Advanced Polymer Composites
for structural applications in construction

ACIC 2004

Edited by
L. C. Hollaway, M. K. Chryssanthopoulos and S. S. J. Moy



WOODHEAD PUBLISHING LIMITED

ADVANCED POLYMER COMPOSITES FOR STRUCTURAL APPLICATIONS IN CONSTRUCTION

ACIC 2004

Proceedings of the Second International Conference, held at the University of Surrey, Guildford, UK on 20–22 April 2004

Edited by L. C. Hollaway, M. K. Chryssanthopoulos and S. S. J. Moy

WOODHEAD PUBLISHING LIMITED
Cambridge, England

Published by Woodhead Publishing Limited, Abington Hall, Abington
Cambridge CB1 6AH, England
www.woodhead-publishing.com

First published 2004, Woodhead Publishing Limited
© 2004, Woodhead Publishing Limited
The authors have asserted their moral rights.

This book contains information obtained from authentic and highly regarded sources. Reprinted material is quoted with permission, and sources are indicated. Reasonable efforts have been made to publish reliable data and information, but the authors and the publisher cannot assume responsibility for the validity of all materials. The publisher makes no representation, express or implied, with regard to the accuracy of the information contained in this book and cannot accept any legal responsibility or liability for any errors or omissions.

Neither the authors nor the publisher, nor anyone else associated with this publication, shall be liable for any loss, damage or liability directly or indirectly caused or alleged to be caused by this book.

Neither this book nor any part may be reproduced or transmitted in any form or by any means, electronic or mechanical, including photocopying, microfilming and recording, or by any information storage or retrieval system, without permission in writing from the publisher.

The consent of Woodhead Publishing Limited does not extend to copying for general distribution, for promotion, for creating new works, or for resale. Specific permission must be obtained in writing from Woodhead Publishing Limited for such copying.

Trademark notice: Product or corporate names may be trademarks or registered trademarks, and are used only for identification and explanation, without intent to infringe.

British Library Cataloguing in Publication Data
A catalogue record for this book is available from the British Library.

ISBN 1 85573 736 1

Printed by Antony Rowe Limited, Chippenham, Wilts, England

CONTENTS

Preface xi

Part I: Keynote Papers

Polymer Composites in Fire
J. M. Davies, Y. C. Wang and P. M. H. Wong UMIST, Manchester, UK 3

Characterization and Health Monitoring of FRP Bridge Systems
V. M. Karbhari, H. Gua and L. Lee, University of California, San Diego, USA, and C. Sikorsky, Department of Transport, Sacramento, USA 18

Durability of Advanced Polymer Composites in the Civil Infrastructure
V. M. Karbhari, University of California, San Diego, USA 30

A Prospective View of Adaptive Materials in Bridge Engineering
U. Meier, EMPA, Dübendorf, Switzerland 43

Composites: Construction Materials for the New Era
A. Mosallam, University of California at Irvine, USA 45

Static and Fatigue Strength of Steel Girders Strengthened with CFRP Laminates
M. Tavakkolizadeh, Jackson State University, USA and H. Saadatmanesh, The University of Arizona, USA 59

Understanding and Modelling the Compressive Behaviour of FRP-confined Concrete
J. G. Teng and L. Lam, The Hong Kong Polytechnic University, Hong Kong, China 73

Upgrading Concrete Structures using Advanced Polymer Composites
T. C. Triantafillou, University of Patras, Greece 89

A Fair Dinkum Approach to Fibre Composites in Civil Engineering
G. Van Erp and S. Ayers, University of Southern Queensland, Australia 101

Part II: FRP Strengthening of Concrete and Masonry Structures

An Experimental Study on Strain Distributions in FRP in Shear-strengthened RC Beams at Debonding
S. Y. Cao, Southeast University, China, J. F. Chen, Edinburgh University, Z. Hao and J Chen, Southeast University, China 117

Bond Tests on Concrete T-shaped Sections Strengthened with CFRP
F. Ceroni, University of Sannio, Italy, S. Matthys, Ghent University, Belgium, M. Pecce, University of Sannio, Italy and L. Taerwe, Ghent University, Belgium 126

Shear Strengthening of Reinforced Concrete Structures Using FRP Composites
S. R. Denton, J. D. Shave and A. D. Porter, Parsons Brinckerhoff, Bristol, UK 134

A Theoretical Strategy for Moment Redistribution in Continuous FRP-strengthened Concrete Structures
T. Ibell, University of Bath, UK and P. Silva, University of Missouri-Rolla, USA 144

Bond-Slip Models for FRP Sheet/Plate-to-Concrete Interfaces
X. Z. Lu, Tsinghua University, Beijing, China, J. G. Teng, The Hong Kong Polytechnic University, Hong Kong, China, L. P. Ye and J. J. Jiang, Tsinghua University, Beijing, China 152

Moment Redistribution in Adhesively Plated RC Beams and Slabs
D. J. Oehlers, I. Liu and R. Seracino, University of Adelaide, Australia 162

Arching Action in FRP Reinforced Concrete Slabs
S. E. Taylor and B. Mullin, The Queen's University, Belfast, Northern Ireland 170

A View Point of Crack Propagation and Failure Modes of FRP Strengthened Flexural RC Elements
E. Andreou, D. B. Tann, R. Delpak, University of Glamorgan, UK 179

Retrofitting of Damaged Concrete Beams with High Performance Polymers
R. Y. Xiao and W. B. Almajed, University of Wales, Swansea. UK 187

RC Column Lateral Prestressing with Composites
M. A. Ciupala, K. Pilakoutas, A. A. Mortazavi and N. Taranu, University of Sheffield, UK 195

Experimental Behaviour of FRP-confined Slender RC Columns under Eccentric Loading
Z. Tao, Fuzhou University, China, J. G. Teng, Hong Kong Polytechnic University, China, L-H. Han, Fuzhou, University, China and L. Lam, Hong Kong Polytechnic University, China 203

Bond Analysis of Masonry Structures Strengthened with CFRP Sheets
M. A Aiello and S. M. Sciolti, University of Lecce, Italy 213

Strengthening with FRP Bars of URM Walls Subject to Out-of-Plane Loads
N. Galati, University of Missouri-Rolla, USA, G. J. Tumialan, Simpson Gumpertz and Heger, USA, S. Secondin, University of Padua, Italy and A. Nanni, University of Missouri-Rolla, USA 222

Part III: FRP Strengthening of Metallic and Timber Structures

Elastic Analysis of Adhesion Stresses Between a Beam and a Bonded Strengthening Plate
J. Cadei, Independent Consultant, Guildford, UK and T. Stratford, University of Edinburgh, UK 235

Experimental Characterization of Steel Elements Reinforced by Adhesively Bonded CFRP Plates
P. Colombi, N. Panzeri and C. Poggi, Polytechnic of Milan, Italy 245

The Strengthening of Wrought Iron Using Carbon Fibre Reinforced Polymer Composites
S. S. J. Moy, J. Clark and H. Clarke, University of Southampton, UK 258

Analysis of the Stresses in the Adhesive Interface of Metallic Beams Reinforced with Composite Plates
S. S. J. Moy, P. J. Deng and M. M. K. Lee, University of Southampton, UK 266

Strengthening of an Artificially Degraded Steel Beam Utilising a Carbon/Glass Composite System
N. Photiou, L. C. Hollaway and M. K. Chryssanthopoulos, School of Engineering, Civil Engineering, University of Surrey, UK 274

Fracture Mechanics 2D-FEA of a Cracked Steel Plate with a CFRP Patch
T. D. Righiniotis, E. Aggelopoulos, M. K. Chryssanthopoulos, School of Engineering, Civil Engineering, University of Surrey, UK 284

Flexural Behaviour of Glulam Beams Reinforced with CFRP Rods
F Micelli, V Scialpi and A La Tegola, University of Lecce, Italy 292

Use of CFRP Connectors in Glulam Flexural Joints
V Scialpi, F Micelli and A La Tegola, University of Lecce, Italy 300

Analytical and Experimental Study on Bonded-in FRP Bars in Glulam Timber
L. De Lorenzis, V. Scialpi and A. La Tegola, University of Lecce, Italy 308

Part IV: Development of FRP Materials and Systems

A New Glass Fibre Reinforcement for Anti-corrosion Composites
P. C. Almenara and P. Thornburrow, Saint-Gobain Vetrotex, France 319

Advanced Polymer Composite and Concrete Beam and Slab Systems
A. G. Bloodworth and J. R. Szczerbicki, University of Southampton, UK 327

Composite Recycling in the Construction Industry
A. Conroy, S. Halliwell and T. Reynolds, BRE, Watford, UK 335

The Use of Advanced Composite Materials in Long Span Civil Engineering Infrastructure
H. N. Garden, Taylor Woodrow Technology, Bedfordshire, UK 343

Polymer-layered Silicate Nanocomposites in Civil Engineering
I. Hackman and L. C. Hollaway, University of Surrey, UK 353

Modelling a Composite/Concrete T-beam Utilising a Finite Element Technique
J. Hulatt, L. C. Hollaway and A. M. Thorne, University of Surrey, UK 361

Static and Fatigue Behavior of GFRP Bridge Decks Adhesively Bonded to Steel Girders
T. Keller and H. Gürtler, Swiss Federal Institute of Technology Lausanne, Switzerland 369

Combined Pressure/Tension Behaviour of Adhesive-bonded GFRP Pipe Joints
J. M. Lees, University of Cambridge, UK 377

Aspects on the Behaviour of Bolted Joints for Pultruded Fibre Reinforced Polymer Profiles
J. T. Mottram, C. Lutz and G. C. Dunscombe, University of Warwick, UK 384

Recycling Technologies for Thermoset Composite Materials
S. J. Pickering, The University of Nottingham, UK 392

Innovative Developments for Bridges Using FRP Composites
G. Sedlacek and H. Trumpf, RWTH, Aachen, Germany 400

GFRP Composite Rock Bolt with Head of Large Bearing Capacity
K. Sekijima, Kurasoku Kensetsu Consultant Co Ltd., K. Ikeda, Shimizu Corp. and T. Nishimoto, Asahi Glass Matex Co. Ltd., Japan 412

Static and Dynamic Behaviour of CFRP Prestressed Concrete Lighting Columns
G. P. Terrasi, SACAC Ltd, Switzerland and J. M. Lees, Cambridge University, UK 420

Deployable FRP Tapered Box-beam Bridge
R. G. Wight, C. R. Shyu, R. Tanovic, M. A. Erki and P. J. Heffernan, Royal Military College of Canada, Canada 428

Part V: Analysis, Design and Testing

The Influence of Shear-flexibility on the Elastic Critical Load for Frames of Pultruded Fibre Reinforced Plastic Section
A. Abbaker and J. T. Mottram, University of Warwick, UK 437

Fire Testing of Concrete Beams with Fibre Reinforced Plastic Rebar
A. Abbasi and P. J. Hogg, Queen Mary, University of London, UK 445

Experimental and Numerical Approach to Buckling of Laminated Composite Sandwich Panel
M. A. Aiello, University of Lecce, Italy, P. Corvaglia, Consorzio CETMA, Italy and L. C. Hollaway, University of Surrey, UK 457

Fire Behaviour of Reinforced Concrete Columns Confined with Fibre-reinforced Polymers
L. A. Bisby and M. F. Green, Queen's University, Canada and V. K. R. Kodur, Institute for Research in Construction, National Research Council of Canada 465

Stresses in Simple Shear Test Specimens for Steel or FRP-to-Concrete Bond Strength: A 3D Finite Element Study
J. F. Chen, Edinburgh University, UK, and W. K. Pan, Nottingham University, UK 473

Performance of a Fibre-reinforced Polymer Bridge Deck Under Dynamic Wheel Loading
A. F. Daly and J. R. Cuninghame, TRL Ltd, UK 483

Global Buckling of FRP Pultruded Thin-walled Members Under Axial Compression
L. De Lorenzis and A. La Tegola, University of Lecce, Italy 493

Thermal Effects on Bond Between FRP Rebars and Concrete
N. Galati, B. Vollintine, A. Nanni, and L. R. Dharani, University of Missouri-Rolla, USA, and M. A. Aiello, University of Lecce, Italy 501

F E Modelling of Mechanical Interaction of Lugged FRP Rods with Concrete, Comparison Between Experiment and Simulation
A. R. Khoei and H. R. Irannejad, Sharif University of Technology, Iran 509

Minimising Damage and Delaying Failure of Composite Laminates
L. N. McCartney, NPL Materials Centre, Teddington, UK 517

Dynamic Response of Initially Stressed Composite Sandwich Plates
A.K. Nayak, R. A. Shenoi and S. S. J. Moy, University of Southampton, UK 525

Numerical Simulation as a Tool for Manufacturing, Failure and Impact Prediction of Textile Reinforced Composites
A. K. Pickett, Cranfield University, UK 535

Euler Buckling of Partially Stiffened Pultruded GRP Columns: A Comparison of Shell Finite Element and Beam-Column Model Predictions
G. J. Turvey and A. Afifi, Lancaster University, UK 545

Shear Failure Strength of Web-Flange Junctions in Pultruded GRP Profiles
G J Turvey andY Zhang, Lancaster University, UK 553

Use of FBG Sensors for Matrix Crack Detection in GFRP Composites
M. Ussorio, H. Wang, S. L. Ogin, A. M. Thorne and G. T. Reed, University of Surrey, UK and S. C. Tjin, Nanyang Technological University, Singapore 561

Use of an FFT Band Pass Filter for Crack Detection by an Embedded Polarimetric Sensor
H. Wang, S. L. Ogin, A. M. Thorne and G. T. Reed, University of Surrey, Guildford, UK 567

The Importance of Dynamic Behaviour in the Design of Laminated Composite Beams
S. H. R. Eslimy-Isfahany, Isfahan University of Technology, Isfahan, Iran, J. R. Banerjee. City University, London, UK 575

Part VI: Durability and Long-term Performance

Effect of Fatigue Cycling on the Strength of RC Beams Externally Strengthened with CFRPs
C. Gheorghiu, P. Labossière and J. Proulx, University of Sherbrooke, Canada 585

The Role of Durability in Reliability-based Design of Composite Materials for Civil Structures
N. L. Post, J. V. Bausano, J. J. Lesko, S. W. Case and J. C. Duke, Virginia Tech, USA 593

Numerical Simulation of Long-term Behaviour of Concrete Structures with Externally Bonded Continuous Fibre Sheet
T. Shimomura, H. Kasahara and K. Maruyama, Nagaoka University, Japan 602

Influences of Freeze and Thaw Cycles and Elevated Temperature on the Properties of FRP Composites
D. B. Tann and R. Delpak, University of Glamorgan, UK 611

Environmental Effects on Tensile Properties of FRP Laminates Made Using Wet-lay-up Method
M. Tavakkolizadeh, Jackson State University, USA and H. Saadatmanesh, The University of Arizona, USA 619

Behaviour of FRP-confined Concrete Stub Columns under Long-term Sustained Loads
Q. Yu, L-H. Han and Z. Zhang, Fuzhou University, China 633

Fatigue Behavior of Double-lap Joints from Pultruded GFRP Laminates
A. Zhou, T. Tirelli and T. Keller, Swiss Federal Institute of Technology, Lausanne, Switzerland 641

Part VII: Certification, Inspection and Quality Assurance

Strengthening Concrete Structures with Fibre Composite Materials: Updating Technical Report 55
J. Clarke, The Concrete Society and A. Darby and T. Ibell, University of Bath, UK 651

Near Surface Mounted Reinforcement for Strengthening – UK Experience and Development of Best Practice
N. Farmer, Tony Gee and Partners, Cobham, UK 659

A Performance-based Qualification Scheme for Composite Materials Systems to be Used in the Civil Infrastructure
A. R. Hutchinson and J. G. Broughton, Oxford Brooks University, S. Frost and R. J. Lee, AEA Technology, N. Farmer and I. Smith, Tony Gee & Partners, S. Luke and L. Canning, Mouchel Parkman, UK 667

A Review of the Use of Fibre Reinforced Composites by the UK Highways Agency
N. Loudon, Highways Agency, UK 675

Field Testing and Long-term Monitoring of West Mill Bridge
L. Canning and S. Luke, Mouchel Consulting, West Byfleet, B Täljsten, Skanska Teknik AB, Sweden and P. Brown, Oxfordshire County Council, Oxfordshire, UK 683

CIRIA C595 – Strengthening Metallic Structures using Externally-bonded FRP
T. Stratford, University of Edinburgh, UK., J. Cadei, Independent Consultant, Guildford, UK. L. C. Hollaway, University of Surrey, UK 693

Structural Health Monitoring of CFRP-strengthened Beams Using Dynamic Testing
C. M. Tan, Mouchel Parkman, Manchester, J. S. Owen, University of Nottingham, S. R. Pearson, AEA Technology Rail, Derby and S. Luke, Mouchel Parkman, Manchester UK 701

Part VIII: Case Studies

Maunders Road Overbridge – The Behaviour and In-service Performance of Cast Iron Bridge Girders Strengthened with CFRP Reinforcement
I. Smith, Tony Gee and Partners, Cobham, UK 711

In-service Performance of FRP Structures
S. Halliwell, BRE, Watford, UK 719

Fibre Composites in Coastal and River Defences
C. K. Jolly, Cranfield University, UK 727

Rehabilitation Design and Evaluation of the Hawthorne Street Bridge FRP Deck Installation
K. Kessler, J. Lesko and T. Cousins, Virginia Tech, USA 738

Strengthening Highway and Railway Bridge Structures with FRP Composites – Case Studies
S. Luke and L. Canning, Mouchel Parkman, West Byfleet, UK 747

The Development of Composite Materials for Strengthening Structures
M. Richardson, Sika Ltd, Welwyn Garden City, UK 755

FRP Strengthening of Building and Civil Structures in Sweden – A Review and Future Aims
B. Täljsten, Luleå University of Technology and Skanska Teknik AB, Sweden and A. Carolin, Skanska Teknik AB, Sweden 763

Index of Authors 771

PREFACE

Over the past three decades Advanced Fibre/Polymer (FRP) Composites have emerged as a viable alternative, to the more conventional civil engineering materials of construction, for new structures and for strengthening/rehabilitation of existing structures and bridge. For new structures, the material is used in conjunction with concrete materials, as reinforcement, as cables for prestressing concrete members and as one of the component parts used in innovative structural systems, such as hybrid FRP/concrete structural members and FRP bridge decks. For existing structures, the advantages of repair and rehabilitation using FRP are increasingly being appreciated in many different countries, and for a large variety of structural forms and types of deterioration or damage. Amongst civil/structural engineers there has been a growing awareness of the importance of the specific weight and the stiffness, the corrosion and non-magnetic characteristics of the FRP material. The shortcomings of the material, such as the creep rupture phenomena, some of the durability aspects and the long-term interaction of loading and damage have encouraged research in these areas in many research institutes. It is necessary for engineers and designers to dispel, through research, practice and design guides, any mysteries associated with FRP composites, which might exist. This task is greatly enhanced by international meetings and fora for dissemination and discussion of mutual and original ideas to promote advances in the application of fibre reinforced polymers in construction.

The conference is the second to be held under the auspices of a network concerned with Advanced Polymer Composites for Structural Applications (CoSACNet), which was funded between January 2001 and January 2004 by the UK Engineering and Physical Sciences Research Council. CoSACNet has now been incorporated into the Network Group for Composites in Construction (NGCC), co-ordinated by the Building Research Establishment.

This book contains the proceedings of the International Conference on Advanced Polymer Composites in Construction (ACIC 2004) held at the University of Surrey between April 20th and 22nd 2004. It is divided into 8 sections. The papers presented in these sections cover a wide spectrum of topics and are contributed by researchers and practicing engineers from many countries. They report the current state of the art and point to the future directions in research and to the utilisation of the material in industry.

The ACIC Conference series is being organised by the Universities of Surrey and Southampton and the BRE, with support from UK industrial and regulatory bodies involved with the application of composites technology in construction:

- CIRIA
- The Concrete Society
- Highways Agency
- London Underground
- National Physical Laboratory
- Network Rail
- Scott Bader

We would like to thank these organisations for their enthusiasm and support, and look forward to the next ACIC conference in 2006. We would also like to thank the reviewers of the papers, and, above all, thanks are due to all the contributors for the careful preparation of their manuscripts and to all the keynote speakers for their support. Our thanks go to Professor R A Shenoi and Professor P A Smith who have spearheaded the development of CoSACNet and who have offered their generous advice and support to the organisers of this conference. Thanks are due to Mrs Penny Briggs who was involved in the day to day running of the organisation of the conference.

L. C. Hollaway
M. K. Chryssanthopoulos
S. S. J. Moy

April 2004

PART I

KEYNOTE PAPERS

This page intentionally left blank

POLYMER COMPOSITES IN FIRE

Professor J Michael Davies
Yong C Wang and Petter M H Wong

Manchester Centre for Civil and Construction Engineering
UMIST, P O Box 88, Manchester M60 1QD, UK

INTRODUCTION

In many applications of polymer composites in construction, there is a requirement for adequate performance in the case of fire. In purely qualitative terms, composite materials respond to fire in a similar manner to wood. When the material is relatively thin, it burns away quite quickly. An example of this was given in the author's paper to the previous ACIC Conference (Davies and Currie, 2002), where empty filament-wound GRE pipes were shown to experience a total loss of strength after about 90 seconds when exposed to a hydrocarbon fire. Conversely, when composite material is relatively thick, it quickly forms a protective char and can then survive for relatively long periods before it loses a significant proportion of its strength. Its survival in such conditions is further helped by the fact that the pyrolysis is endothermic. Unfortunately, unlike wood, economic considerations usually preclude thick, heavy polymer composite members in typical structural applications.

It follows that, in general, polymer composite members are likely to require some form of fire protection. Pipes in offshore construction again provide the initial guidance as to what might be required. Thin-film intumescents are sometimes favoured in steel construction because of their appearance and durability. However, when used with composites, they do not react sufficiently quickly and unacceptable damage takes place before the protective char can form. Thick film intumescents have been used in practice to protect the pipes in fire-water deluge systems on offshore rigs but this solution is unlikely to find favour in more conventional structural engineering applications. Special protective materials can be included in the lay-up (Davies et al, 1994) but these are unlikely to provide sufficient protection for major structural elements. We are therefore left with the passive fire protection solutions that are generally used with, for example, beams and columns in building construction, namely protective boards, sprayed-on materials or similar systems.

Whatever fire protection system is adopted, it is implicit that the protection is only partial. It is not feasible to prevent any temperature rise during the required survival time of the component and design may be based on the attainment of a limiting temperature distribution in the member concerned. There has, of course, been a vast amount of research into the performance of fire-protected steel construction in this context but the considerations with polymer composites are rather different. In the first place, polymer composites are comparatively poor conductors of heat so that the usual assumption of constant temperature throughout the member concerned is unlikely to be valid. Secondly, the deterioration in the material properties of polymer composites commences at much lower temperatures than other construction materials. These two considerations mean that accurate thermal modelling is an essential pre-requisite to any consideration of structural performance in fire. In order to estimate the strength and stiffness of a fire-protected structural member, we first need to know the temperature distribution throughout the member concerned, taking into account the contribution of the fire-protection material. We also need detailed information regarding the

deterioration of the strength and stiffness of the composite material throughout the whole temperature range to which elements of the member are subjected. There is not a great deal of information in the technical literature regarding these considerations.

A PRACTICAL SCENARIO

As much academic research into the structural behaviour of polymer composites has suffered from the lack of an identified end use, it is helpful to have in mind a practical scenario when carrying out the sort of research described in this paper. Although there are many other possible applications, it seemed to the authors that it might be feasible to replace light gauge steel wall studs in steel framed house construction by pultruded composite sections. Two potential problems that strongly influence the design of steel stud walls are unseen corrosion within the wall cavity and the thermal bridges provided by the steel members. Pultruded sections would immediately overcome these disadvantages by the very nature of the material. Although they would be more expensive, the wall studs do not represent a major part of the total cost of the building so that his solution may turn out to be economically feasible. Clearly, a fundamental factor would be the performance in fire and, in this application, there is natural fire protection in the form of fire-resistant lining boards (gypsum boards or similar). It follows that, in all aspects of design (structural and building physics), it is essential to consider the walls as a system in which the various elements complement each other. Here, we will bear this in mind as we consider the fire performance of polymer composite construction systems.

In a related application, there has been significant interest in the use of polymer composites in the construction of wall panels for offshore rigs where the characteristics of light weight and corrosion resistance show to particular advantage and are more than sufficient to meet the additional costs. Offshore, the fire performance is a major design consideration which has to be considered in the context of a hydrocarbon fire.

As discussed above, the prediction of the fire performance has to be considered in two stages. First we will consider the thermal modelling of the assembly of composite members, fire protection materials, and other elements of the construction. Then we will consider the material properties of the polymer composite members (pultrusions) at elevated temperature with a view to combined thermo-mechanical modelling.

It is implicit in what follows that the standard design situation takes the form of a fire resistance test in which the assembly, or one face of it is exposed in a furnace to a standard time-temperature curve. For on-shore applications the relevant curve is well-known and is defined in the ISO standard 834. For offshore applications, and other situations involving liquid or gaseous hydrocarbons, a more severe time-temperature curve is used.

THERMAL MODELLING OF POLYMER COMPOSITE CONSTRUCTION

The behaviour of Glass Reinforced Plastic (GRP) and fire protection materials in fire

In the initial stages of the exposure of a GRP laminate to fire, the incident heat flux will be transferred through the laminate by conduction and there will be no chemical reaction. The resulting temperature distribution will depend on the thermal properties of the materials and the boundary conditions. As the temperature rises to 200-300°C, pyrolysis occurs and gaseous products are created. The resin degrades to form a char

and this char layer will build up as the pyrolysis front moves further into the laminate. Due to its low thermal conductivity, the char layer forms a thermal barrier, helping to keep the interior of the laminate cool. Once the pyrolysis reaction is completed, the temperature of the charred laminate continues to increase and transient heat conduction is governed by the thermal properties of the remaining fibres.

When the surface temperature exceeds about 1000°C, carbon-silica reactions occur in which the carbon residue from the pyrolysis reactions and the silica filler react chemically. Finally, the residual char oxidises and erodes away and the remaining glass fibres will eventually burn out.

Almost every mathematical model of combusting GRP laminate has been developed bearing in mind the above material decomposition behaviour. Most of the models consider the decomposition process up to the completion of the pyrolysis reaction. The later stages, involving carbon-silica reactions, are of reduced interest as most of the material strength will have been lost.

Mathematical models describing the fire behaviour of combustible materials have been developed over many years, starting with the combustion of wood (Kung, 1972; Kansa et al, 1977). These have been developed from the unsteady state heat equation by including terms which describe the ablative processes which take place. The main considerations in the modelling are as follows:

Decomposition

Plastic materials are organic in nature and are inherently combustible. In the current state-of-the-art, it is not possible to model the manner in which they decompose and burn from the basic chemical reactions. In the numerical models, therefore, decomposition is generally modelled using a (first order) Arrhenius equation (1) to relate the mass loss to the heat of reaction:

$$\frac{d\rho_r}{dt} = -A\rho_r \exp\left(\frac{-E_A}{RT}\right) \quad (1)$$

where ρ_r is the instantaneous density of the partially pyrolysed resin (kg/m^3)
E_A is the activation energy (J/mol)
R is the gas constant (8.314 K/K.mol)
T is the temperature (K)
A is the pre-exponential factor (s^{-1})
And t is time in seconds

Resin pyrolysis is assumed to be one way until it is totally consumed.

Formation of char

Similarly, current models can only deal with the macroscopic behaviour of char formation without explaining the fundamental process. In the simple approach of Henderson et al (1985), a plastic composite is separated into rigid material and char depending on the ratio of m/m_0 where m_0 is the initial mass and m is the remaining mass obtained from the first order Arrhenius equation. Some investigators have attempted to include degrees of charring into the pyrolysis process but this is fraught with difficulty and is not thought to be warranted in the current state of the art.

Delamination

During fire resistance tests on composite laminates, loud 'bangs' may be heard as sudden delamination occurs. This is particularly the case when phenolic resin laminates are tested and it is usually attributed to the internal pressure due to vaporisation of the

chemically bonded water within the resin when the temperature rises to over 100°C. At about 200°C, this pressure overcomes the tensile strength of the matrix and tears the laminate accompanied by a sudden release of energy. This, in turn, creates a discontinuity in the thermal properties of the matrix with a significant local decrease in thermal conductivity.

Davies and Wang (1998a) obtained acceptable results by using a simple model to describe this phenomenon. A single value was assumed for the temperature at which delamination takes place and, after delamination, the appropriate boundary conditions for a small air gap betenn two infinitely large flat surfaces are inserted into the global model at the plane of delamination.

Moisture content

The rate of heat transfer in a hygroscopic material is significantly influenced by the evaporation of any physically or chemically entrapped moisture (Davies et al, 1993). During the heating of a hygroscopic material, a complex process of dissociation (dehydration), vaporisation and migration of moisture takes place. Energy is required to break the chemical bond of the water and then to evaporate and move the moisture. A simple and successful approach is to convert these energies into additional specific heat of the material as described by Davies et al (1993).

The mathematical model

The testing and modelling of the behaviour of composite laminates subject to fire has been the subject of collaborative research over a period of more than 10 years at the Universities of Manchester and Newcastle under the auspices of the 'Composites Offshore' rolling programme. The basic principles have been described, for example, by Davies and Wang (1996) and Dodds et al (2000). There are subtle differences between the approaches developed at Manchester and Newcastle, and this paper will describe the model developed by Wang (1995) within the authors' research group at Manchester. As both were calibrated by the same extensive test programme, which was carried out in the fire engineering laboratory at the University of Manchester, they give rise to similar results.

The relationship of these models to others that have been described in the technical literature will be discussed later. Wang's model is essentially simple yet it can replicate the main features of the pyrolysis process and the consequent heat transfer behaviour.The main assumptions are:

- The material is assumed to be homogeneous
- There is thermal equilibrium between the decomposition gases and the solid material but there is no accumulation of these volatile gases in the solid material.
- The feedback of the heat released by the flaming combustible volatiles in a small-scale fire resistance test (or indeed in a real post-flashover fire) may be neglected owing to its relatively small contribution when compared to the heat flux created by the furnace.

Based on the principles of the conservation of mass and energy, the one-dimensional energy equation in a member undergoing thermal decomposition, pyrolised convection and energy sink due to pyrolysis is:

$$\frac{\partial}{\partial t}(\rho h) = \frac{\partial}{\partial x}\left(k\frac{\partial T}{\partial x}\right) - \frac{\partial}{\partial x}\left(m_g h_g\right) - Q\frac{\partial \rho}{\partial t} \qquad (2)$$

where, in addition to quantities described above,

h is the enthalpy (J/kg)
k is the thermal conductivity (W/m°C)
x is the spatial variable (m)
h_g is the enthalpy of gas (J/kg)
m_g is the mass flux of gas (kg/m^{2}s)
Q is the heat of decomposition (J/kg)

If the accumulation of gasses is ignored, the conservation of mass may be written:

$$\frac{\partial m_g}{\partial x} = -\frac{\partial \rho}{\partial t} \tag{3}$$

where the mass flux at any spatial loacation and time can be calculated by integration of equation (3).

Equation (2) can be modified by expanding the first three terms and substituting in the specific heat and continuity equations:

$$\rho C_p \frac{\partial T}{\partial t} = k\frac{\partial^2 T}{\partial x^2} - m_g C_{pg}\frac{\partial T}{\partial x} - \frac{\partial \rho}{\partial t}\left(Q + h - h_g\right) \tag{4}$$

where C_p is the specific heat of the material (J/kg°C)
C_{pg} is the specific heat of the gas (J/kg°C)

This is the basic equation of heat transfer which can be solved numerically by either finite difference or finite element methods and both have been used in practice. Solving the equation is not, however, the main difficulty. The difficulty is in assigning (temperature dependent) numerical values to the various properties in the equation.

A similar equation to (4) has been given in polar coordinates (Davies and Wang, 1998b; Davies et al, 2000) for modelling the performance of pipes (empty or containing either stagnant or flowing water).

Boundary conditions

The boundary conditions on the exposed and unexposed surfaces of a member may either be a prescribed temperature or a prescribed radiation and convection condition. The authors have had limited success in finding the appropriate thermal insult from a furnace following a prescribed time-temperature curve (either celulosic or hydrocarbon) so that the measured hot face temperature is generally used as the boundary condition on the exposed side. On the unexposed side, the heat loss to an ambient environment is taken to be:

$$q = q_{con} + q_{rad} = h(T)\left(T_a - T\right) + E\sigma\left(T_a^4 - T^4\right) \tag{5}$$

where T is the surface temperature (K)
T_a is the ambient temperature (K)
$H(T)$ is the surface heat transfer coefficient, which is calculated according to an empirical formula for natural convection adjacent to a vertical panel
E is the emissivity
σ is the Stefan-Boltzman constant (5.67 x 10^8 W/m^{2}K^4)

Thermal and transport properties

Table 1 shows typical values for the thermal and transport properties that have been used within the authors' research group (Wang, 1995). These have been chosen partly on the basis of published values and partly by curve fitting test results.

In general, these properties vary with temperature and the table shows how a linear distribution of such properties across the section is assumed. In the case of thermal conductivity, the relevant equation is

$$k = k_0 + \Delta T \quad (6)$$

where k_0 is the thermal conductivity at ambient temperature. At the beginning of the heating process, Δ_1 is generally negative, indicating a reduction in thermal conductivity due to the formation of low-conductivity char. As te heating continues, the char will be oxidised and erode away, leaving the fibres alone. During this phase, Δ becomes positive and approaches the value for a crumbling glass mat.

Table 1 Thermal and transport properties of some materials

Product	Thermal Conductivity $k = k_o + \Delta T$ (W/m°C)	Specific Heat $C_p = C_0 + C_1 T$ (J/kg°C)	Kinetic Parameters Eq. (1) $A(s^{-1})$, E_A(J/mol)	Heat of Decomposition (J/kg)
GR Polyester panel	$k_o = 0.26$ $\alpha_1 = -0.0001356$ $\alpha_2 = 0.002$	$C_o = 1200$ $C_1 = 0.8$	*Cellulosic Fire*: A = 1200 [400] E_A = 54000 [70000] *Hydrocarbon Fire*: A = 1200 [600] E_A = 54000 [68000]	-2500000
Ameron pipes (epoxy resin)	$k_o = 0.24$ $\alpha_1 = 0$ $\alpha_2 = 0.0012$	$C_o = 1270$ $C_1 = 0.23$	*Cellulosic Fire*: A = 800 E_A = 56000 *Hydrocarbon Fire*: A = 1200 E_A = 52000	-30000
Phenolic laminates	$k_o = 0.28$ $\alpha_1 = 0$ $\alpha_2 = 0.0018$	$C_o = 1300$ $C_1 = 0.3$	*Hydrocarbon Fire*: A = 1200 [600] E_A = 60000 [58000]	-1600000
Vermiculux	$k_o = 0.28$ $\alpha_1 = -0.00008$ $\alpha_2 = 0$	$C_o = 800$ $C_1 = 0.2$	N/A	N/A
Voidfill 7D	$k_o = 0.0396$ $\alpha_1 = -0.00012$ $\alpha_2 = 0$	$C_o = 1470$ $C_1 = 0$	N/A	N/A
Gypsum board	$k_o = 0.24$ $\alpha_1 = 0$	$C_o = 950$ $C_1 = 0$	N/A	N/A

Values in [ ] represent kinetic parameters at the cold face

Other numerical heat transfer models

In addition to the above, a number of other heat transfer models have been developed by other authors. Most of these have their origins in the work carried out at the Universities of Manchester, Newcastle and Salford under the auspices of the EPSRC-

Table 2 Summary of mathematical models simulating the heat transfer behaviour of polymeric materials at elevated temperatures

Model by	Proposed Year	Dimensions		Solution Method		Order of Arrhenius Equation		Thermal Properties (k, C_p)		Transport/ Kinetic Properties (A,E_A)		Sources of Kinetic Properties		Pyrolysis	Moisture effect	Carbon-silica reactions	Assump *				
		1-D	2-D	Finite Difference	Finite Element	1st	Higher order	Constant	Temp dependent	Constant	Temp dependent	TGA/ testing	Literatures/ manufacturer catalogue				1	2	3	4	5
Henderson *et al.*	1985	•		•			•		•	•		•		•	x	•	•	•	•	•	•
Wilcox *et al.* ψ	1994	•		•		?		•		•			•	•	x	x	?	?	•	x	x
Gibson *et al.* **	1994	•		•		•		•		•			•	•	x	x	?	x	•	x	x
Wang	1995		•		•	•			•	•			•	•	•	x	•	•	•	•	•
Looyeh *et al.*	1997	•			•	•		•		•			•	•	x	x	•	•	•	•	•
Looyeh *et al.*	1998	•			•	•			•	•		•		•	•	x	x	•	•	•	•
Dodds *et al.*	1999		•	?		•		?		?		•		•	?	x	x	?	•	x	x
Dodds *et al.*	2000	•		•		•		•		•		•		•	x	x	x	•	•	•	•

Assumptions of the different mathematical models:
1: Zero value for the final density of the resin material
2: No expansion and/or contraction of the laminate material
3: Thermal equilibrium between the decomposition gases and the solid material
4: The accumulation of the generated volatile gases is ignored
5: No feedback of heat by the combustible volatiles to the panel

• - applicable to the model
x - not applicable to the model
? - unknown
ψ - does not consider delamination of phenolic
** - does not consider char formation

funded rolling research programme "Composites Offshore". Table 2 summarises these models and their main assumptions, including the earlier model by Henderson et al (1985) to which reference was made in the early stages of the EPSRC-funded research.

VALIDATION OF THE THERMAL MODELS

The thermal models referred to above have been extensively validated against furnace fire resistance tests carried out initially at the University of Salford and later at the University of Manchester. In many of the tests, thermocouples embedded in the test specimens provided detailed information regarding the internal temperature distributions.

Some typical results for panels are given in Davies and Wang (1996), for pipes in Davies and Wang 1998b and for delaminating phenolic material in Davies and Wang 1998a. Extensive validation of the Newcastle model for relatively thick composite laminates is given in Dodds et al (2000). Of particular interest in the context of fire protection are some early results obtained for plasterboard (Davies et al, 1993). Figure 1 shows a typical result a 25 mm thickness of plasterboard with a moisture content of 19.4%. Evidently, the mathematical model is well capable of predicting the fire insulating properties as evidenced by the agreement between the measured and calculated cold face temperatures. Equally important is the way in which the cold face temperature is held fairly steady at about 100°C for, in this case about one hour, while the moisture in the plasterboard is evaporated away. When all of the moisture has been lost, the deterioration becomes relatively rapid. This is typical of hygroscopic materials and demonstrates that it is essential to include the moisture effect when modelling them.

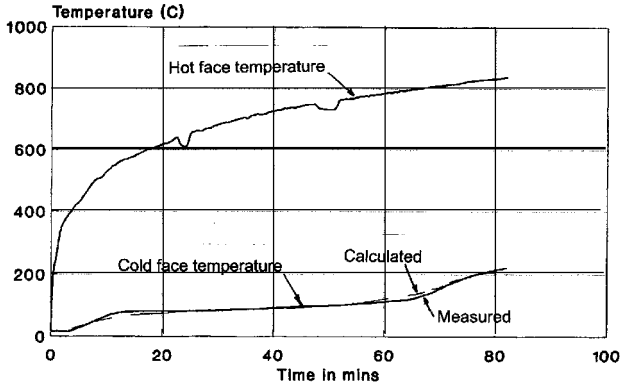


Figure 1: Measured and calculated response of plasterboard in a fire test

THERMO-MECHANICAL MODELLING

In principle, having established a valid thermal model for an assembly including polymer composite components, the extension to a thermo-mechanical model is relatively simple. Assuming an appropriate finite element formulation, the same element mesh can be used for both the thermal and mechanical parts of the analysis and standard structural elements can be used. A simplification, which does not require the

generation of any additional software, is to use the results of the thermal modelling to carry out discrete structural analyses at certain time stages of the thermal analysis.

The main barrier to the immediate implementation of such thermo-mechanical modelling is the lack of information regarding the relevant mechanical properties of polymer composites as the temperature rises. These materials commence to lose both strength and stiffness at much lower temperatures than the vast majority of construction materials and, indeed, they cease to function in structural engineering terms at temperatures at which other structural materials such as steel, concrete and masonry are virtually unaffected.

Mechanical properties of GRP at elevated temperature

Due to the varying distribution of fibre reinforcement, a number of researchers have found that there are significant variations in the material properties around the section of a typical pultrusion. In particular, the fibres tend to migrate away from the corners with the result that these regions are significantly less strong and stiff than the plane areas. Notwithstanding the fact that most standard tests involve the testing of coupons cut from the plane parts of the section, the authors are of the opinion that these are likely to be misleading and that more reliable results will be obtained if tests are carried out on short lengths of complete section. Thus, Currie et al (2001a) carried out carried out compression tests on commercially obtained pultruded channel sections of nominal dimensions 100 x 30 x 4mm x 400mm long.

The tests were carried out in an electrically heated kiln within a reaction frame and were carried out under conditions of steady temperature. Two tests were carried out at each temperature and the average results are summarised in Table 3.

Table 1 Results of compression tests on GRP channels at elevated temperature

Temp. (°C)	Ambient	60	90	120	150	200	250
Stress (N/mm^2)	103	63	60	27	23	9.5	8.7
E (N/mm^2)	22.2	12.9	15.6	10.0	7.5	6.7	6.6

There was significant scatter in the individual test results and the averages do not follow as smooth a curve as might be expected. The results may have been influenced by small variations in the eccentricity etc in the test set up but it is likely that variation in the properties of the material is also a major contributing factor.

There was a change in failure mode as the temperature was increased. Below 120°C, failure was by (explosive) splitting along the web-flange junction, a failure mode that has been observed by other researchers; at intermediate temperatures, failure was more in the nature of local buckling and, above 200°C, end crushing was observed. These changes of mode can be attributed to increasing softening of the resin matrix.

These results give some very general guidance regarding percentage reductions in the properties of pultrusions in general. It is significant that the compression modulus 'E' reduces more slowly than the strength.

In the above series of tests, failure in the lower range of temperatures is evidently influenced by the tendency of the specimens to undergo local and/or distortional buckling with resulting transverse bending stresses. For this reason, Wong et al (2004) have recently carried out an extended series of compression tests on much shorter specimens of 30mm length. Because of the short length, reliable measurement of the compression modulus was not possible. However, good results were obtained for the

strength and these are summarised in Figure 2. The failure stresses are significantly higher than those observed by Currie et al and there is less scatter. The basic trend is similar.

Wong (2004) has also carried out tensile tests on FRP reinforcing bars at elevated temperature and Wong et al (2003) have extended the study of compression members to include columns of practical lengths but these topics are outside the detailed scope of this paper.

This paper is primarily about the performance of members whose load-bearing stress system is essentially unidirectional (axial compression and bending). In the analysis, the properties in the direction of the primary stresses clearly predominate. However, for finite element analysis, it necessary to include the full range of mechanical properties, including those in other planes. Wong (2004) gives detailed consideration to this topic and makes proposals for estimating the necessary properties at elevated temperature. A briefer account of this topic is given in Wong et al (2004).

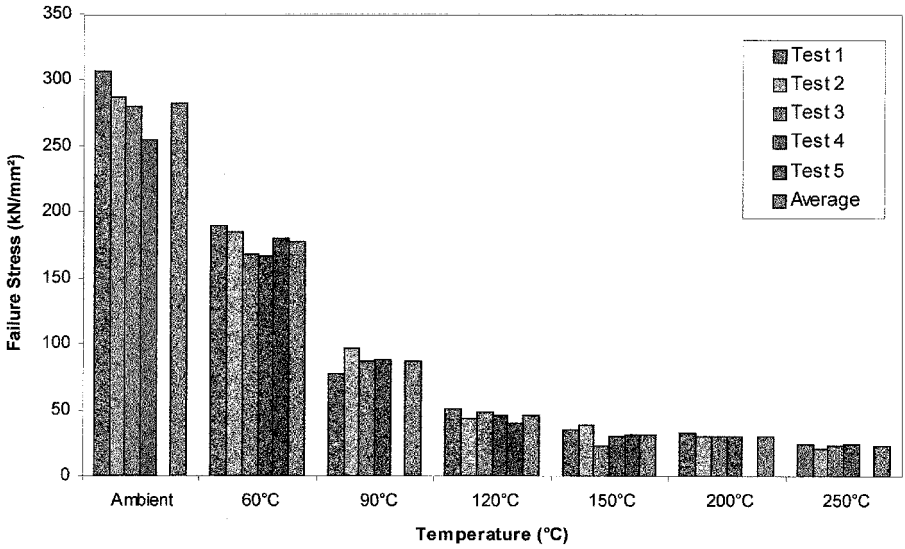


Figure 2 Compression test results on short lengths of putrusion

APPLICATION TO WALL PANEL ASSEMBLIES

Some initial consideration to the design of wall panels incorporating GRP components was given by Davies et al (1995). They considered alternative ways of designing a wall unit for an offshore rig with the following specification: Span 4.0 metres; Wind loading 2.0 kN/m^2; Limiting deflection span/180; Fire rating H120 (120 minutes fire resistance in a hydrocarbon fire). Both "pure" sandwich panels and panels incorporating GRP stringers were considered and it was found that the stringer solutions were to be preferred.

Figure 3 shows a stringer panel that meets the design criteria with a total weight of 31.5 kg/m^2. This is in contrast to a fire protected steel solution which would have a weight of 48 kg/m^2. For the tests, the stringers were formed by wrapping GRP round a former of

Vermiculux and ceramic fibres were incorporated in the lay up of the faces. They could equally have been pultrusions. Designs with panel weights as low as 20 kg/m^2 were considered to be feasible but these were not proved experimentally.

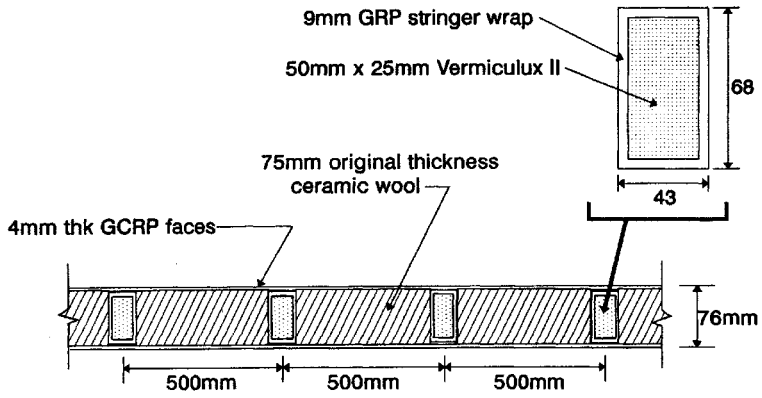


Figure 3 Stringer panel with a weight of 31.5 kg/m^2

Thermal modelling of the tested designs was also undertaken and Figure 4 shows the results for a "pure" sandwich panel consisting of two GRP skins and a 60mm Vermiculux core when subjected to a hydrocarbon fire test.

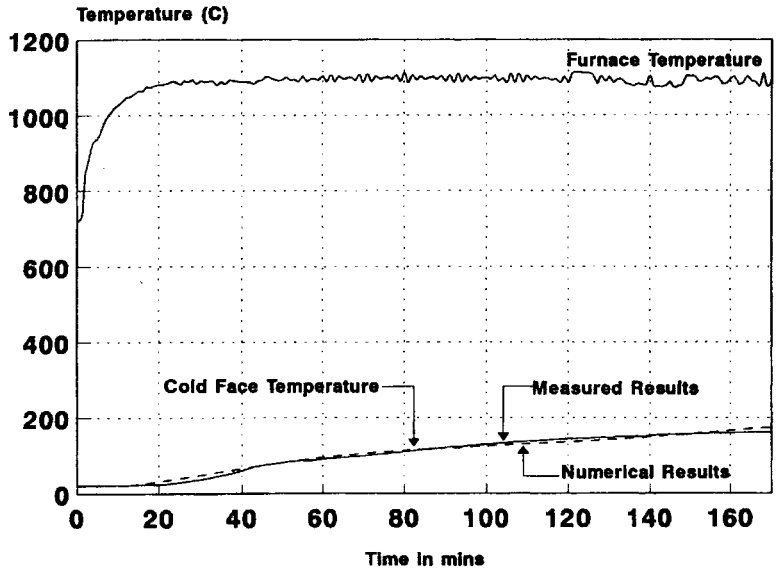


Figure 4 Comparison of hydrocarbon fire test results and theoretical modelling

Further consideration of this topic was given by Currie et al (2001b) and both "pure" sandwich panels with a lightweight phenolic foam core and (pultruded) stringer systems with either plasterboard or phenolic laminate faces were compared. A panel with a steel stringer was included for comparison. Figure 5 illustrates the alternative systems that were considered.

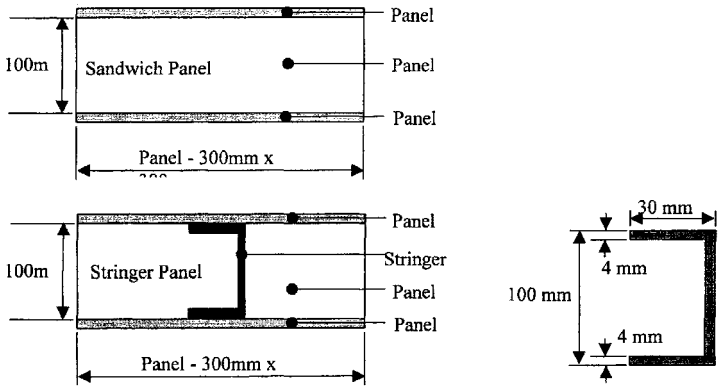


Figure 5 Sandwich panel and stringer construction

The following nine systems were subject to furnace fire resistance tests following the standard cellulosic time-temperature curve

Sandwich panels:	Ph-MW-Ph Pl-Phf-Pl	Pl-MW-Pl	Ph-Phf-Ph
Stringer panels:	Ph-GRP+MW-Ph Ph-GRP+Phf-Ph	Pl-GRP+MW-Pl Pl-GRP+Phf-Pl	Pl-St+MW-Pl

In the above,	Ph	is a 3mm thick phenolic laminate face panel
	Pl	is a 12.5mm thick plasterboard face panel
	Phf	is a phenolic foam core with a density of about 35 kg/m^3
	MW	is a mineral wool core
	GRP+MW	is a Fibreforce GRP stringer surrounded by mineral wool
	ST+MW	is a 1.2mm thick cold-formed steel channel stringer surrounded by mineral wool
	GRP+Phf	is a Fibreforce GRP stringer surrounded by phenolic foam

The phenolic foam core material did not perform very well and when the fire breached the hot face, the core burned through quickly and the tests had to be aborted. However, the density used was very low and sandwich panels are now on the market with much higher phenolic foam core densities (60-80 kg/m^3) and an impressive performance in fire.

Table 4 shows some results for the panels with mineral wool core material. All five panels showed more than 120 minutes of fire resistance according to both the insulation and integrity criteria. The panel with the steel stringer had by far the highest cold face temperature rise but this was still within acceptable limits. There was very little difference between the fire performance of the other systems.

Table 5 shows the measured temperatures in the stringers of the two GRP+MW stringer panels. It can be seen that the higher thickness of the plasterboard face and the dwell time at a temperature of about 100°C resulted in lower stringer temperatures. Over most of the area of the stringers, these temperatures are sufficiently low for a significant proportion of the strength to be retained.

Table 4 Cold face temperatures (°C) after 30, 60 and 120 minutes fire testing

Facing material	Panel type	After 30 mins	After 60 mins	After 120 mins
Ph	Sandwich	28	40	87
Ph	GRP stringer	23	35	106
Pl	Sandwich	35	39	83
Pl	GRP stringer	23	30	72
Pl	Steel stringer	38	91	135

Table 5 Temperature profiles (°C) in GRP stringer panels

Location of thermocouples	After 30 minutes		After 60 minutes	
	Phenolic faces	Plasterboard	Phenolic faces	Plasterboard
Hot face	831	730	899	888
Hot flange	717	315	835	774
Hot end of web	688	284	833	783
Web 25mm	333	81	609	465
Web 50mm	147	69	410	239
Web 75mm	x	58	x	86
Cold end web	36	40	61	51
Cold flange	36	39	61	49
Cold face	23	23	35	30

x denotes no reading due to a faulty thermocouple

Each of the tested constructions has been subject to successful numerical thermal modelling and Table 6 summarises some of the results.

Table 6 Temperatures (°C) found by fire testing (FT) and numerical modelling (NM)

Facing Material	Panel Type	After 30 minutes				After 60 minutes				After 120 minutes			
		Cold face		Hot face		Cold face		Hot face		Cold face		Hot face	
		FT	NM	FT	NM	FT	NM	FT	NM	FT	NM	FT	NM
Phenolic	Sandwich	28	30	807	800	40	79	900	908	87	104	985	1009
Plasterboard	Sandwich	35	21	756	788	39	53	867	901	83	91	973	1005
Phenolic	Stringer	23	24	831	795	35	55	899	907	106	106	985	1008
Plasterboard	Stringer	23	20	730	776	30	36	888	898	72	82	969	1004

CONCLUSIONS

This paper has shown that polymer composites can be used in fire-sensitive situations and that their fire performance can be adequately predicted by numerical modelling. In discussing the various issues involved, an attempt has been made to give a brief summary of the state of the art.

Particular attention has been paid to wall constructions which include polymer composite components and it has been shown that GRP sandwich and stringer panels have useful practical applications.

REFERENCES

Currie P M, Davies J M and Wang Y C (2001a) Behaviour of short columns of pultruded GRP channels at elevated temperatures, Int. Conf. on FRP Composites in Civil Engineering, Hong Kong, 1443-1452.

Currie P M, Davies J M Wang Y C and Wong P M H (2001b) Performance of GRP sandwich panels and stringer systems under fire conditions, Int. Conf. on FRP Composites in Civil Engineering, Hong Kong, 1453-1462.

Davies J M, Hakmi R, and Wang H-B (1993) Numerical temperature analysis of hygroscopic panels exposed to fire, Proc. 8th Int. Conf. On Numerical Methods in Thermal Problems, Swansea.

Davies J M, McNicholas J B and Dewhurst D (1994) Ceramic fibre fire protection of GRP pipes and panels, 6th Int. Conf. on Fibre Reinforced Composites, University of Newcastle upon Tyne.

Davies J M, Dewhurst D and McNicholas J (1995) Performance of sandwich panels in fire; 2. Offshore applications, Sandwich Construction 3, 3rd Int. Conf. on Sandwich Construction, Southampton, 899-909.

Davies J M and Wang H-B (1996) A numerical and experimental heat transfer study of GRP panels subject to standard cellulosic and hydrocarbon fire tests, Proc. 7th Int. Fire Science and Engineering Conference, Interflam'96, Cambridge, March, 123-132.

Davies J M and Wang H-B (1998a) Glass-reinforced phenolic laminates subject to hydrocarbon fire tests, FRC'98, 7th Int. Conf. On Fibre Reinforced Composites, University of Newcastle upon Tyne.

Davies J M and Wang H-B (1998b) Heat transfer analysis of GRP pipes in fire-water systems exposed to fire, OMAE'98, 17th Int. Conf. On Offshore Mechanics and Arctic Engineering, Lisbon.

Davies J M, Dewhurst D and Wang H-B (2000) FRP pipe fire performance: Modelling and testing, Composite Materials for Offshore Operations – 3, University of Houston – CEAC, 269-279.

Davies J M and Currie P (2002) GRP offshore - applications and design for fire, Proceedings Advanced Polymer Composites for Structural Applications in Construction, ACIC 2002, Southampton, April.

Dodds N and Gibson A G (1999) Characterisation and modelling of composites for fire performance in structural applications, Int. Conf. Composites in Fire, University of Newcastle upon Tyne.

Dodds N, Gibson A G, Dewhurst D, and Davies J M (2000) Fire behaviour of composite laminates, Composites A, 31, 689-702.

Gibson A G, Wu Y S, Chandler H W, Wilcox J A D and Betess P (1994) A model for the thermal performance of thick composite laminates in hydrocarbon fires, Int. Conf. on Composite Materials in the Petroleum Industry.

Henderson J B, Wiebelt J A and Tant M R (1985) A model for the thermal response of polymer composite materials with experimental verification, Composite Materials, 19, 579-595.

Kansa E J, Perlee H E and Chaiken R F (1977) Mathematical model of wood pyrolysis including forced convection, Combustion and Flame, 29, 311-324.

Kung (1972) A mathematical model of wood pyrolysis, Combustion and Flame, 18, 185-195.

Looyeh M R E, Betess P and Gibson A G (1997) A one-dimensional finite element simulation for the fire performance of GRP panels for offshore structures, Numerical Methods and Heat Flow, 7 (6), 609-625.

Looyeh M R E and Betess P (1998) A finite element model for the fire performance of GRP panels including variable thermal properties, Finite Elements in Analysis and Design, 30, 313-324.
Wang H-B (1995) Heat transfer analysis of components of construction exposed to fire – a theoretical, numerical and experimental approach, PhD thesis, Civil Engineering and Construction, University of Salford.
Wilcox J A D, Gibson A G and Chandler H W (1994) Modelling the fire behaviour of GRP panels, 6th Int. Conf. on Fibre Reinforced Composites, University of Newcastle upon Tyne.
Wong P M H (2004) Thermal, mechanical and structural performance of fibre reinforced polymer (FRP) structures at ambient and elevated temperatures, PhD thesis, University of Manchester.
Wong P M H, Wang Y C and Davies J M (2003) Behaviour of fibre reinforced plastic (GRP) columns at elevated temperatures, CIB-CTBUH Int. Conf. on Tall Buildings, Malaysia.
Wong P M H, Davies J M and Wang Y C (2004) An experimental and numerical study of the behaviour of glass fibre reinforced plastic (GRP) short columns at elevated temperatures, Composite Structures 63, 33-43.

CHARACTERIZATION AND HEALTH MONITORING OF FRP BRIDGE SYSTEMS

V.M. Karbhari, H. Guan and L. Lee
University of California San Diego, La Jolla, CA, USA

C. Sikorsky
California Department of Transportation, Sacramento, CA, USA

INTRODUCTION

Although fiber reinforced polymer (FRP) composites are increasingly being used in civil infrastructure in applications ranging from use as reinforcement in concrete to use as external strengthening measures for deteriorating concrete and steel in the form of externally bonded reinforcement, and to application in decks and girders, there are still significant concerns related to long-term integrity and durability. While some of these concerns are based primarily on the lack of history of use of these materials and the concern related to field implementation without well established specifications and codes, other concerns are based on the actual lack of information related to the capability of components and systems fabricated of FRP composites to continue showing adequate performance over long service-lives. Although a reasonable case can be made to show the long-term durability of structures fabricated using aerospace grade composites and having well established maintenance and inspection procedures, the same cannot be established for systems being advanced for use in civil infrastructure, due to lack of data. There is hence a need to monitor existing structures in an attempt to not only gain a record of field performance, but to also realistically establish measures for long-term use potential. In addition there is also a need for establishment of cost-effective measures of structural health monitoring for conventional non-FRP systems as a means of being able to autonomously determine the structural and functional viability of life-lines on a continuous basis.

Currently, bridge structures are inspected at routine intervals till significant distress is noted after which the period between inspections is decreased and the level of inspection is increased till such time that the distress has been corrected by replacement or repair. This time-based monitoring is inefficient not just in terms of resources but also since it does not minimize "down-time" of the structure. Since bridges form a critical part of a nation's lifelines they also have immense effects on the economies of the region since they serve as routes for the transfer of goods and services. The decrease in "down-time" due to maintenance, rehabilitation, or even replacement is a critical facet of this and hence a move to a condition-based assessment of structures is essential. The implementation of condition based assessment, however, requires that changes in structural response be monitored often as a result both of normal operation and extreme events. This can be done through the implementation of a true structural health monitoring system which could enable autonomous and continuous recording and assessment of pre-determined response parameters associated with materials, components and/or the entire system.

This paper discusses the in-field characterization and health monitoring of bridges that incorporate FRP elements and demonstrates the viability and usefulness of such measures not only for FRP systems but for all critical elements in the built environment.

APPLICATION TO A FRP BRIDGE SYSTEM

The Kings Stormwater Channel Bridge, a two-lane highway bridge recently completed on Route 86 in California, utilizes the concept of the Carbon Shell Bridge System (CSS). The bridge consists of a two-span beam-and-slab superstructure with multicolumn intermediate piers. The superstructure is composed of 6 longitudinal carbon shell girders with 10 mm wall thickness and 0.34 m inside diameter, which are connected across their tops with a modular FRP deck system consisting of interlocking pultruded profiles bonded together with additional face sheets placed by wet layup. The girders are attached to the abutment end diaphragm and the center cap-beam by continuing the carbon shell into the reinforced concrete elements, and providing a conventional steel reinforcement anchorage. Details related to the bridge components, testing, and installation can be found in Karbhari et al [1] and Zhao and Karbhari [2].

Prior to the opening of the bridge, two separate load tests were conducted. The first was unexpected, due to the movement of a paver over the bridge, whereas the second was a planned test using specific trucks. The paver loading represented approximately one-half the flexural demand by the design truck loading regime. It should be noted that the "paver" test was conducted prior to the construction of the side barriers which are expected to contribute to the overall system stiffness. Once the barriers were constructed a second test was done in order to simulate the actual design loading on the bridge using three trucks that approximated the full flexural demand. Overall results are listed in Table 1 for purposes of comparison.

Table 1: Results of Initial Load Tests

	Paver Test	**Paver Test x 2**	**2-Truck Test**
Moment demand equivalence	50%	100%	100%
Deflection (mm)	8.5	17	9
L/D ratio	L/1180	L/590	L/1120
Max. Strain (με)	~400	~800	~400

As can be seen from Table 1 the response to load is well within expected deflection and strain levels and the bridge can hence be considered to be performing in accordance with the design requirements. Within a few months of the opening of the bridge a flash flood caused significant flow in the stream below the bridge with debris including trunks of trees, some of which were trapped below the bridge with repeated impact taking place between the roots and the girders. In order to assess the response of the bridge after this event as well as to conduct a routine assessment of bridge performance a second load test was performed. Since the purpose of the investigation was the assessment of overall bridge response it was decided to consider a number of different traffic conditions as listed in Table 2. The tests were conducted with two water trucks, designated as Truck A and B, with known axle spacing and axle weight. In addition normal traffic on the highway was also used as an auxiliary method of loading. Truck A is a 3-axle water truck with a total weight of 224.2 kN. The load on the front axle is 71.2 kN and the two rear axles have a load of 76.5 kN each. Truck B is a 5-axle water truck with a total weight of 326.8 kN, of which the front axle has a load of 51.3 kN, the next two axles have a load of 64.2 kN each, and the two rear axles have

a load of 73.6 kN each. Results in Table 2 clearly indicate that the overall performance is above that required by design criteria.

Table 2: Overall Results of Second Load Test

Load Condition	Maximum Mid-Span Deflection (mm)	Deflection-Span Ratio**	Peak Strain (%)	% of Allowable Strain Under Service I Conditions
Rolling loads	7.16	L/1400	300	12
Full-lane load	9.25	L/1088	403	16
Two-lanes loaded	8.20	L/1226	377	15
Brake test*	7.34	L/1370	291	12
Predicted 3-AASHTO design trucks without the dynamic amplification factor	11.09	L/906	625	25
Predicted 3-AASHTO design trucks without the dynamic amplification factor	14.76	L/682	831	33

* From 48 km/h to a stop

** Based on maximum mid-span deflection and a span length of 10.06m

Although these tests clearly demonstrated that the bridge had not undergone any structural damage, there was concern raised about future needs to monitor the bridge both to assess any slow deterioration as a result of the flood and the resulting impact from tree trunks, and as a means of raising the confidence of the engineers in the technology. It was also considered that since the bridge, although on a critical state route, was in an isolated location it would serve as a good demonstration of the implementation of web based structural health monitoring.

NDE and Damage Detection Overview

The implementation of a health monitoring system requires not just the positioning of sensors and transmission of data, but also the development of a system to analyze the incoming data, compare it with the ideal "undamaged" response, and then ascertain whether there are any changes in structural response and assess the level of damage, if any. The term structural health monitoring has gained wide acceptance over the past decade as a means of monitoring structural response to enable an early warning of an unsafe condition using real-time data. It should, however, be emphasized that a system which merely detects indications of damage or degradation without connecting it to structural response measures such as stiffness, deflection, frequency etc. is of little use to the owner of that structure.

Vibration based methods are often used as a means of assessing structural response and can primarily be classified as belonging to either the forced vibration, or ambient vibration methods. The forced vibration method relies on the introduction of excitation through the use of a hammer, shaker or other equipment placed on the

structure. This requires interruption of the normal operation on the structure but provides a high level of stability in obtaining modal parameters. In addition, since conditions are controlled, the results are fairly easy to analyze. However, it is almost impossible to automate this method for use on large structural systems for long-term use. In contrast the ambient vibration method (also known as the output only method) relies on ambient excitation such as that due to traffic or extreme events such as earthquakes. This does not interrupt normal operations and is amenable to continuous automated use. However, the achievement of an appropriate signal-to-noise ratio is essential for obtaining good results, and consequently the method requires a higher degree of development.

Irrespective of method used, there are five general steps that have to be completed i.e. (1) measurement of structural dynamic response, (2) extraction of modal parameters, (3) determination of changes, usually based on changes in mass or stiffness, (4) use of analytical tools for damage localization and estimation of damage severity and (5) use of these measures to assess changes in capacity and service-life.

Time Domain Decomposition and Damage Detection

In the case of the Kings Stormwater Channel bridge the method of ambient vibrations was adopted as a means of measuring the dynamic response of the structure. The time domain decomposition (TDD) method is then used to extract parameters. The basic theory of this method lies on the well established theory in linear algebra that any vector can be spanned by its basis. The output of linear dynamic system can then be expressed in terms of it's mode shapes.

$$\vec{\ddot{y}}(t) = \sum_{i=1}^{N} \ddot{q}_i(t)\vec{\phi}_i \qquad (1)$$

where $\vec{\ddot{y}}(t)$ is the system response, $\ddot{q}_i(t)$ is the generalized coordinate, and $\vec{\phi}_i$ is the ith mode shape.

For a discrete time system, $t = k\Delta t$,

$$\vec{\ddot{y}}(k) = \sum_{i=1}^{N} \ddot{q}_i(k)\vec{\phi}_i \qquad (2)$$

By applying a band-pass filter to the output signal measured from the system, with the passing band set at the desired frequency of ith mode, the result will only contain the system response due to the ith mode. For systems of p measuring points:

$$\begin{bmatrix} \ddot{y}_{1i}(1) & \cdots & \ddot{y}_{1i}(N) \\ \vdots & \ddots & \vdots \\ \ddot{y}_{pi}(1) & \cdots & \ddot{y}_{pi}(N) \end{bmatrix} = \begin{bmatrix} \phi_{1i} \\ \vdots \\ \phi_{pi} \end{bmatrix} \begin{bmatrix} \ddot{q}_{1i}(1) & \cdots & \ddot{q}_{1i}(N) \end{bmatrix}$$

or,

$$\left[\vec{Y}_i\right] = \vec{\phi}_i \vec{\ddot{q}}_i^{\,T} \qquad (3)$$

The output energy correlation of the ith mode can then be represented by the matrix $[E_i]$, where,

$$[E_i] \equiv [Y_i][Y_i]^T = \vec{\phi}_i \vec{\ddot{q}}_i^{\,T} \vec{q}_i \vec{\phi}_i^{\,T} = \vec{\phi}_i Q_i \vec{\phi}_i^{\,T} \qquad (4)$$

This $p \times p$ real semi-positive symmetric matrix can be also decomposed as:

$$[E_i] = U\Sigma U^T$$

$$= [\vec{u}_1 \ldots \vec{u}_p] \begin{bmatrix} \sigma_1 & & 0 \\ & \ddots & \\ 0 & & \sigma_p \end{bmatrix} \begin{bmatrix} \vec{u}_1 \\ \vdots \\ \vec{u}_p \end{bmatrix} \tag{5}$$

$$= \vec{u}_1\sigma_1\vec{u}_1^T + \ldots + \vec{u}_p\sigma_1\vec{u}_p^T$$

where the positive numbers, $\sigma_1 \geq \sigma_2 \geq \ldots \geq \sigma_p$ are the singular values of $[E_i]$. The $p \times p$ real orthonormal matrix, U, is the singular matrix of $[E_i]$, and the columns of U consist of orthogonal vectors, $\vec{u}_1 \cdots \vec{u}_p$. Comparing equations (4) and (5) reveals that the singular vectors also form a basis of matrix $[\vec{Y}_i]$, therefore,

$$\vec{\phi}_i = \vec{u}_1 \quad \sigma_1 \neq 0 \quad \sigma_2 \cdots \sigma_p = 0 \tag{6}$$

where the ith mode shape is given by the first singular vector u_1. The natural frequency of the ith mode can be obtained from the auto-spectrum of the single degree of freedom system:

$$\vec{q}_i^T = \frac{1}{\vec{\phi}_i^T\vec{\phi}_i}\vec{\phi}_i^T[Y_i] \tag{7}$$

The TDD technique as briefly described above provides a methodology for the extraction of mode shapes as the first step, followed by obtaining the corresponding natural frequencies as the second step. Although the TDD method requires frequency information for filter design and for the assessment of the natural frequency, it does not require the use of discrete Fourier Transforms. This enables use of a more computationally efficient technique of modal parameter extraction.

Considerable amount of research has been conducted in the area of damage detection using modal parameters, in which, mode shape changes [3], mode shape curvature [4], modal strain energy [5], flexibility changes[6], and other modal parameters are used to estimate the location and severity of the damage inside the structure. In the present scheme the damage index method [7] is used wherein for a linear, undamaged structure, the ith modal stiffness of a linear undamaged structure can be described as

$$K_i = \vec{\phi}_i^T C \vec{\phi}_i \tag{8}$$

where, $\vec{\phi}_i$ is the ith modal vector and C is the system stiffness matrix. The contribution of jth member to i^{th} modal stiffness is then given by

$$K_{ij} = \vec{\phi}_i^T C_j \vec{\phi}_i \tag{9}$$

The fraction of modal energy of the ith mode contributed by the jth member, also called modal sensitivity, is defined as

$$F_{ij} = K_{ij} / K_i \tag{10}$$

Correspondingly, using * to represent the damaged structure, we can define the fraction of modal energy of a damaged structure as

$$F^*_{ij} = K^*_{ij} / K^*_i \tag{11}$$

in which,

$$K^*_{ij} = \vec{\phi}_i^{*T} C^*_j \vec{\phi}_i^* \quad K^*_i = \vec{\phi}_i^{*T} C^* \vec{\phi}_i^* \tag{12}$$

and,

$$C_j = E_j C_{jo} \qquad C_j^* = E_j^* C_{jo} \tag{13}$$

A fundamental aspect in this method is that the modal sensitivity for the ith mode and j^{th} member remain unchanged for both the undamaged and damaged structure, i.e.

$$F_{ij} / F_{ij}^* = (K_{ij}^* K_i)/(K_i^* K_{ij}) = 1 \tag{14}$$

Therefore by substituting equations (8-11) into (14), a damage index β_j for the jth member, can be obtained as

$$\beta_j = \frac{E_j}{E_j^*} \quad damage\,indicated\,when \quad \beta_j > 1$$

$$\beta_j = \frac{\gamma_{ij}^* K_i}{\gamma_{ij} K_i^*} = \frac{\phi_i^{*T} C_{jo} \phi_i^* K_i}{\phi_i^T C_{jo} \phi_i K_i^*} \tag{15}$$

and the severity of damage can be estimated by:

$$E_j^* = E_j \left(1 + \frac{dE_j}{E_j}\right) = E_j(1+\alpha_j) \tag{16}$$

where

$$\alpha_j = \frac{\gamma_{ij} K_i^*}{\gamma_{ij}^* K_i} - 1$$

in which, $\gamma_{ij} = \vec{\phi}_i^T C_{jo} \vec{\phi}_i \quad \gamma^*_{ij} = \vec{\phi}_i^{*T} C_{jo} \vec{\phi}^*_i$.

Instrumentation and Network

The response of the bridge is characterized through the use of 63 accelerometers, 20 strain gauges, 4 linear potentiometers, 1 temperature sensor, and a pan-tilt-zoom (PTZ) camera. The accelerometers are Model 3140 single axis accelerometers from ICSensors, Inc. The Model 3140 is a high-performance signal conditioned accelerometer with a dynamic range of +/- 2g. The accelerometers were placed in a grid with one axis parallel to each girder. In addition along alternate lines accelerometers were also placed to measure horizontal acceleration. Bonded resistance strain gauges were attached to the bottom of the deck, middle section of the girder, and bottom of the girder at sections with high shear demand. Three girders carrying the most load, i.e., girder 2, 3 and 4, were chosen for the monitoring of slippage monitoring. Also, strain gages were be attached at the mid-span of the two central girders (3 and 4), which are considered to be subject to more vehicular load than other girders and hence will exhibit more shear deformation. Linear potentiometers were also placed at mid-span of the two central girders to measure deflections in each span.

Data is transmitted over an extensive High Performance Wireless Research and Education Network (HPWREN) already in place in southern California. It provides TCP/IP based network access with up to 45 Mbps backbone transfer rate and up to 115 Kbps transfer rate to remote nodes like the Kings Stormwater Channel bridge site. The utilization of the HPWREN wireless network enables fast and reliable communication between the data analysis software running on servers located at UCSD and data acquisition hardware located at bridge site. Also, it enables real-time monitoring of the bridge response by multiple users over the Internet with a industry-standard TCP/IP protocol link.

Web Site and Data Analysis Overview

After the data is collected at the bridge site, controlled by a program running on the data-logger, raw data is sent over the wireless network to a server located at University of California, San Diego in La Jolla. A Matlab based program then autonomously analyzes the raw data, generate results and sends these a web-server. End users can then access these results using a standard web browser, the first page of which is shown in Figure1.

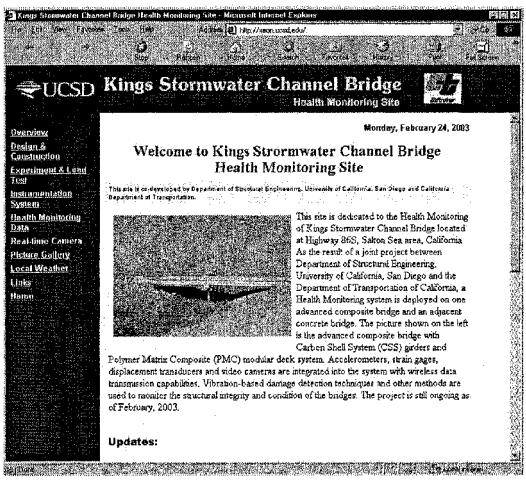


Figure 1: First Page on Web Browser

The web-based user interface enables users with an appropriate internet connection to monitor the bridge's behavior and assess pertinent serviceability, reliability and durability aspects related to the structure. By making use of data stored on the central server users can also access historical data to make comparisons and/or to determine effects of specific events. For the purposes of the current investigation an event is defined as a significant excitation to the bridge, usually caused by single or multiple vehicles crossing the bridge. In terms of measurement, an event is usually a time period over which the bridge is subject to excitation and measurements are taken. Both raw data and processed data are analyzed and stored with reference to the specific event through a date-time stamp. Users can either choose to plot sensor records pertaining to a single event, multiple events, or even records of multiple sensors selected by location. In addition it is possible for the user to view data in real time including the movement of traffic on the bridge through screens such as shown in Figure 2.

Using the data analysis methodology explained in brief earlier, users also have the option of determining the natural frequency and mode shapes of the structure under a specific set of events, and of determining location and severity of damage, if any. Results of this analysis can be compared on the same site with results generated from an ANSYS based finite element model of the bridge, which is routinely updated so as to represent the current state of the bridge. This provides the user with the capability of not only comparing modes, frequencies and severity indexes, but also of reviewing data against pre-determined thresholds that signify levels of acceptable response.

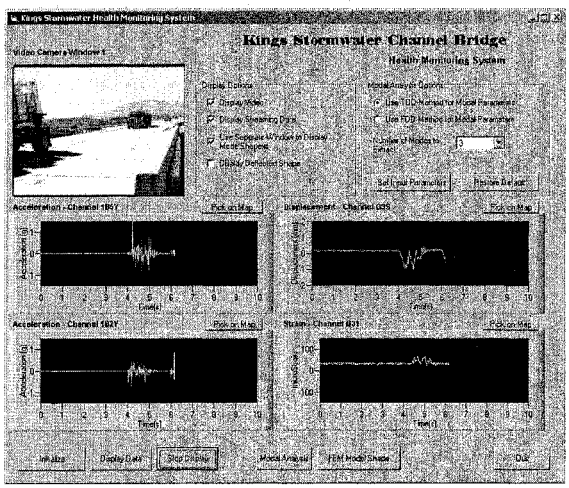


Figure 2: Screen for Real-Time Data Access Including Video Image of Traffic

The system is now fully operational and data is being used both for purposes of structural health monitoring and as a research tool for assessment of bridge response and even to further understand traffic flow.

APPLICATION TO A FRP REHABILITATED STRUCTURE

Rehabilitation of bridge decks with fiber reinforced polymer (FRP) composites is becoming a popular alternative to traditional repair methodologies, such as bonding of steel plates, concrete overlay, or shortening of slabs. However, the Although durability is a major issue, evaluation of the effect of rehabilitation with FRP on an actual bridge structure is rarely addressed. In order to validate the change in a system due to rehabilitation and subsequent environmental degradation of the FRP composites in the field, a global nondestructive evaluation procedure is necessary, which can assess changes in the system over time and ultimately, the change in capacity of the system. Here, it is appropriate to apply techniques in structural health monitoring of bridge structures, where the objectives are to identify, locate, and estimate the severity of damage or improvement in a system. Often, the changes in a system are quantified in terms of changes in stiffness. One such approach utilizes changes in modal strain energy of the system to determine fractional stiffness changes due to damage or maintenance measures on a bridge structure [8]. Estimating the remaining service life of a bridge structure is a primary component of the structural health monitoring scheme and more importantly a means to determine inspection intervals as well as appropriate repair strategies for the system. As a general rule, a methodology for estimating the remaining service life of a system must be able to incorporate unbiased field observations from the structure, such that a correlation between field measurements and life prediction exists. More specifically, for FRP rehabilitated structures, the estimation of remaining service life must also include durability characterization of the FRP composite. The estimation of the remaining service provides a means to determine the criticality of existing structures, but also acts as a design tool to determine adequate levels of rehabilitation in terms of the reliability of the system and desired extension of

service life for an existing deficient structure. In this section the application of the methodology to a rehabilitated bridge structure is elucidated.

The Watson Wash Bridge is located on California Interstate 40, approximately 10.3 km east of Essex Road in the Mojave Desert. The bridge structure, constructed in 1968, consists of two parallel structures each of which is a skewed, two-lane bridge 225.9 m long. The superstructure consists of a cast-in-place reinforced-concrete deck and girder structural system with sixteen 12.8 m central spans and two shorter spans of 10.5 m at each abutment. The 15.6 cm thick deck spans transversely across six girders at 2.13 m centers. The bridge component contains 18 spans and five bays in each span. A visual inspection of the bridge shows the development of transverse and longitudinal cracks on the soffit of the bridge deck and local punching shear potentially caused by increased traffic loads and steel reinforcement deficiencies. The bridge was rehabilitated through external bonding of FRP in the form of both wet layup of fabric and adhesive bonding of prefabricated (pultruded) strips. The rehabilitation was conducted to provide an extended service-life of a few additional years, sufficient to enable design and planning for a replacement structure.

In determining the remaining life of an FRP rehabilitated structure, a condition based monitoring approach is implemented which involves the following, 1) acceptance that damage is present or will occur, 2) an adequate method of inspection is available, 3) adequate strength is retained in the damaged structure. Damage accumulation is measured in terms of a cumulative stiffness loss in the system then correlated to a measure of performance. The reliability, β, defined by system probability of failure is used as the performance measure for the slab. Following procedures from the California Bridge Design Specification and using simple measures of reliability the initial calculated reliabilities and the estimated wheel load capacities for deck slabs in two critical locations are provided in the Table 3

Table 3: Initial Reliability Estimates

Location	**Initial Reliability**	**Wheel Load Capacity**
8-1	2.403	126.73 KN
9-5	3.271	157.35 KN

An estimation of time-dependent reliability, $\beta(t)$, can be developed by introducing time-dependence to variables within the second moment reliability equation:

$$\beta(t) = \frac{\mu[R,t] - \mu[S,t]}{\left(\sigma^2[R,t] + \sigma^2[S,t]\right)^{1/2}} \tag{17}$$

where, μ, denotes the mean value; σ^2 is the variance; R is resistance; S is demand; t is time. The remaining service life of the system is determined by solving for time, t, at the target reliability of the structure; the target reliability for this evaluation is 1% probability of failure or β = 2.33. Only FRP degradation, specifically modulus of CFRP, is considered in this analysis, since the durability of the CFRP rehabilitation is the primary focus. It is assumed that all variables are normally distributed and their respective variations are not time dependent. Degradation of the CFRP modulus, for both pultruded and wet lay-up composites, is empirically modeled from an accelerated aging test of wet lay-up manufactured CFRP exposed to deionized water at 23°C for 18 months using a simple exponential form as

$$E_{frp}(t) = E_{frp0}e^{\psi \cdot t} \quad (18)$$

where ψ is the exponential decay constant determined from a curve fit of wet lay CFRP immersed in deionized water at 23°C for 18 months, -0.078/year; E_{frp0} is the initial measured modulus of the CFRP and t is time in years.

As the modulus of CFRP changes with time, the forces contributing to section equilibrium also change resulting in a time dependent neutral axis depth, $c(t)$. The resulting time-dependent reliability formulation for a rehabilitated bridge deck slab is shown below,

$$\beta(t) = \frac{M_y(t) - M_T}{\left(\sigma^2[M_y(t)] - \sigma^2[M_T]\right)^{\frac{1}{2}}} \quad (19)$$

Applying the time-dependent reliability formulation an estimate of the remaining service life of the structure can be determined for the limit of $\beta = 2.333$. The remaining life estimates for 9-5 is 13.06. The demolition of the Watson Wash Bridge after the extended service period provided a unique opportunity to conduct destructive testing on specific rehabilitated locations of the bridge simulating deterioration of a CFRP rehabilitated bridge deck. Damage scenarios were applied to the two previously identified critical locations of the structure, locations 8-1 and 9-5. The damage sequence in each bay was as follows: (1) Removal of one longitudinal strip; (2) Removal of four transverse strips; (3) Punch out of bridge deck. shows the damage cases applied to location 8-1. The cumulative measured stiffness losses associated with each damage scenario are provided in Table 4.

Table 4: Measured Cumulative Stiffness Loss

Location	Damage Case 1	Damage Case 2	Damage Case 3
8-1	-7.0%	-11.0%	-16.0%
9-5	-8.0%	N/A	-16.0%

In the condition monitoring scheme, a method of inspection is necessary to measure the change in performance of the system. Utilizing stiffness changes measured from the global NDE assessment, the reliability following each damage scenario can be determined using the simple beam relationship for a strip of slab. Each damage scenario applied to the deck rehabilitation can then be considered a single instance in time at which damage severity, in terms of stiffness loss is measured. Therefore, the measured percentage stiffness change is applied directly to the flexural stiffness in equation to acquire an updated resistance measure of the system and a reliability estimate. The reliabilities at locations 8-1 and 9-5 are provided in Table 5 following each damage scenario.

Table 5: Instantaneous Reliabilities

Location	Pre-Rehab t_{pre}	Post-Rehab t_{post}	Damage 1 t_1	Damage 2 t_2	Damage 3 t_3
8-1	1.648	2.403	2.104	1.909	1.670
9-5	1.648	3.271	2.956	N/A	2.593

An approximation of the available capacity of the slab structure can then be made using the following simplifying assumptions

1. Measured stiffness changes are a result of damage in the deck slab only
2. A representative strip of the slab can be used to conduct the analysis

3. A linear relationship exists between measured stiffness changes and the capacity of the slab
4. The yield curvature remains constant with damage
5. Damage is defined as a loss in stiffness

and capacities, as estimated, are listed in Table 6

Table 6: Estimate of Slab Wheel Load Capacity (kN)

Location	Pre-Rehab t_{pre}	Post-Rehab t_{post}	Damage 1 t_1	Damage 2 t_2	Damage 3 t_3
8-1	105.82	126.73	117.50	112.21	105.75
9-5	105.82	157.35	144.34	N/A	131.34

An assessment of the wheel load capacities of the rehabilitated deck slabs shows that location 8-1 decreases to a load level below the pre-rehabilitated load level of the structure. Although, the wheel load capacity is greater than the design truck of 71.2 KN, the associated reliability is an important parameter to assess the safety of the rehabilitated slab. With the total accumulated damage severity, the reliability in location 8-1 is 1.67, well below the limit of 2.33. Location 9-5, shows the CFRP rehabilitation design is capable of accommodating damage severity levels of 16% with a wheel load capacity of 131.34 KN and a corresponding reliability of 2.593. Providing an estimate of the wheel load capacity of the slab and its associated reliability is useful, but does not indicate the duration at which the slab is able to sustain a minimum level of performance. Each of the damage scenarios represents time intervals where damage occurred within the rehabilitated slab structure. By incorporating the field stiffness measurements with the time dependent reliability formulation, an approximation to the remaining service life of the structure is possible. If the damage scenarios are representative of stiffness changes in the structure caused by deterioration of the rehabilitation at intervals of time, then an estimation of the remaining life is possible. For location 9-5, incorporating the three damage severity cases, the structure is likely to have a 1% probability of failure in approximately 10.6 years. The remaining life estimate for location 9-5 shows that its design is adequate to extend the service life of deck slab above a reliability of 2.33 and corresponding wheel load capacity of 123.04 kN. The remaining life estimate for location 8-1 indicates that the punching shear rehabilitation provides, at best, a temporary solution for the bridge deck, which tolerates degradation of CFRP for approximately 1.4 years above a reliability of 2.33 and corresponding wheel load capacity of 124.476 kN.

SUMMARY AND CONCLUSIONS

The paper describes the results of an on-going investigation into the development of health monitoring systems for bridge structures. The first example shows the implementation of an autonomous assessment of the state of the bridge through interrogation of response data as well as comparison of the data to predetermined thresholds. The latter enables the owner's representatives to rapidly access the health of a bridge without having to physically visit the bridge-site unless warranted by specific conditions. Research is ongoing on further developments in damage identification, severity estimation, and linking these measures to serviceability and remaining service life. The second example shows how similar data can be used to provide estimates of remaining life of the structure.

It is expected that the further development of the system will result in the establishment of a comprehensive methodology for autonomous health monitoring of structural systems to the point where true condition based physical inspection and monitoring would become a reality. The integration of damage identification and finite element based tools further provides assistance to the engineer in assessing health immediately rather than having to resort to expensive closures while assessments are made off-line.

ACKNOWLEDGEMENTS

The research was conducted with support of the California Department of Transportation, which is gratefully acknowledged.

REFERENCES

[1] Karbhari, V.M., Seible, F., Burgueno, R., Davol, A., Wernli, M. and Zhao, L. 2000. Structural characterization of fiber-reinforced composite short- and medium-span bridge systems. *Applied Composite Materials*, 7(2/3), pp. 151-182.

[2] Zhao, L. and Karbhari, V.M. 2001. Investigation of stress states and failure mechanisms of a cellular FRP composite bridge deck system. *Proceedings of the 16th technical conference of the American Society of Composites*, paper #201, 12 pp.

[3] West, W. M. 1984. Illustration of the use of modal assurance criterion to detect structural changes in an orbiter test specimen." *Air Force Conference on Aircraft Structural Integrity*, pp. 1-6

[4] Pandey, A. K., Biswas, M., and Samman, M. 1991. Damage Detection from Changes in Curvature Mode Shapes. *Journal of Sound and Vibration*, 145(2), pp. 321-332.

[5] Stubbs, N., Kim, J.-T., and Topole, K. 1992. An efficient and robust algorithm for damage localization in offshore platforms." *ASCE Tenth Structures Congress*, pp. 534-546.

[6] Aktan, A.E., Lee, K. L., Chuntavan, C., and Aksel, T. 1994. Modal Testing for Structural Identification and Condition Assessment of Constructed Facilities. *12th International Modal Analysis Conference*, pp. 462-468

[7] Stubbs, N., and Osegueda, R. 1990. Global non-destructive damage evaluation in solids." *The International Journal of Analytical and Experimental Modal Analysis*, 5(2), pp. 67-79.

[8] Stubbs, N., S. Park, C. Sikorsky, and S. Choi., "A Global Non-destructive Damage Assessment Methodology for Civil Engineering Structures," *Intl J. of Sys. Sci.*, 31(11), 1361-1373, (2000).

DURABILITY OF ADVANCED POLYMER COMPOSITES IN THE CIVIL INFRASTRUCTURE

V.M. Karbhari
University of California San Diego, La Jolla, CA, USA

INTRODUCTION

Fiber-reinforced polymer (FRP) composites are increasingly being used in civil infrastructure in applications ranging from reinforcing rods and tendons, wraps for seismic retrofit of columns and externally bonded reinforcement for strengthening of walls, beams, and slabs, composite bridge decks, and even hybrid (FRP composite in combination with conventional materials) and all-composite structural systems. Although the claim of long-term durability of fiber reinforced polymer (FRP) composites is often one of the major considerations in the selection of this class of materials over conventional materials, there is significant concern related to this aspect, especially because of the requirements of long service life without levels of inspection and maintenance that are used in the aerospace arena.

Historically, the lack of durability data and the need for a high level of safety has led to the use of high factors of safety in design such as 4-6 in the marine industry and as high as 8-12 in the area of tanks and pipes. This however, not only increases cost and weight of the composites, but also changes performance attributes to the point where the inherent tailorability of the composite is often sacrificed. A recent study identified critical gaps in the durability knowledge of FRP composites for use in civil infrastructure [1]. It was noted that environments of the type seen in civil infrastructure can cause significant degradation to types of FRP composites, and that there is in reality a lack of validated data and a comprehensive knowledge of lifetime durability related to some material systems likely to be used in civil infrastructure. A number of critical facets were emphasized and the top research needs were identified as listed below:

- Collection, assessment and appropriate documentation of available data. A substantial amount of data is already available but is scattered in the literature and not in a form to enable use in civil infrastructure. Large amounts of data are also not easily accessible and it is critical that these be retrieved and reported. Loss of this data would result in an enormous duplication of time-consuming effort at tremendous cost. The available data needs to be assessed, and after validation, needs to be presented in a form useable by the civil engineer/designer.
- Testing over extended (18+ months) time periods. Tests conducted over short time periods (less than 18 months) can yield misleading results due to effects of post-cure and slow interphase and fiber level degradation, and can provide an erroneous level of comfort in some cases.
- Testing under combined conditions (stress, moisture, solution, temperature, and/or other regime) at both the materials and structural levels is critical. Although tests conducted under controlled isolated conditions are important for the development of an understanding of degradation mechanisms and models for life-prediction, combined effects can be much more severe and in most cases will dominate overall response.
- Assessment and characterization of the effects of incomplete and under cure, especially for ambient temperature cure systems is essential. Too often designs are based on performance related to post-cured systems neglecting the fact that even extended periods of ambient cure may not be able to duplicate effects of post-cure,

and that incomplete cure can potentially increase the susceptibility of the FRP composite to moisture/solution related accelerated degradation.

- Development of standardized solutions and conditions for laboratory studies that closely simulate actual field conditions. The characterization of representative "short-term" exposure periods for tests that enable accurate extrapolation of effects over longer time periods is essential, and can only be completed though the use of multi-disciplinary efforts.
- Development of appropriate resin systems, gel coats, and coatings that would serve as protective layers for the bulk composite against external influences including environmental conditions, intended and accidental damage.

Although significant research is continuing to be conducted as related to the durability, there is a critical lack of data pertaining to specific aspects such as variability of wet layup composites used for strengthening, characterization of synergistic effects of sustained load and hygrothermal conditions, and results of longer term testing on the basis of which better predictions of service-life could be made. Based on the need for high levels of safety and long service lives, and in light of concerns related to lower levels of quality control (as compared to the aerospace arena), processing in ambient and often poorly controlled conditions (as would be seen in wet layup used for external strengthening), aspects related to creep and stress-rupture of glass fibers, and overall effects of a harsh and varying environment, it is clear that additional studies are needed in this area.

EFFECT OF SYNERGISTIC ENVIRONMENTS

The material under study is representative of that used in prefabricated profiles. The composite is a 58% volume fraction unidirectional pultruded E-glass/vinyl-ester composite composed of a thermosetting vinyl-ester resin (Reichhold, Dion VER 9102) reinforced with unidirectional single-end E-glass fibers (PPG 113). All specimens were cut to dimensions of 25.4 cm x 2.54 cm x 0.141 cm, and were pre-conditioned in a humidity chamber for 6 weeks at 40°C and 18% relative humidity (R.H.) in order to obtain a stabilized base-line. In order to characterize the effects of hygrothermal exposure, specimens were kept both in controlled ambient conditions (22°C and 60% RH) and immersed in deionized water (at 22, 40, and 60°C). The synergistic effects of imposed strain, moisture and temperature were investigated through the use of a bending fixture to enable sustained levels of 0, 30 and 45% ultimate tensile strain at each of the exposure conditions. Specimens were removed at routine intervals from the environmental exposures for testing. In addition, at selected times, samples were re-dried in a humidity chamber for 6 weeks at 40°C and 18% R.H. (i.e. the same duration and conditions as used for pre-conditioning) to enable the desorption of water molecules and provide an assessment of performance regain.

Beyond studies related to moisture uptake, a minimum of 4 specimens from each exposure condition and time period were tested in tension (in the fiber direction) following ASTM D3039 procedures. Tests were conducted immediately after removing samples from exposure conditions, and after the period of reconditioning (to assess property regain). The surfaces of conditioned specimens used in the sorption study were systematically examined for superficial damage through visual inspection. In addition the surfaces that exhibited some amount of degradation were then examined under a scanning electron microscope (SEM). Some of these specimens were also placed in an oven at 500°C for about 15 hours to burn away the resin. Subsequently, the remaining glass fibers were ultrasonically cleaned in acetone to dissolve any residual

sizing from their surfaces. The bare fibers were then placed on a carbon taped-aluminum pin, gold coated and finally observed in the SEM to investigate fiber damage through fiber pitting and cracking.

The characteristics of moisture uptake for the composite specimens are shown in Figure 1. After 24 months of exposure the moisture content in specimens without additional strain was 0.39%, 0.63% and 0.78% in 22°C, 40°C and 60°C deionized water, respectively. At 22°C the moisture gain appears to be progressive and apparently unaffected by bending strains, which suggests that the tensile and compressive stresses, on opposite faces due to bending, have opposing effects on diffusion that compensate each other, as observed previously [2]. Similar conclusions can be drawn for the specimens under 0% and 30% ultimate tensile strain immersed in deionized water at 40°C. However, specimens subjected to 45% UTS start showing divergence from the normal response after about 5,375 hours of immersion at 40°C with a sudden increase in weight gain after 7,964 hours at an apparent moisture content of 0.55%. The final weight gain increase continued till failure by delamination at a recorded weight gain of 0.86% after 11,995 hours of immersion. This anomalous behavior has previously been observed by Rogers [3] and was attributed by Weitsman to the occurrence of irreversible degradation and material breakdown [4]. It is noted that a similar, but significantly more severe, anomalous response was exhibited by specimens under 45% UTS immersed in deionized water at 60°C, wherein the dramatic increase in weight gain was seen to initiate after 2,036 hours of immersion at an apparent weight gain of 0.53% with failure by delamination occurring after 2,711 hours at an apparent weight gain of 1.18%.

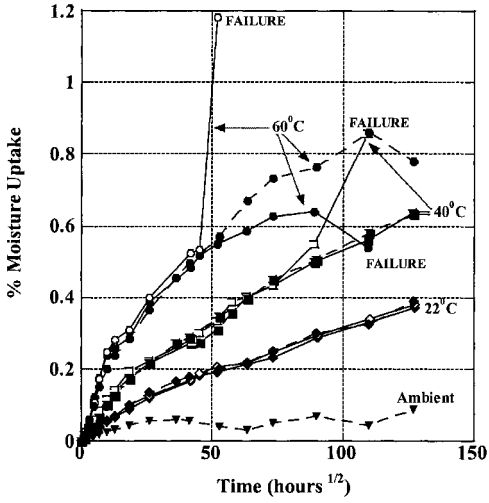


Figure 1: Apparent weight change in composites under various exposure conditions (dashed lines represent samples without any imposed strain, solid lines with filled symbols represent samples with 30% imposed strain levels, and solid lines with unfilled symbols represent samples with 45% imposed strain levels)

The dramatic final increase in weight gain, observed at 40 and 60°C under 45% UTS, is attributed to the occurrence of mid-plane separation as a consequence of high differential internal swelling stresses developing across the composite centerline. Once a critical moisture content of approximately 0.5wt% is attained, it appears that, under the severe imposed bending strains, the greater moisture sorption through the composite

thickness under tension generates high hydrostatic tensile stresses along and across the centerline interface causing midplane separation. As debonding and delamination progress, additional routes for water penetration are created, which explain the subsequent rapid weight increase prior to final failure. On the other hand, elevated temperatures combined with lower bending strains only allowed the occurrence of early leaching-out of material either through the desorption of partially reacted or unreacted low-molecular weight elements (e.g., styrene, resin flexibilizers, etc.), and hydrolysis of polymer groups, causing a final decrease in weight gain. Degradation and leaching of the fiber-matrix interphase is also expected to result in an apparent weight decrease, as the density of the fiber sizing is greater than that of water. These latter damage mechanisms are believed to be responsible for the apparent weight loss after 18 and 12 months of exposure at 60°C, and 60°C & 30% UTS, respectively. The reason for the substantially lower moisture content at 60°C & 30% UTS compared to 60°C may be the superficial layer of resin being removed at a higher rate, especially under tensile stresses, thereby contributing to the loss of material and decrease in the level of apparent weight gain.

It is seen that experimental moisture uptake data are in better agreement with the Langmuir-type model than the Fickian one. In the Fickian model, water molecules are assumed to dissolve in the surface layers of the polymer and migrate into the bulk with the concentration gradient acting as a driving force. The diffusion coefficient, D, is conventionally assumed to be concentration-independent and the saturation moisture content, M_∞, is defined by a single fixed value. The Langmuir-type model, on the other hand, is analogous to the Langmuir theory of adsorption isotherms on surfaces, and as developed by Carter and Kibler [5], assumes a simple linear diffusion theory involving sources and sinks of diffusing water molecules. Water molecules are, therefore, either bound to the polymer or free to diffuse with a diffusion coefficient D. The overall results from both models are summarized in Table 1.

Table 1: Estimated equilibrium moisture contents and diffusion coefficients using both Fickian and Langmuir diffusion models

Temperature	M_∞ [%]		D [$mm^2.s^{-1}$]	
[°C]	Fickian	Langmuir	Fickian	Langmuir
22	0.33	0.47	1.56×10^{-8}	1.63×10^{-7}
40	0.55	0.66	1.66×10^{-8}	2.75×10^{-7}
60	0.76	0.85	2.86×10^{-8}	6.74×10^{-7}

Although the use of one-dimensional diffusion models is useful to approximate and compare diffusion coefficients and equilibrium moisture contents among various composite systems, it is based on a simplifying assumption that diffusion is isotropic. It has been demonstrated that, for fiber-reinforced polymer composites, diffusion along the fiber/matrix interfaces is much faster [6] and can play an important role [7]. This additional longitudinal diffusion through debonded regions in conjunction with the progressive degradation of the polymer matrix and interphase via hydrolysis reactions [8, 9] could explain the unattained equilibrium stage after 2 years of exposure. Moisture saturation of the resin may, in fact, be concealed by a range of damage mechanisms affecting moisture sorption within the composite, and inherently not be detectable by common gravimetric studies for such materials. Nevertheless, assuming that a global saturated state would exist, with regards to the present results predicted by the Langmuir-type model, the moisture saturation content is found to be linearly dependent

upon temperature, while the diffusion coefficient obeys an Arrhenius relationship with temperature.

The change in the ultimate tensile strength of specimens exposed to the various environmental exposures is shown in Figure 2 as a function of exposure time. As expected, a clear decrease in composite strength with increasing immersion time and temperature is seen. It is observed that, without the addition of strain, exposure to deionized water for a duration of 668-678 days results in a strength retention of 82% at 22°C, 60% at 40°C and 46% at 60°C. The reduction in tensile strength is comparatively slow, but continuous in the 22°C immersion case, whereas it is initially more pronounced in the 40°C and 60°C immersion cases prior to approaching a very slow asymptotic decrease.

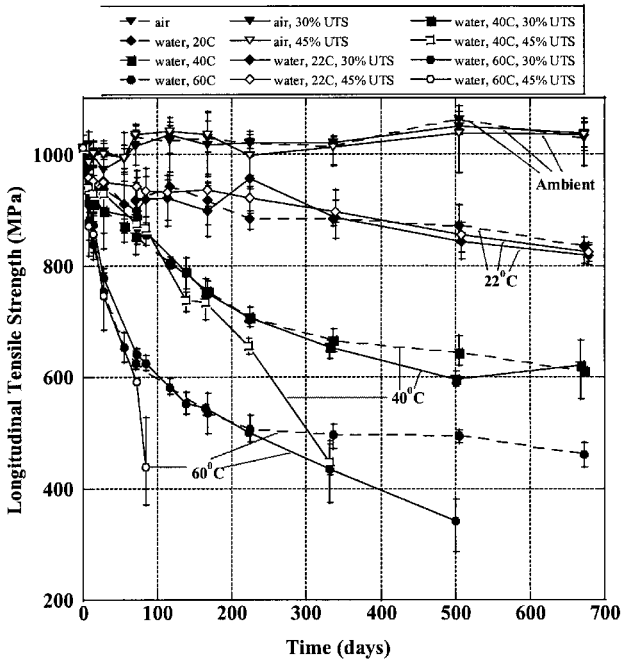


Figure 2: Longitudinal tensile strength of specimens as a function of temperature and period of immersion in deionized water, and level of imposed strain (dashed lines: samples without imposed strain; solid lines with filled markers: samples under 30% UTS; solid lines with hollow markers: samples under 45% UTS.

SEM examination of glass fiber surfaces of composites immersed in deionized water at 60°C indicate that signs of severe pitting and cracking are only seen after 18 months of immersion (Figure 3). The lack of substantial apparent damage at the fiber level prior to this indicates that other non-fiber-volume related damage mechanisms are probably responsible for the initial drop in strength. At the macroscopic level a progressive change in tensile failure mode from a brush-like failure characterized by longitudinal splitting (for unaged or somewhat damaged material) to central fiber rupture (for severely damaged material) was observed as a function of immersion time and increasingly severe environment. This transition can be attributed in part to the degradation of the fiber-matrix bond, since fiber pull-out and smoother fiber surfaces

are indicative of poorer interfacial bond strength due to increased degradation at the level of the bulk resin and interface. It is noted that the tensile failure mode, of longitudinal splitting, exhibited by specimens immersed at 60°C remained virtually unchanged throughout the first 8 months of immersion, implying that the initial reduction in strength is caused primarily by physical and chemical changes within the polymer matrix rather than by degradation at the fiber and/or interface levels.

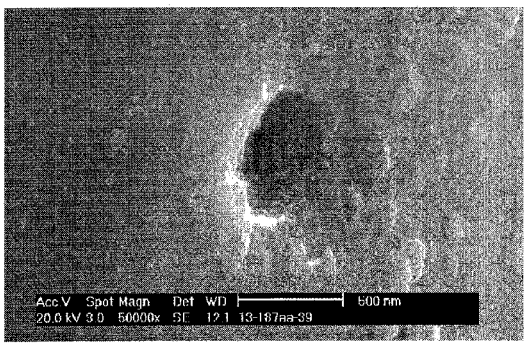


Figure 3: SEM Images of fiber pitting following immersion of composite specimens in deionized water at 60°C for 504 days (≈18 months).

Although there is no perceptible influence of bending stain over the completed exposure time period on the tensile response of composites immersed in deionized water at 22°C, effects are noted at higher temperatures. Specimens exposed at 40°C under 45% UTS, and 60°C under both 30% UTS and 45% UTS show a pronounced decrease in strength retention as compared to the unstrained specimens immersed at the same temperatures. The departure from the unstrained response occurs after a period of 2 months-immersion at 60°C under 45% UTS, 6 months-immersion at 40°C under 45% UTS, and 8 months-immersion at 60°C under 30% UTS. The lower tensile strength exhibited by these specimens can be attributed to severe fiber and interface degradation. Stress corrosion of E-glass fibers is known to generate weak zones that reduce fiber strength and enhance crack propagation, especially in conjunction with moisture, and these effects can clearly be observed.

Degradation of the interface, on the other hand, modifies the magnitude and nature of stress transfer from a broken fiber to its neighbors, and results ultimately in changes in failure mechanisms as well as in a reduction in the overall load-bearing capacity of the composite. SEM micrographs show the presence of superficial fiber cracking and debonding following immersion at 40°C under 30% UTS for 18 months. An increase in the level of imposed strained to 45% UTS results in an increased level of degradation as evidenced by the coalescence of fiber surface cracks and extensive debonding after only 12 months of immersion. An increase in temperature to 60°C, at an imposed strain level of 30% UTS causes, in addition to numerous fiber surface cracks, the development of significant fiber pitting and loss of material presenting further evidence of irreversible deterioration at the fiber level, accelerated by stress corrosion mechanisms. As can be seen in Figure 2, the highest bending strain appears to have a greater detrimental effect on the composite tensile strength than the highest exposure temperature. This is confirmed by the longer time to failure exhibited by the specimens at 60°C under 30% UTS as compared to those at 40°C under 45% UTS and

60°C under 45% UTS. The failure times, (referring to the exposure times at which specimens were found to have failed within the bending fixture) are summarized in Table 2 for the corresponding environmental exposure conditions.

Considering that coupons were tested both immediately after periods of immersion (wet state), and after a fixed period of reconditioning (dry state) equal to that of initial preconditioning (i.e. 6 weeks at 40°C and 18% RH), it is of interest to assess percentage retention in tensile strength as a function of exposure condition and period, in both cases. Overall results for some time periods are given in Tables 2-4. It should, however, be noted that for purposes of true assessment within each case (wet and dry), base lines have to be considered differently. In the wet case the base-line, $\sigma_{wet,o}$, relates to specimens tested immediately after the period of preconditioning, whereas in the dry case the base-line, $\sigma_{dry,o}$, relates to specimens subjected to the full period of both preconditioning and reconditioning, such that

$$\% \text{ Strength Retention (Wet)} = \frac{\sigma_{wet,t}}{\sigma_{wet,o}} \text{ x } 100$$

$$\% \text{ Strength Retention (Dry)} = \frac{\sigma_{recon,t}}{\sigma_{dry,o}} \text{ x } 100$$

where $\sigma_{wet,t}$ is the tensile strength following immersion for a time period, t, and $\sigma_{recon,t}$ is the tensile strength following both immersion for a time period, t, and specified reconditioning. As with most vinylester-based composites, use of elevated temperatures results in post-cure, and reconditioning therefore causes an increase in the average value of the baseline tensile strength from 1011.5 MPa (representing $\sigma_{wet,o}$) to 1059 MPa (representing $\sigma_{dry,o}$). Overall, strength retention, as expected, decreases with increase in time, temperature of immersion, and level of imposed strain. As noted previously, the effects are the least severe at 22°C, although there is clear degradation at the longest time period, which is apparently substantially irreversible. A comparison of strength retention levels also appears to suggest that up to time periods close to failure, with the exception of the 60°C – 45% UTS case, the effect of imposed strain, within the limits investigated in this study, is fairly minor.

Table 2: Percentage Retention in Tensile Strength in the "Wet" and "Dry" State With Imposed Bending Strain = 0 ($\sigma_{wet,0}$ = 1011.5 MPa, $\sigma_{dry,0}$ = 1059 MPa)

	Temperature of Deionized Water					
Time	**22°C**		**40°C**		**60°C**	
[days]	**Wet**	**Dry**	**Wet**	**Dry**	**Wet**	**Dry**
0	100	100	100	100	100	100
14	93	101	90	100.5	83	92
28	94	103	89	98.5	74.5	85.5
71	91	101	84	91	62	69
116	93	95	80	84	57.5	61
168	91	99	75	81	53	57
336	87	98	66	69	49	52
672	82	90	60	60	46	47.5

Table 3: Percentage Retention in Tensile Strength in the "Wet" and "Dry" State With Imposed Bending Strain = 30% UTS ($\sigma_{wet,0}$ = 1011.5 MPa, $\sigma_{dry,0}$ = 1059 MPa)

	Temperature of Deionized Water					
Time	22°C		40°C		60°C	
[days]	Wet	Dry	Wet	Dry	Wet	Dry
0	100	100	100	100	100	100
14	91	97	91.5	97	86	91
28	93	101	89	95	77	82
73	89	99	87.5	94	63	68
85	91	98	85	92	62	65
139	91	97	78	83	55	58.5
165	89	100	74	81	54	59
332	87.5	99.5	65	68	43	48
668	81	92	61	58	FAILURE	FAILURE

Table 4: Percentage Retention in Tensile Strength in the "Wet" and "Dry" State With Imposed Bending Strain = 45% UTS ($\sigma_{wet,0}$ = 1011.5 MPa, $\sigma_{dry,0}$ = 1059 MPa)

	Temperature of Deionized Water					
Time	22°C		40°C		60°C	
[days]	Wet	Dry	Wet	Dry	Wet	Dry
0	100	100	100	100	100	100
14	94	99	92	98	85	89
28	94	102	92	94	74	76
73	93	98	86.5	90	58	55
85	92	99	86	88.5	43	49
113	92	98	73	80	FAILURE	FAILURE
168	92.5	99	72	78	(t=139)	(t=139)
340	88.5	96	44	47		
678	82	87	FAILURE (t=500)	FAILURE (t=500)		

However, an increase in imposed strain level does result in a more dramatic decrease and more sudden failure once a threshold is reached. For example, after 165-168 days of immersion in 40°C deionized water, the level of retention in "wet" strength is 75%, 74% and 72% under 0%, 30%, and 45% UTS, respectively. After 332-340 days of immersion at the same temperature, the level of strength retention is still about equal, namely 66% and 65% under 0% and 30% UTS, respectively, whereas the strength retention under the higher level of 45% UTS is now as low as 40%. As can be seen from Table 3, failure occurs in samples immersed in deionized water at 60°C and under 30% UTS at about 668 days at retention strength levels lower than 43% and 48%, for the "wet" and "dry" cases, respectively. Under the higher level of 45% UTS, failure after immersion in 40°C deionized water occurs at about 500 days with strength retention levels lower than 44% and 47%, in the "wet" and "dry" conditions, respectively. However, immersion at the higher temperature of 60°C results in failure at a shorter immersion time of about 139 days with strength retention levels lower than 43% and 49%, in the "wet" and "dry" cases, respectively. This suggests the existence

of a threshold at which failure will take place with time period dependent on both temperature of immersion and the level of imposed strain.

Finally, it is also of interest to note that up to a moisture gain level of approximately 0.25%, which is attained over a period of time ranging from 4 to 282 days, depending on the temperature of deionized water and the level of imposed strain there is no discernable degradation at the fiber and interface level. The level of strength retention after immersion for the corresponding times is found to be between 86 and 91%, but this is substantially regained on reconditioning, indicating that the effects are largely reversible and due primarily to matrix plasticization.

Consequently, in order to investigate the influence of temperature and bending strains on the composite tensile strength, the tensile strength was plotted against the sorbed moisture content to a limit of $M_m = 0.25\%$. It was found that linear relationships with a high degree of correlation can be obtained both for individual temperature-strain combinations, and for the entire set collectively, indicating the significant and probably dominating effect of sorbed moisture till this juncture (i.e. $M_m = 0.25\%$) on the decrease in strength. Taking all data together it can be determined that due to immersion in deionized water, on average, tensile strength decreases by 490 MPa per percent sorbed moisture in the range considered.

In accordance with most previous published research, there is a very small effect of exposure conditions on the tensile modulus within the relatively short exposure durations investigated. Overall results for retention of longitudinal tensile modulus after a 2-year period of immersion show that with the exception of failed specimens, changes from the initial values are almost insignificant. However, specimens immersed in deionized water at 60°C under 30% UTS exhibited a reduction of about 24% in modulus in the test period prior to failure (t = 332 days). It should also be noted that all specimens initially experienced about a 10% increase in modulus, presumably due to slow postcure over the first 2-3 months of immersion with values returning to the original levels after about 6 months of immersion.

These results clearly show significant interactions between imposed loads (represented here as strains) and hygrothermal conditions. The use of elevated temperatures is well established as a means of acceleration and hence these results are being studied further to develop predictive models.

MATERIALS VARIABILITY IN WET LAYUP

The strengthening of concrete structures through the use of externally bonded FRP composite systems essentially raises concerns related to durability at two levels, namely the durability of the FRP material itself and the durability of the bond between the FRP material and the concrete substrate. Intrinsically the latter includes the durability of the resin/adhesive at the interface between the FRP composite and the concrete substrate. Under the aegis of the Civil Engineering Research Foundation's (CERF) Highway Innovative Technology Evaluation Center (HITEC) program a comprehensive protocol, for the evaluation of durability of FRP systems for strengthening, has been established [10]. One of the primary concerns is that intrinsic variability in the as-fabricated properties would cause not only deviation from expected as-designed performance, but also to the overall durability of the material.

In order to assess the variability accruing from field conditions on properties of the FRP composites themselves process panels were fabricated simultaneous with actual material that was bonded to the deck soffits, as part of a field rehabilitation of the slabs on a bridge, both at the initiation and completion of work on each bay under

consideration. These process panels were intended to serve as indicators of property variation based on field conditions and were allowed to cure in the same conditions as the FRP composites bonded onto the deck soffit concrete substrate, prior to being transported to the laboratory for characterization using tensile tests The designs (number of layers and spacing) were based on the use of nominal properties for the material with the design values being based on normalized values as listed in Table 5. It should be noted that normalization was done by fabric thickness.

Table 5: Nominal Design Values for Wet Layup

Layers	t (mm)	Test Values E (GPa)	Test Values σ (MPa)	Normalized E (GPa)	Normalized σ (MPa)
1	1.15	65.16	718.8	73.79	814.1
2	2.02	64.92	887.1	64.92	887.1
3	3.11	60.18	745.9	61.33	760.2

Overall results for wet layup panels obtained through field fabrication and pooled by thickness are shown in Table 6.

Table 6: Overall Properties Showing Scatter

	t (mm)	Tested σ (MPa)	Tested E (GPa)	Normalized σ (MPa)	Normalized E (GPa)
1 Layer Thick Specimens					
Avg.	1.102	1042	70.37	1127	76.27
SD	0.048	118.7	5.406	93.98	5.233
c.v.	1.135	0.785	0.001	0.574	0.001
Max.	1.168	1243	79.94	1243	88.01
Min.	1.013	874.6	62.05	962.9	71.12
2 Layer Thick Specimens					
Avg.	1.877	1101	78.96	1101	78.96
SD	0.056	111.6	4.071	111.6	4.071
c.v.	0.757	0.699	0.001	0.699	0.001
Max.	1.946	1263	86.31	1263	86.31
Min.	1.778	888.7	74.84	888.7	74.84
3 Layer Thick Specimens					
Avg.	2.741	1008	82.70	1008	82.70
SD	0.127	142.2	5.380	142.2	5.380
c.v.	1.176	0.973	0.001	0.973	0.001
Max.	2.865	1118	90.59	1118	90.59
Min.	2.588	802.1	78.63	802.1	78.63

Table 7: Performance Characteristics of Wet Layup FRP Composites by Location

Property		8-3	8-5	9-3	9-5
1 Layer Thick Specimens					
Thickness (mm)	Avg.	1.072	1.102	1.125	1.082
	SD	0.020	0.045	0.030	0.081
	cv	0.432	1.016	0.686	1.905
	Max	1.097	1.156	1.173	1.173
	Min	1.049	1.029	1.085	1.003
Modulus (GPa)	Avg.	71.16	66.72	70.53	73.17
	SD	10.58	2.828	9.567	12.52
	cv	0.001	0.001	0.001	0.001
	Max	89.29	71.12	90.68	94.18
	Min	59.61	63.13	50.24	53.70
Strength (MPa)	Avg.	1071	1122	956.6	1120
	SD	76.19	54.19	107.2	154.6
	cv	0.489	0.331	0.772	0.952
	Max	1213	1208	1148	1309
	Min	946.0	1050	806.1	911.1
2 Layer Thick Specimens					
Thickness (mm)	Avg.	1.839	1.910	1.885	1.862
	SD	0.066	0.025	0.018	0.091
	cv	0.914	0.330	0.254	1.270
	Max	1.918	1.943	1.920	1.986
	Min	1.760	1.854	1.849	1.770
Modulus (GPa)	Avg.	78.86	78.78	79.12	78.93
	SD	4.430	5.765	8.098	9.546
	cv	0.001	0.001	0.001	0.001
	Max	85.36	88.81	96.64	100.1
	Min	72.88	69.01	62.02	68.28
Strength (MPa)	Avg.	1191	1094	1149	920.2
	SD	99.77	122.0	80.26	92.94
	cv	0.579	0.772	0.483	0.696
	Max	1397	1288	1293	1055
	Min	1060	864.5	972.1	782.1
3 Layer Thick Specimens					
Thickness (mm)	Avg.	-	2.845	-	2.637
	SD	-	0.064	-	0.071
	cv	-	0.584	-	0.686
	Max	-	3.005	-	2.705
	Min	-	2.786	-	2.471
Modulus (GPa)	Avg.	-	79.41	-	85.99
	SD	-	5.469	-	19.56
	cv	-	0.001	-	0.002
	Max	-	89.71	-	135.1
	Min	-	70.29	-	69.97
Strength (MPa)	Avg.	-	1057	-	960.1
	SD	-	56.40	-	176.9
	cv	-	0.365	-	1.269
	Max	-	1134	-	1154
	Min	-	963.3	-	696.4

Results of the tests for the wet layup panels differentiated by the thickness are reported in Table 7 by location as Span-Bay. It can clearly be seen that there is not only significant scatter within values of a set but from set to set. A comparison of nominal values with the results obtained from process panels clearly shows that in the case of

FRP composites fabricated by wet layup not only are the values in some cases below the nominal ones used in design, but the scatter is also fairly large. This raises a concern related to the overall margins of safety due to the rehabilitation scheme used.

Tables 8 and 9 provide a comparison of the number of fabric strips that would be required if the mean, maximum, and minimum values of performance, as tested, were used, with the number required by the design, and the actual number applied in the field.

Table 8: Comparison of Number of Wet Layup Fabric Strips in the Longitudinal Direction

Layers	Design	Avg.	Max.	Min.	Field
1	3.99	3.40	2.75	5.16	4
2	1.99	1.78	1.40	2.26	4
3	1.33	1.16	0.71	1.37	-

Table 9: Comparison of Number of Wet Layup Fabric Strips in the Transverse Direction

Layers	Design	Avg.	Max.	Min.	Field
1	53.81	45.80	37.09	69.53	-
2	26.91	23.95	18.90	30.49	28
3	17.94	15.66	9.58	18.51	21

It should be noted that in some cases the number of fabric strips applied in the field was higher than that required due to use of a higher safety factor for a specific span-bay combination. As can be seen from Tables 8 and 9 the use of just the average values does meet the requirements of design in most cases. However, considering that there is substantial scatter, one could justifiably wonder as to the effects of the lower levels and it is clear that in all cases the minimum values obtained through testing do not meet the design requirements. A summary of safety margins through the use of the different levels is given in Table 10.

Table 10: Summary of Safety Margins

No. of Layers	Average Value	Maximum Value	Minimum Value
1	1.18	1.45	0.77
2	1.12	1.42	0.88
3	1.15	1.87	0.97

The results clearly emphasize the level of scatter for which the lower tail appears to increase as the number of layers decreases. A comparison of values shows that design requirements are met if the value used for design is actually computed as

Average Test Value – 1(Standard Deviation)

for strength, and

Average Test Value – 1.5(Standard Deviation)

for the modulus, based on test results of in-process panels, rather than the nominal values initially used. The difference in these is clearly due to fabrication under field conditions rather than in the facilities of the fabricators wherein a higher level of care is obviously taken in fabrication of the specimens. Further analysis is being undertaken on this data as well as on other sets obtained from similar field installations to provide a

validated set of guidelines for the determination of actual values to be used for design based on effects of field installation. Durability testing is ongoing.

SUMMARY

Although fiber reinforced polymer (FRP) composites have shown that good durability characteristics can be achieved in aerospace, automotive and marine applications, there is enough evidence that the conditions of fabrication, and service conditions (load and environment) need to be considered very carefully. The harsh, changing environment faced in civil infrastructure as well as the exigencies of cost and field fabrication necessitate that FRP materials considered for use in civil infrastructure be carefully characterized and that effects such as variability due to field manufacturing, and accelerated degradation due to synergistic effects be investigated, especially as related to the long service-lives required in civil infrastructure. Results, to date, however show that these materials have immense advantages for the built environment and can result in substantial increases in service-life with reduced maintenance as long as aspects related to materials selection, process and environmental conditions are appropriately considered.

ACKNOWLEDGEMENTS

The research was conducted with support of the California Department of Transportation, and the National Science Foundation, which is gratefully acknowledged.

REFERENCES

[1] Karbhari, V.M., Chin, J.W., Hunston, D., Benmokrane, B., Juska, T., Morgan, R., Lesko, J.J., Sorathia, V. and Reynaud, D., *ASCE Journal of Composites for Construction*, 7[3], 2003, pp. 238-247.

[2] Kasturiarachchi, K.A. and Pritchard, G., Composites, 1983, 14 [3], pp. 244-250.

[3] Rogers, C.E. "Solubility and Diffusivity, in Physics and Chemistry of the Organic Solid State," Vol. 2. Interscience Publishers, New York, 1965, pp. 509-635.

[4] Weitsman, Y.J. "Effects of Fluids on Polymeric Composites – A Review." Mechanical and Aerospace Engineering and Engineering Science, The University of Tennessee Report MA ES98-5.0-CM, August 1998.

[5] Carter, H.G. and Kibler, K.G., Journal of Composite Materials, 1978, 12, pp. 118-131.

[6] Kaelble, D.H., Dynes, P.J. and Maus, L., Journal of Adhesion, 1974, 6 [3], pp. 239-258.

[7] Morii, T., Ikuta, N., Kiyosumi, K. and Hamada, H., Composites Science and Technology, 1997, 57, pp. 985-990.

[8] Prian, L. and Barkatt, A., Journal of Materials Science, 1999, 34, pp. 3977-3989.

[9] Chin, J.W., Hughes, W.L. and Signor, A., Proceedings of the 16th Technical Conference of the American Society for Composites.

[10] Civil Engineering Research Foundation: HITEC Evaluation Plan for FRP Composite Systems for Concrete Repair and Strengthening, 18 pp, 2001

A PROSPECTIVE VIEW OF ADAPTIVE MATERIALS IN BRIDGE ENGINEERING

Professor Urs Meier
EMPA, Dübendorf, Switzerland

Adaptive Material Systems are, like biological systems, able to react autonomously to changes in their surroundings by adapting their characteristics in an appropriate way while in use. When it comes to reducing vibration or optimising physical states in general, adaptive material systems are of vital significance for future developments in lightweight bridges made of fibre reinforced polymers (FRP).

Knowledge from the fields of sensors, actuators, signal transmission, control systems, and the use and characterization of multifunctional composite materials is necessary for the development of adaptive material systems for civil engineering applications. The aim is to incorporate all these functions "monolithically" into the fibre reinforced polymers. The pilot production of "Active Fibre Composites" (AFC) based on piezoelectric fibres in a polymer matrix, intended to be used as actuators and sensors, is described. The same is true of Electro-Active Polymer Systems (EAP). Both techniques function, but have significantly different characteristics. AFCs exert large forces with small deformation while EAPs give large deformation and low force levels.

It is nowadays possible to realize bridge spans of almost 2 km using conventional materials an passive damping systems. Projected bridges schemes for the Strait of Messina and Strait of Gibraltar envisage 3-5 km spans. One outline proposal shows that even 8 km spans could be structurally feasible. As spans increase, the ratio of self-weight to live load becomes less favourable. Given their excellent specific strengths and elastic moduli, carbon fibre composites are particularly suited to use on wide-spanning bridges. This, of course, relates only to the static component (dead load, service loads) of structural performance. Allowance must also be made for the dynamic component (wind, earthquakes, moving loads). Conventional design approaches are hardly able to deliver spans exceeding 2 km, where the dynamic component becomes the decisive factor. Here, adaptive material systems offer the only solution. Such systems are capable, in service, of reacting independently to changes in ambient conditions and adapting their characteristics accordingly. In most cases, the basic components will be underpinned by corresponding sensors, actuators and data-processing elements. The concept of "adaptive material systems" is applicable wherever increasingly complex demands overstep the limits of conventional solutions. In such cases, the standard approach may involve a disproportionate amount of effort or formidable technical challenges, making simpler, more economical alternatives an absolute necessity. At the same time, adaptive material systems open up a whole new range of options, hitherto unfeasible with conventional materials. One possibility would be the described construction of bridges with extremely long spans. For instance, a stay cable capable of real-time response to changes in loads and geometry could be actively dampened when subject to vibration from wind action. Distributed piezoelectric fibres integrated in the carbon composites, asd called active fibre composites (AFC) would assume the associated sensory and actuation functions. Bridge carriageway beams set in vibration by wind action are another example, as conventional measures, such as changing the aerodynamics of the

cross-section, remain ineffective with wide-span bridges. Active microsystems are required that use microflaps to adapt the boundry surface of the structure to the relevant airflows and so eliminate the risk of flutter instability.

In the construction sector, the current annual turnover of carbon fibre totals some 1,500 tonnes worldwide. This roughly corresponds to three-quarters the amount used in the aviation and aerospace sectors. It should however be remembered that, at present, use of this material in the construction industry is almost exclusively limited to the post-strengthening of existing structures, with the new-build share remaining negligible. Use of carbon fibre composites for the tension tether legs of an off-shore platform anchored at a depth of 1,100 m would generate a 600-tonne requirement per platform. Similarly, an 8 km span bridge using CFRP built across the Strait of Gibraltar (as yet an utterly unrealistic prospect) would need 105,000 tonnes of the material.

Only the "monolithic" concept of distributed adaptive material systems will open up entirely new applications in bridge engineering which have not previously been achievable with conventional systems.

COMPOSITES: *CONSTRUCTION MATERIALS FOR THE NEW ERA*

Ayman Mosallam, Ph.D., P.E.

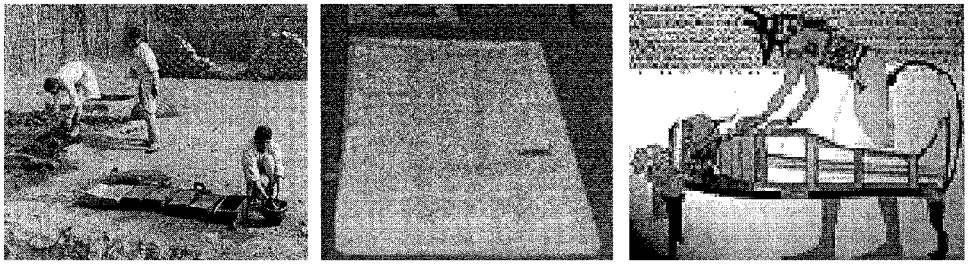
University of California at Irvine
Irvine, California, USA

ABSTRACT

With over fifty years of excellent performance records in the aerospace industry, fiber-reinforced-polymer (FRP) composites have been introduced with confidence to the construction industry. These high-performance materials have been accepted by the civil engineers and have been utilized in different construction applications such as repair and rehabilitation of existing structures as well as in new construction applications. This paper provides an overview of the successful and unique applications of FRP composites in construction. The paper also presents a state-of-the-art review on code and specification developments in the USA and worldwide.

BACKGROUND

The history of composites goes back few thousands years. For example, ancient Egyptians have used natural fibrous composites in building small houses (*straw-reinforced-clay bricks*), in fabricating natural compression molded cross-ply papyrus papers as well as in developing the linen wrapping system for their mummies to increase the ductility of the dried brittle dead bodies (*see Figure 1*).



(a) **(b)** **(c)**

Figure 1: Ancient Egyptians Utilization of Natural Composites:
(a) Fibrous clay blocks, (b) Compression molded cross-ply papyrus sheets, (c) Mummies Linen Wrapping Systems

Composites are no stranger to civil engineers. For decades, civil engineers have dealt with different forms of composite materials, including wood (*natural orthotropic composites*), plywood (*laminated natural composites*), and concrete (*particulate composites*). Polymer composites are "engineered" materials encompassing a wide range of materials where two or more, physically distinct and mechanically separable, components are combined together to form a new material which posse's properties that are notably different from those of its individual constituents. The primary load-carrying component is the fibers, while the matrix acts as a binder, an environmental protector, and stress distribution phase of the laminate. Fibers are available in different types, grades and shapes. Typical types of structural fibers include glass (*E, S, AR grades*), Aramid (Kevlar), and carbon fibers with different grades. Two types of polymers are available namely thermoplastic and thermoset polymers. In most of the structural applications, thermoset resins such as epoxies, unsaturated polyesters, vinyl esters, aminos, phenolics, and urethane are preferred. However, in recent years, few thermoplastic composite systems have been introduced and are being evaluated for civil engineering structural applications.

There are several attractive features that qualify these materials in performing their unique tasks, including: (i) *tailorability* which provides the structural engineer with a flexible tool in adding stiffness and or strength to the member in different directions, and (ii) *lightweight* of composites provides several benefits including minimizing additional masses, ease of handling and application, eliminating or minimizing the need of heavy equipment, and increasing the site safety. In addition, composites have a relatively high-energy dissipation capability. This property is important in absorbing seismic or blast energy, and it may act as polymer dampers at flooring area and connections zones.

HOW COMPOSITES DIFFER FROM OTHER CONVENTIONAL CONSTRUCTION MATERIALS

When dealing with fibrous polymeric composites, the civil engineer should be aware of two major mechanical properties:

1- Anisotropy: Unlike steel and similar isotropic materials where mechanical properties are independent of the applied load directions, composites, by nature, are anisotropic materials and hence thermo-mechanical properties vary in different directions. For this reason, the structural engineer should be aware of this property when specifying laminate fiber architecture. However, wood is orthotropic material and all engineers realize the difference between the parallel and perpendicular to grain properties of wood, and

2- Viscoelasticity: Due to the viscoelastic nature of polymeric composites, it is essential to understand thoroughly the creep performance of the composite system under varying stress levels and at different environmental conditions. This information is critical in determining the allowable long-term stresses and prediction of the long-term deformation of the system through the development of a viscoelastic modulus. This information is also essential for the design and specifications of the composites system in determining the limit-state required to determine the maximum allowable stress of the laminate. When composite shells are subjected to a relatively high sustained loading conditions, sudden failure may occur (*creep rupture or static fatigue*) if not designed properly. This process is characterized by a delayed failure

and it occurs for polymer composites members under ambient conditions, while same phenomena can also observed to metals but at relatively high temperatures. It is important for structural engineers who are accustomed to dealing with metals and who always assumes that if the material is capable of withstanding the applied "*static*" load, in the short-term, it probably will perform well in the long-term under ambient temperatures. This is not the case with polymer composites where it is necessary to use long-term design limit-states, particularly due to the fact that some composites are tough at short times tend to become embrittled at long times. Again, this is not news for engineers dealing with both concrete and wood structures where both of these materials are viscoelastic. In fact, the American Concrete Institute (ACI 318) includes this design concern by calculating the long-term deflection of flexural concrete members. All wood structures design codes include provisions for creep and long-term serviceability.

COMPOSITES IN REPAIR & REHABILITATION APPLICATIONS

General

One of the successful and most popular structural applications of FRP composites is the external strengthening, repair and ductility enhancement of reinforced concrete (RC) columns in both seismic and corrosive environments *(see Figures 2 and 3).* In this process, several laminates of composites are bonded to the pretreated concrete surface in the hoop and/or longitudinal directions for enhancing the member ductility and/or upgrading the axial stiffness of the RC column. In early 1990's, the majority of the applications focused on the ductility enhancement of concrete columns (see *Figure 4*), especially in seismic areas. In this particular application, the fibers are exposed to tension due to the Poisson's effect that, in turn, provide the required hoop stresses without adding to the column's stiffness (*i.e. stiffness/strength decoupling*).

Based on the successful performance of composites in columns applications, the use of FRP composites has been extended to cover other RC structural members, including beams and slabs where composite laminates are securely bonded to the bottom, top, or sides of RC beams and slabs for upgrading the flexural, shear, and torsional capacities of such members (*see Figure 4).*

In recent years, composites have been used to repair and strengthen other structural members including unreinforced and reinforced masonary, wood and steel. Figure 5 shows one of the pioneering field applications of composites for structural upgrade of a portion of the Sauvie Island Steel Bridge in Portland, Oregon [Mosallam (2003)[a,b]].

Types and Forms of Composite Repair Systems

Currently, three composite repair methods are available, including:

- Wet/Hand Layup: In this method, the fibers are in the form of either unidirectional or multidirectional waived, or stitched fabrics. After preparing the member surface and applying a primary epoxy-based coat, the saturated fibers are applied by hand to the location indicated in the engineering drawings *(see Figure 6),*

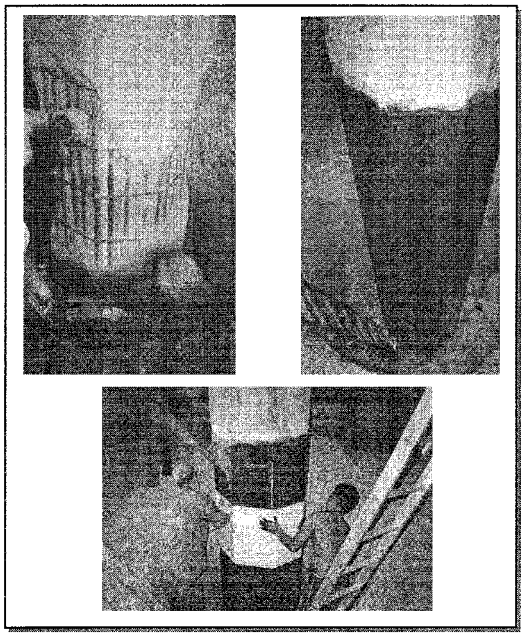


Figure 2: Corrosion Repair Application of FRP Composites in Saudi Arabia (*Courtesy of Sigma Composites, LLC, USA*)

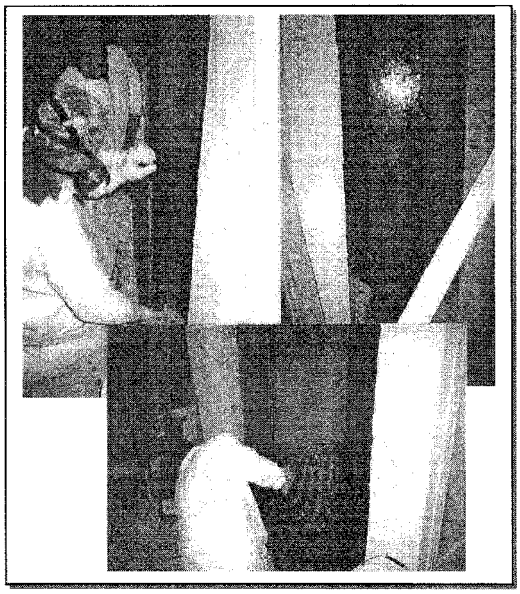


Figure 3: Seismic Application of FRP Composites for RC Column Strengthening (*Courtesy of SCCI, USA*)

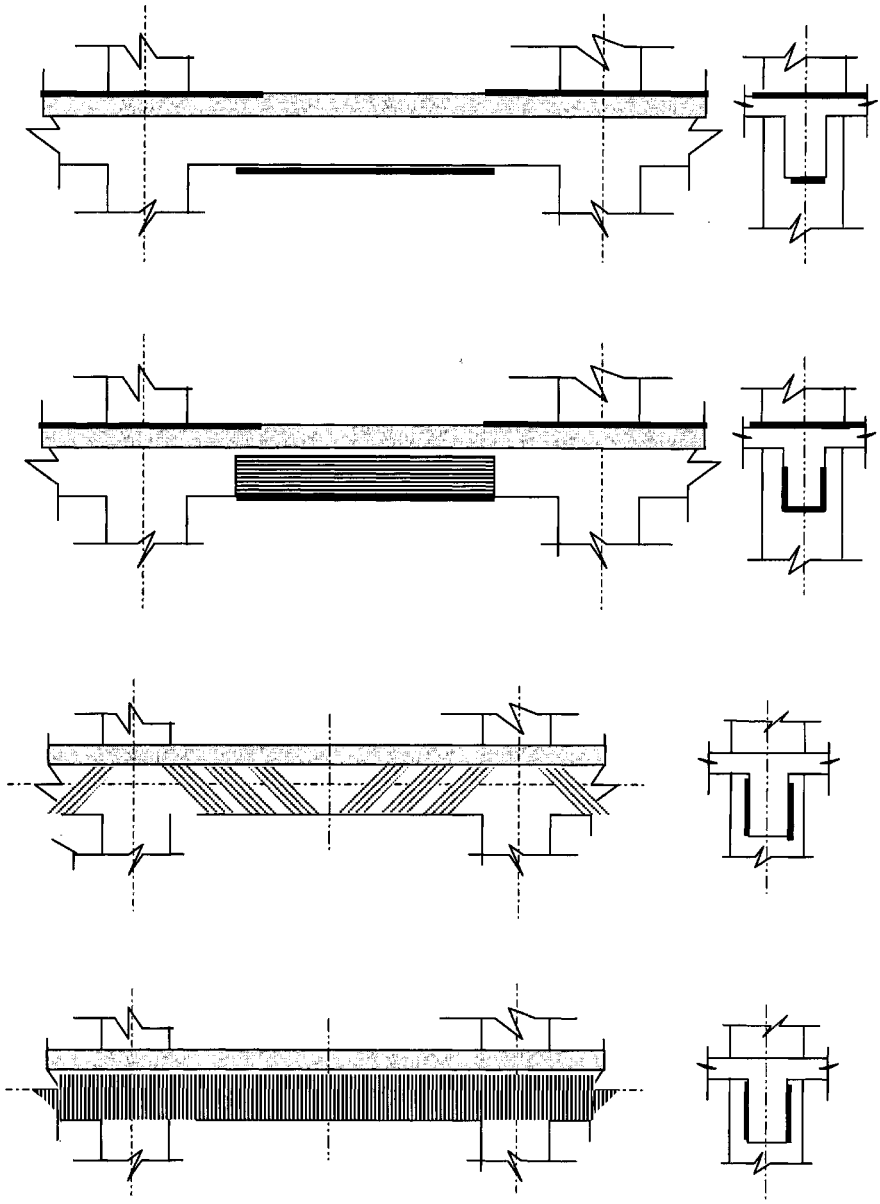


Figure 4: Typical and the Preferred FRP External Flexural and Shear Reinforcement of Continuous RC Floor Beam *[Mosallam (2002)]*

- Prefabricated Composite Laminates or Shells In this method, the composites are in the form of either unidirectional strips or shells. In the case of flat members such as beams and slabs, prefabricated composite strips are bonded to the specified locations using epoxy after surface treatment *(see Figure 7).* In this case, sanding or removal of the outmost matrix-rich layer is performed to ensure sufficient bondline strength between the composites and the concrete surface. For columns, prefabricated shells with majority of fibers in the hoop direction are used. After surface preparation, a thin coat of epoxy is applied, and the shell is placed at the required location per the engineering drawings. Straps are used to squeeze out any excess resin. It is critical that the split lines are staggered with a phase angle of 90°, and
- Automated Machine Lamination: In this method, the fibers are either dry or pre-impregnated. Thermal blanket or mobile curing oven is usually used to achieve the complete cure of the composite laminate *(see Figure 8).*

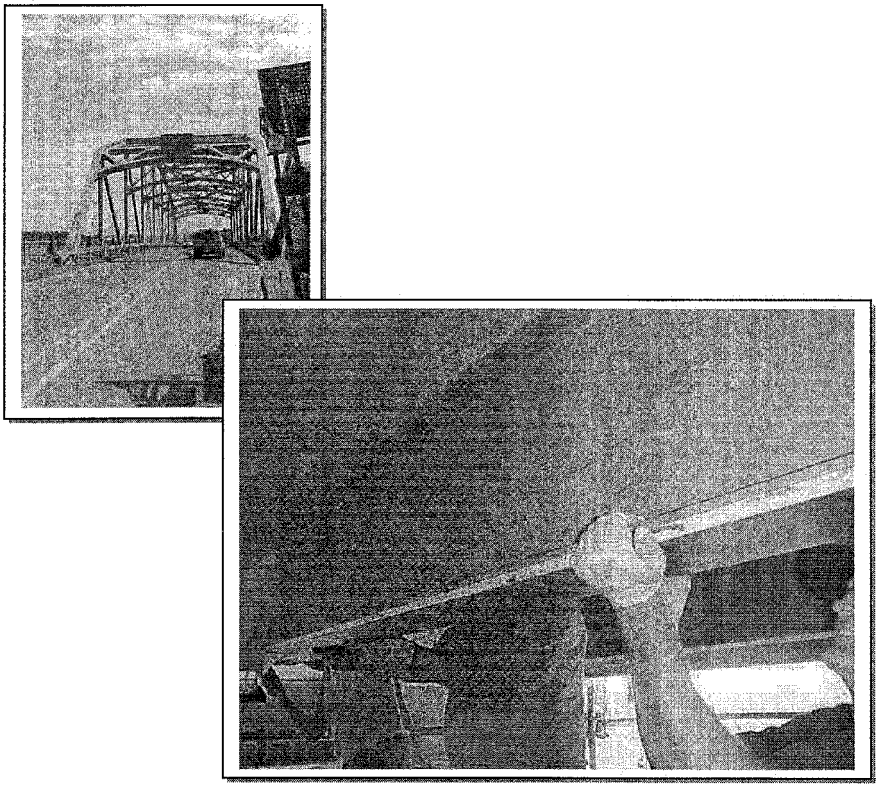


Figure 5: FRP External Flexural Strengthening of the Sauvie Island Steel Bridge Girders *[Mosallam (2003)[b]]*

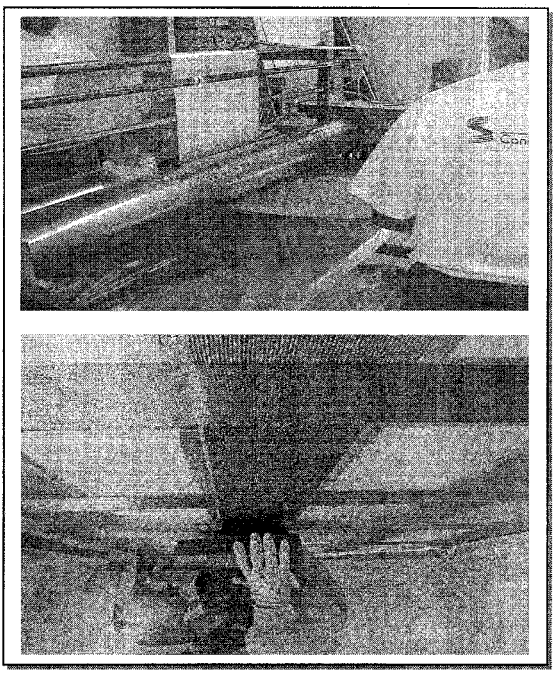


Figure 6: Wet/Hand Layup Process [*Courtesy of SCCI, USA*]

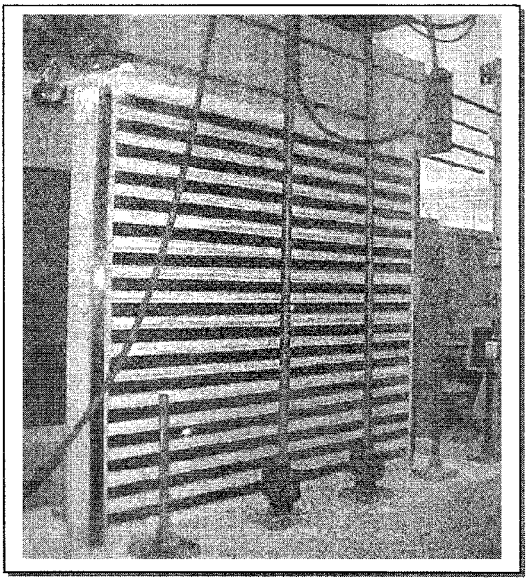


Figure 7: Precured Composite Strips Shear Wall Strengthening Application [*Haroun et al. (2003)*]

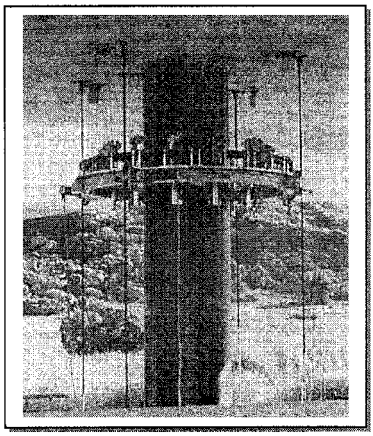


Figure 8: Automated Machine Layup *[XXSYS Company, USA]*

POTENTIAL APPLICATIONS OF COMPOSITES REPAIR & REHABILITATION SYSTEMS

As it was mentioned earlier, due to its unique properties, composites can provide the structural engineers with the answer to many structural problems.

Some of the potential FRP strengthening applications are:

- *Concrete and steel fluid tanks,*
- *Offshore structures and platforms,*
- *Blast-resistant upgrade (see Figure 9),*
- *Wooden beams and columns,*
- *RC and masonry chimneys,*
- *Tunnels (see Figure 10),*
- *Historical structures and monuments,*
- *Concrete and steel pipes (see Figure 11)*, and
- *Aluminum structural members.*

ALL-COMPOSITES STRUCTURES AND BRIDGES

In addition to the repair and reinforcement application of composites in construction, composite materials are being used to build the entire structure such as warehouses, building, highway bridge decks and other civil engineering structures. One of the popular types of composites in construction applications is pultruded composites. For decades, pultruded fiber reinforced polymeric (PFRP) composites have been used as secondary structural members in several construction applications such as petrochemical plants plate forms, cooling towers structures, and water and wastewater treatment plants applications. The typical volume fraction of fibers for "off-the-shelf" sections is in the range of 40% to 45% which are concentrated in the longitudinal direction (unidirectional). In the recent years, several companies in USA and Europe started to produce more optimized primary

structural shapes with different fiber architectures for buildings and bridges applications *(see Figures 12 and 13).*

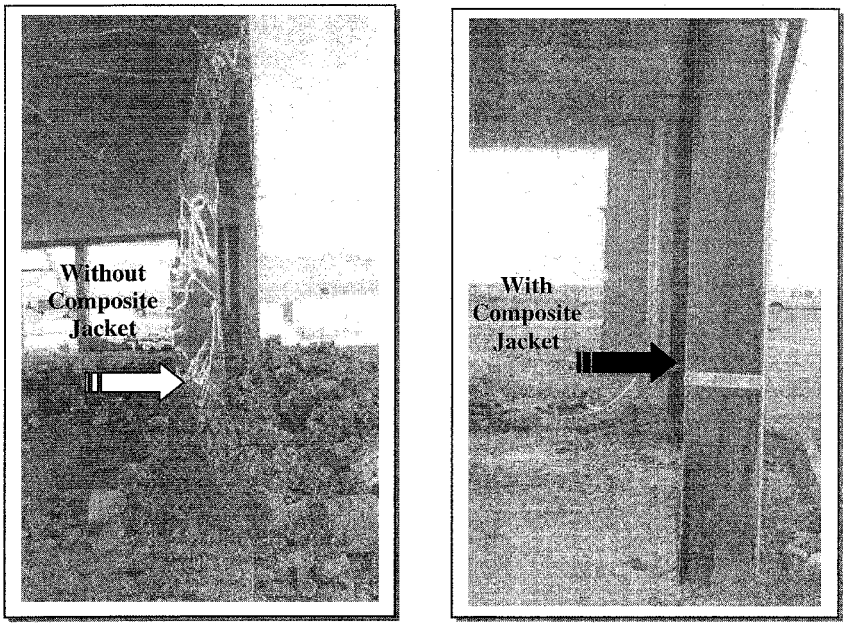


Figure 9: Blast-Resistance Enhancement of Reinforced Concrete Structures
[*Courtesy of SCCI, USA*]

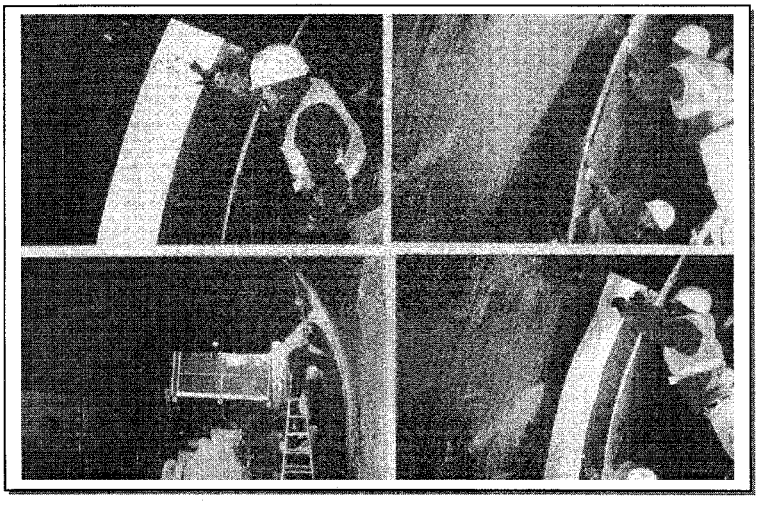


Figure 10: Strengthening of Tunnels Using Polymer Composites
[Source: TONEN Corp., Japan]

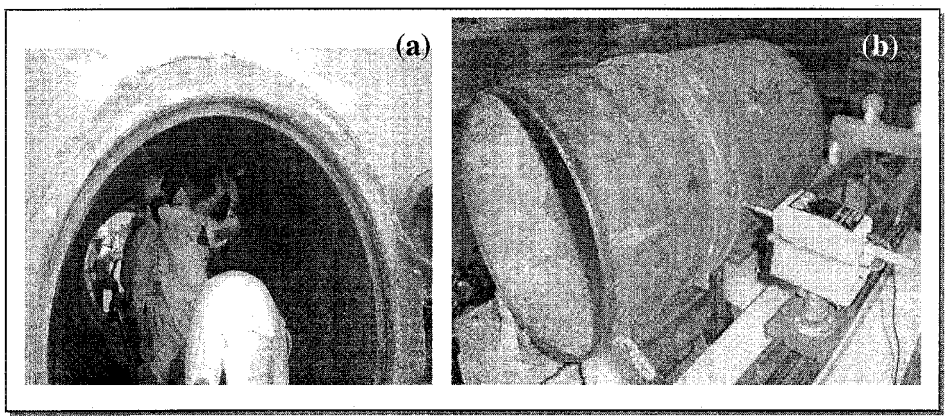


Figure 11: Strengthening of: *(a) Concrete Pipes, (b) Steel Pipes*

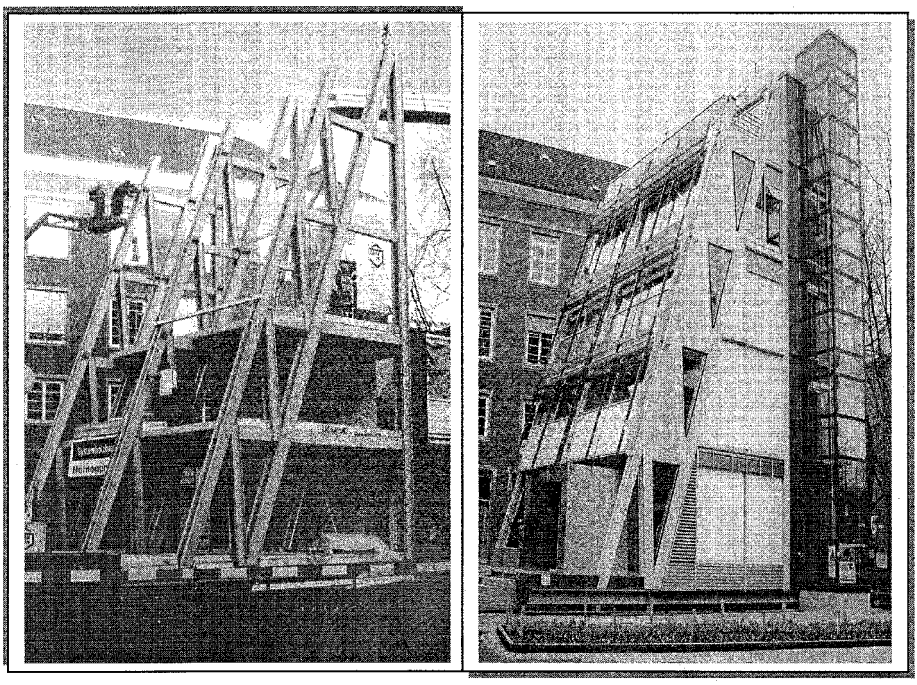


Figure 12: The All-Composite "Eyecatcher" Building in Switzerland
a) Pultruded Frame Skeletons b) The Completed Structure
[Source: Fiberline Composites A/S]

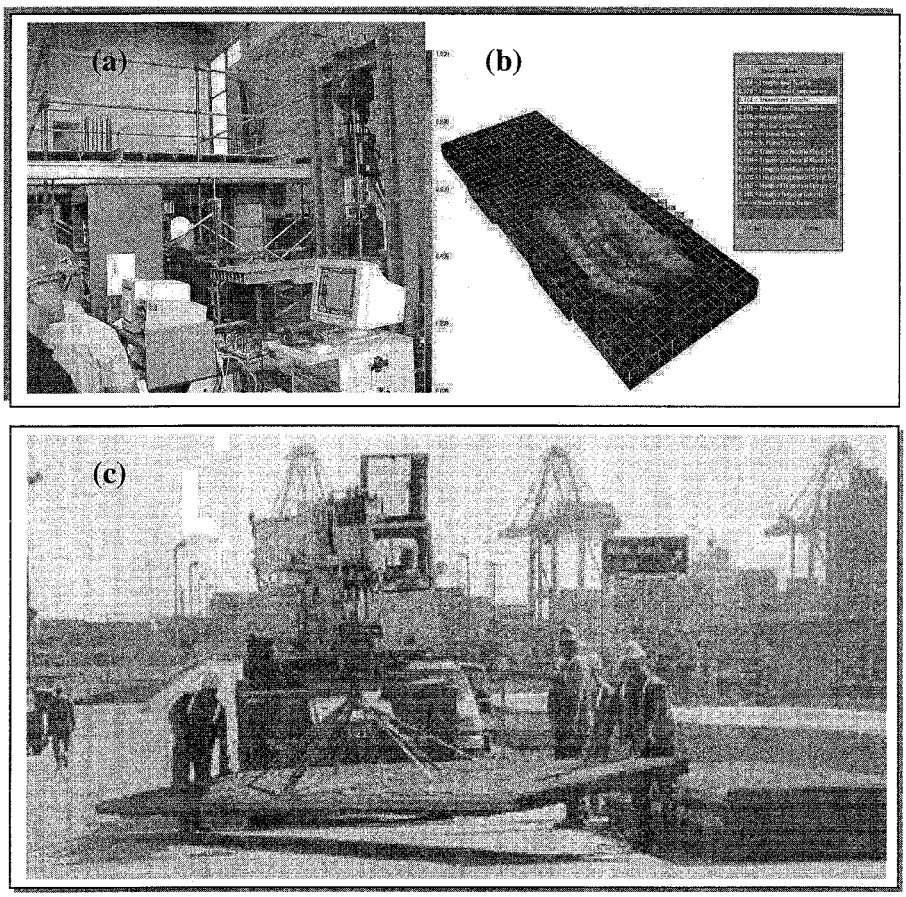


Figure 13: FRP Composites Bridge Deck Evaluation and Application
(a) Full-Scale laboratory Verification, (b) Virtual Testing (GENOA-PFA)
(c) Field Application (The Shuyler Heim Bridge, Long Beach, CA, USA)
[Mosallam and Haroun (2003)]

OTHER APPLICATIONS

FRP composites can also be used as an internal reinforcement for concrete and masonry members. Currently, FRP internal reinforcements are produced in several forms including FRP rebars and grids, and FRP prestressing cables. There are several applications where composites are the preferred choice as internal reinforcement to concrete and masonry, including:

1- *Corrosion environments (e.g. waterfront and marine structures, desalination plants, parking garages and bridges exposed to deicing salts (see Figure 14),*
2- *Structural members of the magnetic resonance imaging (MRI) hospital units, due to the electromagnetic transparency of composites, and*

3-Electrical applications of E-glass composites internal reinforcement due to its non-conductivity properties that contributes in avoiding electrical-related hazards and interference at high voltage environments. (e.g. reinforced concrete power poles, foundations of structural systems in power stations, etc.)

FRP composite rebars are available in standard lengths and diameter, grids. According to ACI 440 (2001), the tensile strength of commercially produced composites rebars varies from 70 to 230 ksi (483 to 1,600 MPa) for GFRP, and from 87 to 535 ksi (600 to 3,690 MPa) for CFRP. The longitudinal modulus of elasticity ranges from 5.1 to 7.4 ksi (35 to 51 GPa) for GFRP, and from 15.9 to 84 ksi (120 to 580 GPa) for CFRP. The ranges for rupture strain for GFRP and CFRP rebars are 1.2 to 3.1%, and 0.5 to 1.7%, respectively.

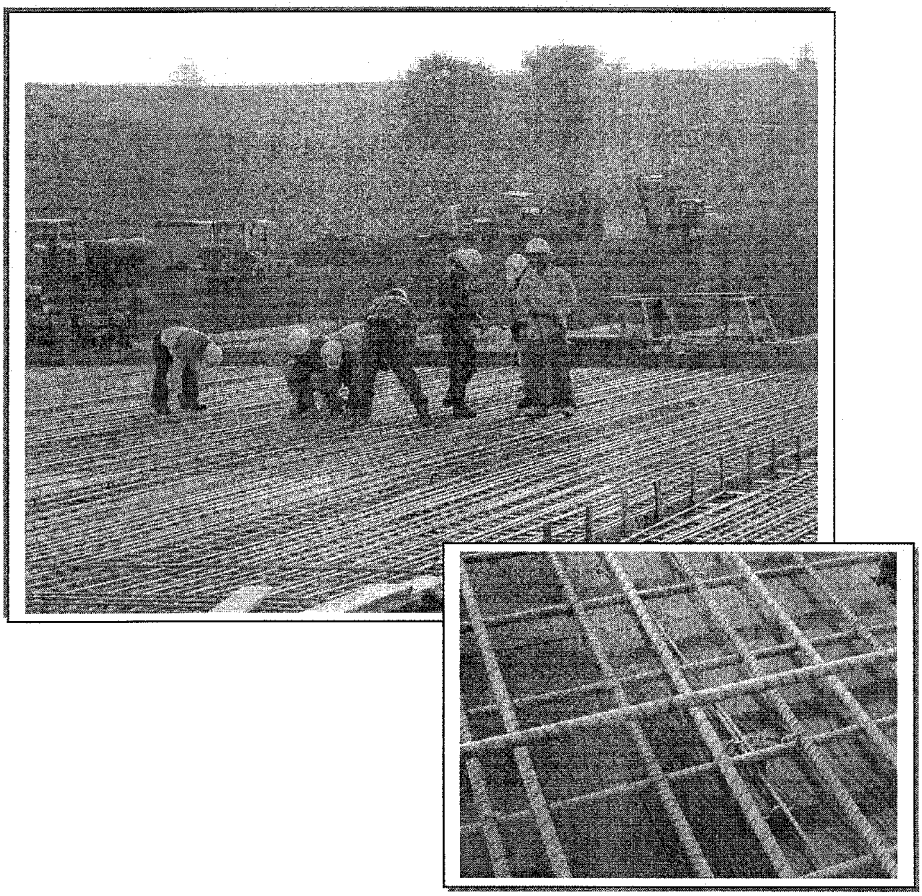


Figure 14: FRP Composite Reinforced Bridge Deck
[Source: Hughes Brothers Company, Canada]

Over the past few years, a number of studies on the durability and long-term performance of frp internal reinforcement were reported (e.g. GangaRao and Vijay (1997), Sen et al. (1998)). The majority of the durability studies concluded the sensitivity of GFRP reinforcing materials to alkaline environment found in fresh concrete. The strength degradation of GFRP rebars can reach values up to 75%, while the stiffness degradation, in many cases, can reach to a value up to 20% (ACI 440 (2002)).

For this reason, it is the author recommendation, to limit the use of GFRP as primary reinforcement in a high pH alkaline environment to low stress level exposure to minimize the possibility of the development of microcracks in the matrix, which open the doors for alkaline attack of the E-glass. Another alternative is using Alkaline-Resistant (AR) glass fibers, although the cost may be higher relative to E-glass fibers. For heavier stress environments, carbon-based composite reinforcements are highly recommended. Again the cost may be the issue, but the reliability in this particular environment is higher.

For a comprehensive coverage of the construction and design aspects of FRP composite internal reinforcement of concrete members, the reader is referred to a recent document published by the American Concrete Institute (ACI 440.1R-02 (2003)).

CODES & STANDARDS DEVELOPMENTS

In the United States, since the early 1990's, several professional organizations have been working in developing standards and design guidelines for the use of composites in construction applications. This includes the pioneering initiatives of the American Society of Civil Engineers (ASCE) through the SCAP Committee, where two design and selection manuals were published in early 1980's, and a recently a new manual, developed by the author (Mosallam (2004)), on design of composite joints (*in press*). The American Concrete Institute (ACI) through the effort of the ACI 440 Committee has been active in developing and publishing state-of-the-art reports and design guides for different concrete-related applications of composites. Both the American Society of Testing Materials (ASTM) and the American Association of State Highway and Transportation Officials (AASHTO) have developed, and in the process of developing, several documents for related to construction applications of FRP composites.

The International Code Council (ICC) has published two valuable documents on strengthening of concrete and masonry structures using FRP composites (AC 125, and AC 178). In the international level, several design and code documents have been published including documents published by the Japanese Concrete Institute (JCI), the Canadian Society of Civil Engineers (CSCE), the European Code (EuroComp), the Swedish Bridge Code, the Australian Industry Code, and recently, an official code of practice for FRP repairs has been developed in Egypt by the Housing and Building Research Center (HBRC) in Egypt.

CONCLUDING REMARKS

As we entered the 21st century, we need advanced construction materials to renew and prolong the service life of our infrastructure. Advanced composites material is one example of high performance materials that can assist the civil engineers to achieve this challenging goal.

REFERENCES

A. S. Mosallam[a] . *Static and Cyclic Behaviors of Steel Girders Strengthened with FRP Composites*, Report No. ST-MULTCO-0103, Submitted to Multnomah County Bridge Section Facility in Portland, Oregon, February 2003.

A. S. Mosallam[b]. *Field Application of FRP Strengthening System For The Sauvie Island Bridge Steel Girders,* APP-MULTCO-10-03, Submitted to Multnomah County Bridge Section Facility in Portland, Oregon, October, 2003.

A. S. Mosallam, *Chapter on Composites in Construction*, Chapter 45, Materials Selection Handbook, Edt. Kutz, John Wiley Publishing Co., NY, USA, 2002), 53 ps.

M. A. Haroun, A. S. Mosallam and K. H. Allam *'In-Plane Shear Behavior of Masonry Walls Strengthened by FRP Laminates'*, 2nd International Workshop on Structural Composites for Infrastructure Applications, NSF/HBRC, Cairo, Egypt, December 17-18, CD ROM, 2003.

A.S. Mosallam. *Design for FRP Composite Connections*, in press, ASCE Manuals and Reports on Engineering Practice #102, American Society of Civil Engineers (ASCE), Virginia, USA, 2004.

A. S. Mosallam, and M.A. Haroun 'Structural Evaluation, Repair and Construction of a Composite Highway Bridge Deck', 2nd International Workshop on Structural Composites for Infrastructure Applications, NSF/HBRC, Cairo, Egypt, December 17-18, CD ROM, 2003.

H.V.S GangaRao and P.V. Vijay. 'Ageing of Structural Composites under Varying Environmental Conditions', Non-Metallic (FRP) Reinforcement for Concrete Structures, FRPRCS-3, V.2, Japan Concrete Institute (JCI), Tokyo, Japan, pp. 91-98, 1997.

R. Sen, M. Shahawy, J. Rosas and S. Sukumar "Durability of Aramid Pretensioned Elements in Marine Environment," ACI Structural Journal, 1998, V. 95, No.5, Sept.-Oct., pp. 578-587.

Guide for the Design and Construction of Concrete Reinforced with FRP Bars. ACI 440.1R-02, American Concrete Institute, Farmington Hills, Michigan, USA, 2003.

Acceptance Criteria for Concrete and Reinforced and Unreinforced Masonry Strengthening Using Fiber-Reinforced Polymer (FRP) Composite Systems, AC 125, ICC Evaluation Services (ICC-ES), Whittier, California, 2003, http://www.icc-es.org

Acceptance Criteria for Inspection and Verification of Concrete and Reinforced and Unreinforced Masonry Strengthening Using Fiber-Reinforced Polymer (FRP) Composite Systems, AC 178, ICC Evaluation Services (ICC-ES), Whittier, California, 2003, http://www.icc-es.org

STATIC AND FATIGUE STRENGTH OF STEEL GIRDERS STRENGHTENED WITH CFRP LAMINATES

Mohammadreza Tavakkolizadeh[1] and Hamid Saadatmanesh[2]
[1] *Jackson State University, Jackson, Mississippi, USA*
[2] *The University of Arizona, Tucson, Arizona, USA*

ABSTRACT

The use of advanced composite materials for rehabilitation of deteriorating infrastructure has been embraced worldwide. Many new techniques have used the lightweight, high strength and the corrosion resistance of fiber reinforced polymers laminates for repair and retrofit applications. Epoxy bonding of Carbon Fiber Reinforced Polymers (CFRP) sheets to the tension area of steel girders improves the ultimate load carrying capacity and stiffness of the member while reducing the stresses and extending the fatigue life. CFRP laminates can be incorporated in design of new structures as well as for repair of damaged structures. Several experimental studies of single span steel and composite girders strengthened and repaired with CFRP laminates have been conducted during the past decade. This paper presents the summary of the result of those studies.

INTRODUCTION

In the last few years, the use of Fiber Reinforced Polymers (FRP) for strengthening and repair of the structures has become very popular. Several studies have addressed the effectiveness of epoxy bonded FRP sheets to the concrete and masonry structures in order to increase their ultimate load carrying capacity, stiffness and in some cases even ductility[1]. These techniques have become very popular with structural engineers and practitioners in recent years. Because of the relatively low stiffness of the concrete, wood or masonry compared to Glass Fiber Reinforced Polymers (GFRP), they have become the materials of choice in the civil engineering field. The comparatively lower cost of these composites compared to carbon based composites initially resulted in more applications of GFRPs. However, GFRPs are sensitive to alkaline environments could deteriorate with time if not properly protected. In the last few years the Carbon Fiber Reinforced Polymers (CFRP) have become readily available and used more in repair and retrofit applications. The higher strength and stiffness in addition to their excellent resistance to aggressive environments were the primary reasons for that trend.

In case of strengthening of steel girders with FRP plates, the low modulus material will not be effective and only the utilization of high strength and high modulus carbon based composite would be practical. A few researchers have investigated the feasibility of using CFRP for repair and strengthening steel girders and the results indicted that the method can be very effective. The main concerns, however, has been the possibility of galvanic corrosion between the two dissimilar materials (carbon and steel). The concern was addressed by a study conducted at The University of Arizona[2].

Steel-concrete-CFRP composite girders or composite girders strengthened with CFRP plates have performed satisfactorily in large-scale tests conducted over the past decade. In two different studies conducted at the University of South Florida[3] and the University of Delaware[4] the effectiveness of this technique was examined. The result was very promising. They reported a significant increase in load carrying capacity and stiffness after yielding for steel-concrete composite girders retrofitted with CFRP plates.

No study on the fatigue behavior of steel beam retrofitted with epoxy bonded CFRP was found in the literature. However, in a study conducted at the University of Maryland[5], adhesive bonding and end bolting of steel cover plates to steel girders provided a substantial improvement in the fatigue life of the system. They reported an increase in the fatigue life of more than twenty times, compared to the welded cover plates.

EXPERIMENTAL STUDIES

The feasibility and effectiveness of epoxy bonding of CFRP sheets on improving the ultimate load carrying capacity of steel girders[6], restoring the lost ultimate load carrying capacity and stiffness of damages steel beams[7] and girders[8], and improving fatigue strength of steel beams[9] were examined by testing a number of small-scale steel beams and large–scale composite girders at the University of Arizona.

Materials

Tack Coat: A two-component viscous epoxy was used for bonding the laminate to the steel flange surface. The tack coat had a pot life of 30 minutes at room temperature and was fully cured after 2 days at 25°C. This epoxy immediately reached high tack consistency and was ideal for over-head applications.
Epoxy: A two-component less viscous epoxy was used for bonding the laminates to each other. The epoxy had a pot life of 1 hour at room temperature and was fully cured after 7 days at 25°C. This epoxy had a longer gel time and much lower viscosity and was used in between CFRP sheets to insure the least entrapped voids.
CFRP: A unidirectional pultruded carbon fiber sheet with width of 76 mm and thickness of 1.27 mm was used. An average tensile strength of 2137 MPa, tensile modulus of elasticity of 144.0 GPa and Poisson's ratio of 0.34 were obtained by uniaxial tension test.
Steel: W355×13.6 and S127×4.5 A36 hot rolled sections were used for the experiments. Average yield strengths of 368.4 and 333.65 MPa, moduli of elasticity of 187.9 and 197.1GPa and Poisson's ratios of 0.302 and 0.303 were obtained from the W sections and S sections, respectively.
Concrete: Concrete was ordered from a ready mix plant with slump of 100 mm and maximum aggregate size of 10 mm. Twelve 75×150 mm cylinders were made were tested under uniaxial compression right before the beam tests.

Strengthening

The effectiveness of epoxy bonding of CFRP sheets on improving the ultimate load carrying capacity of composite girders was examined by testing three large-scale girders strengthened with pultruded carbon fiber sheets. In order to observe the effectiveness of this technique, three different thicknesses of CFRP laminates were considered. Identical girders were strengthened with 1, 3 and 5 layers of CFRP sheets. The overall lengths of CFRP sheets were identical and cut-off points for each layer were staggered to prevent premature failure at termination points due to stress concentration[10].

Four point bending tests were performed using a 2,200 kN test frame. Loading was applied by an MTS-244.41 hydraulic actuator and Enerpac-RRH10011 hydraulic jack with capacities of 500 kN and 1,000 kN, respectively. The Enerpac had to be used since the capacity of the MTS actuator was limited to 500 kN. The load was measured by two MTS-

661.23A-02 load cells with a capacity of 500 kN and the deflection was measured by a DUNCAN 600 series transducer with a range of ±75 mm. Monotonic loading was performed under actuator displacement control with a rate of 0.025 mm/sec. A total of three unloadings were carried out during each test; before steel yielded, after steel yielded and at 500 kN load level. The load, midspan deflection and strains at different points were recorded with a Daytronic System 10 data acquisition system interfacing with PC through Microsoft Excel software. The clear span was 4.78 m and the loading points were 0.5 m apart as shown in Figure 1. The loading points and supports were made using rolling blocks, and one sphere blockhead was used to transfer the load from the hydraulic jack to the spreader beam.

Three composite girders tested in the present study were retrofitted by epoxy bonding of 1, 3 and 5 layers of CFRP sheets to the entire length of their tension flanges. They were subjected to monotonic loading with a constant rate of loading of around 2 mm/min with few unloadings in the elastic and the post-elastic regions. In the elastic region, data were collected at specified load levels, and after yielding, they were collected at specified deflection levels. The concrete slab supported the compression flange of the steel beam and there was not any local or lateral buckling in the flange of girders before compression failure. The shear studs provided a good composite action between concrete slabs and steel beams without any slippage. The wooden blocks that supported the web under the loading points and at the reactions, prevented any web crippling. The load-deflection plots for the retrofitted composite girders are shown in Figures 2 through 4.

Retrofitting with One Layer of CFRP Sheet: The load-deflection behavior of this girder is shown in Figure 2 with heavy solid line. At the beginning of the experiment, there was a slight non-linearity in the response due to transverse shrinkage cracks in the slab. An unloading at the 200 kN load level exhibited no permanent deformation or nonlinear behavior and traced back the initial plot closely. The extreme fiber of the tension flange yielded at a load of 272.6 kN. At this load level, the stress in the CFRP sheet was 202.3 MPa. Thereafter, the stiffness of the girders gradually decreased and the curve became progressively nonlinear while yielding proceeded through the flange and into the web.

Beyond 355 kN load level, several longitudinal cracks in the concrete slab and along the edges of the flange started to appear. The unloading loops at levels of 400 kN and 500 kN displayed a slight hysteresis especially for the second unloading. The girder failed with crushing of the concrete slab at 528.0 kN. The CFRP stress at the failure was about 1589.8 MPa the values of about 75% of CFRP ultimate strength. Just before failure, the edges of the CFRP sheet started to show signs of rupture as a few strands snapped.

Retrofitting with Three Layers of CFRP Sheets: The heavy solid line represents the load-deflection behavior of this retrofitted girder in Figure 3. The load-deflection behavior of the beam started fairly linear and the unloading in the elastic region at 200 kN load level displayed no permanent deformation. At a load of 275.8 kN, the tension flange started to yield and the stress in the CFRP sheet reached 192.5 MPa. Afterward, the stiffness of the girders constantly decreased and the curve became continuously nonlinear.

Several longitudinal cracks in the concrete slab along the edges of the top flange of steel beam started to appear at 400 kN load level. At a load level of 475 kN, a complete unloading and reloading was performed. A slight hysteresis was observed during the loop. The girder failed prematurely by debonding of the last two layers of the CFRP sheets from the first sheet at 553.4 kN load level. The stress at the CFRP sheet was about 901.2 MPa well below its ultimate strength (42%). Partially cured tack coat used

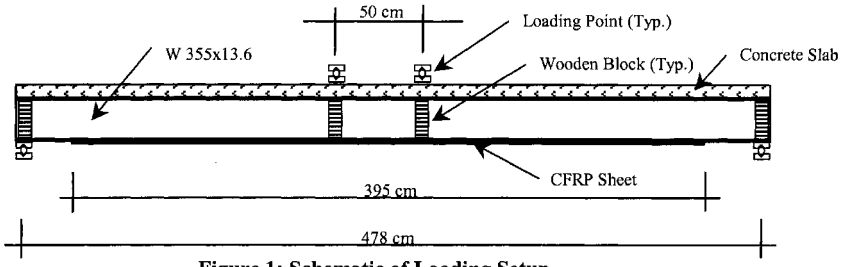


Figure 1: Schematic of Loading Setup

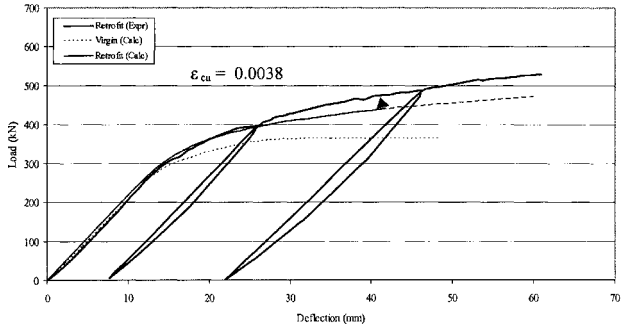


Figure 2: Load vs. Deflection of the Girder Retrofitted with One Layer of CFRP Sheet

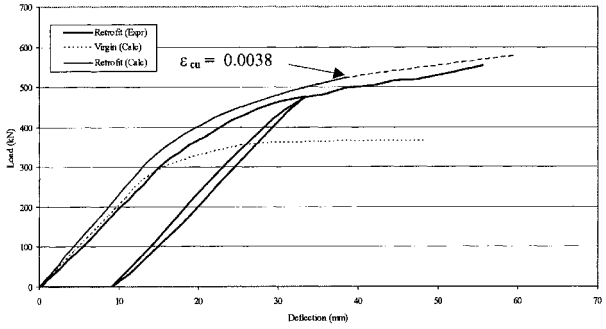


Figure 3: Load vs. Deflection of the Girder Retrofitted with Three Layers of CFRP Sheet

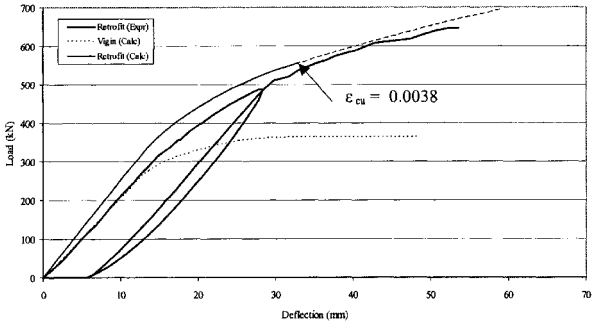


Figure 4: Load vs. Deflection of the Girder Retrofitted with Five Layers of CFRP Sheet

between the CFRP sheets was the cause of failure.

Retrofitting with Five Layers of CFRP Sheets: The issue of premature failure of 3-layer retrofitted girder was corrected for this specimen. The CFRP sheets were sand blasted harsher to expose the carbon fibers and the lower viscosity epoxy, was mixed well used in between layers. The tack coat was mixed thoroughly and only used to attach the 5-layer CFRP laminate to the steel flange.

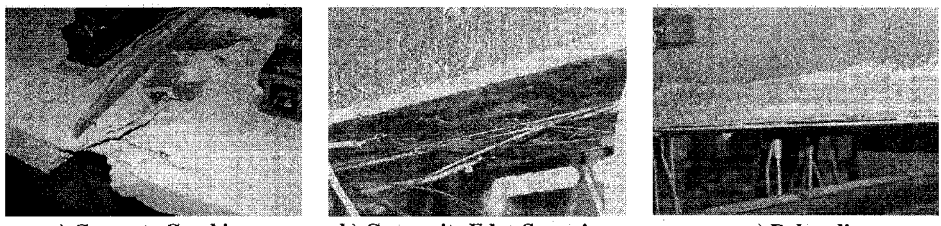
The load-deflection behavior of the retrofitted girder is shown in Figure 4 with heavy solid line. The initial non-linearity due to the transverse cracks in concrete slab existed in this girder as well. The cracks were closed at 100 kN load level and the beam started to show a higher stiffness of 21.99 MN/m compare to 19.61 MN/m as for the beginning. Elastic unloading after reaching 200 kN load level showed no permanent deformation or hysteresis effects. The yielding of the tension flange started after reaching a load of 279.1 kN. The CFRP sheet was experiencing a tensile stress of 184.9 MPa at that point. After yielding of the steel started, the stiffness of the girder gradually decreased and yielding extended to the web as well as the rest of the flange.

Several longitudinal cracks similar to those in previous beams appeared after reaching the 425N load level. These cracks started to grow and widen significantly as loading increased. A complete unloading and reloading conducted around 475 kN load level displayed a modest hysteresis very similar to that in previous girders. The girder failed with crushing of the concrete slab and progressive debonding of the slab from the steel beam at one end due to the excessive widening of longitudinal cracks at 645.8 kN. The CFRP stress at the failure was about 903.7 MPa, which is far below its ultimate strength (42%). The shear plains in the tension flange and web of the steel beams were clearly visible toward the end of the experiments. After concrete failure, the compression flange of the steel beam started to buckle due to disintegration of supporting slab.

Effect of the Retrofitting on Stress and Strain Reduction: Increasing the cross sectional area of the section could reduce the stress level in tension flange of a girder. The tensile modulus of the CFRP sheets was about 2/3 of the modulus of steel and the thicknesses of these sheets were moderately small. The adhesive layer that connected the two materials was relatively soft. Therefore, not a significant improvement in the stiffness of the girder in the elastic region was anticipated. The 5-layer system displayed the most reduction in stress with an average reduction of 13.7 MPa compared to the other two retrofitting systems. After yielding, the effectiveness of the CFRP laminates was much more profound. Tensile strains in the tension flanges of the retrofitted composite girders decreased significantly. The tensile strain in the flange decreased with an average of 20.6, 39.2 and 52.6 % for 1, 3 and 5 layer systems compared to the virgin girder at 350 kN. For higher load levels, the effectiveness of the retrofitting was apparent. The significant improvement could limit the permanent deformation of the girders experiencing unexpected and sudden overload.

Failure Modes: The steel-concrete-CFRP system could display several distinct failure modes including: concrete crushing, CFRP debonding, CFRP rupture, web crippling and shear stud failure. Meanwhile, the wooden blocks placed between the flanges at support, and under loading points prevented web crippling. Shear studs were designed for a slab with 35 MPa compressive strength.

Compression crushing of concrete (Figure 5-a) was the dominating failure mode in all three retrofitted girders. In the one-layer system, the concrete failure happened when the CFRP sheets started to show sign of failure by snapping along their edges (Figure 5-b). In the three-layer system, the debonding of the CFRP sheet (Figure 5-c) caused a



a) Concrete Crushing b) Composite Edge Snapping c) Debonding

Figure 5: Failure Modes

premature failure. The five-layer system did not display any premature failure and, again the compression crushing of concrete became the failure mode of that girder.

Repair

The feasibility of epoxy bonding of CFRP sheets on restoring the ultimate load carrying capacity and stiffness of composite girders was examined by testing three large-scale girders repaired with pultruded carbon fiber sheets. In order to observe the effectiveness of this technique, three different damage levels of 25, 50 and 100 % loss of tension flange were considered and different thicknesses of CFRP laminates were used. The tension flanges of the girders were cut with different total depths of 43, 86 and 171 mm to simulate 25, 50 and 100% loss of tension flange, respectively. These girders were then strengthened by epoxy bonding of 1, 3 and 5 layers of CFRP sheets to the bottom surface of tension flange. Concrete slabs with two different compressive strengths were used. The cut-off points for each layer were staggered to prevent premature failure at termination points due to stress concentrations.

Four-point bending tests were performed with similar descriptions as mentioned in the previous section. All three girders were subjected to monotonic loading with few unloading cycles. The loading was applied under displacement control regime with the constant rate of 0.025 mm/s. The specimens were designed for failure under concrete crushing, but other possible modes of failures that could occur were CFRP sheet rupturing, CFRP sheet debonding, flange local buckling and web crippling. The load-deflection plots for the repaired composite girders are shown in Figures 6 through 8.

Girder with 25% Flange Damage, Repaired with One Layer of CFRP Sheets: The load-deflection behavior of the first repaired composite girder is shown in Figure 6. The concrete slab had an average compressive strength of 29.1 MPa. The girder showed a fairly linear response to the load from the beginning. During the unloading cycle in the elastic region (not shown), no sign of permanent deformation and non-linearity was observed. The elastic stiffness of the girder was 19.6 kN/mm. The bottom flange of the girder started to yield at 166.6 kN load level. The CFRP sheet was under tensile stress of 170.3 MPa equal to 8% of its ultimate strength at that point. Proceeding in to post-elastic region, the girder was twice unloaded and reloaded. At the 449.5 kN load level, the CFRP sheet started to show signs of failure (i.e. snapping of the edge fibers) while it was carrying 2045 MPa, equal to 96% of its tensile strength. The girder failed at a 471.8 kN and an ultimate deflection of 49 mm. The ultimate tensile stress in CFRP was 2298.0 MPa, 7.5% above its average tensile strength. Ultimate compressive strain in the top of the concrete slab reached 0.0018, which is very close the peak strain value. A few longitudinal cracks were observed in the concrete slab but they did not have any effect on the result due to their limited width. At the midspan, between two loading points, the web and flanges displayed clear shear plane due to yielding but there was no

buckling and crippling. In other words, the concrete slab and wooden blocks stayed effective in supporting the compression flange and web up to the failure.

Girder with 50% Flange Damage, Repaired with Three Layers of CFRP Sheets: The concrete slab of the second specimen had a compressive strength of 16.6 MPa. The lower strength concrete was used to change the mode of failure to over-reinforced compression crushing of concrete. As shown in Figure 7, the load deflection response of the composite girder was initially linear with a slight curve due to transverse cracks (shrinkage). The stiffness of the girder in the elastic region was 20.4 kN/mm. The unloading and reloading in the elastic region did not show any permanent deformation or hysteresis. The behavior continued to be linear until the tension flange of the girder reached its yielding strain at 136.5 kN. The CFRP sheet was under a small tensile stress of 71 MPa equal to 3.5% of its strength. Continuing loading of the girder into its post-elastic regime, two unloading and reloading cycles were performed. While both cycles showed slight amount of hysteresis, the energy dissipation in the second cycle was more pronounced. Debonding of the CFRP sheet from the steel girder in the midspan at the cut location (20 mm on each side) started at the load of 480 kN. The lower stiffness in the second and third cycles was due to softening of the concrete and development of longitudinal cracks in the slab, which started to appear at the 475 kN load level. The longitudinal cracks in the slab started to widen at 530 kN and became expanded at 580 kN. The debonding in the midspan grew to 45 and 70 mm on each side of the cut at load levels of 600 and 660 kN, respectively. The concrete slab of the composite girder was almost divided into three longitudinal strips (along the edges of compression flange) at the ultimate load of 658.5 kN, when the girder deflected 74.3 mm. The tensile stress in CFRP sheet was 1606 MPa, equivalent to 75% of its strength. The concrete slab was under a strain of 0.0029 and clearly failed in compression. The continuation of the loading was terminated due to buckling and crippling of the compression flange and web after disintegration of the slab. Tensile stress in CFRP sheets went up to 1748 MPa before termination of the experiment. Overall, the repair was successful and the ultimate deflection of the girder was 1.5% of the clear span.

Girder with 100% Flange Damage, Repaired with Five Layers of CFRP Sheets: This specimen was build of the concrete slab with a compressive strength of 29.1 MPa. The load-deflection behavior of the repaired girder is shown in Figure 8. The girder started carrying the load with a fairly linear response. The elastic stiffness of the girder was 19.9 kN/mm and during the elastic unloading (not shown) there was not any sign of permanent deformation or stiffness change. The linear response continued up to the 162.2 kN load level at which an extrapolated prediction of the strain at the bottom face of the tension flange reached the yielding strain. The CFRP sheet stress was 194.4 MPa equal to 9% of its ultimate strength. Continuing loading, the longitudinal cracks appeared at 287 kN and a complete unloading and reloading was performed at 300 kN. There was minimal hysteresis in the loop and the loop closed out at the point that unloading had started. The reloading stiffness was 20.1 kN/mm very similar to the stiffness at the initial loading. After reaching the load level of 311 kN, plate started to debond from the steel girder at the cut location in the midspan. Approaching the load level of 380 kN, the failure signs of the CFRP ends were noticed. The girder failed at the load level of 434 kN, due to sudden and complete debonding of the CFRP sheets (initiated from the end) and subsequently the rupture of steel web and failure of concrete. At the peak load, the CFRP laminate was carrying 840.1 MPa tensile stress equal to 40% of its strength and concrete strain was 0.0016 well below its failure point.

Effectiveness of the Proposed Technique: After analyzing the experimental results of repaired composite girders repaired with CFRP sheets, a comparison was made with the

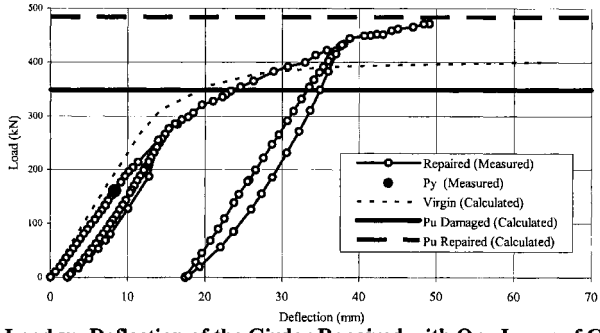


Figure 6: Load vs. Deflection of the Girder Repaired with One Layer of CFRP Sheet

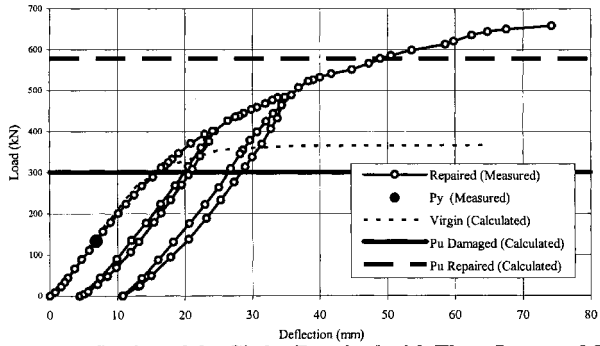


Figure 7: Load vs. Deflection of the Girder Repaired with Three Layers of CFRP Sheets

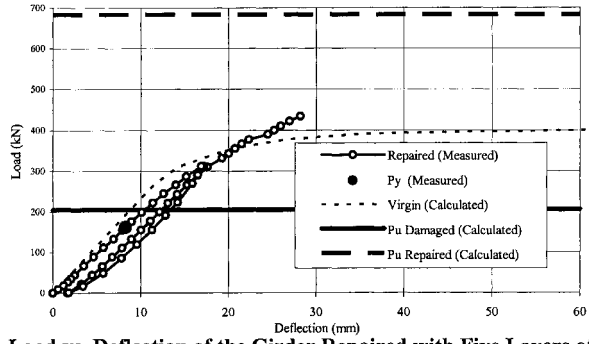
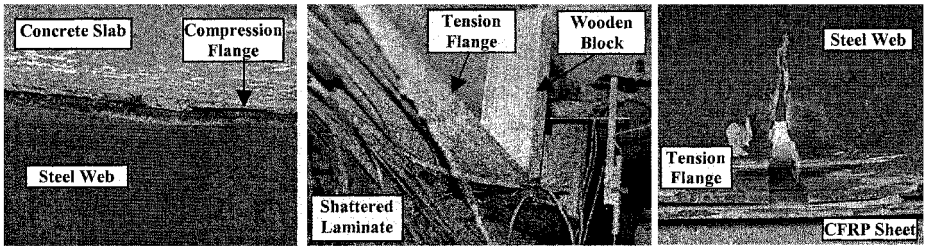


Figure 8: Load vs. Deflection of the Girder Repaired with Five Layers of CFRP Sheets



a) Flange Instability **b) Ruptured Sheet** **c) Web Rupture**

Figure 9: Failure Modes

theoretical values obtained with the incremental deformation method. The load carrying capacities of virgin and retrofitted girders were calculated for concrete slab with compressive strengths of 29.1 and 16.6 MPa and tabulated in Table 1. Three repaired girders were able to carry ultimate loads higher than the calculated values for the virgin specimens. The girder with 25% loss and 1 layer of CFRP displayed 19.1%, while the girder with 100% loss and 5 layers of CFRP showed 9.6% increase. The girder with 50% loss and 3 layers of CFRP, which was made with the concrete slab with lower strength, demonstrated 80.2 % increase.

The predicted values for the elastic stiffnesses of the virgin composite girders made with 29.1 MPa compressive strength concrete was 23.1 kN/mm. The repair technique was not able to recover the loss of the stiffness completely for two girders with higher compressive strength concrete. Average stiffness of the girders were 21.0 (-8.9%) and 20.0 kN/mm (-13.5%) for 25 and 100% loss of flange, respectively. The repaired girder with lower compressive strength (50% loss) recovered the lost stiffness due to the damage completely and displayed the stiffness of 196.7 kN/cm compared to the predicted value of 19.2 kN/mm (+2.4%). Table 2 summarizes the experimental and theoretical values of the stiffnesses of the virgin and repaired girders.

Failure Modes: Crushing of concrete was the dominating failure mode for the girder with 50% loss of its tension flange that was repaired with three layers of CFRP sheets. The CFRP sheets forced the slab to carry the maximum compressive strain of beyond 0.29% before failure. Meanwhile, the extent of damage to the slab and widening of longitudinal cracks after failure allowed the flange and web to buckle (Figure 9-a).

The tension rupture of CFRP sheets (Figure 9-b) was the distinct mode of failure for composite girder with the 25% loss of tension flange area that was repaired with one layer of CFRP sheet. The slab supported the compression flange and prevented buckling despite developing a few longitudinal cracks along the edges of the compression flange. The rupture of the CFRP sheet was sudden and there was no sign of bond failure between CFRP sheet and the steel flange. The concrete slab barely reached its peak strength. The failure of the bond between CFRP laminate and steel flange was the mode of failure in the girder with 100% loss of tension flange, repaired with 5 layers of CFRP sheets. Failure progressed quickly from the first sign of debonding at the cut in the midspan (72% of failure load) to the progressive sign of debonding at the end of the sheets (88% of failure load) and eventually the complete failure. The web of the girder ruptured at the same time as the CFRP sheets debonded (Figure 9-c). The compressive strain in concrete was 0.16%, well below its capacity.

Fatigue

The effectiveness of CFRP sheets on improving fatigue strength of steel girders was examined by testing a number of small-scale steel beams strengthened with pultruded carbon fiber sheets. In order to create a fatigue sensitive detail, tension flanges of steel beams were cut to create a notch on each side. The CFRP patches with identical lengths were then bonded on to the cut sections. Different stress ranges of 69 to 379 MPa were considered in the study.

The four point bending tests were performed using an MTS-810 testing machine. A special bending fixture was constructed to allow the placement of beam specimens in the testing machine. The load was measured by an MTS-661.31E-01 load cell with capacity of 2000 kN and the deflection was measured by a DUNCAN 600 series transducer with a range of ±75 mm. The clear span was 1.22 m and the loading points were 200 mm apart. In order to prevent any movement of the specimen during the

Table 1: Calculated and Experimental Load Carrying Capacity of Virgin and Repaired Girders

Repair Techniques [Concrete Strength]	Measured (kN)	Calculated (kN)	Virgin Calculated (kN)
25% loss & 1 Layer [f_c'= 29.1 MPa]	471.8	484.1	396.2
50% loss & 3 Layers [f_c'= 16.6 MPa]	658.5	578.3	365.4
100% loss & 5 Layers [f_c'= 29.1 MPa]	434.0	683.5	396.2

Table 2: Calculated and Experimental Stiffnesses of Virgin and Repaired Girders

Repair Techniques	Measured Stiffness kN/mm		Calculated Stiffness (Virgin) kN/mm	
	Elastic	Post-elastic	Elastic	Post-elastic
25% Loss & 1 Layer	21.0	6.7	23.1	0.3
50% Loss & 3 Layers	19.7	4.6	19.2	0.2
100% Loss & 5 Layers	20.0	10.1	23.1	0.3

experiments, two ends of the beam were tied down to the roller supports using two steel brackets. The loading blocks were designed with a counter seat for the compression flange to prevent their movement during the experiment.

A total of fifteen unretrofitted specimens and six retrofitted specimens were tested under different stress range cycles (R=0.1). The Cyclic loading was performed under load control mode for nine different stress ranges. Loading was applied in consecutive half-sine shape segments with a frequency of 5 to 10 Hz. Retrofitting system under this frequency range did not illustrate any noticeable increase in temperature that could affect the bond or properties of the epoxy. The initiation and growth of cracks was monitored using a magnifying glass and the length of the crack for specified number of cycles was recorded. In order to facilitate the observation, a permanent marker and acetone were used periodically as a penetrating dye. The test stopped when the growth of the crack caused excessive midspan deflection of 5 mm or more, compared to the initial elastic deflection. The data points obtained in this study for unretrofitted and retrofitted specimens are also plotted in Figure 10.

Unretrofitted Beams: In order to establish a reliable set of control data, seven pairs of unretrofitted beams were subjected to constant stress range cycles of 138, 172, 207, 241, 276, 310 and 345 MPa. One unretrofitted beam was subjected to the stress range of 69 MPa also. Among all of the unretrofitted specimens, only two specimens at stress ranges of 69 and 138 MPa did not fail before 1,200,000 cycles as shown in Figure 6 with solid circles (under cycled).

A linear regression of the data points, not containing the run-out, resulted in the mean S-N line with a coefficient of regression of 0.980. Using reliability techniques, 95% confidence level for 95% survival was used for establishing the design line.

$$\text{Mean: } \log S = 13.260 - 0.282 \log N \;\&\; \text{Design: } \log S = 13.086 - 0.282 \log N$$

The slopes of the lines (1 / [-3.54] = -0.282) were less steep as compared to the AASHTO curves Category C and D with the slopes of -0.308 and -0.326, respectively. The smaller slope suggested longer fatigue life especially under high cycle fatigue. Researchers have shown that the results of small-scale testing overestimate the fatigue strength of beams[11].

The crack initiation and propagation in all unretrofitted specimens were similar. The crack always initiated from the tip of one of the cuts. Then, the crack started to

move toward the near web/flange junction. After reaching the top of the near fillet section of the web, it continued to go up on the near side of the web while the crack front was still growing horizontally to reach the far side of the web. In a few remaining cycles of the beam, the crack grew to reach the tip of the opposite cut. The shear failure occurred at the last moment in the far cut tip and caused complete failure of the flange and further rupture of the web until the deflection limit was violated and the experiment was stopped. A typical failed specimen is shown in Figure 11.

Figure 12 displays a plot of the crack length vs. number of cycles after crack initiation. For crack length of less than 20 mm, the specimens exhibited a stable crack growth (constant crack growth rate) under various stress ranges. The stable crack growth rates were established by linear interpolation of data the points. The rates of 0.52, 0.62, 1.15,1.23 and 2.09 μm/cycle for the stress ranges of 207, 241, 276, 310 and 345 MPa were obtained. The number of cycles and the crack length in which stiffness decay was apparent are displayed with solid circles (stiffness drop). The decrease in the stiffness in all of the specimens was detected when the crack length was between 13 and 15 mm.

Retrofitted Beams: After close consideration of the test results of unretrofitted specimens, it was decided to conduct the fatigue test of retrofitted beams under higher stress ranges. The three lower stress ranges were eliminated, and the stress range of 379 MPa was added. Therefore, a total of six retrofitted beams were subjected to constant stress range cycles of 207, 241, 276, 310, 345 and 379 MPa. As a result, there was not any under cycled specimen in this group.

Similar to unretrofitted beams, the design curve for retrofitted beams was established and their respective equations are as follows:

$$\text{Mean: } \log S = 14.765 - 0.253 \log \quad \& \quad \text{Design: } \log S = 14.584 - 0.253 \log N$$

The slope of these lines (1/ [-3.96] = -0.253) was smaller than the slope of the unretrofitted lines (-0.282) and the lines were also less steep as compared to the AASHTO curves Category B and C with the slopes of -0.297 and –0.308, respectively.

The crack initiation and propagation in all retrofitted beams were similar, but different from those of unretrofitted specimens. The crack always initiated from the tip of one of the cuts. The crack then started to move toward the web. After reaching the fillet section of the web, debonding at the near edge of the CFRP sheet started. While crack front moved to the far side, the debonding at the edge continued to grow. Even after crack front reached the far cut tip, the debonding remained fairly stable (constant rate of debonding). At this stage, the far edge of the CFRP sheet started to debond. Except for the 207 MPa stress range, the failure of the sheet happened after approximately 50 mm of debonding on each side of the notch on both edges. A typical failed specimen is shown in Figure 11.

During the experiments, for monitoring the crack growth, the same crack lengths as those for unretrofitted specimens were considered and the number of cycles for reaching those specified lengths were recorded for different stress ranges. Linear extrapolations similar to the previous section resulted in an estimate of the number of cycles for the crack initiation. Figure 13 displays the relationship between the crack length and the number of cycles after crack initiation. The stable crack growth rates were established by linear interpolation of data points in the initial stage where crack growth rate is constant. These rates were 0.12, 0.20, 0.41, 0.50, 0.72 and 0.89 μm/cycle for the stress ranges of 207, 241, 276, 310, 345 and 379 MPa, respectively. These growth rates were 25% to 40% of the growth rate for unretrofitted beams. After comparing the result of

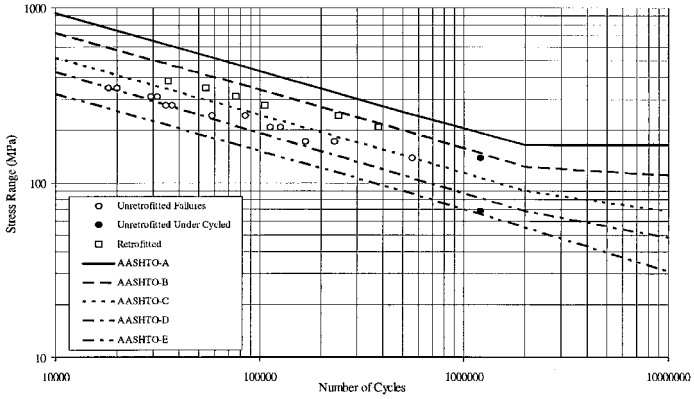


Figure 10: S-N Plot for All the Data Points and AASHTO Categories

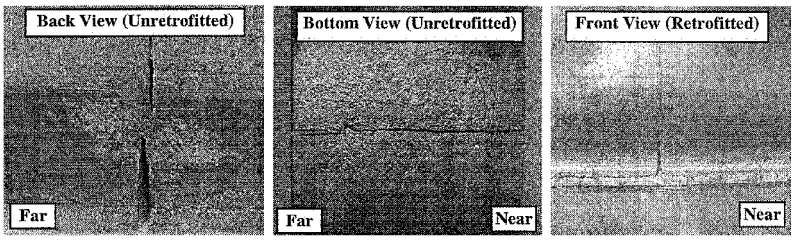


Figure 11: Typical Failure of Unretrofitted and Retrofitted Beams

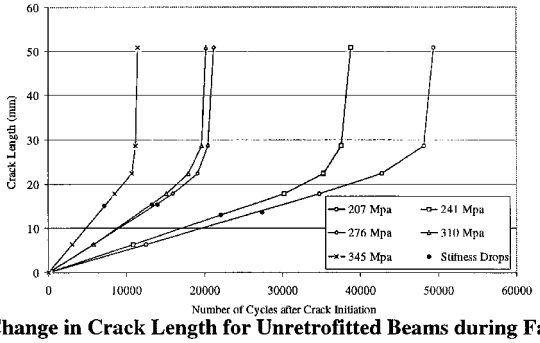


Figure 12: Change in Crack Length for Unretrofitted Beams during Fatigue Tests

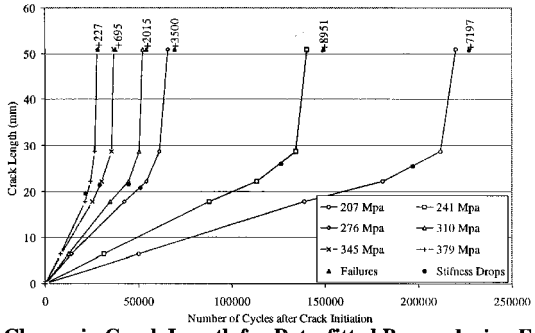


Figure 13: Change in Crack Length for Retrofitted Beams during Fatigue Tests

retrofitted beams to those for unretrofitted beams, the benefits of patching in limiting the crack growth was observed. The number of cycles between crack initiation and complete loss of tension flange increased by factors of 4.5, 3.6, 3.1, 2.5 and 3.2 for the stress ranges of 207, 241, 276, 310 and 345 MPa, respectively.

Similar to unretrofitted specimens, for crack lengths less than 20 mm, the specimens exhibited a stable crack growth under various stress ranges. Solid circles shown in Figure 13 are representing the beginning of apparent stiffness drop. The decrease in the stiffness for four higher stress ranges began when the crack length was between 19 to 21 mm (crack front between near fillet and near web). For the two lower stress ranges, only after the crack lengths reached 25 to 27 mm (crack front started to grow up in the near web), the stiffness of the beam started to decrease. The numbers of cycles to which the specimens failed are shown in Figure 13 by solid triangles. The numbers next to the solid triangles indicate additional cycles after the complete loss of the tension flange. The effect of patches in extending the fatigue life of the beams beyond the total tension flange loss was more pronounced in the lower stress ranges.

CONCLUSIONS

Test results of retrofitting intact, damaged and notched steel beams by epoxy bonding of CFRP laminates for static and fatigue loadings are very promising. Based on the results of the experimental investigation, the following conclusions are drawn:

Strengthening:

1. Ultimate load carrying capacities of the girders significantly increased by 44%, 51% and 76% for 1-layer, 3-layer and 5-layer retrofitting systems. In addition, the yield load of the girders continuously increased as a result of retrofitting (272.6, 275.8 and 279.1 % kN for 1, 3 and 5 layer system).
2. The effect of CFRP bonding on the elastic stiffness of the girders was not significant, due to the flexibility of adhesive.
3. While, the analytical models indicated that the ductility of the retrofitted system was less then the virgin girders, all three retrofitted girders deflected between 50 ~ 60 mm which is about 1/100 ~ 1/80 of the clear span.
4. The effect of retrofitting on the stress level in the tension flange in the elastic region was insignificant (5% difference between 1 and 5 layer system at 200 kN). While in the post-elastic region, the significant reduction in tensile strain was observed (21, 39 and 53 % for 1, 3, and 5 layer system, respectively).

Repair:

1. Ultimate load carrying capacities of the girders significantly increased by 20%, 80% and 10% for 25% damaged and 1-layer, 50% damaged and 3-layer and 100% damaged and 5-layer repairing systems.
2. The effect of CFRP bonding on the elastic stiffness of the girders was significant. The technique restored the elastic stiffness of the girder to 91%, 102% and 86% of the intact girder for 25% loss and 1-layer, 50% loss and 3-layer and 100% loss and 5-layer repairing systems.
3. The effect of the technique on improving the post-elastic stiffness of the repaired girder was much more pronounced. The stiffness was increase 21, 19 and 32 times compared to the intact girder.
4. While, the analytical models indicated that the ductility of the retrofitted system was less then the virgin girders, repaired girders with small to moderate loss of their tension flange deflected between 50 ~ 75 mm which is about 1/100 ~ 1/65 of the clear span.

Fatigue:

1. Fatigue life of a detail can be improved by epoxy bonding a CFRP patch to the member. Retrofitted specimens experienced longer fatigue lives of between 2.6 to 3.4 times the unretrofitted specimens for stress ranges of 345 to 207 MPa, respectively. This improvement is equivalent to upgrading the detail from AASHTO category D to category C.
2. Design S-N curve for unretrofitted and retrofitted cut specimens were $S \cdot N^{3.54} = 1.22 \times 10^{13}$ and $S \cdot N^{3.96} = 3.84 \times 10^{14}$, respectively. The slope of the S-N curves for the specimens (retrofitted and unretrofitted) in a log-log space is slightly smaller than the slope of the ASSHTO design curves.
3. In both retrofitted and unretrofitted cases, the crack growth was stable for the crack lengths of up to 20 mm. The stable crack growth rates decreased by an average of 65% as a result of retrofitting.
4. The average total number of cycles to failure after crack initiation for retrofitted specimens was 3.5 times the one for unretrofitted specimens. The retrofitted specimens were able to carry a few extra cycles even after the tension flange had completely cracked especially under lower stress ranges.

REFERENCES

[1] Saadatmanesh, H. "Fiber Composite for New and Existing Structures." *ACI Structural Journal.* (1994) 91(3), pp. 346 - 354

[2] Tavakkolizadeh, M., Saadatmanesh, H. "Galvanic Corrosion of Carbon and Steel in Aggressive Environments." *Journal of Composites for Construction, ASCE.* (2001) 5(3), pp. 200-210

[3] Sen, R. and Liby, L. "Repair of Steel Composite Bridge Sections Using Carbon Fiber Reinforced Plastic Laminates." *FDOT-510616,* Florida Department of Transportation, Tallahassee, Florida (1994)

[4] Mertz, D. and Gillespie, J. "Rehabilitation of Steel Bridge Girders Through the Application of Advanced Composite Material." *NCHRP 93-ID11,* Transportation Research Board, Washington, D.C., (1996), pp.1-20

[5] Albrecht, P., Sahli, A., Crute, D., Albrecht, Ph. and Evans, B. "Application of Adhesive to Steel Bridges." *FHWA-RD-84-037,* The Federal Highway Administration, Washington, D.C. (1984), pp. 106-147

[6] Tavakkolizadeh, M. and Saadatmanesh, H. "Strengthening of Steel-Concrete Composite Girders Using Carbon Fiber Reinforced Polymers sheets", *Journal of Structural Engineering, ASCE,* (2003) 129(1), pp.186-196

[7] Tavakkolizadeh, M., Saadatmanesh, H. "Repair of Cracked Steel Girder Using CFRP Sheet." *Creative Systems in Structural and Construction Engineering,* Balkema, Rotterdam, Holland, (2001), pp. 461-466.

[8] Tavakkolizadeh, M. and Saadatmanesh, H. "Repair of Damaged Steel-Concrete Composite Girders Using CFRP Sheets", *Journal of Composites for Construction, ASCE,* (2003) 7(4), pp. 311-322

[9] Tavakkolizadeh, M. and Saadatmanesh, H. "Fatigue Strength of Steel Girders Strengthened with Carbon Fiber Reinforced Polymer Patch", *Journal of Structural Engineering, ASCE,* (2003) 129(2), pp. 30-40

[10] Schwartz, M. "Composite Material Handbook." 2nd Edition, McGraw-Hill, Inc, New York, NY. (1992)

[11] Fisher, J. W. "Bridge Fatigue Guide: Design and Details." *Publication T112-11/77,* AISC, New York, NY. (1977)

UNDERSTANDING AND MODELLING THE COMPRESSIVE BEHAVIOUR OF FRP-CONFINED CONCRETE

J.G. Teng and L. Lam

Department of Civil and Structural Engineering,
The Hong Kong Polytechnic University, Hong Kong, China

ABSTRACT

One important application of fibre reinforced polymer (FRP) composites in the retrofit of reinforced concrete (RC) structures is to provide confinement to columns for enhanced strength and ductility. As a result, many theoretical and experimental studies have been carried out on the compressive behaviour of FRP-confined concrete. This paper provides a critical review of existing studies on this subject, with the emphasis being on the revelation of the fundamental behaviour of FRP-confined concrete and the modelling of this behaviour. Although the paper is explicitly limited to concrete confined with FRP jackets in which the fibres are oriented only or predominantly in the hoop direction, many of the observations made in this paper are also applicable or relevant to concrete confined with FRP jackets with a significant axial stiffness, as found in concrete-filled FRP tubes as new columns.

INTRODUCTION

Fibre reinforced polymer (FRP) composites have found increasingly wide applications in civil engineering due to their high strength-to-weight ratio and high corrosion resistance. One important application of FRP composites is as wraps or jackets for the confinement of reinforced concrete (RC) columns for enhanced strength and ductility. In FRP-confined concrete subject to axial compression, the FRP is principally loaded in hoop tension while the concrete is loaded in tri-axial compression, so that both materials are used to their best advantages. Both the strength and the ultimate strain of concrete can be greatly enhanced as a result of FRP confinement, while the high tensile strength of FRP can be fully utilised. Instead of the brittle behaviour exhibited by both materials, FRP-confined concrete possesses greatly enhanced ductility.

This paper provides a critical review of existing studies, with the emphasis being on the revelation of the fundamental behaviour of FRP-confined concrete, and the modelling of this behaviour. The paper is limited to concrete confined with FRP jackets in which the fibres are oriented only or predominantly in the hoop direction as such jackets are commonly used in column retrofit. Nevertheless, many of the observations made in this paper are also applicable to concrete confined with FRP jackets with a significant axial stiffness, as found in concrete-filled FRP tubes as new columns.

BASIC BEHAVIOUR OF FRP-CONFINED CONCRETE

Confining action of FRP jackets

When a concrete cylinder confined with an FRP jacket is subject to an axial compressive stress σ_c, it expands laterally. This expansion is confined by the FRP jacket which is loaded in tension in the hoop direction. The confining pressure provided

by the FRP jacket increases continuously with the lateral strain of concrete because of the linear elastic stress-strain behaviour of FRP, in contrast to steel-confined concrete in which the confining pressure remains constant when the steel is in plastic flow. Failure of FRP-confined concrete generally occurs when the hoop rupture strength of the FRP jacket is reached. For FRP jackets with fibres oriented only or predominantly in the hoop direction, the lateral (radial) confining pressure acting on the concrete core σ_l is given by

$$\sigma_l = \frac{E_{frp}\varepsilon_h t}{R} \tag{1}$$

where E_{frp} is the elastic modulus of FRP in the hoop direction, t is the thickness of the FRP jacket, ε_h is the hoop tensile strain in the FRP jacket, and R is the radius of the confined concrete core, respectively. The lateral confining pressure reaches its maximum value f_l at the rupture of FRP, given by Equation 1 with ε_h being the FRP hoop rupture strain $\varepsilon_{h,rup}$. The FRP hoop rupture strain is generally not the same as the ultimate tensile strain of the FRP from tensile tests of flat coupons as discussed in some detail later in the paper. The ratio between the confining pressure f_l when the jacket ruptures (i.e. the maximum confining pressure) and the compressive strength of unconfined concrete $f_{co}^{'}$ is commonly referred to as the confinement ratio.

Axial stress-strain behaviour of confined concrete

Figure 1 shows typical stress-strain curves of carbon FRP (CFRP)-confined concrete and unconfined concrete, obtained by Lam et al. [1] from compression tests on 152 mm x 305 concrete cylinders. Also shown in this figure are those from compression tests conducted by Sfer et al. [2] on a 150 mm x 300 mm concrete cylinder with active confinement at a constant lateral pressure of 1.5 MPa, and by Candappa et al. [3] on 100 mm x 200 mm concrete cylinders with active confinement at lateral pressures of 4 and 12 MPa respectively. The unconfined concrete cylinder strengths of these specimens are in the range of 32-42 MPa and all these tests were conducted under displacement control. For the purpose of comparison, the axial stress σ_c is normalized by the compressive strength of the unconfined concrete $f_{co}^{'}$ while the axial strain ε_c or lateral strain ε_l is normalized by the axial strain of the unconfined concrete at its peak stress ε_{co}. The axial strains of concrete are defined as positive and the lateral strains negative. The CFRP had a nominal thickness of 0.165 mm per ply, an elastic modulus around 250 GPa based on the nominal jacket thickness and an ultimate tensile strain of 1.52 %.

The two axial stress-axial strain curves of CFRP-confined concrete shown in Figure 1 feature a monotonically ascending bi-linear shape. By contrast, the axial stress-axial strain curves of actively confined concrete feature a descending branch. This is because in the case of FRP-confined concrete, as the axial stress increases, the confining pressure provided by the jacket also increases instead of remaining constant. If the amount of FRP provided exceeds a certain threshold value, this confining pressure increases fast enough to ensure that the stress-strain curve is monotonically ascending. This bilinear phenomenon was also previously observed by Xiao et al. [4] for concrete stub columns confined with steel tubes before the yielding of steel. His steel tubes were primarily used as transverse reinforcement and were not directly loaded in the axial direction. Monotonically ascending stress-strain curves have been observed in the

majority of existing tests on FRP-confined concrete. Naturally, if the amount of FRP is small, a descending branch is possible and has been observed in tests [5-7].

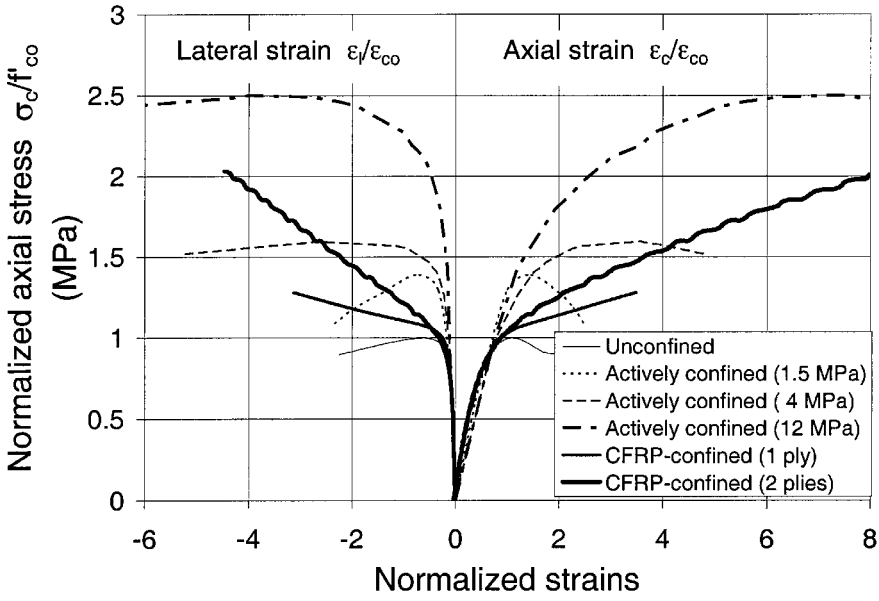


Figure 1. Axial stress vs axial and lateral strains of FRP-confined and actively confined concrete

Dilation properties

The dilation properties of unconfined concrete and actively confined concrete have been well established [8,9]. Under axial compression, unconfined concrete has an initial Poisson's ratio (the lateral-to-axial strain ratio at ε_c = 0, given as absolute value) between 0.15 and 0.22 and experiences a volumetric reduction or compaction up to 90% of the peak stress. Thereafter the concrete shows volumetric expansion or dilation as a result of the rapidly increasing lateral-to-axial strain ratio. Unstable dilation after the initial compaction has also been observed in actively confined concrete in tri-axial compression tests, although at a higher confining pressure, the dilation is less pronounced as described by Pantazopoulou [9].

A number of studies have been concerned with the dilation properties of FRP-confined concrete [6,10-14]. Mirmiran and his co-workers [10-12] compared the volumetric responses of FRP-confined concrete with those of plain concrete and steel-confined concrete which behaves similarly to actively confined concrete after the yielding of the confining steel. They demonstrated that for steel-confined concrete, unstable dilation occurs when steel yields, but for FRP-confined concrete, the linearly increasing hoop stress of the FRP jacket can eventually curtail the dilation if the amount of FRP is sufficiently large.

In Figure 2, the normalized lateral strain is plotted against the normalized axial strain for all the specimens examined in Figure 1. It can be seen from this figure that the normalized lateral-to-axial strain curve of the FRP-confined specimen initially follows that of the unconfined specimen but gradually deviates from it as the axial strain increases, and then sequentially intersects each of the corresponding curves of the

actively confined specimens. Huang et al. [15,16] observed that at these points of intersection, the current confinement ratio of the FRP-confined specimen is almost equal to the confinement ratio of the corresponding actively confined specimen. Here, the current confinement ratio for a given state of deformation is defined as the ratio between the confining pressure provided by the FRP jacket as defined by Equation 1 and the unconfined concrete strength. Moreover, they found that the lateral strain-axial strain responses of unconfined, actively confined and FRP-confined concrete can all be approximated by the following unified equation:

$$\frac{\varepsilon_c / \varepsilon_{co}}{1+8\sigma_l / f_{co}^{'}} = 0.85\left\{\left[1+0.75\left(\frac{-\varepsilon_l}{\varepsilon_{co}}\right)\right]^{0.7} - \exp\left[-7\left(\frac{-\varepsilon_l}{\varepsilon_{co}}\right)\right]\right\} \quad (2)$$

Equation 2 is based on the same sign convention for concrete strains as that adopted in plotting Figure 1. The hoop strain in the FRP jacket is assumed to have the same magnitude as the lateral strain of the concrete but the opposite sign. Figure 3 shows the performance of Equation 2 for the specimens examined in Figures 1 and 2.

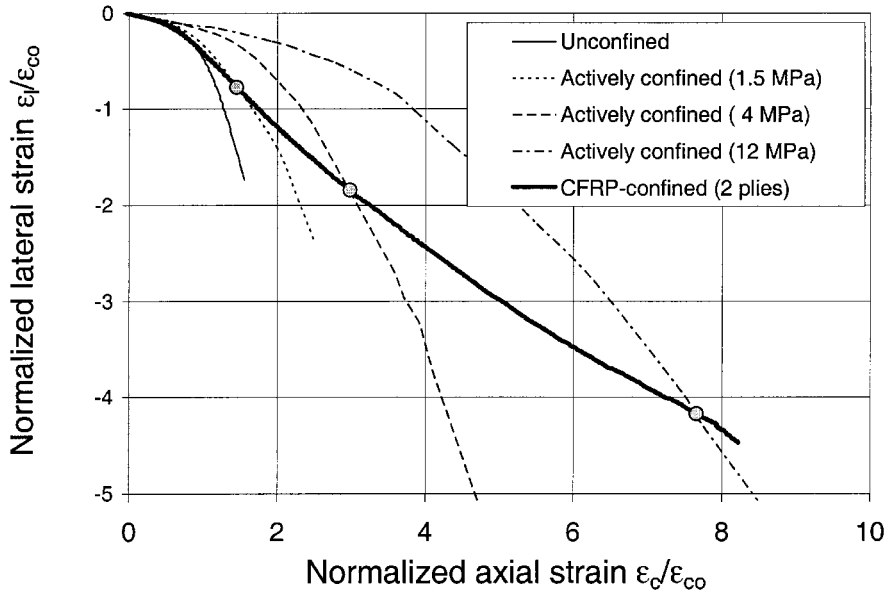


Figure 2. Lateral strain vs axial strain of FRP-confined and actively confined concrete

Ultimate condition

As eventual failure of FRP-confined concrete is by the rupture of the FRP jacket, the ultimate condition of the confined concrete, often characterized by its compressive strength and ultimate axial strain, is intimately related to the ultimate tensile strain or tensile strength of the confining FRP jacket in the hoop direction. In most existing theoretical models for FRP-confined concrete, it has been assumed that tensile rupture of FRP occurs when the hoop stress in the FRP reaches its tensile strength from material tests, either flat coupon tests [17] or ring splitting tests [18]. However, extensive experimental results have shown that the material tensile strength of FRP cannot be reached in FRP-confined concrete as the hoop rupture strains of FRP measured in FRP-

confined cylinder tests have been found to be considerably smaller than the ultimate tensile strains obtained from material tensile tests [6,19,20]

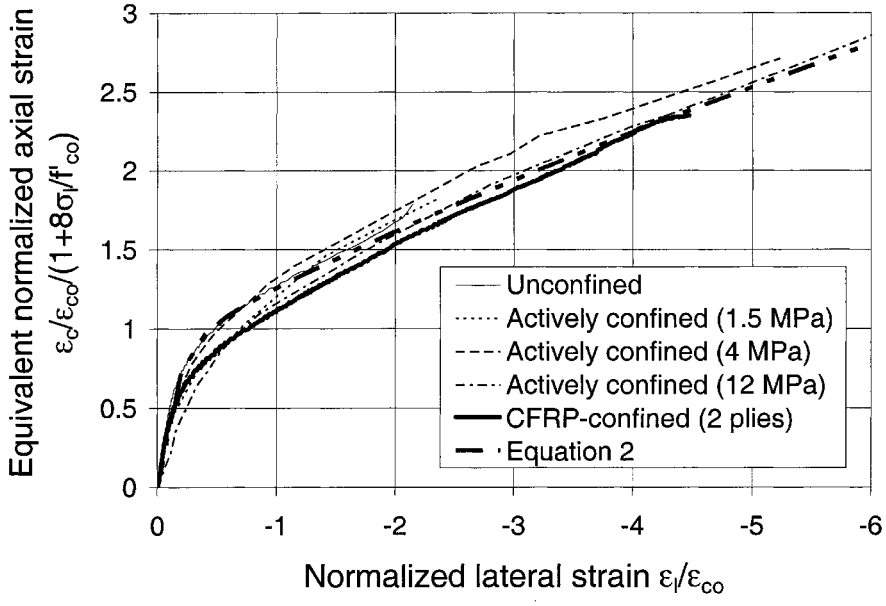


Figure 3. Performance of Equation 2

This uncertainty with FRP hoop rupture strains has led to difficulties in predicting the ultimate condition of FRP-confined concrete, particularly the ultimate axial strain. This is because the ratio between the FRP hoop rupture strain and the material ultimate tensile strain varies with the type of FRP [21]. De Lorenzis and Tepfers [22] showed that of the models they reviewed and assessed [6,12, 23-29], none was able to predict the ultimate axial strain with reasonable accuracy if the hoop strain in the FRP jacket at rupture is taken to be equal to the material ultimate tensile strain. Xiao and Wu [6], Jin [30] and Moran and Pantelides [31] suggested the use of a reduced FRP strength. Lam and Teng [21] recently suggested that in developing confinement models, the actual hoop rupture strain $\varepsilon_{h,rup}$ measured in the FRP jacket should be used to evaluate the stress in the FRP rather than simply using the FRP material tensile strength f_{frp}.

Several causes have been suggested for the difference in the ultimate tensile strain between FRP tensile test specimens and FRP jackets confining concrete [6, 19-22,29]. These suggestions are generally speculative without sound experimental evidence. Lam and Teng [32,33] recently conducted the first carefully planned study involving comparative experiments in an attempt to clarify the causes for the reduced strain capacity of FRP when used to confine concrete. The experimental program covered flat coupon tensile tests [17] and ring splitting tests [18] on CFRP and GFRP specimens, and compression tests on concrete cylinders wrapped with one to three plies of CFRP and GFRP. Based on the test observations, Lam and Teng [32] concluded that the average hoop rupture strains of FRP measured in FRP-confined concrete cylinders are affected by at least three factors: (a) the curvature of the FRP jacket; (b) the deformation non-uniformity of cracked concrete; and (c) the existence of an overlapping zone in which the measured strains are much lower than strains measured elsewhere. While the effect of curvature is material dependent, which means that the curvature of the FRP

jacket has a stronger detrimental effect on CFRP than on GFRP in the context of their study, the non-uniformity of strain distribution is independent of the type of FRP.

In addition, Harries and Carey [34] recently investigated the effect of bond between the FRP jacket and the concrete core on the hoop rupture strain $\varepsilon_{h,rup}$. Their test results showed that on the unbonded specimens which contained a 0.08 mm thick plastic wrap between the FRP jacket and the concrete, the hoop strains were nearly uniform around the circumference. However, the average hoop rupture strains of these specimens did not appear to be higher than those measured on the specimens with the FRP jacket bonded to the concrete. Thus, the role played by adhesive bonding in reducing the hoop rupture strain has not been clearly established by these tests.

STRESS-STRAIN MODELS

From the large number of studies on FRP-confined concrete, many stress-strain models have resulted. These models can be classified into two categories: (a) design-oriented models, and (b) analysis-oriented models. In the first category, stress-strain models are presented in closed-form expressions, while in the second category, stress-strain curves of FRP-confined concrete are predicted using an incremental iterative numerical procedure in which the interaction between the concrete core and the confining FRP is explicitly accounted for. Design-oriented models are more suitable for direct use in design, but analysis-oriented models are more versatile and powerful and are particularly suitable for use in nonlinear computer analysis.

Design-oriented models

Apart from models representing the stress-strain curve of FRP-confined concrete with two or three strictly linear segments [6,35,36], two expressions have frequently been exploited in describing the stress-strain behaviour of FRP-confined concrete: an equation proposed by Sargin [37] and a four-parameter stress-strain curve proposed by Richard and Abbot [38].

The equation proposed by Sargin [36] has the following form:

$$\frac{\sigma_c}{f_{co}^{'}} = \frac{A\frac{\varepsilon_c}{\varepsilon_{co}} + (D-1)\left(\frac{\varepsilon_c}{\varepsilon_{co}}\right)^2}{1+(A-2)\frac{\varepsilon_c}{\varepsilon_{co}} + D\left(\frac{\varepsilon_c}{\varepsilon_{co}}\right)^2} \tag{3}$$

where A and D are constants controlling the initial slope and the descending path of the stress-strain curve respectively. Equation 3 has been used in stress-strain models for steel-confined concrete [39,40] and unconfined concrete [41]. The well-known Hognestad [42] parabola is a special case of Equation 3 with A = 2 and D = 0. Ahmad et al. [43] used Equation 3 to represent the whole stress-strain curve of FRP-confined concrete, with $f_{co}^{'}$ and ε_{co} being replaced by the stress and strain at the peak stress of FRP-confined concrete. Their model does not feature a bilinear shape. In all other models [25, 27,28,44-46] which exploit Equation 3 or a modified version, the stress-strain curve consists of two segments with only the first segment being represented by Equation 3 or the Hognestad parabola while the second segment is defined using a separate expression.

The four-parameter curve of Richard and Abbot [38], which was proposed to describe the elastic-plastic behaviour of structural systems, is given by

$$\sigma = \frac{(E_1 - E_2)\varepsilon}{\left\{1 + \left|\frac{(E_1 - E_2)\varepsilon}{f_o}\right|^n\right\}^{1/n}} + E_2\varepsilon \quad (4)$$

where σ and ε are the stress and the strain respectively, f_o is a reference stress, E_1 is the initial modulus, E_2 is the plastic modulus, and n is the shape parameter controlling the transition from the first portion to the second portion of the stress-strain curve. An advantage of Equation 4 is that the bilinear shape of a stress-strain curve can be described by a single equation. Consequently, Equation 4 has been used in a number of stress-strain models for FRP-confined concrete [12,31,47-49] and a model by Toutanji and Saafi [50] for concrete confined with FRP-reinforced PVC tubes. A model proposed by Campione and Miragia [51] uses a modified form of Equation 4.

The present authors recently developed a design-oriented model [21] based on a careful interpretation of a large test database assembled by them from the open literature. This model consists of a parabolic first portion with its initial slope being the elastic modulus of unconfined concrete and a linear second portion which intercepts the stress axis at the strength of unconfined concrete. The parabolic first portion meets the linear second portion with a smooth transition. This model allows the use of test values or values suggested by design codes for the elastic modulus of unconfined concrete and accounts for the effect of FRP confinement on the non-linear response of concrete before the transition point. It reduces to the design stress-strain curve for unconfined concrete recommended by Eurocode 2 [41] provided the same initial elastic modulus is used, which is an important advantage of the model in practical applications.

Analysis-oriented models

A number of analysis-oriented models for FRP-confined concrete [14,29,52-54] have been developed on the basis of the assumption that the axial stress and axial strain of concrete confined with FRP at a given lateral strain are the same as those of the same concrete actively confined with a constant confining pressure equal to that supplied by the FRP jacket. This assumption is equivalent to assuming that the stress path of the confined concrete does not affect its stress-strain behaviour. The validity of this assumption has recently demonstrated by Huang et al. [15,16]. Based on this assumption, an active confinement model for concrete can be used to evaluate the axial stress and axial strain of FRP-confined concrete at a given confining pressure and the interaction between the concrete and the FRP jacket can be explicitly accounted for by equilibrium and radial displacement compatibility considerations. As a result, the stress-strain curve of FRP-confined concrete can be generated as a curve that crosses a series of stress-strain curves for the same concrete confined with a range of lateral pressures. A model proposed by Mander et al. [55] or a modified version has been used as the active confinement model in the above five models for FRP-confined concrete. The lateral strain at a given axial strain, which is the key for an accurate analysis-oriented model, is found by different means in these models.

Apart from the above five models based on an active confinement model, other approaches have also been used for modelling FRP-confined concrete. Harmon et al. [13] developed a model for FRP-confined concrete based on the concept of crack slip and separation in the concrete. Becque et al. [56] proposed a model based on Gerstle's [57,58] octahedral stress-strain models with some modifications. In addition, the plasticity model proposed by Karabinis and Rousakis [59] for FRP-confined concrete

may also be classified as an analysis-oriented model, although the numerical integration required by the plasticity approach makes it more complicated than other analysis-oriented models.

A recent model developed at The Hong Kong Polytechnic University [15,16] followed an approach similar to that adopted in the five models based on an active confinement model. In this model, Equation 2 is used to determine the lateral strain-axial strain relationship, and a modified version of Mander et al.'s model [55] is to used determine the stress-strain curve under current confining pressures, as demonstrated in Figure 4.

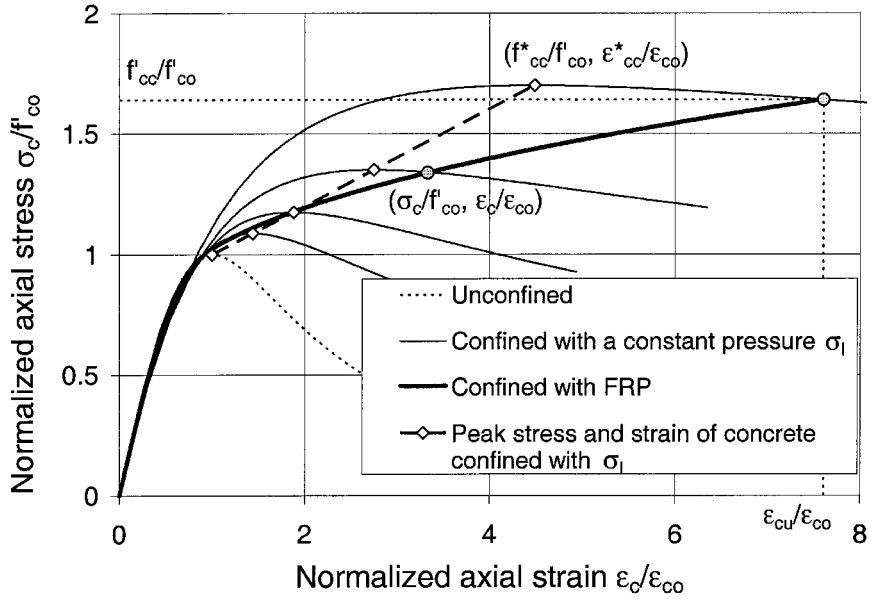


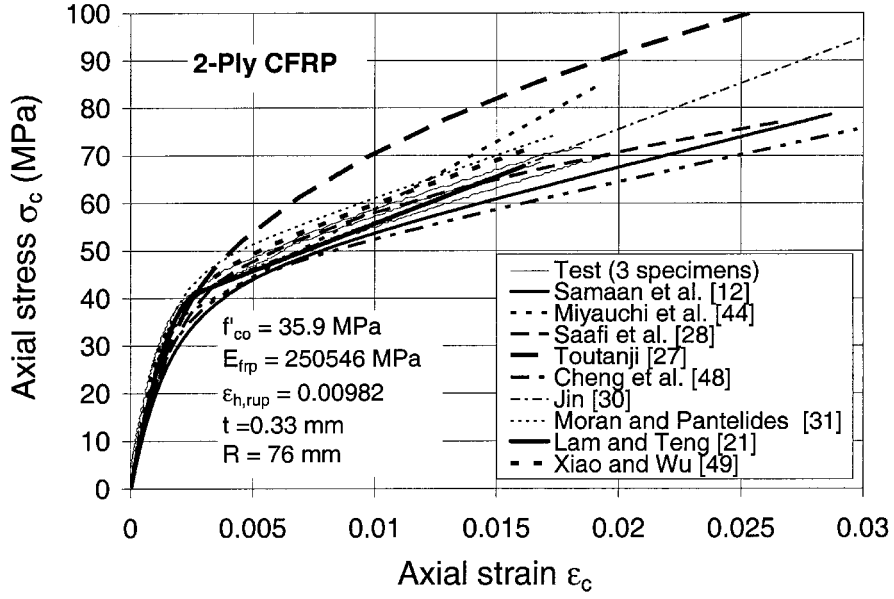
Figure 4. Generation of a stress-strain curve in an analysis-oriented model of FRP-confined concrete based on an active confinement model

PERFORMANCE OF STRESS-STRAIN MODELS

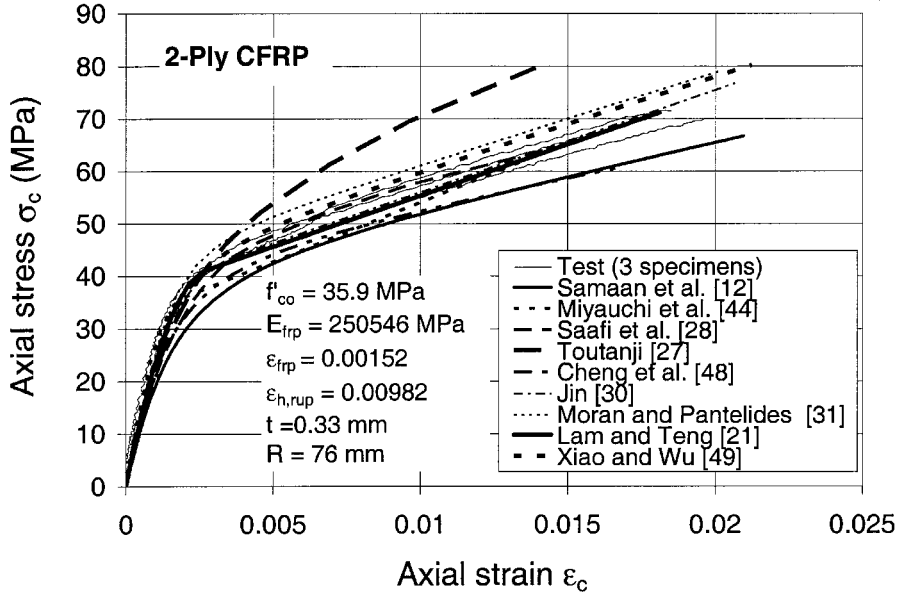
To assess the performance of existing stress-strain models, their predictions are compared here with results from tests on three CFRP- and two GFRP-wrapped concrete cylinders (152 mm × 305 mm) recently conducted by the authors [32,33]. These tests were carefully conducted with hoop strains measured at 8 points around a circumference. The hoop strains used for comparison here were averaged from strains measured outside a 150 mm overlapping zone. It should be noted that the conclusions reached in this section are in agreement with those reached through similar comparisons undertaken by the authors using the test data of Xiao and Wu [6] which are not reported here due to space limitation.

The comparisons between the test results and the predictions of the design-oriented models and analysis-oriented models are shown in Figures 5 and 6 respectively. The details of the specimens are also shown in these figures. The elastic moduli and material ultimate tensile strains of the FRPs were obtained from flat coupon tests according to ASTM D3039 [17] and calculated based on the nominal thicknesses which were 0.165 mm per ply for the CFRP and 1.27 mm ply for the GFRP. In predicting the stress-strain

curves, the elastic modulus E_c and initial Poisson's ratio ν_c of unconfined concrete were either those specified in an individual model or taken to be $E_c = 4730\sqrt{f'_{co}}$ (MPa) and $\nu_c = 0.18$ if they are not specified in the model. The axial strain at the compressive strength of unconfined concrete ε_{co} was assumed a constant value of 0.002 for all models for a more direct comparison even though Huang et al. [15] originally suggested $\varepsilon_{co} = 0.0022$ for use with their model.

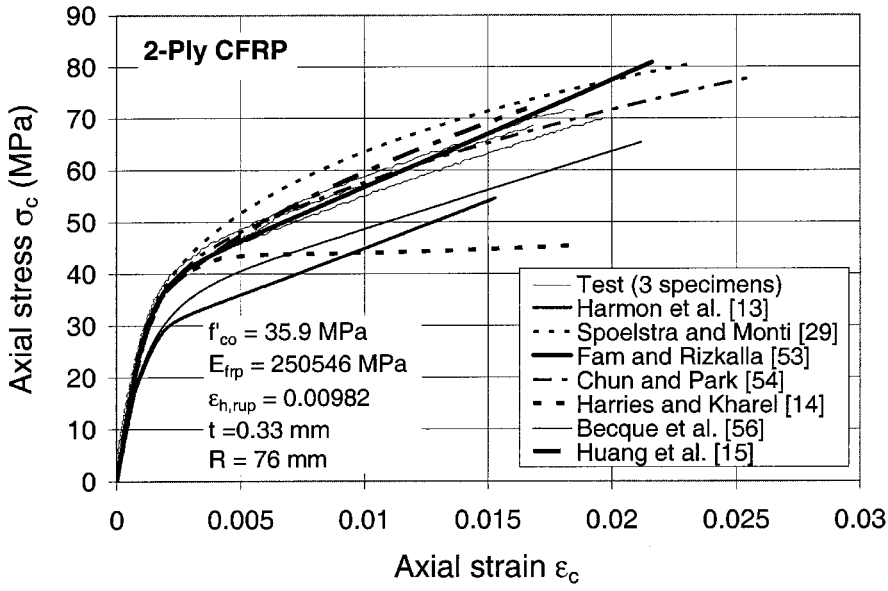


(a) Using the original definition of FRP hoop rupture strain

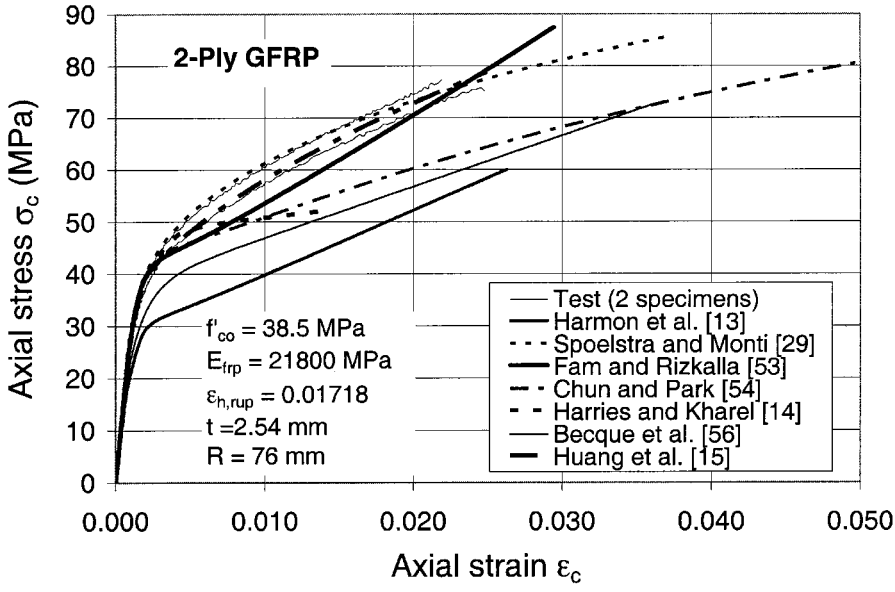


(b) Using the test FRP hoop rupture strain

Figure 5. Performance of design-oriented models



(a) Specimens confined with 2 plies of CFRP



(b) Specimens confined with 2 plies of GFRP

Figure 6. Performance of analysis-oriented models

Figure 5 shows comparisons between stress-strain curves from tests on CFRP-confined concrete and those from the more accurate design-oriented models [12,21,27,28,30,31,44,48,49] as identified in a preliminary comparison. In Figure 5a, comparisons are made for the CFRP-confined cylinders where the hoop strain or stress in the FRP at rupture as defined in the original model is used. For the models of Xiao

and Wu [49] and Jin [30], reduction factors of 0.50 and 0.96 are used for the ultimate FRP tensile strain respectively, according to their definitions. For Moran and Pantelides' model [31], the CFRP hoop rupture strain is taken as 0.0085 based on their own suggestion. For Lam and Teng's model [21], the CFRP is assumed to reach 58.6% of the material tensile strength, which is the average value from a large test database [21]. For other models, the FRP tensile strength from flat coupon tests is used. In Figure 5b, the actual average hoop rupture strains obtained from the confined concrete tests are used for all models. It can be observed from Figure 5a that if the hoop strain at the rupture of the FRP jacket is assumed the value specified in the original model, the three models using a substantially reduced value for this rupture strain [21,31,49] perform better than the other models. However, if the actual hoop rupture strain is used instead, then the performance of the other models becomes better. Among these models, the models of Saafi et al. [28], Jin [30], Moran and Pantelides [31], Xiao and Wu [49], and Lam and Teng [21] give closer predictions of the shape of the stress-strain curve and the ultimate condition.

Figure 6 shows comparisons between stress-strain curves obtained from both tests conducted on CFRP and GFRP-confined cylinders and analysis-oriented models. The predicted stress-strain curves terminate at the point where the average FRP hoop rupture strain from the tests is reached. For the CFRP-confined concrete cylinders (Figure 6a), the models of Spoestra and Monti [29], Fam and Rizkalla [53], Chun and Par [54] and Huang et al. [15] perform well and are superior to other models. However, for the GFRP-confined concrete cylinders (Figure 6b), only the model by Huang et al. [15] provides close predictions.

The above comparisons suggest that central to a design-oriented model is an accurate definition of the ultimate condition. Provided that the ultimate condition of FRP-confined concrete is accurately defined, the stress-strain curve can be closely matched using different forms of equations. For analysis-oriented models, the key for accurate predictions is the lateral-to-axial strain relationship for FRP-confined concrete.

FRP-CONFINED CONCRETE UNDER CYCLIC COMPRESSION

While the behaviour of FRP-confined concrete under monotonic compression has been extensively studied, only a very limited amount of work has been conducted on the behaviour of FRP-confined concrete subject to cyclic compression [1,10,60-63].

Figure 7 shows typical axial stress-axial strain curves of FRP-confined concrete under monotonic and cyclic compression, obtained from tests conducted by Lam et al. [1] on concrete cylinders confined with CFRP. It can be seen from Figure 7 that the envelope curve of the cyclic stress-strain curve almost coincides with the stress-strain curve obtained from monotonic loading. This confirms that a stress-strain model based on monotonic tests can be used to predict the envelope curve of the stress-strain responses of FRP-confined concrete under cyclic compression. Figure 7 shows that under repeated unloading/reloading cycles, the stress at the same unloading strain ε_{un} decreases and the residual strain (plastic strain) at zero stress ε_{pl} increases as the number of cycle increases. This indicates that in developing a cyclic stress-strain model, the loading history has to be taken into account. Such a model is under development at The Hong Kong Polytechnic University [1]. The following equation has been developed to predict the plastic strain ε_{pl} for unloading from a point on the envelope curve at a strain ε_{un}:

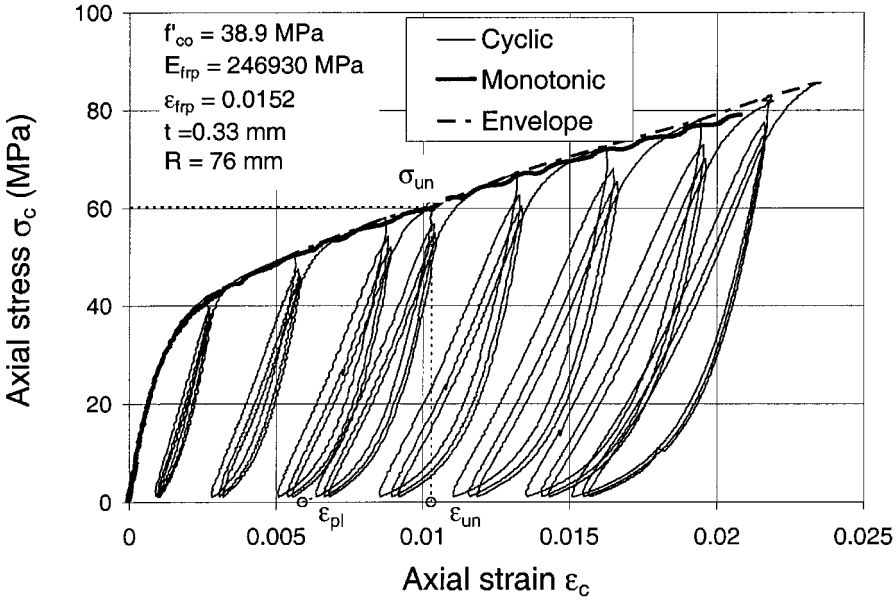


Figure 7. Stress-strain curve of CFRP-confined concrete under cyclic compression

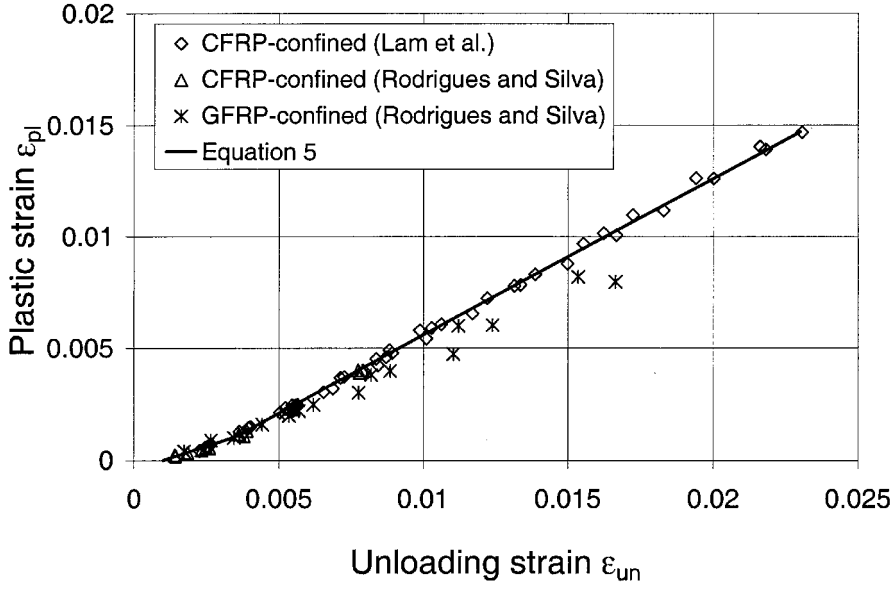


Figure 8. Predictions of the plastic strain

$$\varepsilon_{pl} = \begin{cases} 0, & 0 \le \varepsilon_{un} < 0.001 \\ 0.42\varepsilon_{un} - 0.00042, & 0.001 \le \varepsilon_{un} < 0.0035 \\ 0.7\varepsilon_{un} - 0.0014, & \varepsilon_{un} \le 0.0035 \end{cases} \quad (5)$$

Figure 8 shows that Equation 5 predicts closely the results from tests conducted by Lam et al. [1] as well as those conducted by Rodrigues and Silva [60] on CFRP-confined concrete specimens (Figure 8). For the GFRP-confined specimens tested by Rodrigues and Silva [61], the test data fall slightly below the predictions (Figure 8).

CONCLUDING REMARKS

This paper has provided a critical review of existing research on normal strength concrete uniformly confined with FRP jackets with which most existing studies have been concerned. For such FRP-confined concrete, it may be concluded that the large number of studies on FRP-confined concrete have led to a good understanding of its behaviour and many stress-strain models, the latest of which provide close predictions of test results. While there will inevitably be further refinement of models for such FRP-confined concrete, much more attention should be directed to several other issues of FRP-confined concrete which have received limited attention. These include (a) FRP-confined high strength concrete; (b) interaction between steel confinement and FRP confinement; (c) concrete with non-uniform confinement as found in FRP-confined rectangular and other non-circular sections and sections under eccentric compression; (d) FRP-confined concrete subject to cyclic loading; and (e) concrete confined by hybrid FRP composites. The limited existing research on FRP-confined concrete subject to cyclic compression has been noted in the paper, while a detailed survey of existing work on FRP-confined concrete in rectangular columns has been presented by Lam and Teng [64].

ACKNOWLEDGEMENT

The authors are grateful for the financial support received from the Research Grants Council of the Hong Kong SAR (Project No: PolyU 5059/02E), the Natural Science Foundation of China (National Key Project No. 50238030) and The Hong Kong Polytechnic University provided through its Area of Strategic Development (ASD) Scheme for the ASD in Urban Hazard Mitigation.

REFERENCES:

1 L Lam, J G Teng, C H Cheung and Y Xiao, 'Behavior and modeling of FRP confined concrete under cyclic axial compression', in preparation.

2 D Sfer, I Carol, R Gettu and G Etse, 'Study of the behavior of concrete under triaxial compression, *Journal of Engineering Mechanics,* ASCE, 2002, **128**(2),156-163.

3 D C Candappa, J G Sanjayan and S Setung, 'Complete triaxial stress-strain curves of high-strength concrete', *Journal of Materials in Civil Engineering*, ASCE, 2001, **13**(3), 209-215.

4 Y Xiao, M Tomii and K Sakino, 'Triaxial behavior of confined concrete' (in Japanese), *Concrete Research and Technology*, 1991, **2**(1), 1-14.

5 M Demers and K W Neale, "Strengthening of concrete columns with unidirectional composite sheets", 4th Int Conf *Short and Medium Span Bridges*, Montreal, Canada, Canadian Society for Civil Engineering, 1994.

6 Y Xiao and H Wu, 'Compressive behavior of concrete confined by carbon fiber composite jackets', *Journal of Materials in Civil Engineering,* ASCE, 2000, **12**(2), 139-146.

7 C Aire, R Gettu and J R Casas, 'Study of the compressive behavior of concrete confined by fiber reinforced composites', Int Conf *Composites in Constructions,* Porto, Portugal, A.A. Balkema Publishers, 2001.

8 W F Chen, *Plasticity in Reinforced Concrete*, McGraw-Hill Inc., New York, U.S.A., 1982.

9 S J Pantazopoulou, 'Role of expansion on mechanical behavior of concrete', *Journal of Structural Engineering*, ASCE, 1995, **121**(12), 1795-1805.

10 A Mirmiran and M Shahawy, 'Behavior of concrete columns confined by fiber composites', *Journal of Structural Engineering*, ASCE, 1997, **123**(5), 583-590.

11 A Mirmiran and M Shahawy, 'Dilation characteristics of confined concrete', *Mechanics of Cohesive-Frictional Materials,* 1997, **2**, 237-249.

12 M Samaan, A Mirmiran and M Shahawy, 'Model of concrete confined by fiber composite', *Journal of Structural Engineering,* ASCE, 1998, **124**(9), 1025-1031.

13 T G Harmon, S Ramakrishnan and E H Wang, E.H. 'Confined concrete subjected to uniaxial monotonic loading', *Journal of Engineering Mechanics*, ASCE, 1998, **124**(12), 1303-1308.

14 K A Harries and G Kharel, 'Behavior and modeling of concrete subject to variable confining pressure', *ACI Materials Journal*, 2002, **99**(2), 180-189.

15 Y L Huang, L Lam, J G Teng and L P Ye, 'Analysis-oriented stress-strain model for FRP-confined concrete', in preparation.

16 Y L Huang, L Lam, J G Teng and L P Ye, 'Stress-strain model for concrete confined with FRP', 3rd Cross-strait Conf, *Structural and Geotechnical Engineering*, Taibei, Taiwan, Taiwan University, 2003.

17 ASTM D3039/D3039M – 95, 'Standard test method for tensile properties of polymer matrix composites materials', *Annual Book of ASTM Standards*, Vol. 14.02, 1995.

18 ASTM D 2290 – 92, 'Standard test method for apparent tensile strength of ring or tubular plastics and reinforced plastics by split disk method', *Annual Book of ASTM Standards*, Vol. 15.03, 1992.

19 M Shahawy, A Mirmiran and T Beitelman, 'Test and modeling of carbon-wrapped concrete columns', Composites *Part B: Engineering*, 2000, **31**, 471-480.

20 S Pessiki, K A Harries, J T Kestner, R Sause and J M Ricles, 'Axial behavior of reinforced concrete columns confined with FRP jackets', *Journal of Composites for Construction,* ASCE, 2001, **5**(4), 237-245.

21 L Lam and J G Teng, 'Design-oriented stress-strain model for FRP-confined concrete', *Construction and Building Materials*, 2003, 17(6&7), 471-489.

22 L De Lorenzis and R Tepfers, 'Comparative study of models on confinement of concrete cylinders with fiber-reinforced polymer composites', *Journal of Composites for Construction*, ASCE, 2003, **7**(3), 219-237.

23 M N Fardis and H Khalili, 'Concrete encased in fiberglass-reinforced plastic', *ACI Journal*, 1981, **78**(6), 440-446.

24 H Saadatmanesh, M R Ehsani and M W Li, 'Strength and ductility of concrete columns externally reinforced with fiber composite straps', *ACI Structural Journal*, 1994, 91(4), 434-447.

25 K Miyauchi, S Nishibayashi and S Inoue, 'Estimation of strengthening effects with carbon fiber sheet for concrete column", 3rd Int Conf *Non-Metallic (FRP) Reinforcement for Concrete Structures*, Sapporo, Japan, 1997.

26 S Kono, M Inazuni and T Kaku, 'Evaluation of confining effects of CFRP sheets on reinforced concrete members', 2nd Int Conf *Composites in Infrastructures (ICCI '98)*, Tucson, Arizona, U.S.A., 1998.

27 H A Toutanji, 'Stress-strain characteristics of concrete columns externally confined with advanced fiber composite sheets', *ACI Materials Journal*, 1999, **96**(3), 397-404.

28 M Saafi, H A Toutanji and Z Li, 'Behavior of concrete columns confined with fiber reinforced polymer tubes', *ACI Materials Journal*, 1999, **96**(4), 500-509.

29 M R Spoelstra and G Monti, 'FRP-confined concrete model', *Journal of Composites for Construction,* ASCE, 1999, **3**(3), 143-150.

30 X N Jin, *Experimental Study of the Mechanical Properties of Axisymmetrically Confined Concrete (in Chinese)*, PhD Thesis, Harbin Institute of Technology, China, 2002.

31 D A Moran and C P Pantelides, 'Stress-strain model for fiber-reinforced polymer-confined concrete', *Journal of Composites for Construction*, ASCE, 2002, **6**(4), 233-240.

32 L Lam and J G Teng, 'Ultimate condition of FRP-confined concrete', *Journal of Composites for Construction*, ASCE, tentatively accepted.

33 L Lam and J G Teng, 'Hoop rupture strains of FRP jackets in FRP-confined concrete', 6th Int Symp *Fibre-Reinforced Polymer (FRP) Reinforcement for Concrete Structures,* Singapore, World Scientific, 2003.

34 K A Harries and A Carey, 'Shape and 'Gap' effects on the behavior of variably confined concrete', *Cement and Concrete Research*, 2003, **33**(6), 881-890.

35 V M Karbhari and Y Gao, 'Composite jacketed concrete under uniaxial compression–verification of simple design equations', *Journal of Materials in Civil Engineering,* ASCE, 1997, **9**(4), 185-193.

36 G Wu, Z Lu and Z Wu, 'Stress-strain relationship for FRP-confined concrete cylinders', 6th Int Symp *Fibre-Reinforced Polymer (FRP) Reinforcement for Concrete Structures (FRPRCS-6),* Singapore, World Scientific, 2003.

37 M Sargin, *Stress-Strain Relationship for Concrete and the Analysis of Structural Concrete Section*, PhD Thesis, University of Waterloo, Ontario, Canada, 1971.

38 R M Richard and B J Abbott, 'Versatile elastic-plastic stress-strain formula', *Journal of the Engineering Mechanics Division*, ASCE, 1975, **101**(EM4), 511-515.

39 S H Ahmad and S P Shah, 'Complete triaxial stress-strain curves for concrete', *Journal of the Structural Division*, ASCE, 1982, **108**(ST4), 728-742.

40 S H Ahmad and S P Shah, 'Stress-strain curves of concrete confined by spiral reinforcement', *ACI Journal*, 1982, **79**, 484-490.

41 ENV 1992-1-1, *Eurocode 2: Design of Concrete Structures – Part 1: General Rules and Rules for Buildings,* European Committee for Standardization, Brussels, 1991.

42 E Hognestad, *A Study of Combined Bending and Axial Load in Reinforced Concrete Members*, Bulletin Series No. 399, Engineering Experiment Station, University of Illinois, Urbana, U.S.A., 1951.

43 S H Ahamd, A R Khaloo and A Irshaid, 'Behaviour of concrete spirally confined by fibreglass filament', *Magazine of Concrete Research*, 1991, **43**(156), 143-148.

44 K Miyauchi, S Inoue, T Kuroda and A Kobayashi, 'Strengthening effects of concrete columns with carbon fiber sheet', *Transactions of The Japan Concrete Institute*, 1999, **21**, 143-150.

45 D Lillistone and C K Jolly, 'An innovative form of reinforcement for concrete columns using advanced composites', *The Structural Engineer*, 2000, **78**(23/24), 20-28.

46 M Arduini, A Di Tommaso, O Manfroni, S Ferrari and M Romagnolo, II: confinamento passivo di elementi compressi in calcetruzzo con fogli di materiale composito, *Industria Italiana del Cemento*, 1999, **11**, 836-841.

47 Q Yu, 'A study on the stress-strain relationship of FRP-confined concrete in axial compression' (in Chinese), *Industrial Construction*, 2001, **31**(4), 5-8.

48 H L Cheng, E D Sotelino and W F Chen, 'Strength estimation for FRP wrapped reinforced concrete columns', *Steel and Composite Structures*, 2002, **2**(1), 1-20.

49 Y Xiao and H Wu, 'Compressive behavior of concrete confined by various types of FRP composites jackets', *Journal of Reinforced Plastics and Composites,* 2003, **22**(13), 1187-1202.

50 H Toutanji and M Saafi, 'Stress-strain behavior of concrete columns confined with hybrid composite materials', *Materials and Structures*, 2002, **35**, 338-347.

51 G Campione and N Miragia, 'Strength and strain capacities of concrete compression members reinforced with FRP', *Cement and Concrete Composites*, 2003, **25,** 31-41.

52 A Mirmiran and M Shahawy, 'A new concrete-filled hollow FRP composite column', *Composites Part B: Engineering*, 1996, **27B**(3-4), 263-268.

53 A Z Fam and S H Rizkalla, 'Confinement model for axially loaded concrete confined by circular fiber-reinforced polymer tubes', *ACI Structural Journal*, 2001, **98**(4), 451-461.

54 S S Chun and H C Park, 'Load carrying capacity and ductility of RC columns confined by carbon fiber reinforced polymer, 3rd Int Conf *Composites in Infrastructure*, San Francisco, California, USA., in CD-Rom format, 2002.

55 J B Mander, M J N Priestley and R Park, 'Theoretical stress-strain model for confined concrete', *Journal of Structural Engineering,* ASCE, 1988, **114**(8), 1804-1826.

56 J Becque, A K Patnaik and S H Rizkalla, 'Analytical models for concrete confined with FRP tubes', *Journal of Composites for Construction*, ASCE, 2003, **7**(1), 31-38.

57 K H Gerstle, 'Simple formulation of biaxial concrete behavior', *ACI Journal*, 1981, **78**(1), 62-68.

58 K H Gerstle, 'Simple formulation of triaxial concrete behavior', *ACI Journal*, 1981, **78**(5), 382-387.

59 A I Karabinis and T C Rousakis, 'Concrete confined by FRP materials: a plasticity approach', *Engineering Structures*, 2002, **24,** 923-932.

60 C C Rodriques and M G Silva, 'Experimental investigation of CFRP reinforced concrete columns under uniaxial cyclic compression', 5th Int Conf *Fibre-Reinforced Plastics for Reinforced Concrete Structures*, Cambridge, UK, Thomas Telford, 2001.

61 C C Rodriques and M G Silva, 'The behaviour of GFRP reinforced concrete columns under monotonic and cyclic axial compression', Int Conf *Composites in Constructions,* Porto, Portugal, A.A. Balkema Publishers, 2001.

62 A Ilki and N Kumbasar, 'Behavior of damaged and undamaged concrete strengthened by carbon fiber composite sheets', *Structural Engineering and Mechanics*, 2002, **13**(1), 75-90.
63 Y T Shao, *Behavior of FRP-Concrete Beam-Columns under Cyclic Loading*, PhD Thesis, North Carolina State University, USA., 2003.
64 L Lam and J G Teng, 'Design-oriented stress-strain model for FRP-confined concrete in rectangular columns', *Journal of Reinforced Plastics and Composites*, 2003, **2**(13), 1149-1186.

UPGRADING CONCRETE STRUCTURES USING ADVANCED POLYMER COMPOSITES

Thanasis C. Triantafillou
University of Patras, Patras, Greece

ABSTRACT

Externally bonded fibre reinforced polymers (FRP) have been employed extensively throughout the world in numerous rehabilitation applications of reinforced concrete structures. This paper focuses on upgrading (e.g. strengthening, seismic retrofitting) of RC elements using FRP for shear, flexure and confinement. The key concepts and mechanics are summarized and a brief description of recent developments related to seismic retrofitting of beam-column joints, placing of FRP inside slits and confining according to alternative FRP wrapping techniques are presented.

INTRODUCTION

Strengthening of existing reinforced concrete (RC) members is quite often necessitated by: (a) The inadequacy of transverse reinforcement, which may lead to brittle *shear failure* in members like columns, beams, beam-column joints and shear walls. This mechanism is typically associated with inclined cracking (diagonal tension), sometimes combined with cover concrete spalling, rupture or opening of the transverse reinforcement and rebar pull-out (in the case of joints). The shear capacity of sub-standard members can be enhanced by providing externally bonded FRP with the fibres in the transverse to the member axis direction, in the case of columns, shear walls and beams, or in the direction of both the beam and the column direction, in the case of beam-column joints. (b) *Poor confinement in flexural plastic hinge regions* (e.g. column ends), where flexural cracking may be followed by cover-concrete crushing and spalling, buckling of the longitudinal reinforcement or compressive crushing of the concrete. A ductile flexural plastic hinging at the column ends can be achieved through added confinement in the form of FRP jackets with the fibres placed along the column perimeter. (c) *Poor detailing in lap splices* at the lower ends of columns. The flexural strength of RC columns can only be developed and maintained when debonding of the reinforcement lap splice is prevented. Such debonding occurs once vertical cracks develop in the cover concrete and progresses with increased dilation and cover spalling. The associated rapid flexural strength degradation can be prevented or limited with increased lap confinement, again with fibres along the column perimeter. (d) The inadequacy of longitudinal reinforcement in beams and columns, which may lead to premature *flexural failure* (early yielding of steel rebars, possibly followed by concrete crushing). The flexural capacity of concrete members can be enhanced through the use of externally bonded FRP strips or fabrics or near-surface mounted strips or rods, with the fibre direction parallel to the member's axis. (e) The inadequacy of lateral *stiffness*. It should be made clear that FRP reinforcement cannot alter the stiffness characteristics of existing elements; hence the FRP strengthening technique is not applicable if the structural intervention aims at increasing stiffness rather than strength and/or ductility.

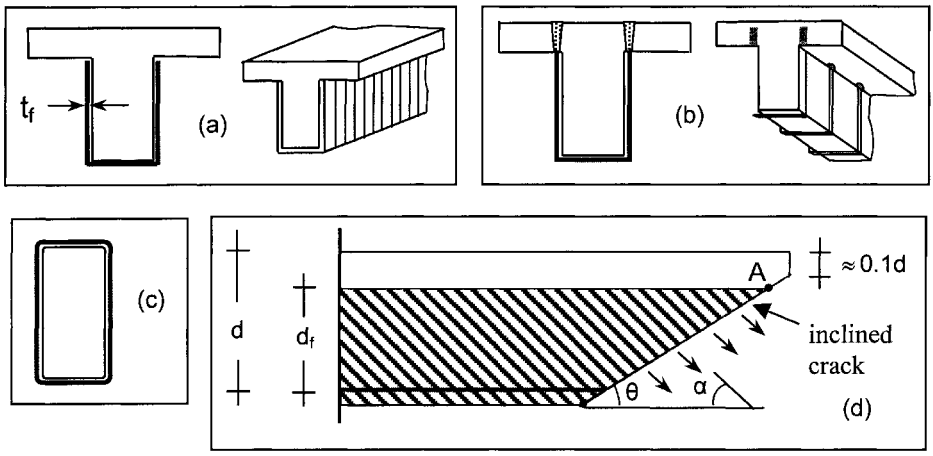


Figure 1 Shear strengthening: (a) beams with U-wrapped FRP; (b) beams with FRP strips anchored in the compression zone; (c) fully wrapped column; and (d) forces carried by FRP at shear crack.

CONCEPTS AND MECHANICS OF UPGRADING WITH FRP

General

The actual increase of RC member strength and deformation capacity effected through FRP reinforcement may be quantified by approaches similar to those used in the case of conventionally reinforced members. The FRP materials are mobilized in tension when crossing cracks that develop due to tension failure of concrete. In the case of column-type members, beam-column joints and beams failing in shear, cracking usually occurs in directions parallel to the compression field that develops in the member, whereas flexural cracks develop perpendicular to the member axis, in areas of high tensile stresses.

Shear strengthening of columns, beams and shear walls

Shear capacity, a strength issue, can be added by FRP jackets both on flexural members (e.g. beams, columns) or shear walls similar to adding shear strength through internal stirrup reinforcement (Figure 1).

In flexural members, the shear strength of a jacketed member is the sum of the jacket contribution (V_{fd}) and the contribution of existing mechanisms, namely concrete (V_{cd}) and stirrup reinforcement (V_{wd}). Of course, it should be recognized that the existing mechanisms may have sustained damage during previous loading; hence, the residual (reduced, compared to the full) contributions of concrete and stirrups should be considered. In design format, the following equation may be adopted for the FRP contribution:

$$V_{fd} = 2t_f d_f (\varepsilon_{fe,d} E_f)(\cot\theta + \cot\alpha)\sin^2\alpha \qquad (1)$$

where t_f = thickness of FRP, d_f = height of FRP crossed by the shear crack (taken equal to 0.9d in case of closed jackets, where d = effective depth of cross section), E_f = elastic

modulus of FRP, $\varepsilon_{fe,d}$ = design value of effective FRP strain, θ = angle of diagonal crack with respect to the member axis; and α = angle between principal fibre orientation and longitudinal axis of member. The effective FRP strain depends on the FRP failure mode (fracture or debonding), the rigidity ($E_f t_f$) of the jacket in the direction of the fibres and the strength of concrete (e.g. Triantafillou and Antonopoulos 2000).

From the relatively limited data available in the literature (e.g. Paterson and Mitchell 2003) on shear strengthening of shear walls it may be deduced that FRP jackets perform more or less the same as in flexural members; they act as horizontal reinforcement with a strain that decreases as the thickness and/or the elastic modulus (along the perimeter) of the jacket increases.

Shear strengthening of beam-column joints

Strengthening of RC joints is a challenging task, which poses major practical difficulties. A variety of techniques applicable to concrete elements have also been applied to joints, with the most common ones being the construction of RC or steel jackets. As an alternative to conventional jackets, which require intensive labour and artful detailing, FRP materials have been used successfully as strengthening materials of exterior beam-column joints (with deficiency in shear strength) by placing the fibres parallel to the beam and column directions (Figure 2).

In a recent study Antonopoulos and Triantafillou (2003) conducted a comprehensive experimental programme, which comprised the investigation of several design parameters through 2/3-scale testing of 18 exterior joints. The parameters under consideration included: area fraction of FRP, distribution of FRP between the beam and the column, column axial load, internal joint (steel) reinforcement, initial damage, carbon versus glass fibres, sheets versus strips, effect of transverse beams. A typical result is shown in Figure 3, which illustrates that even very thin jackets (two 0.12 mm thick CFRP sheets in the beam direction and two in the column direction) may provide substantial increase in the shear capacity (as well as in the stiffness and energy dissipation).

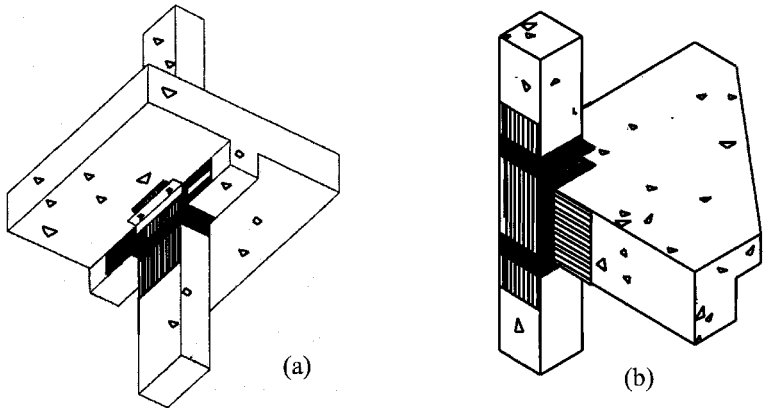


Figure 2 Shear strengthening of (a) interior and (b) exterior beam-column joints.

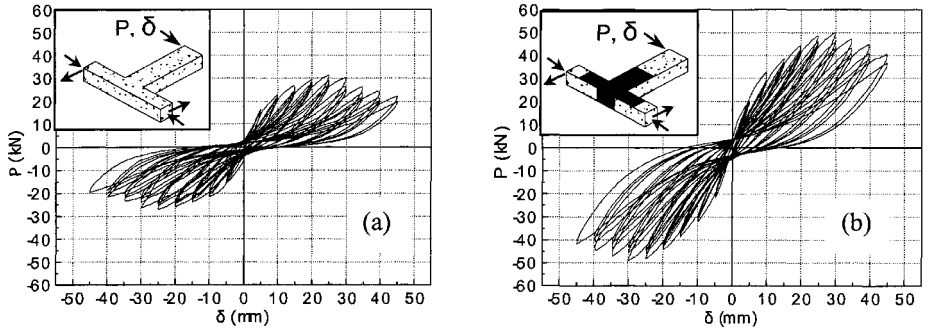


Figure 3 Lateral force-displacement response of shear-critical joints: (a) unstrengthened joint, (b) joint strengthened with CFRP sheets (two layers in the vertical and two in the horizontal direction).

This experimental study was followed by the development of an analytical model (Antonopoulos and Triantafillou 2002) for the prediction of the shear capacity of FRP-strengthened joints (through stress and strain analysis), which was found in excellent agreement with test results.

Confinement

The basis of the FRP contribution is the transverse passive pressure σ developing in the concrete in response to the jacket forces. This pressure is, in general, non-uniform, especially near the corners of rectangular cross sections. As an average value for σ in the cross section one may write:

$$\sigma_\ell = 0.5\left(\sigma_{\ell,h} + \sigma_{\ell,b}\right) = 0.5k_e\left(\frac{2t_f}{b}E_f\varepsilon_f + \frac{2t_f}{h}E_f\varepsilon_f\right) = k_e\frac{t_f E_f \varepsilon_f (b+h)}{bh} \qquad (2)$$

where ε_f = circumferential FRP strain and k_e = effectiveness coefficient. For continuous FRP jackets with fibres in the direction perpendicular to the member axis, k_e is defined as the ratio of fully confined area (A_e in Figure 4) to the total cross sectional area A_g.

Depending on the cause of FRP mobilization, σ may be seen as (a) confining pressure thereby increasing the strength and deformability of encased concrete, (b) jacket contribution to bond-splitting resistance thereby preventing lap-splice failures, (c) lateral support to longitudinal rebars against buckling and (d) jacket contribution to shear capacity. Whereas the last mechanism has already been discussed earlier, (a) – (c) are briefly described next.

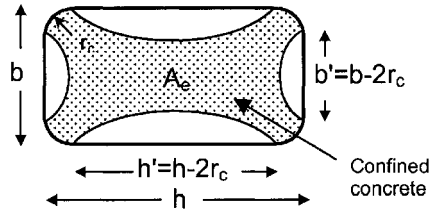


Figure 4 Effectively confined area (defined by parabolas) in rectangular column.

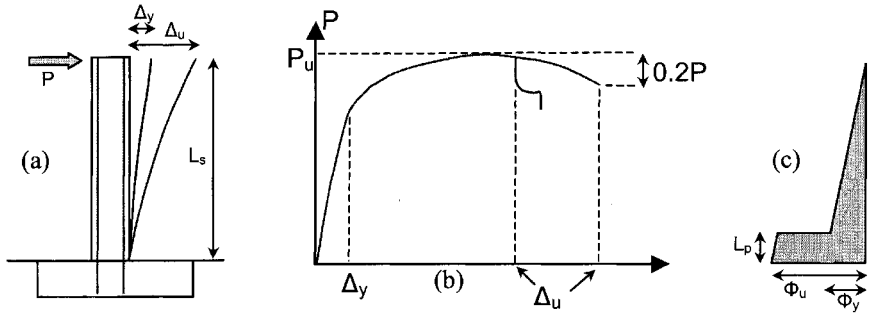


Figure 5 (a) Laterally loaded column, (b) load-displacement diagram, (c) distribution of curvature.

Strength and deformability

Analytical and experimental studies of the stress-strain response of FRP-confined concrete have been conducted by numerous researchers (see e.g. the reviews in Lam and Teng 2002, De Lorenzis and Tepfers 2003). Most of the FRP confinement models give the stress at ultimate strain, f_{ccd}, and the associated strain, ε_{ccud}, as functions of the respective unconfined values, f_{cd} and ε_{cud}, and the confining stress at ultimate, σ_{ud}, as given in eq. (3) – (4). Note that σ_{ud} is given by eq. (2) with $E_f\varepsilon_f$ replaced by f_{fd}, the design tensile strength of FRP.

$$\frac{f_{ccd}}{f_{cd}} = 1 + k_1\left(\frac{\sigma_{\ell ud}}{f_{cd}}\right)^{k_2} \tag{3}$$

$$\frac{\varepsilon_{ccud}}{\varepsilon_{cud}} = 1 + k_3\left(\frac{\sigma_{\ell ud}}{f_{cd}}\right)^{k_4} \tag{4}$$

$k_1 - k_4$ are empirical constants.

The increase in ultimate strain capacity of concrete is of particular interest in seismic retrofitting, when the objective of interventions is the increase of ductility, which may be quantified by the displacement ductility factor μ_Δ, defined as the ratio of displacement at ultimate, Δ_u, to displacement at yield, Δ_y (Figure 5).

The method of selecting the jacket thickness for a specified ductility factor μ_Δ is a relatively straightforward procedure: First the equivalent plastic hinge length L_p for a given column is calculated based on the yield stress and diametre of longitudinal rebars. From L_p and μ_Δ the curvature ductility factor $\mu_\Phi = \Phi_u/\Phi_y$ is established. The yield curvature Φ_y may be found from moment-curvature analysis of the cross section, whereas the maximum required curvature Φ_u may be obtained (again from section analysis) in terms of the ultimate concrete strain. Hence the required value for ε_{ccud} can be established and an appropriate confinement model can be used to solve for the required FRP thickness.

Alternatively, empirical relations between μ_Δ and the jacket characteristics (described through σ_{ud}) may be used, such as the one provided below (Tastani and Pantazopoulou 2002), which applies in the case of bending in the plane parallel to h:

$$\mu_\Delta = 1.3 + 12.4\left(\frac{\sigma_{\ell ud,h}}{f_{cd}} - 0.1\right) \geq 1.3 \tag{5}$$

Prevention of lap-splice failures

As a remedy to anchorage problems, FRP jackets are wrapped externally so that the fibers are oriented normal to anticipated splitting cracks at lap-splice regions. The capacity, F, of a given anchorage length ℓ_s is obtained in terms of the bond stress τ_b acting on the lateral surface of the bar. Using the frictional resistance model to represent interfacial steel-to-concrete bond (Figure 6), the value of τ_b is taken proportional to the lateral pressure exerted upon the lateral bar surface by the concrete cover, transverse stirrups and FRP wrapping. Hence the FRP contribution to prevent lap-splice failure, and hence activate yielding (at a stress f_{yd}) of a rebar with cross sectional area A_b is calculated from the following equation:

$$A_b f_{yd} = p_c \mu \sigma_\ell \ell_s \tag{6}$$

p_c is the likely cover spalling path (Priestley et al. 1996) and $\sigma = \sigma_{ud}$. Therefore, the required FRP thickness to prevent lap-splice failure may be obtained as follows:

$$t_f = \frac{bhA_b f_{yd}}{(b+h)p_c \mu f_{fde} \ell_s} \tag{7}$$

The frictional mechanism is meaningful so long as splitting cracks are narrow; for this reason a transverse strain limit in the order of 0.001-0.002 may be adopted, which limits f_{fde} to this strain times E_f.

Resistance to rebar buckling

The increase in deformation capacity of a RC member attained through FRP jacketing could be accompanied by a dramatic increase in the strain demand developed in the concrete compression zone and the longitudinal reinforcement, hence buckling of the rebars may dominate the response at an axial strain level which depends on the ratio of stirrup spacing to rebar diameter, s/d_b. It may be shown (Syntzirma and Pantazopoulou 2003) that the critical s/d_b ratio corresponding to rebar stress f_s is given by the relationship $s/d_b = 0.785(E_r/f_s)^{1/2}$, where E_r is the double modulus of steel at stress f_s. Therefore, for any given rebar and s/d_b, the axial compression strain of the rebar at buckling, hence the deformability of concrete, may be determined.

Experimental evidence suggests that FRP wraps may not mitigate rebar buckling, unless large amounts of confinement are provided. This is owing to the local stress concentration caused on the FRP at the mid-span between stirrups by the bending bar, resulting in brittle fracture of the jacket. However, Priestley et al. (1996) have suggested that buckling may be prevented in circular columns of diameter D if the volumetric ratio of the FRP jacket ($4t_f/D$) exceeds the following limiting value:

$$\frac{4t_f}{D} \geq \frac{0.45nf_s^2}{E_r E_f} \tag{8}$$

where n = number of rebars in the cross section. A plausible extension to rectangular columns would be

$$\frac{k_e 2(b+h)t_f}{bh} \geq \frac{0.45nf_s^2}{E_r E_f} \tag{9}$$

which can be used to obtain the required FRP thickness.

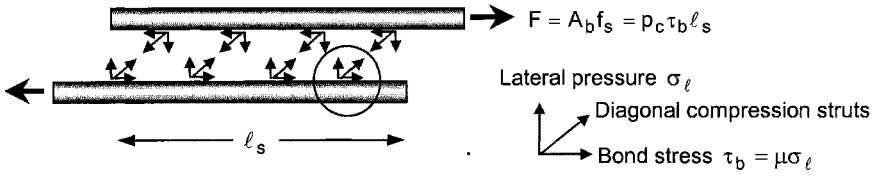


Figure 6 Stress transfer through friction along the lap-splice length

Alternative confinement systems

Column wrapping through the use of FRP has been applied extensively worldwide, especially in seismic regions. The "traditional" method comprises wrapping with the required number of FRP layers using *full bond*, which implies coverage of the concrete surface as well as full impregnation of the sheets with epoxy resin (Figure 7a). Labor as well as materials costs associated with this technique can be reduced significantly, by wrapping fiber tapes in an unbonded state. A few alternatives have been investigated by the author, two of which are shown in Figure 7b-c.

Figure 7b shows wrapping of successive fiber tapes with resin only at a short distance near the ends. Figure 7c illustrates an interesting concept, which comprises the following steps: (a) Wrapping of the first fiber tape (solid lines in Figure 7c) in a spiral configuration, starting from one end (top of column) and stopping at the other (bottom of column); resin is applied only at the two ends, to ensure stability of the tape. (b) Application of the next tape in exactly the same manner, but wrapping is applied in the opposite direction. (c) Steps (a)-(b) may be repeated as many times as needed to achieve the required number of layers. (d) Wrapping of two horizontal tapes (minimum two layers) with full epoxy bond, at the top and bottom of the column, in order to ensure proper anchorage of the spirally wound tapes.

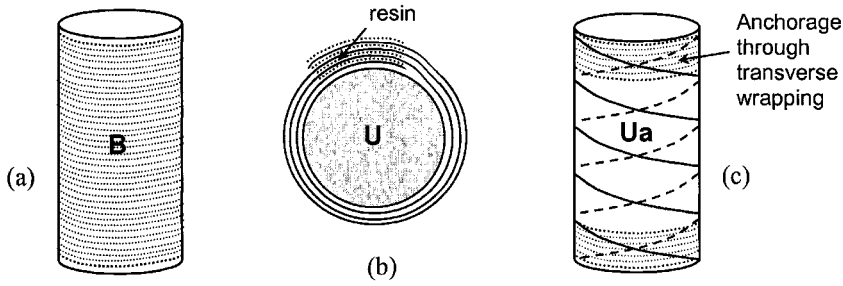


Figure 7 Alternative FRP wrapping systems: (a) full bond through epoxy resin, (b) Unbonded jacket, and (c) Application of unbonded spirally wound sheets in two directions, in combination with end anchorage.

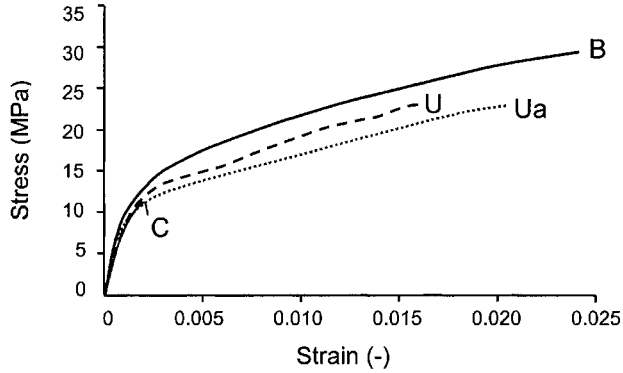


Figure 8 Stress-strain curves for concrete confined with FRP. C: control specimen; B: fully bonded jacket; U: unbonded jacket; Ua: unbonded spirally wound sheets anchored at their ends. All specimens are wrapped with 2 layers of 0.12 mm carbon fiber sheets.

The effectiveness of unbonded wraps is not expected to be as high as that of fully bonded ones. As shown in Figure 8, both configurations, U and Ua, resulted in slightly reduced strength and deformability compared to B. However, these reductions might be acceptable in certain applications. For instance, if the aim of wrapping is to increase deformability, unbonded wrapping, especially when combined with end strips, is an acceptable solution.

Flexural strengthening

Externally bonded strips or sheets

RC beams or slabs may be strengthened in flexure through the use of epoxy-bonded FRP reinforcement to the tension side. The analysis for the ultimate limit state (ULS) in this case follows well-established procedures for reinforced concrete member design, provided that: (a) the contribution of FRP is taken into account properly and (b) special consideration is given to the issue of bond between concrete and FRP. Crucial to the ULS calculation is the identification of failure modes, which may be summarized as shown in Figure 9.

Modes (1) – (3) may be treated by standard cross section analysis, assuming that the FRP behaves linear elastically to failure. Debonding failure modes, (4) – (6), require the calculation of the maximum anchorable force, which may be given in terms of the bond length, the axial rigidity characteristics of the FRP, the tensile strength of concrete and empirical constants. Finally, mode (7) can be analyzed by checking the shear capacity at the FRP termination. Detailed treatment of these failure mechanisms may be found e.g. in *fib* (2001) and Teng et al. (2001).

Pretensioned strips

In some cases it may be advantageous to bond the external FRP reinforcement onto the concrete surface in a prestressed state. Both laboratory and analytical research (e.g. Triantafillou et al. 1992, Garden et al. 1998) shows that prestressing represents a significant contribution to the advancement of the FRP strengthening technique, and

methods have been developed to prestress the FRP composites under real life conditions. However, these methods involve the use of special anchorage devices, which increase the cost and, mainly, the complexity of the technique; thus, simplicity in application, on of the technique's key advantages might be lost.

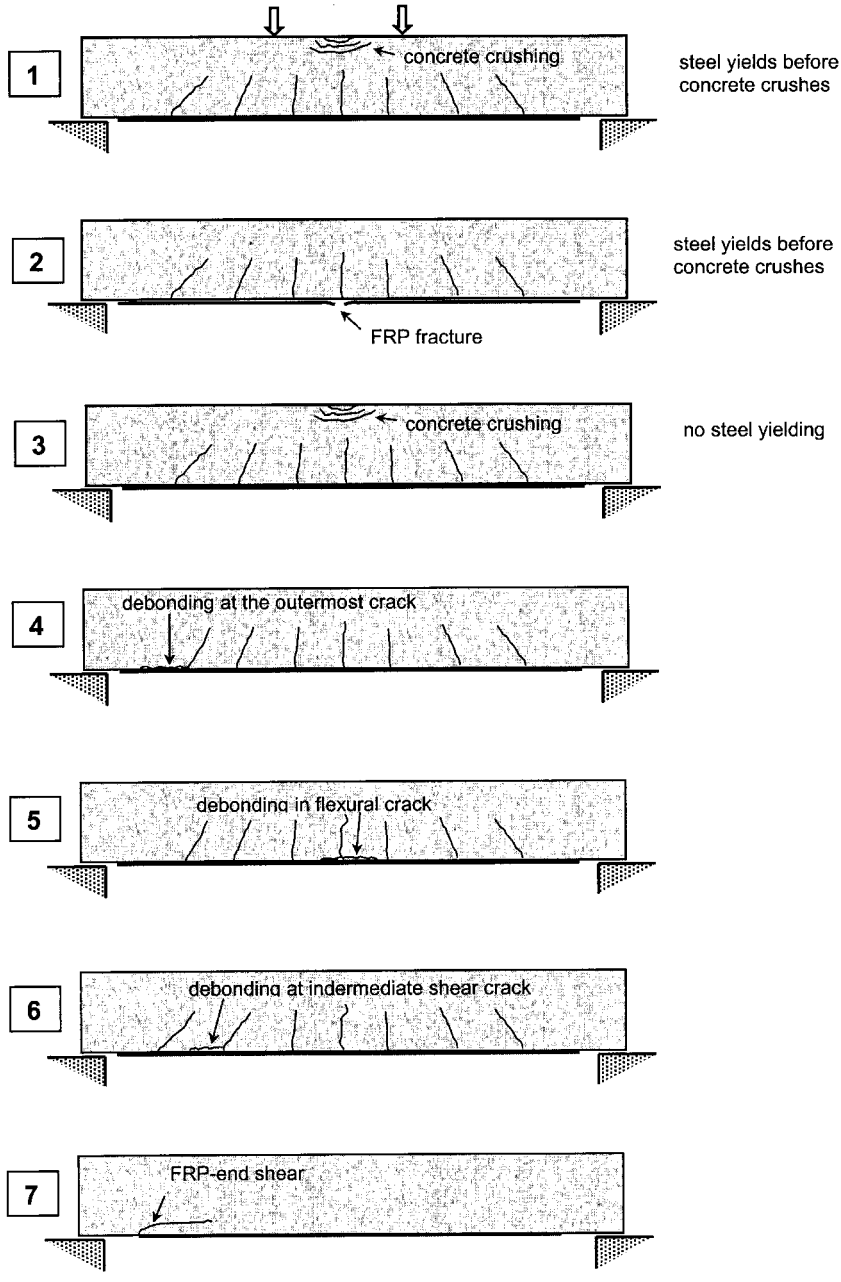


Figure 9 Failure modes of RC beams strengthened with FRP in flexure.

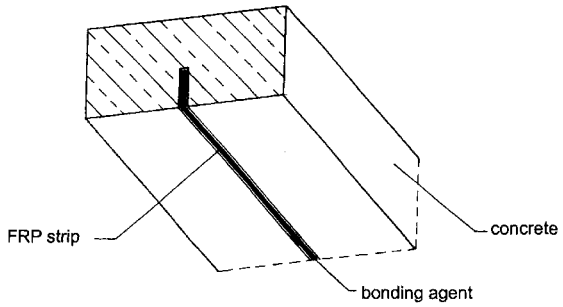


Figure 10 Flexural strengthening with FRP placed inside slits.

FRP inside slits (near surface mounted reinforcement)

FRP inside slits may be thought of as a special method of supplementing reinforcement to concrete structures. The slits are cut into the concrete structure with a depth smaller than the concrete cover. FRP strips e.g. with a thickness of 2 mm and a width of 10-20 mm are bonded into these slits (Figure 10) using epoxy-based or mortar-based adhesives.

Bond tests and beam tests have been carried out to study the mechanical behaviour of the system (e.g. Blaschko and Zilch 1999, De Lorenzis 2002). It was shown that a higher anchoring capacity compared with FRP strips bonded onto the surface of a concrete structure is obtained. The mechanical behaviour is stiffer under serviceability loads and more ductile in the ultimate limit state. The tensile strength of the FRP can be reached in members with additional reinforcement consisting of strips in slits, if there is enough load carrying capacity of the compression zone in the concrete and for shear. The bond behaviour with high strength and ductility allows to bridge wide cracking without peeling-off. Finally, the strips are protected against accidental impact.

Placing FRP inside slits is a particularly effective method for flexural strengthening of RC columns, when the maximum moment develops in the critical regions (column ends). This is the case, for instance, when the width of columns is approximately equal to that of beams, hence the application of epoxy-bonded strips that continue through the beam column joints is not feasible (Figure 11b). The use of FRP inside slits in RC columns subjected to a combination of bending moment and axial load is extremely beneficial for the combination of flexural capacity and axial load capacity, provided that the FRP does enter in the compression zone. This is illustrated in the interaction diagrams shown in Figure 12, which illustrate how the normalized axial load versus bending moment envelope opens at low axial load levels as the volumetric fraction of FRP increases. ρ_{eq} in Figure 12 is the equivalent volumetric fraction of reinforcement, defined as

$$\rho_{eq} = \rho_s + \rho_f \frac{E_f}{E_s} = \frac{A_{s,tot}}{bd} + \frac{A_{f,tot}}{bd}\frac{E_f}{E_s} \tag{10}$$

where $A_{s,tot} = 2A_{s1} = 2A_{s2}$ = total area of longitudinal steel reinforcement (placed symmetrically in the cross section), $A_{f,tot} = 2A_f$, A_f = cross sectional area of FRP in

each side of the cross section, b = width of cross section, d = static depth, E_f = elastic modulus of FRP and E_s = elastic modulus of steel.

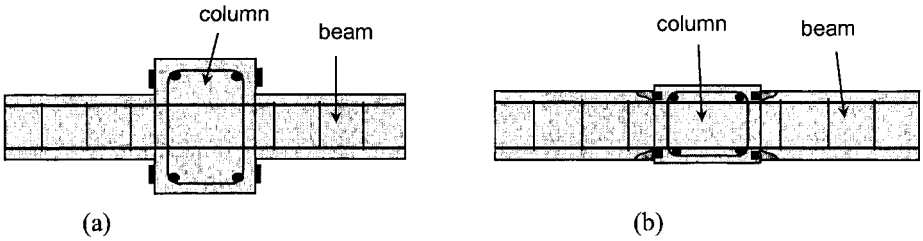


Figure 11 Cross sections of columns with externally placed FRP reinforcement for increased flexural resistance at the critical cross sections (top and bottom). (a) Externally bonded strips in wide columns; (b) FRP placed inside slits.

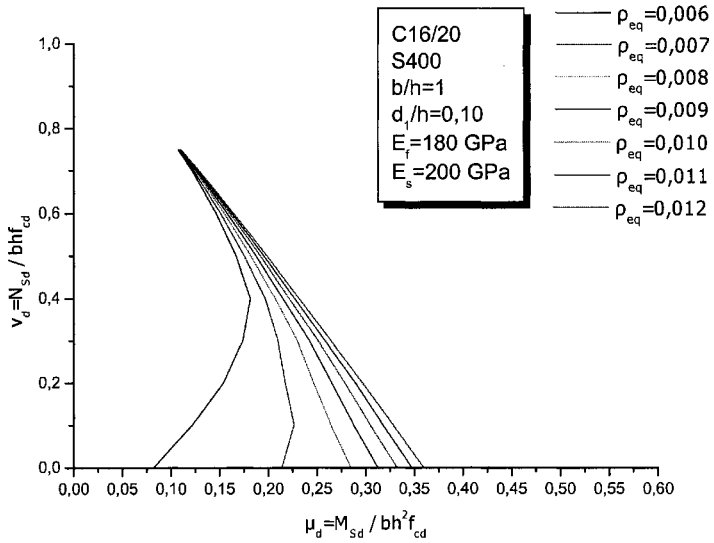


Figure 12 Normalized axial force – bending moment interaction diagram.

CONCLUSIONS

Externally bonded FRP have been employed extensively throughout the world in numerous rehabilitation applications of reinforced concrete structures. Extensive analytical and experimental studies have shown that FRP in the form of strips or sheets can be quite effective in applications where the intervention aims at increasing the flexural capacity (e.g. beams, slabs, columns), the shear capacity (e.g. beams, columns, shear walls, beam-column joints) or the confinement (e.g. for ductility, in lap-splice regions, to delay buckling) in RC elements. Relatively new applications of the FRP-strengthening technique, namely the use of unbonded wrapping and the placement of

reinforcement inside slits are of great potential, thus expanding the range of applicability of advanced composites in the upgrading of concrete structures.

References

1 T C Triantafillou and C P Antonopoulos, 'Design of concrete flexural members strengthened in shear with FRP', *J Comp Constr, ASCE*, 2000, **4**(4), 198-205.

2 J Paterson and D Mitchell, 'Seismic retrofit of shear walls with headed bars and carbon fiber wrap', *J Struct Engrg*, 2003, **129**(5) 606-614.

3 C P Antonopoulos and T C Triantafillou, 'Experimental investigation of FRP-strengthened RC beam-column joints', *J Comp Constr, ASCE*, 2003, **7**(1), 39-49.

4 C P Antonopoulos and T C Triantafillou, 'Analysis of FRP-strengthened RC beam-column joints', *J Comp Constr, ASCE*, 2002, **6**(1), 41-51.

5 L Lam and J G Teng, 'Strength models for fiber-reinforced plastic-confined concrete', *J Struct Engrg*, 2002, **128**(5), 612-623.

6 L De Lorenzis and R Tepfers, 'Comparative study of models on confinement of concrete cylinders with fiber-reinforced polymer composites', *J Comp Costr*, 2003, **7**(3), 219-237.

7 S Tastani and S J Pantazopoulou, 'Design of seismic strengthening for brittle RC members using FRP jackets', 12th Europ Conf *Earthquake Engineering*, Elsevier Science Ltd, 2002.

8 M J N Priestley, F Seible and M Calvi, *Seismic Design and Retrofit of Bridges*, John Wiley and Sons Ltd, 1996.

9 D V Syntzirma and S J Pantazopoulou, 'Assessment of deformability of old-type RC members using capacity-based prioritizing of failure modes', fib Symp *Concrete Structures in Seismic Regions*, Athens, 2003.

10 fib Bulletin 14, *Externally Bonded FRP Reinforcement for RC Structures*, Technical Report, 2001.

11 J G Teng, J F Chen, S T Smith and L Lam, *FRP Strengthened RC Structures*, John Wiley and Sons Ltd, 2001.

12 T C Triantafillou, N Deskovic and M Deuring, 'Strengthening of concrete structures with prestressed FRP sheets', *ACI Struct J*, 1992, **89**(3), 235-244.

13 H N Garden, L C Hollaway and A M Thorne, 'The strengthening and deformation behaviour of reinforced concrete beams upgraded using prestressed composite plates' *RILEM Mater and Struct, 1998,* **31**, 247-258.

14 M Blaschko and K Zilch, 'Rehabilitation of concrete structures with CFRP strips glued into slits' 12th Intern Conf *Composite Materials*, Paris, 1999.

15 L De Lorenzis, *Strengthening of RC Structures with Near-Surface Mounted FRP Rods*, PhD Thesis Dissertation, University of Lecce, 2002.

A FAIR DINKUM APPROACH TO FIBRE COMPOSITES IN CIVIL ENGINEERING

Gerard Van Erp and Stephen Ayers

University of Southern Queensland, Toowoomba, QLD, 4350 Australia

INTRODUCTION

As in many other developed nations in Europe and North America, Australian asset owners are actively seeking solutions for the rehabilitation and replacement of deteriorating civil infrastructure. While the reasons for this interest are somewhat different in Australia than in other parts of the world, major asset owners are faced with the same problem of having decreasing budgets to address an ever increasing demand for structural replacements or upgrades.

Over the past ten years, Australian researchers have actively pursued the development of new structural systems utilising fibre composites to address this industry need. While much of this work has gone largely unnoticed by the rest of the world, the research is now paying dividends with a range of new systems providing design solutions which not only offer unprecedented levels of functionality but do so at a cost which is directly competitive with traditional structural materials. Several of these systems have been successfully demonstrated in real world projects and are now being developed into commercial offerings.

In addition to this work, the Australian composites industry has been investing in a program to put composites technology on a more competitive footing with traditional structural materials such as timber, steel and reinforced concrete. Current programs include the development of design documentation such as codes and standards, as well as the establishment of an appropriate regulatory framework which can ensure confidence in manufacture, supply and installation of composite products.

This paper presents an overview of Australian research into infrastructure applications of fibre composites and associated industry development programs.

DEVELOPMENT OF NEW FIBRE COMPOSITE STRUCTURES

Australia's First Fibre Composite Bridge

While the lack of harsh winters and associated salting of roads removes one of the major causes of bridge deterioration that exists in the USA and Europe, Australia too faces a major bridge replacement program. There are approximately 40,000 road bridges of 7m span or larger in Australia, with a total asset value estimated around $10 billion. Of these, about 10,000 are of timber construction, mostly on the Eastern Seaboard. While old forest hardwood timber is a durable material, many of these bridges, in excess of 60%, were built before the 1940's and were designed to lower loading standards than would be required today. Many of these structures require major rehabilitation or replacement now or in the near future. Hardwood as a structural material is a rapidly diminishing resource and infrastructure owners are actively seeking alternative solutions. With their purported high durability and ability to mimic timber performance through judicious design, fibre composites have become an area of significant interest.

The first fibre composite bridge in the Australian public road network was installed on 19 February 2003 (Figure 2). This installation was the culmination of a development and innovation process lasting over 5 years and involving a wide range of interested parties including; Queensland Department of Main Roads (QDMR), the Roads and Traffic Authority of New South Wales (RTA), the Department of Industry Science and Resources (DISR), Fibre Composite Design and Development (FCDD), Wagners Composite Fibre Technologies (WCFT), the Cooperative Research Centre for Advanced Composite Structures (CRC-ACS) and consulting engineers Connell Wagner and Cardno MBK.

The project originated with a generic design exercise commissioned by the RTA which sought to identify which particular fibre composite bridge technologies should be encouraged. This involved the development of a performance specification that met RTA requirements and the submission of two conforming design concepts. One of these was a novel local concept developed by FCDD, the second was put forward by the CRC-ACS together with engineering consultant Cardno MBK. This design incorporated the latest technology from the United States.

The FCDD solution was selected as the preferred alternative based on a set of agreed selection criteria. The concept combined the high compression capacity of plain concrete with the high strength/low weight characteristics of fibre composites [1]. The design concept was based on the traditional plank bridge concept, where individual beams are laterally post tensioned to create a bridge (Figure 2).

The advantages of this concept include:

- No joints between deck and girders (the girders are the deck);
- Excellent resistance against flood loading and side impact;
- Significant redundancy in the structure due to large number of beams;
- The concept is well understood by bridge engineers;

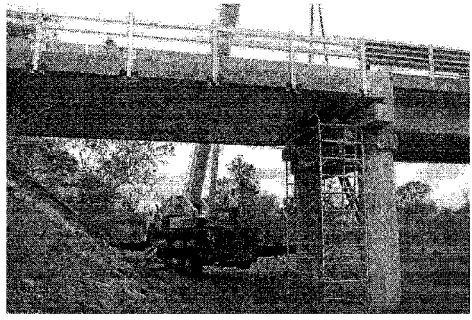


Figure 2. Installation of Australia's first fibre composite bridge

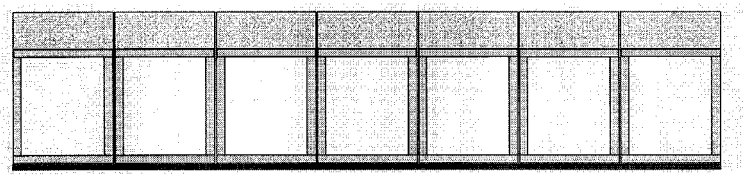


Figure 2. Principle of Australia's first fibre composite bridge deck

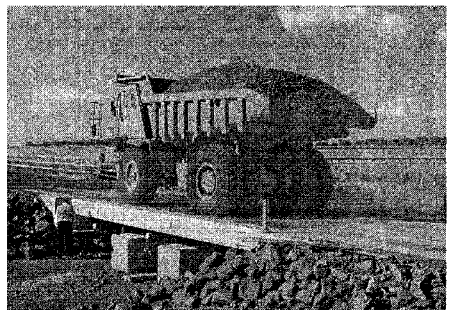


Figure 3. Full scale prototype of composite bridge under test

- Significant understanding of the bridge behaviour can be obtained through testing of individual beams.

The beams in the successful design were a box section formed using glass reinforced, isophthalic polyester pultruded profiles. Additional carbon fibre reinforcement was incorporated into the base of the deck to enhance stiffness. Plain concrete was used to form a compression flange on top of the beams.

FCDD partnered with Wagners Composite Fibre Technologies, the RTA and QDMR to develop the concept into a working prototype which was installed on a Wagner's owned quarry site near Toowoomba, Queensland (Figure 3) in early 2002. An extensive series of field tests followed, revealing that the concept exceeded expectations in terms of its technical performance. Based on this development work, RTA developed a project to install one of these new generation bridges for trial purposes.

The selected installation site was an existing timber span (circa 1940) on a bridge over the Orara River at Coutts Crossing in northern New South Wales. Consulting engineers Connell Wagner were engaged by WCFT to review and modify FCDD's fibre composite bridge concept to suit the site specific requirements at Coutts Crossing. The new bridge deck design was seen to offer substantial benefits over traditional bridge deck design, including:

- Installation in only 5 days, instead of 8 to 10 weeks for the conventional alternative,
- 90% savings on traffic control costs, and
- 75% saving on bridge transportation costs.

The bridge was constructed by WCFT under the supervision of FCDD and installed in February 2003. Initial site testing shows that the bridge is performing well. The RTA will continue to periodically monitor the bridge in coming years.

The Brisbane RiverWalk Project

RiverWalk is a 34 km long trail along the banks of the inner city reaches of the Brisbane River. The RiverWalk concept caters for jogging, cycling, walking and recreation and joins people and the river together. It is an important transport link catering for nearly 20,000 person trips per day. In keeping with the theme of providing a variety of experiences, a section near the Story Bridge has been designed as a floating walkway (Figure 4). The walkway is 850 m long and 5.4 m wide. It has 600 mm freeboard and is

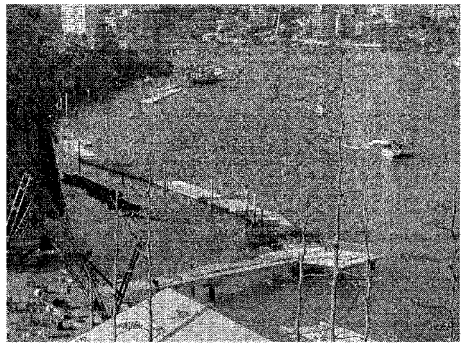


Figure 4. Brisbane's Floating Walkway

provided with universal access. The walkway consists of 288 individual concrete floats connected by beams called walers.

The original waler design utilised timber and steel which are the traditional materials for this type of structure. However, due to the aggressive marine environment, these walers would require replacement every 10 to 15 years which made them the weak link in the 100 year design life required for the walkway. In a bid to find a better alternative, Brisbane City Council approached FCDD about the possible use of fibre composites for the walers. Based on a detailed set of specifications including structural performance, vandal resistance, boat impact and aesthetics, FCDD developed a revolutionary new waler beam concept using a patented combination of polymer concrete, 3-dimensional fibre composite reinforcement and a special filled resin system. The beam concept was designed to carry a wide range of static and dynamic loads and was extensively tested before being applied in the RiverWalk (Figure 5).

Although having twice the cost of timber and steel, the whole-of-life costs of composite walers are significantly lower. BCC was impressed with the cost-performance benefits of this concept and it was decide to use this concept for all 600 beams in the walkway project. All the walers for the project were fabricated by FCDD at their Toowoomba research facility.

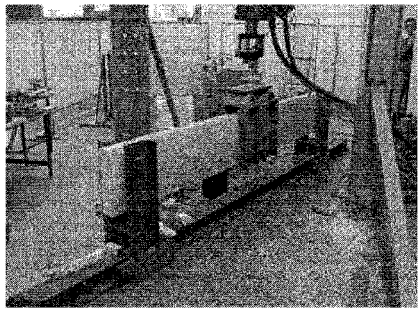


Figure 5. Testing of fibre composite walers

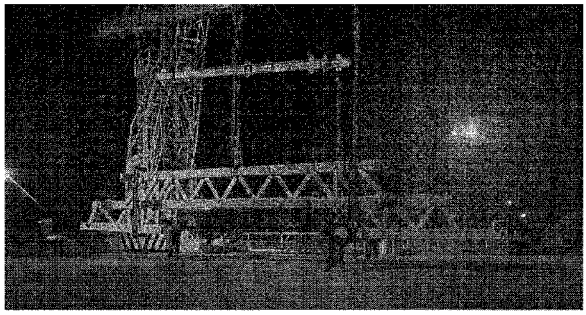


Figure 6. 18m long fibre composite truss

Innovative Fibre Composite Truss Structure for RiverWalk

One area of the floating walkway that presented a serious structural challenge was the downstream end. This section of the walkway supports a 20m span, 5m wide pedestrian bridge, which provides access from the waterfront onto the floating walkway. In order to distribute the highly concentrated loads from the bridge over a number of pontoons, an 18m long structural member was required. A large part of this member is submersed in saltwater. The extremely high dynamic loads and harsh environment made traditional design solutions a prohibitive option.

A special fibre composite truss was developed for this application (Figure 6). Because of its low weight (5000 kg), the truss offered significant benefits in terms of construction and installation time. Estimates on an alternative stainless steel solution were nearly three times the price of the composite truss. The truss has been designed to carry an ultimate bending moment of 700KNm, is 2.5m deep and has a 1.4m deep cut out to accommodate the pedestrian bridge. It provides an extremely durable and high capacity solution to a difficult engineering problem.

REHABILITATION OF CONCRETE STRUCTURES

Strengthening of West Gate Bridge Approach Spans

In 2001 one of the world's largest carbon fibre strengthening programs was undertaken in Melbourne, Victoria. The West Gate Bridge in Melbourne links the western industrial and residential areas to the main city and is one of the cities busiest transport corridors. The 650m long bridge comprises a pre-cast, segmented box girder with pre-cast, post-tensioned cantilever frames and a composite reinforced concrete deck slab. The structure was designed in the mid 1960's.

The construction of additional approach lanes to the bridge required the placement of an additional traffic lane within the existing roadway. The bridge was originally designed for a maximum of 8 traffic lanes and thus it was determined that strengthening of the structure was required to accommodate the new lanes.

URS Australia Pty Ltd undertook a structural assessment of the concrete approach spans on behalf of the Victorian state road authority (VicRoads). This assessment determined that the bridge had insufficient capacity for:

- Global hog of the box girder over piers at serviceability limit state

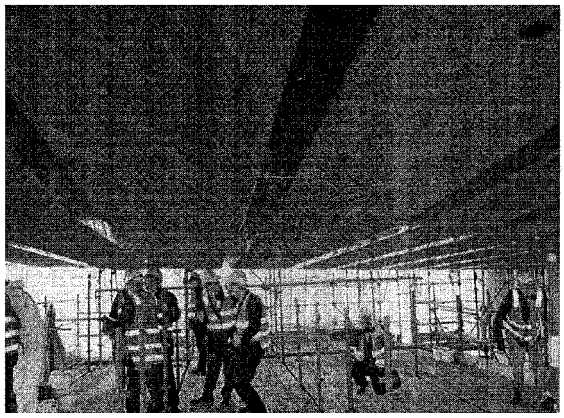


Figure 7. Inspection of strengthening system

- Combined shear and torsion near the piers at ultimate limit state
- Local sag moments in the deck slab at ultimate limit state
- Local bending capacity in the cantilever frame at ultimate limit state.

VicRoads decided to undertake the necessary strengthening works via a Design and Construct contract. The overall project cost was of the order of A$10 million. URS Australia Pty Ltd joined with Abigroup and Savcor to launch a successful bid for the project, which was awarded in May 2001. The use of fibre composite laminates was a key component in the winning bid.

Strengthening of the structure was achieved through a combination of external post-tensioning using longitudinal steel tendons, as well as the application of bonded FRP strips and sheets (Figure 7). BBR Systems Ltd (Zurich) supplied the FRP products for the project. FRP was used for both flexural, shear and torsional strengthening. To achieve adequate anchorage, the shear and torsional laminates were slotted into the concrete deck using a special concrete cutting saw.

The cantilever frames were strengthened for flexure. FRP was placed near the top of the pre-cast concrete frame to increase the tensile capacity, however due to the over-reinforced nature of the cantilever, it was also found necessary to provide bottom flange compression strengthening in the form of steel plates.

The scale and complexity of the FRP strengthening undertaken in this project was unprecedented at the time and has demonstrated the cost effectiveness of FRP for strengthening large span concrete bridges in Australia.

Research Into Externally Bonded Plates for Rehabilitation of Concrete Members

In addition to real world applications such as the West Gate Bridge, Australian researchers are also involved in fundamental research to better understand this type of system. The Centre for Infrastructure Diagnosis, Assessment and Rehabilitation at the School of Civil and Environmental Engineering, University of Adelaide is involved in research into retrofitting using externally bonded plates [2,3]. Areas of research include:

- Seismic retrofitting of rectangular columns
- Critical crack debonding of adhesively plated beams (Figure 8)
- Intermediate crack debonding of adhesively plated beams

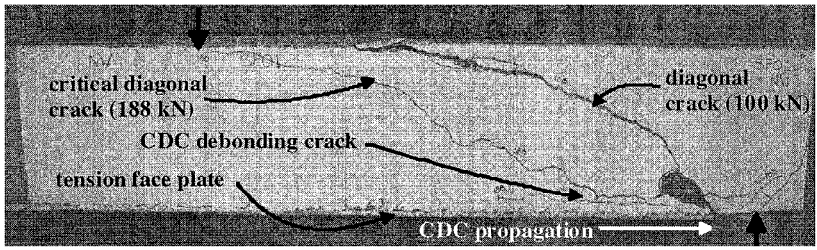


Figure 8. Investigations into critical crack debonding of adhesively plated beams

- Debonding of adhesively plated masonry
- Bolted plated beams

The centre is also working on the development of generic design rules for all forms of plating which allow the designer to develop their own application techniques. Research in this area encompasses:

- plate fixing techniques including adhesive bonding and/or bolting
- plate materials including steel, aluminium, carbon FRP and glass FRP
- plate positioning such as tension face, side and compression face plates
- plate geometry including flat plates, and angle or channel sections
- plate function such as the enhancement of the strength or ductility

Comprehensive design rules have now been developed for plating RC beams and slabs which covers all forms of plating and can be used to quantify both the strength and ductility.

Researchers within the Department of Civil Engineering at Monash University, Melbourne, are also investigating bonded FRP / concrete systems. Research has included:

- investigation of end cover separation and shear crack debonding failure mechanisms in rectangular concrete beams with bonded FRP plates
- shear strengthening of reinforced concrete T-beams with L-shaped CFRP strips (Figure 9) , and
- torsional strengthening of rectangular concrete beams with externally bonded CFRP sheets.

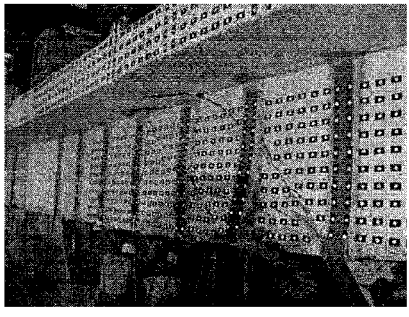


Figure 9. Experimental investigation of shear strengthening of concrete T-beams with CFRP strips at Monash University

REHABILITATION OF TIMBER STRUCTURES

Replacement of Hardwood Timber Beams

The decreasing access to hardwood timber both in terms of volume and quality, has created strong national demand for alternatives solutions from asset owners with large inventories of hardwood timber structures. FCDD has been developing hybrid composite/timber beams for several years, and is in the process of commercialising a range of products to meet the needs of specific markets.

The concept is based on the use of plantation softwood for the bulk of the beam, with composite reinforcement modules being used to increase the strength and stiffness up to that of a typical Australian hard wood beam (see Figure 10). The plantation timber is laminated veneer lumber (LVL), because this type of timber product has less variability than sawn timber, resulting in more predictable properties. The main function of the timber is to provide the shear capacity to the beam, as well as maintaining the separation between the reinforcement modules.

The reinforcement modules use a combination of composite materials and have a Modulus of Elasticity of 60GPa with a failure strength of around 200MPa. The modules are bonded to the timber using a high strength epoxy adhesive. The stress in the adhesive is relatively low due to the large surface area of the module

Figure 11 shows a comparison between the load-displacement behaviour of a typical hybrid composite/timber beam and that of a range of Australian hardwood beams. F34 hardwood has a characteristic flexural strength of 100MPa and a Modulus of Elasticity of 21500MPa. This type of beam used to be readily available but is very rare these days. Figure 11 also shows that the hybrid beam can be designed to have a ductile failure mode which gives significant warning of failure.

The Rail Infrastructure Corporation of NSW has identified a number of applications for this type of beam. These include:

- shorter span beams with a typical cross section of 300x300mm^2 and a span of 7m, and
- longer span girders (18m and 23m) which require shallow abutment depth and a flat soffit, to minimise earthworks and retain minimum track clearances.

A number of tests have been carried out in the development of these hybrid composite/timber beams, aimed at verifying the strength, stiffness, failure mode, and predictability. The first 5 hybrid beams will be installed in two separate bridges early in 2004.

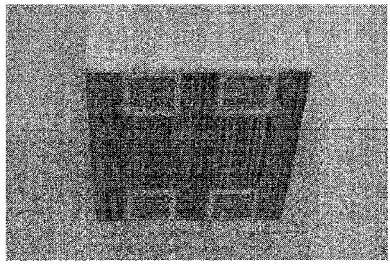


Figure 10. Example of hybrid beam cross-section

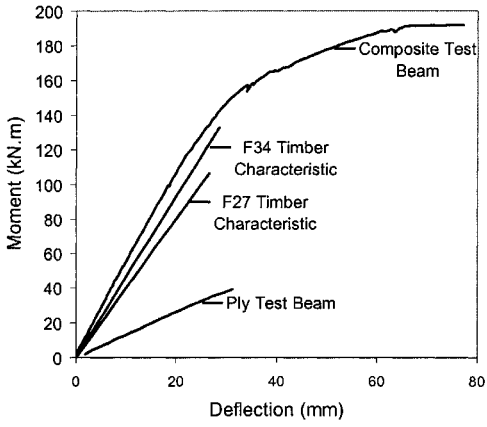


Figure 11. Behaviour of new hybrid composite beam compared with Australian timbers

DESIGN CODE DEVELOPMENT PROGRAM

The market growth restrictions imposed by the lack of appropriate design codes and standards from composites in civil infrastructure applications have been well documented. Recognising this significant barrier to broad utilisation of fibre composites in civil engineering, Fibre Composites Design and Development (FCDD) embarked on a major initiative to develop an Australian Code of Practice for the structural design of fibre composites. This initiative was developed as part of a broader program of industry development with the Composites Institute of Australia and key civil engineering industry stakeholders. Funding for this program has been provided by the Australian Federal Government and the Queensland State Government, with additional support from a range of industry stakeholders.

The primary objective of the Australian code development program was to create a platform whereupon practicing structural engineers could begin to employ fibre composite materials in their design solutions. It was believed that by opening up the world of composites to a wider segment of the structural engineering community, new and innovative structural forms would emerge to incorporate these materials in a more functional and economically viable manner.

Recognising that most current design codes for timber, steel and reinforced concrete, have evolved from an established technology base and history of application, Australian developers believed that the most appropriate initial step in creating a regulated design system was the preparation of an industry based Guide of Best Practice. The aim of this document is not to provide highly prescriptive design guidance on specific structural elements like the more established material codes due to the relative infancy of the infrastructure composites technology. Instead, the document has been developed to provide engineers with sufficient foundational guidance to begin exploring new structural systems utilising composites.

As documented earlier in this paper, researchers at FCDD have demonstrated that cost effective, real-world structures using fibre composites are achievable. However most of these new composite systems take a significantly different form than those

traditionally targeted at the infrastructure market. It is thought that as more engineers explore ways of using composites in their particular applications, a range of other forms and techniques will also emerge. Furthermore, it is considered likely that many of these new systems will also be distinctly different from those currently in the marketplace. Over time improved knowledge and market forces will result in some of these concepts becoming accepted practice while others will fall by the wayside. As this occurs, the successful forms and practices will be incorporated into more prescriptive design codes.

The key at this early stage is to provide the framework necessary for these new forms to be explored and it is believed that the cornerstone of this framework is the provision of accurate and reliable materials data.

One of the core assumptions underlying the Australian work is that the true potential of fibre composites can only be exploited through the use of sophisticated analysis techniques such as finite element analysis. Research experience at USQ has shown that, with correct material data and in the hands of suitably skilled personnel, these tools can be effectively used to develop new structural systems within acceptable levels of confidence. However, to effectively utilise these tools, there is a need to provide engineers with materials data which they can have confidence in.

Australian researchers have moved to address this need on two fronts:

- the development of the National Composites Certification Scheme; and
- the development of a Guide of Best Practice on Materials Properties for the Design of Fibre Composite Structures.

A handbook to assist practicing engineers in interpreting and using the Guide of Best Practice is also under development.

The National Composites Certification Scheme

The National Constituent Certification Scheme (NCSS) is designed to provide a mechanism for standardising the determination and reporting of materials data. The aim is to establish a scheme wherein a central industry body monitors and certifies the performance of all composite materials and constituents sold into the Australian civil infrastructure market. The adopted approach is quite similar to that established by the Australian plywood industry [4].

A standardised program of material characterisation will be established and a centralised laboratory will evaluate all submitted materials in accordance with the prescribed methods. The obtained results will be compared against an established set of objective performance criteria and on the basis of this comparison materials will be awarded a performance grading. The allocated grade will be ratified by an independent certification committee operating under the NCSS. The manufacturer will then be given the right to market the product with trademarked product labelling indicating the allocated grade.

Certification of a product will be for a 5 year period with potential for renewal after that time. During the period of certification, the product may be periodically checked by the NCSS. Products found to deviate significantly from original certification will then be subject to review and possible revocation of their certification. Disqualification of a product will require removal of trademarked grading signage from all products and associated literature.

The NCSS will operate under the auspices of the Composites Institute of Australia's Polymer Composites in Construction (PCiC) division. The scheme will be overseen by a committee with representation from key industry stakeholders.

The initial stage in establishing the NCSS has been the development of a characterisation and grading program for polymer matrix materials used in fibre reinforced laminates. A draft characterisation program has been prepared and is currently under review. This project was undertaken with the support of six of Australia's largest resin suppliers.

The project also involved an experimental investigation of around twenty five matrix systems put forward by the participating manufacturers. The systems have been subject to a wide array of characterisation testing to evaluate proposed test methods and to assist in developing property data for the Guide of Best Practice. This initial program for matrix systems will be used as a model for further work on reinforcements, adhesives and core materials.

Guide of Best Practice on Material Properties for Design

The Guide of Best Practice on Material Properties for the Design of Fibre Composite Structures builds on the work of the NCSS by providing design engineers with the information necessary to begin exploring structural systems involving fibre reinforced composites. The guide has been designed to provide engineers with the material data necessary for input into standard finite element analysis software. It sets out procedures for determining characteristic material properties either from standardised material tables contained within the guide or through direct testing of a specific material combination.

The guide contains a number of standardised material property tables for basic lamina forms. The fundamental forms addressed are:

- Unidirectional laminae
- Woven laminae (based on unidirectional laminae but modified by the direction percentage of fibre and a weave factor)
- Random fibre laminae

This is consistent with the approach of the earlier British tank design standard BS4994 [ref].

Table 1 shows an example of a characteristic property table for unidirectional laminae. Similar tables are provided for the other lamina forms. At this point in time only E-glass and HS carbon reinforcements have been addressed in the guide. Other reinforcements will be added to the guide as required. Experimental work to develop the values for each property is currently underway.

The lamina grade is defined by the certified grade of constituent materials used. The engineer selects the grade of constituent material necessary based on the nature of the structure being designed and the criticality of the component. A set of characteristic properties can then be determined for tension and compression loading parallel and perpendicular to the fibre axis and for in-plane shear.

There are several points worth noting about the adopted approach. Firstly, stength and stiffness properties parallel to the fibre axis are defined in terms of Normalised Unit values (N/mm per kg/m^2 of reinforcement). These properties are fibre dominated and this system is seen to better characterise fibre dominated behaviour [5]. Properties perpendicular to the fibre axis remain in traditional stress units. The guide provides for simple conversion between the two systems of units.

Secondly material capacities are primarily defined in terms of strain limits not strengths. Strength values are determined as a product of the modulus and strain values. This has been done to encourage a focus on strain based design which it is felt is more

Table 1 - Example of characteristic material property table for unidirectional laminae in draft Guide of Best Practice

Property		Symbol	Lamina Grade	Value / Formula	Units
Parallel to the Fibre Axis					
Normalised Unit Modulus		E_{N1}	ALL		N/mm per kg/m^2
Characteristic Strain Limit	Tension	ε'_{1T}	A – A		%
			B – A		
			B – B		
	Compression	ε'_{1C}	A – A		%
			B – A		
			B – B		
Normalised Unit Strength*		f_{Nik}	ALL	$f_{Nik} = E_{Ni}\varepsilon'_{ik}$	N/mm per kg/m^2
Perpendicular to the Fibre Axis					
Modulus of Elasticity		E_2	ALL		MPa
Characteristic Strain Limit	Tension	ε'_{2T}	A – A		%
			B – A		
			B – B		
	Compression	ε'_{2C}	A – A		%
			B – A		
			B – B		
Characteristic Ultimate Stress	Tension	f'_{2T}	ALL	$f'_{2T} = 0.9E_2\varepsilon'_{2T}$	MPa
	Compression	f'_{2C}	ALL	$f'_{2C} = 0.75E_2\varepsilon'_{2C}$	MPa
In-Plane Shear					
Shear Modulus		G_{12}	ALL		MPa
Characteristic Shear Strain Limit		γ'_{12}	ALL	2.0	%
Shear Strength		V_{12}	ALL		MPa
Poisson Interaction					
Poisson's Ratio		ν_{12}	ALL	0.25	

appropriate to composite materials where multiple materials are often combined within the one system.

The procedure adopted in the guide for determination of characteristic properties has been deliberately kept simple to encourage wider adoption of guide by practicing engineers. It is acknowledged that a significant number of simplifying assumptions have been made in this process, however it is believed that the end result retains acceptable levels of engineering accuracy while facilitating ease of use.

The Guide of Best Practice has been developed for use in a limit state design methodology. Thus, the determined a set of characteristic properties for the lamina are modified by a series of reduction factors to yield the design properties. The guide sets out a total of six modification factors for ultimate capacity. The first three factors address material property variation due to production processing, with the key issue being the level of control adopted in the fabrication process. The other three capacity factors address property alteration due to service conditions. These account for environmental exposure, service temperature and load duration. A stiffness modification factor is also used to address variations in modulus over time. The draft of the guide gives values for the modification factors based on the literature. Work is underway to verify these factors through directed experimental testing.

The current guide document is an initial draft and it is recognised that there are still a range of fundamental materials issues and implementation issues which must be addressed. A consultation process with key industry stakeholders is currently underway and research work to improve fundamental knowledge is ongoing. However, while there is still much work to do, it is believed that this document represents a significant step forward for the Australian engineering and composites communities, finally providing interested engineers with a real way forward into the realm of composites technology.

CONCLUSION

This paper has presented a brief survey of development efforts into infrastructure composites within Australia. It has been shown that several new and innovative structural systems using composites are reaching a point of commercial reality within the Australian market. It is believed that the continuing development of these systems and others like them, in combination with national programs to provide engineers with necessary design guidance, will see composites gain an increasing foothold in the Australian civil engineering market over the coming years.

REFERENCES

1. G.M. Van Erp, T.J. Heldt, L. McCormick, D. Carter and C. Tranberg, 'Development of an Innovative Fibre Composite Deck Unit Bridge', Proceedings of the IABSE Symposium. Melbourne. 2002.
2. D.J. Oehlers, 'Development of design rules for retrofitting by adhesive bonding or bolting either FRP or steel plates to RC beams or slabs in bridges and buildings', *Composites - Part A: Applied Science and Manufacturing*, v 32, n 9, September, 2001, p 1345-1355.
3. M.S. Mohamed Ali, D.J. Oehlers and S.M. Park, 'Comparison between FRP and steel plating of reinforced concrete beams' *Composites - Part A: Applied Science and Manufacturing*, v 32, n 9, September, 2001, p 1319-1328
4. S. Dorries, 'PAA Quality Control Policy and Specific Rules for Product Certification', Newstead, Plywood Association of Australia, 2000.
5. S.R. Ayers and G.M. Van Erp, 'An Australian Industry Code of Practice for the Structural Design of Fibre Composites', *Proceedings of the Institution of Civil Engineers – Structures and Buildings*. accepted for publication.
6. Composite Materials Handbook. Volume 1 Polymer Matrix Composites. Guidelines for Characterisation of Structural Materials, MIL-HDBK-17-1F. US Department of Defence. 2002.

This page intentionally left blank

PART II

FRP STRENGTHENING OF CONCRETE AND MASONRY STRUCTURES

This page intentionally left blank

AN EXPERIMENTAL STUDY ON STRAIN DISTRIBUTIONS IN FRP IN SHEAR-STRENGTHENED RC BEAMS AT DEBONDING

S. Y. Cao [a], J. F. Chen [b], Z. Hao [a] and J. Chen [a]
[a] *College of Civil Engineering, Southeast University, Nanjing 210096, P. R. China*
[b] *Institute for Infrastructure and Environment, Edinburgh University, UK*

ABSTRACT

Substantial research has been carried out on the shear strengthening of reinforced concrete (RC) beams with fibre reinforced polymer (FRP) composites. The beams may be strengthened with various methods including the wrapping of FRP around the entire cross-section, and the bonding of U jackets and side strips. For most beams strengthened with FRP wrapped around the entire section, the shear failure process starts with FRP debonding from the sides of the beam, leading to eventual failure by FRP rupture. Most previous research has been concerned with the ultimate failure of FRP wrapped beams when FRP ruptures, but debonding of FRP from the sides of the beam may also constitute a limit state in design, either as a serviceability limit state or a lower bound to the ultimate limit state. This paper presents an experimental study on this debonding failure in which beams with completely wrapped FRP strips were tested. Particular attention is paid to the development and distribution of strains in the FRP strips intersected by the critical shear crack and the contribution of FRP to the shear strength of the beam at the complete debonding of the critical FRP strip.

INTRODUCTION

Experimental studies (Chajes 1995, Norris *et al.* 1997, Chaalal *et al.* 1998, Li *et al.* 2001, Cao 2001, Khalifa and Nanni 2002, Taljsten 2003) showed that the shear strength of reinforced concrete (RC) beams can be substantially increased by bonding fibre reinforced polymer (FRP) composite strips or sheets as external shear reinforcement. Common methods of shear strengthening include side bonding, U-jacketing and wrapping around the entire cross section (Teng *et al.* 2002). Previous studies (Chen and Teng 2003a) have established clearly that such strengthened beams fail in shear mainly in one of the following two modes: tensile rupture of the FRP and debonding of the FRP from the sides of the RC beam, depending on how the beam is strengthened. Available experimental data indicate that almost all beams strengthened by wrapping failed due to FRP rupture. Some beams strengthened by U jacketing (e.g. Chajes *et al.* 1995) also failed in this mode. In contrast, almost all beams strengthened by side bonding only, and most strengthened by U jacketing, failed due to FRP debonding. Chen and Teng (2003a,b) have recently developed two predictive ultimate strength models and put forward consistent design proposals for both failure modes.

Although in the FRP rupture failure mode, the ultimate shear strength is controlled by the tensile rupture of FRP, debonding of the FRP generally precedes final failure. For the common situation where the FRP shear reinforcement is in the shape of strips, the failure process usually starts from the debonding of the most highly stressed FRP strip (i.e. the critical FRP strip) intersected by the critical shear crack, leading to eventual failure by FRP rupture. For beams strengthened with complete wrapping, the beam is often able to carry additional loading following the complete debonding of the critical FRP strip. It may be noted that at the ultimate state, most FRP strips rupture near one of the corners of the beam where there are stress concentration and bending effects which

are not present away from the corners. This rupture failure stress can be significantly lower than the tensile strength of FRP tested under uni-axial loading (such as that obtained from coupon tensile tests). Chen and Teng (2003a) proposed a reduction factor of 0.8 for design to consider these effects. However, the actual reduction may be sensitive to details such as the radius and smoothness of the corners. Therefore, the additional load that can be carried by the beam following the debonding of the critical FRP strip may vary considerably for nominally the same beam details.

Existing studies have been predominantly concerned with the ultimate shear strength of RC beams strengthened with FRP. However, debonding of the FRP from beam sides may also constitute a design limit state for two reasons. Firstly, the debonding strength which is less likely to be affected by construction details at beam corners may be taken as a more reliable lower bound to the ultimate load for conservative design. Secondary, the debonding of FRP strips is at least a serviceability limit state for most structures. This paper presents an experimental study on the behaviour of FRP wrapped beams focussing on the debonding of the critical FRP strip.

It has been demonstrated in Chen and Teng (2003a,b) that the strain (or stress) distribution in FRP along the critical shear crack is an important factor influencing the contribution of FRP to the ultimate shear capacity of the beam. Similarly, this is also expected to be one of the key factors influencing the contribution of FRP to the shear resistance of the beam at the debonding of the critical FRP strip. Therefore, the emphasis of this study is on the development and distribution of strains in FRP strips intersected by the critical shear crack and the contribution of the FRP to the shear strength when debonding of FRP occurs.

TEST PROGRAM

A total of 18 simply supported RC beams were tested in three batches, of which 6 were tested as un-strengthened reference beams. All beams had a length of 2m and a rectangular cross-section of 150mm wide and 250 mm deep with an effective depth of 222.5 mm. The first batch consisted of 6 beams designated Ba, Bb, Bc, Bd, Be and Bf, which were strengthened by wrapping glass fibre reinforced polymer (GFRP) strips with a tensile strength of 260MPa and a Young's modulus of 20.5 GPa based on a nominal thickness of 1.27 mm. The concrete used for this batch had an average cube compressive strength of 30 MPa. There were also 6 beams in the second batch, designated L1, L2, L3, L5, L6 and L7. The concrete used had a lower average cube compressive strength of 17.8 MPa. They were strengthened by wrapping with GFRP strips with a tensile strength of 112 MPa and a Young's modulus of 5.3 GPa based on a nominal thickness of 1.2 mm. The low strength materials used in this batch led to a distinctive range of properties. The beams in the third batch, A1, A2, A3, A4, A5 and A6, were strengthened by wrapping carbon fibre reinforced polymer (CFRP) strips with a tensile strength of 3635MPa and a Young's modulus of 249 GPa based on a nominal thickness of 0.167 mm. The concrete used had an average cube compressive strength of 30.5 MPa. It should be noted that the nominal thicknesses for the two GFRP products are close to the actual thicknesses obtained from a wet lay-up procedure while the nominal thickness of the CFRP corresponds to the fibre thickness. This different definition of nominal thickness is partly responsible for the low strengths and elastic moduli reported for the two GFRP products.

The main parameters considered in these tests were the shear span-to-depth ratio and the amount of external FRP reinforcement. Five shear span-to-depth ratios, namely 2.92, 2.70, 2.47, 1.8 and 1.35, were used in these 18 beams. The external FRP

reinforcement index ω_{frp} ranged from 0.09% to 1.1%. Here ω_{frp} is defined as

$$\omega_{frp} = \rho_{frp} \frac{E_{frp}}{E_c} = \frac{2A_{frp}}{bs_{frp}} \frac{E_{frp}}{E_c} \quad (1)$$

in which A_{frp} is the cross-sectional area of an FRP strip, s_{frp} is the centre to centre spacing of FRP strips, b is the width of the beam, E_{frp} and E_c are the elastic moduli of FRP and concrete respectively. Table 1 lists the main parameters of all specimens.

All except the reference specimens were pre-loaded under four point bending until a diagonal shear crack became visually clear. Actual value of pre-load is listed in Table 2. Thereafter they were fully unloaded and then strengthened by wrapping FRP strips around the entire cross-section within the test shear span (one of the shear spans with less steel shear reinforcement and expected to fail during the test). Strain gauges were bonded to the FRP strips where they were intersected by the critical shear crack from preloading. The pre-crack patterns and the positions of FRP strips and strain gauges are shown in Figure 1. The strengthened beams were loaded to failure.

Table 1 Test specimens

Specimen	Type of FRP	Shear span-to-depth ratio	Angle of critical shear crack, Degree	w_{frp} mm	s_{frp} mm	ω_{frp} %
L1	------	2.92	------	------	------	------
L2	GFRP	2.92	26.1	25	50	0.176
L3	GFRP	2.92	23.3	25	100	0.088
L5	------	1.80	------	------	------	------
L6	GFRP	1.80	43.3	25	50	0.176
L7	GFRP	1.80	36.7	25	100	0.088
Ba	------	2.47	------	------	------	------
Bb	GFRP	2.47	29.1	20	40	0.495
Bc	GFRP	2.47	33.7	20	80	0.266
Bd	------	1.35	------	------	------	------
Be	GFRP	1.35	50.6	20	40	0.528
Bf	GFRP	1.35	44.4	20	80	0.261
A1	------	2.70	------	------	------	------
A2	CFRP	2.70	39.6	30	100	0.549
A3	CFRP	2.70	38.0	30	150	0.369
A4	------	1.80	------	------	------	------
A5	CFRP	1.80	40.6	30	100	0.549
A6	CFRP	1.80	43.0	30	50	1.098

EXPERIMENTAL RESULTS AND DISCUSSIONS

Failure Process

In general, all test beams had a similar failure process. Due to the presence of FRP strips, obvious new cracking was not seen when the applied load reached the level of preloading. As the load increased further, the pre-crack started to propagate slowly and new cracks gradually appeared. Local debonding of some FRP strips initiated at or near the critical shear crack. For the GFRP strengthened beams, the debonded area was easily recognisable because the GFRP changed in colour from yellow to white. The precise moment of debonding commencement could not be determined with certainty. For the

CFRP-strengthened specimens, it was difficult to pinpoint the location of local debonding as there was no obvious change in colour of the CFRP in the debonded zone. For both GFRP and CFRP strengthened specimens, some noise was heard during the debonding process.

At a sufficiently high load level, the most highly stressed strip completely debonded from the sides of the beam (the bond between the FRP and the top and bottom surfaces of the beam remained intact). For most specimens, this was followed by the complete debonding of most of the FRP strips intersected by the critical shear crack from the sides of the beam. Only Specimens Be and Bf failed immediately by FRP rupture at one of the corners of the beam because the corners of these two beams were not well rounded so their ultimate failure loads were same as their debonding loads of the critical FRP strip. For all other specimens, the debonding of most strips intersecting the critical shear crack was not the ultimate limit state as the load could be further increased significantly.

After the complete debonding of most FRP strips intersected by the critical shear crack, the beams showed rapid development of cracking and deformation as the load was further increased. The ultimate load was reached when one of the FRP strips ruptured (mostly near the corner of the beam). Successive rupture of the other FRP strips intersected by the critical shear crack immediately followed and the beam collapsed.

Because of the difficulties and uncertainties associated with the determination of the initiation of debonding, the load at the complete debonding of the most highly stressed FRP strip is defined in this study as the FRP debonding load. Table 2 lists the pre-crack load V_0, the FRP debonding load V_d and the ultimate load V_u for each specimen.

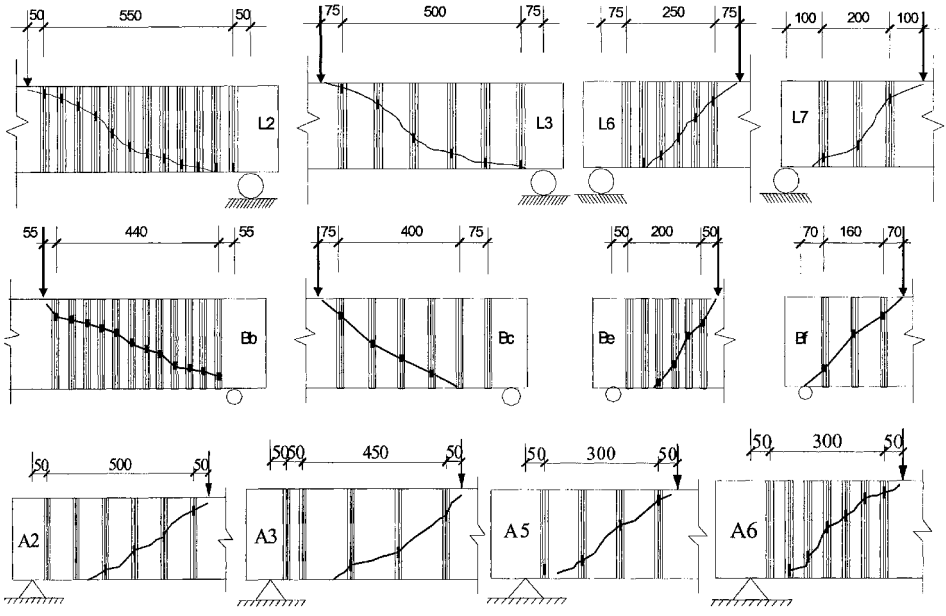


Fig. 1. Positions of FRP strips and strain gauges relative to the critical shear crack

Strain Distribution in FRP along the Critical Shear Crack

Figure 2 shows typical strain distributions in FRP strips measured by strain gauges installed along the critical shear crack. It is seen that the strain distributions are non-uniform and close to being parabolic at all load levels. The FRP contribution to shear resistance of the beam may be found from the product of the strain distribution factor and the maximum stress in the FRP at the considered state as demonstrated by Chen and Teng (2003a). As in Chen and Teng (2003a), the strain distribution factor D_{frp} is defined here as the ratio of the average strain of FRP strips intersected by the critical shear crack to the maximum FRP strain at the considered load level. For discrete FRP strips, it can be described as

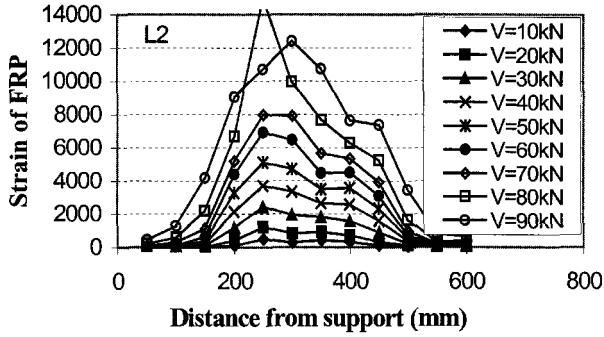
$$D_{frp} = \frac{\sum_{i=1}^{n} \varepsilon_{frp,i}}{n\varepsilon_{frp,\max}} \approx \frac{\int_0^l \varepsilon_{frp}(x)dx}{l\varepsilon_{frp,\max}} \tag{2}$$

where l is the horizontal projection of the critical shear crack, $\varepsilon_{frp,i}$ is the strain of the ith FRP strip, n is the total number of FRP strips intersected by the critical shear crack and $\varepsilon_{frp,\max}$ is the maximum strain in these FRP strips.

Figure 3 shows the deduced strain distribution factor D_{frp} at various load levels relative to the debonding load. It shows that D_{frp} increases slightly as the load increases. Figure 4 shows that the increase of reinforcement reduces D_{frp} slightly when FRP reinforcement index is less than 0.5%. However, results for two specimens with shear span to depth ratio equal to 1.8 show that the increase of reinforcement index beyond 0.6 increases D_{frp}, but this needs further confirmation due to the limit of test points. The shear span to depth ratio λ is shown to have a more significant effect on D_{frp} (Fig. 5). D_{frp} at debonding decreases as λ increases.

Table 2 Pre-load, debonding load and ultimate load of specimens (kN)

Specimen	Pre-load V_0	Debonding load V_d	Ultimate load V_u	Specimen	Pre-load V_0	Debonding load V_d	Ultimate load V_u
L1	——	——	64	L5	——	——	115
L2	48	90	104	L6	79	130	162
L3	55	73	99	L7	79	135	150
Ba	——	——	66	Bd	——	——	150
Bb	50	120	136	Be	54	178	178
Bc	63	104	121	Bf	61	161	161
A1	——	——	141	A4	——	——	183
A2	84	170	185	A5	142	208	227
A3	77	162	187	A6	147	210	217



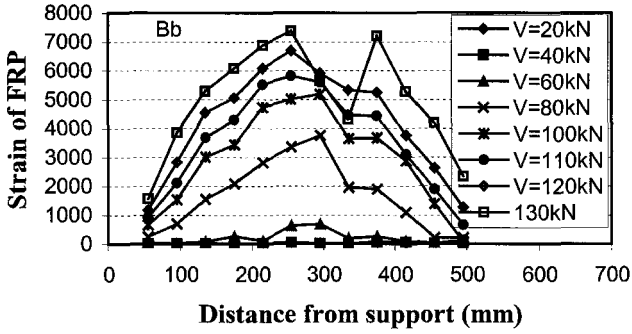
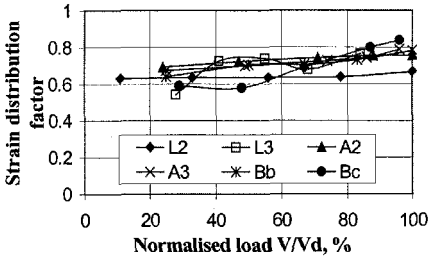
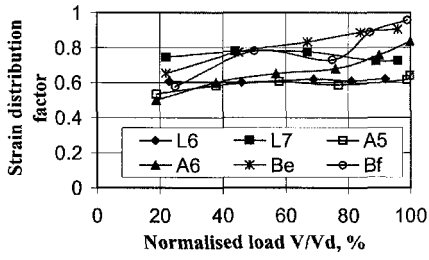


Fig. 2 Typical strain distributions in FRP along the critical shear crack



a) shear span to depth ratios >2



b) Shear span to depth ratios <2

Fig. 3 Strain distribution factor D_{frp} versus load

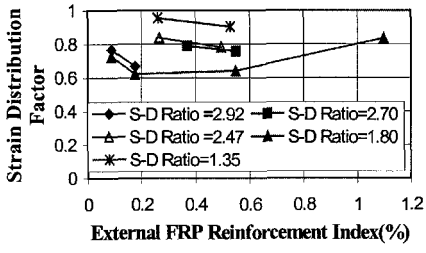


Fig. 4 D_{frp} versus ω_{frp} at debonding

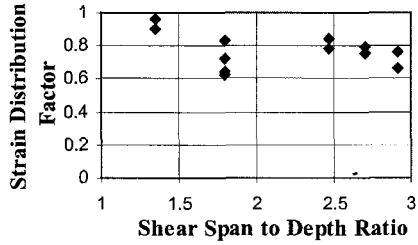


Fig. 5 D_{frp} versus λ at debonding

CONTRIBUTION OF FRP TO SHEAR RESISTANCE AT DEBONDING

For a specimen with a critical shear crack angle θ, the contribution of the FRP strips to the shear resistance when FRP debonds can be established from equilibrium consideration as follows

$$V_{frp} = \sum_{i=1}^{n} 2t_{frp} w_{frp} E_{frp} \varepsilon_{frp,i} = 2t_{frp} w_{frp} E_{frp} \frac{h_{frp} ctg\theta}{s_{frp}} D_{frp} \varepsilon_{frp,\max} \quad (3)$$

in which h_{frp} is the effective height of FRP on the sides of the beam and t_{frp} is the thickness of FRP.

Apart from the geometrical parameters and mechanical properties of the materials involved in Eq. 3, the main factors influencing the shear resistance include the maximum FRP strain $\varepsilon_{frp,max}$, the FRP strain distribution factor D_{frp} and the critical shear crack angle θ. The effects of these three factors are discussed below. It may be noted that the strain distribution factor D_{frp} varies with the load. Of particular interest here is the value of D_{frp} when the most highly stressed FRP strip completely debonds from the sides of the beam.

As discussed in the previous section, D_{frp} depends chiefly on the shear span-to-depth ratio λ. From both the experimental results here and analytical investigations (Zararis *et al.* 2001), the critical shear crack angle θ also depends chiefly on λ. For convenience of practical applications, it is thus desirable that a single coefficient $D_{f\theta}=D_f ctg\theta$ be defined to represent the effects of both D_{frp} and θ. Within the tested range of $1.4 < \lambda < 3$, the following relationship between $D_{f\theta}$ and λ may be used as an approximation (Fig. 6):

$$D_{f\theta} = 0.169 + 0.413\lambda \quad (4)$$

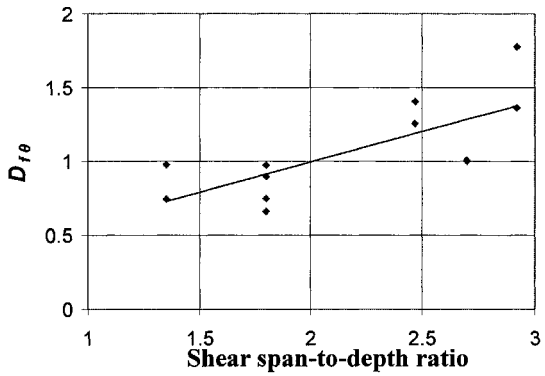


Fig.6 Relationship between $D_{f\theta}$ and λ

Before complete debonding, the behaviour of FRP strips bonded to the sides of the beam resembles that of FRP strips in single or double FRP-to-concrete shear tests (Chen et al. 2001, Chen and Teng 2001, Chen and Teng 2003b). It may be noted that numerous research (e.g. Chajes *et al.* 1996, Bizindavyi and Neale 1999) has shown that there exists an effective bond length L_e beyond which an extension of the bond length L cannot significantly increase the bond strength. In the present case where the FRP is wrapped around the whole circumference of the beam, the portions of an FRP strip bonded to the top and the bottom sides of the beam provide some support to the FRP on the sides before it is completely debonded. Therefore, the stress in the most highly stressed FRP strip at debonding, even if $L < L_e$, can reach or even be larger than the

bond strength with $L = L_e$. This indicates that the stress in the FRP at debonding can be assumed conservatively as that when $L > L_e$ independent of the actual bond length L. Following a similar treatment to that used in Chen and Teng (2003b) and using $\beta_L = 1$ (for $L > L_e$), the maximum strain of the FRP at debonding, $\varepsilon_{f,max}$ can be expressed as

$$\varepsilon_{f,\max} = \frac{0.427\beta_w\sqrt{f_c'}L_e}{E_{frp}t_{frp}} = 0.427\beta_w\frac{\sqrt[4]{f_c'}}{\sqrt{E_{frp}t_{frp}}} \quad (5)$$

in which the strip width coefficient

$$\beta_w = \sqrt{\frac{2 - w_{frp}/s_{frp}}{1 + w_{frp}/s_{frp}}} \quad (6)$$

A comparison of the predicted strains with those observed (Fig. 7) shows that the predictions from Eq. 5 is indeed an estimate of the lower bound as expected.

Figure 8 shows a comparison of the predicted FRP contributions to the shear resistance at debonding with the experimental results. Whilst there is a general agreement between the two, a significant scatter exists. One factor which may be significant is that the experimental FRP contribution was obtained from subtracting the failure load of the relevant reference beam from the debonding load of the strengthened beam. This means a) a large scatter expected to exist in the shear strength of concrete beams is passed onto the FRP contribution so that the scatter of the deduced FRP contribution is larger than that of the concrete beam because the FRP contribution is usually a small portion of the total shear resistance of the strengthened RC beam; and b) it is assumed that the shear contribution of internal steel reinforcement and concrete reach their respective ultimate values at debonding. A more detailed discussion is provided in Cao et al. (2003).

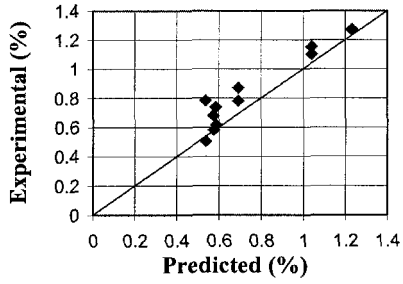


Fig.7 Predicted versus measured maximum FRP strain at debonding

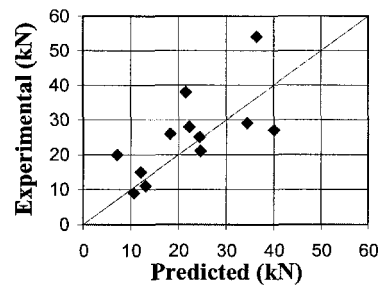


Fig.8 Predicted versus measured FRP contribution to shear strength at debonding

CONCLUSIONS

For RC beams shear strengthened with FRP strips wrapped around the entire section, the state when the most highly stressed FRP strip debonds from the sides of the beam may constitute a design limit state. It may be taken as a reliable lower bound to the ultimate limit state for conservative design which may be desirable given the brittleness of shear failure, and should certainly be treated as a serviceability limit for most structures. This paper has presented an experimental study on shear strengthened RC beams with completely wrapped FRP strips, with particular attention to the strain

distribution in FRP along the critical shear crack and the shear resistance of the beam at debonding. The FRP strain distribution was shown to be highly non-uniform and must be taken into account in predicting the shear resistance contributed by the FRP through the use of a stain distribution factor which depends chiefly on the shear span-to-depth ratio. An empirical model was proposed to predict the FRP contribution to the shear strength of strengthened RC beams at debonding and was shown to compare reasonably well with the experimental debonding loads.

ACKNOWLEDGMENT

This work presented forms part of collaborative research between Southeast University, China and the University of Edinburgh, UK. The authors would like to acknowledge the financial supports provided by the Foundation for University Key Teacher by the Ministry of Education of China and the University of Edinburgh. They would also acknowledge Hwa Ying Foundation for Education and Culture sponsoring the first author's visiting scholarship at the University of Edinburgh. They would like to thank Professor J.G. Teng of The Hong Kong Polytechnic University for his valuable contributions to the work presented in this paper.

REFERENCES

1. M J Chajes, T F Januszka, D R Mertz, T A Thomson and W. W. Finch, Shear strength of RC beams using external applied composite fabrics, *ACI Struct. Jnl*, 1995, **92**(3), 295-303.
2. T Norris, H Saadatmanesh and M R Ehsani, Shear and flexural strengthening of RC beams with carbon fiber sheets, *ASCE Jnl of struct. Eng.*, 1997, **123**(7), 903-911.
3. O Chaallal, M J Nollet and D Perraton, Shear strengthening of RC beams by externally bonded side CFRP strips, *ASCE Jnl of Comp. for Const.*, 1998, **2**(2), 111-113.
4. A Li, J Assih and Y Delmas, Shear strengthening of RC beams with external bonded CFRP sheets, *ASCE Jnl of Struct. Eng.*, 2001, **127**(4), 374-380.
5. S Y Cao, J Chen and J W Pan, Experiment study on shear performance of RC beams retrofitted by GFRP strips, *Proc., Int. Conf. on FRP Composites in Civil Eng.*, Hong Kong, China, 12-15 Dec. 2001, Elsevier, 677-683.
6. A Khalifa and A Nanni, Rehabilitation of RC beams with shear deficiencies using CFRP composites, *Construction and Building Material,* 2002, **16**(3),135-146.
7. B Taljsten, Strengthening concrete beam for shear with CFRP sheets, *Construction and Building Materials*, 2003, **17**(1), 15-26.
8. J G Teng, J F Chen, S T Smith and L Lam, *FRP Strengthened RC Structures*, Chichester, John Wiley & Sons, 2002.
9. J F Chen and J G Teng, Shear capacity of FRP-strengthened RC beams: FRP rupture, *ASCE Jnl of Struct. Eng.*, 2003, **129**(5) 615-625.
10. J F Chen and J G Teng, Shear capacity of FRP-strengthened RC beams: FRP debonding, *Construction and Building Materials*, 2003, **17**(1), 27-41.
11. P D Zararis and G C Papadakis, Diagonal shear failure and size effect in RC beam without web reinforcement, *ASCE Jnl of Struct. Eng.* 2001, **127**(7), 733-742.
12. J F Chen and J G Teng, Anchorage strength model for FRP and steel plate bonded to concrete, *ASCE Jnl of Struct. Eng.,* 2001, **127**(7), 784-791.
13. M J Chajes, W W Finch, T F Januszka and T A Thomson, Bond and force transfer of composite material plate bonded to concrete, *ACI Struct. Jnl*, 1996, **93**(2), 208-217.
14. L Bizindavyi and K W Neale, Transfer length and strength for composites bonded to concrete, *ASCE Jnl of Composite for Construction*, 1999, **3**(4), 153-160.
15. S Y Cao, J F Chen, Z Hao and J Chen, Shear behaviour of RC beams wrapped with FRP strips at debonding, *in preparation.*

BOND TESTS ON CONCRETE T-SHAPED SECTIONS STRENGTHENED WITH CFRP

F. Ceroni[(1)], S. Matthys[(2)], M. Pecce[(1)], L. Taerwe[(2)]

(1) University of Sannio, Engineering Dept., Benevento, Italy
(2) Ghent University, Dept. of Struct. Eng., Magnel Lab. for Concrete Research, Belgium

ABSTRACT

Innovative techniques based on fibre reinforced polymer (FRP) laminates externally bonded to existing structures appear to be interesting alternatives to traditional solutions for the seismic upgrade and repair of buildings and civil structures. Interface failures represent a typical issue of FRP laminates externally applied to reinforced concrete elements, due to high stress concentrations in the anchorage zone of most types of application. Experimental tests to evaluate the efficiency of anchorage systems to avoid the delamination failure at the end of FRP laminates have been performed. Efficiency of the anchorage is evaluated either in terms of ultimate strength or in terms of ductility of the system.

INTRODUCTION

The use of advanced composites, such as fibre reinforced polymers (FRPs), as structural reinforcement for concrete structures is gaining more and more interest. Especially, the use of externally bonded FRP reinforcement is nowadays becoming a standard technique for strengthening of existing structures. Given the high strength of FRPs and structural adhesives, the stress transfer capacity of FRP laminates or sheets bonded to concrete is restricted by the limited tensile strength of the concrete and the high stress concentrations at the anchorage that cause interface failure. Moreover, for shear strengthening of T-shaped cross-sections, the available effective anchorage length may be very limited.

When the external reinforcement is used to upgrade structures in seismic areas (confinement of columns, strengthening of beam-column joints), the ductility is a key issue of the design. Thus, brittle failure due to the debonding has to be avoided and anchorage systems may be designed for both strength and ductility considerations.

Several types of anchorage have been studied and tested by several researchers [1-7]. The efficiency of a bond anchorage (FRP bonded to concrete) can be due to adequate transfer length, as provided by formulations of various authors [3,8,9]. Additional anchorage capacity may be obtained by gluing fibres transversal to the direction of the reinforcement. Another common solution consists into applying at the end of the external reinforcement steel or FRP plates bonded or bolted. For using bolts to fix FRP laminates it is generally suggested to apply an additional layer of multidirectional fibres; because sections where bolts are placed on unidirectional sheets could be starting points for local debonding [10].

Experimental tests [4] on reinforced concrete ties externally bonded with FRP sheet anchored with steel U-shaped devices embedded in the concrete have shown that the anchorage allows not only to have an increase of the ultimate strength, but also an increment of the ductility of the strengthened member with higher displacements at ultimate conditions. This was also found in [11].

An anchorage system for sheets has been recently developed by the methodology of the near-surface mounted FRP rods. It consists into realizing a groove in the concrete transversally to the fibre direction at the end of the FRP reinforcement: the sheet is positioned in the groove, an FRP

bar is put in the groove to fix the sheet and the hole is then filled by epoxy resin. This system was tested as anchorage for external FRP shear reinforcement [7], giving a very good efficiency.

To realize sufficient anchorage capacity for shear reinforcement of T-beams or confinement of column in configurations with wing walls (figure 1), some authors [5,6] have proposed a configuration where fibres are placed in the form of a fan. The largest part of the fan is fully bonded to the FRP, while in the summit fibres are braided to form a string that is then inserted in a hole through the element that make obstacle to a wrapping anchorage. A similar anchorage configuration is mentioned in fib bulletin 14 [3] consisting in the realization of a hole filled with resin, then a glass tow is forced through in the hole and the ends are splayed outwards in a circle and are bonded on the FRP sheet. These types of anchorage can be very useful, eg. for T-beams strengthened in shear, and several configurations have been proposed and tested by [5], varying distance between fans, number of carbon layers and geometrical properties of the elements.

To investigate different solutions to strengthen T-shaped sections in a more efficient way, bond shear tests have been executed in the Magnel Laboratory for Concrete Research on concrete specimens strengthened with carbon fibre FRP (CFRP). Fourteen tests have been executed investigating the bond behaviour between concrete and CFRP when dealing with a T-shaped section and for different strengthening configurations, mainly with respect to additional mechanical fixings.

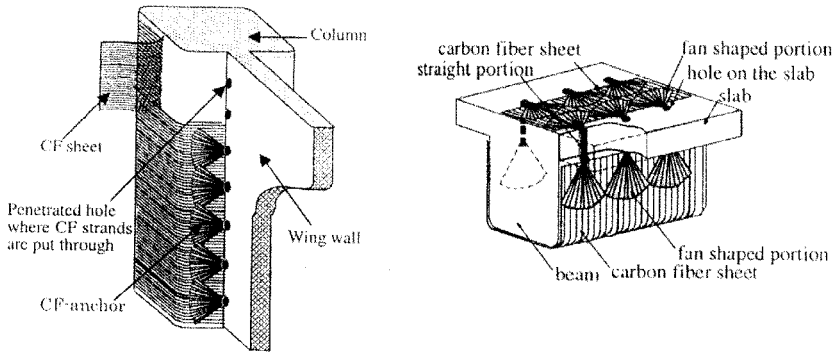


Figure 1. Configurations proposed in [5,6]

TEST PROGRAM

Test set-up

An experimental program of 14 specimens was designed to study the efficiency of different anchorage solutions at the end of external FRP reinforcement. Specimens are composed by concrete blocks connected by carbon FPR laminates loaded in tension by applying compression to the concrete. The configuration of the specimen is a T shape that simulates real geometrical conditions of beam-column connections, footing zone of columns and T beams. Each specimen is made by two concrete blocks with a superior prismatic block (dimension 300mm x 300mm x 250mm) and an inferior T shaped block (dimension 700mm x 300mm x 250mm for the flange of the T and 300mm x 300mm x 250mm for the web). The two blocks are connected during casting, manipulation, preparation and moving the specimen in the tensile machine, by a stiff plastic tube and a wooden box to keep the alignment of the two blocks. This wooden box is placed during the casting in the space between the two blocks (300 mm height) in order to sustain the superior block after removing the framework and until the testing procedure starts.

On two opposite sides of the specimens (sides with the T-shaped section) CFRP laminates are applied with a width of 100 mm. In six specimens the CFRP is provided along the web, according to the configuration shown in figure 2a. For the other eight specimens (configuration 2b) the anchorage systems are realised by extending the FRP on the flange of the T-section (90° angle).

Five of the specimens have been tested without additional anchorage devices, yet using different bond lengths. The remaining specimens comprised different types of additional anchorage devices. An overview and details of the different configurations are provided in table 1 and figure 2.

Table 1 Characteristics of specimens

Specimen	Anchorage type
TA1-1& TA1-2	Laminate applied only on vertical plane: vertical bond length = 250 mm
TA2-1& TA2-2	Laminate applied on vertical plane and extended to horizontal one, vertical bond length = 250 mm
TA3-1	Laminate applied on vertical plane and extended to horizontal one, vertical bond length = 100 mm
TA3-2	Laminate applied on vertical plane and extended to horizontal one + steel plates bonded on FRP: vertical bond length = 250 mm, FRP length before steel plates: 150 mm
TA4-2	Laminate applied on vertical plane and extended to horizontal one + steel plates bonded on FRP and bolted on both sides of FRP: vertical bond length = 250 mm, FRP length before steel plates: 120 mm
TA4-1	Laminate applied on vertical plane and extended to horizontal one + FRP laminate plates bonded: vertical bond length = 250 mm, FRP length before steel plates: 120 mm
TA5-1	Laminate applied on vertical plane with an FRP bar cut-in at the end: vertical bond length = 100 mm, FRP length before FRP bars: 50 mm
TA5-2	Laminate applied on vertical plane with an FRP bar cut-in at the end: vertical bond length = 250 mm, FRP length before FRP bars: 150 mm
TA6-1	Laminate applied only on vertical plane with a bond length of 250 mm + FRP plates bonded at the end
TA6-2	Laminate applied only on vertical plane with a bond length of 250 mm + Steel plates bonded at the end
TA7-1	Laminate applied on vertical plane with a bond length of 250 mm + extension on horizontal plane with FRP bar cut-in in the corner
TA7-2	Laminate applied on vertical plane with a bond length of 100 mm + extension on horizontal plane with FRP bar cut-in in the corner

To have confinement of the concrete, internal reinforcement is provided with steel stirrups. For specimens having the FRP laminate on the vertical and horizontal plane, the 90° angle of the concrete block at the intersection of the two planes was rounded by an epoxy filling having a curvature radius of 25 mm.

Series TA1 and TA2 are reference ones because they have no extra anchorage for the FRP laminate. For all tested specimens the FRP laminate is anchored to the concrete of the superior block by gluing a steel plate and applying a mechanical external anchorage system, in order to avoid a debonding failure in this part. No bond is provided between the CFRP and the wooden box separating the two concrete blocks.

Materials

For concrete characterization (table 2) compression tests were performed on 3 cylinders (Ø150 mm x 300 mm) for each batch at 28 days to have the cylindrical compressive strength, $f_{c,cyl.}$ At the age of testing, compression tests were performed on 3 cubes (150 mm side) to have

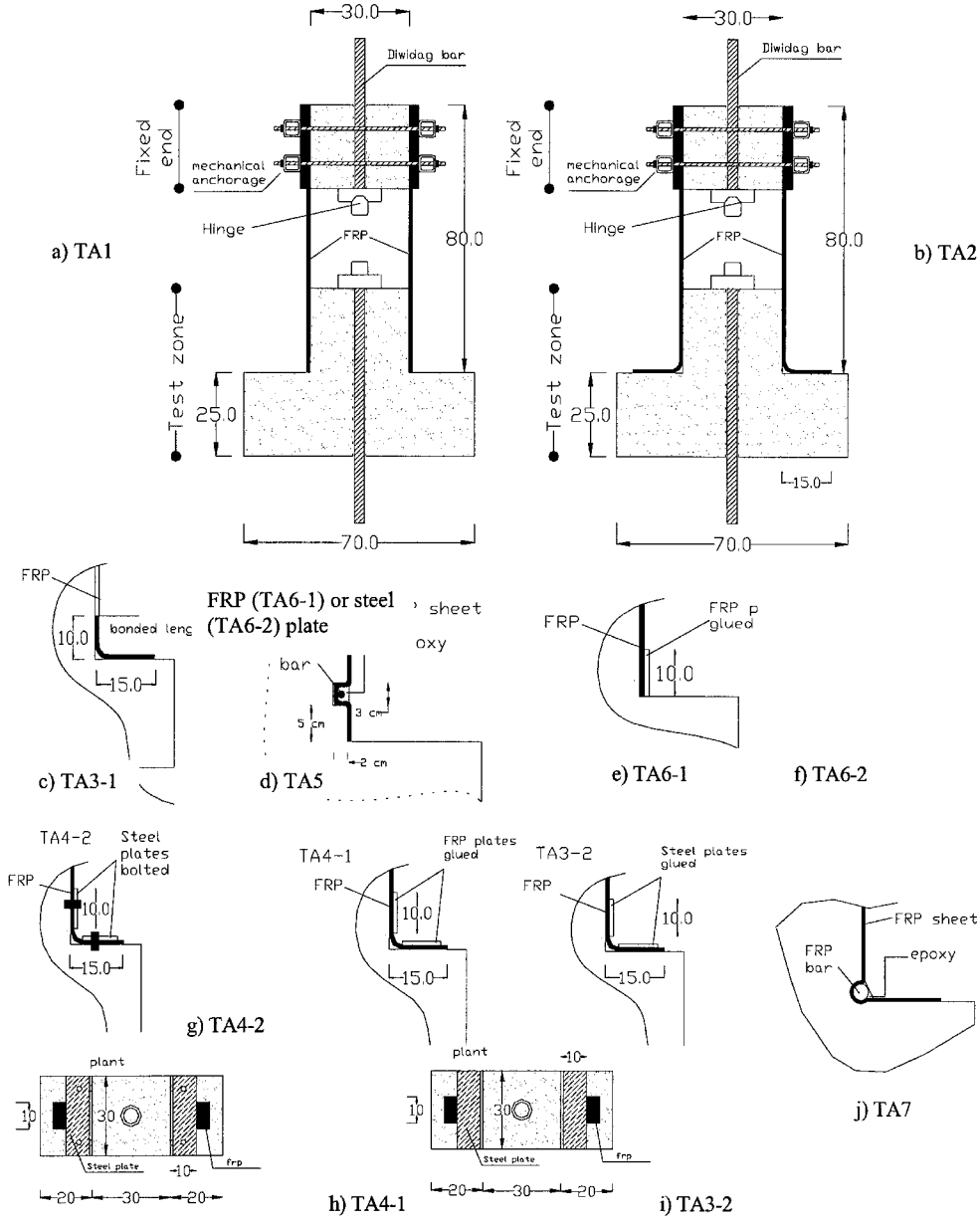


Figure 2 Specimen configuration

the cubic compressive strength $f_{c,cub}$, 3-point bending tests on 3 prisms (150 mm x 150 mm x 600 mm) to have the tensile strength $f_{ct,b}$, splitting test on the 6 remaining halves of the bending tests to have the tensile strength $f_{ct,sp}$, and compression test on cylinders (Ø150 mm x 300 mm) to determine the secant E-modulus E_c (between 0.5 MPa and 1/3 of the compressive strength).

The internal steel reinforcement is made by deformed steel bars S500 (characteristic yield strength 500 MPa). The external FRP is a wet–lay–up system; the thickness, s, the ultimate strength, f_u, and strain, ε_u, the Young's modulus, E_f, as declared by the manufacturer, are respectively 0.111mm, 3400 MPa, 1.4%, 230000MPa.

Table 2 Mechanical properties of the concrete

Batch	$f_{c,cyl}$ [MPa]	$f_{c,cub}$ [MPa]	$f_{ct,b}$ [MPa]	$f_{ct,sp}$ [MPa]	E [MPa]	Batch	$f_{c,cyl}$ [MPa]	$f_{c,cub}$ [MPa]	$f_{ct,b}$ [MPa]	$f_{ct,sp}$ [MPa]	E [MPa]
TA1	37.2	45.0	3.95	3.48	32634	TA5	38.2	42.6	4.8	3.6	32139
TA2	40.3	44.7	4.01	3.49	32631	TA6	39.7	35.6	4.19	3.08	31913
TA3	39.7	42.7	4.01	3.34	36223	TA7	38.6	35.4	3.91	3.36	32826
TA4	40.6	46.3	5.18	3.44	30585						

Measurements and loading scheme

Several strain gauges were applied on the FRP laminates: one strain gauge was applied at the middle of the unbonded FRP and at least 2 times four strain gauges were glued along the bonded part on both sides of the specimen according to the scheme of figure 3. In addition, four LVDT transducers were positioned on both sides of the specimen at the beginning of the bonded zone, in order to measure the slip between concrete and FRP, as shown in figure 4. The measured slip is at the loaded end of the laminate.

The loading arrangement provides tension to the FRP laminate by compression on both the concrete blocks, pulling them apart. To achieve this loading condition by using a tensile loading machine, the specimen contains two central diwidag steel bars inserted in the plastic tube (the latter been put in the concrete blocks during casting). One end of each bar was fixed to the block by a bolted steel spreader plate (Figure 5), while the other end was clamped in the testing machine. In the central zone between the two blocks, the plastic tube is cut to insert the steel bars and spreader plates. Prior to testing the wooden box is dismantled, so that the only connection between the two concrete blocks is provided by the CFRP. The tests were carried out in displacement control way with a speed of 0.1 mm/min.

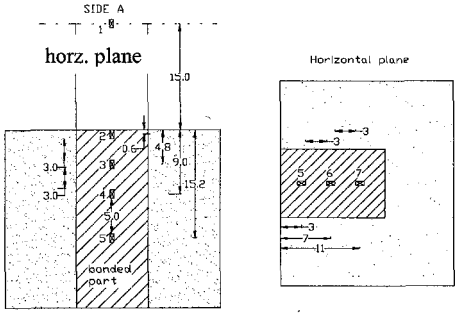


Figure 3 Location of strain gauges

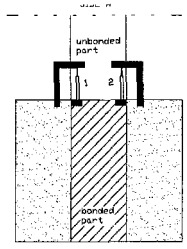


Figure 4 Position of LVDT transducers

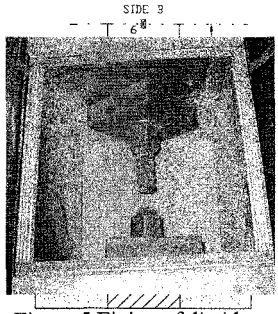


Figure 5 Fixing of diwidag bar at the concrete blocks

TEST RESULTS

Failure mode

The maximum theoretical ultimate load of the specimens, assuming sufficient anchorage capacity to obtain CFRP fracture in tension, is equal to 78 kN, considering the mechanical and geometrical properties of the CFRP given by manufacturer. In table 3 the results of the tests are summarized in terms of maximum load and failure modes. Some examples of failure modes are reported in figure 6.

The delamination load of the bonded interface, calculated according to fib bulletin 14 (2001), is equal to 31.3 kN assuming a tensile strength of concrete equal to the average bending tensile strength (4.3 MPa) of all batches. The transfer length corresponding to this load is 80

mm. The maximum load of specimens of batch TA1, characterized by CFRP applied only on the vertical plane without additional anchorage, is very near to the prediction according to fib bulletin 14 [3].

For the specimens without additional anchorage devices, when the CFRP is applied also on the horizontal plane (specimens TA2-1, TA2-2), a reduction of about 30% of the maximum load was observed with respect to series TA1 (with CFRP only along the vertical plane). This result is probably due to local effects in the corner. This observation is less pronounced when the bond length of laminate on the vertical plane is shorter (specimen TA3-1 has a bond length of 100mm instead of 250mm).

Table 3 Test results

Specimen	F_{max} [kN]	Failure mode
TA1-1	33.41	Delamination
TA1-2	29.36	Delamination
TA2-1	20.95	Delamination + fracture of fibres at the beginning of the bonded side
TA2-2	20.94	Delamination on vertical plane with propagation on the horizontal plane
TA3-1	26.71	Delamination on vertical plane with propagation on the horizontal plane
TA3-2	29.00	Delamination on vertical plane with detachment of steel plate
TA4-1	45.00	Detachment of FRP plate with tensile rupture of fibres in the angle
TA4-2	28.77	Delamination of fibres and tensile failure in the corner, anchorage intact
TA5-1	46.60	Failure of fiber in tension at the groove after delamination
TA5-2	25.50	Failure of fiber in tension at the groove after delamination
TA6-1	48.80	Delamination with slip of fibres from anchorage
TA6-2	49.30	Delamination with slip of fibres from anchorage
TA7-1	47.50	Failure of fibre in tension at the end of the superior prismatic block
TA7-2	29.60	Failure of fibre in tension at the groove

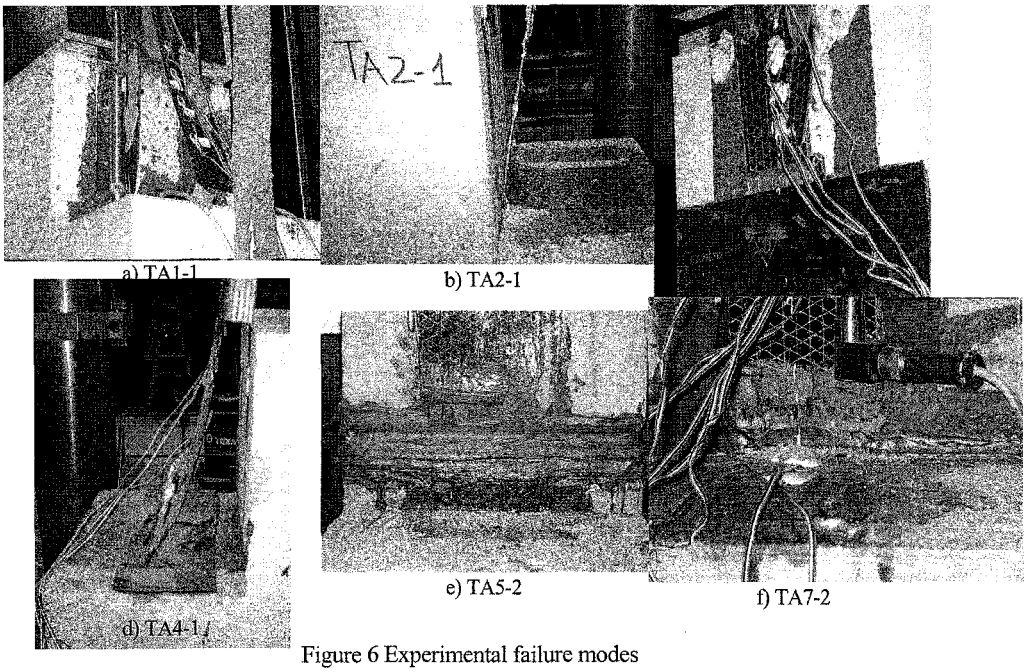


Figure 6 Experimental failure modes

When applying additional anchorage systems, in some cases these are very effective, allowing the CFRP to reach its tensile strength. In other cases the anchorage can not be considered efficient because the ultimate load is less or equal to the failure load of the reference specimens. Detailing and application procedure strongly influence the effectiveness of the system. Application of bolts on steel plates produced concentrated stresses, realization of curved CFRP in a corner is difficult, and grooves for FRP bars produce points where local failure phenomena (local debonding, cutting of fibre, stress concentration) could develop.

When the CFRP is applied only vertically and additional anchorage is provided by a transverse plate (FRP or steel), the failure load can have an increment up to 57% (specimen TA6-2) with respect to the mean value of the reference specimens (TA1-1 and TA1-2). This configuration appears a favourable solution, considering also the easier modality of application.

Strain behaviour

The experimental results in terms of strain distribution along the FRP are reported in figure 8. The point zero of the x axis is assumed at the beginning of the bond length of the laminate. Strain distributions along the FRP laminate evidenced that the effective transfer length is not greater than 100 mm, the remaining part of the bond length is stressed only at failure condition. For this reason some specimens (TA3-1, TA5-2, TA7-2) were realized considering a reduced bond length of 100 mm.

CONCLUSIONS

From the experimental tests information has been obtained about strength, ductility and failure modes for different types of anchorage systems for FRP laminates externally bonded to concrete elements. Given the aforementioned anchorage configurations, the following is noted:

(1) The effective transfer length is not greater than 100 mm and the remaining part of the bond length is stressed only after debonding.

(2) For specimens without anchorage devices, when CFRP is applied also on the horizontal plane, a reduction of about 30% of the maximum load was observed with respect to specimens with CFRP bonded only along the vertical plane. This result is probably due to local effects in the corner.

(3) Detailing of the anchorage and application procedure can strongly influence the effectiveness of the system.

(4) When the FRP is applied only vertically and additional anchorage by means of a transverse plate is used, the failure load can have an increment up to 57% with respect to the mean value of the reference specimens.

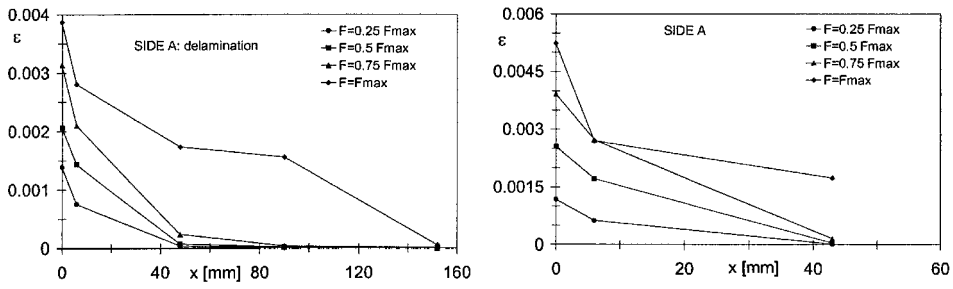


Figure 8 Strain distribution along the FRP

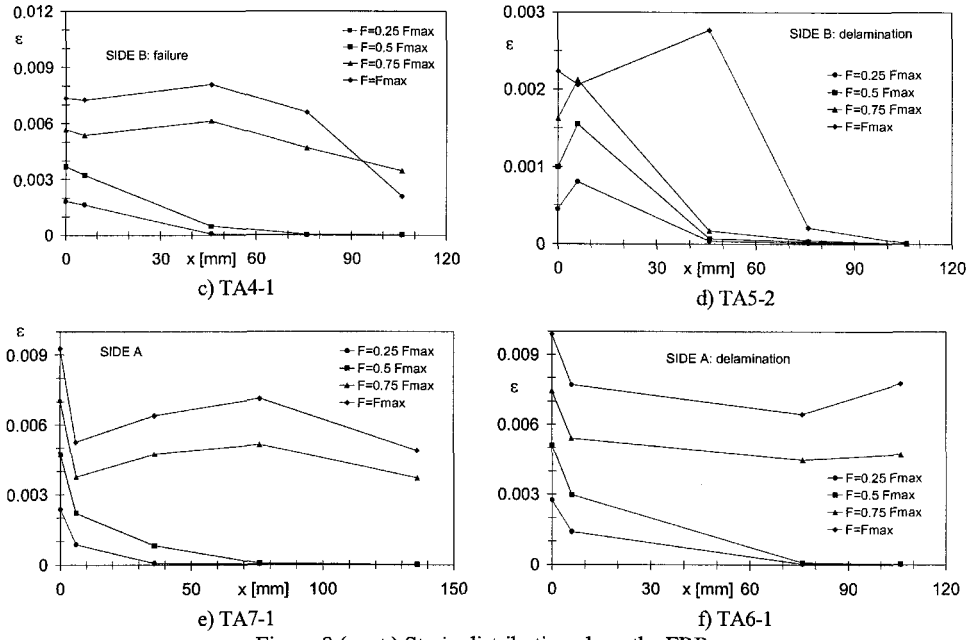


Figure 8 (cont.) Strain distribution along the FRP

REFERENCES

[1] J D Hall, H R Schuman, H R Hamilton III, 'Ductile anchorage for connecting FRP strengthening of under reinforced masonry building', *ASCE Journal of Composite for Construction*, January-February 2002, Vol.6, No.1.

[2] K H Tan, 'Details of FRP reinforcement: an overview', *FRP Composite in Civil Engineering*, Vol.2, pp.1247-1254, Ed. J G Teng, Elsevier Science, 2001.

[3] fib, *FRP as Externally Bonded Reinforcement of RC Structures: Basis of design and safety concept*, fib Task Group 9.3, fib Bullettin 14, International federation for structural concrete, Lausanne, Switzerland, 2001.

[4] M Blaschko, 'Anchorage device for FRP strips', Proceedings of the Fifth Conference on Non-Metallic Reinforcement for Concrete Structures, *Proceedings of FRPRCS5 International symposium*, Cambridge, UK, pp. 1255-1264, Vol. 2, Tomas Telford Editor, July 2001.

[5] Y Jinno, H Tsukagoshi, Y Yabe, 'RC Beams with Slabs strengthened by CF sheets and bundles of CF strands', *Proceedings of FRPRCS5 International symposium,* Cambridge, UK, pp. 981-987, Tomas Telford Editor, July 2001.

[6] K Koayshi, S Fujii, Y Yabe, H Tukagoshi, T Sugiyama, 'Advanced wrapping system with CF-anchor: Stress Transfer mechanism of CF-anchor', *Proceedings of FRPRCS5 International symposium,* Cambridge, UK, Tomas Telford Editor, July 2001.

[7] A Khalifa, A Belarbi, A Nanni, 'Shear performance of RC members strengthened with externally bonded FRP wraps', *Proceedings of 12WCEE Conference*, 2000.

[8] J G Teng, J F Chen, S T Smith, L Lam, *FRP Strengthened RC Structures*, John Wiley & Sons Ltd, 2002.

[9] K Brosens, D Van Gemert, 'Anchorage design for externally bonded carbon fiber reinforced polymer laminates', *Proceedings of FRPRCS4 International symposium*, Baltimore, November 1999.

[10] P Mukhopadhyaya, N Swamy, C Lynsdale, 'Optimizing structural response of beams strengthened with GFRP plates', *Journal of composites for construction*, May 1998.

[11] S Matthys, L Taerwe, J Janssens, D De Neef, 'Innovative strengthening of the reptile building in the Zoo of Antwerp', *Field Applications of FRP Reinforcement: Case Studies*, Eds. S Rizkalla, A Nanni, ACI Fall 2003 Convention Boston, U.S.A., ACI-International SP-215, 2003.

SHEAR STRENGTHENING OF REINFORCED CONCRETE STRUCTURES USING FRP COMPOSITES

S R Denton, J D Shave, A D Porter.
Parsons Brinckerhoff, Bristol, UK

NOTATION

α	Angle between the principal fibres of the FRP and vertical (see Figure 2)
ε_{frpdb}	Strain in the FRP when debonding occurs
$\varepsilon_{frpdb,max}$	Strain in the FRP when debonding occurs when the FRP is fully anchored
ε_{frps}	Effective strain in the FRP
ε_{frpu}	Characteristic ultimate strain capacity of FRP
ρ_f	FRP reinforcement ratio
A_{frps}	Area of FRP (mm^2) for shear strengthening measured perpendicular to the direction of the fibres (see Figure 2). When FRP laminates are applied symmetrically on both sides of a beam A_{frps} is the sum of the areas of both laminates.
b_{frp}	Width of the FRP laminate (mm) measured perpendicular to the direction of the fibres (see Figure 2). For continuous FRP sheet, s_{frp} is taken as 1.0 and b_{frp} is taken as $cos\ \alpha$.
b_w	Width of the concrete beam (mm)
d_{frp}	Effective depth of the FRP strengthening (mm)
E_{frp}	Characteristic tensile modulus of the FRP laminate (MPa)
f_c	Concrete cylinder strength (MPa)
f_{ctm}	Characteristic tensile strength of the concrete (MPa).
k_b	Parameter in the Neubauer and Rostasy[17] FRP anchorage model
$L_{C,max}$	Anchorage length required to develop full anchorage capacity (mm)
s_{frp}	Longitudinal spacing of the FRP laminates used for shear strengthening (see Figure 2). For continuous FRP sheet, s_{frp} is taken as 1.0 and b_{frp} is taken as $cos\ \alpha$.
t_{frp}	Thickness of the FRP laminate (mm)
V_c	Contribution from the concrete to the shear capacity (N)
V_{frp}	Contribution from the FRP to the shear capacity (N)
V_s	Contribution from the steel to the shear capacity (N)
V_u	Ultimate shear capacity of FRP strengthened section (N)

INTRODUCTION

The use of Fibre-Reinforced Polymer (FRP) composites for strengthening reinforced concrete structures has now gained wide acceptance internationally[1,2,3,4]. Initial efforts in this field focussed on the use of FRP composites for flexural strengthening, but more recently there has been increasing interest in the use of these materials to enhance the shear capacity of reinforced concrete beams.

Experimental studies have demonstrated that FRP can be effective in increasing the shear capacity of reinforced concrete beams[5,6,7,8,9,10,11,12] and a number of different design approaches have been proposed[13,14,15,16,17]. However, a review of these design approaches has highlighted some concerns about their application to practical civil engineering structures. In this paper, these concerns are discussed and an alternative, more cautious, design approach is presented.

The behaviour of reinforced concrete in shear is complex. Despite considerable research effort over many years, there remain a number of unresolved issues[18], and research continues in the field[19]. Notwithstanding these limitations, reliable design approaches do exist for shear in reinforced concrete. It is important to recognise, however, that they typically embody significant assumptions as well as empirically determined parameters. It is not yet fully clear how the presence of FRP and its interaction with the structure affects the validity of some of these assumptions and parameters.

These difficulties, combined with the difficulties associated with predicting the behaviour of the FRP itself make the development of reliable approaches for the design of FRP shear strengthening for reinforced concrete beams a particularly challenging problem. Its complexity is illustrated by the significant differences between the approaches that have been proposed and incorporated into design guidelines[1,2,3,4,13,14,15,16,17]. In contrast, there is far greater commonality in the design approaches presented for flexural strengthening.

In understanding the behaviour of FRP strengthening in shear, it is important to recognise that the bond behaviour of FRP differs markedly from conventional embedded steel reinforcement[17,22,23]. In tests on the anchorage of externally bonded FRP, it has been found that beyond a limiting bonded length, of the order of 50-300mm depending upon the FRP stiffness and thickness, no further increase in the ultimate anchorage load-capacity occurs with increased bonded length. This maximum anchorage capacity can be very much less than the ultimate tensile capacity of the FRP (see Figures 4 and 5). The contribution that the FRP makes to the shear capacity can therefore be governed by fracture of the FRP or debonding of the FRP from the concrete. Such debonding is typically associated with the propagation of a failure plane in the concrete close to the surface.

In comparing proposed design methods it is tempting to judge them on the basis of how well they fit experimental data. Whilst such an approach clearly has some legitimacy, it is not necessarily a sensible governing criterion for identifying the "best" method. In particular, where methods include empirically or semi-empirically determined parameters, it can sometimes simply favour later proposals calibrated against a more complete dataset.

Further concerns arise about empirical or semi-empirical approaches when the available experimental dataset does not cover the full range of practical scenarios likely to be encountered by designers. While such approaches may appear reliable for the existing dataset, their extrapolation outside this range is more dubious. It can be extremely difficult to establish reliable bounds on the range of application of empirical or semi-empirical approaches, yet this information is essential to designers.

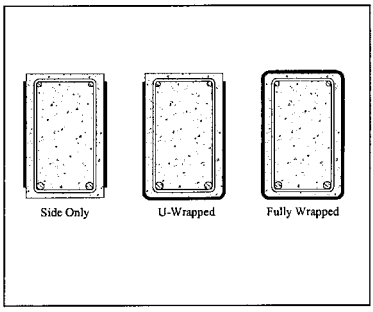


Figure 1 – Strengthening configurations

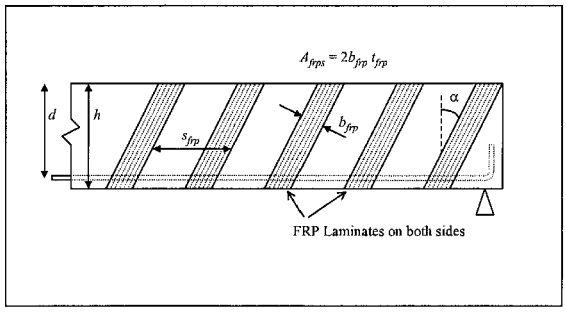


Figure 2 – General notation

In considering alternative proposed design methods, three attributes have been viewed as important. Firstly, the method should be appropriately cautious, reflecting the limitations of the current body of experimental data and the state of understanding. Secondly, it should seek to embody, in a transparent manner, the mechanics that underpin the behaviour of the strengthened beam. Thirdly, it should be reasonably, and systematically, consistent with available experimental data.

The majority of experimental testing of reinforced concrete beams strengthened in shear has used carbon fibre rather than aramid or glass fibre. Although the underlying principles should be common to all materials, the present paper has focussed on the use of carbon FRP.

METHODS OF SHEAR STRENGTHENING

Reinforced concrete beams may be strengthened for shear using FRP plates or fabric sheets. FRP may be bonded to the concrete in various configurations, including: FRP applied only to the sides of the beam (side-only); FRP covering the sides and the tension face of the beam (U-wrapped); or wrapping FRP around the whole perimeter of the beam cross-section (fully wrapped). These configurations are illustrated in Figure 1.

The orientation of the FRP fibres can affect the performance of the strengthening system. Fibres that are inclined to resist the formation of shear cracks (as illustrated in Figure 2) can be theoretically more effective than vertical fibres for shear strengthening. However, if the shear force direction can be reversed or if the FRP is partially or fully wrapped around the beam, systems with vertical fibres are more convenient and are typically used in practice.

Side-only or U-wrapped beams will be more prone to debonding failures than fully wrapped beams. Full wrapping is therefore preferable, but it is not always practicable, for example, where the top of the beam is inaccessible.

EXISTING MODELS AND DESIGN APPROACHES

The existing design approaches considered have been drawn from those incorporated in published design guidelines[1,2,3,4]. These approaches have therefore already received peer review. In addition, the proposals of Chen and Teng[13,20,21] have been considered. Teng *et al.*[22] provide a good general review of shear design methods. Here key points are highlighted and discussed.

All of the design recommendations considered assume that the ultimate shear capacity of an FRP strengthened beam can be expressed as:

$$V_u = V_c + V_s + V_{frp} \tag{1}$$

Generally, it is further assumed that V_c and V_s can be determined from conventional design standards. In some guidelines, warnings are given that it may not be appropriate to assume that the full values of V_c, V_s and V_{frp} act concurrently, however there is little advice on how to deal with this issue in design.

A broadly common approach also underpins the basis upon which the contribution of the FRP to the ultimate shear capacity, V_{frp}, is determined. Assuming a 45° shear crack and that the FRP carries stress solely in the fibre direction, it follows from equilibrium that:

$$V_{frp} = E_{frp}\,\varepsilon_{frps}\,A_{frps}\,\frac{d_{frp}}{s_{frp}}\,(\cos\alpha + \sin\alpha) \tag{2}$$

However, it is in the methods of evaluating the fundamental parameters ε_{frps} and d_{frp} that the differences between the design guidelines manifest themselves. The most significant differences are associated with the evaluation of the effective strain in the FRP, ε_{frps}, which accounts for the variation in strain in the FRP along the shear crack when the ultimate limit state is reached.

All of the design guidelines reviewed recognise that different approaches are appropriate for evaluating ε_{frps} in the case of fully wrapped beams and the case of side-only or U-wrapped beams.

Effective FRP Strain for Fully Wrapped Beams

The simplest approach is that in ACI 440 *Guide for the Design and Construction of Externally Bonded FRP Systems for Strengthening Concrete Structures*[3]. For fully wrapped beams, the effective FRP strain is taken as the lesser of 0.004 and 0.75 times the ultimate strain capacity of the FRP.

The Concrete Society's report TR55[1] incorporates recommendations for evaluating ε_{frps} based upon Khalifa *et al.*[16], although it does highlight some important limitations of the approach. The recommendations in FIB Bulletin 14 *Externally bonded FRP reinforcement for RC structures*[2] are based upon the approach proposed by Triantafillou and Antonopoulos[15]. Both the Khalifa and Triantafillou recommendations are essentially based upon fitting design curves to test results assuming that the ratio of the effective FRP strain, ε_{frps}, to its ultimate strain capacity, ε_{frpu}, is a function of the "axial rigidity" parameter, $\rho_{frp}E_{frp}$, which is proportional to the ratio of the FRP thickness to the beam width, (t_{frp}/b_w). Khalifa expresses the effective strain ratio as a function of $(\rho_{frp}E_{frp})$, while Triantafillou expresses it as a function of $(\rho_{frp}E_{frp}/f_c^{2/3})$. These criteria ostensibly model the fracture of the FRP.

Chen and Teng[13] also assume that for fully wrapped beams the ultimate limit state is associated with fracture of the FRP, although they do note that there may be a loss of aggregate interlock before fracture occurs. They recommend that the effective FRP strain be taken as half the ultimate strain capacity of the FRP. This approach is consistent with assuming a linear variation in FRP strain along the shear crack from zero at one end to the ultimate FRP strain at the other end.

For the case of FRP fracture, Taljsten[4] bases his recommendations on an elastic analysis of the shear strain in the section by Carolin[25]. This analysis gives an effective FRP strain equal to 0.6 times the ultimate FRP strain capacity.

Effective FRP Strain for Side-only and U-wrapped Beams

Both ACI 440[3] and TR55[1] incorporate Khalifa's[16] recommendations for determining ε_{frps} for side-only and U-wrapped beams. These recommendations assume that debonding of the FRP will occur and the effective strain in the FRP is therefore based upon the FRP anchorage capacity. Khalifa uses Maeda's[23] proposals to determine the anchorage capacity.

Both Chen and Teng[13,20] and Taljsten[4] also recognise the significance of debonding and base their design proposals on determining the effective FRP strain from the FRP anchorage capacity. Chen and Teng base the FRP anchorage capacity upon their proposed anchorage model[21]. Taljsten also uses his own anchorage model [24].

The recommendations in FIB Bulletin 14[2] for determining the effective FRP strain for side and U-wrapped beams are based upon the approach proposed by Triantafillou and Antonopoulos[15]. Again, Triantafillou recognises the significance of debonding.

However, rather than basing ε_{frps} on the anchorage capacity of the FRP, it is determined from fitting a design curve to test results assuming that ε_{frps} is a function of only $(\rho_{frp}E_{frp}/f_c^{2/3})$.

Effective Depth of FRP Strengthening

The contribution of the FRP to the shear strength, as modelled by Equation 2, depends on the effective depth of the FRP, d_{frp}. Different design recommendations treat this parameter in various ways.

For fully wrapped beams, most guidelines[1,2,3,15,16] assume that the FRP is effective over the distance from the top of the beam to the tension reinforcement, d. Chen and Teng[13] adopt a more complex approach, which for fully wrapped beams simplifies to $0.9d$. Taljsten[4] also uses $0.9d$, with the top $0.1d$ apparently neglected to account for the compression zone in the concrete.

For beams with FRP bonded only to the sides and U-wrapped beams, the effective width of the FRP strips is reduced in some guidelines[1,16] to reflect the reduced stress that can be developed in the anchorage region within $L_{C,max}$ of the top of U-wrapped and top and bottom of side wrapped beams. This approach is equivalent to reducing the effective depth of the FRP by the same ratio. Chen and Teng[13] have developed an adjustment factor D that is applied to the maximum strain in order to account for anchorage effects. Again, this adjustment is equivalent to a reduction in the effective depth of the FRP.

DISCUSSION OF EXISTING DESIGN METHODS

The design methods proposed by Triantaffilou and Antonopoulos[15] and Khalifa *et al*[16], which are based on fitting design curves to test data, rely on two key assumptions.

Firstly, the body of test data must be representative of the design cases to which the method is applied. However, given the brittle behaviour of FRP-strengthened beams in shear, it is reasonable to anticipate that a size-effect may be significant and therefore the beam size and FRP thickness are likely to be important parameters in this respect. Figures 3a and 3b show the variation in beam depth and effective FRP thickness for most of the tests upon which Triantaffilou and Khalifa's proposals are based. It is clear from these figures that the substantial majority of tests have been undertaken on small specimens with low FRP thicknesses. Many practical design cases are likely to lie outside this range.

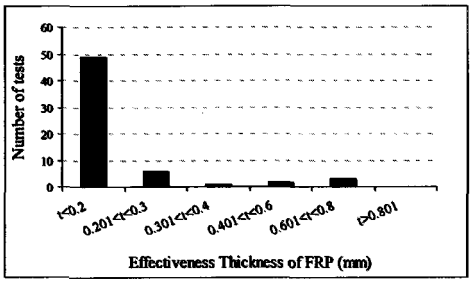


Figure 3a – Range of effective FRP thicknesses used in tests[5,6,8,9,10,11,12,14]

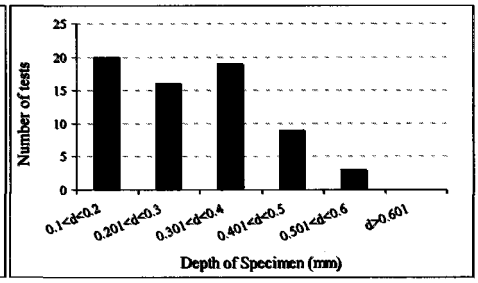


Figure 3b – Range of beam depths used in tests[5,6,8,9,10,11,12,14]

Secondly, the parameters used in fitting the design curves must properly embody the mechanics that underpins the behaviour of the strengthened beam. If this is not the

case, then the design curves will not account for the true influence of the different variables that make up these parameters. This is a particular concern when only a single independent parameter is used. For example, Triantaffilou and Khalifa's approaches appear to assume that ε_{frps} is a function of (t_{frp}/b_w). However, it seems unlikely that the width of the beam is nearly as significant a variable as the FRP thickness, since the mechanics that dictate the FRP behaviour involve the surface concrete and the FRP itself but would seem largely independent of the concrete deeper into the beam. Using their approach the independent significance of t_{frp} and b_w cannot be taken into account.

It seems reasonable to limit the effective strain in the FRP to a value based on the anchorage capacity for cases where debonding is significant[13,16,20,24]. The anchorage model proposed by Maeda[23], and adopted by Khalifa *et al*[16], does not, however, seem to predict the anchorage length well (as also noted by Teng *et al.*[22]), and does not therefore appear well suited to shear strengthening design. Alternative anchorage models, such as those proposed by Neubauer and Rostasy[17] or Chen and Teng[21], which both give similar prediction, would seem more appropriate.

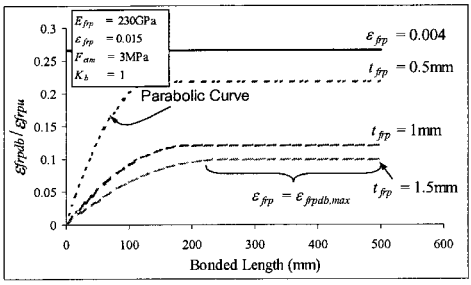


Figure 4 – Variation in FRP debonding strain with bonded length, after [17]

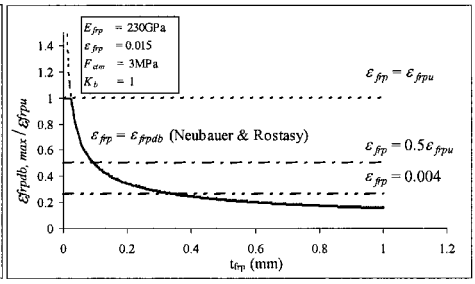


Figure 5 – Variation in FRP debonding strain with FRP thickness, after [17]

Khalifa *et al*[16] and, to a lesser extent, Chen and Teng[13,20] suggest that debonding is only significant in the cases of side and U-wrapped beams. This observation is supported by the fact that in tests the shear failure of fully wrapped beams has almost always been associated with FRP fracture. However, as noted above, the available test data predominantly comprises small beams with low FRP thicknesses. For larger beams with higher FRP thickness, it would seem likely that debonding is also significant for the case of fully wrapped beams, principally because of the potential for V_c to diminish before the FRP fractures. This possibility is acknowledged by Chen and Teng[13,20].

As illustrated in Figure 4, which is based on the anchorage model proposed by Neubauer and Rostasy[17], the strain that can be developed in the FRP before debonding, ε_{frpdb}, increases with the bonded length up to a limiting length, $L_{C,max}$, after which there is no further increase in the anchorage capacity. This maximum anchorage capacity corresponds to a maximum FRP strain, $\varepsilon_{frpdb,max}$. As illustrated in Figure 5, the ratio $\varepsilon_{frpdb,max}/\varepsilon_{frpu}$ decreases with increasing FRP thickness and, crucially, according to this model, debonding is more critical than fracture for all but the thinnest FRP laminates.

Assuming that this anchorage bond model reasonably applies to FRP spanning a shear crack, its implications for a number of different cases can be considered for fully wrapped beams. Although the behaviour of reinforced concrete in shear is complex it is convenient, if rather simplistic, for the present purpose to consider it as having two phases. Initially, the beam will behave approximately elastically. Subsequently, and

after the formation of a shear crack, the displacement of the beam is better characterised by rigid body movements of the two regions of the beam either side of the crack.

If $\varepsilon_{frpdb,max} > \varepsilon_{frpu}$, fracture of the FRP is likely to occur prior to, or as, shear cracking initiates. For such design cases, the behaviour of the beam will be predominantly elastic, and therefore it would seem reasonable to base ε_{frps} on the approach proposed by Taljsten[4] (i.e. taken as $0.6\varepsilon_{frpu}$).

For cases where $\varepsilon_{frpdb,max} < \varepsilon_{frpu}$, debonding will occur before the FRP fractures. Thus, for fully wrapped beams, as a shear crack develops, the FRP will start to debond and the debonded region will propagate in the fibre direction as the shear crack widens. This will occur with an approximately constant stress in the FRP, equal to $E_{frp}\ \varepsilon_{frpdb,max}$, until the debonded region has extended to both the top and bottom of the beam. Once this has happened, it will be possible for the FRP stress to increase until FRP fracture occurs or an alternative failure mechanism initiates.

In this case, the displacement pattern of the beam will be better characterised as two rigid bodies. The crack width will be a maximum at the tension face of the beam and will reduce towards the compression face. Assuming the most onerous case that all the FRP spanning the crack debonds to the top and bottom of the beam, zero crack width at the compression face and FRP fracture at the tension face, the resulting effective FRP strain would be given by $\varepsilon_{frps} = 0.5\varepsilon_{frpu}$, which is the same as the value proposed by Chen and Teng[13,20].

Interestingly, it therefore turns out that the difference between Taljsten's and Chen and Teng's proposals can be understood as being representative of different modes of behaviour. However, perhaps of more significance to designers is that the resulting limits are rather similar so adopting Chen and Teng's lower value for ε_{frps} will not have a significantly adverse affect on the resulting design.

An important qualification arises, however, if it is accepted that when $\varepsilon_{frpdb,max} < \varepsilon_{frpu}$ the FRP must debond over the full depth of the beam for a force greater than the anchorage capacity to be developed in it. It follows from this observation that there is a risk that concrete shear cracks could widen to the point where aggregate interlock would be lost, so that the full V_c could not be relied upon, before fracture of the FRP occurs, particularly in the case of large beams.

If the FRP has debonded over the full depth of the beam, the crack width when FRP fracture occurs can be estimated as the product of ε_{frpu} and the debonded length of FRP, resolved in the direction of crack opening. This approach is likely to overestimate the actual crack widths, but it is unlikely to do so dramatically. Using this method, the variation in crack width with beam depth is plotted in Figure 6 for vertically aligned fibres, where E_{frp} = 230GPa, ε_{frpu} = 0.015 and assuming a 45° shear crack opening normal to its direction. A series of different cases are plotted corresponding to different possible limits on the FRP strain.

Research[26] has shown that the shear stress that can be sustained across a shear crack diminishes as the crack width increases and is substantially reduced for crack widths much in excess of 1mm. Thus, once a shear crack has reached a width of several millimetres, V_c would be expected to begin to diminish rapidly.

From Figure 6 it appears that for the modest beam specimens used in many experimental studies, FRP fracture will occur without V_c reducing significantly. This finding is consistent with the behaviour observed in the tests. However, for beams of a more realistic size, both the peak and average crack opening determined using Chen and Teng's proposed approach (i.e. those corresponding to FRP strains of ε_{frpu} and $\varepsilon_{frpu}/2$) are such that it may be unsafe to rely on the full capacities of the FRP and the concrete to act simultaneously. It also appears that the ACI 440 limits of an average FRP strain

of 0.004, corresponding to a peak value of perhaps 0.008, may similarly not be safe for many practical design cases if V_c is determined assuming conventional design standards are valid.

One approach to deal with this effect is to limit the strain in the FRP to $\varepsilon_{frpdb,max}$, even for the case of wrapped beams. The justification for such an approach lies in the fact that as the shear crack develops and FRP debonding propagates from the shear crack, the FRP can always be expected to mobilise at least its anchorage capacity. Such an approach has been incorporated into the proposed design method summarised below.

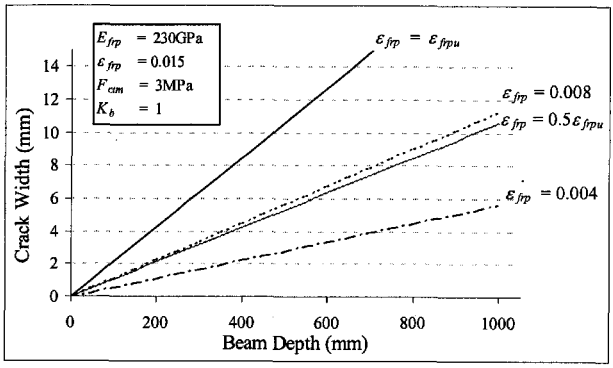


Figure 6 – Variation in crack width with depth for fully-wrapped beams

PROPOSED DESIGN METHOD

The proposed design approach is based on a modified form of Equation 2:

$$V_{frp} = \frac{E_{frp}}{\gamma_{mfE}} \varepsilon_{frps} A_{frps} \frac{(d_{frp} - \frac{n}{3} L_{C,\max})}{s_{frp}} (\cos\alpha + \sin\alpha) \quad (3)$$

where n is taken as zero for a fully wrapped beam, 1.0 when FRP is bonded continuously to the sides and bottom of a beam and 2.0 when it is bonded to only the sides of a beam. The effective depth d_{frp} is taken as the depth from the top of the FRP to the tension reinforcement.

The effective FRP strain is taken as the minimum of:

$$\text{(i) } \varepsilon_{frpu} / 2 \qquad \text{or, (ii) } 0.64\sqrt{\frac{f_{ctm}}{E_{frp} t_{frp}}} \qquad \text{or, (iii) } 0.004$$

The first strain limit of half the ultimate strain capacity is the minimum average FRP strain that could cause fracture of the FRP (based on the lower of the values proposed by Chen and Teng[13] and Taljsten[4]).

The second strain limit corresponds to debonding of the FRP, and is based on Neubauer and Rostasy's[17] anchorage model. While debonding has previously been considered primarily for FRP bonded either to the sides of beams or to the sides and the tension face of beams, it is here proposed that this condition should also be applied for fully wrapped beams for the reasons described in the proceeding section. For small beams such an approach may be conservative, but importantly it is likely to be safe for the cases most frequently encountered by designers.

The final 0.004 strain limit was proposed in early design methods to ensure that the concrete integrity is maintained, and it has been included in ACI 440[3]. This convenient rule of thumb appears to have little rational justification, and as has been shown, does not necessarily prevent wide cracks. However, it is retained simply because it seems sensibly cautious to do so, although it is anticipated that it will be removed once a more complete understanding of FRP shear-strengthened beams has developed.

In Equation 3, the effective depth is reduced by a length equal to $n/3L_{C,max}$. This adjustment accounts for the reduction in force that can be sustained by the FRP in the anchorage regions. The Neubauer and Rostasy [17] anchorage model assumes a parabolic variation of stress with distance (see Figure 4). The force corresponding to the area under the stress curve in the anchorage region is therefore only 2/3 of the maximum stress multiplied by the maximum bond length. This reduction in the FRP contribution can be modelled by subtracting $(n/3)L_{C,max}$ from the effective depth, as in Equation 3. The adjustment is made at the top for U-wrapped beams (n=1) and at the top and bottom for beams with FRP bonded only to the sides (n=2). No adjustment is necessary for fully wrapped beams (n=0).

Figure 7 shows a comparison of experimental measured values of V_{frp} (from [5,6,8,9,10,11,12,14]) and those determined using the proposed design method. There appears to be reasonable agreement. Furthermore, the substantial majority of cases lie on the safe side, with the experimentally measured values exceeding those determined using the proposed design method.

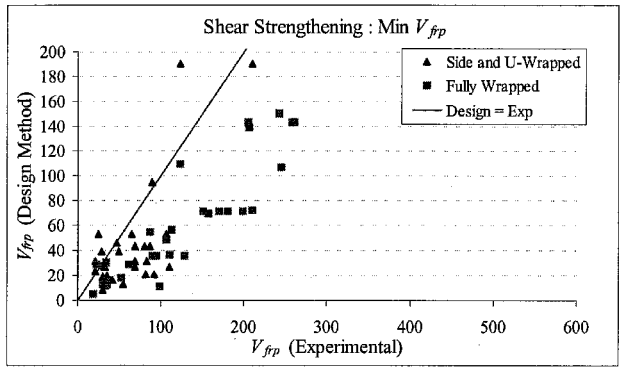


Figure 7 – Comparison of proposed design method with experimental results

CONCLUSIONS

Design approaches previously incorporated into published design guidelines have been reviewed, and potential concerns about the safety of their application to practical design cases have been highlighted.

An alternative design method has been presented. This design method recognises that even for fully-wrapped FRP beams, it is important to take direct account of FRP debonding. The application of this design method shows reasonable agreement with published experimental results. Perhaps more importantly, however, it should be suitable for the kinds of structures that will typically be encountered by designers in practice, which are frequently significantly larger than those used in the majority of experimental programmes to date.

REFERENCES

1 Concrete Society, *Design guidance for strengthening concrete structures using fibre composite materials*, Technical Report 55, Crowthorne, 2000.

2 Fédération internationale du béton, *Externally bonded FRP reinforcement for RC structures*, Bulletin 14, Switzerland, 2001.

3 ACI Committee 440, *Guide for the Design and Construction of Externally Bonded FRP Systems for Strengthening Concrete Structures*, ACI 440.2R-02, 2002.

4 Täljsten, B., *FRP Strengthening of Existing Concrete Structures*, Design Guidance, Luleå University of Technology, 2003

5 Uji, 'Improving the Shear Capacity of Existing Reinforced Concrete Members by Applying Carbon Fibre Sheets', *Trans, Japan Concrete Institute*, 14, 253-266, 1992.

6 Ohuchi et al., 'Seismic Strengthening Design Technique for Existing Bridge Columns with CFRP', *Seismic Design and Retrofitting of Reinforced Concrete Bridges*, R. Park, 495-514, 1994

7 Chajes et al., 'Shear Strengthening of Reinforced Concrete Beams Using Externally Applied Composite Fabrics', *ACI Structural Journal*, May-June 1995.

8 Sato et al., 'Shear Reinforcing Effect of Carbon Fibre Sheet Attached to the Side of Reinforced Concrete Beams', *Advanced Composite Materials in Bridges and Structures*, The Canadian Society of Civil Engineering, 621-627, 1996

9 Miyauchi et al., 'Shear Behaviour of Reinforce Concrete Beams Strengthened with CFRP Sheet', *Trans, Japan Concrete Institute*, 19, 97-104, 1997

10 Taerwe et al., 'Behaviour of RC Beams Strengthened in Shear by External CFRP Sheets', *Non-metallic (FRP) Reinforcement for Concrete Structures*, Vol. 1, Japan Concrete Institute, 483-490, 1997.

11 Fanning et al. 'Shear Strengthening of Reinforced Concrete Beams: An Experimental Study Using CFRP Plates', *Structural Faults and Repair*, London, 1999.

12 Funakawa et al., 'Experimental Study on Shear Strengthening with Continuous Fibre Sheet and Methyl Methacrylate Resin', *Non-metallic (FRP) Reinforcement for Concrete Structures, Vol. 1*, Japan Concrete Institute, 475-482, 1997

13 Chen, J.F. and Teng, J.G., 'A shear strength model for FRP-Strengthened RC Beams', *FRPRCS-5*, Ed. C. Burgoyne, Cambridge, Thomas Telford, London, pp205-214, 2001.

14 Taljsten et al., 'Strengthening of Concrete Structures for Shear with bonded CFRP Fabrics', *Recent Advances in Bridge Engineering, EMPA*, Switzerland, 67-74, 1997.

15 Triantafillou T.C., Antonopoulos, C.P., 'Design of Concrete Flexural Members Strengthened in Shear with FRP', *Journal of Composites for Construction*, November 2000.

16 Khalifa, A., Gold, W.J., Nanni, A. and Aziz, A., 'Contribution of externally bonded FRP to shear capacity of RC flexural members', *ASCE Journal of Composites for Construction*, 2 (4), pp153-203, 1998

17 Neubauer U., Rostasy F. S. 'Design Aspects of Concrete Structures Strengthened with Externally Bonded CFRP Plates', Presented at the *7th International Conference on Structural Faults and Repair*, 2, 109-118, 1997

18 Regan, P.E., 'Research on shear: a benefit to humanity or a waste of time?' *The Structural Engineer* vol. 71 no. 19 5 Oct 1993 pp337-347

19 Shave J.D., Ibell T.J., Denton S.R., 'Shear Assessment of Concrete Bridges with Poorly Anchored Reinforcement', *Structural Faults and Repair*, London, 2003.

20 Chen, J.F. and Teng, J.G., 'Debonding Failure Strength of RC Beams Shear-Strengthened with FRP', *Proceedings of CICE*, Hong Kong, Vol. 1 pp685-693, 2001.

21 Chen, J.F. and Teng, J.G., 'Anchorage Strength Models for FRP and Steel Plates Bonded to Concrete', *Journal of Structural Engineering*, ASCE 127:7, pp784-791, 2001.

22 Teng, J.G., Chen, J.F., Smith S. T., Lam, L., *FRP Strengthened RC Structures*, Chichester, Wiley, 2002

23 Maeda, T., Asano, Y., Sato, Y., Ueda, T., and Kakuta, Y., 'A study on bond mechanism of carbon fiber sheet.' *Non-metallic (FRP) Reinforcement for Concrete Structures, Vol. 1*, Japan Concrete Institute, Tokyo, pp279-286, 1997

24 Taljsten B., 'Defining anchor lengths of steel and CFRP plates bonded to concrete', *Int. J. Adhesion and Adhesives*, Vol 17, No. 4, 1997 pp319-327

25 Carolin, A., *Strengthening of concrete structures with CFRP – Shear strengthening and full-scale applications*. Licentiate Thesis, Lulea University of Technology, Lulea, Sweden, 2001.

26 Walraven, J.C:, *Aggregate Interlock-A Theoretical and Experimental Analysis*; PhD Thesis, TU Delft, Delft University Press; 1980

A THEORETICAL STRATEGY FOR MOMENT REDISTRIBUTION IN CONTINUOUS FRP-STRENGTHENED CONCRETE STRUCTURES

Tim Ibell* and Pedro Silva**
*University of Bath, UK **University of Missouri-Rolla, USA

ABSTRACT

The use of fiber-reinforced polymer (FRP) composites is now a widely-accepted solution for the strengthening of reinforced concrete structures. FRP strengthening schemes offer many well-documented benefits for the retrofit of many existing concrete buildings and bridges. However, the main drawback in using FRP for such purposes is the reduction in ductility that the strengthened structure displays after strengthening. This loss in ductility has led various design guidelines around the world to prohibit any redistribution of bending moments in continuous FRP-strengthened concrete structures. This means that continuous structures, which might have been designed originally under assumptions of moment redistribution, should be designed for FRP strengthening according to elastic distribution of bending moment. This could lead to onerous conditions for such strengthening schemes, particularly in hogging regions. This paper sets out a rationale for the possible appropriate use of redistribution principles for FRP-strengthened concrete.

INTRODUCTION

In today's world, protection of the environment is becoming a major consideration in any building project. Sustainability is a key issue in all its various forms, from embodied energy of materials to energy associated with transport, construction and operation. Strengthening of existing structures avoids the need to demolish and replace, enabling the design life of the current structure to be increased.

Extensive application examples and research exist on flexural strengthening of reinforced concrete structures using FRP[1-4]. The principal advantages in using FRP for such applications lead to a rapid, cost-effective strengthening scheme, so that FRP is now the preferred choice worldwide for retrofit of concrete structures[5].

However, FRP essentially displays elastic behaviour up to brittle failure. Further, the principal failure mode associated with FRP-strengthened concrete structures is peeling of the FRP from the concrete, usually in a brittle manner[6]. Therefore, at first glance, it appears unlikely that moment redistribution should be permitted in FRP-strengthened continuous concrete structures.

However, strengthening of existing continuous steel-reinforced concrete structures, which were designed according to moment redistribution principles, could lead to onerous design conditions, particularly in hogging regions. The degree of FRP strengthening which could be required under such circumstances might become excessive. This is because the original elastic hogging moment *plus* the additional elastic moment (required for strengthening purposes) need now to be resisted at this location, compared with just the original redistributed hogging moment. If it could be shown that

sufficient ductility exists in an FRP-strengthened region, it would be beneficial to be able to carry out limited moment redistribution to alleviate this problem.

Further, fundamentally there are two redistribution issues which need to be addressed. The first relates to redistribution of bending moment *into* an FRP-strengthened region, while the second relates to redistribution of bending moment *out of* an FRP-strengthened region. This paper addresses both issues and suggests levels of redistribution which could be adopted that directly conform with redistribution principles in existing design codes-of-practice around the world[7,8].

MOMENT REDISTRIBUTION IN FRP-STRENGTHENED STRUCTURES

Moment redistribution into strengthened zones

There seems to be no logical reason why moment redistribution should be summarily prohibited *into* FRP-strengthened zones in continuous concrete structures. This is because if it can be shown that a remote unstrengthened zone can rotate sufficiently for the strengthened zone to attract bending moment, the requirements for redistribution are met. There is no need to consider the ductility capacity or the rotation capacity of the strengthened zone itself.

Therefore, it is considered appropriate that moment redistribution into FRP-strengthened zones should indeed be permitted in design guidelines around the world if it can be shown that sufficient rotation capacity exists in the rest of the structure to make such redistribution feasible.

Moment redistribution out of strengthened zones

The issue of allowing moment redistribution *out of* FRP-strengthened zones is far thornier. This is because the rotation capacity and/or the ductility of the strengthened zone itself need to be considered under such circumstances. Research in this area is extremely limited, at best, although some work has indeed been conducted[9]. Equally important work has been conducted into the question of ductility[10,11] and rotation capacity[12,13] in FRP-strengthened concrete structures.

If a structure displays ductility, it will also display rotation capacity. However, if a structure displays rotation capacity, it will not automatically display ductility. Therefore, it is the premise of this paper that, in order to define the context within which redistribution should be allowed in FRP-strengthened concrete structures, *ductility* (rather than mere rotation capacity) should be the over-riding concern. In this way, if ductility can be demonstrated, it is certain that a safe design based on redistribution will result.

MOMENT-CURVATURE RELATIONSHIPS

The bridge beam section in Figure 1 is used here to develop example moment-curvature plots with and without FRP strengthening. If one assumes that such a typical concrete structure often carries roughly equal dead and live loading under service conditions, it

may be seen that, on average, the service moment acting on such a structure during strengthening is

$$M_{service} = M_u^{unstrengthened} / (1.4 + 1.6) \approx 0.30 M_u^{unstrengthened} \quad (1)$$

This ignores any live loading that could be acting. Figure 2 shows theoretical moment-curvature plots for this cross section under increasing quantities of FRP strengthening, which have been added while the section is strained under deadweight. It is clear that as more FRP is added to the section, so the ductility, μ (curvature at the ultimate condition, ϕ_u, divided by curvature at steel yielding, ϕ_y) reduces considerably, as shown in Figure 3.

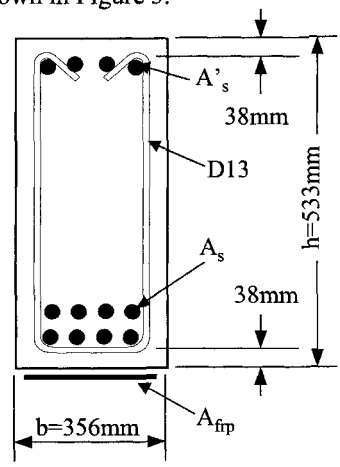


Figure 1 *Typical bridge beam cross section*

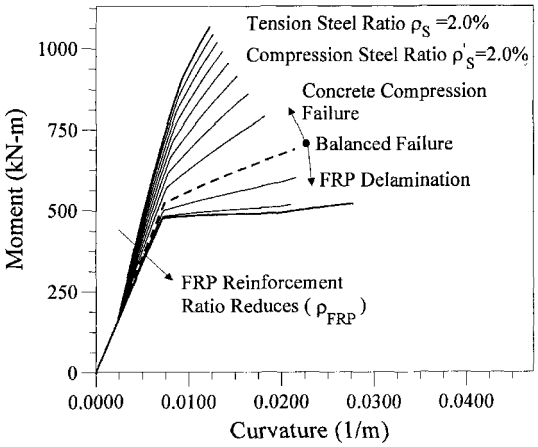


Figure 2 *Moment-curvature plots*

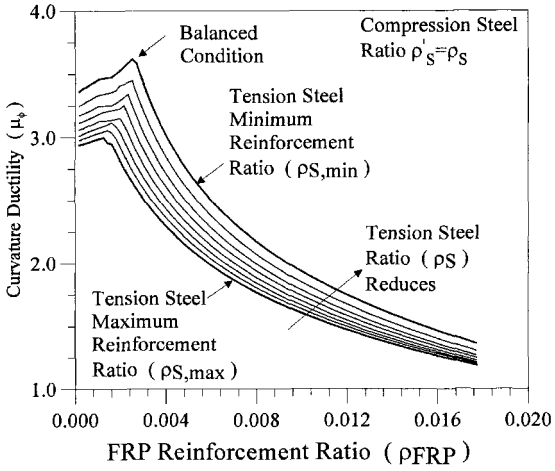


Figure 3 *Ductility ratio under increasing (very high) quantities of FRP*

DUCTILITY EXHIBITED BY FRP-STRENGTHENED CONCRETE

Figure 4 shows a schematic representation of a typical moment – curvature plot for an FRP-strengthened concrete section. Also shown is the moment – curvature plot for the unstrengthened section. The plots are offset horizontally by ϕ_{datum}, corresponding to the datum curvature across the section when the FRP material was added under unpropped conditions. Having removed the datum curvature, that which remains is the effective curvature across the section, which is the additional curvature under strengthened conditions. It may be seen that if the initial moment across the section (at unpropped strengthening) is higher than 30% of the unstrengthened section capacity, the moment – curvature plots shift horizontally to the left. The ductility μ of the section may be defined as

$$\mu = \frac{\phi_u - \phi_{datum}}{\phi_y - \phi_{datum}} \tag{2}$$

and it therefore becomes clear that this ratio increases as the initial service moment on the concrete structure at strengthening increases.

It is undesirable for the initial moment to be *too high* at strengthening, as this could lead to premature yielding of the steel bars under the higher service-load conditions when fully strengthened. However, it is also clear from the above that it is undesirable for the initial moment to be *too low* at strengthening, as this could lead to a low level of ductility.

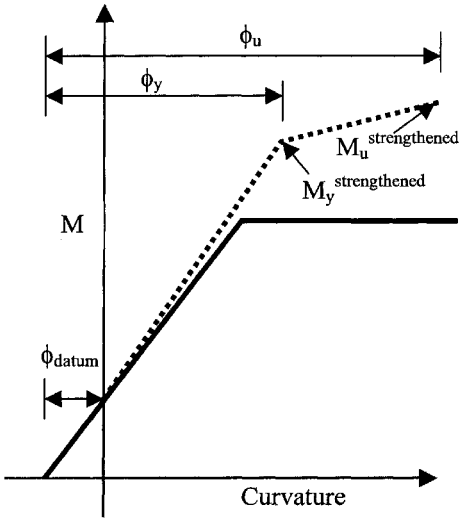


Figure 4 *Schematic moment-curvature plots*

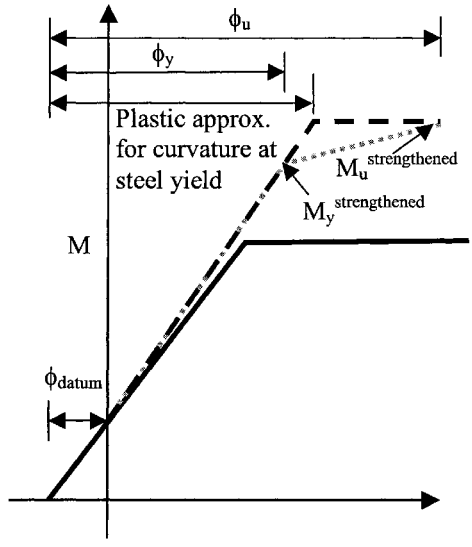


Figure 5 *Fully plastic approximation*

If a measure of ductility is going to be used as a criterion for whether moment redistribution could be carried out or not, it is also important to realise that the FRP-

strengthened section is not fully plastic, but has stiffness under increasing curvature. Figure 5 shows a fully-plastic approximation to this behaviour. Clearly, this model overestimates the stiffness of the response, which is considered to be 'conservative' in the sense that some softening of the section would actually have occurred prior to that which is assumed here. The ductility ratio according to this simplified plastic model may then be recalculated as

$$\mu = \left(\frac{\phi_u - \phi_{datum}}{\phi_y - \phi_{datum}} \right) . \frac{M_y^{strengthened}}{M_u^{strengthened}} \tag{3}$$

which is a lower value than equation (2) would have suggested. Using this approach, it is then possible to calculate a rational level of ductility that the strengthened section would display.

MOMENT REDISTRIBUTION LIMITS OUT OF STRENGTHENED REGIONS

How does the level of ductility found in (3) relate to equivalent levels which are required in present codes-of-practice for conventional reinforced concrete moment redistribution? ACI-318[7] states that the level of redistribution which may be assumed in a steel-reinforced continuous concrete structure is $1000\varepsilon_t$ percent, up to a maximum of 20%, where ε_t is the level of strain in the tension reinforcement, which must be at least 0.0075.

Assuming a singly-reinforced concrete section of effective depth d, such that the strain in the tension steel reaches 0.0075 just as the maximum strain in the concrete reaches 0.003, the curvature at the ultimate limit state is clearly

$$\phi_u = \frac{0.0105}{d} \tag{4}$$

Further, the area of reinforcement, A_s, which is necessary for this strain state to exist is given by

$$A_s = \frac{(0.9)(0.003)(0.85)bdf_c'}{0.0075 f_y} \tag{5}$$

where b is the breadth of the section, f'_c is the cylinder compressive strength and f_y is the yield strength of the steel reinforcement. Then, assuming this area of steel, it may be shown that the depth to the neutral axis, c, when the steel first yields is $c = 0.46d$. The curvature at first yield is then

$$\phi_y = \frac{0.0023}{d - 0.46d} \tag{6}$$

where it is assumed that the yield strain of the steel reinforcement is 0.0023. Therefore, by dividing equation (4) by equation (6), we find that the ductility ratio $\mu = 2.47$. This

implies that as long as the ductility ratio across the section is at least 2.47 and the strain in the tension steel is at least 0.0075, moment redistribution could be allowed in conventional steel-reinforced concrete structures.

It is suggested here that similar criteria be imposed on FRP-strengthened sections for moment redistribution *out of* such locations. It is suggested that as long as the ductility ratio in such sections is at least 2.50, say, and as long as the *total* strain in the tension steel is at least 0.0075, moment redistribution should be permitted out of such sections.

At strengthening, it may be estimated that the strain in the tension steel bars will be in the region of 30% of the yield strain. This translates to a strain of roughly 0.0007. To prevent peeling failure, it is usual for the strain limit in the FRP to be taken as about 0.8%[4]. At this level of strain on the soffit, the total strain in the tension steel bars would be

$$\varepsilon_t = 0.0007 + \frac{(d-c)}{(h-c)} 0.0080 \tag{7}$$

If we assume that generally $h \cong 1.10d$ for most large concrete structures, it turns out that for the strain in the steel bars to reach 0.0075, the depth to the neutral axis, c, is about $0.43d$, which is large. If the depth to the neutral axis is less than this, as is usual, the total strain in the steel bars exceeds 0.0075. Therefore, it is clear that the criterion that the steel strain must be at least 0.0075 appears to be met under normal conditions of FRP strengthening. Further, it is clear from Figure 3 that the ductility ratio in the particular FRP-strengthened section (Figure 1) is above this threshold level of 2.50 under practical conditions (FRP percentage less than 0.4%). But, what level of ductility could we hope to achieve *in general* from an FRP-strengthened structure and would it exceed 2.50, the required minimum?

If it is assumed that the section is strengthened while a deadweight moment of 30% of the ultimate unstrengthened capacity is applied, it is clear that the value of ϕ_{datum}, defined in Figures 4 and 5, is equal to 30% of the curvature in the unstrengthened section at steel yielding. Under fully-strengthened conditions, it may be shown that the curvature at steel yield, ϕ_y, for a strengthened section is given by

$$\phi_y = \frac{\varepsilon_y}{d - \left(\frac{\sqrt{\left(m_s A'_s + m_s A_s + m_f A_f\right)^2 + 2b\left(d' m_s A'_s + d m_s A_s + h m_f A_f\right)} - \left(m_s A'_s + m_s A_s + m_f A_f\right)}{b} \right)} \tag{8}$$

where ε_y is the steel yield strain, d' is the depth to the top steel reinforcing layer, h is the overall depth of section, m is the relevant modular ratio and A is the relevant reinforcement area, with subscript s referring to steel and f referring to FRP. Further, the curvature at the ultimate condition is given by one of the following two equations, depending on whether concrete crushing or FRP delamination is the critical failure mode.

$$\phi_u = \frac{\varepsilon_{fu} b}{hb - \sqrt{\left(m_s A'_s + m_s A_s \frac{\varepsilon_y}{\varepsilon_{fu}} + m_f A_f\right)^2 + 2b\left(d' m_s A'_s + h m_s A_s \frac{\varepsilon_y}{\varepsilon_{fu}} + h m_f A_f\right)} + m_s A'_s + m_s A_s \frac{\varepsilon_y}{\varepsilon_{fu}} + m_f A_f} \quad (9)$$

or

$$\phi_u = \frac{1.8 b f'_c \varepsilon_{cu}}{\sqrt{\left(\varepsilon_{cu} E_c \left(m_s A'_s + m_f A_f\right)\right)^2 + 3.6 b f_c \left(d' \varepsilon_{cu} E_c m_s A'_s + \varepsilon_y E_c m_s A_s + h \varepsilon_{cu} E_c m_f A_f\right)} - \left(\varepsilon_{cu} E_c \left(m_s A'_s + m_f A_f\right)\right)} \quad (10)$$

where ε_{fu} is the ultimate design strain for the FRP, ε_{cu} is the ultimate design strain for the concreteand E_c is Young's Modulus for the concrete.

The above values from (8), (9) and (10) are then plugged into equation (3) to yield the ductility ratio, μ. Note that it is assumed in the above equations that under strengthened conditions, the tension steel always yields, the compression steel is always elastic and the concrete is elastic if the FRP peels. It may easily be shown that, generally, it is FRP peeling that is the more critical failure mechanism for reasonable quantities of FRP. Therefore, equation (9) is usually more critical than equation (10) in terms of ultimate curvature prior to failure.

Using this approach, and plugging in various values across a spectrum of practical scenarios, it turns out that under usual conditions the value of ductility ratio is always above 2.50. This implies that moment redistribution should indeed be allowed to be conducted out of such strengthened zones, based on a minimum level of ductility, and in accordance with the principles laid out in ACI-318, themselves based on the work of Mattock[14].

It is suggested here that should the ductility ratio for a particular situation be found to be equal to or greater than 2.50, a minimum level of moment redistribution should be permitted, namely 7.5%. Should a higher level of redistribution be desired, and it can be shown that the ductility ratio is greater than 2.50, it is advised that a full moment-redistribution analysis be conducted from first principles to justify this.

CONCLUSIONS

This paper has addressed the question of moment redistribution in FRP-strengthened concrete structures by relating such behaviour to the level of ductility at critical sections. In particular, it has been shown that moment redistribution *into* FRP-strengthened zones should be permitted, and that moment redistribution out of FRP-strengthened zones should be permitted if the ductility ratio across the critical section is at least 2.50.

ACKNOWLEDGEMENTS

The authors would like to acknowledge the financial support of the Fulbright Commission for the partial funding of this research.

REFERENCES

1. Tumialan G., Nanni A., Ibell T.J. and Fukuyama H. (2002) FRP composites for strengthening infrastructure around the world. *SAMPE Journal*, Vol.38, No.5, Sept/Oct, pp.9-15.
2. Meier U. ***et al.*** (1993) Strengthening of structures with advanced composites. *Alternative Materials for the reinforcement and prestressing of concrete*. Ed. J.L. Clarke, Glasgow, p153.
3. Task Group 9.3 (2001) *Externally bonded FRP reinforcement for RC structures*. Technical Report, Bulletin 14, Lausanne.
4. The Concrete Society (2000) *Design guidance for strengthening concrete structures using fibre composite materials*. Technical Report 55, Crowthorne.
5. Teng J.G., Chen J.F., Smith S.T. and Lam L. (2002) *FRP-strengthened RC structures*. John Wiley and Sons, UK, 245pp.
6. American Concrete Institute, ACI 440.2R-02. (2002) *Guide for the design and construction of externally bonded FRP systems for strengthening concrete structures*. ACI, Farmington Hills, USA.
7. American Concrete Institute, ACI 318. (2002) *Building code requirements for structural concrete*. ACI, Farmington Hills, USA.
8. British Standards Institution, BS 8110. (1997) *Structural use of concrete: Part 1: Code of practice for design and construction*. London, BSI.
9. El-Refaie S.A., Ashour A.F. and Garrity S.W. (2003) *Sagging and hogging strengthening of continuous reinforced concrete beams using CFRP sheets*. ACI Structural Journal, Vol.100, No.4, July-August, pp.446-453.
10. Burgoyne C.J. (1997) *Rational use of advanced composites in concrete*. Keynote Lecture, *Procs 3rd Int. Symp. on Non-Metallic (FRP) Reinforcement for Concrete Structures, FRPRCS-3*, Vol.1, Sapporo, Japan, October, pp.75-88.
11. Naaman A., Park S. and Lopez M. (2001) *Parameters influencing the flexural response of RC beams strengthened using CFRP sheets*. Proceedings of FRPRCS-5, Cambridge, UK, July.
12. Lees J.M. (1997) *Flexure of concrete beams pre-tensioned with aramid FRPs*. Ph.D. dissertation, University of Cambridge, March.
13. Casadei P., Denton S., Ibell T. and Nanni A. (2003) *Moment redistribution in continuous CFRP-strengthened concrete members*. Proceedings of Composites in Construction 2003 - International Conference, Rende, Italy, September.
14. Mattock A.H. (1959) Redistribution of design bending moments in reinforced concrete continuous beams. Proceedings of the Institution of Civil Engineers, Vol.13, pp.35-46.

BOND-SLIP MODELS FOR FRP SHEET/PLATE-TO-CONCRETE INTERFACES

X.Z. Lu[1], J.G. Teng[2], L.P. Ye[1] and J.J. Jiang[1]
[1] *Department of Civil Engineering, Tsinghua University, Beijing, PR China*
[2] *Department of Civil and Structural Engineering, The Hong Kong Polytechnic University, Hong Kong, PR China*

Abstract: A meso-scale finite element model is first presented for simulating the debonding behavior of FRP-to-concrete bonded joints in simple shear tests. In this model, both the FRP plate/sheet and the concrete are modeled using elements of mesoscopic sizes so that the shapes and paths of cracks during the entire debonding process can be appropriately captured. Results obtained from this model are next presented to provide insight into the debonding failure process. Finally, based on a finite element parametric study and existing test results, three bond-slip models of different levels of sophistication are presented. These proposed models are far more accurate than all existing bond-slip models.

INTRODUCTION

External bonding of fiber reinforced polymer (FRP) plates or sheets has emerged as a popular method for the strengthening of reinforced concrete (RC) structures. In this strengthening method, the performance of the FRP-to-concrete interface in providing an effective stress transfer is of crucial importance. Indeed, a number of failure modes in FRP-strengthened RC members are directly caused by debonding of the FRP from the concrete. Therefore, for the safe and economic design of externally bonded FRP systems, a sound understanding of the behavior of FRP-to-concrete interfaces needs to be developed and a reliable bond-slip model established. It should be noted that term "interface" in this paper represents the adhesive and the adjacent concrete responsible for the relative slip between the FRP plate/sheet and the concrete prism except when it is used in the phrase "concrete-to-adhesive interface" to refer to the physical interface.

In various debonding failure modes, the stress state of the interface is similar to that in a shear test specimen in which a plate is bonded to a concrete prism and is subject to tension (Figure 1). As a result, a large number of studies, both experimental and theoretical, have been carried out on simple shear tests on bonded joints. Existing studies suggest that the main failure mode of FRP-to-concrete bonded joints in shear tests is concrete failure under shear, occurring generally at a few millimeters from the

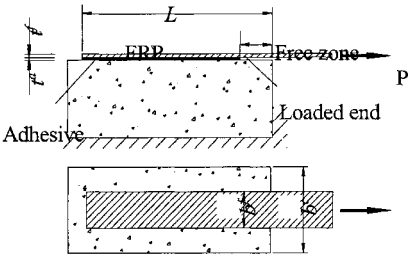


Figure 1. Shear test specimen

concrete-to-adhesive interface [1]. The ultimate load (i.e. the maximum transferable load) of the joint therefore depends strongly on the strength of concrete. In addition, the plate-to-concrete member width ratio also has a significant effect. A very important aspect of the behavior of these bonded joints is that there exists an effective bond length beyond which an extension of the bond length cannot increase the ultimate load. This is a fundamental difference between an externally bonded plate and an internal reinforcing bar for which a sufficiently long anchorage length can always be found so that the full tensile strength of the reinforcement can be achieved.

Existing research has also led to a number of bond stress-slip models based on the direct interpretation of results from shear tests [2,3]. These models suffer from the large scatter generally associated with such test data and also often from the limitation of the test data available to the researchers. As a result, none of them has been found to be of sufficient accuracy when assessed using a large test database [3]. This paper therefore presents a group of new bond-slip models developed in a recent study reported in detail in Ref. [3]. Instead of relying exclusively on test data, a meso-scale finite element model was first developed and employed to establish the various relationships between the bond parameters and the geometric and material parameters of FRP-to-concrete bonded joints. The derived relationships were then fine-tuned through calibration with a large test database. In the following sections, the meso-scale finite element model is first presented, which is then followed by an exploration of the failure mechanism using this model. Three bond-slip models of different levels of sophistication are finally presented and their predictions compared with test results.

MESO-SCALE FINITE ELEMENT MODEL

General considerations

In general, the debonding of FRP from concrete occurs within a thin layer of concrete adjacent to the concrete-to-adhesive interface unless the adhesive is rather weak. The thickness of this concrete layer is about 2~5mm. To simulate concrete failure within such a thin layer, with the shapes and paths of the cracks properly captured, the rotating angle crack model (RACM) [4,5] should be used if elements with a size comparable to the thickness of the concrete layer are adopted. The RACM however has the major drawback that its crack surface parameters have to be empirically derived from the shear tests. Therefore, the present study employed a fixed angle crack model (FACM)[5] in conjunction with a very fine finite element mesh with element sizes being one order smaller than the thickness of the facture zone of concrete. This approach has the simplicity of the FACM for which the relevant material parameters have clear physical meanings and can be found from well established standard tests, but in the meantime retains the capability of tracing the paths of cracks as deformations increase. The present model using very small elements is referred to as the meso-scale finite element model. To reduce the computational effort, the three-dimensional FRP-to-concrete bonded joint (Figure 1) was modeled as a plane stress problem using 4-node isoparametric elements. The effect of FRP-to-concrete width ratio was separately

considered based on the work of Chen and Teng [1].

It should be noted that the present model differs from those employed in existing finite element studies of FRP-to-concrete bond behavior in which an interface element is employed to simulate debonding [e.g. 6,7]. In such models, the interface element has to be based on a bond-slip model which needs to be pre-defined. Such models are not true predictive models, although they may be used with test data to verify/identify interfacial behavior. The present model has the capability of predicting the interfacial behavior from first principles.

Modeling of FRP

As the element size adopted in this study was within the range of 0.25~0.5mm, the FRP plate was modeled with plane stress elements. The use of plane stress elements simplified the modeling procedure in terms of proper interaction between the FRP and concrete. The FRP plate/sheet was treated as an isotropic material.

Modeling of concrete

When concrete is modeled using small elements (here element sizes of 0.25~0.5mm), the element size effect should be considered. According to Bazant [8], the compressive behavior of concrete does not depend significantly on element sizes, so the stress-strain relationship proposed by Hognestad [9] was directly used in the present study to simulate the compressive behavior of concrete.

The tensile behavior of concrete was modeled using the crack band model [8]. The essence of this approach is to control the post-cracking softening branch of the tensile stress-strain curve using the concept of fracture energy in which element sizes are considered. For the linear softening model proposed by Hillerborg, the ultimate tensile strain ε_{cr}^{u} at which the tensile stress decreases to zero is given by [10]

$$\varepsilon_{cr}^{u} = 2G_f^I /(b_{cr} f_t) \tag{1}$$

where G_f^I is the fracture energy of concrete; f_t is the tensile strength of concrete; and b_{cr} is the crack band width (ie the element size). According to the model code of CEB-FIP [11], $G_f^I = \alpha(f_c/10)^{0.7}$, where f_c is the compressive strength of concrete. For concrete of normal aggregate size, $\alpha = 0.03$ [11].

The modeling of the shear behavior of cracked concrete also needs to take into account the effect of element size. Eight different shear models for cracked concrete were compared in the present study, which identified the following model developed at Dalian University of Technology [12] in China as the best performing model [2]:

$$\tau = (0.543 w^{-0.585} + 0.1999)\sqrt{f_c}\,\Delta^{0.72} \tag{2}$$

where w is the crack width and Δ is the relative slip between the crack surfaces, both in mm. Equation (2) was therefore adopted to model the shear behavior of cracked concrete in the present study.

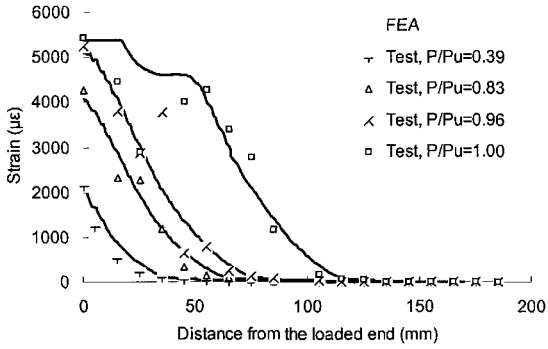


Figure 2. Comparison of strain distributions in the FRP sheet

Implementation

The concrete model described above was implemented into the general purpose finite element package MSC. MARC [13] as a user subroutine. Before finalizing the finite element model, a number of issues were first examined for accurate predictions, including the post-peak softening scheme and the element size [2]. The final finite element model employed an element size of 0.5mm, with a linear softening branch for concrete subject to tension.

The finite element model was verified by detailed comparison with the results of 12 shear test specimens [2]. A close agreement was achieved for all 12 specimens. A typical comparison of the distribution of longitudinal strain on the FRP plate is shown in Figure 2.

DEBONDING PROCESS

The process of crack propagation is difficult to observe in laboratory tests but can be easily predicted by the finite element model. It should however be noted that the actual process of debonding is more complicated than is predicted by the present model, as real concrete is an inhomogeneous material. Nevertheless, the present finite results provide useful insight into the failure mechanism.

Figure 3 shows a set of diagrams of crack strain (total tensile strain minus elastic strain) contours corresponding to different slips at the loaded end. The state each diagram represents can be identified by comparing its slip at the loaded end to the slip value s_0 when the local bond strength is reached at the loaded end and s_f when the ultimate load P_u is first attained. For this specimen, s_0= 0.0585mm, and s_f = 0.154mm.

Figure 3a shows that even at a load of 28% of the ultimate load, the concrete under the FRP plate near the loaded end has experienced extensive cracking. The cracks can be classified into 3 types: (a) interfacial shallow cracks; (b) interfacial deep cracks; and (c) micro-cracks within a cracked zone under the FRP plate. The same three types of cracks also exist at later stages of deformation as shown in Figure 3b~e.

The depths of the interfacial shallow cracks are about 0.5~1mm, whose widths are small and relatively uniform. This thin layer is subject to high tensile stresses as well as high shear stresses as it is directly bonded to the FRP. The depths of the interfacial deep cracks are 2~5mm. The widths of these cracks are relatively large. They are caused by

shear stresses and will control the final debonding strength and the slip of the interface. The overall depth of the cracked zone of concrete is about 5~10mm. They are also caused by shear stresses and some will develop into interfacial deep cracks as deformation further increases.

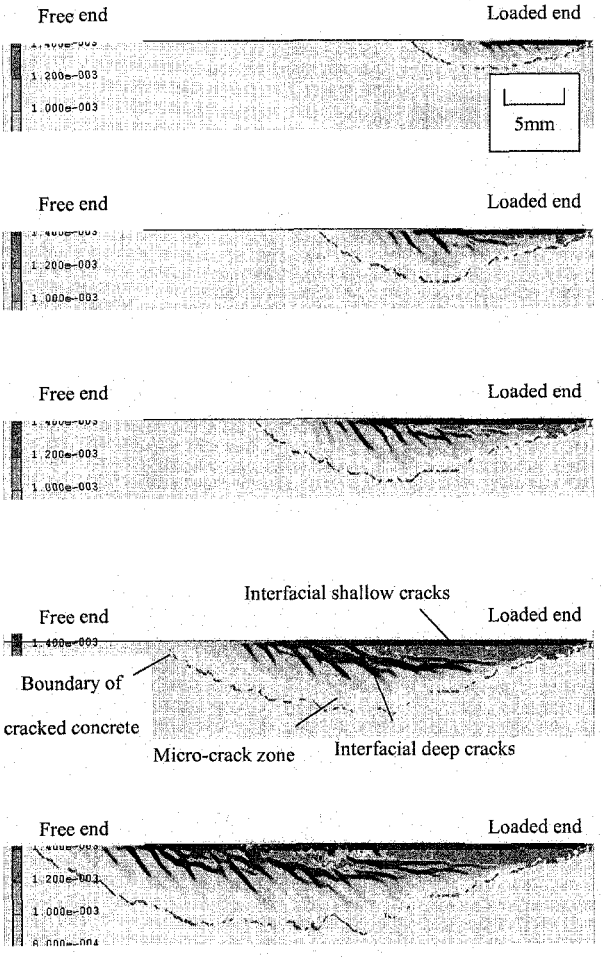


Figure 3. Propagation of cracks in concrete

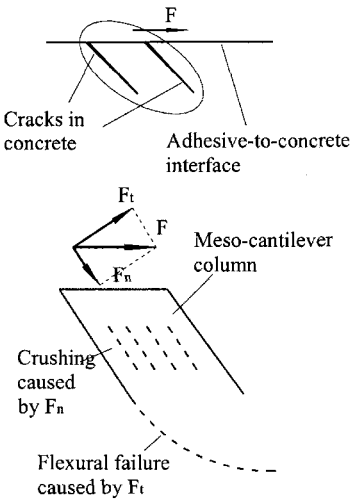


Figure 4. Meso-cantilever column and its failure modes

The above classification of crack patterns also helps explain the failure process. At a low level of loading, the formation of interfacial shallow cracks at angles of 45~60° to the interface leads to the appearance of small cantilever columns (i.e. meso-cantilevers). With further increases in loading, these cantilevers may grow longer as the shallow cracks grow into deep cracks or may fail if the shear force acting on the cantilever reaches a critical value. The shear force F on the cantilever leads to axial compressive stresses which can cause crushing failure, or flexural tensile stresses at the root which is responsible for flexural failure at the root (Figure 4). It is worth noting that debonding

as observed in laboratory tests corresponds to the progressive flexural failure of the meso-cantilevers, except near the loaded end where debonding is mainly due to the crushing of the meso-cantilevers.

LOCAL BOND -SLIP MODELS

General

The finite element model, following verification, was deployed to study the local bond-slip behavior as from such a model, the stress in and the slip of the FRP plate at any point along the plate under any level of loading can be obtained easily. The interfacial shear stress can be deduced from the longitudinal stresses in the FRP plate. Due to localization of cracks, the deduced shear stresses show substantial local fluctuations so a smoothening procedure was applied [3]. A typical bond-slip curve obtained from this procedure is shown in Figure 5, where E_f is the elastic modulus of FRP plate, G_a and t_a are the shear modulus and thickness of the adhesive layer, respectively.

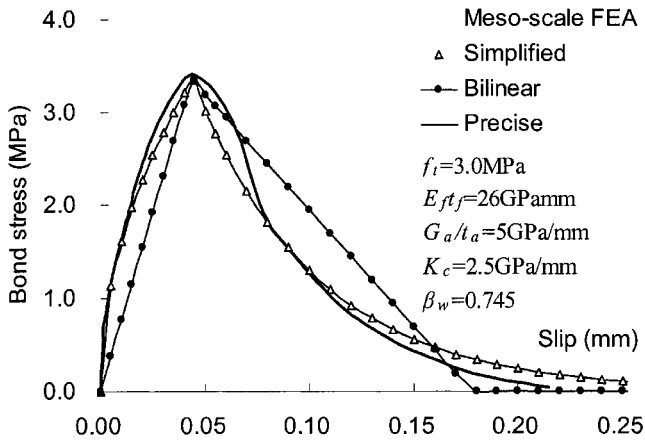


Figure 5. Bond-slip curves

In order to develop bond-slip models, a finite element parametric study was carried out to establish the relationships between various bond parameters and geometric and material parameters. This parametric study showed that the local bond strength τ_{max} and the corresponding slip s_0 are almost linearly related to the tensile strength of concrete f_t, while the total interfacial fracture energy G_f is almost linearly related to $\sqrt{f_t}$. Based on such finite element bond-slip curves and some calibration with a large test database, three bond-slip models were developed [3].

Precise model

The first of the three bond-slip models is referred to as the precise model as it takes explicit account of the effect of the adhesive layer, which is important when the adhesive is much softer than those currently in common use. It has been reported that very soft adhesive layers can increase the interfacial fracture energy [14]. The prediction of the precise model is almost identical to that of the simplified model presented below for normal adhesives.

The precise model describes the ascending and descending branches separately using the following equations:

$$\tau = \tau_{\max}\left(\sqrt{\frac{s}{s_0 A} + B^2} - B\right) \quad \text{if } s \le s_0 \tag{3a}$$

$$\tau = \tau_{\max} \exp[-\alpha(s/s_0 - 1)] \quad \text{if } s > s_0, \tag{3b}$$

where $A = (s_0 - s_e)/s_0$, $B = s_e/[2(s_0 - s_e)]$

The local bond strength $\tau_{\max}$ and the corresponding slip s_0 are given by

$$\tau_{\max} = 1.5\beta_w f_t \tag{3c}$$

$$s_0 = 0.0195\beta_w f_t + s_e \tag{3d}$$

where $s_e = \tau_{\max}/K_0$ is the elastic component of s_0 and the FRP-to-concrete width ratio β_w can be expressed as

$$\beta_w = \sqrt{(2.25 - b_f/b_c)/(1.25 + b_f/b_c)} \tag{3e}$$

with b_c and b_f being the widths of the concrete prism and the FRP plate respectively (Fig.1). The initial stiffness of the bond-slip model is defined by:

$$K_0 = K_a K_c/(K_a + K_c) \tag{3f}$$

where $K_a = G_a/t_a$ and $K_c = G_c/t_c$. G_c is the elastic shear modulus of concrete and t_c is the effective thickness of concrete whose deformation forms part of the interfacial slip and may be taken as 5mm unless this thickness is specifically measured during the test.

The parameter α controls the shape of the descending branch and is given by

$$\alpha = \tau_{\max} s_0 / \left(G_f - G_f{}^a\right) \tag{3g}$$

where the total interfacial fracture energy can be expressed as:

$$G_f = 0.308\beta_w{}^2 \sqrt{f_t} f(K_a) \tag{3h}$$

while the fracture energy of the ascending branch $G_f{}^a$ can be calculated as:

$$G_f{}^a = \int_0^{s_0} \tau ds = \tau_{\max} s_0 \left[\frac{2A}{3} \left(\frac{1+B^2A}{A} \right)^{3/2} - B - \frac{2}{3} B^3 A \right] \tag{3i}$$

Here, $f(K_a)$ is a function of the stiffness of the adhesive layer. Based on finite element results, for normal adhesives with $K_a \geq 2.5$GPa/mm, the effect of adhesive layer stiffness on G_f is very small, so it is proposed that $f(K_a)=1$ for normal adhesives. A precise definition of $f(K_a)$ requires further work. The prediction of the precise model for an example FRP-to-concrete bonded joint is shown in Figure 5 and is seen to compare very well with the prediction of the meso-scale finite element analysis.

4.3 Simplified model

The precise model is accurate but complicated. For normal adhesives, a simplified model without a significant loss of accuracy can be easily obtained. This is because the initial stiffness of the bond-slip curve is much larger than the secant stiffness at the peak point when a normal adhesive of a reasonable thickness is used. Therefore, the initial stiffness can be approximated as infinity. Furthermore, the interfacial fracture energy G_f has little relationship with the stiffness of the adhesive layer. Based on these two simplifications, the following simplified bond-slip model can be obtained:

$$\begin{cases} \tau = \tau_{\max} \sqrt{\dfrac{s}{s_0}} & \text{if } s \leq s_0 \quad (4a) \\ \tau = \tau_{\max} e^{-\alpha\left(\frac{s}{s_0}-1\right)} & \text{if } s > s_0 \quad (4b) \end{cases}$$

where $$s_0 = 0.0195 \beta_w f_t \tag{4c}$$

$$G_f = 0.308 \beta_w{}^2 \sqrt{f_t} \tag{4d}$$

$$\alpha = \frac{1}{\dfrac{G_f}{\tau_{\max} s_0} - \dfrac{2}{3}} \tag{4e}$$

and $\tau_{\max}$ and β_w can be found from Eq. 3(c) and 3(e).

The bond-slip curve of the example bonded joint predicted by the simplified model is also shown in Figure 5, where it can be seen that there is little difference between this model and the precise model as a normal adhesive is used in this bonded joint. For all practical purposes, the simplified model is sufficient for normal adhesive joints but much simpler than the precise model.

Bilinear model

Further simplification was made to the simplified model, leading to a simple bilinear model which can be used to derive an explicit design equation for the ultimate load. This bilinear model has the same local bond strength and total fracture energy, so the ultimate load remains unchanged if the bond length is longer than the effective bond length. This bilinear model is described by the following equations:

$$\tau = \tau_{\max} s / s_0 \quad \text{if } s \le s_0 \tag{5a}$$

$$\tau = \tau_{\max}(s_f - s)/(s_f - s_0) \quad \text{if } s_0 < s \le s_f \tag{5b}$$

where $s_f = 2G_f / \tau_{\max}$ and $\tau_{\max}$, s_0 and β_w can be found using Eq.3(c), 4(c) and 3(e). The prediction of the bilinear model is also shown in Figure 5 to illustrate the differences between this and the other two models.

Table 1 provides the statistics of comparisons of the ultimate load between the three proposed models and 254 shear test results. Very close agreements are seen. The strain distributions in the FRP sheet numerically predicted with the proposed bond-slip models are also in close agreement with test results. A typical comparison is shown in Figure 6 for Specimen PG1-2 tested by Tan [15]. Further extensive comparisons are available in Ref. [3] where it is demonstrated that the proposed models are far more accurate than all existing bond-slip models.

Table.1 Comparison of ultimate load between test results and proposed models

Model	Precise model	Simplified model	Bilinear model
Average error	0.1%	0.1%	0.1%
Standard deviation	0.155	0.155	0.156
Correlation coefficient	0.910	0	0.908

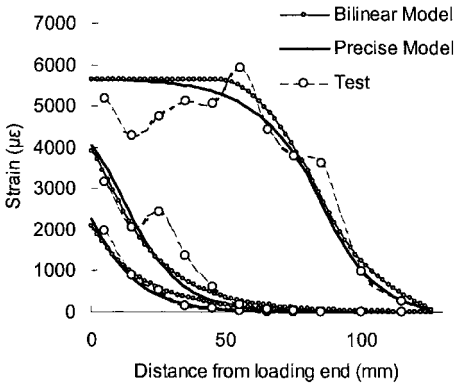


Figure 6. Comparison of strain distributions in the FRP sheet for Specimen PG1-2

CONCLUSIONS

A meso-scale finite element model has been proposed for the simulation of debonding behavior in FRP-to-concrete bonded joints and has been shown to produce accurate predictions. Results obtained from this model showed that debonding is due to the formation and failure of inclined meso-cantilever columns in the concrete. Based on a finite element parametric study and existing test results, three bond-slip models of different levels of sophistication have also been proposed. These proposed models are

far more accurate than all existing bond-slip models.

ACKNOWLEDGEMENT

The authors gratefully acknowledge the financial support provided by the Natural Science Foundation of China (National Key Project No. 50238030) and The Hong Kong Polytechnic University through the Area of Strategic Development (ASD) Scheme for the ASD in Mitigation of Urban Hazards

REFERENCES:

1. J F Chen and J G Teng, 'Anchorage strength models for FRP and steel plates bonded to concrete', *Journal of Structural Engineering, ASCE*, 2001 127(7) 784-791
2. X Z Lu, L P Ye, J G Teng and J J Jiang, 'Meso-scale finite element model for FRP sheets/plates externally boned to concrete', in preparation.
3. X Z Lu, J G Teng, L P Ye and J J Jiang, 'Bond-slip models for FRP sheets/plates externally bonded to concrete', in preparation.
4. X Z Lu, Z Tan, L P Ye and J J Jiang, 'Finite element analysis for debonding in the interface between FRP sheet and concrete', *Engineering Mechanics*, 2003 in press
5. J G Rots and J Blaauwendraad, 'Crack models for concrete: discrete or smeared? Fixed, multi-directional or rotating?', *HERON*, 1989 34(1)
6. Z S Wu and J Yin, 'Fracture behaviors of FRP-strengthened concrete structures', *Engineering Fracture Mechanics*, 2003 70(10) 1339-1355
7. Z S Wu, *Element-level study on stress transfer based on local bond properties*, Technical Report of JCI Technical Committee on Retrofit Technology, 2003 44-56
8. Z P Bazant and J Planas, *Fracture and size effect in concrete and other quasibrittle materials,* Boca Baton, CRC Press, 1997.
9. E Hognestad, *A study of combined bending and axial load in reinforced concrete members*, University of Illinois Engineering Experiment Station, Bulletin Series No. 399, Bulletin No.1, 1951
10. J G Rots, P Nauta, M A Kusters and J Blaauwendraad, 'Smeared crack approach and fracture localization in concrete', *HERON*, 1985, 30(1)
11. CEB-FIP Committee, Model Code 90, Lausanne, 1993
12. Q L Kang, *Finite element analysis for reinforced concrete*, Beijing, China Water Power Press, 1996 120-126
13. *MSC.Marc User's Manual, 'Volume A (Theory and User Information)'*, MSC. Software Corporation, 2003
14. J G Dai and T Ueda, 'Local bond stress slip relationship for FRP sheets-concrete interfaces', Proceedings of the 6th International Symposium on *FRP Reinforcement for Concrete Structures*, Singapore, World Scientific Press, 2003 143-152
15. Z Tan, *Experimental Research for RC Beam Strengthened with GFRP*, Master Dissertation, Beijing, Tsinghua University, 2002.

MOMENT REDISTRIBUTION IN ADHESIVELY PLATED RC BEAMS AND SLABS

Deric John Oehlers, Irene Liu and Rudolf Seracino
Centre for Infrastructure Diagnosis, Assessment and Rehabilitation
School of Civil and Environmental Engineering, University of Adelaide, Australia

ABSTRACT

It is common practice these days to retrofit RC beams and slabs by adhesive bonding FRP or steel plates to their surfaces. However, research has shown that these external plates can debond prematurely at relatively low strains, due to intermediate crack (IC) debonding, and in a brittle fashion. Because of these low IC debonding strains, it can be shown, through the standard use of neutral axis depth factors at ultimate, that the ability of the plated section to redistribute moment to other sections is severely limited and to such an extent that guidelines often preclude moment redistribution. This limitation may have little effect on plating RC bridges but it can, at least theoretically, severely limit the use of plating in buildings where ductility is a requirement.

Tests on steel and FRP plated continuous beams have shown that moment redistribution can occur and a design procedure has been developed to determine the amount of moment redistribution for any type of plated section, such as tension face plates and side plates, and for any type of plate material, such as steel or FRP. In this paper, an analysis approach to quantify the amount of moment redistribution is described. A parametric study is then used to illustrate how the plate material and geometric properties affect moment redistribution; in particular, the study looks at the effect of using carbon FRP plates and glass FRP plates, as well as steel plates that have been designed to either debond prior to yielding or yield prior to IC debonding.

In summary, the paper will show that plated sections can redistribute moment and, hence, the present restriction can be removed which should extend the use of retrofitting by plating. Furthermore, the moment redistribution analysis procedure allows the engineer the freedom to choose the properties of the plate to design for moment redistribution.

INTRODUCTION

The different concepts of moment redistribution are first described in this paper. It is shown that the simple *flexural rigidity (EI)* approach, for quantifying the amount of moment redistribution that can occur, can be used for plated structures, because plates tend to debond at relatively low strains. An internal continuous beam with the same hogging and sagging reinforcing bars and which is subjected to uniformly distributed loads is used to illustrate the ability of plated beams to redistribute moment.

In the first parametric study, the same steel plates are used in both the hogging and sagging regions and this example is used to show how the IC debonding strain affects moment redistribution. In the second parametric study, the hogging and sagging regions are plated with either glass or carbon FRP plates of the same axial stiffness EA and this example clearly shows the benefit of glass over carbon FRP as far as moment redistribution is concerned. In the final study, only the hogging region is plated to illustrate the concept of negative moment redistribution, where it is shown how the hogging moment at IC debonding, in comparison with the sagging moment, is larger than that anticipated from an elastic analysis.

MOMENT REDISTRIBUTION

The concept of moment redistribution[1] is illustrated in figure 1 for the case of an *encastre* or *built in* beam of span *L* that is subjected to a uniformly distributed load *w*. When the flexural rigidity EI of the beam is constant throughout its length as in figure 1(a), then the distribution of moment is line A in figure 1(b) where $M_{hog} = 2M_{sag}$. Any divergence from this 2:1 ratio such as line B will be assumed to signify some degree of moment redistribution.

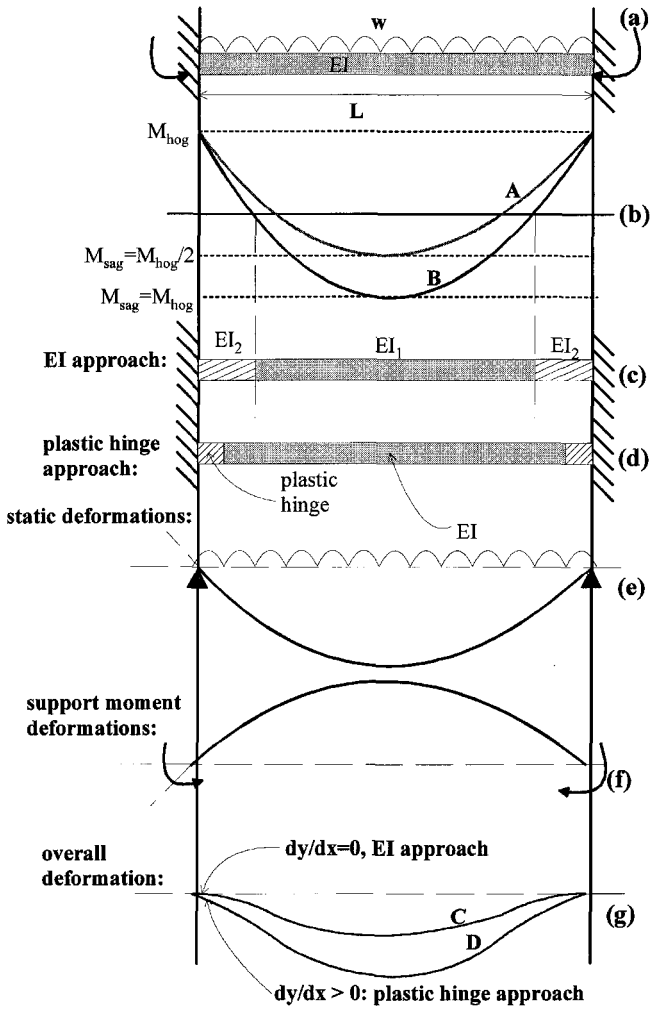


Figure 1 Moment redistribution

The static deformation of the beam is shown in figure 1(e) and that due to the support moments in figure 1(f). The resultant of these deformations is shown in figure 1(g) where the slope at the support maybe finite, as in line D, or zero as in line C. The *plastic hinge* approach shown in figure 1(d) assumes that the support slope is finite, as in line D in figure 1(g), and this finite slope at the supports is allowed for by rotation within the plastic hinges in figure 1(d). In contrast, the *flexural rigidity (EI)* approach

shown in figure 1(c) assumes that the support slope is zero as in line C in figure 1(g), that is any divergence from the *elastic* 2:1 ratio of line A in figure 1(b) is accounted for by variations in the flexural rigidity along the length of the beam as in figure 1(c).

Tests[1-3] on two span continuous beams plated with steel and carbon FRP plates have shown that moment redistribution in plated beams can be accounted for by the *flexural rigidity* approach depicted in figure 1(c). This is probably because IC debonding usually occurs when the maximum fibre strains in the concrete are well below their crushing strain and, hence, before the sectional curvature is sufficient to cause a plastic hinge.

FLEXURAL RIGIDITY APPROACH

The analysis for the flexural rigidity approach[1-3] is depicted in figure 2. The flexural rigidity of the beam within the hogging region is assumed to be constant at EI_2 and that within the sagging region is also constant at EI_1. It may be worth noting that the amount of moment redistribution does not depend on the magnitudes of the flexural rigidities EI_1 and EI_2 but on the relative rigidity that is the ratio EI_1:EI_2. Hence, these flexural rigidities are chosen to represent the proportional change in stiffness between the hogging and sagging regions. For the following parametric studies, the continuous beam has been designed so that plate IC debonding will always occur in the hogging region. Therefore, the hogging flexural rigidity EI_2 is the secant flexural rigidity at the position of maximum hogging moment and at plate IC debonding. The sagging flexural rigidity EI_1 is that at the position of maximum sagging moment.

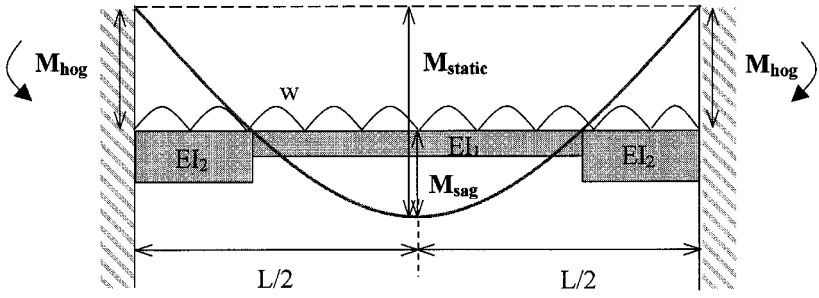


Figure 2 Flexural rigidity analysis

The percentage moment redistribution, %MR, is defined as the change in the hogging moment from that for a beam with a constant EI as in figure 1(a). It is given by the following equation in which M_{db} is the IC debonding moment in the hogging region, that is M_{hog} in figure 2 at IC debonding.

$$\%MR = \frac{\frac{2}{3}M_{static} - M_{db}}{\frac{2}{3}M_{static}} \times 100 \qquad (1)$$

Full details of the steps of the analysis procedure are given elsewhere[1-3].

INTERNAL CONTINUOUS BEAM USED IN PARAMETRIC STUDY

The RC slab of 4 m span in figure 3 was used in the parametric study. The slab was always plated over the hogging region and sometimes plated in the sagging region. The cross-sectional details of 1 m width of slab in the sagging region are shown in figure 4. The hogging region slab was exactly the same as the sagging region but inverted so that the flexural rigidity of the cracked hogging and sagging regions were identical.

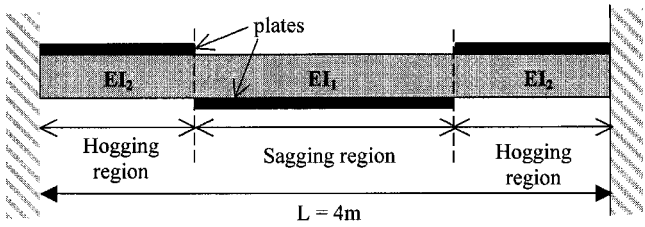


Figure 3 Plated slab in parametric study

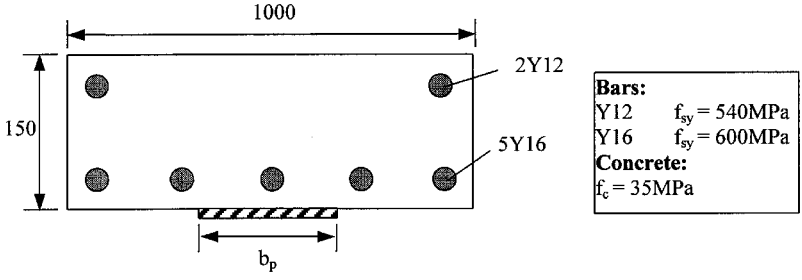


Figure 4 RC slab used in parametric study

STUDY 1: STEEL PLATES IN HOGGING AND SAGGING REGION

In this study, the beam was plated in both the hogging and sagging regions in figure 3 and with identical steel plates of width per meter slab of b_p=225 mm, thickness t_p=2 mm, Young's modulus E_s=200 GPa and yield capacity of f_y=300 MPa. The moment-curvature relationship for both the hogging region and sagging region are identical and given in figure 5 as the curve labeled *full interaction* which was derived from a non-linear analysis.

The slope of the lines that emanate from the origin of the graph in figure 5 are the secant stiffnesses at various IC debonding strains shown in the legend. Also shown are lines that represent the flexural rigidity of the uncracked section $(EI)_{elastic}$, that of the cracked plated section up to plate yield $(EI_{cr})_{plated}$ at B, that at yield of the tension reinforcing bars at C, and that of the cracked unplated section $(EI_{cr})_{unplated}$. The flexural rigidity of the sagging region was held at $(EI_{cr})_{plated}$ and that of the hogging region followed the secant stiffness associated with the whole moment-curvature relationship. Hence, if IC debonding occurred in the hogging region prior to the plate yielding (that is the flexural rigidity of the hogging region is the same as that of the sagging region at $(EI_{cr})_{plated}$) then the percentage moment redistribution would be zero.

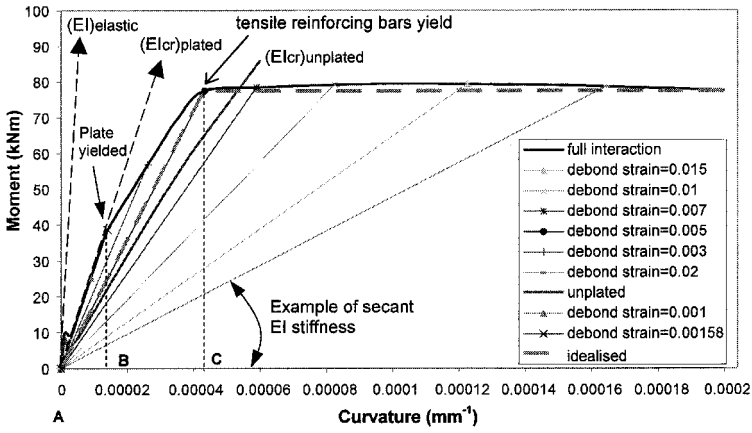


Figure 5 Moment-curvature relationship for steel plated cross-sections

The results of the parametric study are shown in figure 6. The *real moment-curvature* (M/k) plot uses the non-linear *full interaction* curve in figure 5. In the region A-B in figure 6, the hogging region plate debonded prior to the plate yielding. In the region B-C, which starts at an IC debonding strain of about 0.002, the plate debonded after plate yielding but prior to the reinforcing bars yielding. Finally in the region beyond C, debonding occurred after the reinforcing bars yielded that is in the almost horizontal plateau in figure 5. Tests on steel plated beams[1] have shown that steel plates of up to about 3 mm thickness can debond at strains that range from 0.004 to 0.020 which suggests from figure 6 that between 10% to 50% moment redistribution can occur. Hence, substantial moment redistribution can occur in steel plated beams if they are designed properly.

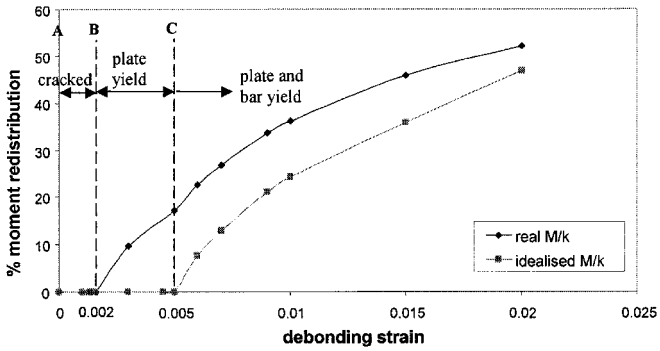


Figure 6 Moment redistribution: steel plated in hogging and sagging regions

It is felt that most practical design will be based on the conservative bi-linear *idealised* M/k curve shown as the broken line in figure 5. When this *idealised* bi-linear curve is used, moment redistribution will only occur if IC debonding occurs after the tension reinforcing bars have yielded. The use of this *idealised* curve gives the results of the *idealised M/k* plot in figure 6 in which for the range of IC debonding strains of 0.004 to 0.020 the moment redistribution varies from 0% to 45%. Hence, some steel plated beams will not be able to redistribute moment but there is a potential

for reasonable amounts of redistribution if the plates are designed to debond at large strains.

STUDY 2: FRP PLATES IN HOGGING AND SAGGING REGION

In this study, both the hogging and sagging regions in figure 3 have been plated with either carbon or glass FRP plates. The plate axial stiffness E_pA_p was maintained constant at $1.0x10^7$ N so that the same moment-curvature relationship in figure 7 applied to all cross-sections. The plate thicknesses t_p were varied from 0.2 mm to 1.2 mm and are shown in the legend in figure 7 and the Young's modulus E_p was assumed to be either 160 or 125 GPa for carbon FRP, or 50 or 25 GPa for glass FRP. The strains at which IC debonding occurred were derived from the research of Teng et al[4].

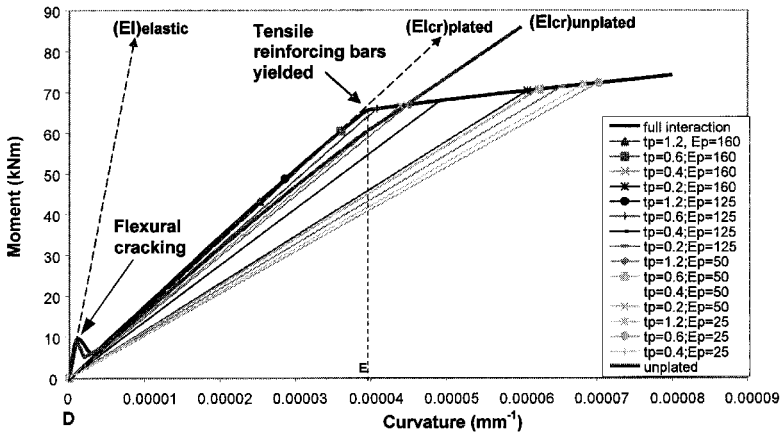


Figure 7 Moment-curvature relationship for CFRP and GFRP plated beams

Compared with the moment-curvature relationship for steel plates in figure 5 which is basically tri-linear with a horizontal plateau, the moment-curvature relationships for FRP plated structures in figure 7 has the typical bi-linear relationship with the gradually rising *plateau*. The results of the FRP parametric study are shown as the lower curve in figure 8 which also shows the results of the steel plated analyses taken from figure 6 for comparison. It can be seen from the lower FRP curve that redistribution only occurs when the IC debonding strain exceeds about 0.0046 which for FRP plates is a relatively high strain[4]. Furthermore, the moment redistribution varies from 0% to 20%. Hence, some moment redistribution can occur with FRP plated beams but the scope is much less than that available for steel plated specimens. The results also show that glass FRP is a better option for moment redistribution than carbon FRP and that moment redistribution only occurs if debonding occurs after the reinforcing bars yield which is obvious but worth stating.

STUDY 3: BEAM PLATED OVER HOGGING REGION

Finally in this study only the hogging regions of the beam in figures 3 and 4 were plated with steel or FRP plates. The moment curvature relationships in figures 5 and 7 still apply but in this case the flexural rigidity of the plated hogging region is always greater than that of the unplated sagging region at the start of loading. The results of

the study are shown in figure 9. For the FRP plated beams, the plate axial stiffness E_pA_p was maintained at $1.0x10^7$ N whilst for the steel plated beams it was maintained at $9.0x10^7$ N to reflect what occurs in practice.

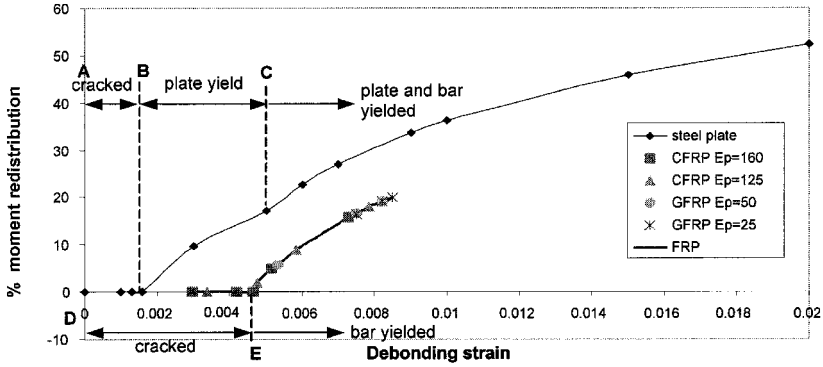


Figure 8 Moment redistribution: FRP plated in hogging and sagging regions

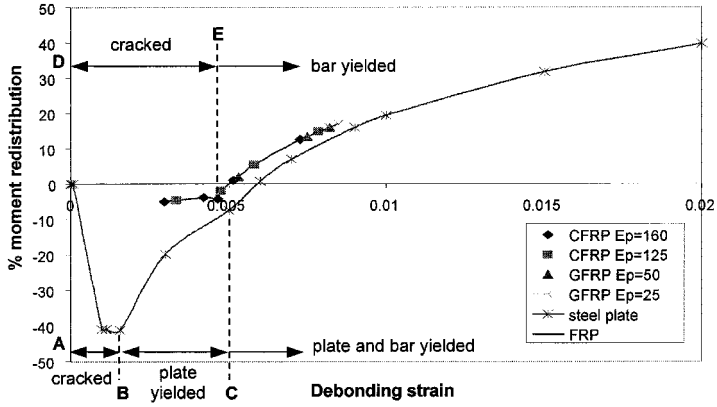


Figure 9 Moment redistribution: beams plated in hogging regions only

Let us first consider the upper curve in figure 9 which are the results for the FRP plated slabs. When IC debonding occurred in the *cracked* region D-E in figure 9, the flexural rigidity of the hogging region was $(EI_{cr})_{plated}$ in figure 7. The flexural rigidity of the hogging region $(EI_{cr})_{plated}$ is greater than that of the unplated sagging section $(EI_{cr})_{unplated}$ in figure 7. Therefore, the hogging region attracts more moment than if EI is constant along the beam so that the hogging moment is more than twice the sagging moment. Hence there is now a negative moment redistribution. That is debonding occurs whilst the hogging moment is greater than that anticipated by an elastic analysis in which EI is constant. Hence, if the beam was designed for the elastic distribution of moment with a constant EI, the beam would fail prematurely due to IC debonding before the sagging design capacity was reached.

After the tensile reinforcing bars have yielded that is beyond point E in figure 9, the secant stiffness of the hogging region gradually reduces from the point marked E in figure 7 as it follows the gradually rising branch. When the secant stiffness reduces to $(EI_{cr})_{unplated}$ in figure 7, there is zero moment redistribution after which

there is positive moment redistribution as shown in figure 9. The FRP curve in figure 9 lies below that in figure 8 which means that the capacity for moment redistribution is less than if both regions were plated. It can be seen that there are circumstances when even assuming that there is no moment redistribution can be unsafe.

The results for the steel plated beams in figure 9 show that at least theoretically negative moment redistribution can be greater in steel plated beams than in FRP plated beams. This is because the axial stiffness of steel plates used in practice tends to be greater than that of FRP plates used in practice. However steel plates when designed to yield prior to IC debonding tend to have a larger IC debonding strain than FRP plates so that the results to the right of point C in figure 9 are more likely to occur in practice, that is steel plates are more likely to have positive moment redistribution capacities.

SUMMARY

- Tests have shown that the ability to redistribute moment in a plated beam can be determined from the variation in the flexural rigidity, probably because plates tend to debond when the strains in the concrete are well below the crushing strain.
- A procedure has been developed for quantifying the ability of a plated beam to redistribute moment which depends on the IC debonding strain and which can be applied to any plate material and for any plate position and shape.
- Steel plated beams can be designed to yield prior to IC debonding although IC debonding does eventually occur. A parametric study of this form of plating showed that the percentage moment redistribution can vary from 0% to 45%. So that there is the potential for substantial moment redistribution but if designed poorly there may be no moment redistribution.
- A parametric study of FRP plated beams showed that the percentage moment redistribution can vary from 0% to 20%. Hence there is the potential for a reasonable amount of moment redistribution but this is mainly restricted to glass FRP plates.
- Furthermore, moment redistribution in FRP plated beams only occurs if IC debonding occurs after the tension reinforcing bars have yielded
- The concept of negative moment redistribution has been introduced where it was shown that poorly designed beams can debond prematurely in a region, that is before the other region has achieved its design moment capacity.
- It is suggested that moment redistribution should be considered in design and that simply allowing for no moment redistribution may not always be a safe assumption.

REFERENCES

1 DJ Oehlers and R Seracino, *Retrofitting RC Structures by Plating: increasing the strength, stiffness or ductility of beams and slabs*. Submitted to Wiley.

2 DJ Oehlers, G Ju, I Liu and R Seracino, 'Moment redistribution in continuous plated RC beams. Part 1 Tests'. Submitted to *Engineering Structures*.

3 DJ Oehlers, I Liu, G Ju and R Seracino, 'Moment redistribution in continuous plated RC beams. Part 2 Design procedure'. Submitted to *Engineering Structures*.

4 JG Teng, JF Chen, ST Smith and L Lam, *FRP strengthened RC structures*. Wiley, 2002.

ARCHING ACTION IN FRP REINFORCED CONCRETE SLABS

Susan Taylor and Barry Mullin
The Queen's University of Belfast, Northern Ireland

ABSTRACT

The corrosion of reinforcement embedded in concrete has been the cause of major deterioration and of high costs in repair and maintenance. Fibre Reinforced Polymers (FRP) exhibit high durability in combination with high strength and light weight. However, the majority of research with FRP bars for reinforcing concrete has been on simply supported beams and slabs where the low value of elasticity of FRP has meant that the service behaviour has often been critical. However, the arching action which occurs in laterally restrained slabs has a beneficial influence on the service behaviour. This paper presents the results of tests on concrete slab with both steel and GFRP reinforcement.

INTRODUCTION

It has become increasingly evident that corrosion of reinforcement due to the effects of de-icing salts has been one of the major factors in the deterioration of reinforced concrete bridge decks. One solution to the corrosion problem is the use of alternative materials to steel reinforcement that do not corrode, such as Fibre Reinforced Polymers (FRP). The majority of recent research using FRP reinforcement has concentrated on simply supported slabs (e.g. Farreira[1] and Alsayed[2]). Deflection in the FRP reinforced sections is greater due to the low modulus of elasticity of the FRP bars compared to steel reinforcement. As a result the deflection criterion may control the design of intermediate and long spanning sections reinforced with FRP bars, as opposed to sections reinforced with steel, where it is usually the ultimate strength which governs the design.

It has been recognised for some time (Ockleston[3]) that laterally restrained slabs exhibit strengths far in excess of those predicted by most design codes. This enhancement in slab strength is due to Compressive Membrane Action (CMA). Previous research, such as that by Kirkpatrick et al [4&5] at Queen's University, has shown that CMA also has a beneficial influence on the service behaviour of laterally restrained slabs. Therefore, by utilising the benefits of new reinforcing materials, such as FRP's, in combination with CMA, it should be possible to produce functional, economic and durable concrete slabs.

This paper presents the results of laboratory tests on six reinforced concrete slab strips with both steel and Glass Fibre Reinforced Polymer (GFRP) reinforcement. The variables were the boundary conditions, reinforcement type and concrete strength. The failure loads of the slabs have been compared to predicted strengths using an arching theory developed at Queen's University of Belfast. The theory has been extended to incorporate the properties of GFRP reinforcement.

Table 1: Test variables

Series No.	Slab No.	Target concrete strength (N/mm^2)	Reinforcement		Boundary conditions
1	S-40-SS	40	Steel	0.5% centre	S/S
	S-40-LR	40	Steel	0.5% centre	F/E + L/R
	S-70-LR	70	Steel	0.5% centre	F/E + L/R
2	G-40-SS	40	GFRP	0.5% centre	S/S
	G-40-LR	40	GFRP	0.5% centre	F/E + L/R
	G-70-LR	70	GFRP	0.5% centre	F/E + L/R

GFRP = glass fibre reinforced polymer
F/E = fixed end
L/R = laterally restrained
S/S = simply supported

EXPERIMENTAL PROGRAMME

Six one-way spanning slabs with varying concrete strengths, reinforcement type and slab boundary conditions were tested (Table 1). Series 1, reinforced with steel bars, were used as a comparison for Series 2, reinforced with GFRP bars. Control samples were taken and the reinforcement types were compared. Previous work by Taylor et al [6] found that when lateral restraint was provided, the slabs could be efficiently reinforced with the bars located centrally. All the slabs were detailed with centre reinforcement.

A line load was applied at midspan of each test slab (figure 1). A steel frame used in previous tests at Queen's University provided restraint (Ruddle[7]). Electronic displacement transducers were located directly below the position of the knife-edge load. Strain gauges were also mounted on each of the reinforcing bars at the midspan region.

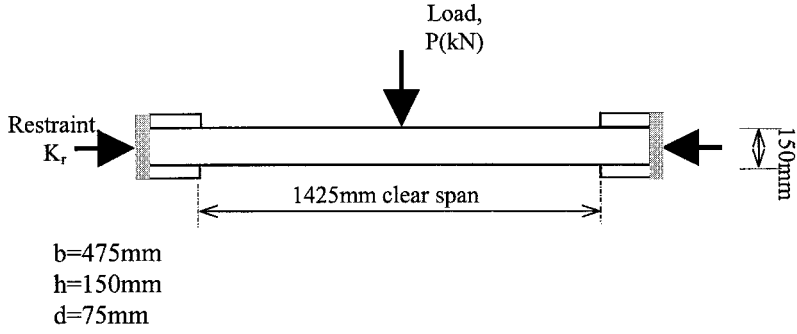


Figure 1: Slab test load arrangement for F/E & L/R boundary conditions

TEST RESULTS

Material properties

The average rupture strength of the GFRP was 504N/m^2 and the average yield strength of the steel reinforcement was 530N/mm^2. The concrete compressive and indirect tensile strengths are summarised in Table 2.

Observed behaviour

The first crack appeared directly below the load point and propagated towards it in all the test slabs. In the simply supported slabs, subsequent cracking occurred to either side of the main crack at increased applied load. The cracking was more pronounced in the GFRP reinforced slab compared to the steel reinforced slab. The GFRP slab split along the midspan region into tow separate halves due to complete rupture of the GFRP bars.

In both the simply supported slabs, the midspan crack developed at a much lower load compared to the equivalent laterally restrained slabs. In the restrained slabs, the width of the midspan crack was lower than the equivalent simply supported slab at any given applied load.

The restrained slabs had a negative support moment which was highlighted by the development of tension cracks in the top face adjacent to the support. When the applied load reached close to the failure load, crushing occurred in both the midspan and the support compression faces. The equivalent GFRP and steel reinforced slabs appeared to behave similarly. At the failure load, crushing of the concrete in the compression zone was evident and this was more pronounced in the slabs with higher concrete compressive strength.

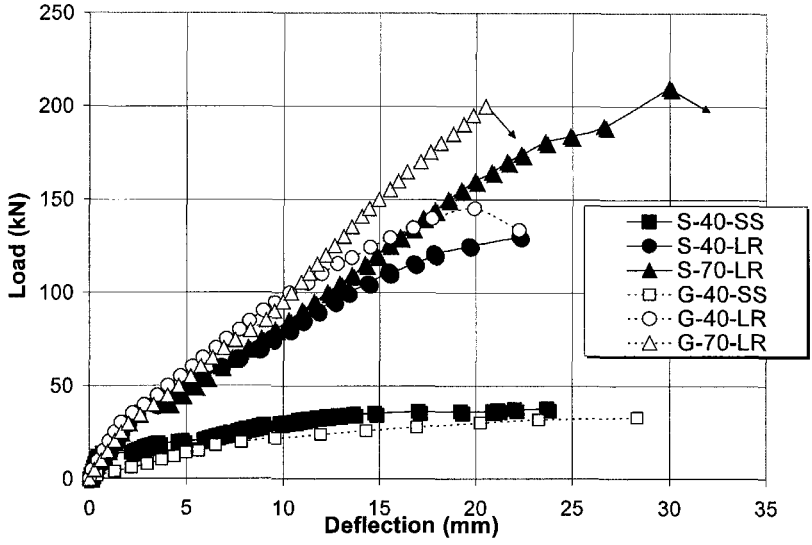


Figure 2: Load vs. vertical deflection at midspan – Series 1 & 2

Slab deflections

The load vs. deflection results for all the test slabs are illustrated in figure 2. The two simply supported slabs failed at similar loads. However, the deflections were higher in the GFRP reinforced slab compared to the steel reinforced slab at the same value of applied load.

At an applied load of 30kN, G-40-SS, reinforced with GFRP, had a midspan deflection over twice that of the equivalent slab reinforced with steel, S-40-SS. This increase in deflection is attributable to the low modulus of elasticity of GFRP bars in comparison to the steel bars. Conversely, in the laterally restrained slabs, the deflections were less in the slabs reinforced with GFRP compared to the equivalent slabs reinforced with steel. At an applied load of 150kN the deflection in slab G-70-SS was 15mm compared to 18mm in slab S-70-SS, that is, 17% less in the former despite the concrete strength being lower.

Reinforcement strains

From the strain measurements in the simply supported slabs, the rupture strain in the GFRP bars and the yield strain in the steel reinforcement were exceeded. However, the rupture strain was not reached in the slab G-40-LR which suggested that the failure mechanism in this slab was by the concrete crushing. This was corroborated by the recovery of strain in the GFRP bars after removal of the applied load. In the laterally restrained slabs reinforced with steel, the yield strain of the steel had been exceeded at the failure load although there was also evidence of concrete crushing.

Ultimate strengths

Table 2 summarises the ultimate strengths and the corresponding deflections at failure. The failure loads have been shown graphically in figure 3. The trend lines clearly show an increase in the ultimate capacity with increasing concrete compressive strength. The ultimate capacities of the slabs reinforced with GFRP were also marginally higher than the equivalent slabs reinforced with steel despite the rupture strength being lower.

Table 2: Test results

Slab No.	f_{cu} (N/mm^2)	f_t (N/mm^2)	Failure load (kN)	Deflection @ failure (mm)	Failure mode
S-40-SS	39.7	2.9	37.4	22	Steel yielding
S-40-LR	41.0	3.1	129.8	22	Crushing/bending
S-70-LR	85.0	2.9	210	30	Crushing/bending
G-40-SS	39.9	3.7	33	28	Crushing
G-40-LR	38.6	3.3	145	20	Crushing/bending
G-70-LR	67.9	3.3	200	21	Crushing/bending

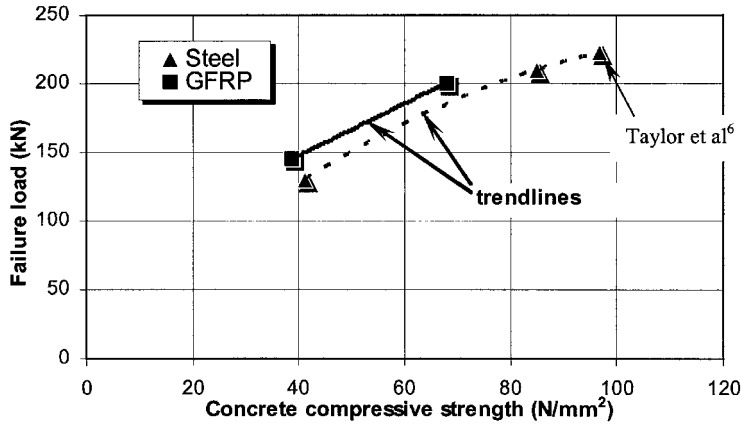


Figure 3: Ultimate failure loads – laterally restrained slabs

BACKGROUND TO ARCHING ACTION

If the edges of a concrete slab are restrained against lateral movement by a stiff boundary, an internal arching mechanism or Compressive Membrane Action is induced as the slab deflects. This enhances the flexural load capacity of the slab. The arching phenomenon occurs in concrete due to the significant difference between its tensile and compressive strengths. The weak strength in tension causes cracking due to the application of load. This shifts the neutral axis towards the compression face. If the edges of the slab are restrained by a stiff boundary, internal arching action is induced (figure 4).

The behaviour at low loading is elastic, region A to B in figure 5, but reaches an elastic-plastic phase, B to C, prior to the peak load at C. This peak load corresponds to the maximum arching effect and, in under reinforced slabs, the maximum bending strength. At increased deflection, the subsequent load capacity reduces. It has been shown that the arching effect is relatively greater in slabs with lower reinforcement percentage, low span to depth ratio and a high degree of lateral restraint. That is, in comparison to the flexural or yield line predicted ultimate strengths which do not consider membrane effects.

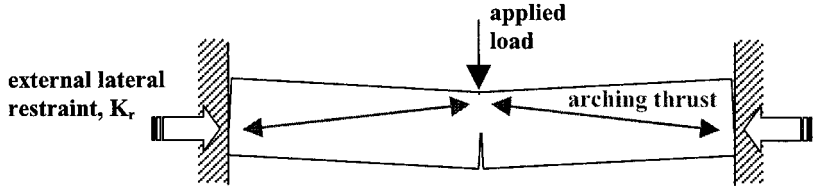


Fig. 4: Compressive membrane action in laterally restrained RC slab

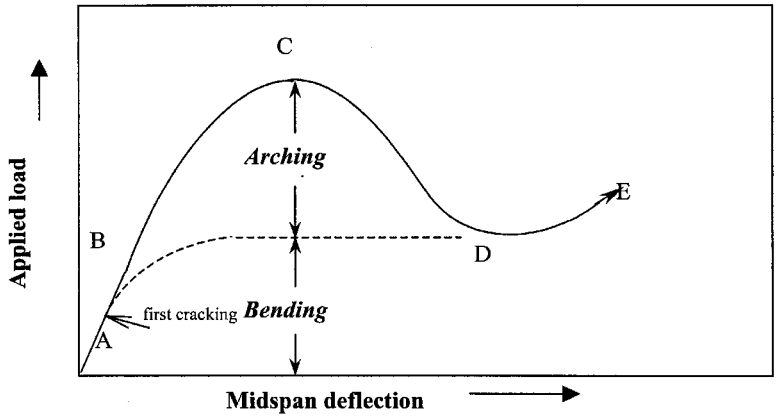


Figure 2 : Typical load vs. deflection for restrained reinforced concrete slab

In a non-linear brittle material, such as concrete, the restraint is effective at the mid-plane as this lies within the tensile zone. The development of arching theory for restrained slab strips has generally been based upon assumptions of elastic-plastic and rigid plastic idealisations. Rankin and Long[8] developed a method for analysing the strength of laterally restrained slab strips.

The theory for the prediction of ultimate capacity was based on the deformation theory of McDowell[9]. The effect of arching and bending were considered separately, although in reality the compressed concrete is due to both the action of arching and bending. This method of analysis was further developed by Taylor et al[6] to incorporate concrete with high compressive strengths (>70N/mm^2). The procedure for assessing the strength of laterally restrained slabs can be outlined by the following calculation flow diagram:

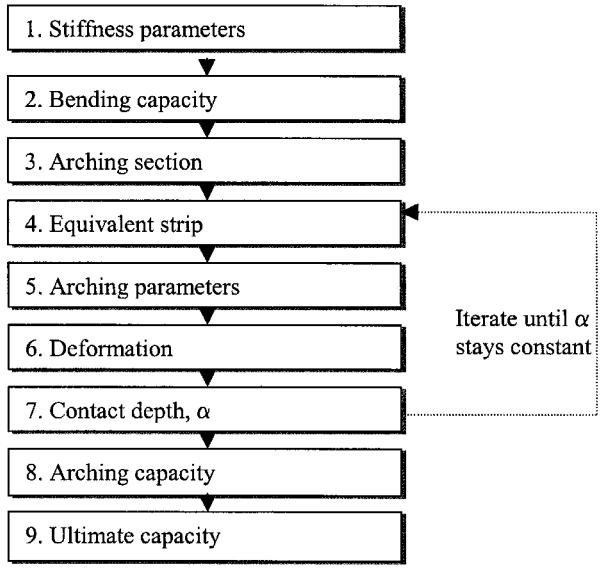


Table 3: Comparison of ultimate failure loads with predicted failure loads

Slab No.	P_T (kN)	P_P (kN)	P_{BS} (kN)	P_T/P_P	P_T/P_{BS}
S-40-SS	37	34	34.5	1.08	1.08
S-40-LR	130	129	69.2	1.01	1.88
S-70-LR	210	184	72.8	1.14	2.88
G-40-SS	33	33	33.0	1.00	1.00
G-40-LR	145	124	65.7	1.17	2.21
G-70-LR	200	163	68.6	1.23	2.92

Load predictions

The design of FRP reinforced concrete members for flexure is analogous to the design of steel reinforced members. A similar approach was adopted for predicting the arching capacity. The material properties, i.e. rupture stress, of the GFRP bars was used directly in the existing method. To facilitate the iterative procedure, a spreadsheet was developed and the predicted failure loads are given in Table 3. These have been shown graphically in figures 6 & 7. The predicted values show good agreement with the test results. The predictions for the GFRP reinforced slabs are slightly more conservative than those for the steel reinforced slabs.

The flexural capacities without arching action were also predicted using the equivalent rectangular stress block in the British Standard[10]. The ratio of actual failure load to the predicted flexural capacity becomes increasingly conservative with increasing concrete compressive strength.

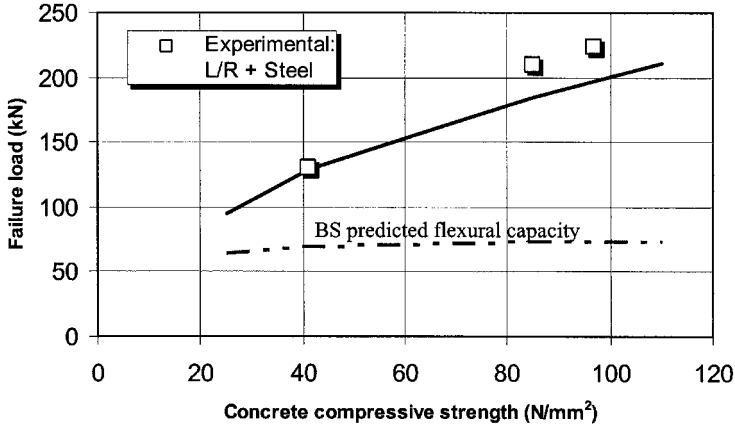


Figure 6: Comparison of ultimate failure loads with predicted failure loads: steel reinforcement

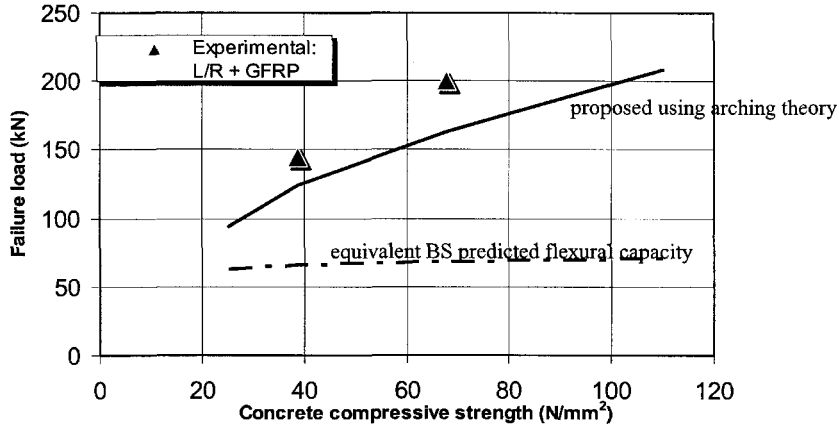


Figure 7: Comparison of ultimate failure loads with predicted failure loads: GFRP reinforcement

CONCLUSIONS

The primary aim of this research was to extend the existing knowledge of arching action in laterally restrained slabs with fibre reinforced polymers bars as the reinforcement, namely GFRP. From experimental and analytical studies the following conclusions have been drawn:-

1. The experimental observations were consistent with the development of compressive membrane action in the laterally restrained slabs.
2. The deflection was significantly greater in the simply supported slab with GFRP compared to the equivalent steel reinforced slab. However, the provision of lateral restraint significantly reduced the midspan deflection and the GFRP reinforced slabs showed better service behaviour compared to the equivalent laterally restrained steel reinforced slabs.
3. The results indicated that the laterally restrained slabs reinforced with GFRP exhibited marginally higher ultimate capacities than the laterally restrained slabs reinforced with steel.
4. The ultimate strength of the laterally restrained slabs was more dependent on concrete compressive strength than the type of reinforcement.
5. GFRP reinforcing bars in laterally restrained concrete slabs are a viable option.

This research has investigated just one type of GFRP bar, there is scope for testing other GFRP bars and FRP's such as carbon FRP to evaluate their effectiveness as a reinforcing material for laterally restrained concrete slabs and beams.

NOTATION

b width of slab
d effective depth of reinforcement
f_{cu} concrete cube compressive strength
f_y steel reinforcement yield strength
h depth of slab
P applied load
P_{BS} predicted ultimate flexural capacity using BS
P_P predicted ultimate capacity using proposed arching theory
P_T test ultimate capacity

REFERENCES

1 A J M Farreira,., P P Camanho, A T Marques, and A A Fernandes, (2001) *Modelling of concrete beams reinforced with FRP re-bars*, Composite Structures, 2001 **53**(1) 815-823.

2 S H Alsayed, Y A Al-Salloum and T H Almusallam, (2000) *Performance of glass fiber reinforced plastic bar as a reinforcing material for concrete structures*, Composites: Part B, 2000 **31** 555-567.

3 A J Ockleston, *Load tests on a 3-storey RC building in* Johannesburg, Structural Engineer, 1955 **33** 304-322.

4 J Kirkpatrick, G I B Rankin, and A E Long, *Strength evaluation of M-beam bridge deck slabs*, The Structural Engineer, 1984 **62**(3) 60-68.

5 J Kirkpatrick, A E Long, and G I B Rankin, *The influence of compressive membrane action on serviceability of beam and slab bridge decks*, Structural Engineer, 1986 **64B**(1) 6-9 & 12.

6 S E Taylor, G I B Rankin and D J Cleland, *Arching action in high strength concrete slabs*, Proceedings of the Institution of Civil Engineers, Structures and Buildings, 2001 **146** (4) 353-362.

7 M Ruddle, *Arching action and the ultimate capacity of reinforced concrete beams*, PhD thesis, Queen's University of Belfast, Northern Ireland, 1989.

8 G I B Rankin, and A E Long, *Arching action strength enhancement in laterally restrained slabs*, ICE Proceedings -Structures and Buildings, 1997 **122** 461-467.

9 E L McDowell, K E McKee and E Sevin, *Arching action theory of restrained masonry walls*, ASCE Journal of Structural Engineering, 1956 **82**(ST) 915-1– 915-18.

10 British Standards Institute, BS 5400 *British Standard for the design of steel, concrete and composite bridges,* London, BSI, 1990.

A VIEW POINT OF CRACK PROPAGATION AND FAILURE MODES OF FRP STRENGTHENED FLEXURAL RC ELEMENTS

E. Andreou, D. B. Tann and R. Delpak
School of Technology, University of Glamorgan, Pontypridd CF37 1DL, UK

ABSTRACT: This study is focused on certain aspects of structural performance of FRP strengthened RC elements in bending. These structural aspects relate to (a) section load carrying capacity, (b) the failure mode and (c) the manner of crack propagation. The study sets out to verify a definitive link between points (b) and (c) and their combined influence on the manner of section deformation until failure. The additional focus of study is to understand the way that the presence of FRP composites changes the extent and intensity of cracking together with the new failure mechanisms and geometry.

The parametric changes in this research have been: (i) beam geometry and loading configuration such as shear span, mechanical spans (load spacing) and (ii) the strengthening arrangement, e.g. FRP type, fibre content and FRP geometry. It was found that the total tension reinforcement (steel and FRP) had a significant influence on structural behaviour. It also determined whether the section reached the full intended deformation capacity, or whether premature failure was triggered.

Finally it was established that there were three limiting cases of total reinforcement ratio, which dictated the deformation and failure characteristic: (1) under-strengthened members where section behaves in a ductile manner similar to conventional flexural RC elements, (2) balanced strengthening, where strength and deformability optimise at approximately the same total reinforcement level and (3) over-strengthened sections which have an unpredictable and brittle nature, frequently brought about by premature failure. The failure modes and crack patterns often have a distinct geometry, dissimilar to that of conventional RC beams.

INTRODUCTION

Apart from the well defined failure modes (flexural and shear), FRP strengthened RC elements often possess additional failure characteristics. As a result, new terms are introduced to describe these modes under which beams fail. It is therefore necessary to define the new terminology, in order to avoid lack of clarity. The terms used in this paper and discussed below, are based on the definitions proposed by Tann[1]:

(a) Debonding of the FRP is used to describe the situation where, the FRP is separated either from the adhesive (this can only happen in the case of plate bonding) or when the FRP/adhesive system is separated from the concrete surface with no substantial amount of concrete attached on it. This usually happens in the case of poor surface preparation or weak bond of the adhesive system. See Failure I in Figures 1 and 2.

(b) Peeling-off of the FRP is used to describe the failure geometry when a debonding type of FRP separation occurs but, in this case some concrete of thickness less than the concrete cover still remains attached to the FRP. See Failure II in Figures 1 and 2.

(c) Tearing-off of concrete cover is used to describe the situation initiated at the plate cut-off point, due to the great concentration of normal (peeling) and shear stresses, which may exceed the maximum shear strength of concrete. It occurs at the internal

steel reinforcement level, with the FRP usually still well bonded to the separated concrete cover. See Failure III in Figures 1 and 2.

d) Delamination is used to describe the condition of physical separation of the FRP composite layers, either in the pre-laminated plate or wet lay-up state. It is usually due to the poor FRP fabrication or application process(es).

In addition to the above failure modes, a full depth concrete crushing failure has also been observed during load testing. This type of failure is different from the conventional compressive concrete failure (which is termed as *Concrete Fracture* in this paper); it takes place within the compression flexural zone and continues through the depth of the beam, usually with a diagonal crack, see Failure V in Figures 1 and 2.

Figure 1 below, shows a schematic of the different failure modes, while Figure 2 includes some tested beams, which failed under one of the above mentioned failure modes.

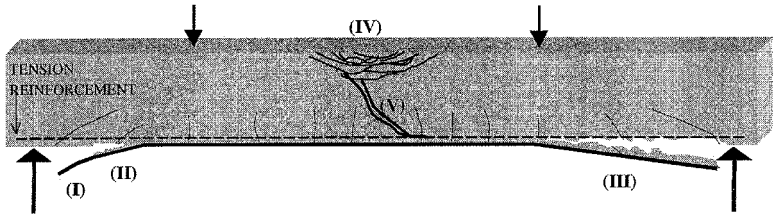
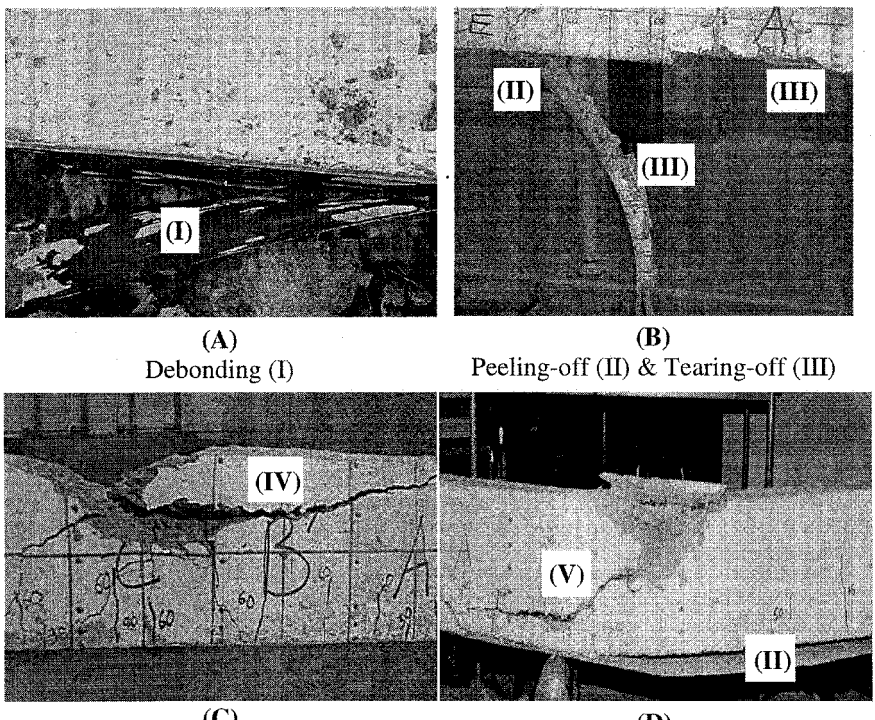


Figure 1: Schematic of failure modes



(A) Debonding (I)

(B) Peeling-off (II) & Tearing-off (III)

(C) Concrete Fracture (IV)

(D) Peeling-off (II) & Concrete Crushing(V)

Figure 2: Typical failure modes of tested beams

FAILURE MODES FROM CURRENT BEAM TESTS

A representative sample of the beam tests carried out during the experimental investigation is presented in Table 1. The failure mode of each system, as well as the beam details, moment at first crack and ultimate moment, are all included. The influence of each factor on the different failure modes is discussed below.

Influence of end-anchorage on failure modes

The beam with the FRP trapped under the supports failed with the concrete crushing through the beam depth, within the constant moment zone. The first visible cracks appeared at about 36kN, but noticeable level of cracks developed closer to failure. Failure was sudden and explosive, with concrete crushing at the beam centre in a triangular shape. A shear crack connected the triangular crushed zone to one end of the beam by becoming horizontal at the internal steel reinforcement level. The FRP peeled-off from the centre and tear continued to one of the beam extremities. It is believed that the end-anchorage of the FRP prevented any premature tearing-off failure and the beam developed substantial deformations up to the point where the ultimate compressive strains of concrete were reached.

Influence of fibre content on failure modes

The influence of the fibre content on beam failure mode is clearly shown upon examination of the beams with 1, 2 and 3 layers of AFRP. Beams with only 1 layer of Aramid failed in the conventional compression manner, while the failure mode is seen to have changed to a premature tearing-off of concrete cover, as the number of Aramid layers increased and an over-strengthened, brittle system resulted[2]. The high stress concentration at the FRP ends resulted in a shear crack at that point, which initiated the tearing-off process of concrete, extending through the weakest plane. The crack spacing of 1 and 2 layer beams was uniform with mostly flexural cracks occurring, while the 3 layer beams exhibited slightly reduced flexure cracking and increased shear cracking.

Influence of adhesive resin used in wet lamination, on failure modes

Two identical, 2-layer Aramid beams were laminated using saturants from two different suppliers. The two beams had the same properties with regards to concrete strength, stiffness and FRP fibre content but exhibited different failure characteristics. The outcome is seen to imply that the resin used influenced the beam mode of failure. The change of failure mode from concrete crushing to tearing-off may be attributed to a stiffer adhesive.

Influence of different FRP types on failure modes

By observing the failure modes of beams strengthened with different FRPs, it can be seen that in general, beams with low total equivalent reinforcement ratio[a] ρ' fail in concrete fracture. The beam strengthened with the glass fabric, failed by debonding of the FRP, which may have been the result of poor bonding.

---

[a] In order to relate the changes of strengthened system performance with the material properties, a parameter, which was called the *Total Equivalent Reinforcement Ratio* (TERR) ρ', of the strengthened beams, was introduced. The TERR, was calculated by taking into account the internal steel reinforcement area, the FRP cross sectional dimensions, the modular ratio (E_{FRP}/E_{STEEL}) of each advanced composite and the beam dimensions[3].

In the case of the beams retrofitted with carbon fabric type *A* & *C*, the FRP was observed to fail in tension, with subsequent concrete crushing and/or tearing-off. These two cases were the only cases throughout the experimental study that the FRP has reached the ultimate tensile strength and failed. This type of failure is not reported to be common, normally owing to the high strength of the FRPs.

Pure tearing-off failure occurred in the case where plate FRP was used. Both the Aramid and carbon plate beams, failed in this manner even though ρ', was relatively low in the case of the Aramid strengthened beam and the system had developed substantial rotation before failure. A possible explanation for this behaviour of the FRP plated beams could be that an adhesive layer was used to bond these plates, which contributed to the "critical" thickness of the FRP/adhesive system. The properties of the adhesive, in this case, influence the strengthened system performance to a greater extent than in the wet lamination case. Therefore, a brittle system could also be the result of a stiff and brittle adhesive.

Influence of shear span and FRP anchorage length on failure modes

The 1.5m long beams, with shear spans of 300mm and 400mm, failed prematurely under a tearing-off type of failure. The small shear spans and FRP anchorage lengths are thought to have resulted in high stress concentrations at the composite ends, which initiated the premature failures. In these cases, cracks appeared at high levels of bending moment and very few cracks developed throughout the test. Beam deformations were low and failure was sudden and occurred without warning. In the case of the beam with shear span of 400mm and zero anchorage length, concrete crushing also occurred during failure, which indicated a more ductile system, since the FRP had practically no effect on beam performance.

The beams with a shear span of 575mm, failed under different modes, in some cases combining concrete crushing and tearing-off, without any clear trend of the influence of anchorage length change. However, all of the beams exhibited a more ductile behaviour than the beams with smaller shear spans both in the deformation levels and failure modes. The first visible cracks appeared at lower moment levels. The presence of cracks was more obvious in these cases.

The failure modes of beams with varied shear span to depth ratios, tested during the experimental programme, are similar to the failure models suggested by Kong & Evans[4] for unstrengthened RC beams. Failure modes are grouped depending on the beam shear span to depth ratio. Beams with ratios between 2.5 and 6, which in this experimental study are the beams with shear span of 575mm, failed in so called a *shear-tension* or *shear-bond* failure. This type of failure initiates with a flexural crack near the support, which with the increase of shear force becomes inclined and propagates towards the point load, but stops at a point below the top of the beam. With increased shear force, the crack widens and propagates along the level of tension reinforcement. The increased shear force presses down the longitudinal steel and causes the weakening of the bond between the concrete and the steel, usually leading to the splitting of the concrete along the steel reinforcement level.

According to the same authors, beams with ratios between 1 and 2.5, similar to the beams with shear span of 300mm and 400mm, fail in a shear-*compression* failure. This type of failure initiates with an independent crack (not as a development of flexural crack), which penetrates into the compression zone at the loading point. At failure, the concrete crushes under the point load, sometimes in an explosive way[4].

The first type of failure suggested by Kong & Evans[4] is similar to the tearing–off type of failure. The mechanisms of the failure are initially the same, but the presence of an external reinforcement results in the tearing-off of the concrete cover. The second type of failure is similar, in the way that is explosive, but again the presence of FRP results in a tearing-off of concrete. Also all the beams tested under this experimental investigation were heavily reinforced in shear, so that a flexural failure was encouraged.

CRACK PATTERNS

The crack pattern of FRP strengthened beams was also seen to be influenced by the FRP fibre content and total equivalent reinforcement ratio as well as the shear span to depth ratio. The first set of visible cracks was delayed, especially in the case of beams with low shear spans, which appeared at a bending moment of more that 15kNm. Beams with low ρ', exhibited a similar crack pattern to that of control, except that the number of shear cracks is seen to have increased slightly. This is due to the greater opportunity for shear cracking, provided by the higher load carrying capacities of the plated beams and the ability of the plate to produce more closely spaced and narrower cracks. With the fibre content increasing, shear cracks increased and became wider, with a reduction of inclination angles. The crack intensity was also substantially reduced in the case of 1.5m long beams. The shear cracks, responsible for the tearing-off failure of strengthened beams, have always initiated from the extremity of the laminate with no visible cracks occurring on the concrete surface beyond the FRP.

The crack propagation patterns and failure modes could generally be distinguished to those indicating a brittle or a more ductile system, resulting from over-, balanced-, or under strengthening of the beams. Figure 3 shows the "averaged" experimental crack patterns of the three most typical beam behaviours. In each case, the experimentally traced cracks of both (and corresponding) sides of two beams were superimposed and the representative crack pattern was traced. The cracks were drawn using three different line types, indicating those which occurred (i) at half the ultimate loads, (ii) those that were the last recorded before failure and (iii) those that were formed after failure had taken place.

A similar illustration to Figure 3 is Figure 4, which shows three different crack propagation patterns, based on the system ductility. The type (A) crack pattern of Figure 4 was generally followed by the control, 1-layer Aramid, the Aramid B, the carbon B and the 2-layer Aramid beam with 400mm anchorage length. Type (B) crack development, occurred in beams with end-anchorage, one of the 2-layer Aramid beams, the carbon B beam and the 2-layer Aramid beam with 200mm anchorage length. Beams with this type of ultimate crack propagation usually failed under more than one mode, which indicated that the system was of intermediate ductility. Type (C) crack pattern is seen to occur in the cases of plated beams, beams with high total equivalent reinforcement ratio and members with low shear span to depth ratios. In these cases the cracks developed at angles less than 30° to the beam soffit, were further reduced and the failure was sudden and explosive.

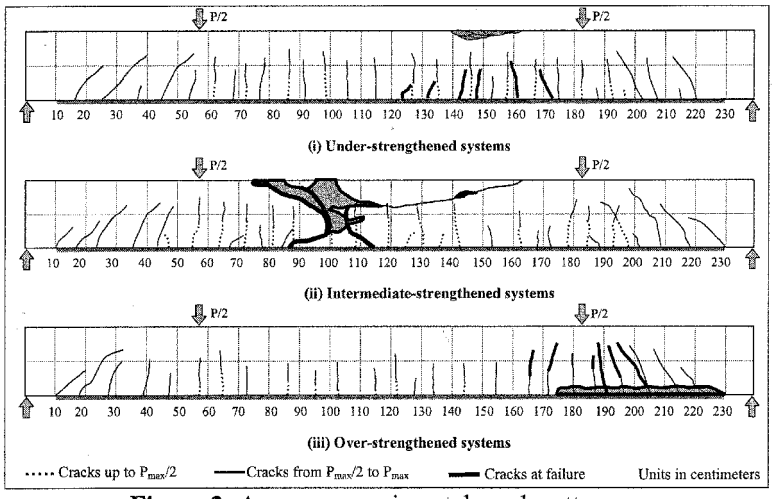


Figure 3: Average experimental crack patterns

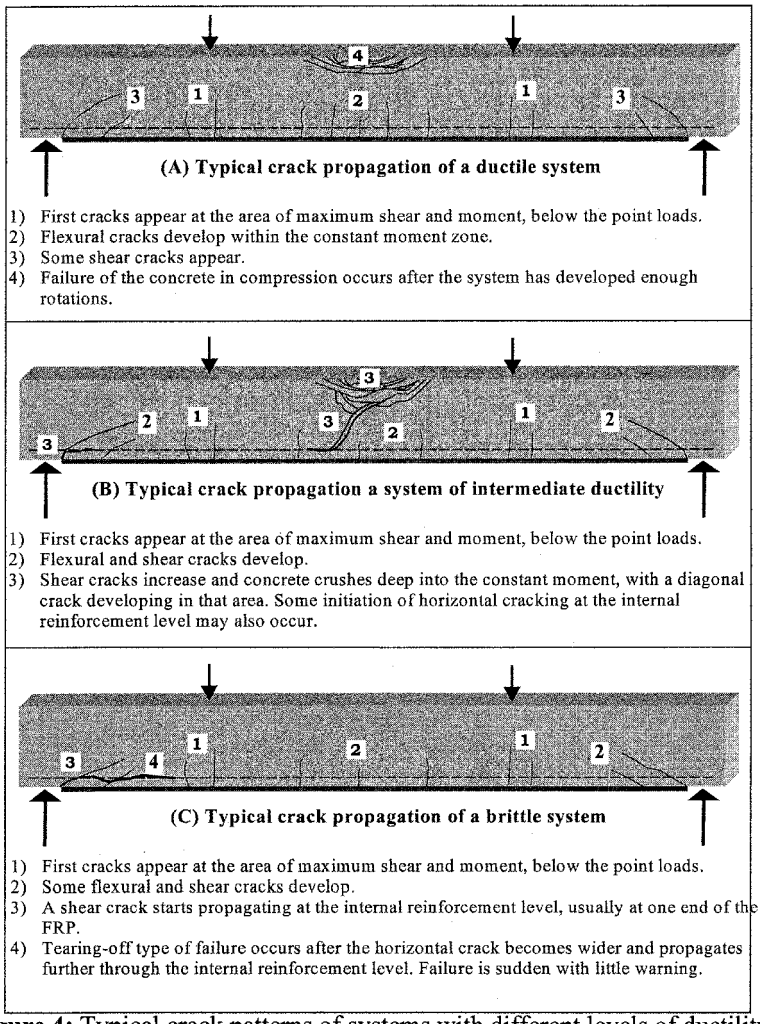


Figure 4: Typical crack patterns of systems with different levels of ductility

Table 1: Summary of beam test results and failure modes

FRP used	*Shear span, ss (mm)*	*TERR[a] ρ' (%)*	*Anchorage length[b], a (mm)*	*Moment at first crack (kNm)*	*Ultimate moment (kNm)*	*Failure mode[c]*
2-L Aramid A[d]	575	0.96	575	10.4	26.4	CC/PL
1-L Aramid A	575	0.88	470	5.8	20.4	CF
1-L Aramid A	575	0.88	470	8.6	20.1	CF
2-L Aramid A	575	0.96	470	8.6	25.0	TR
2-L Aramid A	575	0.96	470	8.6	24.7	CC
3-L Aramid A	575	1.05	470	8.6	23.0	TR
3-L Aramid A	575	1.05	470	11.5	22.4	TR
2-L Aramid B	575	0.86	470	5.8	19.4	CF
Plate Aramid	575	0.94	470	5.8	25.0	TR
2-L Carbon A	575	0.97	470	4.3	22.3	CC/FF/T
1-L Carbon B	575	0.87	470	3.4	20.1	CF
1-L Carbon C	575	0.87	470	3.4	20.7	FF/CF
Plate Carbon	575	1.18	470	5.8	21.6	TR
1-L Glass	575	0.82	470	4.0	19.3	DB
2-L Aramid A	300	0.96	0	17.2	18.6	TR
2-L Aramid A	300	0.96	200	25.9	20.4	TR
2-L Aramid A	300	0.96	290	17.2	20.7	TR
2-L Aramid A	400	0.96	0	17.2	18.0	TR/CF
2-L Aramid A	400	0.96	200	15.8	20.0	TR
2-L Aramid A	400	0.96	350	25.9	23.8	TR
2-L Aramid A	575	0.96	0	5.8	17.0	CF/TR
2-L Aramid A	575	0.96	200	5.8	37.6	CC/TR
2-L Aramid A	575	0.96	400	5.8	23.6	TR
2-L Aramid A	575	0.96	400	5.8	23	CF

Notes:

a) Total Equivalent Reinforcement Ratio;

b) Anchorage length is the FRP length within the shear span of a 4-point loaded beam;

c) Failure Modes: CC = Concrete Crushing through beam depth, PL = PeeLing-off, CF = Concrete Fracture, TR = TeaRing-off, FF = FRP Fracture, DB = DeBonding;

d) Beam strengthened with the FRP anchored under supports;

e) 1-L etc. refers to the number of FRP layers;

f) Aramid A, Carbon C etc. refer to different strengthening systems.

CONCLUSIONS

The behaviour of strengthened beams is associated with the mode at which they fail and the manner that cracks develop. Externally reinforced beams fail in more complicated manner than the traditional RC flexural members do, with reductions in crack widths and intensity. The most common failure modes of externally retrofitted beams are (1) compressive failure of concrete, (2) peeling-off of the FRP, (3) debonding of the FRP and (4) tearing-off of concrete cover. Some of the above failure modes take place prematurely, in a brittle manner and should be prevented.

Failure modes of FRP strengthened beams are influenced by (a) the end-anchorage of the FRP; (b) the FRP fibre content; (c) the adhesive/saturant used; (d) the total equivalent reinforcement ratio and generally the FRP properties; (e) the FRP anchorage length and beam shear span and (f) the concrete and internal reinforcement properties.

ACKNOWLEDGEMENTS

The authors wish to acknowledge the funding and donation of resources from Du Pont de Nemours International S.A. They also appreciate the generous provision of materials and technical advice from MBT (UK) and Ciba-Geigy (Switzerland). The help and advice of Mr. C. Rogers at BRC in Gwent, for provision of reinforcement steel, is also acknowledged. Finally, they wish to express their sincere thanks to the School of Technology (University of Glamorgan) management, in availing R&D resources and allocation of technical support.

REFERENCES

1. D. B. Tann, *Retrofitting of Mechanically Degraded Concrete Structures using Fibre Reinforced Polymer Composites,* Ph.D. Thesis, University of Glamorgan, Pontypridd, 2001.

2. E. Andreou, R. Delpak, R. Pinzelli, and K. Chang, "The application of composite based on Kevlar for the strengthening of RC beams", *Concrete Communication Conference 2000: The 10th BCA Annual Conference on Higher Education and the Concrete Industry,* Birmingham, 2000.

3. E. Andreou, *Performance Evaluation of RC Flexural Elements Strengthened by Advanced Composites,* Ph.D. Thesis, University of Glamorgan, Pontypridd, 2002.

4. F. Kong, and R. Evans, *Reinforced and Prestressed Concrete,* Chapman & Hall, 1987.

RETROFITTING OF DAMAGED CONCRETE BEAMS WITH HIGH PERFORMANCE POLYMERS

Robert Y. Xiao and Wael B. Almajed
Civil Engineering and Computational Engineering Centre
University of Wales Swansea UK SA2 8 PP

ABSTRACT

A research program is being conducted to study the effect of fibrous concrete as a retrofitting material. The paper will represent the experimental investigation and numerical analysis conducted on damaged reinforced concrete beams retrofitted with fibres. Steel, polypropylene and hybrid (steel-polypropylene) fibres are being used for this research programme. Seventeen different types of reinforced concrete beams have been tested. The numerical analysis has been conducted by using finite element software ANSYS. Experimental and numerical results will be compared.

INTRODUCTION

Retrofitting and rehabilitation of existing structures have played an important role in civil engineering construction works[1]. Structures may become inadequate during their service life due to various reasons including: Design and construction errors; deterioration due to corrosion; aging and weathering; damages from overloading; fires and earthquakes etc.[2]. Repairing for the damaged part of a structure is fast and less expensive compared to reconstruction of the whole structure. In addition, engineers have found so many varieties of repairing materials and methods.

In the early 1960s some researchers started to use fibres reinforced concrete, since then interest of using fibre reinforced concrete has been growing rapidly. The use of different types of fibres for many applications has been chronicled throughout the history[3]. Many research papers have been published for the contribution to the development of fibre reinforced concrete[4]. Researchers concentrated on how fibres could improve the performance of brittle-matrix concrete. Research has been developed on using fibres to improve the concrete's flexural resistance, shear resistance and ductility[5][6], energy absorption ability[7][8], impact resistance and concrete's toughness[9].

In this research new types of fibres have been used as retrofitting materials. These include High Performance Polymer(HPP), steel and hybrid steel-polypropylene fibres. All fibres have been provided by Synthetic Industries Ltd.

TEST SETUP

Seventeen steel reinforced concrete model beams with size of *120x150x1000mm* (width, height, length) have been designed and cast for testing as shown in Table 1. The areas of the damaged concrete are considered in mid-span. There are three plain reinforcement beams (control specimen), ten retrofitted beams and four beams with damaged section not repaired. To create the damaged sections in beams (voids) Styrofoam has been used with steel reinforcement cage as shown in Figure 1 before the casting. The voids will be created in the top and bottom of the beam.

Table 1: Summary of Specimens:

Beam Type	Number	Fibre used
Plain Beams (PB)	3	None
Plain Top Void Beams (PTVB)	2	None
Plain Bottom Void Beams (PBVB)	2	None
Polypropylene Fibers Top Beams (PFTB)	2	Short Polypropylene Fibers 0.8%.
Polypropylene Fibers Bottom Beams (PFBB)	2	Short Polypropylene Fibers 0.8%.
Steel Fibers Top Beams (SFTB)	2	Short Steel Fibers 0.6%.
Steel Fibers Bottom Beams (SFBB)	2	Short Steel Fibers 0.6%.
Hybrid Fibers Top Beams (HFTB)	1	Hybrid Fibers S. 0.2% P. 0.4%
Hybrid Fibers Bottom Beams (HFBB)	1	Hybrid Fibers S. 0.2% P. 0.4%

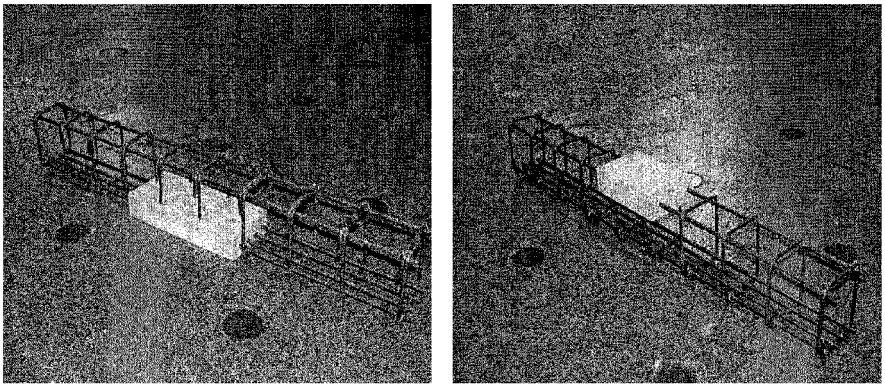


Figure 1: Steel Cages with Styrofoam in top & bottom

Concrete mix design

Concrete has been design according to the BSI specifications. The designed compressive strength f_{cu} of *40 N/mm²* was chosed. Cement used is OPC. Coarse aggregate is crushed limestone, with max. size *10mm*. Fine aggregate is sea sand, with grading zone 4, which has been determined by performing a sieve analysis. The required slump considered is *30-60mm*. The mix Ratio is (*1:0.51:1.95:2.20*) (Cement:Water:Fine aggregate:Coarse aggregate).

Three types of fibres had been used; polypropylene (S-152 High Performance Polymer Fibers HPP), steel (Xorex Steel Fiber)[10] and hybrid (steel-polypropylene), with fibre volume of *0.6%* for steel, *0.8%* for polypropylene and Hybrid fibers *0.2-0.4%* for steel-polypropylene. Bond agent, commercially named V-tie, has been used on the surface of voids to increase the bond strength between old concrete and the new fiber concrete mix.

Test specimens

All Specimens were demoulded after *24* hours and stored in room temperature for curing. Beams with voids were handled carefully and kept six days to gain some strength before removing Styrofoam. Styrofoam was removed and voids were cleaned

and chiselled to make rough surface for strong bonding. After 28 days, the plain beams and two plain beams with voids in top and bottom (PTVB1 and PBVB1), respectively were tested with two-point applied loads until failure. Other beams were ready for the fibrous concrete mix repair by the next day. Retrofitted beams, cubes and cylinders were stored in room temperature for curing. Tested deflections were recorded for all beams by using two LVDTs with digital reading device.

TEST RESULT

The concrete strength has been changed with the addition of fibres in the concrete. Table 2 summaries the variations of the tensile and splitting strength of plain and fibrous concrete.

Table 2: Comparison table between plain mix & fibre mix:

Specimens	Fibre Content %	Compressive Strength N/mm^2 (Average)	Increasing Compressive Strength %	Splitting Tensile Strength N/mm^2 (Average)	Increasing Tensile Strength %
Plain Mix	0.00	42.44	---	2.14	---
Polypropylene Fibers	0.8%	48.45	14.14	2.43	13.52
Steel fibers	0.6%	48.39	14.00	2.38	11.16
Hybrid Fibers	S. 0.2% P. 0.4%	44.81	5.57	2.42	13.30

Results show that retrofitted beams with fibres (all types) in the bottom section are not changed significantly compared to plain beams when voids exist in the bottom of the beam. This is understandable as the fibres have little influence the on flexural strength of beams. The beam was acting in a similar way to plain concrete beam. Beams failed in shear and flexure (as in PB2, PB2 and PFBB2), however, beams that have voids in the bottom behaved differently. Cracks start to occur in the flexural zone then fail in shear (as in PBVB1 and 2).

Beams with voids in the top (damaged beams) were very weak and produce large deflection (*10.41 mm*) with small failure load (*53 kN*). This has indicated that damage occurring in the compression zone of concrete will reduce the beam strength significantly. On the other hand, beams retrofitted with fibres on their top surface have much higher failure loads with relatively smaller deflections.

The bond performance between old concrete and the new fibrous mix was very good, when PFBB2 started to crack in flexure, there were a homogenise cracks from the bottom to the top throughout the two layers. This indicates chiselling the surface of the beam and the bond agent used, were very effective in increasing the bond strength. Table 3 has summarised all tested beam results.

Figure 2 shows the change in the sides of the failure loads for all beam results with the plain beam PB and with the beam that has void on top PTVB. The result shows that the value of all failure loads of the retrofitted beams and the beam with the void on its top surface were decreased compared to the plain beam PB. On the other hand, the result shows a significant increase in failure load up to *23.33%* when compared to the retrofitted beams with that, which had voids on top. The retrofitted beams perform significantly very well, and they exceeded the designed failure load,

however, they are not expected to reach the performance of the normal plain beam PB.

Table 3: A List of the Beam Test Result:

	Beams	Mix	Failure Load *KN*	Max Mid Deflection *mm*
1	PB 1	PM1	75.8	6.32
2	PB 2	PM1	82	7.95
3	PB 3	PM12	83.5	9.6
4	PTVB 1	PM3	46.2	7.9
5	PTVB 2	PM11	53	10.41
6	PBVB 1	PM2	80	6.9
7	PBVB 2	PM11	81	5.07
8	PFTB 1	PM6 & PFM8	62.5	6.32
9	PFTB 2	PM6 & PFM8	60.5	5.97
10	PFBB 1	PM4 & PFM8	73.4	4.75
11	PFBB 2	PM4 & PFM8	87.5	12.39
12	SFTB 1	PM7 & SFM9	60.2	5.89
13	SFTB 2	PM7 & SFM9	57.5	7.95
14	SFBB 1	PM5 & SFM9	76	5.6
15	SFBB 2	PM5 & SFM9	81	5.6
16	HFTB 1	PM3 & HFM10	61.5	5.27
17	HFBB 1	PM2 & HFM10	76.6	6.36

PB = Plain Beams, PTVB = Plain Top Void Beams, PBVB = Plain Bottom Void Beams, PFTB = Polypropylene Fibres Top Beams, PFBB = Polypropylene Fibres Bottom Beams, SFTB = Steel Fibres Top Beams, SFBB = Steel Fibres Bottom Beams, HFTB = Hybrid Fibres Top Beams, HFBB = Hybrid Fibres Bottom Beams

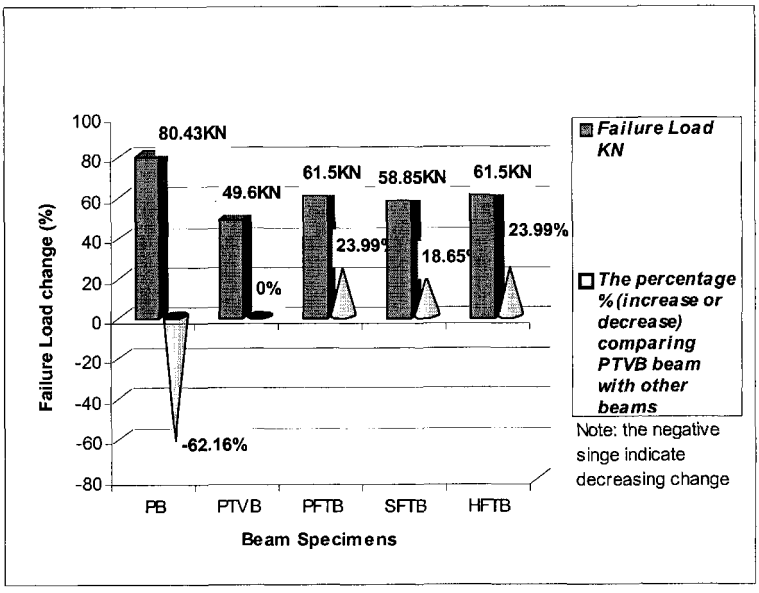


Figure 2: Comparison Chart For All Beams (Failure Loads & Percentage Change).

NUMERICAL SIMULATION

In spite of the traditional way of designing and analysing reinforced concrete, the development of the finite element method has a significant implication on concrete structural analysis in a practical way[11]. However, the simulation of the properties of the reinforced concrete is not an easy task compared with other material analysis such as steel. This is due to the complexity of the concrete composites and uncertainty of its material properties. In addition, it is even more complex when fibres were introduced in finite element analysis.

There are a number of computer programs suitable for reinforced concrete structural analysis, however, modelling of concrete structures incorporating fibres is an issue which has not been taken into consideration in many of these programs. In this research, ANSYS has been used to undertake a non-linear analysis of a concrete structure; the FE program involved a modified material model [12].

Computer modelling

To simulate the effect of concrete, SOLID65 has been used. It is a 3-D solid isoperimetric element with eight nodes and three degrees of freedom at each node. it is used to model the nonlinear behaviour, and can predict the failure mode of brittle materials (like concrete). The element has a cracking capability in tension and crushing capability in compression. In addition, the effect of steel reinforcements can be simulated by adding a LINK8. LINK8 (a spar) is a 3-D uniaxial tension-compression element which can be used to discretise steel reinforcement. It has two nodes with three degree of freedom along *x*, *y* and *z*-axis for each node. In some cases, LINK10 element is used to simulate the shear reinforcement bars as well. The shear transfer coefficient values are between *0.05* and *0.2* depending on the model, the lower shear transfer coefficient represents smooth cracks and the higher shear transfer coefficient represents rough cracks. However, it is recommended that the shear transfer coefficient for open and closed cracks should be set at the same value. The shear transfer coefficient used in this investigation will be *0.05* for an open crack and *0.2* for a closed crack; these values will be considered, in some situations, to help to reach a converged solution for higher applied loads.

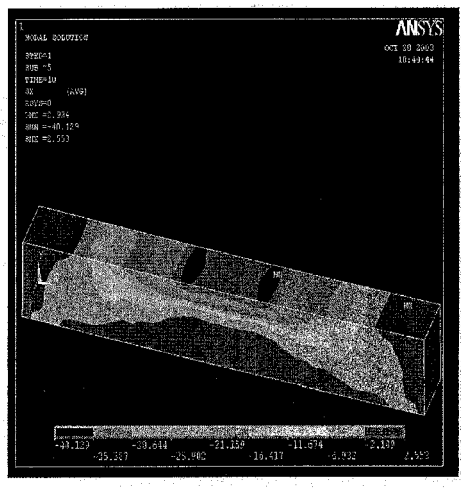


Figure 3: Stress Analysis of the plain

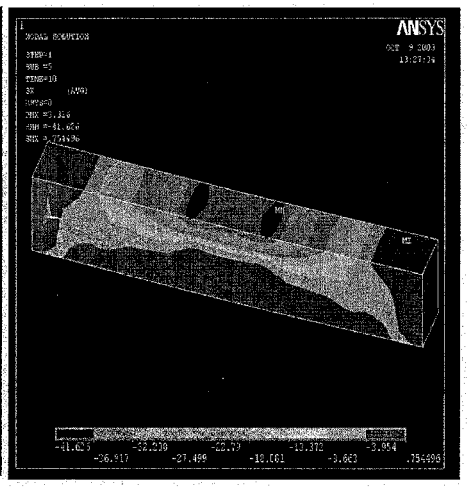


Figure 4: Stress Analysis of the plain

Two different models have been set up and numerically analysed. The first model has been focused on stresses, crushing and cracking behaviour, and on failure load of the reinforced beam model. The second model has been used to obtain more accurate information for deflection, with modified technique for crushing simulation.

The investigation is still undergoing, therefore, a comparison between laboratory work and numerical analysis of the plain reinforced beam will be presented in this paper. The average compressive strength and the average cylinder splitting tensile strength for the mixes that were used to cast the plain concrete beams are *42.44 N/mm^2 2.14 N/mm^2* respectively; those values had been used for predicting the stresses, the crushing and cracking behaviour and the maximum load capacity of the beam. In the numerical analysis the results show that the plain beam PB can sustain a value of *69.194 kN*, the compressive strength at the top of the beam is *40.129 N/mm^2* and the tensile strength in the bottom of the beam is *2.553 N/mm^2* (Figure 3). To show the crashing behavior in the beam, the load was iterated up to *75.398 kN* which is the maximum load that the beam can sustain. The associated maximum compressive stress has a value of *41.626 N/mm^2* on the top of the beam and a maximum tensile stress of *0.7544 N/mm^2* in the bottom of the beam (Figure 4). The solution has demonstrated that the concrete beam could be cracked under the lower tensile stress. It also highlights the need for using fibre for cracking control.

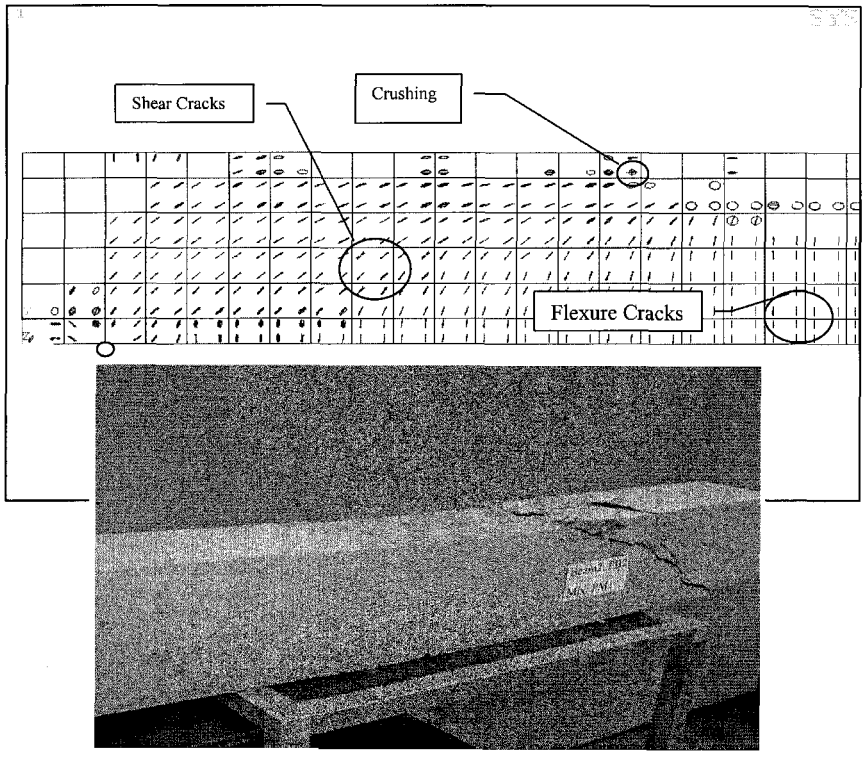


Figure 5 Comparison of crush and crack behaviour beam PB2.

Crush and Crack Behaviour

Figure 5 illustrate the crushing and cracking behaviour of the concrete beam PB2, Vertical lines represent the flexure cracks and the diagonal lines represent the shear cracks. The small diamond shape with (X) inside represent the concrete which is crushed. It can be seen that cracked and crushed simulation has been similarly to beam PB2, the maximum applied load is 75.4KN.

Deflection

To simulate the deflection in Ansys, another model has been set using LINK10 for steel reinforcement and links to disable the crushing function. Figure 6 demonstrates the deflection curve for Beam PB3. The deflection curve of numerical analysis behaves similarly to the laboratory investigation deflection curve.

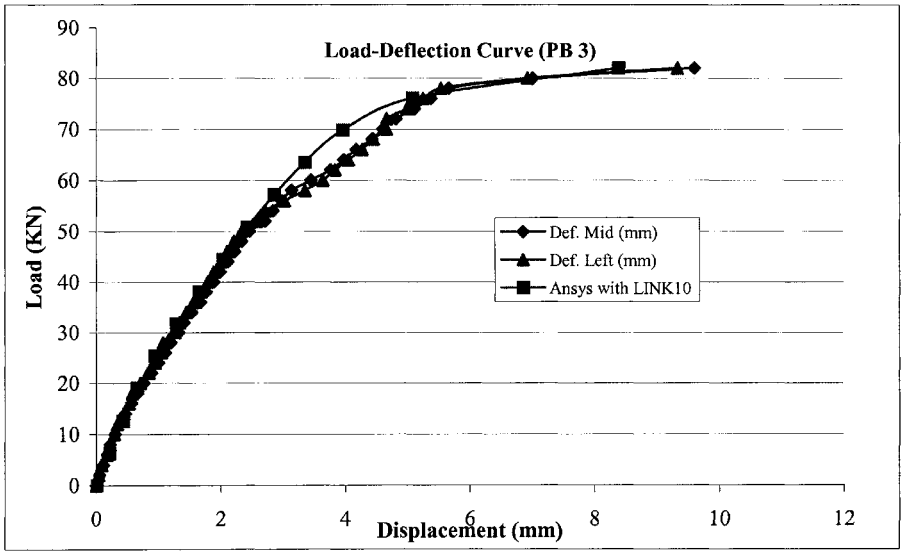


Figure 8: Load deflection curve of PB3 beam.

CONCLUSIONS

From the early test and numerical analysis of this research programme, following conclusions can be drawn.

- The addition of short fibres enhanced the concrete properties, the compressive strength was increased up to *14.14%*, *14%* and *5.57%*, and the tensile strength was increased up to *13.52%*, *11.16%* and *13.3%* for polypropylene, steel and hybrid fibres respectively.
- The performance of the damaged beam, which was retrofitted on its top surface with fibrous concrete, was enhanced. The failure loads of the retrofitted beam compared to the damaged beams were increased by *24.0%*

18.7% and *24%*, when fibrous concrete of polypropylene, steel and hybrid fibres, respectively, were used. .

- The bond between the concrete beam and the retrofitting fibrous concrete was very effective. The bond agent that was used and the way of chiselling the surface of the beam were effective.
- The beam that was retrofitted with hybrid fibres had the best performance in terms of sustaining loads, small deflections and change in failure mode.
- The numerical analysis of the concrete beam shows a close stress magnitude towards the tested values. Cracking and crushing distribution patterns match with tested cracking pattern. The deflection curve is also closely comparable with the lab investigation.

The research is being continuously conducted in this programme. More research results will be published in due course.

REFERENCES

1 Shamim A. Sheikh, 'Performance Of Concrete Structures Retrofitted With Fibre Reinforced Polymers', *Engineering Structures,* 24, 2002, 869–879.

2 Simon Austin, Peter Robins. 'A Repair Application Of Polypropylene Fibers Reinforced Sprayed Concrete', *Fiber Reinforced Cements and Concretes Recent Developments* (Conference Papers Edited by: R. N. Swamy, B. Barr), Elsevier Applied Science, 1989, 21-31.

3 Pobert C. Zellers, P. E., L.S. 'High Volume Application Of Collated Fibrillated Polypropylene Fiber', *Fiber Reinforced Cements and Concretes Recent Developments* (Conference Papers Edited by: R. N. Swamy, B. Barr), Elsevier Applied Science, 1989, 316-325

4 Ronald F. Zollo. 'Fiber-reinforced Concrete: an Overview after 30 Years of Development', *Cement and Concrete Composites*, 1997, 107-122.

5 R. Y. Xiao & C. S. Chin. 'High Performance Polymer Concrete', Advance in Building Technology (Edited By: M Anson, J. M. Ko, E. S. S. Lam), Elsevier Science, 2002, v1, 921-928.

6 A.M. Alhozaimy, P. Soroushian, F. Mirza. 'Mechanical Properties of Polypropylene Fiber Reinforced Concrete and the Effects of Pozzolanic Materials', *Cement and Concrete Composites,* 1996, 18, 85-92

7 G. L. Vodran, M. Nagabhushanam, V. Ramakrishana. 'Fatigue Strength of Polypropylene Fiber Reinforced Concrete', *Transportation Research Record 1226*, 1989, 36-47

8 J. K. Patel, N. B. Desai, J. C. Rana. 'Properties and Application of Steel Polypropylene and polyester Fibre', *Fiber Reinforced Cements and Concretes Recent Developments* (Conference Papers Edited by: R. N. Swamy, B. Barr), Elsevier Applied Science, 1989, 306-315.

9 V. J. Weiss, B. Barr and I.A.I. Ali. 'Fracture Performance of FRC Materials Under Various Curing Conditions', *Fiber Reinforced Cements and Concretes Recent Developments* (Conference Papers Edited by: R. N. Swamy, B. Barr), Elsevier Applied Science, 1989, 157-166.

10 Synthetic Industries, 4019 Industry Drive Chattanooga, TN 37416, USA, http://www.fibermesh.com

11 Antonio F. Barbosa And Gabriel O. Ribeiro. 'Analysis Of Reinforced Concrete Structures Using Ansys Nonlinear Concrete Model', Computational Mechanics, New Trends and Applications, ©CIMNE, Barcelona, Spain, 1998.

12 ANSYS, ANSYS documentations, Manual Set and Theory Reference Manual. ANSYS Inc.

RC COLUMN LATERAL PRESTRESSING WITH COMPOSITES

M. A. Ciupala, K. Pilakoutas, A. A. Mortazavi and N. Taranu
University of Sheffield, UK

ABSTRACT

This paper deals with a novel strengthening technique for concrete columns that uses FRP materials to apply lateral pre-tensioning. The level of pre-tensioning of the FRP jacket is controlled by using different amounts of expansive agent. The technique aims to enhance the capacity and ductility of columns as well as achieve better utilisation of the confining FRP material. It is shown that jacketing columns by pre-tensioned FRP materials can increase the load bearing capacity up to 25% compared with conventional wrapping and up to more than 2 times compared with unconfined concrete. Pre-tensioning is shown to delay the initiation of the fracturing process of the concrete and this can have implication in design. The paper presents details of experimental work undertaken on wrapped concrete specimens with and without pre-tensioning. Results of two different confining materials (CFRP and GFRP) are presented.

INTRODUCTION

Since the 1995 Kobe earthquake, FRP composite systems started being used for the repair and strengthening of RC columns in seismic zones. The confinement of concrete columns with these new materials prevents shear failure, lap splice failure, buckling of the longitudinal reinforcement and premature concrete compressive failure. Confinement can also increase the ductility and the energy dissipation potential of columns.

It has been demonstrated[1,2,3] that the strength of FRP confinement is not well mobilised until the lateral strain in the confined concrete is very high. In lightly reinforced columns, the concrete could crush before the FRP jacket is fully utilised[1,2,3]. Existing design equations which are based on steel confined concrete[4] assume that the confining steel yields before failure. Some of the first models for FRP confinement followed the same logic and considered that the FRP strength is fully utilised. However, many experimental programmes showed that FRP confinement is mobilised at different levels and, hence, models based on steel confinement, were modified using "confinement efficiency factors".

This problem can be overcome by activating the FRP confinement through pre-tensioning. This approach is particularly useful for low modulus materials (such as glass) or when relatively low amounts of confinement are used[1,2,3]. However, it is not easy to apply large pre-tensioning stresses in composites when using the method of pressurised injections. Some researchers[5,6,7] tried to develop lateral pre-tensioning through grout or resin injections, but had limited success in changing the concrete behaviour.

In the technique used in this work, the pre-stressing of the FRP jacket is developed by using an expansive agent[8] (EA), mixed with a cement grout.

The paper presents details of a part of this experimental work with two different types of confining material (glass and carbon) and one level of initial pre-stressing. This research was conducted at the Centre for Cement and Concrete of the University of Sheffield, UK. This research formed part of work undertaken under the EU TMR Network ConFibreCrete and two EU Marie Curie Research Fellowships.

NOVEL TECHNIQUE FOR PRESTRESSING

In this method, a pre-formed FRP confining tube (jacket) is placed around an existing concrete cylinder and the expansion grout (EG), comprising cement, sand and EA, is inserted between the concrete cylinder and the jacket, Figure 1. The jacket confines the expansion of the grout during the hardening period and pressure builds-up due to the reaction of the EG against the concrete core. In practice the FRP jacket can be formed on the top of hollow cylinders and the EG can be injected into the cylinders once the FRP jacket is ready to take load.

To understand the mechanical properties of the EG and to enable the accurate prediction of the lateral pre-tensioning pressure, special experiments were carried out[9,10].



Figure 1. Injection of the expansive grout (EG) into the specimen

After the EG sets (3-4 days), the jacket and grout become an integral part of the column. The expansive pressure of the grout is a function of the confining stiffness[9]. For very low stiffness materials, the expansive pressure can reduce to zero. Figure 2 shows the maximum expansive pressure (MEP) expected to be developed in EG having two different ratios of EA. It can be seen that the relation between MEP and the confinement stiffness (CS) is more or less linear. CS is calculated by multiplying the elastic modulus of the confining material by the thickness and dividing by the radius of the jacket.

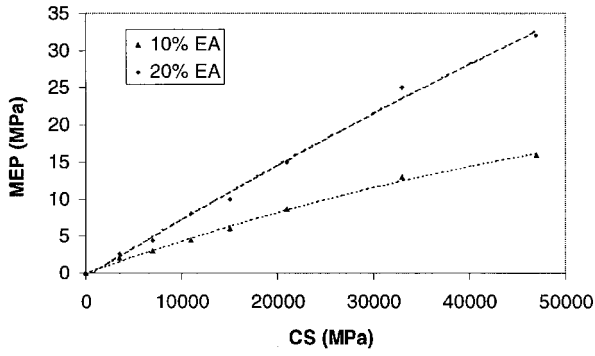


Figure 2. MEP versus CS for two values of EA

SPECIMENS DETAILS, INSTRUMENTATION AND TESTING

The full experimental programme included testing concrete cylinders with different types of confinement. Twenty seven 100mm x 200mm concrete specimens were prepared without any pre-tensioning, 54 specimens were prepared with different levels of confinement pre-stressing and 18 unconfined specimens were tested under compression to determine the plain concrete strength. Four different confining materials were used (steel, glass, aramid and carbon) with different number of layers and ratios of EA. The properties of the materials used in this study are shown in Table 1.

For the measurement of lateral strains, three 15mm surface strain gauges were attached horizontally at the mid-height of each specimen, 120° apart. To measure longitudinal strain, two surface strain gauges of 15mm length were mounted vertically in the middle height of the specimen. In addition to strain gauges, two other devices (DV1 and DV2) were designed to measure lateral and longitudinal strain by using displacement transducers. These devices are shown in Figure 3 and Figure 4.

The tests were undertaken in a servo-controlled hydraulic actuator under displacement control. All specimens were tested under centric (axial) loading.

Table 1. Fibre properties

Fibre type	*t (mm)*	E_{FRP} *(MPa)*	f_{FRPu} *MPa)*	ε_{FRPu} *(%)*
CFRP	0.117	240000	3900	1.55
GFRP	0.135	65000	1700	2.80

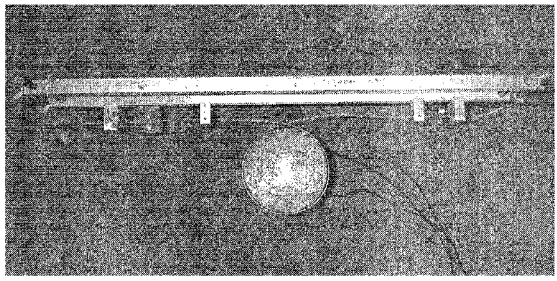


Figure 3. Plan view of the device for lateral strain measurement (DV1)

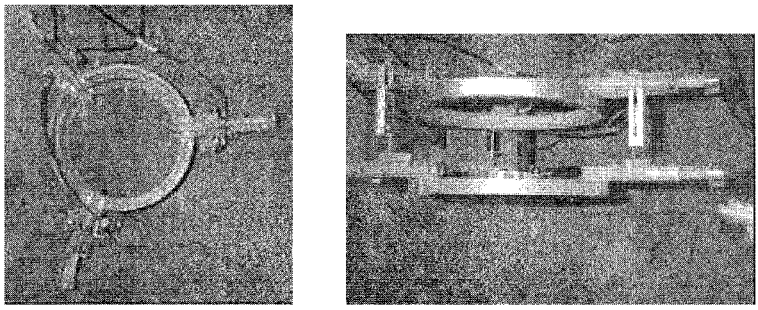


Figure 4. Plan view and elevation of the device for longitudinal strain measurement (DV2)

RESULTS

Two pairs of specimens confined with Glass and Carbon FRP were selected for presentation in this paper. Each pair shows the effect of wrapping and pre-tensioning (using the same amount of EA) of the jacket on the concrete cylinder.

The glass fibre sheet was bi-directional (90°), hence its effective thickness of confinement is 0.0675 mm. For the selected specimens, 3 layers of glass fibre were applied with an overlap of 105 mm. In the first specimen, WG3, the glass fibre sheet was applied directly onto the appropriately prepared concrete core. The second specimen of this pair, PG3-20, had the same amount of glass fibre, but the pre-formed jacket was pre-tensioned with a 7 mm thick EG having 20% EA.

The pair of CFRP confined specimens had only one layer of fibres with the same overlap as for the GFRP specimens. The first specimen, WC1, was wrapped with carbon fibre sheet while in the second specimen, PC1-20, the pre-tensioning grout had the same amount of EA as the second GFRP confined specimen.

GFRP confinement

Figure 5 shows the stress-strain relationship for the two GFRP specimens. Positive strain represents axial compression and negative strain represents lateral tension, as obtained from the averages of strain gauges on the surface of the jacket. No attempt was made to compensate for the effect of the overlap. The vertical axis shows the stress normalised with respect to the unconfined concrete strength f_{co}.

The lateral pre-tensioning strain developed in PG3-20 was around 6000 με. This also led to a modest expansion in the axial direction. This expansion may have been restrained by the glass fibres in the axial direction.

Strengths of 1.7 f_{co} and 1.4 f_{co} were achieved for PG3-20 and WG3, respectively. The failure of WG3 took place when the average lateral strain was around 6500 με (23 % mobilisation of the lateral confinement) whilst for PG3-20 the average lateral strain at failure was around 13000 με (46 % mobilisation of the lateral confinement).

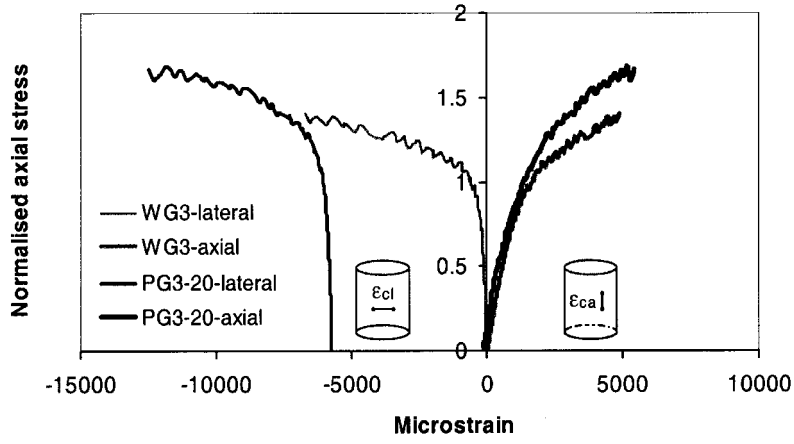


Figure 5. Stress-strain curve for WG3 and PG3-20 specimens

This represents a 100% increase in the utilisation of fibre. In another experiment[11], when 30% EA was used, a 100% utilisation of the glass fibre was achieved.

CFRP confinement

Figure 6 shows the stress-strain relationship for the two CFRP specimens.

The CFRP confined specimens had a similar behaviour to the GFRP confined specimens. The lateral pre-tensioning strain developed in PC1-20 was around 5300 με and this again led to a modest expansion in the axial direction. A strength enhancement of 2.10 f_{co} and 1.70 f_{co} was achieved by PC1-20 and WC1, respectively. The failure of both specimens took place when the average lateral strain in the carbon sheet was in excess of the 1.55% specified by the supplier. Again, there is a substantial difference in the level at which the confinement is mobilised. Hence, it is worth examining the volumetric strains of these specimens.

Volumetric strain

Figure 7 and Figure 8 show the normalised axial stress against the volumetric strain of specimens.

In both cases, at the initial stages of loading, the volume decreases until a critical stress level is reached. At this stage, volumetric dilation begins, which means that concrete cracking is developing rapidly. In the wrapped specimens the critical stress level was always below f_{co}. After this stress level, the strain in the confinement increases rapidly. In the pre-tensioned specimens, PG3-20 and PC1-20, the volumetric dilation is delayed by almost 35% of f_{co} and 50% of f_{co}, respectively.

This is an important advantage in seismic loading, since the damage in the concrete will be delayed and the reinforced concrete element will have a chance to dissipate more energy. In addition, concrete is actively confined even at service loads.

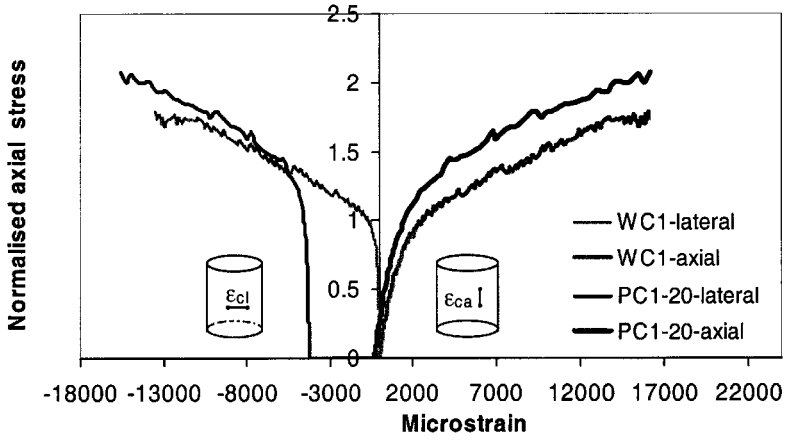


Figure 6. Stress-strain curve for WC1 and PC1-20 specimens

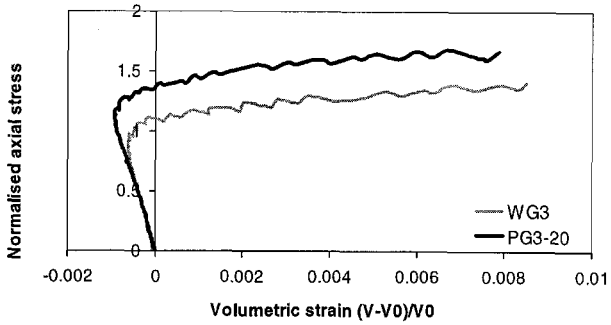


Figure 7. Normalised axial stress versus volumetric strain for WG3 and PG3-20 specimens

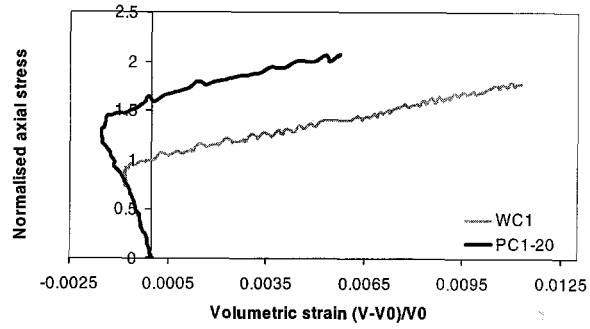


Figure 8. Normalised axial stress versus volumetric strain for WC1 and PC1-20 specimens

Failure mode

Failure was explosive due to the high strain energy stored by the FRP material. Figure 9(a) shows the failure of PG3-20 specimen and Figure 9(b) shows the failure of PC1-20 specimen.

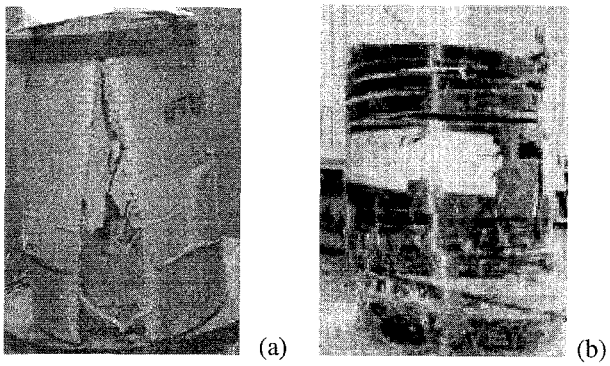


Figure 9. (a) Failure of PG3-20, (b) Failure of PC1-20

As shown in these figures, the mode of failure of the glass fibre confinement is completely different from that of the carbon. This is due to the bi-directional nature of the glass fibre wrapping which at failure has the effect of redistributing lateral strains over the full height of the specimen. In the case of carbon, the failure of the fibres at one location led to the rapid debonding of the filaments over the height of cylinder.

Discussion

Despite the fact that the same amount of EA was used to pretension the Carbon and Glass FRP jacket, the confined specimens behaved differently and achieved different strengths at different lateral and axial strains.

The pre-tensioning has led in both cases to up to 23% higher strengths than the wrapped specimens and, in the case of CFRP confined specimen, this led to the full utilisation of the confinement material.

What is of interest in these two pairs is that the ultimate axial strain appears to be significantly higher in the CFRP confined specimens. It is believed that this is partly due to the fact that the GFRP jackets slipped during testing. As a result, the true strain on the concrete core for GFRP confined specimens is expected to be higher than recorded on the jacket. In this particular case, for PG3-20 at failure, the axial concrete core strain recorded was 7300 με.

CONCLUSIONS

Pre-tensioning of the jacket led to higher strengths and a significant delay in the initiation of the fracturing process of the concrete through cracking. This is expected to lead to a better behaviour both at service loads and under cyclic loading, such as experienced during earthquakes.

ACKNOWLEDGEMENTS

The authors acknowledge the financial support of the Ministry of Energy of the Islamic Republic of Iran, the financial support of the EU for TMR Network ConFibreCrete and the Marie Curie Fellowship Grants HPMF-CT-2001-01279 and HPMF-CT-2002-01553.

REFERENCES

1. A A Mortazavi, K Pilakoutas and K S Son, 'RC column strengthening by lateral pre-tensioning of FRP', *Journal of Construction and Building Materials* (approved for publication 2003).
2. K Pilakoutas and A A Mortazavi, 'Laterally Pre-stressed Concrete with Composites', 5th int conf *Fibre-reinforced Plastics for Reinforced Concrete Structures*, Cambridge, Thomas Telford, 2001.
3. A A Mortazavi and K Pilakoutas, 'Pre-tensioning of Composites by Lateral Pressure', int conf *FRP Composites in Civil Engineering*, Hong Kong, Elsevier Science, 2001.
4. EC8, *Eurocode 8 - Design provisions for earthquake resistance of structures (Draft)*, ENV 1998-1-1, 1996
5. H Saadatmanesh, M R Ehsani and L Jin, 'Seismic strengthening of circular bridge pier models with fibre composite', *ACI Structural Journal*, 1996 **93**(6) 639-647.
6. M J N Priestley and F Seible, 'Design and seismic retrofit measures for concrete and masonry structures', *Construction and Building Materials*, 1995 **9**(6) 365-377.
7. K A Harries and G Kharel, 'Behaviour of modelling of concrete subject to variable confining pressure', *ACI Material Journal*, 2002 99(2) 180-189.
8. Betonamit, 'The non-explosive cracking agent for universal application', Kriscut Plant Hire & Sales co. Ltd, UK, 1998.

9. K Pilakoutas and A A Mortazavi, 'Ductility through external lateral confinement of RC members with FRP', 3rd int conf *Non-metallic (FRP) Reinforcement for Concrete Structures,* Sapporo, Japan Concrete Institute, 1997.
10. A A Mortazavi, '*Behaviour of confined concrete with variable lateral pressure*', PhD Thesis, The University of Sheffield, UK, 2003.
11. A A Mortazavi, K Pilakoutas, M A Ciupala, 'Lateral Prestressing of RC Columns with FRP Jackets', 6th int symp *Fibre-Reinforced Polymer Reinforcement for Concrete Structures*, Singapore, World Scientific, 2003.

EXPERIMENTAL BEHAVIOUR OF FRP-CONFINED SLENDER RC COLUMNS UNDER ECCENTRIC LOADING

Zhong Tao [1], J.G. Teng [2], Lin-Hai Han [1], L. Lam [2]

[1] *College of Civil Engineering and Architecture, Fuzhou University, Gongye Road 523, Fuzhou, Fujian Province, 350002, P. R. China*

[2] *Department of Civil & Structural Engineering, The Hong Kong Polytechnic University, Hong Kong, P. R. China.*

ABSTRACT

This paper presents the results of a recent experimental study aimed at investigating the performance of eccentrically-loaded long circular reinforced concrete (RC) columns strengthened with fibre reinforced polymer (FRP) jackets. Tests were conducted on eight un-strengthened RC columns and eight corresponding columns strengthened with FRP. The main variables explored in this test program include the slenderness ratio and the load eccentricity. The test results showed that FRP-strengthened long columns typically fail by buckling with excessive lateral deflections and with the FRP jacket remaining intact. Significant strength and ductility enhancements may still be expected but these improvements reduce with an increase in either the slenderness ratio or the load eccentricity.

INTRODUCTION

It is well known that the confinement of concrete with a fibre reinforced polymer (FRP) jacket can greatly enhance its strength and ductility. This beneficial effect of FRP confinement has been clearly demonstrated in tests on axially-loaded concrete cylinder specimens and short reinforced concrete (RC) columns [1-4]. In practice, RC columns are usually subjected to intentional or unintentional bending moments and may also be subject to the influence of slenderness. Most research on FRP retrofit of RC columns to date has focused on the seismic retrofit of short RC columns which are subject to cyclic lateral loads plus axial loads in which the FRP jacket is provided mainly as a remedy to shear, ductility and lap splice deficiencies [1,5-7]. A limited number of studies have addressed the strength of FRP-confined RC columns under eccentric loading [1, 8-13], but none of these has been concerned with long columns in which effect of slenderness is important. It is worth noting that the effect of slenderness generally becomes more important in a column confined with FRP. Indeed, FRP confinement may change a column initially classified as "short" to one which needs to be treated as "long" in evaluating its strength.

Against the above background, an experimental study was recently conducted on long columns strengthened with FRP jackets. This paper presents the test results and examines the performance of these FRP-confined columns with particular attention to the effects of slenderness and load eccentricity.

EXPERIMENTAL PROGRAM

General

A total of sixteen circular RC columns were tested in two series. All these columns had corbelled ends and a diameter of 150 mm in the test region, as shown in Figure 1. The total lengths of the columns including the end corbels were 1,200 mm for series I and 3,000 mm for series II, respectively. Each series consisted of four columns without FRP confinement (un-strengthened) and another four columns strengthened with two plies of carbon FRP (CFRP). The four columns of each type were tested under a compressive axial load with eccentricities (e_0) of 0, 50, 100, and 150 mm, respectively. Each series of columns was tested together with three standard plain concrete cylinders (150mm x 300mm) which were for the determination of the cylinder compressive strength of unconfined concrete. In addition, three plain concrete cylinders of the same size wrapped with two plies of CFRP were tested under axial compression to define the behaviour of FRP-confined concrete for comparison with results from the tests on FRP-confined RC columns.

Preparation of test specimens

All RC columns tested in this study had the same internal steel reinforcement as shown in Figure 1. Each column was longitudinally reinforced with four 12 mm deformed steel bars leading to a reinforcement ratio of 2.56%, while the transverse reinforcement consisted of 6 mm plain steel hoops with a centre-to-centre spacing of 100 mm in the test region. The tensile properties of the steel bars from tests are given in Table 1. All steel hoops were anchored with a 135° bend at each end, which extended approximately 60 mm into the concrete core as detailed in Figure 1. The anchorage zone of the steel hoop shifted clockwise along the length of the column to minimize the concentration of the local effect of the anchorage. The clear cover to the steel hoops was 15 mm. All specimens were vertically cast in steel moulds, with the concrete compacted using an external vibrator. The test specimens were cured in the laboratory environment until the day of testing.

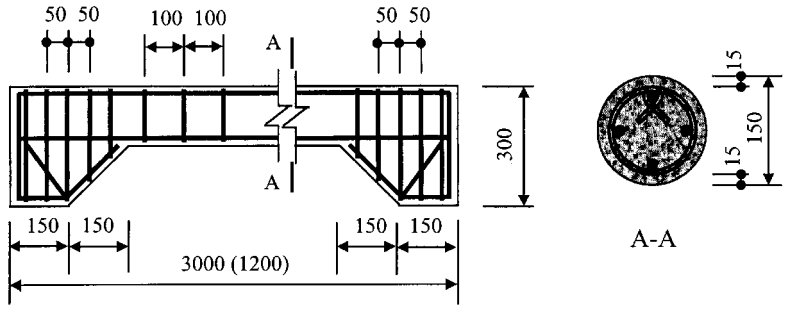


Figure 1 Details of the RC columns

Table 1 Material properties of steel reinforcement

Reinforcement	Elastic modulus (GPa)	Yield strength (MPa)	Yield strain (%)	Ultimate strength (MPa)	Ultimate strain (%)
Longitudinal	196	388.7	0.0020	557.9	0.122
Transverse	216	397.3	0.0019	548.1	0.143

Strengthening using CFRP

CFRP strengthening of columns was achieved by the external wrapping of unidirectional carbon fibre sheets after the concrete had been cured for more than 28 days, with the fibres oriented in the hoop direction. Prior to the wrapping operation, the surface of each specimen was ground, cleaned with water and left to dry. Surface voids were filled with epoxy putty. The finishing end of a sheet overlapped the starting end by 150 mm. The wrapped specimens were left to cure in the laboratory environment at room temperature for about one month before testing.

The tensile properties of the cured CFRP determined from tensile tests of flat coupons according to ASTM D3039 (1995) are given in Table 2, where the values presented are the averages from five test coupons calculated on the basis of the nominal thickness of 0.17 mm for the fibre sheet. The tensile properties of the epoxy as provided by the supplier are also given in Table 2.

Table 2 Material properties of CFRP and epoxy

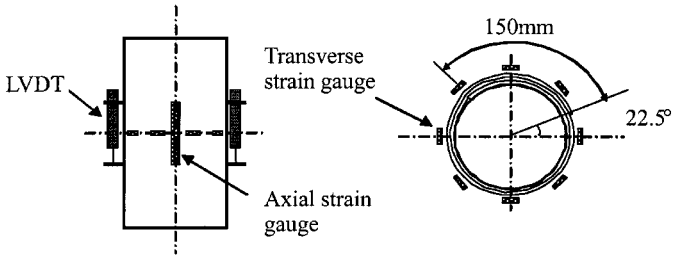
Material	Elastic modulus (GPa)	Tensile strength (MPa)	Ultimate strain (%)	Thickness (mm)
CFRP	255	4,212	1.67	0.170 (nominal)
Epoxy	2.8	48.3	3.1	–

Instrumentation and loading

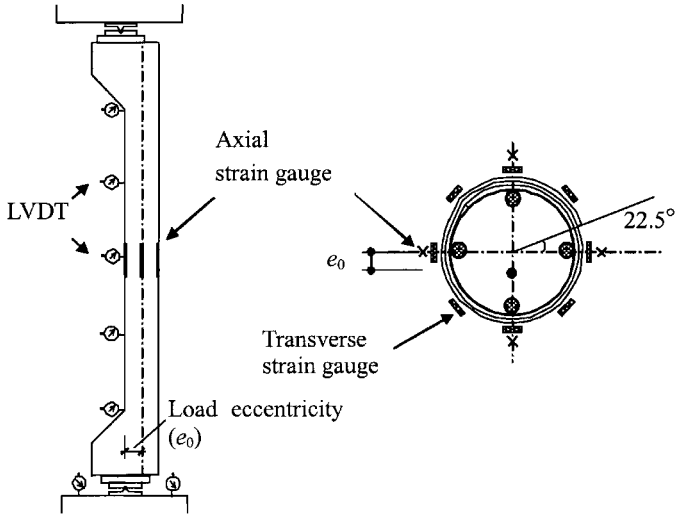
A 5,000 kN capacity testing machine was used for the compression tests of all specimens, and a computerized system was used for data logging. For each plain concrete cylinder, eight strain gauges with a gauge length of 20 mm and evenly distributed around the circumference were installed at its mid-height to measure the hoop strains of the FRP, while two strain gages with a gauge length of 120 mm were used for measuring axial strains (Figure 2a). In addition, two linear variable displacement transducers (LVDTs) at 180° apart covering the mid-height region of 120 mm were used to measure axial shortenings (Figure 2a). Both ends of a plain concrete cylinder specimen were capped with sulphur to produce even and parallel surfaces for uniform axial compression. Axial loading was applied at a rate of approximately 0.24 MPa per second until failure.

For each RC column, eight strain gauges with a gauge length of 3 mm were installed to measure the strains of internal reinforcing bars at the mid-height of the column: four for the four longitudinal bars and another four for a steel hoop. Furthermore, twelve strain

gauges were installed on the surface of each column in the mid-height region, including four gauges with a gauge length of 120 mm for axial strains centred at the mid-height of the column and eight gauges with a gauge length of 20 mm for hoop strains. Of the eight strain gauges for hoop strains, four had the same circumferential positions as the four longitudinal strain gauges so they were installed adjacent to one of the ends of the axial strain gauges. Axial loading was applied through V-shape edges to each column which was installed with steel caps at both ends prior to loading. Grooves of 6 mm in depth were machined on each steel cap to receive the V-shape loading edge so that the load eccentricity could be precisely controlled. The effective length of the column L_0, defined as the distance between the tips of the V-shape edges, was 1,260 mm for the first series of columns and 3,060 mm for the second series. The slenderness ratios of these two series of columns, defined as the ratio between the effective length L_0 and the diameter of the column d, are 8.4 and 20.4 respectively. The axial load was applied at a rate of 2-5 kN/min before the peak load was reached.



(a) CFRP-wrapped cylinder



(b) RC column

Figure 2 Layout of strain gauges and LVDTs

TEST RESULTS AND DISCUSSION

Plain concrete cylinders

Plain concrete cylinders tested at the time of RC column tests showed that the compressive strengths of unconfined concrete for both series of columns were very close, with an average value of 48.2 MPa at an average axial strain of 0.0024.

All three CFRP-wrapped concrete cylinders showed eventual failure by the sudden rupture of the FRP jacket. The stress-strain responses of FRP-confined concrete from these three tests are shown in Figure 3, where tensile hoop strains are taken to be negative while compressive axial strains are taken as positive. In plotting these curves, the hoop strain was found by averaging the readings of the strain gauges outside the overlapping zone, while the axial strain was averaged from the two LVDTs. The average compressive strength and ultimate axial strain of FRP-confined concrete from these three cylinders wrapped with two-plies of CFRP are 102.8 MPa and 0.0243 respectively. The strain gauges for measuring hoop strains debonded prematurely from the FRP jacket before the peak load was reached, and this is why the axial stress-hoop strain curves shown in Figure 3 terminate at loads below the peak loads. For the same reason, the hoop rupture strains could not be accurately determined.

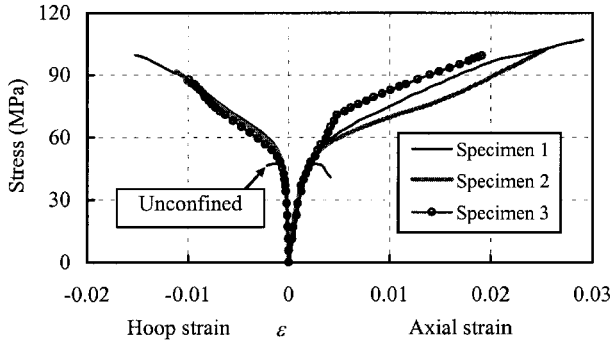


Figure 3 Stress-strain curves from tests on FRP-confined cylinders

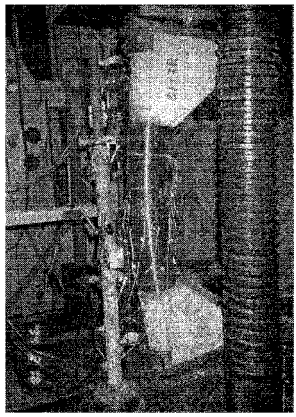
RC columns

The test results of the RC columns are summarized in Table 3, where the strain ε_{cc} at peak load was from the strain gauge located at the extreme compression fibre. All RC columns, with or without CFRP wrapping, failed in a typical flexural mode with large lateral deflections, except specimen C1-1U. Column C1-1U failed in a brittle manner, characterized by the compressive crushing of concrete. This column was thus dominated by the compressive failure of concrete, although significant bending deformations had developed at the time of failure. For all other un-strengthened columns, spalling of compressive concrete was observed after the peak load had been attained. By contrast, in the FRP-confined columns, no concrete spalling was observed due to the presence of an FRP jacket. In addition, rupture of the FRP jacket due to hoop tension which is the

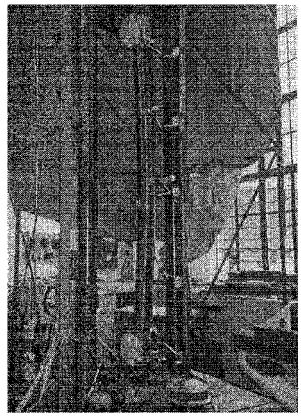
expected failure mode for FRP-confined concrete cylinders and short RC columns, was not observed in these tests even when the specimens were loaded into large deformations. Figure 4 shows typical failure modes of FRP-confined RC columns from both series of tests.

Table 3 Test results of RC columns

Series	Column	L_0 (mm)	L_0/d	e_0 (mm)	Peak load, N_u (kN)	*Strain at peak load* ε_{cc} (με)	*Strengthening ratio* (%)
I	C1-1U	1,260	8.4	0	455	3,104	—
	C1-1S			0	765	13,753	68.1
	C1-2U			50	149	3,095	—
	C1-2S			50	248	5,312	66.4
	C1-3U			100	88	2,631	—
	C1-3S			100	124	5,520	40.9
	C1-4U			150	54.5	—	—
	C1-4S			150	77	8,513	41.3
II	C2-1U	3,060	20.4	0	276	1,814	—
	C2-1S			0	386	2,294	39.9
	C2-2U			50	108	2,494	—
	C2-2S			50	126	2,862	15.0
	C2-3U			100	62.5	2,997	—
	C2-3S			100	71.5	3,253	14.4
	C2-4U			150	39	2,121	—
	C2-4S			150	47.5	5,556	21.8



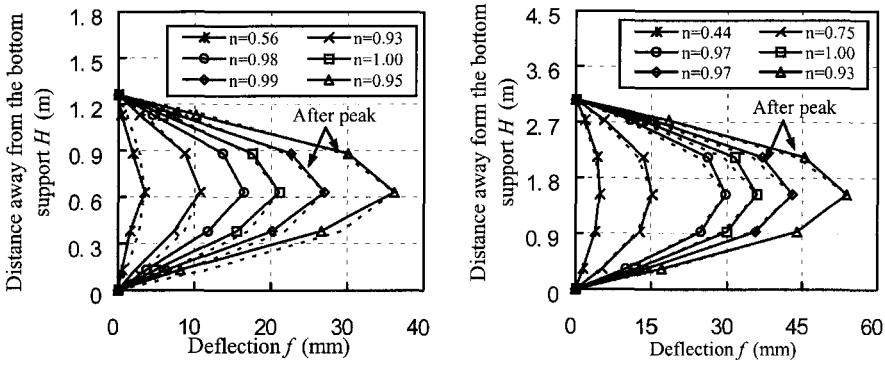
(a) Series I column



(b) Series II column

Figure 4 Typical failure modes of FRP-confined RC columns

The lateral deflections of the columns found from LVDTs are approximately in the shape of a sine half-wave. This observation is illustrated in Figure 5 where the measured deflections of columns C1-2R and C2-2R are compared with corresponding sine curves shown as dashed lines for different levels of axial loads before and after failure. The axial load levels are represented by the axial load ratio n which is defined as the ratio of the applied load to the ultimate axial load N/N_u.



(a) Column C1-2S (b) Column C2-2S

Figure 5 Deflected shapes of columns under different load levels

The axial load (N) is shown against the mid-height lateral deflection (u_m) for all test columns in Figure 6. As expected, an increase in the load eccentricity or slenderness (i.e. the L_0/d ratio) results in a decrease in the failure load as well as an increase in the mid-height deflection at failure, for both wrapped and un-wrapped specimens. It is observed from Figure 6 that the strengthened specimen exhibited a higher flexural stiffness compared with its un-strengthened counterpart. This difference in stiffness is attributed to the high tensile strength of epoxy compared to concrete and hence the less severe tensile cracking in the strengthened specimen, and the effect of FRP confinement on the compressive concrete. The wrapped columns are also seen to show more ductility than their un-wrapped counterparts, and this effect is more pronounced in the shorter columns (Figure 6).

Enhancements in the axial load capacity due to FRP wrapping can be easily gauged using the strengthening ratio defined as the percentage increase in the ultimate load. For the present columns, this ratio varies from 14% to 68%, as listed in Table 3.

Figure 7 shows that both the slenderness ratio and the load eccentricity have a significant effect on the strengthening ratio: this ratio reduces as the column becomes more slender or the load eccentricity increases, as a result of bending becoming more dominant and confinement less effective at the time of failure. However, the strengthening ratio varies little with the load eccentricity when e_0/d exceeds a certain value, and this value depends on the slenderness of the column. This phenomenon is easy to understand, as the behaviour of columns with a sufficiently large load eccentricity is dominated by bending.

Figure 8 shows the effect of FRP confinement on the axial strain at peak load ε_{cc}. It can be seen in Figure 8 and Table 3 that the value of ε_{cc} measured in a wrapped RC column is larger than that of the un-wrapped counterpart, especially for shorter specimens. Nevertheless, it is much smaller than that observed in cylinder compression tests. This demonstrates that the strength of the FRP jacket cannot be fully utilised in long columns as buckling failure occurs with the FRP jacket remaining intact. As a result, the strength enhancement resulting from the FRP jacket for a long RC column may be much less than can be expected for a short column.

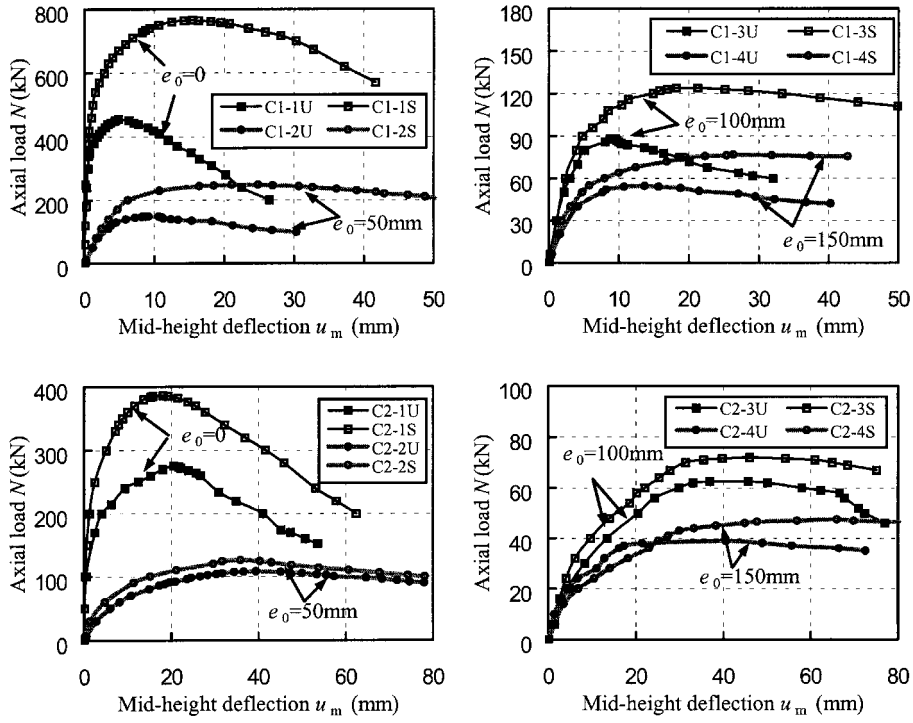


Figure 6 Load-deflection curves

Figure 9 shows typical distributions of hoop strains at peak load measured on un-strengthened and strengthened RC columns. In this figure, tensile strains ($\mu\varepsilon$) are taken to be positive and shown outside the circle representing the perimeter of the column while negative strains are shown inside the circle. The strain distributions in un-strengthened columns are shown as dashed lines while the corresponding distributions in strengthened columns are shown as solid lines. It is observed that in the strengthened columns, the FRP jacket was in tension in the hoop direction in the region where the concrete was in axial compression, but was often in hoop compression in the region where the concrete was in tension. In the un-strengthened columns, the hoop strains measured on the concrete surface showed a similar trend. Larger tensile strains were developed in the FRP jacket for columns with a smaller slenderness ratio and a

smaller load eccentricity, although these strain values are much less than may be found from FRP-wrapped cylinder tests, once again confirming that the FRP jackets were not fully mobilized in these columns.

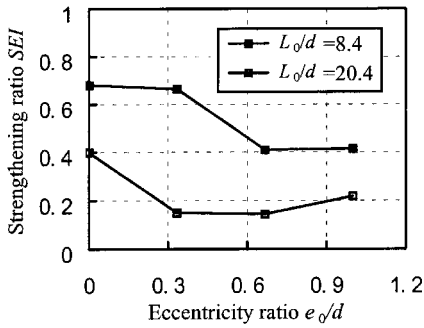


Figure 7 Effects of slenderness and load eccentricity on strengthening ratio

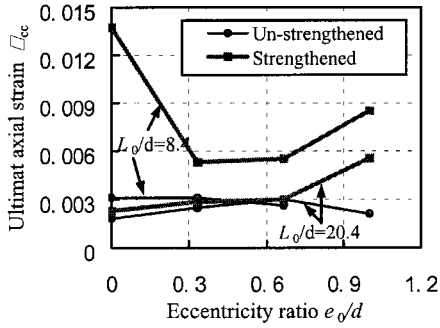
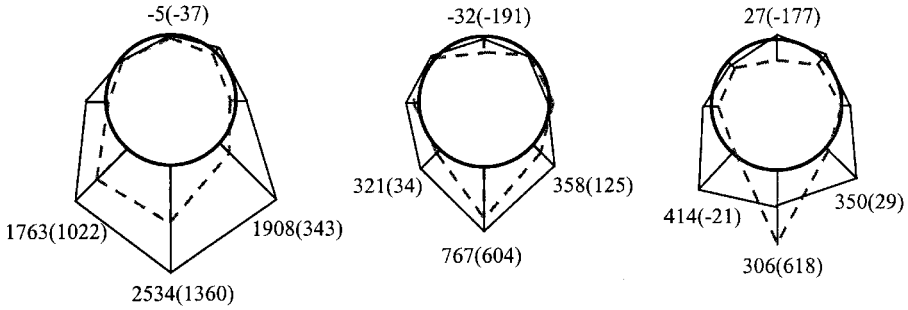


Figure 8 Effect of FRP jacket on ε_{cc}



(a) Specimens C1-3U and C1-3S (b) Specimens C2-3U and C2-3S (c) Specimens C2-4U and C2-4S

Figure 9 Hoop strain distributions at column mid-height

CONCLUSIONS

This paper has presented the results of a recent experimental study aimed at investigating the performance of eccentrically-loaded long circular reinforced concrete (RC) columns strengthened with fibre reinforced polymer (FRP) jackets. Tests were conducted on eight un-strengthened RC columns and eight corresponding columns strengthened with FRP. The main variables explored in this test program include the slenderness ratio and the load eccentricity. The test results showed that the FRP-strengthened long columns typically fail by buckling with large lateral deflections and with the FRP jacket remaining intact. Significant strength and ductility enhancements may still be expected but as expected, these improvements reduce with

an increase in either the slenderness ratio and/or the load eccentricity.

ACKNOWLEDGEMENTS

The authors are grateful for the financial support received from the Science and Technology Development Funds of Fuzhou University (2002-XQ-19), the Research Grants Council of the Hong Kong Special Administrative Region (Project No: PolyU 5064/01E) and The Hong Kong Polytechnic University provided through its Area of Strategic Development (ASD) Scheme for the ASD in Urban Hazard Mitigation.

REFERENCES

1 J G Teng, J F Chen, S T Smith, L Lam, *FRP-Strengthened RC Structures*, John Wiley & Sons, Ltd., 2002.

2 K H Tan, 'Strength enhancement of rectangular reinforced concrete columns using fiber-reinforced polymer', *Journal of Composites for Construction,* ASCE, 2003 **6**(3) 175-83.

3 G Campione, 'The effects of fibers on the confinement models for concrete columns', *Canadian Journal of Civil Engineering*, 2002 **29** 742-50.

4 Y C Wang, J I Restrepo, 'Investigation of concentrically loaded reinforced concrete columns confined with glass fiber-reinforced polymer jackets', *ACI Structural Journal*, 2001 **98**(3) 377-385.

5 A Nanni, M S Norris, 'FRP jacketed concrete under flexure and combined flexure-compression', *Construction and Building Materials,* 1995 **9**(5) 273-281.

6 F Seible, M J N Priestley, G A Hegemier, D Innamorato, 'Seismic retrofit of RC columns with continuous carbon fiber jackets', *Journal of Composites for Construction*, ASCE, 1997 **2**(1) 52-62.

7. Y Xiao, R Ma, "Seismic retrofit of RC circular columns using prefabricated composite jacketing", *Journal of Structural Engineering,* ASCE, 1997 123(10), 1357-1364.

8 H Saadatmanesh, M R Ehsani, M W Li, 'Strength and ductility of concrete columns externally reinforced with fiber composite straps', *ACI Structural Journal*, 1994, 96(4), 500-9.

9 A Parvin, W Wang, 'Behavior of FRP jacketed concrete columns under eccentric loading', *Journal of Composites for Construction*, ASCE, 2000 **5**(3): 146-52.

10 O Chaallal, M Shahawy, 'Performance of fiber-reinforced polymer-wrapped reinforced concrete column under combined axial-flexural loading', *ACI Structural Journal*, 2000 **97**(4) 659-68.

11 H L Cheng, E D Sotelino, W F Chen, 'Strength estimation for FRP wrapped reinforced concrete columns', *Steel & Composite Structures- An International Journal*, 2002 **2**(1) 1-20

12 J Li, M N S Hadi, 'Behaviour of externally confined high-strength concrete columns under eccentric loading', *Composite Structures*, 2003 **62**(2) 145-53.

13 A Fam, B Flisak, S Rizkalla, 'Experimental and analytical modeling of concrete-filled fiber-reinforced polymer tubes subjected to combined bending and axial loads', *ACI Structural Journal*, 2003 **100**(4) 499-509.

BOND ANALYSIS OF MASONRY STRUCTURES STRENGTHENED WITH CFRP SHEETS

M A Aiello, S M Sciolti

Department of Innovation Engineering, University of Lecce, Via per Arnesano 73100 – Lecce Italy.

ABSTRACT

The use of Fibre Reinforced Polymer (FRP) plates and sheets for strengthening masonry structures is a promising technique but further investigations are needed in this area in order to accomplish design requirements. The FRP materials have advantages over steel plates and strips in that they are characterized from a high strength to weight ratio, no electrochemical corrosion problem and ease of erection on site.

Of vital importance in joining two components together is the bonding performance between two very different adherents, as masonry and FRPs. The bond properties will determine the degree of effectiveness of the structural system. A considerable world wide effort has been expended into investigating the bond characteristics between RC elements and composite materials but little work has been undertaken in the sphere of masonry structures.

The present paper reports on part of a research project, still in progress, devoted to the analyses of the bonding characteristics between FRP sheets and typical natural stones utilized for masonry structures in Southern Italy. The test procedure will be given and the results obtained from bond performance will be discussed. Two commercially available CFRP sheets and two different types of masonry blocks have been used in the first stage of the analysis. Bond stresses at the interface between the two adherends have been evaluated and slip values determined.

The influence of the anisotropy of the masonry material has also been considered as well as the bond length parameter.

INTRODUCTION

Reinforcing techniques for strengthening or retrofitting existing structures, using steel plates or Fiber Reinforcing Plastic (FPR) sheets glued to structural members, are the object of several studies presented in the literature. Numerous researches addressed the analysis of bond referring to concrete elements strengthened with steel plate or FRP materials.

Currently, there is an awareness of the use of FRP plates for repair and/or strengthening masonry structures [1, 2, 3, 4]. This technique is not invasive because the reinforcing element is removable; moreover, it has the advantage over steel of a high specific strength and stiffness, ease of erection and corrosion free.

One of the most important aspects to take into account in utilizing steel or composite plate material for strengthening structural members is the adhesion between the two adherends. This might affect the fiber, the adhesive layer and a very thin layer of reinforced material.

These phenomena, and generally the problems related to the reinforcing techniques, have been widely discussed in the last decades for concrete structures [5]; but only in the last few years, the use of these materials in masonry structures has been addressed,

representing a monumental and historical heritage in many European countries [6, 7, 8, 9, 10, 11].

In this context the present investigation refers to the study of the bond between Carbon Fiber Reinforced Polymer (CFRP) and calcarenite ashlars; calcarenite is the most common stone utilized in the construction of masonry structures in Southern Italy.

The study was carried out through an experimental investigation on *naples tuff* and *leccese stone* specimens reinforced with CFRP sheets, glued onto the surface of the stones. Tensile tests were carried out, varying the bond length of the reinforcement, the specification of the FRP sheet, the type of stones, the strengthening procedure and finally anchoring the reinforcement by transverse FRP strips.

The test apparatus and the test procedure have been studied in detail and have been made and improved; and first results, which have been obtained, have been reported [7, 8]. The progress of the research work, related to the first stage of the investigation, is presented in this paper.

EXPERIMENTAL INVESTIGATION

In the present section results of the experimental investigation carried out to characterize material behaviour, particularly related to mechanical properties of masonry stones and of CFRP are reported. Therefore results of bonding tests performed on CFRP sheets bonded to calcarenite ashlars are presented. In particular the affect of the strengthening typology is analysed.

Electrical resistance strain gages have been bonded to the sheet surface, in the longitudinal and transverse direction, in order to evaluate the strain distribution within the reinforcement at each load step up to debonding of the FRP from the stone blocks. Through simple equilibrium considerations, bond stresses at the interface have been evaluated and slip values have been determined.

Mechanical properties of constituent materials

Mechanical properties of materials have been experimentally evaluated. Two kinds of stone have been analysed. Both are calcareous and are utilized in some regions of Italy: the first is called "*Leccese stone*" and the second is the "*Naples tuff*". Two kinds of CFRP sheets have been used, referred to as FRPA and FRPB. The measured mechanical properties are summarized in Tables 1 and 2. More details about tests procedures are reported in a previous study [7, 8]. The anisotropy of the *Leccese stone* has been taken into account; in fact tests have been performed both on specimens loaded in perpendicular direction and in parallel direction with respect to the stratification layers of the limestone.

The tangent elastic modulus has been obtained at a stress level equal to 50% of the ultimate stress; the mean elastic modulus refers to the linear part of the stress-strain curve, the secant elastic modulus refers to the stress level between zero and 50% of the ultimate stress.

Table 1: Mechanical properties of the stones

			Average value	COV
Compressive strength [MPa]	*Leccese stone*	loaded in perpendicular direction	22	11%
		loaded in parallel direction	26	9%
	Naples tuff		5	9%
Flexural strength [MPa]	*Leccese stone*	loaded in perpendicular direction	7	17%
		loaded in parallel direction	4	17%
	Naples tuff		2	27%
Tangent elastic modulus E_t[MPa]	*Leccese stone*	loaded in perpendicular direction	6580	24%
		loaded in parallel direction	8932	12%
	Naples tuff		3012	18%
Mean elastic modulus E_m[MPa]	*Leccese stone*	loaded in perpendicular direction	6884	15%
		loaded in parallel direction	9407	20%
	Naples tuff		2990	16%
Secant elastic modulus E_s[MPa]	*Leccese stone*	loaded in perpendicular direction	8075	28%
		loaded in parallel direction	9630	11%
	Naples tuff		3047	14%

Table 2: Mechanical properties of the FRP sheets

		Average value	COV
Tensile strength [MPa]	FRPA	3846	12%
	FRPB	4458	8%
Young's modulus [MPa]	FRPA	234000	10%
	FRPB	246000	4%

Bonding tests

Bonding tests were undertaken as a type of double lap shear test, in which the reinforcing sheet was bonded onto two opposite sides of the calcarenite blocks measuring 100 x 100 x 250 mm. Each specimen was inserted into a steel box fixed to the bottom of the testing machine. The free end portions of the sheet were fixed on the other side in a special grip of the testing machine and a tensile force was applied. To apply the load a pin was inserted thorough a drilled hole in the sheets. Figure 1 illustrates the set-up and is self explanatory.
Different bond lengths of L=70 mm and L=150 mm were utilised in this experiment. The specimens reinforced with FRPA sheets and having a bond length of 150mm, were tested varying also the strengthening typology. Details regarding the tested specimens are reported in Table 3. The labels that identify the specimens, the final letter "*f*" identifies the specimens strengthened with CFRP sheets and anchored with transverse FRP strips.

Figure 2 shows the position of the electrical resistance strain gauges bonded to both sides of the sheet in the longitudinal direction; a transverse gauges was bonded on to one sheet only to record any eccentricity. The slip between the stone and the composite sheet, at the loaded end, was recorded by a displacement transducer.

TEST RESULTS AND DISCUSSION

Theoretical relationship has been calibrated by the bond stress-slip law proposed from *fib* provisions (CEB-FIP, 2001) and the effectiveness of available theoretical models referring to the service conditions has been checked. Analyzing the results obtained in which the bonded length was varied it has been found that the transfer length is greater than 70 mm. Depending on the kind of stone, the strains distribution,

the bond stress-slip law, the ultimate load as well as the type of failure may vary. In particular the interface stiffness and the bond strength for the *leccese stone* is higher than for *naples tuff*. Considering the effect of the position of the bonded length within the specimens, it has influence on the tests results. This consideration underlines the need of further investigation in order to define a standard bond test able to furnish reliable design indicators. As regards the theoretical analysis, it has been observed that the bond stress-slip law proposed by *fib*, referring to FRP reinforced concrete structures, it appears to be relevant for predicting the interface behavior of FRP strengthened masonry structures. In addition, simplified theoretical models utilized to predict the strains distribution within the composite sheets at the service conditions, gives satisfactory results, assuming mechanical and geometrical properties are accurately defined.

As regard the failure condition, a sudden loss of bearing capacity and a complete detachment of the sheets, together with a layer of calcarenite stone, occurred. In the *Leccese stone* the delamination of the sheet caused, the detachment of a very thin layer of stone. In the *Naples tuff*, however, delamination occurred causing crushing of a thick stone layer, as shown in Figure 3. All test results are summarized in Table 4, where *Fu* is the load value at collapse, τ_{max} is the maximum bond stress experimentally evaluated at the loaded end, *Lo* the transfer length, $\sigma = F_u/(b \times t)$ is the normal stress within the FRP sheet, where *b* and *t* are the width and the thickness of the sheet, respectively, and $\tau_{med} = F_u/(b \times L)$ the average bond stress.

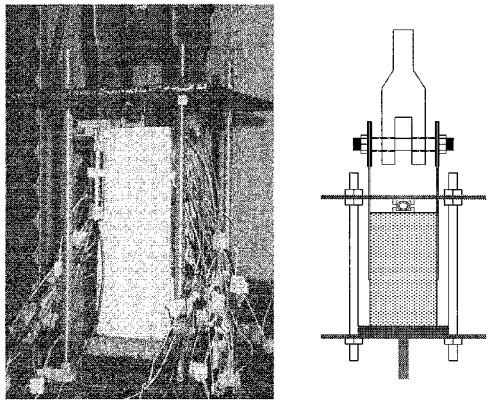


Figure 1: Test apparatus

Table 3: Details of tested specimens

	FRPA		FRPB	
	L=150mm	L=70mm	L=150mm	L=70mm
Leccese stone	150PLA1	70PLA1	150PLB1	70PLB1
	150PLA2	70PLA2	150PLB2	70PLB2
	150PLA1f	---	---	---
	150PLA2f	---	---	---
	---	---	150PLB1s	---
	---	---	150PLB2s	---
Naples tuff	150TA1	---	150TB1	---
	150TA2	---	150TB2	---
	150TA1f	---	---	---
	150TA2f	---	---	---

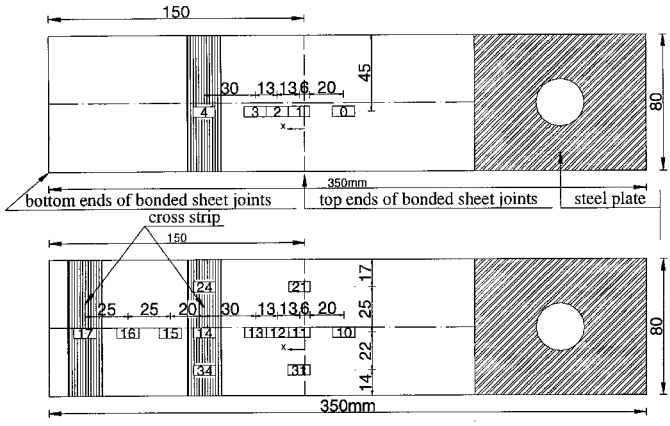


Figure 2: Strain gauges positions

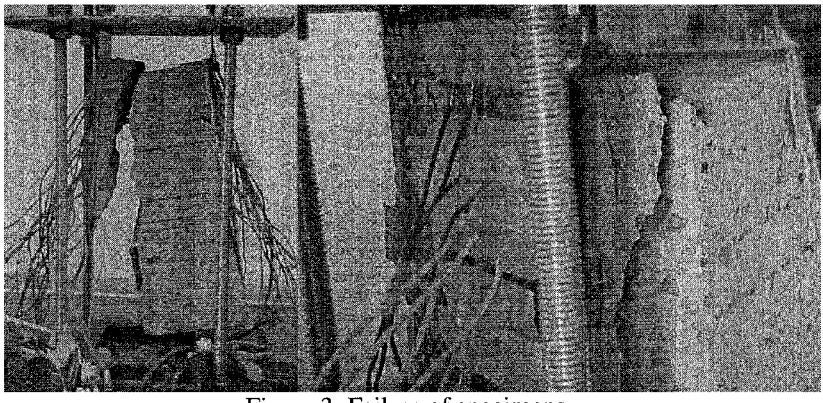


Figure 3: Failure of specimens.

Table 4: Test results

Specimen	F_u [kN]	σ_l [MPa]	τ_{med} [MPa]	τ_{max} [MPa]	L_o	Specimen	F_u [kN]	σ_l [MPa]	τ_{med} [MPa]	τ_{max} [MPa]	L_o
150PLA2*	10,81	819	0,90	5,63	100						
70PLA1	7,56	539	1,27	3,64	>50	150TB1	8,96	605	0,67	---	90
70PLA2	9,08	667	1,57	4,74	>50	150TB2	7,17	489	0,54	2,04	110
150PLB1	9,08	599	0,67	5,92	85	150PLA1f	8,42	631	0,70	1,60	94
150PLB2	9,41	626	0,70	---	90	150PLA2f	8,52	638	0,71	1,62	101
70PLB1	8,98	662	1,58	4,08	>50	150TA1f	6,69	501	0,56	---	---
70PLB2*	9,21	667	1,59	---	>50	150TA2f	6,28	470	0,52	---	---
150TA1	8,09	634	0,70	1,55	120	150PLB1s	13,20	1000	1,10	9,15	73
150TA2	7,88	527	0,58	1,85	130	150PLB2s	12,50	947	1,04	8,01	69

**premature crisis of the specimens before bond failure*

For each specimen the strain values in the transverse direction, recorded on the sheet at the same positions, do not show significant scatters, confirming satisfactory test set-up. The Figure 4 givesthe typical strain paths along the sheet, at various load levels, for certain tested specimens. The strains reported in this figure are the average value of those on the two sides of specimens and forsimilar specimens.

The results of Figure 4 show that the strain distributions at low loads tend to be exponential, also for the specimens anchored with transverse FRP strips. Increasing load, and particularly as failure approaches, the strain distributions become much more non-uniform and non-linear; near the loaded end the strain distribution appears almost uniform indicating a local debonding. The debonding zone increases progressively and the stresses transfer mechanism shifts along the sheet.

The presence of transverse FRP strips seem to improve the bond performance at high load level, in fact the strain patterns appears different from that of specimens without transverse FRP strips. In particular when transverse reinforcement is added a more effective distribution of strains over the whole length of the sheet is observed, thus reducing the decay of the bond performance near the loaded end.

In the Figure 5 results obtained for specimens, with transverse FRP strips are compared with those of similar specimens without transverse FRP strips in terms of strain pattern along the sheet at different load level, up to 50% of the ultimate load (150PLA-150PLAf and 150TA-150TAf). Analysing diagrams it seems that the application of transverse FRP strips did not result in any significant change on deformation values, however a more effective distribution of strains is again confirmed. Probably this result is due to the short length of transverse FRP strips utilized, further investigations are suggested to confirm this last consideration.

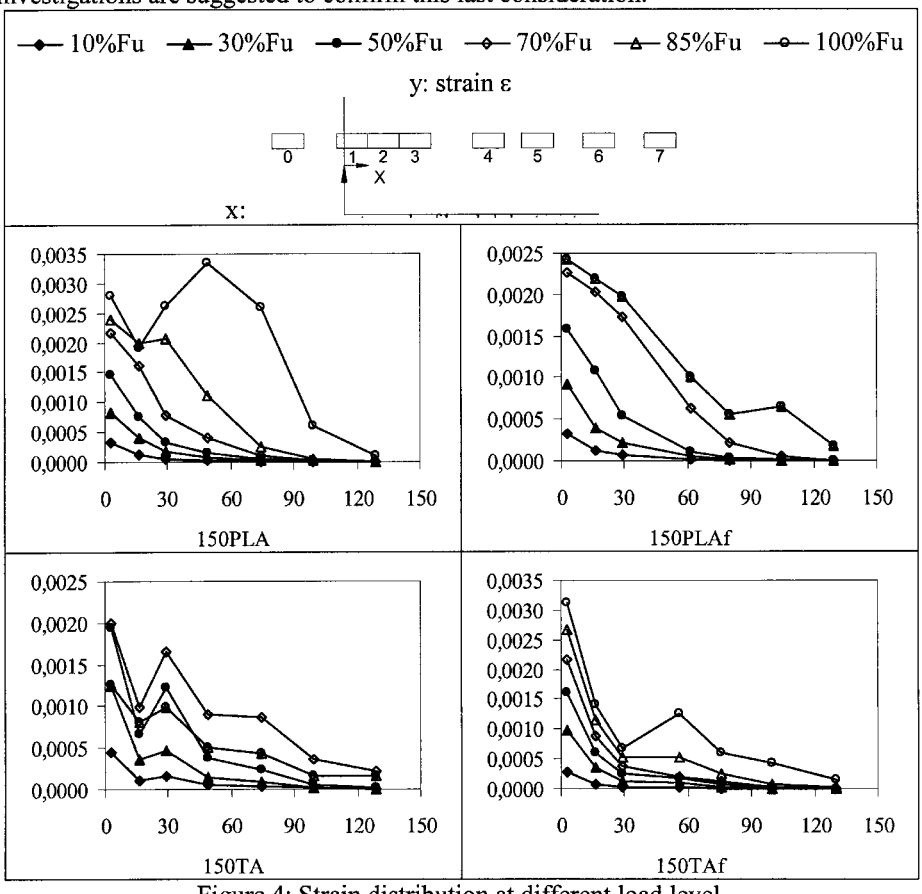


Figure 4: Strain distribution at different load level.

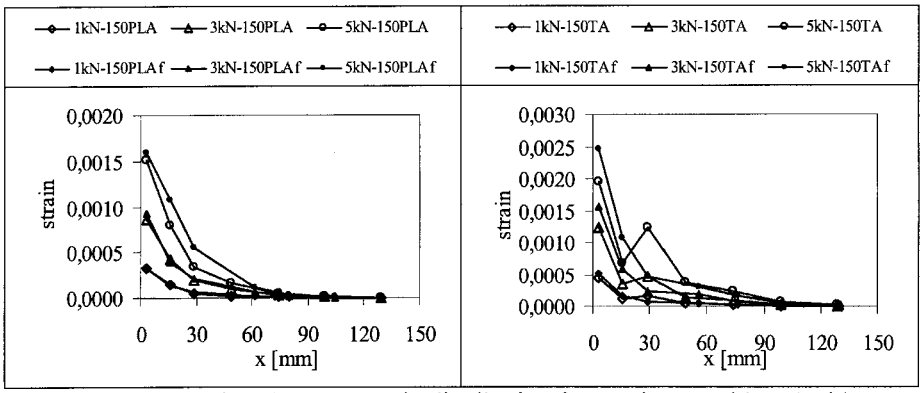


Figure 5: Comparison between strain distribution for specimens with and without transverse FRP strips.

The bond stresses distribution within the reinforcement has been evaluated imposing the equilibrium condition of the sheet with reference to a length Δx that is the distance between two contiguous strain gages positions, $\tau(x)=t\times E_l\times\frac{\varepsilon_i-\varepsilon_{i+1}}{x_{i+1}-x_i}$, where t=sheet thickness; ε_i, ε_{i+1}=strain values in correspondence of two contiguous strain gages; x_i,x_{i+1}=position of two contiguous strain gages measured from the loaded end of the specimen; E_l= elastic modulus of the sheet, determined on the basis of strain values registered on the unbonded sheet of the tested specimens, as reported in more details in other studies [7, 8].

In the Figure 6 the shear stresses versus applied load as a percentage of the ultimate load are plotted at different strain gauge (sg) positions (see also Figure 2 and Figure 4). Curves show as at low load level the stress is almost completely transferred to a small length of the sheet, near the loaded end; when the applied load increases and the de-bonding at the loaded end starts, the transfer length of the sheet increases too; therefore, a longer part of the sheet is involved in the stress transfer mechanism and the peak of the shear stress shifts along the reinforcement.

Neglecting the natural stone strains and assuming the slip is zero at the unloaded end of the sheet, the slip, *s*, at the loaded end, between FRP and masonry can be numerically determined, $s=\sum_i \varepsilon_{l_i}\times\Delta x_i$,being ε_l the recorded strain and Δx_i the sheet element between to contiguous strain gages.

In the Figure 7 typical curves for bond stress-slip are reported for *Leccese stone*. The results show that the behaviour at the interface is characterized by the following steps: at the first stage an elastic behavior is observed and a perfect bond exists between sheet and stone; after the attainment of the peak bond stress it follows a softening branch that ends with a residual bond stress, due to the friction contribution.

In Figure 8 the applied load versus the slip value is reported for a 150PLB1 specimen referring to the ascending branch. The curve obtained when the slip is evaluated by integrating the strains along the sheet is compared with that for the slip values measured by the displacement transducer. A good agreement between the two curves can be observed, evidencing a negligible influence of the interface deformability on the slip values. The reported results relate to the stage before the detachment starting.

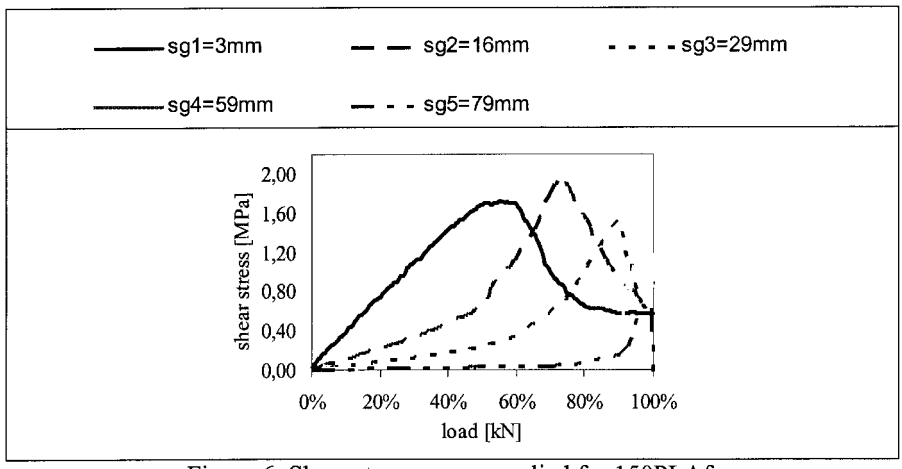


Figure 6: Shear stress versus applied for 150PLAf.

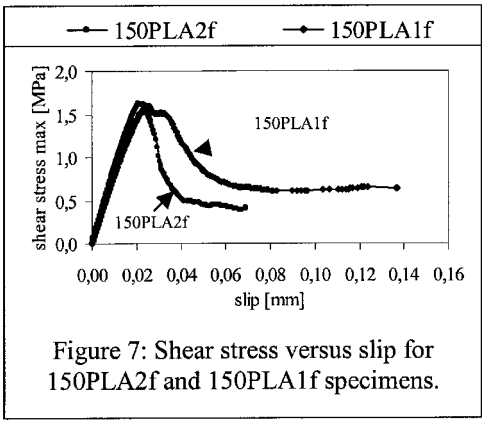


Figure 7: Shear stress versus slip for 150PLA2f and 150PLA1f specimens.

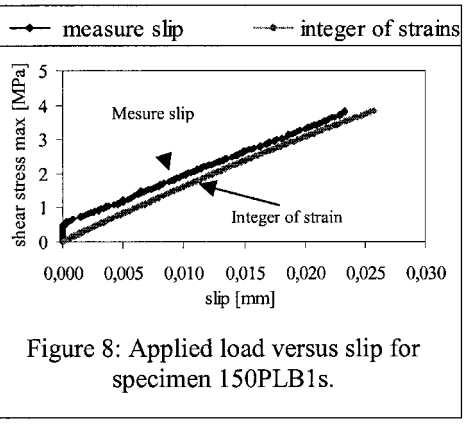


Figure 8: Applied load versus slip for specimen 150PLB1s.

CONCLUSIONS

Results obtained by an experimental analysis aimed to study bond performance between FRP sheets and masonry stones have been reported in the paper. The performed experimental investigation is part of a wider planned research program. On the basis of obtained results it would seem that the transfer mechanism between the masonry and the reinforcement is similar to that obtained for the case of concrete substrate. In fact, the strains path along the sheets varies from an exponential trend, at low load level, to an irregular and ill-defined law, when load increases. The application of transverse FRP strips does not show an improvement in terms of bond strength and strain values; however an improvement of strain distribution along the sheet has been observed. Further analyses are suggested in this area, considering the opportunity of increasing the transverse strips length.

As regard the bond stress-slip laws, it seems that the interface deformability, in the analyzed cases, is very low and therefore the utilized system enough effective.

The progress of the wider experimental investigation should allow a more accurate analysis of the influence of all parameters involved in the bond performance between masonry and composite reinforcement, taking into account also the durability of the system under typical service conditions.

REFERENCE:

1 Avorio A, Borri A, 'Problemi di Collegamento tra Materiali FRP e Strutture Murarie', int conf *Mechanics of Masonry Structures Strengthened with FRP Materials: Modeling, Testing, Design, Control*, Venezia, Italy, 2000.

2 Avorio A, Cecchetti M V, 'Applicazione di FRP su archi e volte in muratura: il caso della chiesa di San Filippo Neri di Spoleto', int conf *Mechanics of Masonry Structures Strengthened with FRP Materials: Modeling, Testing, Design, Control*, Venezia, Italy, 2000.

3 La Tegola A, De Lorenzis L, Micelli F, 'Applications of FRP Materials for Repair of Masonry Structures', *Technology Transfer Seminar Advanced FRP Materials for Civil Structures*, Bologna, Italy, 2000.

4 Nart M., 'Masonry domes strengthened with FRP', int conf *Composites in Constructions – CCC2003*, Cosenza, Italy, Editoriale Bios, 2003.

5 Aiello M A, Pecce M, 'Experimental Bond Behavior between FRP Sheets and Concrete', int conf *Structural Faults and Repair Conference*, London, 2001, on CD.

6 Aiello M A, Galati N, La Tegola A, 'Bond Analysis of Curved Structural Concrete Elements Strengthened using FRP Materials', 5nd int conf *Non- metallic reinforcement for Concrete Structures*, Cambridge, 2001.

7 Aiello M A, Sciolti M S and Pecce M, 'Experimental investigation on bond between FRP sheets and natural masonry blocks', int conf *Structural Faults & Repair- 2003*, London, UK, 2003, on CD.

8 Aiello M A and Sciolti M S, 'Masonry Structures Strengthened with FRP Sheets: the Interface Behaviour', 6nd int cof *Materials Science and Restoration MSR VI*, Karlsruhe, 2003, on CD.

9 Casareto M, Oliveri A, Romelli A, Lagomarsino S, 'Bond Behavior of FRP Laminates Adhered to Masonry', int conf *Accepted for Publication, Advancing with composites 2003, "Plast 2003"*, Milan, Italy, 2003.

10 Ceroni F., Pecce M., Manfredi G. and Marcari A., 'Experimental bond behavior in masonry elements externally reinforced with FRP laminates', int conf *Composites in Constructions – CCC2003*, Cosenza, Italy, Editoriale Bios, 2003.

11 Ceroni F. and Pecce M., 'Experimental and Theoretical crak behavior of RC ties FRP EBR', int conf *Composites in Constructions – CCC2003*, Cosenza, Italy, Editoriale Bios, 2003.

STRENGTHENING WITH FRP BARS OF URM WALLS SUBJECT TO OUT-OF-PLANE LOADS

Nestore Galati
University of Missouri-Rolla, USA
Gustavo J. Tumialan
Simpson Gumpertz and Heger, USA
Stefano Secondin
University of Padua - Italy
Antonio Nanni
University of Missouri-Rolla, USA

ABSTRACT

For the retrofitting of the civil infrastructure, an alternative to Fiber Reinforced Polymer (FRP) externally-bonded laminates is the use ofnear surface mounted (NSM) FRP bars. This technique consists of placing a bar in a groove cut into the surface of the member being strengthened. The FRP bar may be embedded in an epoxy- or cementitious-based paste, which transfers stresses between the substrate and the bar. The successful use of NSM FRP bars in the strengthening of concrete members has been extended to unreinforced masonry (URM) walls, one of the building components most prone to failure during a seismic event. This paper presents the results of an experimental program on the flexural behaviour of URM walls strengthened with (NSM) FRP bars. A total of fifteen URM walls reinforced with NSM FRP bars were tested. The specimens were strengthened with different amounts of reinforcement to observe their improved performance and the mode of failure. The influence of the bar shape (i.e. circular vs. rectangular), dimension of the groove and type of embedding material (i.e. epoxy or cementitious-based paste), were studied. Two types of FRP fabrics, glass (GFRP) and carbon (CFRP), were used as externally bonded reinforcement to provide the benchmark. Strength and pseudo-ductility of URM walls were significantly increased by strengthening with FRP bars. Based on experimental evidence and on the data found in the literature, the paper provides criteria that can be used in the development of design guidelines.

INTRODUCTION

Unreinforced masonry (URM) walls are prone to failure when subjected to overstress caused by out-of-plane and in-plane loads. Externally bonded FRP laminates have been successfully used to increase the flexural and/or the shear capacity of reinforced concrete (RC) and masonry members. The use of near-surface-mounted (NSM) FRP bars is an attractive method for increasing flexural and shear strength of deficient RC members (De Lorenzis et al., 2000) and masonry walls and, in certain cases, can be more convenient than using FRP laminates (i.e. anchoring requirements, aesthetics requirements).

This paper presents an experimental program on 15 URM walls reinforced with FRP bars using the NSM technique and subjected to out-of-plane loads. The influence of five parameters was investigated: type and amount of FRP reinforcement, shape of the FRP bars (i.e. circular or rectangular), groove size and type of embedding material (i.e. epoxy- or cementitious- paste). Also the effectiveness of the FRP reinforcement

for masonry panels having a running or a stack pattern bond type was studied. In addition, based on experimental evidence and on experimental results available in the literature (Turco, 2002 and Fortes et al., 2002), this paper provides criteria that can be used in the development of design guidelines.

TEST MATRIX

As shown in Table 1, fifteen masonry walls were manufactured for this experimental program. Three specimens were built with clay bricks. The remaining twelve were built with concrete blocks. The nominal dimensions of these walls were 1.22 m (48 in) by 0.61 m (24 in); their overall thickness was 95 mm (3¾in) for clay specimens.

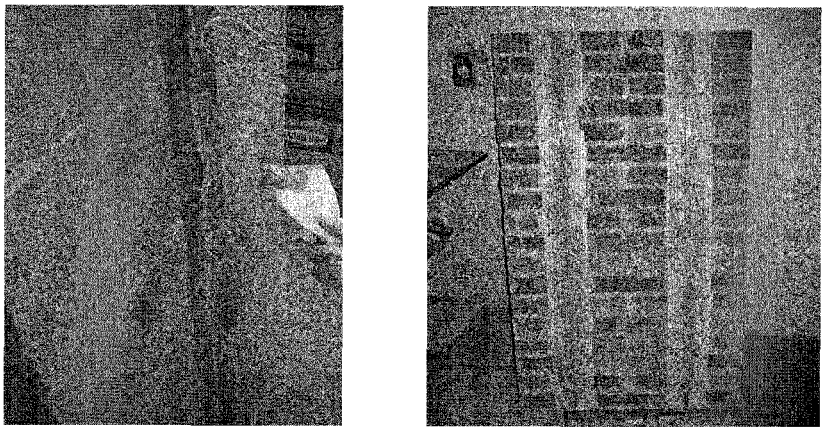
Table 1- Test Matrix

Specimen Designation	Thickness of the Specimen mm (in)	Bar Type	Groove Dimension	Embedment Material
CO1-GTE1	143 (5 ¾)	GFRP Rectangular	Rectangular Groove 17x3 (0.67x0.12)	Epoxy
CO1-GTE2	143 (5 ¾)	GFRP Rectangular		
CL1-GTE1	95 (3 ¾)	GFRP Rectangular		
CL1-GTE2	95 (3 ¾)	GFRP Rectangular		
CL2-CTE1	95 (3 ¾)	CFRP Rectangular		
CO2-GRE21	92 (3 ⅝)	GFRP Circular	Square Groove 2.25 the Diameter of the Bar 14.3 mm (0.56 in.)	Epoxy
CO2-GRE22	92 (3 ⅝)	GFRP Circular		
CO2-GRE23	92 (3 ⅝)	GFRP Circular		
CO2-GRC31	92 (3 ⅝)	GFRP Circular	Square Groove 2.25 the Diameter of the Bar 21.4 mm (0.84 in.)	Cementitious Paste
CO2-GRC32	92 (3 ⅝)	GFRP Circular		
CO2-GRC33	92 (3 ⅝)	GFRP Circular		
CO2-GRE21-SJ	92 (3 ⅝)	GFRP Circular	Square Groove 1.5 the Diameter of the Bar 9.5 mm (0.37 in.)	Epoxy
CO2-GRE22-SJ	92 (3 ⅝)	GFRP Circular		
CO2-GRE21-S	92 (3 ⅝)	GFRP Circular		
CO2-GRE22-S	92 (3 ⅝)	GFRP Circular		

In the case of the concrete masonry walls the thickness varied from 92 mm (3 in.) to 143 mm (5¾ in) (See Figure 1). The walls were constructed using a Type N mortar. All the joints were finished flush with the surface of the masonry unit. All specimens were allowed to cure for at least 28 days before testing. The specimens were strengthened, using the NSM technique, with 6.35 mm (¼in.) and 9.53 mm (in.) diameter deformed GFRP bars and with 2 x 15 mm (0.080 x 0.60 in.) GFRP or with 2 x 16 mm (0.08 x 0.63 in.) CFRP rectangular bars.

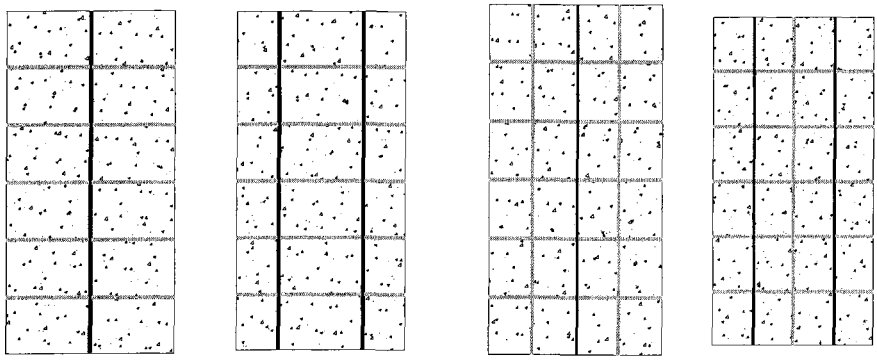
A two-part code was used to identify the specimens. The first part of the code identifies the parent material. Thus, the first two characters identify the type of masonry used "CO" for concrete masonry and "CL" for clay masonry. Since the specimens were constructed using bricks or blocks coming from different stocks, the third number in the code is to identify the stock of the material. From Table 1 it can be observed that four different types of masonry were used: two for the clay walls (CL1

and CL2), and two for the concrete walls (CO1 and CO2).
The second part of the code identifies the type and amount of FRP reinforcement. In particular, the first character is the type of FRP reinforcement used: "G" for GFRP and "C" for CFRP. The second character represents the cross section of the bar used: "T" for rectangular bar and "R" for circular bar. The third character identifies the type of embedding material: "E" for epoxy paste and "C" for latex modified (cementitious grout). For the specimens using rectangular bars the last number represents the number of bars used for the strengthening. For the other specimens, the two numbers following the character "E" or "C" represent the diameter in eighth of an inches and the number of NSM Bars per specimen respectively. The final character "S" or "SJ" indicates that the masonry panels were built with a stack pattern bond type with reinforcement crossing the blocks or placed in the vertical joints (See Figure 2). Thus CO2-GRE21-SJ, refers to a concrete masonry panel, built with a stack pattern bond type, strengthened with one 6.35 mm (¼in.) diameter GFRP bar embedded in epoxy-based paste and placed in the vertical joints.



a) Stack Bond Pattern b) Running Bond Pattern

Figure 1 - Test Specimens



CO2-GRE21-SJ CO2-GRE22-SJ CO2-GRE21-S CO2-GRE22-S

Figure 2 - Reinforcement Scheme for Specimens Built with a Stack Bond Pattern

MATERIAL PROPERTIES

Tests were performed to characterize the mechanical properties of the materials used in this investigation. The average compressive strengths of concrete and clay masonry obtained from the testing of prisms (ASTM C1314) are presented in Table 2. A mortar Type N was used for the walls construction; standard mortar specimens were tested according to ASTM C109. An average value of 7.6 MPa (1100 psi) at an age of 28 days was found.

Table 2 - Compressive Strength of Masonry Walls

Dimensions of Masonry Units mm (in.)	Masonry Type	Specimen Code	Compressive Strength MPa (ksi)
150 x 200 x 400 (5 5/8" x 7 7/8" x 15 3/4")	Concrete	CO1	11.4 (1.6)
100 x 200 x 400 (3 5/8" x 7 7/8" x 15 3/4")	Concrete	CO2	10.5 (1.5)
100 x 200 x 65 (3 3/4" x 2 1/2" x 7 7/8")	Clay	CL1	19.43 (2.8)
100 x 200 x 65 (3 3/4" x 2 1/2" x 7 7/8")	Clay	CL2	15.78 (2.3)

Tensile tests were performed on FRP bars to determine their properties, which are related to fiber content. The average tensile strength, ultimate strain and modulus of elasticity obtained from the testing (ASTM D3039) are presented in Table 3. Details of coupon fabrication and testing procedure are shown elsewhere (Secondin 2003).

Table 3 - Mechanical Properties of FRP Bars

Bar Type	Dimensions of the Bar	Average Maximum Strain %	Average Maximum Stress MPa (ksi)	Average Elastic Modulus MPa (ksi)
#2 GFRP Bar	Nominal Diameter 6.35 mm (0.250 in.)	1.78	824.5 (119.6)	50163 (7276)
#3 GFRP Bar	Nominal Diameter 9.53 mm (0.375 in.)	1.85	760.0 (110.0)	40800 (5920)
GFRP Rectangular Bar	2.06 mm x 15.21 mm (0.081" x 0.599")	2.5	1101.7 (159.8)	44000 (6382)
CFRP Rectangular Bar	2.06 mm x 15.21 mm (0.081" x 0.599")	0.98	1392.4 (201.9)	142740 (20702)

Splitting tensile tests (ASTM C496) were performed on the epoxy-based and on the cementitious-based embedding material used. The splitting tensile strength was found to be 3.58 MPa (0.518 ksi) after 7 days and 5.59 MPa (0.81 ksi) after 28 days in the case of latex modified cementitious paste, and 16.31 MPa (2.36 ksi) after 7 days and 18.54 MPa (2.7 ksi) after 28 days in the case of epoxy-based paste.

TEST SETUP

The masonry specimens were tested under four-points bending (See Figure 3). Loads were applied by 50.8 x 609.6 x 12.7 mm (2 x 24 x ½ in.) steel plates to the external face of the wall. Their distance was 101.6 mm (4 in.) from the midspan. The loads were generated by means of a 12 ton hydraulic jack reacting against a steel frame. Linear Variable Displacement Transducers (LVDTs) were positioned in the middle of the walls to measure the midspan deflection during the tests.
The load was applied in cycles of loading and unloading. An initial cycle for a low load was performed in every wall to verify that both the mechanical and electronic equipment were working properly.

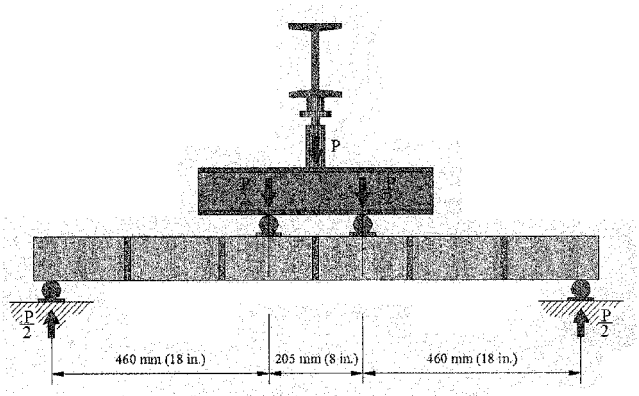


Figure 3 - Test Setup Scheme

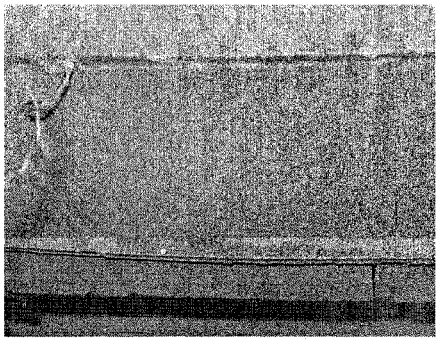
TEST RESULTS

Modes of Failure

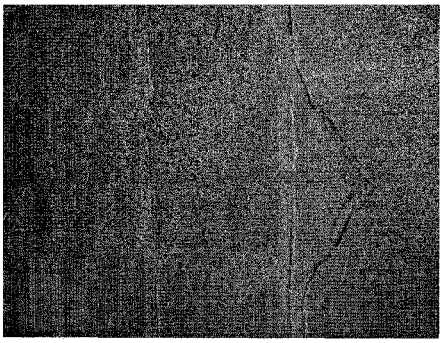
The walls exhibited three different modes of failure (See Figure 4): (1) Debonding of the FRP reinforcement from the masonry substrate; (2) Flexural failure (i.e. crushing of the masonry in compression of rupture of the FRP in tension); and, (3) Shear failure of the masonry at the supports.

FRP Debonding: This was the most frequent mode of failure. Initial flexural cracks were primarily located at the mortar joints (See Figure 4-a). A cracking noise during the test revealed a progressive cracking of the embedding paste. Since the tensile stresses at the mortar joints were being taken by the FRP reinforcement, a redistribution of stresses occurred. As a consequence, cracks developed in the masonry units oriented at 45° (see Figure 4-b) or in the head mortar joints. Some of these cracks followed the embedding paste and masonry interface causing debonding and subsequent wall failure.

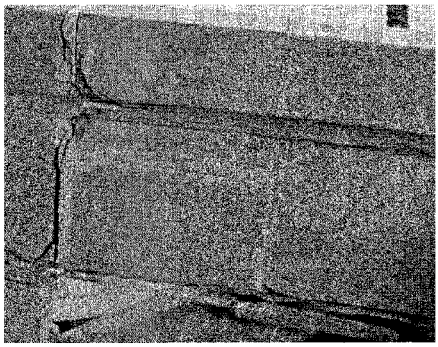
Due to the smoothness of the rectangular bars, for some of the specimens reinforced with rectangular bars debonding was caused by sliding of the bar inside the epoxy. For specimens having a deep groove, debonding was caused by splitting of the embedding material (See Figure 4-c).



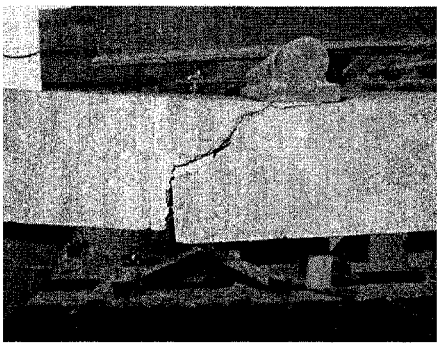
a) FRP Bar Debonding (CO2-GRC32)



b) FRP Debonding: Formation of the 45° Cracks at the Head Joints (CO2-GRC31)



c) Splitting Cracks in the Embedding Material (CO2-GRE22)



d) Flexural – Shear Failure (CO2-GRC33)

Figure 4 - Modes of Failure

Flexural Failure: After developing flexural cracks primarily located at the mortar joints, a wall failed by either rupture of the FRP reinforcement or masonry crushing. FRP rupture occurred at midspan and was observed for the specimens CO2-GRE21 and CO2-GRE22.

Shear Failure: Cracking started with the development of fine vertical cracks at the maximum bending region. Thereafter flexural-shear failure was observed. It was oriented at approximately 45°. In the flexural-shear mode, shear forces transmitted over the crack caused a differential displacement in the shear plane, which resulted in FRP debonding (See Figure 4-d).

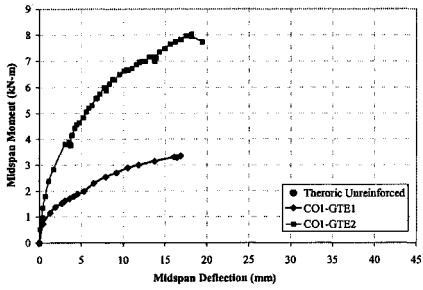
Discussion of Results

Figure 5 shows the Moment vs. Deflection Curves for the six series. It can be observed that the strength and stiffness of the FRP strengthened walls increased dramatically when comparing them to a URM specimen.

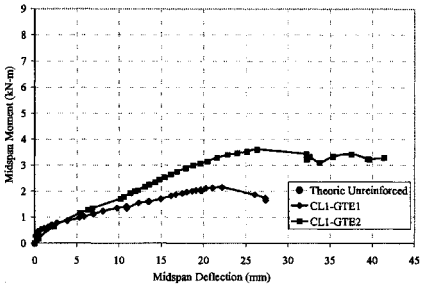
The nominal moments at cracking for the un-strengthened specimens were calculated considering the Masonry Standards Joint Committee recommendations (MSJC-02). From the graphs in Figure 5 they can be stated increments ranging from 4 to 14 times of the original masonry capacity. Since masonry possesses a significant amount of variability this range of values should be taken simply as a reference.

Table 4 reports the test results. The experimental results have been expressed as a function of the amount of reinforcement, ρ_f, $\text{Area}_{FRP}/(\text{Wall Width} \times \text{Wall Thickness})$.

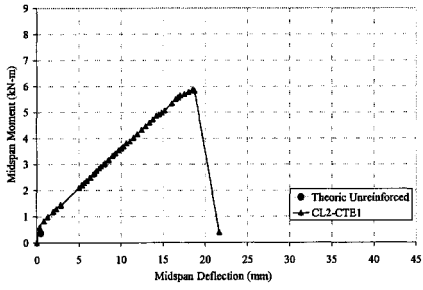
For some of the specimens utilizing carbon or glass FRP rectangular bars, a higher ductility was observed compared with the specimens reinforced with circular bars. In fact, for these specimens the failure was due to the sliding of the bars inside the groove. In these cases, after the failure, the wall could still carry load (because of the friction in the epoxy paste-bar). An interesting observation can be made for specimens built with a stack pattern bond. There is little reduction in the out-of-plane performance by placing the bar in the vertical joints or crossing the masonry blocks.



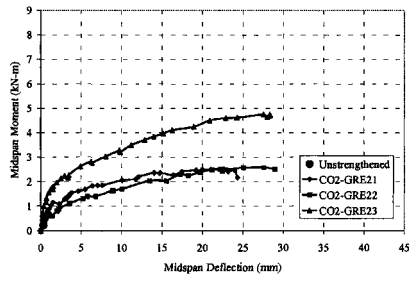
a) Series CO1-GTE



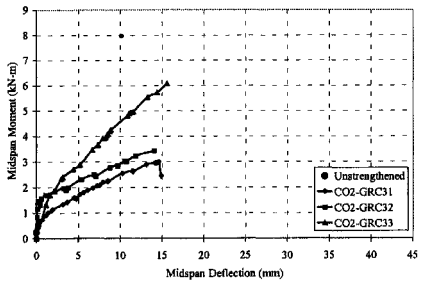
b) Series CL1-GTE



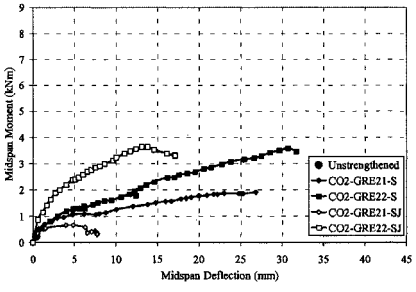
c) Series CL2-CTE



d) Series CO2-GRE2



e) Series CO2-GRC3



f) Series CO2-GRE2x-S

Figure 5 - Moment Versus Midspan Deflection for All the Specimens

The non-adequate performance of wall CO2-GRE21-SJ is attributed to construction problems. This wall had a big mortar joint, therefore the epoxy bordered on the mortar and not on the concrete blocks. It is advisable, as a construction detail, to make grooves bordering the concrete surfaces when bars are placed along the joints.

Table 4 -Test Results

Specimen Name	Amount of Reinforcement ρ_f (x 10^5)	Ultimate Load kN (kip)	Maximum Bending Moment kN-m (k-ft)	Type of Failure
CO1-GTE1	33	14.7 (3.3)	3.35 (2.47)	Debonding*
CO1-GTE2	67	35.1 (7.9)	8.03 (5.92)	Debonding**
CL1-GTE1	50	9.4 (2.1)	2.16 (1.59)	Debonding**
CL1-GTE2	100	16.0 (3.6)	3.66 (2.70)	Debonding*
CL2-CTE1	50	25.6 (5.8)	5.86 (4.32)	Debonding*
CO2-GRE21	54	11.0 (2.5)	2.52 (1.86)	Debonding**
CO2-GRE22	107	11.5 (2.6)	2.64 (1.95)	Debonding**
CO2-GRE23	161	21.6 (4.9)	4.94 (3.64)	Debonding
CO2-GRC31	136	13.1 (2.9)	2.99 (2.20)	Debonding
CO2-GRC32	272	15.0 (3.4)	3.43 (2.53)	Debonding
CO2-GRC33	408	26.6 (6.0)	6.07 (4.48)	Shear
CO2-GRE21-SJ	50	2.84 (0.64)	0.81 (0.60)	Debonding
CO2-GRE22-SJ	101	16.2 (3.64)	3.43 (2.53)	Debonding
CO2-GRE21-S	50	8.4 (1.9)	1.91 (1.41)	FRP Rupture
CO2-GRE22-S	101	15.8 (3.5)	3.60 (2.66)	FRP Rupture

* Debonding due to sliding of the bar inside the epoxy paste
** Debonding due to splitting of the embedding material

Previous Results

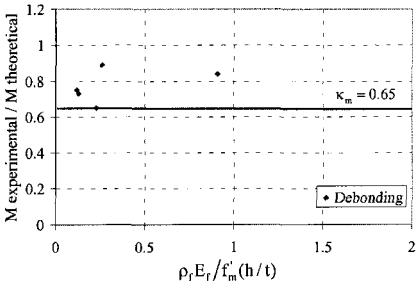
Turco, 2002 conducted an experimental investigation on URM walls reinforced with FRP NSM bars. It was observed that in the case of strengthening with NSM FRP bar, latex modified cementitious paste-GFRP bar system exhibited a better performance when the size of the groove was approximately 2.25 times the diameter but a groove of 1.5 times the diameter was enough when epoxy paste was used.
Fortes et al., 2002 conducted an experimental investigation on concrete masonry walls subject to out-of-plane load. Two reinforcing techniques were compared: CFRP rectangular bars externally bonded to the concrete joints and used as NSM bars. Both were shown to be effective in increasing the ultimate load.

BASIS FOR A DESIGN APPROACH

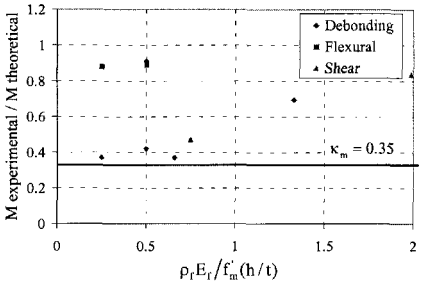
Of the three modes of failure described, the controlling mode is mostly debonding. If a large amount of FRP is provided, shear failure may be observed. The lower limit ratio $M_{experimental}$ / $M_{theoretical}$ has been determined using the design approach developed by Tumialan et al., 2002. It was defined as a reinforcement ratio ω_f, expressed as $\rho_f E_f / f'_m (h/t)$, for masonry walls strengthened with a variety of FRP reinforcement (E_f is the modulus of elasticity of FRP, f'_m is the masonry compressive strength, and h/t is the wall slenderness ratio).

The theoretical flexural capacity of an FRP strengthened masonry wall can be determined based on strain compatibility, internal force equilibrium, and the controlling mode of failure. Theoretical flexural capacity (i.e. optimum capacity) of the strengthened walls was estimated based on the assumption that no premature failure due to debonding or shear could occur. This means that either rupture of the laminate or crushing of masonry would control the wall behaviour.

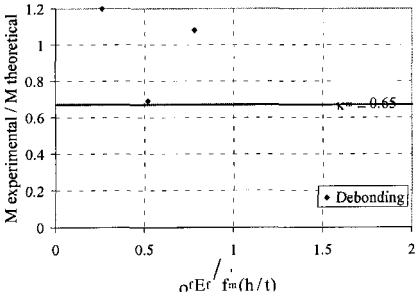
For simplicity and similarly to the flexural analysis of RC members, a parabolic distribution was used for compressive stresses in the computation of the flexural capacity of the strengthened walls. According to MSJC 2002 the maximum usable strain ε_{mu} was considered to be 0.0035 mm/mm (in/in) for clay masonry, and 0.0025 mm/mm (in/in) for concrete masonry. The tensile strength of masonry was neglected. Figure 6 illustrates the relationship between the experimental-theoretical flexural capacity ratio, and the reinforcement ratio ω_f for URM specimens strengthened with FRP systems.



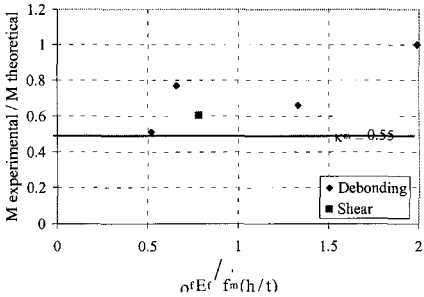
a) GFRP and CFRP Rectangular Bars – Epoxy System



b) GFRP Circular Bars – Epoxy System (dimension of the groove 1.5 the diameter of the bar)



c) GFRP Circular Bars – Epoxy System (dimension of the groove 2.25 the diameter of the bar)



d) GFRP Circular Bars – Latex Modified Cementitious Paste (dimension of the groove 2.25 the diameter of the bar)

Figure 6 - $M_{experimental}$ / $M_{theoretical}$ versus ω_f

Since the flexural capacity is dependant on the strain developed in the FRP bar, it is reasonable to express the effective strain in the bar, ε_{fe}, as the product $\kappa_m \varepsilon_{fu}$, where κ_m is the bond dependent coefficient and ε_{fu} is the design rupture strain. Thus, the effective strain in the FRP bar, ε_{fe}, is limited by the strain controlled by debonding:

$$\varepsilon_{fe} \leq \kappa_m \varepsilon_{fu}$$

FRP Rectangular bars: $\kappa_m = 0.65$

FRP Circular Bars Having a Groove 1.5 the Diameter of the Bar : $\kappa_m = 0.35$

FRP Circular Bars Having a Groove 2.25 the Diameter of the Bar: $\kappa_m = 0.55$

These limits are valid for the case of walls not subjected to sustained load. In walls under sustained load such as retaining or basement walls, creep rupture considerations need to be taken into account (ACI 440.2R-02). Using this approach it is possible to

determine the nominal moment of the section that multiplied by the ϕ factor of the section must be less or equal to the ultimate moment due to the external applied loads.

CONCLUSIONS

1. Flexural strengthening with FRP systems has been proven to remarkably increase the flexural capacity (from 2 to 14 times), strength and pseudo-ductility of URM walls.
2. The test results identified three basic modes of failure. One, shear failure, related to the parent material (i.e. masonry); and two associated with the reinforcing material, debonding and flexural failure (i.e. rupture of FRP or crushing of the masonry). For large amounts of reinforcement, shear failure was observed to be the controlling mode. For other reinforcement ratios, either FRP rupture or debonding was observed, the latter being the most common.
3. In the case of strengthening with FRP rectangular bars, the sliding of the bar in the epoxy caused an increase in the ductility.
4. Based on experimental data obtained in the present and other investigations, it is recommended to consider the maximum usable strain in the FRP Bars as $0.65\varepsilon_{fu}$ for NSM FRP Rectangular Bars utilizing Epoxy Paste and $0.55\varepsilon_{fu}$ for NSM FRP Circular Bars having a groove at least 2.25 times the diameter of the bar and utilizing either Epoxy or Cementitious Paste. The maximum usable strain in the FRP Bars must be limited to $0.35\varepsilon_{fu}$ for NSM FRP Circular Bars having a groove at least 1.5 times the FRP bar diameter and using Epoxy Paste.

ACKNOWLEGEMENTS

The support of the National Science Foundation Industry/University Cooperative Research Center at the University of Missouri–Rolla. The authors would also like to acknowledge the support of the Rolla Technical Institute (RTI).

REFERENCES

1. L. De Lorenzis, A. Nanni, and A. La Tegola, "Flexural and Shear Strengthening of Reinforced Concrete Structures with Near Surface Mounted FRP Rods", *Proceedings of Third International Conference on Advanced Composite Materials in Bridges and Structures*, Ottawa, Canada, pp. 521-528, 2002.

2. V. Turco, N. Galati, J. G. Tumialan. and A. Nanni, "Flexural Strengthening of URM Walls with FRP Systems", *6 th. International Symposium on Fibre-Reinforced Polymer (FRP) Reinforcement for Concrete Structures (FRPRCS-6)*, Singapore, 2003.

3. S. Fortes, J. T. Oliveria and J. A. Barros, "Elementos de Casca em Alvenaria Cerâmica Reforçados com Laminados de Fibras de Carbono", *VII International Seminar on Structural Masonry for Developing Country*, Belo Horizonte, Brazil, 2002.

4. S. Secondin, "Masonry Reinforced with FRP systems," *Tesi di Laurea,* Università degli Studi di Padova, Facoltà di Ingegneria, Padova, Italy, March 2003.

5. Masonry Standards Joint Committee, "Building Code Requirements for Masonry Structures, ACI-530-02/ASCE 5-02/TMS 402-02", *American Concrete Institute, American Society of Civil Engineers, and The Masonry Society*, Detroit, New York, and Boulder, 2002.

6. J. G. Tumialan, N. Galati, S. M. Namboorimadathil and A. Nanni, "Strengthening of Masonry with FRP Bars", *ICCI 2002*, San Francisco, CA, June 10-12, 2002

7. American Concrete Institute (ACI), Committee 440, "Guide for the Design and Construction of Externally Bonded FRP Systems for Strengthening Concrete Structures", October 2002.

This page intentionally left blank

PART III

FRP STRENGTHENING OF METALLIC AND TIMBER STRUCTURES

This page intentionally left blank

ELASTIC ANALYSIS OF ADHESION STRESSES BETWEEN A BEAM AND A BONDED STRENGTHENING PLATE

John Cadei
Independent Consultant

Tim Stratford
The University of Edinburgh

SUMMARY

This paper presents a general closed form solution for the elastic shear and peel stresses in an adhesive layer that bonds a strengthening plate to a beam. The solution takes into account initial strains in the plate, external beam loadings, temperature effects, and forces applied to the end of the plate. Results of some typical load cases are presented in order to illustrate the significance of the stresses.

INTRODUCTION

Strengthening beams and columns by bonding plates to their surfaces is a widely applied technique. Plate bonding has gained new impetus with the use of lightweight fibre-reinforced-polymer composite materials.

Plate bonding relies on the strength of the adhesive layer, and both tests and theoretical work have shown that this strength is governed by stress concentrations which occur due to the mismatch of strains in the beam and plate across the adhesive layer. Concentrations of adhesive stress occur in the vicinity of the geometric discontinuities shown in Figure 1; in particular, at the end of a strengthening, but also at a crack in the substrate, or a bond defect in the adhesive layer.

Several closed form solutions are available, for example see references 1-6. This paper presents a generalised solution that was initially developed during the preparation of CIRIA Report 645 on the 'Strengthening of Metallic Structures using Externally-Bonded Fibre-Reinforced-Polymers'.[7] CIRIA commissioned FaberMaunsell and the University of Surrey to act as research contractors on this project. The useful comments received from the Steering Group members on the bond analysis are gratefully acknowledged, with particular thanks to Steve Denton of Parsons Brinkerhoff, and Simon Frost of AEA Technology.

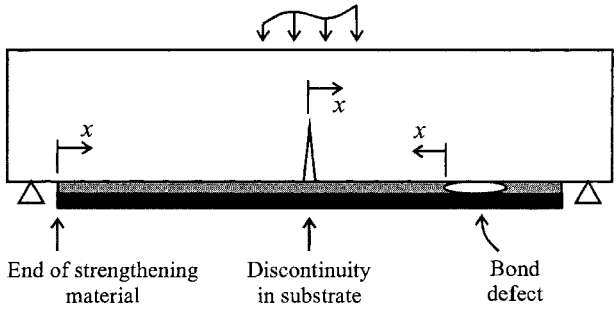


Figure 1 Geometric discontinuities leading to adhesive stress concentrations

BOND ANALYSIS OF AN ELASTIC ADHESIVE JOINT

The bond analysis allows the distribution of shear stress (τ_a) and through thickness, or peel stress (σ_a) along an adhesive joint to be determined. As shown in Figure 1, the

position along the beam is described by the coordinate 'x', measured from the geometric discontinuity. The bond analysis solution and its derivation are given in the Appendix.

The geometric and material properties of the strengthened beam are defined in Figure 2. E & G are the Young's modulus and shear modulus, A is the cross-sectional area, I is the second moment of area, and α is the coefficient of thermal expansion. The subscripts 'b', 'p', and 'a' refer to the beam, plate and adhesive respectively.

The bond analysis is a very useful design tool, as it allows the stress concentrations at the end of a plate to be investigated. However it is worth noting the assumptions made in the analysis:

- The strengthening plate and adhesive layer are of uniform thickness
- All the structural materials behave in a linear-elastic manner (in reality, the adhesive will be non-linear)
- The effects of the longitudinal stress in the adhesive are negligible
- The adhesive layer is long enough for its ends not to interact with one another
- The adhesive layer is continuously bonded to the beam and plate

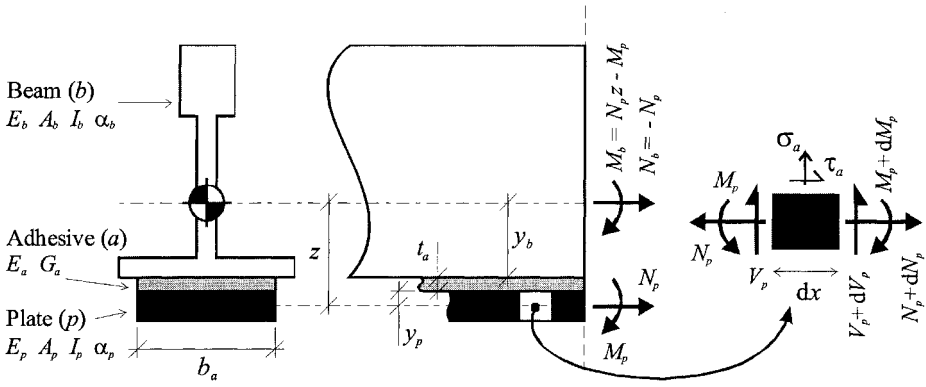


Figure 2 Geometry and material properties of the bonded plate and beam, and equilibrium conditions between the plate, beam and adhesive joint.

RESULTS OF TYPICAL SIMPLE LOAD CASES

A number of characteristic load cases are investigated below to illustrate the use of the elastic bond analysis. For ease of reference, these consider the same beam and strengthening plate that has previously been analysed by Denton.[2]

Cast iron beam			CFRP strengthening plate			Adhesive		
A_b	36 368	mm^2	A_p	576	mm^2	t_a	5	mm
y_b	300	mm	y_p	1.2	mm	b_a	240	mm
I_b	1.691×10^9	mm^4	I_p	276.48	mm^4	G_a	3 800	MPa
E_b	100 000	MPa	E_p	100 000	MPa	E_a	10 000	MPa
α_b	10.22×10^{-6}	1/°C	α_p	0.0×10^{-6}	1/°C			

Load case 1. Uniform temperature rise of 30°C

If the beam and plate are subjected to a uniform temperature rise of $\Delta T = 30°C$ after forming the adhesive joint, the lack-of-fit strains are:

$\Delta\varepsilon_{pa} = 0$ $\Delta\varepsilon_{ba} = 3.06 \times 10^{-4}$

$\Delta\varepsilon_{pb} = -3.06 \times 10^{-4}$ $\Delta\psi_{pb} = 0$

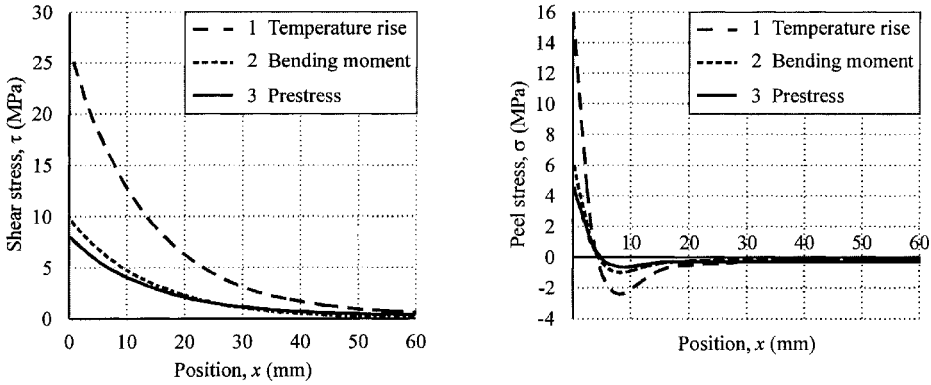


Figure 3 Adhesive stresses due to (1) a uniform temperature rise of 30°C, (2) applied bending moment, and (3) release of prestressed plate

The adhesive stress distributions are shown in Figure 3. The maximum shear stress is 8 MPa, and the maximum peel stress of similar magnitude (5 MPa). However, the zone of influence of the shear stress (60mm) is longer than that of the peel stress (20mm).

Load case 2. Applied beam bending moment

After forming the adhesive joint, the strengthened beam is subjected to a uniform change in bending moment of $\Delta M_{bl} = -200$ kNm. The applied moment produces a lack-of-fit strain in the beam at the adhesive interface of $\varepsilon_{ba} = 6.82 \times 10^{-4}$, but there is no lack-of-fit strain in the plate. The resulting adhesive layer lack-of-fit strains are:

$\Delta\varepsilon_{pb} = -6.82 \times 10^{-4}$ $\Delta\psi_{pb} = 1.18 \times 10^{-6}$ m^{-1}

The adhesive stresses are again plotted in Figure 3, with a maximum shear stress of 10 MPa and a maximum peel stress of (6 MPa). Note that the peak adhesive stresses due to the temperature increase (load case 1) are of a similar magnitude to those resulting from the applied moment.

Load case 3. The situation after the release of a prestressed plate

A strengthening plate can be prestressed using a jacking system. The jacking force is transferred to the adhesive layer after the adhesive has set. If the pre-strain in the plate is 0.1% prior to forming the adhesive joint, the lack-of-fit strains are:

$\Delta\varepsilon_{pa} = -1.0 \times 10^{-3}$ $\Delta\varepsilon_{ba} = 0$

$\Delta\varepsilon_{pb} = -1.0 \times 10^{-4}$ $\Delta\psi_{pb} = 0$

If an auxiliary end anchorage device is not provided, prestress results in high adhesive stresses at the end of the plate, as shown in Figure 3. The peak shear stress is 25 MPa and the peak peel stress is 16 MPa, both of which are higher than load cases 1 or 2.

Load case 4. A crack in the substrate.

Assume that due to the cracking of the substrate, the stress in the plate at the location of the crack is increased to twice the value it has where it is fully bonded. Assume the load change in the plate at the crack location is:

$\Delta N_p = 100$ kN

The corresponding load changes in the beam are then:

$\Delta N_{bt} = -100$ kN $\quad\quad$ $\Delta M_{bt} = -27$ kNm

The associated lacks of fit are:

$\Delta \varepsilon_{pa} = 0$ $\quad\quad$ $\Delta \psi_{pa} = 0$

$\Delta \varepsilon_{ba} = 2.32 \times 10^{-5}$ $\quad\quad$ $\Delta \psi_{ba} = -1.60 \times 10^{-7}$ m^{-1}

$\Delta \varepsilon_{pb} = -2.32 \times 10^{-4}$ $\quad\quad$ $\Delta \psi_{pb} = 1.60 \times 10^{-7}$ m^{-1}

The resulting adhesive stresses are shown in Figure 4. It will be observed that the signs of the shear and peel stresses are reversed compared with the previous load cases. In the previous cases the beam tended to stretch the plate, in this case the plate is tending to stretch the beam. (Note also that this bond analysis assumes plane-sections in the beam, but this is unlikely to be valid just to the side of a crack).

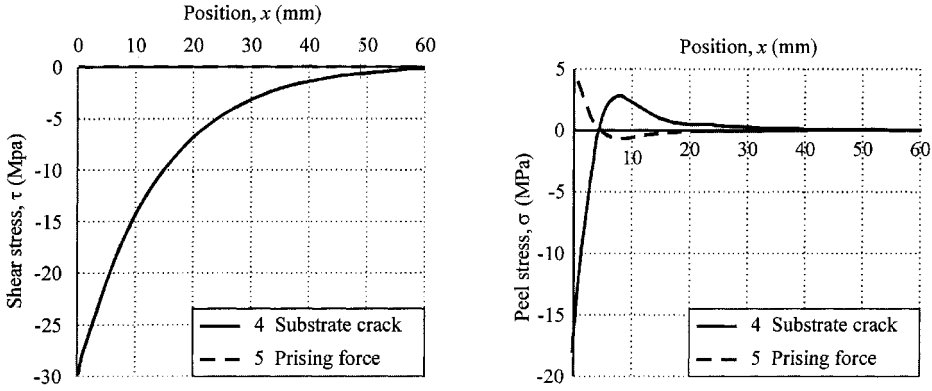


Figure 4 Adhesive stresses due to (4) formation of a crack in the beam, and (5) a prising force at the end of the plate

Load case 5. A prising force applied at the end of the plate.

In this case, a prising force of 2 kN is applied at the end of the plate (acting so as to pull the plate away from the beam). This results in only peel stress in the adhesive, as shown in Figure 4. A prising load test could therefore be used to assess the peel strength of an adhesive system. This load case can also be used to assess the beneficial effect of clamping the end of a bonded plate to resist live load peel stresses.

ADHESIVE STRESSES IN CASES OF MORE COMPLEX GEOMETRY

The bond analysis described in this paper applies to a uniform plate and uniform adhesive thickness. The solution shows that a thicker plate thickness or adhesive layer thickness results in larger peel stress at the end of the plate. Tests have confirmed the inference that tapering the plate to reduce its end thickness improves the strength of the

plate adhesion. The governing differential equations given in this paper are valid for a tapered plate, but their coefficients (f_1, a_1 etc) vary in x as well as the unknown functions N_p, M_p, and the known loading terms $\Delta\varepsilon_{pb}$, $\Delta\psi_{pb}$. A numerical solution method can be used to solve the equations for a tapered plate. For example, the differential equations can be discretised using a finite difference or finite element approach.

CONCLUDING REMARKS

This paper has presented a general closed form solution for the shear and peel stresses in an adhesive layer bonding a plate to a beam member. The plate, beam, and adhesive layer are assumed to be uniform along their length. A number of illustrative elementary load cases relating to a metallic beam strengthened with a carbon fibre plate have demonstrated the adhesive stress concentration effects of applied beam loading, uniform temperature rise, release of plate prestress after curing of the adhesive, the formation of a crack in the beam, and a prising or clamping force applied to the end of the plate. In all cases significant peel stresses arise at the end of the plate. Hence the end of the plate should be located in a region of low beam stress and where necessary prestressed bolts or other supplementary elements should be provided to reduce the tensile peel stresses.

APPENDIX – ELASTIC ANALYSIS OF AN ADHESIVE JOINT

The geometry and material properties of the strengthened beam are described in the main text (Figure 2).

Methodology and assumptions

The analysis of the strengthened beam section determines the shear stress (τ_a) and peel stress (σ_a) acting across the adhesive joint, by examining compatibility requirements across the adhesive interface in the longitudinal direction (shear deformation) and the through thickness direction (peel of the adhesive joint).

The beam and / or plate will typically be under load at that the adhesive joint is formed, and it is important to consider the effect of these pre-strains. The compatibility conditions are written in terms of the *lack-of-fit strains* due to changes in the external loading since the adhesive set.

Equilibrium and constitutive relationships in the beam and plate

The loading applied since the adhesive set is described by the change in stress resultants (ΔN_b, ΔM_b) in the beam and (ΔN_p, ΔM_p) in the plate. The change in temperatures in the beam and plate since the adhesive set are ΔT_b & ΔT_p. Denoting the conditions at the time that the adhesive set as '0', and the conditions at the current time as 't':

$$\Delta N_b = N_{bt} - N_{b0} \qquad \Delta M_b = M_{bt} - M_{b0} \qquad \Delta T_b = T_{bt} - T_{b0} \tag{1}$$

$$\Delta N_p = N_{pt} - N_{p0} \qquad \Delta M_p = M_{pt} - M_{p0} \qquad \Delta T_p = T_{pt} - T_{p0} \tag{2}$$

These changes in the stress resultants result in a lack-of-fit in the strain across the adhesive interface. At the interface between the beam and the adhesive, the lack-of-fit strain ($\Delta\varepsilon$) and curvature ($\Delta\psi$) are:

$$\Delta\varepsilon_{ba} = \frac{\Delta N_b}{E_b A_b} - \frac{\Delta M_b y_b}{E_b I_b} + \alpha_b \Delta T_b \qquad \Delta\psi_b = \frac{\Delta M_b}{E_b I_b} \tag{3}$$

Similarly, the lack-of-fit strain at the plate-adhesive interface is:

$$\Delta\varepsilon_{pa} = \frac{\Delta N_p}{E_p A_p} + \frac{\Delta M_p y_p}{E_p I_p} + \alpha_p \Delta T_p \qquad \Delta\psi_p = \frac{\Delta M_p}{E_p I_p} \tag{4}$$

Load is transferred across the adhesive joint by the stresses (τ_a, σ_a), giving stress resultants in the plate of (N_p, M_p, V_p), acting about the plate's centroid. As shown in Figure 2, these are reacted by stress resultants of (N_b, M_b) about the centroid of the beam:

$$N_b = -N_p \qquad M_b = N_p z - M_p \tag{5}$$

where z is the lever arm between the centroids of the plate and the beam:

$$z = y_p + t_a + y_b \tag{6}$$

Constitutive relationships allow the strains (ε) and curvatures (ψ) in the beam and the plate to be expressed in terms of the plate stress resultants. In the plate:

$$\varepsilon_p = \frac{N_p}{E_p A_p} \qquad \psi_p = \frac{M_p}{E_p I_p} \tag{7}$$

In the beam (using equs (5)):

$$\varepsilon_b = \frac{N_b}{E_b A_b} = -\frac{N_p}{E_b A_b} \qquad \psi_b = \frac{M_b}{E_b I_b} = \frac{N_p z - M_p}{E_b I_b} \tag{8}$$

Equilibrium and constitutive relationships across the adhesive joint

The mean shear stress (τ_a) and peel stress (σ_a) acting across the adhesive joint are assumed to act about the mid-plane of the adhesive layer. By considering equilibrium of a short length of the plate (Figure 2):

- Equilibrium in the x direction gives the shear stress:

$$\tau_a = \frac{1}{b_a}\frac{dN_p}{dx} \tag{9}$$

- For rotational equilibrium (about the top-centre of the plate element):

$$V_p = -\frac{dM_p}{dx} + y_p \frac{dN_p}{dx} = -\frac{dM_p^*}{dx} \tag{10}$$

where M_p^* is the transformed moment about the plate-adhesive interface,

$$M_p^* = M_p - y_p N_p \tag{11}$$

- Equilibrium in the y direction gives the peel stress:

$$\sigma_a = \frac{1}{b_a}\frac{dV_p}{dx} = -\frac{1}{b_a}\frac{d^2 M_p^*}{dx^2} \tag{12}$$

The constitutive response of the adhesive is described by:

$$\gamma_a = \frac{\tau_a}{G_a} = \frac{1}{b_a G_a}\frac{dN_p}{dx} \qquad \varepsilon_a = \frac{\sigma_a}{E_a} \tag{13}$$

Shear compatibility of adhesive layer

Shear compatibility is examined to determine the shear stress across the adhesive interface. The longitudinal displacements at the beam-adhesive (u_{ba}) and plate-adhesive (u_{pa}) interfaces can be expressed in terms of the horizontal and vertical displacements at the centroids of the beam (u_b, v_b) and the plate (u_p, v_p):

$$u_{pa} = \left(u_p + \frac{dv_p}{dx} y_p\right) + \Delta u_{pa} \qquad u_{ba} = \left(u_b - \frac{dv_b}{dx} y_b\right) + \Delta u_{ba} \tag{14}$$

Δu_{ba} and Δu_{pa} are the lack-of-fit displacements associated with the change in load since the adhesive set (equs (1) & (2)).

Differentiating these equations with respect to x gives the corresponding strains at the adhesive interfaces. Writing $\psi = d^2v/dx^2$ for the curvatures gives:

$$\varepsilon_{pa} = \left(\varepsilon_p - \psi_p y_p\right) + \Delta\varepsilon_{pa} \qquad \varepsilon_{ba} = \left(\varepsilon_b - \psi_b y_b\right) + \Delta\varepsilon_{ba} \tag{15}$$

Assuming that the displacement field varies linearly through the adhesive layer, the average shear strain in the adhesive layer is given by:

$$\gamma_a = \frac{\partial u}{\partial y} + \frac{\partial v}{\partial x} = \frac{u_{pa} - u_{ba}}{t_a} + \frac{1}{2}\left(\frac{\mathrm{d}v_p}{\mathrm{d}x} - \frac{\mathrm{d}v_b}{\mathrm{d}x}\right) \tag{16}$$

Differentiating with respect to x and substituting in the longitudinal strains gives:

$$t_a \frac{d\gamma_a}{dx} = \varepsilon_p - \varepsilon_b + \psi_p\left(y_p + \frac{t_p}{2}\right) - \psi_b\left(y_b + \frac{t_a}{2}\right) + \Delta\varepsilon_{pb} \tag{17}$$

$\Delta\varepsilon_{pb}$ is the lack-of-fit in strain across the adhesive layer, which would occur if the adhesive joint was released, due to the loads applied since the adhesive joint set:

$$\Delta\varepsilon_{pb} = \Delta\varepsilon_{pa} - \Delta\varepsilon_{ba} \tag{18}$$

Substituting for the strains using the constitutive relationships (equs (7), (8) & (13)) gives the compatibility equation for shear strain across the adhesive interface:

$$\frac{t_a}{G_a b_a}\frac{d^2N_p}{dx^2} = \left(\frac{1}{E_pA_p} + \frac{1}{E_bA_b}\right)N_p + \frac{M_p}{E_pI_p}\left(y_p + \frac{t_a}{2}\right) + \frac{N_p z - M_p}{E_bI_b}\left(y_b + \frac{t_a}{2}\right) + \Delta\varepsilon_{pb} \tag{19}$$

The unknown variables, N_p & M_p are coupled. To simplify the solution, the difference between the beam and plate curvatures is assumed negligible for the purposes of determining N_p:

$$\psi_p = \frac{M_p}{E_pI_p} = \frac{N_p z - M_p}{E_bI_b} = \psi_b \tag{20}$$

M_p can now be eliminated from equ. (19), giving the governing equation for N_p:

$$-f_1\frac{d^2N_p}{dx^2} + f_2N_p = -\Delta\varepsilon_{pb} \tag{21}$$

where:

$$f_1 = \frac{t_a}{G_a b_a} \qquad f_2 = \frac{1}{E_pA_p} + \frac{1}{E_bA_b} + \frac{z^2}{E_pI_p + E_bI_b} \tag{22}$$

The solution of the governing equation is:

$$N_p = N_{PS} + C_1 e^{-\lambda x} \tag{23}$$

λ is a measure of the relative flexibility of the beam, plate and adhesive:

$$\lambda = \sqrt{f_2 / f_1} \tag{24}$$

To determine the particular solution axial force, N_{PS}, a quadratic variation is assumed for the lack-of fit strain:

$$\Delta\varepsilon_{pb}(x) = \Delta\varepsilon_0 + \Delta\varepsilon_1 x + \Delta\varepsilon_2 x^2 \tag{25}$$

Substituting $\Delta\varepsilon_{pb}$ into equations (21) & (23) gives:

$$N_{PS} = -\frac{1}{f_2}\left(2\Delta\varepsilon_2 \frac{f_1}{f_2} + \Delta\varepsilon_{pb}(x)\right) \tag{26}$$

The constant of integration, C_1, is determined from the axial force in the plate at position x=0, $N_p = N_p\big|_{x=0}$. From equ. (23):

$$C_1 = N_p\big|_{x=0} - N_{PS}\big|_{x=0} \tag{27}$$

The axial force, N_{PS} is now defined, allowing the shear stress in the adhesive to be found using equ. (9):

$$\tau_a = \frac{1}{b_a}\left(\frac{\mathrm{d}N_{PS}}{\mathrm{d}x} - C_1\lambda\, e^{-\lambda x}\right) \tag{28}$$

The maximum shear stress occurs at x=0 (substituting $\mathrm{d}N_{PS}/\mathrm{d}x$ at x=0 from equ. (26)):

$$\tau_{\max} = \frac{1}{b_a}\left(\frac{dN_{PS}}{dx}\bigg|_{x=0} - C_1\lambda\right) = -\frac{1}{b_a}\left(\frac{\Delta\varepsilon_1}{f_2} + C_1\lambda\right) \tag{29}$$

Through thickness compatibility of adhesive layer

The peel stress is found by examining the through-thickness strain in the adhesive, which can be written as the difference in vertical displacement across the adhesive joint:

$$\varepsilon_a = \frac{\partial v}{\partial y} = \frac{v_p - v_b}{t_a} + \frac{\Delta v_p - \Delta v_b}{t_a} \tag{30}$$

Substituting for the strain from equ. (13) and differentiating twice with respect to x:

$$\frac{t_a}{E_a}\frac{d^2\sigma_a}{dx^2} = \psi_p - \psi_b + \Delta\psi_{pb} \tag{31}$$

$\Delta\psi_{pb}$ is the lack-of-fit in curvature across the adhesive interface, which would occur if the adhesive joint was released:

$$\Delta\psi_{pb} = \Delta\psi_p - \Delta\psi_b \tag{32}$$

Substituting for the curvatures using equs (3), (4), (7) & (8) gives the compatibility equation for peel, in terms of the plate moment M_p^* and axial force, N_p (as found above):

$$a_1\frac{d^4M_p^*}{dx^4} + a_2 M_p^* = a_3 N_p - \Delta\psi_{pb} \tag{33}$$

The coefficients are:

$$a_1 = \frac{t_a}{E_a b_a} \qquad a_2 = \frac{1}{E_p I_p} + \frac{1}{E_b I_b} \qquad a_3 = \frac{z - y_p}{E_b I_b} - \frac{y_p}{E_p I_p} \tag{34}$$

The solution of this equation is:

$$M_p^* = M_{PS}^* + C_2 e^{-\beta x} \cos \beta x + C_3 e^{-\beta x} \sin \beta x \tag{35}$$

$$\text{where } \beta = \left(\frac{a_2}{4a_1} \right)^{0.25} \tag{36}$$

Assume that the lack-of-fit curvature can be written as a quadratic function:

$$\Delta\psi_{pb}(x) = \Delta\psi_0 + \Delta\psi_1 x + \Delta\psi_2 x^2 \tag{37}$$

The particular solution moment is found by substituting $\Delta\psi_{pb}$ into equs (33) & (35):

$$M_{PS}{}^* = -\frac{1}{a_2}\Delta\psi(x) + \frac{a_3}{a_2} N_{PS}(x) + \frac{a_3 C_1}{a_1 \lambda^4 + a_2} e^{-\lambda x} \tag{38}$$

The constants of integration C_2 and C_3 are found from the plate boundary conditions at x=0, where the bending moment and shear force are known:

$$M_p^*\big|_{x=0} = M_p\big|_{x=0} - y_p \; N_p\big|_{x=0} \qquad V_p\big|_{x=0} = -\left.\frac{\mathrm{d}M_p}{\mathrm{d}x}\right|_{x=0} \tag{39}$$

Applying the moment boundary condition to equ (35) gives C_2:

$$\begin{aligned} C_2 &= M_p^*\big|_{x=0} - M_{PS}{}^*\big|_{x=0} \\ C_2 &= \left\{ M_p\big|_{x=0} - y_p N_p\big|_{x=0} \right\} + \left\{ \frac{\Delta\psi_0}{a_2} + \frac{a_3}{a_2 f_2} \left(2\Delta\varepsilon_2 \frac{f_1}{f_2} + \Delta\varepsilon_0 \right) - \frac{a_3 C_1}{a_1 \lambda^4 + a_2} \right\} \end{aligned} \tag{40}$$

Applying the shear boundary condition to the first differential of equ (35) gives C_3:

$$C_3 = -\frac{1}{\beta}\left[V_p\big|_{x=0} + \left.\frac{\mathrm{d}M_{PS}^*}{\mathrm{d}x}\right|_{x=0} - \beta C_2 \right] = -\frac{1}{\beta}\left[V_p\big|_{x=0} - \frac{\Delta\psi_1}{a_2} - \frac{a_3 \Delta\varepsilon_1}{a_2 f_2} \right] + C_2 \tag{41}$$

The peel stress is found by substituting the differentials of equs (35) and (38) into equ (12):

$$\sigma_a = \frac{1}{b_a}\left[\begin{array}{l} \dfrac{2}{a_2}\left(\Delta\psi_2 + \dfrac{a_3 \Delta\varepsilon_2}{f_2} \right) - \dfrac{a_3 C_1 \lambda^2}{a_1 \lambda^4 + a_2} e^{-\lambda x} \\ -2\beta^2 e^{-\beta x}\left(C_2 \sin \beta x - C_3 \cos \beta x \right) \end{array} \right] \tag{42}$$

The maximum value of the peel stress occurs at x=0, where:

$$\sigma_{\max} = \frac{1}{b_a}\left[\frac{2}{a_2}\left(\Delta\psi_2 + \frac{a_3 \Delta\varepsilon_2}{f_2} \right) - \frac{a_3 C_1 \lambda^2}{a_1 \lambda^4 + a_2} + 2\beta^2 C_3 \right] \tag{43}$$

NOMENCLATURE

a_1, a_2, a_3	coefficients of peel governing eqn.
A_b, A_p	cross-sectional area (beam, plate)
b_a	width of adhesive layer
C_1	constant of integration for shear
C_2, C_3	constants of integration for peel
E_a	Young's modulus of adhesive
E_b, E_p	Young's Modulus (beam, plate)
f_1, f_2	coefficients of shear governing eqn.
G_a	shear modulus of adhesive layer
I_b, I_p	second moment of area (beam, plate)

M_b, M_p bending moment (beam, plate)
M_{b0}, M_{p0} bending moment at the time the adhesive sets (beam, plate)
M_{bt}, M_{pt} bending moment at the current time (beam, plate)
M_p^* transformed plate bending moment about the plate-adhesive interface
M_{PS}^* particular solution for M_p^*
ΔM_b,ΔM_p change in bending moment since the time the adhesive set (beam, plate)
N_b, N_p axial force (beam, plate)
N_{b0}, N_{p0} axial force at the time the adhesive sets (beam, plate)
N_{bt}, N_{pt} axial force at current time (beam, plate)
N_{PS} particular solution for N_p
ΔN_b, ΔN_p change in axial force since the time the adhesive set (beam, plate)
t_a thickness of adhesive layer
T_b, T_p current temperature at the adhesive interface (beam, plate)
T_{b0}, T_{p0} temperature at the interface at the time the adhesive sets (beam, plate)
T_{bt}, T_{pt} temperature at the interface at the current time (beam, plate)
ΔT_b, ΔT_p change in temperature at adhesive interface since the time the adhesive set (beam, plate)
u_b, u_p longitudinal displacement at the centroid of the beam / plate
u_{ba}, u_{pa} longitudinal displacement at adhesive interface with beam / plate
Δu_{ba},Δu_{pa} longitudinal displacement due to change in external loading at adhesive interface with beam / plate
v_b, v_p vertical displacement (beam / plate)
Δv_b, Δv_p vertical displacement due to change in external loading
V_p shear force in the plate
x position along plate from the start of the adhesive layer
y_b, y_p distance from the adhesive interface to the beam / plate
z lever arm between centroid of beam and centroid of plate
α_b, α_p coefficients of thermal expansion (beam, plate)
β parameter in solution for M_p
γ_a average shear strain in adhesive layer
ε_a average peel strain adhesive layer
ε_b, ε_p strain at centroid of beam / plate
ε_{ba}, ε_{pa} strain at interface between adhesive layer and the beam / plate
$\Delta\varepsilon_{ba}$,$\Delta\varepsilon_{pa}$ lack-of-fit strain due to change in external loading since setting of adhesive, at interface between adhesive and beam / plate
$\Delta\varepsilon_{pb}$ lack-of-fit strain across the adhesive layer, due to change in external loading since setting of adhesive
$\Delta\varepsilon_0 ... \Delta\varepsilon_2$ coefficients of quadratic representation of $\Delta\varepsilon_{pb}$
λ parameter in solution for N_p
σ_a through-thickness / peel stress at the mid plane of the adhesive layer
τ_a shear stress at the mid plane of the adhesive layer
ψ_b, ψ_p curvature (beam, plate)
$\Delta\psi_b$, $\Delta\psi_p$ lack-of-fit curvature due to change in external loading since setting of adhesive (beam / plate)
$\Delta\psi_{pb}$ lack-of-fit curvature across adhesive layer due to change in external loading since setting of adhesive.
$\Delta\psi_0 ... \Delta\psi_2$ coefficients of quadratic representation of $\Delta\psi_{pb}$

REFERENCES

1 A M Albat and D P Romilly, 'A direct linear-elastic analysis of double symmetric bonded joints and reinforcements', *Composite Science and Technology*, 1999 **59**(7) 1127-1137.

2 S R Denton, 'Analysis of stresses developed in FRP plated beams due to thermal effects', *Composites in Civil Engineering 2001*, Hong Kong, 2001, 527-536.

3 S Frost, R J Lee and V K Thompson, 'Structural integrity of beams strengthened with FRP plates – Analysis of the adhesive layer', *Structural Faults & Repair 2003*, London 2003.

4 T C Miller, M J Chajes, D R Mertz and J N Hastings, 'Strengthening of a steel bridge girder using CFRP plates', *New York City Bridge Conference*, 2001.

5 T M Roberts, 'Approximate analysis of shear and normal stress concentrations in the adhesive layer of plated RC beams', *The Structural Engineer*, 1989 **10**(2) 229-233

6 S T Smith and J G Teng, 'Interfacial stresses in plated beams', *Engineering Structures*, 2001 **23** 857-871.

7 CIRIA, 'RP645 - Strengthening Metallic Structures using Externally-Bonded Fibre-Reinforced-Polymers', 2004.

EXPERIMENTAL CHARACTERIZATION OF STEEL ELEMENTS REINFORCED BY ADHESIVELY BONDED CFRP PLATES

Pierluigi Colombi, Nicola Panzeri and Carlo Poggi

Department of Structural Engineering, Polytechnic of Milan, Italy

ABSTRACT

The reinforcing of structures by means of composite materials (plates, laminae or fabrics) is quickly growing in civil engineering applications for rehabilitation and repair of structures as well as for structural improvement operations. In the last decade experimental tests and numerical analyses have been performed on concrete or masonry structures in order to study problems connected to adhesion, stresses at the interfaces, cracks formation on base materials and different thermal elongation. On the contrary the same attention has not been addressed to the reinforcing of steel elements. In this case an experimental analysis of the bonding system is highly recommended in order to use this system with confidence.

Some experimental tests were performed at the Testing Material Laboratory of the Politechnic of Milan in order to characterize the bonding properties of an epoxy resin used in the reinforcement of steel structures by CFRP laminae. The specimens were designed in order to reproduce the most common applications: a double-doubler joint, a double reinforcement of a continuous steel plate and a double reinforcement of a drilled steel plate. The last specimen was studied in order to reproduce the reinforcing of a bolted joint by CFRP patches.

The strains along the whole bond length of the CFRP laminae were recorded by means of several strain-gauges. The results allowed to characterize the force transfer mechanism and to validate the different analytical models available from the literature. Moreover, finite element analyses of the drilled steel plate (where no analytical solutions are available) were performed and the results compared with the experiments. The beginning of the failure mechanism, that generally involves the bonding interface, was detected and provided valuable information to establish relevant failure criteria.

1 INTRODUCTION

For a variety of reasons, steel structures may be found to be structurally unsatisfactory. These deficiencies include design errors, the use of inferior materials or poor construction workmanship. Moreover, an upgrading of the design standards or an increase in the intensity of the applied loads to be supported may render a part of the structure inadequate. Finally, the load carrying capacity of steel elements may be compromised by deterioration of the material as a result of corrosion or fatigue damage. All these reasons contribute to the need for the rehabilitation of metallic structural components. The rehabilitation of steel structures may be undertaken by welding, by bolting or adhesive bonding of steel cover plates to the existing systems. The main disadvantages are:

- durability and corrosion effects [1, 2];
- the need of falseworks to place the heavy plates in position and the consequent traffic disruption;
- the difficulty of fitting complex profiles;
- the sensitivity of the repaired system to fatigue problems due to stress concentration produced by welding or bolting techniques.

To date advanced polymer composites have been used to upgrade a small number of steel or cast iron structures [3] and only a limited number of research projects have been conducted to validate the repair techniques [4-7]. Nevertheless, the high tensile strength and stiffness, the high fatigue resistance and the low self weight, make carbon fiber reinforced polymer (CFRP) composites ideal candidates for upgrading steel structures.

The drawbacks to the use of CFRP reinforcements are its intolerance to uneven bonding surfaces, the potential brittle failure modes and durability of the adhesive joints [1, 8]. Note that, since carbon fibers are electron conductors, relatively high in the galvanic series, when CFRP and metals get in contact in an electrolyte solution (such as sea water or water with de-icing salts), galvanic corrosion of the metal part occurs [4]. Finally, the high stiffness CFRP will have a stiffness of the same order as that of the steel. Significant load transfer take place only in the plastic region or in the elastic region if ultra-high modulus CFRP is adopted. Note, however, that in a rehabilitation project the installation savings can offset the higher material costs if the traffic management costs are included.

The weakest link in the plate bonding of advanced polymer composites to a metallic substrate is the adhesive [8]. The successful strengthening of steel structures with CFRP materials is completely dependent upon the quality and integrity of the composite-steel joint and the effectiveness of the adhesive used. If CFRP pultruded plates were to be used in upgrading a steel member, a two part component epoxy adhesive would invariably be used. The integrity of the joint is highly dependent upon the preparation procedures for bonding the CFRP plates on the, possibly corroded, steel members [3]. In order to produce a chemically active surface, abrasion of the metal is first performed. Then, the surface for bonding must be free from contaminants by solvent cleaning.

In order to study the behaviour of steel-composite assembly, different CFRP steel specimens were prepared and tested. Our attention focused mainly on the adherence problems and on the presence of local stresses near the edge of the lamina or near discontinuities and holes. The experimental results have been compared with the behaviour predicted by analytical and numerical models.

THE EXPERIMENTS

The experiments were performed at the Testing Material Laboratory of the Department of Structural Engineering of the Polytechnic of Milan. Since the objective of the test activities was the understanding of the bonding mechanism, the simplest geometries were adopted. They included a double-doubler joint, a double side reinforcement and a double side reinforcement of a drilled steel plate. The materials mechanical characteristics are reported in section 0 while the descriptions of the specimens can be found in section 0, 0 and 0.

Materials

The composite material used were pultruded CFRP laminae manufactured by SIKA® with a width equal to 60 mm and a thickness equal to 1.4 mm. The nominal values are

	Type	E_x (MPa)	G_{xy} (MPa)	ν_{xy}	f_y (MPa)	f_t (MPa)
Steel	Fe430	210000	80770	0.3	275	430
CFRP laminate	M614	210000	---	---	---	2400
Adhesive	Sikadur 30	4300	---	---	---	15 ÷ 70

Table 1: nominal characteristics of the used materials.

	Type	E_x (MPa)	G_{xy} (MPa)	ν_{xy}	f_y (MPa)	f_t (MPa)
Steel	Fe430	210000	---	---	317.8	433
CFRP laminate	M614	197100	---	---	---	792

Table 2: mechanical characteristic determined by experimental tests.

reported in Table 1 while the experimental ones are reported Table 2. Note that the low f_t value of the CFRP lamina is due to the stress concentration in the grips of the testing machine. In fact the specimens were obtained from a 60 mm width lamina and appropriate end-tabs were not applied. Anyway this value was not significant for the present investigation. The adhesive used in this investigation was a typical thixotropic epoxy resin adhesive, widely used in standard applications, manufactured by SIKA®. Its nominal mechanical properties are reported in Table 1.

Double-doubler joint

The joint was made of two CFRP laminae bonded to two steel plates by two-part epoxy adhesive. The specimen dimensions are reported in

Figure 1. The dimensions were chosen in order to achieve a full force transfer between the joint and the steel plates.

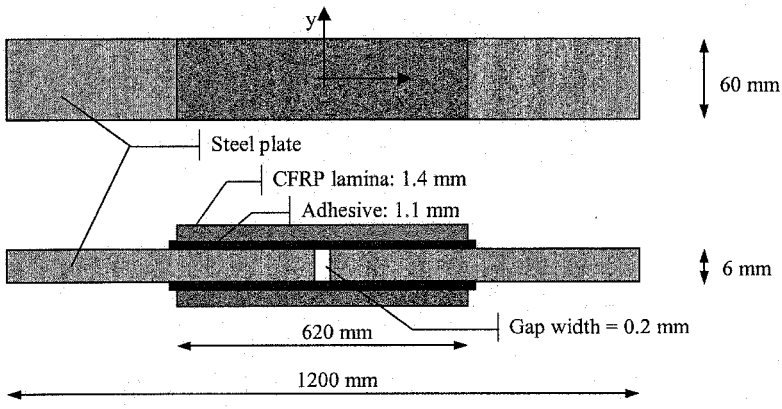


Figure 1: specimen n. 1, double-doubler joint

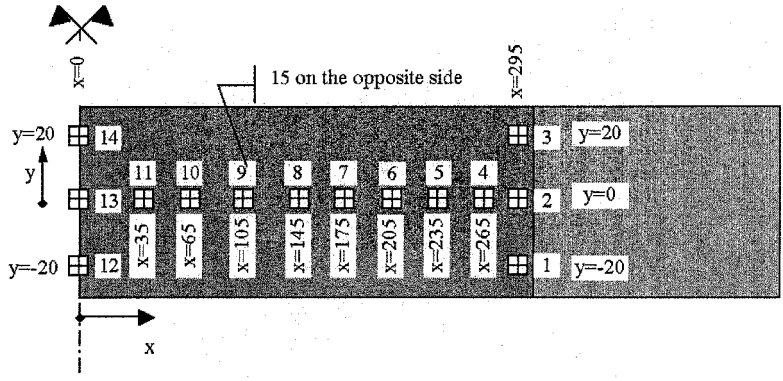


Figure 2: strain gauges positions in specimen n. 1 (distances in mm)

The steel surface was treated with an abrasive disc and then wiped clean by acetone while the CFRP surface was prepared using an abrasive pad. Moreover, the specimen was equipped with fifteen strain gauges applied in the positions described in Figure 2 in order to monitor the load transfer mechanism. The gauge n. 15 was applied on the opposite face in correspondence with the gauge n. 9.

Double side reinforcement

The second specimen was a double side reinforcement of a continuous steel plate using two CFRP laminae bonded by a two-part epoxy adhesive. The specimen dimensions are reported in Figure 3. Also in this case, the steel surface was treated with an abrasive disc and then wiped clean by acetone while the CFRP surface was prepared using an abrasive pad. Moreover, the specimen was equipped with five strain gauges applied in the positions described in Figure 4 in order to monitor the load transfer mechanism.

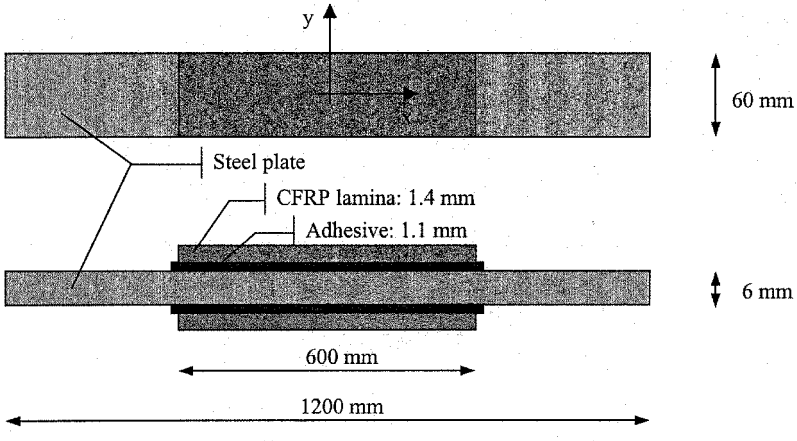


Figure 3: specimen n. 2, double side reinforcement

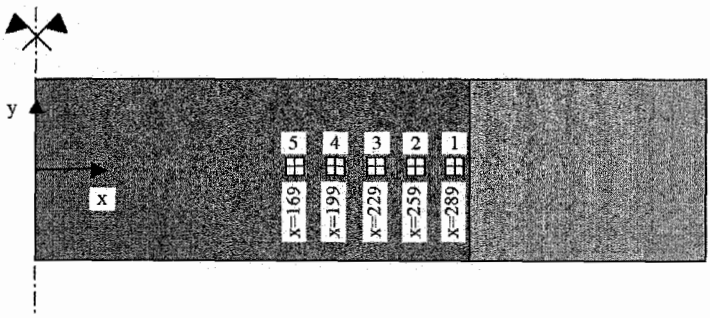


Figure 4: strain gauges position in specimen n. 2 (distances in mm)

Drilled double side reinforcement

This specimen was prepared by bonding two CFRP lamina by two-part epoxy adhesive to a steel plate. Then a 20 mm diameter hole has been drilled through the whole thickness. The dimensions of the specimen are reported in Figure 5.

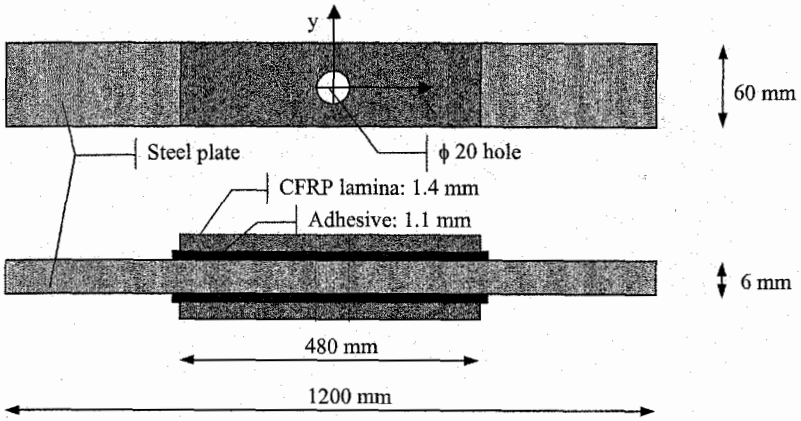


Figure 5: specimen n. 3: drilled double side reinforcement

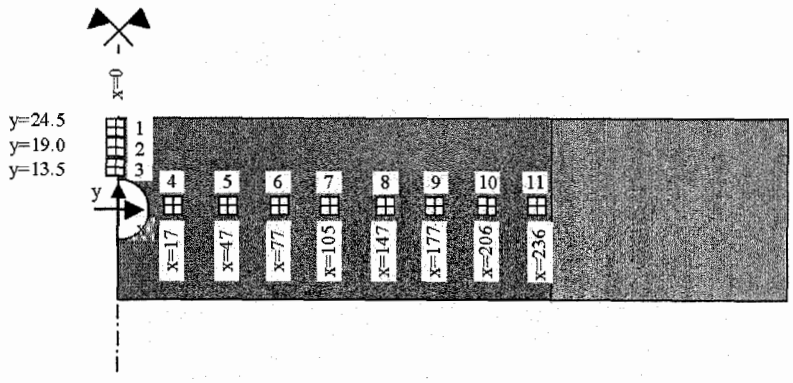


Figure 6: strain gauges position in specimen n. 3 (distances in mm)

The aim of this test was to evaluate the reinforcing capabilities of composite materials if applied to bolted joints. Moreover, the specimen was equipped with eleven strain gauges applied in the positions described in Figure 6. In this case three strain gauges were applied in the transversal direction in order to study the stress distribution near the hole.

TEST RESULTS

All tests have been performed by means of a mechanical testing machine with a maximum capacity of 1000 kN. The tests were performed in displacement control, with a rate equal to 0.5 mm/min in the elastic range and 2 mm/min after yielding.

Double-doubler joint

The strains recorded during the test are reported in Figure 7. It should be noted that:

- the strain gauges number 1 and 8 are not reported due to technical problems;
- the specimen had a linear behaviour up to the steel yield (approximately 100 kN);
- the specimen failure was due to steel/adhesive interface debonding close to the reinforcement edge.

After the substrate yielding large deformation occurred and the debonding of the steel/adhesive interface quickly took place near the reinforcement edge. In fact, from the curves reported in Figure 8 it can be noted that the debonding, denoted by a sudden drop to zero of the relevant strain gages, was initiated near the strain gauges 2 and 4 for a total load of 110 kN.

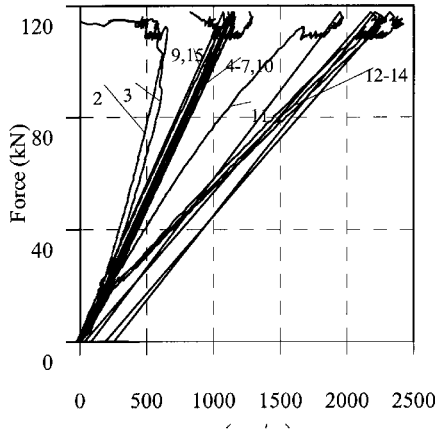


Figure 7: longitudinal deformations in the CFRP patch recorded during the test of specimen n. 1.

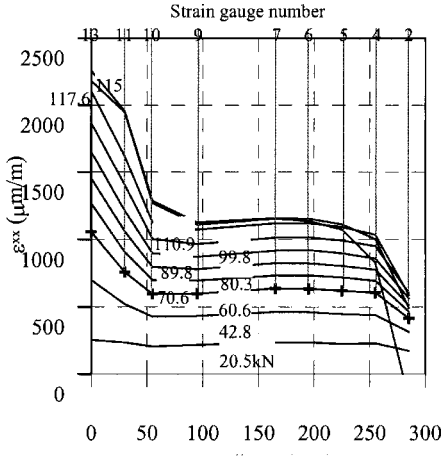


Figure 8: longitudinal deformations in the CFRP patch recorded at different load levels in specimen n. 1. The crosses indicate the strains recorded at a load level of 60.6 kN.

Double side reinforcement

The deformations recorded during the test are reported in Figure 9. It should be noted that:

- the strain gauge n. 1 presents a non linear behaviuor for a total load greater than 70 kN;
- the strain gauge n. 1 is also the first strain gauge which denotes a deformation drop (see Figure 10);
- the specimen failure was due to steel/adhesive interface debonding started from the reinforcement edge.

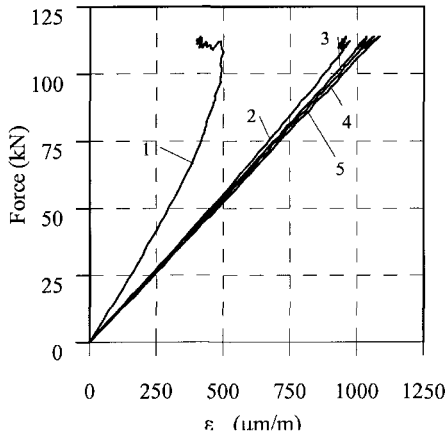


Figure 9: longitudinal deformations in the CFRP patch recorded during the test of specimen n. 2.

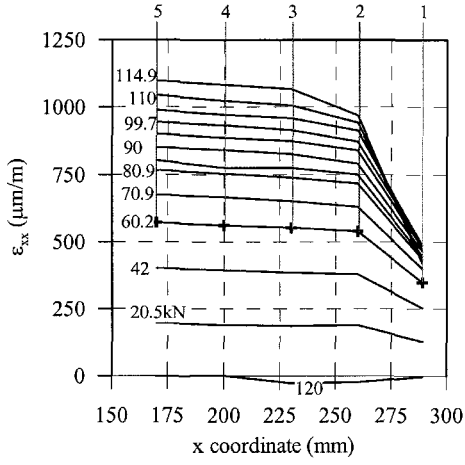


Figure 10: longitudinal deformations in the CFRP patch recorded at different load levels in specimen n. 2. The crosses indicate the strains recorded at a load level of 60.2 kN.

Drilled double side reinforcement

This test was performed in order to study the possibility to reinforce bolted joints by means of CFRP patches. Two possible collapse mechanisms can occur: a rupture near the hole of the whole specimen or the debonding of the CFRP.

The deformations in axial direction recorded during the test are reported in Figure 11. It should be noted that:

- the largest deformations of the composite reinforcement occurred near the hole, for x = 0, in the *x* direction (strain gauges 1-3);
- the failure of the steel-adhesive interface initiated near the edge of the CFRP plates at a load level of 105 kN. For this load level a sudden drop of the deformation recorded by the strain gauge n. 11 was observed (see Figure 12). No debonding was observed near the central hole. This is due to the fact that the shear stresses in the adhesive layer are higher near the edge of the CFRP lamina than in the hole zone.

The axial stresses in x direction calculated from strain gauges measurement 1, 2 and are reported in Figure 13.

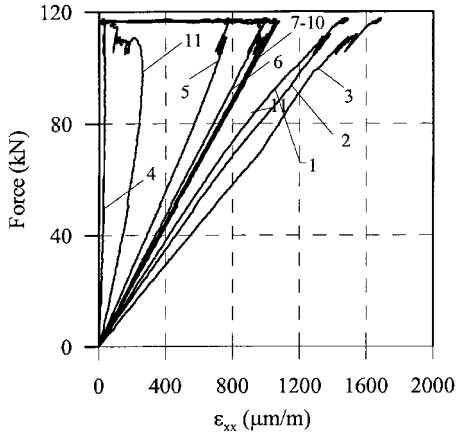


Figure 11: deformation recorded in the CFRP patch during the test of specimen n. 3

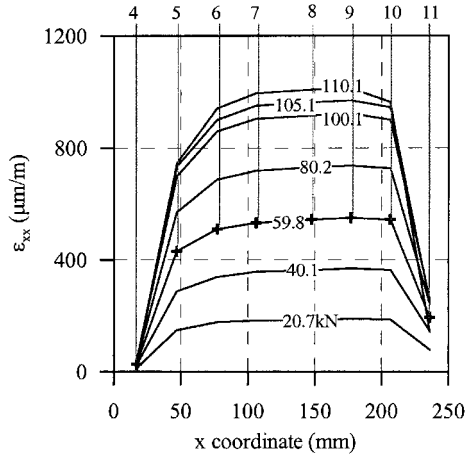


Figure 12: deformation recorded in the CFRP patch at different load levels in specimen n. 3

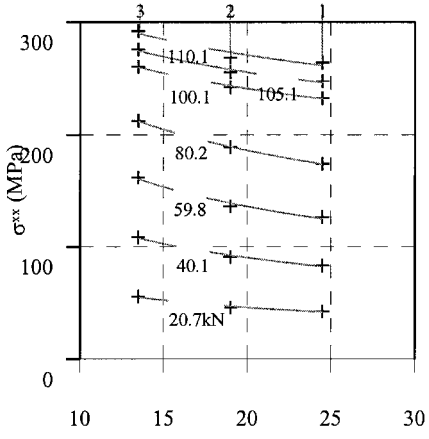


Figure 13: stresses recorded in the CFRP patch at different load levels in specimen n. 3 by strain gauges 1-3. The continuous lines are obtained by a logarithmic best-fit procedure

COMPARISON OF EXPERIMENTAL TESTS WITH ANALYTICAL AND NUMERICAL MODELS

The data collected from the experimental tests reported in section 0 were compared with analytical values obtained using the linear elastic model developed in [9]. The formulation allows to avoid finite elements analyses in order to evaluate the interface stress that occurs in both the double-doubler joint and double side reinforcement. In the case of the double side reinforcement of a hole the model developed in [9] is not applicable, and a finite element analysis become unavoidable to reproduce the experimental results. The geometric and mechanical characteristics assumed for the analytical model are reported in Table 3:

	Thickness (mm)	E (MPa)	G (MPa)	ν
Steel	6.0	210000	80770	0.3
CFRP	1.4	197100	76000	0.3
Adhesive	1.1	---	1500	---

Table 3: geometric and mechanical characteristics assumed in the analytical model

Double-doubler joint

The experimental data obtained from the test of specimen n. 1 are reported in Figure 14 and compared to the corresponding analytical prediction at the load level of 60.6 kN. The figure shows a good agreement although the uncertainty about the shear modulus and the thickness of the adhesive. Note that the strain gauge n. 13 (position x = 0 in the specimen n. 1) recorded strain values sensibly lower than the predicted ones. This is probably due to the fact that during the preparation of the specimen the two steel plates were placed very closed (gap width was approximately equal to 0.2 mm) and the sensor could not record the deformation of the CFRP lamina alone.

The shear stresses at the adhesive interface are plotted in Figure 15 for an axial load of 60 kN. The linear elastic model proposed in [9] predicted shear stresses greater at the joint location ($x = 0$ in Figure 15) than at the reinforcement edge ($x = 300$ in Figure 15). On the other hand, experimental results showed (see Figure 8) that the debonding started at the edge of the reinforcement and not at the joint location. Then, it can be concluded that the inelastic deformation of the steel substrate produced a significant redistribution of the shear stresses at the interface which leads to the debonding at the reinforcement edge and not at the joint location (see the behavior of strain gauges n. 11 and 13 in Figure 7).

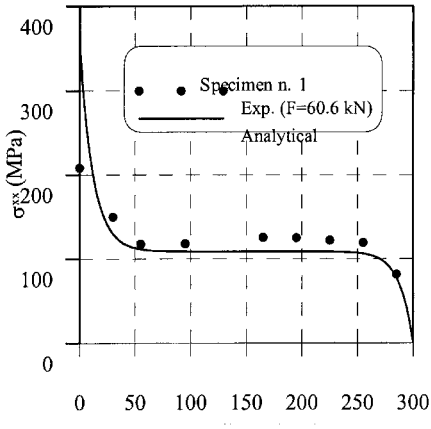


Figure 14: comparison of experimental and analytical values in the CFRP patch for a total load of 60.6 kN in specimen n. 1

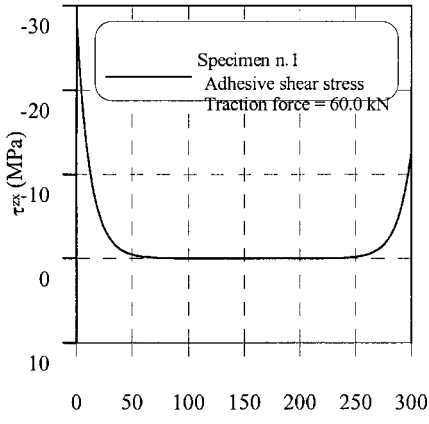


Figure 15: prediction for specimen n. 1 of the shear stress in the adhesive by the model developed in [9]

Double side reinforcement

The behaviour of the double side reinforcement specimen is simpler than the previous one, and certainly it is the most common example of structural reinforcement.

The experimental data obtained from the test of specimen n. 2 are reported in Figure 16 and compared to the corresponding analytical prediction at the load level of 60.2 kN. The figure shows a good agreement even if the real maximum stress of the CFRP seems to be higher than the predicted one.

The shear stresses at the adhesive interface are plotted in Figure 17 for a traction load of 60 kN. The most stressed zone is near the edge of the lamina where debonding took place. Note that also in this case the interface failure was anticipated by inelastic deformations of the steel substrate therefore a shear stress redistribution at the interface was expected (see the behavior of strain gauge n. 1 in Figure 9).

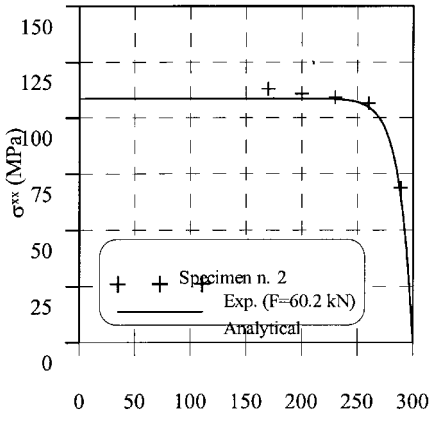


Figure 16: comparison of experimental analytical values for a total load of 60.2 kN in specimen n. 2

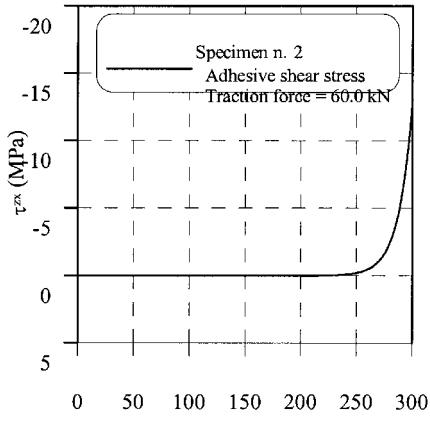


Figure 17: analytical distribution for specimen n. 2 of the shear stress in the adhesive by model developed in [9]

Drilled double side reinforcement

If discontinuities (holes or cracks) are present in a structural element the analytical prediction by means of simple models (like in [9]) cannot be performed and experimental tests become more and more important. These tests results can also be used for the development of adequate finite element models that allow a more in deep investigation of debonding problems. The shear stresses at the adhesive interface and the stress intensity near the hole can be computed only by a finite element model. The lamina behaviour was assumed orthotropic with a transversal Young's modulus equal to one tenth of the longitudinal one, as usual in unidirectional fibre reinforced polymers. The finite element model adopted is reported in Figure 18, while the shear stresses at the steel-adhesive interface are reported in Figure 19. The distribution of the stresses σ_{xx} in the composite reinforcement in the longitudinal direction (x direction in Figure 18) are reported in Figure 20 and compared to the experimental results at the load level $F = 59.8$ kN. The distribution of the stresses σ_{xx} in the steel substrate in the transverse direction (y direction in Figure 18) obtained by finite element analyses are plotted in Figure 21 for two configurations at a load level $F = 60$ kN: the single steel plate and the steel plate

reinforced with CFRP laminae. The stresses have been normalized to the nominal axial stress in the unreinforced steel plate, $\sigma_0 = F/A = 166.66$ MPa. It should be noted that the analytical solution for the stress distribution in the y direction provided a ratio $\sigma_{xx}/\sigma_0 = 3.3$ for $y = 10$ mm while the reinforced plate showed a ratio $\sigma_{xx}/\sigma_0 = 2.5$. This means that the application of the composite patch produces a significant decrease of the stress concentration around the hole region.

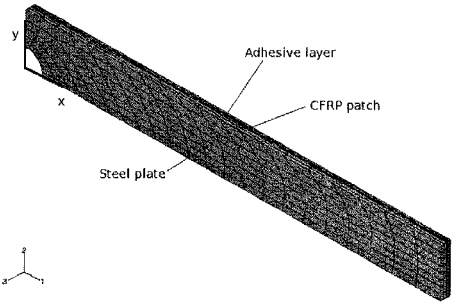


Figure 18: three-dimensional mesh of specimen n. 3.

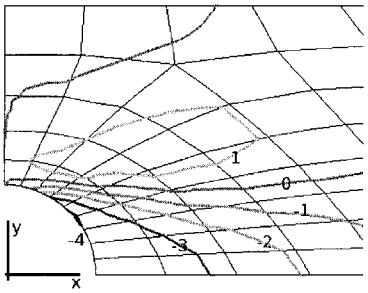


Figure 19: shear stress levels τ_{xz} at the steel-adhesive interface (MPa)

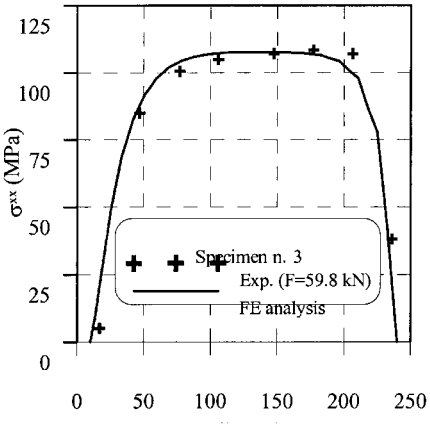


Figure 20: distribution in specimen n. 3 of stresses σ_{xx} in the CFRP reinforcement at a load level of 60 kN.

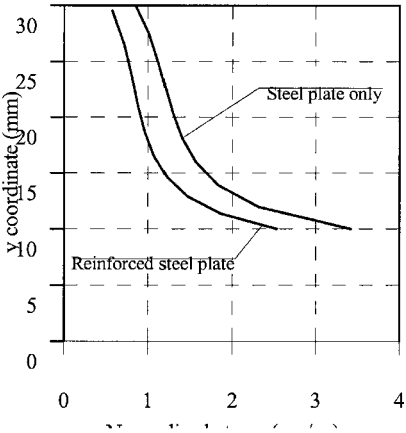


Figure 21: distribution in specimen n. 3 of stresses σ_{xx} in the steel plate (reinforced and unreinforced one) at a load level of 60 kN.

Finally, the distribution of the stresses σ_{xx} in the composite patch in the transverse direction (y direction in Figure 18) are plotted in Figure 22 and compared to experimental results. Even in this case an excellent agreement is evident.

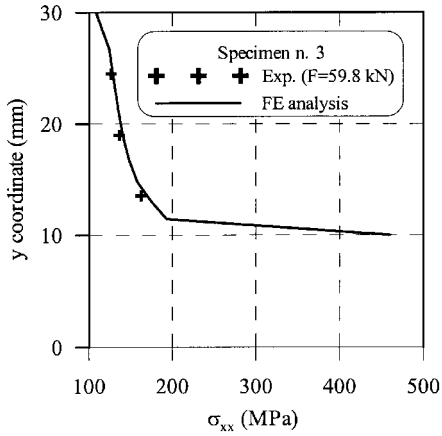


Figure 22: distribution in specimen n. 3 of stresses σ_{xx} in the composite patch at a load level of 60 kN.

CONCLUSIONS

This paper has summarized the observation and results of the first step of an experimental program for the study of the reinforcement of steel element by CFRP patches. Double-doubler joint and double side reinforcements have been investigated together with a drilled double side reinforcement. A single adhesive system configuration has been considered, namely a commercial two-part epoxy adhesive. In each case the failure was produced by debonding of the steel-adhesive interface and no composite damage was observed at the end of the test. Moreover, debonding started, invariantly, at the edge of the composite patch propagating then through the steel/adhesive interface up to failure. This means that the drilled hole, for the investigated reinforcement geometry, does not produce a shear stress concentration capable to start the delamination process. Analytical and numerical models were used to predict experimental results. In particular, the adopted analytical model is capable to predict the reinforcement behavior in the elastic range, but it can not be used to study the debonding phenomena. In fact experimental results showed that it is influenced by the inelastic deformation in the steel plate and eventually in the adhesive layer. The next stage of the research program will be the investigation of steel joints reinforced by CFRP patches and of steel beams strengthened by CFRP laminae. Moreover, a specific debonding model, which takes into account the inelastic phenomena, should be developed in order to predict with confidence the failure load of a reinforced steel plate.

ACKNOWLEDGEMENT

The financial support from the ITALIAN MINISTRY OF INSTRUCTION, UNIVERSITY AND RESEARCH (MIUR) under the research project COFIN02 is gratefully acknowledged. Thanks is also expressed to SIKA ITALIA S.P.A. for supplying the composite materials and to BUILDING IMPROVING S.R.L. for providing the reinforcement installation.

REFERENCES

1 M. Tavakkolizadeh and H. Saadatmanesh. Galvanic corrosion of carbon and steel in aggressive environments. Journal of Composites for Construction, ASCE, vol. 5(3), pp. 200-210, 2001.

2 V.M. Karbhari and S.B. Shulley. Use of composites for rehabilitation of steel structures – determination of bond durability. Journal of Materials in Civil Engineering, ASCE, vol. 7(4), pp. 239-245, 1995.

3 L.C. Hollaway and J. Cadei, Progress in the technique of upgrading metallic structures with advanced polymer composites. Prog. Struct. Engng. Mater., pp.131-148, 2002

4 T. C. Miller, M.J. Chajes, D.R. Mertz and J.N. Hastings. Strengthening of a steel bridge girder using CFRP plates. Journal of Bridge Engineering, ASCE, vol. 6(6), pp. 514-522, 2001.

5 A. Lenwari, T. Thepchatri and E. Watanabe. Prediction of premature separation of bonded CFRP plates from strengthened steel beams using a fracture criterion. Structural Engineering and Mechanics, vol. 14(5), pp. 565.574, 2002.

6 SSJ Moy and F. Nikoudar. Flexural behaviour of steel beams reinforced with carbon fibre reinforced polymer composite. Advanced polymer composites for structural applications in construction, Edited by RA Shenoi, SSJ Moy and LC Hollaway, Thomas Telford, pp. 195-202, 2002.

7 N. Photiou, M. Chryssanthopoulos and L. C. Hollaway, "Characterisation of Adhesively Bonded Composite Plates for Upgrading Structural Steelwork", 10th Int. Conf. on Structural Faults and Repair, London, 1-3 July 2003.

8 VM Karbhari and SB Shulley. Use of composites for rahabilitation of steel structures – determination of bond durability. Journal of Materials in Civil Engineering, vol. 7(4), pp. 239-245, 1995.

9 AM Albat and DP Romilly. A direct linear-elastic analysis of double symmetric bonded joints and reinforcements. Composite Science and Technology, vol. 59, pp. 1127-1137, 1999

THE STRENGTHENING OF WROUGHT IRON USING CARBON FIBRE REINFORCED POLYMER COMPOSITES

S.S.J. MOY J. CLARK H. CLARKE

University of Southampton, UK

ABSTRACT

The paper presents the results of a preliminary investigation into the strengthening of wrought iron structures using carbon fibre reinforced polymer composites (CFRP). It is shown that the production process, in particular the resulting laminar structure, affected the mechanical properties of the wrought iron. This has an influence on the possibility of CFRP strengthening. It is shown that CFRP strengthening is feasible but the possibility of wrought iron delamination in the compression zone needs to be considered.

INTRODUCTION

The use of Carbon Fibre Reinforced Polymer Composites (CFRP) for strengthening and structural upgrade of existing metallic structures has considerable potential. The lightweight, high strength, stiffness and durability of CFRP are offset by relatively high material cost, but where access is limited or connecting conventional material to the existing structure is difficult, CFRP becomes competitive in both applicability and cost. Design Guides [1, 2] for such strengthening are or will be available in the near future.

However, there are concerns about the use of CFRP for strengthening wrought iron structures. Both Design Guides indicate that further research is needed on such strengthening. The railway network of the UK has a significant number of wrought iron bridges, many of which need strengthening following increases in design loading and possibly deterioration of the wrought iron. Consequently there is an urgent need to investigate the applicability of CFRP to wrought iron strengthening.

The concerns surround the nature of the wrought iron itself. It has a peculiar internal structure arising from its manufacturing process. No new wrought iron has been produced in the UK for over 100 years and there has been little research interest in the metal. Railtrack has funded a preliminary research programme in the Department of Civil and Environmental Engineering at the University of Southampton to investigate the nature of the wrought iron in their bridges and to assess its suitability for CFRP strengthening. A detailed report of the research is presented in [3]. This paper presents an overview of the research and gives conclusions and recommendations as to how CFRP strengthening of wrought iron should be progressed.

THE NATURE OF WROUGHT IRON

Wrought Iron is an old form of ferrous metal. It was being produced in the 1820's and was used, particularly in railway infrastructure, up to the end of the 19th century. It has two main constituents, iron and slag. The iron was very pure, containing approximately 0.02% by weight of carbon and small percentages of other impurities such as manganese,

phosphorous, silicon and sulphur. Plain carbon steels have a carbon content of about 2% and cast iron has a carbon content of about 4%. The slag was mainly a silicate of iron, Fe_2SiO_4 [3] and made up about 3% of the total mass.

During manufacture the slag impregnated the iron and in the finished state it was found as inclusions in the metal matrix. The method of production of wrought iron started with a puddling process which resulted in a pasty metal/slag mixture. This was split into small balls weighing about 50kg which were removed from the furnace, hammered into shape and then rolled into a bar. The rolling squeezed out the surplus slag. The process was repeated several times to improve the uniformity of the material and its properties. Experience showed that after six repetitions the optimum properties were achieved.

The hammering and rolling produced relatively thin plates, angle or tee sections, and gave the metal a characteristic laminar structure. To produce large girders the thin components had to be riveted together, as shown in figures 1 and 2. The structure of the wrought iron was very directional. As well as squeezing out the excess slag, the hammering and rolling drew out the slag into long thin fibres in the rolling direction.

Railtrack effectively made available a complete girder from a wrought iron bridge which had been removed after at least 100 years in service and stored in a yard near Wimbledon station. Parts of the top flange were cut out from the bridge and separated into individual plates by removing the connecting rivets. Each plate was about 10mm thick and was distorted as a result of rivet removal. The condition of the metal was good with only light rusting to exposed surfaces. Specimens were cut from the plates and machined flat. The slag fibres were clearly visible but there was no evidence of the laminar structure before loading.

TENSILE TESTING OF THE WROUGHT IRON

Tensile specimens were produced in the direction of the slag fibres and also perpendicular to them. The tensile tests are reported in detail in [3] but the results are summarised in

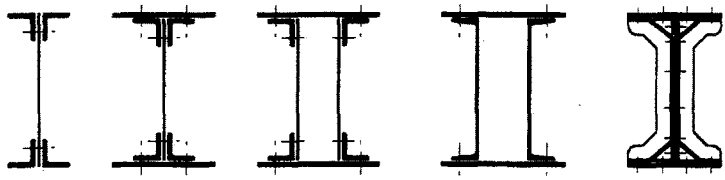


Figure 1: Typical cross-sections of wrought iron girders (from figure 3.7 in [4])

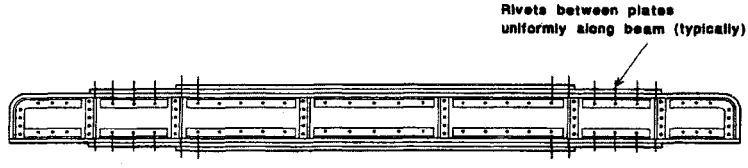
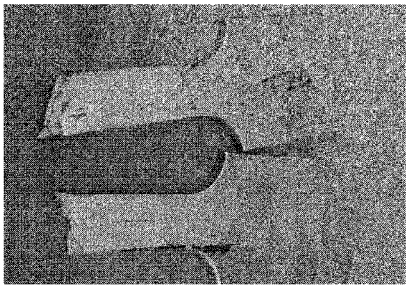


Figure 2: Typical elevation of wrought iron girder (from figure 3.8 in [4])



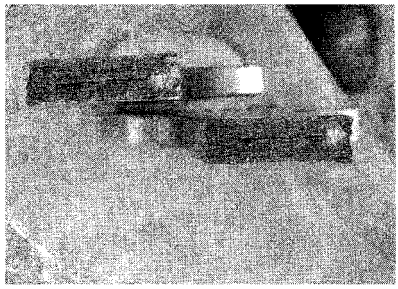


Figure 3: Failed tensile specimen showing slag fibres and laminations of failure surface

Tables 1 and 2. The directional nature of the wrought iron can be seen by comparing the tables of results. There was considerable ductility in the slag fibre direction, with an average elongation at failure of 11.3%, whereas the metal was brittle in the cross fibre direction with an average elongation of 2.6% at failure. The yield stress was slightly

Table 1: Summary of results from tensile specimens, direction of slag fibres.

	Mean Value	Range
Yield Stress (N/mm^2)	234.9	251.9 - 223.0
Young's Modulus (kN/mm^2)	198.6	207.7 - 185.5
Ultimate Tensile Strength (N/mm^2)	312.7	330.0 - 270.1
Elongation (%)	11.3	15.4 - 7.2

Table 2: Summary of results from tensile specimens, perpendicular to slag fibres.

	Mean Value	Range
Yield Stress (N/mm^2)	210.8	226.3 - 170.7
Young's Modulus (kN/mm^2)	205.0	222.7 - 177.5
Ultimate Tensile Strength (N/mm^2)	227.9	244.7 - 206.1
Elongation (%)	2.6	3.4 - 1.9

higher in the fibre direction and because of the ductility the ultimate tensile strength in the fibre direction was 37% higher. There was considerable variability in the results, particularly for properties in the cross fibre direction. The feature of all the tensile tests

was the revelation of the layering in the specimens. Clearly defined planes developed along the thin edges of the specimens which were visible to the naked eye as the load increased. At failure it was observed that fracture would spread through one layer at a time so that distinct fracture surfaces were clearly visible for each layer. It can be concluded that the metal in each layer had slightly different strength and stiffness properties. The specimens with the lowest properties in the fibre direction usually had crystalline inclusions in their fracture surfaces. Figure 3 above, shows a typical failed sample.

COMPRESSION TESTING OF THE WROUGHT IRON

Compression tests were carried out on samples machined in the fibre direction. The specimens were small and stocky to avoid buckling. Table 3 summarises the results.

Table 3: Summary of results from compression specimens, direction of slag fibres.

	Mean Value	Range
Yield Stress (N/mm^2)	244.2	259.5 – 234.8
Ultimate Compressive Strength (N/mm^2)	414.9	446.9 – 385.8

It was not possible to measure strains in the very small specimens and thus it was not possible to determine a Young's modulus in compression. The specimens showed considerable variability. After yield occurred the samples started to delaminate and also to deflect sideways. The most likely explanation is that the individual layers buckled after delaminating because their slenderness ratio was considerably greater than that of the original sample. After failure one specimen had split completely into the individual layers. Figure 4 shows a typical specimen after testing.

INTER-LAMINAR SHEAR STRENGTH OF THE WROUGHT IRON

The laminar structure revealed after the tensile and compressive tests raised questions about the inter-laminar shear strength of the wrought iron. Specimens have been devised to measure this but the amount of machining involved precluded their production and testing in the time scale of this paper. It is hoped to present some results at the conference.

CFRP STRENGTHENING OF THE WROUGHT IRON

Another objective of the research was to investigate the use of CFRP for strengthening the wrought iron. Two types of CFRP were used. K13710 ultra-high modulus CFRP 7.6mm thick preformed plate was used in lap shear tests to investigate the bond between the CFRP and the wrought iron. High strength CFRP Reno sheet was used to investigate the benefits in tensile strength from different thicknesses of CFRP. Reno sheet is a 'prepreg' of carbon fibre in an epoxy resin. It is unusual in that it can be stored at room

temperature and curing is initiated by the heat from the exothermic reaction of additional epoxy resin placed between the layers of prepreg.

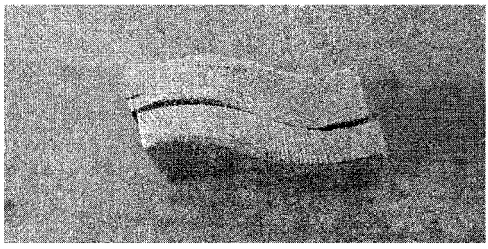


Figure 4: Failed compression specimen showing delamination

The wrought iron specimens were small and it was not practical to have them grit blasted. Thus surface preparation was limited to roughening with a file and emery paper followed by solvent degreasing. This was felt to be the minimum acceptable level of surface preparation and gave the most pessimistic impression of the benefits of CFRP strengthening. The adhesive used to bond the CFRP to the wrought iron was Sikadur 31, a two part epoxy adhesive commonly used in CFRP strengthening. The adhesive was applied in the usual manner to prevent air entrapment. After preparation the various specimens were left for 48 hours to allow the adhesive to cure.

The lap shear specimens tested the strength of the bond between the CFRP and the wrought iron. Table 4 summarises the test results. Two specimens, AS6 and AS8, had to be discarded because of faulty manufacture and testing. The most desirable failure was cohesive failure in the adhesive and this occurred in several specimens. The next most desirable was failure in the CFRP and again this occurred in a number of specimens. Specimens AS4 and AS7 failed by debond at the metal/adhesive interface and AS4 had a very low failure load. This undesirable failure mode was due to the relatively poor surface preparation of the wrought iron. The average shear stress at failure (calculated ignoring AS4) was similar to bond strengths determined between CFRP and steel [4] using the same adhesive. It can be concluded from the lap shear results that with proper surface preparation of the wrought iron (grit blasting) a satisfactory bond can be achieved between the CFRP and the wrought iron.

Tests were carried out on wrought iron tensile specimens (cut in the direction of the slag fibres) reinforced with different thicknesses of CFRP. The CFRP was first tested in tension to determine its tensile strength. Table 5 summarises the test results. The differences in tensile strength for the different thicknesses of CFRP are due to the different proportions of resin used in the fabrication of the CFRP changing the fibre volume fractions in the two thicknesses of specimens. Specimen 5 was the first specimen made and was not satisfactory due to our lack of experience with the materials; hence it has been ignored when calculating the average tensile strength.

Table 4: Summary of results from lap shear tests.

Specimen	Area in shear (mm^2)	Failure Load (kN)	Failure Stress (N/mm^2)
AS1	801.7	14.0 †	17.5
AS2	991.1	14.8 †	14.9
AS3	895.6	12.5 †	14.0
AS4	934.0	9.2 *	9.9
AS5	965.9	15.7 †	16.3
AS6	-	-	-
AS7	842.8	16.0 *	19.0
AS8	1070.9	-	-
AS9	833.7	15.0 †	18.0
AS10	814.8	15.9 #	19.5
AS11	887.8	15.8 †	17.8
AS12	817.7	15.2 †	18.6
AS13	952.6	14.2 †	14.9
		average	17.0

Notes: † CFRP delamination close to adhesive surface
* metal debond
\# failure in the adhesive layer

Table 5: Summary of results from CFRP tensile tests

CFRP Strip	Thickness (mm)	Width (mm)	Area (mm^2)	Failure Load (kN)	Tensile Strength (N/mm^2)
5	0.89	22.93	20.48	14.75	720
6	0.85	23.07	19.54	18.00	921
7	0.91	23.01	20.87	19.20	920
				mean	921*
8	1.45	22.83	33.02	38.50	1165
9	1.44	22.45	32.41	37.50	1157
10	1.51	22.92	34.69	44.80	1292
				mean	1205

*ignoring specimen 5

Several wrought iron tensile specimens were reinforced using the 'prepreg' system however only two were felt to be satisfactory. The results of the tensile tests on these specimens are presented in Table 6. The yield load was taken as the load at which the load-extension graph became non-linear. Test failure was marked by explosive rupture of the CFRP with immediate tensile failure of the wrought iron. Predicted values were based on average measured mechanical properties of the materials and average specimen dimensions. It can be seen that the predicted values are in good agreement with the

measured values. The benefits in terms of increased strength from the CFRP strengthening are obvious and significant.

Table 6: Summary of results from tensile tests on CFRP strengthened wrought iron.

Specimen	Width (mm)	Combined thickness (mm)	Predicted yield load (kN)	Measured yield load (kN)	Predicted failure load (kN)	Measured failure load (kN)	Wrought iron uts (kN)
T23	19.90	8.40	30.8	32.0	59.8	67.0	27.4
T24	20.57	9.33	38.5	39.5	101.1	102.0	28.4

CONCLUSIONS AND RECOMMENDATIONS

The tests reported above and in detail in [3] have shown the following:

- Wrought iron has a laminar structure and directional mechanical properties. In the direction of the slag fibres (the rolling direction during forming) the metal is ductile in tension with an average elongation at failure of 11.3%. In the cross fibre direction it is brittle with an average elongation of 2.6%. There is considerable variability, the results being affected by slag and other crystalline inclusions.
- The wrought iron had a clear yield stress which was similar in fibre and cross fibre directions. The ultimate tensile strength was about 37% greater than the yield stress in the fibre direction due to the ductility of the metal. It was only slightly higher than the yield stress in the cross fibre direction.
- The laminar structure is not apparent in machined unloaded specimens but becomes obvious to the naked eye when load is applied above the yield value.
- Under compression the individual layers start to separate at loads above yield. In one specimen complete delamination occurred.
- The tests showed that CFRP strengthening of wrought iron is possible. The lap shear tests demonstrated that an adequate bond can be developed between the CFRP and the wrought iron provided suitable surface treatment is applied to the wrought iron. Tensile tests on CFRP reinforced specimens showed significant benefits in terms of increased failure load. Failure occurred in the CFRP and was followed by immediate failure of the wrought iron.
- There was no delamination in the wrought iron during the lap shear or tensile tests on CFRP strengthened tensile specimens.
- CFRP strengthening of wrought iron is feasible. The lap shear and tensile tests confirmed this.
- The compression tests revealed a potential problem. CFRP applied to the tension flange of a wrought iron girder will lower the neutral axis which will increase compressive stresses. There is a concern that these stresses may cause

delamination in the wrought iron in compression. However there is a straightforward solution – apply CFRP to both flanges, keeping the neutral axis in the same position.

The tests have been informative about the properties of wrought iron and the possibility of its strengthening with CFRP. As a result of this information the following recommendations are made:

- Wrought iron obtained from different locations in the country should be tested to investigate the effect of different production processes.
- Tests be carried out on wrought iron in poor condition. It has been reported anecdotally that corrosion can affect the interlaminar strength and this should be investigated.
- An actual wrought iron bridge be strengthened with CFRP. A bridge which marginally fails its assessment would be ideal. The bridge should be monitored before and after strengthening to investigate the immediate and longer term benefits of CFRP strengthening.

ACKNOWLEDGEMENTS

The authors thank Railtrack for the financial support which made this work possible. They also thank Messrs Brian Bell and Alan Hardie of Railtrack for their interest in this research.

REFERENCES

1. Editor, S S J Moy. *FRP composites. Life extension and strengthening of metallic structures. ICE design and practice guide.* London, Thomas Telford, 2001. ISBN: 0 7277 3009 6.
2. *Strengthening metallic structures using externally-bonded fibre-reinforced polymers. CIRIA RP645.* To be published Autumn 2003.
3. J Clark. 'The Assessment of Wrought Iron with respect to Strengthening with Carbon Fibre Reinforced Polymers'. *Undergraduate Individual Project Report, Department of Civil & Environmental Engineering. University of Southampton, 2003.*
4. M Bussell. *Appraisal of Existing Iron and Steel Structures.* Ascot, Steel Construction Institute, 1997. ISBN: 1 85942 009 5.
5. S S J Moy. 'Lap-shear tests on specimens cut from CFRP reinforced steel beams'. *Research Report, Department of Civil & Environmental Engineering, University of Southampton, 2001.*

ANALYSIS OF THE STRESSES IN THE ADHESIVE INTERFACE OF METALLIC BEAMS REINFORCED WITH COMPOSITE PLATES

S. S. J. Moy P. J. Deng M. M. K. Lee

University of Southampton, UK

ABSTRACT

The paper presents an analysis of the shear and normal stresses in the interface (metal/adhesive/composite) of a beam reinforced with CFRP. An analytical solution for constant thickness plates and a numerical solution procedure for tapered plates are given. Examples using the analysis are presented and compared with finite element results.

INTRODUCTION

The strength of a structural system depends on its' weakest component. A common composite strengthening scheme for a metallic structure would involve the bonding of preformed carbon fibre reinforced polymer composite (CFRP) plates to the existing metalwork, using an appropriate adhesive, after preparation of the metal surface by grit blasting. Two part epoxy adhesives which cure at ambient temperature are frequently used. However the adhesive interface between the metal and CFRP adherends is potentially a point of weakness. The bond strength of the joint can be affected by the quality of the surface preparation, the curing conditions and the possibility of movement during the curing cycle.

The bending of a metal beam with a bonded CFRP plate causes shear and normal stresses in the adhesive. The discontinuity at the ends of the plate produces peak shear and normal stresses close to the ends and bond failure usually initiates at one end of the plate, when the principal stress in the adhesive exceeds its strength. The ends of the CFRP plate are often tapered to reduce the peak stresses in the adhesive. Denton [1] developed an analysis to determine the adhesive stresses caused by thermal effects. This analysis was improved and extended by Frost et al [2] to include applied loading. Both analyses ignored certain terms to simplify the solution of the governing equations or to give closed form results for the taper situation.

Lap shear tests [3] are used to determine the adhesive strength. The test gives directly the average shear stress in the adhesive at failure and the peak shear and normal stresses can be found using the analysis developed by Goland and Reissner [4]. However the analysis assumed identical adherends which is not the case when CFRP is bonded to a metal.

This paper presents in brief an analysis which includes all the relevant terms in the governing equations. It will be shown that a closed form solution exists for constant thickness CFRP plates and that a numerical procedure gives results for tapered plates. Results are presented of various studies carried out using the analysis.

STRESS ANALYSIS OF THE INTERFACIAL STRESSES

Basic assumptions

1. All materials are considered to be linear elastic.
2. The beam is simply supported and shallow, so that plane sections remain plane.
3. The shear and normal stresses do not vary through the thickness of the adhesive.
4. Shear deformations in the metal beam and CFRP plate are neglected.
5. Bending deformations of the adhesive are neglected.
6. Bending of the CFRP plate is neglected when calculating the interfacial shear stress but is included when calculating the normal stress.

Shear stresses, constant thickness CFRP plate

Figure 1 shows an infinitesimal element of the reinforced beam. In the figure, V, M and N are the shear force, bending moment and longitudinal tension, τ and σ are the shear and normal stresses at the interface and t is the component thickness. The subscripts b, a and p denote the metal beam, adhesive and CFRP respectively. From assumption 3, the shear force and longitudinal tension in the adhesive can be ignored.

The longitudinal equilibrium of the CFRP element, length dx and width b, is given by:

$$(N_p + dN_p) - N_p - \tau b dx = 0 \tag{1}$$

from which

$$\frac{dN_p}{dx} = b\tau \tag{2}$$

and the transverse equilibrium of the CFRP element is given by:

$$V_p + dV_p + \sigma b dx - V_p = 0 \tag{3}$$

giving

$$\frac{dV_p}{dx} = -b\sigma \tag{4}$$

Similar expressions can be found for the element of the metallic beam. Longitudinal force and moment equilibrium of the combined cross section, after some manipulation, require:

$$N_b = -N_p \tag{5}$$

and

$$M_b = N_b(t_b/2 + t_p/2) + M(x) \tag{6}$$

where $M(x)$ is the applied moment. Using the relationships between displacements and strains, stresses and strains, and stresses, forces and moments it can be shown that:

$$\frac{d\tau}{dx} = -\frac{G}{t_a}((\alpha_b - \alpha_p)\Delta T + \frac{(M(x) + N_b(t_b/2 + t_p/2))t_b/2}{E_b I_b} + N_b(\frac{1}{E_b A_b} + \frac{1}{E_p A_p})) \tag{7}$$

where α is a coefficient of thermal expansion and T is change of temperature. Full details are given in [5]. Differentiating equation (7) with respect to x and substituting equation (5) gives the governing equation:

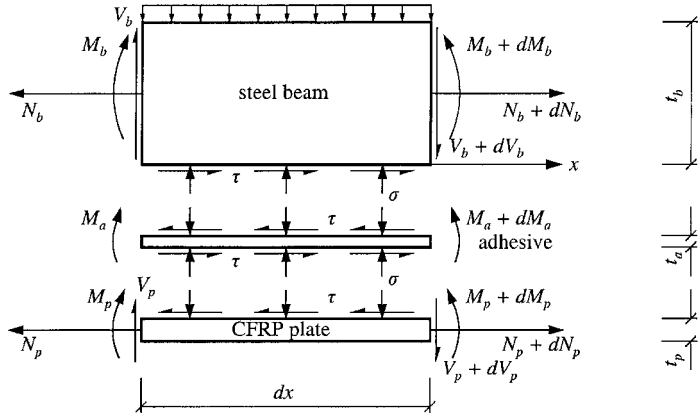


Figure 1: An infinitesimal element of a metal beam with adhesive bonded CFRP plate.

$$\frac{d^2\tau}{dx^2} = \lambda^2\tau - g\lambda^2 M'(x) \tag{8}$$

This has the general closed form solution:

$$\tau(x) = c_1 e^{\lambda x} + c_2 e^{-\lambda x} + gM'(x) \tag{9}$$

where $\lambda = \sqrt{\frac{Gb}{t_a}\left(\frac{(t_b/2 + t_p/2)t_b/2}{E_b I_b} + \frac{1}{E_b A_b} + \frac{1}{E_p A_p}\right)}$ and $g = \frac{Gt_b/2}{\lambda^2 t_a}\frac{1}{E_b I_b}$.

The boundary conditions require the shear stress at mid-span to be zero (from symmetry) and the longitudinal force in the CFRP plate to be zero at each end. Using these and solving the resulting simultaneous equations gives the constants of integration:

$$c_1 = \frac{-\frac{1}{\lambda}e^{-\lambda L_p/2}\left(\frac{G}{t_a}(\alpha_b - \alpha_p)\Delta T + \frac{G}{t_a}\frac{M(0)t_b/2}{E_b I_b} + gM''(0)\right) - gM'(L_p/2)}{e^{\lambda L_p/2} + e^{-\lambda L_p/2}} \tag{10}$$

$$c_2 = \frac{\frac{1}{\lambda}e^{\lambda L_p/2}\left(\frac{G}{t_a}(\alpha_b - \alpha_p)\Delta T + \frac{G}{t_a}\frac{M(0)t_b/2}{E_b I_b} + gM''(0)\right) - gM'(L_p/2)}{e^{\lambda L_p/2} + e^{-\lambda L_p/2}} \tag{11}$$

Normal stresses, constant thickness CFRP plate

Since the normal stress is uniform through the thickness of the adhesive layer, the interfacial normal stress is given by:

$$\sigma(x) = \frac{E_a}{t_a}(v_p(x) - v_b(x)) \tag{12}$$

where v_b and v_p are the transverse displacements at the bottom of the steel beam and the top of the CFRP plate, respectively. These are given by:

$$\frac{d^2 v_b(x)}{dx^2} = \frac{1}{E_b I_b} M_b(x) \tag{13}$$

$$\frac{d^2 v_p(x)}{dx^2} = \frac{1}{E_p I_p} M_p(x) \tag{14}$$

Considering the moment equilibrium of the infinitesimal element of the steel beam:

$$(M_b + dM_b) - M_b - (V_b + dV_b)dx + \frac{1}{2}(\sigma b - q)(dx)^2 + \tau b(t_b/2)dx = 0 \tag{15}$$

Substituting the expression for transverse equilibrium of the steel beam into equation (15) gives:

$$\frac{dM_b}{dx} = V_b - \tau b t_b/2 \tag{16}$$

Similarly,

$$\frac{dM_p}{dx} = V_p - \tau b t_p/2 \tag{17}$$

Differentiating equation (12) three times with respect to x and substituting (13) (14) (16) (17) gives:

$$\frac{d^3\sigma(x)}{dx^3} = \frac{E_a}{t_a}\left(\frac{1}{E_p I_p}(V_p - \tau b t_p/2) - \frac{1}{E_b I_b}(V_b - \tau b t_b/2)\right) \tag{18}$$

where E_a is the elastic modulus of the adhesive. Differentiating (18) gives the governing equation:

$$\frac{d^4\sigma(x)}{dx^4} + \frac{E_a b}{t_a}\left(\frac{1}{E_b I_b} + \frac{1}{E_p I_p}\right)\sigma(x) - \frac{E_a q}{t_a E_b I_b} - \frac{E_a b}{t_a}\left(\frac{t_b/2}{E_b I_b} - \frac{t_p/2}{E_p I_p}\right)\frac{d\tau(x)}{dx} = 0 \tag{19}$$

Assuming that $d^5\tau/dx^5 = 0$ and that the normal stress approaches zero for large values of x, the general closed form solution to equation (19) is:

$$\sigma(x) = e^{-\beta x}(s_1 \cos(\beta x) + s_2 \sin(\beta x)) + m_1 \frac{d\tau}{dx} + m_3 q \tag{20}$$

where

$$\beta = \sqrt[4]{\frac{E_a b}{4t_a}\left(\frac{1}{E_b I_b} + \frac{1}{E_p I_p}\right)}, \quad m_1 = \frac{E_p I_p t_b/2 - E_b I_b t_p/2}{E_b I_b + E_p I_p}, \quad m_3 = \frac{E_p I_p}{b(E_b I_b + E_p I_p)}$$

Substituting the boundary conditions gives:

$$s_1 = \frac{1}{2\beta^3}\left(m_2\tau(0) - m_1\frac{d^4\tau(0)}{dx^4}\right) - \frac{m_1}{2\beta^2}\frac{d^3\tau(0)}{dx^3} - \frac{E_a}{2\beta^3 t_a}\frac{1}{E_b I_b}(V(0) + \beta M(0)) \tag{21}$$

$$s_2 = \frac{m_1}{2\beta^2}\frac{d^3\tau(0)}{dx^3} + \frac{1}{2\beta^2}\frac{E_a}{t_a}\frac{1}{E_b I_b}M(0) \tag{22}$$

Shear stresses, CFRP plate with end tapers

Because of the geometric complexity of the taper at the ends of the CFRP plate, a closed form solution is difficult to derive from the differential equation, but a numerical

approach offers a good alternative. The dimensions of the taper are shown in Figure 2. The changing thickness of the plate in the taper is given by:

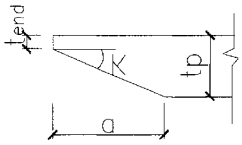


Figure 2: Geometry of the plate taper

$$t_p = t_{end} + kx \qquad 0 \le x \le a \tag{23}$$

$$t_p = t_p \qquad a < x \le L_p/2 \tag{24}$$

where L_p is the length of the plate. As described in [5] the differential equation can be replaced by a finite difference formulation which leads to:

$$\begin{bmatrix} -2-\omega h^2 & 1 & & & & \\ 1 & -2-\omega h^2 & 1 & & & \\ & \ddots & \ddots & \ddots & & \\ & & 1 & -2-\omega h^2 & 1 & \\ & & & 1 & -1-\omega h^2/2 & \end{bmatrix} \begin{bmatrix} N_1 \\ N_2 \\ \vdots \\ N_{S-1} \\ N_S \end{bmatrix} = \begin{bmatrix} Bh^2 \\ Bh^2 \\ \vdots \\ Bh^2 \\ Bh^2/2 \end{bmatrix} \tag{25}$$

where i, h, S are station number, step length and number of stations, respectively, and $h = L_p/2S$. N_i is the axial force in the metal or composite at station i, is a geometric term defined in [5] and $B = \frac{Gb}{t_a}((\alpha_b - \alpha_p)\Delta T + \frac{M(x)t_b/2}{E_b I_b})$. N_i can be found by the solution of these linear equations. Finally, according to equation (5),

$$\tau_i = -\frac{-N_{i+2} + 4N_{i+1} - 3N_i}{2hb} \qquad 0 \le i \le S-1 \tag{26}$$

$$\tau_i = 0 \qquad i = S \text{ (midspan)} \tag{27}$$

Normal stress, CFRP plate with end tapers

The governing differential equation can be replaced by a finite difference formulation as described in [5]. The solution of the resulting simultaneous equations gives the moment M_i at each station. These can then be used with the shear stress to give the normal stress:

$$\sigma_i = \frac{-(M_b)_{i+2} + 16(M_b)_{i+1} - 30(M_b)_i + 16(M_b)_{i-1} - (M_b)_{i-2}}{12h^2 b} + \tau_i' t_b/2 + \frac{q}{b} \tag{28}$$

ANALYTICAL AND NUMERICAL RESULTS

Various analyses have been carried out. In each case a steel beam of 6m span was used with CFRP plate 5m long. The steel beam was a UB, 533×210UB122, and the CFRP was ultra-high modulus plate, 211.9mm wide and 12mm thick. Elastic modulus values of

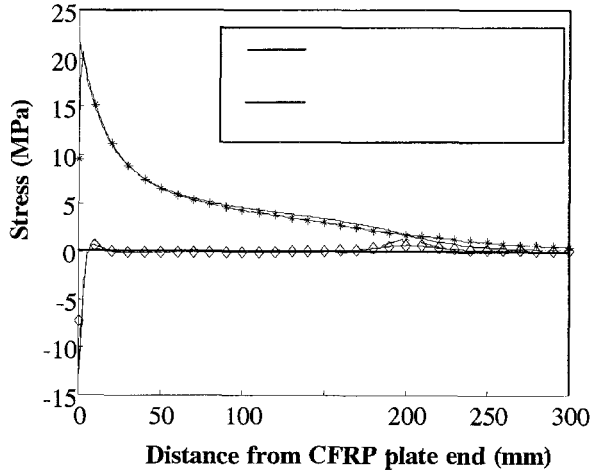


Figure 3: Comparison of analytical and finite element results, thermal load, tapered plate.

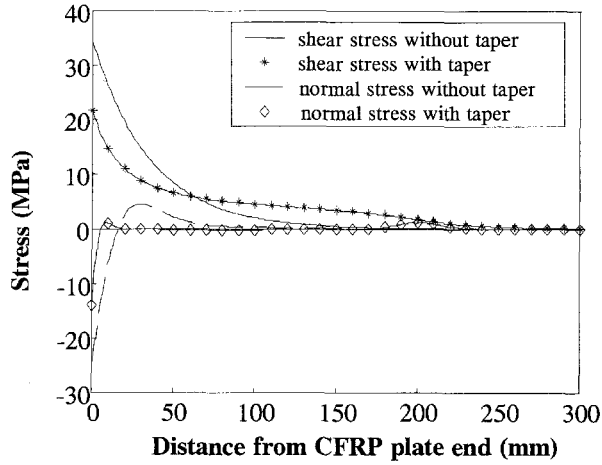


Figure 4: Comparison of stresses, thermal load, plates with and without taper.

	Shear stress		Normal stress	
	Analytical	FE	Analytical	FE
Thermal	36.8%	27.2%	48.4%	51.1%
UDL	37.9%	28.2%	47.4%	55.2%
Concentrated	38.0%	28.9%	45.5%	54.9%

Table 1: Reductions in peak stresses when CFRP is tapered at the ends.

210GPa and 310GPa were used for the steel and carbon respectively and Poisson's ratio was taken as 0.3. A thermal load $\Delta T = 50^0$C, a uniformly distributed load of 106kN/m and a midspan concentrated load of 500kN were used in the analyses. The results were checked by comparison with finite element analyses, details of which are in [5]. Figure 3 shows the results for the steel beam and a tapered CFRP plate. The agreement between numerical and finite element results was very good for both shear and normal stress. The only discrepancy was at the very end of the CFRP plate where the shear stress should drop to zero. This was picked up by the finite element analysis but not the numerical procedure and is a limitation of the analysis. However the peak values were very similar.

Figure 4 shows the benefit of tapering the ends of the CFRP plate. It can be seen that the taper reduces the shear and normal stresses in the adhesive. Table 1 shows the percentage reduction in peak stress. The analysis and finite element results show similar reductions in the peak normal stress. The discrepancy is due to the limitation in the analysis identified above.

Parametric studies have been carried out using the analysis, but only limited results can be presented here. Figure 5 shows the effect of adhesive thickness on the peak stresses. It can be seen that the stresses were reduced as the adhesive thickness increased although there was a penalty because the reinforcement was less effective. However it is common to see adhesive layers several millimeters thick to accommodate imperfections in the original structure. Figure 6 shows the effect of varying the length and slope of the end taper on the maximum shear stress in the adhesive. The stresses have been normalized to the maximum shear stress in the untapered plate. The results clearly show the benefits of a thin tapered end and a long taper. The results for normal stress were similar.

The analytical solutions give the stresses in the adhesive and these can be combined to give a maximum principal stress. The latest Design Guide [6] recommends that this value be compared with measured values from lap shear tests. Recent work [7] indicates that converting the lap shear failure load to principal stress needs care. Representative specimens with CFRP and metal adherends do not behave anti-symmetrically which violates one of the assumptions of the analysis [4] used to calculate the principal values.

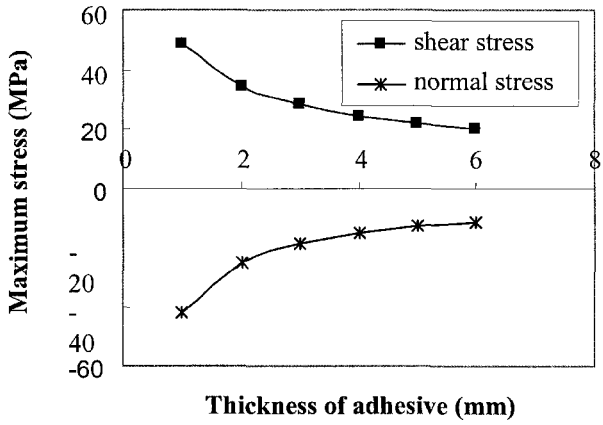


Figure 5: Effect of adhesive thickness on peak shear and normal stresses in the adhesive

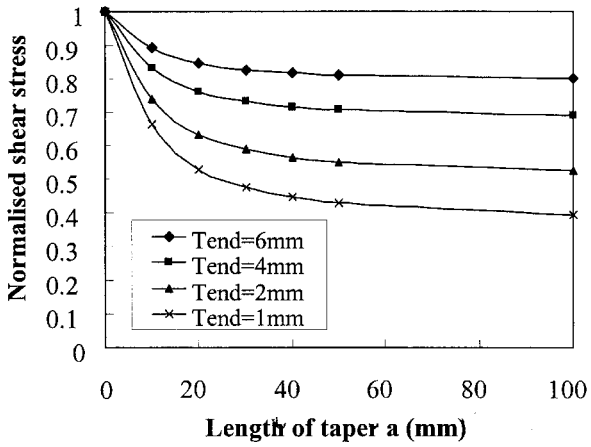


Figure 6: The effect of varying the length and slope of the end taper

CONCLUSIONS

- A closed-form solution to calculate interfacial stresses of steel beams strengthened with CFRP plates under thermal and mechanical loads has been presented briefly, and a numerical solution has been given for CFRP plates with tapered ends.
- The analytical results agree closely with the finite element validations.
- High shear and normal stresses occur in the adhesive close to the ends of the CFRP plate. Tapered ends in the CFRP plates reduce the magnitude of these stresses.
- A parametric study showed that the thickness of the adhesive layer and the geometry of the taper have a significant effect on the magnitude of the stresses in the adhesive.
- Care needs to be exercised when comparing the calculated stresses with the results of the lap shear tests used to determine the adhesive strength.

REFERENCES

1. S.R. Denton, 'Analysis of stresses developed in FRP plated beams due to thermal effects', Proc. "*Composites in Construction 2001*", Hong Kong, 12-14 December 2001, pp 527-536.
2. S.Frost, R.J.Lee, V.K.Thompson, 'Structural integrity of beams strengthened with FRP plates – analysis of the adhesive layer', *AEA Technology Report*, 2003.
3. G.C.Mays, A.R.Hutchinson, *Adhesive in civil engineering*, Cambridge, CUP, 1992.
4. M. Goland, E. Reissner, 'The stresses in cemented joints', *Journal of Applied Mechanics*, 1944 **11.**
5. J. Deng, M.M.K. Lee, S.S.J. Moy, 'Stress analysis of steel beams reinforced with bonded CFRP plate'. *Accepted for publication in Composite Structures.*
6. CIRIA RP645, *Strengthening metallic structures using externally bonded fibre reinforced polymers*, London, CIRIA, 2003.
7. F.Nikoukar, *Strengthening metallic structures with carbon fibre composites*, PhD Thesis, University of Southampton, to be submitted shortly.

STRENGTHENING OF AN ARTIFICIALLY DEGRADED STEEL BEAM UTILISING A CARBON/GLASS COMPOSITE SYSTEM

N Photiou, L C Hollaway and M K Chryssanthopoulos

School of Engineering, University of Surrey, Guildford, Surrey, GU2 7XH, UK

ABSTRACT

The repair and strengthening of deteriorated, damaged and sub-standard steel bridges has become one of the important challenges confronting civil engineers worldwide. To rehabilitate these structures, techniques utilising the lightweight, high strength and corrosion resistance of fibre reinforced polymer (FRP) composites have been proposed. The flexural load carrying capacity of a steel girder can be reinforced significantly by using a two part adhesive or a film adhesive to bond carbon fibre polymer (CFRP) composites its tension flange. This paper discusses the experimental results to investigate the effectiveness of an ultra-high CFRP prepreg in strengthening an artificially degraded beam of rectangular cross-section under four-point loading. Two beams were upgraded, one utilising a U-shaped prepreg unit and the other a flat plate prepreg; both utilised an identical hybrid lay-up of CFRP and glass fibre polymer (GFRP) composite and an adhesive film to bond it to the steel substrate. In the first upgraded beam, the U-shaped hybrid composite was extended up the vertical sides of the beam, to the neutral axis height. Both beams failed when the ultimate strain of the carbon fibre was reached in the pure moment region; the failure load was equal to the full plastic collapse load of the undamaged beam, thus demonstrating the effectiveness of the proposed upgrading scheme. On re-loading the beams after failure, the U-shaped hybrid upgrade continued to act compositely with the steel beam outside of a well confined region corresponding to the original failure location, whereas the beam with the flat plate upgrade exhibited the typical response of a steel beam, owing to debonding having taken place over practically the entire beam length.

INTRODUCTION

Deterioration of the infrastructure concerned with metallic structures is due to several causes but probably the main cause is that of corrosion. In the UK, steel and composite bridges on the national trunk road network managed by the Highways Agency are, in their majority, relatively new but a large number of old (over 100 years) wrought iron and early steel structures are to be found on the railway and canal network. According to the National Bridge Inventory compiled by the Federal Highway Administration some 43% in the USA are made from steel. In addition to corrosion, other problems relate to fatigue sensitive details, the need to increase the service load and a lack of proper maintenance [1, 2]. In many cases, the deteriorated condition will be associated with certain parts of the bridge and it would be more economic to consider repair and retrofit before a decision is made to replace an entire bridge. Repair, upgrading and rehabilitation are invariably more economic than the replacement alternative. Furthermore, in the case of bridges the upgrading and rehabilitation takes less time and reduces service interruption.

A method of providing adequate strengthening capacity to steel structures is by welding or adhesively bonding and end bolting steel cover plates. One of the first structures to use the welded steel cover plate technique was the strengthening, in 1934,

of a 73 year old bridge in France [1] and an example of the adhesively bonded and end bolted steel cover plate technique is that given by [3]. However, these examples revealed serious difficulties with the technique of steel plate bonding/welding; they required heavy lifting equipment to place the plates in position and complicated bonding/welding procedures. Furthermore, if welding is part of the joining process, it can introduce into the material, residual stresses and accentuate possible fatigue problems [4].

The superior mechanical, fatigue and in-service properties of carbon fibre reinforced epoxy (CFRP) composites make them excellent candidates for strengthening and retrofitting of steel girder bridges. However, to date only a limited amount of research appears to have been undertaken [2, 5, 6, 7].

When upgrading a structural steel member with a composite, the type of fibre used in the composite must be chosen carefully. The high modulus carbon fibre/polymer composites will have a stiffness of the same order as that of the steel; this implies that, in plate bonding applications, substantial load transfer can only take place after the steel has yielded. With the ultra-high modulus carbon fibre composites, where the stiffness of the composite material is significantly higher than that of the steel, substantial load transfer will take place even before the steel has yielded, but it should be remembered that the ultimate strain value of this material can be quite low (e.g. 0.4%). Furthermore, the successful strengthening of a steel structure with FRP (or steel) materials is completely dependent upon the quality of the composite/steel joint and the effectiveness of the adhesive used. Previous research at the University of Surrey [8] established the effectiveness and integrity of bonding CFRP plates to steel tensile coupons. In this work, the ultimate strength of a prepreg of ultra-high modulus carbon fibre composite and a compatible film adhesive were compared with that of an identical ultra-high carbon fibre pre-cured composite plate bonded onto the steel coupon specimen with a cold setting two part adhesive, commonly used in the construction industry. The former system had superior bonding qualities to those of the pre-cast composite plate.

A further consideration, when joining carbon fibre to steel, is that of galvanic interaction between the two materials. Contact between CFRP and metals in an electrolyte such as seawater, or Chloride Cl^- contaminated concrete is extremely undesirable, if the metal is highly active and low in the galvanic series. Thus, when carbon (fibre composite) is in contact, a current may flow causing the steel to corrode. Both steel and CFRP composites may be adversely affected when in contact and immersed in sea water. Blisters can form on the surface of the composite, [9, 10]. To overcome this problem a layer of glass fibre composite can be placed between the metal and carbon composite to prevent direct contact between the two materials; this procedure was adopted in the present investigation. An added advantage of incorporating the glass fibre composite between the adhesive and the first layer of CFRP composite, is that higher failure strength of the joint can be obtained [11]. This is due to a more gradual change in shear stress, when load is being transferred to the CFRP composite from the steel via the adhesive and GFRP composite.

This paper will discuss experimental results, which form the first part of a project being undertaken at the University of Surrey, to investigate the effectiveness of an ultra-high CFRP prepreg in strengthening an artificially degraded beam of rectangular cross-section. To eliminate any lateral torsional buckling during the flexural test programme, a rectangular hollow cross-section was chosen for the investigation. Furthermore, in order to induce failure in the tension zone of the beam, a compact (Class 1) section was adopted, thereby delaying failure due to compression flange buckling. In order to create artificially degraded beam, the tensile flange of the beam

was machined to half its original thickness, thus simulating the effect of general rather than localised corrosion; after this operation the corners at the junction of the webs and bottom flange were machined to provide a radius of 5mm.

So far, two beams have been upgraded, one by means of a U-shaped prepreg unit and the other by a pre-cured prepreg flat plate; in both cases the laminates were bonded to the tensile flange of their respective steel beam. Both the U-shaped and the flat plate unit had identical laminate lay-ups; these consisted of unidirectional CFRP composites and $\pm 45^0$ GFRP composites placed along the length of the beam. However, in the hybrid U-shaped composite, the GFRP component was also taken up the vertical sides of the beam to the height of the modified neutral axis. This vertical component was a continuation of the $\pm 45^0$ GFRP composite bonded on the tension flange; it is noted that no CFRP laminates were placed in the webs of the beam. A full explanation of the lay-up is given in the next section.

MATERIALS USED

The carbon fibre/polymer composite material used in the investigation was made from a hybrid of ultra-high modulus, unidirectional carbon fibre and $\pm 45^0$ glass fibre composite. The former component was comprised of two double laminate layers and the latter component of three single laminate layers. The latter fibres were positioned at $\pm 45^0$ to the longitudinal direction of the steel beam.

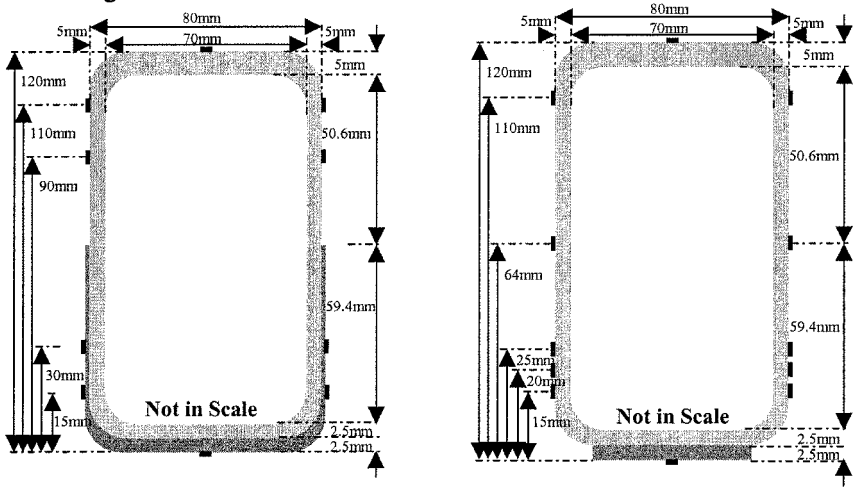


Figure 1a: Schematic diagram of a Steel RHS with an Ultra High Modulus CFRP/GFRP laminate, also showing strain gauge positions

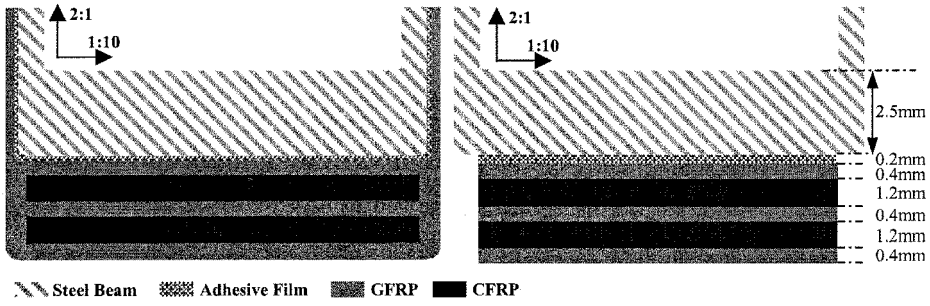


Figure 1b: Schematic diagram of the stacking sequence of the FRP composite components

The hybrid composite laminate layers were stacked as follows: firstly the glass fibre laminate followed by one double laminate of carbon fibre, followed by a single glass fibre laminate, followed by the other double layer carbon fibre and finally another single glass fibre laminate. The first glass fibre laminate was adjacent to the adhesive film and hence separated the steel from the carbon fibres. Figures 1a and 1b depict the strain gauge position and the stacking sequence of the FRP composite components on the steel beam.

Advanced Composite Group (ACG) at Derbyshire manufactured all prepregs as well as the adhesive film. The matrix resin system and the adhesive film, whose typical thickness is about 110-120 microns, were made from a low temperature curing resin system (cure temperature 65^0C), suitable for civil engineering applications. The two upgrading composite systems had projected plan sizes of 210mm by 1600mm and 60mm by 1600mm. Table 1 gives the mechanical properties of the materials used in the composite strengthening system. The steel beam was characterised by a Young's modulus of 205GPa and a 0.2% proof stress of 375MPa. The steel tensile coupons exhibited a continuous stress-strain curve with no distinct yield stress or yield plateau (typically modelled using the Ramberg-Osgood formula). Figure 2 shows the tensile stress-strain response of the FRP and steel materials used.

Table 1: Mechanical properties of the composite strengthening system

Material	Tensile Strength MPa	Elastic Modulus GPa	Ultimate Strain (%)	Poisson Ratio
CFRP (Unidirectional)	1120	270	≈ 0.4	0.32
GFRP (± 45^0 to line of action of load)	215	16	1.7	0.15
Film Adhesive	32	3.7	≈ 0.86	0.37

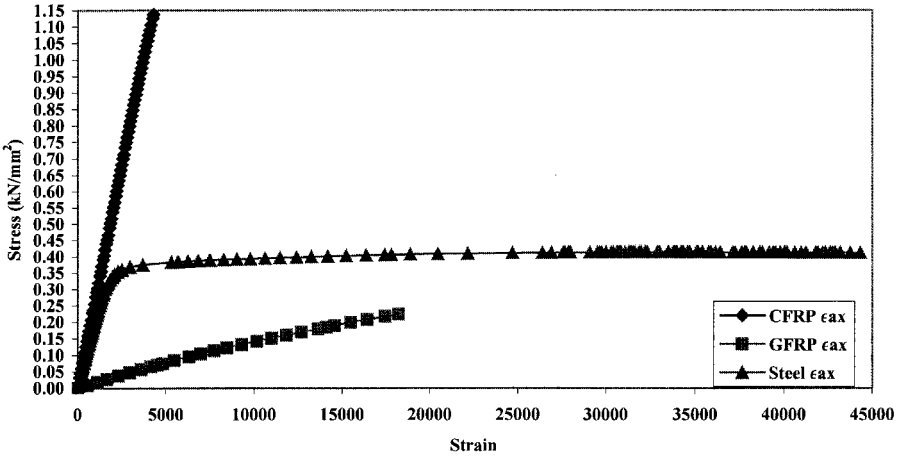


Figure 2: Tensile Stress-Strain response of the FRP and steel materials

UPGRADED BEAM PREPARATION

The first operation in the test programme consisted of cutting the steel beams to a length of 1800mm and machining 2.5mm thickness of material off the flange. This operation was performed by multiple low speed passes, in order to minimise distortions

induced by heat input and residual stress release. Subsequently, all exposed surfaces of the rectangular shaped hollow section steel beams were grit blasted to the Swedish Code SA 2 ½ Grade 3 Dirk grit. Immediately before applying the adhesive film to the surface of the steel, it was solvent degreased using acetone to remove any contaminant materials.

It is necessary to store the composite prepreg at -20^0C immediately after manufacture and to maintain it at this temperature until required for use. Before cutting the prepreg plates to size, the material was allowed to thaw for approximately one hour. The composite plates, for both geometric shaped up-grading systems, were fabricated onto the beam by laminating the four CFRP prepreg layers and the three GFRP prepreg layers in the particular arrangement discussed in the previous section.

The adhesive film was cut to size and laid onto the prepared steel beam. Likewise the prepreg laminates were cut to the design size and laid up as discussed in the previous section. A halar film and breather blanket covered the fabricated composites on the beam and the whole was placed in a vacuum bag. The bag, under a vacuum assisted pressure of 1bar, was transferred to an oven at 65^0C for 16 hours. After curing, the temperature of the oven and sample was reduced to room temperature at a steady rate. The beam was then ready for testing.

TEST PROCEDURE

The two beams were placed in the test rig on a span of 1700mm. The two external loads were positioned at a distance of 200mm on either side of the centre line of the beam. Strain gauges were bonded at strategic positions on both side of the beams at mid-span and down the depth of the beams. The test arrangement is shown in Figure 3. Two displacement transducers were placed on either side of the beam at mid-span to determine the deflections and to indicate any inconsistency in these readings. Displacement transducers were also placed at the two external load positions to determine the curvature of the beams over the pure moment region. A series of four cyclic loading increments were applied to a value one eighth of the estimated failure load before the beams were taken to failure; the load increments were 1kN.

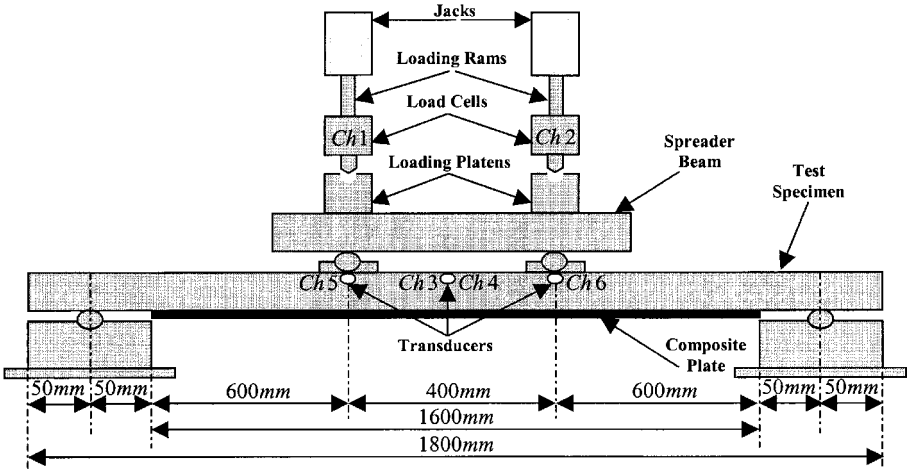


Figure 3: Test Arrangement for beam tests

TEST RESULTS

Failure of Beam 1 (with the U-shaped hybrid composite system) occurred at a load of 46kN per jack and was concentrated in the CFRP composite in a particular location within the pure moment region of the specimen. As confirmed by the strain gauge readings, at this load the CFRP had reached its ultimate strain of about 0.4%. At this point there was no apparent bond failure between the composite and the steel member on either side of the failure section, therefore complete composite action, between the two components, still existed, except of course at the location of failure. Figure 4 shows the average load (per jack) – deflection response of the strengthened beam. Non-linear response can be seen from about 23kN onwards, and this corresponds to the steel in the bottom fibre beginning to exhibit softening response. As can be seen, the load kept increasing to almost twice this value before failure of the ultra-high CFRP took place. In fact, the ultimate load reached by the strengthened beam reached the theoretical plastic collapse load of the full rectangular hollow section steel beam (i.e. before reduction of the bottom flange from 5 to 2.5mm), thus demonstrating the ability of the FRP strengthening system to restore the full bending capacity of the beam. Upon unloading, the beam had a permanent centre deformation of about 12mm. This completed the first cycle to failure, denoted as 'Cycle 1' in Figure 4. The strain distribution within the cross-section, clearly showing the shift in neutral axis position as the steel yielded is shown in Figure 5.

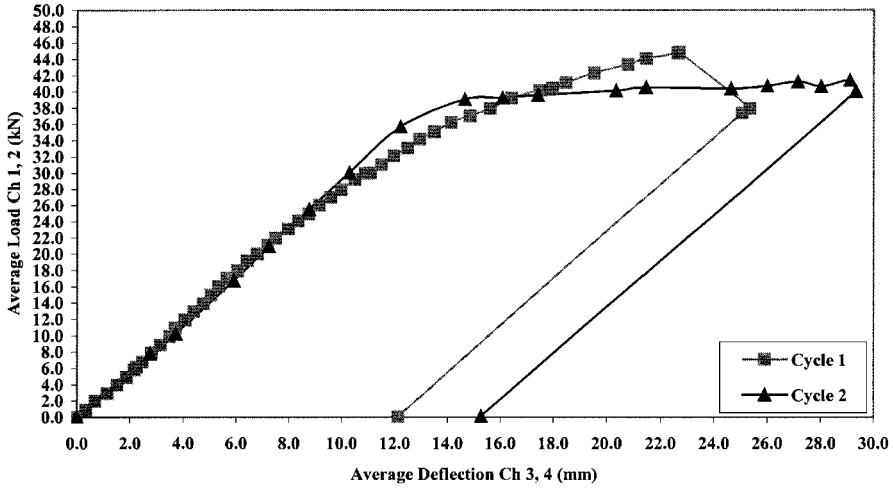


Figure 4: Average Load-Deflection (per jack) response of the strengthened Beam 1

After 15 minutes the beam was reloaded ('Cycle 2' in Figure 4) and the load-deformation characteristic was more typical of a steel member in bending. However, the now damaged strengthened beam, was able to sustain a load of up to 40kN per jack, which was in excess of the capacity of the steel alone, even considering the work hardening afforded to the steel by the first failure cycle. It was clear that the FRP system was still contributing to the strength of the beam due to the adhesive bond still being intact, and thus transferring load to the CFRP and GFRP hybrid system apart from the location where fibre breakage had taken place. These observations were confirmed by the load-strain results for gauges located at the centre of the beam at the top (on steel) and the bottom (on GFRP) shown in Figure 6. These gauges were located 190mm from the CFRP failure position, and were not damaged due to the previous cycle. As can be

seen, the strain gauge on the GFRP recorded 500μ strain at maximum load. This low value indicated that at this specific point on the bond-length, the FRP strengthening system was still developing some considerable strain.

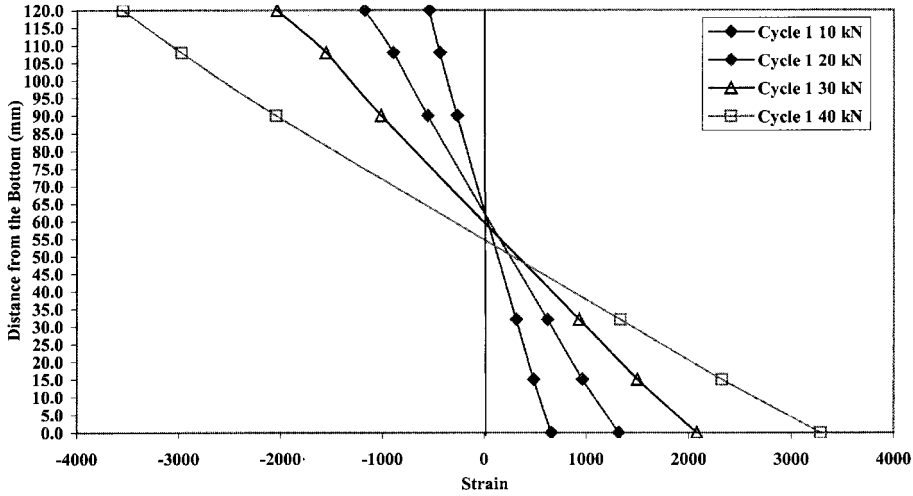


Figure 5: Strain distribution in the strengthened Beam 1

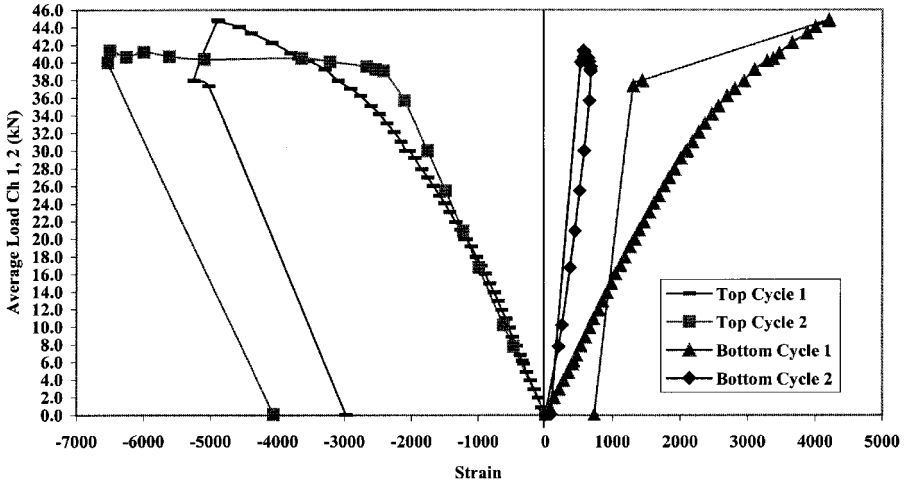


Figure 6: Load-Strain response of the strengthened Beam 1

The corresponding results for Beam 2 (with the hybrid composite bonded to the bottom flange only) are shown in Figures 7 to 9. During the first cycle to failure, the ultimate load reached by the strengthened beam reached an almost identical maximum load, and failure once again occurred as a result of CFRP fibre breakage. However, in this case, the fibre breakage also triggered a more or less complete debonding of the composite system from the steel flange. As a result, the second cycle represented simply the response of the steel beam alone. This is clearly evident in the load-strain results, where it can be seen that the gauge on the GFRP located in the centre of the beam fails to pick up any load during the second cycle.

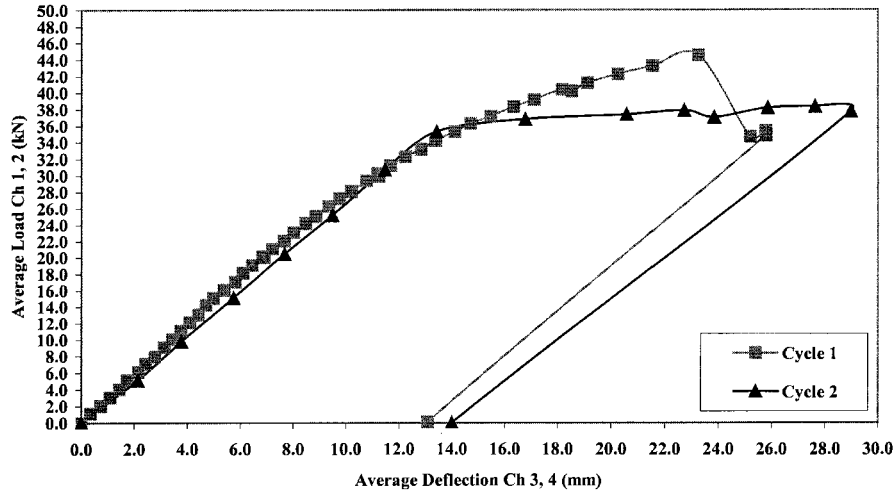


Figure 7: Average Load-Deflection (per jack) response of the strengthened Beam 2

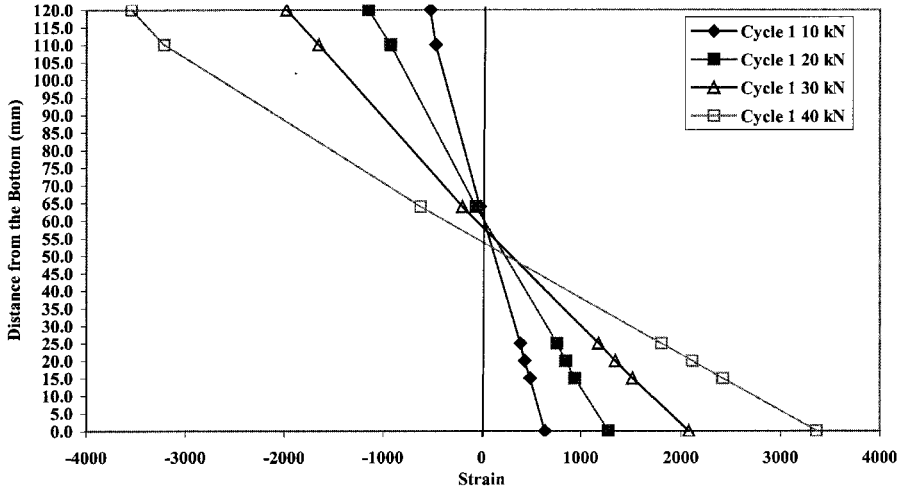


Figure 8: Strain distribution in the strengthened Beam 2

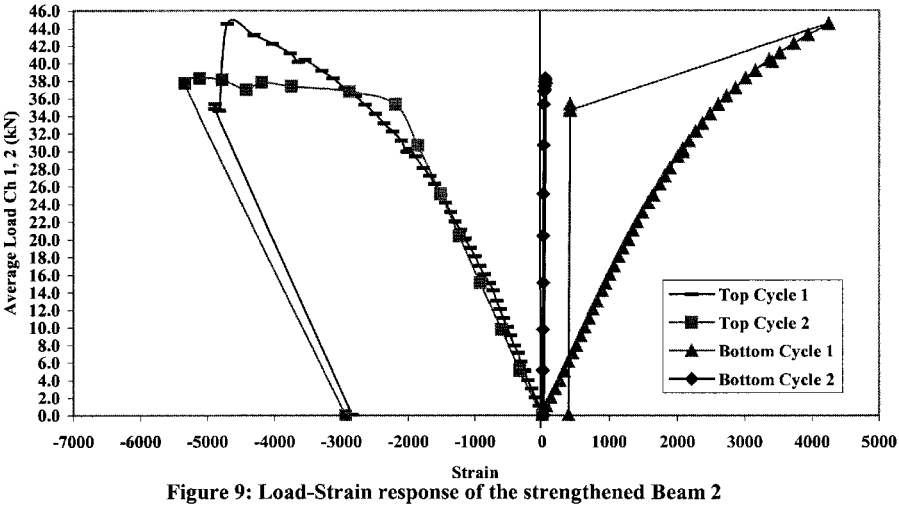


Figure 9: Load-Strain response of the strengthened Beam 2

Thus, although the maximum loads attained by the two strengthening systems are practically identical, the advantage of the U-shaped system over its flat counterpart is that it appears to have the ability to contain the failure and to provide a degree of stiffening even after substantial damage as a result of the ultimate load being reached. Further investigations are currently pursued to examine these alternatives in greater detail, and to model numerically the beam tests.

CONCLUDING REMARKS

This paper has presented experimental results aimed at establishing the effectiveness of a hybrid composite system in flexural strengthening of steel beams. The hybrid system is comprised of ultra-high CFRP prepregs, interleaved with GFRP prepregs, and bonded to the steel substrate using an adhesive film in a single operation. The upgrading system was applied to an artificially degraded beam of hollow rectangular cross-section under four-point loading. It was shown that the strengthened beams could reach the plastic collapse load of the original undamaged steel beam. In both beams, failure was through tensile fibre breakage of the CFRP in the pure moment region. By extending the hybrid composite system, with GFRP prepregs only, up the vertical sides of the beam, to the neutral axis height, it was shown that failure was localised, as opposed to severe debonding that took place when the same strengthening system was applied to the bottom flange only. Further numerical and experimental investigations are being undertaken in order to study in greater detail the relative merits of alternative strengthening systems.

REFERENCES

[1]. Klaiber, F.W, Dunker, K.F, Wipf, T.J. and Sanders, W.W. (1987), 'Methods of strengthening existing highway bridges', NCHRP 293, Transport Research Board, Washington, D.C.

[2]. Tavakkolizadeh, M, Saadatmanesh, H, *'Strengthening of steel-concrete composite girders using carbon fiber reinforced polymers sheets'*, Journal of Structural Engineering ASCE, January 2003, Vol. 129 (1) pp 30-40.

[3]. Albrecht, P, Sahli, A, Crute, P, Albrecht, P, and Evans, B, *'Application of adhesives to steel bridges'*, Report No: FHWA-RD-84-037, Federal Highway Administration, Washington, D. C, 1984, pp 106-147.

[4]. Fisher, J.W. (1997), 'Evaluation of fatigue resistant steel bridges', National Academy Press, Washington, D.C.

[5]. Mertz, D. and Gillespie, J. (1996), 'Rehabilitation of steel bridge girders through the application of advanced composite material' NCHRP 93-ID11, Transportation Research Board, Washington, D.C, pp 1-20.

[6]. Mosallam A.S. and Chakrabarti, P.R. (1997), 'Making connection', Civil Engineering, ASCE, pp 56-59.

[7]. Liu X., Silva P.R. and Nanni, A. (2001), 'Rehabilitation of steel bridge members with FRP composite materials', Proc. CCC 2001, Composites in Construction,

Porto, Portugal, Oct. 2001, Editors, J. Figueiras, L. Juvandes and R Furia. pp 613-617.

[8]. Photiou N.K., Hollaway L.C. and Chryssanthopoulos M.K. (2003), 'Characterisation of adhesively bonded plates for upgrading structural steelwork', Proc. Structural Faults and Repair, ed. M.C. Forde, Engineering Technics Press, Edinburgh.

[9]. Tucker, W.C, Brown, R. and Russell, L. (1990), Journal of Composite Materials, Vol. 24, pp 92.

[10]. Tavakkolizadeh, M, Saadatmanesh, H, *'Galvanic corrosion of carbon and steel in aggressive environments'*, Journal of Composites for Construction, 2001, Vol. 5 (3), pp 200-210.

[11]. Photiou N.K., Hollaway L.C. and Chryssanthopoulos M.K. (2004), 'Selection of CFRP systems for steel work upgrading', Proc. Innovative Materials and Technologies for Construction and Restoration (IMTCR), Department of Innovation Engineering, University of Lecce, Italy.

FRACTURE MECHANICS 2D-FEA OF A CRACKED STEEL PLATE WITH A CFRP PATCH

T D Righiniotis, E S Aggelopoulos and M K Chryssanthopoulos

School of Engineering, University of Surrey, Guildford, Surrey, GU2 7XH, UK

ABSTRACT

Composite patch technology for fatigue life improvement has not yet received much attention in the bridge engineering community, nor has it been approved by relevant certifying authorities, as an effective repair method. Although knowledge exists in the aeronautical field, the conditions to which these structures are subjected, as well as the material specifications used, are very different from civil engineering. This paper investigates the potential fatigue life improvement that may be achieved using CFRP patches on cracked steel members. For this purpose, a two-dimensional steel plate with a crack growing into its thickness direction and a CFRP patch attached through a thin resin film over the crack mouth are modelled and analysed using the FE method. Meshes using conventional 8-noded continuum elements everywhere except the crack tip and 8-noded quarter-point collapsed elements at the crack tip are employed to extract stress intensity factors (SIF). Comparisons between the SIF for the un-patched and patched plates demonstrate the considerable reductions in these parameters resulting from the repair operation. Fatigue life calculations using Paris' model show that the accompanying fatigue life improvement is considerable and that the addition of a CFRP patch can potentially be a viable alternative method of repair.

INTRODUCTION

Fatigue and, ultimately, fracture is one of the main problems that may occur in ageing metallic bridges. Apart from the traditional repair methods employed in order to mitigate this problem, the use of Carbon Fibre Reinforced Polymers (CFRP) for local strengthening of girders or plated structures seems to be a technique worth exploring. For one, repairs based on adhesively bonded fibre-composite patches, introduce the least detrimental fatigue effects to the parent structure compared to mechanically fastened (using welds or bolts) metallic reinforcements. In addition, the usual advantages associated with FRP repair (speed, ease of installation) would also be present.

Research in the field of bonded composite repairs was initially conducted on account of fatigue problems in ageing aircraft. Several investigators have studied various aspects related to the application of composite patch repairs on cracked aluminium aircraft components. Baker [1] presented the benefits of bonded composite patch reinforcement and compared it with the standard mechanically fastened repairs. Jones and Chiu [2] found that externally bonded composite repairs can be used successfully to extend the fatigue life of thick structural components. Schubbe and Mall [3] investigated the fatigue crack growth rate of thick panels under different patch configurations. Denney and Mall [4] examined the effect of debonding on the fatigue response of cracked aluminium panels repaired with bonded composite patches.

FRP materials have been used effectively in civil engineering but mostly for the repair and strengthening of reinforced concrete structures [5]. Only a limited amount of research has been conducted on the application of these materials to metallic structures.

However, due to the existence of many older steel and wrought iron structures, and especially bridges, in Europe and North America, researchers have recently began the study on the potential use of CFRP as a means for repair and strengthening. Recent studies verified that CFRP reinforcements can be used to restore reasonable losses of stiffness and strength in deteriorated steel bridge girders [6-8]. Sen et al. [9] carried out experiments and a non-linear FE analysis to determine the efficiency of CFRP laminates for repairing steel composite bridge members. Tavakkolizadeh and Saadatmanesh [10] performed fatigue experiments on both unretrofitted and retrofitted with CFRP notched steel beams. Colombi et al. [11] have used both experimental and analytical methods to investigate the effect pre-tensioning of CFRP strips prior to bonding has on fatigue life improvement of steel bridge members. Bassetti et al. [12,13] performed full scale fatigue tests on both unretrofitted and retrofitted, with pre-tensioned CFRP strips, riveted cross girders taken from a dismantled ninety-one-year-old railway bridge. Limited research has been conducted with respect to bond durability of FRP bonded steel systems and their resistance to different environmental conditions [14] as well as potential galvanic corrosion problems associated with the interaction of CFRP systems with steel [15]. These studies concluded that there is potential benefit in the use of CFRP for post strengthening of steel members compared to other traditional repair methods.

In the present work, the use of adhesively bonded advanced composite patches for the repair of cracked steel members is studied analytically. Linear, 2D finite element models (FEM) are used in order to model the behaviour of a steel plate with a through-the-width of the plate edge crack, as well as the behaviour of the same plate repaired with an adhesively bonded CFRP (Carbon Fibre Reinforced Polymer) patch. Both configurations are investigated for the simple load case of remote tension.

The study concentrates on the stress intensity at the crack tip and how this is affected by the application of the bonded composite patch. Thus, values of the non-dimensional Y factor are calculated from the finite element analysis and, where applicable, are compared with standard analytical solutions available in the literature.

The results obtained here indicate a significant reduction in Y. This in turn implies an improvement on fatigue life of the cracked component, which was quantified using the well-known crack growth model proposed by Paris and Erdogan [16].

CRACKED CONFIGURATION AND ITS REPAIR

The cracked geometry studied is shown in Figure 1a. It is assumed to be representative of a plate of thickness t_s, which contains a surface crack of length a. The plate is subjected to a remote tensile stress S. This configuration may be seen to represent the two-dimensional equivalent of a surface crack, which in general is characterised by depth (captured here through a) and width in the out of plane direction. This type of crack may be encountered in several different types of bridge detail such as cope holes, gusset plates, longitudinal welds at web-flange connections, flame-cut corners or even bolted and riveted construction.

Figure 1b depicts a typical repair configuration, where a CFRP strip is patched on the surface of the steel plate. A thin layer of adhesive of thickness t_a ensures the stress transfer into the CFRP strip, which has a thickness t_c. For the purposes of this investigation the length of the patch is assumed to be infinite. In practical terms this implies that the adhesive and patch are long enough to ensure no interaction between the patch/adhesive end and the crack tip. Conditions of plane strain are assumed throughout the entire assembly.

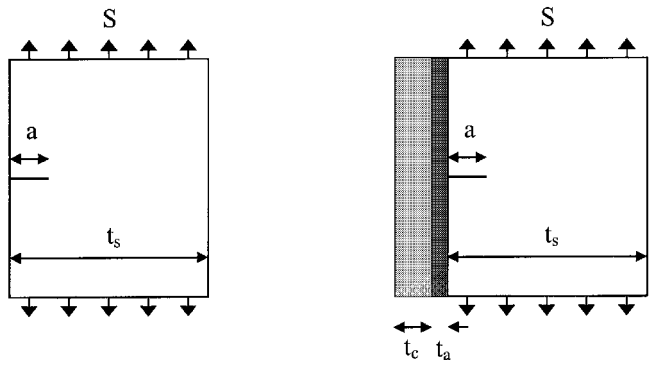


Figure 1: (a) Steel plate containing a surface crack (b) Cracked steel plate with an adhesive layer and CFRP patch

FINITE ELEMENT MODELS

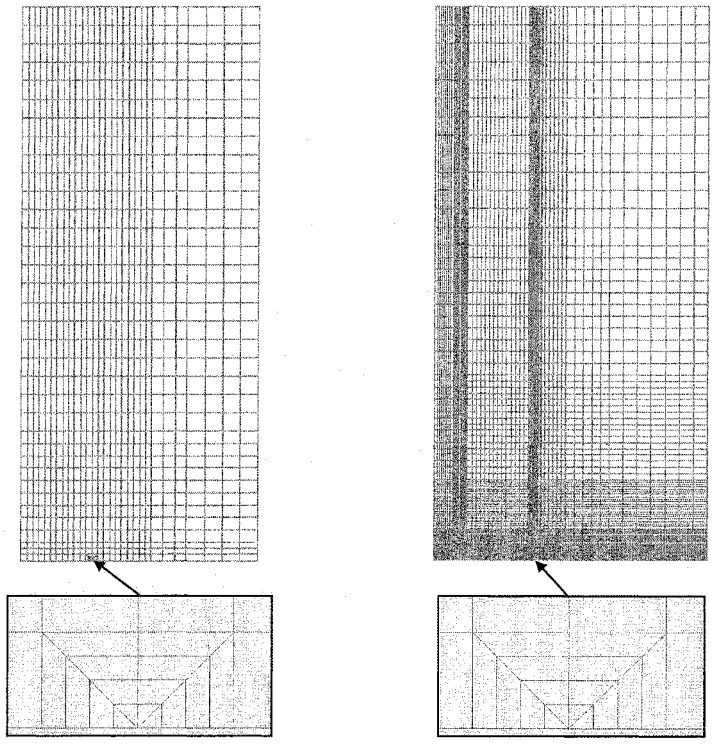
In order to investigate fatigue life improvement of the steel plate as a result of the patch repair, both cracked configurations depicted in Figures 1a and 1b were analysed using the general purpose FE code ABAQUS. The results were obtained in terms of the J integral option available in ABAQUS and converted into stress intensity factors via

$$K = \sqrt{\frac{E_s J}{(1-\nu_s^2)}} \qquad (1)$$

where E_s is Young's modulus and ν_s is Poisson's ratio. Both of these material properties are here considered for the steel as the crack tip is located in steel.

The entire domain was modelled using 8-noded continuum elements. In order to model the crack tip singularity, assuming small scale yielding conditions, the area surrounding the crack tip was modelled using collapsed 8-noded elements with quarter point shift. Due to symmetry, only half of the geometry was modelled. For both patched and un-patched configurations, the number of elements adjacent to the crack tip in the angular direction was varied. Accordingly, 4 and 8 elements around the crack tip were used. The number of rings in the radial direction was kept constant and equal to 4. This allowed J integral evaluation for each of these rings and verification of its path independence (see next section).

For the patched geometry, the point corresponding to the crack mouth on the steel-adhesive interface, was modelled as a second crack tip. Further investigation of this point is underway, whereby a small separation is introduced, but preliminary results indicate that for the deeper cracks ($a/t_s > 0.2$), refined modelling of this region does not affect Y significantly.



(a) (b)

Figure 2: (a) FE mesh of half-plate showing detail of the crack tip in the steel (b) FE mesh of half-plate showing detail of the fictional crack tip in the steel/adhesive interface.

FE analyses were carried out by varying a/t_s from 0.1 to 0.8. Figures 2a and 2b depict typical FE meshes for the patched and un-patched plates. Comparisons were made between the normalised stress intensity factors Y (stress magnification factors) defined as

$$Y = \frac{K}{S\sqrt{\pi a}} \tag{2}$$

and results available in the literature for the un-patched configuration. These comparisons are presented in the following section.

Validation of crack tip modelling

The finite element model used for the un-patched configuration was validated by comparing its results with the results presented in [17]. The un-patched configuration constitutes a surface crack in a finite width strip. A number of different analytical solutions for Y exist in the literature for this type of cracked geometry [18] but the results of Kaya and Erdogan [17] are used here due to their extended range of validity. Accordingly Y is given as

$$Y = 1.1216 + 6.52\left(\frac{a}{t_s}\right)^2 - 12.3877\left(\frac{a}{t_s}\right)^4 + 89.0554\left(\frac{a}{t_s}\right)^6 - 188.608\left(\frac{a}{t_s}\right)^8 + 207.387\left(\frac{a}{t_s}\right)^{10} - 32.0524\left(\frac{a}{t_s}\right)^{12} \quad (3)$$

with a range of applicability of $a/t_s \leq 0.8$.

Differences between the J values reported for each ring were typically less than 1%. Furthermore, comparison between the FE results obtained from Eq. (2) using the average of four values for J and Eq. (3) revealed a maximum difference of 0.56% over all the values of a/t_s considered in the present analyses, as presented in Table 1. The table also reveals that modelling of the crack tip region is very accurate. For this reason, the same crack tip region was also used for the patched configuration.

Table 1: Difference (%) between FE-calculated Y factors and Eq. (3). Number of rings around the crack tip = 4. Number of elements in the angular direction = 4.

a/t_s	0.1	0.2	0.3	0.4	0.5	0.6	0.7	0.8
% Difference	0.56	0.09	0.17	0.02	0.15	0.11	0.17	0.4

Patched configuration

A typical FE mesh corresponding to the patched configuration is shown in Figure 2b. The material properties assumed in subsequent analyses are presented in Table 2.

Table 2: Young's modulus and Poisson's ratio for the three materials used

	E (GPa)	ν
Steel Plate	205	0.3
Adhesive	7	0.3
CFRP	137	0.34

The thickness of the CFRP patch t_c was assumed equal to 0.1 t_s, while the thickness of the adhesive t_a was assumed equal to 0.01 t_s. As the crack tip on the steel/adhesive interface is a fictitious boundary condition, Y values are reported for the right hand crack tip, which is located in the steel. These are depicted in Figure 3. Figure 3 also shows the results of the analyses carried out on the un-patched configuration. It can clearly be seen that introduction of the patch results in a considerable reduction in the Y factors over the entire range of a/t_s values considered here. However, it has to be emphasised that for short cracks (a/t_s less than, say, 0.2), the Y factor for the patched configuration may be different to the one given by Figure 3. This is because the way in which the crack mouth is modelled is expected to influence the steel crack tip conditions. Further work is currently under way to investigate this aspect.

FATIGUE LIFE IMPROVEMENT

Fatigue crack growth may in general be described by the well-known Paris-Erdogan [16] model

$$\frac{da}{dN} = C(\Delta K)^m \tag{4}$$

where N is the number of applied cycles, C, m are the Paris (material) parameters and ΔK is the stress intensity range associated with a stress range ΔS.

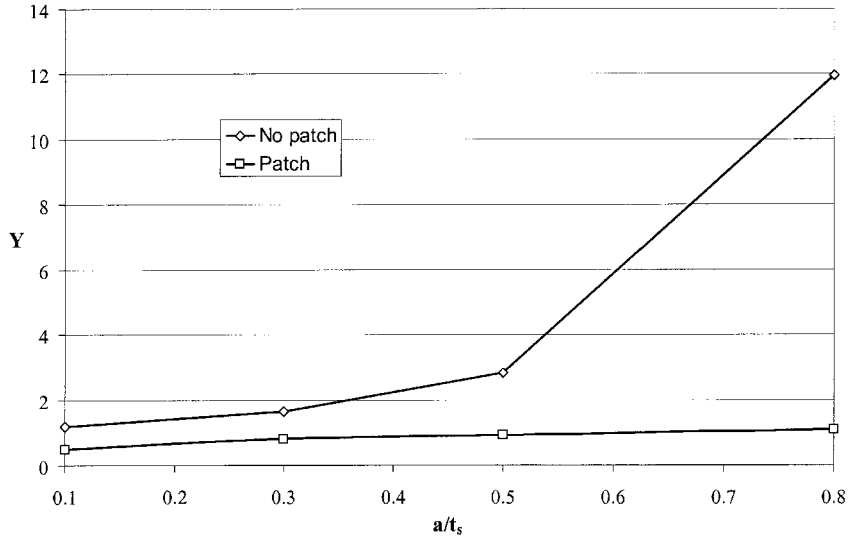


Figure 3: Comparison of Y factors for patched and un-patched plates

For constant amplitude loading (constant stress range) and assuming that C is constant along the crack's path, Eq. (4) leads to

$$N = N_{in} + \frac{\pi^{-m/2}}{C(\Delta S)^m} \int_{a_{in}}^{a_f} \frac{da}{\left(Y\sqrt{a}\right)^m} = N_{in} + N_{rem} \tag{5}$$

where N_{in} is the number of cycles required to initiate and propagate the crack up to a length of a_{in}, a_f is the failure crack length and accordingly N_{rem} is the component's remaining life. In terms of patch repair, N_{in} is the component's age at the time when the patch is introduced and clearly the objective of the repair is to maximize N_{rem}. For a given material (C and m fixed) under given loads (fixed stress range ΔS) the integral is of primary importance. Based on the results presented in previous sections N_{rem} for the un-patched and patched plates may be calculated and compared. For the purposes of this analysis, Y pertaining to the former is given by Eq. (3), while Y pertaining to the latter was obtained from the FE analysis (see Section 3.2) and curve fitted with the following expression

$$Y = 0.166 + 3.7766\left(\frac{a}{t_s}\right) - 6.7244\left(\frac{a}{t_s}\right)^2 + 4.3438\left(\frac{a}{t_s}\right)^3 \quad (6)$$

Table 3 presents the ratio N^p_{rem} / N^u_{rem} where N^p_{rem} is the remaining life corresponding to the patched configuration and N^u_{rem} is the remaining life corresponding to the un-patched configuration. Results are presented assuming a fixed failure crack length of $a_f = 0.6\ t_s$, which is reasonable given steel's resistance to fracture, and for different values of a_{in}. In a more refined analysis, the failure crack may be determined using a failure assessment diagram [19].

Note that in the present context, a_{in} is linked to N_{in}, which in turn reflects the time at which the crack was discovered. Also note that the higher the value of a_{in} the more likely it is that the crack would be detected and, hence, a repair scheme is considered.

Table 3: Fatigue life improvement for different initial cracks and Paris exponents m

	N^p_{rem} / N^u_{rem}	
$(a/t_s)_{in}$	m = 2.8	m = 3
0.05	15.15	19.07
0.1	9.08	10.63
0.2	8.59	9.81

The following points may be made in connection to Table 3:

- As the Y factors are raised to the mth power, fatigue life improvement is highly dependant on m. Accordingly, a higher value of m implies a more drastic improvement.
- Application of the patch towards the end of the plate's useful life implies a smaller fatigue life improvement.
- The improvement in fatigue life is very substantial. However, it has to be borne in mind that the underlying assumption is that no de-bonding takes place during N_{rem}. In reality the high stress concentration encountered at the crack mouth will initiate a crack that will travel along the adhesive/steel interface, adhesive/CFRP interface or within the adhesive [20]. Consequently, the structure will become progressively more compliant with an accompanying increase in Y and hence a reduction in N^p_{rem}. For this reason, the improvements reported in Table 3 should be viewed as an upper bound.

CONCLUSIONS

In this paper the potential improvements in the fatigue life of a steel plate brought about through the application of a CFRP patch were investigated. Based on an LEFM assumption, stress intensity factors were calculated using FE analysis for both un-patched and a patched plates containing a crack. The near tip mesh was validated by comparing the stress intensity factors of the un-patched plate to those reported for the same geometry elsewhere in the literature. Introduction of the patch was seen to reduce significantly the geometry factor Y. This reduction in Y was interpreted in terms of

fatigue life improvement by considering the damage calculated using the well-known Paris-Erdogan crack growth model. Although viewed as upper bound fatigue life improvement estimates, the calculations presented herein indicate that the improvement may be considerable. This improvement will in general depend on the time of patch application and the Paris exponent m as well as the de-bonding process, which is not considered here but is the subject of ongoing research.

REFERENCES

1. Baker A (1999). Bonded composite repair of fatigue-cracked primary aircraft structure. Composite Structures, 47, 431-443.
2. Jones R and Chiu WK (1999). Composite repairs to cracks in thick metallic components. Composite Structures, 44, 17-29.
3. Schubbe JJ and Mall S (1999). Investigation of a cracked thick aluminium panel repaired with a bonded composite patch. Engineering Fracture Mechanics, 63, 305-323.
4. Denney JJ and Mall S (1997). Characterisation of disbond effects on fatigue crack growth behaviour in aluminium plate with bonded composite patch. Engineering Fracture Mechanics, 57, 507-525.
5. Meier U (1995). Strengthening of structures using carbon fibre/epoxy composites. Construction and Building Materials, 9, 341-351.
6. Liu X, Silva P and Nanni A (2001). Rehabilitation of steel bridge members with FRP composite materials. In: Figueiras J, Juvandes L and Furia R editors, Proceedings of CCC 2001 Composites in Construction, Porto, Portugal, 613-617.
7. Miller T, Chajes MJ, Mertz DR and Hastings JN (2001). Strengthening of a steel bridge girder using CFRP laminates. Journal of Bridge Engineering, 6(6), 514-522.
8. Chajes M, Swinehart M, Richardson D and Wenczel G (2003). Bridge rehabilitation using advanced composites: Ashland bridge SR-82 over Red Clay Creek. Conference on Structural Faults and Repairs 2003, London.
9. Sen R, Liby L and Mullins G (2001). Strengthening steel bridge sections using CFRP laminates. Composites: Part B, 32, 309-322.
10. Tavakkolizadeh M and Saadatmanesh M (2003). Fatigue strength of steel girders strengthened with carbon fiber reinforced polymer patch. Journal of Structural Engineering, 129(2), 186-196.
11. Colombi P, Bassetti A and Nussbaumer A (2003). Analysis of cracked steel members reinforced by pre-stress composite patch. Fatigue and Fracture of Engineering Materials and Structures, 26, 59-66.
12. Bassetti A, Nussbaumer A and Hirt MA (2000). Crack repair and fatigue life extension of riveted bridge members using composite materials. In: El-Sheikh S editor, Proceedings of the International Bridge Engineering Conference, Tampa, Florida, 227-238.
13. Bassetti A, Nussbaumer A and Colombi P (2000). Repair of riveted bridge members damaged by fatigue using CFRP materials, in: Advanced FRP Materials for Civil Structures, Bologna, Italy, 33-42.
14. Karbhari VM and Shulley SB (1995). Use of composites for rehabilitation of steel structures – Determination of bond durability. Journal of Materials in Civil Engineering, 7(4), 239-245.
15. Tavakkolizadeh M and Saadatmanesh H (2001). Galvanic corrosion of carbon and steel in aggressive environments. Journal of Composites for Construction, 5(3), 200-210.
16. Paris PC and Erdogan F (1963). A critical analysis of crack propagation laws. Journal of Basic Engineering, 85, 528-534.
17. Kaya AC and Erdogan F (1980). Stress intensity factors and COD in an orthotropic strip. International Journal of Fracture, 16, 171-190.
18. Tada H, Paris PC and Irwin GR (2000). The stress analysis of cracks handbook. ASME Press.
19. BS 7910 (2000). Guide on methods for assessing the acceptability of flaws in fusion welded structures. London: BSI.
20. Buyukozturk O, Gunes O and Karaca E (2003). Progress on understanding debonding problems in reinforced concrete and steel members strengthened using FRP composites. Construction and Building Materials, Article in Press.

FLEXURAL BEHAVIOUR OF GLULAM BEAMS REINFORCED WITH CFRP RODS

Francesco Micelli Vincenza Scialpi Antonio La Tegola

University of Lecce

ABSTRACT

Fibre Reinforced Polymer (FRP) materials are becoming increasingly popular in the civil engineering community, due to their favourable characteristics such as high strength-to-weight ratio, electromagnetic neutrality, and good corrosion resistance. FRP rods are being used as non-metallic reinforcement of newly-constructed concrete members in aggressive environments or as near-surface mounted reinforcement for strengthening of existing concrete, masonry and timber structures. This study investigated the possibility of using Carbon FRP (CFRP) rods as glued-in reinforcement of glulam beams. Full-size beams were tested, with and without the presence of FRP reinforcement. Flexural behaviour of CFRP-reinforced beams was compared with unreinforced beams that were used as control specimens. Different amount of CFRP reinforcement were used in the beam section. The experimental results showed a significant influence of the CFRP rods since the reinforced beams had an increase in ultimate capacity and stiffness. Experimental results were also compared with numerical analysis that was able to furnish results in good agreement with regard to the load and deflection values.

INTRODUCTION

At present, strengthening systems using FRP rods and laminates offer a good potential for application to timber structures in buildings and bridges. They can be used either to enhance flexural and shear strength of existing structures or to decrease the size of new structures for a given required strength.

The first studies dating to the 1960s investigated the use of Glass FRP (GFRP) materials as the reinforcement system of both laminated and solid wood members, while carbon and aramid fibres have been used in some structural applications since the 1990s.Up to the present, different systems for FRP reinforcement of wood structural members have been developed, such as:

- FRP wrapping of wood members with E-glass and carbon fabric reinforcement, using the wet lay-up method;
- FRP adhesive bonding of E-glass pultruted plates to glulam beam;
- FRP tendons for prestressing of laminated wood decks.

Plevris and Triantafillou [1] developed a numerical procedure to predict the behaviour of clear wood beams reinforced with FRP sheets bonded to the tension surface. Triantafillou and Deskovic [2] conducted similar works using prestressed FRP sheets as reinforcement. The programmes showed that small amounts of FRP reinforcement produced significant gains in bending strength and stiffness. Dagher [3] investigated two types of FRP pultruded plates for flexural strengthening of low-grade eastern hemlock glulam beams. The reinforced beams showed substantial gains in strength and stiffness. Tingley [4] used high-strength pultruted FRP laminates to reinforce glulam beams, creating a new composite glulam significantly stronger and stiffer than a conventional unreinforced beam. Hernandez [5] tested Yellow-Poplar glulam beams

strengthened with GFRP sheets that showed an increase in bending stiffness and strength. Dagher used CFRP tendons for prestressing of laminated wood decks in order to improve life-service performance of timber highway bridges. Triantafillou [6] presented experimental and analytical investigations focused on shear strengthening of wood members with FRP laminates. Qiao [7] evaluated the feasibility of improving the performance of wooden railroad crossties by wrapping or encasing the crossties with FRP composites.
In this work an experimental programme is presented in order to show the advantages from the use of near surface glued CFRP rods in terms of flexural behaviour. A significant increase in bending capacity was achieved. A numerical analysis was used to model the behaviour of the reinforced section, and it was found to be in good agreement with the experimental observations.

EXPERIMENTAL PROGRAMME

Specimens and test set-up

Six glulam beam-specimens of European first-quality spruce were prepared, including two unreinforced and four reinforced specimens, of which two specimens had one near-surface glued CFRP rod and two specimens had two CFRP rods. The specimens were 5000 mm long, 120 mm wide and 200 mm high, while the CFRP rods had a diameter of 12.5 mm and peel-ply rough surface. The beams were identified according to the number of bonded rods as GTNR, GTR1 and GTR2, corresponding to a reinforcement area fraction $\rho_f = 0\%$, $\rho_f = 0.51\%$ and $\rho_f = 1.03\%$ respectively. On the bottom lamination of the reinforced beams one or two grooves, 20x15x5000 mm^3 in size were cut using a router. Then, a two-component epoxy resin, with reduced cure-shrinkage and low viscosity, was poured in to the grooves (after application of a primer layer) and the CFRP rods were inserted. After insertion of the rods, the grooves were completely filled with epoxy and the surface smoothed. The epoxy resin was cured for 15 days at room temperature (18°C) before testing.
Table 1 gives the minimum mechanical properties of the glulam according to DIN 1052, while table 2 gives the average test results for uniaxial compressive and tensile strengths of the wood, and the elastic compressive modulus, presented in a previous work resulting from the same research project [8].

Table 1. Minimum properties of first quality glulam (DIN 1052)

Stress Type	Allowable stress (MPa)
Flexure	14.0
Tension	10.5
Compression	11.0
Perpendicular compression	2.5
Longitudinal shear strength	0.9
Shear strength	1.2

Table 2. Experimental mechanical properties of wood (EN 408-97).

Compressive strength parallel to grain [MPa]	32
Direct tensile strength parallel to grain [MPa]	35
Compressive modulus of elasticity parallel to grain [MPa]	8600

The stress-strain relationship of the wood was idealized: the tensile stress-strain curve was assumed to be linear elastic up to failure; the compressive curve was taken as linearly elastic up to the maximum compressive stress, when the fibres start to buckle locally, and a linear softening branch follows. Mechanical properties of CFRP rods and epoxy resin are reported in tables 3 and 4 as certified by the respective manufacturers.

Table 3. Properties of CFRP rod as certified by the manufacturer

Rod surface	Peel-ply
Tensile strength [MPa]	1120
Tensile modulus of elasticity [GPa]	112
Ultimate strain [%]	1.0
Nominal diameter [mm]	12.5

Table 4. Properties of epoxy resin as certified by the manufacturer

Compressive strength at 28 days [MPa]	70
Secant compressive modulus of elasticity at 28 days [MPa]	2900
Tensile strength [MPa]	N/A
Ultimate strain [%]	N/A

The beams were tested to failure under monotonic load in four-point bending with a simply supported span of 4700 mm. The distance between the two applied loads was restricted to 1000 mm to produce a shear span of 1850 mm in order to avoid shear failure. Load was applied with an hydraulic jack and recorded by means of a compression load cell. Deflection at mid-span was monitored using an LVDT on each side of the beam, while deflection at each quarter-span was detected using an LVDT on one side of the specimen. Furthermore, strains were monitored at mid-span of the beam throughout the depth and on CFRP reinforcement by using strain-gauges.

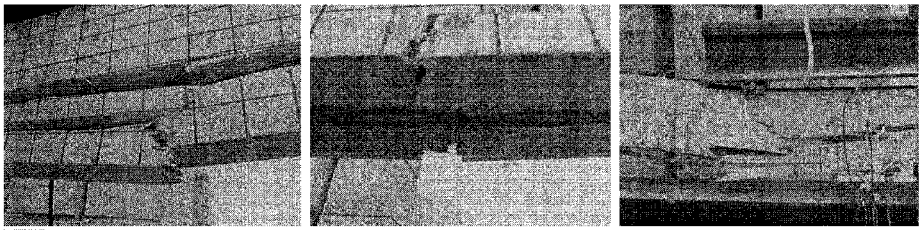
Test results and discussion

Failure modes were governed by the ultimate strain of the timber. Unreinforced beams showed tensile failure in the maximum stress region in one section within the constant-moment zone (Fig. 1-a). Delamination occurred after the breakage of timber fibres. Failure of the reinforced beams was also governed by the tensile strength of the timber. The rupture of tension wood fibres (transversal splitting) (Fig. 1-b) combined with exceeding the bond shear strength at the wood/epoxy interface caused a brittle failure in the beams with one CFRP rod, showing longitudinal splitting close to the constant-moment zone mid-height. The beams reinforced with two CFRP rods showed a wide longitudinal opening in the constant-moment zone propagating up to the compression wooden laminations. This produced the failure of the glulam timber members in combination with localized debonding of the CFRP rod (Fig. 1-c). Both beams reinforced with one CFRP rod showed localized debonding within the constant-moment zone and, consequently, an intact bond between the bar, epoxy and timber outside the same. None of the observed failures was due to either rupturing of CFRP bars or delamination of the reinforcement.

Test results in terms of ultimate load, deflection and stiffness are reported in Table 5. The load versus mid-span deflection curves of all beams are illustrated in Figure 2. The beams with CFRP-reinforcement ratio of 0.51% behaved linearly up to failure achieving an average increase of 26% in load-bearing capacity with respect to unreinforced beams.

The load-deflection behaviour of the two beams with reinforced ratio of 1.03% was linear-elastic up to 50% of the load-bearing capacity, then the slope of the line decreased non-linearly as load increased. In terms of ultimate load an average increase of 82% with respect to unreinforced beams was achieved. This was because the greater reinforcement ratio made the location of the neutral axis near to the CFRP rods reducing the tensile stresses. However the increased compressive stresses caused a compression failure when the extreme wood fibres crushed. This failure produced a pseudo-plastic behaviour in the structural member and, consequently, a more efficient use of structural material.

The stiffness-deflection behaviour showed increases in stiffness for members reinforced with one and two CFRP rods. The average stiffness increase was 8% and 19% with respect to the unreinforced beams, respectively for the case of one or two rods glued as near surface reinforcement. The maximum mid-span deflection at failure was about 140 mm for the beams with two near-surface mounted CFRP bars and about 100 mm for the beams with one near-surface glued CFRP bar.



(a) (b) (c)

Figure 1. Failure modes

Table 5. Average test results

Specimen code	Mid-span deflection [mm]	Quarter-span deflection [mm]	Average ultimate load [kN]	Average stiffness [N/mm^2]
GTNR	76	51	29.29	373
GTR1B	94	63	36.95	402
GTR2B	138	91	53.23	444

Figures 3 shows the experimental data obtained for the typical strain profiles of one and two-CFRP rod reinforced glulam beams tested at different load levels respectively. These profiles report compressive and tensile strains as negative and positive values on the x-axis respectively, and the strain gauges locations on the y-axis corresponding to the compression and tension zone of the cross-section.

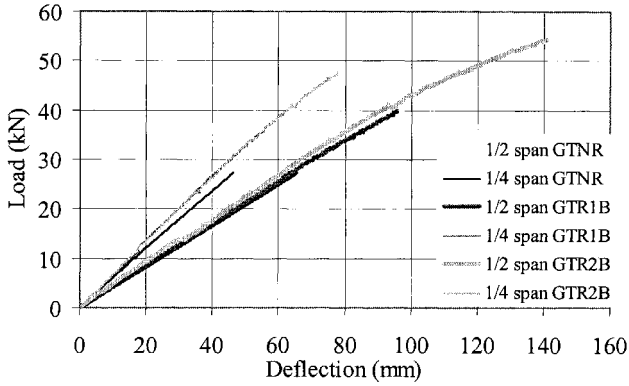
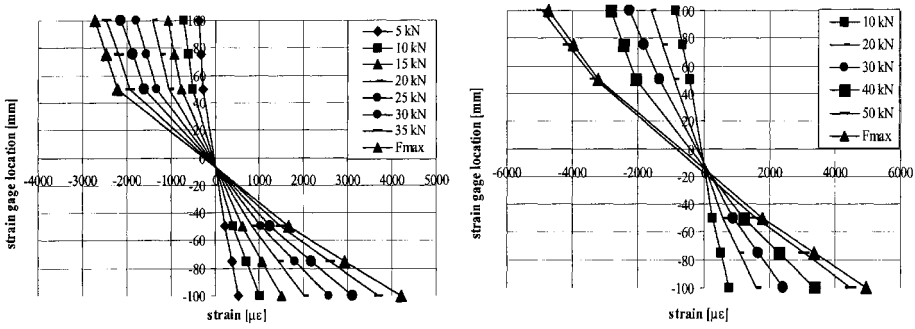


Figure 2. Experimental load versus deflection curves

Data obtained from strain gauges, which were placed on both mid-span cross-section and rods, showed that the assumption of linear strain distribution across the depth (e.g. cross-sections remain plane) was verified approximately for the beams tested. Furthermore, the neutral-axis was placed at 8 mm and 15 mm below the beam mid-height for one and two-CFRP rod reinforced beams respectively prior to loading.
During the first loading phase the strain profiles were nearly linear and the strains measured in the CFRP bars fitted very well with the strain measured in the glulam. This behaviour indicated complete bond between the timber, epoxy and composite material. At higher load levels, compressive yielding in the upper wooden fibres occurred in the beams reinforced with two CFRP bars, and the neutral axis depth increased until the ultimate tensile strain of the wood was reached and, consequently, the beam failed.



(a) (b)

Figure 3.

a -Strain profile at different load levels for beam reinforced with one CFRP rod.

b- Strain profile at different load levels for beam reinforced with two CFRP rods

Figure 4 shows the load versus CFRP-strain curves measured at mid-span and quarter span. It can be seen from Table 6 that the average tensile strain at failure in CFRP bar reinforcing the beams with reinforcement ratio ρ=0.51% was 0.35%, that is about 29% of ultimate strain (ε_u=1.38%), while it was equal to 0.43% for beams with reinforcement

ratio of ρ=1.03%, that is about 34% of the ultimate strain. This showed the effectiveness of the reinforcement in terms of performance.

Table 6. Average tensile strains at failure for reinforced beams recorded

Specimen code	ε_{CFRP} (mid-span)	ε_{CFRP} (span one-third)	ε_{CFRP} (span one-sixth)
GTR1B	0.357%	0.26%	0.155%
GTR2B	0.428%	0.34%	0.131%

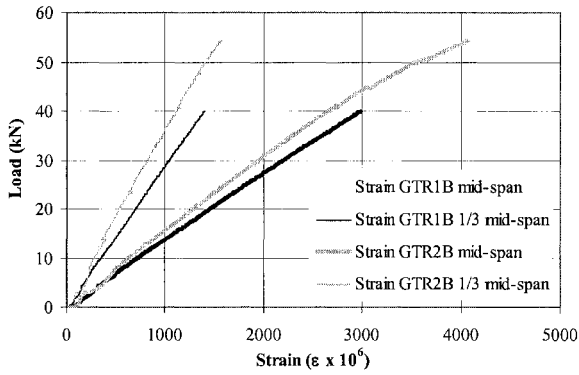


Figure 4. Load versus CFRP-strain curves

ANALYTICAL STUDY

For modelling purposes, it was valid to assume the strain in the CFRP bars to be compatible with the strain in the adjacent timber, a linear strain distribution across the depth and the idealized stress-strain relationship of the materials used.
A simple model based on these assumptions and elastic theory was implemented to predict the moment-curvature of the tested beams that were studied. Considering the mid-span cross section transformed and neglecting the elastic properties of the glue, the neutral-axis location, curvature and ultimate strength were determined by the following equations:

$$\sum F = 0 \Rightarrow \quad \int_{wood} \sigma \cdot dA + \int_{CFRP} \sigma \cdot dA = 0 \qquad (1)\ \text{force equilibrium equation;}$$

$$\sum M = M_e \Rightarrow \quad \int_{wood} \sigma \cdot y \cdot dA + \int_{CFRP} \sigma \cdot dA = M_e \qquad (2)\ \text{moment equilibrium equation}$$

where σ is the stress acting on either wood or CFRP bar element with infinitesimal area dA, y is distance of the same from the neutral-axis, and M_e is external moment acting on beam cross section.
Based on the assumption of plane-sections until failure it is valid to assume:

$$\sigma_{wood} = E_{wood}\varepsilon = E_{wood}\phi y; \quad (3)$$

$$\sigma_{CFRP} = E_{CFRP}\varepsilon = E_{CFRP}\phi y. \quad (4)$$

substituting (3) and (4) in (1) and (2) and considering the transformed section with $n = \frac{E_{CFRP}}{E_{wood}}$:

$$\sum F = 0: \quad \phi\left(E_{wood}\int_{wood} ydA + E_{CFRP}\int_{CFRP} ydA\right) = 0$$
$$\Rightarrow \phi E_{wood}\left(\int_{wood} ydA + n\int_{CFRP} ydA\right) = 0. \tag{5}$$

$$\sum M = M_e: \quad \left(E_{wood}\int_{wood} \phi y^2 dA + E_{CFRP}\int_{CFRP} \phi y^2 dA\right) = M_e$$
$$\Rightarrow \phi E_{wood}\left(\int_{wood} y^2 dA + n\int_{CFRP} y^2 dA\right) = M_e \tag{6}$$

Using equations (5) and (6) the neutral-axis depth y and the curvature Φ are computed:

$$\left(\int_{wood} ydA + n\int_{CFRP} ydA\right) = 0 \qquad (7) \qquad\qquad \phi = \frac{M_e}{E_{wood}\left(I_{wood} + nI_{CFRP}\right)} \qquad (8)$$

The term in parenthesis in (8) is the inertia moment of the homogenized section. In particular, for rectangular cross-section of the glulam beam reinforced with one CFRP rod the equations (7) and inertia moment of the transformed cross-section are written as:

$$y_{n-a} = \frac{\left(bh\frac{h}{2}\right) + nA_{CFRP}\frac{H+h}{2} + (H-h)(b-s)\frac{H+h}{2}}{bh + nA_{CFRP} + (b-s)(H-h)} \tag{9}$$

$$I_h = \frac{1}{3}b\left[y_{n-a}^3 + (H-y_{n-a})^3\right] + \left[\frac{H+h}{2} - y_{n-a}\right]^2\left[nA_{CFRP} - s(H-h)\right] \tag{10}$$

where H=cross-section height, b=cross-section width, s=groove width, h=groove distance from compression side, A_{CFRP}= Area of CFRP reinforcement, E_{wood}=Young modulus of wood and E_{CFRP}=Young modulus of CFRP.
Therefore, it is possible to determine the ultimate moment M_u, the moment vs curvature diagrams and strain in wood and CFRP:

$$\frac{M_u}{I_h}(H - y_{n-a}) = \sigma_{wtu} \tag{11}$$

By comparing theoretical and experimental ultimate moments it was noted that, the ultimate load of the tested beams was accurately predicted. The theoretical moment vs curvature diagrams and strain in CFRP rods were also in good agreement with the experimental results. Figure 5 shows the comparison in terms of load vs deflection.

CONCLUSIONS

An experimental program was conducted in order to investigate the effectiveness of CFRP as glued-in flexural reinforcement of glulam beams. Six full-scale beams were prepared with different CFRP-reinforcement ratio. The preparation of the specimen confirmed that the proposed technique is fast and easy to be appy in real cases.

Test results showed a significant increase in ultimate moment and stiffness, when CFRP rods are glued in the tension side of the cross-section. The presence of one and two 12.5mm diameter CFRP rods produced respectively an increase in ultimate moment of 26% and 82% with respect to unreinforced beams. Failure modes and experimental data showed excellent bond properties between wood and glued CFRP rods; wood properties governed the failure of the beams in all cases. The mechanical behaviour of the specimens can be considered pseudo-linear until failure occurs, although this was less true for the case of high reinforcement ratio.

The analytical prediction of the ultimate moment, moment versus curvature relationship and strain along the cross section in wood and CFRP rods was based on the elastic theory for non-homogeneous beams. In this form an equivalent cross-sectional area was computed (transformed cross-section). Numerical results were found to be in good agreement with experimental data.

Finally, it was shown that the use of CFRP rods for flexural reinforcement of glulam timber beams is effective from a mechanical and technological point of view. The results of this study encourage the use of this technique, but future research is needed.

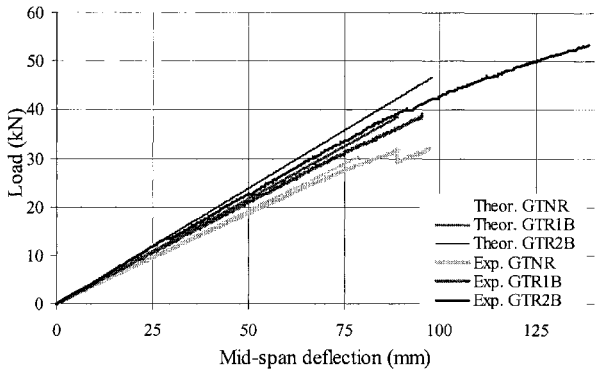


Figure 5. Comparison between experimental and theoretical results

REFERENCES

1 N. Plevris and T.C. Triantafillou, "FRP-reinforced wood as structural material", *Journal of Materials in Civil Engineering- ASCE*, 1992 **3**(4) 300-317.

2 T.C. Triantafillou and N. Deskovic, "Prestressed FRP sheets as external reinforcement of wood members", *Journal Structural Engineering*, **5**(118) 1270-1284.

3 H.J. Dagher, T.E. Kimball, S.M. Shaler and B. Abdel-Magid, "Effect of FRP reinforcement on low grade eastern hemlock glulams", *Nat. Conf. Wood Transportation Structures,* Madison WI. FPL-GTR-94, 1996.

4 D.A. Tingley, P. CC. Gilhamand M.S. and Kent Scottm, "Long term load performance of FRP reinforced glulam bridge girders", *Nat. Conf. Wood Transportation Structures,* Madison WI. FPL-GTR-94, 1996.

5 R. Hernandez, J.F. Davalos, S.S. Sonti, Y. Kim and R.C. Moody, "Strength and stiffness of reinforced yellow- poplar glued laminated beams", Res. Pap. FPL-RP-554, U.S. Dept. of Agriculture, Forest Products Lab., Madison WI, 1997.

6 T.C. Triantafillou, "Composites: a new possibility for the shear strengthening of concrete, masonry and wood", *Composites Science and Technology*, 1998 vol. 58 1285-1295.

7 P. Qiao, and J.F. Davalos and M.G. Zipfel, "Modeling and optimal design of composite-reinforced wood railroad crosstie", *Comp. Struct.*, 1998 vol. 41 87-96.

8 L. De Lorenzis, N. Galati and A. La Tegola, "Strengthening of glulam beams with externally bonded FRP laminates", *CCC 2001 Int. Conf.*, Porto, Balkema Ed. 2001.

USE OF CFRP CONNECTORS IN GLULAM FLEXURAL JOINTS

Vincenza Scialpi Francesco Micelli Antonio La Tegola

University of Lecce

ABSTRACT

Fibre Reinforced Polymer (FRP) composites have been largely used in combination with masonry and concrete structural elements in the last decade. Recent applications showed that new advantages may be achieved also in the field of timber structures, even if at the moment a large use of steel elements is made. This study investigated the possibility of using CFRP rods as glued-in connectors for glulam timber joints that should transfer flexural moment between two adjacent beams. Full-size head joints were prepared and tested. Flexural behaviour of joints was compared with the mechanical properties of mono-piece beams that were used as reference specimens. Three different bonded lengths were used for the construction of CFRP-timber joints. Experimental results showed that the use of CFRP rods in timber joints was successful since the capacity of the CFRP-jointed beams was almost the same as the monolithic beams for the longest bond length that was adopted. This result is important in order to find an adequate alternative to traditional joints made with steel bolts and plates that are not able to create rigid connections and increase dramatically the weight of timber structures.

INTRODUCTION

Mechanical joints in timber structures are made using connecting systems in the form of steel plates, bolts and screws. Current techniques used for flexural head-joints consist of inserting one or more drilled plates that are connected to the timber beams by steel bolts (see Figure 1). The flexural stress is transferred to the connectors that are subjected to shear. This solution is widely adopted, even if technological and mechanical limitations occur: steel plates are heavy, thus transportation costs are high and installation may be dangerous or at least uncomfortable; steel has high thermal conductivity, that may create problems in case of fire; it is impossible to create rigid connections, since the mechanical coupling generates a hinge configuration, even if it is very stiff; aesthetic problems due to the presence of external steel elements.

Innovative techniques employing steel or FRP rods glued-in with resin offer many benefits with respect to conventional methods that use steel plates and bolts. Injecting a resin into the gap between the connector and the wood improves the performance of the joint since it increases the friction at the fastener-wood interface and allows transfer of full load without initial slip caused by the connector displacement. Local crushing of the wood fibres at the bearing interface followed by transverse tension failure is also avoided.

The use of glued steel rod technology for timber connections began in Denmark in the 1980s. In the following years many studies have been carried out in Europe to investigate the reliability of this jointing method. Indeed Europe-wide research projects, such as GIROD [1] and COLORETIM [2], have addressed design recommendations as well as innovative ideas based on the development of special adhesives and possible replacement of steel with FRP. In particular, the objective of GIROD has been to provide design guidelines for glued-in rods that will be included in Eurocode 5.

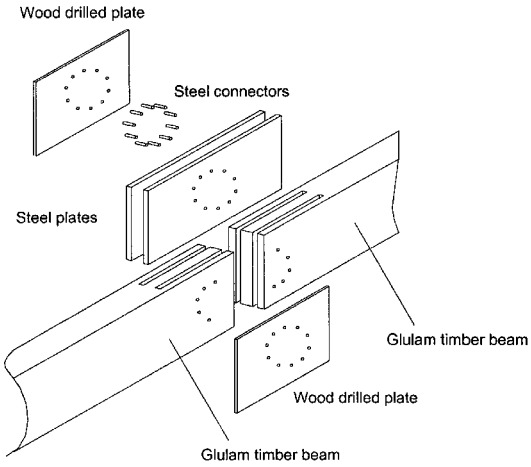


Figure 1. Scheme of traditional head joint for flexural glulam timber members

Similar studies but with different test conditions have also been carried out at the University of Canterbury (New Zealand): Towsend [3] and Deng [4] tested the tensile strength of a single steel rod bonded into glulam using epoxy resin, while Korin [5] tested the tensile strength of single and multiple rods. Firweather [6] carried out tests on several moment-resisting connections showing their ductility and energy dissipation properties; Moss [7] investigated the combined bending and shear behaviour of joints of such timber connections under monotonic and cyclic loading.
Although studies have been undertaken on the use of FRP bars as connectors for existing timber members there appears to be little published evidence of their use in "new-build" application. Moreover, published studies are only related to glass FRP (GFRP) bars since they offer a cheaper solution compared with CFRP. Harvey and Ansell [8] investigated the use of GFRP as an alternative bonded-in rod material to the commonly used steel. They performed pull-out tests to characterise the bonded-in connection and both moment-resisting and shear joints to evaluate their performance.
In this work a new flexural head-joint is presented, experimental results related to mechanical tests are discussed in terms of load-deflection, strain distribution, ultimate strength, and failure mode. The tests revealed the high potential that CFRP offers in combination with glulam timber elements. New possibilities are offered also for contemporary transmission of shear and flexural stresses, and future research will be focused in this direction. In this study only the flexural problem is discussed.

EXPERIMENTAL PROGRAM

Materials and test specimens

Five full-scale glulam specimens were prepared, two monolithic beams that were used as control series, and three joint-specimens that were made using two beams connected with CFRP rods glued by epoxy resin. The length and geometry of the joint-specimens were equal to those of the control beams. The specimens were subjected to mechanical destructive tests under a four-point bending configuration in order to investigate the

possibility of re-establishing the strength of the monolithic beam with the new jointing mentioned above.
Wood beams were built using first quality glulam according to DIN 1052; mechanical properties of the wood were measured in the laboratory; average experimental results are presented in Table 1. The stress-strain relationship of wood was idealized with a stress-strain curve assumed by Bazan [9] that is linearly elastic up to tensile failure; the compressive curve is linearly elastic up to the maximum compressive stress when the fibres start to buckle locally and a linear softening branch follows. Mechanical properties of CFRP rods and epoxy resin are reported in tables 2 and 3 as certified by the respective manufacturers.

Table 1. Experimental mechanical properties of wood (EN 408-97).

Compressive strength parallel to grain [MPa]	32
Tensile strength parallel to grain [MPa]	35
Compressive modulus of elasticity parallel to grain [MPa]	8600

Table 2. Properties of CFRP rod as certified by the manufacturer

Rod surface	Peel-ply
Tensile strength [MPa]	1120
Tensile modulus of elasticity [GPa]	112
Ultimate strain [%]	1.0
Nominal diameter [mm]	12.5

Table 3. Properties of epoxy resin as certified by the manufacturer

Compressive strength at 28 days [MPa]	70
Secant compressive modulus of elasticity at 28 days [MPa]	2900
Tensile strength [MPa]	N/A
Ultimate strain [%]	N/A

Each joint specimen was prepared using two beams 2500 mm long that were jointed in the mid-span by means of two glued-in CFRP bars acting parallel to the grain, in both the tension and compression zones at a spacing of 20 mm. Each structural member had a cross-sectional area of 120x200 mm^2 and a total length of 5000 mm; the CFRP bars had a nominal diameter of 12.5 mm and their surface was made rough by a peel-ply layer. Three different anchor lengths of CFRP-fasteners were chosen: 300, 400, 500 mm in the compression zone with 800, 900, 1000 mm respectively in the tension zone. The test beams were identified as JB300-800, JB400-900 and JB500-1000, according to the length (mm) of the anchorage region in compression and tension side respectively, while monolithic beams were labelled with JNB 1 & 2 (Table 4).
Preparation of joint-specimens is illustrated in Figure 2. Two jointing parts were placed on suitable guides and their mid-span ends were clamped in order to avoid undesired

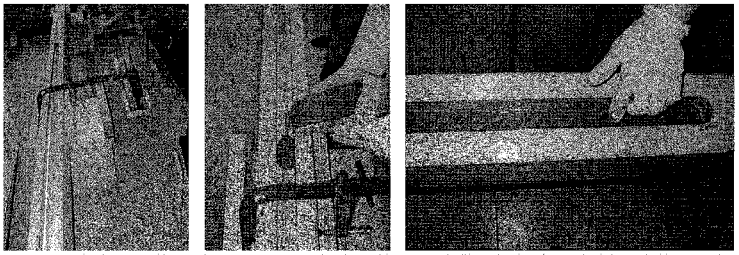
displacements that could change the joint-geometry (Figure 2-a). A layer of epoxy primer was applied on the groove surfaces and, subsequently, the epoxy resin was poured into it in order to insert the rods (Figure 2-b). After insertion of the CFRP rods (Figure 2-c), the grooves were filled with epoxy resin up to a depth of 16mm and they were then covered with a timber lath in order to re-establish the visual appearance of a monolithic structural member. A schematic of the CFRP-timber joint is illustrated in Figure 3.
The specimens (monolithic beams and joint-beams) were tested to failure under monotonic load in four-point bending configuration with a simply supported span of 4700 mm. The test set-up is shown in Figure 4: LVDTs on each side of the beam at mid-span and LVDTs at a each quarter-span (symmetrically with respect to the mid-span) were used to monitor deflections. Electrical strain gauges were bonded to the tension CFRP rods in order to monitor three main locations of the connection: ½ length (corresponding to mid-span) and ¼ length of the rod.

Test results and discussion

For all specimens the failure mode was brittle. Failure of the monolithic beams was caused by tensile failure of the wood in the tension side; followed by longitudinal splitting of the wood fibres. Typical collapse of tested beams is illustrated in Figure 5.
In CFRP-wood joints failure occurred by means of longitudinal splitting in the compression zone (e.g. a wide longitudinal opening within the first or second compression lamination) due to rotation of the two ends at the structural joint during loading, in combination with pulling-out of the tension bars surrounded by a wood wedge (Fig. 6 a-b). This last failure mode was similar to that observed during direct tensile tests (e.g. pull-out tests) performed on CFRP bars glued into glulam blocks parallel to the grain [10].

Table 4. Geometric properties of joint-beams

Specimen code	**Anchorage length in compression side L_c (mm)**	**Anchorage length in tension side L_t (mm)**	**Jointed Beam span L (mm)**
JNB 1 & 2	Monolithic beams used as reference specimens		
JB300-800	300	800	4700
JB400-900	400	900	4700
JB500-1000	500	1000	4700



(a) (b) (c)

Figure 2. Preparation of joint-specimens

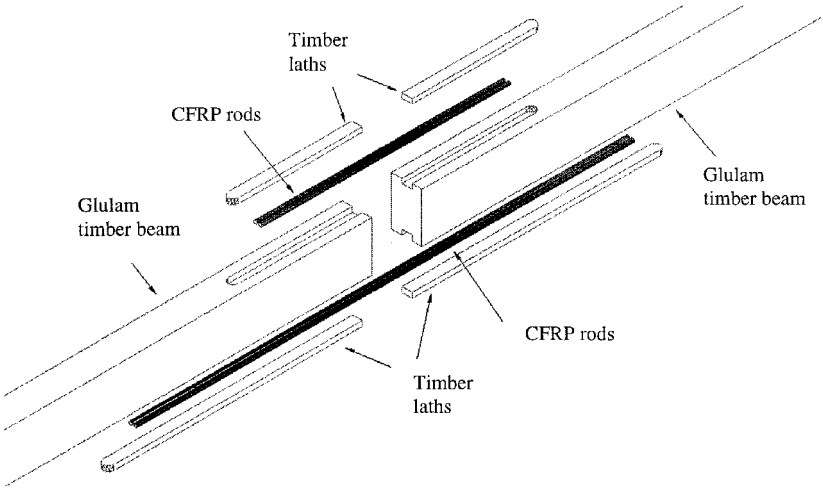


Figure 3. Scheme of the CFRP-timber flexural joint



Figure 4. Test set-up

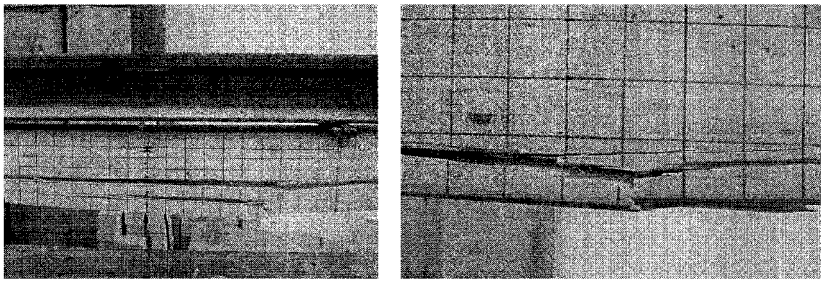
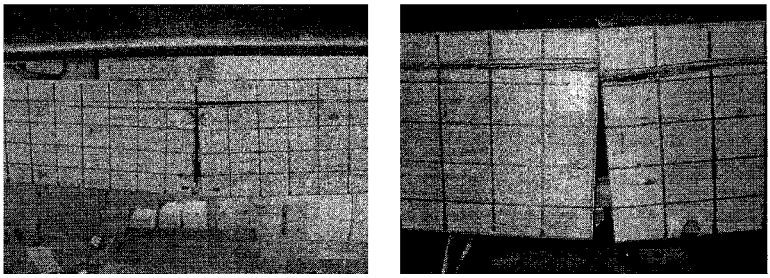


Figure 5. Failure of monolithic beams



(a) (b)

Figure 6. Failure of CFRP-wood joints

a - failure of glulam beam due to longitudinal splitting in the compressive zone in combination with pull-out of the tension bars surrounded by wood wedge

b - detail of the rotation of two structural member jointing ends showing the pull-out of the tension bars surrounded by wood wedge

Test results are presented in Table 5, where maximum load, mid-span deflection, quarter-span deflection and ratio between the maximum load of joints and beams are reported. In particular, it is noted that the JB300-800, JB400-900 and JB500-1000 specimens showed an ultimate load value of about 70%, 74% and 93% of the control beams respectively. That reflects a good bending behaviour of the CFRP-wood connection, especially because it should be considered that in real applications the fastening system would not be placed in the sections with the highest flexural stresses.
Load-deflection curves for joints and control beams are compared in Figure 7. The mechanical behaviour was linear up to failure for all the tested specimens, however the joint-specimens showed local splitting at a load of approximately 15 kN and, consequently a load-loss. This load loss was followed by a region of lower strength and stiffness, compared to the control beams.
It should be noted that the stiffness of the CFRP-connected specimens was almost the same as that of the monolithic beams at service load level; this evidence confirmed the high stiffness of the chemical connection between CFRP and timber.

Table 5. Test results

Specimen	**P_u (kN)**	**1/2 span deflection (mm)**	**1/4 span deflection (mm)**	**$P_{u\text{-joints}} / P_{u\text{-beams}}$ (%)**
JNB	29.29*	76.40*	51.23*	-
JB300-800	20.58	86.40	52.22	70.27
JB400-900	21.76	84.24	50.81	74.29
JB500-1000	27.15	112.09	58.58	92.71

*average results
P_u = maximum load

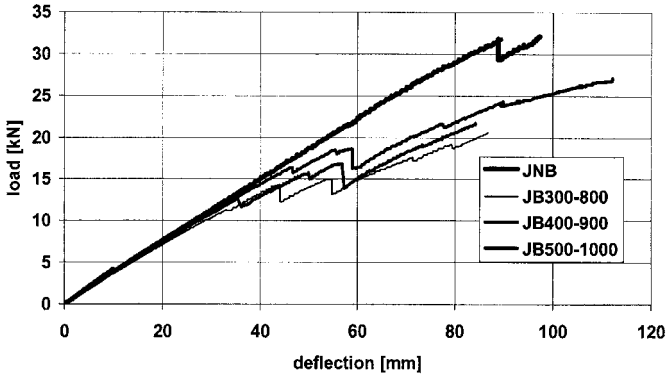


Figure 7. Load - deflection curves for joints and control beams

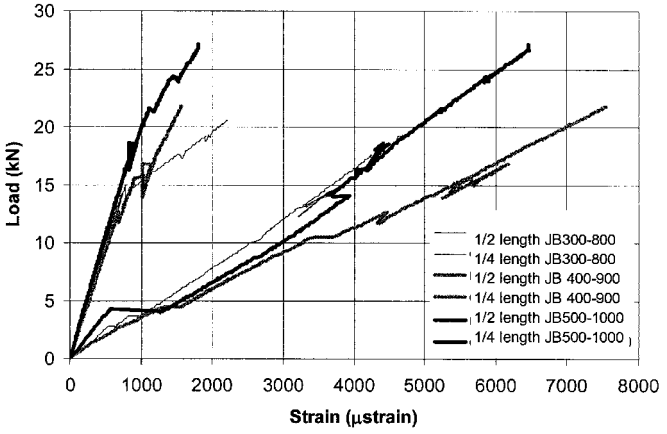


Figure 8. Load – tensile strain curves for CFRP rods

In Figure 8 load versus strain curves are shown for CFRP rods placed in the tension side of the joints. It can be seen that the trend is linear, even if disturbed regions are present, possibly due to the acquisition apparatus. The maximum strain that was monitored in CFRP rods was about 0.77%, 0.75% and 0.50% respectively for JB500-1000, JB400-900 and JB300-800, these correspond to 62%, 60% and 40% of the ultimate strain of CFRP. These values show the effectiveness of the joint in terms of load-carrying capacity and bond performance of the wood-epoxy-CFRP system.

CONCLUSIONS

In this study a new composite system was studied and proposed in order to joint glulam timber beams that should transmit flexural stresses. This system was conceived as a possible alternative to traditional fastening systems that use steel plates and bolts. Numerous advantages were found in terms of installation and in-service behaviour: high stiffness, good aesthetic aspect, ease of preparation and installation. Other aspects should be investigated, since a better fire resistance is also expected for this kind of solution with respect to that using steel connectors.

Mechanical tests were conducted in the laboratory, comparing CFRP-timber joints with monolithic beams. The flexural stiffness of the joints was the same for all the beams under service loads; this highlighted the high stiffness of the chemical connection. The ultimate capacity increased with the anchorage length: an anchored length of 1000 mm allowed the joint to reach 93% of the ultimate load of the control beams, meaning an almost full strength development.
Strain was detected along the CFRP connectors, it was seen that carbon fibres carried 62% of their ultimate stress in the case of an anchorage length equal to 1000 mm. This showed the high performance in terms of bond during the stress-transfer process.
Future research will be addressed to constructing new joints that should transfer shear stresses and flexural stresses, in the same section, using the technique of CFRP-glued rods. In general it should be noted that high bond properties between glulam timber and epoxy-FRP systems allow the introduction of these new technologies in design and construction practice without similar concerns to those in concrete and masonry structure applications, where debonding failure is not easily prevented.

REFERENCES

1 GIROD Project Website: http:// www.sp.se/building/wood/girod.htm

2 COLORETIM EU Website: www.ttlchiltern.co.uk/resarh_projects/pif279/demo/html/

3 P K Townsend, "Steel dowels epoxy bonded in glue laminated timber", Res. Report 90/11, Department of Civil Engineering, University of Canterbury, Christchurch, New Zealand, 1990.

4 J X Deng, "Strength of epoxy bonded steel connections in glue laminated timber". Research Report 97/4, Department of Civil Engineering, University of Canterbury, Christchurch, New Zealand, 1997.

5 U Korin, A H Buchanan and P J Moss, "Effect of bar arrangement on the tensile strength of epoxied end bolts in glulam", *Pacific Timber Engineering Conf*, Rotorua, New Zealand, 1999.

6 R H Faiweather, "Beam column connections in glue laminated timber", Research Report 92/5, Department of Civil Engineering, University of Canterbury, Christchurch, New Zealand, 1999.

7 P J Moss, A H Buchanan, and K L Wong, Moment-resisting connections in glulam beams, *World Conference on Timber Engineering*, Whistler Resort, British Columbia, Canada, 2000.

8 K Harey, M P Ansell, "Improved timber using bonded-in GFRP rods", *World Conference on Timber Engineering*, Whistler Resort, British Columbia, Canada, 2000.

9 I M M Bazan, "Ultimate bending strength ov timber beams", PhD thesis, Nova Scotia Tec. College, Alifax NS, Canada, 1980.

10 V Scialpi, L De Lorenzis, and A La Tegola "Bond of CFRP rods in glulam members", *Composites in Construction CCC 2003 Int. Conf.*, Rende (CS), Italy 2003.

ANALYTICAL AND EXPERIMENTAL STUDY ON BONDED-IN FRP BARS IN GLULAM TIMBER

Laura De Lorenzis, Vincenza Scialpi, Antonio La Tegola
Department of Innovation Engineering – University of Lecce, Italy

ABSTRACT

A promising application of fiber-reinforced polymer (FRP) bars in combination with glue-laminated timber members is their use as bonded-in connectors in place of steel. The advantages related to this solution are the improved durability of the system and the easier and faster application guaranteed by the lightweight properties of FRP materials. In this study, pull-out tests were conducted to study the bond performance of FRP rods epoxied into glulam elements. Based on the experimental curves, the local bond-slip behavior of the joint was calibrated and used to obtain numerically the ultimate load of the joint as a function of the embedment length of the bar. Also, the behavior of the joint in the plane perpendicular to the axis of the bar was modelled for the cases of bar parallel and perpendicular to the grain, showing that splitting bond failure is more critical for bars parallel to the grain, as observed experimentally.

INTRODUCTION

During the last decades, the quality and reliability requirements of glulam have contributed to make it a competitive alternative to reinforced concrete and steel, promoting its use in large structural components. However, the joints of glulam elements often exhibit heavy-weight connection details, which are difficult to install, induce local deformations, and have disturbing appearance. Innovative connection techniques employing steel concealed rods glued in with resin have been shown to offer many benefits with respect to conventional methods of joining, among which greater stiffness and strength, lower weight and cross-grain stress concentration, greater fire resistance, and improvement in appearance.

The use of fiber-reinforced polymer (FRP) bars in place of steel for glued-in timber connections would result in improved resistance to corrosion, lower weight of the connections, easier and faster handling and installation. There appears to be little published evidence of the use of FRPs in "new-build" applications to potential bonded-in rod connections. Davis and Claisse (1998) found uni-axial glass-reinforced joints to be among the two best performing types of joints analysed in their study. Harvey and Ansell (2000) investigated the use of glass FRP (GFRP) as an alternative rod material. They performed pull-out tests on GFRP rods bonded into timber blocks parallel and perpendicular to the grain in order to examine the influence of the rod surface preparation, glueline thickness, bonded length of the rod, adhesive type, moisture content and wood type on the pull-out failure load of the joint.

This study presents the first results of a research project started at the University of Lecce, aimed at investigating the effectiveness of carbon FRP (CFRP) glued-in rods for use as connectors in glulam members. CFRP is stiffer and more durable, although more expensive, if compared to GFRP.

From the experimental point of view, pull-out tests were carried out to investigate the bond behavior of CFRP bars glued in first-quality spruce glulam specimens. Based on the experimental curves, the local bond-slip behavior of the joint was calibrated, and used to obtain numerically the ultimate load of the joint as a function of the embedment length of the bar. Also, the behavior of the joint in the plane perpendicular to the axis of the bar was modelled for the cases of bar parallel and perpendicular to the grain, showing that splitting bond failure is more critical for bars parallel to the grain, as observed experimentally.

SUMMARY OF EXPERIMENTS

As follows, the experimental study on bond of CFRP bars in glulam timber elements conducted by the authors is summarized. For more details, see Scialpi et al. (2003).

The specimens were prismatic glulam blocks with different cross-sectional dimensions and lengths according to the test variables (see Table 1). In each block, a hole with 16-mm diameter was drilled centrally through the entire length and was filled from one end with a two-component low-viscosity epoxy adhesive. A pultruded CFRP rod with 12.5-mm nominal diameter was then glued-in at the center of the block. The applied load was reacted by means of steel threaded rods embedded and glued-in at the corners of the block inserted into a stiffened steel plate.

The test variables were: surface configuration of the bar, bonded length, and direction of the bar axis relative to that of the timber fibers. The CFRP bar surface, spirally wound with a carbon fiber tow, was either sanded or peel-ply roughened. The embedment length ranged from 4 to 24 times the bar nominal diameter. The bars were bonded either parallel or perpendicular to the grain. Three replicates were tested for most combinations of test variables. For the detailed program, see Table 1.

The tests were conducted in displacement-control mode, with a 0.2-mm/min cross-head displacement rate, measuring the relative displacement between the loaded end of the bar and the glulam block (loaded-end slip) by an LVDT.

The type of timber was European first-quality spruce glulam, with direct tensile strength parallel to the grain of 35 MPa and compressive modulus of elasticity parallel to the grain of 8600 MPa. The choice of CFRP bars as connectors among the different types of FRP materials available on the market was motivated by the superior durability performance of CFRP, as well as by its greater stiffness. The sanded bars had a tensile strength of 1771 MPa and an elastic modulus of 136 GPa, the non-sanded bars had a tensile strength of 1900 MPa and an elastic modulus of 112 GPa. The epoxy resin used for embedment had a 70-MPa compressive strength and a 2.9-GPa secant compressive modulus of elasticity.

Test results are presented in Table 1 in terms of maximum load, average bond strength, loaded-end slip at peak load and failure mode. The average bond strength for each specimen has been calculated with reference to both an effective diameter of 16 mm, equal to the external diameter of the annular bondline (diameter of the hole), and the nominal diameter of the bar. The reported values are average from all the replicate specimens.

In specimens with rods glued-in parallel to the grain, failure was determined by longitudinal splitting of the timber block, resulting from tensile failure in the timber perpendicular to the planes containing the fibers. The only exception were specimens with 300-mm embedment length. These failed by pull-out of the bar along with a wooden prism surrounding the bondline, resulting from shear failure in the timber along planes parallel to the fibers. The effect of the bar superficial treatment on the bond performance was rather

weak: since wood was always the weakest link of the connection, the failure modes of equivalent specimens with different rod superficial treatments were similar. However, the bond failure loads of the non-sanded CFRP bars were generally slightly higher.

It is worth noting that current Eurocode design provisions on bonded-in steel bars in timber do not mention splitting among the possible bond failure modes, and prescribe a minimum distance of the bars from the edge of the section of 2.5 bar diameters. In the present study, specimens with bars parallel to the grain had the bar at a distance of 6.4 diameters from the edge, nevertheless they mostly failed by splitting.

1. Pull- out test program and results

Spec. code	In-plane sectional area [mm^2]	Bonded length [mm]	Rod type*	Grain direction with respect to rod axis	Peak load [N]	Loaded-end slip at peak load [mm]	Average bond strength [MPa]	Failure mode****
50CS//		50	S	parallel	7179	0.085	2.86** (3.66***)	1
100CS//		100	S	parallel	20985	0.237	4.17** (5.34***)	1
150CS//	160x160	150	S	parallel	39949	0.659	5.30** (6.78***)	1
200CS//		200	S	parallel	45425	0.495	4.52** (5.79***)	1
300CS//		300	S	parallel	61141	1.631	4.05** (5.18***)	2
AVG. BOND STRENGTH CS//: 4.18 (5.35***) MPa**								
50CNS//		50	NS	parallel	8306	0.289	3.30** (4.22***)	1
100CNS//		100	NS	parallel	18458	0.131	3.67** (4.70***)	1
150CNS//	160x160	150	NS	parallel	33208	0.521	4.40** (5.63***)	1
200CNS//		200	NS	parallel	49839	0.904	4.96** (6.35***)	1
300CNS//		300	NS	parallel	72143	1.856	4.78** (6.12***)	2
AVG. BOND STRENGTH CNS//: 4.23 (5.41***) MPa**								
50CNS⊥		50	NS	perpendic.	16252	0.879	6.47** (8.28***)	3
100CNS⊥	120x230	100	NS	perpendic.	33950	1.066	6.75** (8.64***)	3
150CNS⊥		150	NS	perpendic.	56964	1.816	7.56** (9.68***)	3
200CNS⊥		200	NS	perpendic.	82695	2.340	8.23** (10.53***)	3
AVG. BOND STRENGTH CNS⊥: 7.25 (9.28***) MPa**								

*S: sanded; NS: non-sanded; **computed with the hole diameter; ***computer with the nominal bar diameter
****1: Longitudinal splitting; 2: Pull-out of the bar along with a wooden prism surrounding the bondline; 3: Pull-out of the bar from timber with small wood slivers still attached.

Specimens with rods perpendicular to the grain failed all by pull-out of bar. The bar, surrounded by the adhesive annular layer, debonded from the surrounding timber, keeping small adjacent wooden splinters still attached, and determining the detachment of the superficial fiber layer of the block. These specimens displayed a much higher bond strength than those with bar parallel to the grain and did not exhibit sensitivity to splitting failure, which will be explained later.

ANALYTICAL MODELING

Bond-slip response and theoretical bond failure load

For the range of bonded lengths considered in the tests, the ultimate load showed an approximately linear increase with the bonded length for all variable combinations. Hence, for this type of joints and with bonded lengths shorter than 24 bar diameters, the average bond strength can be considered approximately constant with the bonded length, which

indicates an even distribution of bond stresses along the bonded length at failure. Therefore, the average bond strength indicated in Table 1 can be of immediate design use, provided that this trend is confirmed for longer bonded lengths.

In order to predict the trend of the ultimate load outside the test range of bonded lengths, the local bond slip response of the joints was modelled and used to solve the differential equation of bond. The local bond-slip curve was identified with the average bond stress vs. loaded-end slip curve of the specimens with the shortest bonded length.

Load-slip graphs of rods *perpendicular* to the timber grain showed and ascending branch which could be modelled with the well-known model by Eligehausen et al. (1983) valid for steel bars in concrete, and an almost linear post-peak softening branch. Hence, the local bond-slip curve was expressed as follows:

$$\tau(s) = \tau_m \cdot \left(\frac{s}{s_m}\right)^{\alpha} = C \cdot s^{\alpha} \qquad \text{for } 0 \le s \le s_m \tag{1a}$$

$$\tau(s) = \tau_m + p \cdot (s - s_m) \qquad \text{for } s_m \le s \le s_u \tag{1b}$$

where τ is the local bond stress, s the local slip, τ_m and s_m are bond stress and slip at the peak point, α is a parameter that varies between 0 and 1, p is the slope of the second linear branch and s_u has been assumed as the value of slip at which the bond stress equals zero.

Load-slip graphs of rods *parallel* to the timber grain showed an ascending branch similar to that of the previous specimens. After the peak they displayed in most cases alternating gains and drops in load, due to residual friction and to the effect of imperfections. Hence, the post-peak branch could not be modelled, also because of the notable scatter between different specimens.

The values of the unknown parameters in eq. (1), calibrated by best fitting of experimental results, are reported in Table 2. Parameter α was obtained by equating the area underneath the ascending branch of the experimental curve to the value:

$$A_\tau(0, s_m) = \int_0^{s_m} \tau_m \left(\frac{s}{s_m}\right)^{\alpha} ds = \frac{\tau_m s_m}{1+\alpha} \tag{2}$$

In usual bond test results, the average bond strength decreases with increasing bonded length, due to the non-uniform distribution of bond stresses along the bonded length at ultimate. In this case, the average bond strength was approximately constant with the bonded length within the test range. For this reason, the value of τ_m was taken as the average of all specimens, whereas s_m and α were determined on specimens with 4-diameter bonded length. From the values of s_m it appears that the curves pertaining to sanded bars are stiffer than the others, due to the larger elastic modulus of sanded bars.

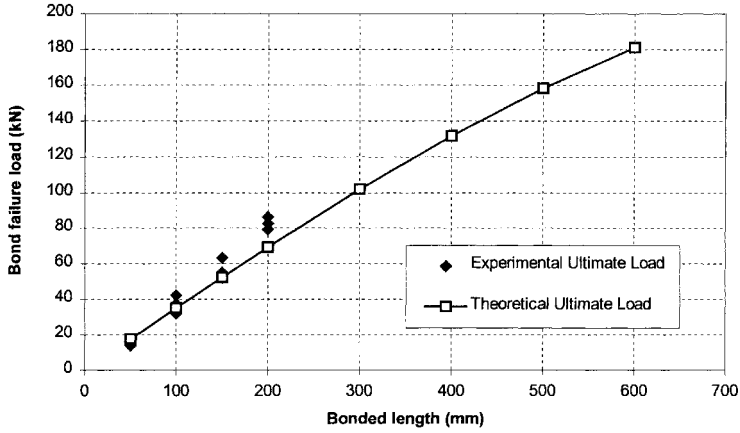
2. Parameters in the local bond-slip relationship

Specimens	τ_m (MPa)	s_m (mm)	α	p (MPa/mm)
CS//	5.35	0.085	0.47	-
CNS//	5.41	0.289	0.44	-
CNS⊥	9.28	0.879	0.42	-1.35

Solution of the differential equation of bond with the calibrated bond-slip curve furnished the bond failure load of the joint as a function of the bonded length, as shown in

Fig. 1 for bars perpendicular to the grain. It may be observed that the experimental bond failure load is predicted with reasonable accuracy and on the safe side. As the theoretical curve displays a deviation from linearity for bonded lengths larger than about 300 mm, using the bond strength given in Table 1 may be unconservative for long bonded lengths. E.g., for a bonded length of 600 mm, the theoretical curve predicts a bond failure load of about 180 kN, versus the value of 219 kN (22% larger) that would result from an average bond strength of 9.28 MPa.

A similar curve for bars parallel to the grain could not be obtained, as the post-peak bond-slip response could not be calibrated.



1. Bond failure load vs. bonded length (bar perpendicular to the grain)

Splitting bond mechanism

As well known, bond is a three-dimensional problem. In the previous section, the bond failure load has been computed solving the differential equation of bond, i.e accounting for the distribution of the bond stresses along the axis of the bar. The constitutive equation governing this distribution is the local bond-slip curve. The parameters defining this curve in turn depend on the configuration of the joint in the plane perpendicular to the axis of the bar, in particular on the depth of the cover and on the possible presence of confinement. This is particularly true in the case of splitting failure, which was the controlling failure mechanism for almost all specimens with bar parallel to the grain. Objective of this section is to compute the value of the local bond strength associated to splitting for the cases of bar parallel and perpendicular to the grain. Glulam is considered transversely isotropic.

Bar parallel to the grain

In his well-known bond model proposed for reinforcing bars in concrete, Tepfers (1973) regarded the radial component of the bond stresses as an hydraulic pressure acting on a thick-walled concrete ring with thickness equal to the miminum cover of the bar in a prismatic section. Since then, the bond action of a reinforcement bar in the plane perpendicular to its axis is often modelled as a uniform pressure, representing the radial

component of the bond forces (Fig. 2). The value of pressure, p, is related to the tangential bond stress, τ, as follows:

$$\tau = \frac{p}{\tan\alpha} \tag{3}$$

The previous equation, written at the ultimate (splitting) stage, corresponds to assuming a Mohr-Coulomb failure criterion, with a zero value of cohesion and a coefficient of friction equal to 1/tanα. The value of α is actually not constant: initially, it depends on existing chemical adhesion and on the surface configuration of the bar, but it will change in different stages of loading. However, a simplifying assumption of a constant α (in particular, of α equal to 45°) is commonly made.

In the case of bar parallel to the grain, the cross-section perpendicular to the bar can be modelled as a thick-walled cylinder with thickness c equal to the minimum cover of the bar in the real prismatic member, and internal diameter equal to the bar diameter d_b (Fig. 2a). It can be easily demonstrated that the transverse isotropy of the system leads to the same solution of the isotropic case, which is independent on the elastic constants governing the constitutive behavior. Hence, solution of this problem is well-known: the radial stresses σ_r are compressive, and the hoop stresses σ_θ are tensile, with maximum value arising for r equal to d_b:

$$\sigma_{\theta\max} = \frac{\left(c+\frac{d_b}{2}\right)^2 + \left(\frac{d_b}{2}\right)^2}{\left(c+\frac{d_b}{2}\right)^2 - \left(\frac{d_b}{2}\right)^2} p = \frac{\left(c+\frac{d_b}{2}\right)^2 + \left(\frac{d_b}{2}\right)^2}{\left(c+\frac{d_b}{2}\right)^2 - \left(\frac{d_b}{2}\right)^2} \tau \tan\alpha \tag{4}$$

Hoop fracture will start when $\sigma_{\theta max}$ reaches the tensile strength of timber perpendicular to the fibers, i.e. for:

$$\tau_{split} \tan\alpha = \frac{2r(1+r)}{2r^2+2r+1} f_{u\perp} \tag{5}$$

where:

$$r = \frac{c}{d_b} \tag{6},$$

$f_{u\perp}$ is the tensile strength of timber perpendicular to the fibers and τ_{split} is the splitting bond strength. For α equal to 45°:

$$\tau_{split} = \frac{2r(1+r)}{2r^2+2r+1} f_{u\perp} \tag{7}$$

Fig. 3 illustrates the $\tau_{split}/f_{u\perp}$ ratio versus the non-dimensional cover thickness r. Such ratio is always less than one, since the maximum hoop stress is always larger than the value of internal pressure.

Bar perpendicular to the grain

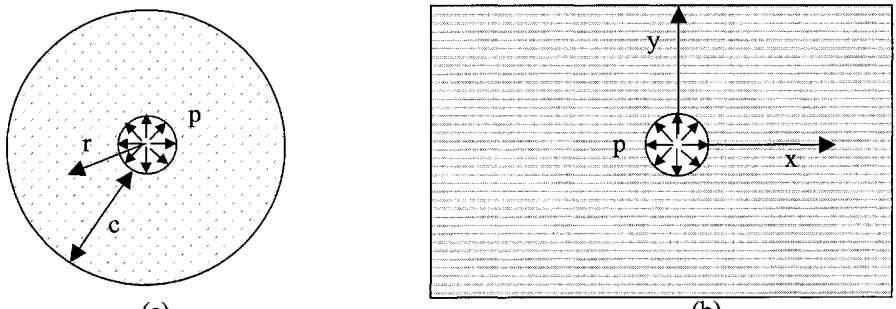
The case of bar perpendicular to the grain is illustrated in Fig. 2b. In order to evaluate the distribution of stresses around a hole in an anisotropic plate under in-plane loading, the solution proposed by Ukadgaonker and Rao (2000), a generalization of Savin's formulation for in-plane loading problems, was used. The distribution of stresses σ_x, σ_y and τ_{xy} around

the pressurized hole was found as a function of the three following parameters: $r_1=E_L/E_T$, where E_L and E_T are the moduli of elasticity parallel (L) and perpendicular (T) to the grain, respectively; $r_2=E_L/G_{LT}$, where G_{LT} is the shear modulus in planes parallel to the grain (LT planes); and ν_{LT}, i.e. the Poisson's coefficient giving strain along the T direction as a result of a unitary stress in the L direction.

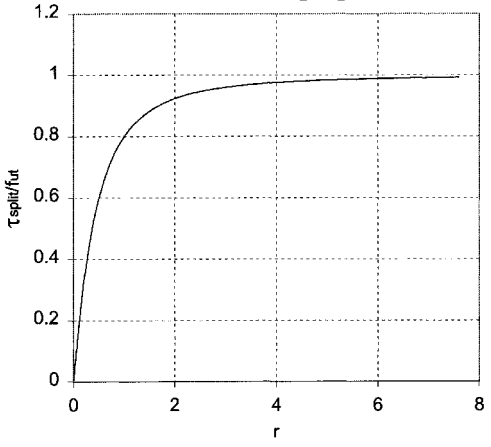
Fig. 4 shows the distribution of σ_y for r_1=30, r_2=15 and ν_{12}=0.35 (values suggested by Giordano, 2000). Since σ_y acts perpendicular to the grain, where the tensile strength is minimum, it can reasonably be assumed that fracture starts when σ_y exceeds $f_{u\perp}$. For the previous combination of parameters, the maximum value of σ_y results equal to 0.735τ, hence the splitting bond stress would be equal to:

$$\tau_{split} = 1.361\ f_{u\perp} \qquad (8)$$

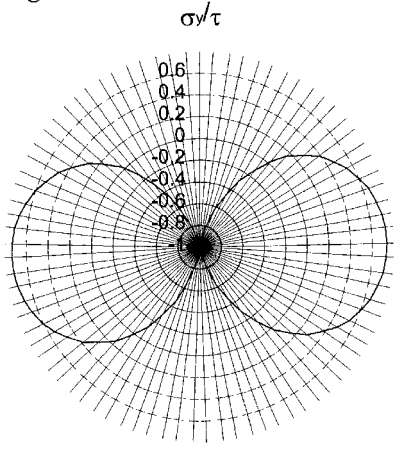
independently on the cover. Comparing eq.s (7) and (8) and recalling that the fraction in eq. (7) was always less than one, it is demonstrated that the splitting bond strength of an element with bar bonded-in perpendicular to the grain is always larger than that of an element with bar parallel to the grain, no matter how large the cover.



2. Bond mechanism in the plane perpendicular to the bar axis for bar parallel (a) and perpendicular (b) to the grain



3. Splitting bond strength vs. cover thickness for bar parallel to the grain



4. Stresses σ_y around the bar for bar perpendicular to the grain

CONCLUSIONS

The main findings of this study are summarized as follows:

- for rods glued-in parallel to the grain the main failure modes were longitudinal splitting and pull-out of the bar along with a wooden prism surrounding the bondline; the occurrence of splitting despite a distance of the bar from the edge of 6.4 diameters contradicts current Eurocode provisions for glued-in steel bars in timber;
- for rods glued in perpendicular to the grain, pull-out failure at the epoxy-timber interface was always observed;
- the bond strength is higher for rods perpendicular to the timber grain than for rods parallel to the grain; also, the bond strength of non-sanded bars is slightly higher than that of sanded bars;
- within the test range, the average bond strength is approximately constant with the bonded length;
- the local bond-slip relationship of bars perpendicular to the grain can be modelled with an ascending branch of the power type and a linear post-peak softening branch. Solving the differential equation of bond the ultimate load vs. the bonded length was found. The theoretical curve is in reasonably good agreement with test results and can be used for conservative design of anchorage;
- modelling of the joint in the plane perpendicular to the bar axis was conducted in the cases of bar parallel and perpendicular to the grain. In both cases, the ratio of the splitting bond strength to the tensile strength of timber perpendicular to the grain was found. In the first case, it depends on the depth of the cover, in the second case, on the ratios of the elastic constants of the transversely isotropic material. For usual values of these ratios, the splitting bond strength is larger for bars perpendicular to the fibers no matter how thick the cover.
- Further research will focuse on a design approach for anchorage and on the effect of moisture content of timber on the bond behavior.

REFERENCES

T.J. Davis, P.A. Claisse (1998), "High performance jointing systems for timber", *Construction and Building Materials*; 12: 415-425.

R. Eligehausen; E. P. Popov; and V. V. Bertero (1983), "*Local Bond Stress – Slip Relationships of Deformed Bars Under Generalized Excitations*", Report No. 83/23, EERC, University of California, Berkeley, CA, 162 pp.

G. Giordano (2000), "Tecnica delle costruzioni in legno", Ed. Hoepli, 850 pp. (in Italian)

K. Harvey, M. Ansell (2000), "Improved timber connections using bonded-in GFRP rods", Proceedings WCTE2000, Whistler Resort, BC, Canada, Poster P04.

V. Scialpi, L. De Lorenzis, and A. La Tegola (2003), "Bond of CFRP rods in glulam members", Proceedings CCC2003, Cosenza, Italy, Settembre 2003.

R. Tepfers (1973), "*A Theory of Bond Applied to Overlapped Tensile Reinforcement Splices for Deformed Bars*", Publication 73:2, Division of Concrete Structures, Chalmers University of Technology, Gothenburg, Sweden, 328 pp.

V.G. Ukadgaonker and D.K.N. Rao (2000), "A general solution for stresses around holes in symmetric laminates under inplane loading", *Composite Structures*, No. 49 (2000), pp. 339-354.

This page intentionally left blank

PART IV

DEVELOPMENT OF FRP MATERIALS AND SYSTEMS

This page intentionally left blank

A NEW GLASS FIBRE REINFORCEMENT FOR ANTI-CORROSION COMPOSITES

Pablo Comino Almenara & Peter Thornburrow
Saint-Gobain Vetrotex

1. ABSTRACT

For centuries, many different materials have been used to make items for use in contact with all types of corrosive products, and today FRP composites are increasingly chosen to replace steel in such applications. The material choice depends on the actual corrosive product concerned, mainly it's chemical type, and the service temperature, and FRP composites are often used because of economics, performance, and ease of manufacture. However, where the application involves contact with an alkaline, cementitious, environment, concern has been raised regarding the durability of glass fibres; one of the greatest concerns being stress-corrosion, which exploits any minor defect, resulting in eventual failure with potentially extremely dangerous and costly consequences, both for manufacturer and end-user.

The development of improved chemical resistant matrices has given FRP composites a big advantage over traditional materials. However, composites may still suffer the effects of corrosion under certain conditions, as corrosion of FRP in acid and alkali media is not only due to the resin, but also to the type of reinforcement present. This paper describes a new glass fibre reinforcement that has, to date, shown the greatest resistance to attack by both acids and alkalis. Comparative tests carried out or validated by the Swedish Corrosion Institute, Stockholm, are described, involving direct exposure of glass fibres to chemical media, and also stress-corrosion testing of laminates using highly corrosion-resistant vinyl-ester resins. Under these severe tests, ARcoteX™ reinforcement proved itself much more resistant and durable than other glass fibres tested.

2. INTRODUCTION

2.1 Corrosion problems of GFRP

Glass fibre composites (GFRP) are extensively used in numerous applications throughout industry, and from the outset, the most widely used reinforcement has been E-glass. The corrosion resistance of this fibre has not inhibited its acceptance, even if it is lower than that of C-glass or boron-free glass, mainly due to economic factors. Nevertheless, there is concern from a series of problems, mainly from the chemical industry, of failures in service caused by corrosion and internal laminate stresses.

It is well recognised that one of the functions of the matrix resin is to protect the reinforcement from environmental attack. It was originally believed that the resistance of the fibre was of little or no importance, and this view still generally applies today. But, at the end of the 70's, it was discovered that GFRP laminates could suffer from stress-corrosion because of internal stresses, which principally affected glass fibres in acid environments[1]. Stress-corrosion is the combined action of stress and environmental corrosive attack. It was recognised that fibres required additional protection, such as a pure

resin surface layer, or gel coat, a resin layer with a superficial barrier film, or a resin-rich coating incorporating a surface veil.

The same approach was adopted in the case of alkali exposure, where specially formulated gel coats and resins have been developed with outstanding chemical resistance. The performance of GFRP in aggressive alkali has been demonstrated by several studies to be largely unaffected by glass corrosion, provided that the fibres are well protected. However, there is always a risk that the protective layer may not be intact, particularly at cut ends, or from damage during handling or installation. Such possibilities have raised concerns over the durability of these materials in structures designed to last for 25 years, or more, and this may contribute to a reluctance to specify composites in some cases.

There is still an important need for further knowledge on the corrosion properties of laminates, resins and glass fibres, as witnessed by the incidence of cracking and damage in GFRP elements due to chemical attack. In some cases, failure by stress-corrosion has occurred even though theory predicted that such cracking should not occur, as the structures were designed to support a maximum stress of 0.2% UTS, and were protected by a chemical barrier.

These failures may have been avoided if a glass fibre with better resistance to stress-corrosion had been used. Access to the fibres by the agent can originate from diffusion into the resin, or through the thermoplastic coating, or via micro-cracks in the surface and/or other laminate defects. If corrosive agents reach the fibres, chemical attack can weaken them.

2.2 Glass corrosion mechanisms.

Two mechanisms, supported by previous published work[2-4] , are proposed for glass corrosion in acidic aqueous environments: 1) an ion exchange mechanism, where metallic Na^+ and K^+ ions in the glass structure are substituted by hydrogen from the acid, followed by dissolution of the glass, and: 2) degradation and dissolution of the silica network (figure 1). For short periods and at low concentrations and temperatures, ion exchange from the glass predominates. This is controlled by diffusion, and after long periods and at high acid concentrations and elevated temperatures, the silica network can dissolve. The interaction between the glass and the chemical environment is characterized by a fast initial mass loss, which then slows with time. If a glass fibre fails, the tip of the crack can continue onto the next fibre, and so on, until failure of the whole laminate occurs. Hence, stress-corrosion resistance can be increased by using a glass fibre which is resistant to the chemical attack. In spite of this, the glass fibre type, and its influence on stress corrosion, has received little past attention.

1. $\equiv Si\text{-}OR + H^+ \leftrightarrow \equiv Si\text{-}OH + R^+$
   Diffusion of ions across the network

2. $\equiv Si\text{-}O\text{-}Si\equiv + H^+ + OH^- \leftrightarrow \equiv Si\text{-}OH + \equiv Si\text{-}OH$
   Dissolution of the network

Figure 1: Glass corrosion mechanisms

The aims of this work, based on more than 3 years of research, are the systematic study and characterization of the corrosion resistance, as measured by the rate of mass loss, of 3 types of glass fibre, including AR-glass (Alkali Resistant Glass), and the stress corrosion behaviour of laminates manufactured with these different glass types.

3. AR-GLASS FIBRES.

During the 60's, AR-glass was developed to resist the strong attack of Portland cements, an extreme alkali environment, in Glass fibre Reinforced Cement (GRC). AR-glass has since been accepted by the building and construction industries, and has been used in several extensive applications. This may be demonstrated by citing examples of prestigious contracts where AR-glass fibre cement reinforcement has been specified, such as those illustrated in tables 1 & 2.

More than 15 years of research has already demonstrated that AR-glass resists both alkali and acid attack, the latter even better than the former for which it was originally developed. However, until very recently, it has not been possible to use AR-glass to reinforce polymer composites, since the surface treatments applied to the fibre degraded with exposure over time, leading to a loss of performance. This difficulty has now been overcome, and AR-glass fibres are now available for use with normal and chemically resistant resins, mainly unsaturated polyester, vinyl ester and epoxies, for the manufacture of highly resistant and durable GFRP structures. ARcoteX™ is the commercial name of this new reinforcement, which forms the basis of the work described here.

Project:	**AL BAYNUNAH TOWER**
Location:	Corniche Road Abu Dhabi United Arab Emirates.
Architect Name Location:	Messrs. ARKAN ARCHITECTS CONSULTANTS. P.O.Box Box No.7673 Abu Dhabi
Brief Description:	Tallest Building in the U.A.E. Comprises a Five Star Hotel (BAYNUNAH HILTON)& Residential / Commercial Apartments
GRC Description:	More than 6000 GRC panels - curved, Islamic Design with Arabic Calligraphy and the wording 'BAYNUNAH' on all GRC elements.

Table 1: The Al Baynunah Tower

Project:	**HEATHROW EXPRESS TUNNEL**
Location:	Heathrow Airport, U.K.
GRC Contractor:	Techcrete Ltd.
Brief Description:	A £440 million BAA project for a high-speed train service, every 15 minutes, between London Paddington and Heathrow.
GRC Description:	9,000 GRC panels as an architectural lining for platforms, concourse, elevator and lift lobby areas. Also supplied were specialist acoustic elements and enamelled glass signs, as inserts to the GRC panels.

Table 2: Heathrow Express Tunnel. U.K.

Oxide	C-glass	boron-free E- glass	AR-glass
SiO_2	61,70	57,00	62,00
Fe_2O_3	0,08	0,30	0,07
Al_2O_3	5,30	12,50	0,20
CaO	6,60	22,20	5,30
MgO	3,75	4,20	-
Na_2O	14,35	0,80	14,30
K_2O	1,05	0,40	-
B_2O_3	6,35	-	-
TiO_2	-	-	-
F	0,65	-	0,30
ZrO_2	-	-	17,30

Table 3: Composition of the different glass fibres.

4. EXPERIMENTAL

Three different types of commercial glass fibres were studied, all of which are considered suitable for GFRP in corrosive applications. These are: C-glass (Chemical glass), AR-glass (ArcoteX™ Alkali Resistant glass), and boron-free E-glass. Their chemical compositions are given in Table 3. Tests were performed on both the pure glass fibres and laminates reinforced with the different types.

4.1 Tests on glass fibres.

Fibres were exposed to hydrochloric acid and sodium hydroxide respectively, at different concentrations (from 0.3 to 5M) and different temperatures (from 30 to 50° C), and the weight loss measured; the pH was maintained constant to within ±0,1.

4.2 Laminate tests.

Uni-axial laminates (3mm thick, 50 vol.% glass content) were made by winding filaments around a suitable mandrel using a vinyl ester resin, and post cured at 100°C. CSM laminates (4mm, 16 vol.% glass content, approx. 35 wt.%) were also prepared using a vinyl ester resin, and four layers of 450g/m^2 chopped strand mat. The edges of the samples were sealed with a 1-2 mm thick epoxy coating.

Stress-corrosion tests on the laminates were carried out in 3-point bending under constant stress, and their behaviour was evaluated by relating the time to failure. In addition, after failure, the fracture surfaces were studied by electron microscopy.

5. RESULTS

5.1 Pure glass fibres

Figures 2 & 3 show the results of corrosion resistance of the glass fibres tested in an acid environment, using a logarithmic scale to accommodate the large differences seen. The

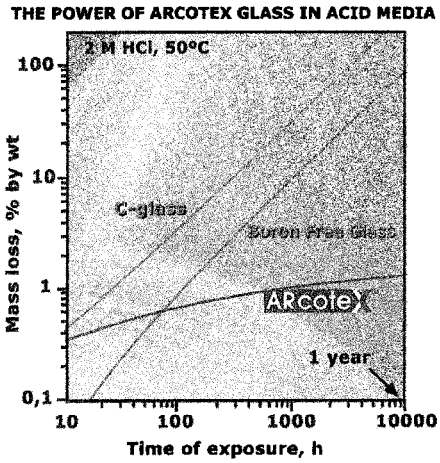


Figure 2 : Acid resistance of different glasses in 2M HCl at 50°C

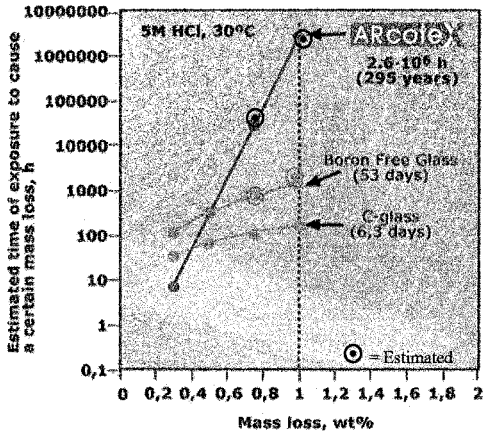


Figure 3: Acid resistance of different glasses in 5M HCl at 30°C.

mass losses were corrected for that caused by the water-soluble portion of the sizing, and also corrected and normalized to the same specific area of the fibre (1000 cm^2/g). The corrosion resistance of C-glass is much lower under these exposure conditions. For a short time, both boron-free E-glass and AR-glass show similar results, but after an extended period it is predicted that AR-glass will outperform the other type. The results obtained indicate that the corrosion process is different for each type of glass, i.e., it depends on the glass composition, and a higher corrosion resistance for ARcoteX™ was demonstrated.

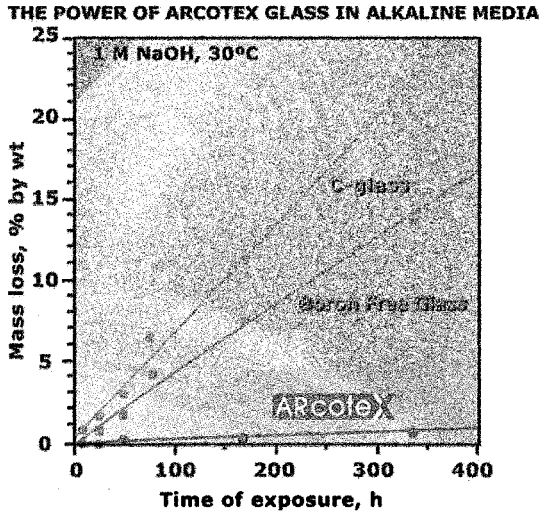


Figure 4: Mass loss of the 3 types of glass fibres vs. exposure time in 1M NaOH at 30°C.

The results also show that the acid resistance of the fibres depends greatly on the temperature, with all fibres showing a faster rate and greater mass loss as the temperature increases. The difference between the corrosion resistance of boron-free E-glass and AR-glass increases at higher temperatures. AR-glass shows the highest corrosion resistance between the fibres tested under these conditions, with the long-term mass loss predicted to be about 1%.

Figure 4 shows the mass losses in 1M NaOH at 30°C. There are no large differences in corrosion resistance between C and boron-free E-glasses under these conditions, the resistance is low in both cases. Nevertheless, the superior resistance of AR-glass is clearly seen as expected.

Figures 5 and 6 show the huge difference in behaviour, resistance and durability of ARcoteX™ fibres compared with other glass types in low and high concentrations of NaOH at 30°C. The degradation of all glass types is worse at higher temperatures, except for AR-glass fibres which remains constant. In this case, standard E-glass has been included to give a wider comparison, showing a similar or worse behaviour than C-glass. So, it is in an alkali medium, where ARcoteX™ glass fibre, at different concentrations and temperatures, shows a big improvement in behaviour and greatly increased durability.

5.2 Laminate results.

The study was continued to determine if there was a relation between the corrosion resistance of fibres under constant load, and the stress-corrosion properties in a laminate manufactured from the different types of glass.

Figure 7 compares the stress-corrosion resistance, in 1M HCl at 25°C, of uni-axial laminates containing the different fibre types. The time to failure depends greatly on the on the applied load. Electron microscope studies on the fracture surfaces indicate that every failure occurred through stress-corrosion of the glass fibres, except for the ArcoteX ™ laminates. This is evident from the failure behaviour. In the case of ARcoteX™, the stress

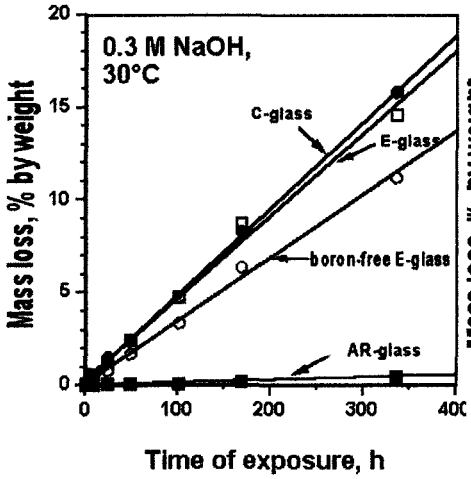


Figure 5: Mass loss of four glass fibre types

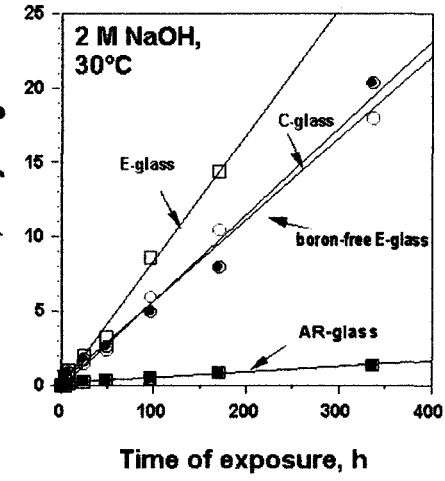


Figure 6: Mass loss of four glass fibre types vs exposure time in 2M NaOH at 30°C

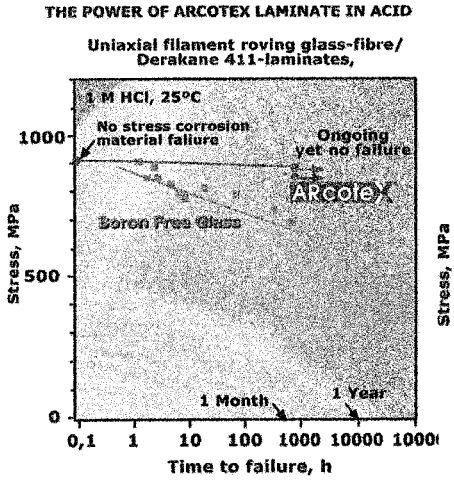


Figure 7: Comparison of the stress-Corrosion Properties of uni-axial laminates.

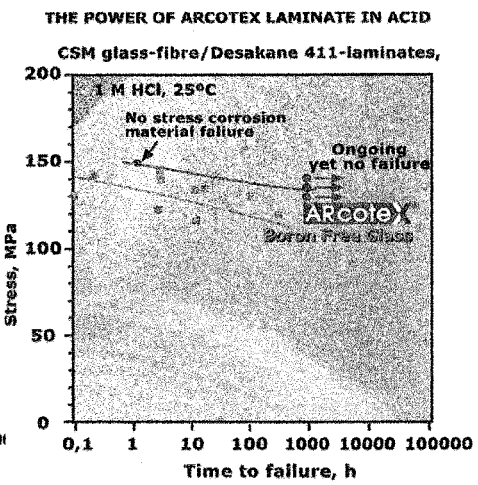


Figure 8: Comparison of the stress-corrosion properties of CSM laminates.

in acid is similar to that in air, i.e., about 900 Mpa, and almost unaffected by the acid environment, indicating that no stress-corrosion is occurring.
Figure 8 shows stress-corrosion data for CSM laminates in 1M HCl at 25°C. The data dispersion is much greater than in uni-axial laminates due to the irregular orientation of the fibres within the plane of the laminate. Nevertheless, the same order of performance applies with respect to fibre type as for the uni-axial laminates, although the differences are not as large, possibly due to the lower glass contents.

6. PRINCIPAL APPLICATIONS IN CONSTRUCTION

The important consequences in construction of corrosion of steel initiated research on pultruded rebars and other FRP elements for structural reinforced concrete, for both pre-cast and on-site use. Rebars based on high alkali resistant resins and reinforcements, including carbon fibres, have been successfully developed, and are being used in contracts the world over. Work is progressing rapidly to provide solutions to other corrosion problems associated with steel reinforced concrete, so new structures, rehabilitations and repairs in works suffering from corrosion of their reinforcement are being considered using composites. Usually, the materials employed are manufactured by pultrusion, or from pre-pregs, using thermosetting resins, as is the case for strengthening pillars, columns and beams.

Pipework, sewers and drainage systems also suffer corrosion from aggressive chemical attack. This is already an established market for GFRP, where it is customary to employ a chemical resistant reinforcement in the lining of pipes to protect the main body from contact with the contents. ARcoteX™ will provide a greater long service life protection in such applications than more traditional reinforcements.

Applications in agriculture and cattle farming are also beginning to develop rapidly, particularly those where a high resistance to chemicals arising from decomposition and contact with animal waste is required.

7. CONCLUSIONS AND DISCUSSION

Huge differences in the corrosion resistance (as measured by weight loss) of C, boron-free E and AR-glass fibres have been demonstrated. ARcoteX™ stands out because of its excellent long-term corrosion resistance in both alkali and acid media. In the short term, at low concentrations and temperatures, the acid resistance of boron-free E-glass is similar to that of ARcoteX™ but differs strongly in the long term and at higher concentrations and/or temperatures. The resistance to alkali is, however, poor for both C and boron-free E glass fibres. C-glass fibres are easily damaged by both alkali and acid, and mass losses can be high. A correlation between the corrosion resistance of the fibre and the stress-corrosion properties of associated laminates has been demonstrated.

So far, only the corrosion resistance to HCl and NaOH have been studied. It is known that other acids, like H_2SO_4, can show differences, because the acid anion can influence the speed of the reaction, e.g., by forming an insoluble precipitate, such as $CaSO_4$, on the fibre surface. Nevertheless, it is believed that the corrosion rates for the different fibres are similar, although higher mass losses can be reached with other acids.

Another aspect that should not be ignored, is that within each type, the glass composition can vary, and with this the corrosion resistance[4], e.g., different E-glasses can show different corrosion results in acid tests.

Stress-corrosion effects, or those due to stresses that aid corrosion, can be found even in laminates theoretically not subjected to stress, through minor defects during manufacture or use. A level of 0.2% of ultimate stress can be easily reached, and little cracking can appear at first. However a corrosive environment will have access to the fibres, because the protective coating never stops diffusion, it merely delays it, so the requirements for stress-corrosion may already present, with the risk of expensive and harmful failure. The risk can be reduced by choosing a corrosion resistant glass, such as ARcoteX™.

Applications for laminates and pultruded elements in construction represent the fastest development and range of applications today, structural as well as protective, in new installations as well as the repair and strengthening of existing structures and buildings. ARcoteX™ can offer an excellent, and economic solution to the high cost of certain alternatives in use today, such as carbon fibre reinforcements.

8. ACKNOWLEDGEMENTS

Special thanks to Gunnar Bergman and Stefanie Römhild of the Swedish Corrosion Institute, as authors of the research that forms the basis of this paper, and with whom Saint-Gobain Vetrotex has co-operated in launching the ARcoteX™ products range.

9. REFERENCES

1. H. H. Collins, *Plastics & Rubber: Materials and Applications*, Feb 1978, 6-10
2. A. Paul, *Journal of Material Science* **12** 1977, 2246-2268
3. F. Devreux, Ph. Barboux, *Journal of Materials Science* **36**, 2001, 1331-1341
4. G. Bergman, N. Steinhed, Unpublished data, Swedish Corrosion Institute, 1998

ADVANCED POLYMER COMPOSITE AND CONCRETE BEAM AND SLAB SYSTEMS

A.G. Bloodworth & J.R. Szczerbicki
School of Civil Engineering and the Environment, University of Southampton

ABSTRACT

This paper reports on an investigation into the feasibility of a structural slab system consisting of a sheet of carbon fibre reinforced polymer (CFRP) in tension and concrete in compression. The system is a development of a design for an APC/concrete composite Tee beam, in which the APC serves as both permanent formwork and tension reinforcement. The design, fabrication and testing of the system are described. Particular issues to be addressed were (a) to obtain an optimal profile for the CFRP formwork, and (b) to provide an adequate bond between CFRP and concrete utilising an adhesive. The behaviour of the slab system at the ultimate and serviceability limit states is described.

INTRODUCTION

The use of advanced polymer composites (APCs) as a replacement for steel reinforcement for use in conjunction with concrete in new structures has been the subject of recent research. APCs have a number of advantages over steel, such as high strength to weight ratio and corrosion resistance. Their lightness makes them easier and safer to handle on site. They are also increasingly finding application in strengthening and upgrading of both concrete and metallic existing structures.

One possible way in which APCs may be used to reinforce concrete is by using 'bars' which are completely encased in concrete, this may be considered a direct replacement for steel reinforcement. However, this may not be the most efficient means of using high-performance materials, which are expensive and are ideally used in thin plate sections. An alternative to the rebar system, that takes advantage of the lightness of the APC materials during the construction process, is the use of these materials as a permanent formwork, on to which concrete is cast to form a composite section.

The possibility of using APC material as permanent formwork for the construction of a beam has been investigated [1,2]. The cross-section used in the Southampton project is shown in figure 1, and consists of a carbon fibre reinforced polymer (CFRP) material. However, a drawback with the concept was that, in order to utilise the concrete efficiently, a large amount of CFRP tension reinforcement was required to bring the neutral axis down to mid-depth. The section then became 'over-reinforced' and brittle failure was predicted to occur in the concrete first, which is undesirable. Failure, under these conditions, actually occurred in the bond between the concrete and CFRP.

This paper presents a development of the CFRP/concrete composite beam concept into that of a slab, drawing on the lessons learned with the beam experiment. It is found possible to utilise the CFRP's properties much more effectively in this arrangement, and the bond between the materials becomes less critical to the overall performance of the structure.

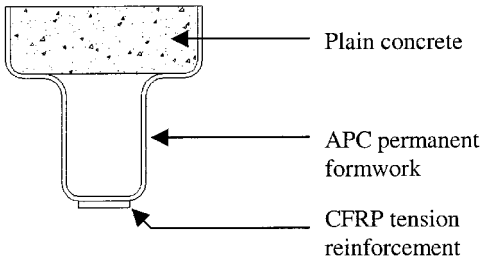


Figure 1. Cross-section of APC/concrete composite beam

DESIGN OF THE SLAB SYSTEM

Design principles

The aim was to model at approximately one-third scale a floor slab spanning one way with a span of 3 m. An overall thickness of 50 mm was chosen. Although it would have been desirable to have made the slab thinner than this, this was regarded as problematic using normal aggregate, even though 10mm aggregate was used.

The design concept, finally chosen, consisted of a corrugated CFRP profile which could be placed in position first and used to support the weight of the wet concrete during the construction phase. At this stage of the project it was not economic for a specific single mould to be constructed, with an optimum shape, on to which to lay-up the CFRP composite. Therefore, a commercially-available corrugated steel sheet was used as the mould. The cross-section of the slab is shown in figure 2.

The analysis of the slab cross-section was based on Engineer's small deflection bending theory. The stress-strain relationship for the concrete was assumed to be non-linear with the characteristic given in BS 8110. The failure strain of concrete was taken as 0.0035. The CFRP was assumed to be linear elastic with a modulus of elasticity of 164 kN/mm^2 and a tensile strength of 860 N/mm^2. These data were obtained from a combination of manufacturer's data and previous tests on coupon samples [2]. The failure strain of the CFRP was thus calculated to be 0.0052.

The corrugated shape of the CFRP was assumed to be of trapezoidal shape in order to carry out the analysis. The cross-section was analysed assuming that failure occurred in the CFRP before the concrete. The analysis predicted the neutral axis at the ultimate limit state to be 19 mm below the top surface of the concrete.

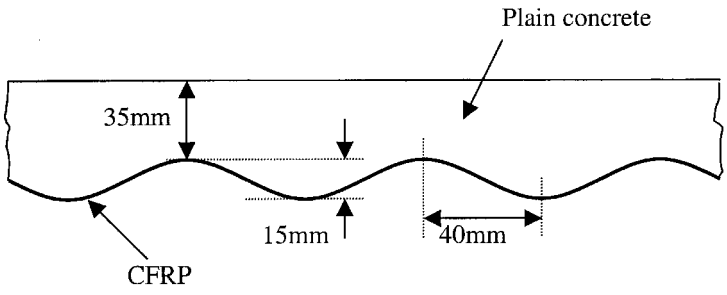


Figure 2. Cross-section of CFRP/concrete composite slab

Finite element analysis

A linear elastic finite element analysis of the slab was carried out in order to assist with the positioning of strain gauges on the slab, and with interpretation of the results.

CONSTRUCTION OF THE SLAB SYSTEM

Advanced polymer composite

The CFRP membrane was formed using a single layer of pre-impregnated ('prepreg') material consisting of a biaxial stitched fabric in high-strength carbon with a total weight of 400 g/m^2 and a hot-melt low-viscosity epoxy resin. The use of prepreg was found to be advantageous to achieve the required profile shown in figure 2 whilst minimising the risk of voids or other manufacturing defects as can sometimes occur in resin infusion. A curing temperature of 120°C and a curing time of 45 minutes were used for the prepreg.

Concrete

The concrete was designed in accordance with[3] to achieve a characteristic strength f_{cu} of 40 N/mm^2 (target mean strength 53 N/mm^2) at 28 days, using 10mm aggregate. Due to the lack of steel reinforcement, it was possible to use a low slump concrete with a target slump of 30 – 60mm, with a water-cement ratio of 0.42.
Cube tests at 28 days confirmed the concrete characteristic strength to be 57 N/mm^2. Further cube tests at 4 months when the slab was tested in the laboratory showed that the concrete strength at that time was around 70 N/mm^2.

Adhesive bond

A bond between the CFRP and the concrete was formed by means of a two-part epoxy adhesive, which was spread on to the surface of the cured CFRP prepreg immediately before the wet concrete was poured.

TESTING

Testing arrangement and loading

The slab was set up between the platens of a column testing machine, which provided sufficient working area. The slab was set up as simply supported in the direction of the corrugations, with the concrete surface uppermost. The effective span was approximately 900 mm. A concentrated load was then applied by means of a 10 t hand jack, spread over an area of 150 mm^2 in the centre of the slab, by means of a steel plate, see figure 3.

Instrumentation

Load was measured by the load cell in the column testing machine and also by the

pressure gauge on the hand jack, and good agreement between these two values was achieved throughout.

Gauges attached to the surface of the concrete and to the underside of the CFRP material measured strains; figure 4 shows the gauge locations. At each location, gauges were placed on both the upper concrete surface and the lower extreme fibre of the CFRP. Between locations A and B on the top surface of the slab, a further gauge was attached to the CFRP surface at the top of a corrugation, to give further confirmation of the position of the neutral axis of bending. The strains were logged by a data-logger. Only data from gauge location A is reported in this paper.

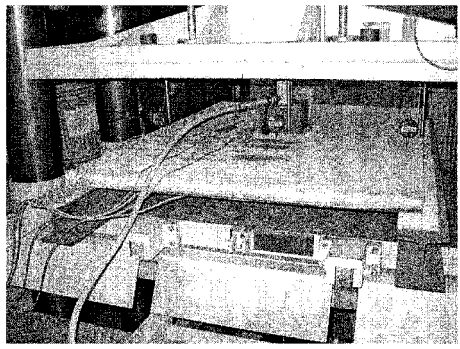


Figure 3. Slab arrangement for testing

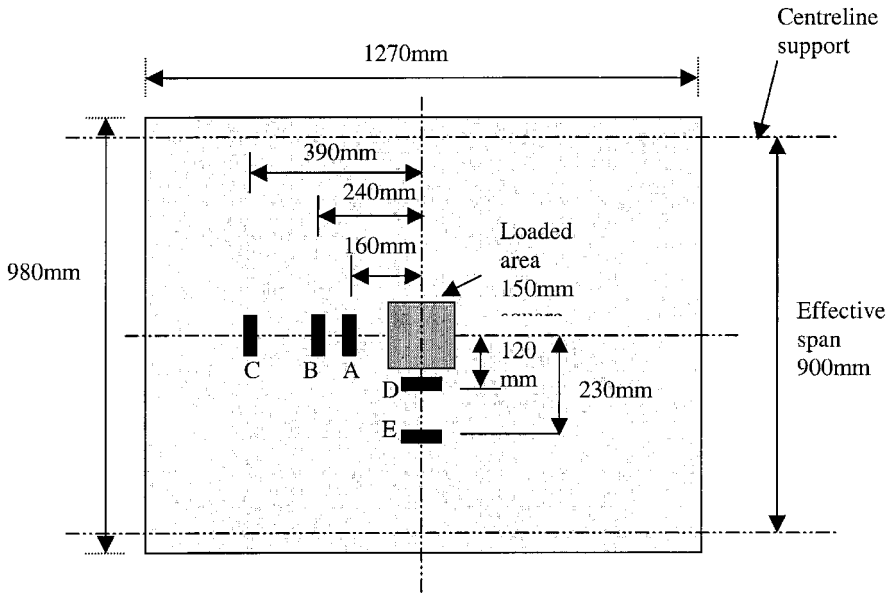


Figure 4. Plan on slab showing locations of strain gauges

Slab performance in testing

The graph of load against deflection measured close to the application of the load is shown in figure 5. The graph shows the behaviour over the entire test. Following an elastic region in which an unload-reload loop was carried out, a peak load of 18.65kN was reached at A. At this point, a failure was observed in the transverse direction of bending, just to one side of the load, in which the profile of the CFRP layer straightened locally and debonded from the concrete over one corrugation, and a crack opened up in the concrete across the whole width of the slab.

This crack undoubtedly reduced the carrying capacity of the slab, but it was still possible to increased the load further and induce a bending failure in the major direction of bending. This occurred at a load of 19.5kN at point B in figure 5, repeated in figure 6. Figure 6 shows that at this point the strain in the CFRP at location A, in the major direction close to the load, had reached approximately 5000με, in good agreement with the expected tensile strain capacity of the CFRP. As further displacement was imposed on the slab by the jack, the strain in the CFRP began to increase rapidly, but the applied load did not increase. The creep rate on each load increment was also observed to increase, and occasional cracking and splitting sounds were heard.

On unloading of the slab, a permanent deflection of 5mm was observed, as shown in figure 5. The slab was reloaded and it was found that large deflections up to 25mm were possible, with the formation of what appeared to be a plastic hinge in bending in the major direction across the entire width of the slab (figure 7). When the maximum concrete strain reached approximately 0.0035, crushing of the concrete was observed on the surface and the slab failed catastrophically by debonding of the concrete from the CFRP over one quarter of the slab.

The position of the neutral axis could be inferred from the strains in the top and bottom fibres of the section at each gauge location, assuming small deflection theory. It was found that in the first part of the test, the neutral axis was at approximately mid-depth, 25mm below the concrete surface. This indicated that the tensile strength of the concrete was not exceeded at these low loads. As the test proceeded, the neutral axis rose gradually, to about 10mm below the concrete surface when the ultimate load was reached. This was higher than predicted by the design.

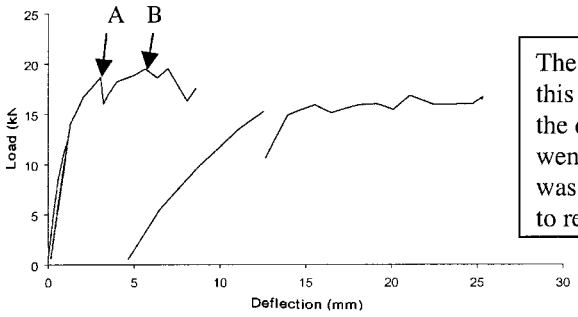


Figure 5. Load against deflection for the entire test

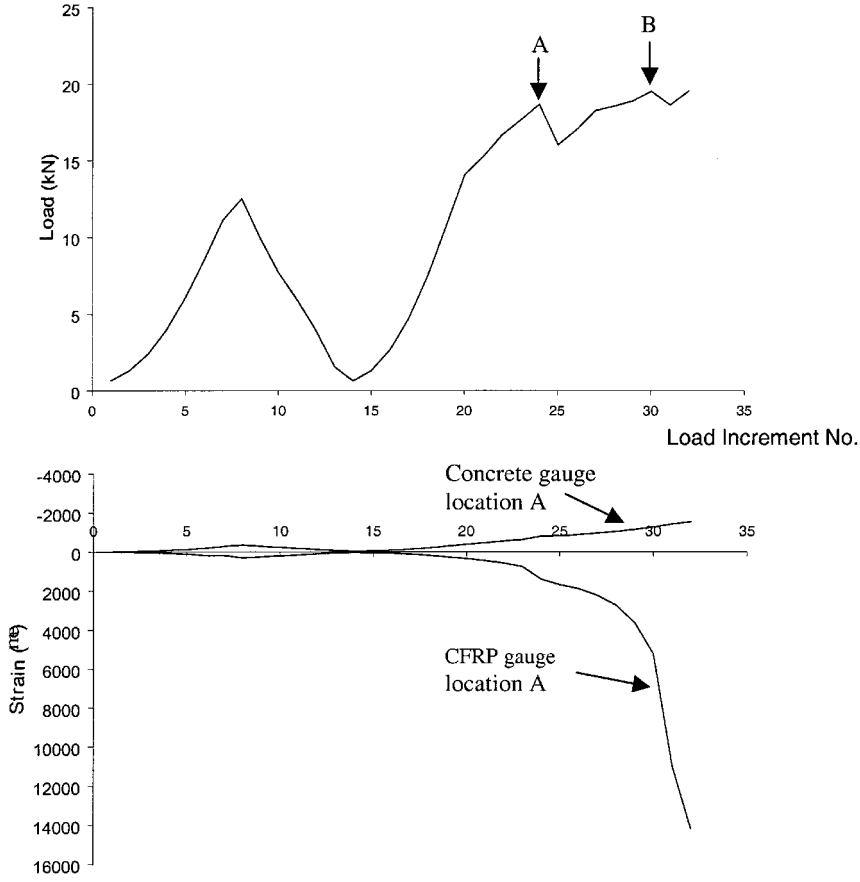


Figure 6. Variation of load and strains at location A during the test

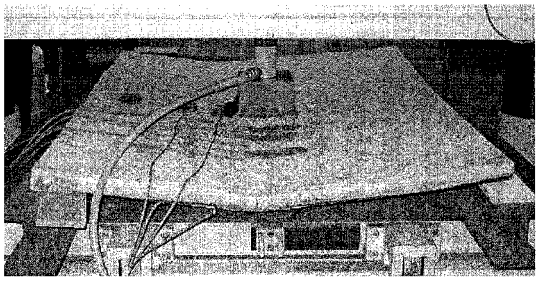


Figure 7. The ultimate failure condition of the slab

As acceptable data had been obtained for the modulus of elasticity of the CFRP and the strain in that material, at the ultimate load, was in accordance with predictions, the most likely explanation for this discrepancy in the neutral axis position, compared to the design prediction, lay with the stiffness assumed for the concrete. If the cross-section was back-analysed with an initial modulus of elasticity, assumed for the concrete, to be $8000\sqrt{(f_{cu}/\gamma_m)}$ (compared with $5500\sqrt{(f_{cu}/\gamma_m)}$ suggested by [4]) and with f_{cu} taken as 70N/mm^2 and γ_m taken as 1.0, reasonable agreement with the experimental observations of neutral axis position could be obtained. The ultimate moment capacity predicted by the analysis was calculated to be 18.45kNm/m width of slab. This compares with an observed moment capacity of approximately 5kNm/m assuming that the crack developed in the minor direction at point A, in figure 5, meant that part of the slab was no longer carrying significant load. This indicates that once the slab cross-section close to the load had reached its peak strength in the major direction of bending, its strength must have decreased as the CFRP yielded, redistributing the load outwards towards the edge of the slab.

The load-deflection behaviour of the slab during the early part of the test is shown in more detail in figure 8. Point C is the location where non-linear behaviour is becoming significant. It was also the position where the neutral axis began to rise from the mid-depth as discussed above. The deflection at this point was 1.29mm which equates to span/682, and the applied load was 14.3kN which is equal to the ultimate load divided by 1.36. If point C is regarded as the point of serviceability limit state failure, then the deflection may be seen to be well within limits normally expected for a floor slab in a building.

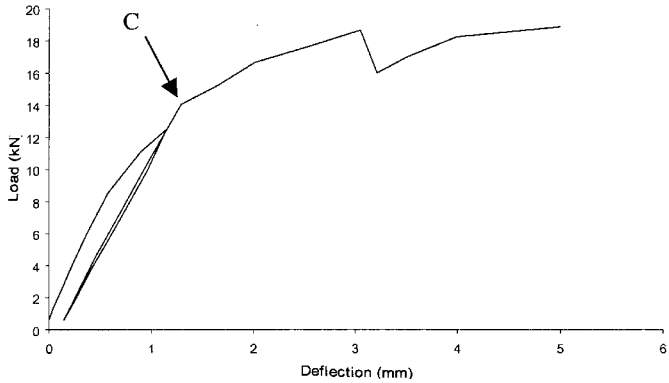


Figure 8. Load against deflection for the early part of the test

SUMMARY AND CONCLUSIONS

This paper presents the design, construction and testing of a slab system comprising carbon fibre reinforced polymer acting as permanent formwork as well as tension reinforcement, and plain concrete in compression.

It was found that at the ultimate limit state, the predicted failure strains of the concrete and of the CFRP were achieved. A successful bond between the CFRP and concrete was achieved by means of an adhesive that was applied to the CFRP prior to pouring of the concrete. The system proved capable of tolerating large plastic deformations. At the serviceability limit state, structural performance was satisfactory, with almost entirely elastic behaviour and low deflections being obtained.

ACKNOWLEDGEMENTS

The second author is grateful for the support of the Institution of Structural Engineers, who awarded a Young Researcher Grant in April 2003 in support of the project.

REFERENCES

[1] J. Hulatt, L C Hollaway, and Thorne, A M., "The use of advanced polymer composites to form an economic structural unit". *Construction and Building Materials*, 2003 **17** 55-68.

[2] J R Szczerbicki, *'Design of a beam comprising advanced polymer composites and concrete'*. Project Report, Department of Civil and Environmental Engineering, University of Southampton, 2003.

[3] British Standards Institution. *Structural use of concrete.* BSI, Milton Keynes, 1997, BS 8110 Part 1.

[4] D C Teychenné, R E Franklin and H C Erntroy. *Design of normal concrete mixes, second edition*, Construction Research Communications Ltd., 1997.

COMPOSITE RECYCLING IN THE CONSTRUCTION INDUSTRY

Amanda Conroy, Sue Halliwell and Tim Reynolds
BRE, Watford, UK

INTRODUCTION

Fibre reinforced polymers (FRPs) are increasingly being used in construction due to their light weight, ease of installation, low maintenance, tailor made properties, and corrosion resistance. The UK FRP industry produces 240,000 tonnes of products a year with 11% of this being for the construction industry. Current and impending waste management legislation will put more pressure on the industry to address the options available for dealing with FRP waste. Such waste legislation focuses on dealing with waste through the waste hierarchy and will therefore put more pressure on solving FRP waste management through recycling and reuse.

At present the most common disposal method for UK FRP waste is landfill. To assist in the transition from disposal in landfill to recycling, the FRP industry needs to consider designing materials and components for easier deconstruction, reuse and recycling at the end of the product life.

EU DIRECTIVES

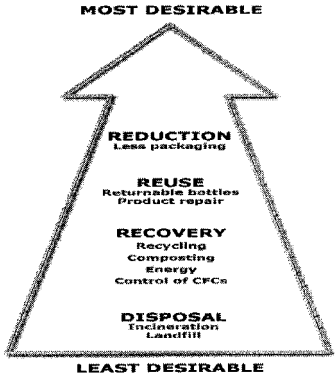
EU directives such as End of Life Vehicles (ELV) and Waste Electrical and Electronic Equipment (WEEE) will put more pressure on solving FRP waste management through recycling and reuse. The ELV directive states that by 2015, 85% of ELVs will have to be reused or recycled (excluding energy recovery), with only 10% incinerated with energy recovery, and only 5% going to landfill[1]. Whilst this new legislation does not impact on the construction industry, currently in negotiation is the proposed EU recommendation on Construction and Demolition Waste, which if adopted will have a significant effect. FRP suppliers could lose their market share to metal and other industries if they cannot ensure that their FRP components can be reused or recycled at the end of their life.

THE WASTE HIERARCHY

According to the waste hierarchy, the options for FRP waste management in order of preference are waste minimisation, reuse, recycling, incineration with energy recovery / composting, and lastly incineration without energy recovery / landfill (see figure 1).

Waste Minimisation

The most cost effective and environmentally beneficial option of waste management is not to produce the waste in the first place. By reviewing the manufacturing process it may be possible to identify a method which results in less production waste. Waste minimisation does not assist in complying with the ELV directive, but may be useful to consider in the face of increasing landfill charges and the development of corporate environmental policies. It could also identify where practicable cost savings can be made.



1. The Waste Hierarchy



2: Disposal of waste FRP

BRE carried out an extensive survey of FRP manufacturing techniques in the UK. Waste takes a variety of forms such as off-cuts, overspray trimmings, trimming dust, trimming from vacuum infusion, defective items and trials runs, plus obsolete moulds. Most automated processes are very efficient and there is little scope for improvement in terms of reducing generated waste, although waste may be generated at the beginning and end of production runs, or if components fail to meet accepted standards e.g. through a faulty set up.

Most of the waste produced is disposed of by landfill. Some manufacturers bear the cost of sending bulky waste via skip container to landfill using a contractor, and there is considerable scope for reducing this burden, Figure 2. Contamination of FRP waste which could be recycled with other waste such as resin containers, release agent, rainwater, cleaning rags etc is an important issue.

Reuse

Reuse is high in the hierarchy, but it is debatable how practical this might be. An FRP component is composed of at least two constituents working together to produce material properties that are different from the properties of these elements on their own[2]. The way in which FRPs are used, their applications and how they are secured to existing structures must be considered with a view to deconstruction and reuse at the end of that application's life[3,4]. The manufacturing process must be examined to identify any possible modifications to improve design for future reuse or recycling. Avoiding embedded metal fixings which are difficult to separate prior to grinding is one example.

Many FRP items are bespoke in nature, being especially designed for a particular application or building (e.g. mouldings and facade panels), meaning that it is very unlikely such products will to be able to be reused for another, different application. Items such as FRP swimming pools, cess pits and pipes are designed with very long service lives and are not installed with recovery or reuse in mind. One possible option is a downgrading of product use e.g. tanks and silos for use in agriculture. However, there is potential to reuse FRP features such as domes, clock towers and chimneys. Indeed, reuse of items like cabins and gatehouses already takes place.

Structural items such as sections or I beams may be difficult to reuse since it is difficult to re-calculate their load carrying properties as recovered items, or reliably access any degradation or creep effect. This is quite different from the situation for recovered steel girders, large section timbers, and old bricks, for example, all of

which are reclaimed and have a market value today. Without reference to the original manufacturer it will be difficult to derive the strength characteristics such as shear and bending of an FRP section with unknown matrix/fibre combination and makeup. FRP sections also tend to be produced to meet a particular set of circumstances and conditions so will often not be transferable to a different use. The designer of a building or structure will have a duty of care to make sure it is sound and a material cannot be reused if its strength properties are unknown or in doubt. This also applies to any fixings, bolt holes etc for FRP claddings and mouldings. Similarly, care must be taken with reuse of cladding or roofing to ensure its fire-resisting properties are known.

Development of modular and prefabricated systems should allow reuse if this aspect is considered at the design stage, especially in respect of the type of site applied sealing and gluing of joints.

Although FRP manufacturers have largely solved issues relating to UV stability and colour fading of their products, many fascia panels and mouldings may be surface degraded. This will affect the ability to re-use such components. FRP claddings and mouldings can be refurbished, by painting for example. FRP components are economical to produce, and this counts against reuse of existing items if they require labour intensive inspection, cleaning, decontamination or repair.

Recycling

Production waste

FRP production waste is generally disposed of since the raw materials used in FRP manufacture are relatively inexpensive (with the exception of aramid and carbon fibres). Quantities of waste produced are usually low in comparison to product volume. If the waste is to be recycled, it may need further treatment such as heat curing before grinding.

Building site waste

Little or no FRP off-cut waste is generated on new-build construction sites. FRP components are designed for a particular use, being pre-moulded and made to measure. This is quite different from the situation with many traditional building components - timber joists, for example, need to be cut down on site from standard sizes.

Deconstruction waste

Current volumes of FRP deconstruction waste are minimal compared to other forms of waste and are presently sent to landfill. However, as the quantities of FRP used in a wider variety of applications increases over the next decade or so, the eventual volumes of post-application FRP will increase. Landfill taxes are predicted to increase sufficiently to discourage disposal and promote reuse or recycling in the future. The FRP industry has to address the situation and identify possible solutions in order to maintain the viability of their products in the construction sector.

There are two main types of resin used for FRPs: thermoplastics and thermosets. Thermoplastic FRPs can be recycled by remelting and remoulding. However, this is not the case for thermoset FRPs which dominate the construction FRP market. One

option for thermoset FRPs is grinding, with the resultant recyclate being used as a filler in new FRP materials[2]. Other treatments can be used to return the FRP back to its original constituents in order to reclaim the fibres. One such approach is thermal treatment of the FRP. Thermal decomposition of FRPs has been trialed in order to recover fibres. The FRP (either thermoset or thermoplastic) is heated at temperatures greater than 260°C (500°F) which causes the fibres to separate from the polymers[5]. Another approach is chemical degradation where FRP is placed in chemicals and heated in order to reclaim the fibre. However reclaimed fibres from this process tend to be more brittle because of the chemicals used, which in turn require disposal.

A number of options for the use of FRP recyclate have been identified[6]. Recyclate could be used for reinforcement in polymer lumber[7] (a reinforced thermoplastic replacement for wood). Recyclate fibre could be used to improve the strength of asphalt, e.g. asphalt for bridge decking, which could possibly accept small amounts of contamination. In speciality Sheet Moulding Compound (SMC), recyclate could be incorporated in between two layers of virgin glass. This process broadcasts the recyclate instead of mixing it with resin. The mixing operation of Bulk Moulding Compound (BMC) can use recyclate, and possibly gains some reinforcement from residual fibres in the recyclate.

Existing FRP recycling pilot plants in countries including France, Germany, Italy and the Netherlands have proved that composite recycling is possible. However, more markets need to be identified for the recyclate produced; few exist at present.

An alternative to traditional FRPs is the development of single-polymer-composites, for example a polypropylene matrix with high strength polypropylene fibres as the reinforcement[8]. This 'all-polypropylene' composite can be recycled resulting in a polypropylene blend that can be reused to remake all-polypropylene composites or can be used for other polypropylene applications. By combining polypropylene honeycombs with polypropylene skins, all-polypropylene sandwich panels with great stiffness can be produced.

Incineration with energy recovery and composting

FRPs have a high calorific value therefore incineration with energy recovery is a viable option for FRP waste.

Incinerator operators actually charge more for accepting FRP waste because the high calorific content together with toxic emissions tends to overload the system, meaning they cannot process as much domestic refuse. It must be borne in mind that the production of electricity from energy recovery is a secondary concern and that the prime business of the incinerator is to dispose of domestic refuse. By burning relatively small quantities of FRP waste, large volumes of domestic waste (of which there is an unlimited supply) must be sent to landfill.

The use of ecocomposites is a growing alternative to FRPs. They use plant fibres as an environmentally friendly and low-cost alternative to glass fibres. Natural fibre FRPs are from renewable resources and can be composted or incinerated at the end of their life. The European automotive industry is investigating the possibility of using natural fibre reinforced thermoplastics to benefit the environment whilst saving weight (natural fibres are 50% lighter than glass fibres) and cost at the same time[9]. Wood flour is also being investigated as an alternative to mineral fillers. These technologies can be used for both thermosets and thermoplastics.

Natural fibres can easily compete with glass fibres in terms of stiffness, but their tensile, compressive and impact strength are relatively low compared to glass fibres.

By modifying the resin systems, ecocomposites can be designed to be either stable or biodegradable[10]. As mentioned above, mechanical recycling is preferred over incineration and landfill. However, mechanical recycling of natural fibre composites could prove problematic as they tend to degrade near the processing temperature of most thermoplastics.

Composting is unlikely to be practicable for combinations of natural fibre and resins such as polyester resin. Plenty of clean plant matter from municipal collection of garden waste, together with agricultural waste such as chicken litter is available for the compost industry to use and building components with difficult to separate organic matter will not be considered.

Incineration without energy recovery and landfill

Incineration without energy recovery and landfilling of composites waste are the least preferred options because they result in a loss of the energy content which could be harvested by incineration with energy recovery. Landfilling of composite waste appears to be the most common disposal option at present in the UK because, although on the increase, the cost of disposal of waste is still relatively low. The fate of surplus new or used FRP components depends on the cost effectiveness of the options available. Thus, until landfill taxes increase to a value where recycling or incineration become viable alternatives, or legislation changes, most of the FRP waste produced will end up disposed of in the ground.

END PRODUCTS FROM RECYCLATE

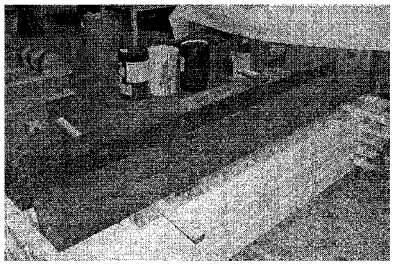
There are certain criteria which must be met in order for utilisation of waste FRP in a product to be economically and technically viable. In this instance ground FRP waste is considered:

- The use of ground FRP should be beneficial to the product i.e. the FRP should have either a structural/reinforcing role or weight saving role, not just act as an inert filler.
- The mix of materials should be synergistic.
- The product should not have to be reinforced with other material or made thicker to compensate for some deficiency caused by inclusion of ground FRP.
- It should not be merely a novel disposal method such as some component of a geotechnical fill.
- The re-use method should be realistic in respect of the likely volumes of recyclate available.
- The re-use of FRP should not make the ultimate recycling of the product difficult (some types of "plastic wood" can be easily recycled or burned without pollution).
- The product should not pose environmental problems or health and safety problems in use - e.g. from abrasion, wear related loss of glass fibres, or during cutting and drilling.
- The product should not be a substitute for something which is actually made from a more sustainable material in the first instance, such as plantation timber.
- The combination of ground FRP with some other waste material should not divert this waste from an existing higher end re-use chain.
- The product should have a suitably long service life.

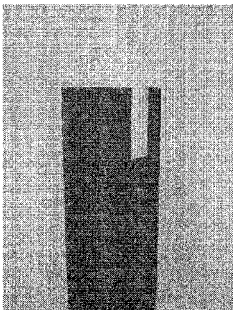
- The product should be cost effective.

BRE has developed, for demonstration and evaluation, several products made from ground GRP

GRP/plastic lumber "Waste Pile"



3. GRP/plastic lumber



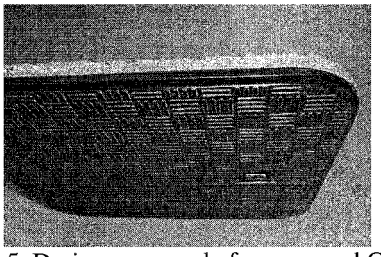
4. GRP/plastic lumber with bolted tenon joint to solid timber

This application offers an alternative to tropical hardwoods or treated softwood for some types of lightly loaded piles such as groynes, footbridge foundations, jetties, boardwalk posts and similar applications. The material can be sawn, drilled and notched like natural timber. The inclusion of ground GRP into the waste mixed plastic results in a composite which is 70% stiffer.

Other possible end markets for the ground GRP/waste plastic composite include:

- Retaining wall components
- Small foundation pads
- Footbridge decking
- Pavement slabs
- Support pads for temporary fencing
- Crash barrier components
- Bollards

GRP/polyester composite

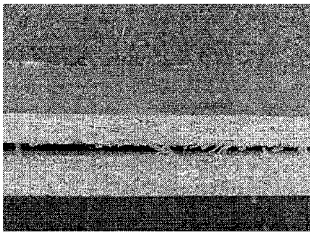


5. Drain cover made from ground GRP and polyester resin

This product is formed from a dough moulding compound, and although incorporates new resin it can be made with low-skilled labour. It offers chemical resistance with

low weight and is non-conducting, being envisaged for applications such as petrol stations etc.

GRP reinforced wood particleboard



6. Ground GRP/wood flake blend particleboards

Ground FRP can be incorporated into panel products. The GRP/wood chip blend particleboard was found to have superior properties to P5 grade commercial chipboard used in domestic flooring:

- Modulus of elasticity (MOE) 2800N/mm^2
- Bending strength 35N/mm^2

Ground GRP has the advantage of requiring no drying before use (unlike wood chip), and is not prone to moisture absorption or expansion in use.

ECODESIGN

The use of Ecodesign could aid the construction industry in its search for ecologically friendly products. Ecodesign takes into consideration the life cycle of the materials used and the methods of interactions they have with the environment[11]. It looks at reducing the environmental impact of a product over its life cycle without impacting on quality. Ecodesign concentrates on ensuring that products are easier to disassemble and uses mainly components that are more easily reused or recycled. Using these principles in the design process can increase profitability by eliminating waste at the beginning of the product's life cycle rather than at the end.

Ecodesign can thus feed into any part of the waste hierarchy and is in effect an application of the Best Practicable Environmental Option (BPEO). However, despite the fact that Ecodesign offers optimal solutions it lacks the range and detail of information to make an informed decision for all materials and components.

CONCLUSIONS

FRPs are increasingly being used in construction due to their low weight, durability and tailor made properties. The UK FRP industry currently produces 240,000 tonnes of product a year with 11% of this being for the construction sector. FRP is widely considered to be un-recyclable, and at present the most common disposal method for such material is landfill. Nevertheless several recycling options have been developed for this material including reintroduction of ground FRP waste into the production process, pyrolysis to generate fuel gas and fluidised bed recovery of glass fibres.

Waste FRP has also been used experimentally in the production of wood/plastic composites, road asphalt and concrete. Incineration with energy recovery or in combination with the production of cement is also an option.

Current and impending waste management legislation will put more pressure on the industry to address the options available for dealing with FRP waste. EU waste management directives on landfill, incineration, construction and demolition waste, end-of-life vehicles, electrical and electronic equipment, and UK government policy such as the waste strategy 2000, the sustainable construction strategy, the landfill tax, and local government policy could all influence the FRP industry. Such waste legislation focuses on dealing with waste through the waste hierarchy and will therefore put more pressure on solving FRP waste management through recycling and reuse.

Waste management is becoming increasingly important within the FRP and construction industries, especially with the implementation of EU directives concerning waste management.

Further work is needed to examine the effect of contamination of waste streams on end-product properties. Improving the quality of the fibre element of the ground GRP could also be achieved by work on shredder technology.

ACKNOWLEDGEMENTS

This research was carried out as part of the Construction Innovation Research Programme of the UK Department of Trade and Industry.

REFERENCES

1. GPRMC Press release – EU Waste legislation becoming more severe, 2001 www.gprmc.be/PressReleases.htm
2. Hobbs, G. & Halliwell S. 'Recycling of Plastics and Polymer Composites', Composites and Plastics in Construction Conference, Watford, UK, September 1999
3. Halliwell, S. Advanced Polymer Composites in Construction, BRE Information Paper IP7/99. Garston, CRC, 1999
4. Hurley, J., McGrath, C., & Bowes, H. Deconstruction and Reuse of Construction Materials. CRC, London, 2001
5. Jody, B.J.,Daniels, E.J., & Pomykala, J.A. 'Thermal Decomposition of PMC for Fiber Recovery', SPE Annual Recycling Conference, 1999
6. Simmons, J. 'Recycling Thermoset Composites in North America', JEC Conference, March 2001
7. George, S.D., & Dillman, S.H. Recycled Fiberglass Composite as a Reinforcing Filler in Post-consumer Recycled HDPE Plastic Lumber. Western Washington University.
8. Cabrera, N., Alcock, B., & Peijs, T. 'All-Polypropylene Composites for Ultimate Recyclability', EcoComposites Conference, London, September 2001
9. Peijs, T. 'Markets and Trends in Ecocomposites for Automotive Applications and Beyond', EcoComposites Conference, London, September 2001
10. Riedel, U., Nickel, J., & Hermann, A. 'Bio-composites: State of the Art and Further Perspectives', EcoComposites Conference, London, September 2001
11. Cranfield University & WE&E Consulting. A Brief Guide to Ecodesign.

FURTHER INFORMATION

Network Group for Composites in Construction www.ngcc.org.uk
NetComposites www.netcomposites.com

THE USE OF ADVANCED COMPOSITE MATERIALS IN LONG SPAN CIVIL ENGINEERING INFRASTRUCTURE

H.N. Garden EurIng MEng PhD CEng MICE ICIOB

Taylor Woodrow Technology, Technology Centre, Stanbridge Road, Leighton Buzzard, Bedfordshire LU7 4QH, UK

ABSTRACT

This paper describes a composites initiative in which Taylor Woodrow Technology used prepregs for a long span demonstrator application. Polymeric composites comprise fibres of (typically) glass, carbon or aramid embedded within a resin matrix. The fibre and resin choices will influence the static and dynamic mechanical properties of the composite, as well as its impact resistance. These are tailored to satisfy the structural requirements of new-build or rehabilitation schemes. The use of composites in combination with concrete, for new construction, is considered in this paper. The materials used were carbon and glass fibre reinforced polymers (CFRPs and GFRPs).

INTRODUCTION

Composite materials, also known as fibre reinforced polymer (FRP) materials, comprise strong and stiff reinforcing fibres embedded in a polymer-based matrix resin. FRPs possess high strength-to-weight ratios and excellent electrochemical corrosion resistance, resulting in low maintenance costs. The main material types used as reinforcing fibres in are glass, carbon and aramid. Prepreg is an abbreviation for pre-impregnated, which refers to the fibre mats having been given a certain amount of resin, only partly-cured, so that the material can be moulded and then heat and pressure can be applied to complete the stalled resin cure process. The part-cure ensures the material has the flexibility required for hand laminating.

New construction with composites has become an area of increasing interest in the civil and structural engineering arenas. Many organisations are investigating ways of developing the benefits of composites identified from other industries – eg. automotive and aerospace. The technology transfer into construction is being co-ordinated by various bodies, such as the Building Research Establishment's Network Group for Composites in Construction (see www.ngcc.org.uk). Developments in the use of composites for new construction will be found in many texts – eg. Garden (1999), BBRI (2000), Hollaway and Head (2001). The structures have included bridges, piles, highway overhead sign gantries, earth reinforcement systems, topside systems of offshore oil platforms, and many others. The growing national and international interest in the use of composites has resulted from advances in low cost manufacturing methods, reduced material demand in high cost areas (eg. defence), the ability to mould complex shapes and the economic viability of composites when combined with conventional materials.

THE ECONOMIC USE OF COMPOSITES WITH CONCRETE IN CONSTRUCTION

Introduction

Taylor Woodrow was the Project Manager for a €2.1M BRITE-EURAM programme called 'COMPCON' (Contract No. BRPR – CT – 98 – 0693). The other partners are the Advanced Composites Group (UK), the University of Surrey (UK), Dragados y Construcciones SA (Spain), TNO Bouw (Holland) and HGB-Netherlands Pavement Consultants (Holland). The project demonstrated how advanced polymer composite materials can be used in combination with concrete to produce economic, efficient and durable structural components for new construction. The work is described in detail in Wilson (1999).

The Project adopted the term, 'Duplex', to mean a combination of concrete and FRPs that forms structural elements which provide optimum properties derived from the individual characteristics of each material. Long span beams were identified as the elements for prototype development in this initiative. These have potential in long span applications including stadia, bridges, offshore structures, docks, piers and swimming pools, in each of which there is a need for lightweight and superior structural properties to eliminate intermediate supports and long term durability to minimise maintenance costs. The purpose of this Project was to overcome the barriers to the transfer of beneficial FRP technology into the construction industry. The potential benefits of these beams are currently being exploited by the project partners through feasibility submissions to a number of client organisations for long span applications.

Project development

Figure 1 shows the basic form of the initial element considered by the project team. Concrete possesses a high compressive strength so this material is located at the top of the beam. The glass and carbon fibre composites have high tensile strengths so they are most effectively located below the neutral axis. This basic form is being progressively modified to optimise the structural properties of the beam. There are other structural elements that would also benefit from the proposed form of construction, such as columns and shells; the application of the technology to elements other than beams is discussed in the final project report (presently confidential).

It has been identified that this form of beam can be up to two times as expensive as conventional concrete elements for short spans but the cost of manufacture is comparable for a large number of long span items. Significant cost savings are expected in the installation of long span Duplex components due to their lower weight. Also, the Duplex items will be more durable so added value over the lifetime of a structure is anticipated. The economic assessment in this regard is continuing.

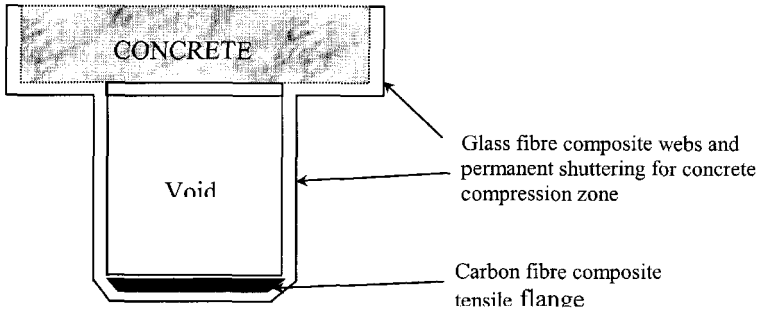


Figure 1 Basic section form being tested and improved.

The specific project goals were:

- a technique for developing a good long term bond strength between the concrete and the composite when the concrete is cast against the cured composite;
- a process for fabricating large, high quality composite / concrete sections under construction site conditions.

The investigations included fire performance, concrete / composite structural interaction and design approaches.

The composite materials being pursued were prepregs which were developed to cure at relatively low temperatures (65°C), which can be achieved by simple heaters. The method lends itself to on-site manufacture of elements. An advantage of this approach would be reduced transport costs for the finished members, and the flexibility to install the elements in remote areas. It has been identified that rapid and light construction would be a benefit in developing countries or war-damaged regions, for example. The concept is being developed for warehouse applications and bridges, in which the shape freedom of the composites would be an advantage architecturally in addition to the light weight and high strength.

Full scale tests

Full scale demonstrator beams were manufactured by Taylor Woodrow and Dragados. Both beams were constructed as shown in Figure 2. They were 18 metres long. The tests were four-point load trials, with the loads arranged at third-points. Brief details of the manufacture testing are given here.

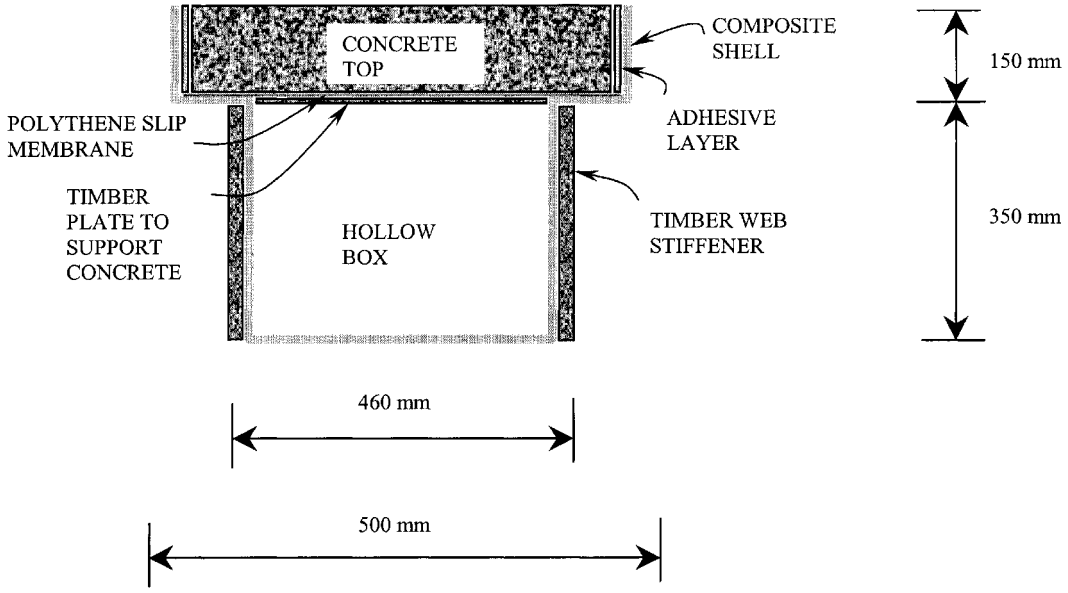


Figure 2 Section constructed as a demonstrator beam.

The Taylor Woodrow beam was load tested to destruction so that the failure mode and ultimate capacity could be determined.

Manufacture of test beams

The composite materials used in the beams were glass- and carbon-fibre prepregs. They were laminated in separate layers, according to the sequence in Figure 3. Laminating was achieved by dispensing the rolls of prepreg from a purpose-made trolley (Figure 4), which provided a simple system for demonstration purposes. The composite was laminated on a male mould tool. The laminating was undertaken by construction industry operatives, with no previous experience of handling composite materials, thereby demonstrating some of the technology transfer objectives of the project. The web stiffeners were half-rounds of timber, laminated over with a single glass-fibre layer, to prevent web buckling. They were spaced at 500 mm intervals in the shear spans only.

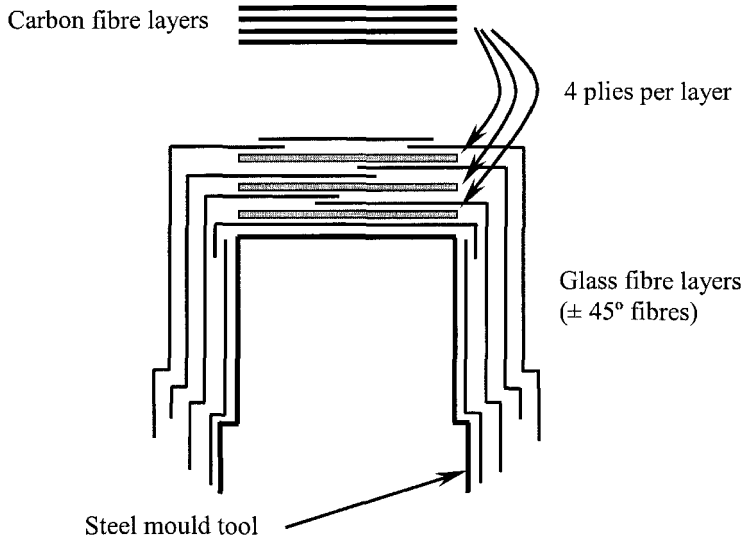


Figure 3 Laminating sequence for demonstrator beams.

The composite was cured under vacuum bag and in an heated enclosure. The cure temperature was achieved using electrical rod heating elements and a polystyrene enclosure, with a temperature of 65°C.

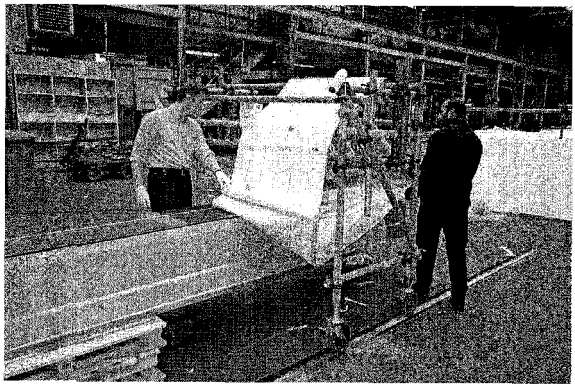


Figure 4 Laminating process for demonstrator beams.

The laminated composite section was struck from the steel mould using air ports to carefully 'blow' the composite off. This section was then turned over (to orientate it in the correct position) and the concrete was cast into the upper part. The composite part on its own (ie. without the concrete) was sufficiently lightweight (150 kg) to be able to manoeuvre it by hand (Figure 5). A timber former layer was located at the base of this upper part, merely for casting purposes (although the timber remained in place). A polythene sheet was laid on the timber before casting the concrete (Figure 6), to ensure that there could be no structural contribution from the concrete / timber interface. The only intended bond was along the sides of the upper composite part, achieved using an epoxy mortar adhesive. The adhesive was trowelled onto the composite before the

concrete was cast (Figure 7). The two materials cured concurrently. A layer of polythene, draped over the beam, ensured that there was adequate moisture during the 28-day concrete cure period.

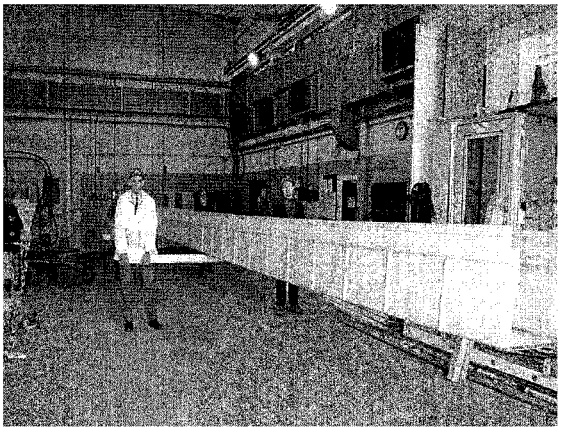


Figure 5 Carrying the composite part to demonstrate its light weight.

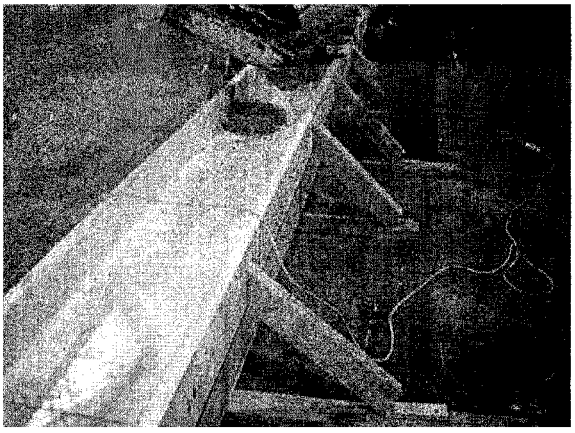


Figure 6 Casting the concrete into the upper composite part. Note the polythene layer.

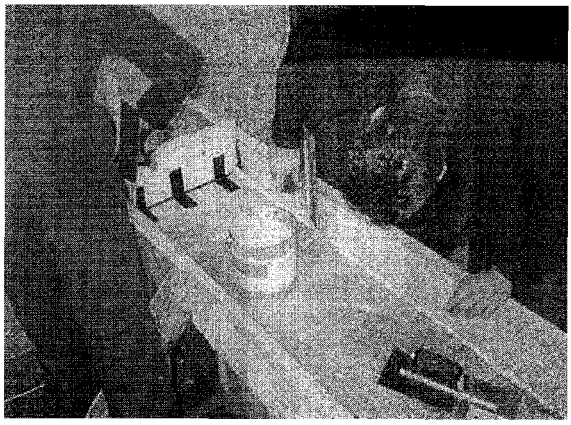


Figure 7 Placing epoxy mortar adhesive before casting the concrete.

Load testing of demonstrator beams

The load test, at 80% of the ultimate load, is shown in Figure 8. The load was applied via hydraulic jacks in increments of 1 kN. The maximum value was 237 kN (total load), giving a bending moment (in the central bending region between the load positions) of 592.5 kNm. The mode of failure was mainly cohesive fracture of the concrete near the sides of the beam (Figure 9), although isolated locations of adhesive failure between the concrete and composite were found. The collapse of the beam was sudden and it was very difficult to observe the onset and propoagation of damage in the materials before collapse.

Buckling of the side panels in the shear spans was observed by a change in light reflection from the resin surface of the composite as the panels lozenged. It is thought that side panel buckling caused the onset of beam failure.

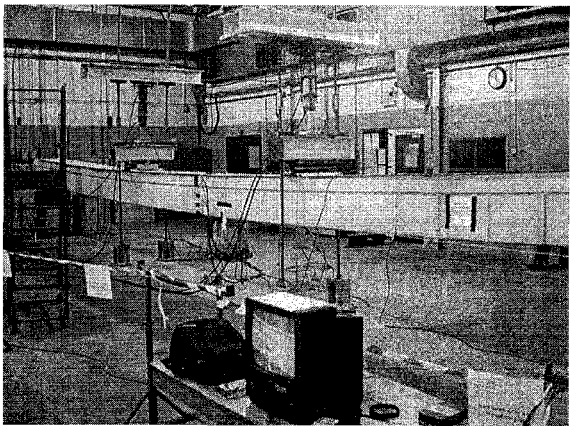


Figure 8 Demonstrator beam at Taylor Woodrow under 80% of the maximum load.

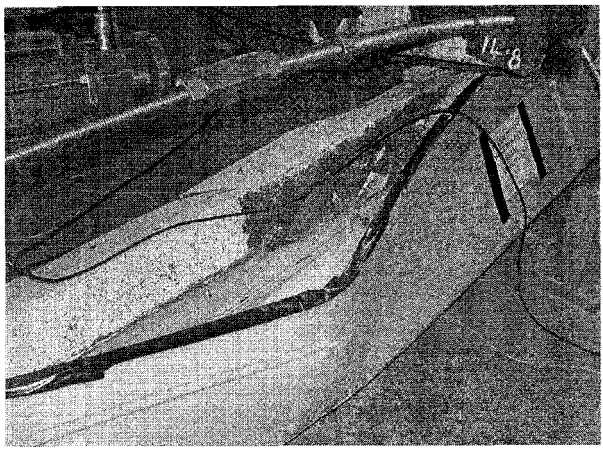


Figure 9 Part view of beam failure mode.

The depth of the beam at mid-span was instrumented (Figure 10) to give compressive and tensile strain results, from which the assumption of plane sections remaining plane was confirmed (Figure 11). The neutral axis lay approximately at the concrete / timber interface, which was the intention. Details of the design approach will be the subject of a later document by the project team.

Figure 12 shows the variation of the strain recorded by the diagonal gauges on the side panels, as a function of applied load. This behaviour is typical of that observed in traditional structures (eg. steel girders). Gauges D2 and D10 were aligned along a line of compression. This strain changed towards a tensile mode after a certain load, which was the load corresponding to the points of contraflexure in the curve. This load level coincided with that at which the tensile strain in the orthogonal gauges, D1 and D9, increased at a greater rate than previously, suggesting a redistribution of stress in the side panels associated with lozenging.

The load was applied incrementally in 1kN intervals.

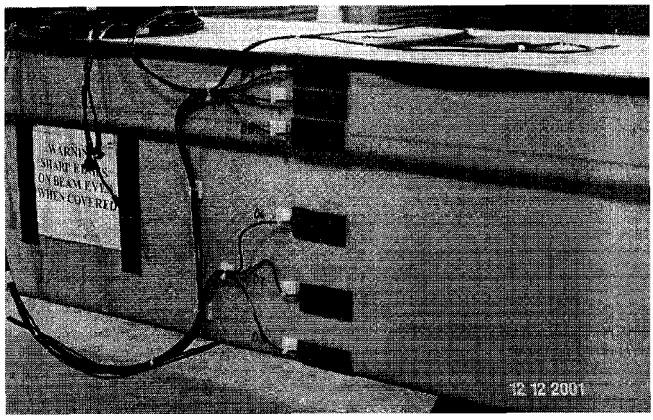


Figure 10 Strain gauge positions at mid-span.

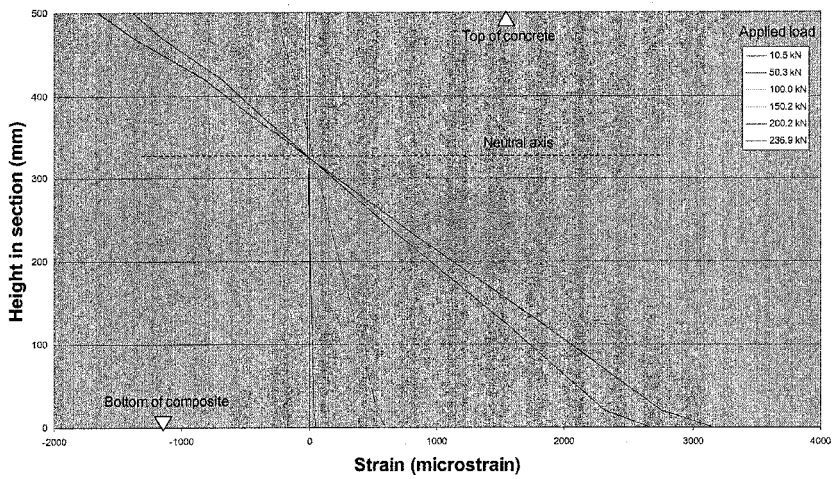


Figure 11 Section strains at mid-span with increasing applied load.

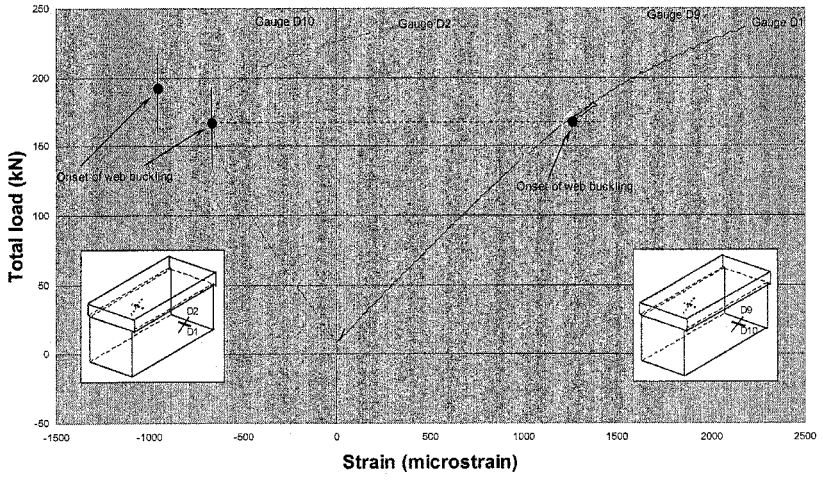


Figure 12 Web buckling behaviour detected by side panel strain gauges in the shear spans.

Interpretation of beam load test results

The assumption of plane sections remaining plane in the region of predominantly bending was shown to be valid. This means that the traditional principles of flexural design will apply to the calculations for such Duplex sections. The design of the web stiffener layout needs to be optimised for any given beam loading configuration (or

combinations of). Sudden brittle failure is undesirable, but appropriate instrumentation of the construction element can be used to indicate strain levels, which can be compared with failure values. A much greater programme of investigation would need to be undertaken to establish such failure criteria.

SUMMARY, CONCLUSIONS AND FINAL COMMENTS

Polymer composites have a significant role to play in infrastructure development and that their benefits in new construction are identified. The ability to mould composites to any shape is one of their greatest advantages. Programme benefits in new-build schemes are envisaged and the full potential of composites is being assessed for long span uses. Their combination with concrete has been seen to achieve the best properties of both materials.

REFERENCES

Garden, H.N. (1999), 'Composites and Plastics in Construction', *Conference held at the Building Research Establishment (BRE, Garston, UK), 16th – 18th November 1999.*

Hollaway, L.C. and Head, P.R. (2001), 'Advanced Polymer Composites and Polymers in the Civil Infrastructure', *Elsevier.*

Wilson, M.J.M. (1999), 'The economic use of advanced polymer composites with concrete in structures (COMPCON)', *Proc. 2nd Annual Workshop of the EC-ECCREDI TRA-EFCT (Targeted Research Action – Environmentally Friendly Construction Technologies.*

POLYMER-LAYERED SILICATE NANOCOMPOSITES IN CIVIL ENGINEERING

I. Hackman and L. Hollaway

University of Surrey, UK

INTRODUCTION

Nanocomposites are one of the many types of new materials that use the principle of nanotechnology to improve the physical properties of materials, or to generate new ones. Nanotechnology is the term used to describe all activities where the range of interest is on the nanoscale. In this range the interaction between atoms and molecules occurs and from which all the observable macro-material properties are derived. Therefore, being able to influence bonding and structure on this level will enable the properties of a material to be significantly altered. A conventional composite is formed by bonding and surface interaction on a macroscopic scale, in a nanocomposite these mechanisms occur on a nanoscale.

Fibre reinforced polymer composites are increasingly being used in the civil infrastructure ranging from internal and external reinforcement of concrete, wraps for seismic retrofit of columns, composite structural systems and bridge decks. The intrinsic lightweight and tailor-ability of composites have clearly aided their rapid utilisation, however, there are concerns related to their overall durability particularly when under load and exposed to harsh and changing environmental conditions. Nanocomposites have the potential to reduce the permeability of polymer composites against ingress of corrosive substances and to aid their fire resistance properties.

CLAY TYPES AND STRUCTURE

Montmorillonite is part of the smectite family of clays, and as nanoparticles perform more favourably than other forms of smectite clay.

There are four main reasons why these clays are ideal for use as nanoparticles in nanocomposite materials.

- The clay layers have a high strength and stiffness along their length, higher than glass fibres.
- The high aspect ratio enables large surface areas ($700m^2/g$) of the clay to be in contact and bond with the polymer.
- They can be modified more easily than most other groups of clays, this high level of intercalation chemistry enables the clays to be chemically altered to aid their bonding and dispersion in the polymer.
- They are naturally occurring and can be purified at a relatively low cost.

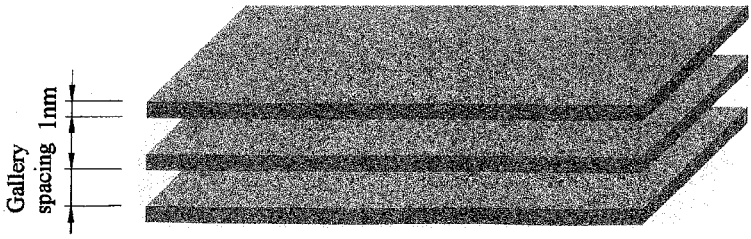


Figure 1. Structural representation of montmorillonite clay layers.

Smectite clays naturally form layer upon layer of oxide sheets that only have a weak interaction holding the layers together (Figure 1). These sheets are around 1nm thick and vary from 20nm to 2000nm in length and width, depending on the type of smectite clay. Montmorillonite is typically about 250nm in length and width, resulting in massive surface areas of $700m^2/g$. These large surface areas make them exceptional at altering the properties of a composite.

The layers have a crystalline structure that is composed of "two silica tetrahedral sheets fused to an edge-shared octahedral sheet of nominally alumina or magnesia" [1]. Between these layers is a gap known as the gallery layer, which fills with water when wet and causes the clay to swell. Completely dry clays will have a very small gallery layer of only a few nanometres. This spacing changes when used in nanocomposites, the way in which the gap changes alters the properties of the resulting nanocomposite.

CHEMICAL MODIFICATION

Chemical modification of the montmorillonite clay is required to enable the clay layers to be dispersed and achieve full interfacial interaction with the polymer material. The clays are naturally hydrophilic and will not easily be dispersed into an organic liquid.

Therefore, to produce a nanocomposite with clay and polymer well mixed, the clay must be changed from a hydrophilic substance to an organophilic (hydrophobic) substance. This modification of the clay, so that it may be integrated with the organic polymer, is known as compatibilization.

The most common compatibilization process is onium-ion modification, which involves ionically bonding a new group of molecules to the surface of the clay layer. This group of molecules consists of a small hydrocarbon chain typically containing an ammonium functional group. The molecule is organophilic and thus provides the required dipole moments so that the material as a whole is organophilic and can mix with the organic polymer. A typical example of the organophilic functional group used for this purpose is $C_{18}H_{37}NH_3^+$.

TYPES OF POLYMER-LAYERED SILICATE NANOCOMPOISTES (PLSN)

The way in which the clay layers are dispersed in the polymer material will influence the interfacial bonding and the level of interaction between the clay layers and the polymer. There are three distinct types of material that can be formed by the introduction of these clay layers into the matrix, standard composites, intercalated and exfoliated nanocomposites.

Conventional composites

In a conventional composite the clay acts only as inert filler, this can easily be achieved in any polymer. If the clay has not undergone any compatibilization treatment the clay layers will not separate and bond with the polymer (Figure 2). There will be no, or very little interfacial bonding between the clay and the polymer, therefore the clay will provide no reinforcement. There will be no layer separation and the polymer will not enter the clay gallery layer. This type of composite is often used as an inexpensive way to fill out the polymer and reduce costs, providing no property improvements. As the clay has not undergone any treatment it is a cheap and effective filler.

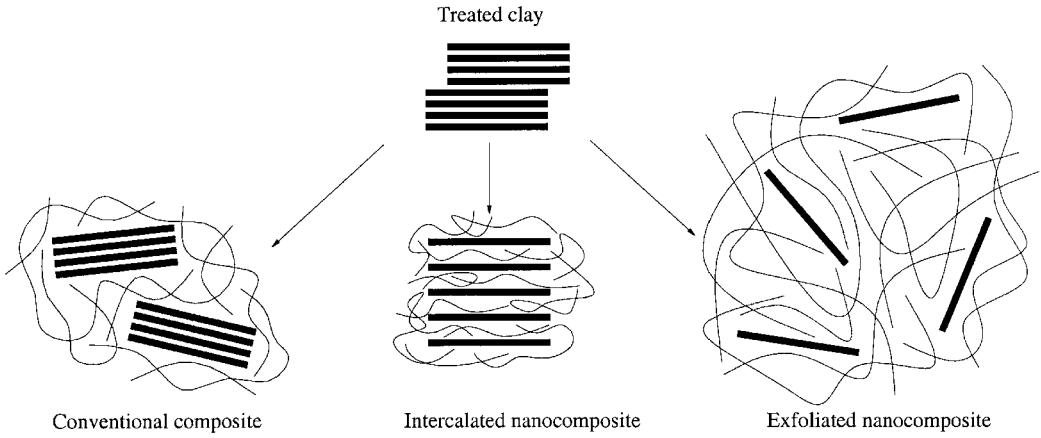


Figure 2. Types Of PLSN.

Intercalated nanocomposites

An intercalated nanocomposite is formed when the clay layers are separated by a fixed amount (Figure 2). Only a small quantity of polymer molecules will enter this increased size gallery layer, causing a degree of interfacial bonding between the polymer and clay layers. The clay layers act as reinforcement for the polymer, although the fixed layer separation is unable to provide the maximum reinforcement. They could potentially provide more reinforcement if they were separated further and orientated in different directions.

Exfoliated nanocomposites

An exfoliated nanocomposite is formed when the clay layers are dispersed in the polymer with random separation and orientation (Figure 2). The clay layers should be evenly distributed throughout the matrix provided sufficient mixing allows the layers to disperse. The distance between clay layers will depend on the clay loading, the higher the proportion of clay in the nanocomposite the closer the clay layers will be to each other. The clay layers will be sufficiently separated to allow full interfacial bonding and to contribute all their strength to the reinforcement of the nanocomposite. They will be orientated at random, so providing reinforcement in every direction, and will therefore provide a greater degree of reinforcement to the nanocomposite than the fixed layer separation and fixed orientation of an intercalated nanocomposite.

PROPERTY IMPROVEMENTS

Mechanical property improvements

The mechanical improvements generated by the inclusion of nanoparticles in a polymer have been well researched, the majority of the most important polymers have all been used to construct nanocomposites and have shown increases in tensile strength and modulus. Current research has focused on the use of thermoplastic resins as it is easier to exfoliate the clays into these polymers, although many thermosets have also been used. An innovative exfoliation mechanism is being researched at the University of Surrey whereby the clays are introduced to a small amount of thermoplastic polymer where they are readily exfoliated. The resulting mixture is combined with thermosetting polymers and the fully exfoliated state of the clays is maintained.

Polyamide-6 (Nylon)

The Toyota research group, in the late 1980s and early 1990s produced the first ever nanocomposites using polyamide-6 [2]. With a 4.2wt% addition of silicate material the tensile strength increased from 69Mpa to 107Mpa (55%), tensile modulus from 1.1Gpa to 2.1GPa (90%), flexural strength by 60% and flexural modulus by 126% compared with the pristine polymer.

Lan et al [3] in conjunction with Nanocor, a leading producer of clay nanoparticles, achieved a similar increase of properties using polyamide-6. They recorded a tensile modulus increase from 3.1GPa to 5.9GPa (90%) and a flexural modulus increase from 3.4GPa to 5.4GPa (58%) at clay loading of 6wt%.

Little research has been conducted into the performance of nanocomposites containing reinforcing fibres, however, Wu et al. [4] have combined chopped strand glass and carbon fibres in a nanocomposite. They incorporated 3wt% nanoparticles in a number of composites containing different amounts of 6mm long chopped strand glass or carbon fibres. They found that a 3wt% polyamide-6 clay nanocomposite provided better reinforcement than 10% carbon or glass fibres and that at every fibre content tested, the nanocomposites provided a higher level of reinforcement.

Epoxy

Wang et al. [5] have conducted studies of epoxy nanocomposites and found that extensive mechanical property improvements can be achieved at a variety of clay loadings. They found an increase in tensile strength and modulus of 183% and 87% respectively with a 5wt% addition of clay, and a 466% and 250% increase respectively with a 15wt% addition of clay. These increases in tensile properties are quite considerable and represent a significant increase in strength and stiffness for the relatively cheap addition of clay.

Becker et al. [6] conducted tests into the flexural modulus of nanocomposites using high performance epoxy resins. They produced nanocomposites with clay loadings of 2.5%, 5%, 7.5% and 10% using three different high performance epoxy resins. They recorded flexural modulus increases of 25%, 22% and 23% at 10% clay loading for the three different types of epoxy.

Polyester

Lee et al. [7] have conducted research into polyester nanocomposites varying from 1wt% to 30wt% clay loading. They observed consistent tensile strength and modulus improvements at every amount of clay loading and only a small reduction in strain at break. They recorded increases of 9.4%, 13.7% and 19.7% in tensile strength and 7.2%, 10.8% and 21.4% in tensile modulus at clay loadings of 3wt%, 5wt% and 10wt% respectively.

Barrier property improvements

The reduction in permeability that can be attained from the exfoliation of PLS into polymers depends on the agent being investigated. The improvements recorded range from three fold to zero, depending on the agent involved. The permeability reduction achieved also depends upon the specific aspect ratio of the clay being used. High aspect ratio clays have a higher surface area and therefore reduce the permeability by a larger amount than lower aspect ratio clays. This is illustrated in Figure 3 [8], which shows the change in relative permeability for a range of minerals with different aspect ratios.

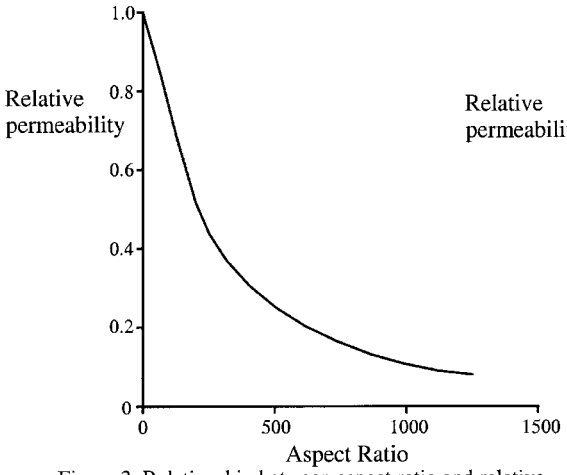


Figure 3. Relationship between aspect ratio and relative permeability [8].

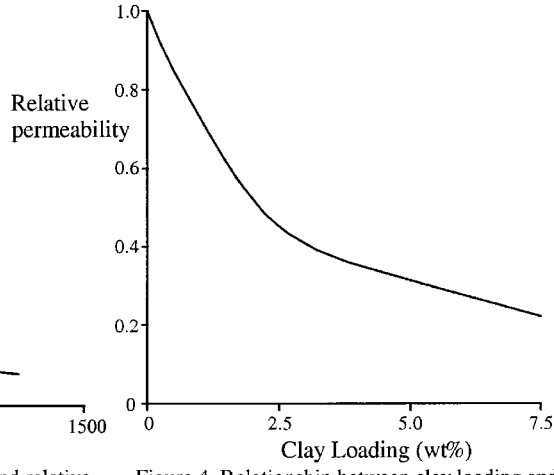


Figure 4. Relationship between clay loading and relative permeability [8], for a 250 aspect ratio montmorillonite clay.

Montmorillonite has an aspect ratio of approximately 250, it would therefore be expected to achieve a reduction in permeability of one half for a montmorillonite nanocomposite. However, this reduction in permeability is also a function of the clay loading that is applied to the nanocomposite. Figure 4 [8] shows how the relative permeability of a nanocomposite with a 250 aspect ratio clay changes with increasing clay loading.

The improvements in barrier properties that have been accomplished in reality are similar to these theoretically expected values. Beall et al [8] have reported reductions of 600%, 240% and 144% compared to the pristine polymer for water vapour transmission rates for various different modified clay types in HDPE nanocomposites.

Wang et al. [5] have conducted research into the weight gain for various different agents in an epoxy nanocomposite containing 9.1wt% clay loading. They found a reduction in weight gain of 6.35% for sodium hydroxide, 36% for water and 56.9% for sulphuric acid all after 15 days.

Chen et al. [9] have conducted research into the barrier properties of exfoliated aerospace epoxy nanocomposites (Shell Epon 862). They found a 20% reduction in the weight gain of a 6wt% clay nanocomposites when immersed in methanol after 104 days. They also conducted research into the uptake of acetone [10] for a 6wt% nanocomposite, recording a reduction in weight gain of 46% after 37.5 days.

Fire property improvements

The majority of research concentrates on the properties of heat distortion temperature (HDT), peak and mean heat release rate (HRR) and mass loss rate (MLR).

Okada et al. [2], in the first investigations into nanocomposites conducted tests on the HDT of nylon-6 clay nanocomposites. They reported an increase from 65°C to 145°C (123%) with a 4.2wt% addition of clay nanoparticles. Similar increases have been reported by Beall [8], an increase from 58°C to 150°C (158%) at a 5wt% clay loading.

Comprehensive research into the fire properties of a variety of different polymer nanocomposites has been conducted by Gilman and published in various papers [11] [12] [13]. It was found that the additions of PLS to all polymers tested resulted in large reductions in peak and mean HRR and mean MLR. However, the specific heat of combustion for some of the nanocomposites was decreased by a small amount.

RESEARCH CONDUCTED AT SURREY

A preliminary investigation was undertaken to ascertain the basic processing, manufacturing and analytical techniques required to produce and observe exfoliated nanocomposites. Basic experiments were devised to observe the characteristics of nanocomposites compared to standard composites.

Materials and preparation

Four different types of nanoparticle were acquired from the manufacturer Sud-chemie. Three treated nanoparticles (A, B and C) containing different amounts of chemical modification, with approximate relative amounts of treatment 0.7, 0.85 and 1 respectively. The fourth nanoparticle (D) was an unmodified clay of the same type, montmorillonite.

All specimens were prepared using three layers of unidirectional E-glass with an epoxy matrix material. Specimens were vacuum bag cured for ten hours at room temperature.

Nanoparticles were introduced into the resin and mixed briefly by hand and then by a high speed and shear mixer for 24 hours to exfoliate. The hardener was then added to the mixture and the specimens produced via a wet lay-up technique.

Testing procedure

Mechanical properties were examined using standard tensile testing sizes and procedures. 5wt% and 10wt% nanocomposites were produced for all four types of nanoparticle for comparison with standard composite specimens.

Barrier property specimens were placed in a high temperature and pH environment for long periods to simulate an aggressive environment. The high pH breaks down the fibre-matrix bonds in the specimens, therefore, a specimen with lower permeability will sustain less damage and retain more of its original strength. The remaining strength was then tested in the same way as the mechanical property specimens. All nanocomposite specimens contained 5wt% nanoparticles for the barrier tests.

Fire properties were tested via UL94 flammability testing techniques carried out in a controlled environment with precise specifications. 5wt% and 10wt% nanocomposite and standard composite specimens were produced for comparison.

Test results

To ensure that the nanocomposites contained fully exfoliated nanoparticles, the key to attaining increases in performance, an exfoliated check was conducted. A sample of raw clay and a powdered sample of nanocomposite were analysed using X-ray diffraction. The sample was fully exfoliated, containing no consistent spacing of nanoparticles.

Mechanical property results

No consistent trend was observed, indicating that the nanocomposites had neither a higher tensile strength or modulus than the standard composite specimens (figure 5). However, due to the high quantity of glass fibres used any increase in strength of the matrix would have caused only a tiny increase in the overall strength of the specimen. A wide range of results (from specimen to specimen) was observed due to the un-homogeneity of composite materials, causing the slightest increase in strength to be unnoticed within the results spread.

Barrier property results

During the environmental testing two different exposure conditions were used, nanocomposite A (Nano A) and standard composite 1 (Comp 1) were tested for 2000 hours at pH13 and 38°C. Nanocomposite specimens B, C and D (Nano B, C and D) and standard composite 2 (Comp 2) were tested for 1000 hours at pH13 and 50°C.

All specimens suffered a large decrease of strength (figure 5) after environmental exposure, however, the treated nanoparticle nanocomposites (A, B and C) retained more of their strength than the untreated nanoparticle D nanocomposite and the standard composite specimens. The nanocomposites achieved a change in strength by 33%, 28.8%, 26% and -26% respectively, these increases of strength for nanocomposites A, B and C represent a potentially major increase in service life for a component subjected to an aggressive environment. The large decrease in strength of the untreated nanoparticle D indicates that using cheap fillers in a polymer subjected to aggressive conditions could significantly reduce the service life of the component with only a small cost saving.

Fire property test results

Fire testing conducted via 94V and 94HB testing was inconclusive, no conclusions could be drawn from the results of the flammability testing. Further research is required into the flammability properties of nanocomposites.

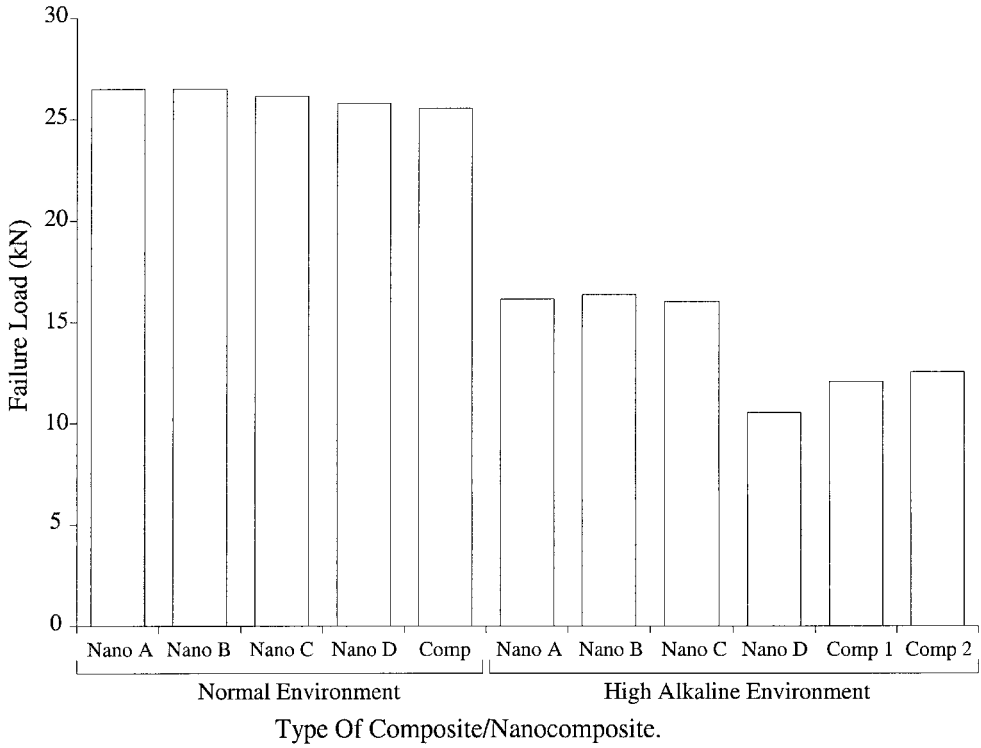


Figure 5.

CONCLUSIONS

Clay nanocomposite materials are a new and developing area of nanotechnology that have the potential to offer many wide ranging benefits to current matrix polymers. They have not thus far been incorporated in any form of product or used to produce any form of structure. However, their ability to increase the service life of materials subjected to aggressive environments could be utilised to increase the durability of glass and carbon fibre composites. This advantage would allow the use of composite materials in situations where their performance under aggressive environments is currently thought to be inadequate for the in-service conditions. The increase in service life would allow composite materials to be used with more confidence in their long-term durability and therefore used in a wider range of circumstances.

REFERENCES

1 R A Vaia, 'Structural characterization of polymer-layered silicate nanocomposites', In: Polymer-clay nanocomposites, edited by Pinnavaia, Wiley & Sons Ltd 2000, p.231.

2 A Okada, Y Kojima, A Usuki, M Kawasumi, Y Fukushima, T Kurauchi and O Kamigaito, 'Mechanical properties of Nylon 6-clay hybrid', Journal of materials research, 8(5), 1185 (1993).

3 T Lan, J Cho, Y Liang, J Qian and P Maul, 'Applications Of Nanomer® In Nanocomposites: From Concept to Reality', Society of Manufacturing Engineers, EM02-249, (2002).

4 S Wu, F Wang, C Ma, W Chang, C Kuo, H Kuan and W Chen, 'Mechanical, thermal and morphological properties of glass fiber and carbon fiber reinforced polyamide-6 and polyamide-6 / clay nanocomposites', Materials Letters, v49, n6, (July 2001), p.327-333.

5 Z Wang, J Massam and T J Pinnavaia, 'Epoxy–Clay Nanocomposites', In: Polymer-clay nanocomposites, edited by Pinnavaia, Wiley & Sons Ltd 2000, p.127.

6 O Becker, R Varley and G Simon, 'Morphology, thermal relaxations and mechanical properties of layered silicate nanocomposites based upon high-functionality epoxy resins', Macromolecules, v36, n5, (Mar 11 2003), p.1616-1625.

7 S Lee, H Park, H Lim, T Kang, X Li, W Cho and C Ha, 'Microstructure, tensile properties and biodegradability of aliphatic polyester/clay nanocomposites', Polymer v43, n8, (Feb 18 2002), p.2495-2500.

8 G W Beall, 'New conceptual model for interpreting nanocomposite behaviour', In: Polymer-clay nanocomposites, edited by Pinnavaia, Wiley & Sons Ltd 2000, p.270.

9 C Chen and D Curliss, 'Morphological development and barrier properties of exfoliated aerospace epoxy-organoclay nanocomposites', Proceedings of the 47th international SAMPE symposium, Long Beach California, 2002.

10 C Chen and D Curliss, 'Organoclay-aerospace epoxy nanocomposites', Proceedings of the 46th international SAMPE symposium, Long Beach California, 2002.

11 J W Gilman, 'Flammability and thermal stability studies of polymer layered (clay) nanocomposites', Applied clay science, 15 (1999) p.31-49.

12 J W Gilman, T Kashiwagi, A Morgan, R Harris, L Brassell, M Van Landingham and C Jackson, 'Flammability of polymer clay nanocomposites consortium: year one annual report', National institute of standards and technology, U.S. Department of Commerce.

13 J W Gilman and T Kashiwagi, 'Polymer-layered silicate nanocomposites with conventional flame retardants', In: Polymer-clay nanocomposites, edited by Pinnavaia, Wiley & Sons Ltd 2000 p.193–205.

MODELLING A COMPOSITE/CONCRETE T-BEAM USING A FINITE ELEMENT TECHNIQUE

J.Hulatt, L C Hollaway and A M Thorne

University of Surrey

ABSTRACT

Since the 1970s, when 'all polymer composite' structures were first seriously introduced into the construction industry the uses of advanced polymer composites (APC) have gradually increased. From the 1990s to the present time a considerable volume of APCs have been used in the flexural and shear upgrading of reinforced concrete and metallic structural members, in the wrapping of concrete columns and in forming a small volume of FRP rebars. Currently, APCs are being considered in combination with the more conventional civil engineering materials to form Hybrid systems in which two or more materials are used compositely to form a structural member; the individual materials are used to their best structural advantage.

This paper will discuss a numerical analytical study undertaken using a finite element technique to predict the loading behaviour of a hybrid T-beam that incorporates concrete in the compression region and APC material in the tensile region of a beam. The numerical method estimates the stresses and deflections of a beam under four point loading conditions, when they have been designed to fail by buckling of the web or by failure of the adhesive material which bonds the concrete to the permanent shuttering. The solutions will be compared with the experimental results, which have been discussed in a previous paper by the same authors.

INTRODUCTION

Although Advanced Polymer Composites (APC) materials were first developed in the early 1940s for military and aerospace applications, the general use in civil engineering has only been evident in the past thirty years. Initially, their use was confined to non-structural applications such as formwork liners or cladding panels. Although there was a high cost associated with composite materials and their production techniques, this was off-set by their inherent advantages, such as high strength and stiffness to weight ratios and their corrosion resistance. However, as the costs of the raw materials reduced and improvements were made in the manufacturing techniques by the introduction of automated methods, the use of APCs in rehabilitation and in structural applications increased[1].

It is suggested that, in future, one of the predominant uses of APC in the construction industry will be in conjunction with the more conventional materials, for instance, a combination of APC and concrete to form a hybrid system in which both materials perform to their best advantage. The current study utilises a 1.5 m span hybrid T-beam manufactured from carbon fibre reinforced polymer (CFRP), glass fibre reinforced polymer (GFRP) and concrete. The concrete and APC are located in the compression and tension regions, respectively, of the beam. This system eliminates the use of steel rebars and hence any problem that might occur with degradation of the steel rebars. The APC material used in this study utilises a heavyweight carbon fibre fabric, which was designed specifically for civil engineering applications.

The objective of this paper is to discuss the finite element technique that was utilised to predict the short-term behaviour of a hybrid T-beam. A three-dimensional model of the beam was assimilated using the pre-processor Patran 2000[2], with the analysis and post-processing undertaken using ABAQUS v5.8[3]. The model was varied depending on the configuration of the T-beam; two different beams were modelled, one that was designed to fail by buckling of the webs and one by a shear bond failure at the interface of the composite permanent shuttering and the concrete. The numerical model was used to compare deflections and stresses with experimental data published in references [4,5]

PREPREG MATERIALS

The APC material utilised in this study is a pre-impregnated (prepreg) material supplied by Advanced Composites Group (ACG). This material has been developed by ACG to be appropriate for the civil engineering industry. The ply thicknesses are much greater than those used in the aeronautical industry, this allows the necessary thickness to be achieved with a minimum number of plies. Details of the two materials predominately used in the manufacture of the hybrid T-beams, namely unidirectional (UD) CFRP and $\pm 45^0$ GFRP, are described in reference[6]. A number of environmental tests, undertaken at University of Surrey, have shown that this material compares favourably with other APC materials used in construction.

BEAM MANUFACTURE AND EXPERIMENTAL TESTING

The two different configurations of hybrid T-beams were designed, (one to fail by web buckling (Type A) and one to fail by shear bond at the interface between the concrete and composite (Type B)), and were manufactured using the vacuum bag method; reference[4] gives the full details. Initially, the composite part of the beam was manufactures by laying up the correct configuration of plies of APC material onto a male mould; the whole was then debaulked and cured in an oven at 65^0C for 16 hours. After trimming and the placement of the stiffeners into position in the beam, concrete with a target strength of 40 N/mm^2 was poured. Two design variations in Type A beam were modelled and tested experimentally; beam A1 and A2 had GFRP stiffeners placed at 75 mm centres whereas beams A3 and A4 had timber stiffeners positioned at the same locations. Stiffeners were omitted at a distance of 300mm from the supports to induce buckling at these locations. Beams B5 and B6 (analysing the shear bond failure) contained double the thickness of GFRP in the webs and contained the full compliment of stiffeners.

Both beam types were experimentally tested statically in 4-point bending after the concrete had cured for 28 days. Further details of the manufacturing methodology and experimental static testing are given in reference[5].

NUMERICAL MODELLING

A finite element (FE) analysis was developed so that the structural performance of the model hybrid beams could be verified before the beam was fabricated. The same FE analysis package have been utilised throughout this study, namely ABAQUS v5.8[3] as the analysis tool and post processor and Patran 2000[2] as the pre-processor. The FE technique is described in reference[7] and consequently, detailed explanations of the FE theory will not be given here.

Beam Type	Beam Number	Layers of GFRP in web	Stiffening method	28 day concrete compressive strength
A	1	2	GFRP	39.8
	2	2		42.9
	3	2	Timber	37.9
	4	2		35.9
B	5	4	GFRP	36.1
	6	4		38.3

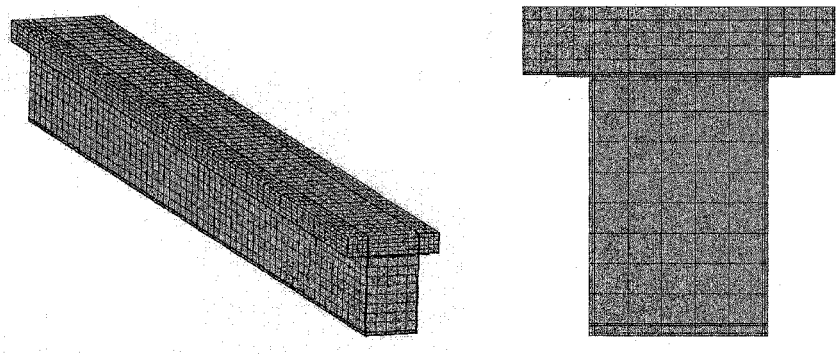
Table 1: Summarising the different beam configurations

Beam Geometry

Patran 2000 is used to generate the solid geometry of the intended model, to mesh it with the desired elements and then to automatically provide the required ABAQUS input deck. Patran 2000 interface was more user friendly when compared to text editing the input file of ABAQUS. A complete 3D model was created using solid elements for both the concrete and composite layers. ABAQUS allows the solid section to be split up into different layers of composite material with varying thicknesses, material properties and fibre orientations. For example, the two parts of the web were created using a solid element with a width of 2.16 mm. This was then split up into four lamina of 0.54 mm (as was fabricated experimentally) with a fibre orientation of +/-45°. The solids were then meshed utilising 20-node brick elements (known as hex20 in Patran or C3D20 in ABAQUS). An example of the completed beam geometry is shown in Figure 1; this shows the model for the Type B beams; the set-up for the analysis of the Type A beams was essentially the same. A full beam was modelled to allow a buckling analysis to be undertaken on the same model, the results of which are given in reference[4].

Linear FE analysis

Initially a linear FE analysis was completed on both beam types. This was undertaken so that the behaviour of the beams up to serviceability loads could be quickly



Full Beam Elevation

Figure 1: FE model utilised for the analysis of Type B beams

modelled before the experimental program commenced. The behaviour of the beam was shown to be non-linear after the serviceability load had been exceeded, therefore, a further non-linear analysis was undertaken to model the beam as it approached failure.

The load was applied as a pressure to the top surface of both types of beam under the same conditions as the experimental set-up (i.e. a 50 mm width plate to spread the load at each load point). The boundary conditions were simply supported such that the vertical and transverse directions were fixed (again to simulate the actual conditions of the experiment). A bearing plate was also simulated at the support. The FE model in all cases assumed that there was a perfect bond between the concrete and composite materials. This was an acceptable assumption as shown by small-scale shear pull-off tests undertaken during the project; in these tests the bond did not fail.

A number of difficulties arose when trying to model concrete using the FE analysis technique. These included the heterogeneous nature of the material and the random manner in which the aggregate was located within the concrete. In the linear FE analysis, the concrete was assumed to be an isotropic material with linear stress-strain characteristics. Consequently, only the longitudinal stiffness (in compression) and the Poisson's ratio were required for the analysis; values of 28 kN/mm^2 and 0.2 were included for the longitudinal stiffness and Poisson's ratio respectively. These values were taken from published data, reference[8], after variations in them were shown to have only minor effects on the overall behaviour of the beams.

As the APCs used in this investigation were orthotropic materials, it was important to obtain the mechanical properties in three directions, namely longitudinally, transversely and through the thickness. The properties of the UD CFRP and +/-45° GFRP composites used in the linear FE analysis are given in Table 2. The properties of the materials in the other directions were generally obtained from the material supplier. The value of the Poisson's ratio for the +/-45° GFRP was greater than 0.5. This is unusual for conventional engineering materials but such a value is consistent for modern elastomeric materials. This value will only give a singularity in the finite element computation if the exact value of 0.5 is used.

Mechanical Property	+/-45° GFRP	UD CFRP
Longitudinal stiffness (kN/mm^2)	13.14	85.73
Transverse stiffness (kN/mm^2)	13.14	6*
Through-thickness stiffness (kN/mm^2)	6*	6*
Longitudinal Poisson's ratio	0.57	0.23
Transverse Poisson's ratio	0.3*	0.1*
Through-thickness Poisson's ratio	0.3*	0.1*
Longitudinal shear modulus (kN/mm^2)	4.61	4.24
Transverse shear modulus (kN/mm^2)	6*	3*
Through-thickness shear modulus (kN/mm^2)	6*	3*

* Taken from Manufacturer's data

Table 2: Showing the properties used in the linear FE analysis for the different composite materials

Non-linear FE analysis

As expected, the actual performance of the hybrid beams after serviceability loads was non-linear. Consequently, to obtain an understanding of the behaviour of the beams towards failure, it was necessary to develop a FE model to take into account the non-linearity of the beam system. There were three basic types of non-linearity which could have been significant in the analysis of the beam, (i) geometric, (ii) boundary and (iii) material. For the hybrid beams used in this study, the main concern was the non-linearity of the materials and the geometric non-linearity of the beam Type A (designed to buckle in the webs).

ABAQUS allows the non-linearity of materials to be defined by the user in the form of solution-dependent variables, for example strain. In this study, the longitudinal strain was paired with different mechanical properties to give corresponding data sets. At each increment of load, the strain of the material was calculated and the stiffness, Poisson's ratio or stress was modified to the value given in the data sets. If the strain was between two values defined in the data sets, linear interpolation was used to calculate the corresponding stiffness etc.

The non-linearity of concrete has been extensively studied. For the purpose of this study, it was decided to use the material properties from reference[8] for the non-linearity of the concrete; these are presented in Table 3. The CONCRETE command within ABAQUS allowed the compressive stress to be paired with the plastic strain.

The same solution-dependent methodology utilised with the concrete properties was undertaken for the +/-45° GFRP, i.e. the strain at a given load was calculated before modifying the stiffness and Poisson's ratio with the different value. Only the longitudinal properties were varied as the transverse and through thickness properties were not obtained experimentally. The values used in the analyses are given in Table 4.

Compressive Stress (kN/mm^2)	Plastic Strain
0.02	0
0.03	0.0005
0.04	0.001125
0.05	0.001875
0.06	0.0031875
0.065	0.004675
0.07	0.006125
0.075	0.008875
0.08	0.012375
0.085	0.017373

Table 3: Showing the non-linear stress-strain properties used for the concrete

Strain	Longitudinal Stiffness (kN/mm^2)	Poisson's ratio
0	16.93	0.547
0.003	14.48	0.552
0.006	12.46	0.584
0.009	10.58	0.614
0.012	9.00	0.640
0.015	7.77	0.664
0.018	6.77	0.674
0.020	6.23	0.675

Table 4: Showing the non-linear properties used for the +/-45° GFRP material

RESULTS

The results of the numerical modelling of both types of beam are compared with experimental values published elsewhere references[4,5]. The comparisons of the linear, non-linear and experimental results are plotted in Figures 2, 3 and 4; these show plots of load-deflection, load-microstrain on the concrete and load-microstrain on the flange respectively.

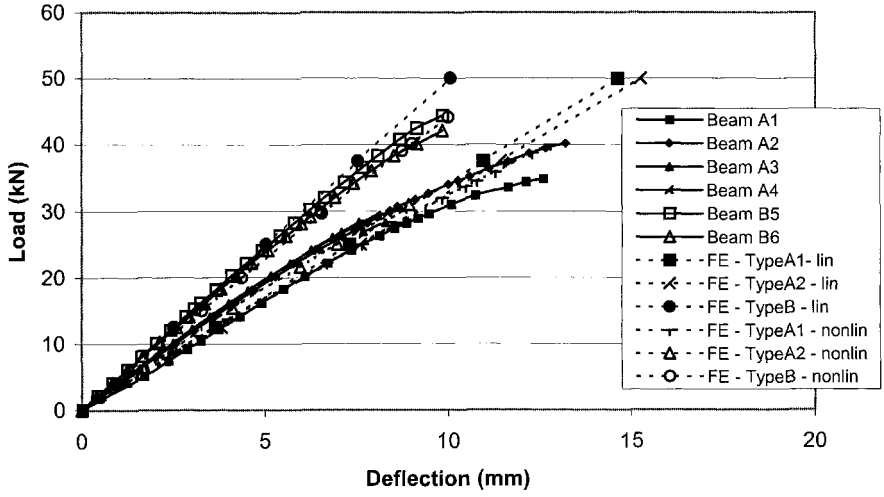


Figure 2: Plot of load against deflection for all beams

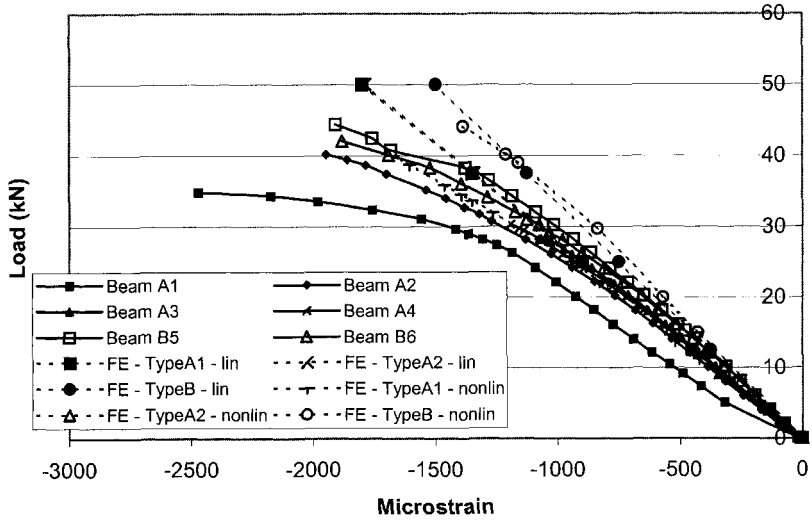


Figure 3: Plot of load against microstrain on the concrete surface for all beams

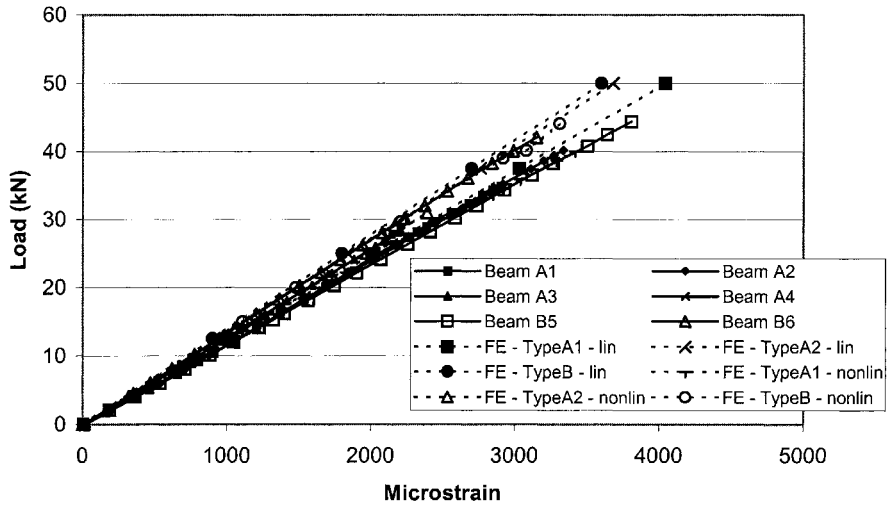


Figure 4: Plot of load against microstrain on the flange for all beams

As expected, the results show that the non-linear FE curves provide a more accurate representation of the behaviour of these types of beam. The heterogeneous nature of the compressive concrete in the beam caused the concrete strain to be highly non-linear. Consequently, after the serviceability load had been exceeded, the non-linear FE analysis more accurately modelled the experimental results.

DISCUSSION

The linear FE analysis, with the use of linear material properties, provided an acceptable comparison to the behaviour of the hybrid beams at serviceability loads (50% of ultimate); in all of the models that have been developed, the linear FE analysis was within 5% of the experimental results at serviceability. However, as the non-linearity of the experimental curves increased, after the serviceability loads, the percentage difference between the FE model and the experimental curves became more apparent. Indeed, the average difference between the load against deflection, load against strain on the concrete surface and load against strain on the flange plots towards failure were 5%, 15% and 2% respectively.

The differences between the experimental results and FE models are likely to be caused by a number of reasons. These include, to varying degrees; (i) the variability of the APC materials, (ii) the variability of the concrete properties, (iii) the simplification of the modelling of stiffeners and diaphragms, (iv) the bond between the concrete and APC material was assumed to be perfect (see previous comment) and (v) slight variations in the cross-sections of the beams due to manual manufacturing techniques. Although the non-linear FE analysis certainly improved the accuracy of obtaining the deflection plot, particularly when compared to the linear analysis, there was still a 15% difference in the value of the strain on the concrete surface as certain beams approached failure. The capability of the non-linear analysis to accurately

predict the behaviour of the strain in the concrete was most likely hampered by the variability of the material and by the reliance of the non-linear material property data.

CONCLUSIONS

The investigation concluded that the geometry of hybrid beams could be effectively modelled in three dimensions utilising Patran 2000 as a pre-processor and ABAQUS v5.8 as the analysis tool and post processor. The linear FE analysis accurately predicted the load-deflection behaviour of the Type B beams at serviceability loads (20 kN). The linear prediction of the deflection for the Type A beams was less accurate due to the discrepancies in the behaviour of the thin walled web. The prediction of the strain in the concrete and flange was within 5% of experimental values at serviceability loads for all beam types. After serviceability loads, the linear analysis could not accurately predict the load-deflection behaviour or the change in strain of the concrete due to the non-linearity of some of the constituent materials. However, as the CFRP is linear-elastic to failure, the linear analysis compared well with the experimental values for the strain in the flange for all beam types. The results of the non-linear analysis improved the accuracy of the model to predict the behaviour of the beams. This was particularly evident with the plots of load against deflection and the strain in the concrete after serviceability loads.

ACKNOWLEDGEMENTS

The authors gratefully acknowledge the financial support provided by the European Commission. Thanks are also due to the Partners of COMPCON, Dr H. Garden (Taylor Woodrow), Mr E. Shahidi & Dr T. Cordon (ACG), Ir F. Tolman (HBG), Ir T. Siemes & Ir G. van den Berg (TNO) and Mr F. Hue (Dragados).

REFERENCES

1) V. M. Karbhari and L. Zhao, 'Use of composites for 21st century civil infrastructure', *Computer Methods in Applied Mechanics and Engineering*, 2000 **185** 433-454.

2) PATRAN, Version 2000, MacNeil-Schwendler Co. 2000.

3) ABAQUS user's manual – version 5.8, Hibbit, Karlsson & Sorenson, Pawtucket, R.I. 1998.

4) J Hulatt, L. Hollaway and A. Thorne, 'The use of advanced polymer composites to form an economic structural unit', *Construction and Building Materials*, 2003 **17** 55-68.

5) J Hulatt, L. Hollaway and A. Thorne, 'Short term testing of hybrid T-beam made of new prepreg material', *Journal of Composites for Construction*, 2003 **7/2** 1-10.

6) J Hulatt, L. Hollaway and A. Thorne, 'Preliminary investigations on the environmental effects on new heavyweight fabrics for use in civil engineering', *Composites: Part B*, 2002 **33** 407-414. Not complete.

7) K-J Bathe, 'Finite element procedures in engineering analysis', Prentice-Hall, Inc., Englewood Cliffs, New Jersey, 1982.

8) A. M. Neville, 'Properties of concrete', Fourth Edition, Longman 1995.

STATIC AND FATIGUE BEHAVIOR OF GFRP BRIDGE DECKS ADHESIVELY BONDED TO STEEL GIRDERS

Prof. Dr. Thomas Keller, Herbert Gürtler
Composite Construction Laboratory (CCLab), Swiss Federal Institute of Technology
CH-1015 Lausanne, Switzerland

ABSTRACT

This paper documents the results of a research project, funded by the Swiss Federal Roads Authority and industry partners and carried out at the Composite Construction Laboratory (CCLab) of the Swiss Federal Institute of Technology in Lausanne. The research project concerns the development of hybrid bridge concepts and corresponding dimensioning methods, using GFRP bridge decks, steel main girders and adhesive connections.

INTRODUCTION

Bridge decks are a promising application of glass fiber-reinforced polymers (GFRP). The favorable characteristics of GFRP bridge decks are a high strength combined with a small dead load (approximately 20% of a concrete deck) and a large tolerance for frost and de-icing salts. The small dead load enables short installation times with minimum traffic interference as well as a possible increase of the live load of existing bridges via replacement of the heavy concrete decks [1].

In order that GFRP bridge decks can be used economically and competitively in the future, they must be able to participate in the bridge's longitudinal direction as the upper chord of the main girders. Such participation is known as composite action. Full composite action is characterized by a plane strain distribution in the composite section, fulfilling the hypothesis of Bernouilli (cf. Figure 1). First, this requires a stiff shear connection of the GFRP deck with the main steel or concrete girders. In this respect, within this project, adhesive bonding is considered a reliable and economical connection technique.

In addition, for full composite action, the shear transmission must be guaranteed also within the GFRP deck itself from the lower to the upper face panels in the bridge's longitudinal direction. For that purpose, together with a sufficient in-plane shear resistance, a sufficient in-plane shear stiffness of the deck is required. Furthermore, for an efficient global contribution, a sufficient in-plane compression stiffness and resistance of the GFRP deck is necessary.

Within this research project, these deck parameters were determined for an existing pultruded deck system, using a new experimental method on small-size deck specimens. The resulting parameters served for the dimensioning of two full-size hybrid girders, consisting of the same pultruded deck system adhesively bonded to steel girders. The results of the experiments performed on these hybrid girders represent the basis for a future deck type independent dimensioning method for hybrid GFRP girders.

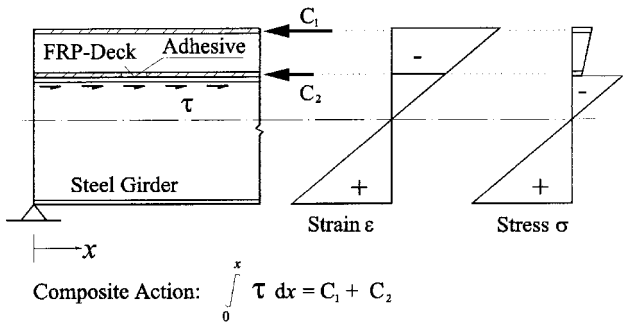


Figure 1: Principle of full composite action between steel girders and FRP bridge decks.

EXPERIMENTAL PROGRAM

Small-size experiments on deck specimens

The previously mentioned deck parameters were determined for an existing pultruded GFRP deck system (DuraSpan 766). The experimental set-up is shown in Figure 2. Two different loading and support configurations were used in order to measure the in-plane compression and in-plane shear behavior. Three specimens with height 730 mm and width 600 mm, composed of 3 pultruded shapes each, were examined in each configuration.

The specimens, arranged between two steel plates 800x800x80 mm, were concentrically or asymmetrically loaded transversely to the pultrusion direction along the whole 600 mm width. The load was applied displacement-controlled at a rate of 1.5 mm/min. The load-displacement behavior was measured, among other things. The detailed set-up, instrumentation and program are described in [2].

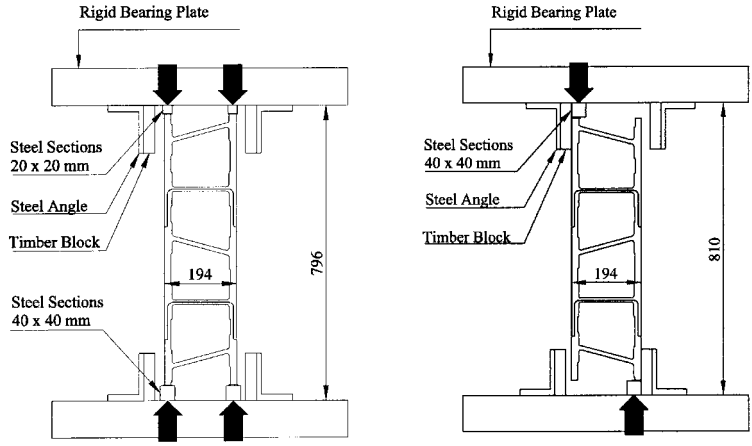


Figure 2: Experimental set-up for in-plane compression and shear experiments.

Full-size experiments on hybrid girders

The static and fatigue behavior of two identical full-size experimental girders (called Fix 1 and Fix 2) was investigated in a four-point loading configuration (cf. Figure 3). The hybrid girders consisted of a welded steel girder S355 and an adhesively bonded GFRP bridge deck. The length of the girders was 7.90 m, the span 7.50 m. The steel girders' height was 500 mm, the dimensions of the upper flanges were 220x10 mm, the lower flanges 250x15 mm and the webs 475x10 mm. The GFRP decks had a width of 1.50 m and a depth of 194 mm. The adhesive layers between the GFRP decks and the upper flanges of the steel girders had a width of 196 mm. With a hard and soft shim arrangement, tolerances of the upper flange of up to 4 mm could be compensated for, having, at the same time, a guaranteed minimal thickness of the adhesive layer of 6 mm [4].

A two-component epoxy adhesive (SikaDur 330) was used for the deck-to-girder connections. The stress-strain behavior of the adhesive in tension and compression was investigated according to ISO 527 and ASTM 695 in a preceding research project at the CCLab [3]. The resulting properties are represented in Table 1.

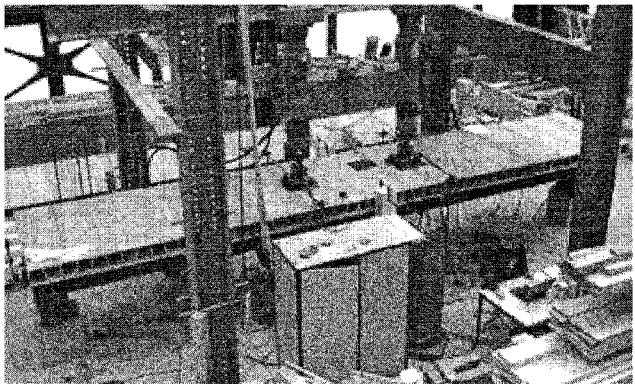


Figure 3: Four-point set-up for full-size hybrid girders.

Table 1: Tension and compression properties of the epoxy adhesive used

Type of loading	Failure stress [MPa]	Failure strain [%]	E-Modulus [MPa]
Tension (5 specimen)	38.1 ± 2.1 (failure)	0.97 ± 0.13 (failure)	4'552 ± 138
Compression (5 sp.)	-80.7 ± 2.6 (max.)	-3.68 ± 0.08 (max.)	3'050 ± 33

The above described girder dimensions resulted from a preliminary dimensioning of a reference bridge of 15 m span and 12 m width for three lanes subjected to traffic loads according to Eurocode 1. The goal was to have a similar shear stress magnitude in the adhesively bonded girder-to-deck connections of the experimental girders under four-point-loading as in the bridge girders under Eurocode loading. The relatively small span of 15 m was chosen because, as the calculations showed, the maximum shear stresses in the adhesive layer decrease with increasing span due to the decreasing contribution of the GFRP deck to the stiffness and resistance of the hybrid girders. Choosing a span smaller than 15 m was considered as not reasonable.

The preliminary dimensioning of the bridge and the experimental girders was done as for bridges with steel girders and concrete decks, assuming full composite action and using the characteristic deck values indicated in Table 2. The determinant design criterion for the bridge main girders at the serviceability limit state (SLS) was a maximum deflection of 1/600 of the span. At failure load (FLS), it was required that failure of the hybrid girders would occur in the GFRP decks due to compression loading during the yielding of the bottom steel flanges in order to have a ductile behavior. The corresponding maximum shear stresses in the adhesive connections at failure were estimated to 2.1 MPa. Subjected to these stresses, failure neither in the adhesive connections, nor through shear loading in the GFRP decks themselves was expected.

Accordingly, the following estimated experimental loads per jack and maximum deflections at mid-span resulted from calculation: 2x80 kN and 8 mm at SLS and 2x415 kN at FLS. Before the quasi-static experiment up to failure, the second girder (Fix 2) was subjected to ten million fatigue load cycles between 2x10 kN and 2x40 kN at a frequency of 2.0 Hertz. The corresponding shear stresses in the connection varied between 0.05 and 0.2 MPa which matched again with the variation of the stresses in the girders of the reference bridge subjected to Eurocode 1 fatigue loads. The ten million load cycles correspond to approximately 600 truck loads per day per lane during 250 days per year and during 70 years of service life.

In order to investigate the increase of the stiffness and failure load due to composite action, a reference steel girder with identical dimensions but without GFRP deck was examined. The details of the set-up, instrumentation and program for the three girders are described in [4].

EXPERIMENTAL RESULTS

Small-size experiments on deck specimen

The main results of the small-size experiments are shown in Figure 4. More detailed information is available in [2]. Idealized axial and shear stress - strain curves were derived from the measured load-deformation behavior. Due to system redundancy, the deck specimens showed an excellent system ductility, above all under shear loading. The resulting characteristic deck system values for in-plane compression and shear loading are summarized in Table 2.

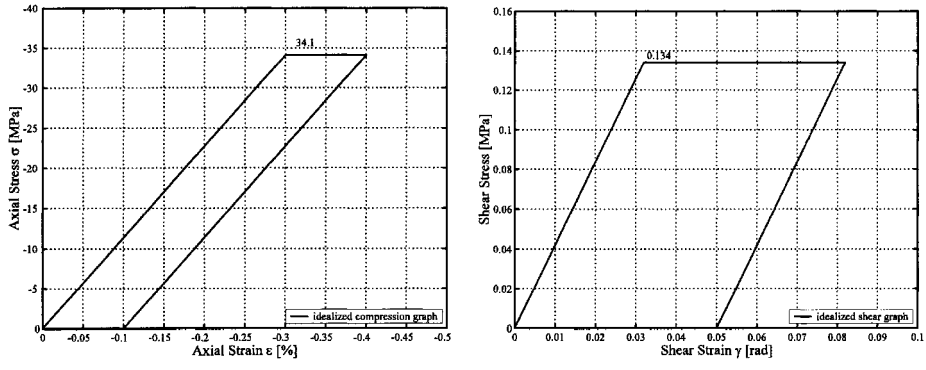


Figure 4: Idealized axial and shear stress-strain behavior of the GFRP deck system used.

Table 2: Characteristic deck system values of the GFRP deck system used

Type of loading	Modulus [MPa]	Failure stress [MPa]
In-plane compression	E-Modulus: 11'700	-34.1
In-plane shear	G-Modulus: 4.9	0.134

Full-size experiments on hybrid girders

Quasi-static experiments up to failure were carried out for girder Fix 1 and for girder Fix 2 after the ten million fatigue cycles. The behavior of the girders up to the SLS loads was linear elastic (cf. Figure 5). Exceeding the elastic limits, first local delamination failures occurred in the deck due to Vierendeel action (transverse bending in the webs). Subsequently, both girders showed an almost identical and very ductile behavior. At 280 kN per jack, the lower steel flange of girder Fix 1 began to yield, at 305 kN per jack the upper steel flange yielded as well. The corresponding loads for Fix 2 were 230 kN and 320 kN respectively.

At a load of approximately 380 kN per jack, both girders were unloaded in order to study the unloading and reloading paths and the residual plastic deformations. The different paths were almost identical and parallel to the initial elastic loading paths. The residual plastic deformations were approximately 55 mm for both girders.

At a load of 405 kN per jack for girder Fix 1 and 415 kN per jack for Fix 2, one of the epoxy bonded joints in the lower deck face panels between the jacks failed in shear in each girder. The vertical mid-span deflections at the onset of failure were 140 mm for Fix 1 and 172 mm for Fix 2.

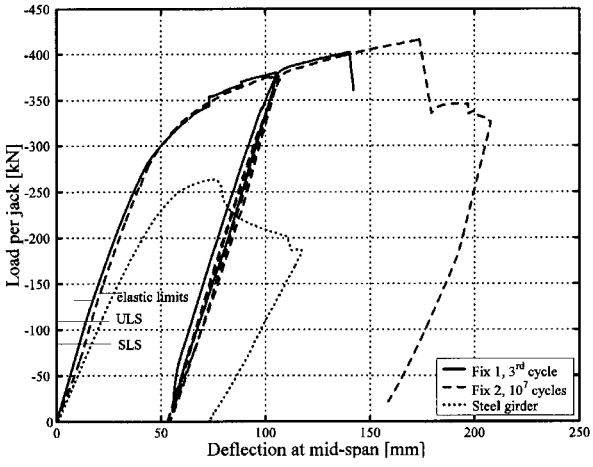


Figure 5: Measured load-deflection behavior of the experimental girders at mid-span.

As the experiments were conducted displacement-controlled, the loads decreased immediately after these failures. The Fix 1 experiment was stopped at this point while the Fix 2 experiment was continued displacement-controlled. The load of Fix 2 decreased to 340 kN per jack (cf. Figure 5). With increasing vertical deflection, the

adhesive connections between the decks and the upper steel flanges began to open in the area between the jacks. Thereby, the failure occurred in the outer layer of the GFRP deck, not in the adhesive. The upper steel flange, which was no longer fixed, showed considerable plastic out-of-plane deformations, similar those of the reference girder (cf. below). Subsequently, two supplementary hinges formed in the deck due to further failures in the transversal joints and resulted in the upward buckling of the deck (cf. Figure 6, residual deformation after discharging). The experiment was stopped at 207 mm vertical deflection which corresponded to a ratio of span/36.

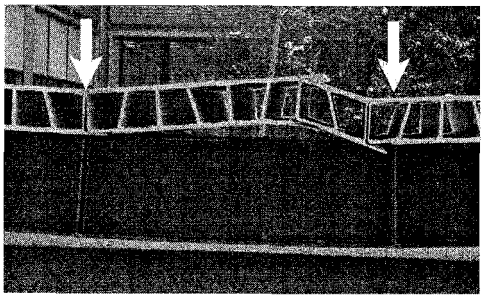


Figure 6: Failure of girder Fix 2 (residual deformation after demounting).

Figure 5 shows also the behavior of the reference steel girder. The upper flange began to yield at approximately 185 kN per jack. At approximately 250 kN per jack, the upper yielding flange began to buckle at one location between the jacks. The load then dropped down after having reached a maximum of 263 kN per jack and 75 mm vertical deflection. The experiment was stopped at 117 mm deflection at mid-span.

The axial strain distributions in the cross-sections at mid-span for girder Fix 1 and Fix 2 were also measured [4]. The measured strain distributions of both girders were almost identical but didn't remain plane over the whole section height. The measured axial strains in the upper face panels at failure were approximately 30-40 % smaller than the strains in the lower deck face panels what explains also the initial failure in the lower face panel. Thus, although the load was fully transmitted through the adhesive girder-to-deck connections, only partial composite action was achieved. The precedent fatigue experiment didn't influence the strain distribution in girder Fix 2.

DISCUSSION

Composite action

The prediction of the girders' behavior assumed full composite action between all components of the cross-sections. As the experiments showed, the adhesive connections between GFRP decks and steel girders were sufficiently stiff and resistant in order to guarantee a full composite action between steel girders and lower deck face panels at all load levels up to failure. The decks themselves, however, were too flexible in their planes in order to fully activate the upper face panels. Therefore, the upper face panels could only partially contribute to the resistance.

Nevertheless, at the SLS and FLS, the influence of the reduced composite action was not very pronounced. The predicted maximum deflections of the girders and failure loads still matched the measured values quite well (cf. Table 3).

The total safety factor amounted to FLS/SLS = 405/80 = 5.1 for girder Fix 1 and 5.2 for girder Fix 2. Deflections at the SLS were decreased by approximately 23% and failure loads increased by approximately 56% compared to the behavior of the reference steel girder. In particular, the improved behavior at the SLS due to composite action is mentionable since, normally, the SLS is determinant in the design of hybrid GFRP girders.

On the other hand, it should be noted that the possible contribution of this deck system type to the stiffness and resistance of a composite girder decreases markedly with increasing span due to the low compression stiffness of the deck, independently of the portion of composite action within the deck itself.

Table 3: Comparison prediction - measurements

Girder	SLS - max. deflection [mm] predicted / measured	FLS - failure load [kN] predicted / measured
Fix 1	8 / 10	2x415 / 2x405
Fix 2	8 / 13	2x415 / 2x415

Fatigue behavior

The fatigue experiment performed on girder Fix 2 showed no indications of degradation or damaging of the girder. Significant changes in the parameters measured and observed (deflections, stiffnesses, strains, failure loads, local and global failure behavior) weren't observed comparing to girder Fix 1. Neither an increase in the hysteresis loop area nor a slope decrease or a lateral shift of the loops could be observed [4].

Dimensioning method

The design criteria used for the hybrid GFRP girders are close to the design criteria for steel girders with concrete decks and shear stud connections. A dimensioning method for hybrid girders with GFRP decks can, therefore, be based on the well-established dimensioning method for steel girders with concrete decks. The following main modifications need to be introduced:

1) The in-plane deck properties of shear and compression stiffness and resistance must be considered.

2) According to the in-plane shear stiffness of the GFRP deck, the portion of participation of the upper deck face panel and the resulting portion of composite action must be considered.

3) The verification of the shear studs behavior must be replaced by a verification of the adhesive connection behavior.

Based on these conceptual aspects, a detailed dimensioning method for hybrid girders, consisting of steel main girders with adhesively bonded GFRP decks, independent of the deck system type, will be developed in the next project stage.

CONCLUSIONS

In the following conclusions, it will be differentiated between research results only valid for the bridge deck system used (marked as ''specific'') and results of general validity for adhesively bonded hybrid GFRP girders (marked as ''general''). The main conclusions at this project stage are:

1) The serviceability limit state is determinant for the design of adhesively bonded hybrid GFRP steel girders (general).

2) Composite action between GFRP bridge decks and steel main girders can increase stiffness and resistance and reduce deflections considerably (general).

3) The portion of composite action in the GFRP deck itself must be verified (general). A reduced composite action was noted for the deck type used. The influence of the reduced composite action, however, was small (specific).

4) The efficiency of the GFRP deck system used as top chord of a composite girder decreases with increasing span. The decrease depends on the deck stiffness in the longitudinal direction (general).

5) Adhesive connection between GFRP bridge decks and steel girders is an advantageous, reliable and economic technique which allows for full composite action (general).

6) Established dimensioning methods with only few modifications can be used (general).

7) It is reasonable and useful to consider the proposed in-plane properties of GFRP decks and the associated experiments for the measuring of these properties. The experiments could be standardized (general).

8) The investigated girders resisted ten million fatigue cycles without any degradations or damage (specific for the deck used, general for adhesive connections).

The main questions that still must be answered concern the behavior of continuous girders (top chord in tension) and the behavior of the adhesive connections in the transverse direction (out-of-plane tension stresses due to uplift forces and deck fixation). Corresponding investigations are currently underway at the Composite Construction Laboratory.

ACKNOWLEDGEMENTS

The authors wish to acknowledge the support of the Swiss Federal Roads Authority; Martin Marietta Composites, Raleigh USA (supplier of the DuraSpan 766 bridge deck elements) and Sika AG, Zurich, Switzerland (supplier of the SikaDur 330 epoxy adhesive).

REFERENCES

1 T Keller, *Use of fibre reinforced polymers in bridge construction*, Structural Engineering Documents 7. International Association for Bridge and Structural Engineering, ISBN 3-85748-108-0, 2003.

2 T Keller, H Gürtler, '*In-plane compression and shear behavior of GFRP bridge decks*', Journal of Composites for Construction, manuscript number CC/2003/022394.

3 T Keller, J de Castro, M Schollmayer, '*Load-carrying behavior of adhesively bonded GFRP-sandwich girders*', Journal of Composites for Construction, manuscript number CC/2002/022333.

4 T Keller, H Gürtler, '*Composite action and adhesively bonded connections between GFRP bridge decks and main girders*' Journal of Composites for Construction, manuscript number CC/2003/022440.

COMBINED PRESSURE/TENSION BEHAVIOUR OF ADHESIVE-BONDED GFRP PIPE JOINTS

J. M. Lees,
University of Cambridge, UK

ABSTRACT

An analysis of bonded GFRP pipe joints is presented. The formulation is based on the theory of beams on elastic foundations where the hoop stiffness of the pipe and coupled sections are modelled as an elastic foundation. A number of different load cases are considered where the relative values of axial load and internal pressure are varied. It is found that the presence of internal pressure will potentially improve the performance of an adhesive-bonded joint under axial tension.

INTRODUCTION

Adhesive joints are widely used as tensile connections for glass fibre reinforced polymer (GFRP) filament wound pipe sections. These joints are typically manufactured using either a bell and spigot system or a coupler to connect two pipe sections (see Fig. 1). This report will focus primarily on the latter system although a number of the principles noted have analogies in a bell and spigot joint.

One important issue in the design of GFRP pipe systems is the material anisotropy which poses certain challenges that do not arise when dealing with an isotropic material like steel. In an isotropic material, the material strengths in all directions are the same. Thus if a thin-walled isotropic pipe section is closed and fully pressurised then, since the hoop stresses will be twice the longitudinal stresses, there will be a reserve capacity for additional axial loads. In an anisotropic material such as filament wound GFRP, the properties in the longitudinal and hoop directions will differ and be a function of factors such as the resin system, the fibre properties, the volume fraction and the winding angle. For pipe applications, most manufacturers design the composite sections for the 1:2 pressure conditions and for example ± 55° winding angles are commonly used[1]. The result is that the mechanical properties in the longitudinal direction tend to be weaker than in the hoop direction and the Poisson's ratios in the axial and hoop directions differ. However, a further consideration is that pipe systems may be subjected not only to pressure but also to other loading conditions. For example, longitudinal stresses will develop as a result of bending and applied axial loads e.g. due to thermal expansion.

In the current work, an analysis that investigates the behaviour of anisotropic- GFRP adhesive-bonded joints subjected to a variety of loading conditions is carried out. In particular, the behaviour due to the interaction of tensile axial loads and internal pressure is considered.

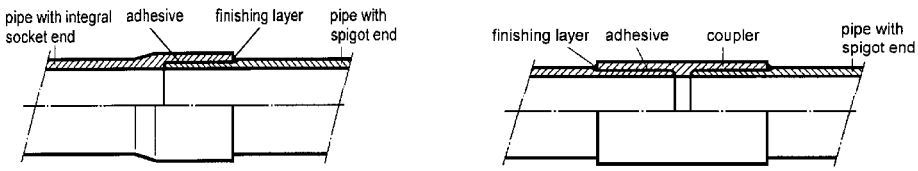


Figure 1. Pipe joints (a) bell and spigot and (b) coupler

Property	
Axial tensile stress	75 MPa
Axial tensile modulus, E_a	12 GPa
Hoop tensile stress	210 MPa
Hoop tensile modulus, E_h	20.5 GPa
Shear modulus	11.5 GPa
Poisson's ratio (axial*/hoop), μ_{ah}	0.65
Poisson's ratio (hoop*/axial), μ_{ha}	0.38
Glass content (by volume)	52±7%

*first index is contraction direction, second is load direction

Table 1. Pipe material properties[2]

JOINED PIPE SPECIMENS

The pipe joint considered in the analytical programme consists of two sections of 80 mm internal diameter, 3.2 mm thick GFRP filament wound pipes connected using a coupler. In order to make a connection, the ends of the pipe sections are shaved. To produce a joint, adhesive is applied to the shaved pipe ends and the inside face of the coupler. Each end of pipe is then inserted into the coupler and the joint is heat cured. The properties of the pipes have been supplied by the manufacturer and are shown in Table 1. The dimensions of shaved pipe sections used and the couplers provided by the same manufacturer are shown in Fig. 2.

The analytical work presented here is being carried out in conjunction with an experimental programme on adhesive-bonded pipe joints. As part of the programme, an innovative testing rig where the tension and pressure can be applied independently has been developed. The pressurisation rig is self-equilibrating and thus only applies pressure to a defined section of the joint and pipe section (shown schematically in Fig. 3). The tensile loading system uses grips manufactured in accordance with ASTM D 2105-97[3].

ANALYTICAL FORMULATION

To investigate the interaction between the pressure and tension, an analysis based on the theory of beams on elastic foundations was undertaken. In the following, the equations for a beam on an elastic foundation are presented (further details can be found in Hetenyi[4]) and the application of the formulae to cylindrical sections is discussed in connection with the analysis of the GFRP pipe joints.

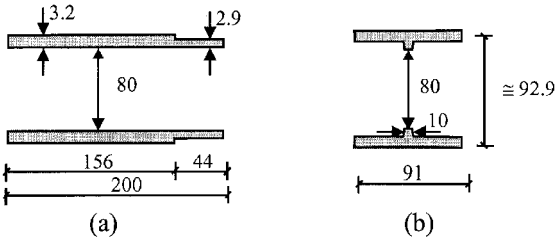


Figure 2. Section through (a) pipe and (b) coupler (all dimensions in mms)

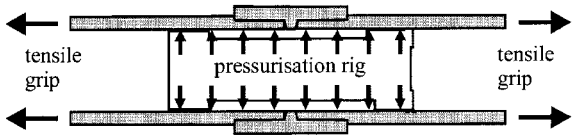


Figure 3. Schematic diagram of loads applied to joined section

Beams on elastic foundations

A small beam element of length dx, supported on an elastic foundation with a modulus k is shown in Fig. 4(a). The applied distributed load is denoted as q and the shear forces and moments are Q and M respectively. The beam deflection is noted as y which is defined as positive downwards. From vertical equilibrium:

$$\frac{dQ}{dx} = ky - q \tag{1}$$

Differentiating the equation of beam bending twice and noting that $Q=dM/dx$ gives:

$$EI\frac{d^4y}{dx^4} = -\frac{d^2M}{dx^2} = -\frac{dQ}{dx} \tag{2}$$

From Equations 1 and 2, an expression for the deformation of a beam on an elastic foundation can then be determined:

$$EI\frac{d^4y}{dx^4} = -ky + q \tag{3}$$

In unloaded regions where $q = 0$, Equation 3 reduces to:

$$EI\frac{d^4y}{dx^4} = -ky \tag{4}$$

The solution of Equation 4 is of the form $y = e^{mx}$ which leads to:

$$y = e^{\lambda x}(C_1\cos\lambda x + C_2\sin\lambda x) + e^{-\lambda x}(C_3\cos\lambda x + C_4\sin\lambda x) \tag{5}$$

where

$$\lambda = \sqrt[4]{\frac{k}{4EI}} \tag{6}$$

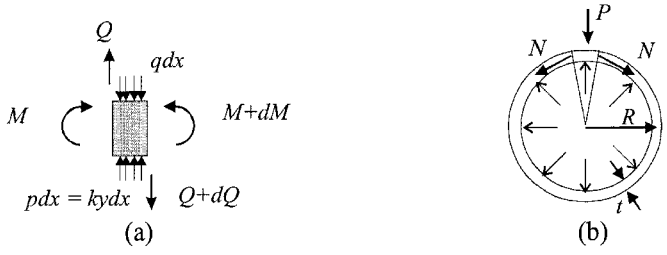


Figure 4. Beam on elastic foundation (a) forces acting on an element (b) pipe analogy

Since relationships between the deflection, the rotation θ, moment and shear are known:

$$\frac{dy}{dx} = \tan\theta \,, \; -EI\frac{d^2y}{dx^2} = M \,, \text{ and } -EI\frac{d^3y}{dx^3} = Q \qquad \text{(7a-c)}$$

then, once an expression for y has been found, these quantities can all be determined by taking the appropriate derivatives.

The deflection of an infinite beam is considered initially and the appropriate boundary conditions used to determine the unknown constants C_1, C_2, C_3 and C_4. Once the infinite case has been solved, this solution can be used to find the deflections of semi-infinite or finite beams by imposing appropriate end conditioning forces and the principle of superposition.

Advanced composite cylindrical pipe and coupler analysis

In order to apply this theory to the current work, the hoop stiffness of the pipe and coupled sections are modelled as an elastic foundation. The sections are assumed to be thin-walled with an axially symmetric load. The small diameter pipes and couplers used in this study are not particularly thin-walled, but nevertheless, the formulation provides a possible closed-form methodology to demonstrate the influence of combined pressure and tension loadings. A further complication is that Hetenyi's derivation is based on the use of isotropic materials whereas the GFRP pipes are anisotropic. Thus in the following, a distinction is made between the hoop and the longitudinal properties and Hetenyi's equations are modified to reflect the material anisotropy.

If an internal pressure is applied to a cylindrical section, the section will expand by a radial displacement y. This displacement will generate a circumferential tension (see Fig. 4(b)) and the resultant of these forces in the radial direction, which opposes the expansion is:

$$P = \frac{E_h t}{R^2} y \qquad (8)$$

where t is the thickness of the cylinder, R is the cylinder radius and E_h is taken to be the hoop modulus of elasticity. Hence it is possible to consider a longitudinal element (taken as a unit width for simplicity) as a beam on an elastic foundation of modulus k where (see Fig. 4(a)):

$$k = \frac{E_h t}{R^2} \qquad (9)$$

For an anisotropic material, the flexural rigidity term EI is as follows:

$$EI = \frac{E_a t^3}{12(1-\mu_{ah}\mu_{ha})} \qquad (10)$$

where E_a is the axial modulus of elasticity and μ_{ah} and μ_{ha} are the Poisson's ratios relating the hoop loading to the axial contraction and the axial loading to the hoop contraction respectively.

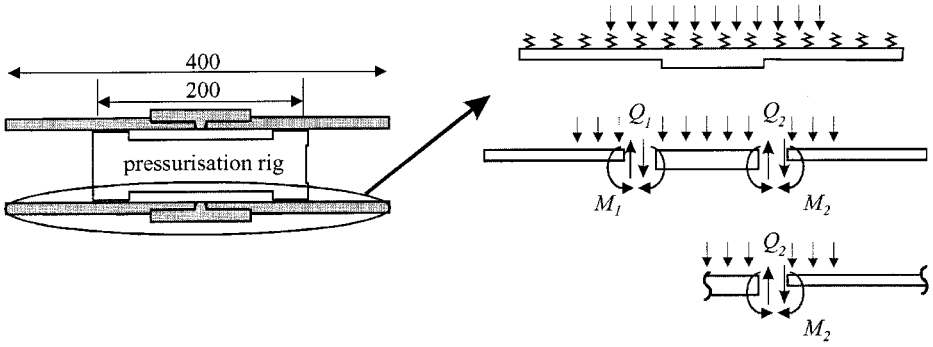


Figure 5. Joined pipe section subjected to tension and pressure loading

ANALYSIS OF JOINED PIPE SECTIONS

In the model of the pipe joint, the shaved end of the pipe plus the coupler are taken to be a composite cylindrical section (see Fig. 5). The adhesive interface is assumed to be fully bonded and not explicitly taken into account. However, this could be included in a more rigorous analysis. Thus the free lengths of pipe are modelled as cylinders with a constant thickness and the coupled section is modelled as a cylinder with a larger thickness. In the first instance, the material properties of the coupled section are assumed to be the same as the pipe sections.

The problem is broken down further by considering the coupled section and the pipe-only sections to be separate beams. In this way standard load cases can be superimposed on each beam. Once the deflections for each load case have been calculated, the rotations, moments and shears can be determined by taking the appropriate derivatives. Further details can be found in Hetenyi[4]. Compatibility conditions for the displacement and rotation at the end of the joint can then be used to connect the beam sections. A summary of the applied loads and continuity reactions are shown in Table 2 and Fig. 5. It is of note that the characteristic lengths of both the pipe and the coupled sections are quite long (i.e. $\lambda L > \pi$) , hence both the pipe and coupler can be considered as semi-infinite without an undue loss of accuracy. As the problem is symmetrical, only the loading on the right hand side of both the coupled section and the pipe are shown in Table 2. Due to the configuration of the pressurisation rig, pressure was applied only to a specified region of the pipe (case 1(b) in Table 2). The influence of the axial load was simplified by representing the load as a uniform contraction.

RESULTS AND DISCUSSION

A programme was written in MATLAB[5] incorporating the relevant equations. Four different load conditions were considered. In the first case, a working pressure of 32 bar and an applied axial tensile load of 20 kN were applied simultaneously (this roughly corresponds to a 1:2 loading ratio). In the second case, the system was not pressurised but an axial load of 60 kN was applied. In the third case, the working pressure was applied with an axial load of 60 kN, and finally a case where a pressure of 16 bar was applied in conjunction with an axial force of 60 kN was included. The predicted displacement profiles along half the length of the joined pipe system for each of these cases are shown in Fig. 6. In this figure, a negative deformation corresponds to a contraction.

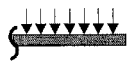
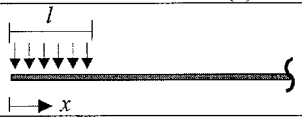
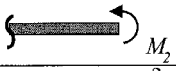
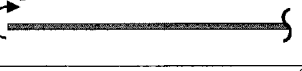
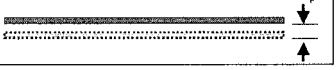
		coupled section	pipe (right hand side)
		semi-infinite beam (a)	semi-infinite beam (b)
pressure	1) uniform load		
continuity reaction	2) shear		
continuity reaction	3) moment		
axial load	4) uniform contraction		

Table 2. Beam models and load cases

Since the axial load was modelled as a uniform contraction, it can be seen that the pipe contracts in the unpressurised regions. In the pressurised regions, the sections either expand or contract depending on the relative values of the pressure and the axial load. When the pressure is relatively high, the sections tend to expand. At low pressures and a moderate level of applied axial load, the pressurised regions exhibit an overall contraction.

The critical point in terms of an adhesive joint performance is at the end of the coupled region where the stress concentrations are the highest. In particular, the development of peeling stresses in this region are detrimental for an adhesive joint since these can lead to premature failure due to a crack propagating through the adhesive and/or adherend.

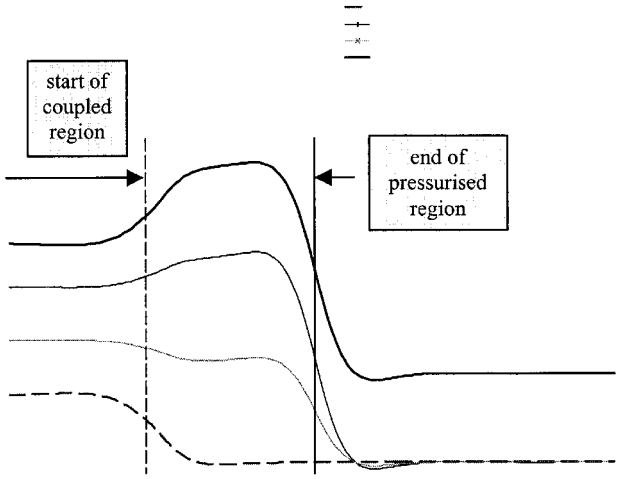


Figure 6. Predicted deformations along the length of a joined pipe section

For the two cases considered where the pressure was 16 bar or lower, it can be seen from Fig. 6 that the adjacent pipe-only section tries to pull away from the coupled region resulting in undesirable tensile peeling stresses. In contrast, when higher internal pressures are applied, the adjacent pipe regions expand to a greater extent than the stiffer coupled region thereby pressing the pipe against the coupler and generating compressive stresses at the end of the joint.

This behaviour suggests that the most critical loading for an adhesive joint will be when the internal pressure is low and the axial load is high since under these circumstances tensile peeling stresses will be generated at the end of the joint. This also suggests that a joint capacity based on closed end pipe joint tests (1:2 pressure conditions) may give unconservative results for an adhesive joint where axial loads occur in the absence of pressure. Further experiments are being carried out to confirm the joint performance under combined loading conditions and the results will be the subject of a future publication.

CONCLUSIONS

A preliminary analysis of the behaviour of an adhesive-bonded GFRP joint has shown how pressure and tension effects can potentially interact. In particular, an internal pressure pushes the pipe section against the coupler and helps to reduce any peeling stresses in the adhesive joint. Thus the analysis demonstrates that it is likely that axial loads not connected to pressurisation are most critical for an adhesive joint.

ACKNOWLEDGEMENTS

The author would like to thank Allan McRobie for his invaluable help and guidance with the analysis of the joint behaviour. This work was in part funded under EPSRC grant GR/R09770.

REFERENCES

1. UKOOA, *Specification and Recommended Practice for the Use of GRP Piping Offshore*, UK Offshore Operators Association. March 1994

2. Wavistrong Epoxy Pipe Systems, *Engineering Guide for Wavistrong Filament Wound Epoxy Pipe Systems*. Future Pipe Industries B.V. Hardenberg, Netherlands. 1997.

3. ASTM D 2105-97, *D2105-97 Standard Test Method for Longitudinal Tensile Properties of "Fiberglass" (Glass-Fiber-Reinforced Thermosetting-Resin) Pipe and Tube*. ASTM. 1997

4. M. Hetenyi, *Beams on Elastic Foundation: Theory with Applications in the Fields of Civil and Mechanical Engineering*, University of Michigan Studies Scientific Series XVI, 1961

5. The Mathworks Inc, *MATLAB*, Version 6.1.0.450, Release 12.1, 2001

ASPECTS ON THE BEHAVIOUR OF BOLTED JOINTS FOR PULTRUDED FIBRE REINFORCED POLYMER PROFILES

J T Mottram[1], C Lutz, and G C Dunscombe
School of Engineering, University of Warwick, Coventry, CV4 7AL

ABSTRACT

Two small test series are presented to study new aspects on the behaviour of bolted joints for Pultruded Fibre Reinforced Polymer (PFRP) profiles. One plate-to-plate test series considers the effect on resistance of subjecting multi-bolted joints for 10 minutes to a constant load, which increases in 5% increments from 80% of the stroke controlled ultimate load. In the second series, a structural steel connection test procedure is adapted to determine the approximate static coefficient of friction for PFRP on PFRP. Salient results are presented and the findings from the two test series are shown to be relevant to the evaluation and refinement of current design procedures.

Key words: Joining technology, Materials characterisation, Safety and reliability

INTRODUCTION

PFRP structural shapes and systems consist of thin-walled composite profiles having overall dimensions up to 1000 mm and wall thicknesses up to 25 mm [1-3]. Reinforcement is E-glass fibre in two forms, namely unidirectional (UD) rovings and continuous filament (or strand) mats. The matrix is a thermoset resin such as polyester or vinylester, which often contains filler and other additives. PFRP members are used in primary load-bearing structures with steel bolts being the preferred method of connection [4]. Primary joints are expected to provide strength and stiffness to the PFRP structure throughout its life [5]. Failure of such joints would constitute major structural damage and be hazardous to life. The safe and reliable design of bolted joints is therefore clearly a priority.

Mottram and Turvey [6] have recently written a review on the physical testing of plate-to-plate PFRP bolted joints. Its aim was to consider what the test data offers us for the appraisal of existing connection design procedures [5, 7]. In their review the authors present information on the 16 series of tests that for, single-bolted and multi-bolted, double lap joints provide some 1700 ultimate strength results. They found that different joint variables had been studied since the 16 series had different objectives, to reflect the current state of guidance on joint design and installation in the pultruders' design manuals [1-3] and elsewhere [5].

A majority of previous PFRP test joints [6] had the bolting tightened to the finger-tight condition and were ultimately failed subjected to monotonic stroke or load rates. Of the many variables that can be changed in bolted joint detailing, previous testing [6] has not considered either the effect on resistance of holding a constant load or the effect of varying bolt torque on the load transferred by friction (i.e. via shear forces over the contacting surfaces). In this paper the authors presented preliminary results from two small test series which had the objective of initiating investigations on the behaviour of these two aspects for the structural performance of PFRP bolted joints.

CONSTANT LOAD TESTS

The purpose of the constant load tests is to find out if the resistance of bolted joints changes by the procedure in which a concentric load is applied.

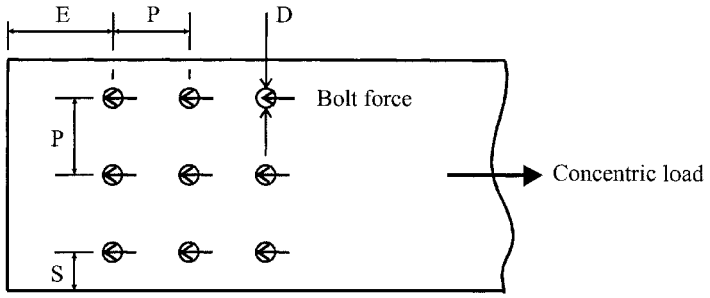


Figure 1. Plate-to-plate joint geometry definitions, D is bolt diameter, E is end distance, S is side distance, and P is pitch distance.

Figure 1 shows the 3×3 multi-bolted joint type used. The material is PFRP EXTREN® Series 625 flat sheet of 6.35 mm nominal thickness [1]. Bolting is steel of size M10 and grade 8.8. There was no thread in contact with the PFRP and the plain shank had a diameter (D) of 9.8 mm. Holes were drilled using a tungsten carbide tipped drill bit. For the drilled hole diameter of 10 mm this gave a 0.2 (0.1-0.3) mm hole clearance. Bolt torque was the finger-tight condition, believed to be < 3 Nm [8]. Joint resistance was established with the direction of concentric load parallel to the orientation of the UD rovings in the PFRP flat sheet.

Two different 3×3 joints were tested using a test fixture that subjected a joint to double-lap shear with the central plate of PFRP, and the two outer plates of 8 mm thick structural grade steel. No washers were present, such that the steel and PFRP plate faces were in full contact. Both joints had the geometric ratios E/D and P/D constant at 6 and 4, respectively. In the first joint group the geometric ratio S/D was 2. This ratio was increased to 4 in the second group.

Three specimens per group were also tested subjected to a constant stroke rate of 0.01 mm/s. Initial damage and ultimate failure occurred at the same maximum load; the ultimate load. When S/D = 2, the stoke controlled ultimate loads, in ascending order, are 72.3, 73.4 and 75.7 kN, while they are higher at 85.3, 92.2 and 95.1 kN when S/D increases to 4. Load increments for the load control tests are based on the minimum load from these three ultimate loads. Thus the 100% load is 72 kN for the first group (S/D = 2), and 85 kN for the second group (S/D = 4). In the load control tests the load was applied at a rate of 0.3 kN/s to 80% of the 100% load, and kept constant for a period of ten minutes. If ultimate failure had not happened, the load was increased by 5%, at a rate of 0.3 kN/s, and held constant again for ten minutes. This load procedure was repeated until the joint failed. Six specimens of both groups were tested under this constant load test procedure. Figure 2 shows the typical tension plane fracture across the first row of bolts. Because the Dartec 9500 testing machine attempted to maintain the load rate after a specimen ruptured there is considerable pullout of UD rovings, until the grip travel is exhausted. The same mode of failure is seen in the stroke control tests; however the separation of the two fractured parts is much smaller when the stroke travel is stopped.

For the joints with S/D = 4, four of the six specimens failed when the load is 90%

and the other two failed at 95%. A similar result is obtained with the second group of specimens, having S/D =2, with three specimens failing at 90% and at 95% of the joint's minimum ultimate failure load from the three stroke controlled tests.

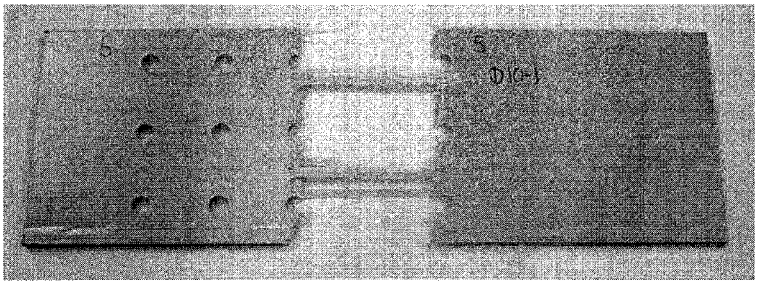


Figure 2. Ultimate failure mode after constant load control test.

This small test series demonstrates that the stroke controlled resistance of 3×3 bolted joints can be 10% higher than the resistance when a constant load is maintained for only 10 minutes before the next load increment. Since such a reduction in resistance is likely to increase, if the period of constant load is that in practice, it is important that this physical behaviour is not neglected when monotonic stroke or load rate test data [6] is used to evaluate and refined bolted joint design procedures [5, 7].

BOLT TORQUE AND LOAD TRANSFER BY FRICTION

It is well known that the clamping force generated by bolt torque is beneficial in increasing the strength of PFRP bolted joints [8]. Of the 1700 ultimate strength results discussed in [6] about 18% had a bolt torque higher than the finger-tight condition. It is also recognised that PFRP material creeps without exposure to elevated temperature [9], such that there would be relaxation of the PFRP compression stresses generated by the clamping force. To date no work has been reported which characterises the time-dependency relaxation of the clamping force with bolt pre-load.

Considering what current practice offers [1-3], it is seen that PFRP joint detailing is likely to have a bolt pre-load, induced via a specified torque (there is, however, no consensus on what tension stress the bolt should experience). To comply with UK (European) steelwork practice [10] and Clause 5.2.2.3(6) in [5], it is, however, observed that bolting in PFRP joints should just be tightened to the finger-tight condition. This low pre-load is expected to take into account factors such as poor on-site practice, the effect of long-term creep, cyclic loading, fatigue and vibration or their combination, and the likelihood that little connection load [11] is transferred by friction. For the reasons just given, the strength design of bolted joints [5, 7] should not be expected to be based on including any additional resistance offered by the bolting having a high pre-load [8].

Both European [10] and American [12] structural steelwork practices recommend bolting to have a pre-load only when the joint is slip-critical (e.g., to design against fatigue failure). For bearing type joints, no pre-load is required and this is meet by the bolting tightened to the snug-tight condition [12]. This condition is defined as the tightness that exists when all parts in a joint are in firm but not necessarily continuous contact; it can be considered to be equivalent to the finger-tight condition found in PFRP joints [6]. There are also high-strength friction grip bolts [10, 12], where slip in the steel connection is not permitted at the SLS or ULS [5], and for these joints the load is carried entirely by static frictional (shearing) force. Given our reliance on transferring

steelwork practice into PFRP practice, it is therefore not too surprising to hear that PFRP fabricators often apply a high bolt torque, with the expectation that the friction between the contacting faces, will aid in carrying the joint forces.

A small test series has therefore been completed, after adapting a testing methodology from structural steelwork [10], to determine the static coefficient of friction of bolted connections. Figure 3 shows the PFRP plate-to-plate test specimen with two 1×2 bolted joints. The outer plates are of PFRP EXTREN® Series 525 flat sheet of 6.35 mm nominal thickness, while the two inner plates of nominal thickness 9.53 mm are taken from the web of a standard Pultex series 1525 wide flange profile [3]. The specimen has geometry with E = 40 mm, P = 80 mm, and width (2S) = 116 mm. The separation between the ends of the two inner plates is 40 mm. The UD rovings are aligned to the concentric tension load. In the steel connection test procedure both inner plates are allowed to slip. As Figure 3 indicates only one of the inner plates (right-side) had clearance holes, which allows for the relative slip. Two types of specimens were prepared. One is for M12 bolting and the other for M16 bolting. At the 'fixed' side the clearance for the two bolt holes in the three plates is about 0.2 mm, while at the 'slip' side it also 0.2 mm in the two outer 6.35 mm plates and 2 to 4 mm for the inner 9.35 mm plate. Non-lubricated (as-received) grade 8.8 bolts were used with standard steel washers against nut and bolt head. For M12 bolting the washers had outer and inner diameters of 24 and 13 mm, respectively, and thickness of 1.45 mm. Washers for the M16 bolting had outer and inner diameters of 29 and 17 mm, respectively, and thickness of 1.85 mm.

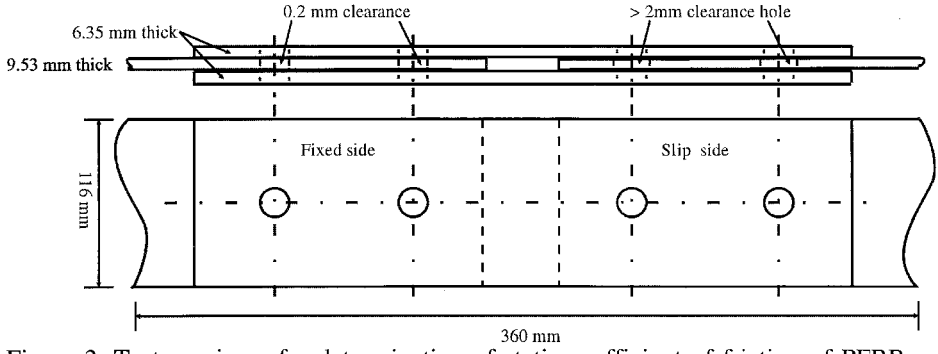


Figure 3. Test specimen for determination of static coefficient of friction of PFRP on PFRP.

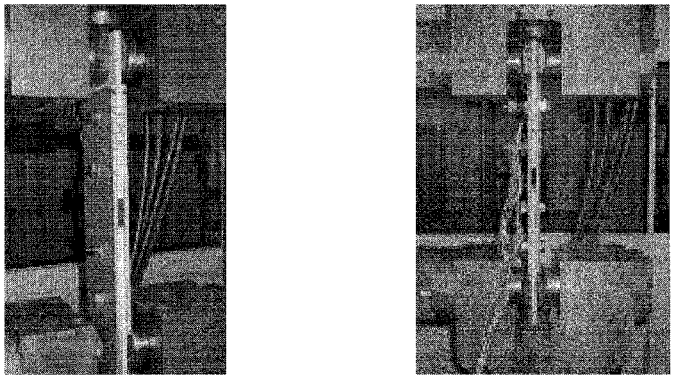


Figure 4. (a) Test specimen in Dartec grips (b) and with bolt load cells.

Figure 4(a) shows a test specimen in the Dartec testing machine. To set-up the specimen the fixed side had the bolts torque to 70 kNmm (Nm) after ensuring that the two bolts were bearing against the inner and outer plates (no slippage could occur). For the slip side the inner plate was pushed against the two bolts in the opposite sense to the tensile loading. This ensured that the amount of slip could be 2 mm or higher. Testing was carried out with the bolt torque on the slip side increased from 10 to 50 kNmm, in 10 kNmm increments. To set the torque a hand-held MHH torque meter (wrench) was used with a range of 0-800 $kgcm^2$.

Tensile load was applied by way of a constant stroke rate of 1 mm/min. Testing continued until slip occurred (and static friction was overcome) and, later, there was additional load carried by bolt bearing on the slip side. The test procedure was repeated three times for each bolt diameter and each torque increment.

It is well known that high strength bolts from the same lot yielded extreme values of bolt tension (±30%) from the mean tension desired by the pre-load applied [12]. The average variation is in general ±10%. This variance is caused mainly by the variability of the thread conditions, surface conditions under the nuts, lubrication, and other factors that cause energy dissipation without inducing tension in the steel bolt. Experience in field use of high strength bolts has confirmed the erratic nature of the torque versus tension relationship [12].

To help establish what the bolt tension (and the normal force) is, the authors designed a simple bolt load cell. This consisted of a steel tube of length 25 mm and outer and inner diameters of 22 and 17 mm. The ends of the tube were smooth and parallel. Four 6 mm TML strain gauges (type FLA-6-120-11) were placed at 90° intervals around the tube to measured axial strain. The two load cells were calibrated by using the same bolts and torque method used in the coefficient of friction tests. Figure 4(b) shows a specimen with the two load cells mounted and operational.

The results presented in what follows are preliminary, and were influenced by a number of error sources. Figure 5 shows, for M12 bolting, typical load-stroke curves at the five torque increments. The existence of a rapid load increase at strokes of 3 mm shows that additional load is being carried through bolt bearing. The sudden change in load-stroke response when slip starts to occur allows the slip load (maximum load transferred by shearing) to be established quickly and reliably. During the dynamic friction phase of the test the load is fairly constant and similar to the peak static value. Table 1 presents the load slip results, along with the mean slip load from a group of three tests and the group's Coefficient Of Variation (COV).

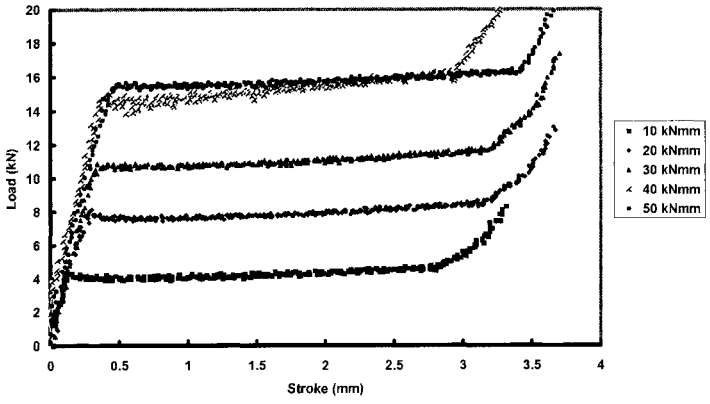


Figure 5. Load-stroke curves for M12 bolting and different torques.

1. Slip loads for M12 and M16 bolt sizes and bolt torques from 10 to 50 kNmm.

Torque (kNmm)	M12 Slip load Test 1	Test 2	Test 3	M12 mean slip load (kN)	M12 COV %	M16 Slip load Test 1	Test 2	Test 3	M16 mean slip load (kN)	M16 COV %
10	5.4	6.0	4.3	5.2	16	2.8	1.2	3.3	2.4	45
20	8.3	8.2	8.3	8.3	1	3.5	4.0	5.0	4.2	18
30	13.8	12.4	10.8	12.3	12	5.5	6.0	8.2	6.6	22
40	15.8	15.7	17.2	16.2	5	8.0	5.2	6.3	6.5	22
50	15.0	17.1	18.2	16.8	10	17.5	10.9	11.5	13.3	27

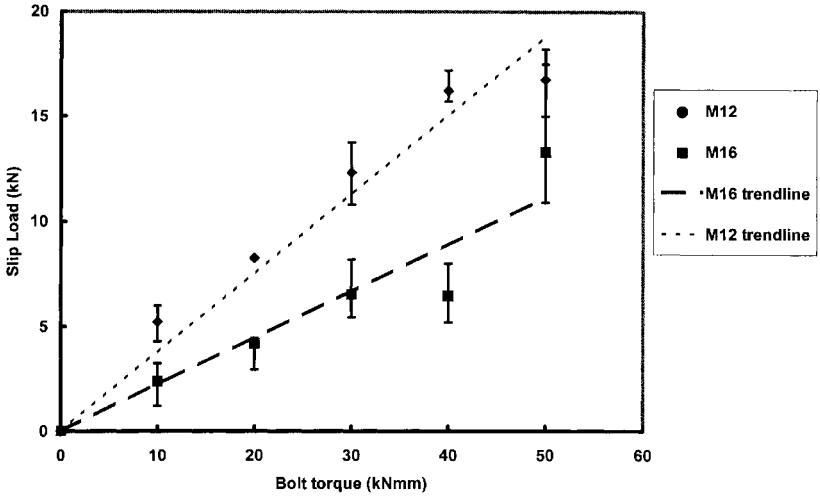


Figure 6 . Load-slip results with scatter bars and trendlines (intercept through 0,0).

After disassembling a specimen it was observed that the PFRP mating surfaces displayed 'mild wear' marks where the location of the UD rovings bundles [6] make the surface raised. This contacting condition was fairly consistent throughout the test series. Figure 6 displays the results in Table 1 and shows the linear trendlines with the intercept forced to be zero. It can be seen from Table 1 and Figure 6 that within each specimen batch (Tests 1 to 3) there is a considerable slip load variation. This will in part be associated with the known variation in bolt tension for a constant applied torque [12].

The results for the M16 bolting give higher variations (see the COV column in Table 1), and for a torque of 40 kNmm appear to be wrong. In practice the bolting is always tightened by a torque wrench (meter) attached to the nut end. Because of a combination of the bolt length and the HMM torque meter's dimensions this was not the procedure used for the M16 bolting. Now the torque meter had to be attached to the bolt head to enable a bolt to be tightened. This is one reason why the M16 results in Table 1 and Figure 6 can be considered to be less reliable.

Lets now determine the approximate value of the static coefficient of friction. Assuming that the Young's modulus of the steel in the load cells is 210 GPa, their calibration gives, for M12 and M16 bolts respectively, the bolt tension (in kN) per bolt torque (in kNmm) as 0.44 and 0.40 kN per kNmm. There are two bolts, so on the slip side of the specimen the normal force can be taken as doubled these values. It can be noted that when the two load cells were employed (Figure 4(b)) in a load-slip test there can be a 30% difference between their mean axial strains, which are themselves

calculated from the four strain gauge readings per cell. Furthermore, there can be a significant difference (> 20%) between the individual gauge values. In Figure 6 the linear trendlines can be used to determine the slip force (and the maximum static frictional force) per unit torque. For M12 bolting the frictional force is therefore 0.38 kN per kNmm and for the M16 bolting it is 0.22 kN per kNmm. This force is for two sliding surfaces. The approximate coefficient of friction for PFRP on PFRP is therefore $(0.5\times0.38)/(2\times0.44) \approx 0.22$ from the M12 bolting tests, and $((0.5\times0.22)/(2\times0.40) \approx 0.14$ from the less reliable M16 tests. A coefficient of 0.2 is typical of advanced polymeric composites on steel and at the lower bound of the range (0.2 to 0.3) for dry (non-lubricated) steel [12]. The lower coefficient for the M16 bolts is probably due to the operator using the MHH torque meter to tighten the bolt via the bolt head instead of the nut.

With high-strength friction grip bolts [10, 12] slip in the connection is not permitted at the SLS or ULS, and for these joints the load is carried entirely by static frictional force (there is no bolt bearing). With the bolt not resisting any load in bearing, the maximum bolt tension is based on not exceeding 75% of the steel's proof stress. Grade 8.8 bolts have a proof stress of > 600 N/mm^2. Therefore, the maximum bolt tension, to 1 kN, is 38 kN for M12 (the tensile stress area is 84.3 mm^2) and 71 kN for M16 (the tensile stress area is 157 mm^2). To estimate the maximum tensile load, at which slip might be expected to occur, lets reduce by 30% the maximum bolt tension and assume the coefficient of friction is 0.2. These conditions give for PFRP on PFRP a slip load per bolt of 5.3 for M12 and 10 kN for M16, respectively. However, to achieve this static frictional load the average through-thickness compressive stress over the washer bearing area would need to be about 1.2 and 1.7 times higher than the recommended maximum of 68 N/mm^2. This maximum stress, to prevent PFRP crushing, is given on page 717 in reference [5]. Using 68 N/mm^2 as a limit on the through-thickness compression stress and the areas of the standard washers for M12 and M16 bolts the maximum pre-load tension can only be about 0.6 and about 0.4 of 38 kN and 71 kN, respectively.

Using the physical test results, from the literature reviewed in [6], it can be estimated that, for both M12 and M16 bolting, the ultimate load for a 2×1 bolted joint with concentric loading is > 35 kN. For this bolt bearing failure load the PFRP thickness is 9.35 mm, the joint geometry is S = 2D, P > 2D and E > 4D, and the bolt torque is the finger-tight condition. If the safe working load is taken to be 30% of the ultimate load, it will be > 10.5 kN, which is much higher than the load for slippage to occur if bolting has its maximum recommended pre-load. And this is before there is any relaxation in the bolt tension due to the PFRP material creeping.

Based on the results of this small test series it seems clear that a joint design procedure cannot be developed which relies on a pre-defined bolt tension to ensure that the joint loading is transferred by friction. It is therefore recommended that designers and fabricators continue to comply with current design practice, in which bolt bearing is assumed to be the only mechanism for the load transfer in bolted plate-to-plate joints.

CONCLUSIONS

Two small plate-to-plate test series have been conducted to investigate two aspects of PFRP bolted joints that had not previously been studied. The constant load tests show that the stroke rate controlled resistance of 3×3 joints can be 10% higher than the resistance when a constant load is maintained for a period of only 10 minutes. Using an experimental method devised for steel connections it is found that the maximum shearing force transmitted by friction between PFRP flat sheets gives a static coefficient

of friction of about 0.2. By measuring the bolt tension with a load cell the authors confirm that, for a predetermined torque, the bolt tension (and hence the normal force) is far from constant. From this preliminary study it seems that a joint design procedure cannot be developed which relies on the entire joint force being transferred by friction. Finally, the findings from these two joint test series should not be ignored when monotonic test data is used to evaluate and refined current bolted joint design procedures.

ACKNOWLEDGEMENTS

EPSRC is acknowledged for its support to part of the research through grant GR/N11797. The authors are grateful to technical support from Mr C. Banks.

REFERENCES

[1] Anon, *EXTREN Design Manual,* Strongwell, Bristol VA, 1989.
[2] Anon, *Fiberline Design Manual for Structural Profiles in Composite Materials*, Fiberline Composites A/S, Kolding, Denmark, 1995.
[3] Anon, *The New and Improved Pultex Pultrusion Design Manual of Pultex Standard and Custom Fiber Reinforced Polymer Structural Profiles*, Creative Pultrusions Inc., Alum, Bank, PA, 1999.
[4] G J Turvey, 'Bolted connections in PFRP structures,' *Progress in Structural Engineering and Materials*, 2000 **2**(2) 146-156.
[5] J L Clarke (Ed.), *Structural Design of Polymer Composites - EUROCOMP Design Code and Handbook*, E & FN Spon, London, 1996.
[6] J T Mottram and G J Turvey, 'Physical test data for the appraisal of design procedures for bolted joints in Pultruded FRP structural shapes and systems', *Progress in Structural Engineering and Materials*, 2003 **5**(4) 195-222.
[7] L J Hart-Smith, 'Mechanically fastened joints for advanced composites – Phenomenological considerations and simple analyses', 4th Int Conf *Fibrous Composites in Structural Design,* Plenum, New York, 1980 543-574.
[8] C Cooper and G J Turvey, 'Effects of joint geometry and bolt torque on the structural performance of single bolt tension joints in pultruded GRP sheet material', *Composites Structures*, 1995 **32**(1-4) 217-226.
[9] D W Scott and A-H Zureick, 'Compression creep of a pultruded E-glass vinylester composite', *Composite Science and Technology*, 1998 **58**(8) 1361-1369.
[10] Anon, *European Recommendations for Bolted Connections in Structural Steelwork*, Publication No. 38, 4th Ed., ECCS, CECM and EKS, March 1985.
[11] R Prabhakaran and J Robertson, 'An experimental investigation of load-sharing in a multi-bolt pultruded composite joint', 2nd Int Conf *Composites in Infrastructure (ICCI'98)*, University of Arizona 1998 Vol. II 355-368.
[12] G L Kulak, J W Fisher and J H A Struik, *Guide to Design Criteria for Bolted and Riveted Joints*, 2nd Ed., American Institute of Steel Construction, Chicago, 2001.

RECYCLING TECHNOLOGIES FOR THERMOSET COMPOSITE MATERIALS

S J Pickering
School of Mechanical, Materials, Manufacturing Engineering and Management
The University of Nottingham, UK

ABSTRACT

The technologies for recycling thermoset composite materials are reviewed. Mechanical recycling techniques involve the use of grinding techniques to comminute the scrap material and produce recyclate products in different size ranges suitable for reuse as fillers or partial reinforcement in new composite material. Thermal recycling processes involve the use of heat to break the scrap composite down and a range of processes are described in which there are various degrees of energy and material recovery. The prospects for commercially successful composites recycling operations are considered and a new initiative within the European composites industry to stimulate recycling is described.

INTRODUCTION

Thermoset composite materials are used in a wide range of applications in industries such as automotive and construction. They come in a variety of forms. At the cheaper end, polyester resins are combined with short glass fibres and cheap fillers to produce moulding compounds for applications where high mechanical properties are not required. For demanding uses, continuous carbon fibres and epoxy resins are used for critical applications in the aerospace industry. In Europe, approximately 1 million tonnes of composites are manufactured each year [1]. Although there are many successful uses for thermoset composite materials, recycling at the end of the life cycle is a more difficult issue. However, the perceived lack of recyclability is now increasingly important and seen as a key barrier to the development or even continued use of composite materials in some markets [2].

Problems in recycling thermoset composites

The problems in recycling thermoset composites are as follows.

Thermosetting polymers are cross linked and cannot be remoulded, in contrast to thermoplastics which can easily be remelted. Some thermosetting polymers can be converted relatively easiliy back to their original monomer, such as polyurethane. However, the more common thermosetting resins, such as polyester and epoxy are not practical to depolymerise to their original constituents.

Composites are by their very nature mixtures of different materials: polymer, fibrous reinforcement (glass or carbon fibre) and in many cases fillers (these may be cheap mineral powders to extend the resin or have some other function, such as fire retardants). There are few standard formulations and for most applications the type and proportion of resin, reinforcement and filler are tailored to the particular end use.

Composites are often manufactured in combination with other materials. For example there may be foam cores or metal inserts to facilitate fastening onto other components.

In addition to these specific problems there are the other problems associated with recycling any material from end-of-life components. Such as the need be able to deal with contamination and the difficulty of collecting, identifying, sorting and separating the scrap components to be recycled.

The need to recycle

Concern for the environment, both in terms of limiting the use of finite resources and the need to manage waste disposal, has led to increasing pressure to recycle materials at the end of their useful life. Where it is economically cost effective to recycle, materials recycling operations are already well established and driven by economics, for instance in the metals industries. Polymers are generally more difficult to recycle and the economic incentives to recycle are less favourable, particularly when waste disposal in landfill is relatively cheap. Consequently, in order to protect the environment, legislation has to be introduced often combined with the use of economic instruments (such as taxes) to encourage recycling to take place [1].

Waste management is now a high priority within the European Union and there is a well known heirachy of routes for dealing with waste. In decreasing order of desirability these are:

- Prevent waste through prevention at source during manufacture
- Reuse a product
- Recycle material
- Incinerate waste
    - with material and energy recovery
    - with energy recovery
    - without energy recovery
- Landfill

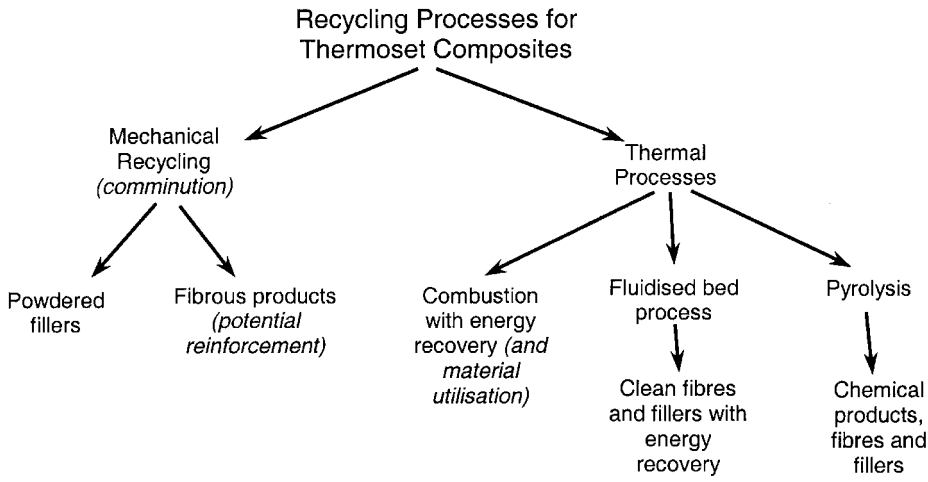
For many years, and in the UK in particular, composite waste has been disposed of in landfill. A recent EU Directive on Landfill of Waste (Directive 99/31/EC) will result in a reduction in the amount of organic material landfilled. As a consequence of this it is already illegal to landfill composites waste in many EU contries.

Other directives deal with particular waste streams. The End-of-life Vehicle Directive (Directive 2000/53/EC) will require that by 2015 all vehicles disposed of must be 85% recyclable, only 10% energy recovery will be allowed and 5% landfill. This means that vehicles manufactured now must meet this requirement as vehicles have a life expectancy of over 10 years. A directive on waste electrical and electronic equipment has recently been issued (Directive 2002/96/EC) and it is likely that there will be regulations concerning construction and demolition wastes soon.

As a consequence of this increasing legislation there is a need for recycling routes to be established and the potential technologies are described next.

RECYCLING TECHNOLOGIES

A number of recycling technologies have been proposed and developed for thermoset composite materials and these are summarised in Figure 1. There are fundamentally two categories of process: those that involve mechanical comminution techniques to reduce the size of the scrap to produce recyclates and those that use thermal processes to break the scrap down into materials and energy. Each will be considered.



1. Recycling processes for thermoset composite materials

Mechanical recycling

Mechanical recycling techniques have been investigated for both glass fibre and carbon fibre reinforced composites, but the most extensive research has been done on glass fibre. The technique used is usually to initially size reduce the scrap composite components in some primary crushing process. This would typically involve the use of a slow speed cutting or crushing mill to reduce the material to pieces in the order of 100mm in size. This facilitates the removal of metal inserts and, if done in an initial stage where the waste arises, the volume reduction assists transport. The main size reduction stage would then be in a hammer mill or other high speed mill where the material is ground into a finer product ranging from typically 10mm in size down to particles less than 50μm in size. Then a classifying operation, typically comprising cyclones and sieves, would be employed to grade the resulting recyclate into fractions of different size. The technology is described in more detail in [3].

In the mechanical recycling process all of the constituents of the original composite are reduced in size and appear in the resulting recyclates which are mixtures of polymer, fibre and filler. Typically the finer graded fractions are powders and contain a higher proportion of filler and polymer that the original composite. The coarser fractions tend to be of a fibrous nature where the particles have a high aspect ratio and have a higher fibre fibre content. A number of companies have been involved in developing the recycling activity at an industrial scale, among them ERCOM in Germany and Phoenix Fiberglass in Canada [3].

Applications for recyclate are many and varied. Both Phoenix and ERCOM were founded to recycle sheet moulding compounds (SMC) and bulk moulding compounds (BMC) materials and they have been successful in finding uses for their recyclates as constituents into the SMC/BMC they were produced from [3]. The fine recyclate grades can be substituted for fillers in new composites comprising typically up to 25% of the weight of new material. At filler substitution levels of 10-20% the mechanical properties of the SMC containing recyclate are unchanged but at higher substitution levels some loss in strength occurs particularly on impact strength. As the density of the recyclate is lower than conventional mineral fillers (e.g. calcium

carbonate) it results in a material with a lower bulk density. Whilst these powdered recyclates have been widely and successfully used it might be argued that the higher value present in the polymer and reinforcement is lost when the composite is only recycled as a filler.

The coarser, more fibrous grades can be used to partially substitute for the virgin glass fibre in new composites and substitution levels of up to 50% can be achieved but with some degradation of mechanical properties at the higher loadings. The glass fibres in the recyclate are less efficient at reinforcement than virgin glass and so cannot be used as a direct substitute for glass fibre. The production of fibrous recyclate in which the reinforcement potential of the fibre can be utilised is also an attractive means for mechanically recycling carbon fibre composites where the carbon fibre has very high value as a reinforcement.

There have been many research studies of other applications for recyclate. At Brunel University [4] a novel twin-screw extrusion process was developed as an integrated compounding process in which coarsely ground recyclate could be compounded with thermoplastics to produce a moulding compound. Various additives could be added during the extrusion process to enhance the coupling of the recyclate with the polymer to produce enhanced mechanical properties and so deliver more value from the recyclate.

The value of re-cyclate can be enhanced if it can be used in a way to exploit some of its unique properties. At SICOMP in Sweden [5] a glass fibre based reinforcement RECYCORE has been produced that consists of a core containing a coarse recyclate. The recyclate core has a particle size from 1 to 25 mm and can comprise up to 70% of the weight of the reinforcement. The particular benefit is that the recyclate gives the core a high permeability that allows it to act as a flow layer along which resin can flow during impregnation. At Bristol University [8] work has been done to investigate the way in which recyclate can be used to provide more damping in a composite so that it is more effective in noise insulation.

Coarse recyclate has also been used as a reinforcement in asphalt and in the manufacture of plastic lumber from recycled thermoplastics where recyclate can be used as an alternative to wood fibre [6,7].

Thermal Processing

Combustion with Energy and Material Utilisation

Thermosetting polymers have a calorific value of about 30 MJ/kg and they can thus be burned as a source of energy. As the most commonly used fibres and fillers are incombustible, the calorific value of the composite depends directly on the proportion of polymer. Trials have shown [9,10] that composites can successfully be burned and energy recovered. Mixing scrap composites at 10% loading with municipal solid waste has been shown to be a practical way to dispose of scrap if landfill is prohibited [10]. In order to recover some value from the incombustible material burning scrap composites in cement kilns is an effect route as the glass reinforcement and mineral fillers commonly used in composites contain minerals that can be incorporated in cement [11]. Alternatively if scrap composites are co-combusted with coal in a fluidised bed combustor [12] any calcium carbonate filler in the composites will absorb oxides of sulphur from the combustion of the coal and so reduce the sulphur emissions.

Fibre recovery using a fluidised bed thermal process

The fibre reinforcement has potentially the most recoverable value in a composite. The theme of research at the University of Nottingham over the past 10 years has therefore been to develop a fluidised bed process to recover high grade glass and carbon fibre reinforcement from scrap glass and carbon fibre reinforced composites [13,14]. Scrap composites are initially reduced in size to about 25mm and fed into a fluidised bed. This is a bed of silica sand with a particle size of about 0.85 mm. The sand is fluidised with a stream of hot air and typical fluidising velocities are 0.4 to 1.0 m/s at temperatures in the range of 450 to 550 °C. In the fluidised bed the polymer volatilises from the composite and this releases the fibres and fillers to be carried out of the bed as individual particles suspended in the gas steam. The fibres and fillers are then separated from the gas stream which can then pass into a high temperature secondary combustion chamber where the polymer is fully oxidised. Energy may subsequently be recovered from these hot combustion products.

The process has been developed for the recovery of both glass fibre and carbon fibre. The fibre product is in a fluffy form comprising individual fibre filaments typically of mean length from 6 to 10mm by weight. The fibres are clean and show very little surface contamination. Mechanical property measurements show that glass fibres typically suffer a 50% reduction in tensile strength but retain the same stiffness as the virgin fibre. Carbon fibres show a lower strength degradation of typically 20% with retention of the original stiffness.

The most promising applications for the recovered fibres are those that require short fibres in a disperse form such as in bulk moulding compounds or non-woven veil or tissue products. A particular advantage of the fluidised bed process is that it is very tolerant of mixed and contaminated materials. Mixtures of composites of any polymer type can be processed and the process is tolerant of painted surfaces or the presence of foam cores in composites of sandwich construction. Metal inserts moulded into a composite do not have to be removed before being fed into the fluidised bed as any metals are retained in the bed and could be separated by re-grading the sand.

Pyrolysis Processes

In a pyrolysis process a combustible material is heated in the absence of oxygen. In these conditions it breaks down into lower molecular weight organic substances (liquids and gases) and there is also a solid carbon char product. Pyrolysis offers a method of recovering material from the polymer in a scrap composite that has the potential to be used as a feedstock for further chemical processing.

Pyrolysis processing of scrap composites has been investigated by a number of workers. In the USA, the SMC Automotive Alliance undertook research on pyrolysis in the early 1990s. [15]. The processing temperature was 700 to 1000°C in a batch processing plant designed for tyre pyrolysis. The process produced a fuel gas used to provide heating for the pyrolisation chamber, some liquid oil products and a solid residue which comprised the inorganic fibres and fillers and a char residue. The solid residue was ground to a powder and investigations carried out to assess its value as a filler in the manufacture of new composites.

More recently, pyrolysis of composites has been investigated at the University of Leeds [16]. Lower temperatures were used ranging from 350 to 800°C and the solid residues were separated into fibres and fillers. A range of composites, mainly glass reinforced, were investigated. It was found that the liquid oils produced from the

process contained some potentially valuable chemicals or could be used as a fuel. The glass fibre was found to be covered in a layer of char and this could be removed by oxidising in air. The glass fibres were found to be degraded by the process and operating at about 450°C was an optimum in terms of limiting the fibre strength degradation to about 50% of the strength of virgin glass fibre.

A pyrolysis process has also been investigated for the recycling of carbon fibre composites [17]. In this work pyrolysation took place at a low temperature (up to 350°C) in the presence of a catalyst. It was claimed that strength degradation of the recycled fibres was less than 20% but that some resin still remained on the fibre surface. A gasification process has also for carbon fibre composites [18]. In this process the scrap is heat along in a controlled flow of oxygen at temperatures of 600°C. The polymer is converted to shorter chain hydrocarbons and gases (H_2 and CO) and the carbon fibres can be recovered for reuse.

A pyrolysis process is currently being developed in Denmark for the recycling of composite wind turbine blades [19]. In this process the wind turbine blade is cut up into pieces of about 1m in size and placed in a large batch reactor where they are heated in the absence of air. Air is introduced towards the end heating cycle to oxidise any char so that clean glass fibre and fillers are recovered. The gaseous and liquid products of the pyrolysis are used as a source of energy and the recovered solid products (glass fibre and filler) have potential for use as reinforcement in a similar way to the fibrous fractions produced from the mechanical recycling processes.

ENVIRONMENTAL ACCEPTABILITY

Although the heirachy of waste management routes appears to give preference to those recycling routes that maximise material recovery, the mechanical recycling of valuable fibres and resins as fillers does not necessarily give the best environmental return. Pyrolysis process have the potential to produce chemical feedstocks from the polymer but these may be difficult to refine from the mixture of products produced. If a pyrolysis process only produces chemicals suitable for use as fuels then an energy recovery process with high quality fibre recovery may be more acceptable. Only environmental audits of the recycling routes can identify which are the most acceptable and this work has yet to be done in detail.

PROSPECTS FOR COMMERCIAL OPERATION

Although there has been much research into different methods for recycling thermoset composites a truly successful commercial operation has yet to be achieved anywhere in the world. Phoenix Fiberglass in Canada ceased operating in 1996 and the ERCOM company and other similar operations have not been able to find sufficient markets for recyclate to operate at commercially viable levels of production [6]. At a recent seminar on composite recycling held at SICOMP in Sweden in 2003 a workshop was held to identify the barriers to composites recycling and a questionnaire was circulated to obtain the opinion of the delegates [21]. The clear message was that cost and lack of markets were the main barriers to the implementation of composites recycling operations but that new legislation was the main driver towards recycling. The key issue is that the costs of recycling operations, whether they be mechanical recycling or other forms of thermal recycling mean that the recyclates currently produced are too expensive to give a clear market advantage over alternative existing materials [7,21]. Furthermore commercially viable operations would require large throughputs and

markets need to be developed to consume these quantities of recyclate. Either the recyclates must find higher value end markets and this may mean developing new higher grade recyclates or the cost of the recyclate must reduce to allow the recyclates to penetrate further into existing markets.

Recent changes to waste management legislation and likely future directions mean that recycling routes are urgently needed to be in place for thermoset composite materials if they are to continue to have a place in the market. Recognising that composite recycling activities need stimulation and financial assistance if they are to succeed, the GPRMC, the European composites industry trade association is proposing a European Composites Recycling Concept (ECRC) [20]. Under this scheme a 'Green label' will be given to composites from manufacturers who adopt this scheme and this will guarantee that the components will be recycled appropriately in accordance with the legislative requirements at the time. Composites manufacturing companies which join the scheme will pay money into a fund that will manage composites recycling on a pan European scale and finance the recycling activities. The scheme is currently in its early stages and will initially focus on composites in the automotive industry.

Glass fibre composites comprise the bulk of the thermoset composites currently manufactured. The production volumes of carbon fibre composites are several orders of magnitue lower but carbon fibre is a much more valuable material, typically at least ten times the cost of glass fibre. The prospects are therefore potentially more attractive for carbon fibre recycling.

CONCLUSIONS

A considerable amount of research has been done to investigate potential recycling techniques for thermoset composite materials and some of the key work has been described in this paper in the area of mechanical and thermal recycling processes. Despite this there is no commercially viable composites recycling activity anywhere in the world, largely as a result of markets not being available at the right price for the recycled materials that are produced. European legislation now requires that recycling routes are available for composites as other waste management methods will not be allowed. The European composites industry is responding with a European Composites Recycling Concept to manage waste from composites and stimulate recycling activities.

REFERENCES

1. G Bos, 'EU waste legislation and the composites industry', Seminar on *Recycling of Composite Materials*, IFP SICOMP, Molndal, Sweden, 14th - 15th May 2002.

2. G Sims and G Bishop, 'UK Polymer Composites Sector – Competitive Analysis and Foresight Study'. Final Report, July 2001, Published by NPL Materials Centre.

3. J Scheirs, *Polymer Recycling - Science Technology and Applications*, John Wiley and Sons Ltd (UK), 1998.

4. M Bevis, CE Bream, PR Hornsby, K Taverdi, KS Williams 'Thermoset recyclate as a functional filler for polymers' Proc of 56th Ann Tech Conf *ANTEC 98*, Part 3, April 26-30, 1998, Atlanta, USA, Soc of Plastics Engineers.

5. M Skrifvars, 'Introduction to Composites Recycling', COMPOSIT Thematic Network Workshop, *Recycling of Composite Materials in Transport*, SICOMP, Pitea, Sweden, 16th June 2003. Papers available at: http://www.compositn.net

6. GPRMC Press Release 2003-2. European Composites Industry Association, Diamant Building, Boulevard A, Reyerslann 80, BE-1030 Brussels, Belgium. http://www.gprmc.be

7. S Halliwell and T Reynolds, 'Markets for Fibre Reinforced Polymer Recyclate', Network Group for composites in Construction, 3rd annual conf *Fibre Reinforced Polymers in the Built Environment*, Nottingham International Clothing Centre, UK, 12th November 2003.

8. R Thomas, FJ Guild, RD Adams 'The dynamic properties of recycled thermoset composites' Proceedings of 8th International Conference on *Fibre Reinforced Composites - FRC2000*, Newcastle upon Tyne, September 2000, pp549-556 .

9. SJ Pickering and M Benson, 'The Recycling of Thermosetting Plastics' Plastics and Rubber Institute, 2nd int conf. *Plastics Recycling*, 13-14 March 1991, London, p23/1-10.

10. B Nystrom, 'Energy Recovery from Composite Materials', Seminar on *Recycling of Composite Materials*, IFP SICOMP, Molndal, Sweden, 14th - 15th May 2002.

11. SJ Pickering and M Benson, 'Recovery of materials and energy from thermosetting plastics' 6th European Composite Materials Conf, *Recycling Concepts and Procedures,* Bordeaux, France, Sept 1993 p41-46. Publ. by European Association for Composite Materials, Bordeaux.

12. NJ Fenwick, SJ Pickering 'Using waste materials to reduce emissions – combustion of glass reinforced plastic with coal in a fluidised bed' Conference on *Engineering Profit from Waste IV*, 9-11 November 1994, I.Mech.E. London. Conference C493. pp157-166

13. SJ Pickering, RM Kelly, JR Kennerley and CD Rudd, 'A fluidised bed process for the recovery of glass fibres from scrap thermoset composites', *Composites Science and Technology*, 2000 **60**, pp 509-523

14. HLH Yip, SJ Pickering and CD Rudd, 'Characterisation of carbon fibres recycled from scrap composites using fluidized bed process' *Plastics, Rubber and Composites*, 2002, **31**(6), pp278-282

15. CN Curcuras, AM Flax, WD Graham and, Hartt GN 'Recycling of thermoset automotive components' *SAE Technical Paper Series*, 910387, 1991, 16p.

16. AM Cunliffe, N Jones and PT Williams 'Pyrolysis of composite plastic waste' *Environmental Technology* 2003 **24** pp653-663

17. RE Allred, 'Recycling process for scrap composites and prepregs' *SAMPE Journal* 1996 **32**(5) pp46-51

18. JF Unser, T Staley and D Larsen, 'Advanced composites recycling' *SAMPE Journal* 1996 **32**(5) pp52-57

19. E Grove-Neilsen, 'Material and thermal recycling of wind turbine blades and other fibreglass items by ReFiber ApS', COMPOSIT Thematic Network Workshop, *Recycling of Composite Materials in Transport*, SICOMP, Pitea, Sweden, 16th June 2003. Papers available at: http://www.compositn.net

20. F Harbers, 'Green FRP recycling label - the step towards closing the loop' COMPOSIT Thematic Network Workshop, *Recycling of Composite Materials in Transport*, SICOMP, Pitea, Sweden, 16th June 2003. Papers available at: http://www.compositn.net

21. COMPOSIT Thematic Network Workshop, *Recycling of Composite Materials in Transport,* SICOMP, Pitea, Sweden, 16th June 2003. Papers available at: http://www.compositn.net

INNOVATIVE DEVELOPMENTS FOR BRIDGES USING FRP COMPOSITES

Prof. Dr.-Ing. G. Sedlacek, Dipl.-Ing. H. Trumpf
Institute of Steel Construction, RWTH Aachen

ABSTRACT

Lightweight and corrosion resistant fibre-reinforced-polymer profiles have found increased application in bridge and industrial constructions in recent years. The Institute of Steel Construction and Lightweight Structures at RWTH Aachen has already developed an emergency single-lane road-bridge for MLC-12 and a span of 20.0 m utilising glass-fibre-reinforced-polymers (GFRP) composites, which has been tested successfully under real conditions. A second research-project was launched in spring 2003 with the aim of designing a FRP-bridge for MLC-40 with a span of 30.0 m.

The paper presents the main results of the first lightweight bridge and the experiences from the proving tests. Main objectives of the first bridge were the structural design, hybrid connections and the extensive test programme. Finally proving tests on the prototype bridge have been performed under service loads and environmental conditions to verify the design and to calibrate the dynamic behaviour simulated with special software.

These results are currently being used to design and optimise the new bridge, which will be erected at the end of 2004. New types of strengthened bolted connections, advanced cross-sections for the deck plate and optimised members are currently being investigated.

1. INTRODUCTION

There is a demand for lightweight emergency bridges that are suitable for air-transport, hand erection by unskilled workers and which may be used for light support vehicles for humanitarian services.

Already completed bridge structures manufactured from pultruded fibre-reinforced polymer profiles in Pontresina (CH) –truss bridge[1], Kolding (DK) –cable stayed bridge[2], Leida (ES) –arch bridge[3] and Oxfordshire (GB) –girder bridge[4] convincingly demonstrate construction, resistance and durability aspects.

The Institute of Steel Construction at the RWTH Aachen has been awarded a project by the "Wehrtechnischen Dienststelle für Pionier- und Truppengerät, Koblenz" to develop an economical solution for such light-weight, single lane bridges constructed from FRP, for a spans of 20.0 m and MLC-12 loadings (MLC-14 exceptional loadings) in 1999.

Due to the low total stiffness and shear resistance of fibre-reinforced profiles compared to steel a special design for the structure and the connections had to be developed to meet the requirements of the material characteristics. In the first project hybrid-connections were used; this is a first step to the combination and the strengthening of the material utilising bolted connections, which can be readily dismantled.

This first FRP-bridge for MLC-12 has been successfully erected and tested in 2001 and 2002 under serviceability loading and environmental conditions. A second research-project was launched in spring 2003 with the aim of designing a FRP-bridge

for MLC-40 and a span of 30.0 m. For these increased demands new strengthened bolted connections, advanced cross-sections for the deck plate and optimised members had to be developed. The developments are accompanied by numerical investigations and will be tested in full-scale static and dynamic test series.

This paper deals with the design, the testing programme and the detailing of the first glass-fibre-reinforced-polymer bridge. A description will be given of the developments of the second bridge, which will be erected in December 2004.

2. DESIGN OF THE STRUCTURE

2.1 Technical requirements

The following technical requirements for the first bridge have been agreed in the technical specifications:

- load class MLC 12, exc. load class MLC 14, impact factor 1.2
- mud load of 0.75 kN/m² (uniformly distributed)
- design span length 20.0 m, minimum clear roadway width 2.75 m (one way)
- hand erection with unskilled workers with 6 persons in 3 hours
- vehicle crossing speed up to 25 km/h, min. temperature range -37° C up to +44° C
- difference in altitude betw. bank supports 3 m, suitable concept for shorter spans
- possible replacement of every FRP-member, dismountable connections
- launching of the bridge by crane, helicopter or by a launching nose
- the structure should be suitable for bridging gaps in bridges that have been partly destroyed

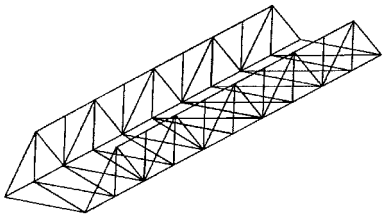
2.2 Design of the bridge structure

Due to the high resistance of the FRP in the longitudinal direction and low shear resistance a truss structure, shown in Figure 1, was chosen.

To allow the replacement of damaged FRP-members and -elements the bridge deck is not integral with the truss structure, but will act as a separate structural member and also as wind bracing under traffic-loads. To avoid long ramps and to enable the placement of the bridge onto an existing damaged bridge a trough cross section has been chosen, Figure 2. The pre-design resulted in an economic truss depth of about 2000 mm for a maximum span length of 20.0 m, Figure 3.

To analyse the stability of the top chords of the truss with U-frame action, the stiffness of the U-frame is represented by the diagonal members, vertical struts and high second moment of areas for the top chord; this provided stability. Furthermore, the knee of the U-frame is strengthened to provide a rigid connection between the cross beams and the vertical struts. The end plates are used as partial ramps to provide a short and a slightly inclined access to the bridge.

For the first project a simple design, for the deck elements has been used (viz. a plate constructed from flat-profiles and rectangular hollow sections). The development of optimised FRP-bridge decks will be undertaken in an additional research programme by designing sophisticated cross sections similar to the Warren-truss in the ASSET-Project [4] supported by FE-simulations, production of deck elements and full-scale fatigue tests, discussed in section 4.



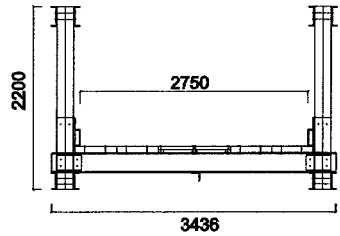


Figure 1 and 2 Static System and U-frame of the mobile light-weight fixed bridge

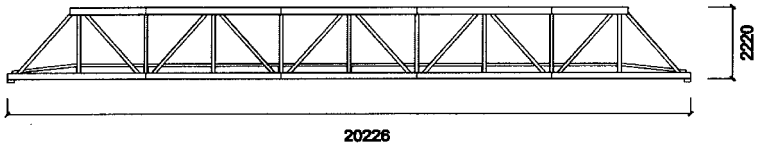


Figure 3 Elevation of the bridge with five segments

2.3 Materials

For the pultruded FRP-Profiles the market offers a selection of different profile-types (similar to rolled steel profiles) manufactured from different matrices and glass-fibre qualities, e.g. Fiberline Design Manual[5]. For the design generally available profile types with the quality E23 were chosen in accordance to the material characteristics specified in EN 13706[6]. The material characteristics of the manufacturer have been verified by standardised tests and requirements to EN 13706. The resistances of the 5%-fractile values of the delivered profiles were up to 35% higher than required in the specification. To obtain an independent static design all checks were done with the material characteristics according to the EN 13706. In Table 1 the main design values for the FRP-Profiles E23 are specified and compared to the design values obtained from independent material tests, evaluated to EN 1990 Annex D.

Table 1 Material characteristics according to EN 13706 E 23 compared to design values evaluated from tests according to EN 1990 Annex D

FRP material constants	Notation	Resistance E23	Design values obtained from tests evaluated according to EN 1990-D
Tension, longitudinal	$f_{t\,II,k}$	240 N/mm²	296 N/mm²
Tension, transverse	$f_{t\perp,k}$	50 N/mm²	51 N/mm²
Compression, longitudinal	$f_{c\,II,k}$	240 N/mm²	276 N/mm²
Compression, transverse	$f_{c\perp,k}$	70 N/mm²	104 N/mm²
Shear resistance	$f_{\perp,k}$	25 N/mm²	31 N/mm²
Young's modulus, longitudinal	$E_{II,k}$	23.000 N/mm²	31.232 N/mm²
Young's modulus, transverse	$E_{\perp,k}$	8.500 N/mm²	10.566 N/mm²
Shearing modulus	G_k	3.000 N/mm²	3.103 N/mm²

To redistribute the internal forces, the FRP-Profiles have been strengthened with bonded steel plates in the area of the joints. For this, stainless steel hybrid connections, material number 1.4571, were used to guarantee the durability and reliability against corrosion. Various selection tests have been performed to check the applicability of different adhesives for the bond between FRP and stainless steel. A solvent free, thixotropic 2-component impregnation resin on epoxy resin basis has been selected after evaluation of the test results. The pot life is about 90 minutes for 15°C and 30 minutes for 35°C. After seven days the tension strength is about 30 N/mm² in accordance to the DIN 53455 / EN ISO 527-1 [7].

2.4 Hybrid connections

Due to the low shear resistance of pultruded FRP-profiles and the high shear forces in the connection areas the ends of the profiles are reinforced by bonded stainless steel plates. Bonded connections are well known and a wide variety of different adhesive's based on 1 or 2-component epoxy resins, polyurethans, acrylats, silicones etc. exist in the market. Furthermore, many papers have been published in the last decades mainly concerning the chemical composition, their interaction, bonding forces (e.g. adhesion, cohesion, etc.), mathematical and numerical models and test specimen, reference[8]. For simple overlapping joints with hybrid materials under shear forces a basic approach to determine the shear stress distribution in the joint may be determined, reference[9]. For adhesive/bolted connections the stress distribution is unable to be determined from reference[9] because of the complex three-dimensional effects. In Figure 4, a simplified shear stress distribution involving the strain in the steel plate and in the FRP is shown. The internal forces in the bolts are transferred by shear and bearing to the stainless steel plate. The adhesive joints transmit these forces by means of shear stresses into the FRP-profile. The maximum peak of the strain difference between both materials in the joint is the maximum shear strength of the adhesive.

These simplified shear stress distributions can also be determined by FE-analyses. Such numerical investigations give a fair degree of accuracy when the plastic restoring stresses, which compensate the parabolic stress distribution, are considered.

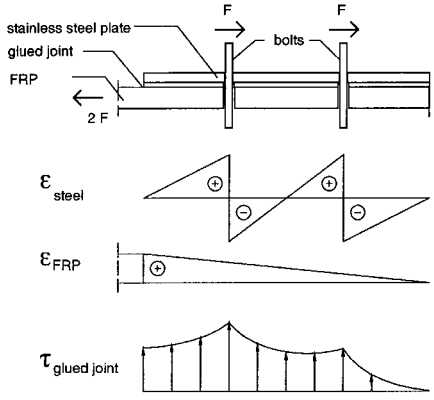


Figure 4 Simplified shear stress distribution for bolt-adhesive connections

The adhesive is applied to the prepared surface by using a trowel or brush. The required thickness of the adhesive for a maximum ultimate resistance is about 0.2 mm.

2.5 Member weights

The member weights recorded in Table 2 have been determined from the static design. All truss members are readily dismantled and therefore interchangeable. The weight of each truss member allows lifting by two workers without any lifting tools.

Table 2 Material quantities

Pos.	Element	Profile	Amount	Length [m]	Weight [kg]	Σ Weight [kg]
1	Top chord	2 U 240 / 72 / 12	12	4,00	32,0	384,0
1.1	Top chord, end.	2 U 240 / 72 / 12	8	2,15	17,2	137,6
2	Bottom chord	2 U 200 / 60 / 10	12	4,00	22,2	266,4
2.1	Bottom chord, end.	2 U 200 / 60 / 10	8	4,09	22,7	181,6
3	Cross girder	2 U 240 / 72 / 12	18	3,44	27,5	495,0
3.1	Cross girder, end	2 U 240 / 72 / 12	2	3,44	24,4	48,8
4	Vertical struts	2 □ 100 / 100 / 8	36	2,20	11,8	424,8
5	Diagonal members	2 □ 100 / 100 / 8	40	2,75	24,8	992,0
6	Wind bracing	L 100 / 100 / 10	10	3,30	9,3	93
7-9	Deck elements	build up profile	30	4,00	46,0	1380,0
10	Coating	Primer, Minerals	-	-	2,5kg/m²	90,0
11 - 29	Stainless steel	18 differ. plates	-	-	-	575,0
30 - 41	Connection items	11 differ. items	-	-	-	339,6
Sum						5,4 t

3 TEST PROGRAMME

3.1 Overview

Various tests have been performed to check the ultimate resistance of the truss connections and the applicability of design rules from standards and the literature.
The test specimen, the loading and the aims of the tests have been presented in Figure 6. The further results of the tests, load-displacement curves are in references.[10,11]..

3.2 Diagonal members and vertical struts and their connections

All connections have been tested with stainless steel plates of varying thickness, t = 2, 3 and 4 mm. After several pre-loading steps up to 50 % of the calculated ultimate load, the connections were then tested to failure. Some examples that demonstrate the load-deflection characteristics of these hybrid-connections are given in Figure 5. All specimens have shown an elastic-plastic load-displacement curve. The displacements depend, in particular, on the first loading steps, mainly on the slip in the clamping devices. The stiffness of the connection is decreasing up to a specific load depending on the plate thickness (e.g. 250 kN for a plate thickness of t = 2 mm).

The failure always occurred by delamination of the FRP-Profile only 1 - 2 mm below the adhesive joint surface. Just before failure, the load increases due to the activation of the bearing capacity of the bolts in the FRP. The failure mode is characterised

by very ductile load-deflection behaviour and confirms the results of the pre-test series that the adhesive has sufficient ultimate resistance. From theory reference9 and Figure 4, the greatest value of ultimate load was reached when bonding a thin stainless steel plate (t = 2 mm) onto the FRP-profiles with a ratio of: $\psi = (E_1 * t_1)/ (E_2 * t_2) = 2.28$

The influence of the stiffness-ratio has been verified in the test programme. Therefore as expected, the relation between the bearing capacity of the stainless steel reinforcement and ultimate resistance of the bonded joint (optimised stiffness-ratio is $\psi_{opt} = 1$) had to be investigated. Wherever possible, the thickness of the stainless steel plate was taken as 2 mm. The safety factor obtained from a probabilistic evaluation of tests for all connections is about $\psi = 1.75$.

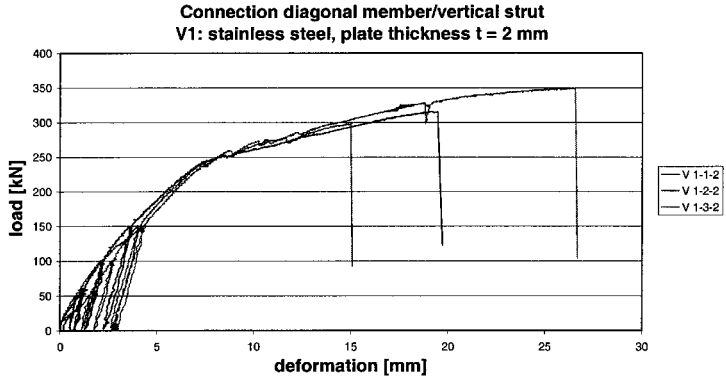


Figure 5 Load-deflection-curve diagonal members and vertical struts

3.3 Temperature tests

In order to verify the temperature behaviour of the bonded connections two test series have been performed. In accordance with the standards, e.g. DIN EN 1465 [12], the ultimate resistances of FRP-FRP and FRP-stainless steel specimen under constant and alternating temperatures were tested.

For the specified temperature range from -37°C up to +44°C the following test programme according to DIN EN 1465 was developed:

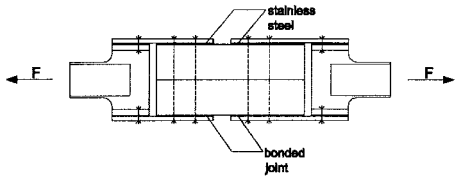
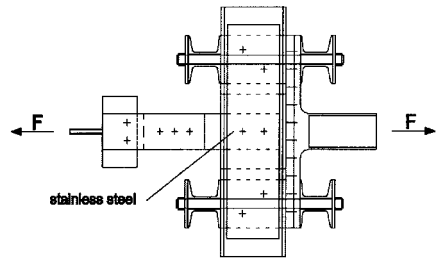
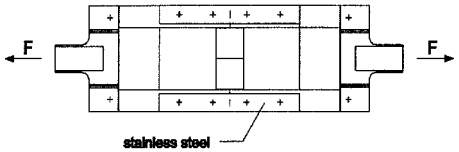
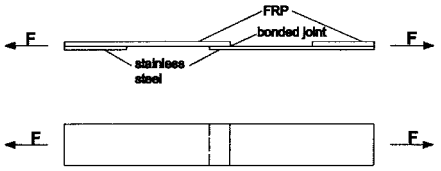
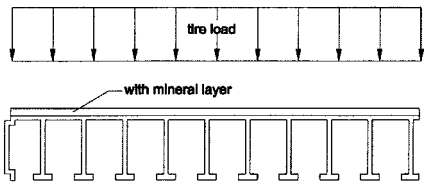
- constant temperatures: -40°C, -25°C, -10°C, +23°C, +40°C and +55°C
- three specimens for each constant temperature

Temperature sensors were used to measure the temperatures in the adhesive joint. Most of the failures occurred due to delamination of the FRP. Only two specimens have shown a combined delamination with a cohesive failure. Although there was a degree of scatter, the results show a tendency for a decreasing strength of above 50°C. The same test set-up was used during temperature cycling. The following load histogram has been applied to the specimen:

- pre-loading by 20% of the calculated ultimate load
- 8 temperature cycles between -25°C and +40°C (under static pre-loading)
- 30 min. loading time for each max. temperature limit (under static pre-loading)

After the whole specimen has been heated or cooled, which was measured by special sensors, the loading time was considered. The test results have shown that there is no significant influence of the cycled temperature on the ultimate resistance of bonded connections.

For constant and alternating temperatures the ultimate resistance of bonded connections is sufficient for the postulated temperature range.

No.	Objectives	Test specimen	Parameters varied
1	Connections of the diagonal members and vertical struts		- stainless steel plate thickness t = 2, 3 and 4 mm
2	Truss joints		- stainless steel plate thickness t = 2, 3 and 4 mm
3	Chord joints		- stainless steel plate thickness t = 2, 3 and 4 mm - profiles U 200 and U 240
4	Temperature behaviour		- constant temperature -40°C, -25°C, -10°C +23°C, +40°C, +55°C - alternating temperature -25°C up to 40°C
5	Coating system for the bridge deck with a finish layer		- 6 sharp edged gravel's - 22 coating systems - crossings - steering-in-place

The test programme has been supplemented by proving tests on the prototype bridge

Figure 6 Overview of the test programme

3.4 Coating system with sand finish for the bridge deck elements

In the framework of this research project an extensive test programme has been undertaken to specify the best coating system, which consists of a primer and a mineral finish for lightweight FRP-deck elements. In a pre-test series the sharp-edged grave, which caused most damage to FRP-decks was from six different samples of gravel.

The main test programme consisted of 'the wheel crossing- and the steering-in-place' tests for 22 coating systems obtained from different fabricators. Before the tests, all specimen were weighed to determine the coating weight per unit area. Furthermore, the first grip- and throatness tests were performed with the pendulum test set-up[13]. The combined grip- and throatness values were determined at five different measuring points per specimen exposed to the air- and coating temperature.

The whole test programme was undertaken on 22 coating systems from various fabricators. After every tenth 'wheel crossing' the truck was 'steered-in-place', which is the most damaging for the coating. At specified intervals visual inspections were made in conjunction with further grip- and throatness tests. After 200 crossings combined with the 'steering-in-place' tests a preliminary selection of coating systems was undertaken; these selected coating systems were then tested to failure.

At the end of the tests, table 3 has shown that most of the coating systems are in excess of the minimum required grip- and throatness value of 60 reference[13]. Nevertheless, a significant depth of local damage of the mineral layer was detected, which sometimes has destroyed the surface of the FRP-element.

After considering the coating weight per unit area, the local damage and the combined grip- and throatness values a coating system with a coating weight of 2,2 kg/m² was chosen. This coating system showed no local damage and a small abrasion of the mineral layer only.

The chosen coating system has been applied on the final deck elements of the prototype bridge and has shown an excellent performance under realistic conditions.

Table 3 Extract from the test programme coated FRP deck elements for lightweight structures (without manufacturers specifications)

Element No.	Specification	Fabricator	Weight	Grip- and throatness test Crossings				
				0	50	100	200	400
1	ABC	XYZ	1,3 kg/m²	79,5	78,0	82,0	74,9	79,7
2	ABC	XYZ	5,0 kg/m²	56,5	70,6	73,2	65,7	74,7
3	ABC	XYZ	5,5 kg/m²	47,7	50,4	55,6	42,0	49,5
4	ABC	XYZ	4,1 kg/m²	90,2	83,8	80,2	77,7	76,7
5	ABC	XYZ	2,2 kg/m²	95,5	89,4	86,4	79,4	79,4
...	...	...	...	...	...	...	...	...
22	ABC	XYZ	7,2 kg/m²	84,5	83,8	81,4	79,5	83,9

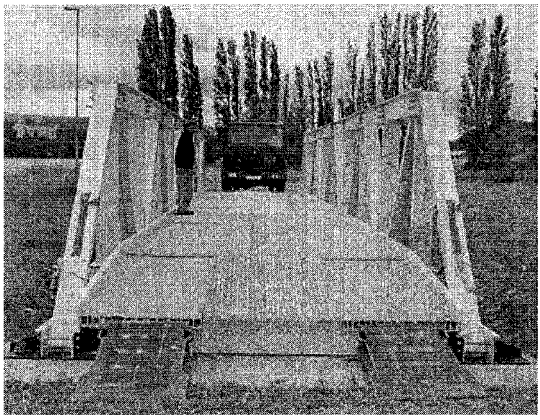
3.5 Proving of the prototype bridge

The prototype of the lightweight fixed bridge was constructed and dismantled several times before delivering to the client for further proving tests in summer 2002.

The load classes chosen for the proving tests were trucks of MLC-7, MLC-12 and MLC-14, Figure 7. All the critical truss members, those members of interest and the

connections were strain gauged at selected positions, and encoders were placed in position, Figure 8. The areas of specific interest are the reinforced areas of the bolted hybrid connections and the segmental joints.

In total, over 6000 longitudinal crossing, with speeds up to 40 km/h, have been made to date most crossings were made with the load class MLC-12. In addition, visual inspections have been carried out at frequent intervals.



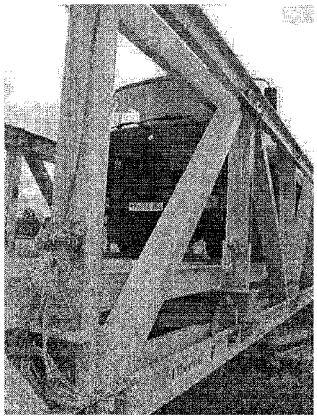


Figure 7 and 8 Prototype light-weight fixed bridge during proving tests at the „Wehrtechnischen Dienstelle für Pionier- und Truppengerät"

The maximum deformation at mid-span under MLC 14 load of 35 mm was only 30% of the expected displacement according to the static analytical analysis. This can be explained by the higher mechanical properties of the material used (see section2.3 – factor 1,35 for the longitudinal modulus of elasticity) and the strengthening of the truss joints by bonded stainless-steel plates. All deformations were fully elastic – no residual deformations were detected.

The measured stresses in the truss members and joints confirmed the utilisation ratios from the design checks.

During the proving tests no fatigue problems of the structure or the truss joints have been detected to date. This confirms the results of other research projects[4], which have estimated good fatigue resistances of fibre-reinforced materials.

In the final test the ultimate load on the total structure was determined. For this ultimate test special plates with dimensions of the MLC-footprints were fixed onto the deck plate in mid-span in accordance with the MLC axle-dimensions. The bridge was loaded statically, in increments, with steel blocks according to the axle load-tables for MLC, Figure 9.

After each load increment (each 1 t) the bridge was left for some time to investigate creep effects. Simultaneously, the strains and deflections were measured and compared with the static design. All strains and deflections measured in these final tests were elastic and no creep effects were detected. The first failure occurred at a load level of MLC-42 in the lower truss joint at mid-span at the position of the rear axle. This first failure was followed by a second failure in the upper truss joint in the first chord field, which caused a local instability of the top chord and this was followed by the total collapse of the bridge, Figure 10.

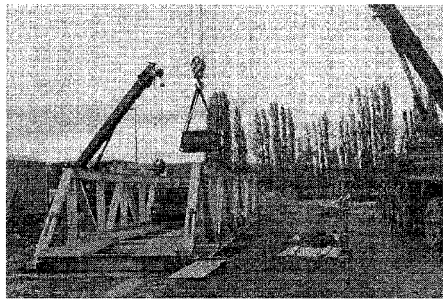


Figure 9
Loading in various steps for the ULS

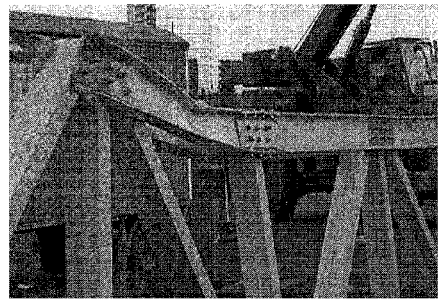


Figure 10 Collapse of the bridge due to connection failure and local instability of the top chord under MLC-42 loads

4. NEW FRP-BRIDGE FOR MLC-40 AND A SPAN OF 30.0 M

For the second research-project, which was launched in spring 2003, the loadings on the bridge have been increased up to a total load of MLC-40, with a span of 30.0 m. Further main technical requirements, such as dismountable connections and truss members, have been incorporated according to the specifications listed in section 2.1.

The design of the new FRP-bridge is based on the experiences of the test programme and the proving tests of the first bridge. Various modifications and improvements have been suggested and discussed with the client and manufacturers. The investigations on FRP-profiles carried out within the new research project comprise the following main objectives:

- feasibility study of an optimised design with special regard to the specifications and the material characteristics,
- development and testing of new dismountable connection techniques,
- optimisation and production of a new pultruded hollow deck plate with webs that form a Warren-truss,
- adapting the rovings and mats of each member according to their specific loading by the laminar theory.

A Warren truss with two vertical truss planes has been chosen where the second truss plane will be used for spans above 20.0 m, Figure 11. Further optimisation design steps will follow to achieve the most economic lightweight design using both standard and new cross sections.

With regard to the connection techniques, various tests are being undertaken, for instance, strengthening with carbon layers, adapter bushings and inductive bonded collar jackets, Figure 12. The local strengthening by using inductive bonded collar jackets has already shown an increased bearing capacity of 100% in the pilot tests. Now the optimised dimensions of the collar jackets, the clearance of the holes and the best inductive application method are being investigated.

The new pultruded hollow deck plate forming a Warren truss is being developed with special regard to the fatigue resistance. The deck plate will also act as a stiffening element for the U-frame action of the truss. Various parameter studies are being examined to determine the optimised dimensions, focussing on the transition radius. Within this investigation FE-simulations and the fracture mechanics method are being used to reach a modular lightweight element which ensures sufficient fatigue resistance.

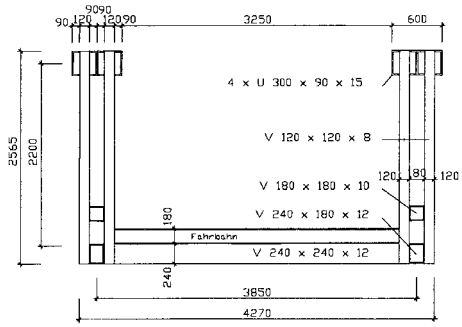


Figure 11
Pre-design of the second FRP bridge

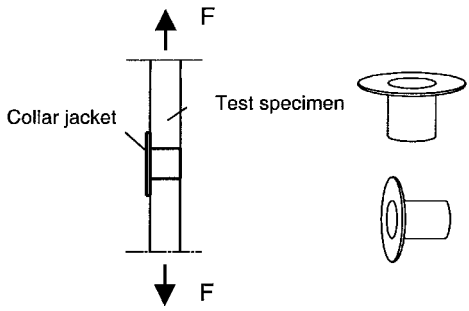


Figure 12 Strengthening the bearing capacity by inductive glued collar jackets

New sophisticated software will be used to determine the optimised position of the rovings and mats of each truss member the stresses and serviceability demands based on the laminar theory. As a first step, the stiffness characteristics of each layer (micro-mechanics) are determined followed by the calculation of stresses and strains (macro-mechanics). Finally the failure modes are determined using the strength hypothesis by Puck [14]. The developments will be tested under static and dynamic loading on full-scale specimens. Finally all of these investigations will flow together in an optimised design of a sophisticated modular lightweight FRP bridge.

5. CONCLUSIONS

The paper presents the design and test programme for a lightweight fixed bridge made of glass-fibre-reinforced-polymer profiles, which was built as a prototype in the Summer 2002 for proving tests. The design and static verification shows that the existing rules and publications are not sufficient to determine the ultimate resistance for hybrid connections, designed as combined bolt/adhesive connections. The test programme showed that there was sufficient ultimate resistance to all connections and framework joints. The final ultimate loading test showed full elastic behaviour and confirmed sufficient robustness (designed for MLC-14, ultimate load MLC-42).

In the new research project these experiences will be used to extend the span to 30.0 m and to increase the load up to MLC-40. By using optimised FRP-cross sections (extension of the available range of sections and shapes) for the truss members and the deck a further 30% of weight will be saved. Furthermore, sophisticated dismountable connections are developed to meet the requirements of the material characteristics. For the final carriageway hollow deck plate elements with webs that form a truss in transverse direction have already been designed.

In order to verify and to extend the rules for FRP-structures and connections further tests and numerical simulations are under examination taking into account various geometric cross-sections and FRP-qualities.

6. ACKNOWLEDGEMENT

Sincere thanks are given to the Ministry of Defence for sponsoring the research project and the "Wehrtechnischen Dienststelle für Pionier- und Truppengerät, Koblenz" for the personnel, logistic and technical support for building up the prototype bridge and performing the proving tests. Special thanks go to the "Technischen Schule des Heeres/ Fachschule des Heeres für Technik, Aachen" for the personnel support during fabrication, transport and providing the production hall.

The test programme has been performed with Dipl.-Ing. U. Castrischer; the production with unskilled students has been carried out under the direction of cand.-Ing. J. Kowalewsky. Sincere thanks are given to Fiberline Composites A/S in Kolding, Sika AG in Zürich and Roadcoat in Mörfelden/Walldorf for supporting the research-project by delivering the materials for the test programmes and the prototype bridge.

REFERENCES

[1] Künzle, O., Strehler, B., 'Static and Dynamic Testing of Fibre-Reinforced Bridge Girders', *Structural Engineering International*, SEI Volume 9, Number 4; Nov. 1999.

[2] Braestrup, M.W., 'Footbridge Constructed from Glass-Fibre-Reinforced Profiles', *Structural Engineering International*, SEI Volume 9, Number 4; November 1999.

[3] Sobrino, J.A., Pulido, M[a] D., 'Towards Advanced Composite Material Footbridges', *Structural Engineering International*, SEI Volume 12, Number 2; May 2002.

[4] Luke, S., Canning, L., Collins, S., Knudsen, E. Brown, P. Taljsten, B., Olofsson, I., 'Advanced Composite Bridge Decking System – Project ASSET', *Structural Engineering International*, SEI Volume 12, Number 2; May 2002

[5] Fiberline Design Manual/ Design- und Konstruktionshandbuch für Konstruktionsprofile aus Verbundwerkstoffen, Fiberline Composites A/S, 1995.

[6] EN 13706, 'Reinforced plastics composites - Specifications for pultruded profiles', Part 1,2 and 3; CEN /TC 249.

[7] DIN 53452, EN ISO 527-1, ‚Plastics - Determination of tensile properties -, Part 1: General principles', German version EN ISO 527-1: 1996.

[8] Habenicht G., *Kleben - Grundlagen, Technologie, Anwendung*, 3. Auflage, Springer Berlin Heidelberg New York 1997.

[9] Volkersen, *Die Schubkraftverteilung in Leim-, Niet- und Bolzenverbindungen*, Energie und Technik, 1958.

[10] Castrischer U., *Konstruktive Entwicklung und statische Bemessung einer mobilen Leichtbau-Festbrücke aus pultrudierten glasfaserverstärkten Polymeren mit Hybridverbindungen*, Diploma thesis, Lehrstuhl für Stahlbau; RWTH Aachen, 2001.

[11] Sedlacek, G., Trumpf, H., Geßler, A., Castrischer U., *Abschlussbericht und Statische Berechnung: Pionier-Leichtbau E/K 41C/V 0085/V 5115, Konstruktive Entwicklung und statische Bemessung einer mobilen Leichtbau-Festbrücke aus pultrudierten glasfaserverstärkten Polymerprofilen mit Hybridverbindungen*, Lehrstuhl für Stahlbau; RWTH Aachen 2002 – unpublished -

[12] DIN EN 1465, 'Adhesives - Determination of tensile lap-shear strength of rigid-to-rigid bonded assemblies (ISO 4587: 1979 modified)', German version EN 1465: 1994

[13] Forschungsgesellschaft für das Straßenwesen, Arbeitsgruppe: Fahrzeug und Fahrbahn, ‚Arbeitsanweisung für kombinierte Griffigkeits- und Rauhigkeitsmessungen mit dem Pendelgerät und dem Ausflussmesser; Forschungsgesellschaft für Straßenwesen', Ausgabe 1972

[14] Puck, A., Festigkeitsanalyse von Faser-Matrix-Laminaten (Modelle für die Praxis), Carl Hanser Verlag, München, 1996

GFRP COMPOSITE ROCK BOLT WITH HEAD OF LARGE BEARING CAPACITY

Kenzo Sekijima[1], Kentaro Ikeda[2], Takashi Nishimoto[3],
[1]*Kurasoku Kensetsu Consultant Co., Ltd,* [2] *Shimizu Corporation,*
[3]*Asahi Glass Matex Co., Ltd.*

ABSTRACT

Nowadays, the New Austrian Tunneling Method (NATM) is most popular in Japan. Shotcrete and a steel rock bolt are used as the main supports of this method. However, when a tunnel is constructed in a corrosive environment as a hot spring, a steel rock bolt may be corroded within a long term and lose their supporting effect. Moreover, a long steel rock bolt is heavy and difficult for handling in a narrow space like as a tunnel.

Recently, since fiber reinforced polymer (FRP) is light in weight, moreover it has a high strength and an excellent durability, it has been applied in the civil engineering field. Especially, it is used as reinforcement or prestressing tendon for concrete members.

In the field of NATM, a glass fiber reinforced polymer (GFRP) rock bolt has sometimes been applied. However, the bearing capacity of the head was only a quarter or one fifth of the tensile capacity of the rod. It was only effective as a temporary support but not as a permanent one.

Therefore, the authors have developed a new GFRP composite rock bolt. It had a special type of GFRP head, the rod was composed of GFRP and lauan wood, and the bearing capacity of the head was greater than the tensile capacity of the rod. In order to clarify the difference of the supporting effect between the GFRP composite rock bolt and a conventional steel rock bolt, three kinds of test were carried out, namely the tension test in a laboratory, the pull-out test and the long-term measurement in some tunnels.

OUTLINE OF GFRP COMPOSITE ROCK BOLT

Rod

The rod of the GFRP composite rock bolt was composed of three layers. The center part was made of a cylindrical lauan wood and its diameter was 20 mm. Glass fibers impregnated with vinylester resin were arranged around the lauan wood in the longitudinal direction. Then, glass fibers impregnated with vinylester resin were wound spirally on the surface of the longitudinal glass fibers to improve the bond property between the rod and grout in a hole of the rock. The outer diameter of the rod was approximately 28 mm.

Head

The head of the GFRP composite rock bolt was also composed of three parts. At the center of the head, there was a GFRP bulb in contact with the end of the lauan wood. Then, the longitudinal glass fibers impregnated with vinylester resin were arranged from the surface of the lauan wood to the surface of the GFRP bulb. The function of the GFRP bulb was to prevent the longitudinal glass fibers from slipping in when they were

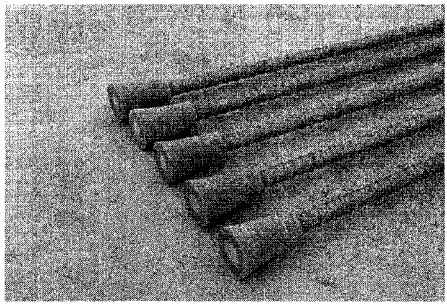


Figure 1 GFRP composite rock bolt

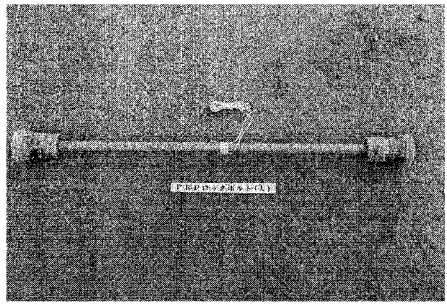


Figure 2 Specimen for tension test

applied to a tensile force. Then, glass fibers impregnated with vinylester resin were wound on the surface of the GFRP bulb in the circumferential direction. Finally, the outer shape of the head became a truncated cone as shown in Figure 1. The height and the maximum diameter were 95 mm and approximately 60 mm, respectively. The base of the head could support a bearing force of the bearing plate.

TENSION TEST OF GFRP COMPOSITE ROCK BOLT

Specimen

The specimen was shown in Figure 2. The number of the specimens was five. The length of the specimens was 900 mm, however, the maximum diameter of the GFRR bulb in the head was 40 mm (FT-1), 34 mm (FT-2 and FT-3) and 28 mm (FT-4 and FT-5), respectively.

Test method

The specimen was set vertically. Both bases of the heads of the specimen were gripped with the two-cut bearing plates, and then they were pushed apart by the cross heads of the testing machine. In this way, bearing forces were applied to the bases of the heads and a tensile force was applied to the rod. The load and the strain of the rod were measured until a failure of the specimen.

Table 1 Test result of tension test

Specimen	Maximum diameter of bulb (mm)	Initial tensile rigidity (kN)	Ruptute load of wood (kN)	Strain at rupture of wood (%)	Ultimate load (kN)	Ultimate strain (%)	Failure mode
FT-1	40	11,700	109	0.98	178	1.95	R
FT-2	34	12,300	89	0.73	155	1.81	S
FT-3	34	11,300	104	0.96	172	2.38	S
FT-4	28	13,100	124	1.30	153	1.76	S
FT-5	28	11,800	111	0.97	147	1.98	S
Average	-	12,000	107	0.99	-	-	-

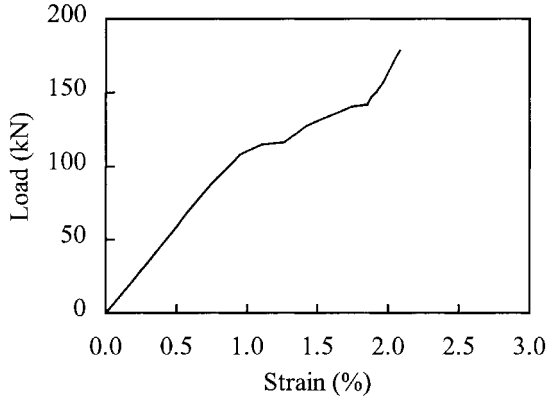


Figure 3 Load-strain relationship (FT-1)

Test result

Failure mode

The test results are shown in Table 1. All specimens failed due to a complete rupture of the lauan wood and a partial rupture of the longitudinal glass fibers. However, there were two types of failure modes of the head. In the case of FT-1, the GFRP bulb did not slip (mode R). The bearing capacity of the head was greater than the tensile capacity of the rod. On the other hand in case of FT-2 to FT-5, the GFRP bulb slipped in from the circumferential glass fibers (mode S).

Mechanical property

Figure 3 shows the load-strain relationship of FT-1. It was almost tri-linear. Those of the other specimens were similar to it. The first change of the tensile rigidity was caused by a rupture of the lauan wood. Since the elongation of the lauan wood was smaller than that of the longitudinal glass fibers, the lauan wood ruptured first. After this point, the tensile force was transferred from the lauan wood to the longitudinal glass fibers. This phenomenon was called a hybrid effect. Then, the glass fibers became the main material to support the tensile force in place of the lauan wood. This load varied slightly between the various specimens.

The ultimate load of FT-1 was the greatest of all specimens tested and its failure mode was appropriate. The head of FT-1 was adopted for the following tests.

PULL-OUT TEST IN TUNNEL

The stratum of the site was a breccia-tuff. The width and height of the tunnel were 6,500 mm and 5,500 mm, respectively. The tunnel was being constructed by a top heading method. The thickness of the shotcrete was 150 mm. The steel rock bolt was made of deformed steel bar D25. The diameter was 25 mm, and the nominal cross-sectional area was 506.7 mm^2. Its specification was SD295A (nominal yield strength was more than 295 N/mm^2). Its length was 2,500 mm.

Specimen

The GFRP composite rock bolt had identical rod and head as those of FT-1 in the tension test. Its length was 2,500 mm, and five wire strain gages were bonded on to the surface of the rod with a space of 500 mm. The number of the specimens was five.

The steel rock bolt was made of deformed steel bar D25; its length was also 2,500 mm. The head of the specimen was screwed. In order to bond the wire strain gages, two rectangular grooves were cut on its surface. Consequently, the reduced cross-sectional area of the steel rock bolt became 421.9 mm^2. Ten wire strain gages were bonded on to the surface of the grooves with the same spacing as that of the GFRP composite rock bolt. The number of the specimens was three.

Test method

First, holes were dug at the side wall of the tunnel with a crawler drill jumbo. Then, cement mortar was grouted and the specimens were inserted. This method was common for the GFRP composite rock bolt and the steel rock bolt.

Figure 4 shows the test apparatus for the pull-out test. The steel ram chair, on which a center hole jack and a load-cell were tightened, was set horizontally at the side wall. Then, the head of the specimen and the prestressing bar were connected with a coupler. A tensile force was applied to the rod of the specimen by pulling the head with the jack.

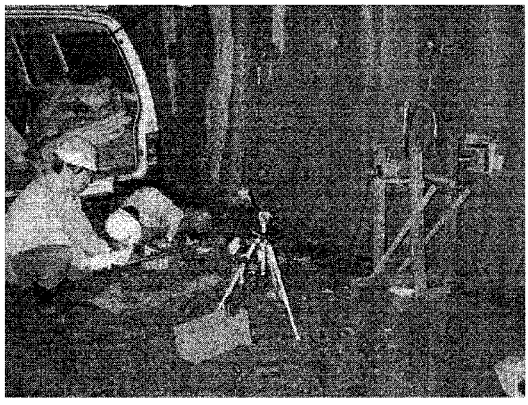


Figure 4 Test apparatus for pull-out test

Table 2 Result of pull-out test

Specimen	Ultimate load (kN)	Failure mode
FP-1	62.8	Rupture of rod at base of head
FP-2	154	Rupture of rod at base of head
FP-3	142	Rupture of rod at base of head and failure of head
FP-4	152	Rupture of rod
FP-5	152	Rupture of rod
SP-1	133	Rupture of screwed head
SP-2	98.1	Stop of test
SP-3	98.1	Stop of test

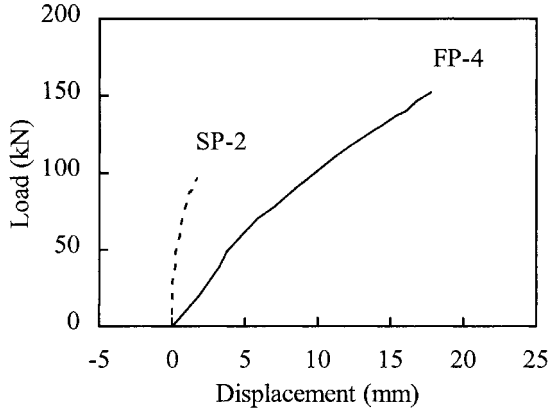


Figure 5 Relationship between load and displacement of head

Since the end of the prestressing bar and a dial gage was connected with a steel wire, the displacement of the head could be measured. The load, the strain of the rod and the displacement of the head were measured during the test duration.

Test result

Failure mode

The test results are shown in Table 2. The ultimate load of the GFRP composite rock bolt depended on the rupture of the rod but not on the bond failure between the rod and the cement mortar grout. The bearing capacity of the head was greater than the tensile capacity of the rod, and the spiral glass fibers gave a good bond property to the rod.

Displacement of head

Figure 5 shows the relationships between the load and the displacement of the head of the GFRP composite rock bolt FP-4 and the steel rock bolt SP-2. The displacement of FP-4 was much larger than that of SP-2, because the tensile rigidity of the former was smaller than that of the latter, namely only one eighth; furthermore, the bond properties were different[1,2].

Distribution of longitudinal and bond force

Figure 6 and Figure 7 show the distribution of the longitudinal forces of FP-4 and SP-2, respectively. The longitudinal force of FP-4 was calculated from the measured strain by making use of the load-strain relationship of FT-1 shown in Figure 3.

In case of SP-2, the greatest part of the bond force occurred near the side wall of the tunnel. However, in case of FP-4, the bond force became larger at the inside of the rock in accordance with an increase in the load. As the tensile rigidity of the GFRP composite rock bolt was small, its elongation became large, consequently, the bond between the rod and the cement mortar grout was lost and the load was transmitted to the inside of the rock[1,2].

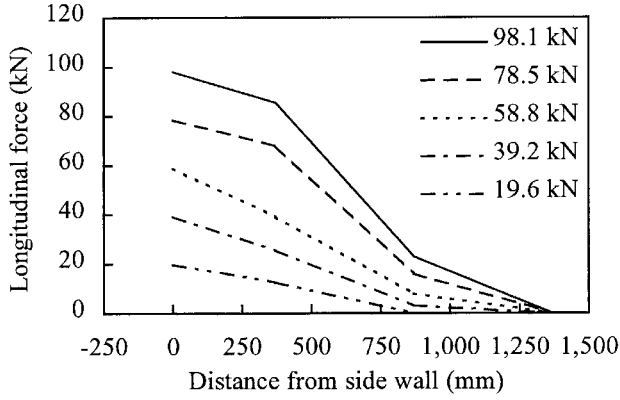


Figure 6 Distribution of longitudinal force (FP-4)

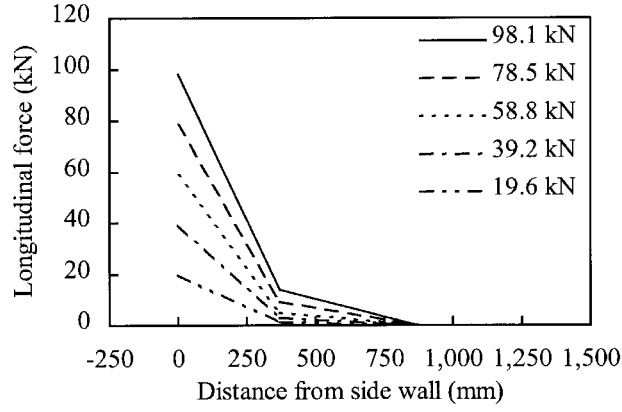


Figure 7 Distribution of longitudinal force (SP-2)

LONG-TERM MEASUREMENT IN TUNNEL

The stratum of the site was a combination of siltstone and sandstone. Both the width and height of the tunnel were 7,320 mm. The tunnel was also being constructed by a top heading method. The thickness of the shotcrete was 150 mm. The steel rock bolt was made of deformed steel bar D25. Its specification was SD295A and its length was 3,000 mm. Steel arched timbering was used, too.

Specimen

The GFRP composite rock bolt had identical rod and head as those of FT-1 in the tension test. Its length was 3,000 mm, and six wire strain gages were bonded on to the surface of the rod with a space of 500 mm. There were twelve specimens.

The steel rock bolt was made of deformed steel bar D25; its length was also 3,000 mm. The head of the specimen was screwed. Six electrical resistance strain gages were bonded on to the surface of the grooves with the same spacing as that of the GFRP

composite rock bolt. The number of the specimens was eight.

Test method

After an excavation of the top heading or the bottom heading and shotcreting, holes were dug immediately with an air auger. Then, cement mortar was grouted and the specimens were inserted.

The GFRP composite rock bolts were inserted between the original designed steel rock bolts (cross section I and II), because the plan of the arrangement of the steel rock bolts could not be changed. On the other hand, the steel rock bolts for the specimens were inserted in place of them (cross section III). The distance between each cross section was 1,000 mm.

The strains of the specimens were measured for more than 60 days.

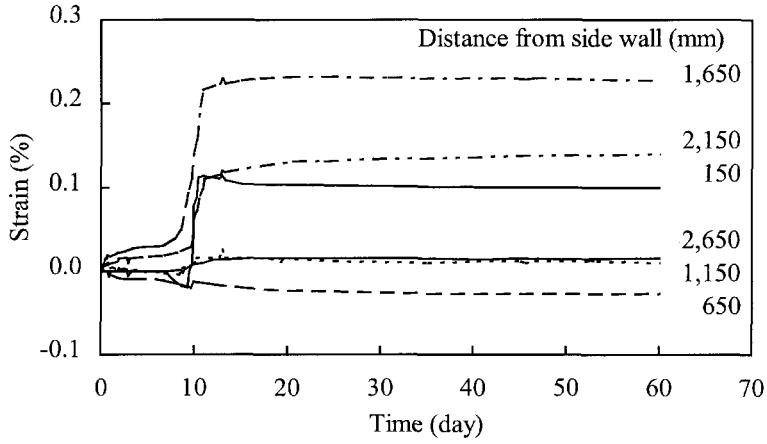


Figure 8 Time-dependent change of strain (FL-3)

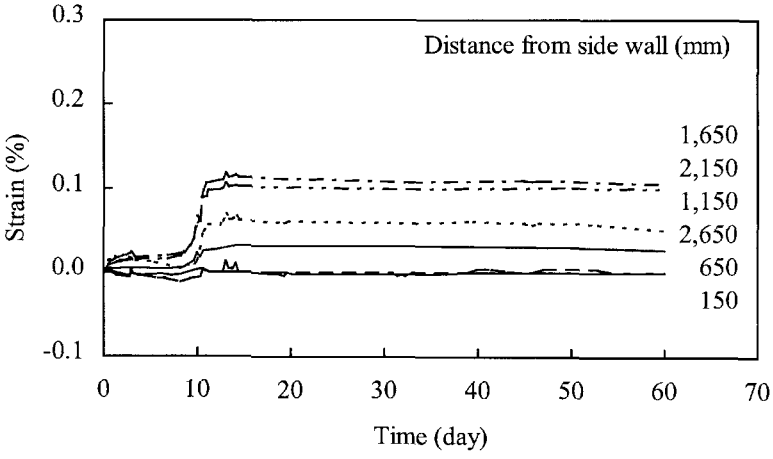


Figure 9 Time-dependent change of strain (SL-1)

Test result

Time-dependent change of strain

Figure 8 and Figure 9 show the time-dependent change of the strains of the GFRP composite rock bolt FL-3 and the steel rock bolt SL-1, which were inserted at the left side wall over the spring line of the tunnel (cross section II and III), respectively.

After the lower face had passed the cross sections, namely ten days later, the strains suddenly became larger, and then, they became stable. The strains of FL-3 were much larger than those of SL-1. Since the tensile rigidity of the GFRP composite rock bolt was only one eighth of that of the steel rock bolt, the effect to confine the strain of the rock was small[3].

Longitudinal force

The strains of the GFRP composite rock bolt were larger than those of the steel rock bolt, however, the longitudinal forces of the former were smaller than those of the latter, because the tensile rigidity of the GFRP composite rock bolt was smaller[3].

CONCLUSIONS

The bearing capacity of the head of the GFRP composite rock bolt was greater than the tensile capacity of the rod.

The tensile rigidity of the GFRP composite rock bolt was smaller than that of the steel rock bolt.

The displacement of the head of the GFRP composite rock bolt was much larger than that of the steel rock bolt at the pull-out test in the tunnel. Moreover, their bond properties were different.

The strains of the GFRP composite rock bolt were larger than those of the steel rock bolt, however, the longitudinal forces of the former were smaller than those of the latter at the long-term measurement in the tunnel.

The GFRP composite rock bolt can be used as a permanent support and it will be effective for a soft rock.

REFERENCES

1 Ikeda, K., Sekijima, K. and Nishimoto, T. 'Development of new FRP rock bolt and its properties', Proceedings of the 43rd conference of the Japan Society of Civil Engineers, 1988. (in Japanese).

2 Ikeda, K., Sekijima, K. and Okamura, H., 'New materials for tunnel support', 13th congress, Helsinki, IABSE, 1988.

3 Sekijima, K., Ikeda, K., Mihara, Y. and Nishimoto, T., 'Long-term measurement of longitudinal force of FRP rock bolt', Proceedings of the 44th conference of the Japan Society of Civil Engineers, 1989. (in Japanese).

STATIC AND DYNAMIC BEHAVIOUR OF CFRP PRESTRESSED CONCRETE LIGHTING COLUMNS

Dr. Giovanni P. Terrasi[1] and Dr. Janet M. Lees[2]
[1] *SACAC AG, Lenzburg, Switzerland,* [2] *University of Cambridge*

INTRODUCTION

In 2000, a 27 m carbon fibre reinforced polymer (CFRP) prestressed concrete electricity pylon was installed in Switzerland[1]. The pylon was manufactured by combining two high strength materials; centrifugally-cast high strength concrete (HSSC) and non-corrodible, lightweight and high strength CFRP tendons (see Fig. 1).

After this successful application, the potential of transferring the technology to lighting columns was identified. Road environments are known to be very aggressive, causing corrosion at the fixture of plain steel, steel-reinforced or steel-prestressed concrete lighting posts. In a steel-prestressed concrete structure a large concrete cover (40-50 mm) is required in order to protect the steel from aggressive environments. In contrast, CFRP is very durable thus only a relatively small concrete cover (15-20 mm) is necessary. As a result, CFRP prestressed poles are lighter than equivalent steel-prestressed poles and benefit from lower transportation and installation costs.

The focus of this project was the development of an 8 m nominal height CFRP prestressed high strength concrete lighting column (Carbolith®, see Fig. 2) fulfilling the requirements of the relevant European Standard EN40 Series[(2)(3)(4)(5)]. A particular design consideration was the influence of an electrical fuse box opening on the column behaviour. Both the static and dynamic behaviour of the lighting poles were considered.

LIGHTING COLUMN DETAILS

The configuration and dimensions of the prototype 9.2 m (8 m nominal height) tapered cylindrical lighting columns are shown in Figure 3.

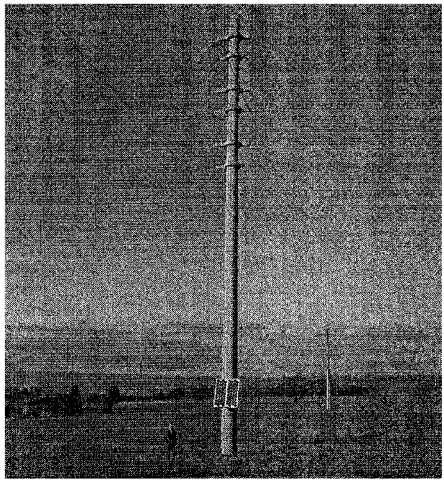


Figure 1: 27 m CFRP prestressed electricity pylon (owner: NOK)

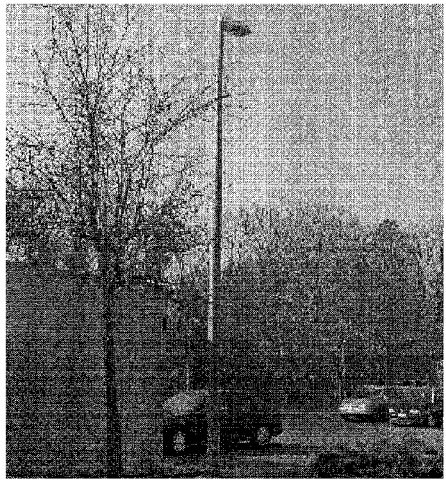


Figure 2: Installed Carbolith® lighting column (height 8 m)

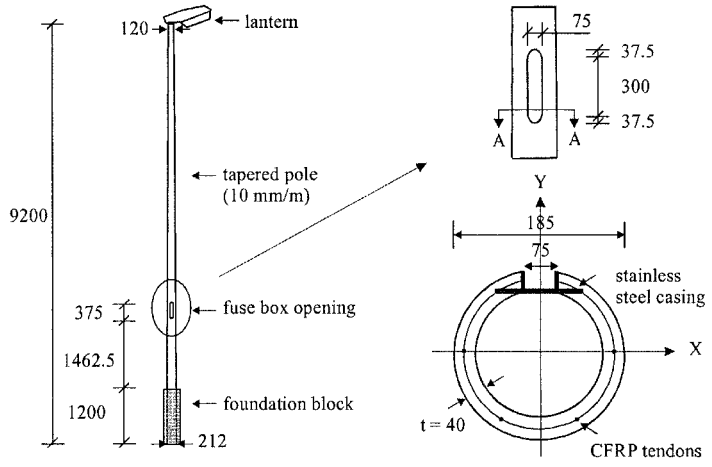


Figure 3: Pole details (all dimensions in mm)

The lantern type and the geometry and position of the electrical fuse box opening were chosen to reflect common practice in central Europe. The poles were tapered and the outer diameter varied from 120 mm at the tip to 212 mm at the foot. The average wall thickness of the pole was 40 mm ± 10 mm (measured at the tip and foot surfaces).

The poles were centrally prestressed with six pultruded CFRP tendons of diameter 4 mm (minimum tensile strength = 2'200 N/mm^2, E = 160'000 N/mm^2) with an initial prestress force of 16.6 kN (σ_{p0} = 1'320 N/mm^2). The tendons had a ceramic coating on the outer surface to improve the bond properties. The total central prestressing force in the pole was 100 kN (at prestress transfer). The need for an electrical fuse box opening 1.5 m from the top of the foundation was an important design consideration. The opening was defined and reinforced by a stainless steel casing consisting of two deflector-beams to deviate the two tendons running through this region (see Fig. 3).

A total of five prototype poles were manufactured for the experimental programme. There was no shear reinforcement in poles 1 and 2 but three different types of shear reinforcement were adopted for pole numbers 3, 4 and 5. In pole 3, a PVA geogrid (180 kN/m-transverse, 180 kN/m-longitudinal, 90/0°, over a length of 3.8 m) was used and in pole 4, an aramid-fibre geogrid (150 kN/m-transverse, 30 kN/m-longitudinal, 90/0° over a length of 5 m) was incorporated. Both geogrids had a mesh size of 30 mm. The shear reinforcement of pole 5 consisted of rolltruded CFRP tape with an average tensile strength of 2'500 N/mm^2 and a Young's Modulus of about 150'000 N/mm^2 which was spirally wound around the longitudinal tendons with a pitch of 35 mm.

Typical mechanical properties of the HSSC mix were; a minimum 28 day compressive cube strength of over 90 MPa, a minimum tensile strength of 5 MPa, a Young's Modulus of 38,550 MPa and an ultimate strain of 0.0035. Two weeks after production, a reinforced concrete foundation block with dimensions 360 × 360 × 1200 mm was cast over the foot region of each of the five pole specimens (see Fig. 3) resulting in a 1.2 m fixture length for the planned cantilever tests.

APPLIED LOADING AND DESIGN PHILOSOPHY

The most relevant loading condition for the lighting columns was the wind. The average unfactored wind pressure on the pole was 600 N/m^2 which was calculated by

assuming installation in a flat area with occasional small structures, a basic wind velocity at 10 m above sea level of 30 m/s and a mean shape factor of 0.52. Based on the manufacturer's geometric data and a shape coefficient of 1.0, the resulting unfactored wind pressure on the lantern was calculated in accordance with EN 40-3-1[4] to be 1'325 N/m^2. A partial wind load factor of $\gamma_f = 1.4$ (for transient wind gust action) was used[4] and the partial load factor for the self-weight was $\gamma_G = 1.2$. In order to determine the increase in load resulting from the dynamic behaviour of the column caused by wind gusts, a lateral free vibration analysis was carried out. The analysis was performed by considering a 10 mm/m tapered cantilever beam of free length 8 m, made of pure concrete (uncracked HSSC, $E_{co} = 40\times10^9$ N/m^2), with round cross section, an outer diameter of 200 mm at fixture and a constant wall thickness of 40 mm. The fuse box opening and the corresponding reinforcing steel casing were not taken into account, while a single mass of 18 kg (the lantern) was considered on top of the pole. The first two eigenvectors (mode shapes) and the corresponding eigenvalues (first two vibration frequencies) were calculated by defining an equivalent two-degree-of-freedom system under the assumption of two adequate bending shape functions in order to compute an equivalent mass- and stiffness-matrix from the kinetic and potential energy for solving the corresponding eigenvalue problem (Rayleigh-Ritz method). Considering that the damping ratio ζ of a fully prestressed concrete beam is very low[6] (in the range of 0.7%), the damping force was neglected in the computation model and the energy conservation principle could be applied. The first two free vibration frequencies of the lighting column with a lantern, f_1 and f_2, were calculated to be 1.97 Hz (with a basic period of vibration $T_0 = 0.51$ sec) and 9.68 Hz respectively. The first vibration frequency was then used to determine the design factor β for the dynamic behaviour of the poles. A value of $\beta = 1.25$ (used as a multiplier on the static loads) was calculated following the specification standard in EN40-3-1[4]. For a pole without a lantern (no mass on the top of the pole), the first vibration frequency was found to be $f_1 = 2.29$ Hz.

The service load conditions were determined by considering the unfactored ($\gamma_f = \gamma_G = 1.0$ and $\beta = 1.25$) characteristic design loads (self-weight and wind[4]). The pole was designed to be fully prestressed at maximum service load in order to limit deflections. The formation of bending cracks is to be avoided so that the moment of inertia of the entire cross section is available to sustain the service moment. In the uncracked state the pole behaviour was analogous to that of an elastic cantilever.

By multiplying the serviceability test loads by the factor $\gamma_u = 1.7$, the minimum ultimate test loads required by the EN[4] were obtained (see Table 1). To calculate the predicted ultimate bending moments of resistance, an inelastic analysis based on the short-term stress/strain curves of CFRP and high strength spun concrete was carried out. The characteristic material strengths were reduced by appropriate partial material safety factors (1.15 for the CFRP tendons and 1.3 for the dense spun concrete). As in classical prestressed concrete analysis, the equilibrium of internal forces and moments was considered assuming perfect bond and the principle of plane sections remaining plane. Since the section geometry and concrete prestress varied along the length, each pole cross-section was considered separately. One important design consideration is the location of the fuse box relative to the load direction. Thus the combined interaction of X-X flexural moments (where the fuse box was on either the compressive or tensile face), Y-Y flexural moments (fuse box on the neutral axis) and torsional moments due to the lantern eccentricity was taken into account.

STATIC AND DYNAMIC TESTS

The experimental programme included freeze-thaw durability, torsion, static bending/torsion and dynamic tests (free bending vibration). However, this paper will report primarily on the static bending/torsion and the dynamic test results.

The five prototype specimens (poles 1-5) were tested in Cambridge, UK. Each pole was fixed to the strong floor by prestressing the end foundation block (see Fig. 4). All the pole specimens were centrally supported by means of a trolley to 'compensate' for the self-weight moment in the vertical plane. The off-axis tensile load was introduced at the tip of the pole by a specially manufactured steel clamping rig.

Bending/Torsion tests

In the main bending/torsion cantilever tests, the fuse box opening was positioned on the compression edge for poles 1 and 3 (M_{+x}), along the neutral axis for pole 2 (M_y) and on the tension edge for poles 4 and 5 (M_{-x}) (see Table 1).

The poles had an effective bending lever arm of 7.99 m and a torsion lever arm of 0.14 m (the load eccentricity was imposed using the clamping rig). The clamping rig at the pole tip was pulled horizontally using a threaded rod connected to an electric motor, that transferred its rotation onto a nut via a chain-gear (see Fig. 4)

The deflection of the pole during testing was determined using Linear Resistance Displacements Transducers (LRDTs). Additional displacement transducers were installed to identify any tendon pull-in or any unexpected rotation of the foundation block (see Fig. 4). The torsion angular displacement was the only data measured by hand using a spirit level inclinometer bonded over the tip of the pole. The measurement of the crack pattern (crack widths, lengths and positions) was carried out at a reference test load of 1.2 kN. The testing regime consisted of applying the load in steps of 0.1 kN up to the serviceability test load, unloading in steps of 0.1 kN back to 0 kN, reloading in steps of 0.1 kN up to the minimum ultimate test load ($\gamma_u = 1.7$), unloading to 0 kN and finally, loading until failure.

Dynamic tests (free bending vibration of cantilever poles)

The free bending vibration of poles 4 and 5 was measured prior (pole 4 and 5, un-cracked state) and during (pole 4, cracked state) the static cantilever tests.

In order to determine reasonable values of the damping ratio, the support at 5.0 m from fixture was changed from the trolley to an even smoother crane support for 3 measurements of pole 4 (with an 8 m long strap on which the pole was hanging).

All tests commenced through an initial manual deflection of the pole's tip by 30 mm, 40 mm or 50 mm followed by a sudden release of the cantilever leaving it to vibrate freely (until all motion stopped). The time-decay of the tip deflection (at intervals of 5 ms) was measured by a calibrated LRDT of total range 150 mm bonded to the pole at 20 mm from its end. In order to check the displacement monitoring, the free vibration tests of poles 4 and 5 were also recorded by a digital video camera positioned in front of the pole's tip (recording the vibration of the pole's tip with a frequency of 25 frames/sec). The analysis of the time indexed ($\Delta t = 0.04$ sec) pictures of the pole tip was a simple and efficient manner to check the vibration frequencies determined from the LRDT signals.

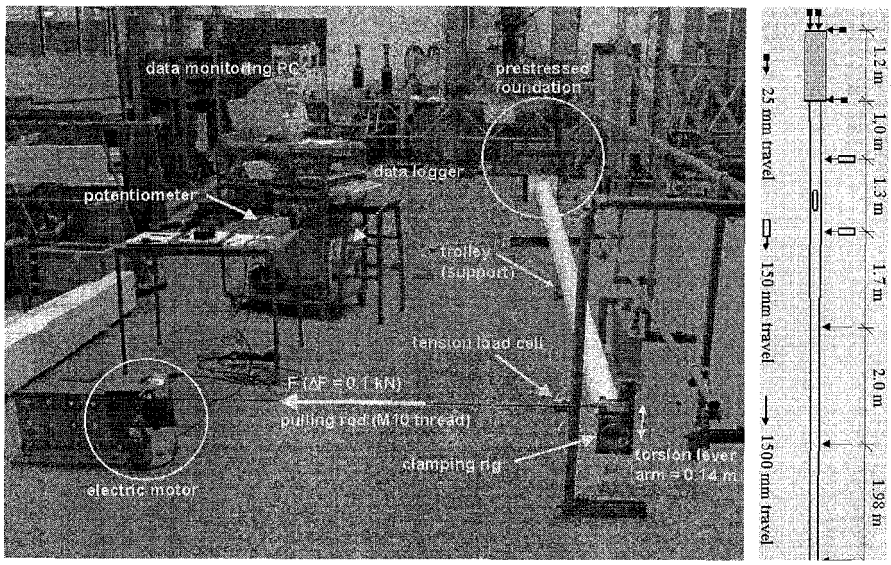


Figure 4: Experimental set-up (detail: LRDT positions and travel ranges)

RESULTS AND DISCUSSION

Bending/Torsion tests

The main results of the bending/torsion cantilever tests of poles 1-5 are shown in table 1. The experimental cracking loads (between 0.80 and 1.0 kN) were greater than the serviceability test loads calculated for the poles according to EN 40-3-1[4] (where $F_{ser}^{x,-x} = 0.56$ kN, $F_{ser}^{y} = 0.506$ kN). The EN serviceability deflection criteria were also easily satisfied. The poles could therefore be confidently considered to be fully prestressed under serviceability conditions. Furthermore, there was ample reserve load capacity after cracking so the appearance of cracks would provide a warning, well before failure, that the structure had been subjected to load levels higher than anticipated.

pole no.	Fuse opening location / load direction: ←	EN service test load (kN)	EN min. ultimate load (kN)	*Exper. deflect. at service test load (mm)*	*Exper. crack load (kN)*	*Exper. ultimate load (kN)*	*Exper. failure mode*
1	M_{+x}	0.56	0.95	*51.8*	*0.80*	*1.64*	*CFRP*
2	M_{y}	0.50	0.86	*42.6*	*0.86*	*1.79*	*CFRP*
3	M_{+x}	0.56	0.95	*52.0*	*0.95*	*1.89*	*HSSC*
4	M_{-x}	0.56	0.95	*47.7*	*0.90*	*1.56*	*CFRP*
5	M_{-x}	0.56	0.95	*51.2*	*1.0*	*1.64*	*CFRP*

Table 1: Summary of EN requirements and experimental results

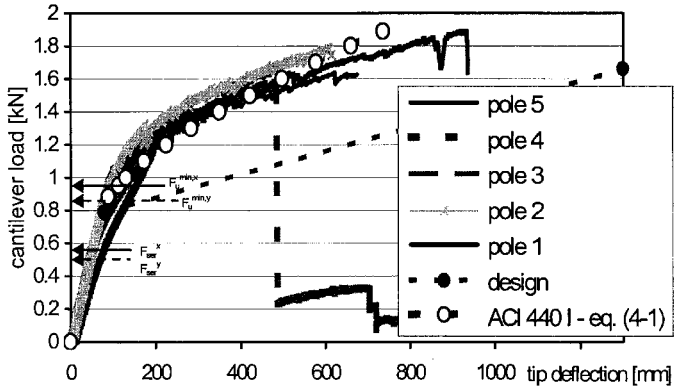


Figure 5: Load vs. tip deflection behaviour of poles 1-5 tested in bending/torsion

The deflections started to increase rapidly after cracking of the pole occurred. Large deflections were noted in the later stages of testing and the tip deflection varied between 475 mm and 925 mm immediately prior to failure (Fig. 5). The high rotation capacity came from the opening of thin, well-distributed bending cracks, originating from the fixture/opening area: A high deformation capacity in the cracked state could therefore be achieved, despite the use of two brittle materials (CFRP and HSCC).

The pole failure loads (between 1.56 and 1.89 kN) were considerably higher than the EN minimum required ultimate loads (0.86 kN and 0.95 kN) which indicates factors of safety in excess of the minimum requirements. Several failure modes were observed, depending on the testing position and on the shear reinforcement configuration. Poles 1 and 2 failed by the sudden snapping of the CFRP tendons on the tensile edge at cross sections near the fixture. Pole 3 (with the opening on the compression edge) contained additional longitudinal passive PVA reinforcement. This reinforcement acted to increase the tensile capacity of the cracked pole in the area of the opening and at the fixture and shifted the failure from the tensile to the compressive edge (HSSC). Poles 4 and 5 were tested with the box opening at the tensile flange, therefore the bending resistance of the area around the lower opening edge was reduced since the two CFRP tendons running next to the tensile edge were deflected inwards. Consequently, poles 4 and 5 failed by the sudden snapping of the CFRP tendons on the tensile edge near the lower edge of the opening.

The load vs. deflection behaviour of all 5 poles (see Fig. 5) was nearly bilinear, with a high bending stiffness in the uncracked state and then a gradual loss of stiffness after cracking. More details on the bending/torsion tests are given in [7]. The static experiments confirmed that both the serviceability and ultimate limit state static bending/torsion performance of the Carbolith® poles fulfilled the EN requirements.

Dynamic tests

The main results of the free bending vibration tests of the cantilever poles 4 and 5 are summarized in table 2. The basic vibration frequency f_1 was determined from the average damped vibration period T_d over 10 exponentially decreasing sinusoidal amplitude cycles in the tip deflection vs. time plots (Fig. 6). A computation of the damping ratio ζ_m was carried out through consideration of the time decay of the vibration amplitude again over 10 cycles. The comparison of the average basic vibration frequencies measured for the un-cracked poles 4 ($f_{1,m}$ = 2.45 Hz) and 5 ($f_{1,m}$ = 2.57 Hz)

pole nr.•test nr. state	deflection at start	support at x = 5 m	$f_{1,m}$ [Hz]	f_1^{video} [Hz]	f_1^{d} [Hz]	ζ_m [%]
pole 5 uncracked	40-50 mm	Trolley	2.57	2.55	2.29	1.736
pole 4 uncracked	30-50 mm	Trolley	2.45	2.44	2.29	1.259
pole 4 uncracked	30-50 mm	Crane	2.48	2.48	2.29	0.904
pole 4 cracked	30-50 mm	Trolley	2.43	2.40	2.29	2.782

Table 2: Free bending vibration tests of poles 4 and 5. $f_{1,m}$ / ζ_m are the average experimental basic vibration frequency/damping ratios determined from the time-decay curve of the tip deflection, f_1^{video} is the frequency value determined by digital video analysis of the vibration process

with the calculated basic frequency f_1^d = 2.29 Hz of the pole without lantern, shows that the chosen Rayleigh-Ritz computation model (neglecting the fuse box opening and assuming a tapered cantilever beam of free length 8 m, made of pure concrete) gave an accurate and slightly conservative approximation of the experiments, that is sufficient for serviceability design purposes. The somewhat higher value of $f_{1,m}$ measured for pole 5 was probably due to a higher bending stiffness of this pole (caused by a larger concrete wall thickness) in comparison with pole 4. The measured damping ratio for the uncracked poles was in the range of 1.5% (1.74% for pole 5 and 1.26% for pole 4) when using a trolley support at 5 m form their rigid fixture, while it decreased to about 0.9% when pole 4 was hanging on a crane at the same position. This value is probably very near the natural damping ratio of the cantilever poles in the uncracked state and is consistent with the value of 0.7% given in [6] for fully prestressed concrete poles. From this, one can conclude that the support by a trolley produced a higher horizontal friction reaction than the crane. On the other hand it was expected that the difference in basic vibration frequency of pole 4 due to a change of support type would have been very low. This was also the case after cracking pole 4 in the static cantilever test, where $f_{1,m}$ decreased from 2.45 Hz to 2.43 Hz (the pole was loaded to a cantilever point load of 1.2 kN in the second cycle of the static test, that induced 10 fine vertical bending cracks in its fixture region). The higher energy dissipation in the crack sections produced a considerable rise in the damping ratio of pole 4 with a mean value increase from 1.26% to 2.78%.

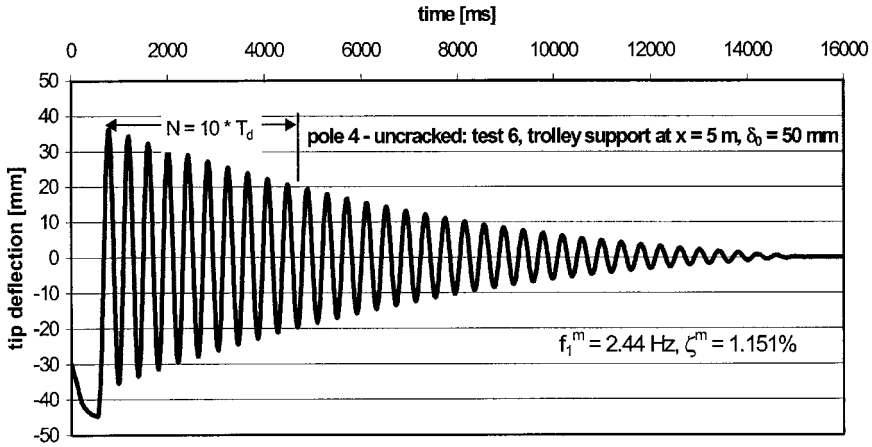


Figure 6: Free bending vibration test of pole 4 (uncracked)

CONCLUSIONS

(1)The full prestressed design of the CFRP prestressed high strength spun concrete lighting column was verified by testing five specimens in accordance with EN-40-3-2[4]. The serviceability, structural and minimum ultimate load requirements were fulfilled by all the pole specimens tested in cantilever bending/torsion.
(2) The poles showed sufficient bending rotation capacity to make up for the lack of plasticity of the brittle CFRP prestressing tendons.
(3) The three different types of shear reinforcement had no practical effect on the static behaviour of the cantilever specimens in the bending/torsion moment ranges achieved in the tests although the 0-90°-biaxial PVA geogrid reinforcement proved to be advantageous in increasing the ultimate load capacity of the pole.
(4) The ultimate load capacity was roughly the same regardless of whether the fuse box was on the compressive or tensile flange. A slightly higher capacity was obtained when the fuse box opening was located on the neutral axis. Except where the PVA geogrid was used, all the poles failed due to tendon rupture.
(5) The free bending vibration tests performed on two of the five cantilever specimens showed basic vibration frequencies and damping ratios in the range expected from the design calculations. The assumed coefficient β for describing the dynamic behaviour of the columns (following EN 40-3-1[4]) to compute the characteristic wind action could be verified by the experimental validation of the lateral free vibration analysis method adopted (Rayleigh-Ritz method).
(6) It is expected that the poles will provide a durable and cost-effective alternative to steel-prestressed and reinforced concrete poles for use in pedestrian and low speed traffic areas.

REFERENCES

1. Terrasi G. P., Bättig G., Brönnimann R.,"High-strength spun concrete poles prestressed with CFRP", FRPRCS-5, ISBN 07277-3009-6, University of Cambridge, England, Ed. C. Burgoyne, pp. 1103-1112, 2001
2. CEN/TC 50 "Lighting columns and spigots": European Standard EN 40-1: 2000: Definitions and terms, European Committee for Standardization CEN, Brussels
3. CEN/TC 50 "Lighting columns and spigots": European Standard EN 40-2: 2000: General requirements and dimensions, European Committee for Standardization CEN, Brussels
4. CEN/TC 50 "Lighting columns and spigots": European Standards EN 40-3-1: 2000, EN40-3-2: 2000, prEN 40-3-3: 1999 (final draft): Design and verification, European Committee for Standardization CEN, Brussels
5. CEN/TC 50 "Lighting columns and spigots": European Standard EN 40-4: 2000: Specification for reinforced and prestressed concrete lighting columns, European Committee for Standardization CEN, Brussels
6. Bachmann H. et al, "Vibration Problems in Structures: Practical Guidelines", Birkhäuser Verlag Basel, 1995
7. Terrasi G. P., Lees J. M., "CFRP Prestressed Concrete Lighting Columns", Field Applications of FRP Reinforcement: Case Studies, Editors: S. H. Rizkalla and A. Nanni, American Concrete Institute International, SP-215, pp 55-74, 2003

DEPLOYABLE FRP TAPERED BOX-BEAM BRIDGE

R.G. Wight, C.T. Shyu, R. Tanovic, M.A. Erki, P.J. Heffernan
Department of Civil Engineering
Royal Military College of Canada
Kingston, Ontario K7K 7B4

INTRODUCTION

The Canadian Forces are replacing many of their tracked vehicles with wheeled vehicles in a move towards a "primarily wheeled Army" for cross-country mobility. Wheeled vehicles can achieve higher roadway speeds, require lower capital and maintenance costs, and, being lighter weight than tracked vehicles, can be more easily deployed. To compensate for the loss of cross-country mobility associated with this change, there arises a need for lightweight, inexpensive, short span bridges. The bridges would be mounted on vehicles and erected with minimal support. Owing to its favourable properties, FRP was the target material for the construction of these bridges. Investigations into a structural concept, adapted to the material properties of commercially available glass FRP (GFRP) pultruded products, are presented, along with preliminary test results of a 4.8 m prototype box-beam bridge.

DESIGNING FRP STRUCTURES – THE CHALLENGES

The introduction of fibre reinforced polymers (FRP) for civil engineering structural applications is in its infancy, but the favourable properties of FRP, such as high strength to weight ratio, corrosion-free characteristics, high degree of free formability and good fatigue resistance are very attractive to designers. The aeronautical/aerospace and automotive industries have successfully replaced primary and secondary metallic components with FRP, and many lessons could be drawn from these developments (1). Indeed, finding replacements in civil engineering construction for steel, that is heavy and susceptible to corrosion, is presently driving structural designers to consider FRP. However, there are many challenges in using FRP for structures, stemming primarily from the fiercely competitive construction industry and the requirement for large volumes of FRP compared to those used in the aeronautical/aerospace and automotive industries. Pressure to keep initial construction costs down drives the push to keep material costs low, and this dictates that FRP material production and quality control are necessarily inferior to those used in other industries (2). Hence, production of FRP for civil engineering structures is mainly through the automated pultrusion process, with its present limitations on fibre volumes, laminate configurations, and structural profiles. Therefore, while FRP holds great promise for certain structural applications, designers confront economic realities that challenge them to optimize FRP production that will in turn improve FRP material properties. These challenges are driving the push for innovations in FRP structural form and its associated connection technology.

The all-FRP structures and bridges built to date have mainly relied on the uneconomic practice of material substitution wherein the pultruded FRP members mirror structural steel profiles, namely channels, I-sections, rectangular tubes and flat plates (3). With the exception of tubular members, the free edges of the other types of profiles are inherently weak in FRP members, because of the different stress-strain characteristics of the laminae that make up the pultruded profile. Delamination can occur at low loadings at

these free edges. Additionally, the intersection between web and flanges is also a source of weakness, as the pultrusion process, without close intervention, omits the additional reinforcement of these critical zones. Keller (4,5), a pioneer in innovative FRP structures, makes the case that to make truly better use of FRP for structures new structural concepts are needed that will be adapted to the specific FRP material properties and the emerging improvements in pultrusion. These new structural concepts need to move away from the linear components seen in steel construction toward closed-cell and surface structures that are more suited to the FRP material properties.

THE PROPOSED STRUCTURE AND TESTING PROGRAM

Mindful of the challenges outlined in the previous section, it was decided that built-up box-beam components would fulfil the need for the transportable, lightweight, short span bridges discussed in the Introduction. The goal was roll-on/roll-off capability, with minimal terrain preparation for deployment of the bridge. Owing to the low rigidity of GFRP, the moment of inertia was maximized at mid-span, resulting in tapered box-beams. First, a balsa wood model, 600 mm long × 150 mm wide, was constructed to aid the design team in developing the final structure and in determining the fabrication sequence. Figure 1 shows a single track of the proposed bridge, consisting of a horizontal base plate, two triangular shape web plates, and an inclined ramp or top plate with a slope of 9.4°. The overall width of the box-beam is 1.2 m, and its length is 4.8 m. Without the wearing surface, the maximum height at mid-span is 0.5 m, and the minimum height at the ends is 0.102 mm. The full structure would consist of two tracks, lightly laced together with bolted GFRP sections.

The box-beam is built from hollow tube sections, 50.8 mm × 50.8 mm × 6.4 mm (2 in. × 2 in. × 1/4 in.), and plate sections, 6.4 mm (1/4 in.) thick, using adhesive bonding throughout. Hollow tube sections, a pair at the top and bottom, reinforce the web plates, such that the box-beam is essentially two built-up I-beams joined together by the top and bottom plates. Five equally spaced internal diaphragms, consisting of the same built-up I-beam components as for the webs, provide global lateral and torsional stability, as well as local stability to the top plate. Gusset plates, of the same plate material used throughout, connect the outer longitudinal tubes at the ends and the apex of the box-beam.

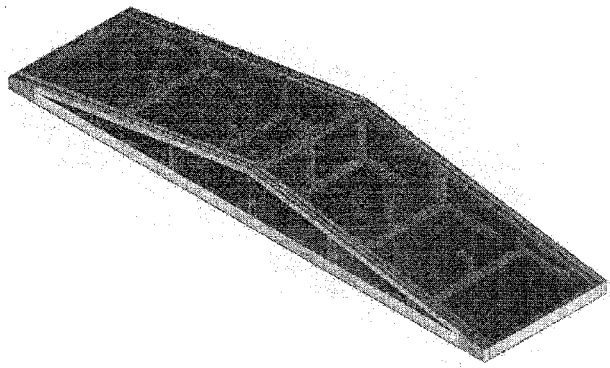


Figure 1. Model of the tapered box-beam.

The hollow tubes and plates are pultruded sections with alternating layers of randomly oriented fibres and unidirectional fibre rovings in a vinyl ester resin matrix for the hollow tubes and an isophthalic polyester resin matrix for the flat plate. The amount of glass fibre by weight for these sections is between 45 and 50%. Table 1 lists the mechanical properties of the sections and adhesive. The low modulus of elasticity in both tension and compression are noted, as are the anisotropic properties of the sections. The orientation of all the main plates of the box-beam, namely top, bottom and web plates, is with the unidirectional fibre rovings parallel to the longitudinal axis of the box-beam. In the webs of the internal diaphragms, the unidirectional rovings are parallel to the vertical axis of the box-beam. A commercial GFRP grating was chosen for the wearing surface and was bonded to the top plate of the box-beam. The grating also provides additional stability to the top plate. Without the grating, the weight of the box-beam is approximately 380 kg (840 lbs). The assembly sequence of the box-beam was established from the experience with the assembly of the balsa wood model. Figure 2 shows the fabrication stage at which the internal diaphragms have been placed.

Structural adhesive was used to connect the box-beam. Bolting was not considered, because of low connection failure loads for bolted FRP components in bearing, shear out, and tensile splitting (6). However, bonding the components presented construction challenges that required meticulous quality control throughout fabrication. Therefore, the single-track box-beam was fabricated under close supervision in the structural laboratory at RMC. Owing to size and shipping limitations of the GFRP components, additional joints were introduced in both the web members and the bottom plates, with

Table 1 Material properties for GFRP sections and adhesive

Property		Hollow Tubes*	Plates**	Adhesive***
Tensile Strength (MPa)	LW	258.4	137.8	16.9
	CW	55.1	68.9	16.9
Young's Modulus (MPa)	LW	19 292	12 402	388
Compressive Modulus (MPa)	LW	19 292	12,402	92
	CW	8 268	6,890	92
Poisson Ratio	LW	0.36	0.31	0.4
	CW	0.36	0.29	0.4
Elongation	LW	n/a	n/a	55%
Shear Strength (MPa)		40[a]	41.3[c]	
		8[b]		15-20[d]

Notes:
LW: lengthwise parallel to the longitudinal fibres;
CW: crosswise direction which perpendicular to the longitudinal main fibres.
* Design Guide, Creative Pultrusions Incorporated.
PULTEX, Vinyl Ester 1625 Series, 45-50% fibre by weight
** Design Manual, Strongwell Company (formerly MMFG).
EXTREN - Flat Sheets Polyester 500/525 Series Standard Fibre Content
*** data sheets, Ashland Chemical Company. Pliogrip 6600/7700 Series.
[a] cross-sectional shear; [b] interlaminar shear; [c] perpendicular shear; [d] lap shear

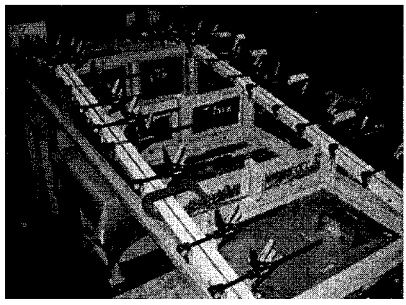


Figure 2. Fabrication stage showing the internal diaphragms.

an attempt to locate these in zones of eventual lower stresses. The bonding area of the sections was grit blasted, removing 1 to 1.5 mm of surface epoxy, until the glass fibres were exposed. The sanded surface was air blasted and solvent- wiped. The structural adhesive was applied to the prepared areas, and the components were joined with a constant adhesive thickness of 0.5 mm, achieved with round metal beads or electrical wire (both beads and wire having a 0.5 mm dia.). The components were clamped for four days until the structural adhesive was cured. The recommended clamping pressure was between 0.10 and 0.14 MPa (15 to 20 p.s.i.). Since the curing process took place at ambient temperature immediately following the application of the adhesive, it was essential to have the clamping applied as early as possible. Moreover, because long pieces of hollow tube and large pieces of flat sheets were involved, widely spaced small diameter bolts were also used to facilitate clamping.

The design vehicle for the bridge will be a eight-wheel light armoured vehicle, having a gross weight of approximately 135 kN. Since deflection and stability criteria controlled the design of the single track box-beam, it was decided to test the box-beam under a much greater load than would be encountered due to vehicle loading. The maximum test load was a patch load of 125 kN. Cold weather in situ testing using a vehicle is planned for early 2004. The laboratory tests were done initially on the structure without the grating wearing surface to de-couple the behaviour of the box-beam from that of the grating, and the structure was tested in three-point simple supported quasi-static loading. Figure 3 shows the completed box-beam with a mid-span patch load and without the wearing surface grating. At the apex, the patch load was nominally 250 mm × 250 mm (10 in. × 10 in.), which owing to the change in slope resulted in a contact area of 260 mm × 254 mm. Displacement control, 2 mm/min to 100 kN, reduced to 1 mm/min to 250 kN, was used. Strain gauges and LVDTs were placed at critical sections on the plates and hollow tubes of the tapered box-beam and its diaphragms. The following test results are for the first laboratory test with the patch load at the apex or mid-span of the box-beam. Tests results for a patch load applied at varying longitudinal and transverse locations on the box-beam, without and with the wearing surface grating, will be presented at the Conference.

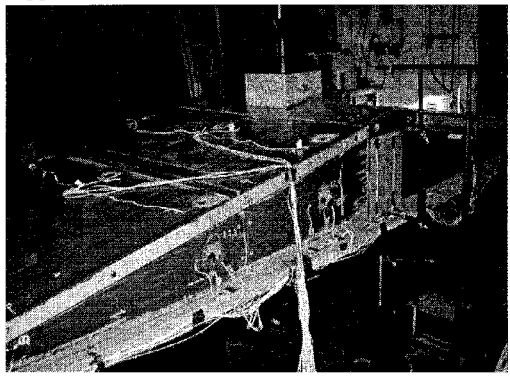


Figure 3. Completed box-beam with mid-span patch load, without the wearing surface grating.

RESULTS AND DISCUSSION

The results obtained from the laboratory test at mid-span, without the grating wearing surface, confirmed that the load-displacement behaviour of the tapered box-beam was linear elastic throughout. At the maximum load of 125 kN, the deflection of the box-beam directly below the mid-span patch load was 24.6 mm, compared to two analyses that predicted 25 mm. The analyses consisted of a simplified strength of materials calculation of the tapered built-up cross section and a 3-D linear finite element analysis, with frame elements representing the hollow tubes and shell elements representing the plates. This mid-span deflection corresponds to approximately $l/200$, where l is the span length. However, the patch load of 125 kN on the single track is over 90% of the gross vehicle weight, so that 125 kN is more than twice the total load expected in service, acting through the single patch load. Therefore the mid-span deflection would likely be better than $l/400$, which is acceptable. At mid-span, the deflections below the outer two webs were both 23 mm, indicating good transverse stiffness at this section. Lateral displacements were also measured at mid-span and were negligible, suggesting also good lateral stability, as expected for a symmetrical, closed section.

At 125 kN, the maximum stresses in the different components of the box-beam were in the range of $1/10^{th}$ to $1/7^{th}$ of the maximum strengths as reported by the suppliers of the materials, confirming that the box-beam is over designed for strength. Therefore, instability, excessive local deformations, or debonding failure will likely trigger ultimate failure. Indeed, without the grating wearing surface, significant local deflections of the top plate between the diaphragms were observed during the test. At 125 kN, these were in the range of 20 mm either upward or downward. Figures 4 and 5 show the observed downward and upward local deflections of the top plate at 125 kN. Figure 6 shows the longitudinal strains in the top plate midway between the vertical webs and at 1900 mm from the left support ($1/3^{rd}$ span). Plate bending occurs at the mid-span patch load of approximately 25 kN. It is expected, however, that subsequent tests with the wearing surface grating will result in improved stability of the top plate.

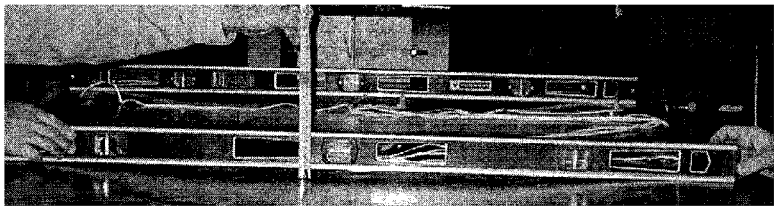


Figure 4. Top plate deformations downward due to mid-span patch load of 125 kN.

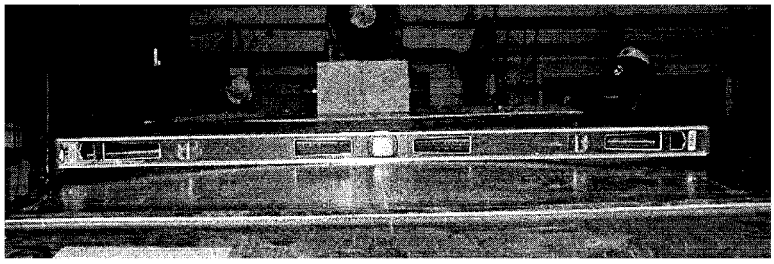


Figure 5. Top plate deformation upward due to mid-span patch load of 125 kN.

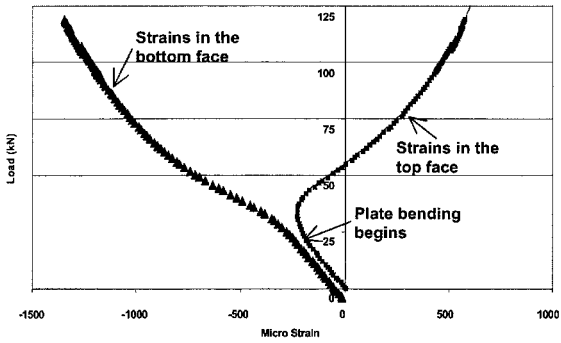


Figure 6. Top plate longitudinal strains at 1450 mm from left support (approx. 1/3rd span) showing plate bending at mid-span patch load of approx. 25 kN.

CONCLUSIONS AND RECOMMENDATIONS

To investigate the appropriateness of lightweight, inexpensive, short span bridges for the Canadian Forces' new fleet of wheeled vehicles, a 4.8 m span prototype tapered box-beam was constructed using commercially available GFRP pultruded sections. The low modulus of elasticity in tension and compression were considered in the development of the structural concept presented. The paper discussed the construction of the box-beam that used bonded connections throughout and reported upon the first laboratory test for an assumed maximum load at mid-span. The load-displacement behaviour of the tapered box-beam was closely predicted by both a simplified strength of materials calculation of the built-up cross section and a 3-D linear finite element analysis that included the diaphragms. At the maximum test load, the displacements were acceptable, and the test showed good transverse stiffness and good lateral stability at mid-span. The low modulus of elasticity of the plates led to significant local deflections of the top plate between the diaphragms. Since this first test was conducted without the wearing surface grating, it is expected that subsequent tests with the grating will result in improved stability of the top plate.

REFERENCES

1 J.R. Vinson and R. Sierakowski, *The behavior of structures composed of composite materials*, Solid Mechanics and Its Applications, Volume 105, Kluwer Academic Publishers, Dordrecht, The Netherlands, 2002.

2 V.M. Karbhari, 'Durability of composites for civil engineering infrastructure – myth, mystery or reality'. *Advances in Structural Engineering*, 2003 **6**(3) 243-255.

3 Th. Keller, 'Towards structural forms for composite Fibre Materials', *Structural Engineering International*, 1999 **9**(4) 297-300.

4 Th. Keller, 'Overview of fibre-reinforced polymers in bridge construction', *Structural Engineering International*, 2002 **12**(2) 66-70.

5 Th. Keller, 'Use of fibre reinforced polymers in bridge construction', *Structural Engineering Documents - Volume 7*, International Association for Bridge and Structural Engineering, Zurich, 2003.

6 G.J. Turvey, 'Bolted Connections in PFRP Structures', *Progress in Structural Engineering and Materials*, 2000 **2**(2), 146-156.

This page intentionally left blank

PART V

ANALYSIS, DESIGN AND TESTING

This page intentionally left blank

THE INFLUENCE OF SHEAR-FLEXIBILITY ON THE ELASTIC CRITICAL LOAD FOR FRAMES OF PULTRUDED FIBRE REINFORCED PLASTIC SECTION

A. Abbaker and J. T. Mottram

School of Engineering, University of Warwick, Coventry, CV4 7AL

ABSTRACT

By way of numerical examples this paper presents the influence of shear-flexibility on the elastic critical load for frames of Pultruded Fibre Reinforced Plastic (PFRP). Design of frameworks requires, not only checks on the joints and the members but also checks for the overall stability of the structure. This paper presents a plane frame analysis that can be used to predict elastic critical loads. To cope with members of advanced composite material the generalised column-beam element is shear-flexible. The analysis accounts for second-order P-Δ effects by the inclusion of shear-flexible stability functions, and semi-rigid action by the inclusion of the non-linear moment-rotation characteristics of the joints. Four simple examples are used to show the performance of the frame analysis tool. It is found that by increasing the shear-flexibility of the members the elastic critical load reduces and that this reduction depends on the joint stiffness. To ignore it presence in the design of PFRP frames might therefore result in an unsafe situation.

INTRODUCTION

Pultruded FRP (PFRP) structural sections consist of a number of thin-walled panels connected to form open or closed cross-sectional shapes [1-3]. Such sections are formed using E-glass fibre reinforcement and a thermoset resin matrix. PFRP sections are used in primary load-bearing trusses and braced frame structures with bolting being the preferred method of connection [1-3, 4]. Because of the small off-the-shelf range in shapes and sizes, beams and columns members are often the wide-flange sections, which are characterised by having the same breadth and depth dimensions and the same flange and web panel thicknesses. Section modulus in flexure is about 24 GPa (E) and the section in-plane shear modulus is about 4 GPa (G). The material tensile/compressive strengths are > 200 MPa along a section's length, and about half this stress in the perpendicular directions. Under short-term loading the material is linear elastic to failure. Structural failure is characterised by excessive deflection or by an instability mode (the material has high strength-to-modulus ratios). Yielding, which is associated with material rupture is an uncommon failure mode. Being lightweight and resistant to corrosion, sections are increasingly used where these advantages are required [4].

Despite the current similarity in construction with conventional steelwork [5], there has been limited computational modelling to analyse PFRP frame behaviour [6]. When designing frames it is important to consider various aspects of local and global stability. Overall stability might be relevant since it could be the governing ultimate Limit State to design against. When material non-linearity is unimportant, existing numerical procedures [6] can enable us to predict the elastic critical load. This critical load is that which the resistance offered by the elastic frame to any random disturbance is zero [7].

When a frame's thin-walled members are isotropic (e.g., steel) the elastic critical load can be determined with shear deformation neglected [8]. For the equivalent sized members of advanced composite material, the ratio of the longitudinal flexural modulus (E) to the shear modulus (G), in the plane of the deforming member, will be much higher [8]. Now, if the analysis neglects shear deformation, the elastic critical load may be overestimate [9] and this could result in a non-conservative frame design.

In this paper the results from a new analysis tool are presented for the critical buckling loads of four shear-flexible frame examples. The geometry for these simple frames are based on a standard section size which is commonly used in PFRP structures for both beam and column members [1, 2, 4]. The research studies, for the first time, the combined influence of semi-rigid joint action and material shear-flexibility on the critical buckling load of frame structures.

ANALYSIS OF SHEAR-FLEXIBLE FRAMES

With the specific aim of analysing the behaviour of shear-flexible frames a plane frame analysis tool was written by Zheng [6]. His coding was developed with the aim of incorporating modelling features that are relevant to the practical applications of PFRP sections in frameworks [4]. As a result, it involves the non-linearities due to second-order P-Δ effects and semi-rigid joint action [6]. Material non-linearity is not included since advanced composite materials are linear elastic to material yield (i.e. rupture). Timoshenko's procedure [8] was used to formulate the stiffness matrix for the shear deformable elements.

In the analysis of steel frames it is required to consider the second-order effects [10]. Should a frame (usually unbraced) be classified as 'sway sensitive' then the P-Δ effects, not associated with linear analysis, become significant and a second-order analysis is necessary to take account of the additional bending moments induced as a result of frame deformation. Second-order effects are introduced into the frame analysis by the stability function approach [11]. Zheng [6] formulated new functions that are shear-flexible. They are dependent on the geometric properties and elastic constants of the members, and therefore do not remain constant as they do when elements are isotropic. When Mottram and Aberle [8] reviewed the literature on shear-flexible stability functions they found that there were mistakes in the formulation of the functions presented by Zheng [6]. This was not a handicap to Zheng's contribution since his frame analysis did not concern the determination of stability [12].

In Zheng's analysis a semi-rigid joint is treated as part of the shear-flexible beam-column member and therefore has not physical size. It is assumed that only its rotational displacement is relevant in the numerical analysis and by employing this assumption the element's stiffness matrix remains unchanged. To take account of semi-rigid action the analysis modifies the loading side of the governing matrix equation [6]. A Guassian-elimination method is used to solve the set of linear simultaneous equations and to solve the non-linear problem a robust convergence procedure is needed [6].

The authors have modified the coding of Zheng so that it can be used to predict the elastic critical load of shear-flexible frames. Zheng's shear-flexible stability functions have been changed to the correct functions given in references [7] and [8]. The stiffness matrix of a stable frame has the property of positive definiteness. This matrix property can therefore be used to characterise the stability of the system. When the loading on the frame attains its critical value the stiffness matrix ceases to be positive-definite and is singular; the determinant of the matrix is zero. The modified shear-flexible frame

analysis therefore performs a test to check that the determinant of the overall stiffness matrix is positive, until it becomes zero. Mathematically, the situation for singularity cannot be exactly obtained [13]. Instability is therefore flagged, only when the sign of the determinant becomes negative, as this corresponds to a state of unstable equilibrium.

RESULTS AND DISCUSSION

The four examples used to evaluate the performance of the shear-flexible frame analysis have beam and column members of length, L, 400 cm, with the geometric properties of a 20.3×20.3×0.953 cm wide flange pultruded section [1, 2]. For this wide flange section the nominal major second moment of area, I, is 4127.8 cm^4 and the nominal cross-sectional area, A, is 56.31 cm^2 [1, 2].

Shear-rigid members and rigid joints - Example 1

To validate the overall stability analysis, the authors use established numerical results for the elastic critical loads of portal frame problems with isotropic 'shear-rigid' members. Fig. 1 presents two simple portal frames of height 400 cm and width 400 cm. The four joints are numbered 1 to 4. Joints 2 and 3 are fixed while at the Base joints 1 and 4 can be Fixed (FB) or Pinned (PB). A single element is used between two joints. The value of E is 20 GPa, and since the elements are shear-rigid the ratio E/G is mathematically zero. The left-sided frame is loaded to excite the sway situation, while the right-sided frame is for the no-sway situation. In the sway case the frame is subjected to two vertical point loads (P) at joints 2 and 3, as well as a very small sway-excitation horizontal load at joint 2. For the no-sway case the difference is to have the excitation 'load' as very small opposing moments at joints 2 and 3.

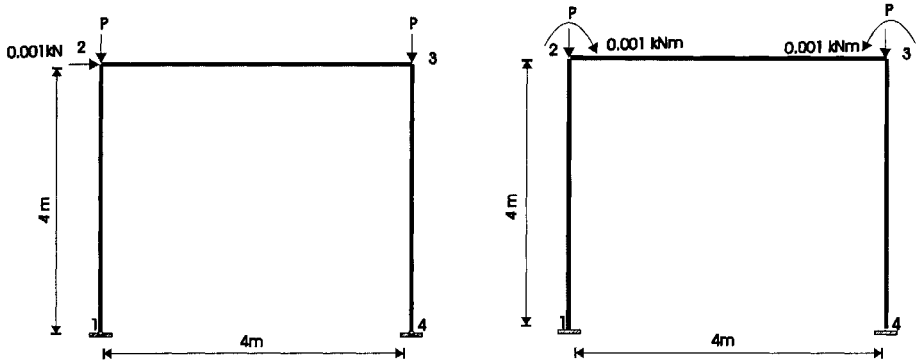


Figure 1. Portal frames under sway and no-sway loading cases.

1. Comparison with elastic critical loads from the authors' frame analysis.

Frame problem	Author [ref]	ρ_{cr}	Abbaker and Mottram ρ_{cr}	Difference %
Sway with PB	Timoshenko [14]	0.184	0.184	-0.10
Sway with FB	Chajes [15]	0.744	0.745	0.10
No sway with PB	Horne [16]	1.285	1.283	-0.15
No sway with FB	Coates [13]	2.550	2.548	-0.10

Notes: PB is pinned joints at base and FB is fixed joints at base.

Presented in Tab. 1 are elastic critical loads for the first overall buckling mode of the sway and no-sway cases, with a fixed (FB) or pinned base (PB). These are given using the non-dimensional load parameter ρ_{cr}. ρ_{cr} is defined by P_{cr}/P_E, with P_{cr} the elastic critical load and P_E the elastic Euler buckling load of the column member (with pinned ends). For the PFRP column member P_E for Euler buckling about the major axis is about 509 kN. It is assumed that that the frame cannot deform out of the plane and so buckling about the minor-axis is fully restrained. The existence of failure by local flange buckling is not considered, and this omission will be discussed later. Column two in Tab. 1 gives the elastic critical load using the theoretical analytical approaches described in references [13] to [16]. Column three gives the ρ_{cr}s from the authors' frame analysis tool. There is excellent agreement between the numerical results for the four different frame problems in Example 1. The maximum difference is only 0.15%.

Shear-flexible members and rigid joints - Example 2

Advanced polymeric materials possess elastic constants giving the ratio E/G from 5 to 80 [8]. The higher this ratio is, the higher is the influence of shearing on the behaviour of members and the framework itself. The equivalent ratio for steel is only 2.6, and this low value justifies the neglection of shear deformation in 'isotropic material' frame analysis [8, 16]. PFRP members can have the E/G ratio in the range 5 to 10, and because the ratio for higher then for steel the effect of the shear-flexibility should be investigated.

Al-Sarraf [7, 9] theoretically investigated the stability of the sway mode of the two-storey frame single bay shown in Fig. 2(a). ρ_{cr} was predicted when the second moment of area (I) and length (L) of all the members are constant. For the frame with shear-rigid members, Al-Sarraf [7] predicted lower and upper bounds, to give $0.5122 < \rho_{cr} < 0.5377$. The bounds differ by only 4.9%. Later, Al-Sarraf [9] extended his investigation to analyse the shear-flexible situation, using the correct shear-flexible stability functions given in his paper. To illustrate the influence of shear-flexibility on ρ_{cr} (now $\rho_{crsh} = P_{crsh}/P_E$), the results from the new frame analysis are presented in Fig. 2(b). To 'excite' the sway-mode a very small horizontal load is applied at joint 3. The principle variable is the moduli ratio E/G ranging from 2.5 to 80. In Fig. 2(b) the non-dimensional shear-flexibility parameter u ($= \frac{\beta P_E}{GA} = \frac{\beta \pi^2 EI}{L^2 GA}$), is used [8]. In this example and Example 4 the shear correction factor β is 3.07.

From the plot in Fig. 2(b) it is clear that as the shear-flexibility parameter u increases (i.e. E/G increases from 2.5 to 80), the elastic critical load ρ_{crsh} reduces from 0.504 to 0.325. This example shows that the elastic critical load can decrease by up to 35% when the members are very shear-flexible. For PFRP members with E/G between 5 and 10, instability will occur at an elastic critical load that is < 95% of the shear-rigid frame value [1]. This simple example therefore shows the relevance of including shear-flexible when analysing the stability of frameworks of advanced composite material.

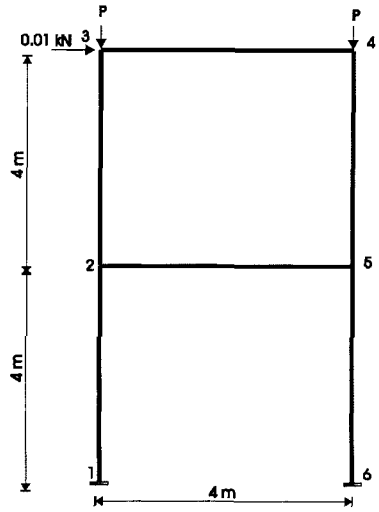


Figure 2(a). Two-storey , sinlge bay sway frame

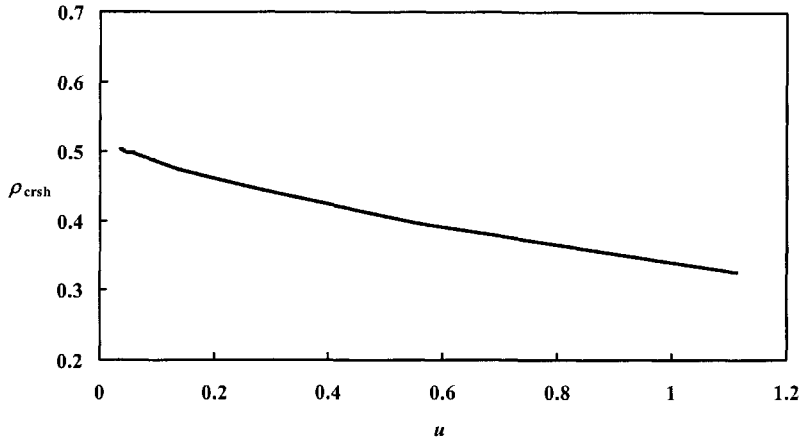


Figure 2(b). ρ_{crsh} with u.

Shear-rigid members and semi-rigid joint action - Example 3

The real moment-rotation characteristics of beam-to-column and column-to-base joints play an important role in the overall response [6] and failure of frames. Here we will consider joints with a constant rotational stiffness. It is noted, however, that the frame analysis can equally cope with non-linear moment-rotation characteristics [6, 12]. Let the linear rotational joint stiffness be S_j and the flexural stiffness of the connected shear-rigid beam be EI/L. To classify steel joints, Annex J in Eurocode 3 [17] states that the joint is rigid if the shear-rigid parameter $(S_jL)/(EI)$ is > 8 for a braced frame and ≥ 25 for an unbraced frame. Joints are said to possess a rotational stiffness for the pinned condition when $(S_jL)/(EI) < 0.5$. If S_j lies between the two boundaries the joint will contribute semi-rigid action to the shear-rigid frame's deformation.

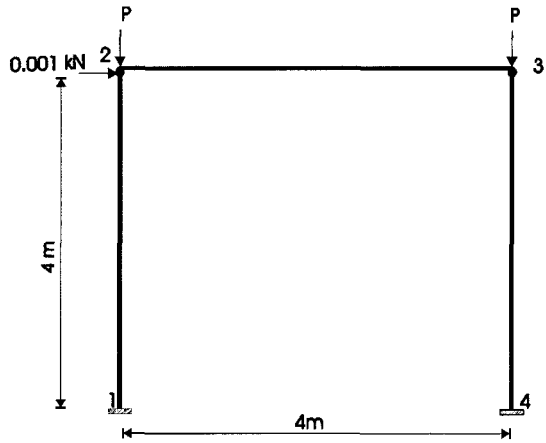


Figure 3(a). Portal sway frame with semi-rigid beam--column joints.

Fig. 3(a) shows an unbraced portal frame for the sway mode of failure, having semi-rigid beam-to-column joints at joints 2 and 3. The column-to-base joints at column ends 1 and 4 remain fixed (i.e. $S_j = \infty$). E is 20 GPa, and since the members are shear-rigid the ratio E/G is mathematically zero. Fig. 3(b) plots ρ_{cr} against $(S_jL)/(EI)$ to show the influence of the semi-rigid action on the frame's elastic critical load. As $(S_jL)/(EI)$ increases from 0.29 (pinned joints) to 25 (rigid joints), ρ_{cr} increases from 0.302 to 0.671. Over the full range of joint stiffnesses this example shows a 122% increase in the critical load. Now, if $(S_jL)/(EI)$ increases from 25 to ∞ (for the unbraced frame), there is only another 10% increase in ρ_{cr}. This simple example emphases the findings used to prepare Annex J of Eurocode 3 [17] that there is no practical benefit when the frame is shear-rigid on having the parameter $(S_jL)/(EI) > 25$.

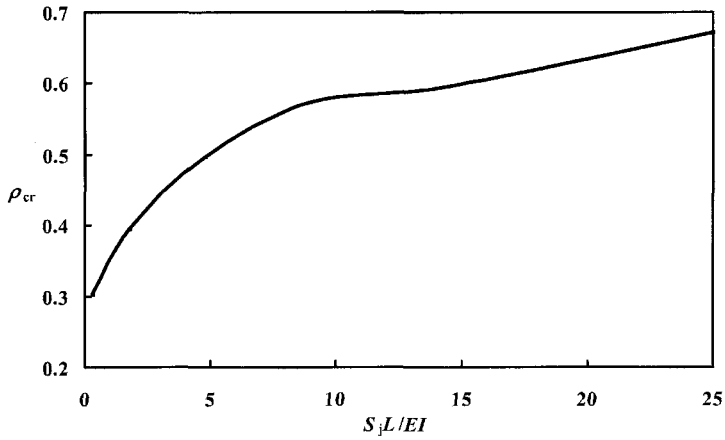


Figure 3(b). ρ_{cr} with $(S_jL)/(EI)$.

Shear-flexible members and semi-rigid joint action - Example 4

Using the same say frame problem in Example 3, the three plots in Fig. 4 show the variation of the elastic critical load with joint stiffness, for members having moduli ratio E/G = 6, 20 or 80 (i.e. u = 0.0833, 0.2776 or 1.1106). To simplify the discussion the

shear-rigid parameter ($(S_jL)/(EI)$) for joint classification will also be used when the members are shear-flexible. For the pinned joint condition, given by $(S_jL)/(EI) < 0.5$, the relative change in ρ_{crsh} is about 4% as E/G changes from 6 to 80. Whereas, for the rigid joint condition given by $(S_jL)/(EI) = 25$, the equivalent change in shear-flexibility has a greater influence on ρ_{crsh}, resulting in a 50% decrease. This can be linked to the influence of a member's shear-flexibility being much higher when the beam's ends are fixed [18]. There is also evidence in Fig. 4 to suggest that the shear-rigid parameter $(S_jL)/(EI)$ will, at the joint classification boundaries, be lower as the members' shear flexibility increases.

LOCAL FLANGE BUCKLING AND OTHER FAILURE MODES

For the standard 20.3×20.3×0.953 cm wide flange section Lane [19] has measured the elastic critical local buckling load of a concentrically loaded column to be 360 kN (or $0.707\rho_{cr}$). Mottram *et al.* [20] have applied different moment gradients to major-axis pinned-pinned columns of the same PFRP section and found that local buckling can be the failure mode resulting from the combined axial compression and flexural compression stresses. For the frame examples presented above it can therefore be said that a local buckling failure could occur when the applied load is $< 0.707\rho_{cr}$. As a result we observe that, as the joints' stiffness increases towards the rigid situation (i.e. $(S_jL)/(EI) > 25$), a local instability is more likely to precede the overall frame mode. Future revisions to the authors' software will enable other potential modes of failure to be determined as the frame analysis progresses to determine the ultimate mode and its critical loading.

CONCLUSIONS

A new frame analysis tool is presented which can predict the elastic critical load of plane frameworks with shear-flexible members. By way of four simple examples it is shown that this instability load reduces with increase in member shear-flexibility, and that this reduction is influenced by semi-rigid joint action. Because the critical load reduces, the effect of shear-flexibility should be included when analysing the stability of frames of PFRP section. It is also essential for the frame analysis to determine the critical loading for other modes of failaure, such as elastic local flange buckling, as these might occur at a loading below the overall mode predicted by the current version of the software.

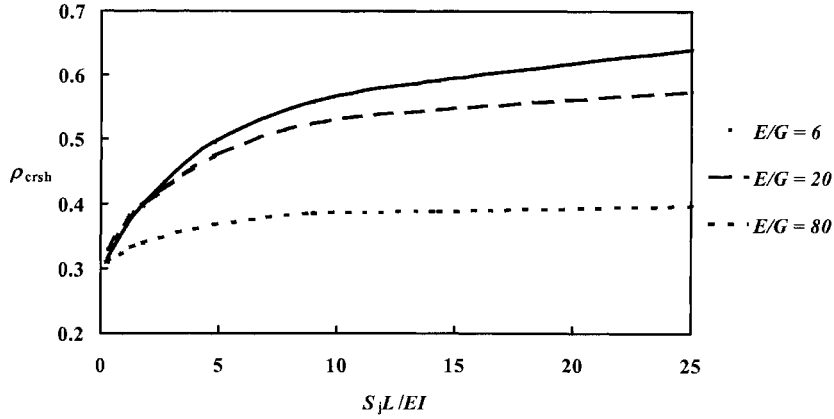


Figure 4. ρ_{crsh} with $(S_jL)/(EI)$ and elastic moduli ratio E/G.

REFERENCES

[1] Anon, *EXTREN Design Manual,* Strongwell, Bristol VA, 1989.

[2] Anon, *Fiberline Design Manual for Structural Profiles in Composite Materials*, Fiberline Composites A/S, Kolding, Denmark, 1995.

[3] Anon, *The New and Improved Pultex Pultrusion Design Manual of Pultex Standard and Custom Fiber Reinforced Polymer Structural Profiles*, Creative Pultrusions Inc., Alum, Bank, PA, 1999.

[4] G J Turvey, 'Pultruded GRP frames: Simple (conservative) approach to design: a rational alternative and research needs for improved design', Int. Workshop on *Composites in Construction: A Reality*, Reston, ASCE Special Publication, 2002, 258-266.

[5] G W Owens, P R Knowles and P J Dowling (Eds). *Steel designers' manual*, 5th Ed. Cambridge, Blackwell Scientific Publications, 1994.

[6] Y Zheng, *Connection Behaviour and Frame Analysis for Structures of Pultruded Profiles*, PhD thesis, University of Warwick, UK, 1998.

[7] S Z Al-Sarraf, 'Upper and lower bounds of elastic critical loads', *The Structural Engineer,* 1979 **57**A(12) 415-421.

[8] J T Mottram, and M Aberle, 'When should shear-flexible stability functions be used in elastic structural analysis?', *Proc. Institution of Civil Engineers: Structures and Buildings*, 2002 **152**(1) 31-40.

[9] S Z Al-Sarraf, 'Shear effect on the elastic stability of frames', *The Structural Engineer*, 1986 **64**B(2) 43-47.

[10] J Graham, 'An elastic-plastic second order plane frame analysis method for design engineers', *The Structural Engineer*, 2003 **81A**(10) 31-35.

[11] K I Majid, *Non-linear Structures*, London, Butterworths, 1972.

[12] J T Mottram and Y Zheng, 'Analysis of a pultruded frame with various connection properties', 2nd Int. Conf. *Composites in Infrastructure (ICCI'98)*, Arizona, University of Arizona, 1998 Vol II 261-274.

[13] R C Coates, M G Coutie and F K Kong, *Structural Analysis*, London, Chapman and Hall, 1994.

[14] S P Timoshenko, *Theory of Elastic Stability*, New York, McGraw-Hill, 1936.

[15] A Chajes, *Principles of Structural Stability Theory*, Prentice-Hall Inc. Englewood Cliffs, New Jersey, 1974.

[16] M R Horne and W Merchant, *The Stability of Frames*, Oxford, Pergamon Press Ltd, 1965.

[17] DD ENV 1993-1-1:1992 *Eurocode 3: Design of Steel Structures, Revised Annex J. Joints in building frames,* British Standard Institution 2000.

[18] G J Turvey, 'Flexure of pultruded beams with semi-rigid end connections', *Composite Structures,* 1999 **47** 571-580.

[19] A Lane, *An experimental investigation of buckling mode interaction in PFRP columns,* PhD Thesis, University of Warwick, UK, 2002.

[20] J T Mottram, N D Brown and D Anderson, 'Buckling characteristics of pultruded glass fibre reinforced plastic columns under moment gradient', *Thin-Walled Structures,* 2003 **41**(7) 619-638.

FIRE TESTING OF CONCRETE BEAMS WITH FIBRE REINFORCED PLASTIC REBAR

A. Abbasi and P.J. Hogg

Queen Mary, University of London, Department of Materials, London E1 4NS

Abstract

The behaviour of glass fibre reinforced polymer (GFRP) rebars reinforced concrete beams when exposed to fire are presented in this paper. The experimental programme involved fire tests based on British Standard 476 on two full-scale GFRP rebar reinforced concrete beams with dimensions in cross section 350mm x 400mm and 4400mm total length with a span length of 4250mm. The beams were designed and constructed according to Eurocode 2 and ACI-440. The purpose of this work was to evaluate the fire resistance of the GFRP reinforced concrete (RC) beams. GFRP rebars with thermoset resin were used for reinforcing beam 1 and GFRP rebars manufactured with thermoplastic resin were used for reinforcing beam 2. Shear reinforcement for beam 1 was GFRP stirrups and for beam 2 steel stirrups were used. Degradation in the flexural capacity due to fire was evaluated and compared. In this study loaded heating tests were implemented with the aim of collecting basic data for the validation of the model presented in the preceding papers.

INTRODUCTION

Most building structures must satisfy the requirements of building codes, which relate to the behaviour of those structures in a fire. Fire ratings for buildings refer to the time available in a fire before the structure collapses. The relevant property of the composite rebar is not its flammability or reaction to fire, but rather its ability to continue to sustain loads in an environment of rapidly rising temperatures. The properties of steel at different temperatures are well known as are the thermal properties of the material and this allows the modelling of structures with some degree of accuracy to predict a time scale for the ultimate loss of structural integrity. Data is required for glass fibre reinforced plastic (GFRP) rebar in order for similar calculations to be made. GFRP rebar have a wide range of potential applications but its advantages and limitations must be ascertained so it can be used appropriately. UK Building Regulations 2000[1] has identified the specific requirements for each category of structural element in a building in terms of resistance to collapse (load bearing capacity). The minimum period of fire resistance for the elements of most structures is 90 minutes.

In this study, glass fibre reinforced concrete beams using continuous fibre bars as main reinforcements were subjected to heating under load tests. The three beams in this project were designed based on Eurocode 2[2] and ACI 440[3] recommendations and constructed at Queen Mary London University premises. In addition another full-scale beam with the same dimensions and GFRP reinforcement ratio was constructed and tested as a control at room temperature. This test was carried out for the evaluation of flexural behaviour of the beam and to choose a sustained load for the fire test. The

results of these tests are included. The objective of the study was to determine the fire resistance of GFRP reinforced concrete beams experimentally and to validate the predictive models for fire resistance, which had been introduced in previous papers[4,5] by the same authors.

BEAMS FOR THE TEST PROGRAMME

The reinforced concrete beam specimens were cast, using marine gravel as coarse aggregate. The dimensions of the beams were 350 x 400mm in cross section, 4400mm overall length and 4250mm supported span. The concrete composition for these beams is given in Table 1. In addition, three 100mm concrete cubes were cast using the same concrete. These gave an average compressive strength of 42 MPa after 28 days of casting.

Table 1. Concrete composition used for casting the testing beams

Item	kg/m^3
Ordinary Portland Cement (OPC)	380
20mm aggregate	700
10mm aggregate	360
Sand	735
Water	148
Water reducing admixture	(1% of OPC) 3.8 kg/m^3

Control beam and beam 1

GFRP rebar reinforcements for the control beam and beam 1 were supplied by Hughes Brothers, Inc. Figure 1a illustrates the various GFRP pieces. From left to right; L-shaped #7 (22mm) used for end rebar U-shaped #3 (9mm) used as stirrups rebars by attaching two pieces together and a cut piece of # 4 (12mm) used for the main reinforcement. Figure 1b shows the arrangement of the reinforcements in the section of the beam.

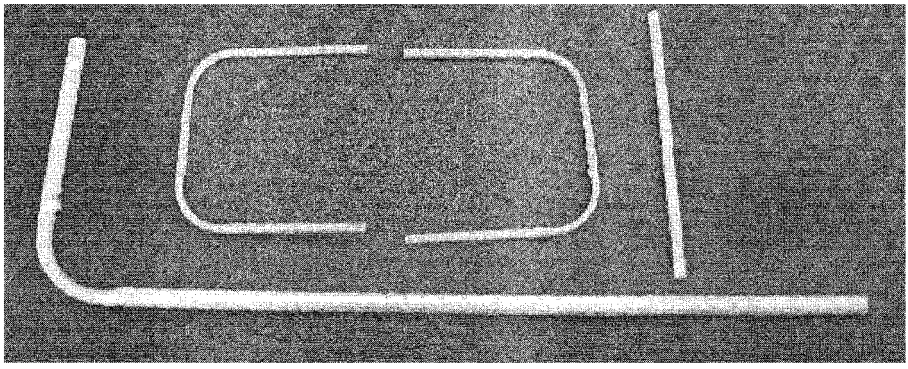


Fig 1a GFRP rebar shapes used as reinforcement for control beam and beam 1

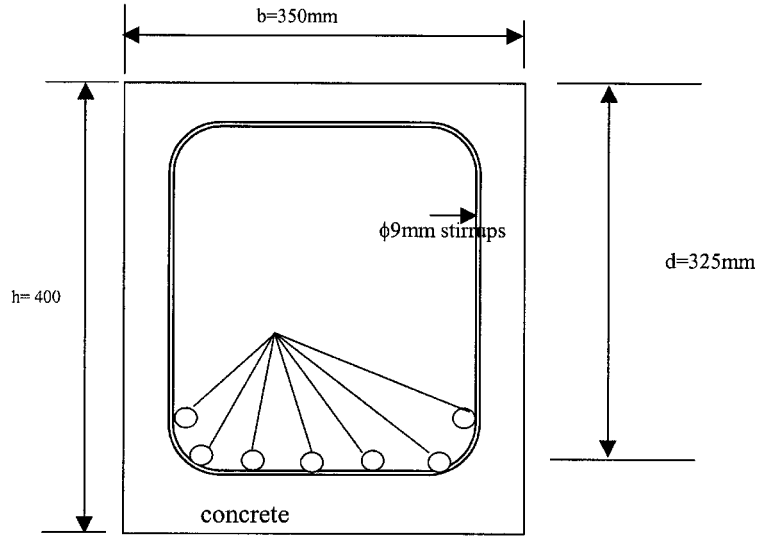


Fig 1b Beam cross section with reinforcement arrangement

Beam 2

Beam 2 was reinforced by GFRP rebar manufactured by the Dow Chemical Company. This rebar utilised a thermoplastic polyurethane resin matrix. Figure 2 illustrates the various pieces provided used for the construction of beam 2. From left to right; L-shaped #4 rebar used for end rebar, steel stirrup and a cut piece of # 4 (12mm) GFRP rebar used for the main reinforcement. Table 2, Table 3 and Table 4 give details of the reinforcement specifications used in this work. Same reinforcements arrangement as shown in Figure 1b used in beam 2.

Table 2 GFRP rebars specifications for control beam, beam 1 and beam 2

Specimens	Bar size (mm)	Cross sectional Area (mm^2)	Nominal Diameter (mm)	*Tensile strength (MPa)	*Modulus of Elasticity (GPa)
Control & Beam1	9	84.32	9.53	760	40.8
	12	144.85	12.70	690	40.8
	22	382.73	22.23	586	40.8
Beam2	12	130.69	12.8	≈1000	≈41

* Manufacture's data

The 10mm steel stirrups used for fabrication in beam 2 has tensile strength of 414MPa at yield and a Young's modulus of 200GPa.

Table 3 Control beam, beam 1 and beam 2

Tension reinforcement		Top reinforcement		Width of the beam (b)	Effect. depth of the beam (d)	Height of the beam (h)	Balance reinforcement ratio (ρ_{fb})	Ratio of GFRP reinforcement (ρ_f)	$\frac{\rho_f}{\rho_{fb}}$
Bar size	No. of bars	Bar size	No. of bars	(mm)	(mm)	(mm)	%	%	
12mm	7	12mm	2	350	325	400	0.45	0.89	1.98

Table 4 Specimens characteristics

Specimen	Main reinforcement			Tensile main reinforcement	A_t* (cm^2)	Tensile reinforcement ratio
	Type of fibre	External profile	Binder			
Control	Glass	Spiral	Vinyl ester	7 of ϕ12	10.14	0.89
Beam 1	Glass	Spiral	Vinyl ester	7 of ϕ12	10.14	0.89
Beam 2	Glass	Molded surface	Polyurethane thermoplastic	7 of ϕ12	10.14	0.89

* Total cross sectional area of tensile main reinforcement

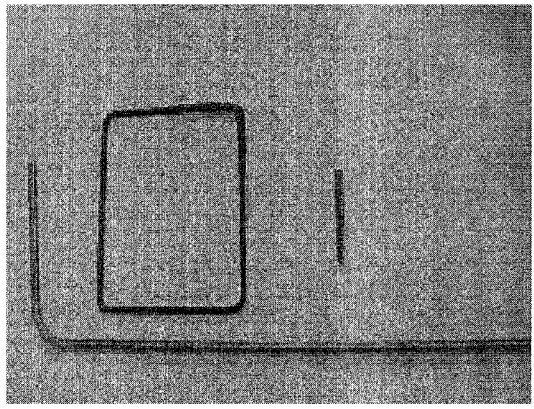


Fig 2 GFRP rebar shapes and steel stirrup used as reinforcement for beam 2

TESTING OF THE CONTROL BEAM AT ROOM TEMPERATURE

In order to evaluate the flexural behaviour of the proposed beam the flexural six point bending test was carried out at room temperature. The beam was subjected to increasing load in increments of 5-10kN, until final failure. The load was stopped at each increment for two minutes for observation. Load was applied with a hydraulic jack at four points on the beam. Vertical deflection was measured at mid centre using an LVDT transducer. The loading of the beam resulted in the load deflection curve shown in Figure 3. The initial linear relationship between load and deflection became non-linear after an applied load of approximately 60kN. This was accompanied by the onset of cracking in the concrete in tension face. The code of practice specifies a maximum deflection allowable of L/250 where in this case is 17.0mm and this is exceeded at a load of 90kN. A load of 40kN was selected for the fire test as being below the concrete cracking threshold.

The load was increased to a maximum of 310 kN which produced a deflection in the beam of 98mm. During unloading the whole beam moved back to the same position as prior to loading. This shows that recovery of the beam is not impeded by plastic deformation of the rebar as would be the case with steel reinforced beams. Modulus of elasticity in bending (E_B) of the control beam can be calculated from experimental results using Equation 1 given in ASTM D790M (1986)[6].

$$E_B = \frac{L^3 m}{4bh^3} \quad (1)$$

Where E_B= modulus of elasticity in bending

L = support span, 4250mm
b = width of beam, 350mm
h = height of beam, 400mm
m = slope of the tangent to the initial straight-line portion of the load-deflection curve, N/mm of deflection.
From the load/deflection curve obtained from experimental results presented in Figure 3 the slope to the initial loading is obtained as 12500 N/mm and the slope for the second part of the curve is obtained as 2500 N/mm. By substituting the above in Equation 1 initial and secondary beam modulus is obtained as 10.7 GPa and 2.1 GPa respectively.

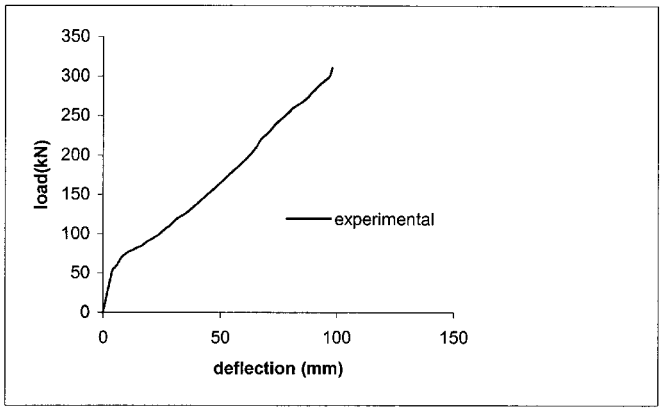


Fig 3 Load-deflection curve for control beam

FIRE TEST PROGRAMME

Instrumentation

Specimens for the fire test were equipped with thermocouples. The thermocouples were embedded in the concrete to obtain temperature distribution during fire test. The thermocouples used were "PTFE insulated k type twisted cables". The ends of the thermocouples were precisely located by placing them in 20x30mm miniature columns 400mm long, cast in the formwork prior to concreting the beam itself. Thermocouples were also attached to rebars and stirrups for beam 1 and beam 2. Figure 4 show the thermocouples (TC's) embedded in concrete in four location along the beam A, B and C at each four thermocouple were embedded No 1, 2 ,3 and 4 which were 80mm apart in the section of the beam.

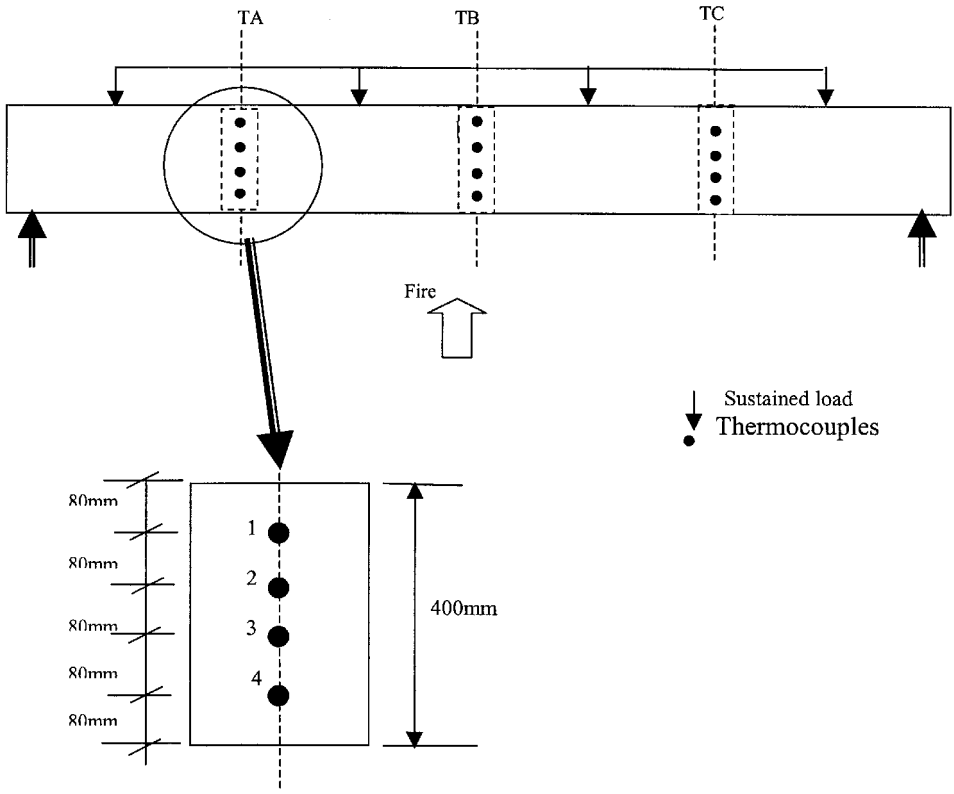
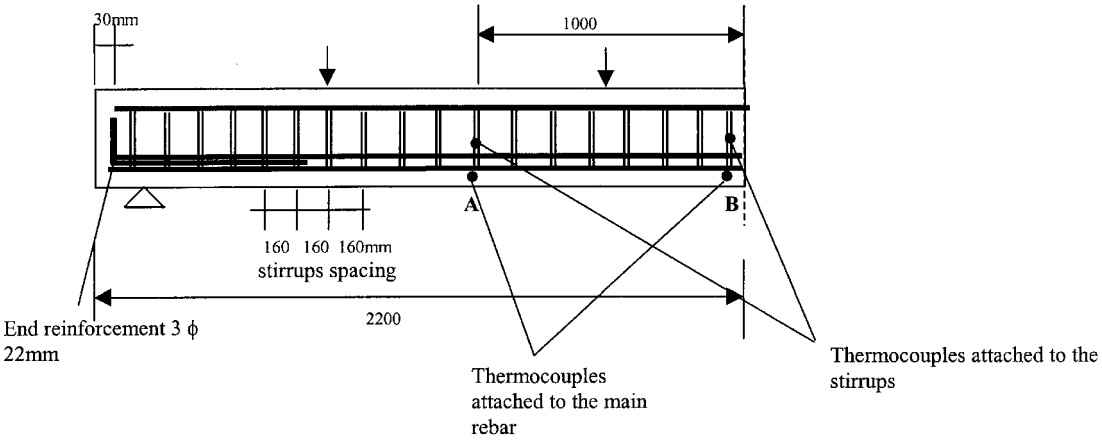


Fig 4 Thermocouples embedded in concrete. Group of thermocouples at A, B and C in concrete Nos. 1-4 at centre line 80mm c/c (3x4=12).

At the location A,B and C thermocouple were also attached to the 3 of the main reinforcements (x,y,z) as shown in Figure 5. Two thermocouples were also attached to the stirrups at location A and B. In total 23 thermocouples were used for each beam. Twelve embedded in the concrete (four at position A, four at position B and four at position C). Nine thermocouples to the rebars at location shown in Figure 5, three at each location. This is the region where the maximum flexural and shear stresses were expected to occur.



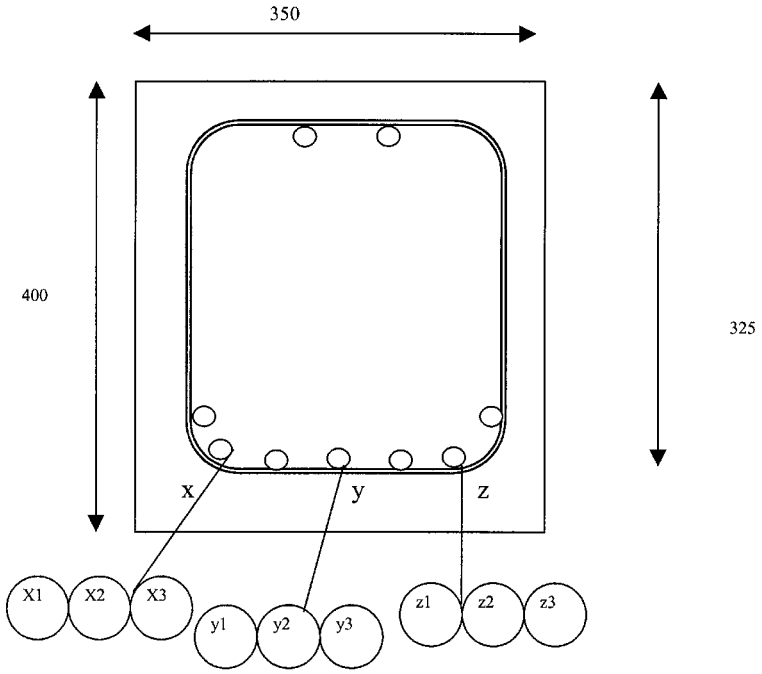


Fig 5 Specimen configuration and measurement points of temperature at the rebars

The experimental set up for the fire test is shown in Figure 6.

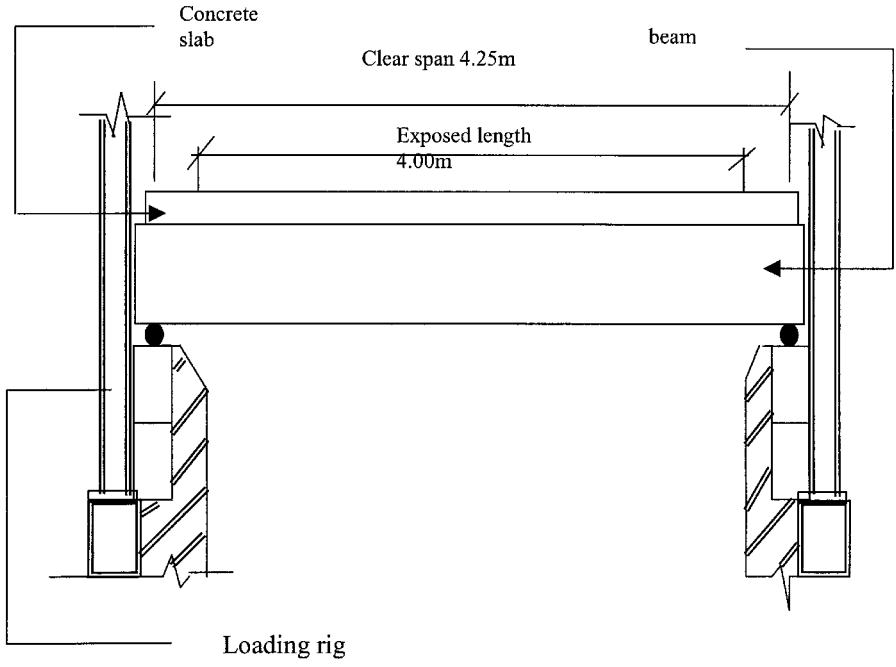


Fig 6 Experimental set up for fire test

Furnace details

The full scale fire testing was conducted at the Building Research Establishment, Watford UK. Furnace details used in this work are as follows; the internal dimensions of the furnace 4m wide x 4m long x 2m deep. Two sides walls contain the burners. One end wall has a door; the other end wall is modular and can be moved. The flue exit is in the floor at one end of the furnace. The top of the furnace is closed off with a test specimen, or a set of refractory-lined steel cover slabs. The furnace is lined with 1400 grade insulating brick (density approx. 880 kg/m^3) to comply with British Standard, ISO and EN requirements. Burners were gas-fired nozzle mix burners. A total of 20 burners, arranged with 10 along two opposite sides of the furnace, approximately 1200mm above the floor. The loading rig sat above the furnace, running centrally along the length, parallel with the walls containing the burners. The rig provides a span of 4.25m for the beams. The load to a beam is applied hydraulically from above with four points of loading. The maximum test load is approximately 440 kN. The beam specimens were heated on three sides. The furnace temperatures were recorded, monitored and controlled to follow the standard fire curve in accordance with BS 476: Part 20[7]. The temperatures were measured at ten points in the furnace near the beam surface.

Test procedure

About one week prior to each fire test, the test beam was taken to the furnace room for instrumentation. At the start of the fire test 40kN load was applied by a hydraulic jack at four points 1m apart uniformly placed on the beam span. This was kept constant during each test by a hydraulic jack load cell monitor which was sat outside the furnace. The deflection was measured at mid-span point, using "Linear Voltage Deflection Transducers". The beam was placed centrally at the roof level of the furnace. The walls of the furnace were constructed with bricks. The roof was made with precast prestressed slabs, which were painted with fire resistance paint with insulation at the top. The gap between the slab-insulation and the beam were carefully packed with insulation, rock wool and ceramic wool, to protect the instrumentation above the slabs and to allow the beam to deflect freely under load. The four points load were applied on the beam through four pre-made holes in the pre-stressed slab of the roof. The loading rig was the same loading rig that was used for the testing control beam. Ten TC's inside ceramic tubes were hung from ceiling of the furnace to measure the temperature near the surface of the beam during the fire test. It was decided that the test should be terminated when the specimen attained a large deflection, or when it was judged as incapable of sustaining the applied load or showed signs of instability, whichever occurred earlier.

FIRE TEST RESULTS

The sequences of events observed during the fire test on each beam are listed chronologically in Tables 6 and 7 and deflection-time curves are shown in Figure 7. A slow but steady increase in beam deflection was recorded from outset of the test, but this settled down and the beams were effectively stable after approximately 30 minutes at this time the only observed effects were small amount of concrete spalling from the corner of the beams. Cracking in the concrete became evident in both beams after about 75-80 minutes which was accompanied by flaming from the crack regions.

The beams exhibit a suitable increase in deflection which was identified as failure after 94 minutes for beam 2 and 128 minutes for beam 1. The appearance of the beams after failure and cooling to room temperature is shown in Figure 8 and Figure 9. The mode of failure of beam is via flexural-shear cracks and spalling of the concrete. After the fire testing the beam were removed from the furnace. It was observed that beam 1 was splitting in two.

Table 6 Observation of fire test on beam 1

Time (min)	Observations
0	Test started
12	Small amount of spalling at bottom corners of beam
75	400mm long crack evident longitudinally along bottom of beam approximately 300mm in from left hand edge of beam. Flaming from near end on bottom and side of beam
100	Crack has grown to approximately 800mm long and another has formed 40mm up the side100mm long
127	Large chunks have fallen off and a large crack 35mm wide has formed around the whole perimeter at mid length. Cracks are showing all over the beam
132	Load removed
140	Large chunk fallen off
143	Test stopped

Table 7 Observation of fire test on beam 2

Time (min)	Observations
0	Test started
14	Small amount of liquid dripping from bottom of beam
25	Small amount of spalling from corners of beam
50	Spalling evident from top of beam
80	300mm long longitudinal cracks have appeared mid way up near side of beam at left-hand end. Flickering flame on far side of beam
88	Crack on bottom of beam (tension face) opened approximately 2mm wide
92	More flaming from other parts of beam and 100mm long longitudinal cracks appeared mid length on bottom and near side
94	Rate exceeded for deflection
101	Rate of deflection was exceeded
104	Test Stopped

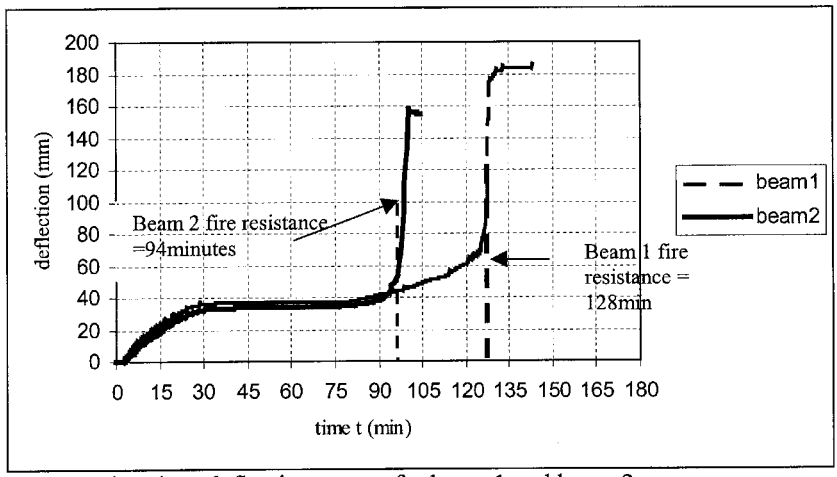


Fig 7 Heating time-deflection curves for beam 1 and beam 2

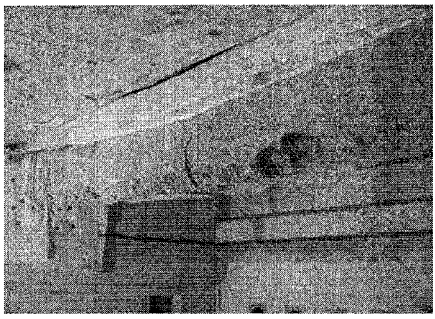


Fig 8 Rupture at the mid centre of the concrete in beam 1 after fire test

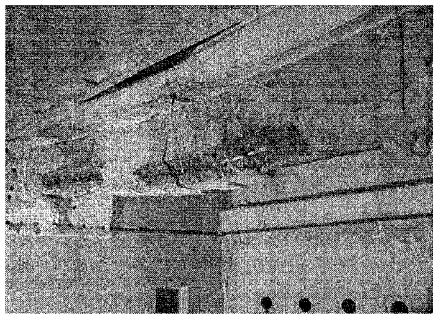


Fig 9 Failure of beam 2 after fire test inside the furnace shows some flexural cracks and rupture in the main reinforcement

Figure 10 depicts the temperatures measured at the mid centre of the beam in positions B, 80mm from bottom of the beam. The temperature increases with time. The ambient high temperature (T°C) at a point located at a distance of "x" mm from the face of the beam is assumed to be a function of fire exposure time. Figure 11 shows the maximum temperature measured at the rebar at each time interval. Figure 12 shows the average temperature at the stirrups. The data excludes some readings, which showed sudden, erratic and abrupt changes. This may be attributed to a possible shorting of a PTFE coated wire and the record showing temperature at a location other than the end of the thermocouple.

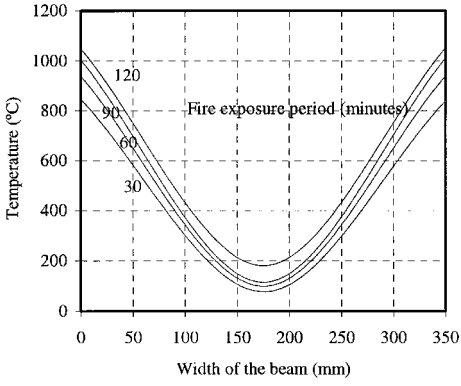


Fig 10 Temperature profile in the cross section of the beam 1 80mm from bottom of the beam for different fire exposure periods. The temperature of each side of the beam is an average reading from TC's in furnace on the each side of the beam.

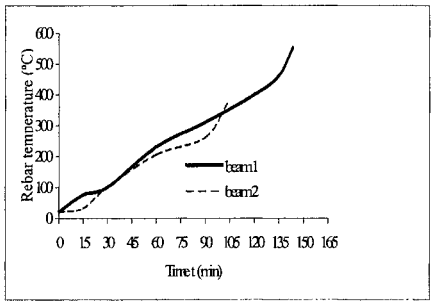


Fig 11 Heating time/ temperature in the rebars for beam1 and beam 2

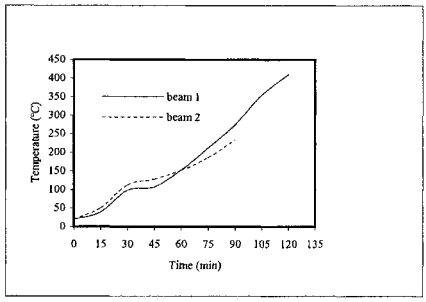


Fig 12 Average stirrups temperature in beam 1 and beam 2

DISCUSSION

All the results of the tested beams in comparison are given in Table 8. The rise in temperature in a concrete cross section, in response to high external temperatures, depends on a large number of factors. These factors include the moisture content of the concrete and the chemical composition of the aggregate and cement. Also, the development of temperature in a beam depends on the heating conditions and the heat transfer characteristics of the environment. However, these factors cannot be conveniently evaluated for the purposes of developing a general design rule. The heating time for beam 1 was 143 minutes with maximum central deflection of 185mm ≈L/23 and the heating time for beam 2 was 104minutes with maximum central deflection of 157.5mm ≈L/27. The deflection/time curves for both beam with fire resistance values is depicted in Figure 7. Sudden deflection in beam 2 was at about 90 minutes. During visual observation subsequent to the completion of heating, the reinforcements were still seen emitting residual flames, this is thought to be due to the high temperature that the fibre bars had reached which aided ignition. The reinforcements which were extracted by chipping away the concrete, were found to have undergone thinning and carbonisation due to combustion.

It would appear from the fire tests using full-scale beams and analysis of the samples remained from the tests, that failure was due to fire penetration through the concrete beam cracks, which developed during testing. This resulted in burning of the matrix of the rebar, which caused interface cracking and de-bonding. This de-bonding resulted in shear cracks along the beam. In beam 1 in which GFRP stirrups was used, the beam split in two pieces after it was taken out of the furnace. Beam 2 was removed from the furnace in one piece, 30mm expansion was measured and beam was bent at the centre. In both beams spalling of the concrete occurred due to the pressure generated by the conversion of moisture in the surface layer of concrete to steam. After the fire test, samples of the rebars were collected from the tension face in middle of the beam in order to evaluate the effect of fire on the rebars. The samples were weighed and compared with unexposed samples. The weight of the rebar in beam 1 and beam 2 had reduced by 22.3% and 33.8% respectively.

Table 8 Results of loaded heating tests

Specimens	Load applied (kN)	Heating time (min.)	Failure mode	Failure time (min.)	Deflection at centre at end of heating (mm)	Average temp of bottom reinforcement at end of heating (°C)
Beam 1	40	143	Flexural failure and residual flames emitted from rebar	128	185	462
Beam 2	40	104	Flexural failure, large cracks at tension face of the beam and residual flames emitted from reinforcements	94	157.5	377

CONCLUSIONS

The fire resistance rating (load bearing capacity) for beam 1 was 128 minutes and for beam 2 was 94 minutes both beams were tested in accordance with BS 476 Part 21[8] 45% of allowable load was applied as service load the deflection was approximately L/23 for beam 1 and L/27 for beam 2. In the criteria for failure under load bearing capacity based on BS 476 : Part 20 (Section 10) [7] the deflection is L/20. The Building Regulations for fire safety recommend that the minimum periods of the fire resistance for the most groups of buildings should be of 90 minutes. These fire tests results indicate show that concrete beams reinforced with GFRP rebar will meet the fire design requirements for the minimum periods of fire resistance (fire endurance). A minimum clear concrete cover of 70mm is recommended for future design of GFRP-RC beams rebars under fire conditions.

Acknowledgements

The authors wish to thank the Materials Department of QMUL for the promotion of this research, Hughes Brothers, Inc. and Dow Chemical Company for providing the rebars, the Building Research Establishment for conducting the fire tests and International Composites and Dow Chemical for direct funding of the fire tests themselves.

REFERENCES

1. The Building Regulations 2000 Fire Safety, Amendments 2002 to Approved Document B (Fire safety) published by TSO (The Stationary Office) and available Online www.tso.co.uk/bookshop.
2. Eurocode 2, "Design of Concrete Structures ", ENV EC2 Part 1.2 1992.
3. ACI Committee, "Guide for the Design and Construction of Concrete Reinforced with FRP Bars", Reported by ACI Committee 440, January 5, 2001.
4. Abbasi, A and Hogg, P J, "A model for predicting the properties of the constituents of a glass fibre rebar reinforced concrete beam at elevated temperatures simulating a fire test " Submitted to Composites part B, 2003.
5. Abbasi, A and Hogg, P J, "A model for prediction the lifetime of FRP reinforced concrete beams under fire conditions" Submitted to Cement and Concrete Composites, 2003.
6. ASTM D 79M - 86, "Standard test method for flexural properties of un-reinforced and reinforced plastics and electrical insulating materials (METRIC)",1986.
7. British Standard Institution, "Fire Tests on Building Materials and Structures", Part 20. Method of Determination of Fire Resistance of Elements of Constructions 1987, BS 476.
8. British Standard Institution, "Fire Tests on Building Materials and Structures", Part 21. Method of Determination of Fire Resistance of load-bearing elements of construction 1987, BS 476.

EXPERIMENTAL AND NUMERICAL APPROACH TO BUCKLING OF LAMINATED COMPOSITE SANDWICH PANEL

Maria Antonietta Aiello*, Paolo Corvaglia** and Len Hollaway***

** Department of Innovation Engineering, University of Lecce, Lecce, Italy*
*** Consorzio CETMA, Brindisi, Italy*
**** Composite Structures Research Unit, School of Engineering, Civil Engineering, University of Surrey, Guildford, UK.*

ABSTRACT

Sandwich panels are widely utilised for different engineering applications. They consist of two stiff and strong material skins and a low modulus material core; a favourable selection of face and core materials allows the sandwich system to develop the optimum structural characteristics, weight and cost for a specific application. The use of high performance materials allows for a considerable reduction in geometrical dimensions; as a consequence, instability issues become of importance and could cause failure of the structural elements before the ultimate material strength is reached.

The objective of the work has been to study the buckling behaviour of flat simply supported sandwich panels with isotropic deformable core and laminated composite faces, the whole being subjected to compressive uniaxial or biaxial in-plane loads. In particular, the experimental evaluation of the critical buckling load of panels with different fibre arrays in the face units has been undertaken; the models were examined under both uniaxial and biaxial loading conditions. In addition, a numerical finite element model was developed and used to compare the results with those of the experimental solution.

The face materials of the panels were made from a GFRP wet lay-up and the PVC foam was used as the core material.

The paper will discuss the issues of the experimental simulation of the boundary conditions, generally acknowledged to be a difficult task whilst undertaking a panel buckling test, and the achievement of the correct loading conditions.

The judicious placement of strain gauges allowed a description of the buckled shape to be obtained and enabled a distinction to be made between the instability failure and material failure of the system.

The development of a finite element model representing the experimental tests and the analysis of the numerical model enabled the failure criteria of the system to be studied in detail. Following these investigations further modifications to the experimental set-up and boundary conditions were suggested to improve the co-relation between experimental and numerical models.

INTRODUCTION

The simplest type of sandwich panel consists of two thin, stiff, strong face material separated by a thick layer of low density core material which is generally much less stiff and strong than the face-material. The bending stiffness of this system can be increased by increasing the thickness of the core material. A judicious selection of face and core material will allow an optimum system to be developed in terms of structural integrity, weight and cost. By utilising high performance materials to reduce geometrical

dimensions, could seriously affect the instability and cause structural failure of the components of the overall system before ultimate strengths were reached.

Whilst a number of studies concerned with buckling of sandwich panels have been undertaken based upon analytical and numerical analysis, refs. [1, 2] relatively little has been done from an experimental point of view, particularly regarding sandwich panels simply supported on all four sides.

Simply supported sandwich panels with face materials of CFRP composite have been tested [3] with different slenderness ratios depending upon whether the type of failure required was a local or global buckling. For the loaded sides of the sandwich panels "end support" consisted of an aluminium V-block that transferred the load to an end-block through a silver steel roller fitting in the lubricated V-block. The end-block clamped the end of the sandwich panel, so loading it uniformly and preventing possible end delamination. The V-block was loaded through a "uniform loading device", which was placed between the external loads and the V-block; this allowed the correction of any possible load eccentricities through a suitable adjustment of bolts. For the unloaded sides of the panel, the support was designed to prevent transverse deflection but to permit rotation. Load/strain data were used to evaluate the buckling load values; the same criterion as that discussed in reference [4] was used, namely the definition of the buckling load as the load at which the strain on the convex side of the panel becomes a maximum. References [4] and [5] particularly emphasise the importance of load alignment during buckling tests on sandwich panels.

Reference [6] used a double cylinder coupling at the supports of the panel and to achieve free rotations, ball bearings were employed. Reference [7] used a similar loading rig, consisting of a cylindrical shaft which clamped the panel ends and bearings, in order to couple the shaft to the loading device.

In the cited works of references [4] and [7] the authors have obtained an uniform stress distribution across the panel and have avoided end delaminations by embedding the ends of the panel in resin and placing the whole in a specially designed rig.

Wadee [8] showed that the ratio between the experimental and the theoretical critical buckling load is highly dependent upon the ratio between the theoretical buckling loads which correspond to the first and the second buckling mode This is particularly so when the latter ratio is close to unity; the former ratio is then much less than unity. This indicated a high sensitivity of the buckling load to real imperfections.

This paper will discuss experimental and numerical analyses undertaken on sandwich panels manufactured from GFRP face material and PVC foam core. Issues associated with the boundary conditions and the success of achieving the correct loading conditions will be discussed. A comparison of the buckling shapes and failure criteria of the panels derived in the numerical and experimental solutions will be made.

EXPERIMENTAL STUDY

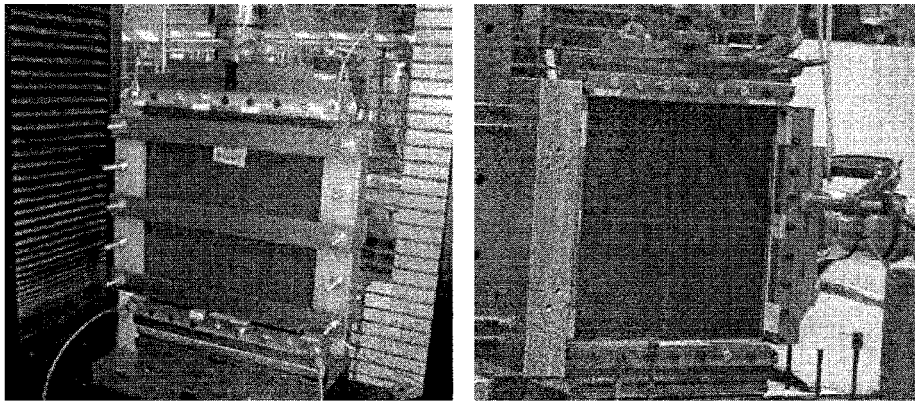
Materials and equipment

The face materials of the panels consisted of a GFRP composite and the core was a PVC foam. The GFRP composite was manufactured by a vacuum assisted wet lay-up process. The vacuum assisted method was used to obtain maximum compaction of the GFRP. On the completed sandwich panels GFRP tabs were bonded on both sides of the two loaded ends in order to avoid local skin compression failure.

The mechanical properties of the foam core were taken from the material data: modulus of elasticity in tension and compression were 50 MPa. and 21 MPa respectively. The mechanical properties of the individual plies of the manufactured face material were experimentally measures; this was undertaken according to the ASTM Standard recommendation (ASTM D3039M, ASTM D4255) except for the in-plane compression tests which were performed utilising a specially developed in-house equipment. The obtained results are as follows: modulus of elasticity E_1 in tension and compression were 18600 MPa and 26600 MPa respectively, and E_2 in tension and compression were 6830 MPa and 5990 MPa respectively. The modulus of rigidity G_{12} was 2190 MPa and the Poisson's ratio ν_{12} was 0.35. When using the data in the numerical analysis, an evaluation of the stress state of each single layer was performed, in order to use the appropriate value of the modulus in either tension or compression E_1 and E_2.

The set-up for the uniaxial and biaxial testing arrangements is shown in figure 1. The uniaxial loaded panel was loaded in the vertical direction by an Instron universal machine at constant displacement rate and the biaxial loaded panel was loaded in a specially developed steel test frame. Both types of loaded panel were constrained by four rigs. The horizontal rigs were longer than the panel dimensions, whilst the vertical rigs, in order to avoid interaction with the horizontal ones, were 30 mm shorter, thus leaving a small unsupported length of 15 mm on both ends of the specimens. Three steel bars were equally spaced down the lengths of the vertical rigs and were rigidly connected to them. This construction was to prevent the vertical rigs from twisting out of the plane of the panels. In the uniaxial test the upper horizontal beam of the test rig was centrally loaded by a hydraulic ram through a steel ball and socket in order to apply a truly vertical frictionless load. At the bottom loading position of the test rig the sandwich panel was loaded through a steel cylindrical roller housed in a machined socket which reacted on a rigid support.

As stated above the biaxial tests were undertaken in a specially developed test frame and two hydraulic jacks, linked to a common pump, applied equal loads onto the horizontal and vertical edges of the sandwich panels; the rig arrangements to apply axial loads to the two edges of the panel were identical to that used in the uniaxial test.



(a) *(b)*

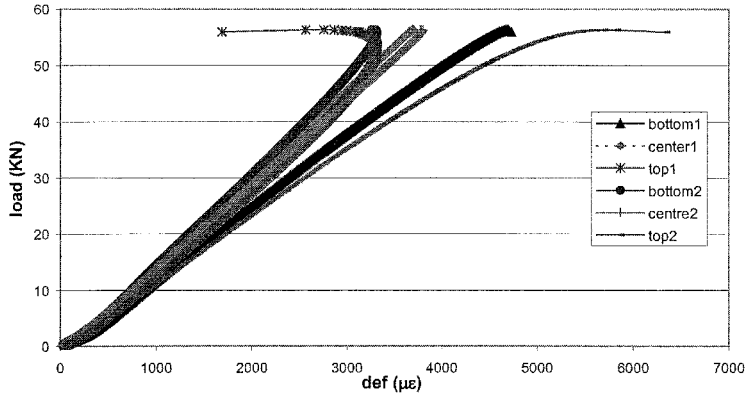
1: Experimental set-up: (a) uniaxial testing, (b) biaxial testing.

The uniaxial tests were performed on square panels of 285 mm side lengths. The core thickness was 7.8 mm and the thickness of the face materials for the uniaxial tests varied between 0.68 mm and 0.87 mm depending upon the test specification. A symmetric and an un-symmetric stacking sequence, respectively [90/0/90] and [0/90], were used for the face materials. The whole was symmetrically placed with respect to the mid-plane of the panel; only the un-symmetrical face material lay-up was used in the biaxial compression.

Results and discussion

During the tests no noticeable deformation of the panels was observed up to a particular load, at which a sudden instability occurred; this was considered as the critical buckling load, and quantitatively defined by means of the load-strain data as reported in the sequel. In the uniaxial tests a shear failure was observed in the vertical unloaded side of the panel close to the horizontal uniformly distributed load. A frame-by-frame analysis of the video of the test revealed that these failures took place immediately after the instability of the panel occurred; the failure of the panel was therefore considered a buckling failure immedialtely followed by a face failure. The analysis of the strain gauge values confirms this conclusion, although localised shear deformations at that position do commence early in the testing of the panel and become large before the final instability failure. The initial buckling load is of low value and the panel is able to support an increase of load until the second order buckling occurred deforming the panel into a highly unstable configuration. This effect may have been due to the existence of an initial imperfection, which would have caused an out-of-plane displacement and thus would prevent the panel from developing the full theoretical buckling load.

Figure 2 shows typical experimental test relationships between load and deformation at particular points on the panel under uniaxial loading. The curves tend to be essentially linear up to certain values of load, beyond which they become non-linear. The two gauges on either side of the panel closed to the top loading position have large deformations with no increase in load; these load values are the critical buckling load [1], [2]. Two tests were carried out for each uniaxial and biaxial configuration. The experimental critical buckling load values are given in table 1 together with the FE analyses. Figure 3 shows qualitatively, the deformed shape of the panel along the un-deformed centre line for axial test (3a) and biaxial test (3b).



2: Load-strain data in uniaxial buckling test on panel with [90/0/90] skins.

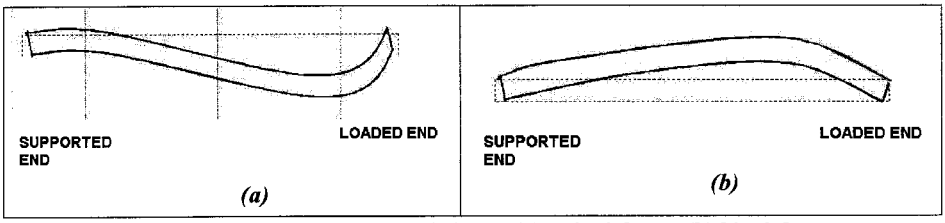
NUMERICAL STUDY

Model development

The finite element analysis was performed using Abaqus (Standard); Abaqus (CAE) was used as the pre- and post-processor. First order 3-D brick elements were used for the core and the rigs, whilst first order stratified shell elements were utilised to model the skins. The degree of mesh refinement was established on the basis of a convergence analysis, with a precision target of 1%.

In order to understand the actual experimental set-up conditions, and as the actual value of the coefficient of friction was unknown, two extreme cases were considered in the FE simulations for the interaction between the panel and the vertical rigs of the uniaxial tests; these two cases were when (a) no friction existed and (b) no sliding existed. In addition, no friction was considered for the remaining interactions in the uniaxial test and for all the contact pairs in the biaxial test simulation.

The critical buckling load values obtained using the above models were considerably lower than the experimental values; the difference between the two techniques as a function of the FE analysis value was 50% This was attributed to a possible partial 'locking' of the ball and the roller in their housing due to the high values of loads being applied. An attempt was made to simulate such effects in the FE analysis by introducing 1-D string elements acting on the rig in such a way as to resist their lateral displacement; the stiffness values were calibrated on the bases of the experimental results for the panel with [0/90] faces. In addition, the partial 'locking' of the ball and roller was also modelled.



3: Qualitative critical deformed shape: (a) uniaxial test; (b) biaxial test.

Table 1 : Experimental and corresponding F.E. critical buckling load (expressed in tons).

LAY-UP AND LOADING	EXPERIMENTAL		F.E.			
			Free rigs rotation		Restrained rigs rotation	
	Single test results	Average value	No friction	Friction	No friction	Friction
[90/0/90] uniaxial	5.63 6.72	6.18	1.46	1.79	5.34	5.69
[0/90] uniaxial	5.00 5.42	5.21	1.37	1.47	4.85	5.21
[0/90] biaxial	4.09 4.14	4.13	1.85	----	3.59	----

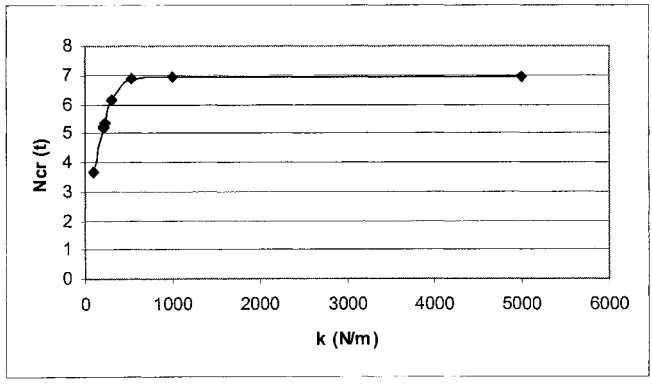
RESULTS AND DISCUSSION

The results obtained from the FE analysis utilising the 1-D spring elements and the experimental analysis are given in table 1. As will be seen, by comparing the column 4 with the column 5 and the column 6 with the column 7, there is only a small difference (2-7%) between applying 'no friction' and 'friction' in the FE analysis and such parameters introduced into the analysis are not critical. Furthermore, the model in which the rigs can freely rotate about the ball and roller gives buckling load values that are considerably lower than the experimental ones. The results for the buckling load when the ball and roller were partially "fixed" are given in column 7 of table 1; these compare well with those for the experimental tests. From the figure 4 it can be seen that the value of the spring stiffness corresponding to the fully fixed condition of the numerical hinge at critical buckling load is about 530 N/m. Thus the degree of fixity in the experimental model in relation to the FE analysis is of the order of 40%, as given by the ratio between the stiffness value (211 N/m) corresponding to the matched experimental result (5.21 t) and the stiffness value (530 N/m) corresponding to saturation value of the critical buckling load (6.9 t).

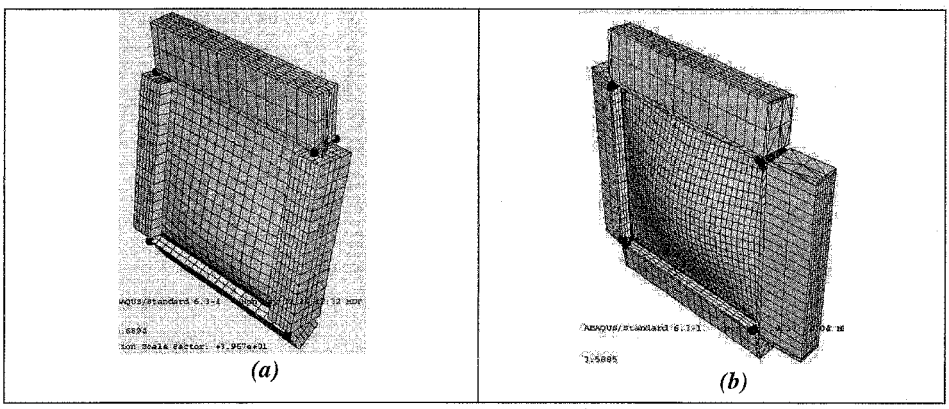
Moreover, for the [0/90] face panel, the experimental buckling load for the uniaxial loading has a higher value than that for the biaxial loading, as would be expected. However, the results obtained for the FE model with free rig rotation, show that the buckling load values are reversed; the biaxial value is higher than the uniaxial value. It can be also seen that when restraints to rotation are applied, the same trend is obtained as in the experimental tests, namely, the biaxial buckling load is lower than the uniaxial load. It should be mentioned here that the application of the 1-D spring element with a particular stiffness developed for a specific model stiffness value (in the present case [0/90] uniaxial) will not necessarily be the correct value to use for other model stiffness values (e.g. in the present case [90/0/90] panels).

From the results it may be concluded that the experimental set-up could be considerably improved by using roller bearings to reduce the friction at the hinges of the rigs.

Figure 5 shows the deformed numerical solutions for the uniaxial and biaxial loaded panels. It can be seen that similar qualitative shapes were obtained for the two panel types experimentally tested in uniaxial and biaxial compression shown in figure 3.



4: Buckling load vs. springs stiffness in the FE model.

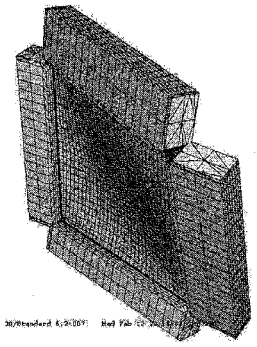


5: Critical deformed shape in the (a) uniaxial test and (b) biaxial test simulation.

With regard to the biaxial test it is worth observing that the out-of-plane displacement corresponding to the second eigenmode (eigenvector = 4.63 t), shown in figure 6, is very pronounced at the top of the panel. Such instability is not compatible with the sample support boundary condition and is due to the lack of restraint at the corner of the top support of the panel. Nevertheless, it corresponds to a considerably higher eigenvalue so it should not occur in the experimental solution; however, in the critical deformed shape, corresponding to the minimum eigenvalue, the actual case is only slightly displaced out of plane.

CONCLUSIONS

In the experimental tests the panel failure was by global buckling although a localised low-load shear deformation (in the uniaxial test) preceded this buckling failure. In addition, a localised compression failure, which followed the buckling was also observed. The buckling failure was interpreted as the result of an initial imperfection due to experimental set-up. Although the results are acceptable realising the aims of the research, it is clear that a further improvement in the experimental set-up could result in a more accurate solution. The classical simply supported boundary conditions were not completely achieved, however, it should be stated that to obtain experimentally a truly axial load and a pinned condition at the supports of a sandwich panel is extremely difficult to achieve. The results of the current experimental work have been critically appraised utilising the finite element technique by introducing various degrees of friction and restraints at the support and it has been shown that the greatest effect on the variability between the experimental and numerical results is from rotation of the experimental support restraints; in the experimental test the panels appear to be partially restrained at the supports whereas they were designed as pined systems. Another weak point in the test set-up of the experimental investigations was the vertical member of the rig. As has been mentioned, these members were slightly shorter than the panel dimensions and therefore an unsupported small length at the top and bottom of the panels existed. This situation could lead to local shear deformations and influence the final buckling of the members.



6: Biaxial test: deformed shape corresponding to the second eigenmode.

Experimental analyses are generally considered to be more accurate than the numerical solutions, because the actual set-up, which would exist in practice, is being tested. Consequently, it might be considered that the above experimental work is the 'ideal' solution. However, the numerical solution is able to be more robustly defined and tends to the mathematical solution. One of the problems with numerical analyses is that the units' material properties, which have to be given precisely for accurate results, have to be measured experimentally and this involves, sometimes, complicated test rigs in order to be able to estimate, say, through thickness mechanical properties or shear properties in three dimensions. These problems do not exist in the experimental solutions.

REFERENCES

1 V.S. Sokolinsky, Y. Frostig, "On the response of sandwich panels with transversely flexible core – special behavior"; *5th International Conference on Sandwich Constructions*, Zurich, 5-7 September, 2000.

2 G. Dreher, "Stability failure of sandwich structures"; *2nd International Conference on Sandwich Constructions*, Gainesville, U.S.A., 9-12 March, 1992.

3 T. R. A. Pearce, J. P. H. Webber, "Experimental buckling loads of sandwich panels with carbon fibre faceplates"; *Aeronautical Quarterly*, November 1973, 295-312.

4 C. de Roover, J. Vantomme, J. Wastiels, K. Croes, H. Cuypers, L. Taerwe, H. Blontrock, "Modelling of a modular pedestrian bridge composed of a concrete deck and a truss girder with IPC sandwich panels"; *Computational techniques for materials, composites and composite structures*, 2000, 327-335.

5 B. K. Parida, R. V. Prakash, A.K. Ghosal, P.D. Mangalgiri, K. Vijayaraju, *Compression buckling behavior of laminated sandwich panels,Composite Materials: Testing and Design, Thirteenth Volume, ASTM STP 1242*, S.J. Hooper, Ed. American Society for Testing and Materials, 1997, 131-150.

6 C. Lainé, G. Rio, "Buckling of sandwich panels used in shipbuilding: experimental and theoretical approach"; 3rd *International Conference on Sandwich Constructions*, Southampton, 12-15 September, 1995.

7 J. C. Roberts, M. P. Boyle, P. D. Wienhold, G. J. White, "Buckling, collapse and failure analysis of FRP sandwich panels"; *Composites: Part B*, 2002 **33**, 315-324.

8 M. H. Wadee, "Experimental evaluation of interactive buckle localization in compression sandwich panels"; *Journal of Sandwich Structures and Materials*, 1999 **1**, 230-254.

FIRE BEHAVIOUR OF REINFORCED CONCRETE COLUMNS CONFINED WITH FIBRE-REINFORCED POLYMERS

Luke A. Bisby[1], Mark F. Green[1], and Venkatesh K.R. Kodur[2]

[1]*Department of Civil Engineering, Queen's University, Canada*
[2]*Fire Risk Management, Institute for Research in Construction, National Research Council of Canada*

ABSTRACT

The use of fibre reinforced polymers (FRP) for strengthening and rehabilitation of reinforced concrete structures has been the subject of numerous research projects and has seen widespread implementation in recent years. However, very little information is available on the behaviour of FRP materials at high temperature, as would be experienced during fire, and this is a primary factor limiting the widespread application FRP-wraps in buildings, parking garages, and industrial structures. This paper presents the results of numerical and experimental studies performed to investigate the fire behaviour of FRP-wrapped (confined) concrete columns, wherein full-scale fire endurance tests were conducted on two circular FRP-wrapped reinforced concrete (RC) columns. The primary objectives of this research project were: to experimentally investigate the behaviour in fire of circular FRP-wrapped and insulated RC columns; to develop and validate numerical models to simulate the behaviour in fire of these members; to investigate techniques to improve their behaviour in fire; and to use experimental data and numerical models to provide guidance to designers regarding the fire behaviour of FRP-wrapped RC columns. Test data are compared with the predictions of a specially developed fire simulation model, and the model is shown to adequately predict the observed thermal and structural response of the members. It is demonstrated that, while currently available infrastructure composites are particularly sensitive to the effects of elevated temperatures, appropriately designed FRP-wrapped reinforced concrete columns are capable of achieving satisfactory fire endurances.

INTRODUCTION

Fibre-reinforced polymers (FRPs) are now widely recognised as efficient and effective materials for the rehabilitation and strengthening of reinforced concrete (RC) structures. One of the most widely used applications of FRP for strengthening concrete structures is as external confining reinforcement for concrete columns. In these applications, adhesively-bonded, circumferentially-wrapped FRP sheets have been shown to increase both the strength and ductility of the concrete columns [1], and design guidelines are now available for use by engineers [2, 3]. However, the performance of FRP materials in fire is not well understood, and a number of significant concerns exist with respect to the fire behaviour of FRP-strengthened concrete members. These concerns must be addressed before externally-bonded FRP reinforcement can be used with confidence in buildings, where building code fire resistance guidelines must be adhered to. This paper presents the initial results of an ongoing experimental and numerical study to investigate the behaviour in fire of FRP-strengthened RC columns, beams, and slabs. Two full-scale fire tests have been conducted to date, and further tests are planned for 2004.

BACKGROUND

In considering the fire behaviour of a structural member, both structural and environmental concerns are important. However, this paper is concerned primarily with the structural performance of FRP-wrapped RC columns – their ability to carry the required loads without failure for the duration of the fire – as opposed to their environmental impact in fire – their contribution to increased flame spread, smoke generation and toxicity. In North America, for satisfactory structural fire endurance, load-bearing columns are required to carry their full unfactored service load for the required duration during exposure to a standard time-temperature curve, as defined in ASTM E119 [4].

FRP in fire

The high-temperature thermal and mechanical behaviour of FRP materials remains poorly understood, and because of the wide variety of often proprietary FRP materials currently available, it is difficult to make generalizations with respect to their thermomechanical behaviour. However, for externally-bonded FRPs used in concrete rehabilitation applications, it can be stated that they are particularly sensitive to the effects of high temperature (in comparison with concrete and steel). Severe deterioration in strength, stiffness, and bond properties can be expected for most FRP materials at temperatures exceeding their glass transition temperature (GTT). To study this behaviour, Bisby [1] assembled a database of results from tests on various FRP materials available in the literature and performed a least-squares regression analysis to develop semi-empirical analytical equations describing variation in strength and stiffness of glass/epoxy and carbon/epoxy FRP materials with temperature. These relationships are shown, along with strength curves for concrete and reinforcing steel at high temperature, as suggested by Lie [5], in Figure 1.

It is important to note that the data used to develop the relationships shown in Figure 1 were obtained from tests on FRPs with unknown matrices, and it is likely that many of these were elevated temperature-cure materials. Thermomechanical data are not currently available for ambient-cure epoxy matrix FRPs, such as those used for concrete strengthening applications, and it is presumed that these FRPs would be more affected by high temperatures. Future testing at Queen's University will shed light in this area.

Given the uncertainties associated with the thermomechanical behaviour of FRPs at high temperature, current design guidelines in North America [3] assume that any externally-bonded FRP reinforcement will be completely lost during fire. Thus, the unstrengthened concrete member must be capable of supporting the unfactored service load for the required duration during fire. In practice, FRP wraps installed in buildings that require fire resistance ratings are provided with supplemental fire insulation in an attempt to maintain the FRP temperature below the matrix GTT for the duration of a potential fire. While both of these approaches are certainly conservative, neither one considers the potential for

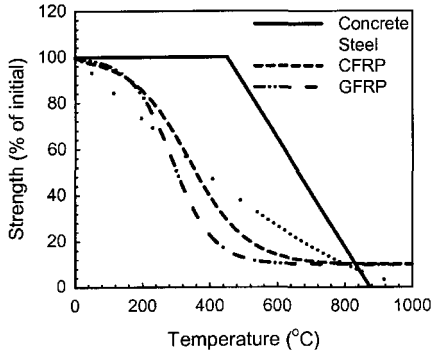


Figure 1: Assumed deterioration of properties with temperature

improvement of structural behaviour through the use of supplemental fire insulation provided on the exterior of the FRP wrap.

Fire tests on FRP-strengthened concrete members

Several test programs investigating the fire performance of FRP-strengthened concrete members have been presented in the literature [6, 7, 8, 9], although none of these studies have examined the performance of fire-exposed FRP-wrapped concrete columns. In the most extensive experimental study conducted to date, a series of full-scale fire tests on reinforced concrete beams and slabs, strengthened in flexure with adhesively bonded carbon/epoxy FRP plates, were conducted by researchers in Belgium [7, 8]. These tests indicated, in part, that there was a need for supplemental thermal insulation applied to the exterior of the FRP plates to prevent premature debonding of the FRP reinforcement during fire.

TEST PROGRAM

In an effort to study the performance in fire of FRP-wrapped reinforced concrete columns, two full-scale fire endurance tests have been conducted at the Institute for Research in Construction of the National Research Council of Canada. The two columns tested to date were identical, except for the amount of supplemental insulation applied to the exterior of the FRP wrap. Insulation was applied to both columns, under the assumption that uninsulated FRP wraps would be completely lost (i.e. complete loss of FRP strength and/or bond properties) very early in the fire exposure. Both columns were wrapped in the circumferential direction with a single layer of a commercially-available carbon/epoxy FRP strengthening system (the Tyfo® SCH system, supplied by Fyfe Co., San Diego), which was applied by wet lay-up using an epoxy adhesive/matrix (Tyfo® S Epoxy). Details of the two columns are provided in Table 1.

Fire insulation

Supplemental fire insulation was applied to the exterior of the FRP wrap over the full height of both columns. The fire insulation consisted of a unique two-component fire protection system (Tyfo® EI/VG Insulation System) which has been developed specifically for fire protection of externally-bonded FRP strengthening systems for concrete. The system consists of a passive layer of a modified spray-applied cementitious plaster (VG) beneath a finish coat of intumescent epoxy paint (EI). The insulation thicknesses applied to the respective columns are provided in Table 1. A more complete discussion of insulation system is available in Bisby [1].

Fire tests

Both columns were fire tested under sustained concentric axial load in the column furnace at the Fire Laboratories of National Research Council of Canada, Ottawa. The furnace temperature was controlled to simulate, as closely as possible, the ASTM E119 standard fire [4]. Both columns were subjected to a sustained axial compressive load of 2515 kN during testing, which is equal to their full unfactored FRP-strengthened service load. This test load was calculated in accordance with ULC S101 [10] guidelines, assuming a one-to-one dead-to-live load ratio and using the ISIS Canada design guidelines [2] to estimate the room-temperature FRP-confined strength of the concrete.

Table 1: Details of the two columns tested to date

column	diam. (mm)	height (mm)	f'_c (MPa)	internal steel reinforcement[§]		FRP wrap*	VG thickness (mm)	EI thickness (mm)
				vertical	spiral			
ISIS-1	400	3810	39	8-20 mm ∅	10 mm ∅	1-layer	32	0.56
ISIS-2	400	3810	40	8-20 mm ∅	10 mm ∅	1-layer	57	0.25

Normal density, type 10, carbonaceous aggregate concrete, strength determined at the time of testing
[§] Specified yield strength = 400 MPa
* Fyfe Co. LLC, Tyfo® SCH-30T carbon/epoxy FRP system

Once installed in the column furnace the columns were loaded to their service load of 2515 kN, and the load was held constant during the fire exposure. Applied load, deformation (overall elongation), internal reinforcement strains, and temperatures in the furnace, insulation, FRP, concrete, and steel reinforcement were all monitored and recorded throughout the tests.

Both columns were able to carry their full service load for more than five hours of fire exposure without showing any obvious signs of failure. Thus, at five hours, the load on the columns was gradually increased until failure occurred by sudden crushing/spalling of the concrete.

NUMERICAL MODELLING

Due to the relatively high costs associated with full-scale fire endurance testing, numerical computer models are now commonly used as tools in fire engineering research. Models can be developed and validated against relatively few full-scale fire endurance tests to allow researchers to inexpensively study the effects of a range of parameters on member behaviour during fire. For the studies presented in this paper, a numerical model was developed to simulate both the heat-transfer and structural behaviour (load capacity and deformation) of circular FRP-wrapped and insulated reinforced concrete columns during fire. The analysis essentially consists of a coupled heat-transfer/load capacity approach which has been programmed for computer. The model output consists of the distribution of temperatures throughout the column cross-section, the variation in load capacity of the column, and the axial elongation of the column under a user-specified sustained load when subjected to fire.

Material properties at high temperature

The development of accurate numerical models to simulate the behaviour of structures in fire requires a detailed understanding of the variation in thermal and mechanical properties of the structures' constituent materials with temperature. For the numerical modelling discussed herein, the thermal and mechanical properties of both concrete and steel, which are readily available in the literature, were assumed based on relationships suggested by Lie [5]. For the carbon/epoxy FRP wraps used in this study, thermomechanical information is extremely scarce, as discussed above. Thus, thermal properties have been assumed herein based on tests of carbon/epoxy aerospace composites as presented by Griffis et al. [11], and mechanical properties have been assumed to adhere to the semi-empirical analytical equations developed by Bisby [1]. The insulation is assumed to be structurally ineffective, and so only the thermal properties are required. These have been assumed based on manufacturer specified information and on thermogravimetric analyses conducted by Bisby [1].

Heat Transfer

The initial portion of the analysis consists of a heat transfer procedure to determine the distribution of temperatures throughout the column at any point in time during its exposure to fire. This is accomplished using an explicit finite difference heat transfer methodology based on elemental energy balances for a radially-discretized column, and is similar to a procedure used previously by researchers at NRC [12] to simulate heat transfer within conventionally-reinforced concrete columns. The column is assumed to be infinitely long and the contribution of the internal reinforcing steel to the heat transfer is assumed to be negligible. The analysis procedure used previously [12] has been modified in the current study to account for the presence of the FRP wrap and the supplemental fire insulation. The variation in thermal properties with temperature of all materials involved is accounted for in the analysis, although the effect of the intumescent finish coat, applied to the exterior of the VG insulation, is not accounted for the analysis (during the fire tests it was observed that the effect of the EI coating was relatively short-lived, and its contribution to the fire endurance of the columns is assumed to be minimal). More complete details of the heat transfer model are presented by Bisby et al. [13, 14].

Load Capacity and Deformation

Once the distribution of temperatures throughout the column has been obtained using the heat transfer analysis, the columns' load capacity and deformation can be approximated at any instant during fire. This is accomplished using a strain-compatibility/equilibrium approach, in which the column cross-section is further discretized into a series of annular elements, which approximates the buckling strength of the column and estimates its axial elongation (or contraction) at any instant. The confining effect of the circumferential FRP wrap is accounted for in the analysis using a modified version of the Monti and Spolestra [15] iterative confinement scheme, in which the confinement model has been modified to account for the degradation of mechanical properties of both the concrete and the FRP with temperature. A complete description of the load capacity model is also presented by Bisby et al. [13, 14].

RESULTS AND DISCUSSION

Both columns behaved similarly during fire testing, with the exception that slightly higher temperatures, larger deformations, and a marginally lower failure load were observed for Column 1 (which had a smaller overall thickness of insulation). The insulation system remained intact for the duration of the tests, and both columns subsequently achieved fire resistance ratings of greater than five-hours according to the ASTM E119 [4] guidelines.

Temperatures

Figures 2 and 3 show temperatures recorded during fire testing at a number of key locations for Columns 1 and 2 respectively. Included in the figures are the temperature of the furnace and the column temperatures recorded at the surface of the insulation, the outside surface of the FRP, and the FRP/concrete interface. Also included in Figures 2 and 3 are the temperatures at the aforementioned locations as predicted by the numerical heat transfer model. For both columns, the recorded temperature at the level of the FRP

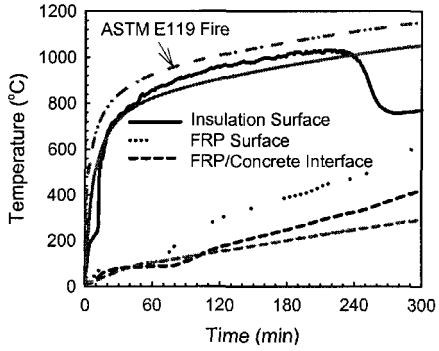


Figure 2: Measured and predicted temperatures for Column 1 during fire exposure (black lines are test data, grey lines are model predictions)

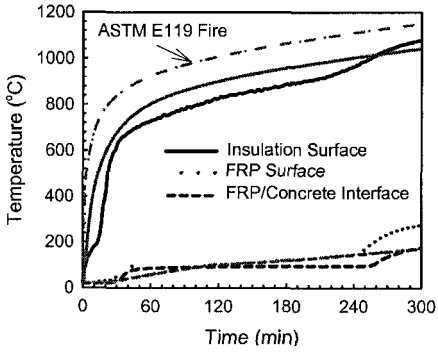


Figure 3: Measured and predicted temperatures for Column 2 during fire exposure (black lines are test data, grey lines are model predictions)

increases fairly rapidly, to temperatures approaching 100 C, but then plateaus at 100 C for a period of time before increasing again later in the fire exposure. This plateauing behaviour can be attributed to the evaporation of both free and chemically-combined moisture from the insulation/FRP interface at temperatures near 100 C. Thus, Column 2, which was protected with nearly twice as much insulation as Column 1, experienced a significantly longer 100 C plateau at the level of the FRP. Examination of the thermal profiles recorded at the surface of the insulation, in comparison with the profiles recorded at the level of the FRP, demonstrates the outstanding thermal protection provided by the insulation system used herein.

The glass transition temperature for the adhesive/matrix used in the current study was quoted by the manufacturer as 93 C. Figures 2 and 3 indicate that the temperature in the FRP remained below the GTT for 33 minutes for Column 1 and 43 minutes for Column 2. It is interesting to consider that these times would change to 58 minutes and 197 minutes if the GTT of the adhesive/matrix could be increased to 105 C. If the fire resistance of FRP-strengthened concrete members is to be defined in the future based on maintaining the temperature of the FRP below its GTT, as some North American building authorities have recently suggested, then adhesive matrices with GTTs in excess of 100 C will result in significantly higher fire resistances for these systems.

The predicted temperatures agree reasonably well with those recorded during testing, with the exception that the numerical model does not accurately capture the 100 C temperature plateau observed in the test data, and tends to underestimate temperatures observed later in the fire exposure. The inability of the model to accurately capture the 100 C plateau is likely due to the fact that it does not explicitly account for moisture evaporation from the insulation. Rather the model artificially increases the specific heat of the insulation near 100 C to account for the energy consumed in the evaporation reaction. The under-prediction of temperatures at later stages of the fire exposure is thought to be due to the formation of small shrinkage cracks in the insulation, which was observed during testing, leading to higher recorded temperatures than those predicted by the model. However, the model's prediction of temperatures is sufficiently accurate to allow for calculation of the overall load capacity of the columns during fire.

Load Capacity

Figure 4 shows a plot of the predicted axial load capacity of both columns as a function of fire exposure time. Also shown are plots giving the loads applied during testing and the failure load for each of the columns. The initial capacity of both columns is predicted to be identical, as should be expected. Under exposure to fire, both columns are predicted to experience only very minor reductions in strength with time, with Column 1 showing slightly more strength deterioration as a consequence of its smaller insulation thickness. Figure 4 also shows points giving the observed failure loads of the columns after 5½ hours of fire exposure. The failure loads for both columns were approximately 1.8 times the axial load capacity required to satisfy the fire endurance guidelines of ASTM E119. Thus both columns achieved greater than a 5-hour fire endurance rating, even though the GTT of the FRP was exceeded within less than one hour during both tests. This suggests that definition of fire endurance for FRP-wrapped RC columns in terms of maintaining the FRP temperature below its GTT, while conservative, may not be required from a fire-safety point of view and may, in fact, be overly restrictive.

Deformation

Figure 5 shows the measured and predicted axial deformations for both columns during the fire tests, and demonstrates that both columns experienced only minor elongations during fire, primarily as a result of very mild thermal expansion. The large contractions shown in the experimental data beyond five hours of exposure are a consequence of the fact that the applied loads on both columns were increased beyond five hours, thus inducing contraction and failure in both tests.

Also evident in Figure 5 is that the numerical model over-predicts the expansion of both columns for the full duration of fire exposure. Nonetheless, the deformations are extremely small, and over-prediction of elongation is conservative from a fire engineering standpoint.

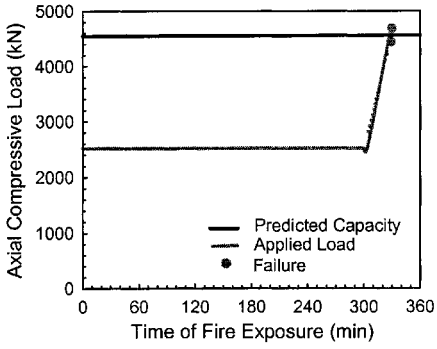


Figure 4: Predicted variation in load capacity with fire exposure time (black lines – model predictions, grey lines – applied loads during testing)

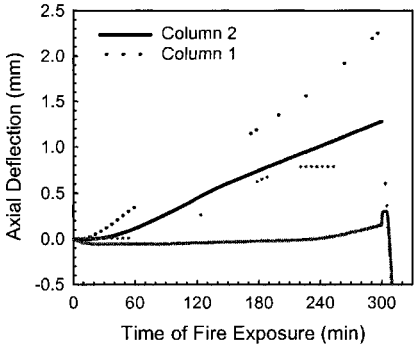


Figure 5: Predicted and observed axial deformation of columns during fire exposure (black lines – model predictions, grey lines – test data)

CONCLUSIONS

Based on the experimental and numerical studies presented in this paper, the following conclusions can be drawn:

1. FRP materials are sensitive to the effects of elevated temperature, and careful consideration of thermal effects on structural performance is required when FRP materials are contemplated for use in building structures.
2. The unique two-component insulation system described herein is an effective fire protection system for FRP-wrapped reinforced concrete columns. The insulation remains intact during exposure to a standard fire, and provides outstanding thermal protection for externally-bonded FRP materials. FRP-strengthened columns protected with this system are capable of achieving satisfactory fire endurance ratings.
3. The numerical model described briefly herein adequately predicts both the heat transfer within, and load capacity and deformation of, FRP-wrapped and insulated reinforced concrete columns during exposure to a standard fire.

ACKNOWLEDGEMENTS

The authors are members of the Intelligent Sensing for Innovative Structures Network (ISIS Canada) and wish to acknowledge the support of the Networks of Centres of Excellence Program of the Government of Canada and the Natural Sciences and Engineering Research Council. The authors would also like to acknowledge the National Research Council of Canada, Fyfe Co. LLC, and Watson Bowman Acme Corp.

REFERENCES

1 LA Bisby, Fire *Behaviour of Fibre-Reinforced Polymer (FRP) Reinforced or Confined Concrete*, PhD Thesis, Department of Civil Engineering Queen's University, Canada, 2003.
2 ISIS, *Design Manual No. 4: Strengthening reinforced concrete structures with externally bonded fibre-reinforced polymers*, Intelligent Sensing for Innovative Structures, Winnipeg, Canada, 2001.
3 ACI, ACI 440.2R-02: Guide for the design and construction of externally bonded FRP systems for strengthening concrete structures, American Concrete Institute, Farmington Hills, USA, 2002.
4 ASTM, Test Method E119-01: Standard Methods of Fire Test of Building Construction and Materials, American Society for Testing and Materials, West Conshohocken, USA, 2001.
5 TT Lie, *Structural Fire Protection*, American Society of Civil Engineers, New York, USA, 1992.
6 M Deuring, *Brandversuche an nachtraglich verstarkten Tragern aus Beton*, Research Report No. 148'795, Swiss Federal Laboratories for Materials Testing and Research, Dubendorf, Switzerland, 1994.
7 H Blontrock, L Taerwe & P Vandevelde, 'Fire Testing of Concrete Slabs Strengthened with Fibre Composite Laminates', 5th An. Symp. *Fibre-Reinforced-Plastic Reinforcement for Concrete Structures*, Thomas Telford, London, 2001.
8 H Blontrock, L Taerwe & P Vandevelde, 'Fire Tests on Concrete Beams Strengthened with Fibre Composite Laminates', *Third Ph.D. Symp.*, Vienna, Austria, 2000.
9 M Saafi & P Romine, 'Effect of Fire on Concrete Cylinders Confined with GFRP', 2nd int conf *Durability of Fibre Reinforced Polymer Composites for Construction*, Avantage Inc., Sherbrooke, 2002.
10 CAN/ULC, *ULC-S101: Standard Methods of Fire Endurance Tests of Building Construction and Materials*, Underwriters' Laboratories of Canada, Scarborough, Canada, 1989.
11 CA Griffis, RA Masmura, & CI Chang, 'Thermal response of graphite epoxy composite subjected to rapid heating', *Environmental Effects on Composite Materials, Vol. 2*, Technomic, Lancaster, USA, 1984.
12 TT Lie and B Celikkol, 'Method to calculate the fire resistance of circular reinforced concrete columns,' ACI Materials Journal, 1991 **88**(1) 84-91.
13 LA Bisby, MF Green & VKR Kodur, 'Fire Behaviour of FRP-Wrapped Reinforced Concrete Columns', *Structural Faults and Repair – 2001*, London, UK, 2001.
14 LA Bisby, BK Williams, MF Green & VKR Kodur, 'Studies on the fire behaviour of FRP reinforced and/or strengthened concrete members,' 2nd int conf *Durability of Fibre Reinforced Polymer Composites for Construction*, Avantage Inc., Sherbrooke, Canada, 2002.
15 MR Spolestra & G Monti, 'FRP-confined concrete model', *J. Composites for Construction*, 1999 **3**(3) 143–150.

STRESSES IN SIMPLE SHEAR TEST SPECIMENS FOR STEEL OR FRP-TO-CONCRETE BOND STRENGTH: A 3D FINITE ELEMENT STUDY

J. F. Chen
Institute for Infrastructure and Environment, School of Engineering and Electronics, Edinburgh University, Edinburgh EH9 3JN

W. K. Pan
School of Mechanical, Materials, Manufacturing Engineering and Management, Nottingham University, Nottingham NG7 2RD

ABSTRACT

One of the key factors affecting the behaviour and reliability of reinforced concrete structures strengthened with externally bonded steel plates or advanced fibre reinforced plastic (FRP) composites is the bond behaviour between the external plate and the concrete substrate. Extensive research has been carried out on external plate-to-concrete bond strength. Many different experimental set-ups have previously been used to determine bond strength. Because of the differences of width and the Poisson's ratio between the test plate and the concrete specimen as well as the details of test set-up, the true stress state in such a test structure is likely to be three-dimensional. However, this 3D nature of stress distribution is generally ignored in theoretical analysis by adopting the plane stress assumption. This paper presents a finite element analysis on the stress distributions in a typical test set-up. Results show that the stress distributions can be significantly different from plane stress assumption.

INTRODUCTION

One of the key factors affecting the behaviour and reliability of reinforced concrete structures strengthened with externally bonded steel plate or advanced fibre reinforced polymer (FRP) composites is the bond strength between the external plate and the concrete substrate (Teng *et al.* 2002a). Extensive research has been carried out on the bond strength between either steel plate or FRP and concrete (e.g. Brosens and van Gemert 1997, Maeda *et al.* 1997, Neubauer and Rostásy 1997, Miller and Nanni 1999, Chen and Teng 2001). This is largely because understanding the bond behaviour is essential before various debonding failures such as intermediate crack induced debonding in flexurally strengthened beams and slabs (Teng *et al.* 2003) and debonding of side plates in shear strengthened beams (Chen and Teng 2003) can be properly understood.

Many different experimental set-ups have previously been used to determine the bond strength, including simple shear tests and bending tests (Chen *et al.* 2001, Teng *et al.* 2002b). Simple pullout shear tests have been more commonly used because of their simplicity (Chen and Teng 2001). Because of the difference of width and the Poisson's ratio between the external test plate and the concrete specimen as well as the details of test set-up, the true stress state is likely to be three-dimensional in these tests. However, this 3D nature of stress distribution is generally ignored in theoretical analysis by adopting the plane stress assumption (e.g. Yuan *et al.* 2001). This paper presents a finite element analysis on the stress distributions in a single shear test (Fig. 1) which has been one of the most commonly used test set-ups.

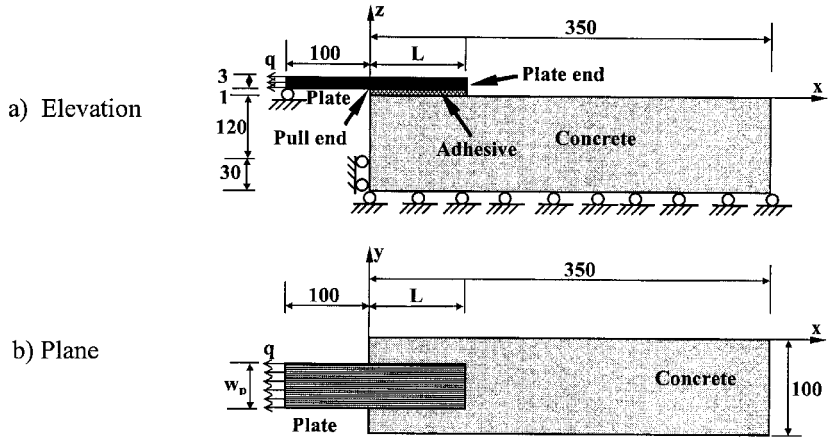


Figure 1. Geometry and boundary conditions for FE modelling

It may be noted that an extensive literature review (Chen and Teng 2001) indicated that most bond strength test specimens failed a small distance (in order of millimetres or even smaller) in the concrete underneath the concrete/adhesive interface. This implies that a rational analysis should be applicable to both FRP and steel plate bonded to concrete because the failure is within the concrete. No distinction is therefore made between FRP and steel plates in this paper.

FINITE ELEMENT MODELLING

General

Linear elastic FE analyses were carried out in this study to investigate the stress states in a typical single shear test. The concrete block was taken to be 350 mm long, 150 mm thick and 100 mm wide. Plate thickness of 3 mm and adhesive thickness of 1mm were used in all the analyses. The Young's moduli were assumed to be 200, 1 and 30 GPa for the plate, adhesive and concrete respectively. The corresponding Poisson's ratios were 0.3, 0.25 and 0.17 respectively.

The geometry, loading, boundary conditions and adopted coordinate system are shown in Fig. 1. Only half of the structure was modelled making use of the symmetrical configuration in x-y plane. The pulling force in the plate was applied by a uniformly distributed tension force q with an intensity of 1 N/mm^2 at the loading end. Vertical restraint was applied to a length of 5mm of the plate from the loading end. Previous study has shown that the height of the vertical free concrete edge on the loading side can significantly affect the stress distribution in the adhesive, but this difference becomes insignificant when the free edge is greater than about 40mm. Because this was not an intended parameter for investigation, a height of 30mm at the bottom on the left hand side of the concrete block is restraint horizontally, leaving a free concrete edge height of 120mm (Fig. 1a).

The analyses were conducted using ABAQUS 5.8. All materials were modelled using 20-node brick elements. Perfect bond between the adhesive and the plate and between the adhesive and the concrete was assumed. A bond length of L=100mm was used in all the analyses presented in this paper.

Mesh convergence

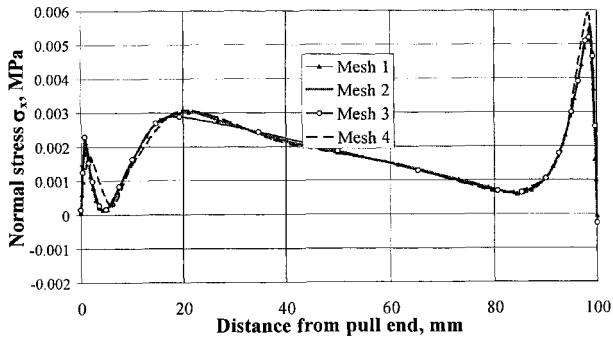
The plate and the adhesive were modelled with 2 and 4 elements respectively through their thicknesses. This shall result in sufficient accuracy based on previous experience in 2D plane stress analysis of the same problem (Chen *et al.* 2001). The concrete block was modelled with elements finest at the adhesive-concrete bond interface and gradually increasing away from this interface. Meshes were also finest near the pull end and the plate end where possible stress singularities exist. They gradually became coarser towards other parts of the structure. It may be noted that slightly larger elements than those used in previous 2D analysis (Chen *et al.* 2001) had to be used here as otherwise the tasks could not be accomplished within the available computational resources.

Four different concrete meshes were used to study the convergence for a typical test with bond length L=100mm and plate width w_p=50mm. The minimum element size, total number of elements and total number of nodes for each of these four meshes are listed in Table 1. Typical results from these meshes are compared below. For brevity, the plate-adhesive interface, adhesive-concrete interface and the mid-section of the adhesive are respectively referred to as PA, AC and MA hereafter.

Table 1 Trial meshes

	Minimum element size, mm	Total No. of elements	Total No. of nodes
Mesh 1	0.36	13178	59000
Mesh 2	0.50	7902	36122
Mesh 3	0.78	3204	15339
Mesh 4	1.88	708	3877

a) Normal stress σ_x at plate centre (y=0)



b) Normal stress σ_x at plate edge (y=25mm)

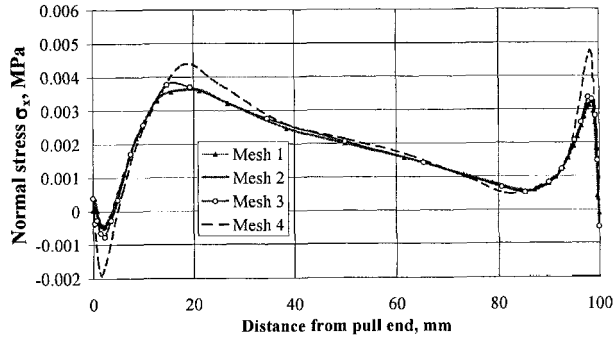


Figure 2. Stresses on MA interface

Figures 2a and b show the distributions of the normal stress σ_x at MA at the middle of the plate (y=0) and along the edge of the plate (y=25mm) respectively. For the four different meshes, Meshes 1 and 2 predicted almost identical results whilst the coarser Meshes 3 and 4 predicted slightly different results. This indicates that Meshes 1 and 2 are adequately fine to predict converged results. The distribution of other stress components confirmed this observation. Results presented hereafter are either directly from predictions of Mesh 2, or that of similar one to Mesh 2.

It may be noted that stresses at PA and AC are not used here for convergence test because the maximum stresses near the pull and plate ends always increase as the mesh becomes finer so no convergence is possible at these locations (Chen et al 2001, Teng *et al.* 2002b) due to stress singularities at two-material wedges (Hein and Erdogan 1971).

STRESSES IN THE PLATE

Figure 3 shows the distribution of the longitudinal normal stress σ_x on the upper and lower surfaces of the plate with L=100mm. Within the bonded part of the plate, there are significant bending stresses near the pull end, with the stress on the upper surface about 30% larger than that on the lower surface at about 10mm from the pull end. It is of interest to note that the bending effect at the edge is more significant than that at the centre. The bending effect reduces gradually as the distance from the pull end x (Fig. 1b) increases and it becomes insignificant at about x=40mm. Near the free end of the plate, the bending effect becomes significant again but the axial stress is close to zero. The stress here is larger on the lower surface than that on the upper surface.

The interfacial shear stress at PA is usually found from the difference of adjacent two strains, measured on the top surface along the bonded part of the plate in experimental studies (e.g. Swamy *et al.* 1986). This method is accurate only when the plate is subjected to pure tension within the bonded part. The existence of significant bending stresses within the plate means that the method can lead to significant errors, especially near the pull end.

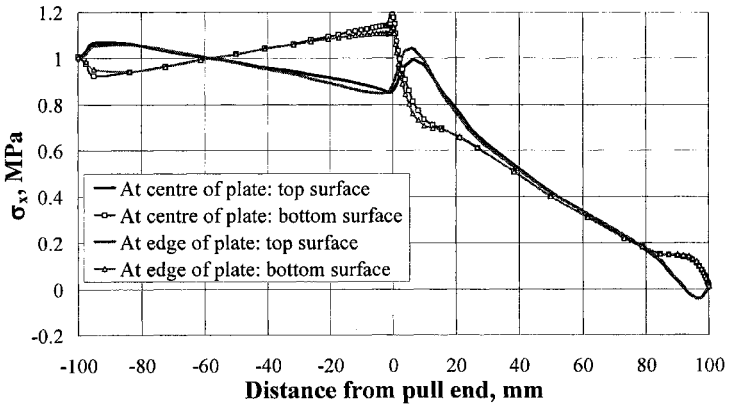


Figure 3. Horizontal normal stress σ_x in the plate

Because a short length (5 mm) of the plate from the loading end is vertically restrained, the reaction force there results in bending stresses in the plate within the unsupported part of the plate. Although it is arguable whether such a restraint realistically represent practical test condition, previous 2D analysis has shown that different boundary at the

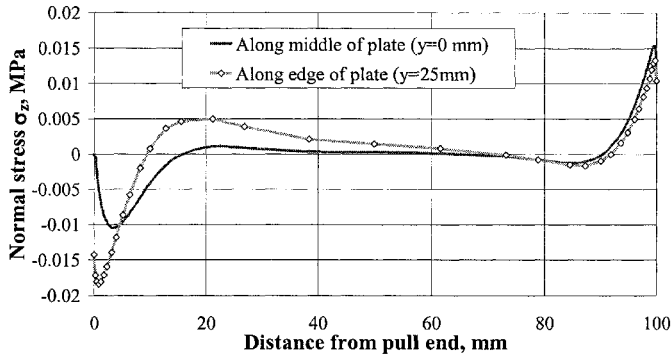
loading end of the plate does not result in significant differences in the stress distribution in the bonded part of the plate (Chen *et al.* 2001).

STRESSES ON MA SECTION

Figures 4a and 4b show the peeling stress σ_z and shear stress τ_{xz} on the mid-section of adhesive (MA) respectively. It is interesting to note that significant differences exist between the stresses at the middle of the plate (y = 0 mm) and those at the edge of the plate (y = 25 mm). Near the pull end, the peak value of the normal stress is – 0.010 MPa at the middle and – 0.018 MPa at the edge of the plate, representing a difference of 80% (Fig. 4a). Near the free end of the plate, the peak normal stress at the middle is larger than that at the edge and the difference is about 15%. These indicate that the stress distribution across the width of the plate (in y-direction) is strongly non-uniform, in contrast to the uniform stress as assumed in 2D analysis. It may be noted that the difference of stresses near the free end of the plate is expected to be strongly dependent on many factors such as the bond length and the plate thickness.

The peak values of the shear stress near the pull end are – 0.046 MPa and – 0.070 MPa respectively at the middle and at the edge of the plate, representing a difference of 52% (Fig. 4b). Although the value of this difference is smaller than that of the peak normal stress, the nonuniformity is significant throughout the whole bond length. The value of the shear stress at the edge is always larger than that at the middle of the plate (Fig 4b), indicating more loading is transferred to the concrete through the adhesive near the edge than that near the middle.

a) Peeling stress σ_z (normal to plate)



b) Shear stress τ_{xz}

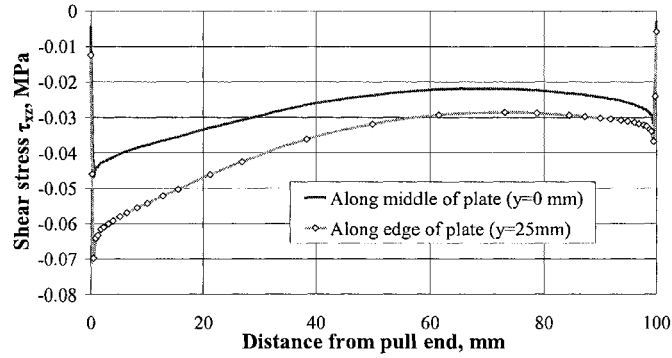


Figure 4. Stresses on MA

It may be noted that a large normal compressive stress σ_z near the pull end may not be of particular concern because concrete is strong in compression. However, both positive and negative shear stresses are detrimental. The significant difference of both normal stress σ_z and shear stress τ_{xz} between the edge and the middle of the plate indicate the strong 3D nature of stress distribution in such a test set-up.

EFFECT OF PLATE TO CONCRETE WIDTH RATIO

Stresses on MA section

Figures 5a and 5b show the effect of plate to concrete width ratio w_p/w_c on the distribution of normal (peeling) stress σ_z at the middle (y=0) and that at the edge (y=w_p/2) of the plate respectively. Along the middle of the plate, the peak (compressive) stress near the pull end reduces quickly as w_p/w_c increases from 0.1 to 0.3 but only reduces slightly when w_p/w_c further increases to 1.0. Near the plate free end, the peak (tensile) stress increases almost linearly as w_p/w_c increases from 0.1 to 1.0 and its value for w_p/w_c=1.0 is about twice that for w_p/w_c=0.1.

a) At middle (y=0)

b) At edge (y=w_p/2)

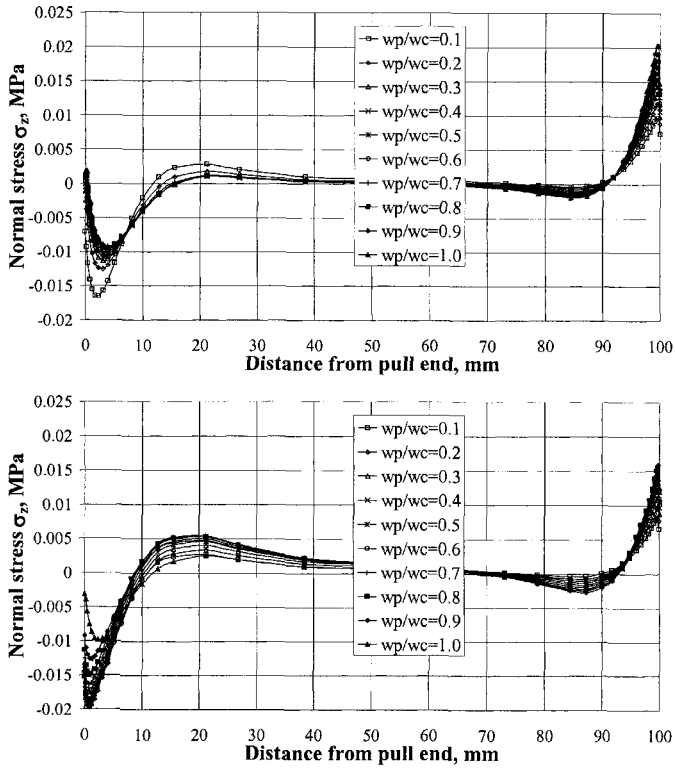


Figure 5. Normal stress σ_z on MA section

The distribution of σ_z along the edge of the plate is overall similar, but the peak stress near pull end is usually larger than that at the middle of the plate and that near the plate free end is usually smaller. The effect of w_p/w_c=0.1 on σ_z near the plate free end is

similar to that at the middle of the plate as above. In contrast to that along the middle of the plate, the peak (compressive) stress reduces slowly initially and then more quickly when w_p/w_c increases from 0.1 to 1.0.

Figures 6a shows that the peak (negative) shear stress near the pull end reduces more quickly initially and then slow down as w_p/w_c increases from 0.1 to 1.0. However, near the plate free end the peak stress increases quickly and then slow down as w_p/w_c *increases. For the peak stress at the edge of the plate (Fig. 6b), it reduces very slightly* as w_p/w_c increases from 0.1 to 0.7 but significant reduction is experienced as w_p/w_c further increases to 1.0. It's increase near the plate free end is however gradual with w_p/w_c.

a) At middle (y=0)

b) At edge (y=w_p/2)

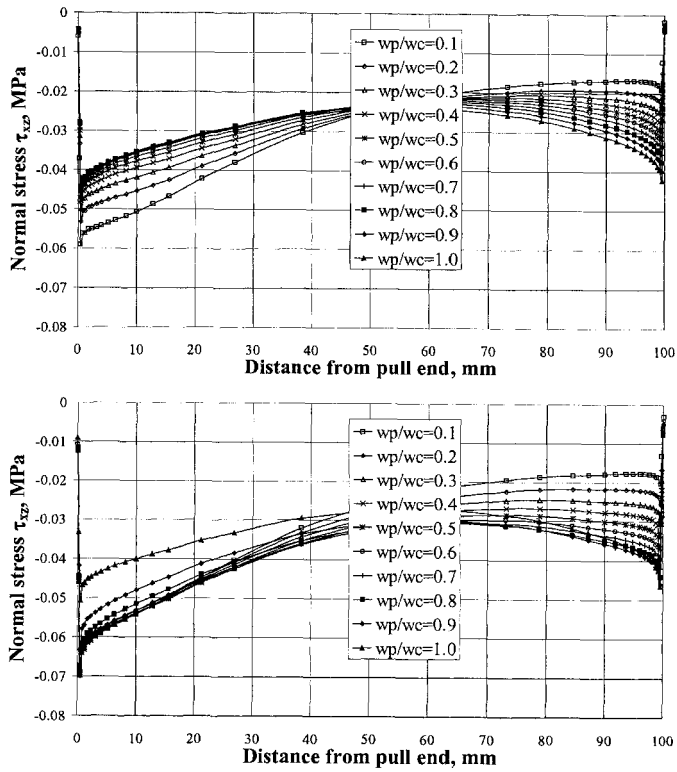


Figure 6. Shear stress τ_{xz} on MA section

From Figs 5 and 6, the following two observations may be made:

a) The stress distributions in such a simple shear test setup is three dimensional as experienced from the difference between the middle and the edge of the plate. There are two contributing factors to this: the difference between the width of the test plate and that of the concrete prism, and the difference between the Poisson's ratios of the materials (the plate, adhesive and concrete).
b) As the plate to concrete width ratio increases, the stresses near the pull end reduces and that near the plate free end increases. This is very similar to the effect of increasing plate thickness (see Chen *et al.* 2001). Therefore, it may be concluded that the axial stiffness $E_p w_p t_p$ has significant effect on the stress

transfer from plate to concrete. As the plate stiffness increases, more loading is transferred from the plate to the concrete away from the pull end.

a) Normal stress σ_z

b) Shear stress τ_{xz}

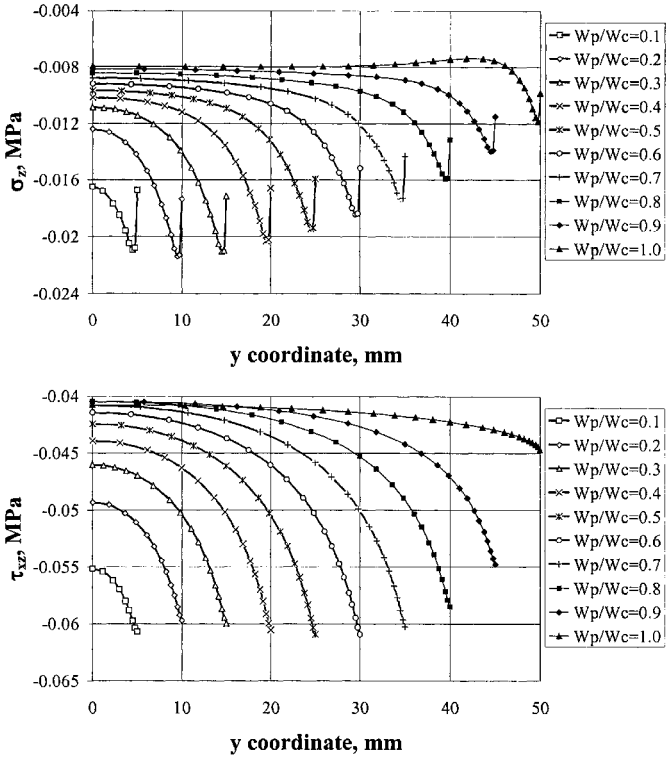


Figure 7. Stresses at x=2.32mm on MA section

The above observations are enhanced by inspecting the stress distribution across the width of the plate (Figs 7a, b). At a distance of 2.32mm from the pull end, both the normal stress σ_z and the shear stress τ_{xz} at MA are highly nonuniform in y direction, and reduce as w_p/w_c=1.0 increases. Note that nonuniformity is also experienced for w_p/w_c=1.0, attributed to the differences of the Poisson's ratios between the materials (otherwise it shall be uniform because both geometry and loading are uniform in this direction so it would be a plane stress problem).

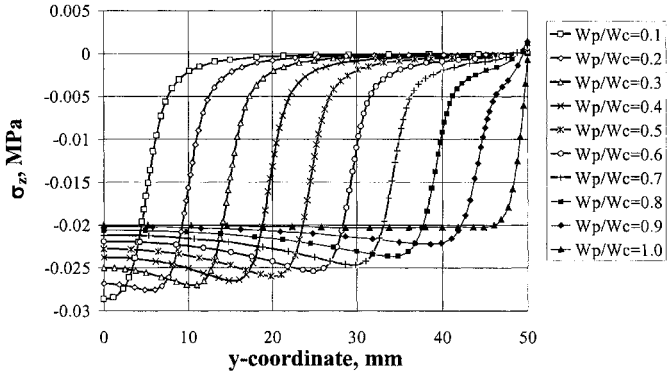
Stresses in concrete

For both steel and FRP plate to concrete bond strength tests, failure for most test specimens occurs in within the concrete a small distance underneath adhesive/concrete interface (Chen and Teng 2001). Therefore, the behaviour of concrete is the predominate factor affecting the failure. In this sense, stresses in the concrete are somewhat more important than that in the adhesive or at the interfaces. Figures 8a and b show the distribution of normal stress σ_z and shear stress τ_{xz} in y direction at x = 2.32 mm from the pull end and z = 2.32 mm below the adhesive/concrete interface. The distribution of both stresses is highly nonuniform. For a given plate width w_p, the magnitude of both stresses increases slightly from the middle of the plate (y=0) as y

increases and reaches their peak values close to the edge of the plate. It then reduces dramatically and approaches zero a small distance (about 5mm) outside of the plate edge. Although both the pattern and magnitude of the stress distribution are strongly dependent on the location being examined, Figure 8 is typical.

Figures 8a and b indicate that the peak normal (compressive) stress σ_z for a smaller w_p/w_c value is slightly larger than that for a larger w_p/w_c value. This does not mean that the plate stress at failure would be smaller in a narrow plate than a wide plate because the compressive stress here is beneficial. Bearing in mind that these stresses are obtained from linear elastic analyses, the slight decrease of the peak shear stress with the increase of w_p/w_c (Fig. 8b) shall not be used to deduce the same conclusion either. This is because the ultimate failure load depends not only on the peak stress values, but also on the stress distribution and redistribution after the occurrence of any plastic deformation. For a narrow plate, although the peak stresses are large near the pull end they only occur in a small amount of concrete. The surrounding concrete can share the loading through stress redistribution once nonlinear deformation occurs in the highest stressed part. In contrast, for a wide plate the majority of the concrete across the width is highly stressed so limited or little stress redistribution can take place. Therefore, results presented in this paper are not really in contradictory to the conclusion reached previously (e.g. Chen and Teng 2001) that the plate stress at failure is higher in a narrow plate than that in a wide plate.

a) Normal stress σ_z



b) Shear stress τ_{xz}

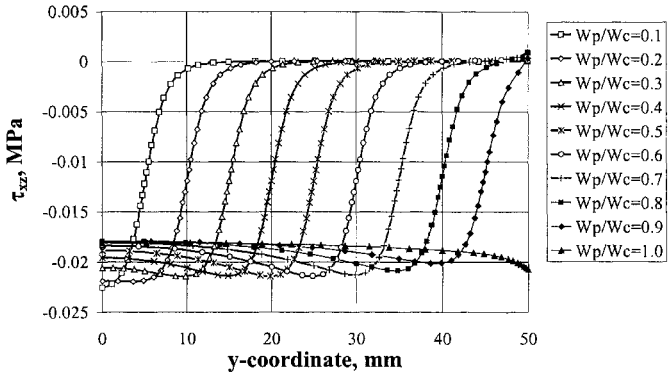


Figure 8. Stresses at x = 2.32 mm and z = –2.32 mm

CONCLUSIONS

This paper has presented a 3D finite element analysis of a simple shear test. The numerical results have shown that the stress distributions in such a simple test setup are highly nonuniform across the width. This three dimensional stress distribution may be attributed to two factors. The first is the difference of the width between the test plate and the test concrete prism. The second is the differences of the Poisson's ratios of the materials (plate, adhesive and concrete). This study also indicates that the axial stiffness of the plate $E_p w_p t_p$ has significant effect on the stress transfer from plate to concrete. As the plate stiffness increases, more loading is transferred from the plate to the concrete away from the pull end.

REFERENCES

1. Brosens, K. and Van Gemert, D. (1997) "Anchoring stresses between concrete and carbon fibre reinforced laminates", *Non-Metallic (FRP) Reinforced Concrete Structures, Proc., 3rd Int. Symp.*, Oct., **1**, 271-278.
2. Chen, J.F. and Teng, J.G. (2001) "Anchorage strength models for FRP and steel plates bonded to concrete", *ASCE Jnl of Structural Engineering*, **127**(7), 784-791.
3. Chen, J.F. and Teng, J.G. (2003) "Shear capacity of FRP strengthened RC beams: FRP debonding", Construction and Building Materials, **17**(1), 27 – 41.
4. Chen, J.F., Yang, Z.J. and Holt, G.D. (2001) "FRP or Steel Plate-to-Concrete Bonded Joints: Effect of Test Methods on Experimental Bond Strength", *Steel & Composite Structures - an Int Jnl*, **1**(2), 231-244.
5. Hein, V.L. and Erdogan, F. (1971) "Stress singularities in a two-material wedge", *International Journal of Fracture Mechanics*, **7**(3), 317-330.
6. Maeda, T., Asano, Y., Sato, Y., Ueda, T. and Kakuta, Y. (1997) "A study on bond mechanism of carbon fiber sheet", *Non-Metallic (FRP) Reinforcement for Concrete Structures, Proc. 3rd Int. Symp.*, **1**, 279-285.
7. Miller, B. and nanni, A. (1999) "Bond between CFRP sheets and concrete", *Proc., ASCE 5th Materials Congress*, Cincinnati, OH, May 10-12, 240-247.
8. Neubauer, U. and Rostásy, F.S. (1997) "Design aspects of concrete structures strengthened with externally bonded CFRP plates", *Proc., 7th Int. Conf. on Structural Faults and Repairs*, ECS Publications, Edinburgh, **2**, 109-118.
9. Swamy, R.N., Jones, R. and Charif, A. (1986) "Shear adhesion properties of epoxy resin adhesives", *Proc., Int. Symp. on Adhesion between Polymers and Concrete*, Sept., 741-755.
10. Teng, J.G., Chen, J.F., Smith, S.T. and Lam, L. (2002a) "*FRP strengthened RC Structures*", John Wiley and Sons, Chichester.
11. Teng, J. G., Zhang, J. W. and Smith, S. T. (2002b) "Interfacial stresses in reinforce concrete beams bonded with a soffit plate: a finite element study", Construction and Building Materials, **16**(1), 1-14.
12. Teng, J.G., Smith, S.T., Yao, J. and Chen, J.F. (2003) "Intermediate Crack-Induced Debonding in RC Beams and Slabs", *Construction and Building Materials*, **17**(6-7), 447-462.
13. Yuan, H., Wu, Z., and Yoshizawa, H. (2001) "Theoretical solutions on interfacial stress transfer of externally bonded steel/composite laminates", *Journal of Structural Mechanics and Earthquake Engineering, JSCE*, 675/1-55, 27-29.

PERFORMANCE OF A FIBRE-REINFORCED POLYMER BRIDGE DECK UNDER DYNAMIC WHEEL LOADING

Albert F Daly and John R Cuninghame
TRL Limited

ABSTRACT

The paper describes the research carried out at TRL Limited on behalf of the UK Highways Agency to examine the performance of fibre-reinforced polymer (FRP) bridge decks under local wheel loading. The objective of the research was to produce a draft standard giving generic design requirements for technical approval of FRP deck systems. The project included the formulation of design guidelines for fatigue. A series of tests was carried out on a full-scale glass FRP bridge deck under static and dynamic wheel loading. The loads were imposed using the TRL Trafficking Test Facility, which replicates the effects of the wheel of a heavy goods vehicle. The deck was subjected to over 4.6 million cycles of a 4 tonne wheel load, equivalent to 30-40 years of service traffic. The paper includes a description of the FRP deck, the dynamic testing and a summary of the performance of the deck.

INTRODUCTION

Background

Most modern short span bridges have concrete decks. In general they are efficient and durable provided proper attention is paid to detailing and standard of workmanship. Concrete is likely to be the most common deck material for some considerable time. However, some concrete bridge decks have suffered corrosion, due in part to the increasing use of de-icing salts. As there is unlikely to be an economically viable replacement for rock salt for de-icing, increasing interest is being shown in materials that are corrosion resistant. In addition, rapid growth in the volume and weight of heavy goods vehicles (HGVs) has led to serious problems and many older bridges no longer meet current design standards. There is therefore, a need for methods of replacing bridge decks to deal with structural deterioration and to increase load capacity, without extensive and expensive bridge works.

Use of FRP in bridge decks

The use of Fibre Reinforced Polymer (FRP) as a primary structural material is developing rapidly in the construction industry. FRP materials have considerable advantages in terms of weight, strength and corrosion resistance, and they have been used for several decades in the aerospace and automobile industries. The 'product life cycle' is much longer in civil engineering so uptake has been relatively slow, but FRP is in use in a number of bridges around the world. As production technology develops and design standards and guidelines become more generally available, these FRP materials will be used more widely to provide cost-effective alternatives to steel and concrete. Potential applications for FRP decks are new design, replacement of under-strength decks in existing bridges, and the provision of temporary running surfaces.

In spite of the advantages, however, there is still a lack of information on the behaviour of FRP components in bridge applications. This has impeded the development of generally accepted guidelines for the design and application of bridge schemes. In response to this, the

UK Highways Agency commissioned TRL Limited to carry out research into the performance of FRP bridge decks with the objective of developing design guidelines.

Outline of research project

The project was to examine the use of FRP in new and replacement bridge decks and produce draft design requirements. A desk study of current research and practice in bridge construction and other FRP applications was carried out to address issues such as design and detailing requirements, resistance to environmental effects, repair and maintenance.

Existing loading rules can be used for FRP decks and global static design is relatively straightforward provided material properties are known. Some design guides are available, but there are currently no fatigue design standards for FRP bridge decks. Local dynamic stresses at details potentially at risk of fatigue due to wheel loading may be difficult to calculate. There are likely to be high stress gradients and the stress cycle may be tensile, compressive or alternating. As these stresses are raised to the power of 10 to obtain fatigue life, it is important that they be calculated with sufficient accuracy. This is similar to the situation for steel orthotropic bridge decks, which are currently beyond the scope of the UK bridge design code (British Standards Institution 1980).

Because of the development costs, it is likely that most FRP decks will be produced as modular systems. The deck system tested was thought to be typical in that it consisted of top and bottom flanges supported by webs running transverse to the direction of traffic flow. The limited number of bridge deck systems that have been developed so far, most notably in the US and Europe are of this form.

Therefore it was decided to carry out full scale tests to study the performance of FRP decks under local wheel loads and provide data on which to base generic fatigue requirements for technical approval of FRP deck systems.

TESTING PROGRAMME

Description of FRP bridge system

The design of the deck used in the dynamic testing was carried out by Maunsell Ltd, UK who developed an FRP bridge deck system consisting of standard glass FRP cellular 'planks' and connectors that can be assembled in a variety of configurations. The units have undercut grooves on the sides, which are used to connect them together using a rod with a 'dog bone' cross-section to provide mechanical interlock; the joints are also glued. This Advanced Composite Construction System (ACCS) has been used in the Linksleader footbridge at Aberfeldy in Scotland and a lifting bridge at Bonds Mill in Gloucestershire, England.

The ACCS deck was not designed to resist local wheel loading, so a new Roadway panel was designed and manufactured. This has a similar geometry to the lighter ACCS plank but with thicker sections to resist direct wheel loads. It was designed to be laid transversely on a sub-structure built up from ACCS planks. The Roadway panel is shown in Figure 1: further details of the design are given elsewhere[2].

Test specimen

A full-scale section of bridge deck was built at TRL. It spanned 4.0m, was 2.12m wide and had a total construction depth of 0.8m: see Figure 2. No surfacing was used (in practice, a thin anti-skid dressing would be sufficient). The deck was instrumented with electrical resistance strain gauges to determine the strain influence lines as the wheel moved along the deck. Displacement transducers were also fitted to measure deflection of the deck under load.

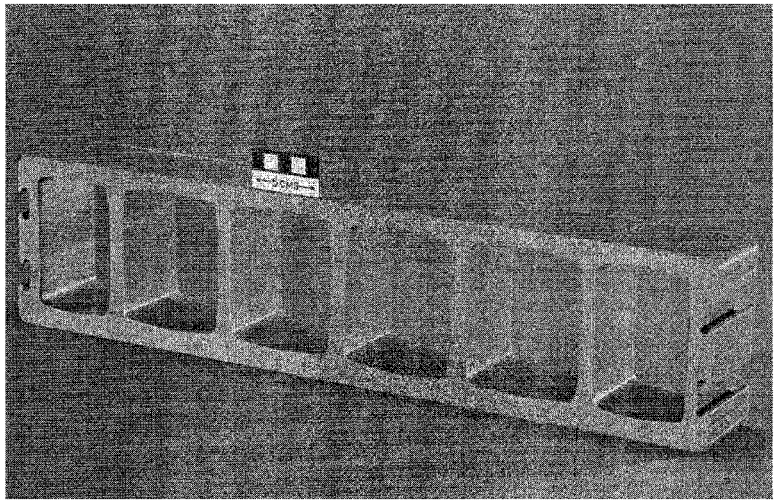


Figure 1 Roadway panel.

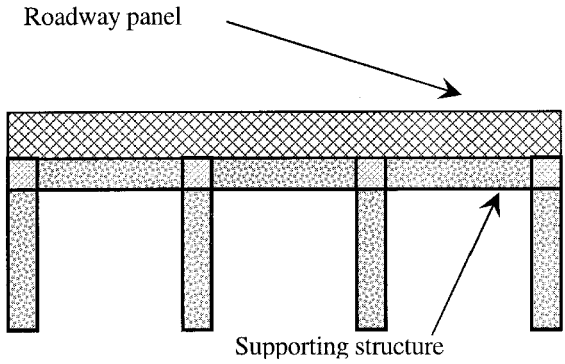


Figure 2 Section through FRP deck.

Test rig

Rolling wheel tests were carried out in the TRL Trafficking Test Facility (TTF). The main features of the TTF are shown in the photograph in Figure 3. It is similar to a conventional pavement test machine, but is smaller and much cheaper to operate. A wheel, either single, twin or 'super-single', rolls along a 3m long track. The wheel load may be up to 5 tonnes and the load may be applied during both forward and reverse passes, or on the forward pass only. The wheel reaches a maximum speed of 20kph and can complete one pass per second (bi-directional), equivalent to 80,000 per day. The wheel, carriage and drive mechanism are set up as a spring-mass system operating at its resonant frequency. This greatly reduces the energy required and hence the cost, of running the rig.

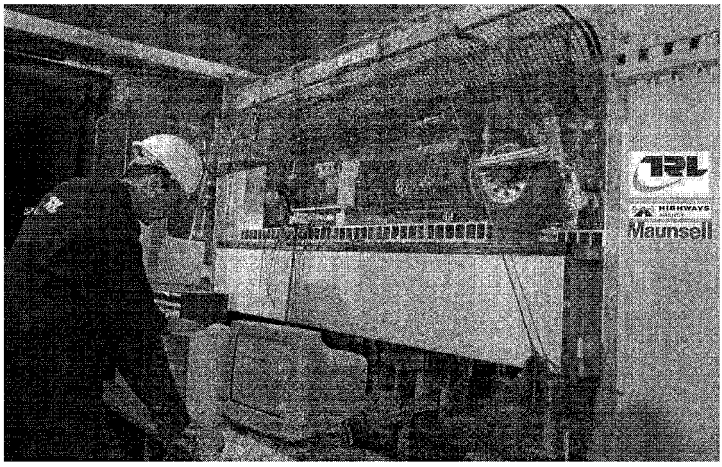


Figure 3 FRP deck in test rig.

Test methodology

Initial static tests were carried out to determine the strain levels in the running surface and to select an appropriate load for the dynamic test. Each series of tests consisted of placing the wheel at various positions on the deck and recording the strains. Transverse and longitudinal influence lines for strain could then be plotted and used to determine the load to be used in the test.

Once the test load level was determined, the dynamic test was started, with the logging system set up to record maximum and minimum values of each gauge output every 10 or so cycles. At various rig cycle counts, a full sweep of strain and deflection was captured and retained to illustrate the behaviour of the deck panel through one loading cycle.

Figure 4 shows a typical influence line, giving the strain at the junction between the web and top flange of the roadway panel as the wheel traversed the deck (see insert in figure). This was one of the locations indicated by analysis to be subject to high stress range due to traffic loading. The strain shown is in the direction of the traffic movement (i.e. longitudinally in the deck, transversely along the Roadway panel). A strain range of 1000 microstrain (tension) to -1290 microstrain (compression) was recorded. This was the highest range of strain recorded in the deck. The influence lines exhibited the expected strain reversal as the wheel rolled over the webs.

Another critical point for fatigue was thought to be in the top flange, mid-way between two webs. Figure 5 shows the influence line for longitudinal strain on the top surface of the second cell of the Roadway panel. Here, the peak strain recorded was -1090 microstrain (compression).

Figure 6 shows the influence line for the strain as the transverse position of the wheel is changed. Again, the strain shown is in the direction of the traffic movement. Two plots are shown, for the maximum and minimum strain as the wheel swept from one end of the deck to the other. The strains recorded for this gauge ranged from 270 (tension) to -950 microstrain (compression).

Influence lines were also recorded for deflection of the deck to indicate the global performance. The maximum deflection was just under 1mm.

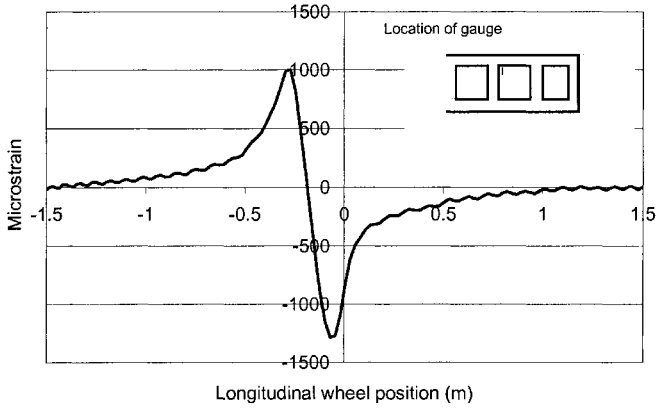


Figure 4 Influence line for strain at top of web.

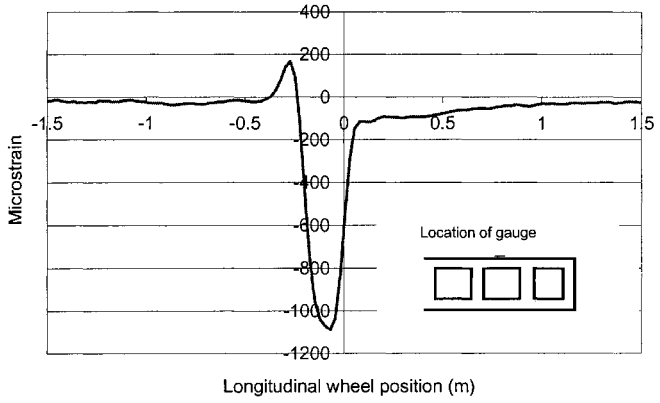


Figure 5 Influence line for strain in top flange.

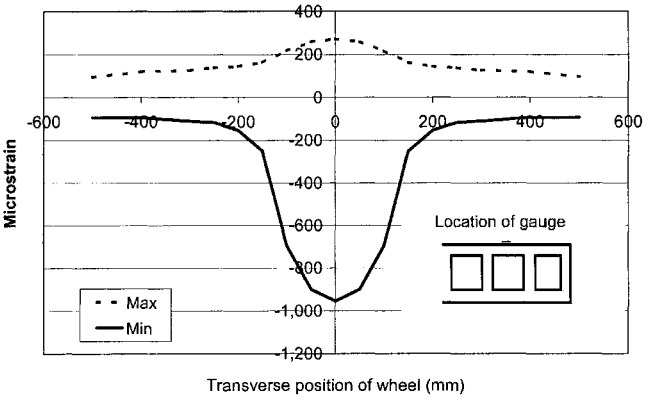


Figure 6 Transverse influence line for strain in top flange.

Once the test load level was determined, the dynamic test was started, with the logging system set up to record maximum and minimum values of each gauge output every 10 or so cycles. At various rig cycle counts, data were recorded continuously to provide influence lines for strain and deflection to monitor any change in behaviour.

TEST RESULTS

General performance of the deck

The dynamic test was continued for as long as possible, within the constraints of the project time-scale. In all, the deck sustained about 4.6 million load cycles.

At various times, the test was stopped and close visual examination of the surface was carried out. Fibre-scope examination of the gauged area inside the Roadway panels did not indicate any damage. Subsequent examination of the surface (including sections and cores taken through the running surface) indicated that there was no visible deterioration and it was concluded that if this was a real structure there would be no cause for concern.

A 500mm section of the Roadway panel, taken from along the line of the wheel loading, was subsequently tested statically to failure. Comparison with a similar test on a not-previously-loaded section indicated no different in strength. This confirmed the above conclusion, that the Roadway panel provided a robust structure capable of sustaining HGV traffic.

Damage in the sub-structure

The only visible damage in the deck was in the substructure. After 247,400 load cycles, damage was noticed adjacent to one of the bearings. This consisted of cracks in the first and second webs of the ACCS plank and debonding of the hard-wood insert (used to prevent local distortion and buckling of the section at the bearing): see Figure 7. At 256,000 load cycles, some debonding was noted in six of the eight supports, although cracks were only apparent at one support. The dynamic movement across these cracks was as 1.1mm.

At load cycle 247,400, it was noted that some of the FRP angles holding the end diaphragms in place had become debonded from the ACCS webs, with relative movement of about 0.07mm occurring. At the completion of the test, two other angles had also become detached.

The only other significant damage was in the glued joint between the ACCS webs and the top flange. This was first noticed because the two surfaces were grinding together and the adhesive was being ground into a fine white powder. Figure 8 shows the joint (viewed from under the deck) at the conclusion of the test. The relative movement at this joint was about 0.5mm.

FURTHER TESTING

The strain data generated by the rolling wheel tests will be used to design a test that can be carried out in a conventional servo-hydraulic testing machine. A short length (500mm) of Roadway panel will be loaded via two steel backed rubber pads loaded alternately to simulate a wheel passing over the panel. Strain gauges installed at the same locations as in the rolling wheel test will be used to set up the loading to give the correct stress distribution. Tests can then be carried out at up to 5Hz, to long endurances, and at several stress ranges to obtain points on an S-N curve, or to provide evidence that fatigue damage will not occur under design traffic loading. The options for testing are discussed in the next section.

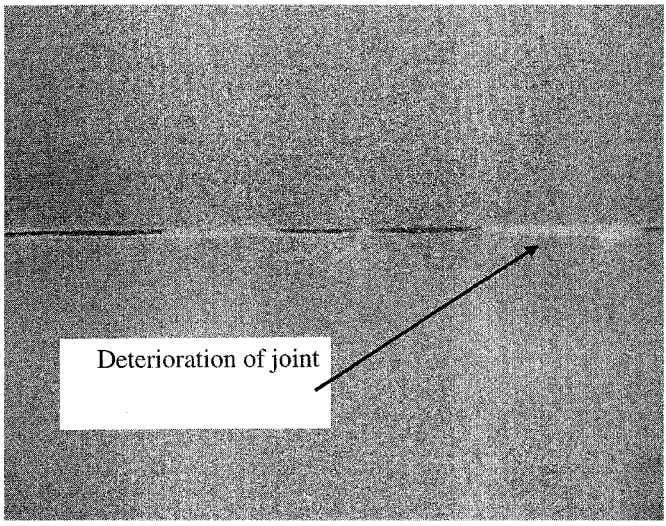


Figure 7 Cracking at support in FRP deck.

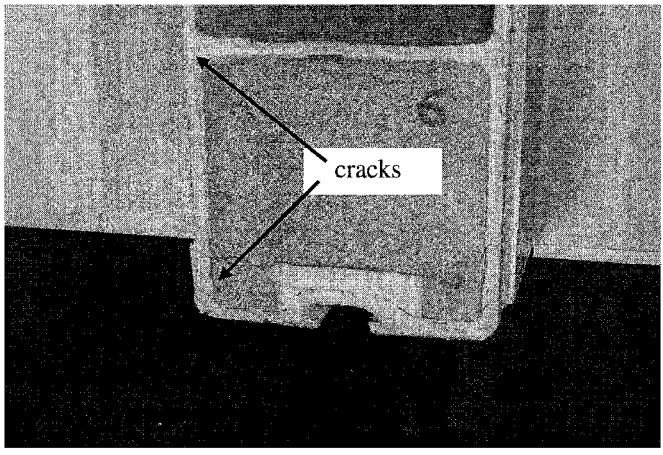


Figure 8 Deterioration of joint in sub-structure.

FATIGUE DUE TO WHEEL LOADING

The rolling wheel tests were carried out to study the behaviour of the FRP deck, to develop a method by which a client could ensure that an FRP deck proposed for use on a UK highway bridge would have an adequate fatigue life. Fatigue damage may be divided into:

- 'Global' damage: for example, the cracking that occurred in the test, adjacent to the bearings. The relevant loading is the total due to vehicles on the span.
- 'Local' damage: where the cyclic stresses are due to individual wheel loads and cracking occurs under, or close to, the wheel tracks. 'Local' cracking is the most common form in lightweight steel decks and it is necessary to ensure that similar cracking does not arise in FRP decks.

It is assumed that FRP decks will consist of components designed and developed by specialists. These components can then be used by non-FRP-specialist bridge designers and the cost of designing and developing the FRP components will be spread over a number of bridges. The use of FRP components in this way is analogous to the use of steel components, e.g. Universal Steel Beams, except that steel components are supported by product standards and are supplied with certified properties. In the absence of product standards for FRP components, it is proposed to base fatigue requirements on testing, at least as an interim measure.

It was recognised that fatigue is only one aspect of the development of an FRP deck and the fatigue strength of FRP materials in general is said to be high compared to welded joints in steel. Therefore, the fatigue requirements should not be so onerous as to form a disproportionate part of the total development costs. The rolling wheel tests have the advantage that all parts of the deck, including joints between components, are automatically included in the test, but the rate of testing is low (1Hz) and the load is limited by the rating of the tyre and the capacity of the rig. It is proposed to base the fatigue requirements for the parts of the deck affected by local wheel loading on a test in which a standard fatigue test machine can be used to simulate the effect of a single wheel.

Traffic loading is the same for any type of deck, so the fatigue design loading in the UK bridge design code (British Standards Institution, 1980) can be used. Maximum axle loads for normal traffic are 60kN for steering axles (30kN per single wheel) and 100kN for rear axles (50kN per twin wheel – 'super-singles' are not included in the code).

On an individual bridge, the number of HGVs and the mix of vehicle types may be different from those in the design code. For example, where an existing concrete deck is to be replaced by an FRP deck, the design loading may be based on a traffic survey. It is envisaged that the specialist FRP designer, or component supplier, should provide fatigue data so that the bridge designer can check that the deck is adequate for the traffic loading on a particular bridge.

Figures 4, 5 and 6 show that the influence lines for potential crack locations in the Roadway panel are short, so a test that simulates the effect of an individual wheel is sufficient. There are two options for the testing regime as described in the following sections.

Assessment without damage summation

All stress cycles due to wheel loads should be below the damage threshold (infinite life).

The most common existing method of fatigue design is simply to limit all dynamic stresses to a value at which damage will not occur. As there are other reasons to limit stress, e.g. to prevent excessive deflection, this approach may not be as over-conservative as it sounds.

To specify a laboratory test to demonstrate that all stresses are below the threshold for fatigue damage, it is necessary to know the number of cycles which corresponds to the constant amplitude fatigue limit. The test would consist of applying the heaviest wheel at the 'worst case' location on the component for that number of cycles. It would be necessary to determine the worst case position of the load, but full influence lines would not be needed.

It seems to be accepted that FRP materials do exhibit a fatigue limit, but the corresponding endurance does not appear to be well defined (very few tests have been continued beyond 10^7 cycles). This problem could be avoided by applying the same number of cycles as the number of wheels passing over the component on a bridge, but this would require between 171 and 685 million cycles depending on the type of road for the normal UK design life of 120 years. Even for a reduced design life of 40 years, the cost of such a test would be too high. It is proposed that the required endurance should be 10^7 cycles.

The test load would be applied through a steel-backed rubber pad 200mm square, to represent a single wheel contact patch. The magnitude of the load would be 30kN multiplied by a partial factor to be defined when the current project is completed. For most details a single loading pad would be sufficient, but where the influence line changes sign (as in the web to

top flange detail), two pads loading alternately would be required to reproduce the correct stress ratio. Alternatively, a factor might be applied to allow for the stress ratio.

A further simplification is proposed, i.e. that the criterion of failure be the static strength of the component at the end of the fatigue test. Fatigue damage may be sub-surface, or in locations where visual inspection is difficult. More sophisticated NDE would add significantly to the cost of the test. Therefore, the component would be tested statically to failure at the end of the fatigue test and the result compared with a similar test on a component that had not been subjected to fatigue loading. The component would be acceptable provided its static load capacity after fatigue testing was within (say) 30% of its 'as-new' capacity. This meets the bridge owner's requirement that the bridge should be capable of carrying the applied loads throughout its life.

Damage summation method

Some damage may occur but the estimated life is greater than the specified design life.

This option requires a method of estimating the total fatigue damage due to all the various wheel loads in the design traffic spectrum. Of the methods currently available, the Palmgren-Miner cumulative damage rule is proposed, as it is relatively simple and already familiar to bridge designers (but there is some doubt whether it is accurate for alternating stresses).

The procedure given in the UK Bridge Design Code, BS 5400 Part 10[1] can be used. The data required to estimate fatigue life is:

- The design traffic loading.
- The relationship between wheel load and stress, i.e. single wheel influence lines.
- A design S-N curve for the detail being assessed.

It is assumed that the assessment will be carried out in terms of stress (or strain) at the crack location. Single wheel influence lines would be calculated or measured for each detail, then the design traffic applied to derive stress spectra.

Design S-N curves exist for steel details which may be at risk of fatigue, following decades of research and testing. No such database of results exists for FRP components. In addition, stress ratio can be ignored when assessing welded steel details (and there is a simple method for non-welded details). For FRPs on the other hand, stress ratio is a significant variable, so has to be reproduced in the tests.

Around six fatigue tests would be required to define an S-N curve for each of the 'at-risk' details (though it may be possible to cover more than one detail with each test, for example producing 'lower bound' curves for details which did not fail). Joints between FRP components would need to be included in the assessment. Once the influence line and S-N data are available, it is a relatively simple matter to estimate the fatigue life for any given traffic loading.

It remains to be seen whether the amount of testing necessary to define a design S-N curve can be justified. A possible compromise option might be to carry out sufficient fatigue testing to define a fatigue limit, e.g. stress at 10^7 cycles, then to assume a design S-N curve based on this value.

Rolling wheel test equivalent life

It is of interest to know the equivalent service life simulated by the rolling wheel test in the TTF rig. The traffic loading in BS 5400 Part 10 was used with two million HGVs per year (the value for a UK motorway). In the absence of a design S-N curve for the Roadway panel, the conservative assumption was made that the fatigue life of the most highly stressed detail on the panel (the top of the web) was about to fail at 4.6 million cycles. This provided one point on a notional S-N curve.

The S-N equation for FRP materials may be expressed by an empirical equation, for example:

$$\sigma_{max}/\sigma_u = 1 - k.\log(N_L)$$

where: σ_{max} is the maximum stress in a cycle
σ_u is the ultimate stress
k is an experimental factor (assumed 0.1)
and N_L is the number of cycles to failure.

The load applied by the rolling wheel (37kN) was around 10% of the ultimate capacity of the panel, so the applied stress was 10% of ultimate. Clearly the test was in the low stress–high cycle region of the S-N curve. It is not known whether the above equation is applicable at endurances greater than 10^7. Its form suggests that all cycles are damaging in proportion to the applied stress. This does not take account of the fact that stresses below the constant amplitude cut-off are not damaging until later in the life of the detail. To avoid this difficulty, it was decided to use an S-N equation of the form:

$$S^m \times N = k$$

where: S is the maximum stress in a cycle.
M is the inverse slope of the S-N line (assumed to be 10 for FRP).
N is the number of cycles to failure.
and k is a constant.

At high stress and low cycles the S-N curves produced by the two equations are similar, but the latter is less severe at high endurances. The constant in the equation which passes through the test point is $k = 4.66 \times 10^{40}$. Applying this equation, along with the influence lines, gives an estimated life for the Roadway panel of 39 years.

CONCLUSIONS

The dynamic testing of an FRP deck has shown that FRP components can provide a robust bridge solution complying with the general requirements of the UK design code and, in particular, are capable of resisting local wheel loads due to heavy vehicles for at least 30-40 years, without major damage. However, careful attention is needed to prevent local damage in highly stressed regions such as web to flange connections and close to bearing supports.

A procedure for fatigue design and a testing procedure are being devised for incorporation into a Highways Agency Standard for FRP decks. It is considered important to minimise the testing requirement so as to encourage development of FRP bridge decks. The results so far suggest that a simple test simulating a single wheel load may be sufficient.

A simple fatigue design method, not requiring a damage summation appears possible, based on demonstrating that fatigue damage will not occur under design traffic loading.

REFERENCES

1. British Standards Institution (1980). BS 5400: Part 10: 1980. Steel, concrete and composite bridges. *Code of practice for fatigue*, British Standards Institution, London, UK, 1980.

2. A F Daly and W A Duckett. The design and testing of an FRP highway bridge deck. *Journal of Research*, Volume 5, No 3, Transport Research Laboratory, Crowthorne, UK, 2002.

GLOBAL BUCKLING OF FRP PULTRUDED THIN-WALLED MEMBERS UNDER AXIAL COMPRESSION

L. De Lorenzis and A. La Tegola
Department of Innovation Engineering – University of Lecce, Italy

ABSTRACT

Fiber-reinforced polymer (FRP) pultruded profiles are increasingly used in the construction industry as primary and secondary load-bearing members, because of their good corrosion behavior, low weight, and high mechanical properties. In this paper, the effect of the actual distribution of the applied compressive stresses on the flexural-torsional buckling load of FRP structural members is analyzed. The static behavior is described by means of the exact theory of thin-walled isotropic beams, developed by Capurso in 1964 and generalized by the authors to transversely isotropic materials. A numerical example is presented for the I-section, showing that the critical load of FRP pultruded profiles may be sensitive to the uniformity of application of the load and hence predictions based on St. Venant's principle may result unsafe.

INTRODUCTION

Structural members made of fiber-reinforced polymer (FRP) pultruded profiles are becoming more and more popular in the construction industry, because of their low weight, high mechanical properties and good corrosion behavior. Due to the low thickness, design of FRP pultruded members is often governed by buckling.

In 1964, Capurso developed the exact theory of thin-walled isotropic beams, in which he removed the limitations related to St. Venant's principle. By means of this theory, the state of stress generated by arbitrary loads acting on the beam can be computed. In a previous work (De Lorenzis and La Tegola, 2003), the authors generalized Capurso's theory to transversely isotropic materials, with particular reference to FRP pultruded profiles. It was shown that, within the range of mechanical properties of common FRPs, the discrepancy between exact and Vlasov formulations may be significantly larger than for isotropic materials. Hence, Vlasov theory may lead to significantly inaccurate predictions of the state of stress.

In this paper, the exact theory of thin-walled beams is used as a basis for the global buckling analysis of thin-walled structural members under axial compression. The influence on the global buckling load of the actual distribution of the axial compressive stresses applied on the two faces of the element is investigated. The analysis is conducted with the energetic approach at first-order level, hence the effect of imperfections and of coupled instability is not taken into account. A numerical example for the I cross-section is presented showing the influence on results of the theory used for describing the static behavior and of transverse isotropy as opposed to isotropy.

GLOBAL BUCKLING ANALYSIS

Given a profile with constant thickness t and generic cross-section with continuous directrix, the coordinate system will have origin in the center of gravity, x and y axis coinciding with the principal axes of inertia of the cross-section and z axis orthogonal to them (Figure 1). Another coordinate system will be (n,s,z), with s curvilinear abscissa

along the directrix of the cylindrical surface and n normal to the surface. Let $u=u(x,y,z)$, $v=v(x,y,z)$ and $w=w(x,y,z)$ be the displacement components of the generic point P in the fixed coordinate system (x,y,z), and $\xi=\xi(n,s,z)$, $\eta=\eta(n,s,z)$ and $\zeta=\zeta(n,s,z)$ its displacement components in the mobile coordinate system (n,s,z).

Assuming that the profile is loaded by two distributions of longitudinal pressures $p_{0z}(s)$ and $p_{lz}(s)$ on the two extreme bases $z=0$ and $z=l$, both equivalent to a normal force and satisfying global equilibrium, the objective of the analysis is to determine the effect of these punctual distributions on the flexural-torsional buckling load. The buckling load will be computed by using the energetic approach based on Dirichlet principle. The second variation of the total potential energy can be expressed as follows (Krall, 1968):

$$\Phi = W + \left(L_2^* - L_2\right) \tag{1}$$

where W is the elastic strain energy corresponding to the transition from the primary configuration C_0 (thought of as undeformed) to the secondary configuration C defined by the displacement components u, v, w. L^*_2 is the second-order work done by the internal stresses present in C_0 for the second-order components of strains:

$$L_2^* = \int_V \varepsilon_{ij}^{(2)} \sigma_{ij} dV \tag{2}$$

whereas L_2 is the second-order work made by the external loads and is equal to zero in absence of hydrostatic loads (Krall, 1968).

ELASTIC STRAIN ENERGY AND SECOND-ORDER STRAINS

The deformed configuration C will be defined assuming transverserly rigid cross-section (global buckling) and zero shear strain at the midplane of the profile. Hence, if $u_0=u_0(z)$, $v_0=v_0(z)$ and $\varphi_0=\varphi_0(z)$ are the x and y displacement components of the shear center and the rotation of the cross-section about it, the following relationships hold:

$$u(x,y,z) = u_0(z) - \varphi_0(z)(y - y_0) \qquad v(x,y,z) = v_0(z) + \varphi_0(z)(x - x_0) \tag{3a,b}$$

$$w(s,z) = -u_0'(z)x(s) - v_0'(z)y(s) - \varphi_0'(z)\omega_z(s) \tag{3c}$$

where x_0 and y_0 are the coordinates of the shear center in the cross-sectional plane (Figure 2), $\omega_z(s)$ is the warping function of the cross-section, and the "'" symbol denotes derivation with respect to z.

W can be easily expressed as follows in terms of u_0, v_0 and φ_0:

$$W = \frac{1}{2}\int_0^l \left[E_z I_y u_0''^2 + E_z I_x v_0''^2 + Z J_t \varphi_0'^2 - E_z C_w \varphi_0''' \varphi_0' \right] dz \tag{4}$$

where E_z is the elastic modulus in the fiber (z) direction, Z is the shear modulus in planes parallel to the z axis, I_x and I_y are the moments of inertia about x and y, J_t and C_w are the torsion constant and the warping constant of the cross-section, respectively.

The second order components of strains are as follows:

$$\varepsilon_z^{(2)} = \frac{1}{2}\left[\left(\frac{\partial u}{\partial z}\right)^2 + \left(\frac{\partial v}{\partial z}\right)^2\right]; \quad \gamma_{zs}^{(2)} = \frac{\partial \xi}{\partial z}\frac{\partial \xi}{\partial s} - \frac{\partial \zeta}{\partial z}\frac{\partial \eta}{\partial z} - \frac{\partial \zeta}{\partial s}\frac{\partial \eta}{\partial s} \tag{5a,b}$$

If the following positions are made:

$$r = (x - x_0)\frac{dy}{ds} - (y - y_0)\frac{dx}{ds}; \quad p = (x - x_0)\frac{dx}{ds} + (y - y_0)\frac{dy}{ds} \tag{6a,b}$$

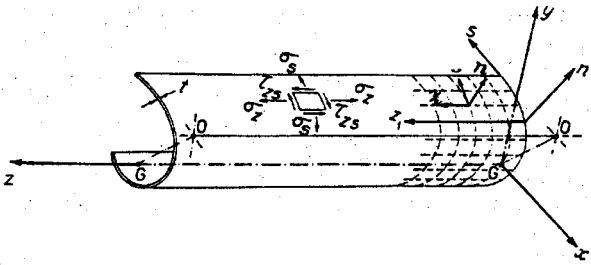
the displacement components in the mobile coordinate system can be expressed as follows:

$$\xi = u_0\frac{dy}{ds} - v_0\frac{dx}{ds} - \varphi_0 p; \quad \eta = u_0\frac{dx}{ds} + v_0\frac{dy}{ds} + \varphi_0 r; \quad \zeta = w \tag{7a-c}$$

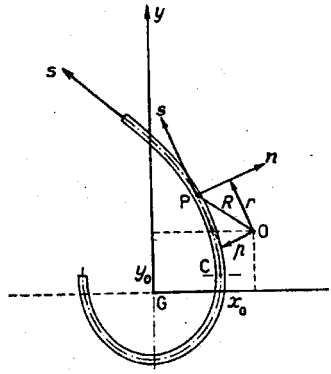
Hence, Eqs. (5) can be easily expressed as a function of u_0, v_0 and φ_0 through eqs. (3) and (7).

STATIC REGIME IN THE PRIMARY CONFIGURATION AND SECOND-ORDER WORK

Capurso's theory is based on a kinematic model where the profile cross-section is considered transversely rigid, but the assumption of zero shear strain at the midplane of the profile is removed. The displacements of any point of the profile are then completely described by the four functions $u_0 = u_0(z)$; $v_0 = v_0(z)$; $\varphi_0 = \varphi_0(z)$; $w = w(s,z)$.



1. Coordinate systems and stress components (from Capurso, 1964a)



2. Cross-section of the profile (from Capurso, 1964a)

By using constitutive relationships and equilibrium conditions, the problem is reduced to a single integro-differential equation with partial derivatives in the unknown function *w(s,z)*, whose solution can take the form of a series of eigenfunctions:

$$w(z,s) = \sum_{n=1}^{\infty} \varphi_n(z)\Phi_n(s) \tag{8}$$

where $\Phi_n(s)$ is the eigenfunction associated to the nth eigenvalue β_n, and φ_n is the corresponding function of *z*. The eigenfunctions $\Phi_n(s)$ are a closed and complete system of orthogonal functions. Since also 1, *x(s)* and *y(s)* are eigenfunctions, corresponding to the zero eigenvalue, it is:

$$\int_A \Phi_n dA = 0; \quad \int_A \Phi_n x dA = 0; \quad \int_A \Phi_n y dA = 0 \tag{9a-c}$$

for every Φ_n corresponding to the non-zero eigenvalues. Computation of the β_n and of the corresponding $\Phi_n(s)$ involves only the cross-sectional geometry of the profile and not the material properties, unlike that of functions φ_n(z) (Capurso, 1964b).

The problem of the determination of stresses and strains for a thin-walled beam loaded only by two systems of longitudinal pressures on the extreme bases, $p_{0z}(s)$ and $p_{lz}(s)$, can be studied by superposition of infinite simple cases: three cases coinciding with the "classical" normal force and bending moments (about *x* and *y*), and infinite cases of "warping moment" according to the respective Φ_n. In fact, any given distribution $p_{0z}(s)$ and $p_{lz}(s)$ can be expressed as:

$$p_{0z}(s) = -\frac{N_z}{A} - \frac{M_x}{I_x}y(s) + \frac{M_y}{I_y}x(s) - \sum_n \frac{M_{on}}{I_n}\Phi_n(s);$$

$$p_{lz}(s) = \frac{N_z}{A} + \frac{M_x}{I_x}y(s) - \frac{M_y}{I_y}x(s) + \sum_n \frac{M_{ln}}{I_n}\Phi_n(s) \tag{10a,b}$$

where N_z, M_x and M_y are the "classical" normal force and bending moments resulting from the distributions $p_{0z}(s)$ and $p_{lz}(s)$ and uniform along z;

$$M_{0n} = -\int_A p_{0z}\Phi_n dA \quad \text{and} \quad M_{ln} = \int_A p_{lz}\Phi_n dA \tag{11a,b}$$

are the nth warping moments applied on the two bases $z=0$ and $z=l$, respectively, A is the cross-sectional area, and $I_n = \int_A \Phi_n^2 dA$.

Since this paper focuses on elements under axial compression, it will be assumed that $M_x=M_y=0$. In the simple case corresponding to the application of the constant term, the only non-zero internal force is the normal force, and stresses are:

$$\sigma_z = \frac{N_z}{A} \qquad \tau_{zs} = 0 \tag{12a,b}$$

The simple case corresponding to the nth warping moment according to Φ_n occurs upon application on the two extreme bases of two pressure distributions proportional to $\Phi_n(s)$:

$$p_{lz} = \frac{M_{ln}}{I_n}\Phi_n; \quad p_{0z} = -\frac{M_{0n}}{I_n}\Phi_n \tag{13a,b}$$

These distributions have zero resultant and zero moment resultant, as follows from eq.s (9). For this reason, M_{on} and M_{ln} can assume different values while keeping global equilibrium. In this case the only non-zero internal force is the warping moment M_n, which can be obtained from:

$$M_n(z) = M_{ln}\frac{\sinh\alpha_n z}{\sinh\alpha_n l} + M_{0n}\frac{\sinh\alpha_n(l-z)}{\sinh\alpha_n l} \tag{14}$$

where α_n is related to the eigenvalue β_n associated to the function $\Phi_n(s)$ as follows:

$$\alpha_n = \beta_n\sqrt{\frac{Z}{E}(\bar{n}-\mu^2)} \tag{15}$$

whereas the stresses are:

$$\sigma_z = \frac{M_n}{I_n}\Phi_n(s); \qquad \tau_{zs} = -\frac{1}{I_n}\frac{dM_n}{dz}\frac{d\omega_n}{ds} \quad \text{with} \quad \frac{d\omega_n}{ds} = -\frac{1}{\beta_n^2}L(\Phi_n) \tag{16a,b}$$

and L is a linear operator.

In eq. (15), E is the elastic modulus in the plane of isotropy (x-y), μ is the Poisson coefficient giving strain in the n-s plane due to a uniaxial stress along z, $\bar{n}$ is the ratio between E and E_z, and Z is the shear modulus in planes parallel to the z axis. Eq. (14) indicates that the internal warping moment $M_n(z)$, consequent from the application of two external warping moments M_{0n} e M_{ln} on the extreme bases, assumes on these bases values equal to the external actions, but then decreases with quasi-exponential trend going from the bases towards the internal of the beam. This decrease is more gradual for low values of α_n and hence for low values of the eigenvalue β_n associated to the eigenfunction $\Phi_n(s)$. Since the eigenvalues were given increasing order, the warping moments with deeper penetration will be those corresponding to the first non-zero eigenvalues. Furthermore, eq. (15) shows immediately that α_n decreases as Z/E and (n-μ^2) decrease.

Finally, the second-order work is as follows

$$L_2^* = t\int_s\int_0^l\left(\sigma_z\varepsilon_z^{(2)} + \tau_{zs}\gamma_{zs}^{(2)}\right)ds\,dz \tag{17}$$

where:

$$\sigma_z = \frac{N_z}{A} + \sum_n\frac{M_n}{I_n}\Phi_n(s); \quad \tau_{zs} = -\sum_n\frac{1}{I_n}\frac{dM_n}{dz}\frac{d\omega_n}{ds} \tag{18a,b}$$

RALEIGH-RITZ METHOD

The determination of the critical load can be accomplished in an approximate way by using Raleigh-Ritz method. For instance, in the case of a beam of length l with flexural and torsional simple supports at both ends:

$$u_0 = \sum_m A_{1m} \sin\frac{m\pi z}{l}; \quad v_0 = \sum_m A_{2m} \sin\frac{m\pi z}{l}; \quad \varphi_0 = \sum_m A_{3m} \sin\frac{m\pi z}{l} \tag{19a-c}$$

For simplicity, in the following the series development will be substituted with its generic (m^{th}) term:

$$u_0 = A_1 \sin\frac{m\pi z}{l}; \qquad v_0 = A_2 \sin\frac{m\pi z}{l}; \qquad \varphi_0 = A_3 \sin\frac{m\pi z}{l} \tag{20a-c}$$

With positions (20), the elastic strain energy can be expressed as follows:

$$W = \frac{l}{4}\left(\frac{m\pi}{l}\right)^2 \left[E_z I_y \left(\frac{m\pi}{l}\right)^2 A_1^2 + E_z I_x \left(\frac{m\pi}{l}\right)^2 A_2^2 + ZJ_t A_3^2 + E_z C_w \left(\frac{m\pi}{l}\right)^2 A_3^2\right] \tag{21}$$

and the second-order work results:

$$L_2^* = \frac{l}{4} N_z \left(\frac{m\pi}{l}\right)^2 \left[A_1^2 + A_2^2 + A_3^2\left(x_0^2 + y_0^2 + \rho_x^2 + \rho_y^2\right) + 2A_3\left(A_1 y_0 - A_2 x_0\right)\right] +$$

$$+ \sum_n k_n \left(M_{\ln} + M_{0n}\right) \cdot \frac{\left(\frac{m\pi}{l}\right)^2}{\alpha_n^2 + 4\left(\frac{m\pi}{l}\right)^2} \cdot t \cdot \left[\frac{\alpha_n^2 + 2\left(\frac{m\pi}{l}\right)^2}{2\alpha_n^2} A_3^2 \cdot I_{s\Phi n} + I_{sn}\right] \text{ where} \tag{22}$$

$$k_n = \frac{\alpha_n}{I_n}\frac{\cosh\alpha_n l - 1}{\sinh\alpha_n l} \qquad I_{s\Phi n} = \int_s \Phi_n(s)\left(x^2 + y^2\right)ds \tag{23a,b}$$

$$I_{sn} = -\left(\frac{m\pi}{l}\right)^2 I_{s11n} A_1^2 - \left(\frac{m\pi}{l}\right)^2 I_{s22n} A_2^2 + I_{s33n} A_3^2 - \left(\frac{m\pi}{l}\right)^2 I_{s12n} A_1 A_2 - \left[I'_{s13n} + \left(\frac{m\pi}{l}\right)^2 I''_{s13n}\right] A_1 A_3 +$$

$$+ \left[I'_{s23n} - \left(\frac{m\pi}{l}\right)^2 I''_{s23n}\right] A_2 A_3 \tag{24a}$$

$$I_{s11n} = \int_s \frac{d\omega_n}{ds} x \frac{dx}{ds} ds; \quad I_{s22n} = \int_s \frac{d\omega_n}{ds} y \frac{dy}{ds} ds; \tag{24b,c}$$

$$I_{s33n} = \int_s \frac{d\omega_n}{ds} p ds; \; I_{s12n} = \int_s \frac{d\omega_n}{ds}\left(x\frac{dy}{ds} + y\frac{dx}{ds}\right)ds \tag{24d,e}$$

$$I'_{s13n} = \int_s \frac{d\omega_n}{ds}\frac{dy}{ds} ds; \; I''_{s13n} = \int_s \frac{d\omega_n}{ds}\left(x \cdot r + \omega_z \frac{dx}{ds}\right)ds; \; I'_{s23n} = \int_s \frac{d\omega_n}{ds}\frac{dx}{ds} ds; \tag{24f-h}$$

$$I''_{s23n} = \int_s \frac{d\omega_n}{ds}\left(y \cdot r + \omega_z \frac{dy}{ds}\right)ds \tag{24i}$$

The conditions:

$$\frac{\partial\Phi}{\partial A_1} = \frac{\partial\Phi}{\partial A_2} = \frac{\partial\Phi}{\partial A_3} = 0 \tag{25}$$

give a system of linear and homogeneous equations in the unknowns A_1, A_2 and A_3. Equating to zero the determinant of the system results in a third-order equation for the critical load. Assuming for simplicity that the cross-section is doubly symmetric (x_0=y_0=0), and that M_{on} and M_{ln} vary proportionally to N_z:

$$M_{0n} = k_{0n} N_z ; \qquad M_{ln} = k_{ln} N_z \tag{26a,b}$$

the matrix of coefficients of the system has the following terms:

$$a_{11} = E_z I_y \left(\frac{m\pi}{l}\right)^2 + N_z \left\{ 1 - \sum_n \frac{4t}{l} k_n \frac{\left(\frac{m\pi}{l}\right)^2}{\alpha_n^2 + 4\left(\frac{m\pi}{l}\right)^2} I_{s11n} (k_{ln} + k_{on}) \right\} \tag{27a}$$

$$a_{22} = E_z I_x \left(\frac{m\pi}{l}\right)^2 + N_z \left\{ 1 - \sum_n \frac{4t}{l} k_n \frac{\left(\frac{m\pi}{l}\right)^2}{\alpha_n^2 + 4\left(\frac{m\pi}{l}\right)^2} I_{s22n} (k_{ln} + k_{on}) \right\} \tag{27b}$$

$$a_{33} = Z I_t + E_z C_w \left(\frac{m\pi}{l}\right)^2 + N_z \left\{ (\rho_x^2 + \rho_y^2) + \sum_n \frac{2t}{l} k_n \frac{(k_{ln} + k_{on})}{\alpha_n^2 + 4\left(\frac{m\pi}{l}\right)^2} \left[\frac{\alpha_n^2 + 2\left(\frac{m\pi}{l}\right)^2}{\alpha_n^2} \int_s \Phi_n (x^2 + y^2) ds + 2 I_{s33} \right] \right\}$$

$$a_{12} = a_{21} = -N_z \sum_n \frac{2t}{l} k_n \frac{\left(\frac{m\pi}{l}\right)^2}{\alpha_n^2 + 4\left(\frac{m\pi}{l}\right)^2} I_{s12n} (k_{ln} + k_{on}) \tag{27c,d}$$

$$a_{13} = a_{31} = -N_z \sum_n \frac{2t}{l} k_n \frac{I'_{s13n} + \left(\frac{m\pi}{l}\right)^2 I''_{s13n}}{\alpha_n^2 + 4\left(\frac{m\pi}{l}\right)^2} (k_{ln} + k_{on}) \tag{27e}$$

$$a_{23} = a_{32} = N_z \sum_n \frac{2t}{l} k_n \frac{I'_{s23n} - \left(\frac{m\pi}{l}\right)^2 I''_{s23n}}{\alpha_n^2 + 4\left(\frac{m\pi}{l}\right)^2} (k_{ln} + k_{on}) \tag{27f}$$

If $k_{ln}=k_{0n}=0$, the matrix becomes diagonal and the "classical" flexural and torsional buckling loads of doubly symmetric cross-sections, the minimum of which is the critical load, are retrieved by equating to zero the diagonal terms (note that the values found are negative, because so far N_z was considered positive for tensile loading). The presence of M_{ln} and M_{0n} introduces a coupling between the three buckling modes even in case of double symmetry. It is also worth noting that, since the eigenvalues were given an increasing order and the terms α_n are at the denominator, the first term of the summation is the largest one, whereas the effect of subsequent terms is more and more unimportant.

Extension of the previous theory to cross-sections with discontinuous directrix is straightforward. The cross-sections used for engineering purposes can always be considered as formed by single parts, each having continuous directrix and constant thickness. Hence, the integrals in eq.s (23-24) must simply be expressed as summations of the relative terms computed on the continuous parts in which the cross-section may be divided.

A NUMERICAL EXAMPLE FOR THE I-SECTION

Let us now consider the common case of the I-section (Figure 3). As a result of the double symmetry of the cross-section, the characteristic functions of the generalized

problem, Φ_n, can be divided into: doubly symmetric; y-symmetric and x-antisymmetric; x-symmetric and y-antisymmetric; doubly antisymmetric. Assuming for simplicity $b = h$ and uniform thickness for web and flanges, the eigenvalues β_n corresponding to the doubly symmetric eigenfunctions are (Capurso, 1964c):

$$\beta_n = n\frac{\pi}{h} \qquad n = 1,2,...,\infty \tag{28}$$

and the corresponding doubly symmetric eigenfunctions are:

$$\Phi_n(s_1) = \cos(\beta_n s_1); \qquad \Phi_n(s_2) = \cos\frac{\beta_n h}{2}\cos(\beta_n s_2) - \frac{1}{2}\sin\frac{\beta_n h}{2}\sin(\beta_n s_2) \tag{29a,b}$$

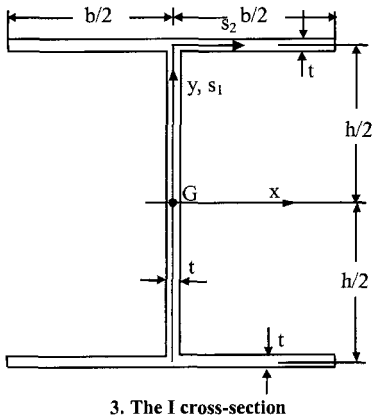
Let us now assume that the I-section profile has h=200 mm and thickness t=8 mm. The member has length l, is simply supported at both ends, and is subjected on the extreme bases to two distributions of axial stresses having a uniform component and a component proportional to the first doubly symmetric eigenfunction:

$$p_{0z}(s) = -\frac{N_z}{A} - \frac{M_{0l}}{I_1}\Phi_1(s); \qquad p_{lz}(s) = \frac{N_z}{A} + \frac{M_{ll}}{I_1}\Phi_1(s) \tag{30a,b}$$

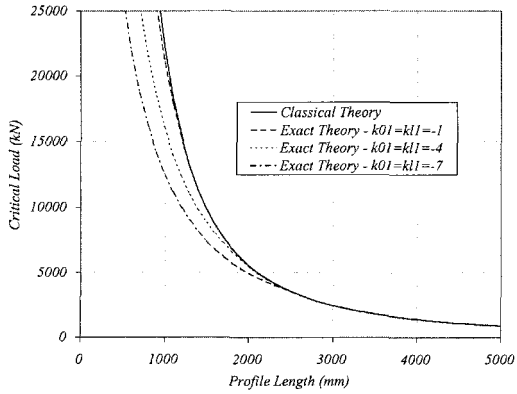
where M_{0l} and M_{ll} are assumed to vary proportionally to N_z, according to eq.s (26). Note that the applied stresses given by eq.s (30) have a resultant equal to N_z and no moment resultant, hence M_{0l} and M_{ll} may assume values independently from each other. The effect on the critical N_z of the actual distribution of p_{0z} and p_{lz} will now be analized. Increasing the absolute value of k_{0l} and k_{ll} results in a distribution of applied pressures whose maximum (punctual) absolute value is larger and larger than the average value. For instance, as the absolute value of k_{0l} changes from 0 to 1, 4 and 7, the ratio of the maximum absolute value to the average changes accordingly from 1 (uniform distribution) to 3.9, 15.8 and 27.6.

In Figure 4 the absolute value of the critical load (always corresponding to m=1) is plotted versus the length of the profile for an isotropic material with Poisson's coefficient equal to 0.3, for three different values of k_{0l}=k_{ll}=k_l. It is evident that, as the absolute value of k_l increases, the critical load predicted by the exact theory is more and more reduced compared to the "classical" one. However, the reduction is appreciable only for very short profile lengths, i.e. in a range of lengths where failure for a steel member is controlled by yielding. In fact, the additional stresses determined by the "warping moments" decrease rather rapidly moving away from the ends of the beam, as indicated by eq. (14), hence their relative importance decreases as the length of the member increases.

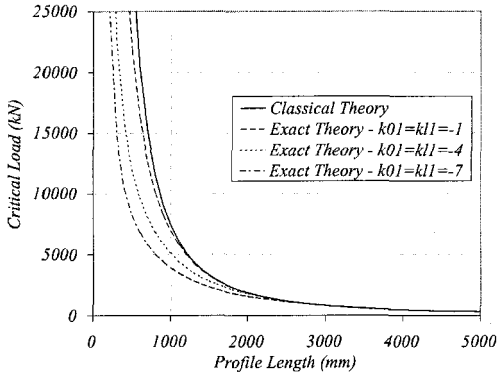
Figures 5-6 are analogous to the previous one but are valid for transversely isotropic materials with Z/E=0.5, $\bar{n}$=0.6 and μ=0.1 (composite 1) and with Z/E=0.2, $\bar{n}$=0.2 and μ=0.2 (composite 2). These properties represent the extreme values of the typical range of elastic constants for pultruded composites. It is evident that the discrepancy between predictions of the classical and exact theories is much more pronounced than in the isotropic case and is appreciable for a wider range of lengths. This because, as already reported by De Lorenzis and La Tegola (2003), the decay lengths of the effect of warping moments are always larger for composite materials than for steel, becoming more than triple for materials with low Z/E ratio, low ratio between transverse and longitudinal moduli, and high Poisson's coefficient μ.. Hence, the critical load of FRP pultruded profiles may be sensitive to the uniformity of application of the load and predictions of the classical theory may result unsafe.



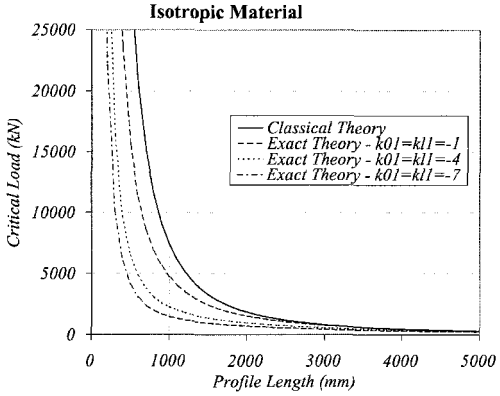
3. The I cross-section



4. Critical Load according to the Classical and Exact Theories – Isotropic Material



5. Critical Load according to the Classical and Exact Theories – Composite 1



6. Critical Load according to the Classical and Exact Theories – Composite 2

CONCLUSIONS

The effect of the actual distribution of the applied compressive stresses (equivalent to an axial force) on the flexural-torsional buckling load of a thin-walled member has been analized. A numerical example clearly showed that the effect of the local stresses arising at the extremities of the beam as a result of non-uniform self-balanced components of the applied pressure distributions may cause the buckling load to decrease. This effect is more pronounced for short element lengths. For steel profiles, the effect is practically negligible in the range of lengths where failure is controlled by buckling. For FRP profiles, the effect may be relevant and predictions of the classical theory may result unsafe to an extent depending on applied stress distribution, shape of the cross-section and elastic properties of the FRP.

REFERENCES

Capurso, M. (1964a-c), "Sul calcolo delle travi di parete sottile in presenza di forze e distorsioni. Note I-II-III", Ricerca Scientifica, 34 (II-A), vol. 6, 213; vol. 6, 241; vol. 7, 5 (in Italian).

De Lorenzis, L., and La Tegola, A. (2003), "Static analysis of pultruded fiber-reinforced polymer thin-walled beams", *Composite Structures*, Vol. 60, No. 3, pp. 231-244.

Krall, G. (1968), "Stabilità e vibrazioni", Edizioni Cremonese – Roma (in Italian).

THERMAL EFFECTS ON BOND BETWEEN FRP REBARS AND CONCRETE

Nestore Galati
University of Missouri-Rolla, USA
Bryan Vollintine
University of Missouri-Rolla, USA
Antonio Nanni
University of Missouri-Rolla, USA
Lokeswarappa R. Dharani
University of Missouri-Rolla, USA
Maria Antonietta Aiello
University of Lecce, ITALY

ABSTRACT

Bond between FRP bars and concrete depends on several parameters comprising environmental agents as the service temperature. As known, FRP bars present high values of the transverse coefficient of the thermal expansion (CTE) with respect to concrete; as a consequence, when temperature increases, tensile stresses take place within the concrete that may produce splitting cracks affecting the bond performance. The present paper is devoted to the analysis of the bond between FRP bars and concrete under thermal loads taking into account already available data on bond slip relationships and thermal behavior. An experimental investigation was carried out on concrete specimens reinforced with a FRP bar and subjected to thermal cycles with a maximum temperature value of 70 °C. After the thermal treatment, pull-out tests were performed at room temperature or higher. Untreated specimens were also tested for comparison. Results are reported and discussed in order to investigate the degradation of the concrete-reinforcement interface under thermal treatment and, as a consequence, the effects on bond-slip laws. Experimental results showed a significant degradation induced by exposure to relatively high temperatures.

INTRODUCTION

The use of FRP bars as reinforcement for concrete elements seems to be an effective solution for overcoming durability problems of traditional steel reinforced concrete structures due to the corrosion of metallic bars. For this reason, the replacement of steel with FRP bars is gaining popularity worldwide. The numerous experimental and theoretical studies carried out in the last years and many structural applications in addition to efforts in many countries to establish the guidelines of practical use of FRP reinforced concrete structures, confirm the increasing interest in this field (Nanni, 2001). However, in order to gain a deeper insight into the structural behavior of such new materials and to guarantee their safe application, further researches are needed in specific areas that concern the structural performance and durability under service conditions (Harris et al., 2003) and among all the effect of the temperature increases.

Unidirectional FRP bars, generally utilized in concrete, present an anisotropic behavior. As a consequence, the coefficient of thermal expansion (CTE) is different in

the longitudinal and transverse directions. In particular, the longitudinal CTE, controlled by fibers, is low and even negative (as in the case of aramidic fibers), while the transverse CTE, controlled by the resin, is up to 3 - 6 times that of the concrete (Gentry et al., 1996). As a result, an increase in temperature produces bursting stresses within the concrete that may cause splitting cracks. This fact involves a degradation of the bond between concrete and reinforcement (Tepfers, 1998; Tepfers, 1979), affecting the structural response.

This paper aims to determine what effect elevated service temperatures have on the bond performance of FRP reinforced concrete members. A total of thirty-six specimens were tested under direct pull-out. The variables investigated were: bonded length, concrete cover and exposure to high temperature. Experimental results showed a significant degradation induced by exposure to relatively high temperatures.

TEST MATRIX

A total of thirty-six specimens for direct pull-out testing were constructed (See Table 1). A 9.5 mm (3/8 in) GFRP bar with different embedment lengths was placed inside a 152 mm^3 (6 in^3) cube of concrete. Three different types of specimens were created based on the position of the bar, namely: centrally placed, and two and three times the diameter from one of the outer faces (See Figure 1). In addition, in order to create different embedment lengths, bond breakers were used. Consisting of soft polyethylene tubing placed over the bar to prevent direct contact with the concrete (See Figure 1). In order to have statistically relevant test results, three specimens for each configuration were tested.

The heat treated specimens were placed into an environmental chamber for 200 hours at a temperature of 70 degrees Celsius and at a humidity of 80%.

Table 1 - Test Matrix

Bonded Length mm (in)	**Thermal Treatment**	**Concrete Cover mm (in)**	**Bar Placement**
76 (3)	no	148 (5.8)	Center
152 (6)	no	148 (5.8)	Center
76 (3)	no	19 (0.8)	2 ϕ from edge
152 (6)	no	19 (0.8)	2 ϕ from edge
76 (3)	no	29 (1.1)	3 ϕ from edge
152 (6)	no	29 (1.1)	3 ϕ from edge
76 (3)	yes	148 (5.8)	Center
152 (6)	yes	148 (5.8)	Center
76 (3)	yes	19 (0.8)	2 ϕ from edge
152 (6)	yes	19 (0.8)	2 ϕ from edge
76 (3)	yes	29 (1.1)	3 ϕ from edge
152 (6)	yes	29 (1.1)	3 ϕ from edge

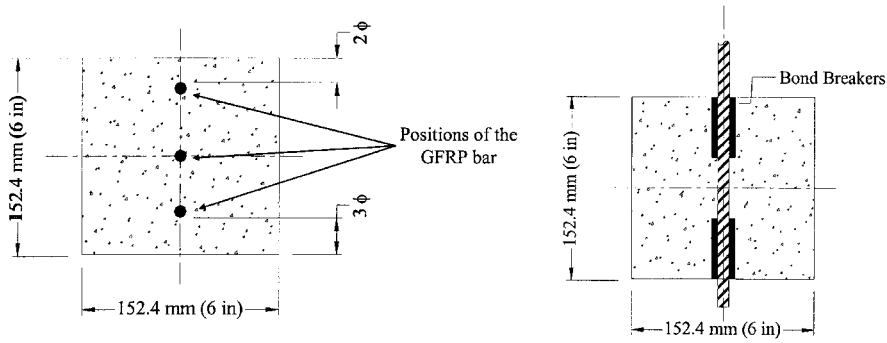


Figure 1 - Thermal Cracking Specimens

MATERIAL PROPERTIES

Tests were performed to characterize the mechanical properties of the materials used in this investigation.

The concrete used for the preparation of the specimens was designed to have a compressive strength of 27.6 MPa (4000 psi). Water to cement ratio for the concrete mixture was 0.45. Components in the concrete mixture were proportioned as follow by weight: 19% Portland cement, 40% crushed limestone, 33% sand, and 8% water. Once the specimens were cast, they were allowed to cure for 28 days at room temperature.

The specimens were built from four different batches of concrete. Table 2 summarizes the average compressive strength (ASTM C39/C39M) and the average tensile splitting strength (ASTM C496) for each batch of concrete.

The GFRP bars were manufactured by Hughes Brothers, Seward, Nebraska. These bars have a surface deformation called: "wrapped and sand coated design". The "wrapped" refers to the spiral glass fibers that are twisted around the bar. This decreases the amount of transverse thermal expansion and increases the mechanical interlock with the concrete. Bars are also sand coated to increases the friction and interlocking bond. The longitudinal and transverse coefficients of thermal expansion, as referred by the manufacturer, are $0.68 \div 0.74 \times 10^{-6}/^{\circ}C$ and $0.29 \times 10^{-6}/^{\circ}C$, per transverse and longitudinal direction respectively.

Table 2– Mechanical Properties of the Concrete

Batch of Concrete	Average Compressive Strength MPa (psi)	Average Splitting Tensile Strength MPa (psi)
1	33.9 (4920)	3.39 (492)
2	28.9 (4200)	3.05 (443)
3	28.6 (4150)	3.03 (439)
4	32.8 (4750)	3.31 (480)

Tensile tests were performed on FRP bars to determine their engineering properties, which are related to fiber content. The average tensile strength, ultimate strain and modulus of elasticity obtained from the testing of the specimens (ASTM D3039) are presented in Table 3. Details of coupon fabrication and testing procedure are shown elsewhere (Secondin 2003).

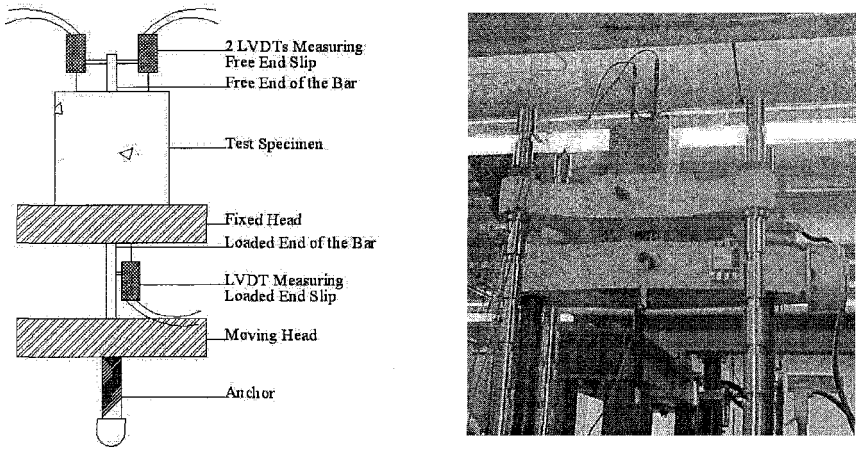
Table 3 - Mechanical Properties of FRP Bars

Bar Type	Dimensions of the Bar	Average Maximum Strain %	Average Maximum Stress MPa (ksi)	Average Elastic Modulus MPa (ksi)
#3 GFRP Bar	Nominal Diameter 9.53 mm (0.375 in.)	1.85	760.0 (110.0)	40800 (5920)

TEST SETUP

The testing was completed using the guidelines listed by ACI 440 (ACI 440-K.09-011) for direct pull-out specimens. As already mentioned before, the specimens were designed as concrete cubes with the bar either embedded in the center or placed two or three times the diameter from one of the outer cube faces. The bar then had a long and a short end. The short end was used to measure the free end slip while load was applied to the longer end.

For direct pull-out testing, the concrete block is held in place while a load is applied to the long end of the bar. The measurements taken were free and loaded end slip of the bar and the load. Two LVDTs were used to measure the free end slip 180 degrees apart from one another. One LVDT was used to measure the loaded end slip because of the lack of room. This setup can be seen from Figure 2.



a) Schematic b) Lab Photograph

Figure 2 – Test Setup for Pull-out Test with Central Bar

As the load was applied, readings were taken every second, until (1) rupture of the FRP bar occurs, (2) the enclosing concrete splits, or (3) sufficient slippage of the free end of the bar occurs (Boothby et al., 1996).

Significant pre-test preparation was the anchoring system. The anchoring system was needed to be able to apply the load without damaging the bars. In fact, unprotected grapping crushes the FRP bar. This crushes the bar causing failure outside the gage length.

The anchor system used consisted of a 200 mm (8 in) long steel pipe, 25 mm (1 in) in diameter. The pipe was placed on the end of the bar to be loaded and filled with a low viscosity epoxy resin. The low viscosity epoxy allowed for the epoxy to fill the pipe without leaving air pockets. The inside of the pipes were threaded to make sure the load was transferred from the pipe to the resin. From Figure 3 one can see that polymer caps were used to keep the pipe aligned with the bar. During testing, the load was applied to the pipe.

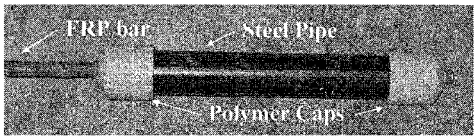


Figure 3 – Anchoring System

For the specimens that had the off-center bar placement, a variation in the setup had to be introduced to prevent any bending on the bar. With reference to the sketch in Figure 4, one can see that another 6 in block was tied to the one being tested. This kept the bar and the block straight, eliminating the bending moment that might have otherwise been created.

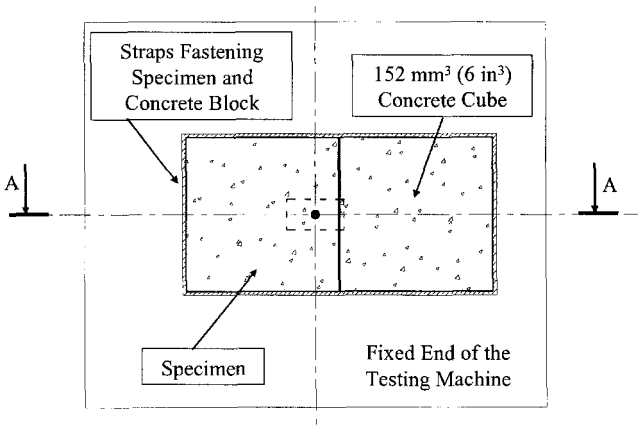
TEST RESULTS AND DISCUSSION

The specimens with 152.4 mm (6in) embedment lengths, 15 times the diameter of the bar, were too long for a 9.53 mm (0.375 in.) diameter bar. In many of the specimens, the bar broke before they would begin to slip.

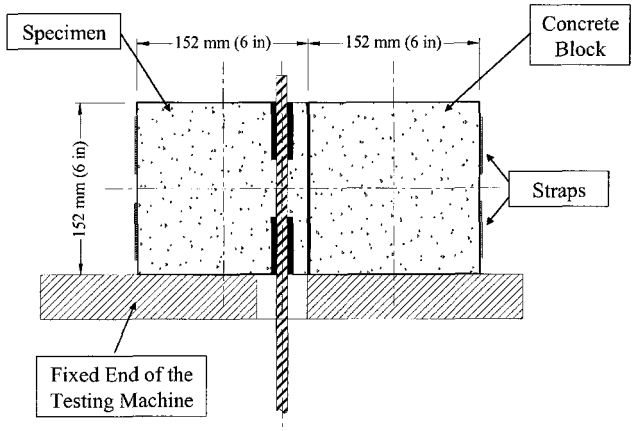
Test results in terms of average ultimate load are summarized in Table 4. By increasing the embedment length the maximum load that the specimens can hold also increases.

From Table 4 it can be observed a 16% maximum reduction in the ultimate load for the thermally treated specimens' consequent to bond degradation. The effects of thermal loads are more evident by looking at the load-slip curves. Typical load-slip curves for the pull-out tests performed are shown in Figure 5.

These curves show the difference between the behavior of the specimens with and without thermal treatment. For the untreated specimens there was almost no slip at the free-end until the load reached its ultimate value. For the thermal treated specimens instead, the same peak bond stress is attained but with higher slip values. The bond failure in this case is caused by the shearing of the matrix material from the fibers in the bar. The GFRP bar consists of a core of glass fibers with an outer layer of resin and sand. As a consequence of the thermal treatment there is a weakening of the matrix and thus it shears off as observed in Figure 6.



a) Side View

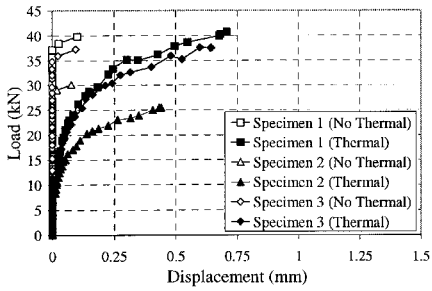


b) Section A - A

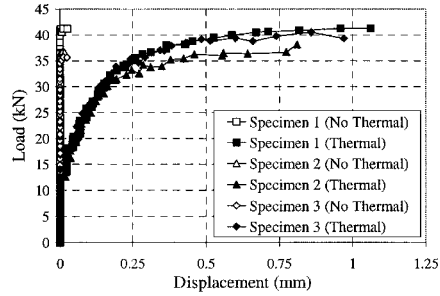
Figure 4 –Test Setup for the Off-Center Specimens

Table 4 – Test Results in Terms of Ultimate Loads

Bar Placement	Bonded Length mm (in)	Ultimate Load kN (kip)		Covariance %		Strength Loss $\frac{P_{NT}-P_T}{P_{NT}}\cdot 100$
		Thermal Treatment (P_T)	No Thermal Treatment (P_{NT})	Thermal Treatment	No Thermal Treatment	
Center	76.2 (3)	33.81 (7.60)	34.70 (7.80)	9.78	5.83	2.56
Center	152.4 (6)	41.15(9.25)	42.26 (9.50)	5.41	6.84	2.63
2 ϕ from edge	76.2 (3)	34.55 (7.77)	35.73 (8.03)	16.73	2.12	3.24
2 ϕ from edge	152.4 (6)	28.77 (6.47)	34.25 (7.70)	12.36	11.04	15.97
3 ϕ from edge	76.2 (3)	39.59 (8.90)	37.81 (8.50)	5.06	14.12	-4.71
3 ϕ from edge	152.4 (6)	30.69 (6.90)	34.70 (7.80)	8.55	26.92	11.54



a) Specimens having a 76.2 mm (3 in) Embedment Length, GFRP bar placed 2 ϕ from edge.



b) Specimens having a 76.2 mm (3 in) Embedment Length, GFRP bar placed 3 ϕ from edge.

Figure 5 - Comparison of Free-End Slips

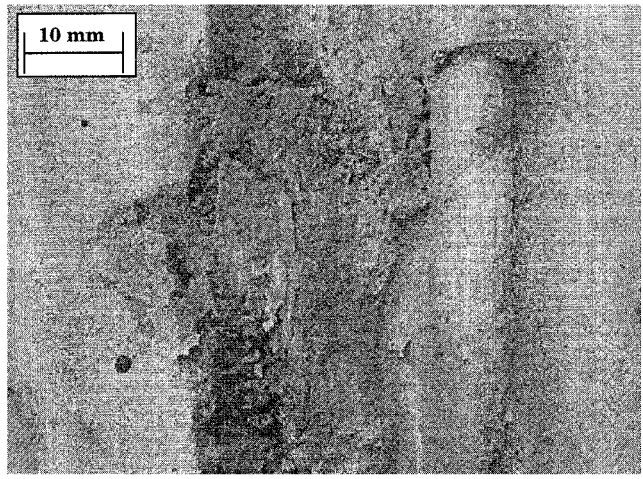


Figure 6- The Shearing of the Resin

CONCLUSIONS

On the basis of the experimental investigations, the following concluding remarks can be drawn:

- The thermal treatment induced in most of the specimens a slight degradation in the bond performance in terms of ultimate load. A more pronounced effect has been observed on the bond stress-slip curves in terms of slip values due primarily to the degradation of the resin;
- In many of the specimens with a 15-diameter embedment length the bar broke before it would begin to slip;
- Future research is to conduct the direct pull-out test at high temperature. This would allow determining any bond degradation when the structure is subject to high temperature and therefore to verify if the current standards are adequate for the use with internal FRP reinforcement.

ACKNOWLEGEMENTS

The support of the National Science Foundation Industry/University Cooperative Research Center at the University of Missouri–Rolla. The authors would also like to acknowledge the support of the Rolla Technical Institute (RTI).

REFERENCES

1. A. Nanni, "Relevant Applications of FRP Composites in Concrete Structures," Proc., CCC 2001, Composites in Construction, Porto, Portugal, Oct. 10-12, 2001, J Figueiras, L. Juvandes and R. Furia, Eds., (invited), pp. 661-670, 2001.
2. K. A. Harries, M. L. Porter, and J. Busel, "FRP Materials and Concrete - Research Needs", Concrete International, Vol. 25, Issue 10, October 1, 2003.
3. T. R. Gentry, "Thermal compatibility of Plastic Composite Reinforcement and Concrete". Advanced Composite Materials in Bridges and Structures, M.M. El-Badry, ed., Canadian Society for Civil Engineering, Montreal, Quebec, 149-156, 1996.
4. R. Tepfers, "Bond between FRP-Bars and Concrete". Division of Building Technology, Chalmers University of Technology, Göteborg, Publication no. 98:3, Work no. 22, 1-16, 1998.
5. R. Tepfers, "Cracking of concrete cover along anchored deformed reinforcing bars". Magazine of Concrete Research, Vol. 31, no. 106, 3-12, 1979.
6. ASTM C 39/C 39M, "Standard Test Method for Compressive Strength of Cylindrical Concrete Specimens"
7. ASTM C496-96: "Standard Test Method for Splitting Tensile Strength of Cylindrical Concrete Specimens"
8. Secondin, S., (2003), "Masonry Reinforced with FRP systems," Tesi di Laurea, Università degli Studi di Padova, Facoltà di Ingegneria, Padova, Italy, March 2003.
9. ACI Committee 440, "Recommended test methods for FRP Rods and Sheets.", ACI 440-K.09-011. American Concrete Institute International, Farmington Hills, MI, 2001.
10. Boothby, T.E., Nanni, A. and Bakis, C.E., "Accelerated Test Methods for FRP/Concrete Systems in Highway Structures." 4th National Workshop on Bridge Research in Progress, I.G. Buckle and I.M. Friendland, eds., 17-19, Buffalo, NY, 1996.
11. Conrad, J.O., Bakis C.E., Bootby, T.E. and Nanni, A., "Durability of Bond of Various FRP Rods in Concrete". CDCC-98, Sherbrooke, Canada, 299,310, 1995.

FE MODELLING OF MECHANICAL INTERACTION OF LUGGED FRP RODS WITH CONCRETE, COMPARISON BETWEEN EXPERIMENT AND SIMULATION

A.R. Khoei and H.R. Irannejad
Department of Civil Engineering, Sharif University of Technology, P.O. Box 11365-9313, Tehran, Iran

ABSTRACT

The main objective of this paper is to present a numerical simulation of mechanical interaction (bond mechanism) of lugged FRP rods with concrete. A finite element analysis is performed and the major causes of bond in lugged rod's interface with concrete are summarized. The concept of ascending and descending behavior of a rib under pull-out load is discussed. A simple procedure is employed to model the crack formation and propagation in the concrete block below the rib. Details and general aspects of model are described and numerical results are compared with experiments. Finally, it has been concluded that the proposed model can be effectively used for the simulation of bond behavior of deformed FRP with surrounding concrete.

INTRODUCTION

The need for infrastructure renewal and the potential advantage of composite material have led to interest in applying them in civil engineering structures[1]. Fiber Reinforced Polymer (FRP) rod is proposed as an alternative reinforcement for concrete structures, particularly in environmental capabilities, such as: chemical and electromagnetic corrosion. The FRP lugged rods are of great importance from the point of view of structural application. It is mainly due to considerable bond resistance in comparison with similar smooth rods. Also, they are famous for their capability to eliminate corrosion and increase the durability of in-cast concrete structures[2].

The major characteristics of polymer-fiber composites are; the low density, significant chemical adhesion, and suitable tensile strength[3]. The FRP rods, tendons, and grids have already been applied in structures in the vicinity of water, such as bridge structures[4].

The nature of contact phenomenon and its simulation result in a better application of these rods in construction of modern concrete structures. The necessity of simulation of mechanical interaction is intensified, considering the fact that carrying out experiences in the laboratory is a time-consuming and expensive task. One of the main aspects of FRPRC, which has been verified experimentally, is the mechanical interaction of various types of this composite material with surrounding concrete, although fewer attempts have been made to investigate it numerically.

MECHANICAL BEHAVIOR OF BOND IN LUGGED RODS

The performance of both reinforced and pre-stressed concrete structures depends on the properties of concrete, reinforcement, and bond behavior between the two components[5]. Friction plays the main role in mechanical interaction of smooth rods while the major cause of bond behavior in lugged rods is mechanical interference, which mainly implies bearing of lugs and concrete blocks below them[6]. There are some minor phenomena

affecting the bond behavior, such as: chemical adhesion, thermal and moisture effects, and cog-wheel behavior between rib and core of reinforcement.

The mechanism of resisting the pull-out load in structures reinforced with lugged rods is mainly based on the bearing between ribs and concrete blocks below them. In fact, it acts before the occurrence of general failure in concrete, such as: 'concrete splitting' and 'rib shear cut-off'. In the case of 'lug shear cut-off', the major factor providing the extra bond strength is the so-called "Cog-Wheel" behavior between the cutted lugs and internal core of reinforcement, which demonstrates an inverse mechanical behavior. In other words, increasing the slip of the reinforcement decreases the shear force in the lug, as shown in Figure 1. This process continues until the interaction of ribs with the core of rod is completely demolished and the interface is destroyed.

The occurrence of rib shear cut-off in lugged rods reinforced concrete is very common. Daniali[7] observed such a failure following the huge slip and bond rupture from experimental test carried out on E-glass fiber deformed bars made by vinylester resin. Bakis et al.[8] conducted an experiment on a unit-rib lugged rod and observed that the failure behavior of a single lug is triangular and has two branches; ascending and descending. In the ascending branch, the pull-out load increases by development of the relative slip until the lug crack takes place. At this stage, the tangential force borne by rib decreases proportionally, as shown in Figure 1.

FE MODELLING OF LUGGED RODS

Apparently, the first rib-scale analysis for FRP bars, which considered the plastic behavior of materials, was carried out by Boothby et al[9]. In the present study, numerical modelling of lugged rods is carried out in rib-scale, which is principally the most accurate and of course time-consuming due to enormous calculation expenses. One of the major aspects of computational modelling is the consecutive process of analysis in order to obtain various segments of output diagrams. In rib-scale model, the rod and concrete are modeled in details.

A finite element analysis of bond behavior which can predict the pull-out and splitting failures could be combined with the experimental observations in order to perceive the progressive failure and calibrate the configuration based bond models applicable to large-scale structural analysis. The FRP material which is modelled in the current simulation is transversely isotropic, with major module of elasticity in longitudinal direction and the minor module of elasticity in the other two orthogonal directions. It is worth noting that the experimental specimens were concrete cubes of 150mm size reinforced with FRP composite rods. However, a similar cylindrical model (with 150mm diameter) is simulated in this study. It is a reliable approximation for modelling, considering the fact that the size of specimens is large enough. Note that an internal hole was bored through the reinforcement in the experiment, and an aluminum strain-probe was placed inside it. Figure 2 illustrates the general shape of an axi-symmetric experimental model employed in this analysis together with the deformed shape of a part of the rod. The implementation of finite element model is shown in this figure. As can be observed from the figure, the concrete region named 'type A' nodes is in connection with the above FRP elements. This implies the bearing interaction of FRP lug and concrete block. "type B" nodes are located on the boundary of external surface of the rib, or inter-lug smooth surface, and the adjacent concrete. The contact elements and nonlinear springs, which model the frictional behavior and adhesion respectively, make the connection points of nodes at this region. The 'type C' nodes are located on

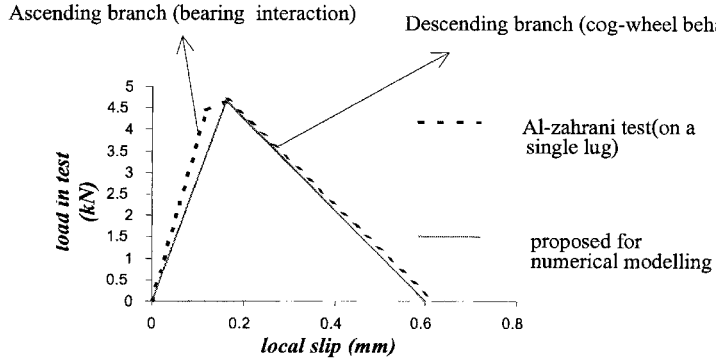


Figure 1 - Load versus slip observed in Al-Zahrani test on a unit-rib specimen.

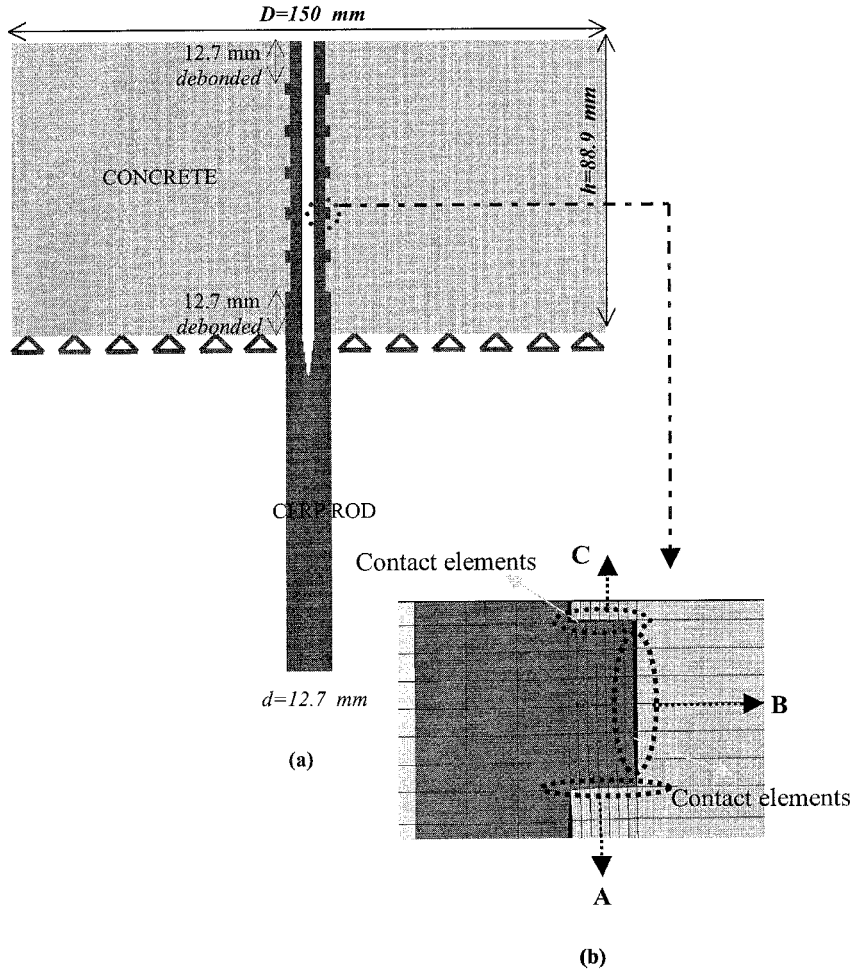


Figure 2 - a) General shape of the model. b) Modelling of interaction in rib-scale.

the upper side of rib and lower side of the concrete block above. A set of contact elements connect nodes of this type at this zone, although these contact elements have no initial interference and length and only define a gap between the rib and the concrete block at the region.

It can be clearly observed that there is no compressive contact between concrete and rib at this region, but a gap is initiated between the lug and concrete block as a pull-out load is exerted at the end of the reinforcement and continues to open with further progress in loading. In order to prevent the influence of end reactions on the general bond behavior and crack propagation, especially in the vicinity of the rib which is near the loaded end, a part of the concrete near the supports is debonded from the adjacent reinforcement by creating a gap. To obtain a better bond distribution and avoid stress concentration around and in the last rib, which is placed near the free end, a similar debonded length is created in the model at the upper zone of the cylinder near the free end. Figure 3 shows typical shapes of models with and without debonded lengths.

Simulation of 'cog-wheel' behavior of lugs

In the case of 'lug shear cut-off', the mechanical behavior of rods follows the descending branch, as shown in Figure 1. In fact, this implies the initiation of the so-called "Cog-Wheel" behavior, which was described in previous sections. In order to simulate this behavior, several nonlinear springs are employed across the interface of lug and the core of rod, as shown in Figure 4. These springs are capable of simulating the inverse proportional relationship between the shear force and slip. Note that before a certain slip; the slip corresponding to the instant of rib shear cut-off, the springs should not play any role in the process of load transfer and bond resistance. This critical slip corresponds to an amount of average shear stress in the lugs which is 38.7 MPa, as observed in a pull-out test on a unit-rib reinforcement by Bakis et al.[8]. In fact, the nonlinear spring becomes active after occurrence of such an average shear stress in rib.

Crack modelling

In order to model the crack propagation through the concrete block below the rib, a simple method is employed here. For this purpose, the elements across the boundary of concrete blocks below the rib and the adjacent concrete cylinder that the tensile stress at corresponding nodes exceeds the tensile strength of concrete (here approximately 4 MPa) are eliminated from the model (killed), as shown in Figure 5. The finite element mesh is so fine that a typical crack width in concrete can be approximated by the width of each element that is 0.2~0.3mm. Thus, it seems to be a reliable procedure.

When the pull-out force is exerted at the end of the rod, a part of concrete block, which is adjacent to the interface of lug and internal core of the rod, is crushed up under compression exerted by the rib on the concrete block and changes into powder. On the other hand, it is heaped below the lug, which becomes soft and creates a micro-gap. To simulate this phenomenon, a method similar to that described above is employed here.

COMPARISON BETWEEN EXPRIMENTAL AND NUMERICAL RESULTS

In order to demonstrate the capabilities of the model, a comparison is performed between the analytical load versus slip variation and the corresponding graph derived from experiment. Note that the experimental results was obtained by a debonded length of 86.5 mm; 75 mm at loaded-end and 11.5mm at free-end[10], and the rod was

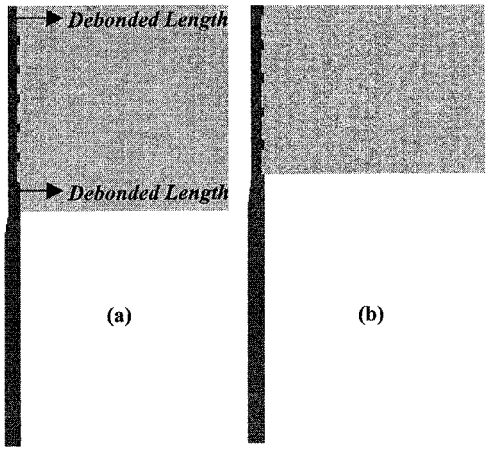


Figure 3 - (a) Model with debonded length. (b) Model without debonded length.

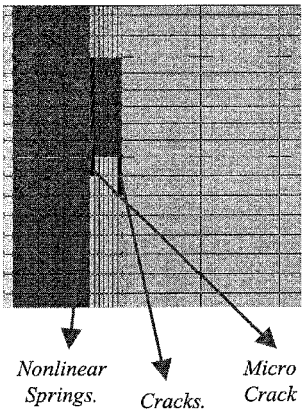


Figure 4 - Layout of nonlinear springs

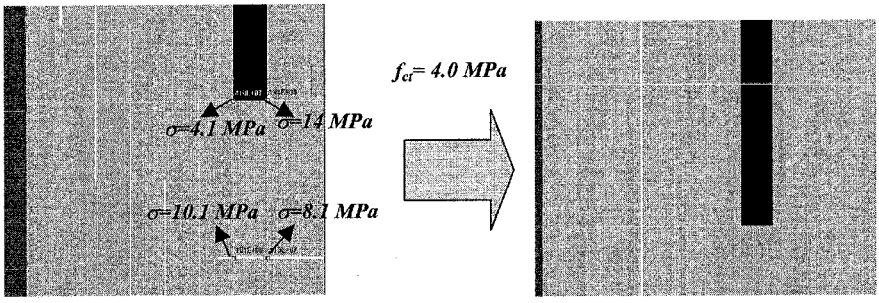


Figure 5- Method of crack formation and propagation modelling.

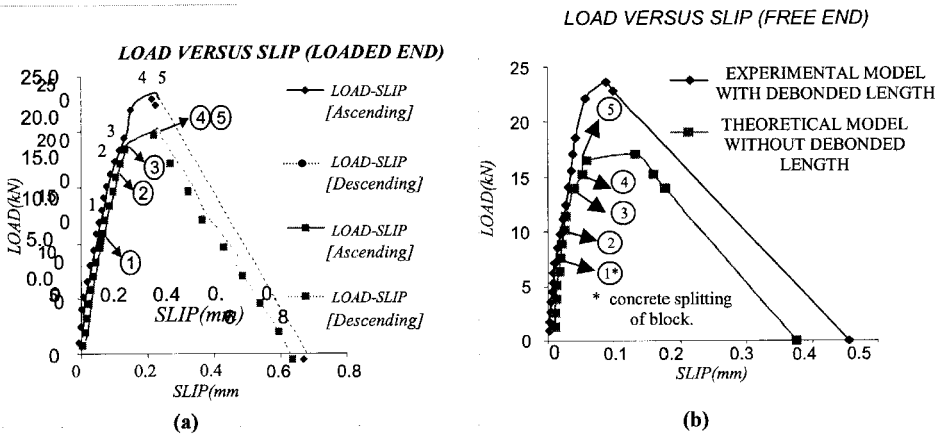


Figure 6-(a) Load-Slip variation: model with debonded length.
(b) Load-Slip curve for free end: comparison of experiment with analysis.

surrounded by concrete with a total length of 150 mm (the embedment length was 63.5mm). In the present simulation, the upper zone of the rod is covered with the concrete cylinder of 88.9 mm length in order to reduce the calculation expenses. So the debonded length of 12.7 mm can be observed both at the loaded-end and free-end parts (note that 88.9-2*12.7=63.5mm), which does not make sense, considering the fact that the real extra length of 61.1 mm of the FRP rod existing in experiment is debonded and does not have any direct contact with the surrounding concrete. The comparison is shown in figure 6. Both ascending and descending branches of bond response are also presented in this figure. The numbers in the circles indicate the load and slip for consecutive split (shear cut-off) of lugs, which occurs one by one from the loaded end toward the free end of the FRP rod.

In addition, due to some limitations in experimental observations and the fact that the system becomes rather unstable after reaching the peak load and the occurrence of it's corresponding slip, a short portion of the descending branch could be obtained in experiments. Figure 7 illustrates the sketched curves of load versus slip according to the output data supplied from test. It may be worth noting that the slip at the loaded or unloaded ends of the bars governs the bond intensity that can be developed under working load conditions[11] since this slip will significantly affect crack width. In order to perform a reasonable comparison between simulation and experiments, the descending part is established by stretching the negative-slope line in Figure 7. In this figure, the dotted line indicates the abstract descending part of the tentative curve, which could be compared with the descending line obtained from analysis (from nonlinear spring force-displacement data) to validate the integrity of the proposed modelling. However, it must be noted that the real experimental bond-slip behaviour may not be identical with those presented in Figures 6 and 7. As it was observed from a similar test carried out on glass/vinylester FRP rods that the decrease of shear stress with development in slip stops at a certain point (approximately equal to 30~40% of the ultimate shear stress), following a sudden jump in shear stress, and a constant shear with development of slip could be observed after the jump takes place[10]. Numerical modelling of this behavior is one of the proposals of the authors for further researches to be carried out in due course, but it is beyond the scope of this article. The suggested method of modelling gives a good evaluation of bond response for the whole ascending branch and a part of descending branch up to an amount of pull-out load nearly 30~40% of the ultimate load.

There are no experimental data for models without the end debonded length in the literature[10], but a numerical simulation of the proposed model without debonded length is carried out here and the output of load-slip graph is illustrated (see Figure 6b). Clearly, approximately 30% decrease of ultimate pull-out load is resulted by the elimination of end debonded lengths. The reason was discussed in previous sections. It is worth mentioning that the preliminary failure in the system is no more the shear cut-off of the lug near the loaded end. In fact, the preliminary rupture is a concrete splitting below the lug located near the loaded end of the reinforcement. The mechanical behavior in both cases is similar.

Figure 8 shows the progressive deformation of lugs by exerting pull-out load. The lug shear cut-off, which takes place after the ultimate pull-out load is fully applied, is illustrated in this figure. The progressive deformation and crack propagation at different stages of loading at the first rib and concrete block for a model with debonded length is illustrated in Figure 9a. Similar results are shown for a model without debonded length (see Figure 9b). the occurrence of concrete splitting in a concrete block below the first lug due to the maximum pull-out load is obvious in Figure 9b. Also, existence of a micro-gap at early stages of loading (approximately 20% of ultimate pull-out load) is

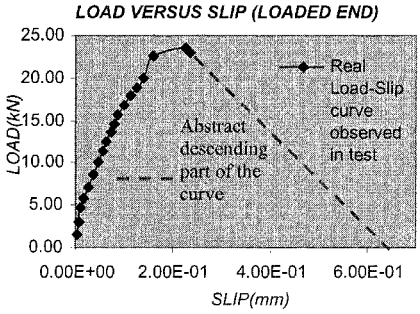


Figure 7- Real Load-Slip curve observed in experiment.

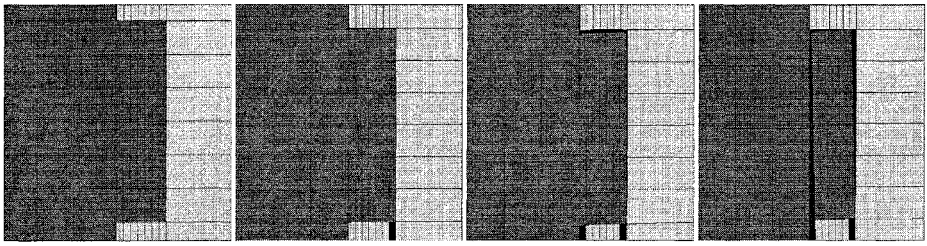


Figure 8- Progressive deformation of lugs.

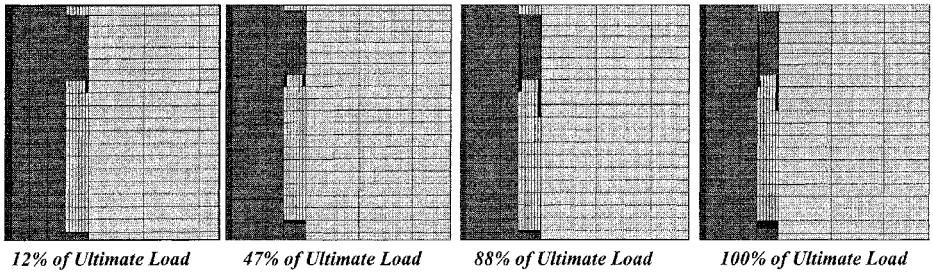


Figure 9- Progressive deformation and crack propagation:
(a) Model with debonded length. (b) Model without debonded length.

vivid for the model with debonded length from figure 9a.

CONCLUSION

In the present paper, a finite element simulation of the lugged FRP rod mechanical interaction with surrounding concrete was proposed. Application of contact and nonlinear spring elements to model the lug mechanical interaction with concrete was described. The method of simulation of the so-called 'Cog-Wheel' behavior of lugs was explained. An approach was presented to simulate the tensile or compressive crack formation and propagation in the concrete blocks. The comparative experimental and numerical graphs for load versus slip variation of model with debonded length were included as validation of the research. The reduction of ultimate pull-out load due to elimination of debonded lengths was investigated numerically. Different failure modes around the first rib of the simulated experimental model were demonstrated and verified separately for models either with or without debonded lengths. Typical shapes for progressive deformation of ribs and crack propagation below the ribs were presented.

REFERENCES

1 J V Cox and J Guo, 'Modelling the stress state dependency of the bond behaviour of FRP tendons', ACI's special publication for the 4th int symp of *Fiber Reinforced Polymer for Reinforced Concrete Structures (FRPRCS-4),* Baltimore, Md., Nov 1999.

2 Alkhadraji, Mettemeyer, Belarbi, and Nanni, Flexural behaviour of FRP-reinforced concrete members, University of Missouri Rolla, CIES 99-15 report, 1999.

3 M W Hyer, *Stress Analysis of Fiber-Reinforced Composite Materials,* Singapore, McGraw-Hill, 1998.

4 L J Malwar, 'Tensile and bond properties of GFRP reinforcing bars', *ACI Materials Journal* , May-June 1995 **92**(3) 276–85.

5 E Cosenza, G Manfredi, and R Realfonzo, 'Behaviour and modelling of bond of FRP rebars to concrete', *Journal of Composites for Construction*, May 1997 **1**(2) 40–51.

6 A Vafai A R Khoei H R Irannejad, 'FE analysis of mechanical interaction of Fiber Reinforced Polymer (FRP) with concrete', Proceeding *6th int conf on civil (ICCE2003)*, Isfahan, Iran, Arkan, eds., May 2003, pp.165-173.

7 S Daniali, 'Development length for Fiber-Reinforced-Plastic Bars', Proceeding 1st int conf *on Advanced Composite Materials in Bridge Structures,* Neyer and Labossiere, eds., sherbrooke, Quebec, Canada, 1992.

8 C E Bakis, V S Uppuluri, A Nanni, and T E Boothby 'Analysis of bonding mechanisms of smooth and lugged FRP rods embedded in concrete', *Journal of Composites Science and Technology*, Aug 1998 **58(8)** 1307–1319.

9 T E Boothby, A Nanni, C Bakis, and H Huang, 'Bond of FRP rods embedded in concrete', Proceeding 10th *ASCE Mechanical Engineering Specialty Conference,* New York, S. Sture, ed., May 1995, pp.114-117.

10 M M Al-Zahrani, S U Al-Dulaijan, A Nanni, C E Bakis, T E Boothby, 'Evaluation of bond using FRP rods with axi-symmetric deformations', *Journal of Construction and Building Materials*, 1999 **13** 299–309.

11 B Benmokrane, B Tighiouart, and O Challal, 'Bond strength and load distribution of composite GFRP reinforcing bars in concrete', *ACI Materials Journal*, May-June 1996 **93**(3) 246–253.

MINIMISING DAMAGE AND DELAYING FAILURE OF COMPOSITE LAMINATES

L. N. McCartney

NPL Materials Centre
National Physical Laboratory
Middlesex, UK, TW11 0LW

ABSTRACT

The construction industry has for many years used composites for non-load-bearing situations, and more recently the development of composites for re-bars, bridge strengthening and the primary structure of small bridges, is extending this use to load-bearing applications. The objective of this paper is to summarise our knowledge of the modelling of damage development and failure in composite laminates and its use when developing recommended methods of designing laminates to minimise damage formation and to delay failure in composite engineering components used in the construction (and other) sectors. The summary will consider the general in-plane loading of general symmetric laminates that are also subject to thermal residual stresses. The major issues discussed concern the effects of ply thickness and ply lay-up on both first ply failure and the subsequent failure of the laminate. Another issue concerns the avoidance of 90° plies on either side of the mid-plane of the laminate and at the free surface, as this can lower the strength and first ply failure stress of some laminates when compared with configurations having a different ply order. On the basis of considering some experimental results and model predictions of first ply failure in general symmetric laminates, it is concluded that:

- Experimental strength measurements for a variety of laminates indicate that there are thickness and ply lay-up dependencies that are ignored when applying conventional failure criteria.
- Initial ply failure should be modelled using an energy based approach as it leads to realistic ply thickness and lay-up effects in contrast to the 'strength of materials' methodology that does not have these practically important characteristics.
- The location of 90° plies in a symmetric laminate should avoid being adjacent to the mid-plane, or at the free surface, as it leads to a lowering of the strength and/or first ply failure stress.
- For carbon fibre composites subject to loading likely to cause ply cracking, the first ply failure stress could usefully be the basis of a criterion for failure. The adoption of such an approach is practical due to the existence of a new software tool to assist with its implementation, and the approach would be of benefit also to engineering components subject to fatigue loading and environmental exposure.

INTRODUCTION

The use of composites in engineering applications has been driven mainly by aerospace and defence applications, although more recently the Formula 1 racing industry has become exceedingly innovative. The construction industry has for many years used composites for non-load-bearing situations, and more recently the development of composites for re-bars, bridge strengthening and the primary structure of small bridges, is extending this use to load-bearing applications. Because of this relatively new type of

application in the construction sector, it is timely to review the state of the art regarding the engineering methods needed to avoid the structural failure of composites. This paper is concerned with physically-based methods of design that can be used to minimise damage formation and delay the onset of the failure of laminated composites. While the methodologies to be considered apply to laminated composites with aligned fibres, the principles to be discussed and conclusions are expected also to be highly relevant to woven laminates.

STATUS OF FAILURE CRITERIA FOR COMPOSITES

Before embarking on a brief review of physically based design methods, it is useful first of all to describe briefly the traditional approach to avoiding failure in composite materials. At its most sophisticated, the methodology involves the engineer in first estimating the stress distribution in those parts of the structure thought to be prone to failure during service. Such locations are often associated with localised details where stress concentrations exist, such as around holes. In such regions the stress field will not be homogeneous, and it certainly will not be uniaxial in nature. The determination of the stress field will often require the use of numerical methods such as finite element analysis (FEA) or boundary element analysis, although sometimes hand calculations can be undertaken, such as for simply loaded plates with holes in the absence of free edge interactions. The next stage in the design procedure is to examine the stress field and apply locally some form of failure criterion.

Engineers often predict structural failure of composite engineering components by the application of one or more of various quadratic failure criteria that are applied to the local stress states of undamaged structures. Such failure criteria are often built into commercial FEA packages enabling the engineer to apply the criteria as part of the post-processing stage of calculations. Linear anisotropic behaviour of the composite right up to the onset of ultimate failure is normally assumed. When adopting this approach the failure criteria that are applied do not take account of the microstructural behaviour of the composite material, i.e. they ignore the effects of progressive damage growth that can lead to a local loss of properties and to the re-distribution of stress within the component. This phenomenon is very similar to plastic flow in metals.

The current status of many composite failure theories has been reported in Parts A and B of the International Failure Prediction Exercise [1]. The conclusions of this initiative were compiled from the results of comparing high quality experimental data with 'blind' predictions by the developers of the various failure models and criteria. Although a range of laminate types and in-plane loading cases were considered, there was no investigation of the effects of ply thickness and ply lay-up. As a result it is not yet possible for the various failure criteria to be evaluated with regard to these practically important effects. Such evaluations would have differentiated between those models (usually energy based such as those described in [2]) that are capable of predicting the effects of ply thickness and ply lay-up on failure, and those models based on 'strength of materials' concepts, where no effect would be expected if statistical aspects are excluded from the analysis.

If a 'strength of materials' approach is taken, and if the thicknesses of the plies in a laminate are simply doubled, then there should be no difference in the applied stresses for initial ply failure and laminate failure. Neither energy-based models, that include a fibre failure criterion, nor experimental results, support this conclusion (see discussion below) implying a thickness dependence to failure criteria that is not usually taken into account when designing laminated composite components. If the plies in a laminate are

re-ordered maintaining symmetry about the mid-plane but altering the lay-up sequence, then again a 'strength of materials' approach would imply that there should be no difference in the applied stresses needed to cause first ply failure and laminate failure. Again both energy-based modelling and experiment do not support the use of the 'strength of materials' approach (see following discussion). To illustrate the importance of ply thickness, Table 1 shows the measured strengths for three types of laminate lay-up. Johnson and Chang [3] have tested a wide range of CFRP (T300/976) laminate geometries, and fully characterised matrix crack induced laminate failure. For each laminate tested, the authors have described the damage progression and given the failure stresses (averages of three or four results) for the laminates tested in uniaxial tension.

Table 1 : Effect of ply thickness on measured strengths (bold) and predicted first ply failure (not bold) of CFRP laminates (Johnson & Chang [3]). Values normalised to the commonly used ply thickness n = 2 are in brackets.

	Measured strength (MPa)		
n	$[30_n/-30_n/90_{n/2}]_s$	$[45_n/-45_n]_s$	$[60_n/-60_n]_s$
1	**469.2 (1.77)** 792.8 (1.51)	**183.3 (1.29)** 145.7 (1.46)	---
2	**264.6 (1.00)** 524.0 (1.00)	**141.9 (1.00)** 99.7 (1.00)	**69.6 (1.00)** 64.9 (1.00)
3	**92.2 (0.73)** 383.7 (0.73)	**116.4 (0.82)** 78.9 (0.79)	**52.5 (0.75)** 51.5 (0.79)
4	**152.3 (0.58)** 334.0 (0.64)	---	**48.2 (0.69)** 43.5 (0.67)

In Table 1 the parameter n describes the thickness of each ply such that when n = 1 the ply thickness is 0.132 mm. It is clearly seen that as n (and the ply thickness) increases the measured strength (bold results) of the laminate decreases substantially. It is emphasised that if conventional failure criteria were used to predict laminate failure using the methods described above then no thickness dependence would be observed at all. The data for strength given in Table 1 clearly indicate that current practice can be grossly in error and this should be noted by engineers taking responsibility for designing load-bearing laminated composite applications in the construction, and other, sectors.

Turning now to the effect of ply lay-up on laminate strength, Johnson & Chang [3] have provided the strength data (averages of three or four results) shown in Table 2. Strength measurements for different types of quasi-isotropic CFRP (T300/976) laminate are given where the lay-up of the plies in the laminate has been varied. It is seen that the $[0/45/-45/90]_s$ laminate has the lowest strength, where the 90° ply is located at the centre of the laminate. The $[45/-45/0/90]_s$ laminate is stronger than the $[0/90/45/-45]_s$ laminate, thus demonstrating that the relationship of ply cracking to strength either may be complex, or the strength values are subject to some scatter.

Further evidence supporting the effects of ply lay-up on failure, and the deleterious effect of placing 90° plies adjacent to the mid-plane, is shown in Table 3. The 'strengths' of four different lay-ups of quasi-isotropic carbon fibre laminates are given which are derived from the measured net section stresses for the failure of open hole tension tests (see Acknowledgements). Note that the laminates A and D, having a 90° ply adjacent to the mid-plane, lead to lower 'strengths' than those for laminates B and C where the 90° ply is located away from the laminate mid-plane.

Table 2: Effect of laminate lay-up on the measured strengths of quasi-isotropic CFRP laminates (Johnson & Chang [3]), and the predictions of first ply failure stress.

Laminate lay-up	Measured strength (MPa)	First ply failure stress (MPa)
$[45/-45/90/0]_s$	560.2	688.8*
$[45/-45/0/90]_s$	511.2	495.9
$[0/90/45/-45]_s$	500.9	688.4*
$[0/45/-45/90]_s$	487.1	448.1
$[90/0/45/-45]_s$	---	431.3
$[90/45/-45/0]_s$	---	394.9

Table 3: Comparison of first ply failure stresses with net section 'strengths' (see Acknowledgement). Results in brackets are normalised relative to laminate C.

	Lay-up A $(45/0/-45/90)_{2s}$	Lay-up B $(45/90/-45/0)_{2s}$	Lay-up C $(45/-45/90/0)_{2s}$	Lay-up D $(45/-45/0/90)_{2s}$
Net section 'strength' (GPa)	0.52 (0.88)	0.57 (0.97)	0.59 (1.00)	0.53 (0.86)
Predictions of first ply failure (GPa)	0.41 (0.80)	0.49 (0.96)	0.51 (1.00)	0.44 (0.90)

To conclude this brief review of laminate failure, it is useful to warn of some other issues that can affect the failure of composite engineering structures, and which cannot be taken into account using conventional approaches to predicting laminate failure:

- Given that in the construction sector bending loading modes are extremely important (e.g. the loading of bridges), it should be noted that conventional failure criteria do not involve bending loads, but require the application of a failure criterion locally within a component. The effects of bending loads were not in fact considered in the Failure Exercise [1] and no guidance is available to engineers, although a method has been developed to predict progressive ply crack formation for combined tensile and bending loads (see for example [2]).
- Failure envelopes, that account for the effects of multi-axial loading on failure, are defined by applying failure criteria to multi-axial stress states without a proper consideration of thermal residual stresses, nor the micro-mechanisms of local damage that contribute to failure. The failure event (however it is defined) in a composite structure is in fact determined by the progressive occurrence and interaction of some or all of the many micro-mechanisms of damage, such as matrix cracking, delamination, fibre fracture and fibre/matrix debonding.
- Failure envelopes are not necessarily the best design methodology for engineers, as the path taken to reach a final multi-axial stress state can affect the failure event. This is because variations of path dependencies will lead to differing initiation and growth of damage prior to the occurrence of failure.
- The prediction of failure under monotonic loading is not necessarily the critical factor determining design criteria. For example, when designing against fatigue damage, the safest and easiest approach is to develop design methods that avoid the formation of any damage that would then lead to the growth of further damage

during fatigue loading. This is also a case of practical importance in monotonic loading design situations, as structural failure in pressure vessels and pipelines can often be taken as the first occurrence of leakage paths arising from ply cracking.

- Environmental considerations also have an important influence on the failure of glass fibre reinforced composites due to stress-corrosion mechanisms that degrade the properties of fibres leading to time-dependent failures. The key issue for this case is being able to use physically based models to estimate the lifetimes of composite coupons, and the time dependence of the residual strength. It is worth noting that ply crack formation can promote the ingress of the environment, and laminates can be designed to avoid such a damage mode.

It is clear that the physically-based prediction of the failure of a composite component is very complex and cannot easily be handled just by the application of a testing programme to generate failure envelopes by gathering data in loading situations that might not be relevant to most composite engineering structures. It is concluded that an approach to composite failure that is not based on the physical mechanisms of material degradation is very unlikely to be of general applicability in engineering design. The remainder of this paper will focus on ply crack formation in laminates and its relationship to laminate failure, as the above discussion has illustrated its importance to a variety of failure modes.

PLY CRACK FORMATION AND ITS RELATIONSHIP TO STRENGTH

In references [2, 4] it was shown that ply crack development during loading (in the absence of shear deformation) is most easily understood by introducing a macroscopic damage parameter D defined by

$$D = \frac{1}{\overline{E}_A} - \frac{1}{\overline{E}_A^o} . \tag{1}$$

In (1) the parameter $\overline{E}_A$ is the effective axial modulus of a laminate (constrained so that in-plane shear strain is zero) having ply cracks in 90° plies, while $\overline{E}_A^o\ (>\overline{E}_A)$ is the corresponding value for the same laminate without ply cracks. Clearly D is zero when the laminate is undamaged. It has been shown [2, 4] that the following relations define, in terms of D, the values of the various thermoelastic constants of a damaged laminate which are satisfied for ANY state of cracking in the 90° plies of a general symmetric laminate (see [2] for formal definitions of the various effective thermoelastic constants)

$$\frac{1}{\overline{E}_t} - \frac{1}{\overline{E}_t^o} = (k')^2 D , \quad \frac{1}{\overline{E}_A} - \frac{1}{\overline{E}_A^o} = D , \quad \frac{1}{\overline{E}_T} - \frac{1}{\overline{E}_T^o} = k^2 D , \tag{2}$$

$$\frac{\overline{\nu}_t^o}{\overline{E}_T^o} - \frac{\overline{\nu}_t}{\overline{E}_T} = k k' D , \quad \frac{\overline{\nu}_A^o}{\overline{E}_A^o} - \frac{\overline{\nu}_A}{\overline{E}_A} = k D , \quad \frac{\overline{\nu}_a^o}{\overline{E}_A^o} - \frac{\overline{\nu}_a}{\overline{E}_A} = k' D , \tag{3}$$

$$\overline{\alpha}_t - \overline{\alpha}_t^o = k' k_1 D , \quad \overline{\alpha}_A - \overline{\alpha}_A^o = k_1 D , \quad \overline{\alpha}_T - \overline{\alpha}_T^o = k k_1 D . \tag{4}$$

In the above inter-relationships the parameters k, k′ and k_1 are constants for undamaged laminates defined by (see [2, 4] for details)

$$k_1 = \frac{\bar{E}_A^o\left[\bar{\alpha}_A^o + B\bar{\alpha}_T^o - C\right]}{1 - \bar{\nu}_A^o B}, \quad k = \frac{\bar{E}_A^o}{\bar{E}_T^o}\frac{B - \bar{\nu}_A^o\frac{\bar{E}_T^o}{\bar{E}_A^o}}{1 - \bar{\nu}_A^o B}, \quad k' = \frac{\bar{E}_A^o A - \bar{\nu}_a^o - \bar{\nu}_t^o\frac{\bar{E}_A^o}{\bar{E}_T^o}B}{1 - \bar{\nu}_A^o B}, \quad (5)$$

where A, B and C are defined by the basic properties of individual plies (in italics)

$$A = \frac{\nu_t}{E_T} + \frac{\nu_a \nu_A}{E_A}, \qquad B = \nu_A, \qquad C = \alpha_T + \nu_A \alpha_A . \quad (6)$$

If $\bar{E}_A$ is *measured* during damage development then in principle the values of the parameters $\bar{E}_t$, $\bar{E}_T$, $\bar{\nu}_t$, $\bar{\nu}_a$, $\bar{\nu}_A$, $\bar{\alpha}_t$, $\bar{\alpha}_A$ and $\bar{\alpha}_T$ can be deduced using the relations (2-4) which are expected to be exact within the assumptions of linear elasticity, stress-free cracks and homogeneous damage at the macroscopic scale. Also if wanting to evaluate the effects of damage formation in a structure using FEA, the relations (2-4) provide a reliable method of locally degrading the properties provided the relationship is known between the effective axial modulus $\bar{E}_A$ and the ply crack distribution.

Ply cracking damage in the 90° plies of a length 2L of laminate is defined by $\{L_1, L_2, \ldots L_n\}$ where n is the number of cracks in length 2L of the 90° plies and where L_I, I = 1...n denote the distances between neighbouring cracked planes. For this case the energy absorption per unit volume for length 2L of laminate is given by

$$\Gamma = \frac{h^{(90)}}{hL}\sum_{j=1}^{M}\delta_j \gamma_j^{(90)} , \quad (7)$$

where $2h^{(90)}$ is the total thickness of all 90° plies in the laminate having total thickness 2h, and where M is the number of potential cracking sites in 90° plies which are ordered in a regular way, e.g. from top to bottom in the plies which are taken in order from the centre of the laminate to the outside, symmetry about the mid-plane of the laminate being assumed. The quantity $2\gamma_j^{(90)}$ is the fracture energy for the jth potential cracking site of the 90° plies. The parameters δ_j describe the crack pattern in the laminate such that $\delta_j = 1$ if the jth site of the 90° ply is cracked and $\delta_j = 0$ otherwise.

Consider progressive cracking between two distinct damage states 1 and 2 having ply crack patterns defined by:

$$\text{State 1} = \{L_1, L_2, \ldots L_n\}, \qquad \text{State 2} = \{L_1, L_2, \ldots L_{n+1}\},$$

and leading to energy absorptions Γ_1 and Γ_2 respectively. It has been shown [2, 4] that the loading conditions (in the absence of shear deformation) required for an additional ply crack to form, are specified by the inequality

$$s > \sqrt{\frac{2\left[\Gamma_2 - \Gamma_1\right]}{\frac{1}{\bar{E}_A^{(2)}} - \frac{1}{\bar{E}_A^{(1)}}}} + s_c, \quad n \geq 0, \quad \text{where } s = k'\sigma_t + \sigma + k\sigma_T . \quad (8)$$

The parameter s is an effective stress that takes full account of the triaxial loading of a general symmetric laminate in the absence of shear loading. The parameter $s_c = -\bar{k}_1 \Delta T$ has the property that when $s = s_c$ the axial stress in the 90° plies of an undamaged laminate is zero. It is also the stress at which the ply cracks in the 90° plies of a damaged laminate

are *just* closed. It is emphasised that the term s_c appearing in (8) takes full account of the effects of thermal residual stresses in the laminate.

When using (7) and (8) to investigate crack formation, the fracture energies $2\gamma_j^{(90)}$ are taken at random from a statistical distribution of fracture energies (normal distribution assumed) and then allocated at random to the various potential fracture sites in the 90° plies. The values of the applied stresses are then regarded as slowly increasing until the fracture condition (8) can be met at one of the potential fracture sites in the laminate. This means that crack formation, for every stage of loading, must be investigated at all remaining potential cracking sites in order to determine the location of the next crack to form. This procedure, carried out using a computer, has to be repeated for every new ply crack that forms during loading. Ply cracking predictions for general symmetric laminates can be made using a new user-friendly software system PREDICT [5], and all predictions presented in this paper have been made using this very useful tool.

When making predictions for first ply failure in CFRP(T300/976) laminates it has been assumed [3] that the basic ply thickness in all laminates is 0.132 mm and the temperature difference between the test temperature and the stress-free temperature of all laminates is -125°C. It has also been assumed that fracture energy (i.e. energy release rate) for each potential ply crack formation site is 157.5 J/m^2, so that the standard deviation of the fracture energy distribution is taken to be zero. The plies are subdivided into 5 layers of equal thickness to increase model accuracy. The laminate length is taken to be 100 mm and the number of potential ply crack formation sites is taken as 200. For the $[45_n/-45_n]_s$ and $[60_n/-60_n]_s$ laminates, ply cracking is assumed to occur in the outer ply as such cracking can occur at a lower stress than that needed to crack the inner ply. Such ply cracking is mixed mode, but no account has been taken of this when predicting damage progression.

The results of predictions, using the model described above, for first ply failure stress are given in Table 1 where, for the $[45_n/-45_n]_s$ and $[60_n/-60_n]_s$ laminates, first ply failure stress is seen to be always less than the measured strength, as expected. This is not the case for the $[30_n/-30_n/90_{n/2}]_s$ laminate as other damage modes, which are not modelled (such as delamination and fibre failure), can lead to failure before ply cracking is initiated. For the $[60_n/-60_n]$ laminates, the first ply failure stress is very close to the measured strength indicating that first ply failure is a very good indicator of laminate strength. It is seen that the trend predicted by the first ply failure predictions follows those of the strength. The key result is that the first ply failure stress and laminate strength both decrease as the ply thickness is increased. First ply failure predictions thus have good potential for predicting the ply thickness dependencies of strength, assuming that the strength for at least one ply thickness has been measured. Similar predictions for first ply failure in quasi-isotropic laminates are made to investigate the effect of ply lay-up, as seen from the results shown in Table 2 where an asterisk is attached if the first ply failure stress exceeds the measured strength. This situation can arise if additional damage modes (that are not being modelled) are occurring, such as delaminations.

The model predictions in Table 3 are for a different type of CFRP laminate (ply thickness 0.25 mm) where the results in brackets are normalised measured 'strengths' and predicted first ply failure stresses with respect to the results for laminate C that exhibits the largest 'strength' and the largest first ply failure stress. It should be noted that the ranking of the laminates according to 'strength' is the same that would result if ranked according to first ply failure stress. It is again seen that when the first ply failure stress is less than the measured strength, the predictions follow the same trends as the

measurements, and the key result here is that the first ply failure stress and the laminate strength depend similarly on the ply lay-up. Another key result demonstrated by the results of Tables 2 and 3 is that the placing of a 90° ply adjacent to the mid-plane, or at the free surface, clearly lowers the first ply failure stress and/or the laminate strength.

CONCLUSIONS

On the basis of comparing with some experimental results model predictions of first ply failure in general symmetric laminates, it is concluded that:

1. Experimental strength measurements for a variety of laminates indicate that there are thickness and ply lay-up dependencies that are ignored when applying conventional failure criteria.
2. Initial ply failure should be modelled using an energy based approach as it leads to realistic ply thickness and lay-up effects in contrast to the 'strength of materials' methodology that does not have these practically important characteristics.
3. The location of 90° plies in a symmetric laminate should avoid being adjacent to the mid-plane, or at the free surface, as it leads to a lowering of the strength and/or first ply failure stress.
4. For carbon fibre composites subject to loading likely to cause ply cracking, the first ply failure stress could usefully be the basis of a criterion for failure. The adoption of such an approach is practical due to the existence of a new software tool to assist with its implementation, and the approach would be of benefit also to engineering components that need to be resistant to fatigue loading and environmental exposure.

ACKNOWLEDGEMENT

The work described in this paper was supported by the Materials Measurement Programme of the Department of Trade and Industry, UK. Airbus is acknowledged for permission to use the experimental results shown in Table 3.

REFERENCES

1. P D Soden, M J Hinton & A S Kaddour, 'Lamina properties, lay-up configurations and loading conditions for a range of fibre reinforced composite laminates', *Comp. Sci. Tech.*, 1998, **58**, 1011-1022, and other papers in the same special issue. Part B of the exercise is published in *Comp. Sci. Tech.* 2002, **62**, 1479-1797.
2. L N McCartney, 'Physically based damage models for laminated composites', *Proc. Instn. Mech. Engrs.* 2003, **217**, Part L: J. Materials: Design & Applications, 163-199.
3. P Johnson and F-K Chang, 'Characterisation of matrix crack induced laminate failure - Part I: Experiments'. *J. Comp. Mater.* 2001, **35**, 2009-2035. Part II: Analysis and verifications, **35**, 2037-2073.
4. L N McCartney, 'Model to predict effects of triaxial loading on ply cracking in general symmetric laminates', *Comp. Sci. Tech.* 2000, **60**, 2255-2279. (see Errata in *Comp. Sci. Tech.* 2002, **62**, 1273-1274).
5. Software system 'PREDICT' which is a specific module of CoDA.
(see http://www.npl.co.uk/npl/cmmt/cog/coda.html)

DYNAMIC RESPONSE OF INITIALLY STRESSED COMPOSITE SANDWICH PLATES

A.K. Nayak, R.A. Shenoi, S.S.J. Moy
University of Southampton, Highfield, Southampton S017 1BJ, U.K.

ABSTRACT

A new finite element formulation is developed to model the transient response of isotropic, laminated composite and sandwich plates under the effect of initial stresses. A four node shear deformable assumed strain plate bending element is formulated based on a refined third order theory. The new plate bending element is validated by comparison with earlier published results in the literature. The results from the present investigation could serve as benchmark for future investigators.

1 INTRODUCTION

Composite materials consist of two or more materials, which together produce desirable properties that can not be achieved with any of the constituents alone. The feasibility of having different lamination scheme and different material properties of each individual lamina provide an added flexibility to designers to tailor the stiffness and strength of the laminate to match the structural requirements of specific applications. A sandwich structure consists of three distinct layers (i.e. the top face, the core and the bottom face) which are bonded together to form an efficient load carrying assembly. The greatest advantage with sandwich construction compared to solid laminates is that the strength and stiffness are increased without a corresponding increase in the weight. During their build and fabrication, sandwich structures are subjected to various edge loads which can lead quickly to failure. Hence it is very important to study the effect of inplane loads on the transient response of composite sandwich plates.

There has been a great deal of interest recently to study the behaviour of sandwich structures under a variety of static and dynamic loading environments [1-4]. Reismann and Tendorf [5] employed the Mindlin plate theory [1-4] to investigate the dynamic response of a plate under the uniform in-plane load. Khdeir and Reddy [6] studied the transient response of symmetric cross-ply laminates with the application of the method of orthogonality of principal modes and the state variable technique. A comparative study of the classical plate theory based on the Kirchoff-Love hypothesis, Mindlin plate theory and third-order theory was presented to illustrate the effect of shear deformation in the analysis of thick composite plates. Noor et al [7] presented the three dimensional results on the buckling analysis of initially stressed composite sandwich plates. Currently there is no exact result available in the literature on the transient analysis of initially stressed laminated and composite sandwich plates.

Chen and Sun [8] analysed the transient response of initially stressed laminated composite plates using a selectively reduced integrated nine node plate bending element based on the first order shear deformation theory with constant shear correction factors. More recently Nayak et al [9-12] developed Lagrange plate bending elements based on a refined third order theory. The developed plate bending elements are free from any major

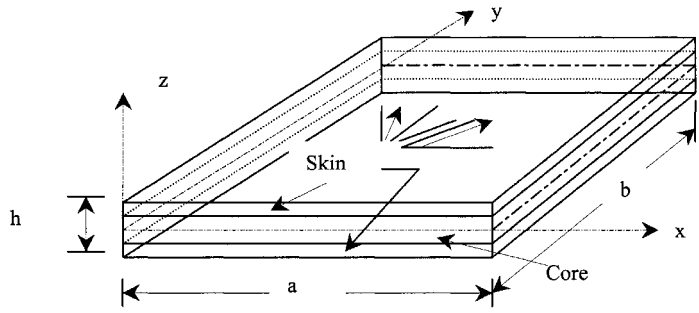


Figure 1: Sandwich plate geometry with laminate reference axes, and fibre orientation

defects like the parasitic spurious zero energy modes and shear locking due to the use of the assumed strain approach. Due to the cubic expansion of inplane displacements in the thickness coordinate and linear expansion of transverse displacement, there is no need for shear correction factors. The use of full integration to evaluate the terms in the energy expressions makes the procedure very straightforward.

The purpose of the present research is to study the transient response of composite sandwich plates under the influence of inplane loads which frequently arise in practice due to the manufacturing processes and assembly techniques. It appears from a literature review that the study on this subject is very scarce. A new four node assumed strain plate bending element is formulated to include the effect of initial stresses in the dynamic analysis of plates. The results from the present investigation could serve as benchmark for future investigators.

2 FORMULATION OF THE PROBLEM

The present higher-order shear deformation theory [9-12] is developed on the basis of the assumed displacement field in the following form (see Figure 1):

$$u_\alpha = u_\alpha^o + z\psi_\alpha - \frac{4z^3}{3h^2}\phi_\alpha \qquad w = w^o \tag{1}$$

where the superscript zero denotes the middle surface displacements; ψ_α are the rotations about the α axes; ϕ_α are the warping functions; h is the thickness of the plate; Greek subscripts range on x and y; u_α are the displacements of a point in the α axes; and w is the displacement in the z direction.

The strain-displacement relations of the higher-order theory are obtained from Equation (1) which can be stated as

$$\varepsilon_{\alpha\beta} = \varepsilon^o_{\alpha\beta} + z\kappa^o_{\alpha\beta} + z^3\kappa^2_{\alpha\beta} \quad \varepsilon^o_{\alpha\beta} = \frac{1}{2}\left(u^o_{\alpha,\beta} + u^o_{\beta,\alpha}\right) \quad \kappa^o_{\alpha\beta} = \frac{1}{2}\left(\psi_{\alpha,\beta} + \psi_{\beta,\alpha}\right) \quad \gamma = \gamma^s_\alpha + z^2\kappa^s_\alpha$$

$$\kappa^2_{\alpha\beta} = \frac{1}{2}\left(\frac{-4}{3h^2}\right)\left(\psi_{\alpha,\beta} + \psi_{\beta,\alpha}\right) \quad \gamma^s_\alpha = 2\varepsilon_{\alpha z} = w_{,\alpha} + \psi_\alpha \quad \kappa^s_\alpha = \left(\frac{-4}{h^2}\right)\phi_\alpha \tag{2}$$

where a comma denotes partial differentiation and repeated indices imply summation.

The stress-strain relations for the lamina in the laminate coordinates (x, y, z) are given by

$$\sigma_{xx} = \overline{Q}_{11}\varepsilon_{xx} + \overline{Q}_{12}\varepsilon_{yy} + 2\overline{Q}_{16}\varepsilon_{xy} \quad \sigma_{yy} = \overline{Q}_{12}\varepsilon_{xx} + \overline{Q}_{22}\varepsilon_{yy} + 2\overline{Q}_{26}\varepsilon_{xy}$$
$$\sigma_{xy} = \overline{Q}_{16}\varepsilon_{xx} + \overline{Q}_{26}\varepsilon_{yy} + 2\overline{Q}_{66}\varepsilon_{xy} \quad \sigma_{xz} = 2\overline{Q}_{55}\varepsilon_{xz} + 2\overline{Q}_{54}\varepsilon_{yz} \quad \sigma_{yz} = 2\overline{Q}_{45}\varepsilon_{xz} + 2\overline{Q}_{44}\varepsilon_{yz} \tag{3}$$

where $\overline{Q}_{ij}$ are the transformed, plane stress reduced elastic stiffness coefficients [9-12], which is given as,

$$\overline{Q}_{11} = Q_{11}c^4 + 2(Q_{12} + 2Q_{66})c^2s^2 + Q_{22}s^4 \quad \overline{Q}_{12} = (Q_{11} + Q_{22} - 4Q_{66})c^2s^2 + Q_{12}(c^4 + s^4)$$
$$\overline{Q}_{16} = (Q_{11}c^2 + (Q_{12} + 2Q_{66})(s^2 - c^2) - Q_{22}s^2)cs$$
$$\overline{Q}_{22} = Q_{11}s^4 + 2(Q_{12} + 2Q_{66})c^2s^2 + Q_{22}c^4$$
$$\overline{Q}_{26} = (Q_{11}s^2 + (Q_{12} + 2Q_{66})(c^2 - s^2) - Q_{22}c^2)cs$$
$$\overline{Q}_{66} = (Q_{11} + Q_{22} - 2Q_{12})c^2s^2 + Q_{66}(c^2 - s^2)^2 \tag{4}$$

where $[Q_{ij}]_k$ is the constitutive matrix at the lamina level; $c = \cos\theta$; $s = \sin\theta$; θ is the angle between the lamina x axis and lamina principal x_i axis. $Q_{11} = E_1/(1 - \nu_{12}\nu_{21})$, $Q_{12} = (\nu_{12}E_2)/(1 - \nu_{12}\nu_{21})$, $Q_{22} = E_2/(1 - \nu_{12}\nu_{21})$, $Q_{66} = G_{12}$, $Q_{55} = G_{13}$, $Q_{44} = G_{23}$ in which E_i is x_i axis elastic modulus; ν_{ij} is the *i-j* plane Poisson ratio; G_{ij} is the *i-j* plane shear modulus.

The equations of motion associated with the displacement field in Equation (1) are

$$N_{xx,x} + N_{xy,y} = I_1\ddot{u}_x^o + I_2\ddot{\psi}_x + \left(-\frac{4}{3h^2}\right)I_4\ddot{\phi}_x$$
$$N_{xy,x} + N_{yy,y} = I_1\ddot{u}_y^o + I_2\ddot{\psi}_y + \left(-\frac{4}{3h^2}\right)I_4\ddot{\phi}_y$$
$$Q_{xx,x} + Q_{yy,y} + q + \overline{N}_{xx}w^o{}_{,xx} + 2\overline{N}_{xy}w^o{}_{,xy} + \overline{N}_{yy}w^o{}_{,yy} = I_1\ddot{w}^o$$
$$M_{xx,x} + M_{xy,y} - Q_{xx} = I_2\ddot{u}_x^o + I_3\ddot{\psi}_x + \left(-\frac{4}{3h^2}\right)I_5\ddot{\phi}_x \tag{5}$$
$$M_{xy,x} + M_{yy,y} - Q_{yy} = I_2\ddot{u}_y^o + I_3\ddot{\psi}_y + \left(-\frac{4}{3h^2}\right)I_5\ddot{\phi}_y$$
$$\left(-\frac{4}{3h^2}\right)(P_{xx,x} + P_{xy,y}) + \frac{4R_{xx}}{h^2} = \left(-\frac{4}{3h^2}\right)I_4\ddot{u}_x^o + \left(-\frac{4}{3h^2}\right)I_5\ddot{\psi}_x + \left(\frac{16}{9h^4}\right)I_7\ddot{\phi}_x$$
$$\left(-\frac{4}{3h^2}\right)(P_{yy,y} + P_{xy,x}) + \frac{4R_{yy}}{h^2} = \left(-\frac{4}{3h^2}\right)I_4\ddot{u}_y^o + \left(-\frac{4}{3h^2}\right)I_5\ddot{\psi}_y + \left(\frac{16}{9h^4}\right)I_7\ddot{\phi}_y$$

The various stress resultants are given by

$$N = [A]\varepsilon_{\alpha\beta}^o + [B]\kappa_{\alpha\beta}^o + [E]\kappa_{\alpha\beta}^2 \quad M = [B]\varepsilon_{\alpha\beta}^o + [D]\kappa_{\alpha\beta}^o + [F]\kappa_{\alpha\beta}^2$$
$$P = [E]\varepsilon_{\alpha\beta}^o + [F]\kappa_{\alpha\beta}^o + [H]\kappa_{\alpha\beta}^2 \quad Q = [A]^s\gamma_\alpha^s + [D]^s\kappa_\alpha^s \quad R = [D]^s\gamma_\alpha^s + [F]^s\kappa_\alpha^s \tag{6}$$

where

$$N = (N_{xx} \quad N_{yy} \quad N_{xy})^T \quad M = (M_{xx} \quad M_{yy} \quad M_{xy})^T$$
$$P = (P_{xx} \quad P_{yy} \quad P_{xy})^T \quad Q = (Q_{xx} \quad Q_{yy})^T \quad R = (R_{xx} \quad R_{yy})^T$$
$$(A_{ij}, B_{ij}, D_{ij}, E_{ij}, F_{ij}, H_{ij}) = \sum_{k=1}^{N}\int_{z_{k-1}}^{z_k}(\overline{Q}_{ij})_k(1, z, z^2, z^3, z^4, z^6)dz \quad (i, j = 1,2,6)$$

$$\left(A_{ij}^s, D_{ij}^s, F_{ij}^s\right) = \sum_{k=1}^{N} \int_{z_{k-1}}^{z_k} (\overline{Q}_{ij})_k \left(1, z^2, z^4\right) dz \quad (i, j = 5,4) \tag{7}$$

The inertias I_i (i= 1,2,3,4,5,7) are defined by

$$\left(I_1, I_2, I_3, I_4, I_5, I_7\right) = \sum_{k=1}^{N} \int_{z_{k-1}}^{z_k} \rho_k \left(1, z, z^2, z^3, z^4, z^6\right) dz \tag{8}$$

In Equation (5), $\overline{N}_{xx}$, $\overline{N}_{yy}$ and $\overline{N}_{xy}$ denote the applied edge loads.

The principle of virtual work equation can be obtained from Equations (5) to (8) in the following form

$$\int_0^t \int_A (\delta\varepsilon_{\alpha\beta}^{o\,T}[A]\varepsilon_{\alpha\beta}^o + \delta\varepsilon_{\alpha\beta}^{o\,T}[B]\kappa_{\alpha\beta}^o + \delta\varepsilon_{\alpha\beta}^{o\,T}[E]\kappa_{\alpha\beta}^2 + \delta\kappa_{\alpha\beta}^{o\,T}[B]\varepsilon_{\alpha\beta}^o + \delta\kappa_{\alpha\beta}^{o\,T}[D]\kappa_{\alpha\beta}^o + \delta\kappa_{\alpha\beta}^{o\,T}[F]\kappa_{\alpha\beta}^2 +$$

$$\delta\kappa_{\alpha\beta}^{2\,T}[E]\varepsilon_{\alpha\beta}^o + \delta\kappa_{\alpha\beta}^{2\,T}[F]\kappa_{\alpha\beta}^o + \delta\kappa_{\alpha\beta}^{2\,T}[H]\kappa_{\alpha\beta}^2 + \delta\gamma_\alpha^{s\,T}[A^s]\gamma_\alpha^s + \delta\gamma_\alpha^{s\,T}[D^s]\kappa_\alpha^s + \delta\kappa_\alpha^{s\,T}[D^s]\gamma_\alpha^s +$$

$$\delta\kappa_\alpha^{s\,T}[F^s]\kappa_\alpha^s) dA dt +$$

$$\int_0^t \int_A q dw^o dA dt + \int_0^t \int_A [G]^T \overline{[N]}[G] dA dt = \int_0^t \int_A [I_1(\ddot{u}_x^o \delta u_x^o + \ddot{u}_y^o \delta u_y^o + \ddot{w}^o \delta w^o) +$$

$$I_2(\ddot{\psi}_x \delta u_x^o + \ddot{\psi}_y \delta u_y^o + \ddot{u}_x^o \delta\psi_x + \ddot{u}_y^o \delta\psi_y) + \left(-\frac{4I_4}{3h^2}\right)(\ddot{\phi}_x \delta u_x^o + \ddot{\phi}_y \delta u_y^o + \ddot{u}_x^o \delta\phi_x + \ddot{u}_y^o \delta\phi_y) +$$

$$\left(-\frac{4I_5}{3h^2}\right)(\ddot{\psi}_x \delta\phi_x + \ddot{\psi}_y \delta\phi_y + \ddot{\phi}_x \delta\psi_x + \ddot{\phi}_y \delta\psi_y) + I_3(\ddot{\psi}_x \delta\psi_x + \ddot{\psi}_y \delta\psi_y) +$$

$$\left(\frac{16I_7}{9h^4}\right)(\ddot{\phi}_x \delta\phi_x + \ddot{\phi}_y \delta\phi_y)] dA dt \tag{9}$$

where $[G] = \begin{bmatrix} w^o{}_{,x} & w^o{}_{,y} \end{bmatrix}^T$ and $\overline{[N]}$ is a matrix containing the inplane edge loads. Note that for implementation purpose, γ_α^s in Equation (9) is replaced by $\bar{\gamma}_\alpha^s$ where $\bar{\gamma}_\alpha^s$ is the substitute shear strains to remove spurious zero energy modes as mentioned in References [9-12].

3 FINITE ELEMENT APPROXIMATION

A four node isoparametric quadrilateral displacement finite element is developed on the basis of a refined higher-order plate theory as discussed in the previous section. The element displacement function approximations can be expressed as

$$u_\alpha^o = \langle N_1, N_2, N_3, N_4 \rangle \langle u_{\alpha 1}, u_{\alpha 2}, u_{\alpha 3}, u_{\alpha 4} \rangle \quad w = \langle N_1, N_2, N_3, N_4 \rangle \langle w_1, w_2, w_3, w_4 \rangle$$

$$\psi_\alpha = \langle N_1, N_2, N_3, N_4 \rangle \langle \psi_{\alpha 1}, \psi_{\alpha 2}, \psi_{\alpha 3}, \psi_{\alpha 4} \rangle \quad \phi_\alpha = \langle N_1, N_2, N_3, N_4 \rangle \langle \phi_{\alpha 1}, \phi_{\alpha 2}, \phi_{\alpha 3}, \phi_{\alpha 4} \rangle \tag{10}$$

where N_i are the shape functions. The shape functions and their derivatives are expressed as

$$N_i = \frac{1}{4}(1 + \xi\xi_i)(1 + \eta\eta_i) \quad \frac{\partial N_i}{\partial \xi} = \frac{1}{4}\xi_i(1 + \eta\eta_i) \quad \frac{\partial N_i}{\partial \eta} = \frac{1}{4}\eta_i(1 + \xi\xi_i) \tag{11}$$

where ξ and η are the natural co-ordinates. The generalized mid-surface strains at any point in the element 'e' from Equation (2) can be expressed in terms of nodal displacements as follows:

$$\varepsilon_{\alpha\beta}^{o\,(e)} = [B_\varepsilon^o]^{(e)}\{\delta\}_{(e)} \quad \kappa_{\alpha\beta}^{o\,(e)} = [B_\kappa^o]^{(e)}\{\delta\}_{(e)} \quad \kappa_{\alpha\beta}^{2(e)} = [B_\kappa^2]^{(e)}\{\delta\}_{(e)}$$
$$\bar{\gamma}_\alpha^{\,s(e)} = [\bar{B}_\varepsilon^s]^{(e)}\{\delta\}_{(e)} \quad \kappa_\alpha^{\,s(e)} = [B_\kappa^s]^{(e)}\{\delta\}_{(e)} \tag{12}$$

where $[B_\varepsilon^o]$, $[B_\kappa^o]$, $[B_\kappa^2]$, $[\bar{B}_\varepsilon^s]$ and $[B_\kappa^s]$ are generated strain-displacement matrices, $\{\delta\}_e^T$ is the element degrees of freedom. For arbitrary value of virtual displacements, the global dynamic equation can be formed from Equation (9) as

$$[M]\{\ddot{\Delta}\} + [K]\{\Delta\} = \{F\} + \lambda_b[K_g]\{\Delta\} \tag{13}$$

Here the unknown vector $\{\Delta\}$ is generated by the assemblage of element degrees of freedom $\{\delta\}_e^T$, e=1,....,total degrees of freedom in the region R. λ_b denotes the buckling parameter (a function of the applied loads $\overline{N_{xx}}$, $\overline{N_{yy}}$ or $\overline{N_{xy}}$). The assembled stiffness, mass, buckling and force matrices for the dynamic analysis are

$$[K] = \sum_e \int_{A_e} [[B_\varepsilon^o]^T[A][B_\varepsilon^o] + [B_\varepsilon^o]^T[B][B_\kappa^o] + [B_\varepsilon^o]^T[E][B_\kappa^2] + [B_\kappa^o]^T[B][B_\varepsilon^o] + [B_\kappa^o]^T[D][B_\kappa^o] +$$
$$[B_\kappa^o]^T[F][B_\kappa^2] + [B_\kappa^2]^T[E][B_\varepsilon^o] + [B_\kappa^2]^T[F][B_\kappa^o] + [B_\kappa^2]^T[H][B_\kappa^2] + [\bar{B}_\varepsilon^s]^T[A^s][\bar{B}_\varepsilon^s] +$$
$$[\bar{B}_\varepsilon^s][D^s][B_\kappa^s] + [B_\kappa^s]^T[D^s][\bar{B}_\varepsilon^s] + [B_\kappa^s]^T[F^s][B_\kappa^s]]dA \tag{14}$$

$$[M] = \sum_e \int_{A_e} [N]^T[M_I][N]dA \tag{15}$$

$$[K_g] = \sum_e \int_{A_e} [X]^T[\overline{N}][X]dA \tag{16}$$

$$\{F\} = \sum_e \int_{A_e} [N]^T\{q\}dA \tag{17}$$

where $[X] = \begin{bmatrix} N_{,x} & N_{,y} \end{bmatrix}^T$, $[M_I]$ is the mass matrix containing inertia terms and $\{F\}$ is the column vector containing the boundary and body force contributions. The Newmark direct integration method [12] is employed to integrate the terms in the energy expression. The parameters used in the Newmark integration scheme correspond to the constant average acceleration method.

4 NUMERICAL EXAMPLES

In this section, some of the examples involving transient analysis of isotropic, laminated and sandwich plates are discussed. Some of the results are also reported by other authors in the literature. The types of forcing functions used presently can be found in Reference [13].

Example 1: Transient analysis of initially stressed isotropic plate

This example is one of the most widely used test examples in the transient analysis. Reismann and Tendorf investigated the dynamic response of an isotropic plate under the uniform in-plane load $P_x = \overline{N}_x$ using the Mindlin plate theory. The same numerical example is taken as a test case to validate the new plate bending element. The example involves a rectangular isotropic plate of length a, width b, and thickness h, having simply supported edges and subjected to a sudden transverse load of intensity q over a square subregion of side $\bar{a}$ located at the center of the plate. The material properties and the

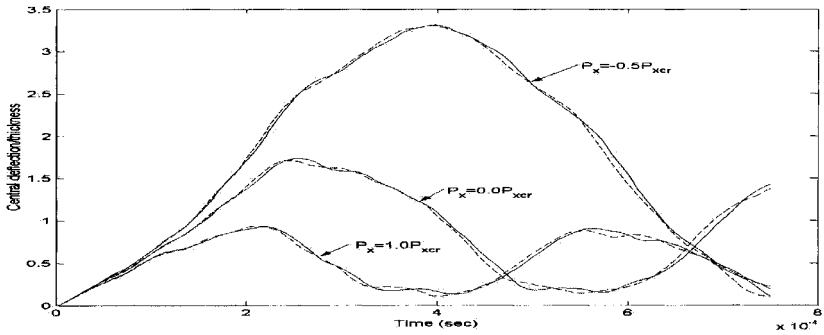


Figure 2: Comparison of the central deflection of the rectangular, isotropic plate subjected to various initial stresses using the present finite element formulation and results from the Mindlin theory ; _____ Reismann and Tendorf ; ---------- Present 4.

parameters of the plate are as follows: $a=20,\ b=28.28,\ h=2.0,\ \bar{a}=4,\ E=216.0e05\ \ \nu = 0.30\ \ \rho = 7.96\ e\text{-}05\ \ q=2.94e05$. A mesh density of 8×10 in a quarter of the plate is used. The time step is taken as 2.5 microsecond. The comparative results from the present formulation and Reismann and Tendorf are shown in Figure 2 where the solid line represents the results from Reismann and Tendorf and the dashed line represents the results from the higher order formulation. As seen from the Figure, the present formulation gives closer agreement with the analytical solution [5].

Example 2: Transient Analysis of initially stressed laminated composite plates (0/90/0)

This example deals with the transient analysis of simply supported square composite plates (0/90/0) for which an analytical solution is available. Since exact results are difficult to obtain for laminated composite plates, the analytical solution given by Khdeir and Reddy [6] serves as benchmark results for validation studies. The following geometrical and material properties are used: $a=b=5h$ and $h=0.1524m,\ E_1=172.369\ GPa,\ E_2=6.895\ GPa,\ G_{12}=G_{13}=3.448\ GPa,\ G_{23}=1.379\ GPa,\ \nu_{12}=0.25,\ \rho=1603.03\ kg/m^3$. The intensity of the transverse load is taken to be $q_o=68.9476\ MPa$. The transverse load $q(x,y,t)$ is given by $q_o F(t)\sin\left(\pi x/a\right)\sin\left(\pi y/b\right)$ where $F(t)$ is for step loading: 1 $0<t<t_1$ and 0 $t>t_1$. The convergence and stability criteria is discussed in detail in Reference[12]. The present results for a mesh density of 9 nodes per side in a quarter plate with 40 μ second as a time step is compared with the analytical solution [6] without the effect of initial stresses. As seen from the Figure 3, the present results are in close agreement with the analytical solution. As the plate is subjected to initial inplane compressive stresses of 0.5 P_{xcr}, the response is higher. Similarly the response is lower when it is subjected to tensile stresses. The reason for this is that the plate is stiffer when subjected to tensile stresses and less stiff when subjected to compressive stresses.

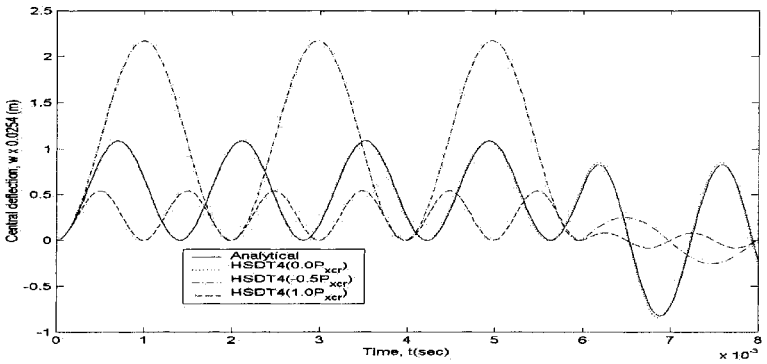


Figure 3: Variation of the central deflection as a function of time for step pulse

Example 3: Dynamic stability of composite sandwich plate $(0/90/0/90/core)_s$

After validating the present finite element formulations for isotropic and laminated composite plates under transient loading, a problem involving stability analysis of structural sandwiches with square planform, simply supported edges and cross-ply composite face sheets with ten number of layers placed symmetrically about a honeycomb titanium core for which an exact solution [7] is available is considered. The material characteristics of the face sheets and the core are given by [7]:
Face sheets:

$E_L / E_T = 19$, $G_{LT} / E_T = 0.52$, $G_{TT} / E_T = 0.338$, $\nu_{LT} = 0.32$, $\nu_{TT} = 0.49$,

Core:

$E_1 / E_T = 3.21 \times 10^{-05}, E_2 / E_T = 2.9 \times 10^{-05}, E_3 / E_T = 0.4, G_{12} / E_T = 2.4 \times 10^{-03}$,

$G_{13} / E_T = 7.9 \times 10^{-02}, G_{23} / E_T = 6.6 \times 10^{-02}, \nu_{12} = 0.99, \nu_{13} = \nu_{23} = 3 \times 10^{-05}$;

where subscript L=the direction of fibers, T=the transverse direction, subscripts *1,2,3*=the *x,y* and *z* directions: ν_{LT} = the major Poisson's ratio. The results from the quarter plate descritizations with 5,7 and 9 nodes per side are shown in Figure 4 for *a/h*=10 and 20 with $2h_f / h$ varied between 0.05 and 0.20, where h_f is the thickness of the face sheets. It can be concluded that the results are in excellent agreement with the exact solution on the refinement of the mesh densities.

Example 4: Convergence and stability check for transient response of initially stressed composite sandwich plate $(0/90/0/90/core)_s$ *under step loading*

This example deals with the transient analysis of simply supported square composite sandwich plates $(0/90/0/90/core)_s$ under step loading. The structural sandwiches considered have square planform with face sheets of eight plies of GE placed symmentrically about a polyvinyl chloride (PVC) foam core. The material characteristics of the face sheets and the core are given by:
Face sheets [12]:

E_L = *128 GPa,* E_T = 11.0 *GPa,* ν_{LT} = 0.25, $G_{LT} = G_{13} = G_{23}$ = 4.48 GPa,
$\rho_f = 1500 kg/m^3$
PVC Foam Core [12]:
E_c = 103.63 MPa, G_c = 50 MPa, ν_c = 0.32, $\rho_c = 130 kg/m^3$

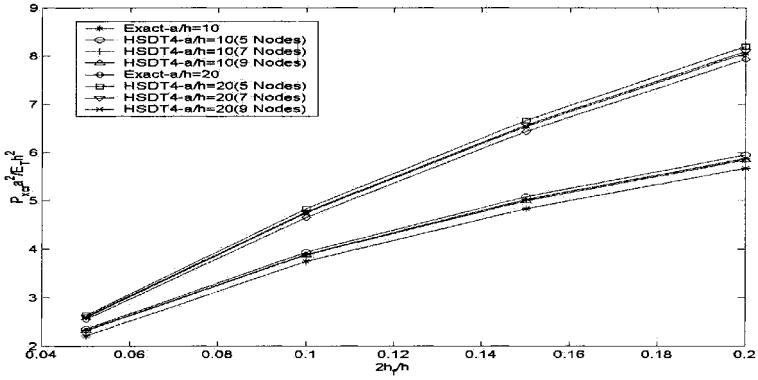


Figure 4: Critical buckling stresses $P_{xcr}a^2/E_Th^2$ for uniaxially loaded simply supported composite sandwich plates.

For this example, *a/h* is 10 and $2h_f/h$ =0.05; For step loading, t_1 is taken as 0.016. Figure 5 shows the center deflection of a simply supported composite square sandwich plate $(0/90/0/90/core)_s$ subjected to initial prestress of –0.5 P_{xcr} for different time steps under step loading. Two mesh densities (12 x 12 and 16 x 16) are considered in the quarter plate. As seen from the figure, it is clear that the solutions converge (as the mesh is refined) and are stable (as the time step is increased). For a given mesh, the solution at a given time increases with decreasing values of the time step. For remaining examples, a 12 x 12 elements mesh in the quarter plate are considered.

Example 5: Transient Analysis of a simply supported sandwich plate $(0/90/0/90/core)_s$ *under explosive blast loading*

This example deals with the transient analysis of simply supported square composite sandwich plates $(0/90/0/90/core)_s$ under explosive blast loading. The material and geometry is same as that of example 4. For explosive blast loading $F(t)$ is given by $e^{-\gamma t}$ where γ is 330 s^{-1}. The results from the present formulation is shown in Figure 6. As seen from the figure, the response is highest when the plate is subjected to failure load.

Example 6: Transient response of composite sandwich plates under various initial inplane stresses subjected to blast loading

In this example, the composite sandwich plate is subjected to various types of inplane stresses and the responses from these applied loads (-0.95 of the critical loads) are shown in Figure 7. The response is lowest when subjected to initial stresses in the x-direction. The plate shows highest response when subjected to biaxial loading. The reason for such behaviour is attributed to the degree of flexibility in the composite sandwich plates. Hence the effect of initial prestress plays an important role in the design of composite plates under transient loading conditions.

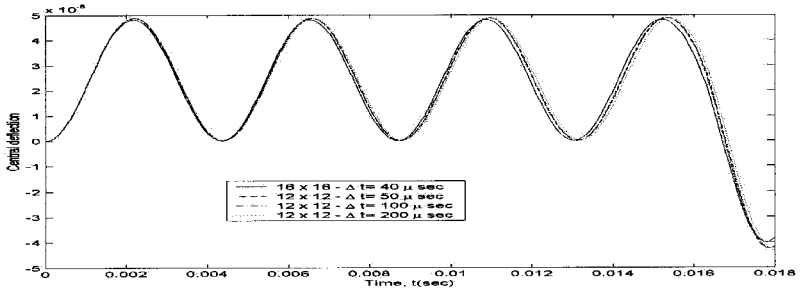


Figure 5: Stability of the Newmark algorithm for a simply supported composite sandwich plate under step loading with various time steps and mesh densities.

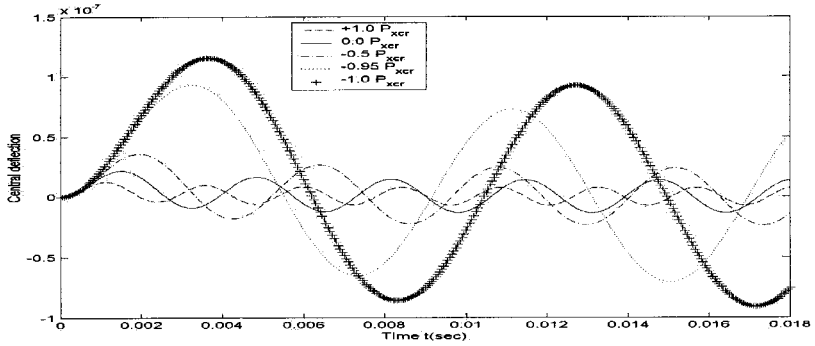


Figure 6: Central deflection of the composite sandwich plate subjected to various initial stresses.

5 CLOSURE

In this paper, transient analysis of initially stressed composite sandwich plates is carried out using the finite element method. Due to the use of the cubic expansion of the thickness coordinate in the inplane displacement and linear expansion of thickness coordinate in the transverse direction, there is no need for shear correction factors. A new four node assumed strain quadrilateral element is formulated based on a refined third order theory. Full integration scheme is carried out for all the terms in the energy formulation in the equilibrium equation which makes the procedure very clean and simple to use. Consistent

mass matrix is used to preserve the total kinetic energy. The results on isotropic, laminated and composite sandwich plates show the generic studies in the dynamic response of structures under initial prestress conditions which occurred in many practical situations. It can be concluded that the present formulation can be used to deal with any type of loading and boundary conditions.

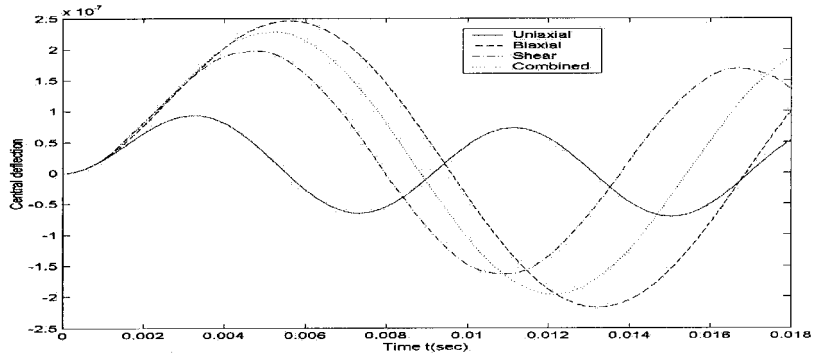


Figure 7: Central deflection of the composite sandwich plates under various initial stresses

REFERENCES

1 E Carrera , 'Historical review of Zig-Zag theories for multilayered plates and shells', *Applied Mechanics Reviews, Trans. ASME,* 2003 56(3) 287-308.

2 A K Noor, W S Burton and C W Bert , 'Computational models for sandwich panels and shells', *Applied Mechanics Reviews, Trans. ASME*, 1996 49(3) 155-199.

3 J Mackerle, 'Finite element analyses of sandwich structures: a bibliography (1980-2001)', *Engineering Computations*, 2002 19(1-2) 206-245.

4 Mallikarjuna and T Kant, 'A critical review and some results of recently developed refined theories of fiber-reinforced laminated composites and sandwiches', *Composite Structures*, 1993, 23(4), 293-312.

5 H Reismann and Z A Tendorf, 'Dynamics of initially stressed plates', *Journal of Applied Mechanics, Trans. ASME,* 1976, 304-308.

6 A A Khdeir and J N Reddy, 'Exact solutions for the transient response of symmetric cross ply laminates using a higher order plate theory', *Composite Science and Technology*, 1989 (34) 205-224.

7 A K Noor, J M Peters and W S Burton, '3-dimensional solutions for initially stressed structural sandwiches', *J. Engg. Mech., ASCE*, 1994 120(2) 284-303

8 J K Chen and C T Sun, 'Nonlinear transient responses of initially stressed composite plates', *Comput. Struct.,* 1985 21(3) 513-520.

9 A K Nayak, S S J Moy and R A Shenoi, 'Free vibration analysis of composite sandwich plates based on Reddy's higher order theory', *Composites Part B-Engineering*, 2002, 1-19.

10 A K Nayak, R A Shenoi and S S J Moy, 'Analysis of damping in composite sandwich plates using plate bending elements with substitute shear strain fields based on Reddy's higher order theory', *Proceedings of IMechE, Part C,* 2002, 1-19.

11 A K Nayak, S S J Moy and R A Shenoi, 'Quadrilateral plate bending elements for multilayer sandwich plates', *Journal of Strain Analysis,* 2003, 38(5), 377-394.

12 A K Nayak, R A Shenoi and S S J Moy, 'Transient response of composite sandwich plates', *Composite Structures, (In press),* 2003.

13 J R Vinson, *The behaviour of sandwich structures of isotropic and composite materials*, Technomic Publishing Co. Inc, USA, page 169, 1999.

NUMERICAL SIMULATION AS A TOOL FOR MANUFACTURING, FAILURE AND IMPACT PREDICTION OF TEXTILE REINFORCED COMPOSITES

Anthony K. Pickett
School of Industrial and Manufacturing Science, Cranfield University

ABSTRACT

During the past two decades Finite Element (FE) simulation techniques have been developed and are now an invaluable tool for the design and optimisation of various manufacturing processes and structural analysis. These techniques have primarily been developed for metals which are relatively simple materials to characterise. Advanced composite materials are also of great interest to a wide range of industries, including the civil engineering sector, and simulation tools to represent these materials in various forming and impact-crash situations are required. Unfortunately the complex nature of these materials makes their numerical simulation a comparatively more difficult task. This paper gives a brief overview of the current state-of-the-art for numerical simulation of draping and impact analysis and presents some new results for advanced composites applications.

INTRODUCTION

The automotive and aerospace industries, in particular, have taken advantage of numerical simulation and two notable applications are metal stamping/forming and crashworthiness analysis. In both cases simulation is now an integral part of the design process and prototype testing is usually only undertaken to confirm the 'virtual' design. In recent years there has been a growing interest to apply these simulation technologies to composite materials. This paper will describe the application of Finite Element simulation to composites draping and impact analysis.

For complex parts accurate prediction of draping is necessary to determine if a fabric can be draped to the desired shape without excessive thinning and distortions, or winkling. Furthermore, the deformed fabric architecture must be known if subsequent impregnation, stiffness, failure or impact analysis of the composite part is to be undertaken. The first serious attempts to simulate metal stamping were undertaken over fifteen years ago and led to a European research project on the subject [1]. This work provided the basis for a further CEC research project [2,3] which adapted metal stamping simulation techniques to the draping of composite sheets. Initially this work only considered continuous fibre reinforced thermoplastics; however, more recently, these techniques have been adapted to include fibre reinforced thermosets, dry fabrics and Non Crimp Fabrics where special attention must be paid to through thickness stitching.

Impact and crash simulation of metal structures is today a well validated technique; however, the application of these methods to composite materials is still a research topic due to the complex failure mechanisms that occur in laminate composites. This paper presents some recent work in this field and outlines techniques to model ply and delamination failure of large scale composite structures. The above mentioned problems are all tackled using a commercial explicit Finite Element code [4] which has, where necessary, had specific new developments added. The next section briefly outlines the explicit solution method and justifies the use of this technique for the range of dynamic, highly non-linear problems, presented in this paper.

FINITE ELEMENT CODES FOR DRAPING AND IMPACT ANALYSIS

Traditionally, implicit solution methods are most commonly used for Finite Element analysis. This technique is well known [5] and involves discretisation of the structure into an assemblage of Finite Elements, application of loading, boundary conditions and assignment of material data. The analysis then computes a global structure stiffness matrix which, after inversion, is used to compute nodal displacements, elements strains and stresses. The method is primarily used for stiffness and stress analysis and specialised orthotropic beam, shell and solid elements are usually available for dedicated composites structural analysis. The global structure stiffness matrix [K] provides the relationship between nodal displacements {u} and applied nodal forces {P} for the structure,

$$\{P\} = [K]\ \{u\} \qquad \text{or by inversion,} \qquad \{u\} = [K]^{-1}\ \{P\}.$$

The nodal displacements are then used to compute element stresses and strains. Problems involving contact and nonlinear material behaviour, such as composite damage, yield a nonlinear stiffness matrix [K]. In this case a CPU intensive iterative solution is necessary to determine the nodal displacements for a given applied loading.

During the past two decades the automotive industry, in particular, has promoted the use of the explicit Finite Element method for specialised applications involving dynamic loading and interface contact; these include, amongst others, crashworthiness and metal stamping simulation. The explicit method uses conventional finite elements to discretise the structure, but a different solution strategy is used. In this case the problem is formulated as a dynamic one using the linearized equations of motion, from which a solution in the time domain is obtained. At each node the dynamic equation of motion are given by,

$$[M]\{\ddot{u}\}_n + [C]\{\dot{u}\}_n + [K]\{u\}_n = \{F_{ext}\}_n\ ,$$

where {u}, {$\dot{u}$} and {$\ddot{u}$} are vectors of nodal displacement, velocity and acceleration, n is the cycle number at time position T_n (after nΔT time steps); [M], [C] and [K] are the Mass, Damping and Stiffness matrices respectively and $\{F_{ext}\}$ is a vector of applied external nodal forces. Material damping can be neglected in short duration dynamic problems and, replacing the term $[K]\{u\}_n$ with the equivalent internal nodal force vector $\{F_{int}\}_n$ gives Newton's second law of motion,

$$[M]\{\ddot{u}\}_n = \{F_{ext}\}_n - \{F_{int}\}_n\ .$$

If a lumped mass distribution is assumed the mass matrix [M] is diagonal and a solution for nodal accelerations {$\ddot{u}$} is trivial,

$$\{\ddot{u}\}_n = [M]^{-1}\ (\{F_{ext}\} - \{F_{int}\})_n\ . \qquad (1)$$

The nodal velocities $\{\dot{u}\}_{n+1/2}$ and nodal displacements $\{u\}_{n+1}$ may then be obtained by integration in the time domain using the central finite difference operators,

$$\{\dot{u}\}_{n+1/2} = \{\dot{u}\}_{n-1/2} + \{\ddot{u}\}_n \Delta T_n\ ,$$

$$\{u\}_{n+1} = \{u\}_n + \{\dot{u}\}_{n+1/2} \Delta T_{n+1/2}\ . \qquad (2)$$

Equations (1) and (2) are 'conditionally stable' and restrict the allowable integration time step to $\Delta T_{critical}$, which is dependent on the smallest element size and material properties.

A comparison of the two methods is given [5]; briefly, the implicit method is superior for static, mildly nonlinear problems; whereas the explicit method is advantageous for medium to high velocity impact problems involving large scale deformation and material nonlinearity. Also, the dynamic integration scheme allows buckling and contact between bodies to be easily treated, both of which are important in draping and impact analysis.

FINITE ELEMENT DRAPING SIMULATION

Numerical analysis of fabric draping was first developed nearly fifty years ago and used geometric mapping techniques in which a 'pin-jointed net', or 'fishnet', idealisation is used [6]. These methods assume the fibres to be inextensible with the crossover points between the yarns acting as pin-joints with no relative slip. The method is still widely used today because it is computationally simple, however, it does have numerous drawbacks. Firstly, it is essentially material and process independent and cannot account for contact interactions, inter-fibre slip and out-of-plane deformations such as wrinkling. Secondly, process parameters such as blankholders, which are often used in practice to prevent fabric buckling, cannot be considered.

In recent years the FE method has been applied to composite fabric draping, for example [7,8]. This technique offers the potential to overcome many limitations of mapping methods since both fabric constitutive laws and processing parameters can be treated. The first attempt to develop a commercial FE code for industrial applications was undertaken within a Brite-Euram project [2] which has resulted in the explicit FE PAM-FORM™ code [9]. This code uses shell elements to represent the fabric, which may be either dry, or impregnated with a temperature and rate dependent viscous resin. The shell formulation allows fibre reorientation during forming and wrinkling to be predicted for both unidirectional and simple plain weave fabrics.

Modelling draping of advanced fabrics

The following outlines recent work which has extended the woven fabric model in PAM-FORM for Non Crimp Fabrics [10]. Non Crimp Fabrics are receiving considerable attention as an advanced fabric preform for Liquid Composite Moulding. The fabric has good drapeability and impregnation characteristics and due to the stitching and absence of crimp provides a final composite part with excellent inplane and through thickness mechanical properties. Figure 1 illustrates the manufacturing process and shows a typical fabric.

Figure 2 shows the main features and constitutive laws used to idealise a stack of two plies of NCF. Parameters for the inplane moduli E_1 and E_2 must be determined via coupon testing and a 'picture frame' test is an effective means to obtain the intra-ply shear G_{12}. The picture frame test also gives the shear locking angle at which point further shear deformation is likely to result in out-of-plane buckling. Friction is present and defined between the plies. In addition special elements, as shown below, are introduced to tie adjacent nodes and represent the stitching. The stitch force-displacement relationship is found from a pull-out test in which one ply is extracted from between a 'blanket' of plies [10].

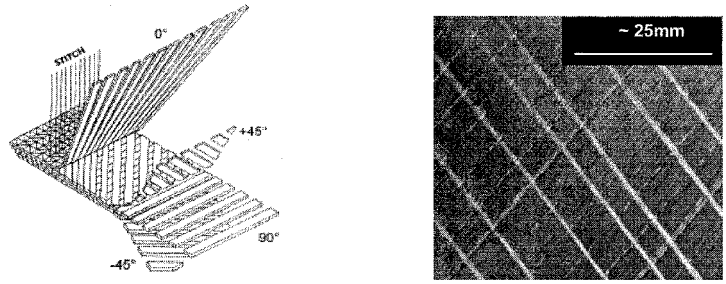


Fig 1: The manufacturing process and an example of a Carbon NCF

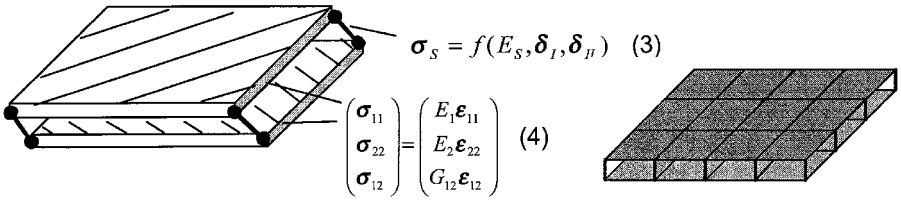


Fig 2: Two stacked plies and the constitutive laws for NCF

Figure 3 illustrates a picture frame test in which a pure shear loading is applied to a biaxial NCF with a tricot stitch at 45° to the fabric tows. The stiffening effect due to tow compaction is clearly visible and is seen to increase to a maximum after about 70° of shear. Information from this test can be directly input into the ply constitutive model. The bias extension tension test, picture frame shear test and a ply pull-out test are all used to calibrate the ply and stitch behaviour. Further, relatively simple tests to determine inter-ply friction, ply-to-tool friction and bending rigidity of the plies are also required and used to calibrate remaining parameters in the numerical constitutive model.

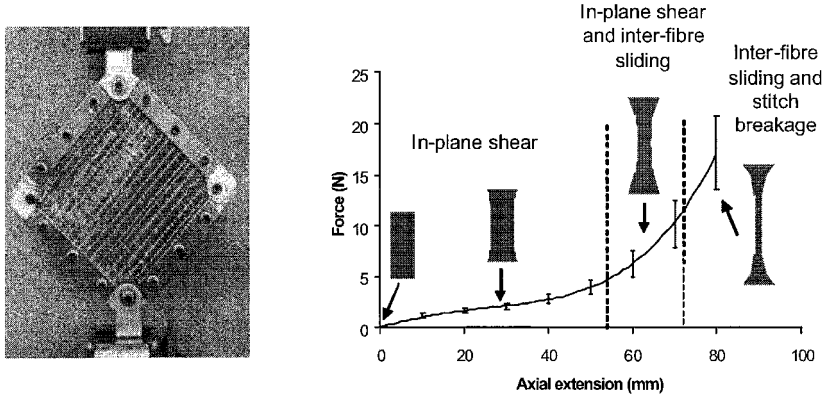


Fig. 3: Example of the NCF picture frame and force-extension results

In order to validate the model experimental draping tests of NCF have been conducted using a double hemisphere mould with vacuum rubber membrane forming. Figure 4 shows example test and simulation results for a biaxial ±45° tricot stitched

NCF. This work has shown a good agreement for both fabric shear strain distributions and deformations of the periphery of the fabric.

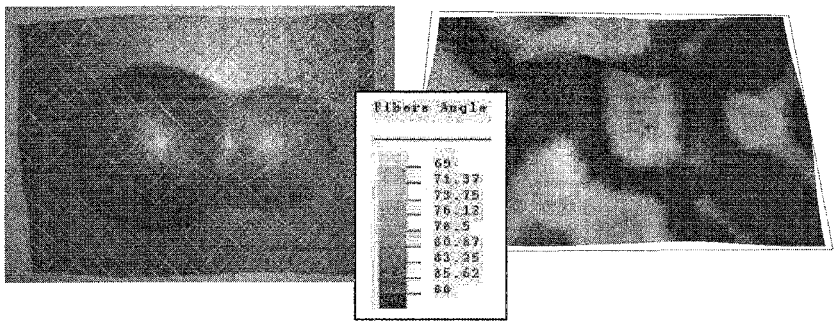


Fig. 4: Experimental draping and simulation results for a biaxial ±45° NCF with tricot stitch under vacuum rubber membrane forming

COMPOSITE FAILURE AND IMPACT MODELLING

Many composite failure models are available that can, if properly calibrated against test measurements, predict ply failure [11]. Generally these models use simple criteria such as maximum strain or stress limits to define failure, or use quadratic formulae with coefficients that must be correlated with coupon tests. Many of these models have been critically reviewed and assessed in a 'Round Robin' exercise [12].

These traditional ply failure models provide a useful means to identify initial ply failure, but are of limited use for impact and crash simulation where progressive ply damage leading to complete rupture of the laminate is required. The damage model must take into account all of the potential failure mechanisms that can occur within the individual plies and must also consider the initiation and growth of inter-ply delamination.

Ply damage models

Ply damage models should be able to model all damage mechanisms including resin micro-cracking due to transverse tension, fibre-matrix debonding due to shear and fibre failure due to longitudinal tension or compression loading. Depending on the loading these mechanisms may develop independently, or in combination. Continuum damage mechanics is a convenient and simple way to treat both ply and delamination failure and is briefly outlined in this section.

Damage is a permanent weakening of the material due to resin micro-cracking, fibre-matrix debonding or fibre failure and occurs prior to complete rupture. In its simplest form damage can be approximated by reducing (damaging) the material elastic properties via a scalar damage parameter (d). The stress-strain relation is then given by,

$$\sigma = E_d \, . \, e \qquad \text{and} \qquad E_d = E_o \, (1 - d),$$

where E_o and E_d are the elastic and damaged moduli respectively, and d is a scalar damage parameter that varies from zero, for strains below the damage initiation strain e_i, and increases to d_u at full material damage strain e_u. Damage d is usually linked to the state of strain, or the strain energy release rate [13]. Complete material rupture at strain

ϵ_u is easily imposed by setting the damage d=1. The evolution of damage and the resulting stress-strain curve are shown in Figure 5.

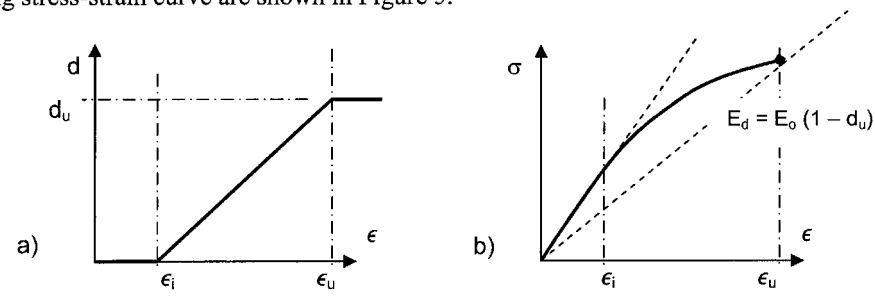


Fig. 5: a) the evolution of damage
b) the corresponding stress-strain relationship

For orthotropic materials there are several material moduli which can be damaged. These mechanical properties and their damage growth, including any interaction of damage, must be determined via appropriate coupon tests. The following illustrates the principles and application of continuum damage mechanics to an orthotropic fabric composite [14]; and is based on the 'Ladeveze' damage model for uni-directional composites [13]. The plane stress orthotropic constitutive law with damage parameters is given by,

$$\begin{Bmatrix}\sigma_{11}\\ \sigma_{22}\\ \sigma_{12}\end{Bmatrix} = \begin{bmatrix} 1/E_1(1-d_1) & -\upsilon_{12}/E_1 & 0 \\ -\upsilon_{12}/E_1 & 1/E_2(1-d_2) & 0 \\ 0 & 0 & 1/G_{12}(1-d_{12}) \end{bmatrix} \begin{Bmatrix}\varepsilon_{11}\\ \varepsilon_{22}\\ \varepsilon_{12}\end{Bmatrix} = [S]\{\varepsilon\},$$

where the compliance matrix [S] comprises of four undamaged elastic constants E_1, E_2, G_{12} and υ_{12} and damage parameters d_1, d_2 and d_{12} for the two principle fibre and shear directions. Usually d_1 and d_2 are uncoupled, but there can be an interaction between d_2 and d_{12}. Calibration of this model requires tension tests in the fibre and transverse directions and a compression test in the fibre direction. A cyclic shear test in which a ±45° fabric coupon is cyclic loaded in tension is used to obtain shear mechanical properties and elastic-plastic properties with damage for the resin.

Delamination modelling

Laminate composites subjected to impact loading are particularly prone to delamination. This failure mode significantly weakens the laminate bending stiffness leading to greater individual ply loading and likelihood of failure. Delamination also absorbs a significant proportion of impact energy and should be properly modelled in any impact analysis.

Modelling delamination using the FE method is difficult since efficient multi-layered elements cannot accurately compute stresses at the ply interfaces and, moreover, cannot treat the separation of plies and load redistributions following delamination. The method presented here is a promising approach to handle the coupled phenomena of ply failure and delamination for large scale composite structures under impact and quasi-static loading. The method involves modelling the laminate as a stack of discrete shell (or solid) Finite Elements in which each element represents one ply, or a sub-set of

plies. These elements are then tied together using interface constraints which characterise the mechanical stiffness, strength and delamination energy absorption of the resin rich interface.

Figure 6a shows the attachment of two plies; arbitrarily called the slave and master plies. At initialisation each slave node on a slave ply is attached to a fictitious 'shadow' node created on the normal vector to the adjacent master ply (element). During deformation the relative movement of the slave and shadow nodes provide the normal and shear displacement contribution (δ_I and δ_{II}) to be used in the mechanical law to compute the elastic-damaging traction and shear resisting forces. The main features of the interface mechanical law are shown in Figure 6b for normal (Mode I) loading. A simple linear elastic law is assumed to the failure stress σ_{Imax}. Thereafter, linear damaging is activated such that, at final separation δ_{Imax}, the fracture energy of the fibre-resin interface has been fully absorbed. That is, the area under the curve corresponds to the fracture energy G_{Ic} of the fibre-resin interface. Thus σ_{Imax}, δ_{Ic} and δ_{Imax} are selected so that the elastic-damage curve fulfils the required criteria. Identical arguments are used to define the shear (Mode II) curve.

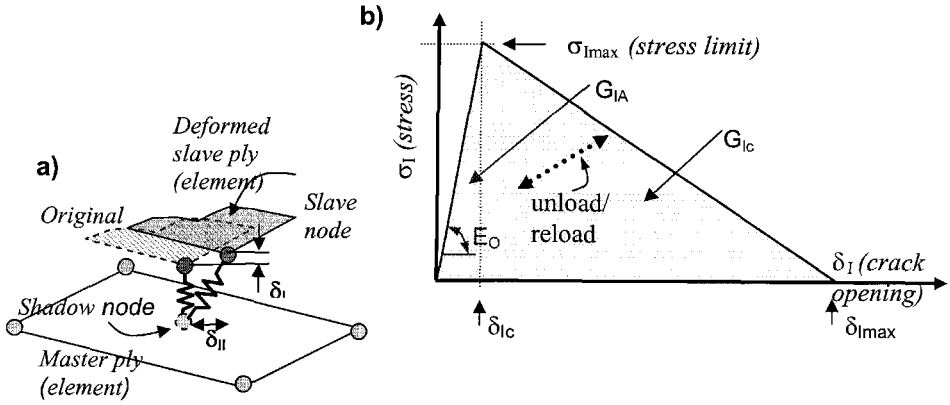


Fig. 6: The interplay delamination model:
a) An attached slave node constrained to a master element ply
b) Diagram of the stress-crack opening curve for Mode I loading

The following formulae describe mode I failure; identical equations are used for mode II by interchanging E_0, σ_{Imax}, δ_I and G_{Ic} with G_0, σ_{IImax}, δ_{II} and G_{IIc}. The resin through thickness normal modulus E_0 relates stress to displacement in the elastic region. At the maximum normal stress σ_{Imax} damage is initiated and the stress displacement law then follows a linear damage equation of the type,

$$\sigma_I = (1-d_I)\cdot E_0 \cdot \varepsilon_I = (1-d_I)\cdot E_0 \cdot \frac{\delta_I}{L_0}$$

where d_I is the damage parameter, varying between the values of 0 (undamaged) and 1 (fully damaged), E_0 is the modulus, L_0 the normal distance between the original position of the slave node and the master shadow node and δ_I is the deformed normal separation distance. The area under the stress-displacement curve in the elastic range G_{IA} is the fracture energy required to initiate damage of the interface and is given by,

$$G_{IA} = \frac{1}{2}\frac{\sigma_{Imax}^2}{E_0} L_0 \ .$$

The total area under the load-displacement curve is the critical fracture energy required for failure of the interface (including both the elastic and damage zones) and is given by,

$$G_{Ic} = \frac{1}{2}\sigma_{\mathrm{I}max}\delta_{\mathrm{I}max} .$$

The values of G_{Ic} and G_{IIc} can be obtained via the standard Double Cantilever Beam (DCB) and End Notched Flexure (ENF) test procedures [15] and [16] respectively.

In real structures there is invariably a strong coupling between normal and shear loading at the interface and a further test procedure is available to determine fracture energy under Mixed Mode Bending (MMB) [17]. This work has shown that, for many materials, a linear coupling model can reasonably represent the mixed-mode failure process; thus the following interaction model is usually assumed,

$$\frac{G_I}{G_{In}} + \frac{G_{II}}{G_{IIn}} = 1 ,$$

where $n=A$ for the onset of fracture and $n=C$ for fracture; G_I and G_{II} are the instantaneous values and G_{In} and G_{IIn} correspond to test values as measured by the DCB and ENF tests. Example solutions using this approach, including validation against DCB, ENF and MMB tests have been presented [18].

Figure 7 shows the experimental setup for a DCB test where a Mode I delamination crack is opened in an aluminium honeycomb composite panel. In this case the delamination model is used to represent the adhesive bonding between the aluminium honeycomb core and the composite facing material and is part of an ongoing investigation to simulate crash of a Jaguar F1 nosecone structure [19]. The DCB experimental procedure is used to determine G_{IC} and Figure 7 shows the good agreement obtained between test and simulation for this mode of failure. A comparison of axial impact loading of this sandwich composite is shown in Figure 8 where, again, a good agreement for impact force between test and simulation is found.

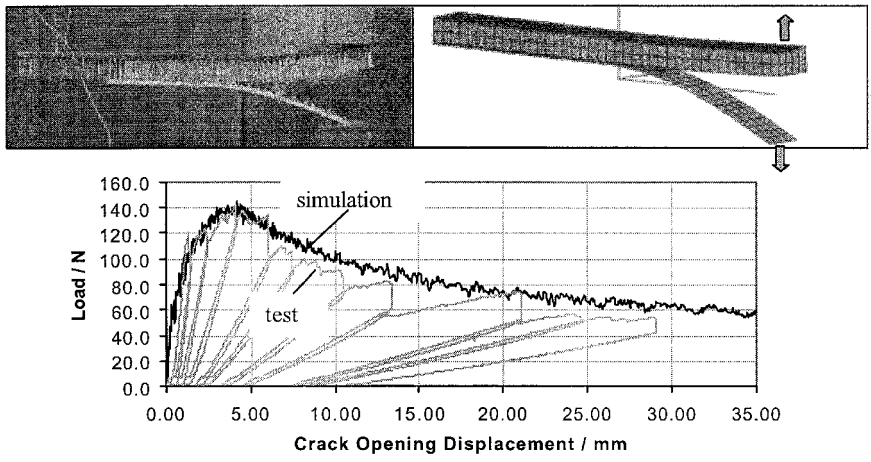


Fig. 7: Comparison of test and simulation for the DCB testing of an aluminium honeycomb composite sandwich panel

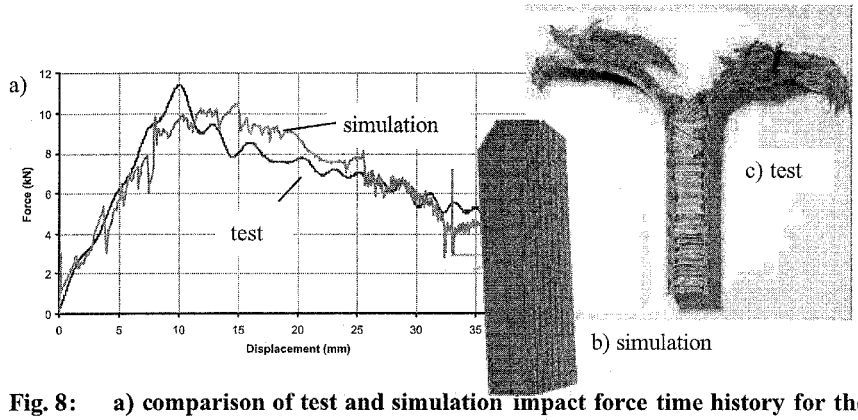


Fig. 8: a) comparison of test and simulation impact force time history for the axial impact loading of aluminium bonded composite sandwich panel
b) the simulation model
c) a test failure specimen

Figure 9 shows the application of these techniques to a structural composite section made of NCF. The problem consists of a hat section simply supported at its base and loaded quasi-statically with a cylindrical impactor. The composite base has 4 blankets (each 0/90/+45/-45) and the upper channel section has 5 similar blankets giving thicknesses of 3mm and 4mm respectively; the specimen is circa 250mm long. In this numerical model each shell element represents one blanket of NCF which are tied together with the delamination model. Both the ply data and the delamination data have been obtained using coupon and delamination tests. The impactor force-time histories (not shown) agree to within 15% of the test results which is a reasonable agreement considering this level on modelling. Ongoing work is considering further refinement of the model in which the blankets are broken down into their individual plies.

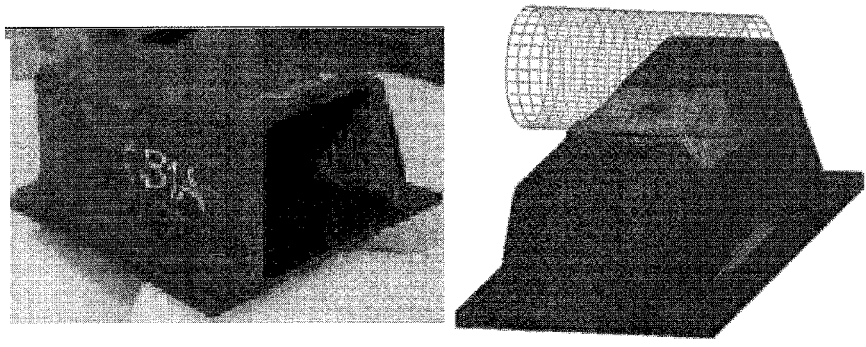


Fig. 9: Test and simulation model for the transverse crushing of a NCF hat section

CONCLUSIONS

In recent year's numerical simulation of composite manufacturing and structural analysis has made significant progress; although they are still not as advanced as comparable techniques currently used for metal manufacturing processes and design.

This paper has demonstrated composites simulation in two important areas; namely, draping and impact analysis and has shown that accurate results are possible. However, future work will also have to consider the important coupling of information between analysis codes so that deformed fabric architecture can be used for accurate resin injection, stiffness, failure and impact analysis.

Acknowledgements

The author would like to thank the CEC European project TECABS for use of the hat section results and Remko Akkerman at the University of Twente for providing the double hemisphere mould used in the draping trials.

References

1 Brite-Euram Project No. BE-3486-89, 'Investigation for an innovative methodology for sheet metal stamping', 1989-1992.
2 Brite-Euram Project No. BE-5092, 'Industrial press forming of continuous fibre reinforced thermoplastic sheets and the development of numerical simulation tools', 1992-1996.
3 A K Pickett, et al., 'Numerical techniques for the pre-heating and forming simulation of continuous fibre reinforced thermoplastics', SAMPE'96, Basel, 1996.
4 The PAM-SOLID code, Engineering Systems International, 20 Rue Saarinen, Silic 270, 94578 Rungis-Cedex, France.
5 R D Cook, D S Malkus and M E Plesha, *Concepts and applications of Finite Element analysis*, Wiley Publ, 1989.
6 C Mack and H M Taylor, Journal of the Textile Institute, 47, 1956.
7 P Boisse, M Borr, K Buet and A Cherouat, 'Finite Element simulation of textile composite forming including the biaxial fabric behaviour', Composite B, Vol 28B, 1997, 453-464.
8 A K Pickett, 'Simulation strategies for automotive composites', Proc. 23rd Int. SAMPE Europe Conference, Paris, April 2002, 47-58.
9 PAM-FORM, Engineering Systems International, 20 Rue Saarinen, Silic 270, 94578 Rungis-Cedex, France.
10 G Creech, A K Pickett and L Greve, 'Finite element modelling of non crimp fabrics for draping simulation', The 6th ESAFORM Conference on Material Forming, Salerno, Italy, April 28-30, 2003.
11 I M Daniel and O Ishai, *Engineering mechanics of composite materials*, Oxford University Press, 1994.
12 M J Hinton, A S Kaddour and P D Soden, 'A comparison of the predictive capabilities of current failure theories for composite laminates, judged against experimental evidence', Composites Science and Technology, **62** (2002), 1725-1797.
13 P Ladeveze and E LeDantec, 'Damage modelling of the elementary ply for laminated composites', Composites Science and Technology', No. 43, 1992, 257-267.
14 A F Johnson, A K Pickett and P Rozycki, 'Computational methods for predicting impact damage in composite structures', Composites Science and Technology, 61, 2001, 2138-2192.
15 ISO international standard DIS15024 'Fibre-reinforced plastic composites – Determination of Mode I interlaminar fracture toughness, GIC, for unidirectionally reinforced materials'.
16 ASTM draft standard D30.06: 'Protocol for interlaminar fracture testing, End-Notched Flexure (ENF)', revised April 24, 1993.
17 J R Reeder and J H Crews, 'Mixed-mode bending method for delamination testing', AIAA Journal, Vol. 28, No. 7, 1989, 1270-1276.
18 N S F Lourenco, A K Pickett and W A Warrior, 'Mixed mode delamination – experimental and numerical studies', Journal of Strain Analysis, 2003.
19 M Temple, 'Numerical simulation of formula one nose cone impact testing', MSc thesis, Cranfield University, UK, 2003.

EULER BUCKLING OF PARTIALLY STIFFENED PULTRUDED GRP COLUMNS: A COMPARISON OF SHELL FINITE ELEMENT AND BEAM-COLUMN MODEL PREDICTIONS

G. J. Turvey and A. Afifi

Engineering Department, Lancaster University, Bailrigg, Lancaster, LA1 4YR, UK

ABSTRACT

A two-dimensional shell finite element (FE) model and a one-dimensional beam-column model are presented for the global (Euler) buckling analysis of partially stiffened pultruded GRP (Glass Reinforced Plastic) WF (Wide Flange) columns subjected to uniform uniaxial compression. By comparison with the buckling loads predicted with the two-dimensional FE model, it is shown that the beam-column model gives accurate predictions of the global buckling loads of simply supported and clamped columns partially stiffened with Type 1 and Type 2 GRP and CFRP (Carbon Fibre Reinforced Plastic) stiffeners. The results obtained also show that Type 1 stiffeners are more effective in raising the buckling load for simply supported columns and, moreover, that there is little benefit in stiffening more than three-quarters of the length of the column. However, for columns with clamped ends both types of stiffener produce similar increases in the buckling load and the greatest increase in the buckling load occurs when the column is stiffened over the whole of its length. Finally, and despite its accuracy, it is shown that the beam-column model is likely to be of limited use for columns with CFRP stiffeners which extend over their whole length, because local or combined mode rather than global buckling occurs for practical column lengths of 3 – 3.5m.

INTRODUCTION

In recent years, the use of fibre-reinforced plastic (FRP) in civil engineering applications has increased dramatically. The increase in use may be attributed to their advantageous properties compared to conventional construction materials, eg. high specific strength and stiffness, low unit mass, high corrosion resistance and low thermal conductivity. However, the first of these advantageous characteristics makes FRPs more susceptible to instability failure modes than conventional steel or aluminium structural components. Consequently, the buckling behaviour of pultruded GRP profiles has been the subject of intensive research, especially over the past decade. A large number of analytical and experimental investigations of the buckling behaviour of open and closed-section pultruded GRP profiles subject to uniform uniaxial compression have been completed (see, for example, [1-6]) and several design formulae have been proposed for predicting their buckling loads.

The buckling loads of pultruded GRP columns are limited by the low stiffness of the GRP material. One way of increasing the buckling loads is to stiffen the profiles. This may be achieved in a variety of ways. For example, some of the GRP rovings could be substituted with CFRP rovings to produce a hybrid fibre pultruded profile. Whilst this is simple to achieve, it has the disadvantage that the stiffness is enhanced uniformly over the entire length of the profile and this may not be efficient from a structural performance standpoint. An alternative approach is to bond stiffening material to the GRP profile. For example, in the case of an I or H-section profile, the flange edges

could be stiffened by bonding on GRP or CFRP strips over part of their lengths. As far as the authors are aware this latter approach has not been investigated for pultruded GRP profiles and this has provided the motivation for the present investigation.

A pultruded GRP WF (Wide Flange) section has been chosen for investigation. Various flange edge stiffening arrangements have been analysed using both FE and simple beam-column models in order to quantify the increase in buckling load due to the different stiffener configurations and to confirm the adequacy or otherwise of the beam-column analysis vis-à-vis the more detailed FE analysis for predicting global buckling loads.

PULTRUDED COLUMNS: MATERIAL AND GEOMETRIC PROPERTIES

The analysis was based around an EXTREN® 500 Series 152 x 152 x 9.5mm (nominal dimensions) WF profile. It was assumed that the column was stiffened by either GRP or CFRP rectangular cross-section (25 x 2.5mm) strips bonded to the flange edges. It was also assumed that the material principal axes of the WF profile and the stiffening strips were coincident. Moreover, it was assumed that the CFRP strip was a uni-directional material. The elastic constants of the GRP and CFRP materials are given in Table 1.

Two types of flange stiffener were chosen for investigation. Both types of stiffener were symmetrically distributed with respect to the cross-section and the length of the column. With Type 1 stiffeners the central portion of the column was stiffened and with Type 2 the ends of the column were stiffened. Sketches of the two types of stiffener are shown in Figure 1.

ANALYSIS MODELS OF FLANGE STIFFENED COLUMNS

Two modelling approaches were used for the buckling analyses of the partially stiffened pultruded GRP columns with simply supported or clamped ends. The first was a two-dimensional finite element model and the second was a one-dimensional beam-column model. Some of the details of these models are presented overleaf.

Table 1 Elastic constants of the pultruded GRP and CFRP materials

Elastic Constants	GRP Profile	GRP Stiffener	CFRP Stiffener
$E_L\,(kN/mm^2)$	23	23	125
$E_T\,(kN/mm^2)$	8	8	9
$G_{LT}\,(kN/mm^2)$	3	3	4.4
ν_{LT}	0.29	0.29	0.34

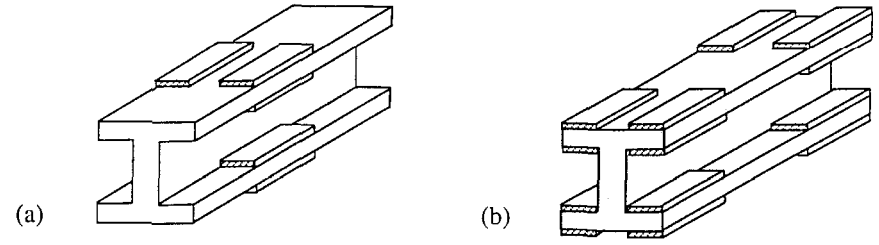


Figure 1: Flange stiffened pultruded GRP WF-sections: (a) Type 1 and (b) Type 2

Finite element model

The two-dimensional finite element model was set up using the ANSYS FE software [7]. Shell 99 elements were used to model the flanges and the web of the WF profile. The Shell 99 element has eight nodes, each with six degrees of freedom. The element accounts for shear deformation effects and is also suitable for modelling laminated anisotropic materials. Hence, the strip stiffeners were treated as distinct laminae within the element. It should be appreciated, however, that the adhesive was ignored in the FE analysis.

The majority of the partially stiffened columns were modelled with 630 elements. There were four elements across each flange and two across the web and 63 elements along the length of the column. Figure 2 shows the FE meshes used for the two types of stiffener.

In the FE models the simply supported and clamped end conditions were simulated by constraining the displacements of the nodes on the end cross-sections of the columns.

For simply supported ends translation in the y-direction was suppressed in the flanges at both ends. Translation in the z-direction was also suppressed in the webs at both ends. In addition, translation in the x-direction was suppressed at the centre of the web at one end and rotation about the x-axis was suppressed at both ends. All of the other nodal freedoms at the two end cross-sections were permitted.

Likewise, for clamped ends translations in the y and z-directions were suppressed at both ends. In addition, translation in the x-direction was suppressed at one end, but permitted at the other, where the load was applied. Rotations about the x, y and z-axes were also suppressed at both ends. The translations in the x-direction at the loaded cross-section were coupled to ensure equal displacements.

The load was applied to one end of the column as a uniform pressure over the web and flanges.

Beam-column model

The beam-column model of the partially stiffened column was based on classical stability functions [8] coupled with the Method of Transformed Sections [9]. This one-dimensional model, consisting of three beam-column elements, provides exact buckling loads for global buckling modes. The beam-column models for the Type 1 and Type 2 stiffeners are shown in Figure 3.

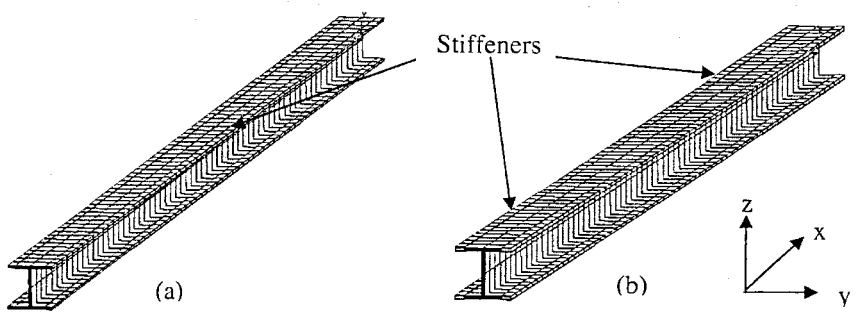


Figure 2: FE models of partially stiffened pultruded GRP columns: (a) Type 1 and (b) Type 2 stiffeners

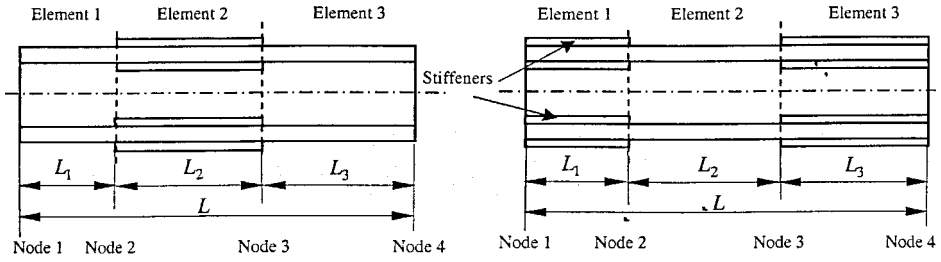


Figure 3: Three-element beam-column models of partially stiffened columns (a) Type 1 and (b) Type 2 stiffeners

The beam-column element is a one-dimensional element with two nodes – one at each end. The nodes have three degrees of freedom – two translations and one rotation. The element has only one elastic constant, namely the elastic modulus of the material. It is, therefore, only really applicable to isotropic materials. However, for those parts of the column stiffened by CFRP strips the elements consist of two materials, viz. GRP and CFRP. Therefore, the Method of Transformed Sections [9] was used to convert the CFRP to an equivalent area of GRP, so that the isotropic beam-column model could also be applied to these portions of the column. It should also be appreciated that the one-dimensional beam column model ignores the effect of the adhesive layers, which bond the stiffeners to the edges of the flanges.

Figure 3 shows the two three-element models for the two types of partially stiffened columns. The results presented later are all for stiffeners which are symmetric with respect to the middle of the column, i.e. $L_1 = L_3$. However, symmetry was not exploited in the analysis.

The boundary conditions are much simpler to apply for the beam-column model. The simply supported condition was simulated by suppressing the deflection at the nodes at each end of the column and the clamped condition was obtained by suppressing both the deflection and the rotation at these nodes.

It should be appreciated that the beam-column model gives exact buckling loads only for global buckling modes, whereas the FE model provides approximate buckling loads for *all* buckling modes (global, local and combined).

NUMERICAL RESULTS AND DISCUSSION

As mentioned in the Introduction, the majority of the results obtained from the two buckling analysis models apply to a 152 x 152 x 9.5mm WF flange column with a length of 6.3m. This is longer than would normally be used in practice, but was chosen to ensure that global buckling occurred in the FE model. The GRP and CFRP stiffeners were 25mm wide and 2.5mm thick. The stiffener lengths were defined in terms of the parameter μ. For Type 1 stiffeners $\mu = \frac{L_2}{L}$ and for Type 2 stiffeners $\mu = \frac{L_1 + L_3}{L}$ and in both cases $L_1 = L_3$. Buckling analyses were undertaken for $\mu = 0, 0.25, 0.5, 0.75$ and 1

for Type 1 and Type 2 GRP and CFRP stiffeners for columns subjected to uniform uniaxial compression and with both ends simply supported or clamped.

For the beam-column buckling analyses the equivalent properties of the transformed sections with GRP and CFRP stiffeners are given in Table 2.

In order to quantify the increases in buckling loads which arise from the use of Type 1 and Type 2 stiffeners for each set of column end conditions (simply supported and clamped), it is convenient to non-dimensionalise the buckling loads with respect to the Euler buckling load of the pultruded GRP column with either simply supported or clamped ends, i.e. with respect to $P_E^{ss}\left(=\pi^2 E_L^{eq} I^{eq} / L^2 = 31.82kN\right)$ or $P_E^{cc}=\left(0.25\pi^2 E_L^{eq} I^{eq} / L^2 = 127.2kN\right)$ respectively.

Table 2: Equivalent elastic and geometric properties of the stiffened beam-column elements after transformation

Equivalent Property	GRP Profile	GRP Profile + GRP Stiffeners	GRP Profile + CFRP Stiffeners
$E_L^{eq}\left(kN/mm^2\right)$	23	23	23
$I^{eq}\left(mm^4\right)x10^7$	0.557	0.758	1.653
$A^{eq}\left(mm^2\right)x10^4$	0.415	0.465	0.687

Table 3: Comparison of FE and beam-column model buckling loads for simply supported columns with Type 1 and Type 2 stiffeners

μ	GRP Profile + GRP Stiffeners				GRP Profile + CFRP Stiffeners			
	Type 1		Type 2		Type 1		Type 2	
	P_A/P_E^{ss}	P_{BC}/P_E^{ss}	P_A/P_E^{ss}	P_{BC}/P_E^{ss}	P_A/P_E^{ss}	P_{BC}/P_E^{ss}	P_A/P_E^{ss}	P_{BC}/P_E^{ss}
0.00	0.9956	1.0000	0.9956	1.0000	0.9956	1.0000	0.9956	1.0000
0.25	1.1565	1.1574	1.0025	1.0204	1.4204	1.4339	1.0113	1.0367
0.50	1.2664	1.2768	1.0452	1.0534	2.0961	2.1269	1.1219	1.1448
0.75	1.3136	1.3623	1.1558	1.1605	2.7756	2.8412	1.4890	1.5048
1.00	1.3576	1.3607	1.3576	1.3607	2.9578	2.9666	2.9578	2.9666

Table 4: Comparison of FE and beam-column model buckling loads for clamped columns with Type 1 and Type 2 stiffeners

μ	GRP Profile + GRP Stiffeners				GRP Profile + CFRP Stiffeners			
	Type 1		Type 2		Type 1		Type 2	
	P_A/P_E^{cc}	P_{BC}/P_E^{cc}	P_A/P_E^{cc}	P_{BC}/P_E^{cc}	P_A/P_E^{cc}	P_{BC}/P_E^{cc}	P_A/P_E^{cc}	P_{BC}/P_E^{cc}
0.00	0.9882	1.0000	0.9882	1.0000	0.9882	1.0000	0.9882	1.0000
0.25	1.1501	1.1507	1.1116	1.1278	1.4095	1.4196	1.3883	1.4162
0.50	1.1745	1.1757	1.1603	1.1754	1.8466	1.8231	1.7680	1.8233
0.75	1.2531	1.2600	1.1721	1.1970	1.9095	1.8812	1.8246	1.8810
1.00	1.3427	1.3616	1.3427	1.3616	2.8459	2.9685	2.8459	2.9685

The first non-dimensionalised buckling loads presented are for columns with simply supported ends. They are listed in Table 3. The buckling loads obtained from the ANSYS FE analysis are denoted by P_A and those obtained from the beam-column stability function analysis are denoted by P_{BC}. Similar results are presented in Table 4 for columns with clamped ends.

The results presented in Table 3 show that the buckling loads predicted by the FE and beam-column models are in excellent agreement except when $\mu = 0.75$ for Type 1 GRP and CFRP stiffeners, where the latter model's buckling loads are 3.7% and 2.4% respectively higher. For the case of partially stiffened columns with clamped ends, the results in Table 4 show that the greatest difference between the buckling loads predicted by the two models is when the column is stiffened over its whole length, i.e. when $\mu = 1$, with CFRP stiffeners. In this case, the difference in the buckling loads amounts to about 4.3%. Thus, it appears that the simple beam-column model, based on stability functions, provides good estimates of the buckling loads of partially stiffened pultruded GRP WF-section columns when global buckling occurs.

It is instructive to plot the non-dimensional buckling loads against the non-dimensional stiffened span in order to establish which types of stiffener are more efficient for each set of column end conditions. Figure 4 shows these plots. Figures 4(a) and 4(b) show the graphs for Type 1 and Type 2 stiffeners respectively for columns with simply supported ends. It is clear that Type 1 stiffeners are more effective in raising the buckling loads than Type 2 stiffeners. Moreover, as expected, the use of CFRP rather than GRP stiffeners produces much larger increases in the buckling loads. The increases in buckling loads are very significant for Type 1 stiffeners. For example, when $\mu = 0.5$, the GRP stiffeners raise the buckling load by about 27%, whereas the CFRP stiffeners produce a 110 – 114% increase in the buckling load. Figure 4(a) also reveals that there is little to be gained by stiffening more than three-quarters of the span with either Type 1 GRP or CFRP stiffeners. The curves in Figure 4(b) suggest the opposite conclusion, namely that with Type 2 stiffeners the buckling load increases rapidly when $\mu \geq 0.5$ and reaches its maximum value at $\mu = 1$, i.e. when the stiffeners extend over the whole span.

Figures 4(c) and 4(d) show the non-dimensional buckling load versus stiffened span plots for both types of stiffener for columns with clamped ends. It is evident that the two figures are very similar, i.e. the type of stiffener has little influence of the buckling loads for the same stiffener material and stiffened span. Moreover, for columns with clamped ends and CFRP stiffeners the buckling load is enhanced significantly when the stiffeners extend over the entire span.

The final results presented are the buckling loads of unstiffened and fully stiffened $(\mu = 1)$ columns with simply supported (see Figure 5(a)) and clamped (see Figure 5(b)) ends. These buckling loads were computed with the FE model in order to show at what column length the global buckling mode is no longer valid.

It is evident, from Figure 5, that for columns stiffened over their whole length with CFRP stiffeners, global buckling only arises when the length of column is greater than 5m for simply supported ends and greater than 7m for clamped ends. These lengths reduce to about 4m and 5m respectively for GRP stiffeners. Therefore, it would appear that the beam-column model may give inaccurate predictions of the buckling loads for columns used in practice, which have lengths of around 3 – 3.5m, especially when CFRP stiffeners are used. This is because the mode of buckling is local or a combination of global and local buckling.

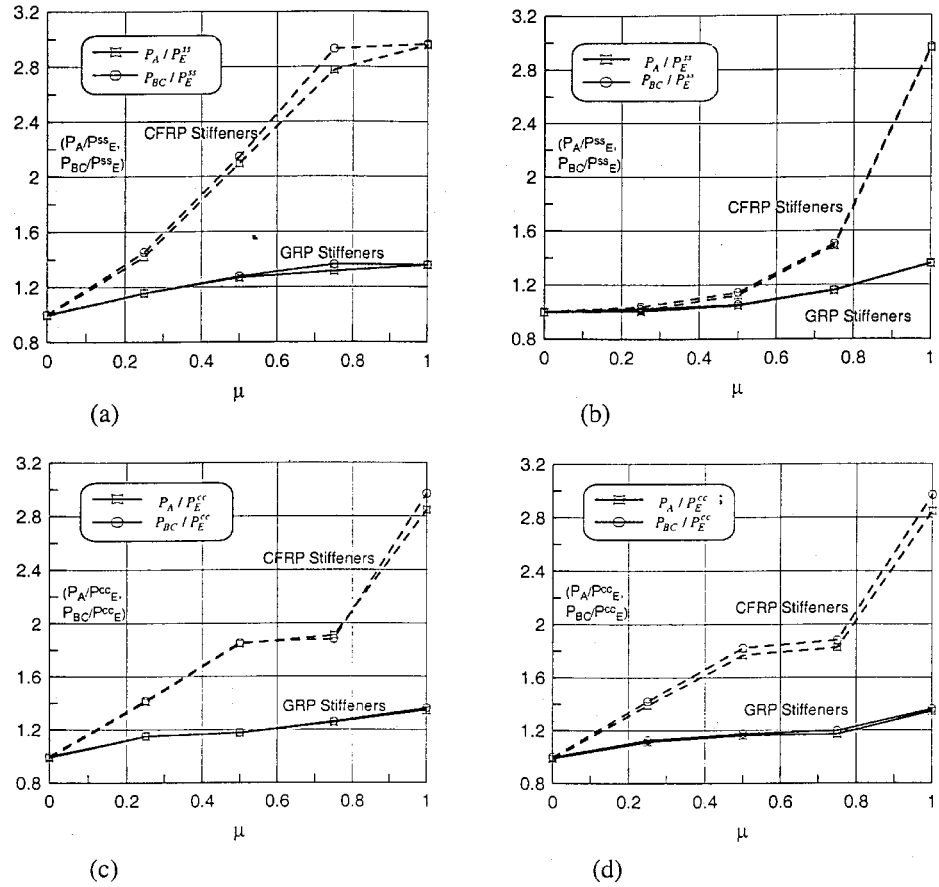


Figure 4: Buckling loads versus stiffened span ratio: (a) Type 1 stiffeners (simply supported ends), (b) Type 2 stiffeners (simply supported ends), (c) Type 1 stiffeners (clamped ends) and (d) Type 2 stiffeners (clamped ends).

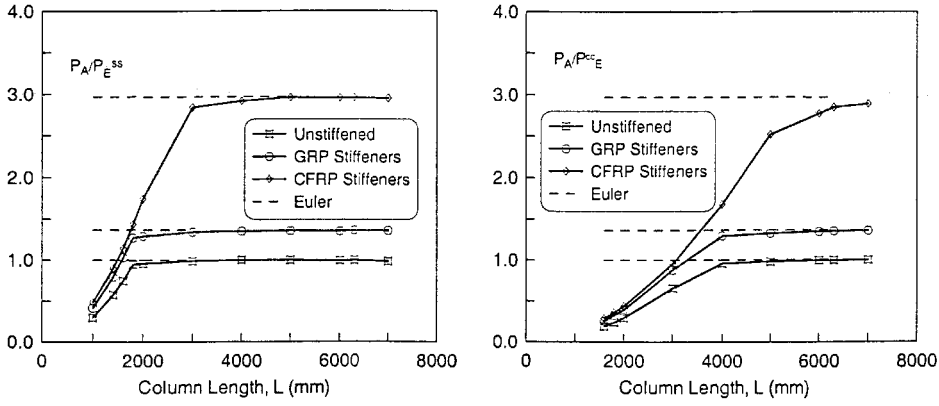


Figure 5: Buckling load versus column length for unstiffened and fully stiffened columns: (a) simply supported ends and (b) clamped ends.

CONCLUDING REMARKS

Two analysis models – a two-dimensional shell FE model and a one-dimensional beam-column model, based on stability functions – have been developed for computing buckling loads of pultruded GRP columns partially stiffened by two types of GRP and CFRP stiffeners. It has been shown that, provided the mode of buckling is global, the buckling loads predicted by both analyses are generally in good agreement. Moreover, it has also been shown that Type 1 stiffeners increase buckling loads of simply supported columns more than Type 2 stiffeners. However, there is little to be gained from stiffening more than three-quarters of the span with Type 1 stiffeners. On the other hand, when the column ends are clamped both types of stiffener produce similar increases in the buckling loads.

It is also shown that stiffening the flange edges with CFRP strips leads to significantly larger increases in buckling loads than when they are stiffened with similar sized GRP strips.

Finally, it is emphasized that the one-dimensional beam-column model may lead to inaccurate buckling load estimates for column lengths used in practice, especially when the stiffeners extend over the whole length of the column, because the buckling mode is local rather than global.

ACKNOWLEDGEMENTS

The second author wishes to record her appreciation to the UK Universities and the trustees of the Peel Trust for financial support through an ORS Award and a Peel Award respectively, without which this research investigation could not have been undertaken. Both authors also wish to express their appreciation to the Engineering Department for supporting their research.

REFERENCES

1. A. Zureick, and D. Scott, 'Short term behaviour and design of fibre-reinforced polymeric slender members under axial compression', *Journal of Composites for Construction, ASCE,* 1997, **14** (4), 140-9.
2. A. Lane, 'Finite element buckling analysis of fibre reinforced plastic columns', Fourth Year Undergraduate Project Report, University of Warwick, May, 1997.
3. D. J. Lee, and P.J. Hewson, 'The use of fibre-reinforced plastics in thin-walled structures'. In *Stability Problems in Engineering Structures and Components,* T.H. Richards and P. Stanley (eds), Applied Science Publishers Ltd, London, 1978, 23-55.
4. A.R. Vakenier, A. Zureick, and K.M. Will, 'Prediction of local flange buckling in pultruded shapes by finite element analysis', *Proceedings of the ASCE Special Conference on Advanced Composite Materials in Civil Engineering Structures,* Materials Engineering Division, ASCE, Las Vegas, Nevada, 1991, 302-312.
5. N. D. Brown. J. T. Mottram, and D. Anderson, 'The behaviour of columns for the design of pultruded frames: tests on isolated columns', In *Fiber Composites in Infrastructure,* H. Saadatmanesh and M.R. Ehsani (eds), University of Arizona, Tucson, **II**, 1998, 248-60.
6. J. T. Mottram, N. D. Brown, and A. Lane, 'The analysis of columns for the design of pultruded frames: isolated centrally loaded columns', *Proceedings of the Eighth European Conference on Composite Materials: Science, Technologies and Applications (ECCM-8),* Woodhead Publishing Ltd, Cambridge, **2**, 1998, 235-42.
7. Ansys Users Manual Version 6.0, ANSYS Inc., Southpointe, Pennsylvania, USA, 2002.
8. P. A. Kirby and D. A. Nethercot, *Design for Structural Stability,* Granada Publishing, London, 1979, 40-62.
9. Case, J., and Chilver, A.H., *Strength of Materials: An Introduction to the Analysis of Stress and Strain,* Edward Arnold Publishers Ltd., London, 1964, 183-93.

SHEAR FAILURE STRENGTH OF WEB-FLANGE JUNCTIONS IN PULTRUDED GRP PROFILES

G.J. Turvey and Y. Zhang

Engineering Department, Lancaster University, Bailrigg, Lancaster, LA1 4YR, UK

ABSTRACT

Ultimate load tests on pultruded GRP WF (Wide Flange) profile beams and columns have shown that final failure is triggered by separation or one or both flanges from the web. Strengths determined from coupons cut from the web and flanges do not provide accurate predictions of web-flange junction strengths, because of the presence of a roving-rich core at the heart of the junction. Therefore, tests have to be carried out on junctions under different loading arrangements to determine junction strengths. Tensile strengths of junctions were reported recently by the authors in [1]. Here, details are presented of a complementary investigation to determine the shear strengths of web-flange junctions. The details include: the preparation of the web-flange junction specimens, a description of a new test rig for determining junction shear strengths and the underlying theory on which it is based, and the shear strengths obtained from junction tests on two sizes of WF profile.

INTRODUCTION

Moment – rotation tests on beam to column connections between pultruded GRP profiles have shown that tearing separation of the column flange from its web may occur when the ultimate moment of the connection is reached [2]. Similar tearing separation failure has been observed in tests on beams [3] and columns [4], where this mode of failure usually follows buckling of the profile's web and flange(s).

In order to promote the use of pultruded GRP profiles in infrastructure applications, it is essential to enhance our knowledge of their ultimate strengths and modes of failure. In this regard, it appears that the majority of research effort has been directed towards understanding and developing tools to predict the onset of buckling in pultruded GRP beams and columns. As far as the authors are aware, only Bank and Yin [3] have attempted to analyse tearing separation failure in pultruded GRP beams subjected to four-point bending. In their analysis model the tension strength of the web-flange junction was assumed equal to the tension strength of coupons cut transversely from the web and flanges. The weakness with this assumption is that coupon tests do not take into account the curvature of the fibre architecture and the roving-rich zone at the core of the web-flange junction. In order to acquire more representative strength data for the web-flange junctions of pultruded GRP profiles, it is necessary to carry out tests on specimens that include the junction.

Turvey and Zhang [1] carried out a series of tension tests on web-flange junction specimens of two sizes of pultruded GRP WF-profiles (102x102x6.4 and 203x203x9.5 mm) referred to as I4 and I8 respectively and obtained tension strengths of web-flange junctions. In their tests it was observed that failure tended to initiate in the roving-rich zone of the web-flange junction as a crack propagating from the centre of the zone parallel to the flange. With increasing load this crack extended and a second crack developed from its centre and ran upwards along the centre of the web. Prior to reaching

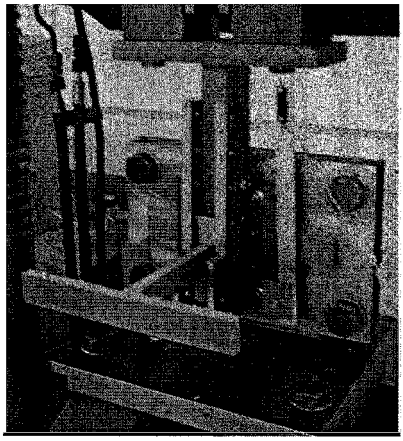
the ultimate tensile failure load, secondary cracks (or delaminations) began to develop in the curved outer plies of the junction.

Tearing failure of the web-flange junction in beam or column failure is a complex phenomenon, because the stresses acting on the junction are complex. It is, therefore, important to characterize the strength of the web-flange junction under a number of simple stress states in order to develop junction failure models. The earlier work of Turvey and Zhang [1], which provides tension strengths of two sizes of web-flange junction, constitutes a useful first step in this direction. Here we report on a complementary set of tests, which have been carried out with the aim of determining the shear strengths and failure modes of web-flange junctions.

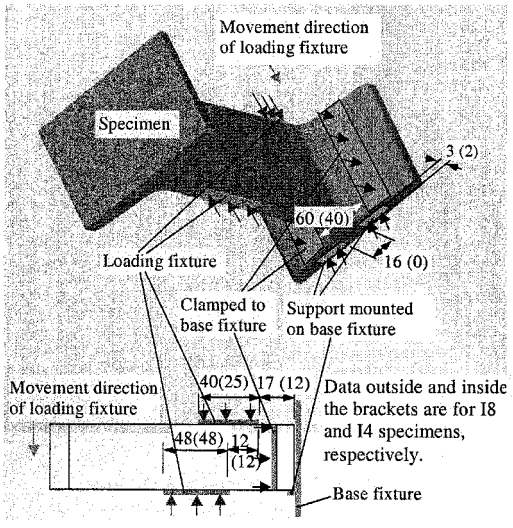
SPECIMEN PREPARATION

Two sizes of the EXTREN® 500 series pultruded GRP WF profiles, i.e., I4 and I8 were chosen for investigation. Test specimens were cut transversely from the profiles using a band saw. Initially, two I4 specimens 25 mm long were prepared for preliminary testing. Thereafter, 36 specimens, 18 from the I4 and 18 from the I8 profile, were prepared by cutting the profiles successively into lengths of 25, 40, 60, 25, 40, ... mm. Each short length of profile provided two test specimens, i.e. one containing the upper and the other the lower web-flange junction of the profile. The specimens were divided into groups according to profile size and length. In each group there were six specimens, three containing the upper and three the lower web-flange junction. The length of the web-flange junction and the thickness of the web of each specimen were measured before testing.

TEST SET-UP



(a)



(b)

Figure 1: Shear testing of web-flange junction specimens (a) photograph of test rig (b) dimensioned sketches showing how the shear load is applied to web-flange junction.

The tests were carried out in a universal testing machine. Fig.1(a) shows a web-flange junction specimen set up ready for testing and Fig.1(b) shows how the specimen is supported and loaded. The flange of the specimen was clamped to the vertical plate of an L-shaped steel base by two steel bars. Two small steel blocks were also fixed to the vertical plate to support the lower edge of the specimen's flange. The horizontal plate of the L-shaped base was fixed to the lower platen of the testing machine. A T-shaped loading fixture was bolted to the upper platen of the test machine. The web of the specimen was located under this fixture. A steel shoe was placed on the upper edge of the web close to the web-flange junction. A steel block of length 48 mm was placed between the loading fixture under the lower edge of the web. This steel block could be adjusted vertically in the loading fixture. During a test, the loading fixture moves downward. Once it makes contact with the upper edge of the web through the steel shoe, the steel block is adjusted to bring it into contact with the lower edge of the web so that rotation of the web is prevented during loading. Load is then applied until the specimen fails.

A displacement sensor (maximum travel = 10mm) was fixed to the vertical plate of the L-shaped steel base. Its tip was kept in contact with the loading fixture in order to record the vertical displacement. During each web-flange junction shear test, load and displacement were recorded automatically at 0.1 second intervals by a data-logging system.

THEORETICAL BACKGROUND TO THE SHEAR TEST

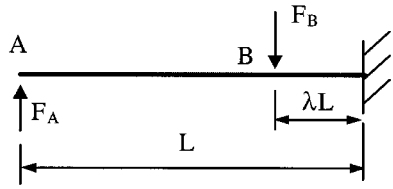


Figure 2: Structural model of web-flange junction test rig

In the test set-up described above, the web of a specimen close to the web-flange junction may be idealised as a propped cantilever loaded as shown in Fig.2. The applied shear force, F, may be expressed as

$$F = F_B - F_A \tag{1}$$

where F_B and F_A are the forces acting at the points B and A, respectively.

Ignoring the effects of shear deformation in the beam, the deflections at A (w_A) and B (w_B) are given by

$$w_A = w_{A_{F_B}} - w_{A_{F_A}} = \frac{L^2}{6EI}\left[F_B\lambda^2(3-\lambda) - 2F_A\lambda^3\right] \tag{2a}$$

$$w_B = w_{B_{F_B}} - w_{B_{F_A}} = \frac{L^3}{6EI}\left[2F_B\lambda^3 - F_A\lambda^2(3-\lambda)\right] \tag{2b}$$

where E is the flexural modulus and I is the second moment of the area. $w_{A_{F_B}}$ and $w_{A_{F_A}}$ are the deflections at point A due to F_B and F_A respectively and $w_{B_{F_B}}$ and $w_{B_{F_A}}$ are the deflections at point B due to F_B and F_A respectively.

If it is assumed that the loading fixture is much stiffer than the specimen, then the beam will undergo the same deflection at points A and B so that

$$w_A = w_B \tag{3}$$

Substituting Eqs.2 into Eq.3 and using Eq.1, the forces F_B and F_A can be expressed in terms of the shear force F at the web-flange junction as

$$F_A = \frac{3}{2\left(1+\lambda-2\lambda^2\right)}F \;;\; F_B = \frac{2+2\lambda-\lambda^2}{2\left(1+\lambda-2\lambda^2\right)}F \tag{4a, 4b}$$

At the web-flange junction, i.e., the clamped end of the propped cantilever beam, the shear force is equal to the applied force F and the bending moment, M, is given by

$$M = F_A L - F_B \lambda L = -\frac{\lambda(2+\lambda)}{2(1+2\lambda)}FL \tag{5}$$

It can be seen that the WF junction is subjected to both a shear force and a bending moment. Therefore, it is more accurate to refer to the test as shear-bending test.

It should also be appreciated that the end support at the web-flange junction in Fig.2 is shown as rigid, whereas in practice it is semi-rigid. Hence, the actual bending moment M at the support may be much smaller than that given by Eq.5.

TEST RESULTS

Load – displacement behaviour

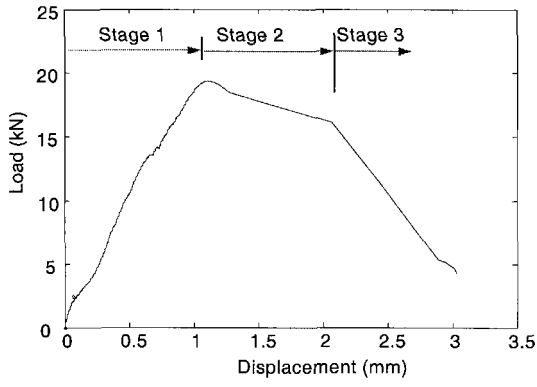


Figure 3: Typical load-displacement curve for a shear test on the web-flange junction of a 40 mm long I8 specimen

Each of the web-flange junction specimens was tested to failure. The loading rate used was in the range 0.2~0.8 kN/min. A typical shear force versus displacement curve for a failure test on a web-flange junction is shown in Fig.3. The response may be sub-divided into three roughly linear stages. The first stage is from zero load to the maximum load of about 19 kN corresponding to a displacement of about 1.1 mm. In the second stage the load reduces to about 16 kN as the displacement increases to 2.2 mm, and in the third stage, the load falls rapidly as the displacement increases to 3.1 mm and final failure occurs. Failure initiates at the web-flange junction as the load approaches its peak value. During the second stage, the failure at the web-flange junction gradually extends causing the load to decrease as the displacement increases. In the third stage the failure propagates rapidly along the web-flange junction causing the web to shear off the flange.

Failure development and failure modes

In the shear tests on the web-flange junction specimens, it was observed that failure generally initiated in the roving-rich core of the junction. The initial crack (or delamination) was shaped like an inverted vee in the majority of the specimens, as shown in Fig.4(a). With increasing load, the crack extended either into the flange along a ply interface, or into the outer plies at the junction. Failure development was mainly due to the high combined shear and bending stresses at the ply interfaces. A typical failure mode observed in the web-flange junction shear tests is shown in Fig.4(b).

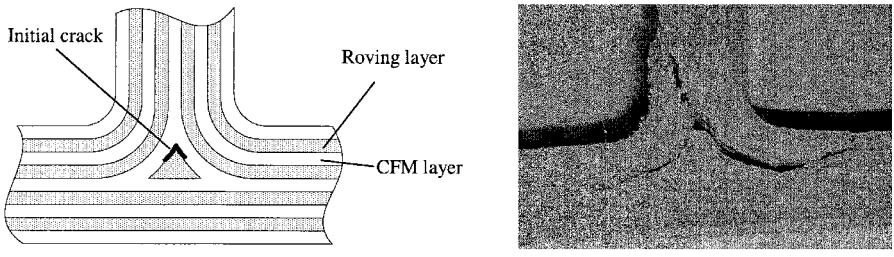
For the three 60 mm long lower web-flange junction specimens cut from the I8 profile, it was observed that failure occurred under the steel shoe due to high bearing stresses.

Shear failure strength

In determining the shear failure strengths from the test results, the shear stress τ is defined as

$$\tau = \frac{F}{bt} \tag{6}$$

where b is the length of the specimens and t is the thickness of the web.



(a) (b)

Figure 4: (a) sketch of the initial inverted vee crack and (b) typical failure mode observed in web-flange junction shear tests

Fig.5 shows the shear stress at failure for all of the I4 and I8 web-flange junction specimens tested. The upper and lower web-flange junctions are denoted by 'upper' and 'lower', respectively. As mentioned above, the 60 mm long lower web-flange junction specimens cut from the I8 profile failed locally. For these three specimens, the shear stresses correspond to bearing failure and their real failure shear strengths are expected to be higher than the values shown in Fig.5.

In Table 1 the shear strengths obtained from the present web-flange junction tests are compared with those obtained from AFPB (Asymmetrical Four-Point Bending) shear tests on V-notched flat coupons [5] and those given in the manufacturer's design handbook [6].

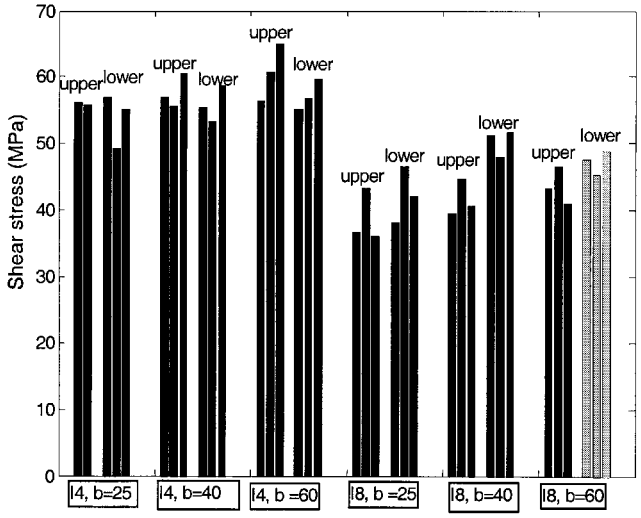


Figure 5: Shear strengths of web-flange junction specimens

Table 1: Comparison of shear strengths

WF-Section (mm)	Test methods	Av. shear strength (MPa)
102 x102 x6.4	Present, b = 25mm	54.7
(I4)	Present, b = 40mm	56.8
	Present, b = 60mm	59.0
	AFPB [5]	84.8
	[6] (ASTM D3846)	41.4
203 x 203 x 9.5	Present, b = 25mm	40.5
(I8)	Present, b = 40mm	46.0
	Present, b = 60mm	45.4
	AFPB [5]	77.9
	[6] (ASTM D3846)	41.4

Effect of parasitic bending on the shear strength of the web-flange junction

In order to obtain an estimate of the effect of bending at the web-flange junction on the shear strength, we must examine the bending stress at the clamped end of the beam. The maximum tensile stress at the clamped end due to bending occurs at the upper edge of the beam and is given by

$$\sigma = \frac{|M|b}{2I} \tag{7}$$

Substituting Eq.5 into Eq.7 and noting Eq.6, we have

$$\sigma = c\tau \tag{8}$$

$$\text{where } c = \frac{3\lambda(2+\lambda)L}{(1+2\lambda)b} \tag{9}$$

From Eq.9 it is seen that c is inversely proportional to the length of the specimen b. It implies, therefore, that the ratio of σ/τ decreases and the shear strength increases as b increases. This is indeed the case for the test results and is clearly shown in Fig.6.

Consider two cases in which the point forces F_B and F_A act at different locations on the propped cantilever. The positions at which F_B and F_A act at are assumed to coincide with the middle points of the steel shoe and the steel block of the test rig, respectively, in the first case, and the right hand end of the steel shoe and left hand end of the steel block, respectively, in the second case. Based on the above assumptions and the dimensions given in Fig.1, the values of c can be calculated from Eq.9. According to the tension test results for web-flange junction specimens obtained by the authors [1], the tension strengths of the web-flange junctions are about 21 MPa and 16 MPa for the I4 and I8 profiles, respectively. Hence, the theoretical failure forces due to bending can be estimated and the corresponding shear stresses $\tau_{\sigma c}$ can be determined from Eq.8. These values are given in Table 2.

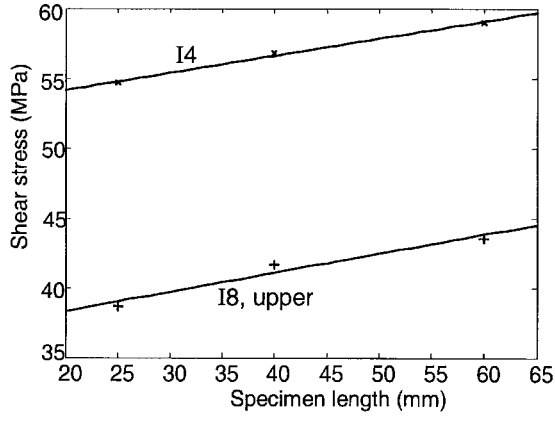


Figure 6: Size effect on the shear strength of web-flange junction specimens

Table 2: Shear stresses $\tau_{\sigma c}$ corresponding to theoretical failure forces in bending

WF-section (mm)	b (mm)	$\tau_{\sigma c}$ (MPa)	
		Case 1	Case 2
102 x102 x 6.4	25	7	18
(I4)	40	12	28
	60	18	42
203 x 203 x 9.5	25	4	10
(I8)	40	7	16
	60	10	25

The web-flange junction shear test results reveal that the failure initiates at much higher shear stresses than those given in Table 2. In other words, the bending effect on the failure of web-flange junction is much less than that determined from the propped cantilever beam analysis assuming a fully clamped support.

CONCLUDING REMARKS

Shear tests have been carried out on web-flange junctions of two sizes of pultruded GRP WF-profile. The shear strengths of the web-flange junctions have been quantified and the failure modes have been identified from the tests. The test results show that the strengths of the web-flange junctions are much lower than those of flat coupons. Moreover, it was observed that failure tended to initiate in the roving-rich zone at the core of the web-flange junction. Because of the effect of the bending moment at the web-flange junction it was found that the shear strength increases as the specimen length increases. In order to reduce further the effect of parasitic bending moments on the shear strengths of the web-flange junction specimens a second series of tests has been carried out on modified specimens. These tests will be reported in a subsequent paper.

ACKNOWLEDGEMENTS

The authors wish to express their gratitude to the UK's Engineering and Physical Sciences Research Council (EPSRC) for providing a grant (GR/R28386/01) to enable the research described herein to be carried out.

REFERENCES

1 G J Turvey and Y Zhang, 'Tearing failure of web-flange junctions in pultruded GRP profiles', 7th int conf (DFC7) *Deformation and Fracture of Composites*, 22nd-24th April, University of Sheffield, 2003.

2 L C Bank, A S Mosallam and H E Gonsior, 'Beam-to-column connections for pultruded FRP structures', Proceedings of 1st Materials Engineering Congress on *Serviceability and Durability of Construction Materials*, Materials Engineering Division, ASCE, 1990, 804-13.

3 L C Bank and J Yin, 'Analysis of progressive failure of the web-flange junction in post-buckled I-beams', *ASCE Journal of Composites in Construction*, 1999 **3**(4) 177-84.

4 D Stubbs, Buckling tests on pultruded GRP short columns in axial compression, Final Year Project Report, Engineering Department, Lancaster University, 1998, pp159.

5 Y Zhang and G J Turvey, Structural integrity evaluation of buckling-triggered failure in pultruded GRP and HF profiles: First Report, Lancaster University, 2002.

6 Anon, *EXTREN Fiberglass Structural Shapes – Engineering Manual*, Morrison Molded Fiber Glass Company (Now Strongwell), Bristol, Virginia, 1989.

USE OF FBG SENSORS FOR MATRIX CRACK DETECTION IN GFRP COMPOSITES

M. Ussorio[1], H. Wang[1], S.L. Ogin[1], A.M. Thorne[1], G.T. Reed[2], S.C. Tjin[3]

[1]*School of Engineering, University of Surrey, Guildford, Surrey, U.K.*
[2]*School of Electronics and Physical Sciences, University of Surrey, Guildford, Surrey, U.K.*
[3]*School of Electrical and Electronic Engineering, Nanyang Technological University, SINGAPORE*

ABSTRACT

Optical fibre Bragg grating sensors have been embedded in a transparent glass reinforced plastic cross-ply laminate. Whilst the coupons were subjected to uniaxial tension, light spectra reflected by the Bragg gratings were recorded and observed for three conditions; prior to damage in the coupon, whilst a crack progresses across the sensor within its gauge length and subsequent to the complete development of the crack across the coupon. By stepping the load at discrete intervals for an individual coupon the characteristic spectrum shift along the wavelength axis was established before and after cracking for the sensor. It was found that the reflected spectrum from the cracked specimen contained distinct side bands not present in the reflection from the undamaged specimen that would enable a damaged specimen to be distinguished from one containing no damage within the gauge length of the sensor. Hence the characteristic change in the recorded spectra due to matrix crack detection might enable a Fibre Bragg Grating sensor to be used to monitor crack development as well as strain in composite materials

INTRODUCTION

Multidirectional laminates manufactured from polymer composite materials are often characterised by a first ply failure consisting of matrix cracks developing parallel to reinforcing fibres in off-axis plies. This damage is typically very difficult to detect, since it generally occurs at internal locations within laminates. However, off-axis matrix cracks result in the reduction of the mechanical properties for the material, which may prove unacceptable in many applications. The use of optical fibre sensors (FOS) for monitoring the health of composite material structures has gained increasing attention from researchers in recent years [1-4]. The applicability of optical fibre Bragg grating (FBG) sensors in several different applications has been demonstrated [5-9], including that of damage detection. In particular, it has been shown [8] that the onset and development of matrix cracks at the location of the FBG sensor in cross-ply laminates affects the characteristics of the sensor's optical output.

In this work, the response of an optical FBG sensor to the development of a single transverse matrix crack in a transparent Glass Fibre Reinforced Polymer (GFRP) cross-ply laminate has been investigated. Quasi-static tensile tests were carried out on composite coupon specimens incorporating an optical fibre in which a FBG had already been written. The coupons were firstly tested undamaged. A single transverse crack was then grown across the coupon in the location of the FBG and the coupon tested again. A comparison of the FBG reflected spectra for the two cases allowed a qualitative understanding of the sensor's output when it interacts with the damage in the polymer composite.

EXPERIMENTAL

In the present study a continuous E-glass fibre-reinforced epoxy resin cross-ply laminate was used with a $(0/90_5/0)$ lay-up and an individual ply thickness of 0.5mm that resulted in a total composite thickness of 3.5mm. A 10mm long Bragg grating was written in the core of a commercial single mode optical fibre. The optical fibre was coated with acrylate and the location of the FBG was evident by a 40mm length of stripped fibre necessary as part of the process of writing the grating into the core. The fibre remained in this condition for embedding into the GFRP composite as it facilitated direct contact with the epoxy matrix during the manufacturing process. 25mm wide GFRP cross-ply tensile specimens were produced from an in-house manufactured laminate, where each coupon contained an optical fibre embedded within one of the longitudinal plies located as close as possible to the 0/90 interface; the location of the FBG sensor was such that it was in the middle third of the coupon's length. Figure 1 is a schematic diagram of the composite laminate with the embedded optical fibre containing the sensor. At the location where end tabs were to be fixed on the coupon specimens the optical fibre had an additional layer of silicone rubber coating applied.

An Amplified Spontaneous Emission (ASE) broadband light source was connected used and analysis of the back reflected optical response of the FBG sensor was carried out on an Optical Spectrum Analyser (OSA). Details of the optoelectronic arrangement are given elsewhere [8].

The initial quasi-static tensile tests on the undamaged coupon were carried out by applying incremental loads and recording each of the corresponding FBG reflected spectra. Thus the linearity of the sensor response to increasing strain in each specimen was confirmed and records of the observed spectrum shapes for increasing strain for the undamaged material were obtained.

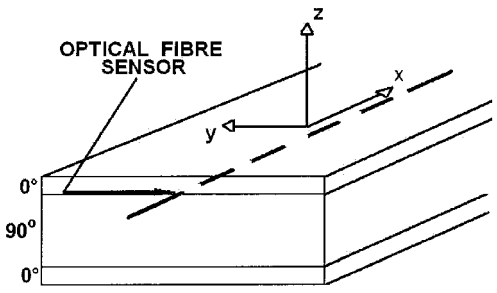


Figure 1. Diagram showing the FBG sensor location in the GFRP cross-ply laminate.

In an attempt to characterise the sensor output when a matrix crack grew past the sensor location, a single crack was slowly grown in the transverse ply of the coupons by manually initiating the crack with a scalpel blade and subjecting the specimens to a few fatigue cycles under a low tensile load. The transverse crack was located at a position, along the specimen length, within the gauge length of the Bragg grating, so that its growth took place in a transverse plane adjacent to the sensor location. As the specimens were transparent, the crack growth could be interrupted before the crack tip had reached the optical fibre as shown in Figure 2. The loading was then incrementally applied so that reflected spectra were obtained for the condition where a) there is no crack present, b) the crack has partly grown but not yet passed the sensor and c) the

crack has fully grown across the coupon. A comparison of the recorded back-reflected spectra for the different crack conditions was then made.

RESULTS AND DISCUSSION

Figure 3 shows the FBG reflected spectra for the undamaged material (i.e. before any crack growth) under discrete increments of the applied tensile load. The reflected spectrum shifts uniformly along the wavelength axis as a result of the enlargement of the grating periodicity due to the uniform longitudinal strain experienced by the optical fibre under the action of the applied load. The back-reflected shape of the spectrum remains unchanged during the shift; a symmetrical shape is present about one main peak.

Figure 4(a) is a digital photograph of the transparent epoxy GFRP coupon showing a crack partly grown across the coupon towards the optical fibre. Figure 4(b) shows the back-reflected spectra for incremental tensile loads when the crack is in this position. The shape of the reflected spectra is unchanged as the transverse crack approaches the sensor location.

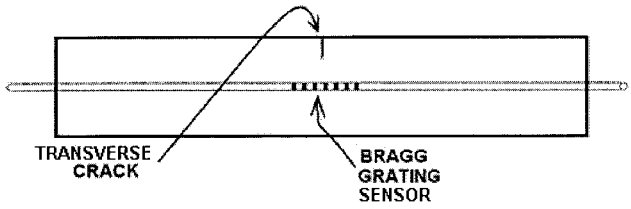


Figure 2. Diagram showing an intermediate step of a transverse matrix crack growth in a cross-ply laminate. In this case, the growing crack tip has not yet reached the location of the FBG sensor.

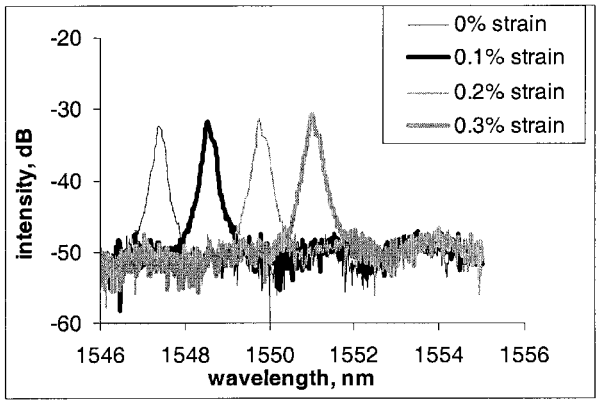


Figure 3. Plot FBG reflected spectra at increasing strains for the undamaged GFRP material.

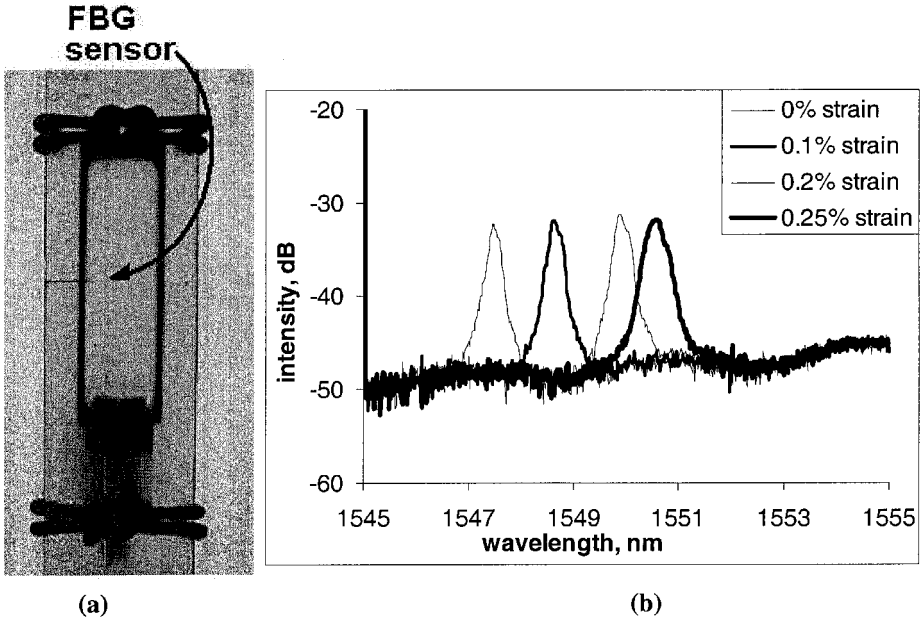
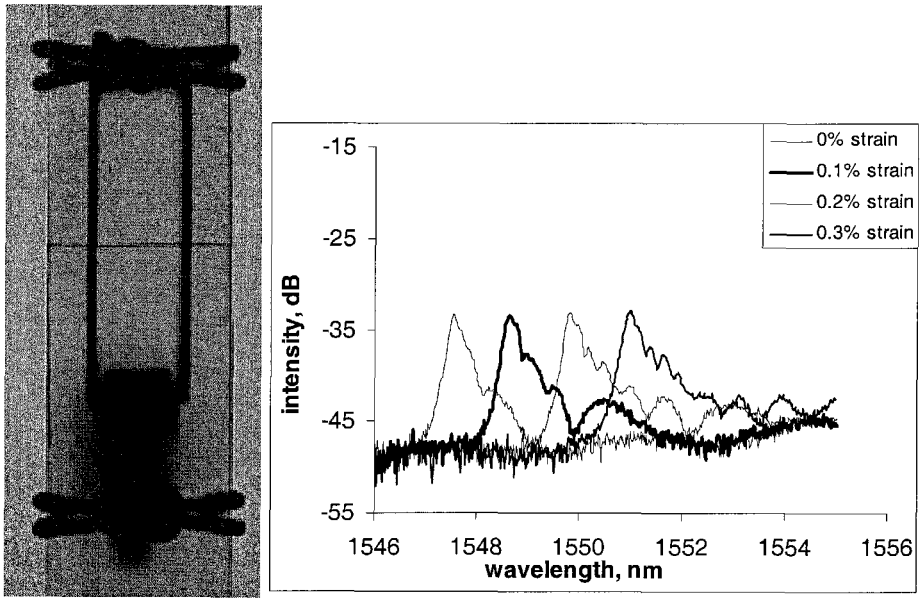


Figure 4. (a) Image of a GFRP cross-ply specimen during a tensile test. A matrix crack has grown partly across the coupon, but has not yet passed the FBG sensor
(b) Plot of FBG reflected spectra at increasing strains for the part-grown crack.

In Figure 5 the spectra are shown when a single matrix crack has grown passed the location of the Bragg grating. Fig. 5(a) shows the transparent cross-ply coupon with the transverse crack fully grown across the width. In this case, the back-reflected spectra become an asymmetrical bell-shape (Figure 5(b)), with a broadening on the side of longer wavelength after the main peak. Additionally, on the same side of the spectra, there are side bands of weaker intensity, than the main peak.

The skewed shape of the reflected spectrum is related to the higher strains in the 0^0 ply as a result of the transverse ply crack. The presence of the crack in the transverse ply produces a strain magnification in the adjacent longitudinal plies. As a result the grating pitch length over a length of approximately 5mm (i.e. approximately two ply thicknesses) of the sensor's total 10mm length undergoes a larger strain than the strain seen by the rest of the grating. Consequently, the region with the strain magnification produces the reflections giving rise to the sideband peaks found in the FBG spectra after cracking, while the remainder of the grating produces the same reflections as found before cracking producing the same main spectrum peak.



(a) (b)

Figure 5. (a) Image showing a GFRP cross-ply specimen during a tensile test. A matrix crack has grown fully across the coupon and has passed the FBG sensor.
(b) Plot of FBG reflected spectra at increasing strains for the fully-grown crack.

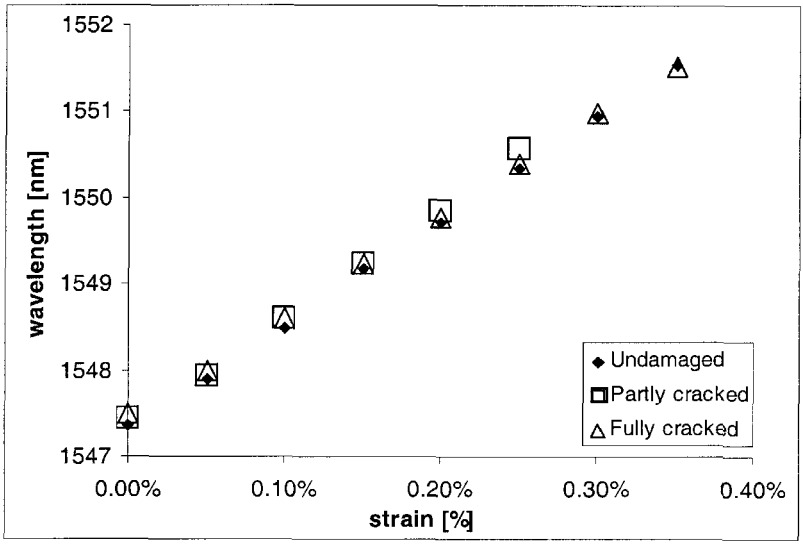


Figure 6. Plot of the wavelength shift undergone by the main spectrum peak in the cases of undamaged material, partially grown crack and fully grown crack.

The shift of the main spectra peaks for incremental tensile loading resulting from the three damage conditions monitored are shown in Figure 6. The wavelength shifts of the peak in each series are the same, confirming that the main spectrum peak results from reflections emanating in the grating regions not influenced by the presence of the crack.

CONCLUSION

An embedded optical FBG has been studied as a damage detection system for matrix cracks in a GFRP cross-ply composite laminate. The spectra reflected in the case of undamaged material had a single peak and a symmetrical shape. After the formation of the crack, the spectra presented a skewed shape, with secondary peaks developed on the longer wavelength side. The secondary peaks present on the spectra back-reflected by the sensor in the damaged material are due to reflections taking place in the region of the 0^0 ply where strain magnification occurs due to the transverse ply crack.

REFERENCES

[1] Kersey A., Davis M.A., Patrick H.J., LeBlanc M., Koo K.P., Askins C.G., Putnam M.A., Friebele J., "Fiber Grating Sensors" *Journal of Lightwave Technology* **15(8)** (1997) 1442-1463.

[2] H. Wang, S.L. Ogin, A.M.Thorne and G.T. Reed, "Use of a polarimetric sensor for damage detection in cross-ply composite laminate", in *Proceedings of ECCM-10*, Bruges (Belgium), June 2002.

[3] Okabe Y., Mizutani T., Yashiro S., Takeda N., "Detection of microscopic damages in composite laminates with embedded small diameter fiber Bragg grating sensors" *Composite Science and Technology* **62** (2002) 951-958.

[4] Guemes J.A., Menendez J.M., "Response of Bragg grating fiber-optic sensors when embedded in composite laminates" *Composite Science and Technology* **62** (2002) 959-966.

[5] M.A. Davis, A.D. Kersey, J. Sirkis, E.J. Friebele, "Shape and vibration mode sensing using a fiber optic Bragg grating array", *Smart Materials and Structures* **5** (1996) p. 759.

[6] V. Dewynter-Marty, P. Ferdinand, E. Bocherens, R. Carbone, H. Beranger, S. Bourasseau, M. Dupont, D. Blageas, "Embedded Fiber Bragg Grating Sensors for Industrial Composite Cure Monitoring" *JOURNAL OF INTELLIGENT MATERIAL SYSTEMS AND STRUCTURES* **9** (1998) p. 785.

[7] L. Dokos, M. Mowlem, A. Chambers, G. Brambilla, V. Pruneri, "Low velocity impact detection and damage assessment in composite materials using fibre Bragg grating sensors", in *Proceedings of ICCM-13*, Beijing – China, July 2001.

[8] M. Ussorio, H. Wang, S.L. Ogin, A.M. Thorne, G.T. Reed, "Use of Fibre Bragg Gratings for Damage Detection in Cross-Ply Laminates", in *Proceedings of Advancing with Composites – 2003*, Milan (Italy), May 2003.

[9] E. Bocherens, S. Bourasseau, V. Dewynter-Marty, S. Py, M. Dupont, P. Ferdinand, H. Berenger, "Damage detection in a radome sandwich material with embedded fiber optic sensors", *Smart Materials and Structures* **9** (2000) 310.

USE OF AN FFT BAND PASS FILTER FOR CRACK DETECTION BY AN EMBEDDED POLARIMETRIC SENSOR

H. Wang[1], S.L. Ogin[1], A.M.Thorne[1] and G.T. Reed[2]

[1]*School of Engineering*
[2]*School of Electronics and Physical Sciences*
University of Surrey, Guildford, Surrey GU2 5XH, UK

Abstract

Polarimetric optical fibre sensors have been embedded within the 0° ply and close to the 0/90 interface of a cross-ply GFRP laminate. The response of the embedded sensor to a transverse crack that passes the sensor in the adjacent 90° ply is a step change of the optical output. In the present study, it is shown that a band pass FFT (Fast Fourier Transform) filter can be employed to enable crack development to be identified in real-time from the optical output.

1. Introduction

Fibre optical sensors are the subject of intense interest for detecting various types of damage in composite materials. Some of the early work on damage detection concentrated on using attenuation of the intensity of the optical output due to fibre failure or bending losses induced in an area of damage [1]. More recent approaches have made use of the potential ability of sensors both to detect damage and to indicate its position. Such work has included the use of optical time domain reflectometry, optical coherence domain reflectometry, fibre Bragg grating sensors, Michelson interferometric sensors and polarimetric sensors [e.g. 2-7].

The present study uses a polarimetric sensor to detect damage development, specifically the growth of matrix cracks in a cross-ply composite laminate. When the strain state around the embedded polarimetric sensor changes, the relative phase of the two orthogonal modes of polarised light transmitted in the core of a polarisation-maintaining fibre changes, producing fringes which are detected at the output optical signals. Previous work [7, 8] has shown that the response of the embedded sensor to such a transverse crack that passes the sensor in the adjacent 90° ply results in a step change of the optical output. However, the step changes are often obscured by the noise of the optical signal and cannot be identified easily. To detect the transverse cracks, it is necessary to carry out a frequency analysis of the optical output.

2. Experimental Method

High-birefringence single-mode polarisation-maintaining Panda fibres (obtained from Fujikura Europe Ltd) were used to manufacture the sensors. Localisation of the gauge length within the optic fibre was achieved by rotating the axes of the fibre through 45° in the sensing section relative to the orientation of the lead-in/lead-out sections of the optical fibre. The sensor embedded in a cured coupon was connected to other parts of the optical path with two 0° splices. Splicing was carried out using a Fujikura fusion splicer. The sensor gauge lengths were in the range from 80 *mm* to 100 *mm*.

The polarimetric fibre optical sensors (FOS) were embedded in cross-ply laminates using a wet lay-up/frame winding technique [9] which produces an optical sensor embedded within one 0° ply of a cross-ply laminate. Coupons were cut from the laminate,

parallel to the 0° ply direction, ensuring that the optical sensor was located towards the centre of the coupon.

Linearly polarized light from a He-Ne gas laser, 633 *nm* operational wave length, was launched into one of the axes of the fibre core and the lead-out fibre was connected to a photoamplifier by a standard connector. Separation of the orthogonal modes of the optical signal was achieved by bending the lead-out part of the optical fibre. This caused the loss of one of the two orthogonal modes through the cladding enabling the optical output to be dependent on the fringes from one mode only [10]. A schematic of the edge of a coupon is shown in Figure 1.

The optical output was converted to a voltage and recorded simultaneously with the load and strain signals by the controller of an Instron servo-hydraulic testing machine (8000) operating at a sampling frequency of 1667 *Hz*. The servo-hydraulic testing machine was operated in load control mode. Standard self-tightening Instron grips were modified to accommodate the optical fibres emerging from the samples. During the tests, a 50 *mm* gauge length dynamic extensometer measured the longitudinal strain. The transparent coupon made it possible to observe the development of transverse cracks directly. The FFT (Fast Fourier Transform) analysis and FFT filter analysis of the optical output were carried out using Origin® software [11].

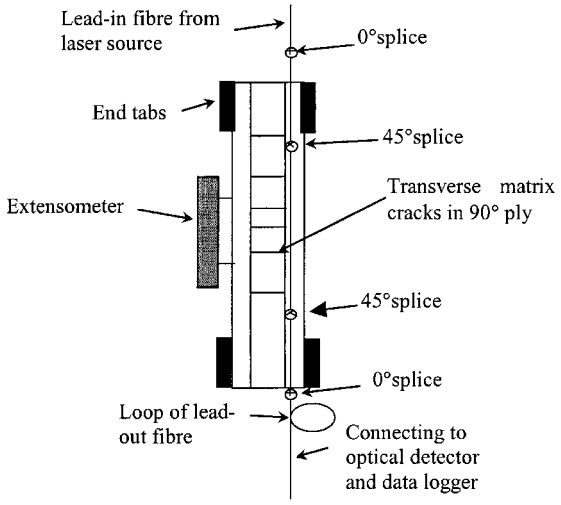


Figure 1. Schematic of experimental arrangement showing a $(0/90)_s$ coupon with transverse cracks in the 90° ply, viewed from the edge.

3. Experimental results and discussion

3.1. FFT analysis of the optical output

The optical response of the polarimetric sensor to a crack which passes the sensor is a step-change in optical output, as shown in Figure 2. However, sometimes, the signals are not so clear. Figure 3 shows the optical signal from a coupon over a 40 second period under quasi-static load when 5 cracks developed as determined from a video recording of the test.

The FFT analysis of the optical signals shown in Figure 3, i.e. when 5 cracks passed the sensor, is shown in Figure 4(a). For comparison, Figure 4(b) shows the FFT analysis of a period of 50 seconds when no cracks occurred. In Figure 4(a), the FFT analysis of optical signal shows peaks at about 20 Hz, 50 Hz, 75 Hz, 100 Hz, 150 Hz, 200 Hz, 320 Hz and a

collection of peaks at about 65 Hz. The spectrum also contains strong contributions from low frequencies (< 5 Hz) due to the irregularity of the experimental optical fringes. The peak at 320 Hz may be induced by the test machine [12]. The optical spectrum shown in Figure 4(b) is almost identical to that shown in Figure 4(a), although there are some small changes in the amplitudes of the peaks. This suggests that the step-changes in the optical signals do not generate additional peaks, even at high frequencies. However, the Fourier transform spectrum of the step change in optical fringes is composed of a series of frequencies extending from almost zero to infinity with decreasing amplitude [13]. The reason why those frequencies cannot be obtained from Figure 4 is because the step-change comprises contributions from a range of different frequencies. The contributions of the step-changes will be similar in amplitude to the original information and cannot be picked out, i.e. the signal to noise ratio is small.

To identify the step-changes in the optical signal, filters need to be employed to observe the time domain signal with the noise frequencies removed. One approach is FFT filtering.

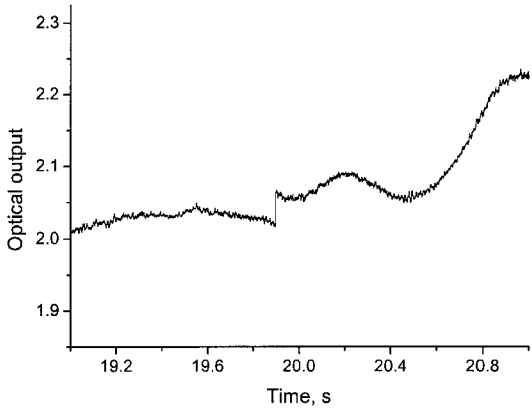


Figure 2. The step-change in optical output when a crack passes the embedded sensor

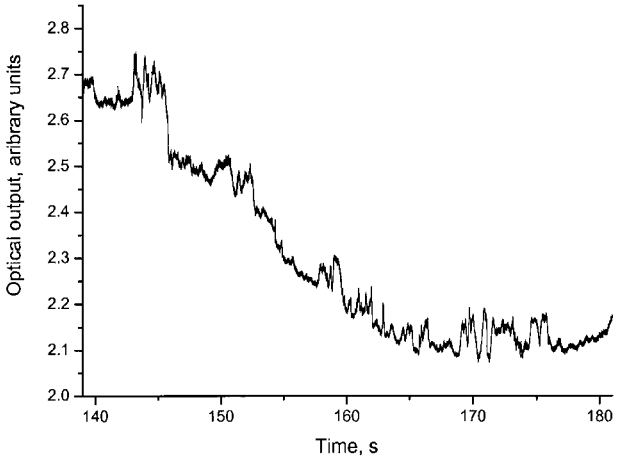


Figure 3. Experimental results from a cross-ply coupon over 40 seconds when 5 cracks passed the sensor.

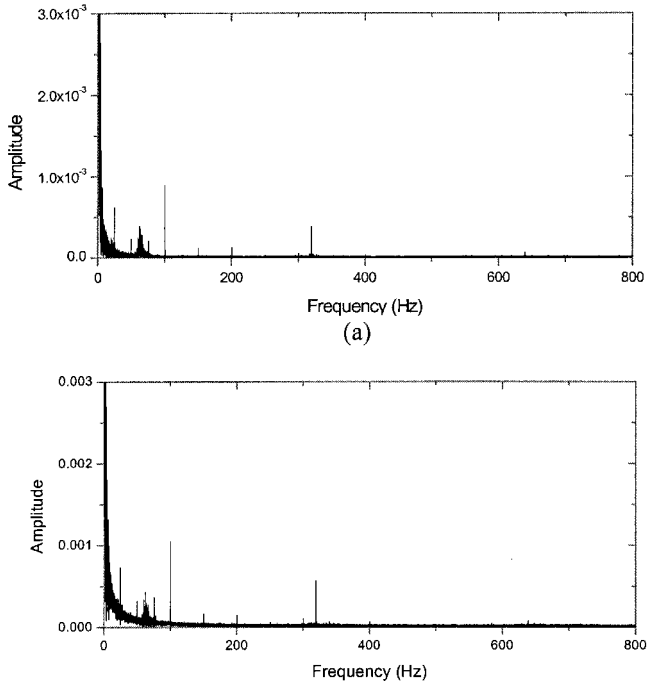


Figure 4 FFT analysis of the optical signals.
(a) FFT analysis of the optical signal shown in Figure 3.
(b) FFT analysis of the optical signal over 50 seconds when no cracks occurred.

3.2 Application of FFT filter to the FFT analysis results

Unlike the FFT analysis, which shows the contributions of different frequency components

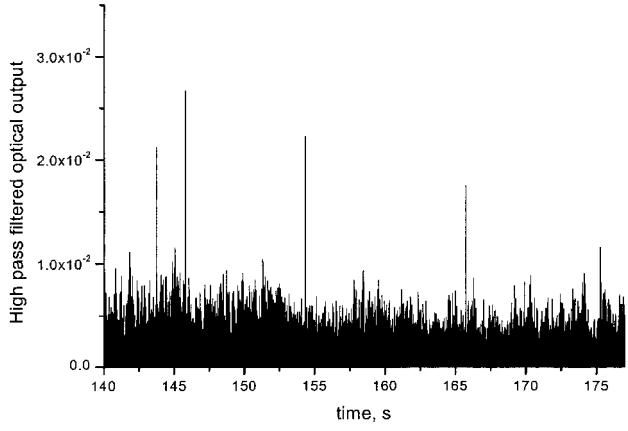


Figure 5 High pass filtered optical signal shown in Figure 5(b) with a value of 50 Hz.

to the spectrum, the FFT filter can provide information about contributions of a band of frequencies to the spectrum over a particular period of time. Thus the contributing frequency of the step-changes in the optical signal can be picked out.

A high pass FFT filter, which only allows frequencies higher than a defined value to pass through, blocks the lower frequencies. A 50 Hz high pass FFT filter has been applied to the set of optical data shown in Figure 4(a) during the period when 5 cracks passed the sensor and the results are shown in Figure 5. It is clear that five peaks emerge: at 143.7 seconds, 145.8 seconds, 154.3 seconds, 165.7 seconds and 175.3 seconds. Careful inspection of the optical signals, which will be shown later, indicates that step-changes can be found at these times, suggesting that the cracks had propagated past the sensor at these particular times. The Fourier filtering process has enabled the contributions of the step-changes to the frequency spectrum to be distinguished from the original information.

The amplitudes shown in Figure 5 are the contributions of all the frequencies higher

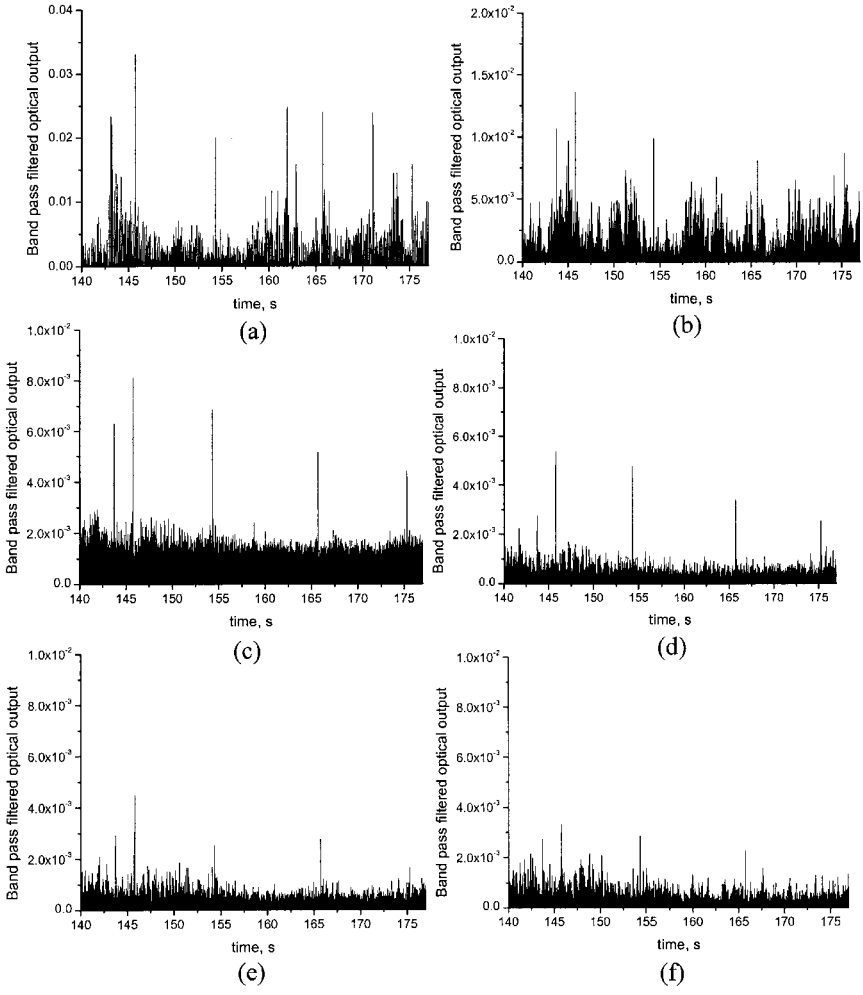


Figure 6 Band pass FFT filtered optical signal shown in Figure 5(b).
(a). 5 – 50 Hz; (b). 50 – 100 Hz; (c). 100 – 150 Hz;
(d). 150 – 200 Hz; (e). 200 – 250 Hz; (f). 250 – 300 Hz;

than 50 Hz to the amplitudes of the five peaks. The signal/noise ratio is improved significantly as the FFT filter is applied, especially to the selected high frequencies. To distinguish the contributions of different frequency components to the spectrum, different band-pass FFT filters have been applied to the set of optical data shown in Figure 4(a) and the results are shown in Figure 6. The contribution of lower frequencies to the five peaks, for example, frequencies lower than 100 Hz, is relatively high. This is shown in Figure 6(a) which employs a band pass filter in the range 5 to 50 Hz and Figure 6(b) which employs a band pass filter of 50 to 100 Hz. However, due to the existence of other noise frequencies lower than 100 Hz, i.e. the frequencies seen in the spectrum of Figure 6(a) at 25 Hz, 50 Hz and the band of frequencies around 65 Hz, the five peaks corresponding to the formation of the five cracks are not easily identified. When the band pass filter moves to higher frequencies (100–150 Hz, 150–200 Hz, 200–250 Hz, 250–300 Hz), the five peaks are easier to recognise, especially in Figure 6(c) and Figure 6(d), for which the band pass filter is between 100 Hz and 200 Hz. When the frequencies of the band pass filter are higher than 250 Hz, the amplitudes of the five peaks are reduced to the level of noise and can hardly be picked out, as shown in Figure 6(f).

Contributions of different bands of frequencies to the amplitudes of the five peaks shown in Figure 6 are plotted in Figure 7. In this figure, the amplitude of each of the five peaks for the different frequency ranges is plotted against the mean value of the frequency range. The figure shows that the Fourier transform spectrum of the step-changes in the optical signal is composed of a series of frequencies. The contributions of different frequencies decrease when the band of frequencies analysed is moved to higher values. Note that in Figure 7, each data point presents the contribution to the amplitude of the peak by a band of frequencies 50 Hz wide (45 Hz for the first column of the data).

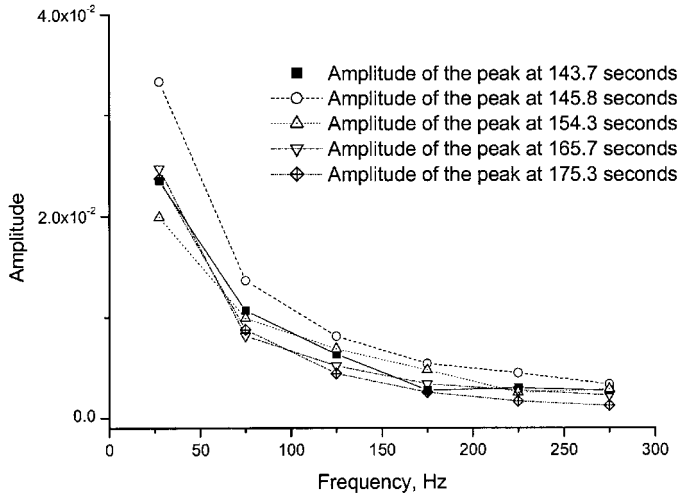


Figure 7 Contributions of different frequencies to the five peaks shown in Figure 6.

The complete FFT band pass filtered results for the optical output signal shown in Figure 3 (when 5 cracks passed the sensor) are shown in Figure 8(a). The lower frequency of the band pass filter was chosen to be 100 Hz to block out irrelevant frequencies, and the higher frequency was chosen to be 300 Hz to obtain a good signal/noise ratio. The detail of the optical output for each crack (labelled A to E) is shown in Figure 8 (b) to 8(f).

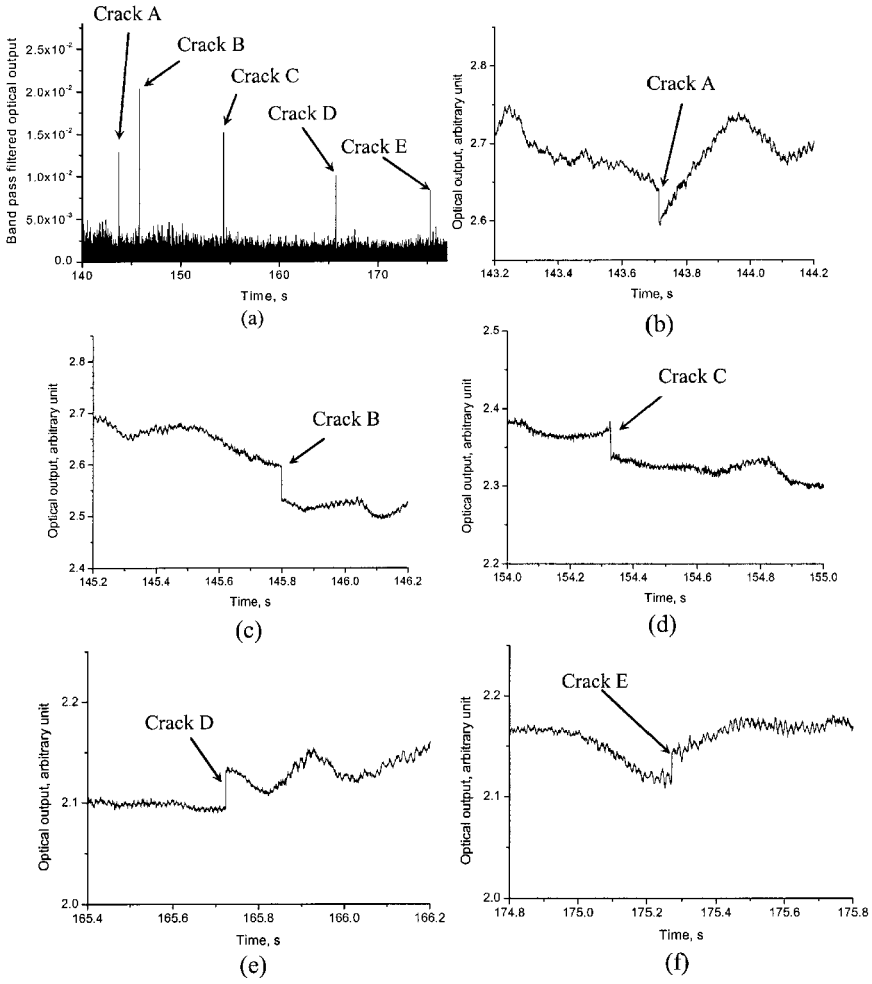


Figure 8 Transverse crack detection by an embedded polarimetric sensor
(a) Band pass filtered optical signal; (b) The optical signals of Crack A;
(c) The optical signals of Crack B; (d) The optical signals of Crack C;
(e) The optical signals of Crack D; (f) The optical signals of Crack E.

4. Conclusion

The optical output signals have been analysed using the FFT function in Origin® software. The results show when a crack passes adjacent to an embedded sensor, components of high frequencies emerge in the Fourier spectrum as a consequence of the step-change in the optical signal induced by the crack. The times when the high frequencies occur can be obtained from a FFT band pass filter analysis and hence the time when cracks occur can be identified. The success of this technique shows that it should be possible to detect transverse cracks in a composite structure in real time using an embedded polarimetric sensor.

References

1. E. Udd, *Fibre Optic Smart Structure*. New York Wiley, (1995).
2. E. Bocherens, S. Bouraseau and V. Dewynter-Marty, 'Damage detection in a radome sandwich materil with embedded fibre optic sensors', *Smart Materials and Structures,* 2000 **9** 310-315.
3. N. Takeda, T. Kosaka, K. Hotate and T. Saida, 'Prelimenary studies on indentification of mechanical loading by distributed fibre optic sensors', *US-Japan Workshop on Smart Materials,* 1997 227-234.
4. I. Kwon, G. Kim and C. Hong. 'Simultaneous sensing of the strain and points of failure in composite beams with an embedded fibre optic Michelson sensor', *Composite Science and Technology*, 1997 **57** 1639-1651.
5. H. Tsuda, I. Takahashi and K. Urabe, 'Damage monitoring of carbon fibre-reinforced plastics with Michelson interferometric fibre-optic sensor'. *Journal of Materials Science*, 1999 34 4163-4172.
6. V. Murukeshan, P. Chan, O. Seng and A. Asundi, 'On-line health monitoring of smart composite structures using fibre polarimetric sensor'. *Smart Materials and Structures*, 1999 **8** 544-551.
7. H. Wang, S. Ogin, . Thorne and G. Reed, 'Use of a polarimetric sensor for damage detection in a cross-ply composite laminate', Proc. of 10th *European Conference on Composite Materials*, 2002
8. H. Wang, S. Ogin, A. Thorne and G. Reed, 'Crack detection around a hole in a cross-ply laminate using an embedded polarimetric fibre optic sensor' Proc. of 14th *Internal Conference on Composite Materials*, 2003
9. E. Barton, S. Ogin, A. Thorne and G. Reed, 'Interaction between optical fibre sensors and matrix cracks in cross-ply GRP laminates—part 1: passive optical fibres', *Composite Science and Technology*, 2000 61 1863-1869.
10. M. Varnham, A. Barlow, D. Payne and E. Tarbox, 'Coiled-birefringent-fibre polarisers'. *Optics Letters*, 1984 9 306-308.
11. Origin Manual, Microcal Softwar, Inc., 1999.
12. H. Wang, Ph.D thesis, University of Surrey, 2003.
13. Kraniauskas P. *Transforms in Signals and Systems*; Addison-Wesley, 1991.

THE IMPORTANCE OF DYNAMIC BEHAVIOUR IN THE DESIGN OF LAMINATED COMPOSITE BEAMS

S.H.R. Eslimy-Isfahany* and J. R. Banerjee+
*Civil Engineering Department, Isfahan University of Technology, Isfahan 84156, Iran.
+ School of Engineering and Mathematical Sciences, City University, London, UK.

ABSTRACT

The focus of this investigation is on improving the performance of composite structures by enhancing their dynamic characteristics. Using linearly-elastic small-deflection theory, an analytical method is developed to perform the response analysis of bending-torsion coupled beams made of composite materials when subjected to deterministic or random loads. The procedure incorporates the dynamic stiffness matrix of a composite Timoshenko beam and then uses generalised coordinates by utilising the normal modes, so that the overall response of the beam is computed by the superposition of all individual responses in each mode. This methodology sets a trend for dynamic response analysis of laminated composite structures with particular reference to thin-walled composite beams. This is an essential step towards computer-integrated design and fabrication of such structural components with due attention to optimisation criteria.

1. INTRODUCTION

The use of composite materials in structures has attracted considerable attention in recent years [1-3]. This is because fibrous composites offer numerous advantages over isotropic materials. Components made of anisotropic composite materials are ideal for structural applications due to their high strength-to-weight ratio, and their ability to be tailored and designed to meet all specific stiffness and strength requirements of a structure. These extraordinary properties have enabled the design engineers to have greater confidence in the materials' potential and their structural applications [1]. Lately, model specifications for FRP materials for use in civil engineering structures have also been proposed [3].

Because of the growing interest in the application of composite materials as structural elements, there is a need for the development of analytical and numerical methods to predict the behaviour of thin-walled composite structures in free vibration and dynamic response [4-10]. It is also equally important to plan for well-designed experiments to achieve a better understanding of the behaviour of composite materials to be used in designing structures, because these materials may behave relatively less predictably than conventional metals at a micro or macro level than expected [2]. Although there is a wealth of literature on the static stress analysis of composite structures [12-13], there are very few published work on the evaluation of dynamic stress analysis in composite structures [6]. This warrants an investigation on the subject matter.

An exact analytical methodology is presented here to address the dynamic response characteristics of a class of thin-walled laminated composite beams in order to facilitate a better understanding and to provide a benchmark for others using less rigorous methods [7, 9, 10]. The dynamic response of the beam is described by its (i) flexural deflection with the corresponding slope and torsional rotation; (ii) dynamic shear force, bending moment and torque at various points; and (iii) normal and shear stresses in the laminates.

2. SOME PRELIMINARIES AND BASIC ASSUMPTIONS

The structural elements in this investigation are straight beams, which may have a flat or thin-walled closed cross-section. Carbon fibre, glass fibre and Kevlar are the main types of fibrous composite materials considered in this study. The flat composite beam is assumed to have symmetric cross-ply (either balanced or unbalanced) and the profile section is assumed to have Circumferentially Asymmetric Stiffness (CAS) configuration [7-8]. A generally used box beam construction is a practical example of the latter.

It firstly is necessary to establish the rigidity properties of the beam. For composite materials, due to the fibrous nature of their make up, the eventual material characteristics will vary with the orientation of the fibres as well as the stacking sequence of the plies. The cross-section of the structure will also affect the mode of deformation and ultimately the stress-strain conditions in the structure. In order to obtain a good estimate of the cross-sectional and other properties of composite structures, considerable efforts have been made in the past two decades [4, 6, 8].

The analysis of dynamic response in this paper includes both geometric and material coupling between bending and torsional deformations of composite beams. Bending-torsion coupling effects in composite beams occur due to material and/or geometric coupling. Material coupling arises from the anisotropic nature of fibrous composites, while the geometric coupling arises from the non-coincident centroid and geometric shear centre of the beam cross-section which are properties of the geometry.

With regard to the damping behaviour, linear viscous damping in shear, flexure and torsion are the only sources of damping taken into account. It is assumed that each point of the cross-section moves with its own local velocity, so that the local damping force, bending moment and torque for each span-wise element are a product of the local velocity and damping terms. Throughout this work, the energy dissipation during vibration and response analysis was included in the form of modal damping after the equations of motion were uncoupled. However, it is possible to include more refined forms of energy dissipation by modelling the composite laminate as a viscoelastic material.

A first-order shear theory is introduced to incorporate the effect of shear deformation. Effect of rotatory inertia and a constant axial load (compressive or tensile) are also taken into account when developing the approach. These effects may significantly affect the dynamic response characteristic of composite laminates.

Warping stiffness and warping inertia are neglected here, because they have relatively less significant effects on the dynamic response of beams with closed cross-section. However, their inclusion in the equations of motion, especially, for beams with open cross-section is currently under investigation, which is beyond the scope of this paper.

The methodology presented may be used for laminated composite beams with non-uniform cross-section to cover many practical applications. This can be achieved either by defining a dynamic stiffness matrix for the non-uniform beam, or by dividing it into a number of elements with uniform cross-sections, so as to model it as a stepped beam.

3. METHODOLOGY

At first, the basic governing differential equations of motion of composite beams under the action of external forces were derived by the authors in their earlier work [9-11] and are presented here. The solution of the governing differential equations of motion is expressed in terms of normal modes and generalised coordinates. The modal analysis of the beam is carried out using the dynamic stiffness method in order to establish free vibration characteristics [7]. The orthogonality condition of the beam is also derived to uncouple the equations of motion in each mode.

Next, the response problem is formulated and the dynamic stresses are determined [9, 10]. The beam is subjected to time dependent forces and/or torques which can be either concentrated or distributed over the length. Both deterministic and random loads

are considered. An important example of a deterministic load is the one that varies harmonically with time. The Duhamel integral is employed to calculate the response to any arbitrary time dependent deterministic load. The random load is assumed to be Gaussian, having both stationary and ergodic properties. The evaluation of the response to random load is carried out in the frequency domain by relating the Power Spectral Density (PSD) of the output to that of the input using the frequency response function.

4. AN OUTLINE OF THE FORMULATION

One example of a bending-torsion coupled composite beam with profile cross-section is shown in Figure 1. The mass and the elastic axes (i.e. the loci of the mass centre and the shear centre of the cross section) of the beam are separated by a distance x_α as shown.

4.1. Governing differential equations of motion

The differential equations of motion of an axially loaded and viscously damped bending-torsion coupled Timoshenko composite beam (Figure 1) are taken in the following form [9]

$$K\psi''' + k'AG(u'' - \theta') - P(u'' - x_\alpha\psi'') - c_1(\dot{u} - x_\alpha\dot{\psi}) - m(\ddot{u} - x_\alpha\ddot{\psi}) = f(y,t) \quad (1)$$

$$Ku''' + GJ\psi'' - P\left\{\left(I_\alpha / m\right)\psi'' - x_\alpha u''\right\} - c_2\dot{\psi} + c_1 x_\alpha\dot{u} - I_\alpha\ddot{\psi} + mx_\alpha\ddot{u} = g(y,t) \quad (2)$$

$$EI\theta'' + k'AG(u' - \theta) - c_3\dot{\theta} - \rho I\ddot{\theta} = 0 \quad (3)$$

where $u=u(y,t)$, $\theta=\theta(y,t)$ and $\psi=\psi(y,t)$ are the transverse displacement and the flexural and the torsional rotation of the flexural axis of the beam, respectively (the flexural axis is defined here as the locus of the shear centres of the beam cross sections), $f(y,t)$ and $g(y,t)$ are the external force and torque acting on and about the flexural axis of the beam, m is the mass per unit length, I_α is the mass moment of inertia per unit length about elastic axis, ρI is the mass moment of inertia about X axis, P is a constant axial load. An over-dot represents differentiation with respect to time and a dash represents differentiation with respect to space. The coefficients c_1, c_2 and c_3 in Eqs.(1-3) are linear viscous damping terms per unit length in flexure, torsion and shear, respectively. In this paper the cross-sectional properties, namely, the bending (EI), torsional (GJ), bending-torsion coupling (K) and transverse shear ($k'AG$) rigidities of the composite beam, are obtained using existing literature [8], which is essentially based on the variational-asymptotical method.

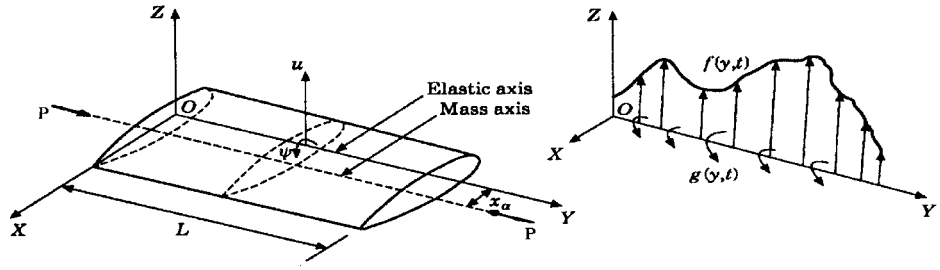
4.2. Free vibration analysis

For undamped free vibration, the external load $f(y,t)$ and torque $g(y,t)$, and the damping coefficients are set to zero. The solutions for principal modes are in the form of [7]

$$U(\xi) = A_1\cosh\alpha\xi + A_2\sinh\alpha\xi + A_3\cos\beta\xi + A_4\sin\beta\xi + A_5\cos\gamma\xi + A_6\sin\gamma\xi \quad (4)$$

$$\Theta(\xi) = B_1\cosh\alpha\xi + B_2\sinh\alpha\xi + B_3\cos\beta\xi + B_4\sin\beta\xi + B_5\cos\gamma\xi + B_6\sin\gamma\xi \quad (5)$$

$$\Psi(\xi) = C_1\cosh\alpha\xi + C_2\sinh\alpha\xi + C_3\cos\beta\xi + C_4\sin\beta\xi + C_5\cos\gamma\xi + C_6\sin\gamma\xi \quad (6)$$



(a) (b)

Figure 1 (a) The coordinate system and notation for axially loaded bending-torsion coupled beam with profile cross-section; (b) Distribution of flexural and torsional loads;

where A_1 -A_6 , B_1 -B_6 and C_1 -C_6 are the three different sets of constants, α, β, γ are functions of mechanical properties of the beam and ξ=y/L.

Orthogonality condition of the principal modes of free vibration can be derived as [10]

$$\int_0^1 [mU_m U_n + I_\alpha \Psi_m \Psi_n + \rho I \Theta_m \Theta_n - m x_\alpha (U_m \Psi_n + U_n \Psi_m)] d\xi = \mu_n \delta_{mn} \quad (7)$$

where μ_n is the generalised mass in the nth mode and δ_{mn} is the Kronecker delta function.

4.3. Response to random loads

The randomly varying excitation can be presented by [5, 6]

$$f(\xi,t) = f(\xi).\chi_f(t) \quad \& \quad g(\xi,t) = g(\xi).\chi_g(t) \quad (8)$$

where $\chi_f(t)$ and $\chi_g(t)$ are stochastic processes and their spectral densities are $S_f^{\chi}(\Omega)$ and $S_g^{\chi}(\Omega)$, respectively. The cross-spectral density for the above loading is

$$S_f(\xi_1,\xi_2,\Omega) = f(\xi_1) f(\xi_2) S_f^{\chi}(\Omega) \quad \& \quad S_g(\xi_1,\xi_2,\Omega) = g(\xi_1) g(\xi_2) S_g^{\chi}(\Omega) \quad (9)$$

For distributed loading, the spectral density functions of the bending displacement and flexural and torsional rotations (i.e. $S_u(\xi,\Omega)$, $S_\theta(\xi,\Omega)$ and $S_\psi(\xi,\Omega)$) are related to the cross-spectral densities of the force $S_f(\xi_1,\xi_2,\Omega)$ and torque $S_g(\xi_1,\xi_2,\Omega)$ by the following relationships [10]

$$\begin{aligned}
S_u(\xi,\Omega) &= \left|\sum_{n=1}^{\infty} f_n d_n(\Omega) U_n(\xi)\right|^2 S_f^{\chi}(\Omega) + \left|\sum_{n=1}^{\infty} g_n d_n(\Omega) U_n(\xi)\right|^2 S_g^{\chi}(\Omega) \\
S_\theta(\xi,\Omega) &= \left|\sum_{n=1}^{\infty} f_n d_n(\Omega) \Theta_n(\xi)\right|^2 S_f^{\chi}(\Omega) + \left|\sum_{n=1}^{\infty} g_n d_n(\Omega) \Theta_n(\xi)\right|^2 S_g^{\chi}(\Omega) \\
S_\psi(\xi,\Omega) &= \left|\sum_{n=1}^{\infty} f_n d_n(\Omega) \Psi_n(\xi)\right|^2 S_f^{\chi}(\Omega) + \left|\sum_{n=1}^{\infty} g_n d_n(\Omega) \Psi_n(\xi)\right|^2 S_g^{\chi}(\Omega)
\end{aligned} \quad (10)$$

in which

$$d_n(\Omega) = 1/\mu_n\left(\omega_n^2 - \Omega^2 + 2i\zeta_n \Omega \omega_n\right) \quad (11)$$

where ζ_n is the non-dimensional damping coefficient in the nth mode given by [9, 14]

$$\int_0^1 [c_1 U_m U_n + c_2 \Psi_m \Psi_n + c_3 \Theta_m \Theta_n - c_1 x_\alpha (U_m \Psi_n + U_n \Psi_m)] d\xi = 2\zeta_n \omega_n \mu_n \delta_{mn} \quad (12)$$

where ω_n is the natural frequency of the nth mode and

$$f_n = \int_0^1 V_n(\xi) f(\xi) d\xi \quad , \quad g_n = \int_0^1 V_n(\xi) g(\xi) d\xi \quad (13)$$

where

$$V_n(\xi) = -a_F U_n(\xi_1) - a_G \Psi_n(\xi_1) \quad (14)$$

The values of a_F and a_G can be either 1 or 0 depending upon whether or not bending and/or torsional loads are present. Finally, the mean square value of the response can be found by integrating the spectral density functions over all frequencies, so that [5]

$$\left\langle u^2(\xi,t)\right\rangle = \int_{-\infty}^{\infty} S_u(\xi,\Omega) d\Omega, \left\langle \theta^2(\xi,t)\right\rangle = \int_{-\infty}^{\infty} S_\theta(\xi,\Omega) d\Omega, \left\langle \psi^2(\xi,t)\right\rangle = \int_{-\infty}^{\infty} S_\psi(\xi,\Omega) d\Omega \quad (15)$$

If the input random excitation follows a Gaussian probability distribution, the response probability will also be Gaussian and therefore, the response can be fully described by its spectral density function.

4.4. Response to deterministic loads

Using Duhamel's integral, the solutions for the bending displacement u, bending rotation θ and twist ψ due to the applied loads can be obtained as follows [10]

$$u(y,t)=\sum_{n=1}^{\infty}q_n(t)U_n(y),\quad \theta(y,t)=\sum_{n=1}^{\infty}q_n(t)\Theta_n(y),\quad \psi(y,t)=\sum_{n=1}^{\infty}q_n(t)\Psi_n(y) \qquad (16)$$

where $\omega_{nd} = \omega_n (1-\zeta_n^2)^{1/2}$. Response of the generalised coordinates $\boldsymbol{q_n(t)}$ can be expressed in terms of initial conditions ($\boldsymbol{A^*_n}$ - $\boldsymbol{B^*_n}$), and generalised forces $\boldsymbol{F_n(t)}$ - $\boldsymbol{G_n(t)}$ as follows

$$q_n(t)=e^{-\zeta_n\omega_n t}\{A_n^*\cos(\omega_{nd}t)+B_n^*\sin(\omega_{nd}t)\}$$
$$+\frac{1}{\omega_{nd}}\int_0^t\{F_n(\tau)+G_n(\tau)\}e^{-\zeta_n\omega_n(t-\tau)}\sin\{\omega_{nd}(t-\tau)\}d\tau \qquad (17\text{-b})$$

$$F_n(t)=-\frac{1}{\mu_n}\int_0^L U_n(y)f(y,t)dy,\qquad G_n(t)=-\frac{1}{\mu_n}\int_0^L\Psi_n(y)g(y,t)dy \qquad (17\text{-c})$$

4.5. Stress analysis

In this investigation, failure criteria of fibrous composite laminates depend on excessive dynamic stresses. To find the stresses in fibres, we firstly need to obtain the internal forces. For instance, in a cantilever beam internal shear force $\boldsymbol{V}$, bending moment $\boldsymbol{M}$ and torque $\boldsymbol{T}$ are defined as follows

$$V=\int_L^y\left[f(y,t)+m(\ddot{u}-x_\alpha\ddot{\psi})\right]dy+V_L,\qquad M=\int_L^y\left[V+\rho\, I\ddot{\theta}+P(u'-x_a\psi')\right]dy+M_L$$
$$T=\int_L^y\left[g(y,t)-(mx_\alpha\ddot{u}-I_\alpha\ddot{\psi})\right]dy+T_L \qquad (18)$$

and $\boldsymbol{V_L}$, $\boldsymbol{M_L}$ and $\boldsymbol{T_L}$ are, respectively, the values of concentrated external flexural force, bending moment and torque at $\boldsymbol{y=L}$ (or $\boldsymbol{\xi=1}$).

Note that, the equilibrium of forces acting on the differential element is considered, when the beam is in maximum displacement, i.e. acceleration is maximum and speed is zero. Therefore, damping forces, which are assumed to be proportional to speed, are not present in the equilibrium. Moreover, damping forces inn a structure are not in the same phase as external and inertia forces and usually, they are relatively smaller than others.

Normal stress (σ_y) in each ply induced by axial load and internal bending moment and, when there is at least one axis of symmetry in a closed cross section, shear stress (τ_{xy}) in each ply induced by internal shear force and torque are, respectively, given by [13]

$$\sigma_y=\frac{E_y P}{\sum_{j=1}^{NE}(E_y\,tb)_j}+\frac{E_y M\,z}{\sum_{j=1}^{NE}(E_y\,I_{xx})_j},\qquad \tau_{xy}=-\frac{E_y V}{tI_{xx}'}\int_0^s t\,z\,ds+\frac{T}{2t\oint dA} \qquad (19)$$

where $\boldsymbol{b}$ is the width of the laminate, $\boldsymbol{t}$ is the thickness of the laminate , $\boldsymbol{z}$ is the ordinate from the neutral plane of the section to the point of the element in equation, $\boldsymbol{s}$ is a general point on the cross-section , $\boldsymbol{E_y}$ membrane equivalent young's modulus value of each laminate in reference $\boldsymbol{y}$ direction for individual element in the section, NE is the number of laminates in the section, $\boldsymbol{I_{xx}}$ is second moment of inertia of each laminate about the neutral plane of the section and $\oint dA$ is the area enclosed by the closed section profile.

5. APPLICATION OF THE METHODOLOGY AND KEY FINDINGS

Based on the proposed methodology, a suite of computer programs is developed and used to predict the free vibration and the response characteristics of thin-walled composite beams, which can be incorporated into a CAD/CAM system. This will increase design accuracy and provide a better understanding about the behaviour of composite structures.

For illustrative purposes, a cantilever composite box beam with following properties is considered (Figure 2), which exhibits material bending-torsional coupling [9].

$E_1 = 206.92 \times 10^9\ Nm^{-2}$
$E_2 = E_3 = 5.17 \times 10^9\ Nm^{-2}$
$G_{12} = 3.10 \times 10^9\ Nm^{-2}$
$G_{13} = G_{23} = 2.55 \times 10^9\ Nm^{-2}$
Thickness=1.016 cm
Length = 203.2 cm
$\nu_{12} = \nu_{23} = \nu_{13} = 0.25$
$\rho = 1529.48\ kgm^{-3}$

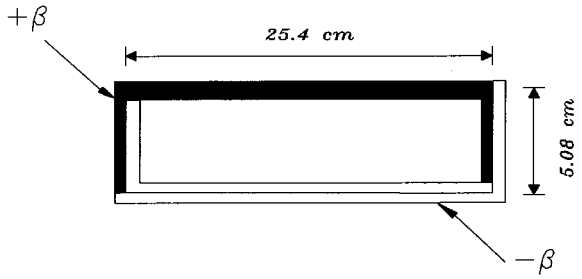


Figure 2 Configuration of the laminated composite beam [9].

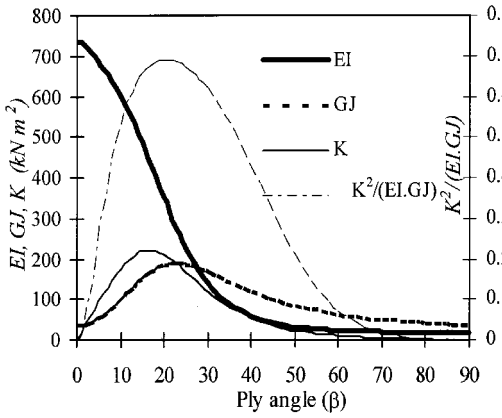


Figure 3 Variation of flexural (EI), torsional (GJ), bending-torsion coupling (K) rigidities and coupling parameter against ply angle.

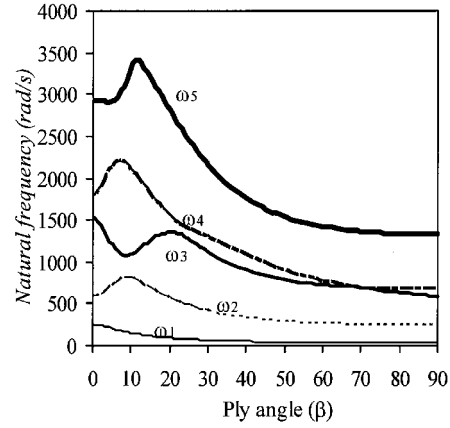


Figure 4 Variation of the first five natural frequencies of the composite beam against ply angle.

The rigidity properties of the beam are calculated by using the theory of Armanios and Badir [8] and their variations with ply angle are shown in Figure 3. Using the dynamic stiffness matrix method, the first five natural frequencies and mode shapes of the beam were computed for various ply angles. The variations of these natural frequencies with ply angle are also shown in Figure 4. The modal interchanges (i.e. flip-over from bending to torsional mode and vice-versa) due to changes in ply orientations were observed in the results for all natural frequencies except for the fundamental [10].

In addition, a detailed parametric study on a range of composite beams was undertaken and numerical results were obtained, fully examined and thoroughly verified [9-10, 14]. In the course of this research, the following insights have been gained into the free vibration behaviour and the dynamic response characteristics of thin-walled laminated fibrous composite beams. For brevity, only the key findings are presented here.

5.1. Importance of shear deformation, rotatory inertia and axial load

The effect of an axial load on the free vibration and dynamic response of the beam can be significant. Effects of a compressive axial load are opposite to those of a tensile load as expected. A compressive load generally reduces the natural frequencies and increases the dynamic response of the beam whereas a tensile load has a stabilising effect, increasing the natural frequencies and reducing the dynamic response.

Shear deformation and rotatory inertia may also affect natural frequencies and mode shapes in almost all modes, since most of the modes of composite beams are generally coupled in bending and torsion. Evidently, the effect will be relatively more significant on

bending dominated modes, but less on torsion dominated modes. Since lower frequencies of short beams are usually torsion dominated, therefore, for such beams these effects are much more prominent on higher modes.

Moreover, changing the slenderness (L/r) ratio can alter a bending dominated mode to a torsion dominated one and vice-versa. For a given L/r ratio, the effects of shear deformation and rotatory inertia are more pronounced in higher natural frequencies. For structural elements with relatively higher L/r ratio, these effects will also be evident on lower modes. However, unlike the metallic Timoshenko beam, the effects of shear deformation and rotatory inertia are not necessarily at their maximum when the slenderness ratio is at its minimum. The reason for this can be attributed to the coupling effect between the bending and torsional modes.

In general, the responses of beams with a greater degree of end constraints (such as clamped-clamped and clamped-simply supported beams) are seen to be more affected by the shear deformation than beams with a lesser degree of end-constraints (such as simply supported-simply supported and cantilever beams). The thicker and stiffer stocky beams are also more susceptible to the effect of shear deformation. In response analyses and reliability studies of such beams, it is therefore important to consider the effect of shear deformations.

5.2. The generalized mass and significance of modal interchange

Two influential concepts on the dynamic performance of composite structures are also considered here. One is the interpretation of normal modes using the concept of generalised mass in each of the modes of vibration, which has not been particularly featured in the existing literature. The other one is the significance of modal interchanges between flexural and torsional modes of vibration, which may occur due to the effects of axial load, shear deformation and/or rotatory inertia as well as the variation in ply angles.

The investigation confirms that illustration of a mode shape in the form of displacements or rotations may not be sufficient to identify the characteristics of a mode, whose main constituent part can be bending, torsion or bending-torsion coupled. This is because, when looking at the mode shape, one is confronted with the idea of an invalid comparison of dissimilar quantities. In the absence of any suitable criteria, the common practice is to compare linear displacement (arising from bending action) with that of torsional rotation (arising from twisting action). This is clearly evident from the literature.

An alternative, but elegant procedure, is based on the concept of generalised mass associated with a particular mode given by Eq. (7) from the orthogonality condition of the principal modes of free vibration of a bending-torsion coupled Timoshenko beam. As it can be seen from Eq. (7), the expression for the generalised mass μ_n has four contributory terms. These are: mU_n^2 which is due to flexure deformation alone, $\rho I \Theta_n^2$ which is due to flexural rotation alone, $I_\alpha \Psi_n^2$ which is due to torsion alone and $2mx_\alpha(U_n \Psi_n)$ which is due to bending-torsion coupling effect. In each of the modes of vibration, the contribution of each term in the above equation is a quantitative measure of the importance of that term to the generalised mass and hence to the response characteristics of that mode.

A small alteration in the thickness and/or the length of a composite beam; inclusion of secondary effects - such as shear deformation or rotatory inertia; variation of ply angles or stacking sequences may change the occurrence order of bending or torsional modes of vibration. Consequently, this will change the dynamic response of such beams. This distinctive feature which does not normally exist in Bernoulli-Euler beams (bending-torsion uncoupled), has not been addressed adequately in the existing literature. The investigation has reaffirmed that due recognition to the modal interchanges must be given when studying the free and forced vibration characteristics of bending-torsion coupled composite beams.

6. FURTHER REMARKS

For cost effective application of fibre reinforced materials, the present methodology can be successfully used as a customised tool for a multidisciplinary optimisation procedure in design and fabrication of composite structures. Moreover, for efficient utilisation of advanced composite materials, the proposed approach can considerably help the development of formal strategies and design solutions in the field of dynamic response.

Furthermore, it is observed that the dynamic stresses in composite beams are greatly influenced by fibre angle, axial load and the effects of shear deformation and rotatory inertia. This investigation has shown that the response induced by material coupling as a consequence of ply orientation can be significant. For optimisation purposes, therefore, it is especially very important to investigate the effect of variation of ply angles and stacking sequences on rigidities, frequencies, mode shapes and ultimately on the dynamic response behaviour of composite beams.

Finally, finite element method is, of course, an alternative route to approach the problem. Although FE method is a universal numerical resource for structural analysis, it has its own disadvantages as well. In FE method, stiffness and inertial properties of the structure are restricted by the number of elements used and the way the elements are defined. Unlike the dynamic stiffness matrix method, FE method generally provides much less accurate modal information when higher frequencies are involved. Moreover, the computer time used for analysis can substantially be saved if explicit analytical expressions for the elements of the dynamic stiffness matrix are used instead of finite element method.

7. ACKNOWLEDGEMENT

The authors are grateful to Mr Adam Sobey who made useful contribution to this work.

8. REFERENCES

1. L.C. Hollaway; "The Evolution of and the Way Forward for Advanced Polymer Composites in the Civil Infrastructure", *Construction and Building Materials*, 2003 **17** 365-378.
2. Lelli Van Den Einde, Lei Zhao and Frieder Seible; "Use of FRP Composites in Civil Structural Applications", *Construction and Building Materials*, 2003 **17** 389-403.
3. L.C. Bank, T.R. Gentry, B.P. Thompson and J.S. Russell; "A Model Specification for FRP Composites for Civil Engineering Structures", *Construction and Building Materials*, 2003 **17** 405-437.
4. J.K. Suresh, C. Venkatesan and V. Ramamurti, "Structural Dynamic Analysis of Composite Beams", *Journal of Sound and Vibration*, 1990 **143** 503-519.
5. G. Cederbaum, I. Elishakoff, J. Aboudi and L. Librescu, "*Random Vibration and Reliability of Composite Structures*", Technicom Publishing Company, 1992.
6. A.S. Abdelnaser, and M.P. Singh, "Random Vibration of Cantilevered Composite Beams with Torsion-Bending Coupling", *Probabilistic Engineering Mechanics*, 1993 **8** 143-151.
7. J.R. Banerjee and F.W. Williams, "Free Vibration of Composite Beams- An Exact Method Using Symbolic Computation", *Journal of Aircraft*, 1995 **32** (3) 636-642.
8. E.A. Armanios and A.M. Badir, "Free Vibration Analysis of Anisotropic Thin-Walled Closed-Section Beams", *AIAA Journal*, 1995 **33** 1905-1910.
9. S.H.R. Eslimy-Isfahany and J.R. Banerjee, "Dynamic Stresses in Composite Timoshenko Beams with Application to Aircraft Wings", *Proceedings of AIAA/ASME/ASCE/AHS/ASC 39th Structures, Structural Dynamics and Materials Conference*, Long Beach, USA, April, 1998, pp. 3201-3211..
10. S.H.R. Eslimy-Isfahany and J.R. Banerjee; "Dynamic Response of Composite Beams with Application to Aircraft Wings", *AIAA Journal of Aircraft*, November-December, 1997 **34** (6) 785-791.
11. S.H.R. Eslimy-Isfahany and J.R. Banerjee, "Significance of Modal Interchange on Composite Beam Dynamics", *Proceedings of The Sixth Annual International Conference on Composite Engineering, ICCE/6*, Orlando, Florida, USA, June 27-July 3, 1999.
12. A. Miravete, "Strain and Stress Analysis in Tapered Laminated Composite Structures", *Composite Structures*, 1990, **16** (1-3) 65-84.
13. M.H. Datoo, *Mechanics of Fibrous Composites*, Elsevier Applied Science, 1991.
14. S.H.R. Eslimy-Isfahany and J.R. Banerjee; "Use of Generalized Mass in the Interpretation of Dynamic Response of Bending-Torsion Coupled Beams", *Journal of Sound and Vibration*, 2000 **238** (2) 295-308.

PART VI

DURABILITY AND LONG-TERM PERFORMANCE

This page intentionally left blank

EFFECT OF FATIGUE CYCLING ON THE STRENGTH OF RC BEAMS EXTERNALLY STRENGTHENED WITH CFRPS

Catalin Gheorghiu, Pierre Labossière, Jean Proulx

Département de génie civil, Université de Sherbrooke, Sherbrooke, QC, J1K 2R1, Canada

ABSTRACT

The overall deterioration of transportation infrastructure due to ageing and increasing traffic loads motivated researchers to look for new ways of repairing and monitoring the existing structures. Numerous studies were conducted and proved the efficiency of bonding fibre-reinforced polymers (FRP) systems on the structural elements such as reinforced concrete (RC) beams and columns. Although there is a huge potential for the use of FRP materials, their large-scale implementation is often impeded by the lack of data on their durability when submitted to extreme loading conditions. This paper presents an experimental project undertaken in order to asses the durability of RC beams externally strengthened with carbon-fibre-reinforced polymers (CFRPs). The beams were loaded in fatigue for various numbers of cycles and then tested quasi-statically to failure. Test results provide an insight on the potential performance of CFRP-strengthened beams submitted to fatigue loading conditions.

INTRODUCTION

In many countries, most of the transportation infrastructure was constructed in the middle of the twentieth century and is approaching the end of its expected life. In addition, there were significant increases in load requirements over that period. These facts illustrate the need for fast, efficient and durable strengthening methods. A technique now gaining popularity is the bonding of carbon-fibre-reinforced polymers (CFRPs) on structural elements. CFRPs are used extensively to strengthen reinforced concrete beams and columns in existing structures.

Although major applications of CFRPs are reported in the literature, design engineers are still concerned by the durability of these products under severe loading and climatic conditions. Some work has been conducted to evaluate the durability of CFRP-strengthened beams submitted to wet-dry cycles (Beaudoin et al., 1998)[1], or continuous immersion (Raîche et al., 1999)[2], and also under freeze-thaw cycles (Green et al., 2000)[3]. These researchers also published results from quasi-static loading of RC beams strengthened with CFRPs. Other studies reported fatigue behaviour of strengthened beams (Brena et al., 2002)[4], and the specimens' response to a combination of fatigue loading and low temperature (Lopez et al., 1999)[5], or fatigue loading and water exposure conditions (Gheorghiu et al., 2003)[6]. However, there are still no extensive data dealing with the beam's response to different fatigue load levels and number of cycles, especially for the characterization of the CFRP-concrete interface.

The objective of the project reported here is to investigate the influence of the fatigue loading on the residual strength of CFRP-strengthened beams. The emphasis was placed on studying the behaviour of the CFRP-concrete interface throughout dynamic and quasi-static loading.

DESCRIPTION OF THE TEST PROGRAM

This section describes the main characteristics of the tested specimens, the properties of their constituent materials, the environmental exposure conditions, the experimental loading apparatus, and the instrumentation and data acquisition systems.

Specimens

The typical geometry and reinforcement of the tested beams are shown in Figure 1. The specimens were fabricated from normal-strength ready-mixed concrete. The concrete strength was measured at three different times along the testing program and had a mean value of 50 MPa. The internal reinforcement is made of smooth and undeformed bars 6.35 mm in diameter and is providing the minimum steel quantity required by the Canadian Standard CSA-A23.3[7] for reinforced concrete. Steel rebars exhibit a yield strength of 600 MPa and a Young's modulus of 200 GPa.

All the beams were externally strengthened with a unidirectional CFRP strip. The main properties of this Sika CarboDur plate are shown in Table 1. The 50-mm-wide plates were bonded to the tension face of the beams with the proprietary mortar of the system on a 400 mm length at both ends, thus leaving a 260 mm unbonded portion in the middle. This configuration was selected to avoid concrete crushing and to trigger failure by delamination of the CFRP, eventually allowing the investigation of the concrete-CFRP interface.

Prior to testing, all specimens were instrumented with strain gauges. One gauge was placed on the concrete surface, and two on the rebars, as shown in Figure 1. Four more gauges were installed on the CFRP, in order to measure the onset of delamination along the CFRP-concrete interface. The load cell was a part of the actuator, and one LVDT measured the midspan deflection of the beams.

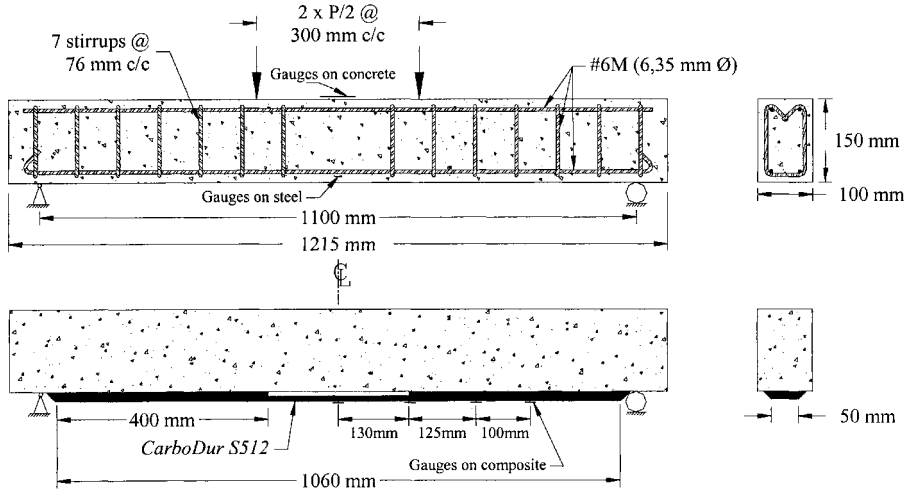


Figure 1: Concrete beam – geometry, reinforcement and instrumentation details

Table 1: Properties of FRP system

System	E_{frp} (GPa)	ε_{frp} (%)	f_{frp} (GPa)	t (mm)
Sika CarboDur	155	1.6	2.4	1.20

Testing Procedure

All beams were submitted first to flexural cyclic loading, and then to quasi-static four-point bending. The only exceptions were the two reference beams tested only quasi-statically. The location of the two loading points is shown in Figure 1. The fatigue test consisted of 400 000, 800 000 and 2 000 000 cycles at a load level of 15 to 35% of the yielding moment. Table 2 indicates the minimum and maximum loads P applied to the beams.

Table 2: Loads applied in fatigue tests

Beam	P_{min} (kN)	P_{max} (kN)	$(P_{min}- P_{max})/P_y$ (%)	$(P_{min}- P_{max})/P_u$ (%)
L-series	6.8	15.9	15-35	12-28

The fatigue load was applied with a MTS hydraulic actuator of 100 kN capacity controlled by a TestStar-II software. The specimens were first loaded statically up to the minimum value of the cyclic load identified in Table 2, then the fatigue load was applied up to the maximum value. Between these extreme values, the CFRP plate remained in tension. At 2 cycles per second, and including preparatory work, 13 days were spent on each beam tested for 2 000 000 cycles. The sinusoidal loading was force-controlled using the TestWare-SX process module. Readings at minimum and maximum loads were taken at every 2000th cycle until cycle 801 000, then they were spaced at every $10\,000^{th}$ cycle to the end of the test. Full cycle readings during the test were taken according to the following sequence: at 1st cycle and every 10th cycle to 200; at every 200th cycle to 1001; at every $20\,000^{th}$ cycle up to 801 000. Then, the space between two consecutive readings was increased to 100 000 up to the $2\,001\,000^{th}$ cycle. For these preset cycles, the frequency was reduced to 0.05 Hz in order to take into account the limitations of the fibre-optic sensor's reading device. The beams were then loaded quasi-statically up to failure under four-point bending. The quasi-static load was applied at the same location as for the cyclic loading, on a Baldwin press of 267 kN capacity, and a load rate of approximately 0.1 kN/s. Data were recorded at every 0.1 kN load increment.

Summary

Table 3 summarizes the characteristics of the tested beams and provides some of the most significant fatigue and static test results. The beam designation is given in first column of the table. The table lists two control specimens A and B that were tested only quasi-statically. The other seven specimens were tested in fatigue for 400 000 (400A,B), for 800 000 (800A,B,C), and for 2 000 000 cycles (2000A,B). The second column in Table 3 give the concrete strength f'_c obtained at the testing time as explained above. The results in the other columns will be commented in the following section.

RESULTS

The results for the control beams will be followed by a discussion on the beams submitted to fatigue loading.

Table 3: Specimens and test results

Beam	f'_c (MPa)	$\varepsilon_{s,fat}$ (με)	$\varepsilon_{c,fat}$ (με)	$\varepsilon_{frp,fat}$ (με)	P_u (kN)	Δ_u (mm)	$\varepsilon_{s,u}$ (με)	$\varepsilon_{c,u}$ (με)	$\varepsilon_{frp,u}$ (με)
A	50	-	-	-	55.6	8.00	2932	-906	4700
B	50	-	-	-	56.7	7.54	2992	-914	5124
400A	50	802	-	1401	56.6	7.74	2552	-	4018
400B†	50	1019	-208	1678	54.7	6.74	2888	-1024	4216
800A†	50	851*	-	1492	56.5	6.92	-	-	4306
800B†	50	1081**	-	1504	55.0	7.42	-	-1084	3894
800C	50	911	-229	1639	57.2	6.78	2680	-916	4040
2000A	50	879	-	1669	58.7	6.80	2610	-	4214
2000B	50	926	-214	1596	59.4	7.43	2602	-1042	4202

† Beams tested at 3 Hz

* Steel strains unexpectedly high starting at *461 000 and **261 000 cycles

Quasi-static test

The beams A and B were tested quasi-statically up to failure without prior fatigue loading. The last five columns of Table 3 give results from these tests. They include the ultimate load P_u and corresponding deflection Δ_u at midspan, as well as the strains $\varepsilon_{s,u}$ in the steel rebar, $\varepsilon_{c,u}$ in the concrete, and $\varepsilon_{frp,u}$ in the CFRP at that section. It can be observed that the ultimate load is slightly larger for the beam B than for the beam A. This increase in strength is accompanied by a slight decrease in the ultimate deflection. The ultimate strains are similar for the two specimens, though the strain in the CFRP is 424 με larger for B than for A. These reference results will be compared to the results obtained for the fatigued beams.

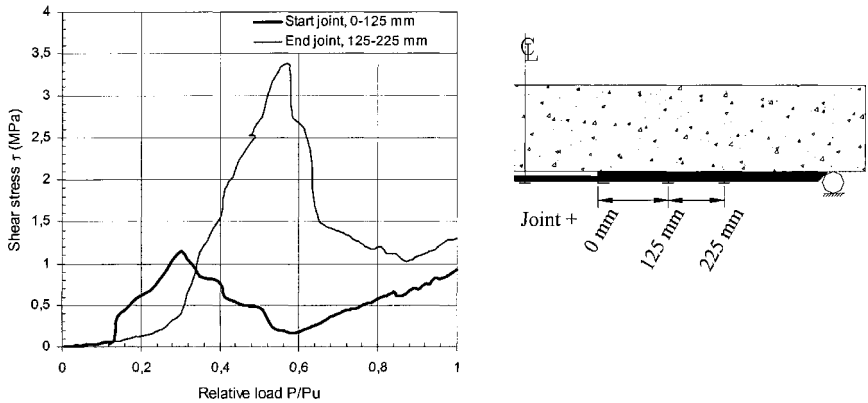


Figure 2: Shear stress as a function of relative load during static test, beam A

The failure mode of all the beams being by delamination it would be useful to investigate the behaviour of the CFRP-concrete interface. From the strain measurements along the CFRP plate the shear stress was calculated and plotted against the relative load (Bizindavyi and Neale, 1999)[8]. The average shear stress was calculated for each region between two consecutive gauges. Figure 2 thus shows two shear stress curves for

the specimen A, and the strain gauges with the two corresponding intervals. For the interval comprised between 0 and 125 mm from the beginning of the joint, the shear stress increases almost proportionately with the load, then decreases suddenly. Simultaneously with this stress decrease in the first interval, an increase in the shear stress can be observed for the interval comprised between 125 and 225 mm. The shear stress continues to increase for the second interval to reach a maximum of 3.4 MPa at about 50% of the ultimate load. Then the shear stress decreases to about 1 MPa at the ultimate load for both intervals.

Fatigue test

Seven beams where tested in fatigue in order to investigate the influence of cycling on the strength and stress transfer at the CFRP-concrete interface. Graphical results for the beam 400B submitted to the minimum number of cycles and for the beam 2000B cycled with the maximum number of cycles are discussed in the following.

For the beam 400B, submitted to the cyclic loads indicated in Table 2, the evolution of strains in the steel rebars and at four different locations along the CFRP reinforcement is shown in Figure 3. Results from each gauge are represented by two curves corresponding to minimum and maximum cyclic loads. The central gauge on CFRP is considered first. The curve with rectangles shows the minimum strains, and the one with solid rectangles indicates the maximum strains through the 400 000 cycles. For the first cycle, the extreme values were 1077 με and 1433 με. At the same time, Figure 3 shows that the strains in the rebars ranged from 717 με to 839 με. As the number of cycles increased, these extreme strains were found to change gradually. For the CFRP, they increased to values comprised between 1167 με and 1678 με, and on the steel rebars, they changed to values between 692 με and 1019 με. These variations can be used to locate the neutral axis and evaluate the change in stiffness of the beam. Similar observations can be made for the other gauges reported in the figure.

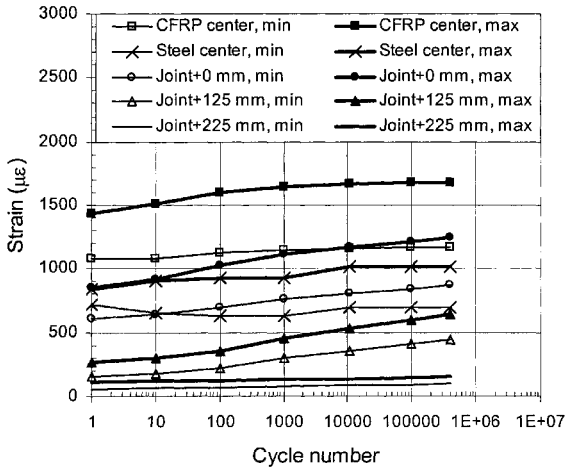


Figure 3: Strain extremes in the steel and CFRP during fatigue test for beam 400B

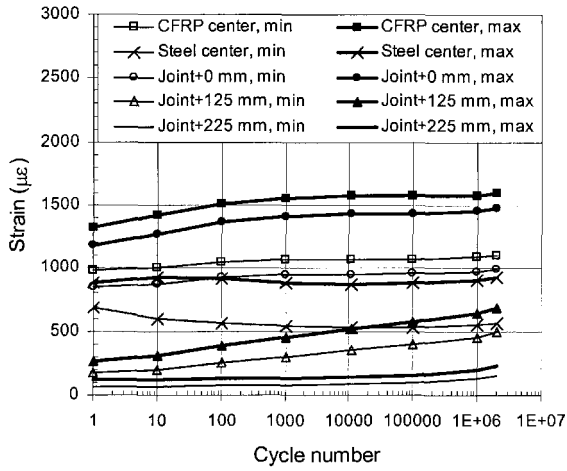


Figure 4: Strain extremes in the steel and CFRP during fatigue test for beam 2000B

The same type of curves are drawn for beam 2000B in Figure 4. Overall they are similar to the ones obtained for beam 400B, though slightly smaller strain values are observed for 2000B. A slight increase in strain is observed for 2000B at the location joint + 225 mm in the last part of the fatigue test. At joint + 0 mm larger strain are observed for 2000B than for 400B. This can be explained by the fact that this particular gauge was not exactly positioned at the beginning of the joint but rather towards the midspan of the beam. For the last cycle, the maximum strains $\varepsilon_{s,fat}$ in steel, $\varepsilon_{c,\,fat}$ in concrete, and $\varepsilon_{frp,\,fat}$ in CFRP, at midspan, are listed in Table 3 for all the tested specimens. To conclude, the strain values for the two specimens indicate that fatigue response of the beams is not influenced by the number of cycles.

Post-fatigue quasi-static test

Following the fatigue cycling the beams were loaded quasi-statically to failure. Table 3 lists the most significant results from these tests. The ultimate load P_u varies from 54.7 to 59.4 kN and, for the parameters used in this study, indicates that there is no clear influence of the fatigue loading on the post-fatigue or residual strength. The ultimate deflection varies from 6.74 to 7.74 mm. Again no trend is observed between the change in ultimate deflection and the number of fatigue cycling. These values are similar with those obtained for the control specimens A and B. However, an 8% decrease in the mean ultimate deflection of the fatigued beams over the mean deflection of the control ones is observed. The mean strain values in the steel rebar and the CFRP plate decreased by 10 and 16%, respectively. For the concrete they are 12% higher than the mean concrete strain of A and B.

In addition to these data, strain values were used to plot the shear stress curves at the CFRP-concrete interface. Comparing the shear stress distribution along the joint for the control specimens A of Figure 1 and 400B of Figure 5(a), one can observe that the fatigue cycling slightly changed the response of the CFRP-concrete interface. For the beam 400B the first interval between gauges located at 0 and 125 mm measures smaller shear stress than beam A on the entire loading duration. Consequently, there is no visible shear transfer from the first interval to the second one. Though the first 125 mm portion of the joint carries smaller stress in 400B than in A, the second interval reached

a relatively high maximum stress of 2.8 MPa, that is 18% lower than for beam A. This maximum value is attained at about 65% of the ultimate load as compared to 50% for the beam A.

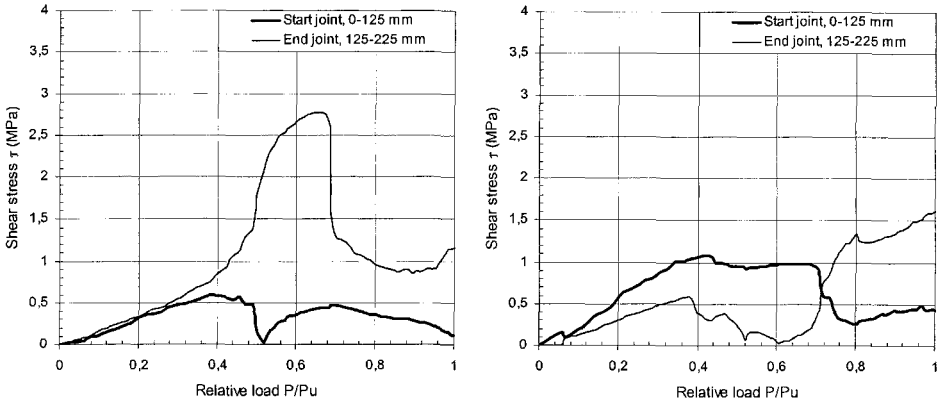


Figure 5: Shear stress as a function of relative load during static test; beam 400B (a) and beam 2000B (b)

If is to compare the shear stress calculated for beam 2000B, Figure 5(b), with the shear stress for beam A, Figure 1, there is a clear difference in the shape of the curves. Although the shear stress transfer is observed between the two intervals a maximum value of only 1.6 MPa is reached at 80% of the ultimate load. The maximum shear stress value for beam 2000B is 43% smaller than that for 400B and 53% smaller than that for A. The significant decrease in shear stress value is a clear indication that the degradation of the CFRP-concrete interface took place. This change in the shear transfer mechanism with cycling can be correlated with the slight increase in strains at joint + 225 mm observed for the beam 2000B during the fatigue test. These two parameters may be considered for future studies on the crack propagation at the interface. However, these variations in the extent of damage and damage mechanism at the interface did not lead into a significant difference in the ultimate capacity of the beams.

CONCLUSION

An experimental program was conducted on the fatigue response of beams externally strengthened with CFRPs. The results provide an insight on the long-term behaviour of a repair system that is gaining widespread use. The effects of fatigue loading on the flexural behaviour of such system was addressed. During the fatigue loading the strains were found to increase gradually. At sections where crack appears the increase is significant. The beam loaded for two million cycles exhibited a slight increase in strain values measured towards the extremity of the CFRP-concrete joint. Following the cyclic tests, the beams were submitted to quasi-static loading up to failure. Results from these tests showed that the number of fatigue cycles had no significant effect on overall beam's response. Curves showing the shear transfer mechanism between CFRP and concrete were also presented. They show that during the delamination process the beams submitted to fatigue cycling measured smaller shear stress values at the interface. In addition, shear stress values are smaller for the cycled beam than those for the control

one. The ultimate deflection and strains in steel and CFRP decreased for fatigued specimens. However, the ultimate load reached by the specimens is not affected by fatigue cycling. Further work needs to be done in order to develop analytical and numerical models for the CFRP-concrete interface, this representing a key parameter for the successful application of these products in Civil Engineering.

ACKNOWLEDGEMENTS

The financing of this research project was provided by the Network of Centres of Excellence ISIS Canada and by the Natural Sciences and Engineering Research Council of Canada (NSERC), and is gratefully acknowledged. The authors also thank Mr. Marc Demers and Mr. Claude Aubé for their assistance in the laboratory.

REFERENCES

[1] Y. Beaudoin, P. Labossière and K.W. Neale, "Wet-dry action on the bond between composite materials and reinforced concrete beams", *1st International Conference on Durability of Fibre Reinforced Polymer (FRP) Composites for Construction*, Benmokrane B. and Rahman H., eds., Sherbrooke, Canada, 537–546, 1998.

[2] A. Raîche, Y. Beaudoin and P. Labossière, "Durability of composite materials used as external reinforcement for RC beams", *Proceedings of the Annual Conference of the Canadian Society for Civil Engineering*, Regina, Canada, 155–164, 1999.

[3] M.F. Green, L.A. Bisby, Y. Beaudoin and P. Labossière, "Effect of freeze-thaw cycles on the bond durability between fibre reinforced polymer plate reinforcement and concrete", *Canadian Journal of Civil Engineering*, 27(5), 949–959, 2000.

[4] S.F. Brena, S.L. Wood and M.E. Kreger, "Fatigue tests of reinforced concrete beams strengthened using carbon fibre reinforced polymer composites", *Proceedings of the Second International Conference on Durability of Fibre Reinforced Polymer (FRP) Composites for Construction*, Benmokrane B. and El-Salakawy E., Editors, Montreal, Canada, 575–586, 2002.

[5] M.D.M. Lopez, A.E. Naanan, L. Pikerton and R.D. Till, "Behavior of RC beams strengthened with laminates and tested under cyclic loading at low temperatures", *Proceedings of the International Conference on FRP Composites in Civil Engineering*, J.G. Teng, Editor, Elsevier, Hong Kong, 415–422, 2001.

[6] C. Gheorghiu, P. Labossière and A. Raîche, "Environmental fatigue and static behaviour RC beams strengthened with CFRP", *Journal of Composites for Construction,* ASCE, 2003 (in print).

[7] CSA-A23.3, *Design of concrete structures,* Canadian Standards Association, Rexdale, Ontario, 1994.

[8] L. Bizindavyi and K.W. Neale, "Transfer lengths and bond strengths for composites bonded to concrete", *Journal of Composites for Construction*, ASCE, 3(4), 153–160, 1999.

THE ROLE OF DURABILITY IN RELIABILITY-BASED DESIGN OF COMPOSITE MATERIALS FOR CIVIL STRUCTURES

Nathan L. Post, John V. Bausano, John J. Lesko, Scott W. Case, John C. Duke
Department of Engineering Science and Mechanics
Virginia Tech, Blacksburg, VA 24061 USA

ABSTRACT

Design guidelines for fiber-reinforced polymers (FRP) used in critical structures must take into account the loss of stiffness and strength these materials experience in service over time. Reliability based design accounts for these losses by the use of reduction factors. These design reduction factors should include scientific and rational backing. In the civil infrastructure, the American Association of State Highway Transportation Officials (AASHTO) load resistance factor design (LRFD) uses statistical methods in structural design, including a strength reduction factor for a particular combination of loads. This approach is very attractive for composite structures as it accounts for the service environment. In this paper, we propose a durability simulation method that combines LRFD and a material property evolution scheme to predict the future reliability of a FRP structure and allows one to rationally select reduction factors given a preselected probability of survival.

INTRODUCTION

FRP composite structures have gained limited acceptance in civil applications through experimental structural implementations, while aerospace applications have seen more routine implementation. To further increase the utilization of these FRP structures new design standards and guidelines must be available for routine implementation of these innovative systems. Load resistance factor design (LRFD) is a reliability based design method that is presently being adopted into regular design practices for conventional material structures. There is also a significant interest in developing a design standard for FRP composites that is consistent with the LRFD standard.

Separately, various suppliers have developed design manuals of various levels (e.g. Hardcore Composites, Strongwell, Corp, Hughes Brothers). These guides provide the user with direction in the component's correct use and allowable loads/stresses under various use conditions. Each clearly defines a material, dimensions, and tolerances for the component and design Equations or tables for various limit states in suitable implementations.

One element missing from these initial efforts is the recognition that over time the strength and stiffness of the FRP structures will change due to combined exposure to load and environment. A major concern when dealing with such changes in the context of an allowable for a design is the reality of potential failure mode changes and how to deal with such events. Although the LRFD approach provides a clear and logical statistical approach to design, it also relies on the existence of one well-defined failure mode and does not account for a change in failure mode.

DURABILITY AND THE LRFD APPROACH

In the LRFD approach, the probability distribution of loads/stress (Loads, Q) is compared to the probability of failure strength of the material (Resistance, R), typically

represented as illustrated in Figure 1 (AASHTO 1998). The region of overlap is related to the risk associated with the situation designed. Selecting the form and size of the structure determines the desired overlap of the two distributions thus defining the stated allowable risk for a given loading condition.

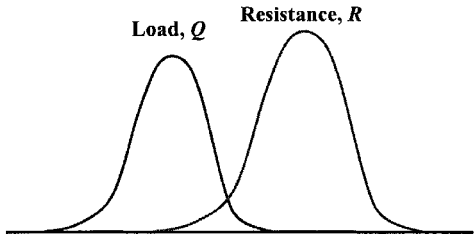


Figure 1: Load and resistance distributions

The basis for statistical description of composite structures lies in Weibull statistics (Weibull 1951), where the cumulative probability distribution function describing the distribution of measured values is given by,

$$F(x) = 1 - e^{-\left(x/\beta\right)^{\alpha}} \tag{1}$$

where α and β are the two parameters used to fit the data. The value of α (the shape parameter) determines the breath of the distribution while β (the location parameter) corresponds to the 63.2% probability.

The reliability of composite structures can change over time because of the strength and stiffness loss the systems exhibit. The loss of reliability defines new lower factors of safety associated with the systems as compared to those developed on the basis of the as received structure. As these FRP structural shapes/components are new to the industry, definitive criteria for reasonable factors of safety based on durability are presently not available.

With this incomplete picture of how one should account for strength and stiffness loss in the life of the design with FRP structures we consider here the development of an durability modified LRFD based simulation approach. Using the commonly reported expression,

$$\phi R_n > \sum \gamma_i Q_{ni} \tag{2}$$

which describes the basis of the LRFD philosophy, we attempt to simulate and track the reduction in the Resistance, R, in the presence of a *factored* (γ_i) load environment, Q_{ni}, including both mechanical and environmental factors. The reduction factor, ϕ□, is not well defined at this point for FRP applications where durability is a concern. We hypothesize that in the presence of a particular set of loads/environments, the strength will change and influence how one chooses ϕ, as illustrated in Figure 2. Possessing such representations, we can go through the normal procedure of computing the probability of failure, P_f, and the partial safety factor ϕ of Equation 2. This procedure is accomplished through the representation shown in Figure 3. When Q>R failure occurs, the probability that this limit state occurs is given by Equation 3. Here the probability of failure is determined from the integral of the overlapping PDF for the loads and the cumulative distribution function (CDF) for the resistances given by

$$P_f = \int f_Q(x) \cdot F_R(x) dx \tag{3}$$

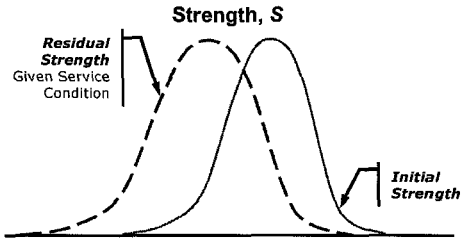


Figure 2: The hypothesized changes in the probability density function describing the statistical distribution in the resistance (strength) of a component or material.

Other researchers have examined the reduction factor of Equation 2 for lognormal distributions. In this case, the reduction factor can be computed from

$$\phi = \left(\frac{\mu_R}{R_n}\right)\exp\left(-\alpha_R \beta V_R\right)$$
$$\beta = \frac{\ln\left(R_n / Q_n\right)}{\sqrt{V_R^2 + V_Q^2}} \tag{4}$$

For the above equations, μ_R is the mean of the resistance, α_R is a "sensitivity coefficient" that depends on the PDF of the resistance curve (typically between 0.5 and 0.6), V_R and V_Q are the coefficients of variation for the resistance and load distributions respectively.

Such an expression can be derived for Weibull statistical representations of load and resistance by the use of first order reliability methods (FORM). An equivalent method of describing the limit state failure probability is by defining a limit state function,

$$G(X_1, X_2, ..., X_m) = 0 \tag{5}$$

where X_m is a random load or resistance variable. By convention failure occurs when $G(X)<0$. In the case of a non-linear limit state function, Hasofer and Lind (Hasofer 1974) proposed a definition of the reliability index β_{HL} to be,

$$\beta_{HL} = \min_{G(u)=0} \sqrt{\sum_{i=1}^{m} u_i^2} \tag{6}$$

where u_m are the normalized stochastic variables X_m with expected values of 0 and standard deviations of 1.

The question that remains unanswered is how to simulate these changes in residual resistance. The residual strength approach developed and advanced by Reifsnider & co-workers (Reifsnider et al. 1995, Reifsnider et al. 1996) is proposed to predict the residual strength.

$$Fr(n) = Fr(0) - \int_0^{\frac{n}{N}} (1 - Fa(n)) \cdot j \cdot \left(\frac{n}{N}\right)^{j-1} \cdot d\left(\frac{n}{N}\right) \tag{7}$$

where

n = elapsed number of cycles
N = life in cycles at applied stress
Fa = normalized applied stress (in terms of a failure criterion)
Fr = normalized remaining strength (in terms of a failure criterion)
j = residual strength fitting parameter (taken to be 1.2)

N, the cycles to failure at an applied stress level can be calculated using

$$N(Fa) = 10^{\frac{Fa-A}{B}} \tag{8}$$

where A and B are curve fit parameters that describe the material's S-N curve

This method of life prediction for FRP materials can combine loads and environments to develop a representation of the residual properties of the composites as a function of time and or cycles (service condition). The approach relies on the mechanistic representation of changes in constituent properties and the presence and development of damage as a result of the applied stresses and environments. Tracking residual strength provides a metric which is compared to the resulting stress level in the critical element (the ply or interface that controls the failure of the composite). When the remaining strength of the critical element equals the stress applied to it, failure occurs. In addition, residual stiffness is tracked in this analysis and can offer an estimate of deflection limit states and they are typically the controlling feature in an FRP structural design. Thus, the necessary tools are available to carry out a simulation that can be used to simulate and suggest appropriate ϕ factors for various applications and service environments. The concepts of this proposed simulation are illustrated in Figure 4.

The simulation begins by securing a representation of the loads (including the hygro-thermal service environment). For purposes of representing this load and environment history in the model we employ a Monte Carlo simulation. Based on the estimated loads, a structural design is completed and the stress analysis allows for the assessment of the condition that controls the design. This stress analysis is used to feed the residual strength/stiffness life prediction model discussed above. Here the life prediction model must be supplied with representations of the functional forms of stiffness and strength loss as a function of exposure to individual degrading phenomena. Work continues in the area of understanding how the combination and synergism of environment and load. However, there are presently some reasonable approximations of how to treat some classical combinations of load and moisture and temperature for glass/polymer composites (McBagonluri et al. 2000, Phifer et al. 2000). Furthermore, our laboratory continues to examine simulations of realistic service environments under accelerated conditions to understand the influence of synergistic effects. These findings will be incorporated in futures efforts to assess durability and codes development. The simulation also requires that we include statistical representations of the phenomena and their combination. This is particularly true of fatigue and those environmental features that influence variability and shift in the phenomena.

Having defined these inputs, we perform the simulation and develop the CDF of the residual resistance for a predefined period of service as shown in Figure 3. Computing the probability of failure and the associated ϕ, we are now left to make a judgment call as to the acceptable level of risk. If the engineer or the community believes that the risk is reasonable for the period chosen, then we are satisfied with the material and its use in the design and select the computed ϕ for the design. If on the other hand the engineer finds the level of risk too high, then he/she is left with the ability to make a second guess on the design to change component sizes or material properties to further separate the resistance from the loads. Repeating the simulation the risk and ϕ are computed and checked again until the engineer arrives at an acceptable level of risk.

With the availability of such a tool the community could develop a series of ϕ's for various material specified FRP components under various exposure to various regions

of the U.S., and traffic characteristics. (The life and therefore the ϕ will be dependent on the load and environmental service condition for the structure.) This could potentially provide an engineer with a table from which to select a ϕ factor appropriate for the design, removing the engineer from the need to run the simulation. Ideally this allows the bridge design community to meld the LRFD approach for conventional structures, which is gaining acceptance, to those that will be developed in the future that include FRP composites. To illustrate the approach, we will consider an example of a preliminary model implementation.

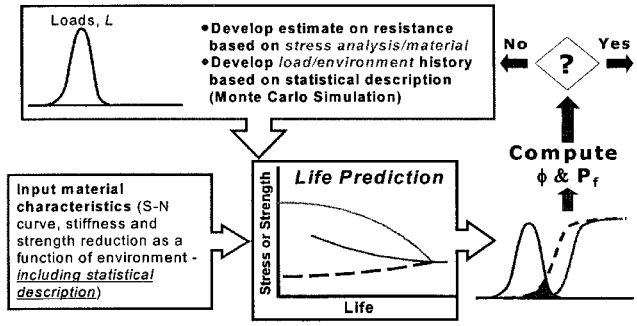


Figure 3: Proposed simulation for the assessment of acceptable ϕ factors.

PRELIMINARY MODEL IMPLEMENTATION:

Experimental data collection

A first implementation of the proposed simulation technique was performed on a pultruded E-glass / Dow Derakane Momentum 610-900 resin composite laminate. The laminate layup was of [CSM/0°/90°/CSM/±45° /CSM $]_s$, where CSM denotes continuous strand mat. The initial quasi-static stiffness and strength were determined experimentally for the material system along with the fatigue performance (S-N curve). The laminate stiffness loss was also tracked for each fatigue sample that was tested to construct the S-N curve.

The quasi-static properties were determined from 15 standard tensile tests. The results are listed in Table 1.

Table 1: Quasi-Static Laminate Properties

Weibull Parameter	Stiffness	Strength
α	17.7	36.2
β (MPa/ksi)	15,445/2,240	258/37.4

To determine the S-N curve 100 individual fatigue tests were performed at an R ratio (minimum applied cyclic stress/maximum applied cyclic stress) of 0.1. The tests were conducted at a wide range of stress ratios (%UTS), which is defined as the maximum applied stress divided by the initial strength. The resulting S-N curve is shown in Figure 4.

Figure 5 is a plot of the laminate stiffness reduction plots for the 35% UTS stress level. Note the normalization to the mean cycles to failure. As shown in Figure 5, at a specific time in normalized lifetime, there exists a definite distribution in stiffness loss. Weibull parameters were calculated to describe this behavior at 1, 5 10, 20, 50, 80, 90,

95 and 99 percent lifetime. Figure 6 shows the "classic" shape at which a laminate of this type losses stiffness. For the first 10% of life, the stiffness loss occurs quickly, followed by a linear reduction in stiffness with cycles. The stiffness loss rate remains linear until just before failure where large losses in stiffness are observed. The Weibull parameters were plotted over normalized cycles to failure, as shown in Figure 6.

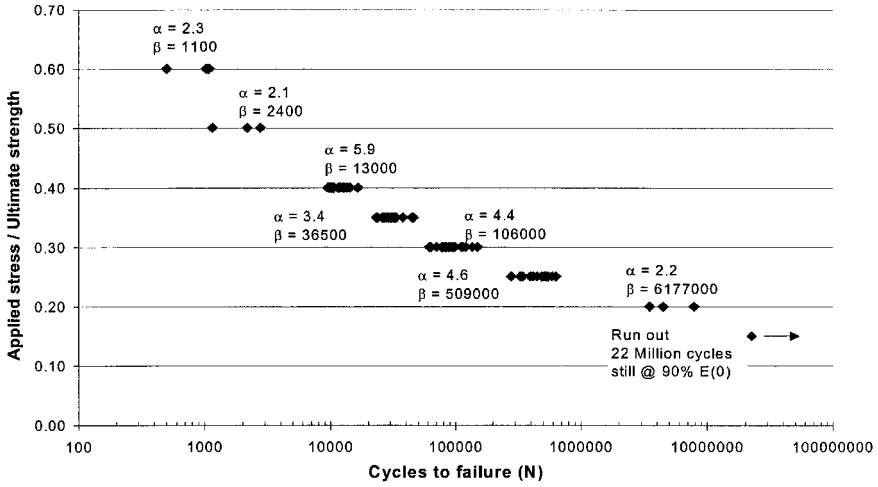


Figure 4: Laminate S-N curve

Modeling results

The Monte Carlo simulation was implemented using the experimental data to determine the distribution of the remaining strength of a simple tensile fatigue process. The simulated test was a fatigue loading at 35% UTS for 18750 cycles (18750 cycles is two standard deviations lower than the mean cycles to failure at 35% UTS) (see Figure 7). The simulation was run for 500 trials, each time calculating the residual strength at the 18750 cycles. From the simulation the Weibull parameters for the variation in remaining strength were determined to be $\alpha = 5.8$ and $\beta = 162$ MPa (23.5 ksi) or 69% of the original non-fatigued strength. The model also predicted that 28% of the samples would fail before they reached the 18750 cycle mark.

Model verification

The validation of the model is a straightforward process. Simply speaking a number of samples were fatigued at the 35% UTS for the prescribed 18750 cycles. After each sample was fatigued it was immediately failed in tension to determine the remaining tensile strength. The Weibull parameters determined experimentally are $\alpha = 10.9$ and $\beta = 163$ MPa (23.6 ksi) or 68% of the original strength. Also 23% of the samples tested failed in fatigue before they reached the 18750 cycle mark. Although the shape parameter was twice (experimentally) that the predicted, the methodology was able to predict the percentage failed and approximate the remaining strength within 2%.

SUMMARY & REMARKS:

We have presented a perspective on the development of design guides for FRP composites based on reliability and the philosophy presented by the AASHTO LRFD approach. As these guidelines are presently developed for systems based on as processed conditions we propose a means to include service environment degradation in the determination of resistance reduction factors, ϕ. Provided with this factor, the engineer can properly select material and component size in completing an FRP design suitable for the longevity in a particular service environment.

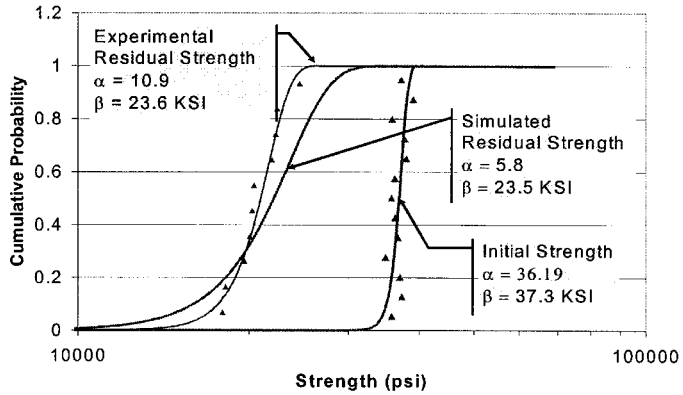


Figure 5: Comparison of measured and simulated residual strength distributions

Preliminary modeling efforts of a simple case show promising results. Currently the simulation is in good agreement with experimental data with regards to the residual strength prediction. The current model does not, however, accurately predict the Weibull shape factor. Completing such a simulation requires further work to understand combined environments and their influence on residual strength and stiffness. Further validation tests must be conducted to assess the accuracy of the approach and its limits. Ultimately the approach must be applied to the growing numbers of systems and FRP designs that hold promise for routine use in the highway bridge structures. Once the residual strength distribution can be adequately predicted the final step would be to implement the LRFD algorithms to determine the resistance factors for the systems at future times.

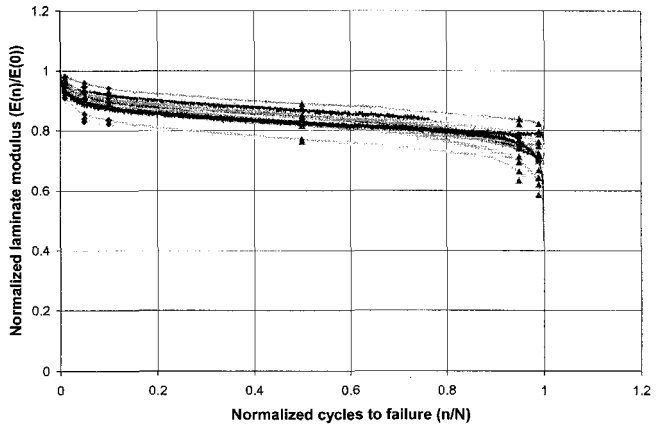


Figure 6: Normalized modulus reduction for 35% UTS

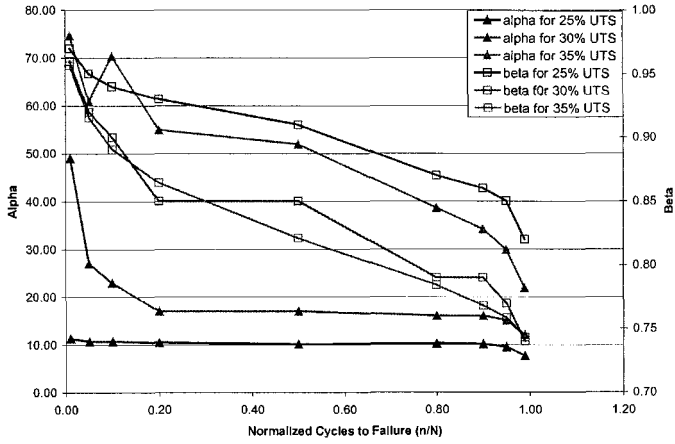


Figure 7: Evolution of Weibull parameters with normalized cycles

REFERENCES

1 AASHTO, "LRFD Bridge Design Specification", 2nd edition. *American Association of State Highway and Transportation Officials*. Washington, D.C. 1998.

2 F McBagonluri, K Garcia, M Hayes, N Verghese, & J Lesko, "Characterization of Fatigue and Combined Environment on Durability Performance of Glass/Vinyl Ester Composite for Infrastructure Applications", *International Journal of Fatigue, 2000* **22**(1): 53-64.

3 W D Neely, *Evaluation of the In-Service Performance of the Tom's Creek Bridge, M.S. Thesis.* Virginia Tech, 2000.

4 S P Phifer, K N E Verghese, J Haramis, & J J Lesko, "Temperature-Moisture-Mechanical Response of Vinyl Ester Resin and Pultruded Vinyl Ester/E-glass Laminated Composites", *ANTEC 2000,* Orlando, Florida, 1999.

5 K L Reifsnider, J J Lesko, & S W Case, "Kinetic Methods for Prediction of Damage Tolerance of High Temperature Polymer Composites", *Composites '95: Recent Advances in Japan and the United States, I. Kimpara, H. Miyairi, and N. Takeda, Ed., Proceedings Japan-U.S. CCM-VII*, Kyoto, Japan, 49-55, 1995.

6 K L Reifsnider, N Iyengar, S W Case, & Y L Xu, "Damage Tolerance and Durability of Fibrous Material Systems: A Micro-Kinetic Approach", *Durability Analysis of Structural Composite Systems, A. H. Cardon (Ed).* A. A. Rotterdam: Balkema.123-144, 1996.

7 Strongwell, "Development of Innovative Manufacturing Technology to Produce Large Phenolic Composite Shapes", *NIST Advanced Technology Program,* 1994.

8 Strongwell, "EXTREN DWB™ Design Guide", 2000.

9 Weibull, & Waloddi. "A Statistical Distribution Function of Wide Applicability", *J. of Applied Mechanics*, 1951 293-297.

10 Hasofer, & Lind. "An Exact and Invariant First Order Reliability Format", *J. Eng. Mech.,*, 1974 111-121.

NUMERICAL SIMULATION OF LONG-TERM BEHAVIOUR OF CONCRETE STRUCTURES WITH EXTERNALLY BONDED CONTINUOUS FIBRE SHEET

Takumi Shimomura, Hiroko Kasahara and Kyuichi Maruyama
Nagaoka University of Technology, Japan

ABSTRACT

A numerical simulation of long-term behaviour of concrete structures retrofitted with externally-bonded continuous fibre sheet is presented. Continuous fibre sheet can improve not only mechanical performance of an existing concrete structure but also its durability. The effectiveness of continuous fibre sheet as a surface insulator was quantified by laboratory tests. Based on this, case studies of numerical service-life simulation of concrete structures with continuous fibre sheet under corrosive environment are demonstrated. The results imply that continuous fibre sheet can extend service-life of concrete structures.

1. INTRODUCTION

In general, performance of a concrete structure under service is gradually deteriorated by loading and environmental attack under service. In order to ensure rational service-life design of concrete structures to be built and to ensure rational ageing management of existing concrete structures, therefore, it would be useful to develop an engineering prediction method for performance of concrete structures as a function of service time. Figure 1 schematically shows the estimated service-life of concrete structures considering upgrading, i.e., repair or rehabilitation, techniques. If we can calculate time-dependent change of structural performance of concrete structures under arbitrary conditions, we can know residual service-life of the structures as the length of time until the calculated value of structural performance meets the minimum acceptable performance[1].

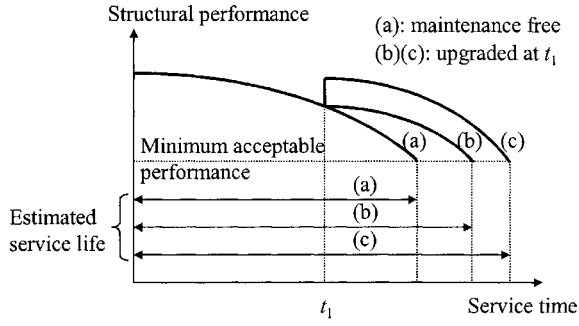


Figure1 Schematic illustration of estimated service-life of concrete structures

If no special maintenance operations are taken during the service-life of a structure, its residual service-life is assumed (a) in Figure 1. On the other hand, if we execute some upgrading operation at the time t_1, the residual service-life of the

structure can be extended as (b) and (c). To evaluate the length of the residual service-life of the structure accurately, we should be able to calculate performance of the structure as a function of service time taking possible upgrading techniques into consideration.

Continuous fibre sheet, which are carbon or aramid textile bonded on concrete surface with epoxy resin, has been used to improve mechanical performance of structures, such as load-carrying capacity and ductility[2)3)]. At the same time, since epoxy resin has very low permeability, the system of continuous fibre sheet and epoxy resin can protect concrete from ingress of aggressive agents, such as chloride ions though this effect has not been enough considered in design. Consequently, continuous fibre sheet can upgrade not only mechanical performance but also durability of existing concrete structures simultaneously. In this sense, continuous fibre sheet is a good example to realize time-dependent performance change of structures as Figure1.

In this study, the effectiveness of continuous fibre sheet as a surface insulator is quantified based on the conducted experimental investigations.

2. OUTLINE OF THE METHODOLOGY

The outline of the computational system considered in this study is shown in Figure 2. Degradation process of concrete structures is calculated step by step with respect to service time by coupling mathematical models for microscopic phenomena in concrete. Since corrosion of reinforcing steel bars embedded in concrete is one of the typical and the serious degradation phenomena of general concrete structures, corrosion problem is focused on here. Hence, we calculate chloride ingress into concrete, corrosion of reinforcement in concrete and structural performance of members with corroded reinforcements at each time step. As results, structural performance is evaluated as a function of time. After retrofitting continuous fibre sheet on the structure, its roles, as an insulator and as an external mechanical reinforcement, are taken into account naturally by means of the mathematical models that are proposed in this paper.

Table 1 Conditions of specimens

Specimen No.	W/C of concrete [%]	Thickness of cover [mm]	CF sheet wrapping
1	60	45	No
2	60	45	Yes
3	60	70	No
4	50	45	No
5	50	45	Yes
6	50	70	No
7	40	45	No
8	40	45	Yes
9	40	70	No
10	30	45	No
11	30	45	Yes
12	30	70	No

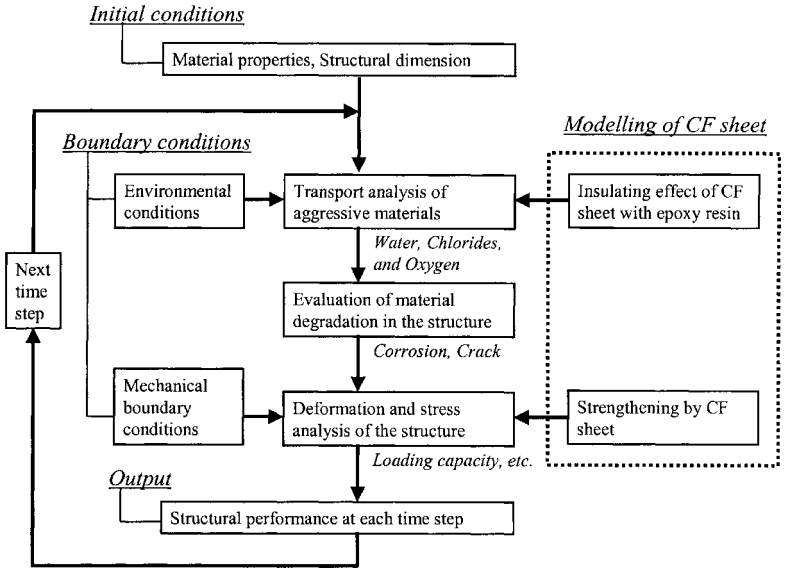


Figure 2 Outline of the computational system

3. INSULATING EFFECT OF CONTINUOUS FIBRE SHEET

3.1 Experiment

Since epoxy resin that is used in bonding continuous sheet on the concrete surface has very low permeability compared with concrete, it is difficult to experimentally measure its insulation effect against ingress of aggressive agents into concrete. Therefore, the electrical permeability test was employed in this study. Cylindrical concrete specimens shown in Figure 3 were used in the test. Twelve specimens, whose experimental parameters are water-cement ratio of concrete, thickness of concrete cover and wrapping of continuous sheet on the surface, were tested. Testing conditions of the specimens are indicated in Table 1.

Setup for the permeability test is shown in Figure 4. Constant electric voltage of 30V was applied to the specimen in NaCl solution. Time-dependent direct current penetrating the concrete was measured.

Concrete cracks were generated in the specimens 1 and 4 around 100 hours by corrosion of reinforcements in concrete. Electric resistance of concrete cover was suddenly lost after cracking. In order to compare permeability of all the specimens under the unified condition, therefore, accumulated electric current until 90 hours is taken as an index for permeability of specimen as shown in Figure 5.

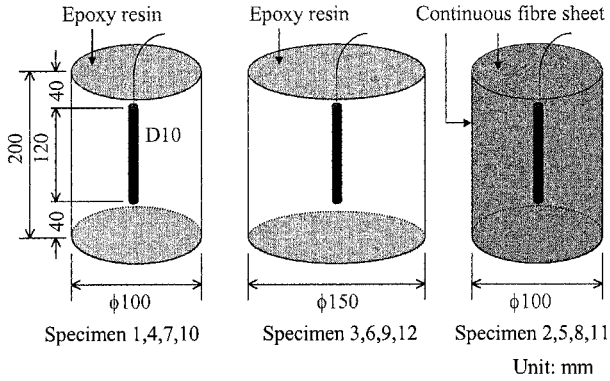


Figure 3 Cylindrical specimen for permeability test

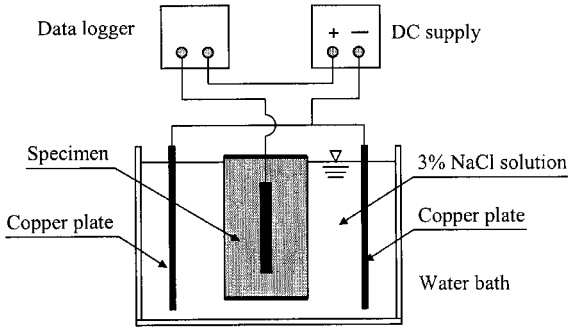


Figure 4 Setup for chloride permeability test

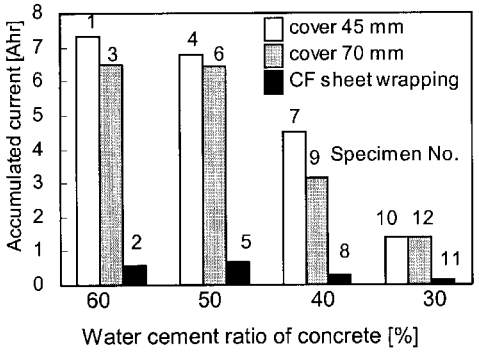


Figure 5 Accumulated electric current of the specimens until 90 hours

Comparing the obtained accumulated electric current without continuous fibre sheet in Figure 5, it is clear that permeability of concrete decreases with decreasing of water-cement ratio and increasing of thickness of concrete cover. These tendencies are very reasonable. In cases that continuous fibre is attached on the surface of concrete, accumulated current became very small in spite of water-cement ratio of concrete. It is verified that the system of continuous fibre sheet and epoxy resin is effective as a surface insulator against ingress of materials into concrete.

3.2 Modelling of insulation effect of continuous fibre sheet

The authors have developed a computational model for the transport process of water and chloride ions in concrete based on pore structure of concrete and thermodynamic behaviour of water in porous media[4)5)6)]. Mass conservation equations of water and chloride are respectively expressed as follows:

$$\frac{\partial w}{\partial t} = -div(J_v + J_l) \tag{1}$$

$$\frac{\partial C_{Clt}}{\partial t} = -div\left(J_{Cldif} + C_{Clf}\frac{J_l}{\rho_l} \right) \tag{2}$$

where, where w is mass concentration of water per unit concrete volume, t time, and J_v and J_l mass flux of vapour and liquid water respectively, C_{Clt} is total mass concentration of chloride per unit concrete volume, J_{Cldif} is mass flux of chloride by molecular diffusion and C_{Clf} is mass concentration of free chloride. The last term in Equation (2) expresses mass flux of chloride ions carried by liquid water that can be obtained from the moisture transport analysis.

It is necessary to execute coupling analysis of water and chloride to evaluate transport of chloride in non-saturated concrete in the atmosphere. However, in case of saturated concrete, molecular diffusion is dominant as transport mechanism of chloride in concrete. The mass flux of chloride by molecular diffusion is formulated as:

$$J_{Cldif} = -K_{Cl} D_{Cl} grad\, C_{Clf} \tag{3}$$

where, K_{Cl} is non-dimensional material factor of concrete as a function of its pore structure, D_{Cl} is diffusivity of chloride ion in liquid water. Mass flux of chloride by molecular diffusion at the boundary surface is formulated as:

$$J_{Cldif} = -D_{Cl}\frac{C_{Clf}(0) - V_o \cdot C_{ext}}{h_{Cl}} \tag{4}$$

where, $C_{Clf}(0)$ is mass concentration of free chloride in concrete at the surface, V_o is porosity of concrete, C_{ext} is mass concentration of chloride in external solution and h_{Cl} is thickness of boundary-layer for mass concentration of chloride.

In order to express insulating effect of the system of continuous fibre sheet and epoxy resin bonded on the surface of concrete, the boundary-layer is apparently increased:

$$h'_{Cl} = h_{Cl} + h_{cf} \tag{5}$$

where, h_{cf} is apparent thickness of the system of continuous fibre sheet and epoxy resin, defined as:

$$h_{cf} = t_{cf} \frac{D_{Cl}}{D_{cf}} \tag{6}$$

where, t_{cf} is actual thickness of the system of continuous fibre sheet and epoxy resin and D_{cf} is diffusion coefficient of chloride in the system, hereafter diffusion coefficient of continuous fibre sheet.

3.3 Determination of diffusion coefficient of continuous fibre sheet

Diffusion processes of chloride in the cylindrical concrete specimens that were used in the electric permeability test were analyzed by the proposed diffusion model. Finite differential method was employed to solve the governing equations numerically[7]. Material parameters for concrete were determined based on the previous study[4]. The driving force in the experiment is the gradient of electric potential, while the driving force assumed in the computational model is the gradient of chloride concentration. Though they are different phenomena in fact, these two transport phenomena may have some correlation with each other since they are both transport phenomena of ions in concrete. Hence, before discussing permeability of continuous fibre sheet, the correlation between the experiment and the analysis is verified using the results of the specimens without continuous fibre sheet (Figure 6).

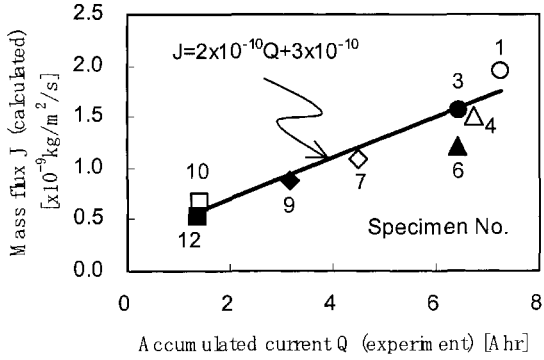


Figure 6 Correlation between the experimental and the analytical results

Table 2 Diffusion coefficient of continuous fibre sheet

Specimen No.	2	5	8	11
W/C [%]	60	50	40	30
Q (experiment) [Ahr]	0.56	0.68	0.28	0.13
D_{cf} [x10^{-14}m^2/s]	2.29	2.99	3.03	4.69

Figure 6 shows the relationship between the experimental and the analytical results performed in this study. Accumulated electric current until 90 hours (Q) is taken as the index of the experimental result, while mass flux of chloride in the steady state (J) is taken as the index of the analytical result. It is clear that the experimental results (Q) and the analytical ones (J) have good correlation in spite of water-cement ratio of concrete and thickness of concrete cover. This result implies that the hypothesis on the correlation between the experiment and the analysis is correct. In Figure 6, an

empirical equation between the experimental results (Q [Ahr]) and the analytical ones (J [kg/m^2/s]) is indicated.

$$J = 2\times10^{-10}Q + 3\times10^{-10} \quad \left(kg/m^2/s\right) \tag{7}$$

It is assumed that this empirical correlation may be adapted to the specimens with continuous fibre sheet. Then, diffusion coefficient of continuous fibre sheet can be determined by trial and error so that the obtained analytical result (J) and the experimental result of the specimen (Q) satisfy the empirical equation. In the analysis, the thickness of continuous fibre sheet (t_{cf}) was set 1 mm.

The diffusion coefficients of continuous fibre sheet, which were obtained by this method from the experimental results of the specimens with continuous fibre sheet, are shown in Table 2. Close values were obtained from the four specimens. The obtained diffusion coefficient of continuous fibre sheet was approximately 3x10^{-14}m^2/s, which is about two orders as small as that of ordinary concrete.

5. NUMERICAL SERVICE-LIFE SIMULATION OF STRUCTURES

In order to verify the reasonableness to take into account the insulating effect of continuous fibre sheet as well as its strengthening effect, service-life simulation of concrete structure was carried out. Flexural capacity of RC beam with continuous fibre sheet shown in Figure 7 under various conditions were calculated as a function of time. Material properties used in the analysis are shown in Table3.

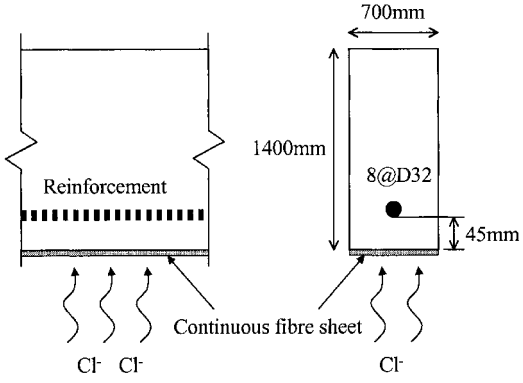


Figure 7 RC beam retrofitted with CF sheet

Table 3 Material properties

Material		Properties
Concrete	Unit water	165kg/m^3
	Water-cement ratio	50%
	Compressive strength	38N/mm^2
	Other mechanical properties	presumed from compressive strength
	Parameters for mass transport	presumed from mix proportion
Reinforcement	Yield strength	400N/mm^2
	Elastic modulus	200000N/mm^2
Continuous fibre sheet	Thickness	1mm (including epoxy resin)
	Tensile strength	390N/mm$^{2*)}$
	Elastic modulus	3000N/mm$^{2*)}$
	Diffusion coefficient for chloride in the system of sheet and epoxy resin	3x10^{-14}m^2/s

Note) Tensile strength and elastic modulus of continuous fibre sheet is calculated setting the thickness of the sheet 1mm.

Table 4 Analytical cases

Case	Time of retrofit of CF sheet	Effect of CF sheet to be considered
1	without CF sheet	--
2	from the initial stage	Insulating and strengthening effect of CF sheet
3	at 10 years	Insulating and strengthening effect of CF sheet
4	at 20 years	Insulating and strengthening effect of CF sheet
5	from the initial stage	Only insulating effect of CF sheet
6	from the initial stage	Only strengthening effect of CF sheet

The structure was assumed to stand under the corrosive environment with airborne salt from the sea. One-dimensional transport analysis was employed to evaluate chloride ingress into concrete as shown Figure 7. Corrosion of reinforcement in concrete caused by chloride and loss of cross-sectional area of the reinforcement due to corrosion were considered. Strengthening effect of continuous fibre sheet was evaluated by the conventional beam theory. Delamination of the sheet was not considered.

Six cases were analyzed as indicated in Table 4. Figure 8 shows the analytical results, in which flexural capacity of the beams as a function of time are plotted. In case 1, in which continuous fibre sheet is not attached, flexural capacity of the beam decreases gradually because of reinforcement corrosion.

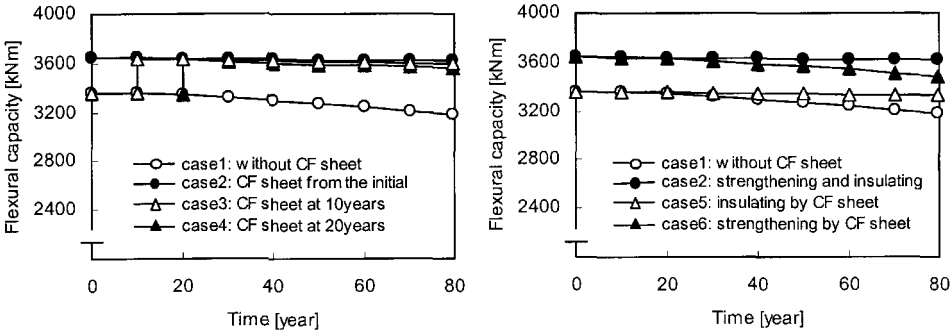


Figure 8 Analytical results: flexural capacity of beam as a function of time

In case 2, 3 and 4, in which continuous fibre sheet is attached, flexural capacity is increased by the strengthening effect of the sheet and the time-dependent decreasing of flexural capacity is avoided by the insulating effect. The 'jump' in flexural capacity in the cases 3 and 4 in the left figure is attributable to the retrofitting of sheet. The rate of deterioration after retrofitting of the sheet is a little different depending on the time of retrofitting. This is due to the difference of chloride concentration in concrete at the time of retrofitting.

The advantage to take into account the effectiveness of continuous sheet both as surface insulator and as external reinforcement is much clear in comparison of the results of case 1,2,5 and 6 in the right diagram.

6. SUMMARY

Coupling the electric permeability test and numerical analysis, diffusion coefficient of chloride in the layer of continuous fibre sheet with epoxy resin was quantified. Through the numerical service-life simulation of RC structure with continuous fibre sheet, the advantage to take into account the effect of continuous sheet both as surface insulator and as external reinforcement was verified.

REFERENCES

1 G Somerville, 'Engineering design and service life', *STATS 21st anniversary conference*, London, E & FN Spon, 1995.

2 Japan Concrete Institute, *Technical Report on Continuous Fibre Reinforced Concrete*, Tokyo, Japan Concrete Institute, 1998.

3 Japan Society of Civil Engineers, *Recommendations for Upgrading of Concrete Structures with Use of Continuous Fibre Sheets*, Tokyo, 2001.

4 T Shimomura and K Maekawa, 'Analysis of the drying shrinkage behaviour of concrete using a micromechanical model based on the micropore structure of concrete', *Magazine of Concrete Research*, 1997 **49**(181) 303-322.

5 T Shimomura and K Maruyama, 'Service life prediction of concrete structures subjected to chloride attack by numerical simulation', *International RILEM Workshop on Life Prediction and Aging Management of Concrete Structures*, Cannes, RILEM Publications S.A.R.L., 2000.

6 T Shimomura and K Maruyama, 'Numerical simulation of performance of concrete structures as a function of service time', *International Conference on Advances in Structures: Steel, Concrete, Composite and Aluminium (ASSCCA'03)*, Sydney, A.A.Belkema, 2003.

7 S V Patankar, *Numerical heat transfer and fluid flow*, New York, Hemisphere Publishing Corporation, 1980.

INFLUENCES OF FREEZE AND THAW CYCLES AND ELEVATED TEMPERATURE ON THE PROPERTIES OF FRP COMPOSITES

D. B. Tann and R. Delpak

School of Technology, University of Glamorgan, Pontypridd CF37 1DL, UK

ABSTRACT: This paper reports the influences of freeze and thaw actions as well as high temperatures on the mechanical properties of various FRP fabric sheets that are commonly used in the construction industry for structural strengthening. One hundred and twenty samples of commercially available Aramid, Carbon and Glass FRP fabric strips were subjected to: (a) freeze and thaw cycles at every three days for a period of nine weeks; and (b) elevated temperatures, for a period of four or six hours everyday consecutively for one week. These samples were then tested to determine their mechanical properties including ultimate tensile strength, failure strain, and elastic modulus. Results are presented and compared with those of the control samples. It was found that high temperature did have a detrimental effect on the mechanical properties of FRP composites, while the freeze and thaw cycles exhibited relatively minor influences.

INTRODUCTION

In recent years, the number of structures that were strengthened by externally bonded fibre reinforced polymer (FRP) composites has been steadily increasing worldwide. A great deal of research work has been carried out on the performance of FRP strengthened members under short-term loading. However, research activities in the area of durability and poor workmanship for the FRP materials are still relatively few. The FRP strengthened structures, depending on the geographical location, could often be subjected to extreme weather conditions. In other cases, elevated temperature in the event of indirect exposure to fire may become an issue of concern as it may adversely affect the in-service mechanical properties of the FRP materials. This paper, therefore, attempts to simulate the adverse environmental and human effects on the FRP properties.

EXPERIMENTAL PROGRAMME

A total of one hundred and twenty FRP tensile tests are reported in this paper. All samples were prepared and tested in accordance with the British Standard [1] BS EN 2561:1995 (BSI, 1995). Firstly the FRP fabric sheets were laminated (in a single layer) with the prescribed resin adhesive. After curing for seven days, the laminate was then cut into tensile test samples and prepared for load testing. All samples were strain gauged at the middle length. Displacement control was used and the load speed was set at 2 mm per minute. The length of all samples was kept at 250 mm, and the width used varied from 13 to 16 mm. This variation in width was necessary since the samples were cut such that no strand was disturbed [2,3]. A typical sample contains six fibre strands. The sample identification was as follows:

The first letter represents the type of FRP. Aramid FRP sheets were represented by the letter **A**; Carbon FRP sheets were represented by the letter **C**; and, Glass FRP sheets

were represented by the letter **G**. Following the first letter, one or two digit(s) denotes the number of the sample. (1 to 20)

The third letter indicates the environmental conditions, while the subscript is related to specific settings. The following three types of accelerated adverse conditions were created in laboratory controlled conditions in which FRP samples were kept.

(a) **Condition 1 – Coded E**. A freeze and thaw environment was created in a special environmental chamber. FRP specimens were exposed to twenty-one continuous freeze and thaw cycles. Each cycle lasted three days, forty-eight hours at –20°C and then twenty-four hours at +25°C, making a total of 9 weeks.
(b) **Condition 2 – Coded T**. An elevated temperature of +180°C was created in a preheated oven, the FRP samples were then lodged in the oven for 4 hours (coded $\mathbf{T_4}$) and 6 hours respectively (Coded $\mathbf{T_6}$) every day for 5 days.
(c) All control samples were denoted by a letter **R**.

The sample G9T_6 is therefore the 9th Glass fibre sample subjected to the 6-hour high temperature condition, and A10R is the10th Aramid control test piece.

The tests were conducted using a standard INSTRON 8502 test machine, which was fully calibrated (by UKAS) to ±1.5 N. The thickness and width of all samples were carefully measured at three positions (at top, middle, and bottom in the gauge length) and were averaged for result calculations. Electrical strain gauges were bonded to each specimen to monitor strain variation at every load increment.

TEST RESULTS AND DISCUSSIONS

Freeze and Thaw Action - A total of 30 samples (10 each for CFRP, GFRP and AFRP respectively) were exposed to the 21 freeze and thaw cycles in the environmental chamber. During load testing, the strains were recorded at every 0.5 kN load increment for the first 2 kN, and subsequently at 1.0 kN interval. The value of elastic modulus of each sample was determined based on the stress-strain graphs, which showed mostly linear elastic behaviour until failure. Hence it was possible to determine the average ultimate strain capacity from the strength and elastic modulus. This was necessary since at occasions, some ultimate strain readings were unavailable due to the breakage of the electrical strain gauge before failure. A typical stress strain graph is shown in Figure 1.

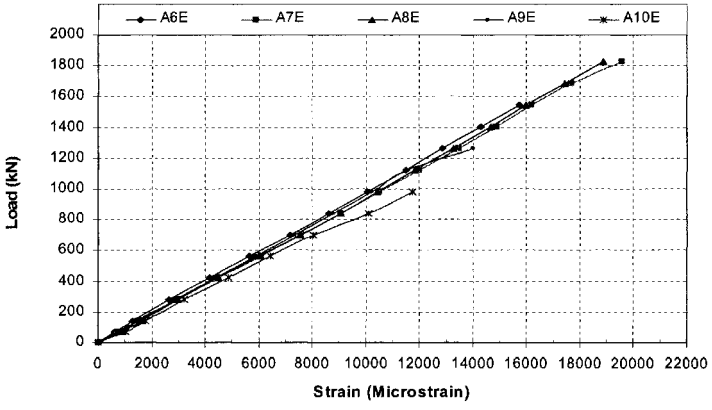


Figure 1. Typical stress-strain graphs (AFRP samples A7E-A10E)

Shown in Tables 1 and 2 are the results of CFRP samples. Given the inevitable (but acceptable) level of data variation, it can be seen that the difference in the two sets of results are negligible, indicating that such freeze and thaw actions had no appreciable influence on the mechanical properties of CFRP composites.

Table 1. Test Results for the **CFRP** Control Samples (1-10)*.

Sample Reference	Tensile Strength (N/mm^2)	Elastic Modulus (kN/mm^2)	Ultimate Strain Capacity (%)
C1R	3530.9	244.7	1.44
C2R	3614.0	241.2	1.50
C3R	3083.4	246.9	1.25
C4R	3483.2	252.8	1.38
C5R	3469.6	239.9	1.45
C6R	3225.9	241.6	1.34
C7R	3444.3	245.8	1.40
C8R	3268.7	239.9	1.36
C9R	3487.4	236.9	1.47
C10R	3541.8	253.9	1.39
Average	**3414.9**	**244.4**	**1.40**
Standard Dev	166.7	5.62	0.07

* Sample thickness = 0.149 mm, average cross section area = 2.359 mm^2.

Table 2. Test Results for the **CFRP** Freeze-and-Thaw Samples (1-10) *.

Sample Reference	Tensile Strength (N/mm^2)	Elastic Modulus (kN/mm^2)	Ultimate Strain Capacity (%)
C1E	3218.6	250.7	1.28
C2E	3669.6	242.3	1.51
C3E	3482.5	231.6	1.50
C4E	2907.0	244.1	1.19
C5E	3910.2	243.2	1.61
C6E	2721.8	202.5	1.34
C7E	3780.6	246.7	1.53
C8E	2986.9	231.4	1.29
C9E	3870.2	247.3	1.56
C10E	3866.9	246.2	1.57
Average	**3441.4**	**238.6**	**1.44**
Standard Dev	448.8	14.19	0.15

* Sample thickness = 0.149 mm, average cross section area = 2.290 mm^2.

Table 3. Test Results for the **GFRP** Control Samples (1-10) *.

Sample Reference	Tensile Strength (N/mm^2)	Elastic Modulus (kN/mm^2)	Ultimate Strain Capacity (%)
G1R	1655.1	84.8	1.95
G2R	2074.1	81.9	2.53
G3R	1915.9	87.7	2.18
G4R	1717.4	81.1	2.12
G5R	1821.3	82.2	2.22
G6R	1866.9	81.1	2.30
G7R	1737.3	85.8	2.02
G8R	1978.1	85.4	2.32
G9R	1899.8	85.2	2.23
G10R	2135.4	95.6	2.23
Average	**1880.1**	**85.08**	**2.21**
Standard Dev	154.6	4.32	0.16

* Sample thickness = 0.162 mm, average cross section area = 2.820 mm^2.

Similarly, two groups of GFRP samples were tested. The results are listed in Tables 3 and 4. Again, no significant difference was noted. Although the current test programme lasted a relatively short period of sixty-three days, it is an encouraging sign that GFRP strengthened structures can sustain extreme adverse weather conditions with little change in the material properties.

Table 4. Test Results for the **GFRP** Freeze-and-Thaw Samples (1-10)*.

Sample Reference	Tensile Strength (N/mm^2)	Elastic Modulus (kN/mm^2)	Ultimate Strain Capacity (%)
G1E	1906.1	83.6	2.28
G2 E	2082.9	88.2	2.36
G3 E	1738.3	79.1	2.20
G4 E	1906.3	86.4	2.21
G5 E	1917.3	94.3	2.03
G6 E	1687.7	77.1	2.19
G7 E	1848.1	85.6	2.16
G8 E	1950.4	82.3	2.37
G9 E	1670.1	83.4	2.00
G10 E	1972.2	95.8	2.06
Average	**1867.9**	**85.58**	**2.19**
Standard Dev	132.5	5.98	0.13

* Sample thickness = 0.162 mm, average cross section area = 2.601 mm^2.

For Aramid samples, again the two groups of samples were tested under identical conditions as those of CFRP and GFRP samples. It was also found that no appreciable differences in the major elastic properties were noted, as illustrated in Tables 5 and 6.

It was further observed that all samples were successfully tested where all failed by rupture of the fibres within the gauge length. Figure 2 shows a typical example of failure mode. (shown here are the GFRP samples G1E-G10E)

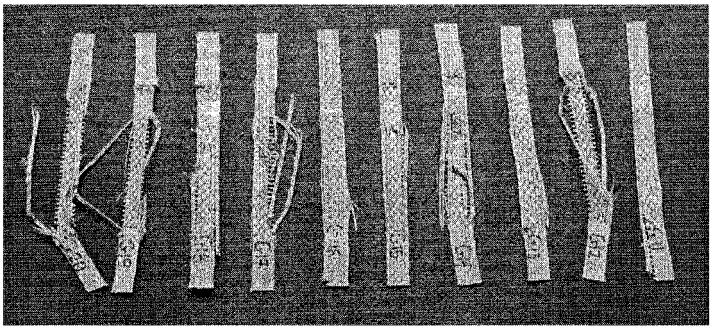


Figure 2. Typical failure mode of FRP samples

Elevated Temperature - For the elevated temperature condition, there were some apparent changes in the mechanical properties. Tables 7, 8 and 9 show the results for three sets of GFRP specimens. It can be seen that as the exposure to high temperature is continued, the ultimate tensile strength decreases, with a slightly faster rate of strain decrease, hence giving an apparent increase in the elastic modulus. However, sample $G12T_6$ failed unexpectedly prematurely, which was not attributed to the elevated temperature effects but imperfect sample fibre alignment.

Table 5. Test Results for the **AFRP** Control Samples (1-10, 2 layers) *.

Sample Reference	Tensile Strength (N/mm^2)	Elastic Modulus (kN/mm^2)	Ultimate Strain Capacity (%)
A1R	1962.3	94.5	2.08
A2R	1939.4	92.2	2.10
A3R	1809.8	90.0	2.01
A4R	1942.6	90.1	2.16
A5R	1446.6	85.5	1.69
A6R	1778.1	95.4	1.86
A7R	1920.6	96.5	1.99
A8R	1863.9	94.5	1.97
A9R	2095.8	96.4	2.17
A10R	2133.6	92.2	2.31
Average	**1889.3**	**92.73**	**2.04**
Standard Dev	191.3	3.46	0.17

* Sample thickness = 0.508 mm, average cross section area = 7.448 mm^2.

Table 6. Results for **AFRP**s in Freeze-and-Thaw Chamber (1-10, 2 layers)*

Sample Reference	Tensile Strength (N/mm^2)	Elastic Modulus (kN/mm^2)	Ultimate Strain Capacity (%)
A1E	1847.8	94.5	1.96
A2E	1894.6	90.0	2.11
A3E	1786.7	95.0	1.88
A4E	2039.1	86.3	2.36
A5E	2024.1	96.7	2.09
A6E	1617.5	96.3	1.68
A7E	2041.7	94.1	2.17
A8E	1811.9	78.7	2.30
A9E	2020.3	97.1	2.08
A10E	2076.6	92.6	2.24
Average	**1916.0**	**92.13**	**2.09**
Standard Dev	149.5	5.77	0.21

* Sample thickness = 0.508 mm, average cross section area = 7.096 mm^2.

Table 7. Test Results for the **GFRP** Control Samples (11-20)*.

Sample Reference	Tensile Strength (N/mm^2)	Elastic Modulus (kN/mm^2)	Ultimate Strain Capacity (%)
G11R	1769.3	76	2.33
G12R	1898.5	82	2.32
G13R	1800.1	85	2.12
G14R	1938.9	86	2.25
G15R	2063.4	92	2.24
G16R	1672.7	82	2.04
G17R	1747.0	80	2.18
G18R	1652.6	73	2.26
G19R	1742.8	81	2.15
G20R	1575.6	76	2.07
Average	**1786.1**	**81.3**	**2.20**
Standard Dev	146.0	5.55	0.10

* Sample thickness = 0.162 mm, average cross section area = 2.820 mm^2.

Tables 10 to 12 list the results for the Aramid samples. It is clear that the exposure to high temperature under extended time results in reduced ultimate tensile strength. The E values also increased significantly within the four-hour heat sample batch but reversed to "near control" values when heat was applied for longer.

Table 8. Test Results for the **GFRP** Samples in (20 hrs at 180°C , 11-20)*.

Sample Reference	Tensile Strength (N/mm^2)	Elastic Modulus (kN/mm^2)	Ultimate Strain Capacity (%)
$G11T_4$	1883.2	86	2.19
$G12\ T_4$	1883.2	97	1.94
$G13\ T_4$	1773.6	86	2.06
$G14\ T_4$	1851.2	88	2.10
$G15\ T_4$	1606.3	90	1.78
$G16\ T_4$	1688.7	82	2.06
$G17\ T_4$	1516.2	84	1.81
$G18\ T_4$	1689.6	89	1.90
$G19\ T_4$	1961.4	89	2.20
$G20\ T_4$	1704.5	80	2.13
Average	**1755.8**	**87.1**	**2.02**
Standard Dev	139.6	4.75	0.15

* Sample thickness = 0.162 mm, average cross section area = 2.755 mm^2.

Table 9. Test Results for the **GFRP** Samples in (30 hrs at 180°C, 11-20)*.

Sample Reference	Tensile Strength (N/mm^2)	Elastic Modulus (kN/mm^2)	Ultimate Strain Capacity (%)
$G11T_6$	1480.4	83	1.78
$G12\ T_6$	785.2	89	0.88
$G13\ T_6$	1739.1	88	1.98
$G14\ T_6$	1478.4	80	1.85
$G15\ T_6$	1727.0	107	1.61
$G16\ T_6$	2025.2	91	2.23
$G17\ T_6$	1893.1	86	2.20
$G18\ T_6$	1330.5	92	1.45
$G19\ T_6$	1839.2	83	2.22
$G20\ T_6$	1744.0	79	2.21
Average	**1604.2**	**87.8**	**1.84**
Standard Dev	356.8	8.07	0.43

* Sample thickness = 0.162 mm, average cross section area = 2.711 mm^2.

Table 10. Test Results for the **AFRP** Control Samples (11-20, 2 layers)*.

Sample Reference	Ultimate Tensile Strength (N/mm^2)	Elastic Modulus (Kn/mm^2)	Ultimate Strain Capacity (%)
A11R	1896.0	83.0	2.28
A12R	2058.8	87.0	2.37
A13R	1984.2	94.0	2.11
A14R	2080.1	86.0	2.42
A15R	1965.1	88.0	2.23
A16R	1992.5	91.0	2.19
A17R	2046.7	88.0	2.33
A18R	1717.0	86.0	2.00
A19R	1941.2	90.0	2.16
A20R	2204.2	91.0	2.42
Average	**1988.6**	**88.4**	**2.25**
Standard Dev	128.4	3.17	0.14

* Sample thickness = 0.51 mm, average cross section area = 7.39 mm^2.

The data obtained in the current tests were considered to be reliable due to the careful configuration and implementation of the laboratory test programme. Figures 3 and 4 show the overall comparison of the normalised results.

Table 11. Test Results for **AFRP** Samples in (20 hrs at 180°C, 11-20, 2 layers)*.

Sample Reference	Ultimate Tensile Strength (N/mm^2)	Elastic Modulus (kN/mm^2)	Ultimate Strain Capacity (%)
$A11T_4$	1643.5	95.0	1.73
$A12\ T_4$	2038.2	99.0	2.06
$A13\ T_4$	1793.3	99.0	1.81
$A14\ T_4$	1520.9	99.0	1.54
$A15\ T_4$	1915.9	100.0	1.92
$A16\ T_4$	1902.4	98.0	1.94
$A17\ T_4$	1903.7	105.0	1.81
$A18\ T_4$	1938.1	101.0	1.92
$A19\ T_4$	1855.3	102.0	1.82
$G20\ T_4$	1895.8	101.0	1.88
Average	**1840.7**	**99.9**	**1.84**
Standard Dev	152.2	2.64	0.14

* Sample thickness = 0.51 mm, average cross section area = 7.051 mm^2.

Table 12. Test Results for **AFRP** Samples (30 hrs at 180°C , 11-20, 2 layers)*.

Sample Reference	Ultimate Tensile Strength (N/mm^2)	Elastic Modulus (kN/mm^2)	Ultimate Strain Capacity (%)
$A11T_6$	1784.9	91.0	1.96
$A12\ 8_6$	1377.0	77.0	1.79
$A13\ T_6$	1335.7	95.0	1.41
$A14\ T_6$	1762.3	100.0	1.76
$A15\ T_6$	1658.5	89.0	1.86
$A16\ T_6$	2048.5	99.0	2.07
$A17\ T_6$	1517.6	85.0	1.79
$A18\ T_6$	1653.8	94.0	1.76
$A19\ T_6$	1931.7	94.0	2.06
$A20\ T_6$	1546.9	90.0	1.72
Average	**1661.7**	**91.4**	**1.82**
Standard Dev	228.3	6.79	0.19

* Sample thickness = 0.51 mm, average cross section area = 7.486 mm^2.

CONCLUSIONS

A series of experimental evaluations were carried out involving 120 FRP samples which included Carbon, Aramid and Glass fibres. Preliminary conclusions may be drawn as follows.

(a) The freeze and thaw actions - 21 cycles at between -20°C (2 days) to +25°C (1 day) in current tests, do not appear have significant influence on the mechanical properties of the common FRP composites used in construction.

(b) Elevated temperature at 180°C for 20 hours (4 hours a day) appeared to marginally reduce the ultimate tensile strength of both GFRP and AFRP fabric sheets. While the elastic modulus apparently increased over those of the control samples by 7% and 13% respectively. The ultimate strain capacity for GFRP and AFRP samples decreased by 10% and 19% respectively. This suggests that as temperature increases the composites become stiffer through brittleness.

(c) When the FRP samples were exposed to high temperature (180°C) for 30 hours (6 hours a day), the elastic modulus appeared to stabilise for the GFRP material, while recovering toward the magnitude of the control samples for the AFRP composites. The ultimate strain capacity remained significantly reduced from the reference values.

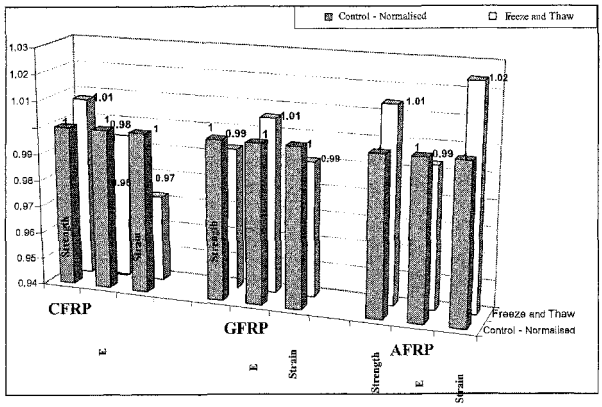


Figure 3. Results comparison of freeze and thaw samples

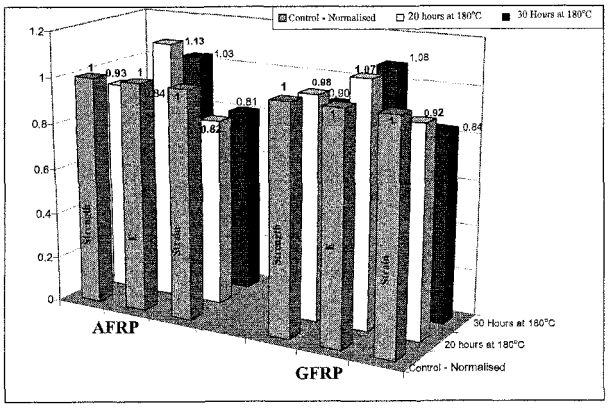


Figure 4. Results comparison of elevated temperature samples

ACKNOWLEDGEMENTS

The tests reported herewith were conducted at the University of Glamorgan Structural Laboratory, the authors wish to acknowledge the contribution of final year project students Efi Ntalia and Adam Hopkins for carrying out parts of the laboratory tests. Senior technical officers Mr Huw Williams operated the Instron testing machine for all samples, and Mr Paul Marshman strain gauged the specimens. Exchem Mining and Construction (UK) Ltd provided all FRP materials and laminating resins.

REFERENCE

1. British Standards Institution, BS EN 2561:1995, *Carbon fibre reinforced plastics – Unidirectional laminates, Tensile test parallel to the fibre direction, 1999, London.*
2. E. Ntalia, "*Evaluation of elastic properties of fibre reinforced polymer (FRP) composites,*" BSc dissertation, University of Glamorgan, Pontypridd, 2002.
3. A. Hopkins, "Mechanical *properties of FRP composite sheets subjected to elevated temperatures,*" BSc dissertation, University of Glamorgan, Pontypridd, 2002.

ENVIRONMENTAL EFFECTS ON TENSILE PROPERTIES OF FRP LAMINATES MADE USING WET-LAY-UP METHOD

Mohammadreza Tavakkolizadeh[1] and Hamid Saadatmanesh[2]
[1] *Jackson State University, Jackson, Mississippi, USA*
[2] *The University of Arizona, Tucson, Arizona, USA*

ABSTRACT

The demand for Fiber Reinforced Plastics (FRP) in rehabilitation of infrastructures is increasing. New techniques utilize the lightweight, high strength and formability of FRP fabrics and laminates in various retrofitting projects. This paper presents the results of a study on the long-term behavior of different types of FRP laminates made using the wet-lay-up technique. A total of 525 specimens were prepared using one type of epoxy and seven different types of fabrics. Unidirectional and bidirectional fabrics made from glass, carbon and aramid were used in this study. The samples were exposed to nine different environments. These environments were simulated using four different chemical solutions with pH of 12.5, 10, 7 and 2.5, and substitute seawater. In addition, four chambers for exposure to ultraviolet radiation, temperature of 60°C, temperature of 50°C with 95% relative humidity and soil with 25% moisture content and active microorganisms were considered. Uniaxial tension tests were performed on the samples after 6000, 12000 and 20000 hours of exposure as well as on control samples, and tensile properties were measured for each specimen. The results showed a significant loss of strength and ultimate strain for glass fiber reinforced plastics (GFRP) in solutions, especially in high pH values, while carbon and hybrid glass-carbon laminates showed very little loss of mechanical properties.

INTRODUCTION

Fiber Reinforced Plastics (FRP) are increasingly attracting the attention of civil engineers because of their unique properties for retrofitting of structures. The excellent tensile strength, lightweight, resistant to electrochemical corrosion and formability of FRPs make them materials of choice for repair and retrofit of structures. These materials have been used in different engineering fields such as aerospace, automotive, marine, chemical, etc. for many years, and in general, they have shown good long-term behavior. The methods of fabrication and quality control in civil engineering projects, however, are quite different from those in aerospace or defense industry. In addition, the FRP used in civil engineering projects are exposed to different environments than those in other fields of engineering. Therefore, in order to address the rising concerns about the long-term performance of FRP in civil engineering projects, durability of these materials and change in their mechanical properties with time must be investigated.

Several investigators have addressed the durability of FRP materials. Most of the research was concentrated on the effect of the moisture and temperature on FRP tendons, rebars, pultruded sections and laminates made with standard vacuum bagging procedures and under controlled-temperature curing cycles for periods of less than a year. The results of such studies have been used initially to answer some of the concerns of structural engineers. However, since durability of FRP materials is significantly affected by their manufacturing process and quality control used during construction, studies are needed to address durability issues specifically for the type of

projects involving the wet-lay-up procedure and the environments in civil engineering applications.

PREVIOUS WORK

As it mentioned before, the existing database on long-term durability of composite laminate could not address all the concerns of practicing engineers. The manufacturing processes of the composite used in these researches were different than the wet-lay-up technique, which is the most common method used in civil engineering projects. The environments considered in most of these studies were not addressing all of civil engineering interests. In addition, most of these studies considered fairly short periods of exposure that may not satisfy the long-term concerns of structural engineers. The existing research on the durability of FRP structural elements can be categorized in four groups:

Laminates

In two studies conducted by Shen[1] and Springer[2], environmental effects on glass fiber reinforced polyester and vinylester composites were investigated. They exposed three different composite laminates to humid air (50% and 100% RH), saturated NaCl solution, diesel fuel, lubricating oil, antifreeze and gasoline at two temperatures of 23°C and 93°C for six months. They obtained the tensile and shear properties of the laminates by conducting uniaxial tension and short beam shear tests. The following conclusions were drawn from testing of over 600 specimens:

Specimens exposed at 93°C showed the highest loss of mechanical properties (~19%) in solutions as compared to those exposed at 23°C (~6%). The vinylester based laminates showed less degradation (~9.5%) compared to the polyester based laminates (~14.5%). Among all of the environments, antifreeze, saturated salt, gasoline and 100% RH showed the strongest effect on the specimens after 6 months exposure with the average loss of 28%, 22%, 15% and 13%, respectively.

In another study conducted by Hexcel Corporation[3] the effects of ozone (at 60°C), salt water, fresh water, alkaline soil (pH=8.5~10.5), high temperature (60°C) and UV radiation on the tensile properties of GFRP laminates were investigated. The laminate, which was made of 920 gr/m^2 glass fabric, had an average thickness of 2 mm. Laminates, after 1000 hours of exposure, did not show any significant degradation of their tensile properties.

Rebars and Tendons

In two studies conducted at The University of Arizona[4], the effect of different environmental exposure on E-glass FRP rebars, pan-based carbon FRP-tendons and aramid FRP-tendons was investigated. They tested the specimens after exposure to seven different solutions, ultraviolet radiation and freeze-thaw cycles. The solutions considered were fresh water (at 25°C and 65°C), alkaline (pH of 12 at 25°C and 65°C), acidic (pH of 3 at 25°C), sea water (3.5% NaCl at 25°C) and deicing salt (7% NaCl +$CaCl_2$ and NaCl +$MgCl_2$ at 25°C). After six months of exposure, they tested the specimens in uniaxial tension and reported a relatively higher strength loss in alkaline (~18%) and deicing salt (~17%) solutions compared to fresh water (4%), sea water (8%) and acidic (5%) solutions. In addition, they reported less degradation in Vinylester based rebars (~10%) in comparison to polyester based ones (~16%). They also

observed that the loss of strength in smaller rebars (~16%) were much higher than the larger diameter rebars (~9%). Meanwhile, they pointed out a limited change in tensile modulus of the FRP rebars as a result of the exposure. Their test results after 1 year of exposure, showed almost no degradation for carbon tendons. In case of the aramid tendons, excellent freeze-thaw and fresh water immersion durability was observed. The acidic solution had the most significant effect on aramid tendons and caused 8% drop in strength, while for the rest of the environments, an average of 5% loss in tensile strength was reported.

Pultruded Sections

Gomez[5] investigated freezes-thaw durability of Pultruded fiberglass composites. They considered two different pultruded laminates with polyester and vinylester matrix. They reported an average reduction in flexural properties of 26% and 20% for vinylester and polyester based laminates, respectively. The reduction in flexural properties of laminates only exposed to solution was 9% and 5% for the vinylester and polyester based laminates.

In another study by Bank[6], the accelerated aging of vinylester based glass pultruded rods was addressed. For specimens immersed in water, they reported flexural strength losses of 14% to 45% for the temperatures of 40°C to 80°C, respectively. In the case of alkaline solutions, only 30% ammonia solution appeared to have had a measurable effect on the properties. The humid environment did not affect the properties either.

Overwraps

Twelve different composite overwrap systems made with E-glass and carbon fiber in epoxy, polyester and vinylester matrices were considered by Steckel[7] in a durability study. The exposures included 100% relative humidity at 38°C, salt water, alkaline solution with pH of 9.5, temperature of 60°C and freeze-thaw cycles. Uniaxial tension tests were performed on 19 mm wide straight coupons with 5 cm long tab with a 7° taper. Short beam shear tests were conducted with a length/thickness ratio of 6~7. The specimens were tested after 3000 hours of exposure. Generally, most specimens showed very good durability in the environments tested. However, only one glass system showed significant reduction in tensile strength (15%) in 100% RH, and one carbon system showed large reduction in shear strength (25%~35%).

EXPERIMENTAL STUDY

In order to investigate the effects of environmental exposure on the mechanical properties of FRP laminates as prepared in a typical civil engineering application, uniaxial tension tests were performed. Composite laminates made from fabrics made of different materials with different weave patterns were tested after exposure to various simulated aggressive environments. Tensile properties such as ultimate strength, modulus of elasticity and ultimate strain were measured for each sample after specific exposure time. By comparing the mechanical properties of the exposed specimens to those for control specimens, the effect of different environments on the composite laminates made using wet-lay-up procedure (typically used in civil engineering applications) was determined.

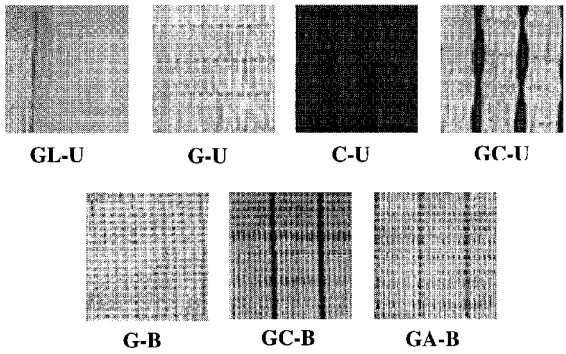


Figure 1: Different Types of Fabrics

Test Variables

The effects of several parameters on the durability of FRP laminates were examined. Nine simulated aggressive environments were considered: (1) Fresh water, (2) Saturated calcium hydroxide, $Ca(OH)_2$, solution (pH of 12.5), (3) Saturated $Ca(OH)_2$ solution (pH of 10.0), (4) Hydrochloric acid, HCl, solution (pH of 2.5), (5) Simulated seawater, (6) Moist alkaline soil with micro organisms, (7) Dry air at temperature of 60°C, (8) Air temperature of 50°C and relative humidity of 95%, and (9) Ultraviolet radiation. Seven different types of fabrics were used: (1) Unidirectional loose glass, GL-U, (2) Unidirectional glass, G-U, (3) Unidirectional carbon, C-U, (4) Unidirectional hybrid glass-carbon, GC-U, (5) Bidirectional glass, B-G, (6) Bidirectional hybrid glass-carbon, GC-B, and (7) Bidirectional hybrid glass-aramid, GA-B, as shown in Figure 1. For designation of different fabrics, letters G, C and A stood for E-glass, pan-based carbon and aramid while U and B represented unidirectional and bidirectional, respectively. The exposure time played an important role in the degradation process. Three different exposure times of 6000, 12000 and 20000 hours were considered.

Materials

Epoxy: A two-component epoxy was used as the matrix for preparing the coupons. The mixing ratio of the epoxy was two-part resin (bisphenal A based) to one-part hardener (polyamine based) by volume. It had a pot life of 45 minutes and full a cure time of 7 days at 25°C.

Fabrics: Seven different unidirectional and bidirectional fabrics were used in the study. The fabrics were made of E-glass, pan-based carbon, and aramid fibers. Three sticky string unidirectional fabrics were used. These included glass, carbon, and glass-carbon hybrid fabrics. Another unidirectional glass fabric with loose fibers sandwiched between two layers of mat was also used. The three-bidirectional fabrics included glass, glass-carbon hybrid, and glass-aramid hybrid. These fabrics were stitched to a glass mat on one side with a polyester thread. Various characteristics of these fabrics are listed in Table 1.

Environments

In order to expose the composite coupons to aggressive conditions similar to those in the civil engineering applications, nine different environments were simulated using

Table 1: Characteristic of Different Fabrics

Designation	Orientation	Fiber Type	Style	Weight (gr/m^2)	Glass Content (Vol.)	Glass Content (Wt.)
GL-U	Unidirectional	Glass	Loose Between Two Mats	650	1	1
G-U	Unidirectional	Glass	Sticky String	400	1	1
C-U	Unidirectional	Carbon	Sticky String	350	0	0
GC-U	Unidirectional	Glass / Carbon	Sticky String	950	0.82	0.87
G-B	Bidirectional	Glass	Stitched to Mat	350	1	1
GC-B	Bidirectional	Glass / Carbon	Stitched to Mat	700	0.88	0.91
GA-B	Bidirectional	Glass / Aramid	Stitched to Mat	600	0.94	0.96

Table 2: Properties of Aggressive Environments

Designation	Temperature	Humidity	pH	Remark	ASTM
W-S- ALK	Ambient	N/A	12.5		C 581
W-W-ALK	Ambient	N/A	10.0		C 581
W- NEUT	Ambient	N/A	7.0		C 581
W-S-ACID	Ambient	N/A	2.5		C 581
OCIEN	Ambient	N/A	7.25		D 1141
SOIL	Ambient	N/A	10.5	MC = 25 ~ 30 %	D 3083
HEAT-D	60°C	RH = 0 ~ 5 %	N/A		D3045
HEAT-M	50°C	RH = 95%	N/A		D 4585
UV-RAD-D	Ambient	RH = 5 ~ 10 %	N/A	UV-A (340 nm)	G 53
RH = Relative humidity; MC = Moisture Content; nm = 1×10^{-9} m					

chemical solutions following ASTM specification. These environments are listed in Table 2.

Solutions: Distilled water with neutral pH of 7 was used to simulate exposure to fresh water. Saturated calcium hydroxide, $Ca(OH)_2$, solutions with pH of 10 and 12.5 were used to simulate exposure to hydrating cement and other alkaline environments. The alkaline solutions were prepared by dissolving $Ca(OH)_2$ in distilled water until saturation. Then NaOH solution was added to control the pH as needed. Acidic solution was used to simulate exposure to low pH environments such as that encountered in sewer pips and wastewater treatment facilities. The solution was prepared by the addition of diluted hydrochloric acid, HCl, to distilled water until reaching the pH of 2.5. Substitute ocean water with pH of 7.25 was used to simulate exposure to marine environment. The major ingredients of this solution were NaCl (24.53 g/L), $MgCl_2$ (5.20 g/L), Na_2SO_4 (4.09 g/L), $CaCl_2$ (1.16 g/L), KCl (0.695 g/L) and $NaHCO_3$ (0.201 g/L). The pH of the solutions was monitored weekly with an electronic pH meter with a resolution of ±0.1. The adjustment to the solutions was made after ±0.2 deviations in pH. All solutions were replaced with new ones every two months to prevent contamination and change in their chemical composition.

Alkaline Soil: In order to simulate exposure to alkaline soil containing microorganism, compost soil was prepared using commercial potting soil and natural fertilizers. The moisture content of the mix was kept between 25 to 30 % (by weight) by adding water periodically. Lime was added to the soil to keep the alkalinity around pH of 10.5.

Cotton strips were used to monitor the biological activity in the mix. A 70% drop in the tensile strength of cotton strips in one week was an indication of satisfactory biological activities. Soil samples were replaced every month to insure the high level of biological activity.

Chambers: The effects of hot-dry and hot-moist climates were measured in two separate chambers. In the first chamber, the temperature was kept at 60°C with presence of minimal moisture. In the second chamber, the temperature was kept at 50°C with the relative humidity of 95%. The temperature was kept at ±1°C from the target value by using a heating element and a thermostat. The relative humidity was kept at ±2% by providing adequate evaporation surface for water containers in the chamber. In the third chamber, the effect of sunlight exposure was studied. A series of 15 Watt Black Light Fluorescent tubes were used to simulate ultraviolet radiation between 300 and 400 nm with a peak of 340 nm and intensity of 30×10^{-6} J/sec/cm^2. Tubes and specimens were 25 cm apart from each other. In all chambers, miniature fans were circulating air to achieve uniform environments.

Sample Preparation

Seven different types of FRP laminates were manufactured using the wet-lay-up technique without heat and pressure treatments. The laminates were 25 50 cm made of one layer of fabric. Fabrics, after saturation with epoxy, were placed between two layers of Mylar sheets. Excessive air bubbles were bled out of the laminate along with extra epoxy using a putty knife and a 12 cm wide roller. Laminates were then placed between two 2-mm thick glass plates on a level surface. The laminates were kept under 1 kPa pressure for 24 hours and then the Mylar sheets were peeled off. The laminates were kept inside the laboratory under ambient temperatures for 6 more days before being cut into strips with dimensions of 2.5 40 cm. The edges of the coupons were smoothened, using grid 100 sandpaper on a flat surface. The exact dimensions and weight of each coupon were measured using a caliper and a digital scale. The resolution of the caliper and scale were ±0.025 mm and ±0.01 gr, respectively.

Experimental Setup

Certain mechanical properties of the composite laminates were sensitive to their thicknesses. Considering the unavoidable variation in the thickness of the coupons made with this technique, twelve coupons were selected randomly as control specimens. The rest of the coupons were then placed in specified environments and their behaviors were monitored over time. A total of 9 coupons for each laminate were placed in each environment in order to be tested at three different times. For each laminate, twelve control specimens were kept inside the lab under ambient conditions and were tested with the first batch of exposed coupons after 6000 hours. Each set of exposed coupons were washed with fresh water and kept inside the laboratory under ambient condition for seven days to dry out, and then their weights were measured. The uniaxial tension tests were performed following ASTM D 3039 using an MTS-810 test machine and MTS-647 hydraulic wedge grips.

During previous experiments, SurfAlloy flat wedges had shown that they could yield desirable results without using tabs on the coupons for gripping purposes. This simplified the test setup considerably. The axial deformation was monitored using an MTS-632.12E-24 extensometer with a gage length of 25.4 mm and accuracy of 10

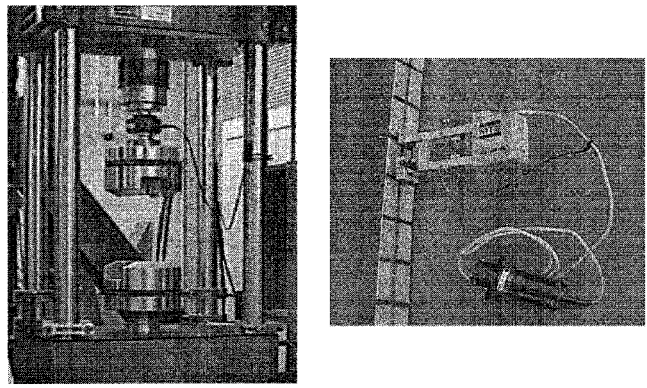


Figure 2: Universal Testing Machine and Extensometer Mounted on a Typical Specimen

microstrain as shown in Figure 2. The load was measured by an MTS-661.20E-03 load cell with a capacity of 100 kN. Displacement controlled loading was used with a rate of 0.025 mm/sec. The values of the load and strain were recorded every second and the data were analyzed using spreadsheet software.

EVALUATION AND ANALYSIS OF THE RESULTS

The first step in analyzing the result was establishing an average value for the tensile properties of the control specimens. Initially, twelve values for each laminate were averaged and considered as the control values. After conducting a correlation analysis, it was observed that the values for the ultimate strength and the modulus of elasticity had a strong correlation with the thickness of the laminates. Therefore, a different approach for these two parameters was considered. A linear regression between the values of these two parameters and the laminate thickness was performed. In these cases, linear control functions replaced the control values. A summary of the averages (AVR), coefficients of variation (COV), and coefficients of correlation (COC) is presented in Table 3.

Table 3: Statistical Characteristics of Control Specimens

Designation	Ultimate Strength (MPa)			Modulus of Elasticity (GPa)			Ultimate Strain (%)		Load / width (KN/cm)	
	AVG	COV	COC	AVG	COV	COC	AVG	COV	AVG	COV
GL-U	286.4	0.22	-0.65	18.9	0.05	-0.83	1.535	0.22	2.88	0.20
G-U	286.6	0.14	-0.72	20.3	0.08	-0.87	1.470	0.20	3.67	0.14
C-U	564.3	0.10	-0.63	56.1	0.07	-0.97	1.000	0.07	4.17	0.07
GC-U	317.0	0.16	-0.64	31.0	0.08	-0.78	1.030	0.19	4.13	0.18
G-B	125.6	0.07	-0.65	9.2	0.08	-0.77	1.432	0.11	0.95	0.08
GC-B	204.4	0.08	-0.80	16.6	0.09	-0.98	1.248	0.05	2.22	0.06
GA-B	168.8	0.10	-0.86	12.9	0.10	-0.98	1.355	0.07	1.82	0.07

AVG = Average Value; COV = Coefficient of Variation; COC = Coefficient of Correlation

After establishing the control values and functions for different laminates, testing of coupons with 6000, 12000 and 20000 hours of exposure began. Three coupons were tested for different environments, exposure times and composite types. The ultimate tensile strength, tensile strain and tensile modulus of elasticity were measured for each laminate. In order to simplify the analysis, all the values for exposed specimens were normalized with respect to their corresponding control values (without exposure). The results are presented in Figures 3 through 12. The change in weight of the laminates in different environments was obtained by subtracting the dry weight of each coupon from the weight after exposure. The weight change results are presented in Table 4.

Freshwater (pH of 7.0)

Freshwater with a neutral pH did not have any significant effect on the modulus of elasticity of the laminates. The ultimate strength of GL-U laminates decreased by 41%, 40% and 48% while the strain at failure dropped by 40%, 47% and 46% after 6000, 12000 and 20000 hours, respectively. The ultimate strength of G-U laminates reduced by 11%, 20% and 26% while the strain at failure declined by 19%, 37% and 32% after 6000, 12000 and 20000 hours, respectively. The ultimate strength of G-B laminates diminished by 23%, 28% and 22% while the strain at failure dropped by 28%, 31% and 35% after 6000, 12000 and 20000 hours, respectively. The ultimate strength of GA-B laminates degraded by 9%, 22% and 24% while the strain at failure fell by 6%, 26% and 27% after 6000, 12000 and 20000 hours, respectively. The carbon and glass-carbon laminates displayed insignificant decrease in their ultimate strength and strain at failure.

Alkaline Solutions (pH of 10.0 and 12.5)

Alkaline solutions did not affect the modulus of elasticity of the laminates. The effect of these solutions on the other tensile properties of carbon based laminates was also insignificant. However, glass based laminates lost significant portion of their tensile properties when subjected to alkaline solutions.

At pH of 10, the strength of GL-U laminates was decreased by 51%, 41% and 46% while the strain at failure dropped by 45%, 41% and 41% after 6000, 12000 and 20000 hours, respectively. The ultimate strength of G-U laminates reduced by 21%, 26% and 29% while the strain at failure declined by 32%, 42% and 38% after 6000, 12000 and 20000 hours, respectively. The ultimate strength of G-B laminates diminished by 18%, 29% and 31% while the strain at failure dropped by 26%, 33% and 30% after 6000, 12000 and 20000 hours, respectively. The ultimate strength of GA-B laminates degraded by 11%, 21% and 30% while the strain at failure fell by 3%, 14% and 29% after 6000, 12000 and 20000 hours, respectively.

At pH of 12.5, the strength of GL-U laminates decreased by 41%, 63% and 69% while the strain at failure dropped by 31%, 56% and 65% after 6000, 12000 and 20000 hours, respectively. The ultimate strength of G-U laminates dropped by 6%, 58% and 58% while the strain at failure declined by 18%, 53% and 61% after 6000, 12000 and 20000 hours, respectively. The ultimate strength of G-B laminates diminished by 17%, 36% and 44% while the strain at failure dropped by 19%, 44% and 46% after 6000, 12000 and 20000 hours, respectively. The ultimate strength of GA-B laminates degraded by 17%, 54% and 46% while the strain at failure fell by 10%, 38% and 44% after 6000, 12000 and 20000 hours, respectively.

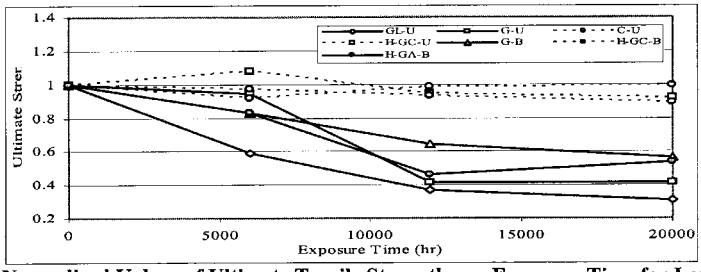


Figure 3: Normalized Values of Ultimate Tensile Strengths vs. Exposure Time for Laminates in Alkaline Solution (pH = 12.5)

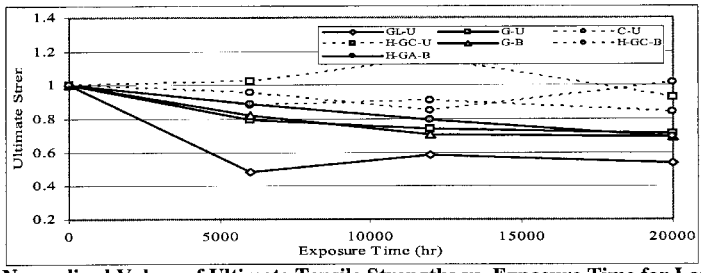


Figure 4: Normalized Values of Ultimate Tensile Strengths vs. Exposure Time for Laminates in Alkaline Solution (pH = 10.0)

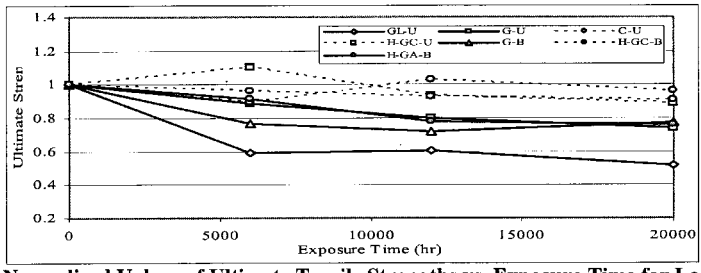


Figure 5: Normalized Values of Ultimate Tensile Strengths vs. Exposure Time for Laminates in Fresh Water Solution (pH = 7.0)

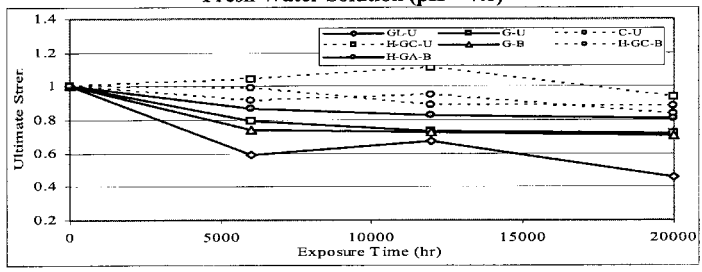


Figure 6: Normalized Values of Ultimate Tensile Strengths vs. Exposure Time for Laminates in Acidic Solution (pH = 2.5)

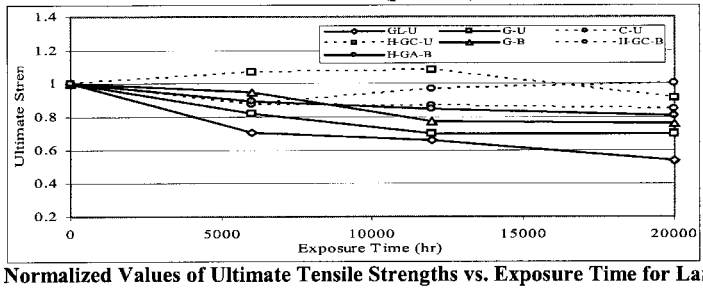


Figure 7: Normalized Values of Ultimate Tensile Strengths vs. Exposure Time for Laminates in Seawater Solution (pH = 7.25)

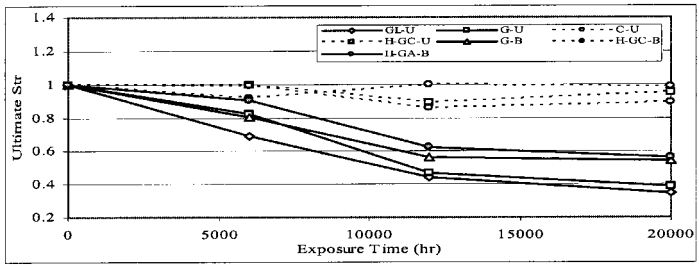


Figure 8: Normalized Values of Strain at Failure vs. Exposure Time for Laminates in Alkaline Solution (pH = 12.5)

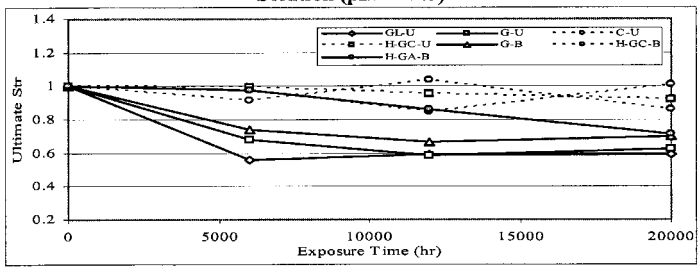


Figure 9: Normalized Values of Strain at Failure vs. Exposure Time for Laminates in Alkaline Solution (pH = 10.0)

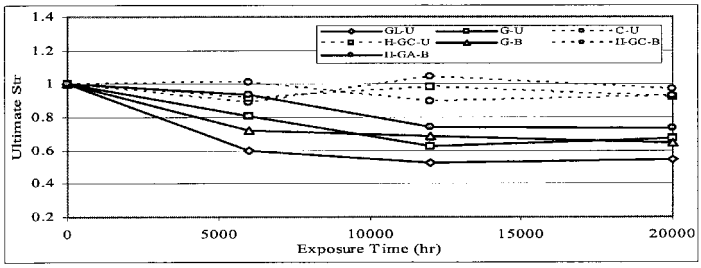


Figure 10: Normalized Values of Strain at Failure vs. Exposure Time for Laminates in Fresh Water Solution (pH = 7.0)

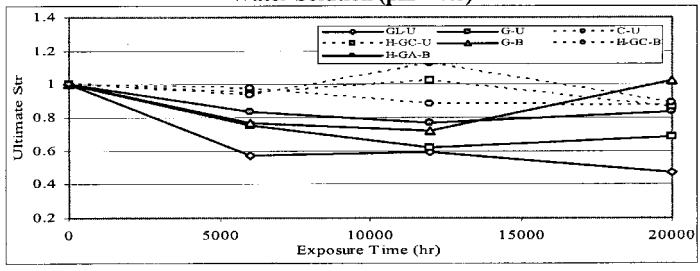


Figure 11: Normalized Values of Strain at Failure vs. Exposure Time for Laminates in Acidic Solution (pH = 2.5)

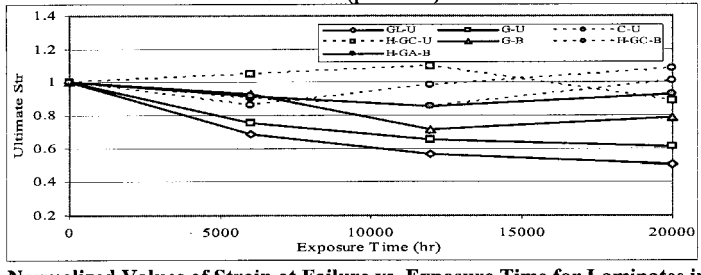


Figure 12: Normalized Values of Strain at Failure vs. Exposure Time for Laminates in Seawater Solution (pH = 7.25)

Acidic Solution (pH of 2.5)

Acidic solution did not affect the modulus of the elasticity of the laminates. The effect of this solution on the other tensile properties of carbon based laminates was insignificant. Exposed to the pH of 2.50, the strength of GL-U laminates decreased by 41%, 33% and 55% while the strain at failure dropped by 43%, 41% and 53% after 6000, 12000 and 20000 hours, respectively. The ultimate strength of G-U laminates reduced by 20%, 27% and 28% while the strain at failure declined by 25%, 38% and 31% after 6000, 12000 and 20000 hours, respectively. The ultimate strength of G-B laminates dropped by 26%, 27% and 29% while the strain at failure reduced by 23%, 28% and 27% after 6000, 12000 and 20000 hours, respectively. The ultimate strength of GA-B laminates degraded by 13%, 17% and 19% while the strain at failure fell by 17%, 23% and 17% after 6000, 12000 and 20000 hours, respectively.

Seawater (pH of 7.25)

Similar to the other solutions, seawater did not alter the modulus of elasticity of the laminates and its influence on the other tensile properties of the laminates containing carbon fibers was not significant. The strength of GL-U laminates decreased by 29%, 34% and 46% while the strain at failure dropped by 32%, 44% and 50% after 6000, 12000 and 20000 hours, respectively. The ultimate strength of G-U laminates reduced by 18%, 30% and 30% while the strain at failure declined by 25%, 35% and 39% after 6000, 12000 and 20000 hours, respectively. The ultimate strength of G-B laminates declined by 5%, 23% and 24% while the strain at failure dropped by 7%, 29% and 22% after 6000, 12000 and 20000 hours, respectively. The ultimate strength of GA-B laminates degraded by 11%, 15% and 7% while the strain at failure fell by 9%, 15% and 7% after 6000, 12000 and 20000 hours, respectively.

Moist Soil with Microorganism

All, but one laminate in this environment displayed minor changes in their tensile properties. The ultimate strength of GL-U laminates decreased by 18%, 19% and 14% while the strain at failure dropped by 26%, 29% and 25% after 6000, 12000 and 20000 hours, respectively.

Effect of Dry Heat (60°C)

When laminates were exposed to dry heat, their mechanical properties were affected by a smaller percentage compared to the other environments. The ultimate strength of G-U and G-B declined by 12% and 11% after 12000 hours of exposure, respectively. The strains at failure of GL-U, G-U and G-B declined by 6%, 18% and 16% after 12000 hours of exposure, respectively.

Heat and Moisture (50°C and 95%RH)

For the laminates exposed to heat and moisture, G-B and G-U laminates displayed the only apparent changes. The ultimate strength of G-U and G-B degraded by 16% and 15% after 20000 hours of exposure, respectively. The strain at failure of GL-U, G-U and G-B fell by 7%, 15% and 18% after 20000 hours of exposure, respectively.

Ultraviolet Radiation

Ultraviolet radiation did not cause any change in the values of the modulus of elasticity of the laminates similar to other environments. With regard to other tensile properties, the laminate did not degraded after exposure. In fact, some showed even a slight increase in their mechanical properties. The UV exposure seemed to help curing of the composites and resulted in improved properties.

Glass FRP

Loose glass fiber laminates, GL-U, showed the lowest durability in the solutions. With the exception of the modulus of elasticity that did not change, their other tensile properties showed continued degradation, especially in alkaline solutions. After 20000 hours of exposure, the ultimate strength and strain at failure decreased by 69% and 65% in strong alkaline solution, 55% and 53% in acidic solution, 48% and 46% in freshwater, 46% and 50% in seawater, and 46% and 41% in weak alkaline solution.

Bundled glass fiber laminates (unidirectional) performed better in the solutions compared to loose fibers. After 20000 hours of exposure, the ultimate strength and strain at failure, respectively, decreased by 58% and 61% in strong alkaline solution, 30% and 39% in seawater, 29% and 38% in weak alkaline solution, 28% and 31% in acidic solution, and 26% and 32% in freshwater.

Bundled glass fibers laminates (bidirectional) performed better in the solutions compared to the other two. After 20000 hours of exposure, their ultimate strength and strain at failure, respectively, decreased by 44% and 46% in strong alkaline solution, 31% and 30% in weak alkaline solution, 29% and 27% in acidic solution, 24% and 22% in seawater, and 22% and 35% in freshwater.

Carbon FRP

None of tensile properties of laminates made from carbon fibers was affected significantly even after 20000 hours of exposure in all of the environments. The exposure time did not show any significant effect on the properties. The normalized values of the properties were varying between 0.85 ~ 1.13.

Hybrid FRP

Glass-carbon laminates (Unidirectional and Bidirectional) showed excellent durability similar to carbon laminates. The exposure time did not show any significant effect on the properties. The normalized values of the properties were varying between 0.80 ~ 1.15. The glass-aramid laminates showed continued degradation with time. Except for their modulus that remained unchanged, the ultimate strength and strain at failure for these laminates, respectively, decreased by 46% and 44% in strong alkaline solution, 30% and 29% in weak alkaline solution, 24% and 26% in freshwater, 19% and 17% in acidic solution, and 19% and 7% in seawater.

Fiber Orientation of FRP

Comparison between the results of G-U and G-B laminates showed that unidirectional laminates had higher degradation of about 7% and 2% in ultimate strength, and 5% and

2% in strain at failure after 6000 and 12000 hours of exposure, respectively. The comparison between the results of GC-U and GC-B laminates showed higher degradation of about 13%, 14% and 10% in ultimate strength, and 6%, 8% and 3% in strain at failure for unidirectional laminates after 6000, 12000 and 20000 hours of exposure, respectively. This is due to the fact that in bidirectional fabrics, matrix dominates properties more than that in unidirectional fabrics. This further indicates that matrix materials are more affected by the environment than do fabrics.

Weight Change for FRP Laminates

The weight change of the laminates in different chambers was analyzed. The specimens exposed to UV radiation displayed an average weight loss of 0.42%, 0.52% and 0.50% after 6000, 12000 and 20000 hours of exposure, respectively. The exposed samples to the dry heat showed continuing weight loss for an average of 1.2%, 1.43% and 1.66% after 6000, 12000 and 20000 hours of exposure, respectively. Samples exposed to the moist heat displayed a lower weight loss of 1.22%, 1.42% and 1.45% after 6000, 12000 and 20000 hours of exposure, respectively due to partial moisture absorption. The samples buried under soil displayed a minimal weight loss of about 0.25%.

The weight changes of the laminate as a result of exposure to different solutions were also analyzed. The exposed specimens were weighted after air-drying in room temperature for 7 days. Specimens submerged in alkaline solution with pH of 12.5 displayed the highest weight loss of 0.26%, 0.76% and 0.78% after 6000, 12000 and 20000 hours of exposure. The alkaline solution with pH of 10.0 produced a weight loss of 0.41%, 0.59% and 0.50% after 6000, 12000 and 20000 hours of exposure, while the specimens in freshwater showed the least weight loss of 0.24%, 0.50% and 0.47% after 6000, 12000 and 20000 hours of exposure. Seawater and acidic solutions, respectively, caused a weight loss of 0.19%, 0.45% and 0.58%, and 0.20%, 0.40% and 0.54% after 6000, 12000 and 20000 hours of exposure.

Table 4: Weight Change of Laminates in Different Environments (%)

Designation	Exposure Time (hr)	W-S- ALK	W-W-ALK	W- NEUT	W-S-ACID	OCIEN	SOIL	HEAT-D	HEAT-M	UV-RAD-D
GL-U	20000	-1.10	-0.04	-0.73	-0.52	-0.24	0.00	-1.42	-1.21	-0.62
	12000	-1.06	-0.71	-1.87	-0.29	-0.33	-0.40	-1.24	-1.48	-0.46
	6000	-0.65	-0.46	-0.18	-0.28	-0.33	-0.30	-1.16	-1.46	-0.62
G-U	20000	-0.40	-0.72	0.28	-0.54	-0.07	0.47	-1.14	-0.97	-0.42
	12000	-0.59	-0.07	0.03	-0.17	-0.18	-0.06	-1.22	-0.70	-0.19
	6000	-0.22	-0.25	-0.09	-0.10	-0.02	0.00	-0.97	-0.76	-0.29
C-U	20000	-0.65	-0.71	-1.32	-0.44	-1.22	-0.64	-2.30	-1.61	-0.39
	12000	-0.97	-0.71	-0.25	-0.62	-0.86	-1.09	-2.04	-2.30	-0.92
	6000	-0.57	-0.39	-0.52	-0.21	-0.50	-0.40	-1.58	-1.61	-0.52
GC-U	20000	-0.03	0.32	-0.07	-0.23	-0.10	0.28	-1.50	-1.23	-0.46
	12000	-0.14	-0.07	-0.23	-0.33	0.03	-0.06	-0.91	-1.07	-0.44
	6000	0.70	0.09	-0.14	0.06	0.62	0.32	-1.02	-0.95	-0.23
G-B	20000	-1.12	-0.47	-0.41	-0.79	-1.07	-0.33	-1.77	-1.30	-0.62
	12000	-0.49	-0.62	-0.07	-0.41	-0.73	-0.46	-1.59	-1.62	-0.80
	6000	-0.23	-0.55	-0.23	-0.18	-0.67	-0.27	-1.14	-1.38	-0.68
GC-B	20000	-1.24	-0.95	-0.47	-0.63	-0.58	-0.60	-1.94	-1.51	-0.42
	12000	-1.14	-0.92	-0.64	-0.30	-0.57	-0.64	-1.59	-1.45	-0.39
	6000	-0.50	-0.61	-0.43	-0.68	-0.25	-0.37	-1.15	-1.30	-0.24
GA-B	20000	-0.90	-0.92	-0.58	-0.63	-0.77	-0.66	-1.58	-2.30	-0.58
	12000	-0.92	-1.03	-0.50	-0.68	-0.54	-0.77	-1.42	-1.34	-0.44
	6000	-0.37	-0.69	-0.12	0.00	-0.18	-0.32	-1.41	-1.10	-0.35

CONCLUSIONS

The effects of different aggressive environments on tensile properties of seven different FRP laminates were investigated. FRP coupons were immersed in five different solutions and kept in four different chambers, which simulated typical harsh environments encountered in the field. Following the analysis of the results from the experiments, these conclusions are arrived at:

1. FRP laminates have excellent durability when they are exposed to hot and humid weather, ultraviolet radiation or moist and biologically active alkaline soil. After more than 27 months of exposure, the mechanical properties of most laminates in tension were minimally affected by these environments.
2. Laminates that are made from, or contain carbon fibers have superb durability and remain completely unaffected even after a long period of exposure to solutions with a variety of pHs and ionic compounds.
3. Glass fiber reinforced plastic laminates are most vulnerable to immersion in solutions. High alkaline solution has the most effect on the laminates. Laminates made of glass fibers are not recommended for application exposed to aggressive solutions, especially the composites made with loose glass fibers.
4. The findings of this study show that unidirectional laminates tend to degrade at a slightly lower rate than bidirectional fabrics do. This is due to more matrix dominance in the bidirectional fabrics.

REFERENCES

[1] Shen, C. and Springer, G. "Environmental Effect on the Elastic Moduli of Composite Materials." *Journal of Composite Materials*. (1977) Vol. 11, July, pp. 250-264

[2] Springer, G., Sanders, B. and Tung, R. "Environmental Effect on Glass Fiber Reinforced Polyester and Vinylester Composites" *Environmental Effects on Composite Materials*, Technomic Publishing company, Inc., Westport, CT. (1981) pp. 126-144

[3] Falabella, R., Neuner, J. and Isley, F. "Environmental Durability and Resin Stoichiometry Studies of TYFO-S High Strength Column Wrapping System" *Report LSR 932822*, Hexcel Corp., Pleasanton, California. (1993)

[4] Tannous, F. and Saadatmanesh, H. "Environmental Effects on the Mechanical Properties of E-glass FRP Rebars" *ACI Material Journals*. (1998) V. 95, No. 2, March-April

[5] Gomez, J. and Casto, B. "Freeze-thaw durability of Composite Materials." *The First International Conference on Composites in Infrastructures*, Tucson, Arizona. (1996) pp. 947-955

[6] Bank, L., Gentry, T., Barakatt, A., Prian, L., Wang, F. and Mangla, S. "Accelerated Aging of Pultruded Glass/Vinylester Rods." *The Second International Conference on Composites in Infrastructures*, Tucson, Arizona. (1998) Vol. 2, pp. 423-437

[7] Steckel, G., Hawkins, G. and Bauer, J. "Environmental Durability of Composites for Seismic Retrofit of Bridge Columns." *The Second International Conference on Composites in Infrastructures*, Tucson, Arizona. (1998) Vol. 2, pp. 460-475

BEHAVIOUR OF FRP-CONFINED CONCRETE STUB COLUMNS UNDER LONG-TERM SUSTAINED LOADS

Qing Yu, Lin-Hai Han and Zheng Zhang
College of Civil Engineering & Architecture, Fuzhou University, Gongye Road 523, Fuzhou, Fujian Province, 350002, P. R. China

A series of tests on the behaviour of FRP-confined concrete stub columns under long-term sustained loading, in addition to providing further tests on the static ultimate strength of the composite columns are performed. The main parameters varied in the tests are: (1) the level of long-term sustained load level, and (2) FRP ratio. After observing the measured data of the axial strain due to long-term sustained load effects in the current tests, it was found that after about 130 days, the process tends to stabilize. Generally, creep effects reduce the ultimate axial strain of the FRP-confined concrete stub columns, while the ultimate strength is not significantly altered. The current tests show that, in general, the current ACI 209R-92 (1992) slightly overestimates the long-term strain of the FRP-confined concrete stub columns.

INTRODUCTION

The use of FRP (fiber reinforced polymer)-confined concrete columns has become widespread in the past decade (ACI Committee 440, 2000; Teng, et al., 2001). FRP-confined concrete columns subjected to service loads, in a building will suffer from the effects of creep and shrinkage of the concrete. In the past, the behaviour of FRP-confined concrete columns under short-term loading has been the subject of many investigations. However, it appears that attention has seldom been given to the influence of long-term sustained load on the behaviour of such columns. This may be attributed to the fact that, except for exceptional cases, the structural strength is not compromised by the creep phenomenon.

The only experimental observation of time-dependent behaviour of FRP-confined concrete columns was reported by Nagib and Mirmiran(2002). They found the shrinkage of the CFFT (concrete-filled FRP tube) columns to be quite negligible. Lateral confinement provided by FRP tube places the core concrete in a tri-axial state of stress, resulting in less creep. In their tests, the maximum level of long-term sustained load was about 30% of the ultimate capacity. The lack of information on behaviour of FRP-confined concrete columns under sustained loads indicates a need for further research in this area.

The main objectives of this study were twofold: first, to report a series of tests on the behaviour of FRP-confined concrete stub columns under long-term sustained loading, in addition, to providing further tests on the static ultimate strength of the composite columns. Secondly, to analyze the effects of ageing at specific loading (τ_0), time under sustained loading (t), of the level of sustained load (long-term sustained load level, n), of the FRP ratio ($\alpha_f = A_f / A_c$, where A_f and A_c are the FRP sheet and the concrete core cross-sectional area respectively), and of the strength of the materials on the long-term creep and shrinkage strains of the column.

EXPERIMENTAL PROGRAM

Specimens preparations

A total of twelve 100 × 200 mm FRP-confined concrete cylindrical specimens were tested. The main parameters varied in the tests are: (1) long-term sustained load level (n), from 0.3 to 0.6, and (2) FRP ratio (α_f), from 0.44% to 0.89%. A summary of the specimens is presented in Table 1. The long-term load level n is defined as followings:

$$n = N_L / (f'_{ccS} \cdot A_c) \quad (1)$$

where f'_{ccS} is the ultimate stress of FRP-confined concrete column subjected to short-term loading, the value of f'_{ccS} was determined according to the tests of the FRP-confined concrete specimens at the day of long-term sustained loads were applied.

1 Summary of Test Information

No.	Specimen	t_f (mm)	α_f (%)	Sustaining Load N_L (kN)	Sustaining load level n	$f'_{cc,ue}$ (MPa) Measured	Average	SI	ε_{ue} (με) Measured	Average	DI
1	L1-0.3-1	0.111	0.44	100	0.3	48.4	49.9	0.940	2365	2551	0.920
2	L1-0.3-2	0.111	0.44	100	0.3	51.4			2737		
3	L1-0.6-1	0.111	0.44	200	0.6	52.6	54.7	1.030	2425	2510	0.905
4	L1-0.6-2	0.111	0.44	200	0.6	56.8			2595		
5	S1-1	0.111	0.44	—	0	51.9	53.1	1	2538	2773.5	1
6	S1-2	0.111	0.44	—	0	54.2			3009		
7	L2-0.3-1	0.222	0.89	150	0.3	62.4	65.1	0.997	3715	4002	0.775
8	L2-0.3-2	0.222	0.89	150	0.3	67.7			4289		
9	L2-0.6-1	0.222	0.89	300	0.6	62.6	64.1	0.985	2528	2637.5	0.511
10	L2-0.6-2	0.222	0.89	300	0.6	66			2747		
11	S2-1	0.222	0.89	—	0	65.6	65.3	1	4920	5162.5	1
12	S2-2	0.222	0.89	—	0	64.9			5405		

Material properties

The number of ply sheets used is 1 and 2. The number of stub nominally identical column specimens for testing is 2 for each configuration/type. The wrap for the specimens was made from one or two 0.111mm layers of carbon fibers (vertical and horizontal, i.e. the same fibre volumn in the axial and longitudinal directions) with epoxy resin. The tensile properties of the FRP laminate and its constituents are shown in Table 2.

2 Properties of FRP Wrap

Materials	Tensile strength (MPa)	Tensile modulus of elasticity(MPa)	Thickness per layer(mm)
Carbon fibers*	3500	235000	0.111
Epoxy resin*	72	3165	--
FRP laminate	1430.7	118000	0.111

* As provided by manufacturer

The epoxy system consists of two parts, resin and hardener, mixed in the ratio of 2:1. The epoxy system was thoroughly hand-mixed for at least 6 min. The concrete cylinders

were cleaned and completely dried before the epoxy was applied. A thin layer of epoxy ($250g/m^2$) was applied to the concrete cylinder. A FRP ply sheet was then applied directly on the surface. Special attention was taken to insure that there were no voids between the FRP sheet and the concrete cylinder surface. After the application of the first lap of the FRP sheet, a second layer of epoxy was applied on the surface of the first layer to allow the impregnation of the second lap of the FRP sheet. Finally, an additional epoxy layer was applied on the surface of the wrapped concrete cylinder. In all cases, the outside layer was extended by an overlap of 100mm to insure the development of full composite strength.

All specimens were left at room temperature for ten days before testing. This was done to insure that enough time had passed for the epoxy system to cure.

To determine the FRP sheet material properties, four tension coupons were cut from a randomly selected FRP sheet. From these tests, the average ultimate strength (f_f) was found to be 1430.7 MPa, the modulus of elasticity was 118×10^3 MPa, and the ultimate strain was 0.011917. The concrete compressive cube strength (f_{cu}) and cylinder strength ($f_c^{'}$) at 28 days were found to be 36MPa and 27MPa respectively. The modulus of elasticity (E_c) of concrete was found to be 32800 MPa. For each concrete mix batch used, three 150mm cubes were also cast and cured in conditions similar to the related specimens. The mix proportions were: cement: 440 kg/m^3; water: 198 kg/m^3; sand: 528 kg/m^3 and coarse aggregate: 1234 kg/m^3. In all the concrete mixes, the fine aggregate used was silica-based sand, the coarse aggregate was carbonate stone. No additives were used in any of the mixes.

The experimental program consisted of two phases, which are described below and designated as long-term service tests, static load versus deformation and ultimate load tests.

Long-term service load tests

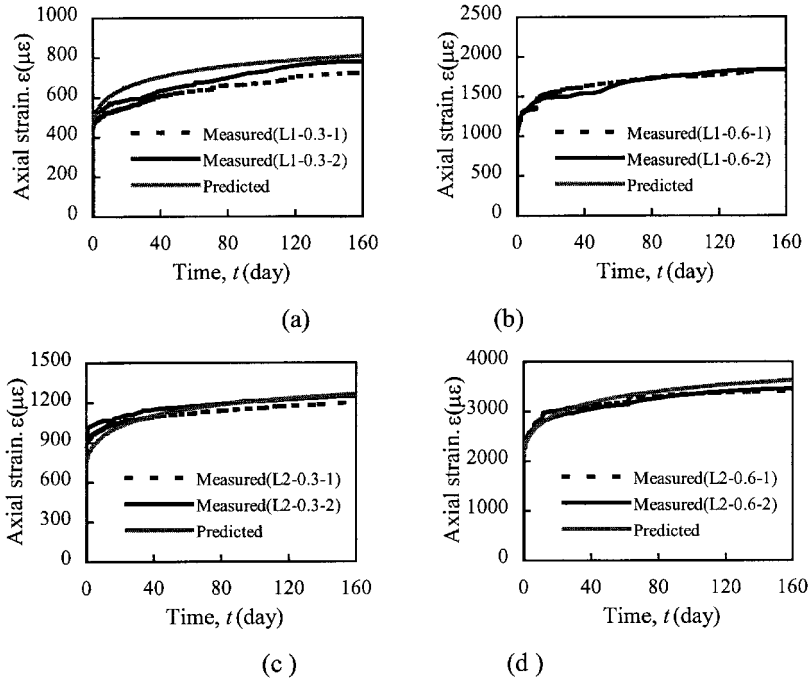
The concrete specimens were placed upright to air-dry until testing. The long-term service load tests were carried out as soon as the age of 180 days after concrete casting was reached. The concrete compressive cube strength (f_{cu}) and cylinder strength ($f_c^{'}$) at that day were found to be 48.3 MPa and 39.6 MPa respectively. The modulus of elasticity (E_c) of concrete was found to be 38630 MPa. The top surfaces of the concrete cylinders were ground smooth and flat using a grinding wheel with diamond cutters. This was to ensure that the load was applied evenly across the cross-section.

The long-term sustained load (N_L) was applied by pre-stressing bars and controlled by means of a load cell. The load was kept constant with adjustments of these bars during the measurement. Eight strain gauges were used for each specimen to measure the longitudinal and transverse strains at the middle height. Two displacement transducers were used to measure the axial deformation. Each displacement transducer was attached with two rigid anchors, the two anchors with distance of 150 mm, were anchored into the column body vertically to the cylinder surface. The values of the sustained loads as well as the long-term sustained load level (n) are shown in Table 1.

The experiment was carried out in a laboratory where the temperature and humidity are almost constant during the whole year, so that the influence of temperature gradient could be kept to minimum values.

Strain measurements were obtained in the central part of the column for the FRP sheet. The long-term service load was sustained for 160 days. After observing the measured data of the axial strain (ε), for about 130 days, it was found that, the process

tends to stabilize. This time is slightly longer than that of HSS (hollow structural steel) columns filled with concrete subjected to long-term sustained loads (Han, et al, 2001; Han and Yang, 2003). Fig.1 shows the tested time-history of the axial strain (ε).



1 Tested time-history of the axial strain (ε).

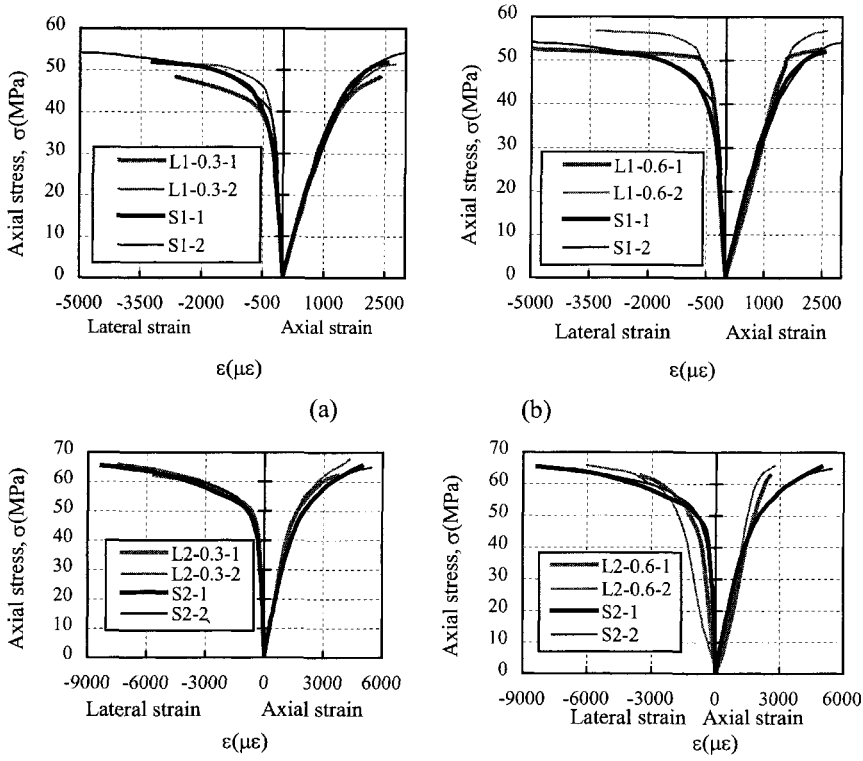
Static load versus deformation and ultimate load tests

At the completion of the long-term service load tests, all the specimens were removed from the creep-loading devices and tested to failure in a compression-testing device. In addition to this, specimens without long-term service load applied were also tested at the same time, with the aim of making comparisons.

The concrete compressive cube strength (f_{cu}) and cylinder strength ($f_c^{'}$) at the day of load versus deformation and ultimate load tests (368 days) were found to be 49.1 MPa and 40.8 MPa respectively.

All of the specimens were tested in pure compression. The tests were performed on a 2000 kN capacity testing machine. Eight strain gauges were used for each specimen to measure the longitudinal and transverse strains at the middle height. The displacement transducers were used to measure the axial deformation.

It was found that patches could be seen near the middle-height of the stub columns at about 80-90% of the ultimate load, an indication that resin has yielded, leaving only the fibers to take the hoop tension. Failure is by fracture of the FRP in the circumferential direction. Upon fracture of the casting, the concrete core crushes and sheds its compressive load. Confining by FRP not only increases the stub concrete column strength, but also enhances the ductility. Total of the tested curves of axial stress ($\sigma = N/A_c$, where is N the axial load) versus the axial strain and the lateral strain (ε) are shown in Fig. 2.



2 Tested axial load (N) versus axial strain (ε) relations

The measureed ultimate stress ($f'_{cc,ue}$), as well as their corresponding strain (ε_{ue}) of the tested specimens is summarized in Table 1.

ANALYSIS OF TEST RESULTS AND DISCUSSIONS

Based on the test results, influence of the long-term sustained load level (n) and the FRP ratio (α_f) on the behaviour of the FRP-confined columns is discussed.

Influence on Strength Index (SI)

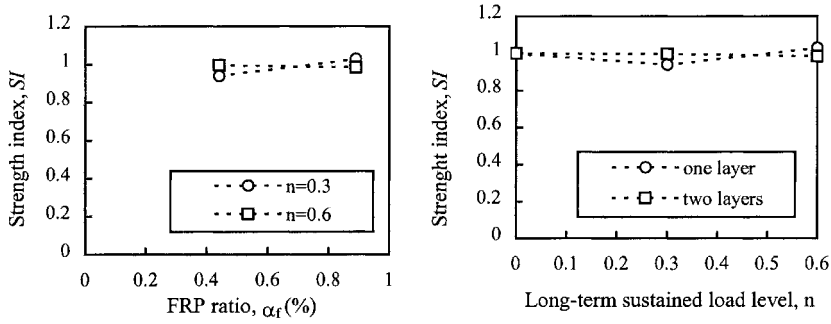
For convenience of analysis, strength index (SI) is defined to quantify the influence of long-term sustained load on the strength of the composite columns. It is expressed as:

$$SI = \frac{f'_{ccL}}{f'_{ccS}} \tag{2}$$

where f'_{ccL} and f'_{ccS} is the measured ultimate strength of specimens with or without long-term sustained loads respectively.

The strength index (SI) so determined is shown in Table 1 and in Fig.3 respectively. Results in Table 1 and in Fig.3 clearly show that both the long-term sustained load level (n) and the FRP ratio (α_f) have moderate influence on the strength index (SI) of the composite columns. It also can be seen from Table 1 that, in general, the ultimate

strength of the FRP-confined concrete stub columns is not significantly reduced due to long-term sustained load effects.



(a) FRP ratio (α_f) (b) Long-term sustained load level (n)

3 Influences of different parameters on strength index (SI)

Influence on Deformation Index (DI)

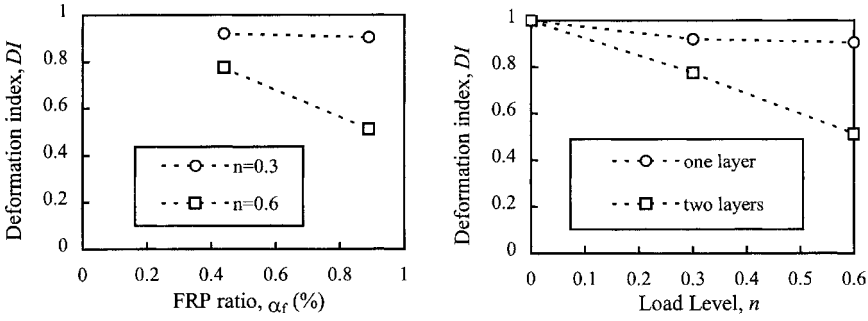
Deformation index (DI) is defined to quantify the influence of long-term sustained load on the deformation properties of the composite columns. It is expressed as:

$$DI = \frac{\varepsilon_{ueL}}{\varepsilon_{ueS}} \tag{3}$$

where ε_{ueL} and ε_{ueS} is the measured ultimate axial strain of specimens with or without long-term sustained loads, respectively.

The deformation index (DI) so determined is listed in Table 1. Results in this table clearly show that both the long-term sustained load level (n) and the FRP ratio (α_f) have influence on the deformation index (DI) of the composite columns.

The deformation index (DI) is plotted in Fig.4(a) against the FRP ratio (α_f), and in Fig.4 (b) against the long-term sustained load ratio (n). It can be seen from Fig. 4 that generally, the deformation index (DI) decreases with the increase of α_f and n.



(a) FRP ratio (α_f) (b) Long-term sustained load level (n)

4 Influences of different parameters on deformation index (DI)

It also can be seen from Table 1 that generally, long-term sustained load effects reduce the ultimate axial strain of the FRP-confined concrete stub columns. A careful examination of the test results revealed that the ultimate strain of the specimens without

applied long-term sustained loads, is about 8% to 49% higher than that of the specimens with applied long-term sustained loads.

Analytical Modeling

The main results, which were determined from the long-term tests, include both creep and shrinkage strain [$\varepsilon_{cr}(t)$ and $\varepsilon_{sh}(t)$]. The total strain (ε_o) was measured in the loaded specimens, and this is comprised of three components, which are highlighted in Equation (4).

$$\varepsilon_o(t) = \varepsilon_{elastic}(t) + \varepsilon_{cr}(t) + \varepsilon_{sh}(t) \tag{4}$$

The creep strain [$\varepsilon_{cr}(t)$] can be expressed as:

$$\varepsilon_{cr}(t) = \varepsilon_{elastic} \cdot \varphi(t, \tau_0) \tag{5}$$

in which $\varepsilon_{elastic}$ is the elastic component of strain of the specimens subjected to the load of N_L, and can be determined by using the model introduced in Samaan, et al.(1998).

The creep fuction and shrinkage law recommended by ACI 209R-92 (ACI Committee 209,1992) are calibrated herein with the test data with good agreement. The models express both the creep coefficient [$\varphi(t,\tau_0)$]and shrinkage strain [$(\varepsilon_{sh})_t$] as a function of time (t) given as follwings:

$$\varphi(t,\tau_0) = [\frac{(t-\tau_0)^{0.6}}{10+(t-\tau_0)^{0.6}}] \cdot \varphi_{max}(\tau_0) \tag{6}$$

where $\varphi_{max}(\tau_0)$represents the ultimate creep coefficient, its average value is given as 2.35(ACI Committee 209,1992). $\varphi_{max}(\tau_0)$ can be taken as 2.35 by several correction factors for different member sizes, environmental conditions and etc. Applying all necessary correction factors for the current tested specimens, leads to an ultimate creep coefficient of 0.7.

$$(\varepsilon_{sh})_t = (\frac{t}{35+t}) \cdot (\varepsilon_{sh})_{max} \tag{7}$$

where $(\varepsilon_{sh})_{max}$ represents the ultimate shrinkage strain(ACI Committee 209,1992), which is taken as $780\,\mu\varepsilon$ by several correction factors for different member sizes, environmental conditions and etc. Applying all necessary correction factors for the current tested specimens, leads to an ultimate shrinkage strain of $31.4\,\mu\varepsilon$.

The average strains determined from the test program are compared with those obtained from the predictive model. Fig.1 shows the comparisons of the time-history of axial strain (ε) for the current tests. Generally, a good agreement is obtained between the predicted and tested curves. However, the current by ACI 209R-92 (ACI Committee 209,1992) do slightly overestimate the creep of FRP-confined concrete columns.

Based on the theoretical model mentioned above, a parametric analysis was performed. The effects of the changing age time at loading (τ_0), time under sustained loading (t), level of sustained load (long-term sustained load ratio n), the FRP ratio (α_f), and strength of the materials on the long-term strain ε_L ($\varepsilon_{cr}+\varepsilon_{sh}$, creep component and shrinkage component of strain respectively) due to creep and shrinkage of the axially loaded column are analyzed.

The analytical results show that the strain of ε_L decreases as the time immediately after loading (τ_0) increases. ε_L increases as the time under sustained loading (t), the long-term load level (n), the strength of FRP (f_f), the FRP sheet ratio (α_f), and the

strength of concrete ($f_c^{'}$) increase.

CONCLUSIONS

The following conclusions can be made based on the limited research reported in the paper.

(1) After observing the measured data of the axial strain due to long-term sustained load effects in the current tests, it was found that after about 130 days, the process tends to stabilize.

(2) The ultimate strength of the FRP-confined concrete stub columns is not significantly altered due to long-term sustained load effects.

(3) Long-term sustained load effects reduce the ultimate axial strain of the FRP-confined concrete stub columns. The test results revealed that the ultimate axial strain of the specimens with applied long-term sustained loads, are about 8% to 49% lower than those of the specimens without applied long-term sustained loads. The reduction increases with the increases of the FRP ratio (α_f) and the long-term sustained load level (n).

(4) The current tests shown that, in general, the current ACI 209R-92 (ACI Committee 209,1992) slightly overestimates the long-term strain of the FRP-confined concrete stub columns.

ACKNOWLEDGEMENTS

The research work reported herein were made possible by the Fujian Province Educational Fund (JB01012), the financial support is highly appreciated.

REFERENCES

1 ACI Committee 209,'Prediction of Creep□Shrinkage and Temperature Effects in Concrete Structures (ACI 209R-92)'□ American Concrete Institute, Farmington Hills, Mich., USA□1992.

2 ACI Committee 440 ,'Guide for the Design and Construction of Externally Bonded FRP Systems for Strengthening Concrete Structures'□ American Concrete Institute, Detroit, Michigan, USA□2000.

3 J G Teng, J F Chen, S T Smith and L Lam, FRP strengthened RC Structures, John Wiley & sons, LTD Press, 2001

4 W Nagib and A Mirmiran,'Time-dependent behaviour of FRP-confined concrete columns'□ ACI Structural Journal, 2002 99(2) 142–148.

5 L H Han, Z Tao and W Liu, 'Concrete-Filled SHS Columns Subjected to Long-Term Loads'□ Proceedings of The First International Conference on Steel and Composite Structures, Pusan, Korea, 2001 1733-1740.

6 L H Han and Y F Yang, 'Analysis of thin-walled steel RHS columns filled with concrete under long-term sustained loads'□ Thin Walled Structures, 2003 41(9) 849-870.

7 M Samaan, A Mirmiran, and M Shahawy, 'Model of Concrete Confined by Fiber Composites'□ Journal of Structural Engineering, 1998 124(9) 1025-1031.

FATIGUE BEHAVIOR OF DOUBLE-LAP JOINTS FROM PULTRUDED GFRP LAMINATES

Aixi Zhou, Tommaso Tirelli and Thomas Keller

Composite Construction Laboratory (CCLab), Swiss Federal Institute of Technology CH-1015 Lausanne, Switzerland

ABSTRACT

This paper investigates the fatigue characteristics of adhesively bonded double-lap joints (DLJs) from pultruded Glass Fiber Reinforced Polymer (GFRP) laminates. Experiments were conducted under room temperature and humidity environment. Results showed that the fracture of the DLJs was in brittle manner. Cracks initiated from the fillets of the joints and then propagated into the GFRP laminates. The failure of the joints was interlaminar failure in the GFRP adherends where fiber mats locate. No cohesion failure and adhesion failure were observed. Experiments showed a fatigue limit of about 25% of the static failure load after 10 million cycles. A 2MPa average shear resistance can be achieved under the fatigue limit, which provides a safety factor of 8-13 for practical design of bonded GFRP joints.

INTRODUCTION

Due to the advantages of lightweight, ease of installation, low maintenance, and long lifetime, and the growth in research and demonstration projects around the world, FRP composites are finding wider acceptance in the characteristically conservative infrastructure construction industry. Since the early 1990s, the use of pultruded GFRP structural shapes for building and bridge applications has increased significantly. As pultruded GFRP profiles become more and more widely used in civil infrastructure, the need for efficient and reliable load-carrying joints that can endure long-term fatigue loadings and environmental attacks has become apparent.

Mechanical fastening (bolting), adhesive bonding and the combination of fastening and bonding have been used for FRP composite connections. Each method has its advantages and disadvantages. However, adhesive bonding is the easiest for a permanent joint. Bonded joints using high strength adhesives are excellently suitable to pultruded GFRP composites due to the composites' brittleness and anisotropic behavior. Since no cutouts are required in a bonded joint, the reinforcing fibers remain continuous, stress concentrations are reduced, and a refined joint geometry is obtained. Therefore, a bonded connection possesses better fatigue and durability performance. Bonded connections reduce production costs due to the simplification of joining. Bonded connections are lightweight compared to fastened joints, which is important for developing advanced lightweight composite structures. Joining via adhesive bonding has shown to be successful for connecting FRP composites in aerospace/aircraft and automobile structures due to numerous research efforts in these fields. In civil infrastructure, adhesive bonding has been used in developing lightweight FRP bridge and building structures.

Fatigue has been a critical issue in developing bonded composite joints. The degradation of highway bridges, buildings, and other civil structures is always associated with fatigue loadings, i.e., cyclic and dynamic loading. The ratio of live load to dead load is the main concern in fatigue resistance of structures. This becomes more prominent for lightweight FRP composite structures. This brings into questions concerning the fatigue performance of the adhesive-bonded FRP composite systems, in particular the fatigue performance of their connections. The fatigue behavior of bonded FRP composite joints is influenced by many factors, such as adhesives, FRP adherends, joint geometries, environmental conditions, loadings, and the quality of the fabrication process etc. Considerable experimental and analytical research has been conducted to investigate the fatigue performance of adhesively bonded composite joints for aerospace/aircraft and automobile applications. Bonded connections for civil infrastructure have essential differences compared to aerospace/aircraft and automobile applications: bonding geometries, the types of materials and fabrication processes, loadings, and environmental conditions. Therefore, it is impossible to directly compare and transfer research results among these different areas.

Efforts have been dedicated to studying the fatigue behavior of connected GFRP pultruded members [3,7], in which the fatigue of bolted joints, bonded joints and the combined bolted/bonded joints was studied without considering environmental effects. Comparisons of the performance of bolted connections and bonded/bolted connections showed that a bonded/bolted configuration was better than a bolted configuration for GFRP connections [7]. It was suggested that, as a safety measure, supplementary bolting should be considered for bonded connections [3]. However, stress concentrations at holes of bolted GFRP pultrusions could be as much as eight times the average net section stress [3]. Apparently, a lack of confidence in the fatigue performance of adhesive-bonded joints from pultruded GFRP composites has limited their wide applications in civil infrastructure.

This research attempts to understand the fatigue performance of bonded GFRP pultrusions through coupon level experiments. To achieve this goal, a series of double-lap joints (DLJs) were prepared and tested under quasi-static and fatigue loadings. The DLJs were chosen due to their ease of manufacture, geometrical symmetry, and a reduction of eccentricities. The strength and failure of the double-lap joints under quasi-static loadings were investigated and used as reference values for fatigue study. Then the fatigue behavior of the double-lap joints was investigated. Though there is no standard for fatigue testing of bonded DLJs from pultruded GFRP laminates, the ASTM standard D3479/D3479M-96[1] was referred in the fatigue testing program.

EXPERIMENTAL DETAILS

Materials and preparation of specimens

Two sets of pultruded GFRP laminates were used in this study: 5mm thick laminates and 10mm thick laminates. The 10mm thick laminates were put inside of the DLJ while the 5mm thick laminates were put as outside adherends. The in-plane dimensions of the laminates are the same for both sets: 500mm in length and 100mm in width. A plot of the DJL specimens is shown in Figure 1. The dimensions were chosen to investigate the fatigue behavior of typical joint sizes in civil infrastructure.

The pultruded GFRP laminates have E-glass fibers in form of roving bundles used as reinforcements in the middle. The direction of the roving fibers runs in the

pultrusion direction. Additional glass fiber mats are used as the outside layers for shear resistance and corrosion protection. The combined mats consist of chopped strand mats (CSM) as well as woven mats (0°/90°). The CSM and woven mats are stitched together to form a mat layer. Four mat layers are used in the 10mm laminates with two layers on the top and two layers on the bottom, as shown in Figure2(a), while two mat layers are used in the 5mm laminates with one layer on the top and one layer on the bottom. A polyester surface veil is added for protection and surface finishing. The average fiber volume fraction of the GFRP laminates is about 46.5%, which was obtained from burn-off tests at 450°C [6]. The glass fibers are embedded in an isophthalic polyester resin.

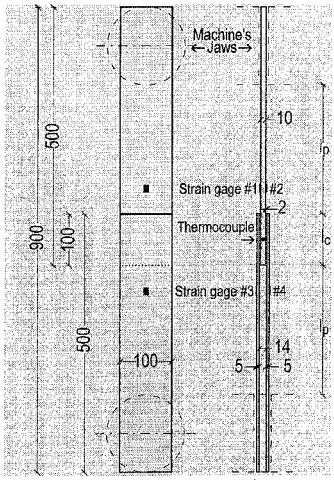
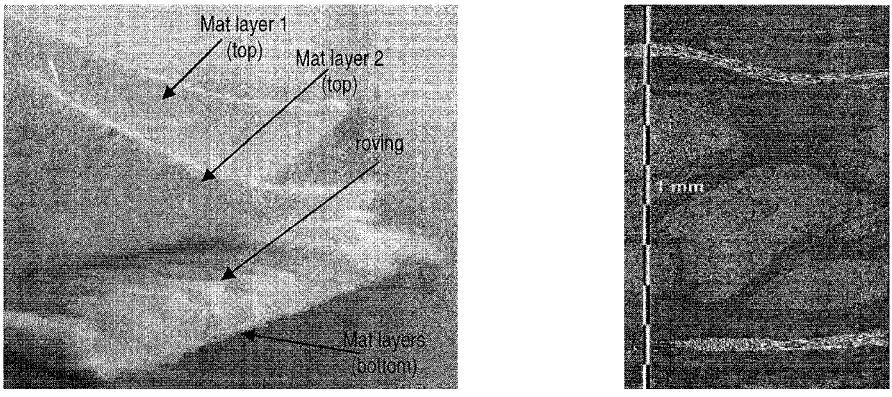


Figure 1: Specimen for this research

GFRP laminates were studied through microscopy to examine the fiber architecture and evaluate the quality of the pultrusion process. The microscopy analyses showed good embedment of the fibers [Figure 2(b)]. The mechanical properties of the GFRP laminates were determined from coupon level tests following standard testing procedures, which are summarized in Table 1. The response of the GFRP laminates to quasi-static loadings was elastic, and brittle failure was observed. The adhesive in current study is a two-component epoxy adhesive. A summary of adhesive mechanical properties is presented in Table 1.



(a) (b)

Figure 2: Fiber architecture (a) and the cross-section of a 10 mm thick laminate (b)

Experimental set-up and loading protocol

Specimens were clamped into a Schenck testing machine with a capacity of 800 kN in cyclic loading (tension and compression) and possible displacement of up to 250 mm. The specimen

length between the grips was 600 mm. At the end of the joints, spacer plates were placed between the 5mm laminates in order to ensure a clamping free of additional end constraints. The experiments were performed in a laboratory environment at room temperature.

Table 1: Material properties of GFRP laminates and adhesive

	Material	Modulus (GPa)	Ultimate Stress (MPa)	Ultimate Strain (%)
GFRP	5mm (11 samples)	34.5[1]±0.64[2]	441±21	1.34±0.10
Laminate	10mm (14 samples)	32.2±2.6	334±14	1.07±0.13
Adhesive	Tension (5 samples)	4.56±0.138	38.1±2.1	0.97±0.13
	Compression (5 samples)	3.05±0.033	80.7±2.6	3.68±0.08

1: Mean Value; 2: Standard Deviation

The locations of strain gages are shown in Figure 1. Thermocouples were implemented to monitor temperature increase in the specimen under high frequency (10 Hz) loading. Measurement showed negligible temperature changes during testing [6]. The final failure of specimens could be studied using a high-speed camera.

For quasi-static tests, specimens were loaded under uniaxial tension up to failure. Loadings were applied as displacement-controlled at a rate of 0.6 mm/min. For fatigue tests, specimen were sinusoidally loaded in tension at an amplitude ratio of R = 0.1, which is defined as $R = P_{min} / P_{max}$, where P_{max} – maximum applied load and P_{min} – minimum applied load. For some specimens, R changed to different values due to the problem of the machine's control system during the testing process. The highest loading in a testing procedure was controlled with the values from 20% to 90 % of the average failure load from quasi-static tests. The fatigue experiments were performed as load-controlled at 1 Hz, 5 Hz and 10 Hz. Fatigue experiments were conducted up to failure or to a maximum of 10 million cycles. Specimens not failed during fatigue testing were subsequently quasi-statically loaded up to failure. The loading protocol, frequencies, and other parameters are summarized in Table 2.

Table 2: Overview of experimental programs

Specimen	Load range ΔP[kN]	Amplitude ratio R	Shear stress amplitude Δτ [MPa]	% of ultimate load	Frequency [Hz]	No. of cycles up to failure N_f
QS1-QS3[1]	0 - 148±9	-	7.4±0.5	100	-	1
F1[2]	13 - 135	0.10	6.1	91	1	132
F2	11 - 110	0.10	5.0	74	1	130
F3	11 - 101	0.11	4.5	68	5	5452
F4	9 - 90	0.10	4.1	61	5	29,038
F5	9 - 90	0.10	4.1	61	5	85,358
F6	12 - 88	0.14	3.8	59	5	54,611
F7	10 - 56	0.18	2.3	38	10	3,926,255
F8	5 - 45	0.11	2.0	30	10	13,238,467 [cracked]
F9	4 – 30 [148[3]]	0.13	1.3 [7.2[3]]	20	5	3,268,994[not failed]
F10	4 – 29 [150[3]]	0.14	1.3 [7.4[3]]	20	10	10,676,849[not failed]

1: QS-Quasi-Static loading; 2: F-Fatigue loading; 3: Ultimate values under QS loadings

EXPERIMENTAL RESULTS

Fatigue crack initiation and propagation

A total of 13 double-lap joint specimens were tested as described: three specimens were tested under quasi-static loadings and 10 specimens were tested under fatigue loadings. Since the failure of the joints was in brittle manner without any signs of observable warning (with the chosen measurement), it was difficult to capture the whole crack initiation and propagation process under fatigue loading using the high speed camera. Because no non-destructive evaluation technique was used in this research, damage initiation and micro-crack forming could not be detected. However, information from the fractured surfaces showed that cracks initiated from the adhesive fillet, then entered into the 10mm thick laminate (the middle laminate of the double-lap joint) at an angle about 40-45°. A schematic representation of crack initiation is shown in Figure 3(a) (dimensions not to scale).

Fatigue crack propagation and the fracture of a specimen were captured using the high speed camera, which is shown in Figure 3(b). After entering into the 10mm thick laminate, the crack propagated within the mats region (outer surface of the CSM or between the CSM and the woven mat) of the laminate in parallel to the laminate-adhesive interface. One exception to the abovementioned crack propagation process should be pointed out. Cracking initiated at the same location as described in Figure 3(a) and propagated about 18mm in Specimen F8 after about 4.1 million cycles. No further crack propagation was observed in this specimen up to 13.2 million cycles, at which the fatigue test stopped.

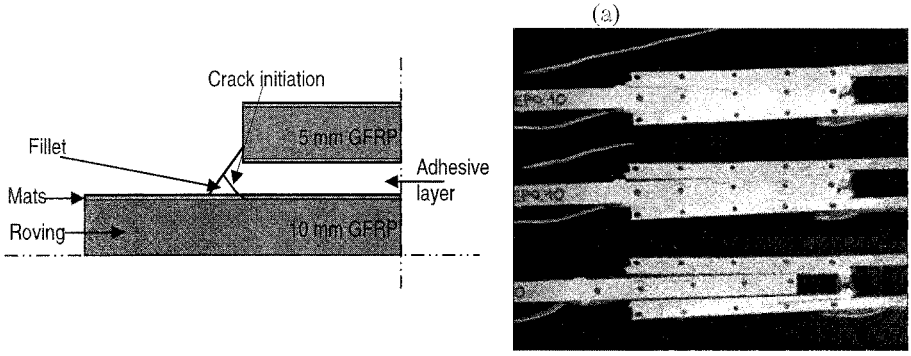


Figure 3: Crack initiation (a) and crack propagation and final failure (b)

Failure surfaces and results from fractography

The fracture of the joints was brittle without visible or audible warnings under quasi-static and fatigue loadings. The brittle fracture of the joint can be seen from their fractured surfaces. A typical fractured surface under fatigue loadings is shown in Figure 4.

Several samples were prepared from the fractured specimens (under fatigue loadings) for microscopic study. A cross-section of a 10mm thick specimen is shown in Figure 5. It is clear that the crack propagated within the mat regions. Results from several other samples also showed that cracks never entered into the roving region of the laminates. The same failure pattern occurred for specimens under quasi-static loadings. The observations indicate that the mat regions are weak regions in resisting interlaminar fracture.

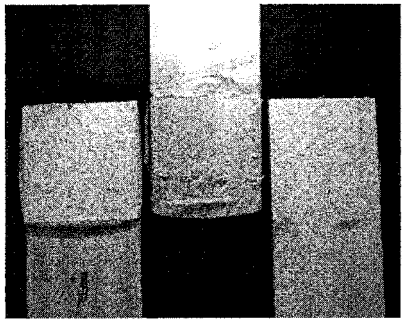


Figure 4: Failure surface of a specimen

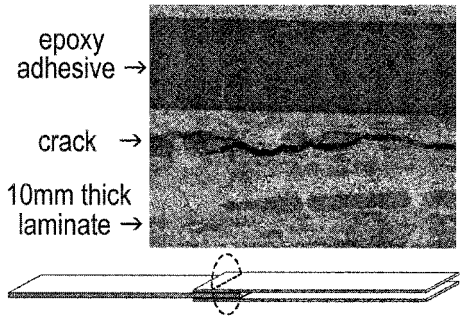


Figure 5: Cross-section of a fractured specimen

Fatigue life curves

Fatigue life curves are shown in logarithmic representation in Figure 6(a) and linear representation in Figure 6(b). The average shear stress amplitudes in the joint, $\Delta\tau$, were normalized with respect to the average ultimate shear stress from the quasi-static tests (7.4 MPa). The linear representation shows a steep drop in the fatigue resistance which is about 30% of the ultimate static value within the first million cycles. A fatigue limit of about 25% of the ultimate static capacity could be achieved [Figure 6(b)]. However, because only 13 samples were tested, more fatigue tests should be conducted to obtain a reliable fatigue limit value. A simple calculation showed a 2.0 MPa average shear stress amplitude can be achieved in the bonded joints at 10 million cycles.

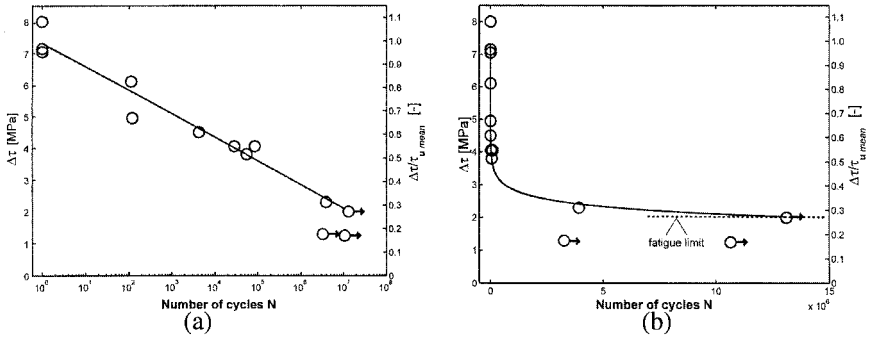


Figure 6: Fatigue life curves in logarithmic representation (a) and linear representation (b)

Other observations

The progressions of the average strains on the 5 mm laminates are shown in Figure 7(a). The abscissa is normalized with respect to the number of cycles at failure (N_f). The strains remained almost constant and, therefore, showed no sign of modulus reduction. The strain measurements on the 10 mm profiles showed the same results. The progressions of the stiffness, EA_c, in the double-lap joints are shown in Figure7(b). EA_c were calculated as follows: $EA_c = (\Delta F \cdot l_c)/\Delta l_c$ with $\Delta l_c = \Delta l_{tot} - \Delta\varepsilon_{a1} \cdot l_p - \Delta\varepsilon_{a2} \cdot l_p$ where ΔF represents the load range, l_c the length of the connection, Δl_c the elongation of the connection, l_p the length outside the joint, $\Delta\varepsilon_{a1}$ the measured average strain amplitude from gages 1

and 2 on the 10 mm profile, $\Delta\varepsilon_{a2}$ the measured average strain amplitude from gages 3 and 4 on the 5 mm profiles and Δl_{tot} the measured total specimen elongation (see Figure 1). The progression curves showed no signs of significant stiffness reduction before the brittle fracture of specimens.

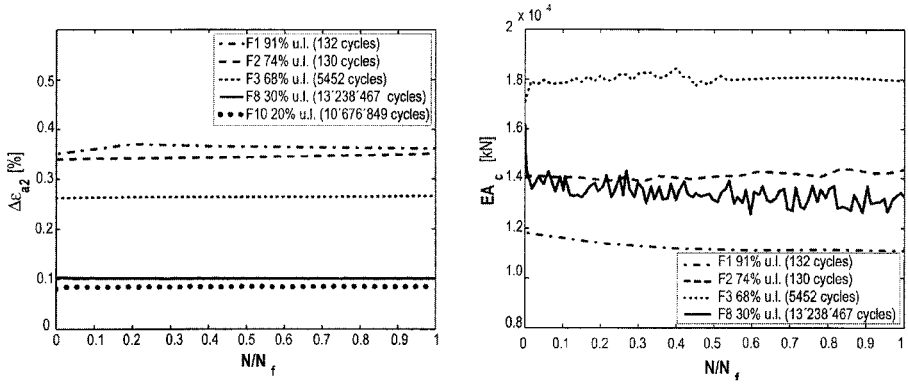


Figure 7: Progression of joint modulus (a) and stiffness (b)

DISCUSSION

The experiments showed a fatigue limit of about 25% of the static failure load or 2.0 MPa average shear stress at R=0.1 after 10 million cycles. The fatigue limit remains far above the fatigue stress amplitudes in adhesive connections of typical GFRP bridge structures (0.15-0.26 MPa) [4,5]. A safety factor of 7.7-13.3 could be achieved in practical fatigue resistance design of adhesively bonded joints. It should be noted, however, that experiments were performed in a laboratory environment without the consideration of environmental effects.

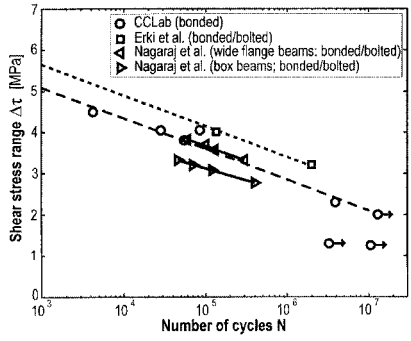


Figure 8: Comparison of fatigue lives of laminates different GFRP joints

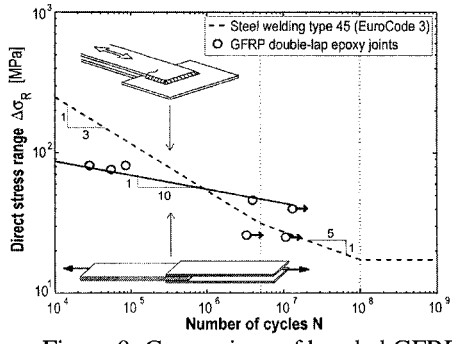


Figure 9: Comparison of bonded GFRP to welded steel connections

A comparison of "cycles-shear stress range" curves from current work with the published results is shown in Figure 8. The slopes of fitted lines are similar for four different pultruded GFRP joints. The "cycles-direct stress range" curve for the DLJ from pultruded GFRP laminates is compared with welded steel joints [2] as shown in Figure 9. The slope of

the fatigue life curve of welded steel joints is constant and amounts to 1:3 for up to 5 million cycles. From 5 million to 100 million cycles the comparable slope is 1:5 [2]. The slope of the adhesive GFRP connections, however, is much flatter with 1:10. Therefore, adhesive-bonded connections from pultruded GFRP laminates are more sensitive to changes in load amplitude than welded steel connections.

Damage initiation and progression before fracture could not be detected with the chosen measurement set-up. However, it cannot be concluded that no damage in the form of micro-cracks inside the materials occurred during the testing process.

CONCLUSION

Fatigue experiments on adhesively bonded double-lap joints from pultruded GFRP laminates were conducted in a laboratory environment. The experiments showed a fatigue limit at approximately 25% of the static failure load at 10 million cycles. This corresponds to average shear stress amplitude of 2.0 MPa in the joints. This value ensures a safety factor of 7.7-13.3 under fatigue loadings in bonded connections of GFRP bridges. Fracture always occurred in a brittle manner within the GFRP adherends without visible or audible warning. The failure of the adherends was interlaminar fracture within the mat regions of the GFRP laminates. No adhesion and cohesion failure were observed. The slopes of fitted lines of the fatigue life curves are similar for bonded and bonded/bolted pultruded GFRP joints. The bonded GFRP joints are more sensitive to changes in load amplitude than welded steel connections. However, additional fatigue tests should be performed to validate the fatigue limit obtained from the above experimental program. Further studies are necessary to investigate environmental effects on fatigue of the bonded joints. Non-destructive evaluation techniques shall be implemented in future studies to detect damage initiation and growth for better understandings of the damage and failure mechanisms in the bonded joints.

ACKNOWLEDGEMENTS

The authors would like to thank the Swiss Innovation Promotion Agency CTI for financial support and Sika AG (Switzerland) and Fiberline Composites A/S (Denmark) for providing adhesives and GFRP laminates.

REFERENCES

1 ASTM, 'Standard test method for tension-tension fatigue of polymer matrix composite materials', Designation D3479/D 3479M-96, ASTM, West Conshohocken, PA, USA, 1996.

2 Eurocode 3, 'Design of steel structures, Part 1-9: Fatigue strength of steel structures', *European Committee for Standardization*, Brussels, prEN1993-1-9, 2003.

3 M A Erki, C Shyu, R G Wight, 'Fatigue behavior of joints for FRP pultruded members', 2nd Int. Conference on *Durability of Fiber Reinforced Polymer Composites for Construction CDCC'2002*, Montreal, Canada, 2002: 449-561.

4 T Keller, 'New bridges and buildings constructed from translucent GFRP sandwich panels and glued GFRP elements', 3rd Int. Conference on *Advanced Composite Materials in Bridges and Structures ACMBS*, Ottawa, Canada, 2000: 785-792.

5 T Keller, 'Recent all-composite and hybrid fiber reinforced polymer bridges and buildings' *Progress in Structural Engineering and Materials*, 2001 3(2) 132-140.

6 T Keller, T Tirelli, 'Fatigue behavior of adhesively connected pultruded GFRP profiles', Composite Structures, In Press, Available online, 14 November 2003.

7 V Nagaraj, Gangarao, V S Hota, 'Fatigue behavior and connection efficiency of pultruded GFRP beams', *Journal of Composites for Construction*, 1998 2(1) 57-65.

PART VII

CERTIFICATION, INSPECTION AND QUALITY ASSURANCE

This page intentionally left blank

STRENGTHENING CONCRETE STRUCTURES WITH FIBRE COMPOSITE MATERIALS: UPDATING TECHNICAL REPORT 55

John Clarke*, Antony Darby** and Tim Ibell
The Concrete Society (*) *and the University of Bath* (**)

INTRODUCTION

Concrete Society Technical Report 55 [1], was published in December 2000. This was the first document to give authoritative, independent design guidance on externally bonded fibre composites (commonly known as FRPs) for strengthening concrete structures. Other guidance is now also available, such as ACI 440.2R [2] and *fib* Bulletin 14 [3], but TR 55 is widely accepted in the UK and many other parts of the world. It was followed in 2003 by Technical Report 57 [4], which gives guidance on many aspects of quality control and inspection. In addition, CIRIA has prepared guidance on strengthening metallic structures using FRP [5].

The number of strengthening applications is increasing rapidly as clients start to appreciate the benefits of this cost-effective technique. Materials and methods are also developing rapidly, along with new approaches, such as the use of near-surface-mounted reinforcement. The decision has therefore been taken to review and update TR 55, in the light of experience gained over the past few years and the developments in materials and techniques.

This paper reviews the current state-of-the-art, giving examples of typical applications, and identifies the key areas in which revision and updating is required.

MATERIALS

The most commonly used fibres for externally strengthening structures are carbon, glass and aramid, which are combined with an epoxy resin. The composite may be factory-made, such as plates or shells for surrounding columns, or may be formed in situ. In the latter case the fibres are in the form of fabrics or tapes, which are impregnated with resin and then applied to the concrete surface. It should be noted that this paper, and the guidance given in the Concrete Society Technical Reports, is not specific to any particular form of fabrication.

APPLICATIONS

Since about the mid-1990s the technique has been used for strengthening many concrete structures throughout the world, including bridges, commercial buildings, industrial plant, chimneys and tunnels. (In addition iron and steel structures and masonry buildings are routinely strengthened using externally bonded FRP.) Some typical applications are given in the following Sections.

Bridges

In the UK there has been a major reassessment of bridge capacities, following the requirement to carry heavier commercial vehicles. This has led to strengthening bridge

decks, with the application of FRP plates on both the soffits and top surfaces [6]. Edge beams have been strengthened using proprietary shear straps. Columns have been wrapped, or encased in shells, to improve impact resistance [7]. In addition, in areas such as California, columns have been wrapped to improve their seismic performance [8].

Buildings

Applications include strengthening floor slabs to carry additional imposed loads or following structural alterations [9]. Columns have been strengthened to carry additional load. One example of the latter is the strengthening of the main columns of a seven-level car park in Manchester so that two further storeys could be added, providing an additional 300 car parking spaces [10]. The approach was chosen in preference to conventional strengthening, because of the speed of installation and the minimal increase in the column dimensions. Other applications have been to replace missing hoop reinforcement in columns [11] or to improve seismic performance [12].

Industrial buildings

Applications in industrial buildings have included strengthening power station cooling towers to resist wind loading [13] and the rehabilitation and strengthening of a tower in a fertilizer plant in Qatar [14]. In addition a number of coastal structures such as piers and jetties have been strengthened [15].

DESIGN ISSUES

Chapters 5, 6, 7 and 8 of the existing Technical Report deal with strengthening design issues. Whilst the current design approaches for strengthening of members are safe within the constraints detailed in the guidelines, revisions (including additions and rationalisation) will be carried out in the light of recent research and experience in practical implementation. The main limitations of current methods, together with proposed changes and additions, are described in the following sections.

Structural design of strengthened members

The current Chapter 5 deals with generic design issues, such as the overall basis of design, material properties, safety factors and behaviour under extreme forms of loading.

The material partial safety factors in the current guidance might be considered overly conservative when compared with other similar guidelines that have been introduced since the publication of TR 55 [2, 3, 16]. In particular, the partial safety factor for glass FRP seems rather high, although glass is rarely used in practical strengthening applications. More importantly, it should be noted that, in general, failure behaviour of strengthened structures is governed by FRP strain rather than ultimate strength. In this context, safety factors relating to modulus of elasticity are important. These safety factors are currently under review.

Current guidance on behaviour under extreme loadings is limited to fire and seismic performance. As well as reviewing these sections, further guidance is to be introduced on impact loading (e.g. vehicle impact of bridge piers), blast loading and protection against vandalism (both deliberate and accidental, e.g. the drilling of holes in FRP on a strengthened structure).

Design of members in flexure

The current design guidelines for the moment capacity of flexural elements are based upon a balanced moment of resistance approach, which occurs when the allowable ultimate design strains in the FRP and concrete occur simultaneously. When the applied design moment is less than the balanced moment, design of the required FRP is relatively straightforward. However, when the design moment is greater than the balanced moment, the process is rather more tedious.

The concept of the balanced moment approach is felt to be unnecessarily complicated. A more practical method, advocated by practising engineers, is to use a trial-and-error approach based upon an initial estimate of the size of FRP and iterating until an economical and safe design is achieved. The proposed method is as follows:

- Calculate the ultimate capacity of the unstrengthened section and ensure that the critical section is at least capable of withstanding the unfactored loading condition, so that collapse should not occur should FRP failure occur.
- Estimate the amount of FRP required assuming the neutral axis remains in the same place as for the unstrengthened case and limiting the strain in the FRP to 0.8%. Since the FRP is usually applied under existing dead load, it is necessary to ascertain the initial notional soffit strain under unfactored dead load by making the usual serviceability limit state assumptions.
- Guess the maximum compressive strain in the concrete and guess a neutral axis position. Assuming plane sections remain plane and remembering to subtract the initial strain in the soffit from the FRP strain, the forces in the concrete, steel and FRP can be calculated based upon suitable stress-strain models.
- The neutral axis can then be adjusted until horizontal equilibrium is obtained.
- The moment capacity can then be calculated by taking moments of the forces about a suitable position. This capacity is then compared with the required ultimate moment.
- If the moment of resistance is less than that required, the initial estimate of the compressive strain is increased (up to a limit of 0.0035) and the process repeated until the moment of resistance is equal to the required ultimate moment.
- Should the required ultimate moment not be achievable for the given quantity of FRP, an incrementally higher quantity of FRP is assumed. The calculated stress-strain criteria must then be assessed such that the maximum tensile strain in the FRP is no greater than 0.008 in order to prevent debonding, the maximum longitudinal shear stress in the adhesive layer is less than 0.8 N/mm^2 and the FRP stress is less than its ultimate design capacity.
- Should the calculated moment of resistance be substantially greater than that required, a lower quantity of FRP could be chosen, and the process repeated. Whilst this approach is iterative, it is conceptually much more straightforward than the balanced moment approach and can be easily programmed using a spreadsheet.

It should be noted that the choice of stress-strain model for the concrete and steel can be important. Whilst it makes little difference whether a parabolic or rectangular stress block is used for modelling concrete under high compression, the idealised steel stress-strain model used may effect the calculations. Although the tri-linear stress-strain model of BS 5400 [17] would appear conservative, and is certainly the case for calculation of the flexural strength of the element, when it comes to calculation of longitudinal shear, a bilinear version (without the truncated corner at yield, similar to

that in BS 8110 [18]) results in higher shear stress, so the tri-linear model may underestimate longitudinal shear. It is therefore suggested that the bilinear stress-strain model be used for steel.

In addition to calculating moment capacity, the issue of separation failure must also be addressed. In most instances peeling can be prevented by providing adequate anchorage length, beyond the length required for flexural strengthening. The existing equations for calculating the resulting anchorage force are acceptable but need clarification for situations when the steel reinforcement has yielded and when members are non-prismatic. In instances where it is difficult to provide sufficient anchorage length, some form of anchorage device is required. Advice on anchorage is to be updated, based on latest findings.

Guidance will be provided on strengthening beams with globally and locally curved soffits. Ideally, the applied FRP should be straight, following the tensile load path. Provided the deviations are small, local curvature or undulations can be taken out by additional thickness of adhesive. Use of pultruded plate, rather than wet lay-up sheet laminate, is therefore appropriate in such a situation. In the case of globally concavely-curved soffits, there is no option but to follow the curve of the soffit. The flexural strength enhancement of FRP is therefore reduced due to the straightening effect in the curved system, causing premature debonding.

Finally, the use of near-surface-mounted (NSM) reinforcement is to be discussed. The first UK application of NSM was in 2002 [19] and its use is likely to gain momentum. The technique has, in certain situations, advantages over standard techniques, due to increased bond area and the fact that it can be applied to negative moment areas of decks and slabs where surface reinforcement might be subject to damage. Guidelines specific to use of NSM for flexural strengthening are to be added.

Shear

Although the current guidelines for shear strengthening are safe, there are issues that need to be addressed. The contribution of the FRP to the shear strength is related to an effective strain. The limiting effective design strain for the FRP is the lesser of 0.004 (which limits crack widths so that aggregate interlock is maintained), an empirical equation for debonding and an empirical equation related to the ultimate strain capacity of the material. In most cases, failure would be due to separation failure before the ultimate strain capacity is reached. Even in cases where shear strengthening wraps around the beam, unacceptable levels of debonding are likely to occur before failure of the FRP itself. The effective strain models are based on curve fitting of experimental work [20], rather than explicitly modelling the mechanics of the failure mode. Although a significant amount of data has been used to derive these expressions, it should be noted that the vast majority of the testing has been done on beams less than 0.4 m deep. As stated in the current guidelines, care needs to be taken if the beam being strengthened is not typical of those by which the equations have been derived. This constrains and limits practical use of the equations.

Whilst it is generally accepted that the value of 0.004 for the effective strain limit to prevent loss of aggregate interlock is acceptable (and indeed is often the limiting case), it is suggested that a more fundamental look at the failure behaviour of the FRP is required to develop models which reflect the mechanical behaviour of debonding and fibre rupture to allow more confident use of the guidelines outside the limits of current experimental investigations. The suggested approach for fibre rupture is simply to assume a linear strain distribution, from zero at the top of a 45° shear crack (i.e. at the

compression face of the beam), to the ultimate failure strain of the FRP at the bottom of the shear crack (i.e. at the tension face of the beam). Thus, the average FRP strain across the entire shear crack is half the ultimate strain of the FRP at shear collapse.

The proposed model for delamination of the FRP is related to anchorage length and is consistent with peeling failure described in the Section on flexural strengthening. The anchorage length depends upon whether the FRP shear strengthening is applied to the sides of the beam, as a 'U' wrap or wrapped round the entire section. The anchorage model used in the flexural design chapter of TR55, based on Neubauer and Rostasy [21], is used to calculate the bond failure force in the FRP above and below the shear crack, depending upon the end conditions. For the debonding failure mode, the total contribution of the FRP to the shear strength of the section is this force integrated over the effective width of the FRP across the shear crack. The limiting shear strengthening provided by the FRP is the lesser of this force, that provided by the limiting strain of 0.004 and that resulting from fibre rupture (considered to occur when the average strain is half the rupture strain).

This design approach is at a preliminary stage and may be overly conservative in its assumptions. However it does form a more logical mechanically-based model from which a simple design basis may be formed without the need to constrain the situations in which it may be applied.

An additional discussion on NSM for shear strengthening will also be included. Although not widely used at present, there are certainly situations where NSM would be more beneficial than sheet strengthening. In particular, when shear strengthening can only be applied to the sides of the beam, NSM will increase the bond strength and increase resistance to separation failure. The issues particular to NSM for shear strengthening will be highlighted.

Columns

For circular columns, the current guidelines treat strengthening in compression and flexure separately. However, in practically all cases axial loading is accompanied by moment, either due to eccentricity of loading or due to other bending actions. It is therefore felt that the two stress resultants should be more fully unified.

Whilst detailed guidelines on circular columns can be given with relative confidence, guidelines on strengthening columns with non-circular cross-sections requires further expansion. In particular, square and rectangular columns are common. Although it is evident that only modest increases in axial strengthening can be achieved by wrapping rectangular columns, explicit guidelines will be added based upon recent work by Lam and Teng [22]. The generally accepted model is based upon a shape factor, developed from a parabolically-defined cruciform area of confinement which is used to modify the strength enhancement of an equivalent circular column. It should be noted, however, that no large-scale rectangular columns (>250 mm maximum dimension) have been tested for comparison with such models and thus this approach should be applied to large columns with caution, particularly under eccentric loading.

Once again, the use of NSM for strengthening columns will be discussed in the context of increasing flexural capacity.

Design flow charts

In order to improve the user friendliness of the guidelines, a set of flow charts will be introduced. Rather than give specific design examples, generic flow charts detailing the

design procedures for flexural, shear and column strengthening will be included to allow the designer to follow the design process in a logical manner.

In addition, a decision flow chart will be added to allow a designer to make informed judgement on suitable types of strengthening systems (plate bonding, wet lay-up, NSM, etc.), types of material (carbon, aramid, glass) and material properties (high stiffness, etc.).

Emerging technologies

Designers will sometimes need to address situations or problems that are not covered by the current techniques described in the design chapters. A new chapter referring to emerging technologies and techniques is to be written. Whilst these techniques may not currently be at a stage where designers can confidently use them, the chapter will present the important practical aspects of the techniques. The designer can then make an informed judgement as to the suitability of the technique for the particular situation and thus allow further investigation into the details of the method to be made. Furthermore, the topics will be categorised so that the designer will know whether the technique has been used and demonstrated in practice or whether it is merely at an experimental stage.

The technique of prestressing using FRP will be discussed in detail. This technique has been used to strengthen bridges, but is not widely used at present, largely due to cost. It is a specialist technique and it is not considered suitable that full detailed design guidance be given. However, the principles and methodology of the technique will be presented to allow the designer to appreciate the issues that are involved. Other emerging technologies that will be discussed are as follows:

- Technologies already used in practice
  - Post-tensioned cable and rope systems
  - FRP anchorage techniques
  - Bolted plate anchors
  - Concrete masonry walls
  - Strengthening against blast
- Technologies at the research stage
  - Gradually-anchored prestressed CFRP laminates
  - Prestressed NSM bars
  - FRP anchor systems
  - Steel-reinforced polymers
  - Moment redistribution in continuous structures
  - Deep embedded bar for shear strengthening
  - Prestressed CFRP straps for shear strengthening
  - Mechanical fastening techniques
  - Hybrid glued and bolted systems
  - Strengthening for torsion
  - Life expectancy modelling

SUMMARY

This paper has outlined the work that is being carried out to revise and update Technical Report 55, which is widely accepted as the standard approach for the design of fibre composite strengthening systems for concrete structures. The resulting Second Edition should improve the effectiveness and reliability of this technique.

ACKNOWLEDGEMENTS

The Authors would like to acknowledge the financial support of the following organisations for the revision of Technical Report 55: Exchem Mining and Construction, Fyfe Co. LLC and Fyfe Asia Pte., Highways Agency, London Underground Ltd., MBT, Network Rail, Toray Europe and Weber SBD. The Authors would also like to thank staff from Mouchel, Parsons Brinckerhoff and Tony Gee & Partners for their contributions to this paper.

REFERENCES

1. The Concrete Society, *Design guidance for strengthening concrete structures using fibre composite materials*, Technical Report 55, Crowthorne, The Concrete Society, 2000.

2. American Concrete Institute, ACI 440.2R, *Guide for the design and construction of externally bonded FRP systems for strengthening concrete structures*, Farmington Hills, USA, American Concrete Institute, 2002.

3. Task Group 9.3, *Externally bonded FRP reinforcement for RC structures*, Technical Report, Bulletin 14, Lausanne, *fib*, 2001.

4. The Concrete Society, *Strengthening concrete structures using fibre composite materials: acceptance, inspection and monitoring*, Technical Report 57, Crowthorne, The Concrete Society, 2003.

5. Construction Industry Research and Information Association, *Strengthening metallic structures using externally-bonded fibre-reinforced polymers*, Report C645, London, CIRIA, In print 2003.

6. B Sadka, 'Strengthening bridges with fibre-reinforced polymers', *Concrete*, 2000, **34** (2) 42–43.

7. L Hollaway, 'The development and the future of advanced polymer composites in the civil infrastructure', *Proceedings of the International Conference on Advanced Polymer Composites in Construction (ACIC)*, Southampton, 2002.

8. J W Bai and M B Hueste, 'Seismic retrofit for reinforced concrete building structures', CBE Final Report, Mid-America Earthquake Center CM-4: Structure Retrofit Strategies, Texas A&M University, 2003.

9. C A Gold and A J Martin, *Refurbishment of concrete buildings: structural and services options*, Guidance Note GN 8/99, Bracknell, BSRIA, 1999.

10. P Russell and A Modi, 'Wrapping the Harbour City car park, Manchester', *Concrete*, 2001 **35** (6), 24.

11. J Thomas and A Tipnis, 'Blue Circle terminals find their strength', Cement Americas, Nov. 1, 2001.

12. M J N Priestley, F Seible and G M Calvi 'Seismic design and retrofit of bridges', Wiley, USA, 1996..

13. Anon, 'Structural reinforcement from MBT FEB, *Concrete*, 2001 **35** (1), 12-13.

14. S Luke, S Godman and H Hamnevoll, H., 'Strengthening the Qafco prill tower, Qatar, with FRP plates', *Concrete*, 2002 **36** (2) 32-33.

15. N Yazdani and A K M Islam, 'Post storm reconstruction model for coastal habitable structures', *International Conference on Coastal Engineering Development, Singapore*, December 2001.

16. A Cripps, B Harris and T Ibell, *Fibre-reinforced polymer composites in construction*, Technical Report C564, London, CIRIA, 2002.

17. British Standards Institution, BS 5400, *Steel, concrete and composite bridges*, Part 4, *Code of practice for design of concrete bridges*, London, BSI, 1990.

18. British Standards Institution, BS 8110, *Structural use of concrete*, Part 1, *Code of practice for design and construction*, London, BSI, 1997

19. N S Farmer, 'Near-surface-mounted carbon fibre reinforcement', *Concrete*, 2003, **37** (1), 20-21.

20. A Khalifa, J William, A Nanni and M I Abdel Aziz, 'Contribution of externally bonded FRP to shear capacity of RC flexural members', *Journal of Composites for Construction, ASCE*, 1998, **2** (4), 195-202.

21. U Neubauer and F S Rostasy, 'Design aspects of concrete structures strengthened with externally bonded CFRP plates, *Proceedings of 7th International Conference on Structural Faults and Repair*, (Editor M C Forde) Edinburgh, Engineering Technics Press, 1997, **2**, 109-118.

22. L Lam and J G Teng, 'Compressive strength of FRP-confined concrete in rectangular columns', *Proceedings of the International Conference on FRP Composites in Civil Engineering*, Elsevier, 2001, **1**, 335-343.

NEAR SURFACE MOUNTED REINFORCEMENT FOR STRENGTHENING – UK EXPERIENCE AND DEVELOPMENT OF BEST PRACTICE

Neil Farmer
Tony Gee and Partners Consulting Engineers

INTRODUCTION

The use of Fibre Reinforced Polymer (FRP) bars, bonded into grooves near the surface of a concrete element, is a relatively new and exciting technique for strengthening structures[1]. In the United Kingdom (UK) this Near Surface Mounted (NSM) reinforcement method of strengthening has been used to enhance the load carrying capacity of two car park structures and provided an opportunity for the author of this paper to provide feed-back on the advantages and disadvantages of using this approach to applying additional non-ferrous reinforcement. A particular challenge for the designers was to determine if existing approaches could be extrapolated and in this respect the paper sets out areas where further research work should be targeted.

HISTORY

The earliest example of the retrofitting technique appears to have taken place in Sweden in 1948. In that case steel bars were used as the reinforcement. By the time the 1990's arrived stainless steel was being used to enhance the intrados of masonry arches and more recently FRP bars have been preferred to strengthen silos, bridge decks and car parks. In the UK, the first major use of FRP bars, in conjunction with the NSM reinforcement technique, was at Trenchard Street multi-storey car park in Bristol in 2002 and this has been followed by a smaller but no less significant application to a car park in Liverpool. The reasons why the method is so beneficial for strengthening near the faces of elements subjected to trafficking are immediately apparent.

BENEFITS

There are three principal benefits of using NSM reinforcement over those that exist for an externally bonded reinforcement solution. Firstly the reinforcement is buried beneath the surface of the element and therefore is protected from damage due to accidental impacts, traction forces, braking forces and deliberate vandalism. Secondly, the top surface of a concrete structure can often be undulating and rough. If structural reinforcement is to be bonded to the surface then extensive preparation, by grinding or scabbling is frequently required. However, NSM reinforcement is set into a groove or slit and is formed in the concrete surface to a depth of approximately 20 mm to 25 mm (Fig. 1). Consequently the surface undulations and roughness are, within reasonable boundaries, more easily accommodated.

In the case NSM reinforcement being used as the strengthening technique, the weak layer of laitance that migrates to the top of a concrete mix during the pouring and vibration process has less influence on the development of a satisfactory bonded joint. For external bonding, extensive grit blasting or needle gunning would generally be required to expose the aggregate and hence provide a fine gripping substrate. However, as the reinforcement is set below the weak surface the aggregate surface is more readily exposed. Notwithstanding that the forming of the grooves produces a suitable surface

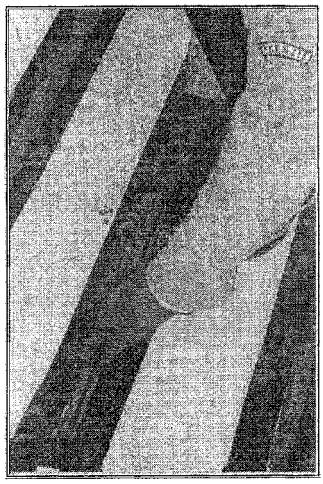


Fig.1 Placing the bars in the adhesive

along the base of the grooves, it is still necessary to use a method of mechanical abrasion to prepare the sides that may otherwise be smooth as a result of saw cutting.

The final advantage is principally one of aesthetics. Following installation the surface profile of the concrete element is substantially as it was prior to the strengthening works taking place. In the case of car parks, where a waterproof membrane is often applied to the surface, it is almost impossible to detect that any works have been undertaken.

On the top surfaces of bridge decks the strengthening measures become less vulnerable to damage during replacement of bituminous surfacing and are exposed to lower temperatures than for externally applied reinforcement.

DESIGN

Currently there are not any national standards for the design of strengthening using NSM reinforcement. However, the American Concrete Institute and the UK's Concrete Society are in the process of producing guidelines.

The principles outlined in the Concrete Society's Technical Report 55 (TR55)[2] were followed in the design of the strengthening measures at both of the car parks in Bristol and Liverpool. It is believed, as the basis of laboratory testing, that the extrapolation of design recommendations for externally bonded reinforcement to NSM reinforcement leads to a relatively conservative design in respect of ultimate strength. Testing in Sweden, Italy and the USA has shown that between 60% and 100% of the failure strain of the bar reinforcement can be developed, whereas the design strain for externally bonded reinforcement is typically around 50% of the failure strain so as to prevent debonding.

Although carbon fibre bars possess high strength and stiffness, in retrofit applications they are usually present in smaller quantities than existing steel reinforcement. As a consequence, under normal working loads they provide a lesser proportion of the contribution to flexural resistance.

As strains increase and approach the yield strain of the steel, the stiffness of the steel decreases, but that of the carbon fibre remains constant. Hence, FRP reinforcement makes a rising contribution to flexural resistance for each uniform increment of strain. It is because of the presence of this non-linear elasto-plastic phase that simple reinforced concrete theory cannot be substituted into FRP-strengthening design. When the steel has completely yielded, any increase in strain results in a large increase in the shear stresses between the FRP reinforcement, the surrounding concrete and adhesive matrices.

The properties of the 7.5 mm diameter bars used in the car parks strengthening described in the case studies presented later in this paper were:

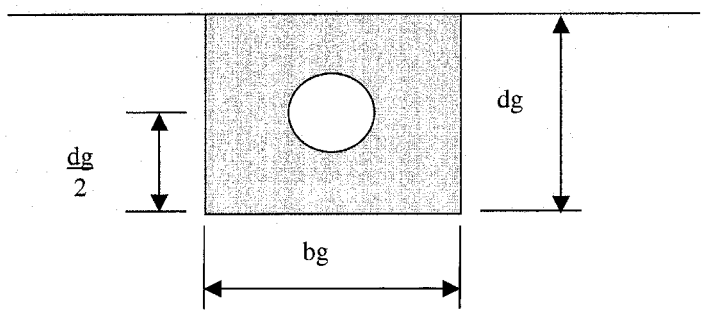
Elastic Modulus (E) = 200 KNmm^2
Failure Strain (ε) = 0.01

The partial safety factors applied to the material properties were:

γmE	=	1.1	Factor on elastic modulus
γm_M	=	1.4	Factor on strength (Manufacturing method)
γm_F	=	1.1	Factor on strength (Fibre type).

Hence the maximum design strain ($\varepsilon_D = \varepsilon/(\gamma m_M \cdot \gamma m_F)$) in the bar was limited to 0.00649.

A check was also carried out on the bond between the concrete and the adhesive, assuming that the fully bonded interfacial width (W) was as shown in Fig. 2.



$$W = 2.\frac{dg}{2} + bg = (dg + bg)$$

Fig. 2

The full depth of the groove was not considered to be effective in resisting longitudinal shear forces since a saw is used to cut the groove in the concrete and this produces smooth surfaces. Even after subsequent roughening the surface texture along the sides of the groove is less rough than along the horizontal bottom surface, it is therefore prudent to reduce the effectiveness in the design calculations.

An area where future research is required is in the relative effectiveness of different preparation methods. The maximum value of longitudinal shear stress recommended in Concrete Society Report TR55 is 0.8 N/mm^2.

Stresses can be calculated assuming that plane sections remain plane. However, account must be taken of existing strains in the concrete at the time of strengthening.

CASE STUDIES

TRENCHARD STREET CAR PARK, BRISTOL

The first major UK application of NSM reinforcement took place at Trenchard Street car park in the heart of Bristol.

In early 2002, consulting engineers Tony Gee and Partners (TGP) had developed a scheme for strengthening the deck slabs with externally bonded fibre-reinforced polymers (FRP). TGP was aware that, although feasible, a new technique being developed in Europe and the USA could provide a more appropriate solution. As an alternative solution they developed an NSM reinforcement proposal that was accepted by Bristol City Council.

The 205 mm-deep perimeter cantilevers slabs at Trenchard Street car park lacked flexural strength where the top layer of steel reinforcement had been depressed, resulting in an excessive cover of up to 95 mm. The initial solution proposed was to grind a recess into the slab into which would be bonded pultruded carbon fibre strips. The strips were to be covered by a layer of adhesive for protection. By using the alternative NSM technique, a stage was removed from the installation process and uncertainties about the quality of the bond surface were reduced.

Application technique

Bar installation began with the cutting of a groove 20mm wide and 20mm deep into the slab using a concrete saw and light percussive tools (Fig. 3). The sides of the groove were roughened as far as was practicable. The top of the groove was taped to provide clean edges and bonding surfaces were coated with epoxy primer. Cleanliness is a pre-requisite to any structural bonding exercise, and surfaces were vacuumed just before the adhesive was applied.

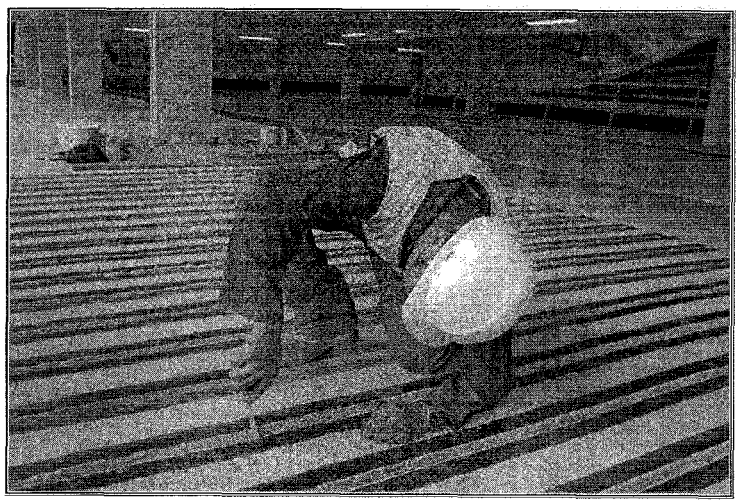


Fig. 3 Cut chases with tape along edges

As the work was undertaken during the summer, it was not difficult to maintain the minimum temperature of 10°C required to cure the resin in the two-part cold-cured epoxy adhesive. This material was mixed and injected into the groove with a sealant gun to a depth of 10mm (Fig. 4). A 7.5mm diameter bar was then positioned in the centre of the groove and the final 10mm layer of adhesive placed and trowelled level with the top of the adjacent slab.

The finished surface was suitable for trafficking by vehicles, despite the fact that grooves had been cut at 250mm centres along almost the entire perimeter of the slab. However, to protect existing reinforcement bar from the corrosive effects of de-icing salts, the surface was finished with a waterproofing membrane, hiding the strengthening work.

Load testing

To check the strengthened slabs could withstand the required loading, a slab was tested to 1.25 times the maximum working load. This showed the adequacy of the strengthening. In addition, comparison with a pre-strengthening test revealed a reassuring increase in stiffness. The load was applied in increments by using water-filled bags and deflection measurements were recorded (Fig. 5). Taking into account all the various potential failure mechanisms, the bars were designed to be loaded to only 12% of their ultimate tensile strength at the ultimate limit state.

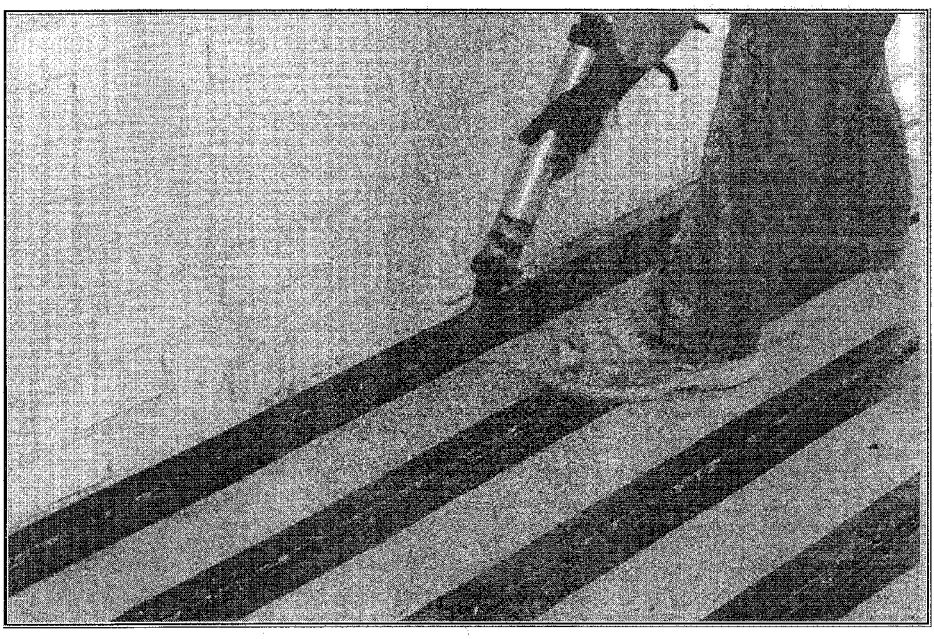


Fig. 4 Filling the grooves with first layer of adhesive

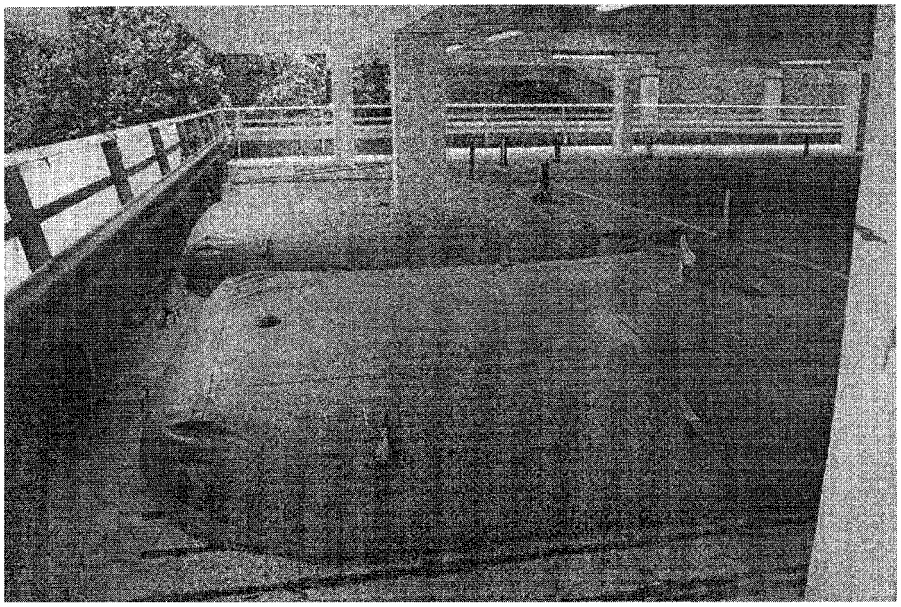


Fig. 5 Load testing using water-filled bags

SMITHDOWN LANE CAR PARK, LIVERPOOL

Over the last thirty years Merseyside Police have utilised a multi-storey car park at Smithdown Lane in the heart of Liverpool. Unfortunately in the latter years of its life cracked and spalling concrete provided evidence that a major repair, strengthening and refurbishment strategy would be required if the facility was to remain operational into the future.

In 1998 specialist consulting engineers Tony Gee and Partners were retained to investigate the mechanisms associated with the visible deterioration and ultimately design and supervise the necessary remedial works. Part of the chosen solution involved the use of fibre reinforced polymer bars bonded into grooves within the top surfaces of the car park decks.

Cracking and corrosion

The five split-levels of the car park included three suspended floor slabs each comprising a hybrid flat slab form of construction with waffle slabs in the mid-span zones.

The absence of a waterproof membrane on the top surface of the slab had exposed the structure to chlorides, in the form of de-icing salts, brought into the car park on the tyres of police vehicles. Cracks in the slab, disposed in a radial fashion around each column, were shown by a structural assessment and intensive investigations to be due to a combination of insufficient steel reinforcement and excessive cover.

This presence of structural cracking and chlorides in the same location had caused the steel reinforcement in the car park slabs to corrode and deteriorate. Elsewhere the effects of thirty years unprotected exposure to adverse environmental conditions had also taken their toll on the performance of the structure.

Enhancing flexural capacity with NSM reinforcement

Most areas of the slabs around the internal columns could only be satisfactorily repaired and strengthened by removing delaminated concrete and installing additional steel reinforcement after the installation of a temporary propping scheme.

The slab around the perimeter of the structure was not as badly affected by chloride ingress but flexural cracking was still giving cause for concern. The chosen solution for strengthening these areas had originally been externally bonded carbon fibre strips, set into a recess for protection against damage from wheel loads. However, in 2002, engineers from Tony Gee and Partners Advanced Composites Group had been involved with the design of the strengthening measures at Trenchard Street Car Park in Bristol involving the novel use of carbon fibre bars in the form of NSM reinforcement. The opportunity to switch the design solution to utilise the more appropriate NSM technique was seized

Strain limits

Research into the NSM technique has taken place in Sweden, Italy and the USA. Where it has been possible to anchor the bars with epoxy adhesive into areas of low shear stresses, it has been shown that in laboratory conditions between 80 and 100 percent of the ultimate capacity of the very high strength carbon fibre bars can be utilised. Accounting for the effects of actual site practices and material variability and following the principles outlined in the Concrete Society's Technical Report 55, a design was produced that limited the interfacial shear stresses at the concrete adhesive interface to less than 0.8 N/mm^2 and the tensile stress in the fibre composite material to 36% of its 2000 N/mm^2 ultimate strength.



Fig. 6 Saw Cutting of Grooves

Installation

Grooves of 20 mm width and 20 mm depth were cut into the slab above the level of the retained steel reinforcement (Fig. 6). Following vacuuming to remove all dust, the groove was primed and then filled with epoxy adhesive to a depth of 10 mm. The carbon fibre "Leonardo" bar, supplied by MBT Degussa, was placed in the centre of the groove before being encased in a final layer of epoxy adhesive and trowelled level. The finished surface was ground level and eventually grit blasted prior to application of an elastomeric membrane.

Surface protection measures

With a span/effective depth ratio of approximately 40:1, the structure had undergone significant deflections in the mid-span regions and vibrations were very noticeable as vehicles impacted the slab at the bottom of the access ramps. In these circumstances it was deemed prudent to provide additional protection to the top of the slab, in particular in areas where tensile cracking would occur.

In the latter positions, around columns, an elastomeric crack bridging membrane was specified while areas in compression were protected with a resin based wearing coat.

RESEARCH REQUIREMENTS

The amount of research work undertaken in respect of NSM reinforcement is very limited in comparison to that relating to externally bonded reinforcement. Areas needing more evaluation include the influence of the following:

- Different methods of concrete surface preparation
- Different methods of bar surface preparation
- Groove geometry
- Groove spacing
- Shear stress at crack discontinuities
- Shear stresses at ends of bars
- Load/deflection behaviour of members with low levels of steel and high levels of FRP reinforcement

It is important to ensure that areas of research work is not duplicated while others are not considered. Consulting Engineers Tony Gee and Partners are collaborating with Cambridge and Edinburgh Universities on a programme of testing to deal with some of these areas of interest. Through networking organisations, such as the UK's CoSACNet, it is hoped that within the next three or four years it will be possible to produce a set of design and construction guidelines that are as comprehensive as those available for externally bonded reinforcement.

REFERENCES

1. Farmer, N. Near-surface-mounted Carbon Fibre Reinforcement, Concrete, Vol. 37, No. 1, January 2003, pp-20-21.
2. The Concrete Society. Technical Report 55: Design Guidance for Strengthening Concrete Structures Using Fibre Composite Materials, The Society, Crowthorne, 2000, 72pp.

A PERFORMANCE-BASED QUALIFICATION SCHEME FOR COMPOSITE MATERIALS SYSTEMS TO BE USED IN THE CIVIL INFRASTRUCTURE

A R Hutchinson & J G Broughton
Oxford Brookes University

S Frost & R J Lee
AEA Technology

N Farmer & I Smith
Tony Gee and Partners

S Luke & L Canning
Mouchel Parkman

ABSTRACT

The growth in the use of composite materials systems for very different applications has signalled the need for more generic guidance in the materials selection, design, application and approval processes. Materials selection can either be prescriptive or performance-based; in the latter case, the performance of the combined system is defined and the testing necessary to verify that performance is prescribed. A performance-based qualification scheme is described that will enable designers to select FRP materials systems based upon performance requirements. The concept of classification schemes that define the requirements of the individual components of a materials system are also introduced; these requirements are linked directly to quality control procedures for on-site application, approvals and long-term assessment. The introduction of such qualification and classification schemes, together with new test methods, will provide engineers with greater confidence in the design and use of FRP materials systems.

INTRODUCTION

Fibre-reinforced plastic (FRP) materials are used increasingly in a large range of civil infrastructure applications, in both new build and repair. The growth in the use of composite materials systems for structural applications, either as the sole material component or for applications that involve concrete, metallic and timber materials, has highlighted the need for more guidance on the design, specification, application and approval processes. A UK DTI-funded project (MMS 6) (www.compclass.org) led by Oxford Brookes University, supported by AEA Technology, Mouchel Parkman and Tony Gee and Partners, is addressing the development of performance-based classification and qualification schemes for FRP material systems. These schemes will enable engineering designers to select FRP material systems based on system performance requirements.

The overall aim of the MMS 6 project is to develop a performance-based qualification scheme to enable designers to select FRP materials systems based upon performance requirements. The specific outputs from the project will include classification and qualification schemes, together with guidance on their implementation, test protocols (laboratory and site-based), and practical application guidance. Test procedures will also be developed for the assessment and acceptance of materials systems on-site, involving the development of manufacturing techniques for on-site fabrication of reliable and consistent test pieces. This latter activity will be linked with the development of in-service monitoring techniques that will employ both destructive and non-destructive testing.

The aims of the MMS 6 project are three-fold:

- To develop a performance-based qualification scheme and component material classification schemes
- To identify, adapt and develop acceptance and quality control procedures associated with on-site applications of materials systems
- To compile guidance on how to incorporate the new classification and qualification schemes, and test procedures, into design and application.

The overall project is split into eleven tasks, structured to meet these aims, as depicted in Figure 1.

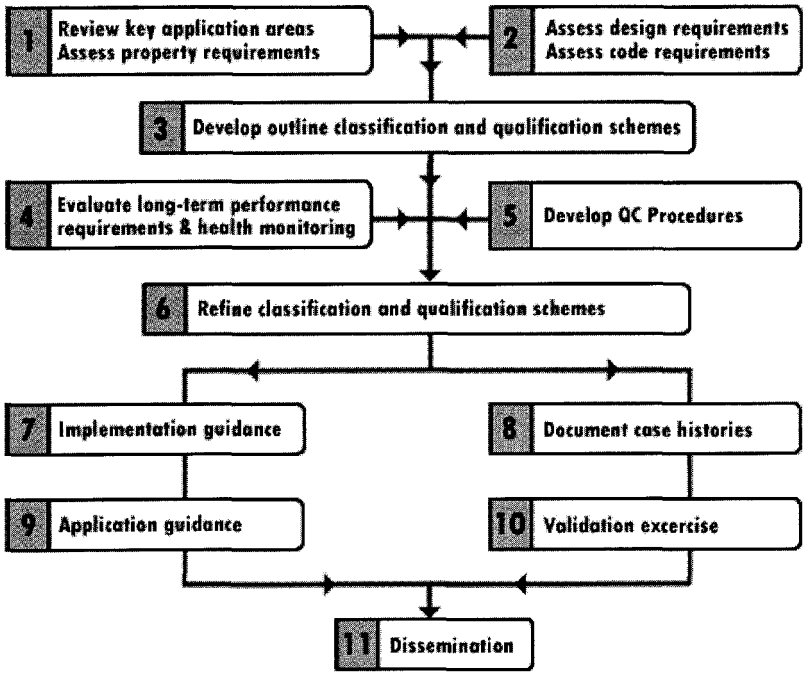


Figure 1. MMS 6 project – work programme

Throughout this paper the following definitions are used:

- COMPOSITE MATERIALS SYSTEMS comprise FRP materials, primers, adhesives or laminating resins (excludes substrate)
- CLASSIFICATION SCHEMES are for individual components of the materials system, e.g. adhesives
- QUALIFICATION SCHEMES provide the materials interface with the design process and installation of the composite materials system to a specific structure.

PRINCIPAL APPLICATIONS

The principal applications of composite materials systems within the civil infrastructure can be split into one of three generic classes:

- Structures – flexural and shear strengthening, stiffening

- Columns – wrapping for impact damage protection and improved seismic resistance
- New build applications – bridges, floors, and beams.

Several reviews of current applications of composite material systems within the civil infrastructure have been carried out for general applications of FRP[1], for concrete[2], for steel, cast iron and wrought iron[3], and for timber[4]. Other relevant sources of information exist [5-13] that provide an excellent overview of current experience, applications, design guidance and material acceptance testing available.

PROCESSES AND PROCEDURES

The four key steps involving the use of FRP materials in any project involve design, specification, application and acceptance. The most common application of composite materials within the civil infrastructure in the UK is associated with flexural strengthening or stiffening of existing structures. In this context, structures imply beams forming parts of bridges, decks or floors. This application has been chosen as the case study for the development of the performance based qualification scheme. For flexural strengthening, the relevant components and definitions are:

- Substrate – parent material comprising the existing structure
- Reinforcement – composite material (fibre and resin)
- Adhesive – bonding agent between the substrate and the reinforcement.

The purpose of a qualification scheme is to identify the stages in the process of design, application and installation where material properties are required to be either defined or measured. The focus of the scheme is on material properties and this covers how they are measured, how they are defined and, importantly, how they are used to assess quality control during application. This last point raises the question as to whether material properties assumed by the designer are actually reproduced during application on site.

The flowchart shown in Figure 2 describes the relationship between the design and installation process and the qualification scheme.

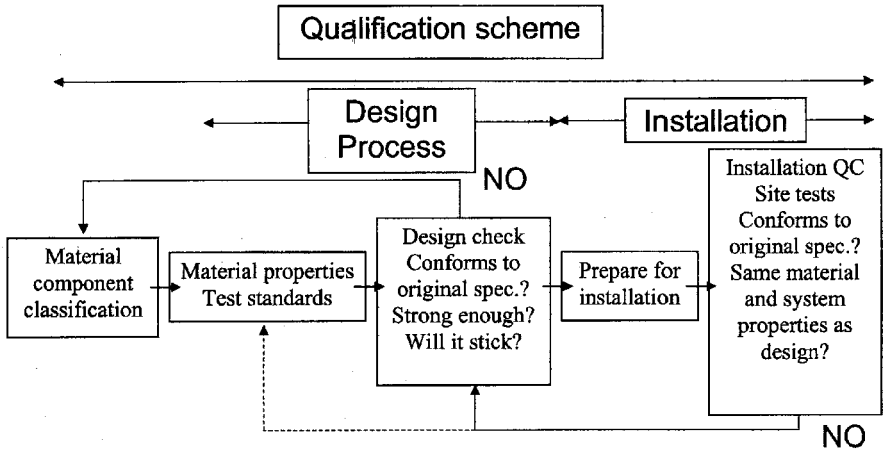


Figure 2. Flowchart summarising the link between design and installation and the qualification scheme

The design process for flexural strengthening can be summarised by the following four steps:

- Material components selection (from classification scheme), including adhesive and composite material
- Material property determination (through appropriate testing)
- Design calculations: the output is the area of reinforcement and stresses within the adhesive layer
- Design check: is the reinforcement strong enough and will the reinforcement remain bonded to the substrate?

It is this final step that links the qualification scheme to the design process. For the designer to check that the design conforms to the original specification, the appropriate performance-based material properties are required. The qualification scheme provides the route, i.e. testing standards and interpretation to obtain these values. Note that if the design does not conform, then the process has to be repeated with alternative material components selected.

The installation process can be summarised by the following three steps:

- Preparation for installation (including substrate surface preparation)
- Application of adhesive and reinforcement
- Quality control checks: does the reinforcement and adhesive conform to the original specification?

The last step links the qualification scheme to the installation process. The qualification scheme will provide the appropriate tests to perform both on-site and off-site, along with the appropriate acceptance criteria. Note that if the installation does not conform to the original specification, i.e. the applied materials are different to that assumed by the designer, then the design can be repeated using the as-measured on-site properties to confirm conformance.

PERFORMANCE-BASED DESIGN APPROACH TO MATERIALS SYSTEM SELECTION

Material selection can either be prescriptive or performance-based. In a prescriptive approach either the materials themselves are defined, e.g. all composite systems for flexural strengthening shall be made from carbon fibre and epoxy resin, or a minimum material property is defined, e.g. all adhesives used in flexural strengthening shall have a minimum lap shear strength of 10MPa. Such a prescriptive approach simplifies the designer's task in terms of material selection but will restrict the flexibility of the design approach in such a way that the design is unlikely to be optimal. Furthermore, it will limit innovation within the design approach and stifle new material developments.

An alternative approach to prescriptive material selection is to base the design and qualification of the material system on a performance-based approach. In such an approach, the material system itself is not prescriptively defined but rather the performance, for example, strain to failure is limited by a Code or Standard and the supplier of the material system demonstrates acceptable performance through testing. Note that the supplier is free to select the materials within the system. This performance-based approach has recently been adopted for the qualification and design of FRP pipes[14].

Despite this performance-based approach, there will be limitations on the range of applications that the composite material system can be applied to for the flexural strengthening of beams. Firstly, material weaknesses of the substrate have to be considered (e.g. delamination resistance of wrought iron or the tensile strength of

concrete). Secondly, the maximum continuous operating temperature of the reinforcing system must be considered (e.g. by limiting this to, say, 20°C below the glass transition temperature of either the adhesive or the laminating resin, whichever is the lowest).

MATERIALS PROPERTIES AND STRUCTURAL REQUIREMENTS

The material properties of the flexural reinforcement, adhesive layer and substrate that are required to design and install to the original design intent are a key element of the QA/QC assessment of the installed reinforcement (Table 1). One of the critical issues with the substrate is defining what quality is required to obtain a sufficient level of adhesion. A Best Practice Guide[15] for the assessment of adherend surface quality provides guidance on the definitions of surface quality.

Item	Key Performance Issues
Substrate (parent material)	• Can the surface be prepared such that a sufficient level of adhesion can be obtained? • Is the resistance to delamination of the substrate sufficient for load sharing with the reinforcement?
Adhesive layer	• Can the adhesive transfer the load between the substrate and reinforcement for the design lifetime? • Will the adhesive remain stuck to the substrate for the design lifetime?
Composite (reinforcement)	• Can the adhesive transfer the load between the substrate and reinforcement for the design lifetime? • Will the reinforcement area be sufficient to provide the required strengthening?

Table 1. Key Performance Issues

CLASSIFICATION SCHEMES

Classification schemes are for individual components of the materials system, such as primers, adhesives, laminating resins and preformed FRP composites. Their use provides the initial materials screen in the design process.

Adhesive materials

The successful application of adhesive materials requires that three fundamental aspects are addressed[16]:

- Working characteristics
- Mechanical performance and bulk property behaviour, including thermal behaviour
- Adhesion and durability.

The working characteristics of an adhesive are critical to successful on-site application, including storage life, usable life and curing requirements. The mechanical properties currently form part of the design requirement and their importance is self-evident. Both of these aspects are handled currently by performance characteristics defined in EN 1504[17]. The third aspect, adhesion, represents the least well understood

of the requirements and yet is crucial for ensuring bond integrity and long-term durability. The performance characteristics defined in EN 1504 are limited in their applicability. In current practice, no QC tests are performed that provide assurance that the adhesive has stuck sufficiently well to the reinforcing or parent materials. Furthermore, there is not normally any direct assurance through testing of the installed system that the adhesive system chosen will be durable for the lifetime of the repair. Appropriate test protocols are required to properly assess adhesion and be linked to QC testing so that a rapid and direct comparison with design data can be made as an assessment of performance and quality of workmanship.

A draft classification, or materials selection, scheme has been devised for adhesive systems that embrace the three essential aspects outlined above. Adhesive systems may be classified using a suite of test procedures that can be shown alongside reference values either for specific application categories (with given loading conditions, parent material type and service environment) or for several categories. The classification does not aim to be prescriptive in terms of setting minimum performance requirements because most design solutions are unique and may require particular property characteristics. However, the framework should ensure that all potential design requirements are met, and that all bulk property and adhesion property requirements are met. The reference data that such Schemes provide will prove useful in design as well as in consideration of QC and long-term test data.

Some new test methods for use on site are under consideration currently that seek to provide alternative and more informative data as compared to the status quo. These methods will embrace working characteristics, adhesion and durability of bonded interfaces. The intent is to rationalise and simplify the contemporary approaches to testing.

Composite materials

Composite materials may be considered either as a prefabricated component or as a site-laminated plate. Prefabricated components may include standard forms such as pultruded rods, bars, beams and plates, or bespoke beams, shells and profiles. Externally bonded reinforcement for flexural strengthening typically involves pultruded plates that can be used either unstressed or prestressed.

A draft classification scheme has been devised for applications involving flexural strengthening. This scheme includes the method of manufacture, the form of composite material, and the loading and environmental requirements that need to be considered for a particular design solution. The performance requirements and test methods associated with three separate aspects are then considered:

- Working characteristics of laminating resins
- Adhesion of laminating resins to different (parent) materials
- Mechanical and physical properties of cured composite materials.

The difficultly of assessing adhesion has been discussed already and methods for addressing this have been considered under the adhesive material classification scheme. On-site manufacture of composite includes wet lay-up, the application of prepreg layers and vacuum infusion. Composite quality is generally far better for prefabricated components.

Composite materials systems may be classified using a suite of test procedures that can be shown alongside reference values. Pathways exist for cross-comparative testing associated with classification, design validation and quality control, in the same way that they do for adhesive materials.

QUALIFICATION SCHEME

A draft qualification scheme has been devised that is based on the flowchart depicted in Figure 2. The principal sequence of steps that is used is:

- Definition of structure, loading and consequences of failure
- Materials system selection, using classification scheme(s)
- Definition of design conditions
- Design input parameters, including partial factors
- Design calculations
- Design checks
- Development of method statement
- Application details
- QA checks
- Inspection and approval checks.

CONCLUSIONS

Performance-based classification and qualification schemes are being developed that will enable engineers and specifiers to select materials systems on the basis of performance requirements. The overall qualification scheme identifies the stages in the process of design and installation where material properties are required either to be defined or measured. It also highlights the question as to whether the material properties assumed by the designer are actually reproduced during application on site. Classification schemes focus on the issue of material properties, how they are measured, how they are defined and, importantly, how they are used to assess the quality control during manufacture and installation.

New QC test methods are being considered for use on site that not only provides more quantitative and meaningful data than current methods, but whose results provide an important link back into the design process. As the MMS 6 project progresses, test methods for the identified critical material properties will be recommended or developed (if no suitable method is available), acceptance criteria formulated and their interpretation in terms of partial factors will be defined. In the authors' view, there is too much emphasis currently on checking component materials that are often well characterised already and not enough on the short- and long-term system performance.

The project is initially focused on developing a qualification scheme specifically for the FRP application of flexural reinforcement. If this development is successful then qualification schemes for other FRP applications will be considered including shear strengthening and column wrapping.

ACKNOWLEDGEMENTS

This paper is based on the early work carried out under contract to the DTI as part of their Materials Metrology Programme within a project, MMS 6, entitled "Classification and assessment of composite materials systems for use in the civil infrastructure (COMPCLASS)". The project's Partners are Oxford Brookes University, AEA Technology, Mouchel Parkman and Tony Gee and Partners. A large Industrial Advisory Group supports the project that comprises materials suppliers, contractors, designers and end-use clients. Further information about the project and a full list of the participants is given in the website: www.compclass.org.

REFERENCES

1. A. Cripps, B. Harris, & T. Ibell. *Fibre-Reinforced Polymer Composites in Construction*, CIRIA C564, London, 2002.
2. Anon. *Design Guidance for Strengthening Concrete Structures using Fibre Composite Materials*, Technical Report No. 55, The Concrete Society, Crowthorne, UK, 2000.
3. Anon. *Strengthening Metallic Structures using Externally-Bonded Fibre-Reinforced Polymers*, CIRIA Report No 645, London 2003.
4. C.J. Mettem & M. Milner. *Resin Repairs to Timber Structures: Volume 1 Guidance & Selection.* High Wycombe UK: TRADA Technology, 2000.
5. L. Hollaway and M.B. Leeming, (eds.). *Strengthening of Reinforced Concrete Structures using Externally Bonded FRP Composites in Structural and Civil Engineering*, Woodhead Publishing, 1999.
6. EUROCOMP. *Structural Design of Polymer Composites – Design Code and Handbook*, E & F N Spon, 1996.
7. S.S. J. Moy, Ed. FRP Composites. *Life Extension and Strengthening of Metallic Structures*, The Institution of Civil Engineers, Thomas Telford, 2001.
8. B. Täljsten. *FRP Strengthening of Existing Concrete Structures – Design Guidelines*, Luleå University of Technology, 2002.
9. C.J. Burgoyne. 'Advanced Composites in Civil Engineering in Europe', *Structural Engineering International* 4/99, 1999.
10. S.M. Halliwell. *Polymer Composites in Construction,* BRE405, 1999.
11. A.R. Hutchinson. *'Forensic Studies of Adhesive Joints,'* Part 6 – Externally Bonded Steel Plate Reinforcement for Concrete Bridges. MTS Project 3 - Environmental Durability of Adhesive Bonds, 1995.
12. A. R. Hutchinson. *Joining of Fibre-Reinforced Polymer Composite Materials,* CIRIA Project Report No. 46, London, 1997.
13. Anon. *Strengthening Concrete Structures with Fibre Composite Materials: Acceptance, Inspection and Monitoring*, Technical Report No. 57, The Concrete Society, Crowthorne, UK, 2003.
14. ISO 14692. Petroleum and Natural Gas Industries: GRP Piping, 2001.
15. R.J. Lee, N.L. Hancox & A.R. Hutchinson. *'The Assessment of Adherend Surface Quality – A Best Practice Guide'*. DTI Report MTS Project 4 - Assessment of Surface Quality prior to Adhesive Bonding, 1998.
16. G.C. Mays and A.R. Hutchinson. *Adhesives in Civil Engineering*, Cambridge University Press, 1992.
17. EUROPEAN COMMITTEE FOR STANDARDIZATION, prEN 1504. Products and Systems for the Protection and Repair of Concrete Structures. Part 4 - Structural Bonding, Brussels.

A REVIEW OF THE USE OF FIBRE REINFORCED COMPOSITES BY THE UK HIGHWAYS AGENCY

Neil Loudon
Highways Agency

ABSTRACT

The United Kingdom Highways Agency have now completed a substantial number of schemes to strengthen existing concrete structures using fibre reinforced composites, mainly column wrapping and deck enhancement. Under consideration are the latest developments in frp technology for strengthening, such as near surface mounted reinforcement systems, but also its use for more fundamental structural applications, such as bridge decking and other parts of the highways infrastructure. There continues to be a lot of activity and interest in the construction industry regarding advanced composites, and therefore it is opportune to summarise and review the current position within the Highways Agency regarding their use, and outline some future activities, to embrace these innovative materials, in research and construction work. The paper does not however address the use of non-ferrous reinforcement for reinforced concrete or applications for suspension or post-tensioning cables.

BACKGROUND

Frp composites consist of high strength fibres, usually composed of carbon, aramid or glass, embedded in a resin matrix. They are not subject to corrosion and are therefore a potential benefit as a low maintenance and durable option for bridge decking and strengthening of structures. An additional advantage is that they can formed into light structures which can be lifted into position with a minimum of disruption to road traffic. Experience in the UK is still relatively limited, but growing rapidly.

Frp bridge decks have been previously used on the Aberfeldy footbridge and Bonds Mill Road Bridge in the UK, and more recently a complete deck was built mainly using frp bonded components at the West Mill Bridge in Oxfordshire. Strengthening schemes are more widespread, and utilise the composites bonded to the structure - there are a number of different production and application techniques. There are however some potential disadvantages in using composites, and areas of uncertainty such as longer term durability, particularly of the resin/adhesive. It is essential that design, installation and management information and best practice is promulgated based on sound research data, to ensure that the materials are used appropriately and can be utilised to their maximum benefit, and can be specified with confidence. However there is likely to be unfortunate consequences if they are used inappropriately, or installed with poor workmanship by unskilled operatives, and so an important message is to understand the limitations of the materials in particular applications.

There is much research work currently being carried out both in the UK and abroad into various aspects of composites and new construction techniques. The Highways Agency commissions some of this research itself and keeps in touch with other work carried out by other researchers and academic institutions, in order to establish its own more specific design guidance, and detailed materials specification.

HIGHWAYS AGENCY – INTRODUCTION OF COMPOSITES

For some years the Agency has been keeping a watching brief on the developments of advanced composites for use in construction. It became clear that materials developed and used in the aeronautical and marine industries had potential uses in bridges and other structures. However it was the advent of the 15 year bridge rehabilitation programme in 1987 and the investigation into 'The performance of concrete in bridges' in April 1989[1], that acted as the catalyst for the introduction of new materials. Greater emphasis was placed on maintenance of the bridgestock. New and innovative solutions were required to strengthen highway structures, to avoid complete rebuilding, and in situations where traffic management and safety constraints, and the need to minimise traffic delays during maintenance operations, were having a significant impact.

Initial ideas involved the use of steel plates bonded to bridge soffits to enhance the bending capacity of bridge decks. To this end the Agency published Advice Note BA30 'Strengthening of concrete highway structures using externally bonded plates' in 1994[2], to provide design rules and an outline specification for steel plate and resin adhesive materials. But it soon became clear that the use of steel plates did not provide all the answers – the plates were heavy, and difficult to handle on site, required rigorous site preparation, as well as significant amounts of bolting through to the concrete substrate. Although they did provide a cost-effective solution to strengthening, nevertheless it was apparent that installation operations would still require extensive carriageway possessions. There were also some concerns about the durability of steel plates and bond to the concrete substrate, and ongoing maintenance liabilities to repaint steel plates periodically. Frp plates were considered as a possible alternative to steel.

In the mid-1990's it also became apparent that some work would be required to upgrade and strengthen bridge supports to withstand greater accidental vehicle impact loadings. Early solutions involved the construction of concrete collars and infill between supports, which were often cumbersome and inelegant solutions, and required long periods to construct. With this in mind the benefits of using composites were considered.

The Highways Agency looked at the available research information and particularly the work to strengthen bridge supports retrofitted for anti-seismic measures. The first practical test was undertaken in 1997 on the A30 Bible Christian Bridge in Cornwall. This was used to assess whether the technique of wrapping bridge columns with composites was viable. It involved the use of glass, carbon and aramid fibre materials applied on three of the bridge supports. The trial was very successful, and proved that the materials were relatively easy to use, although requiring some care and skill as well as environmental controls during installation. Further work ensued at the Transport Research Laboratory, with static and impact testing of various aramid wrapped columns. From this evolved a set of design rules and charts, and some guidance on materials specification. This guidance has now been published as BD 84[3]. As a result many column wrapping schemes have now been undertaken, and these operations are becoming relatively commonplace.

Meanwhile other researchers had been looking at the problems associated with bending deficiencies in bridge decks. In the UK this was undertaken partly through the ROBUST programme, not directly involving the Agency, and also by some pioneering schemes, and by work abroad, particularly the US, Japan and Switzerland. The first Agency scheme was undertaken at M60 Barnes Bridge near Manchester in 1999/2000, and several others have also now been completed. It is expected that a new Standard BD85[4] will be published shortly.

Alongside the strengthening applications, the Agency was also looking at interesting developments in the use of composites for more fundamental structural applications. Initially this was for secondary usage such as the adoption of structural steelwork enclosure to ease access for inspection and maintenance and to provide additional protection against the onset of corrosion. This was first used on the A19 Tees Viaduct, in 1988/89 where a pultruded glass reinforced plastic material in the form of a modular cellular plank system was adopted. Similar arrangements have now been used on a number of bridges based on BD67/BA67[5]. More recently attention turned to the bridges themselves, and decks in particular, to produce options for alternative materials and designs in locations where access was difficult, or carriageway occupation time was very limited. Such situations occur particularly with the construction or reconstruction of bridges over existing railway lines, or where live traffic is involved. Two footbridges have now been built – however the primary support elements are steel suspension cables, although the decks have been formed from grp sections, produced by pultrusion or other techniques.

In the last year several sites have been identified, where it appears to be practical and cost effective to utilise composite decked roadbridges, and benefit from the use of frp in combination with traditional steel girders or precast concrete beams. Another interesting project that is at an advanced stage in planning is expected to utilise glass fibre construction for sign and signal gantries.

HIGHWAYS AGENCY PROJECTS – SELECTED CASE STUDIES

Strengthening - M60 Barnes Bridge at Manchester

The bridge was strengthened in 1999/2000 using carbon fibre plates applied to the soffit of the deck with steel plate strengthening to the top of the deck, rather than composites - principally due to the concerns about damage to frp's beneath surfacing, when subsequent carriageway planing operations are undertaken. In this case the design was based on the approach in Advice Note BA 30[2] dealing with steel plate bonding.

This was an existing 4 span continuous reinforced concrete slab bridge with separate decks carrying the northbound carriageway of the A34, and the combined southbound carriageway of the A34 plus slip road lanes over the M60 Motorway and slip roads near Cheadle. Each deck was skewed at 19 degrees to square. Three spans were constructed from a solid reinforced concrete slab, and the north spans were voided reinforced concrete slabs. Structural assessment of the bridge, completed in 1998, found the superstructure capable of only 17 tonnes assessment live load. The limiting aspect was shear, as the main longitudinal reinforcement was curtailed too close to the hogging regions of the deck at the intermediate supports. Interim measures were installed following the initial assessment, consisting of removal of the hot rolled asphalt surfacing (replaced with a skid resistant waterproofing membrane) and lane reductions. Analysis of the bridge deck for design HA and combined 45 units of HB loading showed that under design loads, strengthening is not only required for shear, but also for bending. The strengthening works to the deck involved increasing the moment capacity of the slab at critical sections by plate bonding. Plate bonding was required both on top of the deck and to the soffit of the slabs adjacent to all intermediate supports. Shear strengthening was effected by the installation of high strength stainless steel threaded bars through the slab at critical sections.

Further strengthening schemes have also now been completed, in some cases they have used carbon fibre bonded plates on the top surface of the deck, but only to

strengthen against relatively minor secondary deck deficiencies. Special consideration is being given to the performance, protection, monitoring and inspection of the buried composites, especially their vulnerability to damage and long term durability. On one further scheme at the A38 Western Interchange in Cornwall carbon fibre plates have been used to strengthen an abutment, and also for the first time to strengthen a deck against minor shear deficiencies using preformed 'L' shaped plates. This is an area where there has been comparatively little site experience, research or published data.

Column wrapping - M11 Coopersale Bridge, Essex

This was the first Highways Agency column wrapping project completed, and the columns were strengthened by wrapping with layers of wet-lay aramid. Design was undertaken on the basis of the published Advice Note BA84[3]. This project was very successful and resulted in about a 50% saving in costs and time, compared to other strengthening schemes. In fact the bridge was destined for demolition and reconstruction, and the use of composites provided part of the justification for retention.

Footbridges – A30 Halgavor and A5 Wilcott Bridges

In the last two years Highways Agency have completed two footbridges utilising composite deck systems. The first such structure to span a Trunk Road was Halgavor Bridge carrying cycle, foot and equestrian users over the A30 in Cornwall. This was a landmark structure representing the best practice in design and construction under the Government's 'Better Public Buildings' initiative launched in October 2000. The suspension bridge which formed a vital link in the 180 mile Cornish Way, and part of the National Cycle Network, promoted by SUSTRANS, and was situated adjacent to the National Trust's Llanhydrock House. It was supported by a £50,000 grant contribution from the Millennium Commission. The bridge has utilised the advantages of traditional construction materials such as concrete and stainless steel, for foundations and suspension cables (as the primary means of support) and glass fibre reinforced composites for the deck. The material had considerable advantages, in being light and easily handled and not subject to corrosion, and therefore offered a low maintenance and durable option for bridge decking. It also allowed prefabrication under factory controlled conditions, and to be lifted into place during a single night time occupation of the Trunk Road, minimising the effects on traffic. The bridge utilised a combination of grp moulding and resin infusion processes, using expertise derived from the marine industry. At the ends of the bridge, traditional skills have been used to construct a typical Cornish drystone wall, to reflect the position of the structure in the landscape, and blending old crafts with modern design and materials.

The second footbridge in Shropshire was similar in form, but utilised a commercially available grp modular pultuded cellular plank deck system. This allowed the deck to be formed from standard components, bonded together to form the box section required for the deck. The completed Wilcott Footbridge which forms part of the new Nesscliffe Bypass is an elegant but simple structure. The use of the grp deck significantly reduced the time to build, and in fact the deck was erected in just two days.

Roadbridges

As mentioned earlier the Highways Agency is seeking opportunities to utilise composites for more fundamental applications. Building on the experience from the two

footbridges, and other structures in the UK and worldwide, opportunities for roadbridges have been investigated. Research has been commissioned at TRL, to investigate the fatigue loading of deck panels, and is aimed at producing generic guidance, on the design of road decks, which will be published in due course.

With the recent Government announcement of a substantial programme of road building including widening existing roads, and new schemes, there are opportunities for innovative solutions for bridging existing carriageways and other obstacles, and for bridge rehabilitation. One option is the use of lightweight frp bridge decks, which can be fabricated adjacent to trunk roads and erected rapidly with minimal road closures. The most economic solution is an frp roadway deck on steel girders or concrete beams, but complete frp decks may be feasible for short span structures. Frp promises low cost off-the-shelf durable bridge systems, which can be easily maintained.

Some of the benefits include:-
a) Safe and durable material for bridge construction
b) Rapidly installed lightweight decks - economic over live carriageways/railways with less disruption to road and rail users, with reduced possession costs and traffic management
c) Durable alternative to orthotropic steel decks for long-span cable stay/suspension bridges
d) Low maintenance as frp's are not affected by de-icing salts
e) Cost effective bridge rehabilitation – reduced deck weight
f) Can incorporate remote high-tech monitoring systems

Key issues for specifiers include:-
a) There are a number of experienced UK designers
b) A draft Standard for the use of frp has been developed (not yet published)
c) Costs are expected to be lower in whole life terms where there are significant traffic delays or railway possessions, and critical construction operations can be reduced in duration
d) Design and detailing requires special expertise
e) Procurement - it is desirable to utilise early contractor involvement
f) Good durability and lower maintenance costs anticipated

Several sites have now been identified where there is potential to utilise frp decks, and over the coming months it is hoped that these schemes will be taken forward.

Gantries

An innovative, aesthetic, low maintenance, standard sign/signal gantry design using frp materials has been developed by the Agency in partnership with consultants, as an alternative to existing steel and concrete gantries, for the ASTIS project in the Bristol area. The preliminary design originally identified a requirement for 45 new portal gantries on the scheme. Following discussions between the designer and the Agency the feasibility of a new gantry design was investigated. A review of the current steel and concrete gantry designs, considering the proposed gantry locations, construction, maintenance and health and safety issues, suggested the benefits of an alternative gantry design. The objectives were to address the issues identified with current gantry designs, and to develop a functional low maintenance and aesthetically attractive design. The

feasibility study demonstrated that an frp gantry would meet the desired project objectives with an equivalent whole life cost to conventional gantries. It has also some other advantages:

a) Spans of 46metres without central supports, to span dual 4 lane motorways
b) Manufacturing resources outside traditional suppliers
c) Slender structure with good aesthetics, low visual intrusion, but still functional
d) Lightweight structure allowing speedy erection, with minimal traffic disruption
e) Gantries could be easily adapted for future re-use as combined use footbridges
f) Whole life costs close to current alternatives
g) 4.5metre fixed sign envelope over the carriageway, to meet current/predicted future needs
h) Future proof in terms of all combinations and layouts of signals and other fixed equipment
i) Frp materials are durable, requiring very low maintenance with a high quality finish. Frp consumes less energy in production than steel or concrete
j) Full scale ergonomic assessment was successfully undertaken for all maintenance operations
k) Unique centrally mounted fixed signs allow a dual access walkway for full access to all installed equipment

It is expected that this project will proceed in the coming months.

MONITORING AND MANAGEMENT

Until recently there has been comparatively little information available on the longer term durability and performance of composites and adhesives used in the construction sector, though there is much that can be inferred from examination of other industries such as maritime and aerospace, where similar materials have been successfully used in aggressive environments for many years. The general expectation is that composites will have service lives of 30 years, probably a lot longer, with minimal requirements for interim maintenance. The initial Agency projects have developed an adhoc approach to 'in service' monitoring, with relatively short intervals between inspections, until greater confidence in performance is gained. Additional composite coupons have been bonded on to structures away from the strengthened areas and on to specimen blocks, which can be subjected to periodic testing.

It is evident that monitoring and testing is an area where there has been comparatively little research and guidance. Other than unsophisticated 'hammer tapping' techniques there are no available robust site test methods, though the use of fibre optics, thermography and acoustic emission appear to be promising. This is important as it will provide a quality control procedure during the installation process, but will also allow periodic management of in-service structures. Together with the development of new testing methods is the need for performance criteria – what is the significance and acceptability of defects in the bond, or in the component materials themselves?

It is generally accepted that it is fairly easy to repair damaged composites, but there is no authoritative guidance available, particularly where the materials are used in

combination with concrete or steel as a means to enhance the strength. Contingency arrangements must be put in place in Maintenance Manuals for schemes under construction, and other guidance produced.

However the situation has considerably improved through the publication of the Concrete Society Technical Report TR57 'Strengthening concrete structures using fibre composite materials: acceptance, inspection and monitoring'[7], produced by a healthy cross industry collaboration, and including the author representing the Agency. This provides guidance for the first time in one document, on the management of frp strengthened structures, and useful information on the state of development of various NDT techniques and monitoring systems.

SPECIFICATION AND TECHNICAL APPROVAL

The Highways Agency has a well developed system of technical approval in place to ensure that consistent standards are adopted for the construction and strengthening of new and strengthened structures. Where no suitable or relevant Agency standards exist, as is often the case with composites, departure from standard procedures apply. However as standards for column and deck strengthening using composites are published, this requirement will be relaxed.

The Highways Agency has not yet published generic specifications for composites, covering materials and installation issues, though previous schemes have used adhoc documentation, subject to departure procedures. The specifications are being developed based on experience, and best practices for manufacture and installation. Key aspects are to ensure that work is only undertaken by suitably experienced contractors and operatives, and using materials that have been subject to rigorous quality control procedures. Suitable performance criteria are also required.

QUALITY ASSURANCE

Alongside Agency initiatives, it is clear that the composites industry needs to work together to ensure that it is regulated. One part of this process is the establishment of certification schemes covering manufacture and particularly installation, to ensure that best practices are adopted. There have been some attempts to rectify this, but the relatively small market for composites and the disparate nature of the composites applications and the range of materials and production techniques does present challenges. A project currently underway as part of the DTi materials metrology programme and lead by Oxford Brookes University, and intended to classify composites, may provide a basis for future certification schemes.

HIGHWAYS AGENCY RESEARCH

As has already been mentioned the Agency has completed a number of research contracts, focussed on strengthening bridge supports. More recent work has investigated the fatigue performance of modular frp bridge decking panels. Another project has considered various aspects of frp's - bond strength between concrete and an frp, minimum bend radius for complex geometric shapes, the effects of voids/debonding and the use for shear strengthening.

The Agency has been involved in several other research activities with partners and undertaken by cross industry collaboration. The author has chaired three Concrete Society Steering Groups to produce design guidance for strengthening concrete

structures using frp (TR55)[6], and the in-service management of such structures (TR57)[7]. The first has found widespread usage worldwide and is currently being updated.

Highways Agency have been very pleased to be involved with the Network Group for Composites in Construction (NGCC), which was established by BRE with DETR funding. The principal aims have been to facilitate the exchange and dissemination of information, and establish research needs, as well as promote the responsible use of composites.

THE WAY FORWARD

It is evident that there is a lot of activity concerning composites, both in terms of research and for actual applications. The construction industry has in the past been accused of being somewhat conservative and slow to embrace innovation. With composites there is an excellent opportunity for all parties in the supply chain to work together to ensure that the benefits of these materials are obtained, but there must be technical guidance to ensure materials are used appropriately.

The Highways Agency is in a position to promote and be pro-active in the adoption of these innovative materials. The main areas for the future concern design guidance, specification, quality control systems, the need for research to plug any potential gaps particularly over the long term durability of composites, and the establishment of appropriate techniques for managing, monitoring and inspecting and testing of composites in service. The provision of training and guidance to Agency staff likely to be involved with composites in the future will also be important.

Particular aspects for the future:-

a) Gradual relaxation of design criteria, building on increased confidence of the performance of composites in service.

b) Improved testing and monitoring techniques.

c) Better information on durability.

d) New applications – use of frp for structural appications, lighting columns, non-ferrous reinforcement, post-tensioning cables, drainage pipes etc..

e) Industry education

REFERENCES

1 Highways Agency, *The performance of concrete in bridges – a survey of 200 highway bridges*, HMSO, April 1989

2Highways Agency, *BA30 Strengthening of concrete highway structures using externally bonded plates,* Stationery Office, 1994

3 Highways Agency, *BD84 Strengthening of concrete bridge supports for vehicle impact using fibre reinforced polymers,* Stationery Office, 2002

4 Highways Agency, *BD85 (draft) Strengthening of highway bridges using externally bonded fibre reinforced polymer*, Unpublished, publication expected 2004

5 Highways Agency, *BD67/ BA67 Enclosure of bridges,* Stationery Office, 1996

6 Concrete Society, *TR55 Design guidance for strengthening concrete structures using fibre composite materials,* Concrete Society, 2000 (currently being updated expected 2004)

7 Concrete Society, *TR57 Strengthening concrete structures using fibre composite materials: acceptance, inspection and monitoring*, Concrete Society, 2003

FIELD TESTING AND LONG TERM MONITORING OF WEST MILL BRIDGE

Dr. Lee Canning, Dr. Sam Luke – Mouchel Parkman,
West Byfleet, Surrey, KT14 6EZ
Prof. Bjorn Taljsten –
Skanska Teknik AB, Sweden
Mr. Peter Brown
Oxfordshire County Council, Oxford.

SUMMARY

West Mill Bridge, the first FRP composite bridge on the European public highway network, spans over the River Cole in Oxfordshire, UK, and was opened on 29th October 2002. The bridge has a span of 10 metres, a width of 6.8 metres and carries two traffic lanes and footpaths.

To determine the in-service structural performance of the bridge, conventional and novel monitoring systems were installed during the fabrication of the bridge superstructure. The data from the initial load test on the bridge is presented and various aspects compared with the predicted design performance. The static deflection of the bridge under the test load was within 15% of the predicted value using theoretical and numerical analyses. The degree of composite action between the decking and main longitudinal beams, in particular, and other secondary structural elements has a significant effect on the global flexural rigidity of the structure, which is discussed in light of the strain data obtained during the load test.

The fabrication of the bridge superstructure was completed in 7 days, and the construction methods used for the FRP composite superstructure of West Mill Bridge are described, highlighting the advantages and disadvantages. Conclusions and observations are presented on the short-term structural performance and the efficiency of the methods used for the construction of West Mill Bridge.

WEST MILL BRIDGE

West Mill Bridge was reconstructed in October 2002. The bridge carries the B4508 over the River Cole in Oxfordshire and had a span of 7.6 metres. The new bridge has a span of 10 metres, and the width was increased to 6.8 metres to carry two lanes of traffic and footpaths. A photograph of the old and new bridges is shown in Figure 1. The new bridge was comprised of reinforced concrete spread footings and abutments with brickwork facing, supporting four longitudinal beams and the bridge deck. The longitudinal beams were manufactured from GFRP composite box beams with uni-directional CFRP composite flanges to provide the required global flexural rigidity (the manufacture and proof testing of the longitudinal beams is described in Taljsten, 2002). The deck consisted of a series of adhesive bonded advanced composite ASSET profiles (described in detail in Luke et al, 2002) spanning transversely, on which the polymer concrete surfacing and epoxy wearing course for the carriageway were located. In addition, reinforced concrete parapet edge beams (using stainless steel) held the parapets in place and in turn were anchored through the ASSET deck. Figure 2 shows the cross-section at midspan of the reconstructed West Mill Bridge.

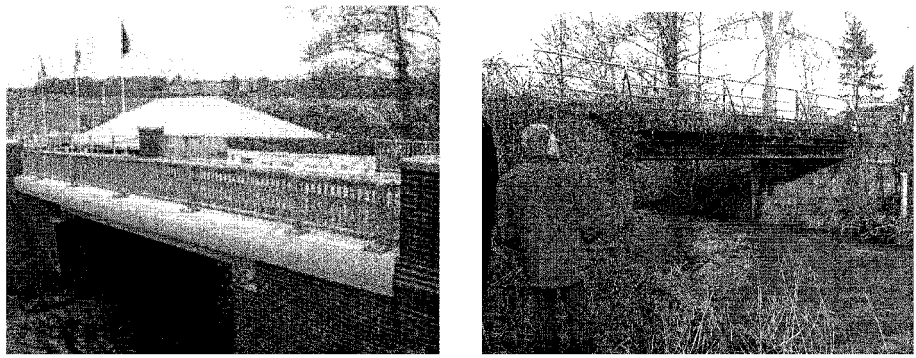


Figure 1 – New and Old West Mill Bridge, Oxfordshire

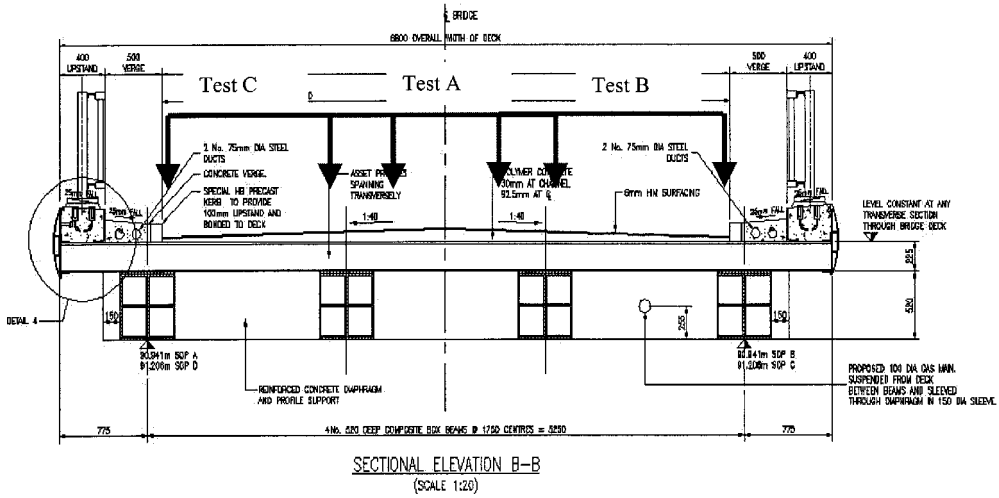


Figure 2 – Cross-section of Reconstructed West Mill Bridge With Load Test Vehicle Locations

INSTRUMENTATION AND LOAD TEST ON WEST MILL BRIDGE

To determine the in-service structural behaviour of West Mill Bridge, dial gauges, electrical resistance strain gauges and optical fibre sensors were installed during the bridge fabrication and installation. Figure 3 and Table 1 show the location and type of each instrumentation point.

A load test was undertaken, using a 28 tonne lorry with a front axle of 7520kg, and two rear axles of 8920kg each , prior to the opening of West Mill Bridge to the public. To obtain a complete description of the structural behaviour, three sets of load tests were undertaken; the first with the lorry travelling in increments at the centre of the carriageway (Test A), the second flush with the Eastern edge of the carriageway (Test B), and the third flush with the Western edge of the carriageway (Test C). The lorry was moved at 1 metre intervals for the first load test, and at 2 metre intervals for the second and third load tests at the edges of the carriageway. Strain and deflection data were

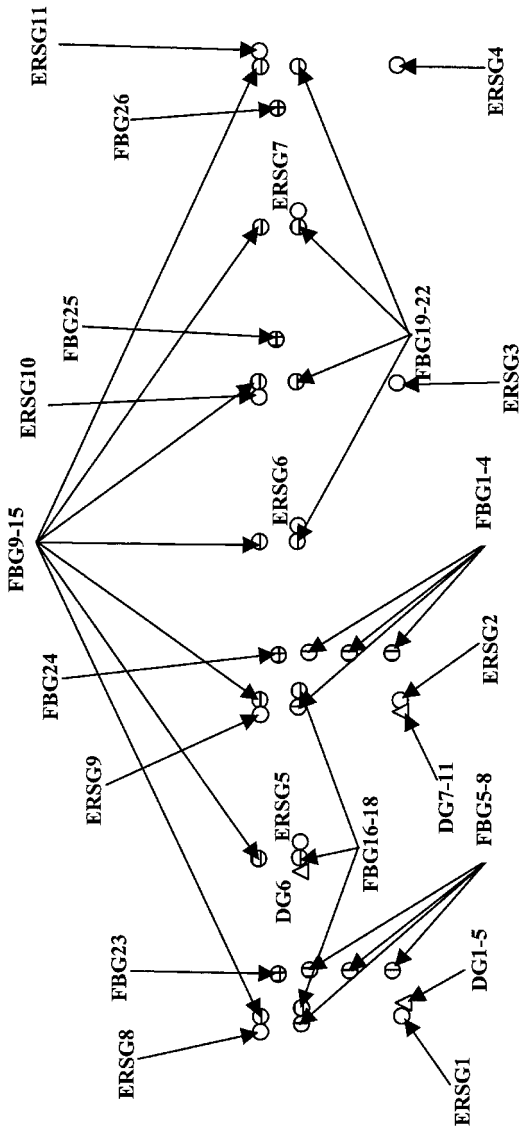


Figure 3 – Location of Sensors on Bridge Superstructure
(FBG = Fibre Bragg Grating, ERSG = electrical resistance strain gauge, DG = deflection dial gauge)

Table 1 – Location and Type of Instrumentation

Reference	Location/Type
FBG1	FBG sensor at bottom of web of internal beam, midspan (longitudinal).
FBG2	FBG sensor at middle of web of internal beam, midspan (longitudinal).
FBG3	FBG sensor at top of web of internal beam, midspan (longitudinal).
FBG4	FBG sensor at internal beam top flange/ASSET deck bottom flange bonded interface, midspan (longitudinal).
FBG5	FBG sensor at bottom of web of external beam, midspan (longitudinal).
FBG6	FBG sensor at middle of web of external beam, midspan (longitudinal).
FBG7	FBG sensor at top of web of external beam, midspan (longitudinal).
FBG8	FBG sensor at external beam top flange/ASSET deck bottom flange bonded interface, midspan (longitudinal).
FBG9-FBG15	FBG sensors at top flange of ASSET deck, midspan (transverse).
FBG16-FBG22	FBG sensors at bottom flange of ASSET deck, midspan (transverse).
FBG23-FBG26	FBG rosette sensors at bonded ASSET deck web interface over Beams 1, 2, 3 and 4, midspan (transverse).
ERSG1-ERSG4	ERSG sensors at soffit of Beams 1, 2, 3 and 4, midspan (longitudinal).
ERSG5-ERSG7	ERSG sensors at soffit of ASSET deck between Beams 1, 2, 3 and 4, midspan (longitudinal).
ERSG8-ERSG11	ERSG sensors at outer surface of top flange of ASSET deck above Beams 1, 2, 3 and 4, midspan (longitudinal). Note ERSG 8 failed.
DG1-DG5	Dial gauges at soffit of Western edge beam, at bearings, ¼ span, midspan, and ¾ span.
DG6	Dial gauge at soffit of ASSET deck between Western edge beam and Western central beam, midspan.
DG7-DG11	Dial gauges at soffit of Western central beam, at bearings, ¼ span, midspan, and ¾ span.

recorded manually and electronically immediately prior to the load test, at each increment, and immediately after the lorry moved off the bridge.

The reasons for the load test were:

i) as a proof test for the client, Oxfordshire County Council,

ii) to obtain baseline data for comparison with any longer-term structural monitoring and data acquisition,

iii) to determine the degree of composite action between the ASSET deck and the longitudinal beams. This data could then be used for further design guidance.

RESULTS OF LOAD TEST ON WEST MILL BRIDGE

Figures 4, 5 and 6 show the longitudinal tensile strain at the lower flange of the longitudinal beams at the quarter and mid-span locations for the three load tests with the lorry located at midspan. In addition, theoretical strains assuming simply supported end conditions are shown in Figure 4, for two particular design assumptions:

i) No composite action between any deck components; the four longitudinal beams provide the flexural rigidity,

ii) Full composite action between the longitudinal beams, ASSET deck, and reinforced concrete parapet edge beams.

It was also assumed for the theoretical calculations that no wheel load distribution occurred through the depth of the ASSET deck.

Figure 7 shows the longitudinal strain profile for Tests A, B and C, at midspan, at the location of Beam 2. Figures 8 and 9 show the maximum deflections measured along the lower flanges of the internal and edge main beams with the lorry rear axles

located at midspan (the front axle being off the bridge deck). The maximum deflection of the ASSET deck soffit between the West edge beam and West central beam, at dial gauge 6, was measured as 1.68mm.

The strain data from the FBGs are shown in Figures 10-14. The steps in strain are due to the incremental movements of the lorry across the bridge. The longitudinal strains measured by the FBGs generally compare well with the strain data gathered from the ERSGs, the maximum measured longitudinal strains being 90 and 75 microstrain respectively. The maximum principal shear strain in the web of the ASSET profile, calculated from the FBG rosette readings in Figure 12, was approximately 100 microstrain. The maximum transverse compressive and tensile strains in the transverse sagging region were approximately 50 and 65 microstrain respectively.

DISCUSSION OF LOAD TEST RESULTS

The measured longitudinal strains on the lower flanges of the main beams show that a large degree of composite action is present between the main beams, ASSET deck and other deck components. From the change in depth of the neutral axis at the outer main beam locations, it is apparent that the reinforced concrete parapet edge beams contribute to the global flexural rigidity of the bridge deck significantly.

The strain profiles and deflections at various transverse locations allow the degree of composite action between various components to be ascertained based on linear elastic bending theory. The strain data in Figures 4, 5 and 6 show that the end conditions as-built were essentially simply-supported with no compressive strains measured in the lower flanges of the main beams near the ends of the span. Table 2 shows the calculated flexural rigidity of the bridge deck from theory, and using the data obtained from the load test.

Table 2 – Theoretical and In-Service Performance of Bridge Deck

Degree of composite action	Flexural rigidity, kNm^2	Height of the neutral axis, mm	Midspan deflection, mm
FRP composite main beams only. (Theoretical)	207,400	260	4.60
FRP composite main beams and GFRP composite deck. (Theoretical)	323,600	335	2.95
FRP composite main beams, GFRP composite deck and RC parapet edge beam. (Theoretical)	641,800	457	1.98
FRP composite main beams, GFRP composite deck and RC parapet edge beam, with spring connections. (FE Model)	552,500	360	2.30
Load Test Results (central beam)	552,500	490-520	2.01

From Table 2, the actual degree of composite action between the ASSET deck and longitudinal main beams from the load test was very high. Other types of structural connections, such as that described in Gangarao et al (1999), generally show a lesser degree of composite action between the advanced composite deck and main beams. The presence of full composite action between the bridge deck components, in the case of West Mill Bridge, effectively doubled the short-term global flexural rigidity of the bridge deck. This is of particular importance, as the design of FRP composite bridges is often critically dependent on the deflection limit, i.e. flexural rigidity.

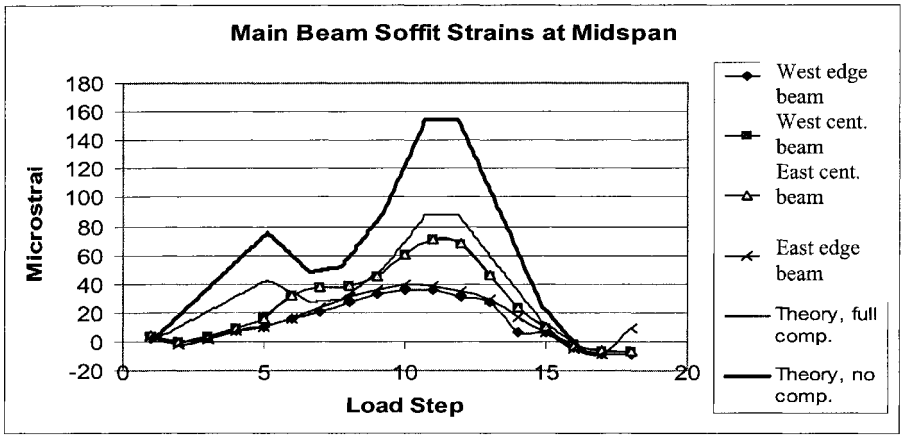


Figure 4 – Longitudinal Strain at Soffit of Beams 1-4 at Midspan for Test A

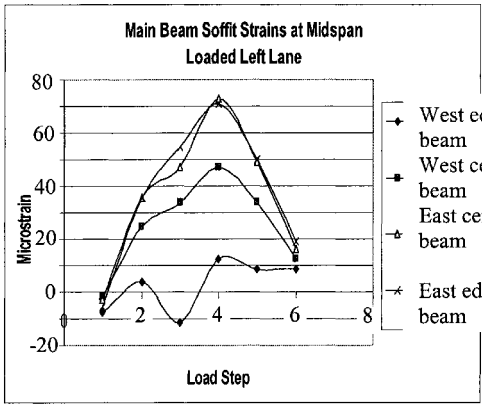


Figure 5 – Longitudinal Strain at Soffit of Beams 1-4 at Midspan for Test B

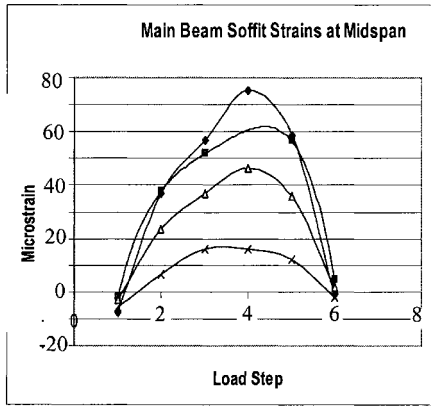


Figure 6 – Longitudinal Strain at Soffit of Beams 1-4 at Midspan for Test C

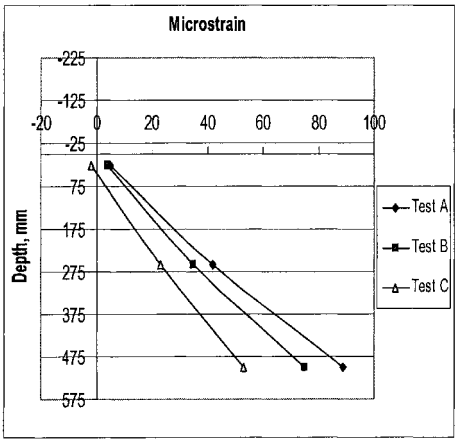


Figure 7 – Longitudinal Strain Profile at Midspan, Western Central Beam

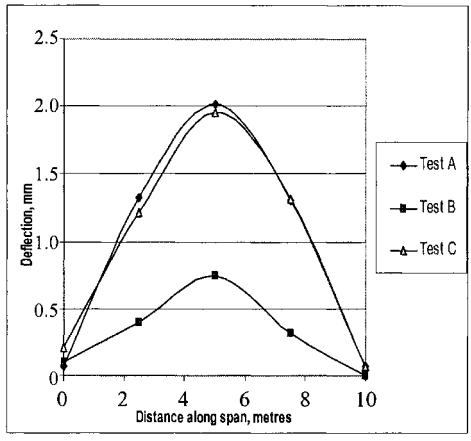


Figure 8 –Deflection Along Soffit of Western Central Beam Under Maximum Load

More effective means of achieving composite action between structural components can possibly allow more efficient FRP composite bridges to be design and constructed. However, this would also be dependent upon the long-term effectiveness of any connections, whether mechanical or chemical (adhesive bonded).

The maximum transverse compressive and tensile strains in the top and bottom flanges of the ASSET profile should theoretically be the same. However, the tensile strains were generally greater than the corresponding compressive strains (for example, FBG21 in Figure 13 and FBG14 in Figure 14). This may be due to the presence of the polymer concrete surfacing and it's stiffening effect on the top flange.

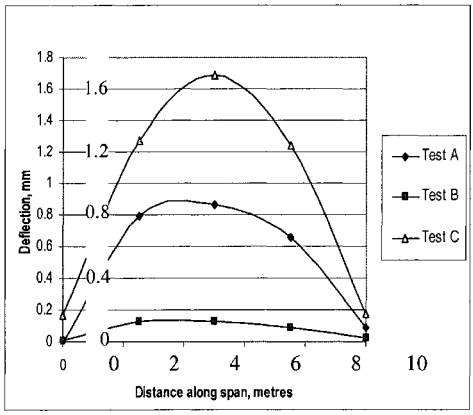


Figure 9 –Deflection Along Soffit of Western Edge Beam Under Maximum Load

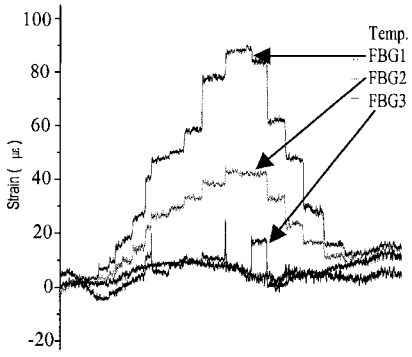


Figure 10 – Tensile Strain Readings on Web of Central Longitudinal Beam, Test A

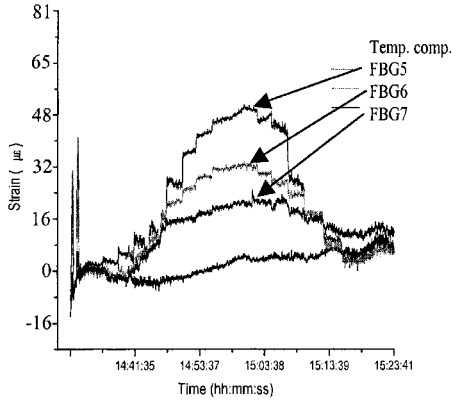


Figure 11 – Tensile Strain Readings on Web of Edge Longitudinal Beam, Test A

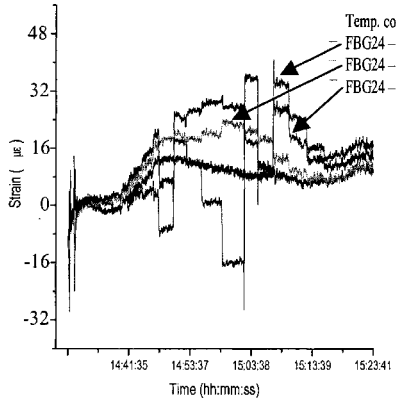


Figure 12 – Typical FBG Rosette Readings on External Web of ASSET Profile

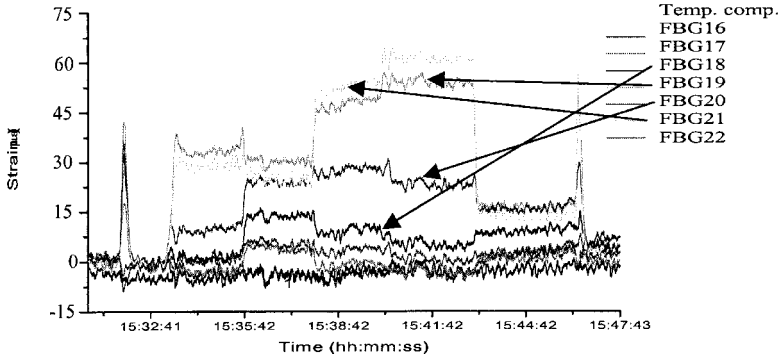


Figure 13 – Transverse Strain Readings on the soffit of the ASSET Profile Deck (Black line – temperature compensation), Test C

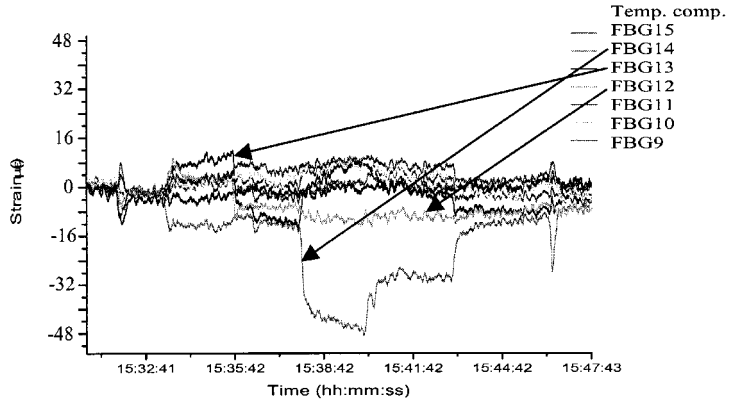


Figure 14 – Transverse Strain Readings on the top flange of the ASSET Profile Deck (Black line – temperature compensation), Test C

STRUCTURAL MONITORING SYSTEM

The application of both electrical resistance strain gauges and optical fibre sensors was, in part, to confirm the viability of using an optical fibre monitoring system for long-term structural monitoring. The maximum difference between the optical fibre results and electrical resistance strain gauge results was 15%, which is relatively small for field applications.

The optical fibre monitoring system is described fully in Gebremichael et al (2003), and consisted of 41 ruggedly protected fibre Bragg Grating sensors (FBGs) on 8 parallel channels. A total of 10 electrical resistance strain gauges were installed to provide the basis of acceptance of the structural performance of the bridge deck by the client, and for comparison with the FBGs. It is possible to monitor these sensors in the long-term, but it is well known that some drift for the results from the electrical resistance strain gauges is probable.

CONSTRUCTION OF WEST MILL BRIDGE

The first stage in the construction of the new West Mill Bridge was demolition of the existing bridge deck and the abutments, due to the increase in deck width. Sheet pile cofferdams were installed on either side of the river using traditional driving methods,

to enable the new reinforced concrete abutments to be constructed. During the abutment construction the site factory for fabrication of the bridge deck was erected adjacent to the existing bridge site, comprising a large tent and hardstanding.

The advanced composite main beams were then located on the hardstanding and the concrete diaphragm beams cast in-situ. The ASSET profiles were transported to site in factory pre-bonded deck panels consisting of 7 bonded profiles. This reduced the amount of site bonding, a specialist activity, to a minimum. The deck panels were then lifted, positioned and bonded one at a time, with the required surface preparation (abrading and degreasing) carried out on the main beams and deck panels. The final stage of fabrication was locating of the composite edge fascia plate on the sides of the bridge deck, bonding of the GFRP composite permanent shuttering for the concrete edge beam, and casting of the concrete edge beams with the parapet post anchor bolts.

Due to the lightweight nature of the bridge deck, weighing approximately 30 tonnes prior to application of the surfacing, of which the composite components weighed 12 tonnes, a relatively small crane was used to lift the bridge deck into position onto the abutment bearing shelf. This is approximately one third of the weight of a comparable reinforced concrete bridge. The polymer concrete and epoxy-based wearing course were then applied on the deck to form the running surface. Other items such as the parapet barrier, expansions joints and earthworks were then completed and the bridge officially opened on 29th October 2002.

Discussion of Construction Process

The items described below relate to construction processes for bridges using FRP composite materials.

The main advantages are:

i) lightweight nature of components, leading to easier handling and faster installation,
ii) lightweight nature of components, leading to the use of lighter cranes (if required),
iii) lightweight nature of components, leading to ease of transport to site,
iv) lightweight nature of components, providing the possibility of minimal foundation/substructure requirements,
v) use of modular construction, leading to simple on-site construction processes,
vi) safer construction environment for site operatives, due to reduced on-site fabrication.

Some disadvantages are:

i) Requirement for environmental control if adhesive bonded joints used,
ii) Increased on-site quality control and site supervision due to novel nature of materials
iii) Increased on-site quality control and site supervision due to high degree of dependence of bonded joints on workmanship.

All these advantages and disadvantages were present during the construction of West Mill Bridge. The programme of construction was 3 months long, of which approximately 2 months was taken for demolition and substructure works, and approximately 2 weeks for associated construction activity, such as installation of drainage and highway approach works. The fabrication of the bridge superstructure took approximately 7 days comprising:

i) Location of the longitudinal beams on the temporary hardstanding.
ii) Location of the end diaphragm steel reinforcement and casting of concrete.
iii) Delivery of 7 ASSET deck panels, each panel consisting of 5 bonded ASSET profiles and weighing approximately 1 tonne.
iv) Surface preparation of the top flange of the longitudinal beams (light grinding and degreasing) and bottom flange of the first ASSET deck panel.
v) Adhesive application on prepared surfaces, precise locating and bonding of first ASSET deck panel.
vi) Surface preparation of webs on adjoining ASSET deck panels and bonding of the subsequent ASSET deck panels.
vii) Surface preparation and bonding of GFRP composite angle sections as permanent shuttering for reinforced concrete edge parapet beam.
viii) Fixing of GFRP composite edge fascia panels using slotted and bolted connections to allow future removal and replacement, if required.
ix) Location of steel reinforcement and through-deck anchor bolts for edge parapet beam and casting of concrete.
x) Installation of edge parapet barriers.

The instrumentation was installed concurrently with the deck fabrication with no loss of field instrumentation. The expansion joints, footpath concrete and kerb, polymer concrete surfacing and epoxy based wearing course were installed once the bridge deck was lifted in by crane.

Further field monitoring of West Mill Bridge is planned and will allow the long-term performance of the bridge to be assessed. In particular, the structural properties of the FRP composite deck, FRP composite main beams and the integrity of the adhesive bond between them, will be assessed to provide information for future specifications and designs.

ACKNOWLEDGEMENTS

The authors would like to acknowledge City University, London, and Cranfield University, Cranfield for the provision and installation of the fibre optic monitoring system, and Oxfordshire County Council as the bridge owner. The authors would also like to thank the European Commission for funding the research and development phase of the ASSET FRP composite deck system.

REFERENCES

Gangarao, H.V.S, Thippeswamy, H.K., Shekar, V., and Craigo, C., 'Development of Glass Fibre Reinforced Polymer Composite Bridge Deck', SAMPE Journal, 35(4), pp12-24, 1999.

Gebremichael, Y.M., Li, W., Meggitt, B.T., Boyle, W.J.O., Grattan, K.T.V., McKinley, B., Fernando, G.F., Kister, G., Winter, D., Canning, L., Luke, S., 'Integration and Assessment of Fibre Bragg Grating Sensors In Europe's First All-Fibre Reinforced Polymer Composite Road Bridge', Journal of Structural Health Monitoring (to be published).

Luke, S., Canning, L., Collins, S., Brown, P., Knudsen, E., Olofsson, I., 'The Development of an Advanced Composite Bridge Decking System – Project ASSET', Structural Engineering International, Volume 12, Number 2, 2002.

Taljsten, B., 'Proof Testing and Manufacture of Main Beams For West Mill Bridge', NGCC 2nd Annual Conference on Design, Specification and Construction of FRP Structures, Solihull, UK, 30th October 2002.

CIRIA C595 – STRENGTHENING METALLIC STRUCTURES USING EXTERNALLY-BONDED FRP

Tim Stratford
The University of Edinburgh

John Cadei
Independent Consultant

Len Hollaway
The University of Surrey

SUMMARY

Fibre-reinforced polymers (FRPs) are being increasingly used to strengthen metallic structures. The current best-practice for this technique is described in the recently published CIRIA report '*Strengthening Metallic Structures using Externally-Bonded FRP*'. The report covers all aspects of a strengthening scheme, including procurement, design, installation, and inspection. It is thus of interest to clients, consultants, contractors, and materials suppliers. This paper gives an overview of the report and summarises its findings. Aspects of particular importance to strengthening metallic structures using FRPs are highlighted and discussed.

INTRODUCTION

Fibre-reinforced polymer (FRP) materials are particularly suited to strengthening and repairing existing structures, and being increasingly used to extend the life of metallic infrastructure. FRP, bonded to the external surface of an existing metallic structure, can be used to provide an increase in strength and stiffness, replace material lost by damage or corrosion, extend the fatigue life, or allow a change in the structure's use.

FRP strengthening for metallic structures is a rapidly developing technique, and many of its applications have been realised in the UK. For example, Figures 1 & 2 show a cast iron bridge and a curved steel beam in a building, both strengthened using FRP. Very little guidance, however, is currently available on the subject. CIRIA (the Construction Industry Research and Information Association) commissioned a report to establish best-practice in the application of FRP-strengthening to metallic structures, and to promote its use. FaberMaunsell and the University of Surrey acted as the research contractors and were responsible for producing the report. The project was guided by a Steering Group and has been reviewed by leading experts in the field.



Figure 1 *Hythe bridge, Oxford. Cast iron beams supporting brick jack arches, strengthened using prestressed CFRP plates. (Photograph by kind permission of Mouchel Parkman).*

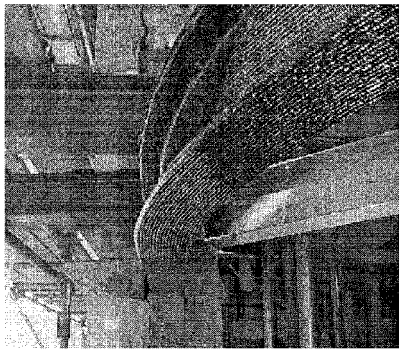


Figure 2 Boots Building, Nottingham. A curved steel beam strengthened using preimpregnated CFRP. (Photograph by kind permission of Taylor Woodrow Technology Centre).

The result of the project is the CIRIA report C595, '*Strengthening Metallic Structures Using Externally-Bonded Fibre-Reinforced Polymers*',[1] published in February 2004. This paper gives an overview of the report and highlights some its important findings.

THE CONTEXT OF THE REPORT

The development of metallic materials and structures is shown in Figure 3, starting with cast iron at the end of the 18th century and wrought iron in the middle of the 19th century. Steel was first produced at the end of the 19th century, and has been continuously developed ever since. The first use of FRP materials for structural strengthening is believed to have taken place in 1991. The initial development of FRP strengthening techniques focused on concrete structures, and the extension of the technique to metallic structures has been a more recent development.

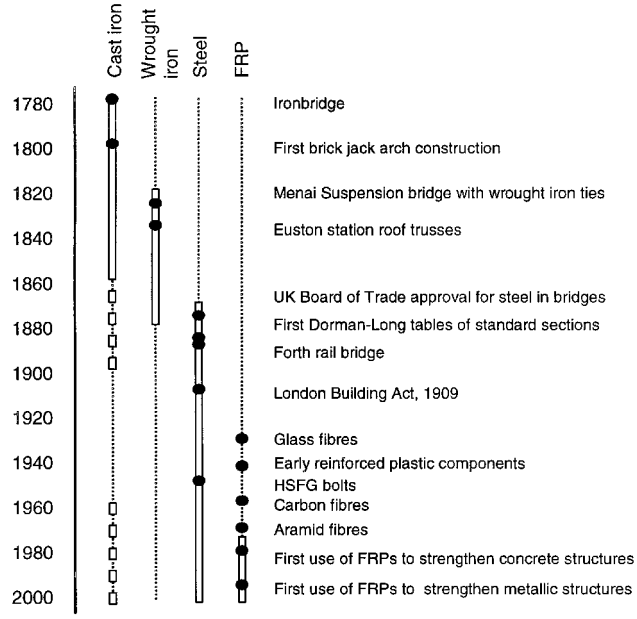


Figure 3 The development of metallic structures and FRP strengthening techniques.

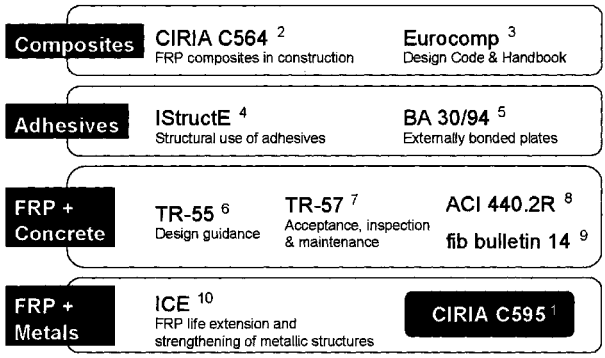


Figure 4 C595 in context

Design codes and guidance for metallic structures are well established. However similarly mature design codes are not available for the structural use of FRP. There are, nevertheless, a number of guidance documents relevant to the use of FRP in construction, as shown in Figure 4.

The use of FRP composites in construction is described by Ciria report C564 [2] and the Eurocomp [3] design code and handbook. Adhesive joints (which form a crucial part of a FRP strengthening scheme), are addressed in the IStructE report 'Structural use of adhesives' [4] and BA 30/94,[5] for externally-bonded plates. There are a number of documents relating to strengthening concrete structures using FRP, such as the Concrete Society reports TR-55 [6] (giving design guidance) and TR-57 [7] (describing operational aspects). Only the ICE Design and Practice guide [10] was previously available for strengthening metallic structures using FRP.

C595 extends the scope of the ICE guide, and complements the information on strengthening concrete structures.

THE CONTENT OF THE REPORT

C595 aims to be a single source of information on strengthening metallic structures using externally-bonded FRP. It is also aimed at a wide audience: clients and owners of structures, installation contractors, design consultants, and materials suppliers and manufacturers. Consequently the report covers a broad range of material, which is summarised in Figure 5.

The structure of the report reflects the four principal stages of an FRP strengthening project: consideration of the materials involved, the design of a strengthening scheme, the installation of the FRP strengthening, and operation of the strengthened structure.

It should be noted that C595 reports on the best-practice at the time of writing, and although the report is innovative in its presentation of the design methodology, no attempt was made to undertake new fundamental research work as part of the project. Since FRP strengthening is a young and developing technology, where there is currently uncertainty regarding an aspect of FRP strengthening for metallic structures, this is noted in the report.

Materials

A vital first step to designing a strengthening scheme is understanding the materials involved and how they work together. Both the existing materials and the strengthening materials need to be characterised.

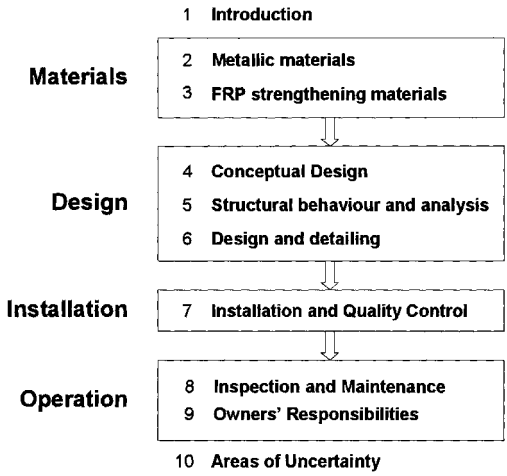


Figure 5 The structure of report C595

C595 is a single source of information, and hence covers all the materials involved in a strengthening scheme. Different sectors of the report's readership are likely to already be familiar with at least part of this information.

The principal metallic materials found in construction are cast iron, wrought iron and steel. Structural forms have developed to take advantage of these materials. These have very different properties; for example, cast iron is brittle and has very different characteristics to ductile steel, and early steels can be of very different quality to modern steels. A range of metallic structures have been successfully strengthened using FRPs. These include struts, bridge beams, parapet posts, spandrel rings and lamp standards made from cast iron and rolled bridge beams, fabricated bridge beams, offshore blast walls, pipelines, and ships made from steel. Wrought iron structures have not yet been strengthened due to the lack of research knowledge on the influence of wrought iron's laminar structure. However, investigations into the feasibility of strengthening wrought iron are reported elsewhere in these Proceedings.[11]

An FRP strengthening system can broadly be split into two components: the fibre-reinforced-polymer material and the adhesive used to bond the FRP to the existing structure. Carbon FRP is usually used to strengthen metallic structures, as efficient strengthening requires a material with a high modulus. Aramid FRP might be used when a non-conducting fibre is desirable, and glass FRPs may be used in combination with carbon FRP (for example around connection details). The bonding component of the system is usually an epoxy adhesive.

An FRP component can either be *preformed*, or formed *in-situ*. If an FRP component is preformed for later bonding to a structure, the distinction between the FRP and adhesive components is well defined. If the FRP is formed in-situ, however, the bonding adhesive is also used to impregnate dry fibres to form the fibre-reinforced-polymer, and there is no clear distinction between the bonding adhesive and the FRP matrix material.

Design

The design process is an important phase in an FRP strengthening project. Options are evaluated during the *Conceptual Design* stage, and the chosen solution is then developed during *Detailed Design*.

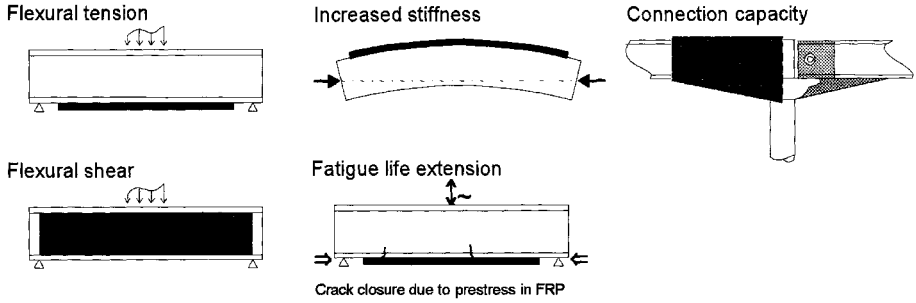


Figure 6 Applications of FRP to extend the life of metallic structures

Conceptual Design

Although the term *'Strengthening'* implies the application of FRP material to improve a structure's strength, it is not always an increase in load capacity that is primarily sought. Figure 6 shows some of the possible aims of FRP strengthening. Strengthening for flexural tension or shear increases the strength and reduces the deflection of a member. An increase in stiffness will also improve the buckling capacity of an axially-loaded member. The strength of a connection detail can be increased by applying FRP locally. By reducing live load stress levels FRP strengthening may also be used to extend the fatigue life of a structure. Prestressed FRP may be used to close fatigue cracks, which may initiate at rivet holes.

Prestressing the FRP may be desirable where a cast iron structure is being strengthened. Cast iron is brittle, and permanent tensile stresses frequently represent a significant proportion of the tensile strength of the material. Prestressing allows a portion of the permanent tensile stress to be transferred from the cast iron to the FRP material. If the strengthening is not prestressed, it needs to have a high modulus to be effective (e.g. ultra-high modulus CFRP).

Steel structures are ductile and hence a lower modulus, non-prestressed FRP can be used, provided that the system is capable of accommodating stress redistribution when the steel yields. FRP can also be used to increase both the global and local buckling capacities of modern thin-walled steel sections.

Good quality wrought iron is also ductile, although it may be laminated (as already noted). Strengthening wrought iron members will often be constrained by the locations of the rivets used to fabricate a member from individual plates.

Detailed Design

Figure 7 outlines the detailed design process. The inputs to this process include the existing structure, materials, design parameters (such as the partial factors), and environmental actions (such as temperature, moisture conditions). These values are used to determine the quantity of strengthening material required, and to check the capacity of the adhesive joint. Dynamic and fatigue effects should also be examined where relevant, and the design is finalised by suitable detailing, including fire protection, where necessary.

Figure 7 provides the framework for design, and shows the principal aspects that must be considered. Detailed analysis of the strengthening is just one part of this framework, and it is convenient to consider this structural analysis separately.

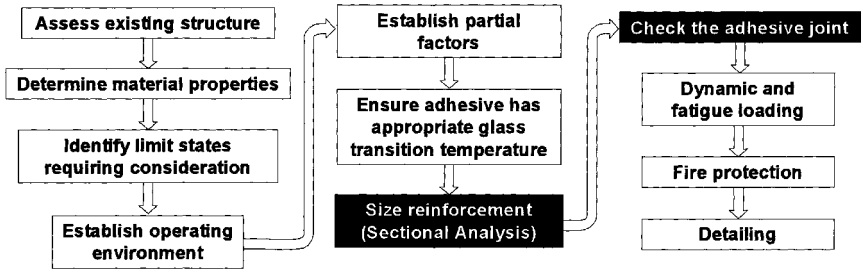


Figure 7 Overview of the design process

Structural Analysis

The strengthened member must be able to carry the imposed loads, but the member must also be checked for temperature effects. The coefficients of thermal expansion of the FRP and the metal can be very different, so that very significant restrained thermal stresses develop within the section and across the adhesive joint. The effects of differential thermal expansion can govern the capacity of the strengthened member, because they may control the strength of the adhesive joint between the strengthening material and the unstrengthened member.

Structural analysis must be carried out of the composite behaviour of all components of an FRP strengthening scheme, namely the FRP material, the existing structure and the adhesive joint between them (as highlighted in Figure 7). The adhesive joint may control the mode of failure and therefore govern the design.

Sectional analysis is used to determine the minimum cross-sectional area of FRP material required to achieve the specified strength or stiffness of the strengthened section. The analysis must take into account the stress in the structure at the time that the strengthening is applied, and is based upon the conventional assumption of flexural stress analysis, that plane sections remain plane. Due to the existence of initial stresses and strains in the unstrengthened member, the analysis must be carried out on a stage by stage basis.

The assumption that the FRP strengthening material and the unstrengthened member act compositely with one another assumes integrity of the adhesive connection between them. It is therefore important to verify that the adhesive connection has adequate strength. The strength analysis of adhesive joints, however, is not familiar to many structural engineers. Concentrations of shear and through-thickness (peel) stress occur across an adhesive joint adjacent to geometric discontinuities, such as the end of the strengthening plate, at a defect in the adhesive layer, or at a crack in the metallic substrate.

There are two approaches to analysing the strength of an adhesive joint: an elastic, stress based approach, and a fracture mechanics based approach. The fracture mechanics analysis is an ultimate approach that does not require a detailed description of the elastic stress distribution within the adhesive joint. Within the project a fracture mechanics solution was developed for a uniform beam with uniform strengthening. It was not possible, however, to develop the fracture mechanics approach for application to a general FRP strengthened member taking into account temperature effects and section variability.

C595 describes the application of an elastic adhesive analysis in detail. The elastic analysis determines the distribution of shear and peel stresses within the adhesive joint. If the peak combined adhesive stress exceeds the strength of the adhesive joint, methods

for reducing the peak adhesive stress must be sought, such as relocating the end of the strengthening plate to a less highly stressed region of the member, or changing the width of the strengthening plate, or changing the geometry of the strengthening near the end of the plate. The elastic analysis of an adhesive joint between a plate and a beam (as presented in C595) is described elsewhere in these Proceedings.[12]

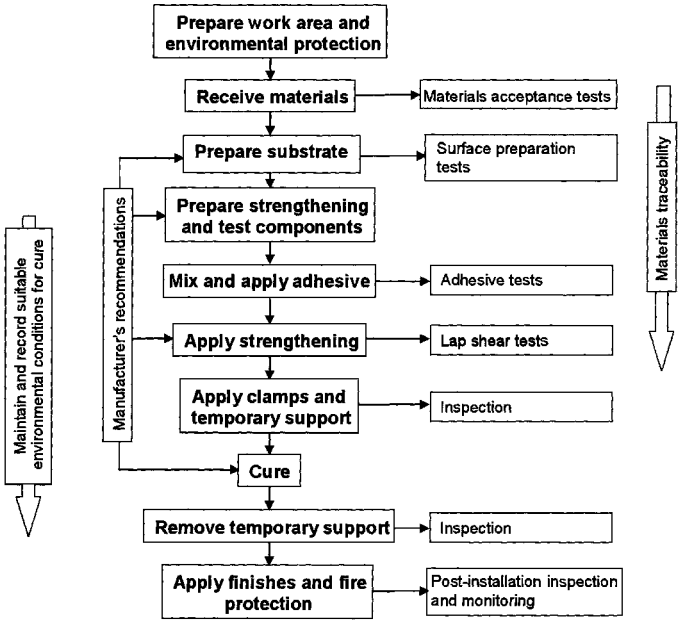


Figure 8 The installation process for FRP strengthening

Installation

A high quality installation is essential for an externally-bonded FRP strengthening system, in order for it to perform as required, and not fail prematurely. Careful planning of the strengthening works, provision of the correct equipment and environment for strengthening, and in particular adequate training of all personnel involved are vital to achieve the required quality of installation.

C595 gives advice on the complete installation process, which is summarised in Figure 8. This includes test procedures to provide assurances that the strengthening has been correctly installed.

Operation

The final section of C595 concerns operational aspects of an FRP-strengthened metallic structure. These are split into (a) inspection and maintenance of the strengthened structure and (b) procurement and management issues, which will be of particular interest to the owners of structures.

Like in any construction scheme, an FRP strengthening project requires inspection immediately after the work is carried out and at regular intervals during the structure's service life. An appropriate inspection and maintenance regime must be established for the strengthened structure. Specific potential defects should be identified, and suitable repair methods described. These are especially important with FRP strengthening, as

future inspections might be carried out by engineers who are not familiar with FRP materials and who may not, for example, be aware of the significance of a defect in the adhesive layer near the end of a plate. Non destructive test (NDT) methods can be used as part of an inspection, though, no single NDT method is likely to provide information on all defects present, and currently available methods of NDT inspection of FRP-strengthened structures are still under development.

C595 outlines the procurement process of an FRP strengthening scheme. This starts with a structural assessment, which establishes to what extent strengthening work is required. Procurement proceeds through conceptual and detailed design, installation, inspection and acceptance of the completed works, and maintenance of the strengthened structure. The decision to use FRP strengthening will depend on an economic assessment (in which savings due to ease of installation are often found to outweigh higher material costs). The environmental impact of the strengthening method and the implications of using FRP strengthening on heritage structures must also be considered.

CONCLUDING REMARKS

This paper has presented only a brief overview of Ciria C595. Nevertheless, it has drawn attention to some important issues to be considered when strengthening metallic structures using FRP. These include an adequate understanding of the materials involved, the importance of the analysis of the adhesive joint, the effects of temperature on the strengthened section, the importance of a high quality installation, and regular inspection of the strengthened structure.

REFERENCES

1 J M C Cadei, T J Stratford, L C Hollaway and W G Duckett, *Strengthening Metallic Structures using Externally-Bonded Fibre-Reinforced-Polymers – C595*, ISBN 086017-595-2, London, CIRIA, 2004.

2 A Cripps, B Harris, T Ibell, *Fibre-reinforced polymer composites in construction – C564*, London, CIRIA, 2001.

3 J L Clarke (ed) *Structural Design of Polymer Composites: Eurocomp Design Code and Handbook*, London, E & F N Spon, Chapman and Hall, 1996.

4 IStructE, *Guide to the structural use of adhesives*, London, SETO, 1999.

5 Highways Agency, *Strengthening of concrete highway structures using externally bonded plates – BA 30/94*, London, 1994.

6 Concrete Society, *Design guidance for strengthening concrete structures using fibre composite materials. - Technical report no. 55*, Crowthorne, UK, 2000.

7 Concrete Society, *Strengthening Concrete Structures with Fibre Composite Materials: acceptance, inspection and monitoring - Technical report no. 57*, Crowthorne, UK, 2003.

8 American Concrete Institute, *Guide for the Design and Construction of Externally Bonded FRP Systems for Strengthening Concrete Structures - ACI 440.2R-02*, Detroit, USA, 2002.

9 Fédération Internationale du Béton, *Externally bonded FRP reinforcement for RC structures - fib bulletin 14*, Lausanne, Switzerland, 2001.

10 S S J Moy (ed), *FRP composites – Life extension and strengthening of metallic structures - ICE design and practice guide*, London, Thomas Telford, 2001.

11 S S J Moy, J Clark and H Clarke, 'The Strengthening of Wrought Iron using Carbon Fibre Reinforced Polymer Composites', *ACIC-2004*, Guildford, 2004.

12 J M C Cadei and T J Stratford, 'Elastic Analysis of Adhesion Stresses Between a Beam and a Bonded Strengthening Plate', *ACIC-2004*, Guildford, 2004.

STRUCTURAL HEALTH MONITORING OF CFRP-STRENGTHENED BEAMS USING DYNAMIC TESTING

Dr C M Tan[1], Dr J S Owen[2], Dr S R Pearson[3] and Dr S Luke[1]

[1]*Mouchel Parkman, St John's House, Queen Street, Manchester, M2 5JB*
[2]*School of Civil Engineering, University of Nottingham, Nottingham, NG7 2RD*
[3]*AEA Technology Rail, Jubilee House, Pride Park, Derby, DE24 8LY*

ABSTRACT

Vibration data have long been considered a useful tool for monitoring the condition of structures, though the reliable implementation of these techniques for bridges has remained elusive. This paper considers their suitability for monitoring the performance of CFRP-strengthened beams. First, the different failure mechanisms are reviewed and the likely sensitivity of each assessed. Then, data collected from the beams used in the ROBUST project are used to investigate the feasibility of both the system identification and statistical pattern recognition paradigms. The results suggest that although the system identification paradigm is insensitive to the small changes of stiffness associated with these repairs, the statistical pattern recognition approach can be used successfully to classify the damaged beams.

INTRODUCTION

Carbon Fibre Reinforced Polymer (CFRP) plates are now being accepted in the UK as an effective alternative to traditional methods of bridge-strengthening. In the past 3 years, over 200 bridges have been strengthened with CFRP plates in the UK alone [1]. As this is a relatively new technology, some bridge owners still have doubts over the durability of CFRP-strengthened bridges. A reliable structural health monitoring (SHM) tool for CFRP-strengthened bridges would therefore be a useful development.

There have been many studies into the application of dynamic testing for the detection of deterioration in bridges [2,3]. The key principle is that damage will result in a loss of stiffness, which is then detected as a change in modal properties (i.e. natural frequencies, mode shapes and modal damping). The use of modal testing to monitor these changes in stiffness has two advantages over other forms of non-destructive testing. First, the modal characteristics provide a global picture of the structural system. Second, it is possible to monitor changes in these modal properties using relatively few sensors strategically placed on the bridge.

The application of these methods to civil engineering structures, and bridges in particular, has led to several studies on full-scale bridges [e.g. 4] laboratory models [e.g. 5] and computational simulations [e.g. 6]. There are several detailed reviews of SHM methodology for civil engineering and the growing literature in the field [e.g. 7]. However, although significant work has been done on detecting and monitoring damage in bridge structures using vibration data, little work has been done to assess their use for monitoring bridge repairs. In this paper, the authors consider the feasibility of using vibration data for the SHM of CFRP-strengthened structures. First, the major damage mechanisms are considered to identify the likely sensitivity of vibration data. Then the results of modal tests on eight post-tensioned beams recovered from the Botley flyover, three of which were strengthened using CFRP plates under the ROBUST project [8], are presented to illustrate a possible solution.

BACKGROUND

In considering the feasibility of using vibration data to monitor bridge structures it is necessary to consider the effects of different failure mechanisms on the vibration signatures. Traditionally, the system identification paradigm has been applied in which changes in natural frequency have been used to infer changes in stiffness, often using techniques such as FE model updating. However, this can be insensitive to small, localised changes in stiffness and the effects masked by environmental changes. More recently the statistical pattern recognition approach has been used [9, 10] in which more subtle changes in the whole vibration signature are monitored.

The failure modes for FRP-strengthened reinforced concrete (RC) beams can be categorised as shown in figure 1 [11]. Of the eleven possible failure modes, modes 8, 9 and 10 are highly unlikely to occur and could therefore be excluded from the study for now. Modes 1, 2, 4 and 11 are pure reinforced concrete failure. Although extensive research has been carried out on the effect of this type of damage on the vibration signatures of RC beams [7,12], the presence of the FRP-strengthening will influence both the relative change of stiffness associated with damage and the vibration behaviour of the cracks in the concrete. It is therefore important to compare the behaviour of damaged beams with and without FRP-strengthening.

Failure mode 3 is a tensile failure of the FRP plate, which will result in a localised reduction in stiffness analogous to a crack forming. Simple dynamic testing/analysis discussed in most papers should be capable of identifying this damage. However, the nature of the crack interface in the FRP plate may cause complications that make the reduction in stiffness less clear. Similarly, modes 5, 6 and 7, which are all peeling modes of failure, will lead to a gradual reduction in stiffness and so a simple dynamic test may have difficulties in identifying the damage at early age. Therefore, for these modes of failure the traditional system identification paradigm seems inappropriate and the alternative statistical pattern recognition technique more suitable.

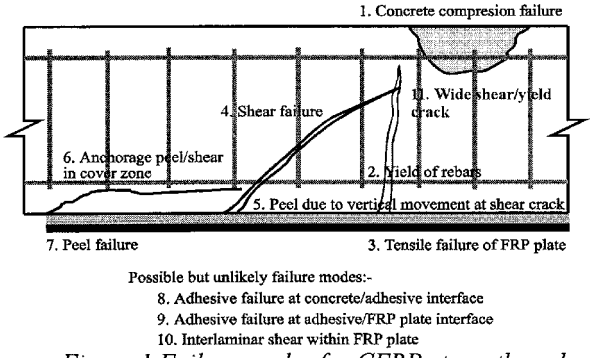


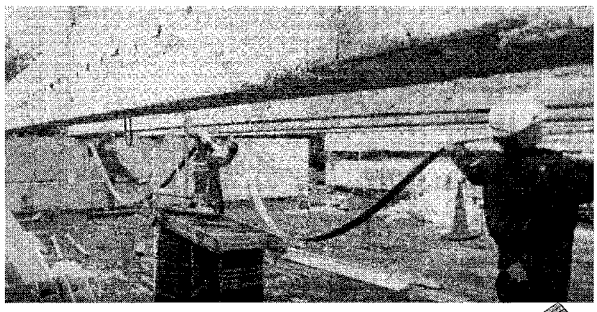
Figure 1 Failure modes for CFRP-strengthened reinforced concrete beams

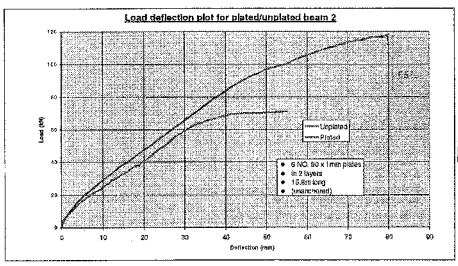
To gain a better understanding of the feasibility of using vibration data to monitor FRP-strengthened RC structures, and to further the understanding of the issues involved, beams removed from the Botley Flyover have been tested. Although not all damage modes could be considered, it was possible to compare strengthened and non-strengthened beams. This, therefore, could provide important information on the effect of FRP plates on the vibration behaviour of damaged concrete.

BOTLEY FLYOVER AND THE ROBUST PROJECT

The Botley flyover was designed in 1957 to carry the A34 Oxford Western By-pass over the A420. The bridge was a three span structure with a centre span of 17.5m and side spans of 6.1m and 8.0m built on a 17° skew. The main deck was constructed from 47 pre-cast post-tensioned concrete beams. In common with a number of other post-tensioned bridges of this period, poor grouting of the tendon ducts led to corrosion of the pre-stressing tendons and subsequent loss of pre stress in the main bridge beams. Therefore, the bridge deck was replaced in 1993. The original bridge beams were removed from site and stored in the open at the Oxfordshire County Council depot at Campsfield near Kidlington, UK. These beams have since been used in several research projects, including the ROBUST project investigating the use of CFRP for strengthening structures.

The ROBUST project was a research project undertaken by Mouchel Parkman to investigate the feasibility of using advanced composite materials for strengthening structures. Approximately 130 flexural tests using pre-stressed and unstressed plates were carried out on model beams in the laboratory and also on the bridge beams removed from Botley flyover (Fig. 2). To supplement the experimental work, Mouchel carried out non-linear, 3 dimensional finite element analysis to calibrate the performance of the beams in the laboratory tests and to provide sufficient data for development of design guidance. A consortium led by Mouchel Parkman has then drawn up a specification for CFRP plate bonding. The results of the ROBUST project have indicated that plate bonding using CFRP plates is a viable and cost effective alternative to other methods of strengthening. The method can be applied to a wide range of structural types to increase their flexural capacity.





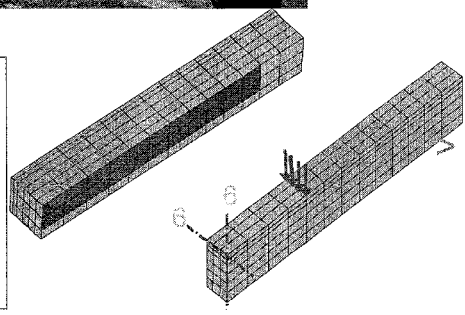


Figure 2: Photograph, results and FE analysis of ROBUST project

DYNAMIC TESTS ON BOTLEY BEAMS

Condition of the Beams

Before dynamic tests were carried out, visual inspection on the beams revealed a wide range of conditions; some beams were badly damaged whilst others displayed little if any cracking. The beams that had previously been used in the ROBUST project had been load tested in 3 point bending resulting in further cracking. For these beams the longitudinal pre-stressing tendons had been cut at intervals by coring the beams and the beams subsequently strengthened by the bonding of carbon fibre plates to the soffit. For two of the beams tested these plates were post-tensioned. Each of the beams was classified according to the level of damage – light (3 beams), heavy (2 beams) or CFRP-strengthened (3 beams), see Table 1 and Fig 3. Finally, it should be noted that all the beams had been stored outside for several years before testing and this had resulted in the growth of moss and general weathering.

Table 1: Summary of the condition of the beams tested. [9]

Beam	FRP plate?	Damage description	Classification
1	No	No visible cracking Some spalling at both ends and along top edge Transverse tendons cored but not removed	Light damage – class 1
2	No	Significant diagonal cracking in top half Cracking between transverse wires at mid height Extensive spalling around transverse tendons Loss of section due to spalling along sides Several small vertical cores	Heavy damage – class 2
3	No	Cracking in top half Significant cracking at mid height between tendons Cracks extend full height near ends Several small and 2 large diameter vertical cores Transverse tendons cored	Heavy damage – class 2
4	Central 5m (post-tensioned)	No visible cracking Some spalling along top edge – reinforcement exposed Longitudinal strands cored at four locations Small cores at mid height	strengthened – class 3
5	Central 5m (post-tensioned)	Cracking in bottom half around main cores Some spalling around main cores Longitudinal strands cored at four locations Small cores at mid height	strengthened – class 3
6	Full length	Cracking extending above mid height around and between main cores Spalling around main cores Longitudinal strands cored at four locations Small cores at mid height	strengthened – class 3
7	No	No visible cracking Shear links exposed by cutting Some spalling at both ends and along top edge Transverse tendons cored but not removed	Light damage – class 1
8	No	No visible cracking Spalling along top edge exposing reinforcement Significant spalling along bottom edge exposing corroded reinforcement Transverse tendons cored but not removed	Light damage – class 1

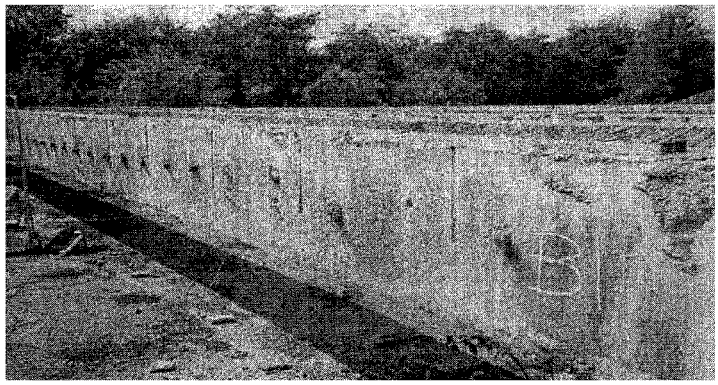


Figure 3: Photograph of typical test beam (class 1)

Experimental Procedure

The modal survey was performed using an instrumented hammer to provide an impulse excitation on the top face of the beams. Two excitation locations, three-eighths span and five-eighths span, were used so that reciprocity checks could be made. The response was measured by seven accelerometers located at one-sixth, one-quarter, one-third, three-eighths, one-half, five-eighths and two-thirds span. Due to the removal of the in-situ concrete distribution slab, the top surface had become uneven and was unsuitable for mounting the accelerometers; instead they were attached to the underside of the beam. All beams were tested using a soft hammer tip, which gave an impact duration of ~ 7ms and a broadband excitation with an approximate frequency range of 0 - 500Hz. Two different excitation magnitudes were used to detect any system non-linearity.

Data Processing

Data was collected using a PC and A/D board. For each hammer test, a total of 8192 samples were taken at a rate of 2000 samples per second, giving a total record length of 4.096 seconds. To avoid aliasing, all signals were filtered at 1000Hz using a set of low pass filters prior to digitisation. The digitised data were then used to obtain an estimate of the system frequency response function (FRF) for each measurement point. To reduce random errors, the FRFs from 20 data records were then averaged using an ensemble averaging procedure; sufficient averages were taken to ensure a value of coherence ~1 close to the natural frequencies.

Modal Parameter Extraction

To determine the natural frequencies, modal damping and mode shapes the FRF data were analysed using Diamond, software developed by Los Alamos National Laboratories specifically for the extraction of modal properties and their use in damage identification [13]. Diamond includes a range of modal parameter extraction methods, though for this study the rational polynomial approach was used. Typically, 20 modes were identified within the range 0-300Hz, though this varied from beam to beam depending on the damage level. For some of the beams the FRF data contained multiple or split peaks, which made both modal identification and systematic comparison between different beams difficult. The natural frequencies for the flexural modes are summarised in table 2.

Table 2: Natural frequency estimates for beams 1 – 8 (Hz)

Flexural Mode	Beam 1	Beam 2	Beam 3	Beam 4	Beam 5	Beam 6	Beam 7	Beam 8
1	4.9	4.4	4.7	5.1	5.1	4.8	4.6	4.7
2	17.9	15.8	16.9	17.4	17.3	16.7	17.0	17.3
3	37.8	36.9	36.8	39.1	39.1	37.3	37.6	37.3
4	62.2	63.0	63.5	66.3	66.4	63.2	63.1	62.2
5		93.3		98.4	99.4	94.3		
6				132.3	133.0	127.0		
7		108.0	106.5	166.5	166.2	153.3		

STRUCTURAL HEALTH MONITORING

Using Natural Frequencies – the System Identification Paradigm

The most basic approach to use vibration data for SHM is to look for changes in the natural frequencies as the level of damage increases. For the beams described in this paper, this should mean that the beams could be classified according to the relative values of the natural frequencies, i.e. the natural frequencies of damaged beams ought to be lower than the corresponding natural frequencies of the modified beams. Figure 4 shows the natural frequencies for each mode of each beam normalized by dividing through by the natural frequency of one of the modified beams. This figure does indeed show that there is a reduction in natural frequency for the more damaged beams, however there is also a significant spread of the results, which makes practical usage difficult. Furthermore, it is essential that comparisons are made between corresponding modes and the number of repeat/multiple modes makes this impossible to achieve with confidence. This is why there are several modes for which there appears to be an increase in normalized natural frequency. In conclusion, there is clearly some reduction in natural frequency with damage, but the lack of confidence in comparing modes between beams in different damage states makes this approach unreliable for SHM purposes.

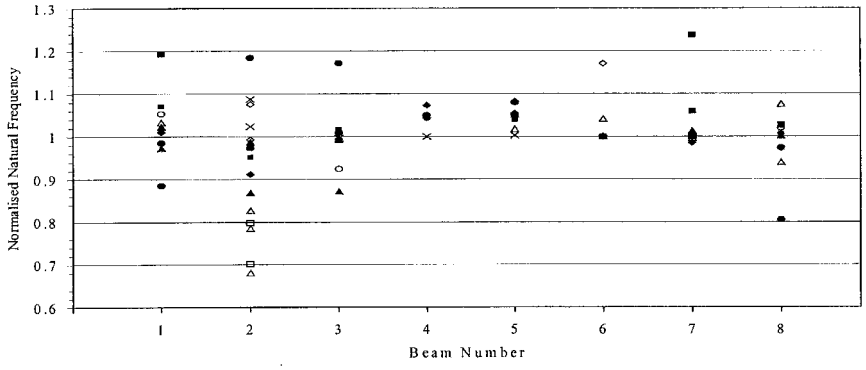


Figure 4: Plot of normalized frequency change against beam number

The Statistical Pattern Recognition Paradigm

The alternative to the traditional system identification paradigm is to use an approach that makes a statistical comparison between the whole of a vibration record, not just the modal behaviour. The approach followed here is to take the vibration data and form the FRFs – as described above. Then, rather than extract modal parameters from these FRFs, the data set is reduced using principal component analysis [14]. This essentially identifies a set of frequency domain functions that contain most of the significant components of the data. The principal components identified can then be used to discriminate between the different data sets. This is illustrated in Fig 5, for the simple case of using just the first two components, and clearly shows that the different beam classes can be identified. A more detailed comparison, using artificial neural networks to perform the pattern recognition based on a larger number of principal components allows the method to be refined further [9].

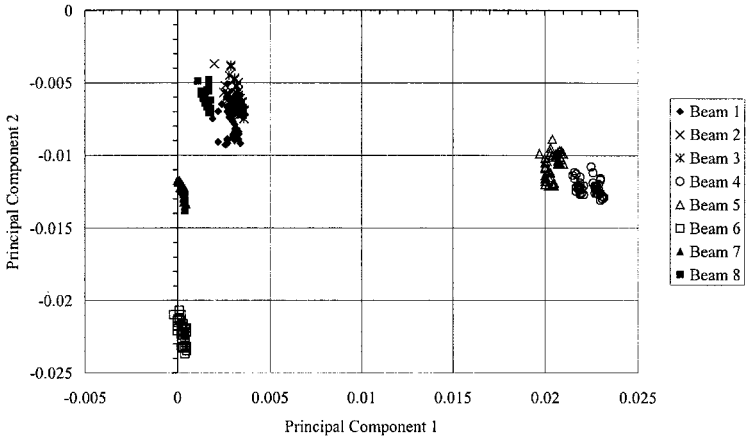


Figure 5 FRFs from single accelerometer using first two principal components

DISCUSSIONS AND CONCLUDING REMARKS

The work presented in this paper has shown that there are indeed small differences in flexural stiffness for bridge beams with different levels of damage and for bridge beams that have been strengthened using CFRP plates. Although these differences in stiffness can be detected through measurements of natural frequencies, these are fairly insensitive to the level of damage and so can lead to ambiguous results. Furthermore, this system identification approach is made less attractive by the difficulty in correlating modes between different damage states. Indeed, heavily damaged beams seem to lack clearly defined vibration modes.

In contrast, the pattern recognition paradigm was clearly able to differentiate between the different damage states using the same vibration data. This suggests that this is a potentially more useful approach to the SHM problem where changes in vibration data are expected to be small, such as when comparing strengthened and un-strengthened RC beams.

A range of different failure modes was identified in the introduction to the paper. The work presented has essentially focused on those failure modes that represent failure of the concrete beam. However, it is also important to consider the implications for the other failure mechanisms, such as peeling or tensile failure of the

CFRP plate. It is expected that initial peeling will result in quite small changes in stiffness, changes that would be expected to be undetectable if using natural frequencies and the system identification paradigm. The pattern recognition approach is potentially more useful in this situation, though this assertion needs to be confirmed with a more thorough investigation.

ACKNOWLEDGEMENTS

The work presented in this paper was supported by the UK Highways Agency.

REFERENCES

1. S Luke, "Composites in civil engineering – an overview", *Ingenia Journal, UK,* 1999.
2. SW Doebling, CR Farrar and MB Prime, "A summary review of vibrational based damage detection methods", *The shock and vibration digest, Vol. 30(2), pp 91-105, 1998.*
3. PC Das, JS Owen, BJ Eccles, MA Woodings and BS Choo, " The role of dynamic testing in the assessment of bridges", *Transport Research Record Part 2: Structures, Vol. 1594, pp 115-124, 1997.*
4. Peeters B. & De Roeck G., "One-year monitoring of the Z24-Bridge: environmental effects versus damage events" *Earthquake Engineering Structural Dynamics, Vol. 30, pp149-171, 2001.*
5. Pearson S. R., Owen J. S. & Choo B. S., "The use of vibration signatures to detect flexural cracking in reinforced concrete bridge decks.", *Key Engineering Materials, Vol. 204-205, pp 17-26, 2001.*
6 Ren, W-X., & De Roeck, G., "Structural damage identification using modal data. I: simulation verification", *Journal of Structural Engineering, Vol. 128, No. 1, pp 87-95, 2002*
7. Farrar, C. R., Doebling, S. W. & Nix, D. A., "Vibration-based structural damage identification", *Philosophical Transactions of Royal Society of London Vol. 359, 131-149, 2001.*
8. J Darby, S Luke and S Collins, "Stressed and unstressed advanced composite plates for the repair and strengthening of structures", *Bridge management, Vol. 4, 2000.*
9. JS Owen, SR Pearson, CM Tan and BS Choo, "The classification of damage/repaired beams using vibration signature", *Transport Research Record, No. 1814, Designs of Structures, pp 135 -144, 2002.*
10. Haritos, N. & J. S. Owen, "The use of vibration data for damage detection in bridges: a comparison of system identification and pattern recognition approaches." *International Journal of Structural Health Monitoring (in press)*
11. S Luke, "Composites in civil engineering" *Institute of Structural Engineering Evening Lectures, Nov 2003.*
12. CM Tan, *Nonlinear Vibration of Cracked Reinforced Concrete Beams*, PhD Thesis, School of Civil Engineering, University of Nottingham, UK, 2003.
13. SW Doebling, CR Farrar and PJ Cornwell, "DIAMOND: A graphical user interface toolbox for comparative modal analysis and damage identification", *Proc. of 6th International Conf. on Recent Advances in Structural Dynamics, Southampton, UK, 1997.*
14. CM Bishop, *Neural networks for pattern recognition* Oxford University Press, UK, 1995.

PART VIII

CASE STUDIES

This page intentionally left blank

MAUNDERS ROAD OVERBRIDGE
THE BEHAVIOUR AND IN-SERVICE PERFORMANCE OF CAST IRON BRIDGE GIRDERS STRENGTHENED WITH CFRP REINFORCEMENT

Ian Smith,
Tony Gee and Partners

ABSTRACT

Maunders Road Bridge was the first Network Rail (then Railtrack) cast iron bridge to be strengthened by the application of FRP composites. Due to the innovative nature of the technique the bridge was instrumented during and after the strengthening process, providing valuable confirmation of the theoretical behaviour of such strengthening schemes.

MAUNDERS ROAD BRIDGE

Maunders Road Bridge in Milton, Stoke-On-Trent is typical of many cast iron bridges built in the 19th century. The deck consists of six simply supported cast iron beams with masonry jack arches spanning up to 1.44m between the beams, with the jack arches being in good condition and no water seepage problems. The beams span onto padstones which are built into masonry wall abutments. The construction of the deck above the jack arches consists of rubble fill, road base material and bituminous surfacing, see figure 1.

As part of the Railtrack 'Bridgeguard 3' programme, the bridge was assessed as having a 7.5 tonne capacity. However, the bridge was the only route into an industrial area that could be negotiated by heavy goods vehicles (two other routes both having even narrower hump-back bridges, both situated on tight double bends) and required a 40 tonne capacity. Furthermore, a number of services, including a large gas main suspended from one parapet, crossed the bridge to supply a residential area.

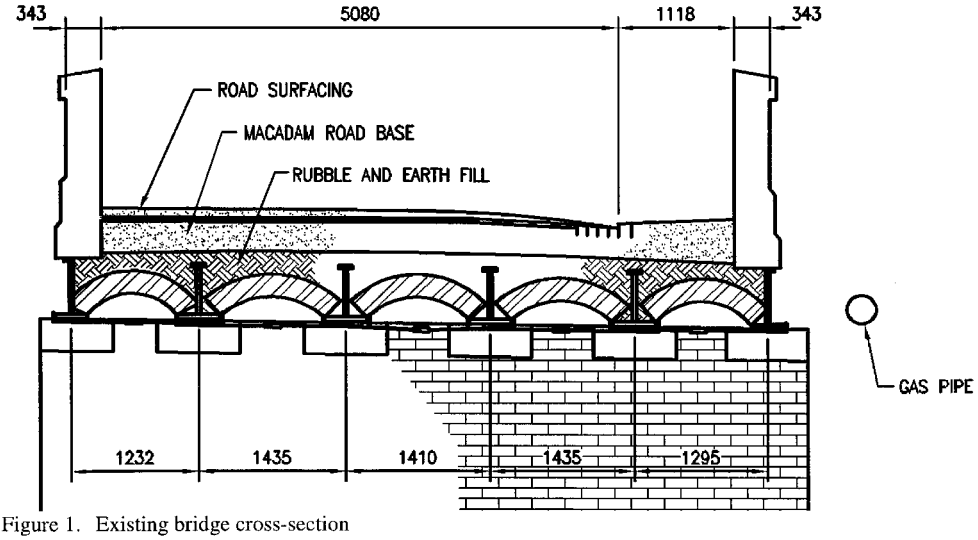


Figure 1. Existing bridge cross-section

Although the line beneath the bridge is mothballed, there are aspirations to re-open it, so permanent propping and in-fill schemes were not appropriate. Following a feasibility study, the strengthening solution adopted was to install externally bonded ultra-high modulus carbon fibre laminates applied to the soffit of each cast-iron beam to increase flexural capacity.

Design issues

Subject to all the constraints identified, CFRP bonding was the most economic method. Steel plates of stiffness equal to the CFRP laminates used would have weighed approximately 0.6 tonnes and would have been virtually impossible to install.

The required strength gain could only be achieved by utilising the strength of the cast-iron / CFRP composite section to withstand dead load effects in addition to the imposed vehicle loads. For this reason, an innovative scheme was adopted where the structure was jacked at the midspan position prior to application of laminates, the jacks being released once the bonding adhesive had cured.

Ancillary elements

The transverse tie-rods at the structure had failed in a number of locations, some fully corroded and some snapped. Works to replace these were included in the project, but the interface between retro-fitted ties and the beam soffit with CFRP applied required precise detailing.

Extensive brickwork repairs were also completed on the structure during the same contract period.

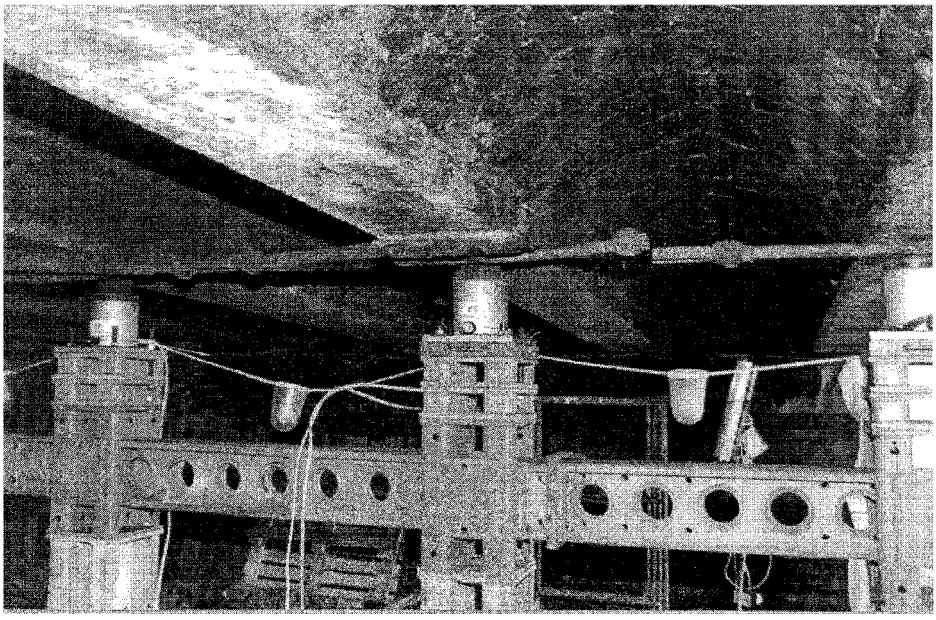


Figure 2. Jacks in place beneath beams before CFRP installed. Also note tie-rod condition.

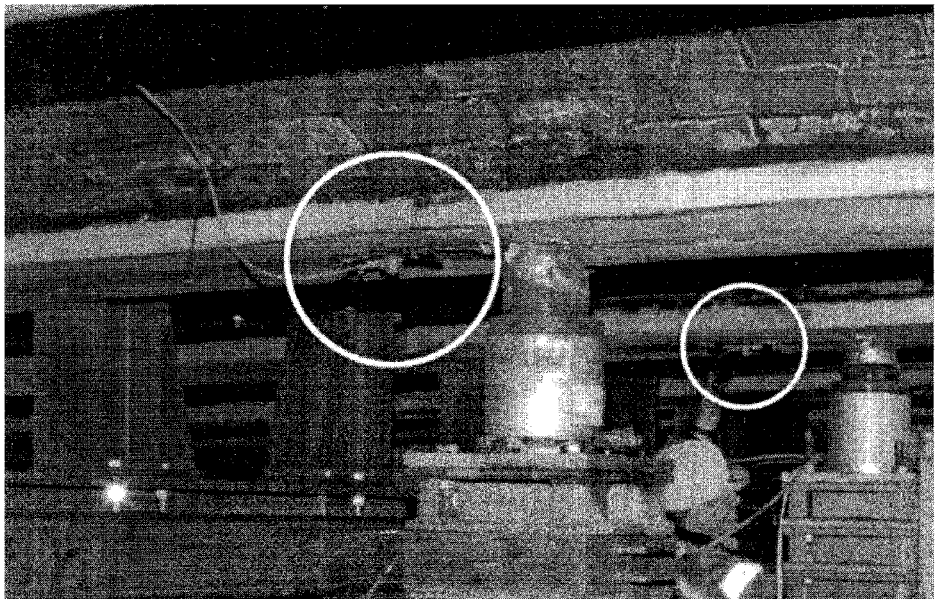


Figure 3. Strain gauges installed on beams before CFRP installed

Construction programme

Deck strengthening works were undertaken during a two week road closure in November 2001, with laminate bonding being undertaken swiftly within a 5 day period. Including the ancillary works (e.g. preparatory groundwork, brickwork repairs) undertaken before and after this closure, the total duration of works on site was seven weeks.

Monitoring and inspection

During the works strain gauges were fixed at midspan to every beam and one of the two laminates bonded to each beam. The data gathered from these was analysed by TGP.

During jacking operations, the beams were also monitored by dial gauges. Although these were mounted on a separate structure from the jacks and the scaffold working platform, this structure was supported from the same concrete base that supported the jacks. In order to ensure that readings were from the deck going up, rather than the base going down, the base was surveyed by optical level before and after jacking and again before and after releasing the jacks. In all cases, no movement of the base was detected.

As part of site QA procedures, acoustic sounding tests were undertaken to ascertain if any voids were present after bonding. These tests are also to be carried out at future inspections. In addition, extra inspections have been made of the structure to try and detect any unexpected behaviour.

Since it is located over a disused railway, the bridge is intended to be used for further testing. In particular, it is intended that it be a 'test-bed' structure to prove the feasibility of new non-destructive testing methods for in-situ testing and inspection. Unfortunately, while we had hoped to have the first results of such testing methods to report, the survey has been postponed and data is not available. However, the data gathered during installation provides some useful conclusions.

CONSTRUCTION MONITORING RESULTS

Since the construction method adopted required jacking up the structure, stiffness values can be deduced both before and after the strengthening had been completed. Although the load applied was upwards (i.e., opposite the normal loading direction), it nevertheless provides some information which is often not known for bridge structures.

Before strengthening

The internal beams were jacked up in six increments to an upwards load of 126kN per beam. Edge beams were jacked to the slightly lower load of 118kN. These values were determined such that even under extreme combinations of the tolerances of known values (structure weight, jack pressures, section properties etc.) there would be no stress reversal in the beams. That is, no part of the cross-section which had been previously subject only to compressive stress would be subject to tensile stress due to the jacking operation. This limit was to minimise the risk of propagation of any cracking that may have been present but undetected in the beam.

The displacements due to jacking for every beam are shown in figure 4. After the first two increments (during which it is assumed that the prop structure was 'bedding in') a substantially linear response was observed, with all beams reacting similarly. The gradient of the deflection / force graph averages 0.028mm per kN.

Since the beams are simply supported, and a known point load at midspan has caused a known deflection, it is possible to calculate the stiffness (EI) of the beam. From the values observed, the stiffness of the beams can be calculated as 372.39 10^{12} Nmm^2.

Since the cross-section and the material of the beams is known, it ought to be possible to compare this with a theoretical calculated value. Unfortunately, however, the appropriate value of elastic modulus for cast-iron is a subject of debate. Suggestions include the Highways Agency document BD21/01 "The Assessment of Highway Bridges and Structures" recommending between 90 and 138 kN/mm^2 and the SCI publication 138 "Appraisal of Existing Iron and Steel Structures" suggesting 66 to 94 kN/mm^2. Other references vary over similarly wide ranges, though these two describe the limits of commonly assumed range.

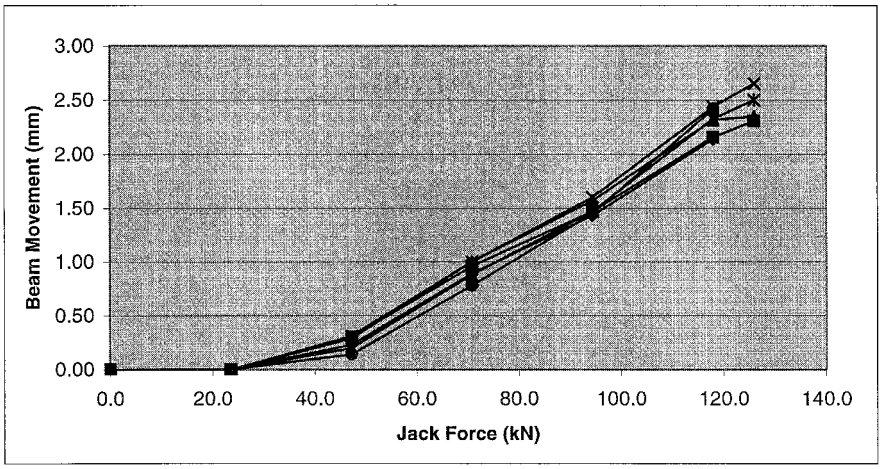


Figure 4. Unstrengthened structure response to jacking

However, even if the most extreme of these values is adopted, the observations from jacking results are much stiffer than theory would suggest. If an extreme value of 138 kN/mm^2 is assumed for the cast-iron, the bridge deck is approximately 1.6 times stiffer than the bare beam. If a value of 92 kN/mm^2 is adopted (the middle of the overlap in the noted ranges), the deck is 2.3 times stiffer than the bare beam.

These figures are not unprecedented. The stiffness values in BD21/01 are taken from ICE paper 5418 "The Strength of Cast-Iron Girder Bridges" published in 1944. This paper records a programme of testing on jack-arch bridges and concludes that beams built into brick jack-arches can exhibit composite action between the beam and the masonry and fill resulting in stiffnesses significantly in excess of the bare beam values. BD21/01 incorporates this conclusion, and for Maunders Rd bridge, would allow increase in stiffness to 1.6 times the bare beam value. This shows implausibly good correlation with the first of the values calculated above, but it seems likely that the true situation is cast-iron of stiffness less than 138 kN/mm^2 and composite action of greater than 1.6 times, since the stiffness enhancement adopted by BD21/01 is a simplified approach expected to be conservative.

As previously noted, the beams had strain-gauges mounted near midspan during the jacking procedure. These correlated well with the dial gauges, giving a strain in the middle portion of the jacking process of 1.12 microstrain per kN

During strengthening

Strain gauges were in place during the bonding operations, which were undertaken during the 24 and 25 November. Ambient temperatures were around freezing at this time, falling below freezing overnight, so the structure was sheeted and heated continuously by space-heaters. Heating was maintained for a cure period of one week, during which the beam temperature (recorded at two strain-gauge locations) varied in the range 10°C to 17°C. When the heating was halted, the structure took three days to cool to ambient (in the range -2°C to 6°C).

After strengthening

After the cure period, the jacks were released. At this stage, dial gauges were not employed, so it is only possible to work from the strain gauge results. Two gauges were now present on each beam – one remaining on the cast iron (installed before jacking) and one on one of the pair of laminates bonded to each beam. Gauges on the cast iron showed approximately 40 microstrain as jacks were released, compared to approximately 100 microstrain during the jacking process. The stiffness had thus increased by a factor of 2.5. This compares with a theoretical prediction of between 2.4 (if the cast iron is assumed to have E=138 kN/mm^2) and 3.2 (if E=92 kN/mm^2), ignoring any composite action with brickwork. This was considered to be a good correlation, and within acceptable values since the design was prepared on the basis of 138 kN/mm^2 for the cast iron.

The strain gauges on the surface of the CFRP showed values typically 45% higher than those on the CI. Since these are offset the thickness of the laminate plus adhesive (around 39-42mm depending on adhesive thickness) the location of the neutral axis can be estimated at 90mm up from the CI soffit. This compares with a theoretical prediction of between 112mm and 91mm for the range of CI stiffness noted above. Again, this was considered to be good correlation.

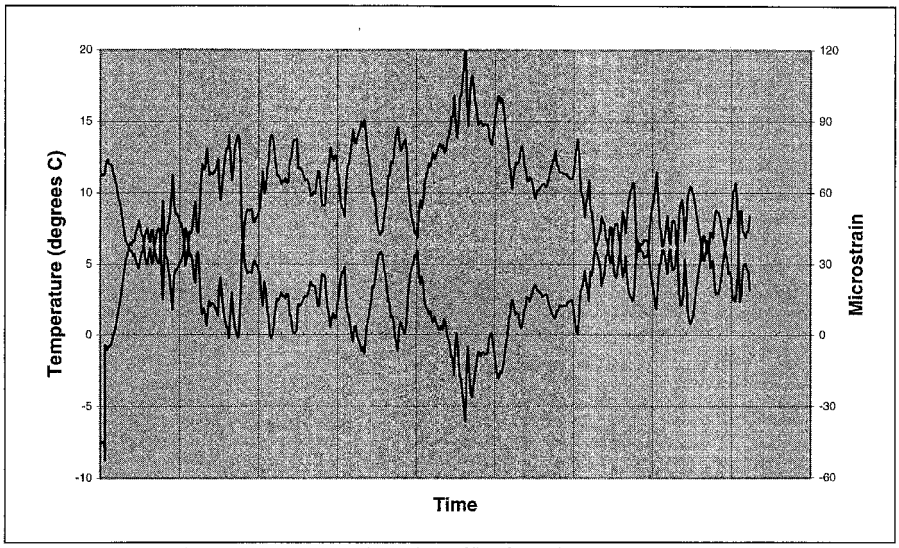


Figure 5. Correlation between average strain at the soffit of cast-iron beams (upper trace) and temperature of the beams (lower trace) from time of release of jacks onwards (gridlines at 1 week intervals)

In service

All strain gauges were left in place for a further two months (till the end of January 2002). During this time the bridge was in use by traffic, but no monitoring of the traffic was undertaken, and data was logged at three hour intervals, so it is not possible to correlate strains with imposed loading.

Temperatures were recorded, however, and the strains in the cast iron show a very close correlation with the temperatures of the beam, as seen in figure 5. This is expected, since the sample interval is large enough and traffic levels low enough that imposed loading would not register on this graph.

SUBSEQUENT INSPECTION

The bridge has been inspected to confirm the ongoing performance of the CFRP strengthening. Most recently, an inspection and tap-test of the taper zone of each laminate was undertaken in June 2003, approximately 18 months after installation of the laminates.

The bridge is still standing, with no immediately apparent signs of distress. Tap-testing the end (taper) zones of the laminates did not reveal any voids.

The beams have been painted, with a paint film extending across the bond line and onto the CFRP, which is not ideal since it could conceal the early stages of delamination were it to occur. Current practice on Network Rail structures requires paint to extend onto the adhesive, but not across the line from adhesive to laminate. This is intended to provide maximum protection for the potentially corroding cast iron surface while maximising the opportunity to inspect the interfaces. This detail is simplified by forming a fillet in the adhesive that extends a little way up the edge of the CFRP laminate.

Water has been leaking through the deck, and there is already some light water-straining on the paint surface (apparently deposited by water running out from the brickwork). However, there are no indications that this is entering the bond or damaging the adhesive interfaces at this time.

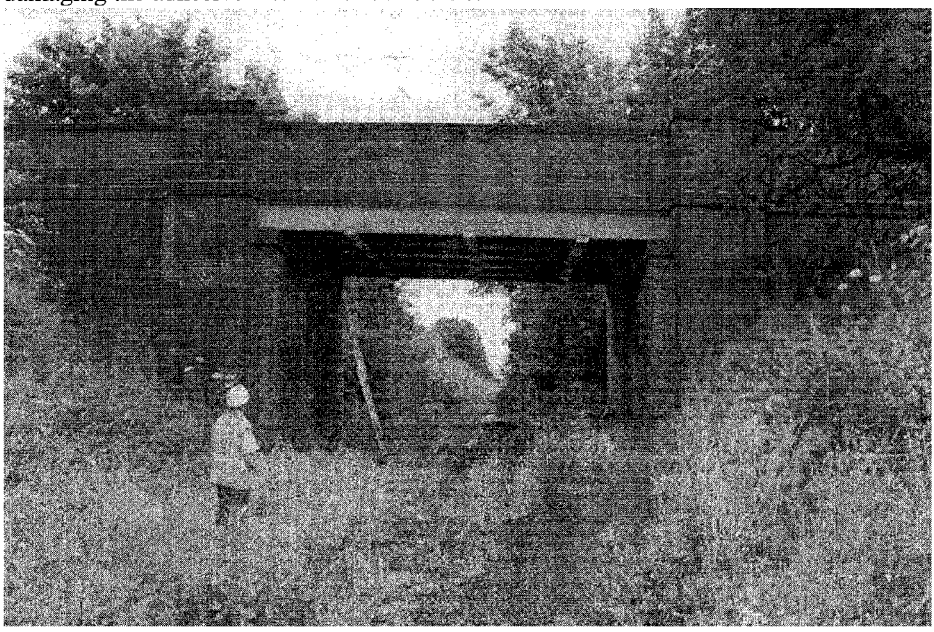


Figure 6. Structure at approximately 18 months after installation of CFRP

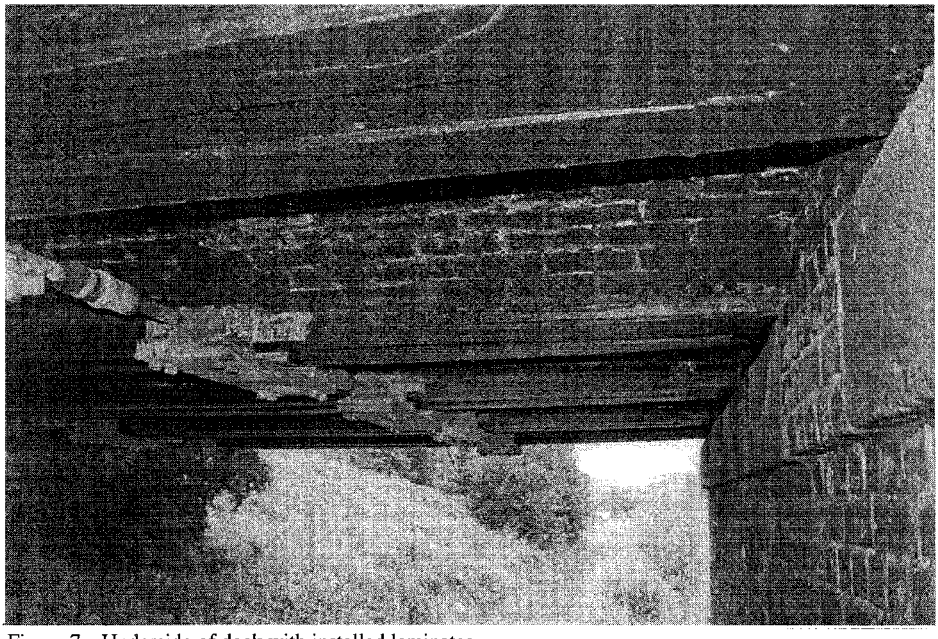


Figure 7. Underside of deck with installed laminates

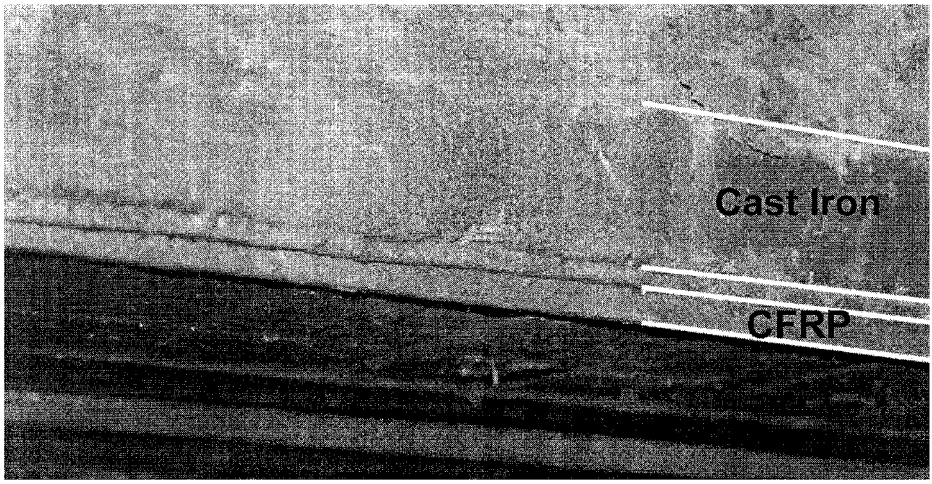


Figure 8. Beam edge near end of laminate, showing adhesive layer between cast iron and CFRP. Laminate at this location is approximately 10mm thick at the centre of the photo.

FUTURE MONITORING

To date, inspection of the bridge has been limited to occasional visual inspections, and tap-testing. The convenient location over a currently disused rail line means that the bridge is a prime candidate for 'proof-of-concept' testing to demonstrate the performance of testing methods in the real bridge inspection situation. Network Rail is currently in discussion with various bodies (both commercial and academic) with a view to evaluating testing methods in such an environment.

CONCLUSIONS

Maunders Rd Bridge was strengthened by the addition of ultra-high modulus CFRP laminates bonded to the soffit of the cast iron main beams by epoxy adhesive. It was the first such Network Rail structure to be strengthened by the technique, and was consequently instrumented during and after the works.

The results obtained during installation validated the assumptions made during the design process, and agreed with work done on cast iron jack-arch decks in the 1940s. They provide reassurance that the structure is behaving in the manner anticipated.

The results obtained in service do not permit conclusions to be drawn regarding performance under imposed loading. However, they do demonstrate the importance of considering thermal effects during design and the magnitude of thermal strains that occur in such a strengthening scheme.

This bridge is ideally suited to prove the practicality of developing test methods for composites on metallic bridges. We look forward to continuing the inspection and assessment of the behaviour of this bridge in future years and hope to develop further insights into cast iron jack arch deck behaviour from ongoing testing exercises on the structure.

ACKNOWLEDGMENTS

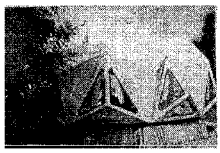
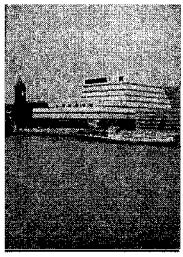
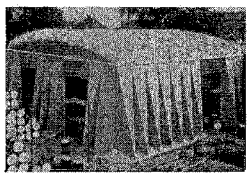
The author would like to thank Network Rail for permission to publish this paper. The views expressed are those of the author and not necessarily the views of Network Rail.

IN-SERVICE PERFORMANCE OF FRP STRUCTURES

Sue Halliwell
BRE, Watford, UK

INTRODUCTION

FRPs have been used successfully over the past 50 years in a wide range of applications in the marine and civil engineering sectors in a diverse range of applications[1]. These include pipes, tanks, slabs, walkways, bridge decks, gratings, column reinforcing wraps and reinforcing bars for concrete. In many of these applications FRPs are exposed to one or more environmental influences. All FRPs are durable inasmuch as they are water resistant, thermally stable and cannot rust. Particular grades of high durability (5-20 year lifetime) FRPs are available for specific applications e.g. FRPs for concrete re-bars incorporate alkali resistant glass fibres in order to resist fibre attack by pore water. In almost all applications, the durability of an FRP may be enhanced by imposing a conservative safety factor (2-4) on the design, and in many such cases additional durability may be achieved by the use of a protective coating and/or the incorporation of light stabilisers and antioxidants.

1: Structures erected in the early 1970s are still meeting performance requirements
1.1Covent Garden Flower Market roof | 1.2 School classroom Preston | 1.3 Mondial House London | 1.4 Modular Stores Building Wollaston

PERFORMANCE REQUIREMENTS

Service Life

Most materials have a finite life. Metals can corrode and can suffer from fatigue. Wood can rot, even preservative treated timber can rot eventually in a severe hazard. Concrete can crack or suffer from various chemical degradation processes. Natural rubber can perish as a result of ozone attack. All these materials have been around for long enough for us to know and make allowance for their weaknesses.

FRPs are no exception to deterioration, but can be designed to meet even the most challenging service environment. There are continuous improvements in resin technology (new improved varieties of resin tend to be developed around every seven years). FRPs are now being specified for applications designed to last for 30, 40 or even 60 years without loss of functional effectiveness. The accelerating trend towards using FRPs in bridges and buildings means a further extension of the required lifetime, possibly to almost a century.

When does an FRP product have to be replaced?

It is sometimes difficult to determine the end of life of a product. There are three key factors:

- the product must remain safe to use despite the stresses and the external weathering they experience over decades
- it must not become too expensive to maintain
- it must continue to meet performance requirements – structural or aesthetic.

The possibility of repair is an attractive feature of FRPs. Their useful life can often be extended because they are more easily repaired than some other materials. Additionally, they can be used to extend the life of structures originally made from another material, such as concrete or metals. In some cases, however, the very ease of replacement of FRP components encourages disposal over repair.

PERFORMANCE IN SERVICE

Causes of deterioration

All construction materials are subject to deterioration in service due to exposure to certain environmental elements. Material deterioration may begin through one or more of the following influences:

- Mechanical stresses, including static loading, fatigue, repeated minor impact, erosion (including water erosion) and abrasion
- Chemicals (water, solvents, fuels, oils, acids, cleaning liquids, atmospheric oxygen, oxidising agents, caustic alkalis etc)
- Radiation (including sunlight)
- Heat, including high temperatures and large and rapid fluctuations in temperature
- Biological attack from bacteria, fungi, insects and marine borers.

Outdoor weathering can involve all five factors simultaneously. Materials can often survive individual threats such as ultraviolet light or a specific solvent, but they can still succumb to a combination of influences.

Biodegradation through micro-organisms, whilst a major factor for other materials (timber in particular), has very little importance in the degradation of most polymers, whether reinforced or not. However, wood-plastic composites can rot and UPVC can host mould fungi. Most FRPs can be buried safely underground for decades without rotting. However, mould and algae adhesion to pre-weathered surfaces can be critical, if the aesthetic appearance of the FRP is of importance.

Fabrication of products

There are obvious links between fabrication procedures, inspection methods and subsequent product durability. Some methods of manufacturing FRPs produce better quality products than others. They introduce fewer defects, allow better control over fibre placement and orientation, enable a higher volume fraction of fibre reinforcement to be used, or lend themselves to better quality control.

Quality control is an important element in the optimisation of material durability. Achieving consistent output involves sound operator training, regular routine screening of raw materials, competent maintenance of processing machinery and good mould tool design. It also requires vigilant oversight of the actual processing operation, including

atmospheric conditions such as humidity, temperature and dust content. Furthermore, it requires the use of up-to-date inspection methods on the final products.

Maintenance

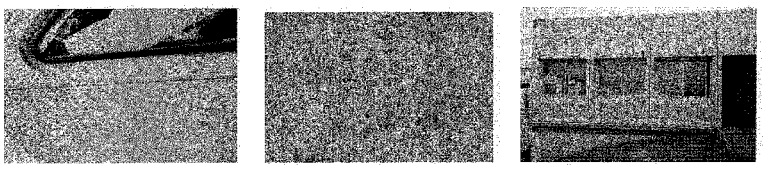
Incorrect maintenance of an FRP structure can deleteriously affect the durability. The use of inappropriate cleaning agents based on strong alkali, solvents or abrasives can damage the surface. Conversely, a beneficial effect can be obtained by the occasional use of a mild cleaning agent and the application of a wax specially formulated for the upkeep of FRP products. Maintenance procedures are detailed in BRE Good Repair Guide 34.

Property Retention as a Guide to Durability

After several decades in service the initial properties of a component will have changed, even in the absence of obvious mechanical damage. It is customary to cite the change in properties with time as a measure of the extent of deterioration, and '% retention' has become by implication a measure of durability[2]. Not all properties change equally rapidly and the selection of significant properties requires careful consideration.

The durability of an FRP article is sometimes considered to be a function of its appearance, including colour changes, loss of surface quality, and so on. Sometimes the changes are more obvious; there may be gross cracking or swelling. At the other extreme, there may be no visible signs of deterioration. Changes may only be apparent when using advanced diagnostic equipment, such as thermography, acoustic emission equipment, ultrasonic instrumentation, an electron microscope or spectrometers for chemical analysis.

Effects of Weathering



2: Changes induced by weathering
2.1 Crazing of surface 2.2 Deterioration of gel-coat 2.3 Un-even discolouration

All materials of construction change in appearance on extended exposure to the weather. Materials such as brick, stone, exposed hardwood, slate and copper are judged to improve aesthetically on weathering. Others such as concrete, painted timber and polymers (including FRPs) become less pleasing on the eye. Whether this factor is important depends largely on the application of the material.

Resins vary a great deal in their ability to withstand outdoor use for long periods. Poor performance can sometimes be completely transformed by trace additives, so the solution becomes one of using the right grade of resin.

The effects of outdoor use on structural FRPs such as glass/polyester or carbon/epoxy laminates are confined to the surface and do not often involve a serious threat to their structural integrity, unless perhaps there is a reduction in impact strength as a result of surface cracking. The effects are mainly cosmetic[3] including:

- Fading and darkening
- Yellowing
- Blooming
- Loss of gloss and chalking

Colour fading or darkening without loss of gloss can be due to the use of unstable pigments or pigment combinations which change colour after exposure. This can be overcome by the appropriate choice of pigment.

Yellowing is due usually to the darkening of the base gelcoat resin, especially in whites. This can be overcome by using a more UV-resistant resin and better UV additives, and by ensuring good cure of the resin.

Blooming is caused by migration of an incompatible pigment or additive to the surface of a gelcoat to give a mat, faded appearance. Certain organic pigments can be the cause of this. Bloom can be removed by polishing, but this is only a short term solution. Judicious choice of the pigment should overcome this problem.

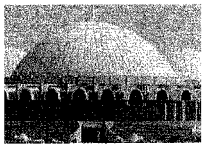
Loss of gloss is normally brought about by erosion of the surface layer of the gelcoat due to chemical and/or physical damage. The colour of the gelcoat then appears to whiten, due to the diffused reflection of light from the matt surface. This is most serious in mouldings with strong bright colours where the phenomenon is most easily observed. On paler colours the effect is less noticeable. Indeed the whiteness of a white structure can even improve by this means because surface dirt is shed, leaving a fresh exposure of white pigment. This phenomenon is termed 'chalking'.

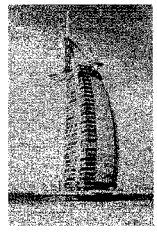
The erosion of gelcoat after many years service that can bring about the eventual mechanical failure of the laminate by exposing the reinforcement underneath. However, the onset of loss of gloss or chalking does not presage the immediate disappearance of the gelcoat which normally lasts for many years longer.

Climate effects

The severity of the weathering effects depends on the climate to which a material is exposed. Climates can be classified into a number of types such as temperate, sub-tropical, desert, arctic and Mediterranean, as well as industrial, rural or marine. In addition, variations occur from season to season and from year to year. It is thus complicated to compare the weathering performance of one material with that of another and to predict accurately the performance in service of a new component.

Despite this, FRPs can be designed to meet specific climatic conditions, however severe. For example, they are finding widespread application in the Middle East.





3: Application in extreme climates
3.1 Sharjah Airport Dome, 1974 3.2 Arabian Towers Hotel Cladding, 1990

Prediction of durability

Predicting the weathering performance of building materials (including FRPs) can be carried out based on artificially accelerated laboratory weathering experiments and field trials. The latter take several years and relatively few organisations have been able to generate large data banks. However, there are now sufficient case histories of FRP products to give us performance data extending over three decades or more. Accelerated methods can be undertaken indoors or outdoors. Accelerated prediction techniques for FRPs are discussed in detail in BRE Information Paper 11/03[4].

Controlling weathering performance with additives

UV Absorbers

UV absorbers are commonly used in the gelcoats on FRP components to absorb UV light and dissipate the absorbed energy. In the first few years of life in temperate climates, the use of a UV agent makes little difference to the weathering properties of a good quality pigmented gelcoat. However, experience shows that patchy yellowing of white gelcoats, which sometimes occurs in these climates, can be overcome by such means. It is thought that this type of discolouration is caused by areas of the gelcoat having a lower pigment content. UV absorbers help to overcome such yellowing of resin.

In the longer term or under conditions of high levels of radiation (such as subtropical climates) UV agents can be shown to improve gloss retention and colour stability. Traditional UV absorbers that have been used for many years are benzotriazole and hydroxybenzophenone derivatives. Other UV agents known as hindered amine light stabilisers (HALS) do not absorb UV radiation, but act by absorbing any free radicals that have been formed.

Fire Retardant Additives

The use of fire retardant additives in gelcoats has a detrimental effect on weathering properties. Thus it is good practice to achieve fire retardancy by using a highly fire retardant resin behind a non-fire retardant gelcoat.

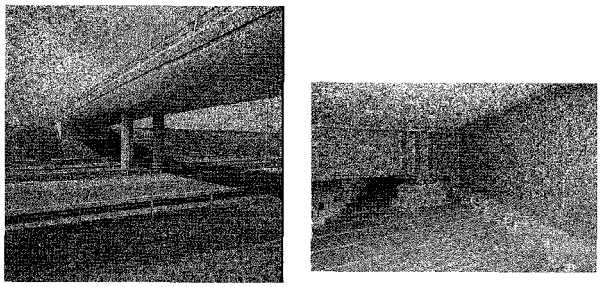
Pigments

Most gelcoats are used in pigmented form in order to hide the substrate and provide a choice of colour. Careful selection of pigments is of importance since this can affect the durability of the finished product.

Case Studies

Most can be learnt about FRP durability and performance in service by examining actual structures. BRE carried out over 25 surveys of existing FRP structures[1]. Several case studies were reported at ACIC 2002, key additional ones are given in this paper.

Bridge enclosure on Second Severn Crossing approach roads

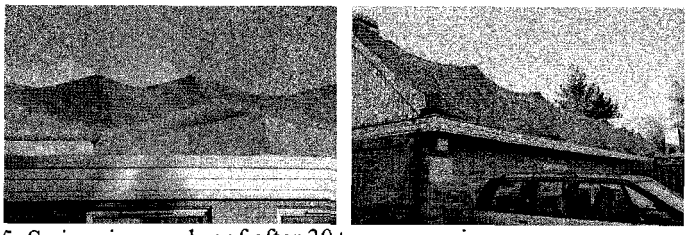


4: Second Severn Crossing approach roads bridge enclosure

In Avon two approach roads of dual two-lane motorway link the M4 motorway at Awkley and the M5 Motorway at Lawrence Weston to a new interchange at the main estuary crossing embankment at Pilning. The total length of the new motorways is 15km. Some 24 new structures are provided, seven of which incorporate advanced composite enclosure systems for improved maintenance life. The scheme also involves the realignment of 12 side roads. Traffic studies, geotechnical investigations, planning and environmental considerations were carried out. Preferred routes were selected after public consultation and the submission of a Parliamentary Bill for which client support was provided at Select Committee stage.

When one of the bridges was inspected by a BRE engineer in September 2001, the interior was found very dry and clean. The system appeared to be working excellently with no sign of water ingress, damp, build up of debris or corrosion occurring. An important aspect to the system is that some ventilation is allowed and that it is not designed to be hermetic, thus any condensation forming is removed. One rig-seal to a bridge column was noted as being adrift and one or two panels appeared to have been marked by site mortar or concrete. Apart from this the exterior was clean, in spite of the dirt and spray from passing traffic, and was aesthetically very pleasing. No visible deterioration to the panels was noted.

Swimming pool roof, Southampton

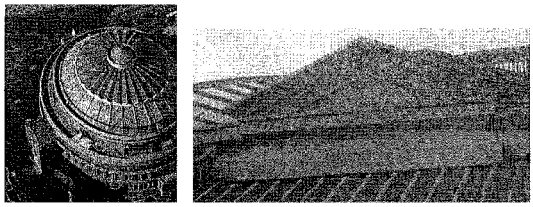


5: Swimming pool roof after 30+ years service

The structure was erected in 1970. It was inspected in 2002. The roof consists GRP pyramidal shaped structures on a metal frame. In general, the condition after 30+ years service was very good, there was some dirt retention. Very little maintenance had been carried out – there had been one successful repair to a corner that was lifting in the wind. The interior of the GRP had been painted, it was thought that this was for

light/heat reasons, and the paint was peeling off in several places making the roof look 'tatty' when viewed from inside. The steel frame was corroding badly.

Royal Albert Hall



6: GRP pediments on the roof of the Albert Hall

GRP roofing pediments were installed in 2002 to replace the existing GRP pediments. Kelsey Roofing installed the previous GRP pediments in 1970 to replace the original timber pediments from 1871 which were painted to resemble the colour of Portland stone.

The performance of the previous GRP pediments was considered acceptable. Integral brackets bolted the pediments on to the interior steel and timber frames of the domes. Some of the brackets were heavily corroded and the GRP was de-laminating from the bracket. Moisture as blown rain was clearly able to get in behind the old pediments.

Repair and Maintenance of FRP Structures

FRPs require little maintenance. Panels facing prevailing winds are generally 'self-cleaning' whilst those in the shadow will become contaminated and require periodic cleaning with a mild detergent solution.

Mechanical damage, during erection or in service, can be patched and an attempt made to match the original but site conditions are not usually favourable for proper curing of the resin and a patch is likely to show after a period of weathering. The quality of the repair will also be influenced by the level of surface preparation, the correct use of repair products and the final finishing of the repair. Many of these aspects depend on the skill of the individual conducting the repair. It is better to replace a complete panel or member if this is practicable.

Restoration of degraded surfaces can be difficult. In the extreme case of the glass fibres becoming badly exposed, they must be scrubbed off completely before any new surface treatment is applied. As with the repainting of all exterior construction substrates, when coating FRP attention should be paid to surface preparation, the specific paints manufacturers instructions ant the supervision of trained labour. Surface preparation, prevailing weather conditions during application and the skill of the painter will all have an influence on the service life of the coating, regardless of paint type.

Conclusions

FRP components have good durability:

- FRP structures perform well if appropriately designed
- several structures in the UK have given over 35 years of service, and are still meeting performance requirements

- where reported failures were not due to the material, but due to a lack of understanding of material properties at the initial design stage or poor detailing in some prefabricated sections.

The following signs of deterioration may be observed. These do not affect the structural performance of the component or building, but may be significant for certain applications:

- crazing
- delamination
- dirt retention
- loss of gel-coat

Improvements in resin and manufacturing technology over the last ten years will lead to improved durability of FRP components and should enable design lives of 60-100 years to be achieved.

References

1. BRE Report 461: Long-term performance in service of FRP in construction

2. Pritchard G (Ed), Reinforced Plastics Durability, Cambridge, Woodhead Publishing, 1999.

3. Halliwell S M. 'Reinforced Plastics Cladding Panels' Proc. Composites and Plastics in Construction, BRE, UK, Nov 1999, Paper 20.

4. BRE Information Paper 11/03: FRP in construction: predicting weathering

5. Halliwell S M. 'In-service performance of GRP in buildings' Paper 8.5, ACIC 2002, Thomas Telford, London 2002.

6. BRE Good Repair Guide 34: Repair and maintenance of FRP structures.

FIBRE COMPOSITES IN COASTAL AND RIVER DEFENCES

Dr Colin K Jolly
Cranfield University Shrivenham, UK

ABSTRACT

Fibre reinforced composites (FRP) offer high strength, chemical resistance, low weight, and freedom to create structurally efficient geometries. Fibre composite products have consequently proved highly competitive in aerospace and petrochemical industry structures. FRP composites have been relatively expensive, and their penetration into the construction industry has been limited. However, as the cost of some traditional materials has increased, FRP unit costs have fallen. Composite-composite combination of FRPs with traditional construction materials, or with recycled bulk materials, now offers more durable options than traditional construction. Though remaining slightly more expensive, these options are in many cases demonstrably more economic on a whole-life cost basis.

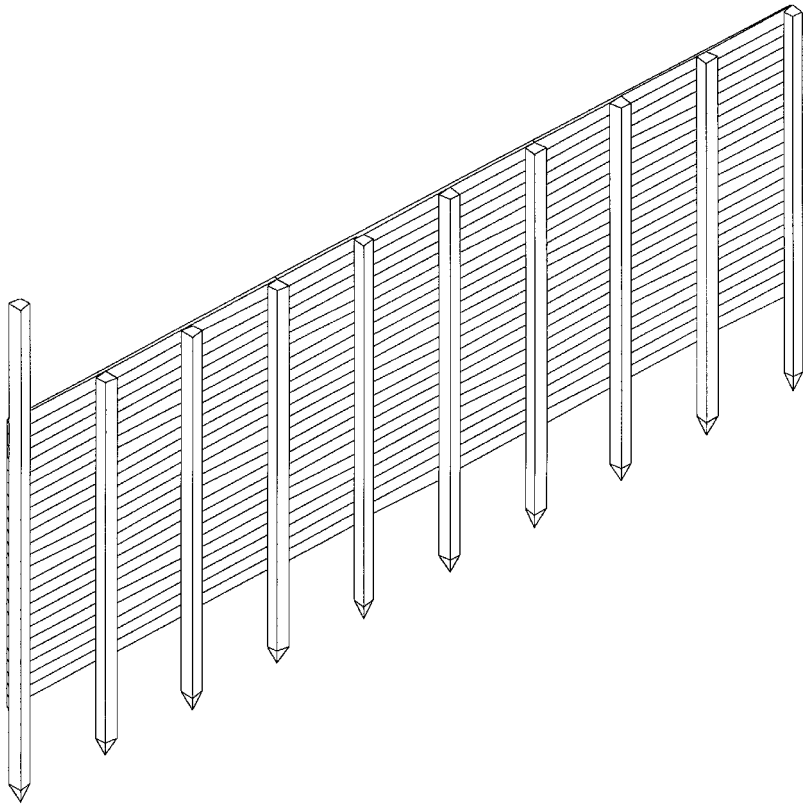
In coastal and river protection works, the cost of repair or reinstatement is extremely high. The chemical aggressiveness of brine and of contaminated river water, particularly as their ambient temperatures rise, is increasing deterioration rates of steel and reinforced concrete. Consequently, coastal and river environments are front runners for becoming economically viable markets for FRPs, as predicted by the author [1]. This paper describes two examples along the south coast of the UK that demonstrate this: one is at Bournemouth, and the other at Hayling Island.

INTRODUCTION

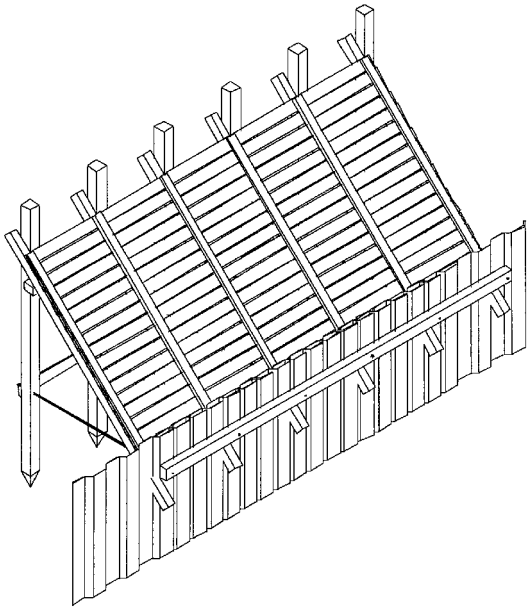
Bournemouth is a town with a population of about 170,000 on the south coast of the United Kingdom. Bournemouth is famous for its seven miles of almost continuous sandy beaches that make it one of the country's most popular holiday resorts. It also has a reputation as a popular retirement area, for foreign visitors learning English, and as a conference venue.

The beaches at Bournemouth are seen as one of its great assets, and the Borough Council takes great care to preserve its high reputation as a resort. The natural tendency of the prevailing southwesterly winds is to create wind drift, wave action and inshore currents that drive the beach sand eastwards, and to form near-to-shore sandbanks. Historically, Bournemouth has used greenheart timber groynes rising up the beach from the king pile at the seaward end to control this littoral drift, as shown in Fig. 1. However, increasing cost, combined with shortage, of greenheart and similar salt-water resistant bulk timber led to an interest in consideration of fibre reinforced plastics. FRP combined with recycled plastics provide a viable alternative material for groyne panel construction, and when combined compositely with concrete are viable for groyne piling.

Hayling Island is a smaller holiday resort further east along the south coast. It is the adjoining island to Portsea, on which Portsmouth is founded, and lies between Langstone Harbour and Chichester Harbour with only its south coast facing open sea. Along the eastern end of this exposed coast, breastwork is used to protect the shoreline, in addition to greenheart timber groynes controlling littoral drift. The general



1. Groyne arrangement at Bournemouth.



2. Breastwork at Havant.

arrangement of this breastwork is shown in Fig. 2, with a steel sheet piled toe tied back to the main piles, and inclined timber bearers to support open-jointed planking.

Geology

The Bournemouth Cliffs are part of Poole Bay. The coast is protected to some extent from the prevailing southwesterly winds by the Isle of Purbeck, particularly Old Harry Rocks, Ballard Point, and Durlston Head. The Cliffs comprise Eocene sands and clays. Until the early 19th century, these cliffs were exposed, and supplied sand directly to the Bournemouth Beaches. As the present holiday town developed, a promenade and sea-wall were built at the foot of the cliffs, which have become largely vegetated.

An eddy in the general west to east longshore drift, caused by the interruption of the Purbecks, and reinforced by ebb flow from Poole Harbour, causes littoral drift from Bournemouth Cliffs westwards towards Sandbanks. Littoral drift from the Cliffs also feeds eastwards towards Boscombe, Branksome, and Hengistbury Head.

The maximum reach for waves incident on the eastern end of Poole Bay is from the southwest, and for the western end is from the southeast. Reversal of littoral drift therefore occurs, depending on each storm's approach direction and the state of the tide.

Similar sand deposits supply the beach at the western end of Hayling Island, where it is largely protected by the Isle of Wight. Towards the eastern end of the beach, there is progressively more flints in the natural material, and this is supplemented by rock and crushed rock supplied to improve protection for the residential areas immediately behind the shore.

Traditional groyne and breastwork material supply

Currently about 8,000 squared greenheart logs are imported to the UK each year. This is approximately 50% of world production, which is almost exclusively from the former British colony of Guyana. The single source of this timber is being rapidly depleted, with indications of severe scarcity within five years. This is a result of former generations' lack of foresight rather than a criticism of the regeneration policies of the foresters. Replanting in recent years has exceeded harvest rates, but these hardwoods only begin to reach maturity after 80 years.

Only opepe is similarly strong, resinous, and thus reasonably resistant to decay in a watery environment, and that is sourced from former French colonies with similar supply problems. Oak is suitable, though not as durable. English oak performs better than the faster-growing European oak or American oak, but none of these are in abundant, cheap supply. Pitch pine is the only softwood with natural resistance in water. Other timbers require treatment with undesirable toxic preservative compounds (e.g. arsenic, creosote).

Industry estimates of time to replacement of the timber in the saline splash zone as: greenheart and opepe, 20-25 years; oak, 12-15 years; pitch pine or treated softwood, 5-8 years.

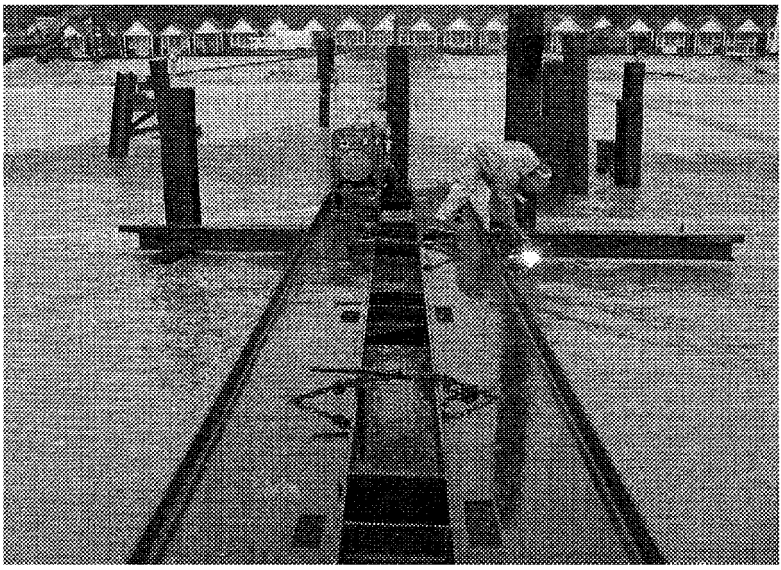
PAST INSTALLATION TECHNIQUES

Piles

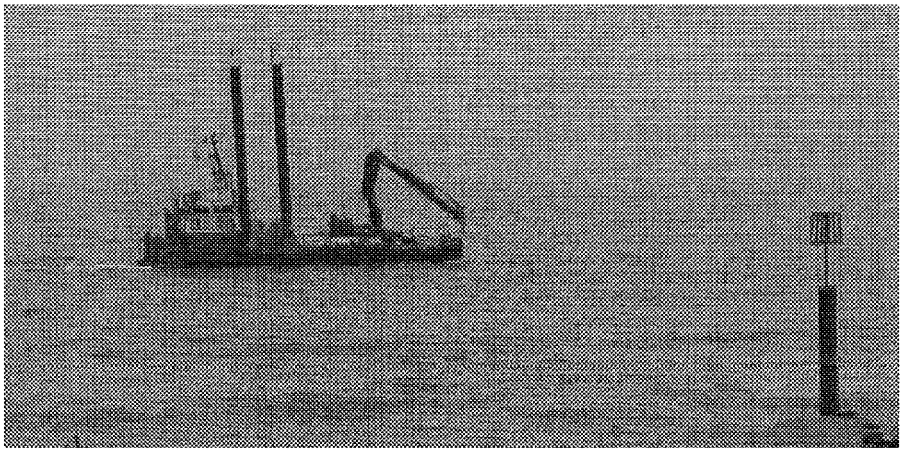
Installation of the groyne piles has developed progressively over recent years. In all cases, the piles are pitched into a guide frame, an example of which is shown in Fig. 3.

Piledriving technique	Advantages	Disadvantages
Hammer	Traditional Suitable for timber	Noisy Damages fibre FRP shell
Hammer on internal mandrel	Traditional Suitable for FRP shells only	Noisy Lost shoe on each shell
Flight auger	Quiet Readily available	Disturbs ground Continuity impractical
Water jet	Quiet Low cost	Disturbs ground Interrupted by boulders
Vibration	Works in many soils Moderately quiet	FRP pile must be precast Inefficient for timber

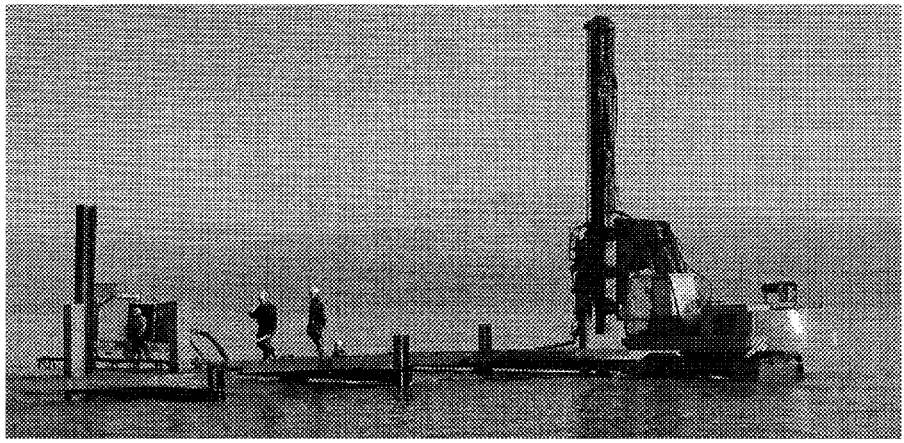
Table 1. Potential techniques for driving timber and FRP composite piles.



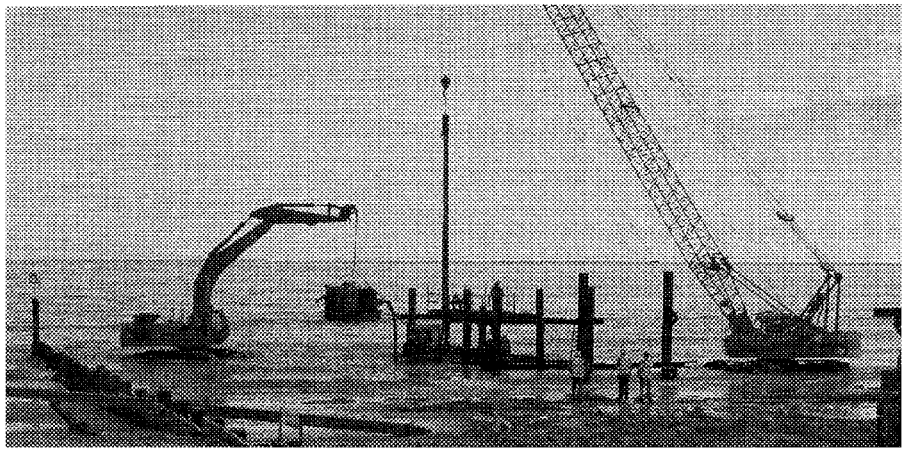
3. Guide frame for pitching piles.



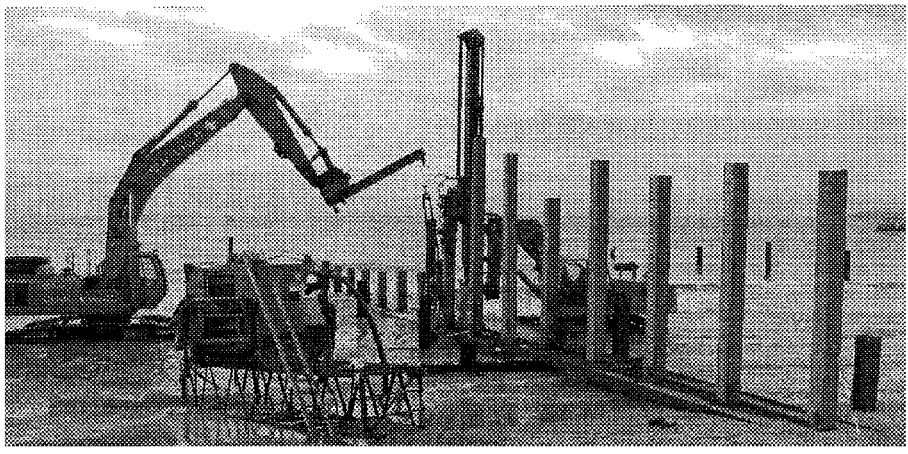
4. A jack-up barge for piling.



5. Front-mounted piling hammer.



6. A large crane-mounted water lance pre-jetting a hole in the seabed.



7. Front-mounted hammer guiding pile into pre-jetted hole, aided by small lance.

Table 1 summarises the merits of different piling techniques for this application. A number of these have been used in the past. Until recently, the piles were driven using a jack-up barge, see Fig. 4. Piles lower down the beach were then installed by a crane, mounted on a temporary pier that was piled in advance and subsequently removed.

Trials using the front-mounted hammer rig shown in Fig. 5 eliminated the need for a temporary pier, improving speed but retaining a noisy process that disturbed residents. Subsequent trials using a large water jet to predrill a hole in the seabed was found to reduce hammer noise considerably, particularly if material settling into the hole was kept mobile by a smaller water-jetting lance.

Both sheet piling and timber piles for the breastwork at Hayling Island are installed using the same hammer driving techniques.

Panels

At present, the lower panels are pre-assembled onto two walings, with the greenheart planks vertical. Plywood is fixed over the entire lower panel surface to assist in preventing sand from washing between the planks, see Fig. 8. Once this adrasive flow starts, the gap between planks rapidly increases, and when it is about 2 mm the groyne ceases to prevent passage of beach material. The groyne then has to be replaced. The walings are bolt fixed through the piles. The resulting holes are near the location of maximum bending moment, so cause loss of pile strength at a critical section.

Fig. 9 shows a sand bund, formed using material excavated from between the piles, to protect the excavation from wave action. This increases the time available for this work at the seaward end of the groyne to approximately 45 minutes on a spring tide. Work here is highly dependant on tides and weather. Sand conditions in the excavation are frequently quick during this tidal work.

The top panel is made up of horizontal planks, individually fixed by to the piles by coach screws. Staggered butt joints at the piles help provide panel moment capacity to distribute load between piles. Indeed, the top planks are often fitted first to provide mutual fixity for the piles when excavating to install the lower panels, and to ensure good alignment of the top of the groyne.

Breastwork planking is installed at Hayling Island with 25 mm spaces between planks to permit waves to pass through and dissipate their energy. Graded angular rock fill lies behind the planking to break up the waves. The water then drains back through the open planking as the wave recedes. There is a tendency for the smaller crushed rock to accentuate the abrasive properties of the beach material.

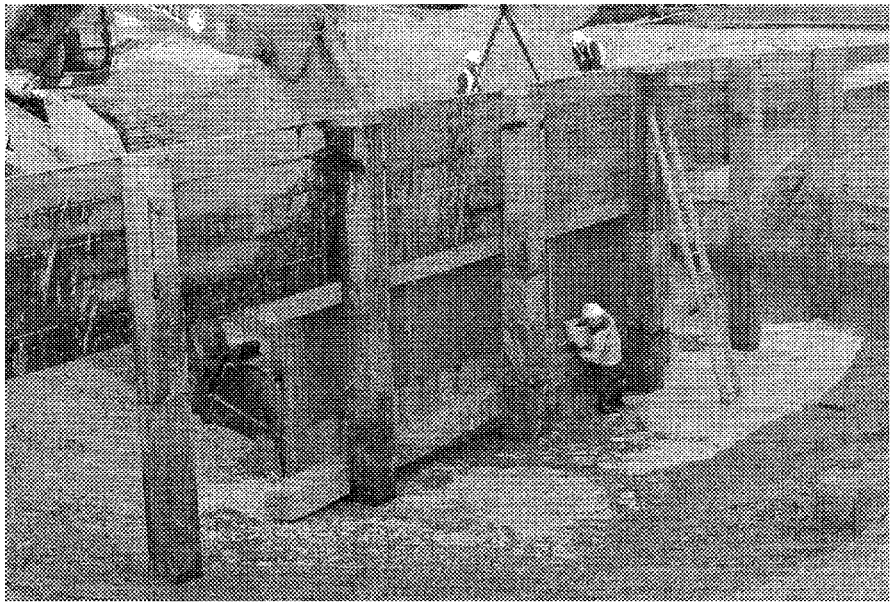
SPECIFICATION

Loading

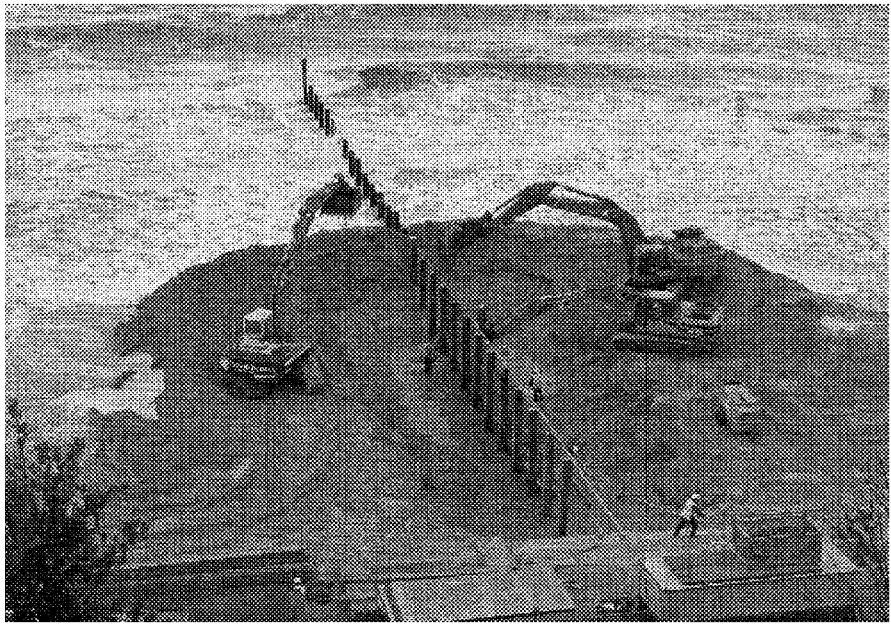
The variable littoral drift forces the groyne at Bournemouth to be designed to resist a 3.0 m difference in beach level between the two sides, and to allow for complete reversal. Consequently, fixings into the piles must be able to resist in tension the full pressure on the panels.

Underlying beach material is sand, silts and clays with maximum particle sizes of about 2 mm in most groyne locations.

The action of waves riding up the high beach side of the groyne, then filtering through the sand, creates unusual downward forces. These have been estimated from



8. Installing the lower panel



9. Forming sand bund to protect lower panel installation.

past experience by Bournemouth Council to develop an effective soil relative density of 2.1, the result of a combination of seepage flow drag and surface tension.

The timber groyne has been demonstrated to work effectively using 6.1 m long, 300 mm square piles at 2.5 m centres, clad with 4.2 m deep panels. The king pile seen

in Fig. 1 is higher to provide support for warnings of underwater hazards to swimmers and navigators.

Materials

Existing installations at Bournemouth use exclusively greenheart timber, marine quality plywood, and stainless steel fixings.

Abrasive wear on the Hayling Island breastwork metal fixings makes it uneconomic to use stainless steel. Most of the fixings for this application are galvanised, since both the metal and the timber are abraded at such a rate that incremental renewal is normally required after between 5 and 8 years. Wear rather than rot of the greenheart forces its replacement after two or three installations of supplementary fixings.

Serviceability

Normal timber deflection criteria are applied for the designs. The plywood is kept at low levels on the groyne panels in an effort to avoid splinters affecting beach visitors. Corners of the sawn finish piles and planking are rapidly abraded so splinters from these are rarely a problem.

Projecting ends of fixings are minimised. Projecting bolt heads are acceptable, but exposed excess lengths of bolt threads are cut back close to the nut face and hammered over.

PROPOSED DESIGN SOLUTION AND INSTALLATION TECHNIQUE

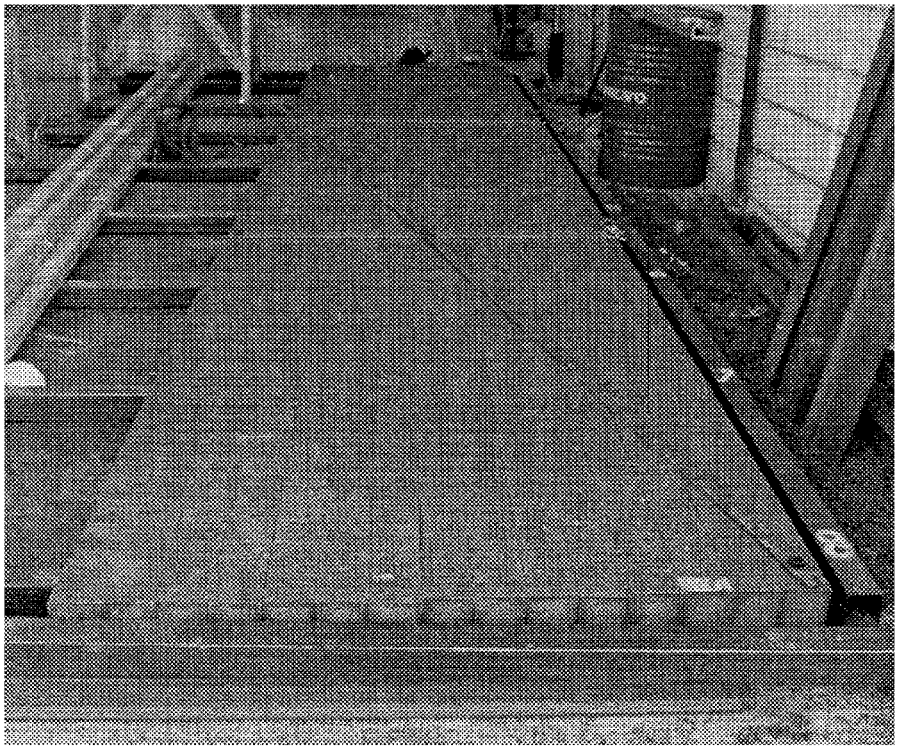
Piles

The proposed solution is for a FRP pile shell, overclad on the external face by recycled waste plastic to give the appearance of timber. The plastic provides additional ultraviolet light protection for the FRP, and has greater abrasion resistance. It thereby protects the public from fibre splinters that would be exposed as the sand surface is abrasively mobilised by wave action. The pile shell is filled with concrete and is designed as a composite column using the design criteria developed by Lillistone and Jolly [2,3]. The design also complies with the more general design recommendations published by the Institution of Structural Engineers [4].

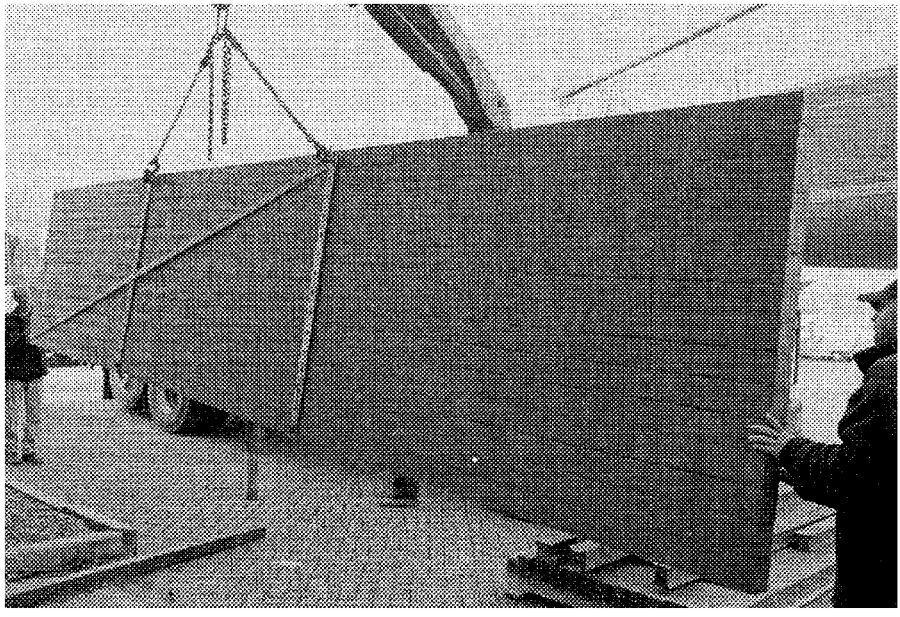
Three options have been designed in detail for the Bournemouth application. The first option was recycling of withdrawn greenheart piles by overwinding with FRP to supplement the declining strength. A design of this option assuming that only service strength of the piles remained proved uneconomic. In fact, a test on one of these withdraw piles that had virtually no loss of gross section but with a single hole created by a marine borer, demonstrated a strength loss in excess of 30%. Enzymes secreted by the boring insect to aid its digestion of the cellulose are believed to account for this high loss. The second option of circular composite piles is most efficient in providing structural enhancement to the concrete infill by triaxial confinement. However, the third option of rectangular composite FRP piles avoid the need for specially moulded extrusions to facilitate concealed fixings, and this became the preferred design.

A filament-winding machine has been specially modified for Plasti Ltd. It has a long bed to produce piles for these and other piling and composite column applications.

FRP pile shells can be hammer-driven using a mandrel inside that rests on a shoe to provide a driving point. A shoe is then lost for each pile. This method has been



10. Jig assembly of groyne panels.



11. Use of washer plates and diagonal bracing during carriage.

demonstrated for driving into highly variable gravel at an inland site. Alternatively the pile can be precast and driven in a similar fashion to the latest technique for timber piles. Better still, the pile shell can be driven silently by water-jetting down the pile core. This method has been demonstrated at full scale in the laboratory [5] for beach material with the same grading as exists at Bournemouth. Bottom driving is more appropriate at Hayling Island because of the inclusion of stones and boulders.

Panels

Recycled plastic is again proposed for the panels and planking. This is an environmentally attractive use for bulk quantities of inert, abrasion-resistant, and rot-resistant waste. Laboratory tests have demonstrated that the proposed material is approximately eight times as resistant to sand abrasion as greenheart timber.

Joints between planks can be formed with FRP box-section tongue inserts into 100 mm thick grooved extrusions. This tongue interlock forms a contorted pathway that makes the onset of particle penetration extremely difficult. The FRP sections are designed to match both strength and stiffness resistance to lateral load of the greenheart. Longitudinal joints are again staggered.

For the groyne, planks are pre-assembled on a jig into panels (see Fig. 10), and then through-bolted to provide rigidity during carriage. Temporary diagonal bracing is used in conjunction with the permanent washer plates to retain the requisite angle to match the beach profile. See Fig. 11.

Pre-drilled washer plates provide for rapid fixing using slightly more numerous, but substantially smaller coach screws. No bolts are required. The need for plywood, walings and sealing fillets is eliminated. The total weight of stainless steel fixings is reduced.

The proposed replacement for Hayling Island planking consists of narrow panels of the same construction as for Bournemouth. Each plank then contains two of the FRP box sections to provide the requisite strength and stiffness.

ECONOMICS

For the materials alone, the cost of piling relative to the current cost of greenheart timber is about 3 for filament wound recycled timber piles, and 5 for composite FRP and concrete piles regardless whether they are circular or square. However, as for most river and coastal works, the material cost is low compared with installation costs. The anticipated life for the FRP piles is 60-70 years. Whole-life cost analysis shows both the FRP composite pile solutions to become justifiably economic at the age when first replacement of the timber piles is required.

For the groyne panels the material cost is slightly less than for the existing installations, mainly because of eliminated components and reduced stainless steel weight. The smaller-section breastwork planking is slightly more expensive, but whole-life cost again shows it to be economic at age of first replacement. This can occur as early as 5 years, and can often occur after 8 years.

Use of the lighter FRP with plastic components, and advantage obtained by more pre-assembly of panels is expected to make the proposed solutions more economic to install, thereby offsetting yet more of the material costs.

A progressive programme of trial installations at Bournemouth has demonstrated that FRP-strengthened, recycled plastic planks wear well. Two panels have been

supplied for installation during this winter's maintenance and renewal season. Trial windings of piling sections are under way.

Plastic samples have been installed at Hayling Island for localised replacement of worn lower planks on the breastwork. This will demonstrate in situ the greater abrasion resistance under the particularly aggressive conditions that prevail there.

CONCLUSIONS

Combination of FRP composites with recycled plastic, and with concrete, to provide doubly-composite sections has been demonstrated to provide an economically viable long-term alternative to tropical hardwood timber for river and coastal protection. Faster intertidal operations are expected to make the economic assessment even more attractive when installation is no longer novel. Use of relatively small quantities of FRP to supply the strength and durability, and to contribute to the stiffness of components, is an efficient use of their properties in this context.

Improvements to the economy of FRP provision are already planned as a production facility for bespoke large components is already available. Specifically designed pultruded FRP sections will also reduce costs. Increased FRP production to supply the massive volumes demanded by the construction industry will help to cut relative costs at a time when traditional hardwood sources are becoming scarce.

Acknowledgements

The author wishes to thank Bournemouth Borough Council, Dean & Dyball Ltd., and Plasti Ltd. for their co-operation in the preparation of this paper.

References

1 C K Jolly, *Present And Possible Applications Of Fibre-Reinforced Composites In The Building And Construction Sectors.* Building Research Establishment Report, Department of the Environment, June 1996.

2 C K Jolly and D Lillistone, *The Stress-Strain Behaviour Of Concrete Confined By Advanced Fibre Composites*, Concrete Communication, British Cement Association, Crowthorne, 1998, 117-136. ISBN 072101540 9.

3 C K Jolly and D Lillistone, *Concrete-filled FRP Circular Columns Under Eccentric Loading,* Fibre Reinforced Composites, Woodhead Publishing Ltd, Cambridge, 1998, 506-513. ISBN 185573375 7.

4 Institution of Structural Engineers, *Interim guidance on the design of reinforced concrete structures using fibre composite reinforcement.* IStructE, London, 1999.

5 G T Bateman, 'Design parameters of a water-jet piling system for hollow tubular piles', *Research dissertation,* Cranfield University, RMCS, Shrivenham, 2002.

REHABILITATION DESIGN AND EVALUATION OF THE HAWTHORNE STREET BRIDGE FRP DECK INSTALLATION

Kristin Kessler, John Lesko, Thomas Cousins
Virginia Tech. USA

ABSTRACT

The Hawthorne Street Bridge is a 75' clear span historic through truss structure over a C&O Railroad/CSX Rail line. There are five 15' bays transversely supported by W14x119 girders. Stringers (W10x33) on 5' centers support the 6-inch thick reinforced concrete deck between girders. The bridge is presently posted at 7 tons with a recommendation to reduce to 5 tons based on a recent load rating. VDOT and the City of Covington desire to upgrade the Hawthorne St. Bridge. The reinforced concrete (RC) deck is in poor condition and recently has been patched after several large pieces of deck fell onto the railroad tracks to the extent that the City closed the structure in February of 2001 to make emergency repairs. In addition, there is a concrete sidewalk that requires rehabilitation and whose weight is critical in the rating of the structure. The proposed rehabilitation would retain the historic cast iron Phoenix truss system while replacing the RC deck, floor beams and stringers. A deck constructed from adhesively bonded pultrusions is presently suggested reducing the dead load from 100 lb/ft^2 to 25 lb/ft^2. Both one and two-way bending analysis of the deck stringer configuration, not including composite action, has been accomplished and validated via scaled model testing. In addition to the bolted connection between the deck and stringers developed for the design, an adhesively bonded condition is also being considered and tested. The details of the design and analysis are presented in conjunction with cost and installation considerations.

INTRODUCTION AND BACKGROUND

There is increasing concern surrounding the aging of the U.S. transportation infrastructure. According to the 2000 Transportation Statistics Annual Report [1] there are over four million miles of transportation media, including highway, rail, and waterways. Among this system of roads there are nearly 160,000 bridges, of which 15% are structurally deficient and 14% are functionally obsolete [1]. To be structurally deficient and functionally obsolete means these bridges suffered from loss of material properties due to degradation and age, and are experiencing traffic they were not originally intended for.

The Hawthorne Street Bridge in Covington, Virginia is one of the many bridges considered structurally deficient. The through truss bridge is a 75' clear span Pratt-truss structure with a roadway width of 22 feet, running over three Norfolk Southern rail-lines as shown in Figure 1. The bridge's historical significance is due to the use of the Phoenix Column in the truss. The Hawthorne Street Bridge is an integral part of lifeline access for the fire station to downtown and with the present positioning, fire trucks have to use a longer route. This is also the only route that emergency vehicles can use during periods of high water to get to the area of the City north of the railroad. All of the other road crossings of the railroad are underpasses, which become inundated during flooding.

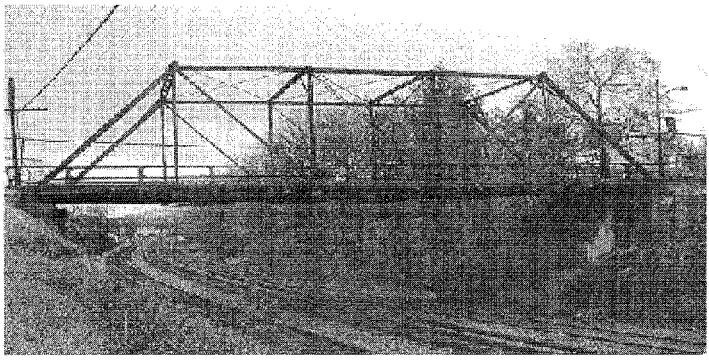


Figure -1: The Hawthorne Street Bridge in Covington, VA.

The current condition of the bridge has required that it be posted at 7 tons, with considerations of lowering that to 5 tons. The structure has a condition rating of 5 (fair condition with all primary elements experiencing only minor section loss). Inspections have shown that the existing W10x33 stringers supporting the deck of the bridge (see Figure 2) are no longer sufficient for meeting American Association of State Highway and Transportation Officials (AASHTO) deflection requirements. The inspections also revealed that the connections of the truss members are rusted to a rigid condition that causes tension members of the truss to sustain compressive loads. Additionally and of primary concern, the reinforced concrete (RC) deck is severely deteriorated and several large pieces of it fell from the structure in February 2001 onto the railroad tracks causing the City to close the bridge to make repairs.

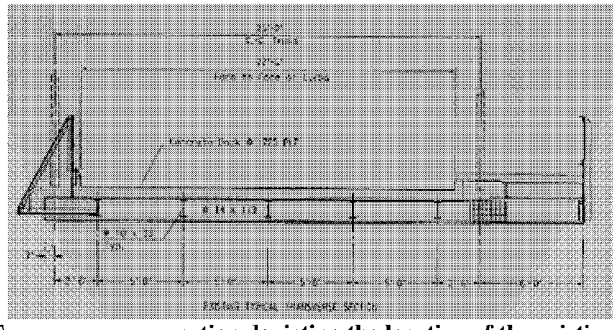


Figure -2: Transverse cross-section depicting the location of the existing members in the Hawthorne Street Bridge.

The Hawthorne Street Bridge is beyond general maintenance, and is in need of a full rehabilitation or replacement; the latter of which is not an option due to the confined areas around each of the abutments and it would result in the destruction of a historically significant bridge. The purpose of the rehabilitation is to greatly reduce the dead weight of the bridge through the use of a Fiber Reinforced Polymer (FRP) deck, as well as to replace some of the existing steel elements of the superstructure. An FRP decking is advantageous to through truss structures because of its high strength to weight ratio, improved durability, resistance to corrosion, and potentially lower life-cycle costs (decreased maintenance). By accomplishing the deck and element replacements, the reduction in dead load will allow for an increased live load, thus allowing the bridge to handle desired and emergency vehicle traffic loads and therefore avoiding partial closure or complete replacement.

REHABILITATION DESIGN OVERVIEW

A successful rehabilitation would ensure that the Hawthorne Street Bridge met AASHTO design requirements enabling emergency vehicles to use the bridge. The proposed design, as shown in Figure 3, replaces the W10x33 sections with W12x40 sections at 5' centers, reduces the width of the walkway from its original 6' to 4.5' and enables the use of a tube-plate deck shown in Figure 4. The deck is made of 6"x6"x3/8" pultruded box beams, two skin plates (1/4" and 1/2" thick respectively), and a wearing surface [2-5]. The design components involved in this rehabilitation include the replacement of the existing deck and stringers. Special considerations were made concerning connection of the deck to the girders, the deck panel-to-panel, and the bridge railing to the steel superstructure. In addition to these replacements, modifications were made to the walkway. All design and replacement decisions were made according to the maximum weight reduction (weight limitations were unknown) as well as maintaining local and global deflection requirements of L/800-L/1000. Ultimately, the bridge should be fully functional, allowing both lanes of traffic to be in full use, with the replacements and recommendations made.

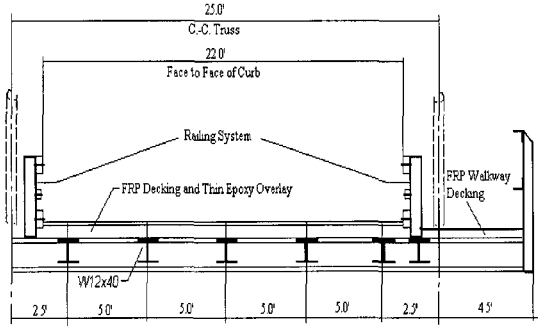


Figure -3: Transverse cross-section of the proposed rehabilitation of the Hawthorne Street Bridge.

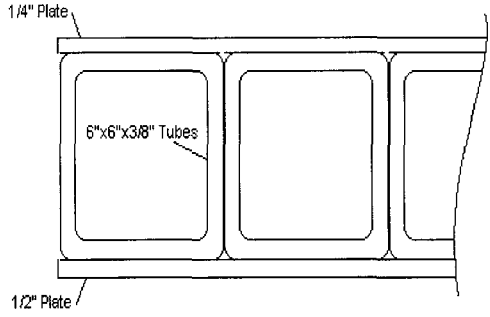


Figure -4: Adhesively bonded pultruded tube-plate deck.

DESIGN FEATURES

Stringer spacing:

Using the appropriate design specifications (VDOT issued), various options for shape, quantity, and location of replacement stringers were evaluated. One way and two way bending analyses were utilized to determine that deflection requirements were met for the selected stringers. Once all options of shape, size, and weight were considered, a cost analysis of these options was performed, and appropriate preliminary selections were made.

The one way bending analysis used a simplified model of a single bridge bay to estimate the necessary size and spacing of the stringers. This estimation was based on weight, size, and deflection constraints. Michael Hayes, a doctorate candidate at Virginia Tech, furnished a computer program that modeled the stringer and composite deck. The program quickly calculates (using Euler-beam modeling) the deflection of each stringer according their quantity and size. Using the program, four loading situations (center-axle, left-axle, dual-axle, and an axle loading over the second stringer) were evaluated for three stringer options (5-W12x45, 5-W12x40, and a combination of 2-W14x48 and 3-W12x45). Using the computer model, the stringers were loaded according to the AASHTO HS20-44 design load. The AASHTO HS20-44 truck is a three axle truck similar to the one shown in Figure 5. It was found that the most deflection occurs when an axle is placed over the second stringer as shown in Figure 6. According to the one way bending model none of the selections met the L/800 deflection requirements for every loading scenario; however, the conservativeness of this analysis was taken into consideration accepting them for further analysis where two way bending was taken into account. The deflection should decrease when considering two-way bending, which will allow for the stiffness of the deck to carry some of the applied load. According to the three stringer selections chosen a preliminary weight versus cost analysis based on stringers alone was preformed, showing that the obvious choice would be the W12x40 sections considering it will minimize the cost and weight.

The three shapes selected using the one-way bending analysis were reanalyzed using a computer program modeling two-way bending. Again the AASHTO20-44 design loads were implemented to analyze the deflection. The two-way bending model used

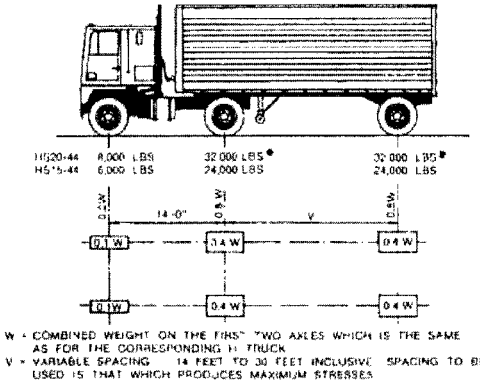


Figure -5: AASHTO HS20-44 truck loading.

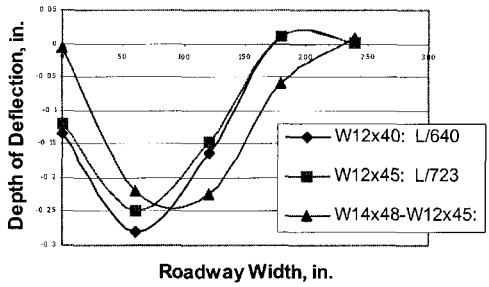


Figure -6: One-way bending deflection results for axle loading over the second stringer.

was developed by Dave Haeberle, in his ESM senior design project. Due to the way in which the program was written the combination of W12x45 and W14x48 sections could not be analyzed; therefore analysis was only performed on the W12x40 and W12x45 sections. The program also limited the location of the loads applied, therefore only the edge and dual loading scenarios could be modeled within reason. A plot similar to the one shown for the one-way bending model was created from the outputted values of deflections for the dual axel loading and is shown in Figure 7.

Combining the results from both the one and two-way bending analysis, the logical choice of stringers is five W12x40 sections at 5 foot spacing. This decision increases the weight contribution of the steel in the bridge, but it brings the functionality of the bridge up to standards. The weight savings from the FRP deck will compensate for this increase.

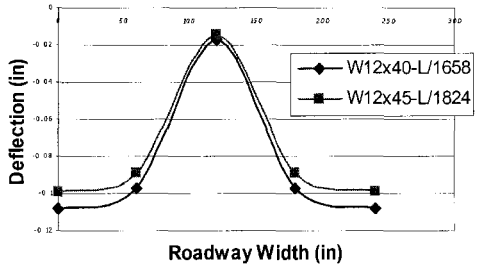


Figure -7: Two-way bending deflection along roadway width for dual axle loading.

Deck-to-girder connection:

The preliminary design, created by VDOT, attaches the panels using a through bolt of the bottom flange of the deck while accessing it through the top of the deck. Considerations of panel size and placement, and expected loading were made, as well as the contribution of the deck to the overall stiffness of the bridge. Using the results of these considerations, the quantity, size, and grade of the bolts and connection was determined.

The criteria for the connection design between the deck and stringers was based upon the Allowable Stress Design method (ASD) [6] and further verified by the mechanics of materials method. Failure modes for which the connections are designed for

are as follows: (1) shear failure of the bolt (2) bearing failure of the deck and (3) moment failure of the deck. The bolts used for this connection will be A-325.

The American Association of State Highway and Transportation Officials (AASHTO) braking force equation, $F_B = 0.25W$, was used to calculate the expected bolt loads (Baker, 1997). For the HS20-44 design truck, a breaking force of 25 kips was calculated and placed 6ft above the breaking surface where it is assumed to be static. AASHTO also specifies that the force under a dual rear wheel, as is the case for the HS20-44, will be twenty percent of the breaking force ($0.2F_B$ = 5 kips, for HS20-44); for the purpose of this design it is assumed that this force is distributed into the nearest two connections.

As previously mentioned, the breaking force will act 6 feet above the breaking surface, which is resolved into a force and moment at the contact surface of the deck and the stringer. The force remains at 5 kips, and the moment (M) acting through the deck onto the bolt was found to be 32.5 kip-ft, when using the equation $M = F_b L$, where L is the summation of the 6 foot distance above the breaking surface and the depth of the deck (0.5ft). With all loads and moments defined, a solution to gain the necessary bolt size was the made using mechanics of materials. Results from this analysis conclude that the minimum bolt diameter is 0.46" with no factor of safety and 0.92" with a safety factor of two. This result shows only a 3% difference from the bolt commonly used in deck connections, 7/8". The 7/8" bolt diameter was then applied to the same failure modes using ASD design, and according to the results, the 7/8" ASTM-325 bolt will be adequate for the deck to girder connections. At this time no conclusions have been made concerning what bolt pattern should be used in the Hawthorne Street Bridge.

Panel-to-panel connections:

The joining of the deck panels is important in terms of constructability as well as panel up-turn. From the manufacturer the panels are produced in 7.5'x22' sections and need a means of being attached to one another in the field. Currently a connection design consisting of two mating pieces is being tested. The design enables the use of a composite I-beam as the joining piece. Figure 8 shows both the male and female pieces in the manner they are to be connected. For testing purposes the I-beam is going to be cut to size to fit around 4" tubes. This design should allow for an ease in both manufacturing as well as installation.

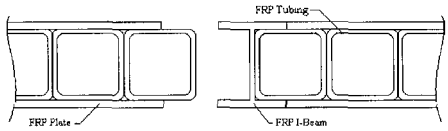


Figure -8: Proposed panel-to-panel connection.

Bridge rail design:

The guard rails for the bridge are being replaced by VDOT to ensure all safety standards are met. Robert Saufley, an engineer at VDOT, has proposed that a variation of the Illinois Steel Railing system be employed. Originally, this railing would be connected through the concrete decking; however it is necessary to modify this connection

because of the FRP deck. The modification includes adding another W-section beneath the location of the railing system in order to have a means to connect the railing to the bridge. Using Load Factor Resistance Design (LRFD)-AASHTO impact specifications, and LRFD end plate connection design the diameter of the bolts and dimensions of the base plates as specified in the original connection were checked and found to exceed the single bolt, flange and web weld size and strength, and plate dimension requirements.

Pedestrian walkway design:

The pedestrian walkway has a large influence on the bridge's behavior. VDOT had originally proposed a plan to reduce the walkway size by 1.5 feet making the width 4.5 feet. A definition of the necessary performance and a redesign of the system have been established. The design includes a decking and connection system as well as additional supporting members.

The Strongwell SAFPLANK decking system has been selected to utilize as the walkway deck in the Hawthorne Street Bridge. Strongwell includes a means of connection with this particular system, using a Carriage Bolt assembly. Since details of the connection of this deck are taken care of the only necessary task was to limit the deflection of the deck to L/800. Additional members were needed for support beneath the deck to maintain this deflection requirement. Using the one-way bending model, and a trail and error approach, it was found that 2-W12x14 steel beams placed at 18" on center as shown in Figure 9, are needed. According to the model, the W12x14 sections minimize deflection to L/951 while keeping their contribution to the bridge's weight minimal. The proposed walkway greatly reduces the weight of the bridge by approximately 14 tons.

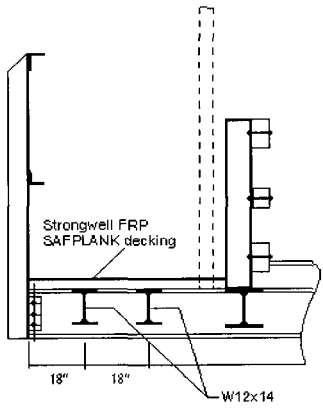


Figure -9: Proposed additional support members in walkway.

System behavior:

In the development of the overall system behavior of the proposed bridge design, a RISA structural analysis model was used to analyze the applied HS20-44 loads required by AASHTO. The difference in this analysis and the two way bending model, is that this RISA model will include the stiffness of the truss and floor beams. The behavior of the entire bridge was analyzed after all the design aspects were obtained. The RISA

model was run to determine live load deflection for one truck, two trucks, as well as the alternative military loading (6 trucks) on the bridge. Deflection results from this analysis considering no composite action between the deck and its supporting stringers are L/1347, L/887, and L/612 respectively. The most accepted criterion for deflection based design is the HS20-44 two-truck loading at mid-span. From the results, the selected W12x40 sections and the FRP decking, with the added truss and floor beam stiffness, meet the deflection range of L/800 to L/1000 with an overall maximum deflection of L/887.

SUMMARY

Considering the current condition of the bridge and the major importance of it for efficient emergency access to the town of Covington, the completion of this project will have a considerable impact on the town. The goal of the rehabilitation is to maintain full use of the bridge without replacing the truss members by reducing the overall weight of the bridge. This process primarily involves replacing all steel members with those which meet AASHTO deflection requirements and replacing the RC deck with a fiber reinforced polymer (FRP) deck on both the roadway and walkway.

The replacement of the steel and decking required investigation of the size of the steel replacements, the details of the deck connection, details of the bridge railing connection, and complete walkway redesign. The process of selecting a replacement for the steel members required utilization of two computer programs, modeling the deflection of a single bridge bay. The first of these models was more conservative than the second, in that it did not account for the varying stiffness of the FRP, however, both models suggested that the use of five W12x40 at 5' centers would meet AASHTO deflection requirements. Using allowable stress design (ASD) and mechanics of materials, the bolt diameter was found to be 7/8" (assuming A325 bolts). Checked using load resistance factor design (LRFD) the bridge railing should follow the specifications for the Illinois Steel Railing with an alteration to which the bolts will be connected (i.e. these bolts will be connected to an additional member beneath the railing location). Finally, the walkway will be limited to 4.5' in width and utilize the Strongwell SAF-PLANK system as well as two additional steel members (W12x14 at 18" centers) to limit deflections. All of these alterations bring the Hawthorne Street Bridge up to date concerning AASHTO specifications and reduce the overall bridge weight by approximately 56 tons, where the majority of the weight savings was from replacing the RC decking with the FRP decking.

REFERENCES

1 Zureick, A., Shih, B., and Muley, E. (1995), "Fiber-reinforced Ploymeric Bridge Decks." *Structure Engineering Review*, 7(3), 257-266.

2 Hayes, M. D., Ohanehi, D., Lesko, J. J., Cousins, T. E., and Witcher D. (2000), "Performance of tube and plate fiberglass composite bridge deck." *Journal of Composites for Construction*, 4(2), 48-55.

3 Coleman, J. T. (2002), "Continuation of Field and Laboratory Tests of a Proposed Bridge Deck Panel Fabricated from Pultruded Fiber-Reinforced Polymer Components." M.S. Thesis, Virginia Polytechnic Institute and State University, Blacksburg, Virginia.

4 Temeles, A. B. (2001), "Field and Laboratory Tests of a Proposed Bridge Deck Panel Fabricated from Pultruded Fiber-Reinforced Polymer Components." M.S. Thesis, Virginia Polytechnic Institute and State University, Blacksburg, Virginia.

5 Zhou, A. (2002). "Stiffness and Strength of Fiber Reinforced Polymer Composite Bridge Deck Systems." PhD Dissertation, Virginia Polytechnic Institute and State University, Blacksburg, Virginia. (Online at http://scholar.lib.vt.edu/theses/available/etd-10072002-164345/)

6 AISC (1989), Manual of Steel Construction, ninth edition, American Institute of Steel Construction, Inc., Chicago, IL.

STRENGTHENING HIGHWAY AND RAILWAY BRIDGE STRUCTURES WITH FRP COMPOSITES – CASE STUDIES

S. Luke and L. Canning

Mouchel Parkman

INTRODUCTION

Throughout the world, a significant percentage of bridges are in a deteriorated state. The main reasons for the poor state of these bridges are lack of good detailing for durability, corrosion of metallic components, damage to the structure and, most importantly, the increase in traffic volume and loads over time.

Strengthening of such bridge structures using FRP (fibre reinforced polymer) composites has become increasingly common in the last decade due, essentially, to their cost effectiveness and the reduction of impact on traffic flow. This paper describes six case studies where FRP composites, in different forms, were used to strengthen RC (reinforced concrete) and metallic bridges. In particular the observed advantages and disadvantages of FRP strengthening techniques are highlighted.

Case Study 1 – Chelmsford Subways Strengthening

The floor and ceiling slabs on a series of three RC pedestrian subways of 3 metres width and 2.5 metres height, under a main road in the city centre of Chelmsford, were assessed as under strength in transverse bending. The main reasons for choosing FRP composites for strengthening in this case were the short installation time, restricted access and overall cost. High-strength pultruded CFRP (carbon fibre reinforced polymer) plates were chosen as the FRP strengthening material due to the flat nature of the surface of the soffit.

Figure 1 shows one of the subways during the FRP strengthening works. The existing granolithic slab over the structural floor slab was removed by diamond-wire sawing, a novel semi-automatic method. This technique allowed the granolithic slab to be 'sliced' off horizontally in sections amenable to removal from the subway, and reduced noise and dust to a minimum.

The surface condition of the concrete slab after diamond-wire sawing was found to be very suitable for FRP plate bonding, confirmed by pull-off testing, hammer-tapping for damaged areas, and visual examination. CFRP plate bonding was carried out in stages along the subway with regular site supervision, after the concrete surface condition and strength was assessed as acceptable by pull-off testing. Prior to covering the floor slab with the pedestrian walkway, all the CFRP plates were tap-tested for voiding and remedial measures (either void injection or bonding of an additional plate) were undertaken where required. Extensive quality control was undertaken, using site prepared CFRP plate lap-shear test samples and adhesive samples. The textured surface finish on the ceiling slab was removed only at the CFRP plate locations to minimise the amount of time spent on re-applying the surface finish.

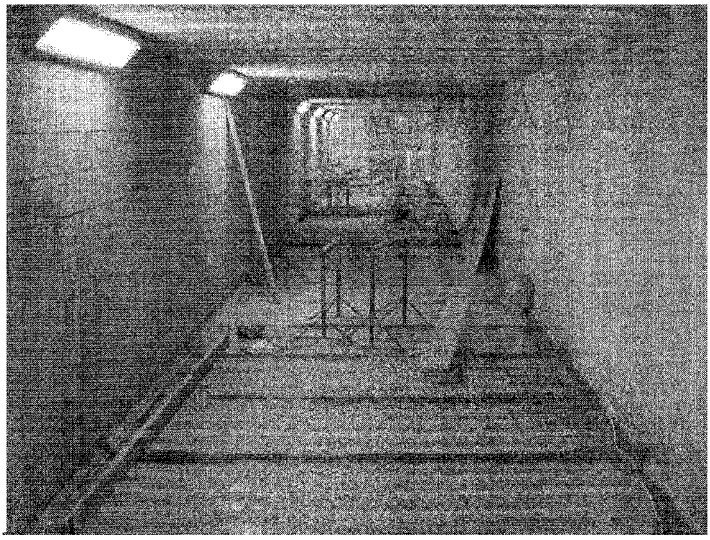


Figure 1 – CFRP Strengthening of Pedestrian Subway

Case Study 2 – M1 Slip Road Strengthening

A slip road onto the M1 required improved parapet containment, which meant the existing deck edge cantilevers were found to be under strength in flexure due to the increased dead load and parapet loads. On the East side of the deck, the surface was flat, whereas, on the West side of the deck, the surface contained a curved step in the surface profile. Therefore, high-strength pultruded CFRP plates were chosen to strengthen the flat deck edge (Figure 2), and a high-strength carbon fibre wet lay-up sheet chosen to strengthen the other deck edge (Figure 3), as this allowed the surface profile to be followed.

The site works began in October 2001 and ended in January 2002. Initially, the deck surfacing was planed off to reveal the structural concrete beneath. The deck cantilever area was then surface-prepared by grit-blasting. Any substandard surface areas were repaired with an epoxy mortar compatible with the CFRP strengthening system. The East Cantilever was strengthened first, using high-strength pultruded multiple CFRP composite plates. To continue the rate of strengthening work during inclement weather, a polythene tunnel enclosure was erected. Using this method, about 1.5 km of pultruded CFRP composite plate was installed in 6 weeks to strengthen a 90m length of the deck. During work on one side of the deck, the other side was left open to traffic. Therefore, the East side of the deck was reinstated and opened prior to works on the West cantilever.

The West cantilever was strengthened in the winter months, again using the polythene enclosure tunnel to allow continual installation to take place in the right environmental conditions for FRP bonding. Approximately 1300 m^2 of CFRP composite wrap was installed in about 4 weeks. The West side of the deck was then reinstated and the bridge opened to traffic.

Throughout the CFRP plate bonding process, extensive quality control was used, i.e. tap-testing of the CFRP composite and site test samples. In addition, long-term in-situ CFRP plates and wraps were located in the vicinity of the bridge to allow future checking of the integrity and condition of the CFRP strengthening system.

Brockley Slip Road was successfully strengthened for the upgraded parapet system on a tight programme and in poor weather conditions. The unusual scenario of using both CFRP composite plates and wraps for essentially the same structural function on either side of the deck enabled valuable comparisons of the two strengthening and installation systems to be made. Furthermore, experience was gained in the logistics and installation methods applicable in poor weather conditions and restricted spaces.

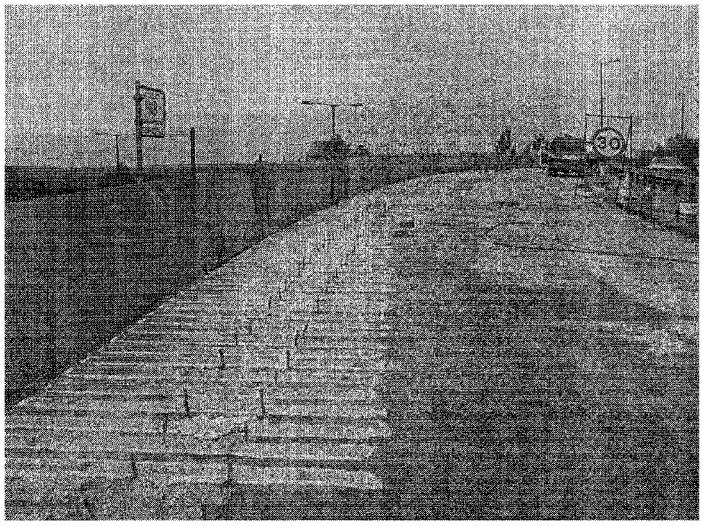


Figure 2 – CFRP Plate Bonding to Strengthen Deck Edge Cantilever

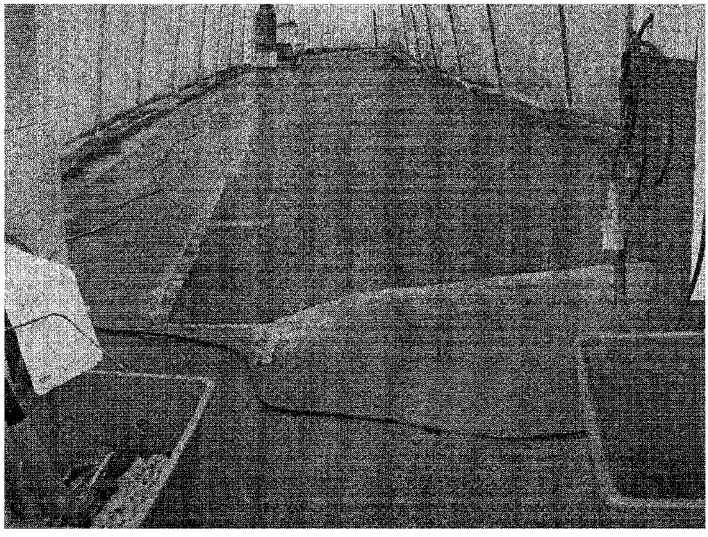


Figure 3 – CFRP Wet Lay-up to Strengthen Deck Edge Cantilever (Within Polythene enclosure Tunnel)

Case Study 3 – Theydon Bois Viaduct Strengthening

A 29 span reinforced concrete viaduct spanning over an above ground LUL railway line and private land was found to be exhibiting extensive concrete spalling and corrosion of the main reinforcement. An assessment of the viaduct showed the overall capacity of the carriageway to be 17 tonnes. An option study showed that removal of the poor quality soffit concrete to good quality concrete, followed by the fixing of additional main reinforcement and the application of sprayed concrete, would strengthen the viaduct to carry the full 40 tonne assessment load. In the non-railway spans, propping of the deck would be used to mitigate the risk of failure of the deck during removal of the soffit concrete.

However, beneath the LUL railway spans propping was not a feasible solution. Therefore it was proposed to bond CFRP plates to the top of the deck, beneath the carriageway surfacing, to provide supplementary support to the deck during this phase of the works. Although it was considered that at this stage propping of the deck would not be required the consequences of any unforeseen movement were such that it was deemed prudent to provide the strengthening. The CFRP plate would then act to increase the hogging capacity of the deck in the event of a failure at midspan, and hence the deck acting as cantilevers from the supports. Multiple factory bonded CFRP plates with gradual curtailment were used to provide an efficient system and to minimise bond stresses. Removal of the carriageway surfacing, bonding of the CFRP plates and reinstatement of the surfacing was undertaken one lane at a time, allowing controlled traffic flow at all times. Over 1000 metres of high strength CFRP plate was applied in total using a tented environment to ensure work could go ahead in adverse weather conditions. Figure 4 shows one lane of the carriageway being strengthened using the large tented area.

In addition, upgrading of the parapets, waterproofing, and drainage were all undertaken during the above deck works.

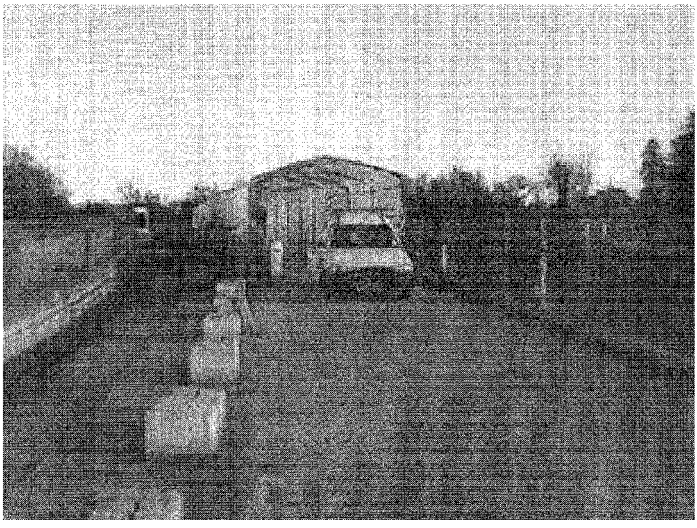


Figure 4 – CFRP Plate Bonding On-going in Tented Area, Single Lane Working

Case Study 4 – Nunnery Bridge Strengthening

Nunnery Bridge is a cast iron beam/brick jack-arch bridge over a river at Castle Hedingham, Essex, with a span of 4.9m. The bridge was assessed as under strength due to the tensile stresses in the bottom flange of the cast iron beams. To strengthen the cast iron beams to the 40 Tonne assessment load, a solution using 16mm thick tapered ultra-high modulus (UHM) CFRP laminates bonded to the soffit of the cast iron beams was proposed. This technique improves the section properties of the cast iron beam and reduces the tensile stresses to acceptable limits. Two options were proposed for the UHM CFRP plates; factory vacuum-bonded multiple 4mm thick pultruded CFRP plates with staggered curtailment of the plates to create a taper , or factory vacuum cured pre-preg CFRP laminates with a more gradual taper to a nominal end thickness of 1mm.

The factory bonded pultruded UHM CFRP plates were used in this particular case, with a minimum tensile modulus of 450 GPa. Prior to CFRP plate bonding works, the cast iron surface was grit-blasted and cleaned to provide a suitable surface condition for adhesive bonding. Pull-off test dollies were bonded to the prepared cast iron surface to ensure the surface preparation was adequate. CFRP plate bonding to the cast iron beams was undertaken using scaffolding for access, whilst the environment was monitored to ensure that the substrate temperature, air temperature, dew point and relative humidity were acceptable for CFRP plate bonding. Due to the thickness of the CFRP plates, temporary clamps were used to ensure a good bond until the adhesive had cured (Figure 5). CFRP plate lap-shear and adhesive test samples were manufactured on site and tested for quality control. The CFRP plates and cast iron beams were finally painted to provide a highly durable strengthened structure.



Figure 5 – Applying pressure and temporary clamps to CFRP plates

Case Study 5 – New Moss Road Bridge CFRP Strengthening

The existing bridge is located on the CLC Liverpool to Manchester (MAJ) railway at Irlam, Greater Manchester. The bridge is a two span structure, and carries the unclassified two lane single carriageway New Moss Road. The original bridge, constructed in 1873, was a single span structure comprising six simply supported cast iron beams with brick masonry jack arches spanning between the beams. In 1956, the bridge was extended to the south by the provision of a second span of reinforced concrete construction, although the track under this span has now been taken up. The structure has a North (cast iron) span and South (reinforced concrete) span.

The cast iron beams in the North span were assessed to be under strength in tensile capacity in the bottom flanges, and the Southern reinforced concrete span was assessed to be under strength in flexure. The Northern span also required replacement of tie-bars as part of the strengthening work. To strengthen the cast iron beams, multiple tapered, factory bonded, pultruded UHM CFRP plates were proposed, and medium modulus (150 GPa) CFRP plates were proposed for the reinforced concrete span to strengthen the structure to the 40 Tonne assessment load. The maximum thickness of the UHM CFRP plates was 24mm, whilst the thickness of the medium modulus CFRP plates on the reinforced concrete span was 2.9mm.

The cast-iron beams were strengthened under normal rules of the route possessions, comprising 8 No. 8 hour night possessions. During the first possession, grit-blasting and priming of the cast-iron beams was completed. Subsequent possessions comprised inspection of the prepared surface, pull-off testing, CFRP plate bonding (Figure 6) and final inspection. During site works, extensive quality control testing was undertaken and a high level of site supervision was provided.

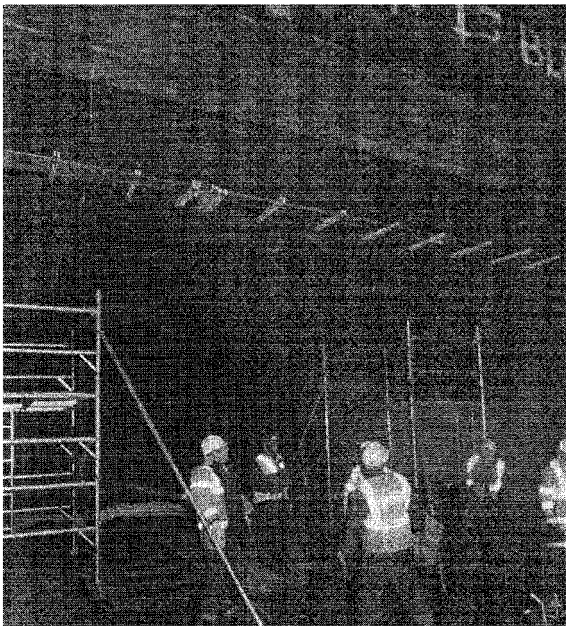


Figure 6 – CFRP Plate Bonding During Overnight Possession

Case Study 6 – St. Michael's Road Bridge CFRP Strengthening

St. Michael's Road Bridge is a reinforced concrete underbridge carrying the Weaver Junction to Liverpool Lime Street Line. The single span bridge crosses St Michael's Road, a disused industrial access road on the outskirts of Ditton in Merseyside. The bridge is understood to have been constructed in the mid 19th century, consisting originally of a deck of metal beams with transverse spanning brick jack arches, supported by brick abutments. The replacement deck, installed in 1959, has an effective span of approximately 6.7m. The deck carries 2 No. tracks and comprises 4 No. precast reinforced concrete deck units (with each deck unit located directly beneath one rail) and 2 No. precast reinforced concrete parapet units.

The bridge deck was assessed as under strength in flexure for the required railway live load, and a strengthening scheme was proposed using thin, medium modulus, pultruded CFRP plates. The strengthening scheme was undertaken within 3 no. 8 hour possessions, to allow CFRP plate bonding to be completed whilst there was no live load on the bridge. Temporary propping on the CFRP plates was used to ensure the live loading had negligible effect on the adhesive bond. Figure 7 shows the bonded CFRP plates on the soffit of the concrete bridge deck.

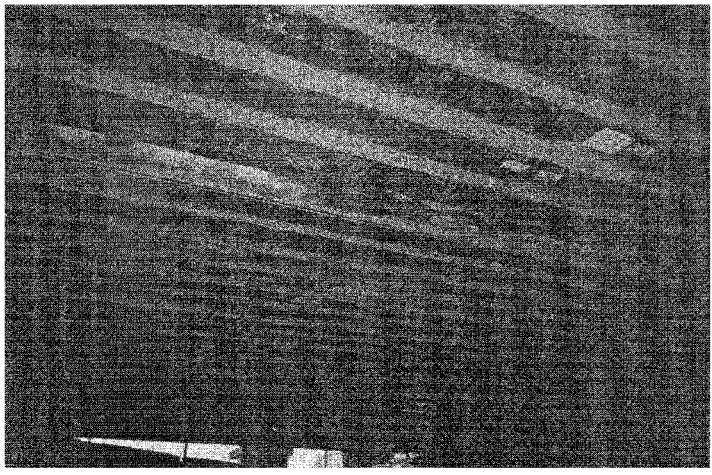


Figure 7 – Completion of CFRP plate bonding

CONCLUSIONS AND OBSERVATIONS

The main observed advantages of using CFRP plate bonding in these projects were:

- Ease of installation in restricted space due to the lightweight nature of the CFRP composite and minimal requirements for plant.
- Speed of installation.
- Flexibility of strengthening method, e.g. the use of CFRP pultruded plates and wet lay-up carbon fibre fabric on Brockley slip road.

These combined advantages lead to an efficient and cost effective technique for strengthening metallic and concrete structures.

However, strengthening using FRP composites requires certain measures not typical for conventional strengthening methods:

- Dependence on weather conditions, although this can be overcome by using a tented environment.
- Detailed monitoring of the environmental conditions for effective adhesive bonding.
- Specialist site supervision, as the success of FRP strengthening schemes are highly dependent on workmanship.

ACKNOWLEDGEMENTS

The authors would like to acknowledge Network Rail, The Highways Agency and Essex County Council. The views expressed in this paper are solely those of the authors and not those of Network Rail, the Highways Agency or Essex County Council.

THE DEVELOPMENT OF COMPOSITE MATERIALS FOR STRENGTHENING STRUCTURES

Martin Richardson

Sika Limited

ABSTRACT

The technique of flexural strengthening of reinforced concrete structures using externally bonded composite reinforcement has been in use for over 5 years. The method of strengthening by bonding steel plate, which had been used in the UK since 1975, has now generally been replaced by the use of composite plates.

The increased acceptance of the method has led to different types of structure and problems being considered for strengthening using composite materials. The flexural capacity of metallic structures such as cast iron and steel can be improved. The resistance of reinforced concrete or masonry against impact, blast and seismic loads can be increased. Reinforced concrete structures deficient in shear can be strengthened. The use of pre-stressed composite plates can relieved both dead and live loads at the same time as overcoming difficult detailing problems.

The success of any new techniques depends on detailed research and development and the long term durability of all the materials used in the strengthening system. The other main system components that should be included in this development are the adhesives used to bond the composite to the structure.

The presentation will introduce each of these strengthening techniques and where possible discuss the completed research and development and mention the long-term durability of the components used.

INTRODUCTION

The technique of bonding external reinforcement to structures was first used in the UK in 1975 on the M5 near Birmingham to strengthen the Quinton Interchange.

The method of strengthening using externally bonded reinforcement, (viz) structural strengthening, can be introduced by providing the answers to some simple questions.

(i) What is Structural Strengthening? (ii) Why do we need it?

(iii) What can be achieved by using the technique? (iv)Where can we use it?

Structural strengthening involves the bonding of additional reinforcement to the external faces of a structural member. This additional reinforcement can incorporate steel plates, composite plates or composite wrapping systems. The method is attractive because it provides a cost effective solution to increasing load carrying capacity, especially when compared to demolition and rebuilding.

One of the main reasons for using the method in the UK is due to the change in requirements of a structure generally to provide increased load-carrying capacity. Other reasons for utilizing the technique might be due to inadequate design, poor quality of construction, structural damage, fire damage, seismic loading, reinforcement corrosion (where the cause must be treated) and the loss of prestress force in the concrete beam.

Strengthening can improve the load carrying capacity of structures by increasing flexural strength, Shear strength, impact resistance, punching shear resistance and redistribute loads around new openings.

Externally bonded reinforcement gives the opportunity to strengthen members without having a significant visual impact on the overall structure. The installation process is fast and can minimise disruption to the function of the structure including any services which might be attached to it.

Structures made from reinforced concrete, steel, cast iron, masonry and timber have all been strengthened to date using a form of the technique. Beams and slabs have been strengthened on both their top and bottom surfaces for flexural upgrading. Columns and beams have been strengthened on their vertical side faces for shear. Slabs have been strengthened around columns to increase punching shear resistance. Various other types of structural elements have been strengthened for many different reasons.

DEVELOPMENT OF STRENGTHENING

Steel Plate Bonding

Steel plate bonding has been used in both buildings and civil structures in the UK since 1975. In 1994 the Highways Agency published BA 30/94 'Strengthening of Concrete Highway Structures Using Externally Bonded Plates'. This provided information on application, design and specification of the technique. The application of steel plates is still the best solution to some strengthening problems that occur today.

Steel plate bonding provides the basis for the establishment of strengthening using externally bonded reinforcement. The process involves the bonding of a mild steel plate with a minimum thickness of 4mm (for handling purposes) to a prepared concrete surface.

The steel plates are fabricated off site to the required dimensions and specification, including holes for anti-peel bolts.

To prevent any corrosion of the steel plate a primer system needs to be applied to the prepared steel surface during fabrication. This primer also provides the critical function of transferring forces from the structure to the steel plate and is hence a crucial part of the system.

Holes for anti-peel bolts also need to be inserted in the steel plate during fabrication. These bolts are required to provide additional resistance to peel forces applied to the bond line due to any residual force in the end of the plate. The bolts have to be positioned carefully to avoid damage to the existing reinforcement in the concrete surface.

Temporary works are required to support the heavy steel plates while the 2-part epoxy adhesive is curing. The curing period is dependant on ambient conditions but is likely to be a minimum of 3 days.

A fillet of adhesive is generally placed around the edge of the plate, this provides additional protection to the bond line but also allows the application of the final corrosion protection system to the steel plates to be lapped out onto the concrete surface. The corrosion protection system is likely to provide a life to first maintenance of 8 years and to major maintenance of 16 years in an exposed environment.

PULTRUDED COMPOSITE PLATE BONDING

The development and use of alternative materials has been a constant process almost since the first use of steel. The installation problems associated with the weight of the steel plates and the potential for corrosion to reduce the durability of the system led to composite materials being considered. In the early 90's much of the research was carried out at EMPA in Switzerland. In the UK a Dti Link project called ROBUST was established to investigate the use of composite materials for strengthening structures. In 2000 the Concrete Society launched Technical Report 55 'Design Guidance for strengthening concrete structures using fibre composite materials'.

The first UK strengthening scheme using composite materials was completed in 1996 at Kings Collage Hospital in London. The addition of a new floor to a building changed the loading requirements of the existing roof to new floor loadings. 1.3Km of Sika CarboDur plates were installed to the soffit of the longitudinal ribs under the slab.

Preparation of the concrete surface for either steel or composite plate bonding is identical. The composite plate is delivered to site in a roll with a diameter of approximately 1.5m. The lightweight nature of the composite material means a roll containing 250m can be easily lifted and moved by a single operative. The roll is cut on site to give the required plate lengths.

The plates are applied to the concrete surface using a similar adhesive to the one used for steel plate bonding. The initial grab of the adhesive is enough to hold the lightweight plate in place during the full cure period of the adhesive, eliminating the requirement for temporary works.

The composite plates are 1.2-1.4mm thick. This means that any residual longitudinal forces in the end of the plate have a much smaller eccentricity to the concrete surface compared to steel plates. In turn this means that peeling forces are lower which generally removes the requirement for anti peel bolts.

As composite materials do not corrode, corrosion protection systems are not required. A decorative coating can be applied to help conceal the strengthening.

INNOVATIONS IN STRENGTHENING

Strengthening Metallic Structures

Interest in strengthening metallic structures was first led by the off shore industry. The civil engineering industry soon realised the opportunity for its use and major bridge owners such as London Underground Limited and Network Rail expressed interest.

In 1996 a DETR/PiT program was set up to develop the use of composite materials in strengthening metallic structures. Detailed areas for investigation included design, specification, materials performance and installation best practise. The main output from this program was the Institution of Civil Engineers design and practise guide ' FRP Composites Life Extension and Strengthening of Metallic Structures'[1], which was published in 2001.

Both cast iron and steel structures have been strengthened with bonded composite plates. Wrought iron is also a material being considered for strengthening.

Another major part of the DETR/PiT program was to carry out full-scale validation of the technique. A London Underground Ltd bridge called D65A was selected for this trial. The bridge consisted of 3 main longitudinal beams with transverse beams

spanning between them. Two of the transverse beams were selected for the trial. A target of a reduction in peak strains in the beams of 25% was chosen and designed for. A known load was pasted over the bridge both before and after strengthening and a reduction of peak strains of 23% was recorded. The discrepancy between the target and the actual reduction in strain was investigated and found to be due to the stiffened beams attracting additional load from other parts of the structure.

The plates for strengthening metallic structures are generally considerably larger than those used for strengthening reinforced concrete. The requirement for increased stiffness of the strengthened element means larger cross sectional areas are required. The fibres used within the plates, although still carbon, have a higher stiffness than those used in the strengthening of reinforced concrete. These requirements mean that plates are generally manufactured to the exact dimensions and properties required for the project, making them bespoke plates.

To provide plates that have a high level of control of fibre alignment, and hence final plate properties, a pre-preg method of manufacturing is adopted. This involves unidirectional fibres being pre-impregnated with an epoxy resin to form a sheet. These sheets are then laid up individually in the required direction and a vacuum used to consolidate the layers and obtain the maximum fibre fraction content. The whole component is then cured in an autoclave. This method of production also allows tapers to be built into the plate, reducing the thickness at the end of the plates to approximately 1mm and in turn reducing forces on the bond line.

The finished plates are then delivered to site flat in a similar way to steel plates. However, they are considerably lighter than the equivalent steel plate. The substrate needs to be prepared to remove all contamination and corrosion products and provide the maximum levels of adhesion of the adhesive. Although the plates are lighter than steel plates they are too heavy for the adhesive to hold in place whilst still curing. Temporary supports are required to maintain pressure between the plate and the substrate while curing takes place. Once cured a final protective coating is applied over the plate and on to the metallic substrate to prevent corrosion of the substrate.

In 2002 the LUL bridge MR46A was strengthened using the Sika CarboDur DML System. The bridge is a single 28m span bridge consisting of mild steel main and transverse beams. Strengthening was required for the bridge to carry the full LUL load requirements. Various Sika CarboDur DML plates up to 13m in length, 30mm thick and 250mm wide were installed.

In more recent times production of plates using aramid fibres has been carried out. The aramid fibre is less conductive than carbon fibres and this is believed to be beneficial in reducing induction forces when strengthening bridges over high voltage cable, a common situation on electrified railways.

BLAST, IMPACT AND SEISMIC STRENGTHENING.

Where blast impact and seismic loads are been considered a range of materials may be suitable. The increase ductility and toughness of fibres such as aramid and glass fibres has seen them used along with carbon fibre for these types of projects. Some strengthening projects utilise the ease of installation of a plate as discussed previously, but more often than not the use of fabric, bonded in-situ, provides the required solution.

Blast and seismic strengthening are generally a small part of the market place with limited design and practical guidance. However, post September 11, interest in protecting strategic buildings against terrorist attack has been increasing. In many

situations the strengthening not only provides an improved resistance to collapse, but also helps to reduce the fragmentation, which can be so dangerous for the users of a building. Seismic strengthening in the UK is at present limited to the nuclear industry. In areas of the world where seismic activity occurs, strengthening against seismic loads becomes the major market for composite materials within the construction industry.

Strengthening columns for vehicle impact loading using composite materials has been common practise within the UK for several years. The installation can be carried out using either the wet or dry application method. The wet method involves saturating the fabric with resin prior to applying it to the concrete surface. The dry method involves applying adhesive to the concrete surface and placing the fabric into the adhesive. Multiple layers of fabric can be applied using either method of application. Due to the unidirectional nature of the majority of fabrics, layers can be applied in different orientations to provide strength in different directions when required. Multi direction materials are available, but are often uneconomic.

In late 2002 the Highways Agency published Bridge Directive, BD84/02 Strengthening of Concrete Bridge Supports Using Fibre Reinforced Polymers[4]. This provides design and specification advice on the use of fabric materials in strengthening of columns against impact.

The SikaWrap range of composite fabrics and the Sikadur range of epoxy adhesives have been developed for both dry and wet application methods. The SikaWrap range of fabrics includes carbon, aramid and glass fibre materials.

The composite strengthening is often used in conjunction with additional reinforced concrete elements to improve fixation of columns at supports.

In August 2003, a project, which was completed in Bristol on the A38 Patchway Viaduct, SikaWrap 300A aramid wrapping system was installed using the dry method of application. As part of the installation trial bands were installed above the area where strengthening was required. Defects were deliberately made in these bands to trial the use of transient pulse thermography in detecting such defects. The system employed by the BRE uses short bursts of powerful light to raise the surface temperature of the strengthening and then to use a sensitive infrared camera to monitor the cooling of the surface. Differences in the way the surface cools show possible defects within the layers of the fabric.

SHEAR STRENGTHENING

Strengthening reinforced concrete structures for shear has traditionally been difficult. Early schemes consisted of bonding bolting steel plates to the outside of beams. The development of the use of composite materials for shear strengthening has been researched since 1997. The use of fabric wrapping systems has provided a solution to strengthening columns where it can be applied to all surfaces of the column. The development of a system of preformed L shaped composite links for use on down stand beams has been carried out by the Swiss Federal Laboratories for Material Testing and Research – EMPA. This system is the Sika CarboShear L Link. It consists of a 40mm wide, 1.2mm thick L shaped plate made of carbon fibre.

Providing sufficient composite material to resist the shear force is relatively simple. The technical difficulty is associated with obtaining the required anchorage to the ends of the composite. Initial research was required to quantify the exact capacity of different types of anchorage. At the bottom of the beam the anchorage is provided by the bend of the link under the beam. At the top of the beam the anchorage is

achieved by bonding the link into the bottom of the slab. The capacity of the anchorage bonded into the slab can reach the tensile capacity of the Sika CarboShear L link at a bond depth of 120mm. The bend anchorage can only achieve approximately 60% of the capacity of the link, and hence is the limiting factor in any strengthening scheme. The conclusions of these initial tests provided information to allow the design concept to be developed.

Full scale validation testing was then carried out on T section beams at EMPA to confirm the design concept.

The beams used for the validation testing were specifically designed for high shear stresses. Four beams were statically loaded with different shear reinforcement, consisting of combinations of both internal steel links and external bonded Sika CarboShear L Links. Additional beams were used to investigate the effect of preload on subsequent strengthening and fatigue.

From the externally bonded shear link tests it was concluded that:

(i) shear load capacity of reinforced concrete (ULS) could be increased, and could also reduce shear defections (SLS).

(ii) by preloading the composite before strengthening, no effect on the performance of the strengthened beam at ULS was realised

(iii) the composite materials used for shear strengthening can readily bear the applied fatigue stresses.

The first trial project using Sika CarboShear L links in the UK was carried in on the A38 Liskard Bypass in Cornwall. The bridge, which is owned by the Highways Agency, consisted of a heavily skewed reinforced concrete slab. The slab had been propped since an assessment has showed that the deck edge zones had inadequate shear strength to resist the combination of torsional and flexural shear. The links were bonded to the edge of the slab and were anchored into the soffit of the parapet stringcourse at the top and lapped under the slab at the bottom. On completion of the strengthening the propping could be removed.

PRESTRESSING COMPOSITE MATERIALS

Limitations of the existing reinforced concrete section means that only 50% of the ultimate strain capacity of the bonded composite material can ever be utilised. In order to fully utilise the full strain of a bonded CFRP plate it has to be prestressed before being bonded. For this reason post tensioning systems suitable for on site application have been developed for strengthening reinforced concrete structures.

The advantages of using prestressed CFRP strips as externally bonded surface tendons are,

(i) The upper range of the strain and stress capacity can be used.

(ii) Strains on the internal reinforcement can be relieved.

(iii) Strengthening can carry both dead and live loads.

(iv) Crack widths can be reduced along with bending deflections, improving serviceability.

(v) Anchorage lengths can be reduced.

The Sika CarboDur Leoba LCII system was developed by Leonhardt, Andra & Partners in association with the University of Leipzig and fully tested at EMPA.

A plate embedded and bonded in a concrete cover recess is used as a jacking platform. The stressing operation is carried out using a hydraulic tandem cylinder miniature jack during the pot life of the adhesive. The system consists of a pultruded

CFRP plate with a defined width and thickness, dead and lives anchorages and jacking systems.

Anchorages are installed by removing the cover concrete and bonding and bolting the base plate in place. The pultruded carbon fibre plate is delivered to site in a roll and cut to the required length. Preparation of the concrete is required to remove any peaks in the concrete surface and provide the required key for the adhesive. The two part cold cured epoxy is the same as used for bonding normal pultruded CFRP plates. The plate is fed into the jacking device and clamped in place. The jack then stresses the plate through friction clamps. A maximum pre-strain of 0.55% is applied to the plate during the installation. The plate can then be locked into place and the jack removed.

An alternative system, the Sika StressHead system, has also been developed by EMPA. The system comprises both live and dead anchorages placed in core holes pre drilled into the reinforced concrete and plates with prefixed end anchors attached.

The exact location of each anchorage is determined on site by carrying out a cover meter survey to minimise or avoid any damage to local reinforcement. This survey gives the exact dimensions of the required plates. The plates with prefixed anchors at each end are then fabricated, tested and certificated for performance. The core holes are then made into the concrete and the anchorages installed. The plates are then inserted into the anchorages and the stressing force applied by jacking against the prefixed anchor on the end of the plate. A maximum tensioning force of 220 kN is applied to each plate.

CONCLUSIONS

There are many new methods of strengthening being developed to take full advantage of the benefits of composite materials. Great care should be taken when considering using any of these new methods. A full review and understanding of the available research should be undertaken prior to such a method as being considered as a viable solution to a problem. Where ever possible full-scale validation trials should be completed to help demonstrate both the practical and technical capability of the systems.

Research and development is often carried out on complete strengthening systems, and whilst it may be simple to define the performance characteristics of the components of each system, care should be taken when substituting alternative unproven and untested materials for these components or wholesale substitution, without completing similar validation.

This paper has attempted to provide an overview of several techniques for strengthening using composite materials. More detailed information on the research and development of the systems and materials discussed is contained within the references.

Correct design, use and specification of systems are essential to guarantee long-term performance and durability. The use of experienced designers, contractors and material suppliers should be encouraged to ensure this.

REFERENCES

1 The Department of Transport, 1994, Strengthening of Concrete Highway Structures Using Externally Bonded Plates, BA 30/94

2 Concrete Society, 2000, Design Guidance For Strengthening Concrete Structures Using Fibre Composite Materials, Technical Report 55

3 Institution Of Civil Engineers, 2001, ICE Design and Practise Guide – FRP Composites Life Extension and Strengthening of Metallic Structures

4 The Highways Agency, 2002, Strengthening of Concrete Bridge Supports Using Fibre Reinforced Polymers, BD84/02

BIBLIOGRAPHIES

5 New Civil Engineer, 21/28 August 2003, Infrared detection spots concrete defects.

6 Heinz Meier, Schweizer Ingenieur und Architekt SI+A, 1998, CFRP L-Shaped Plates

7 EMPA, 2002, Shear Strengthening with prefabricated CFRP L-shaped plates – Test Beams S1 to S6, Report No 116/7

8 New Civil Engineer, 23 November 2000, Stronger Links

9 Hans-Peter Andra, Markus Maier, September 2000, Post Strengthening of RC Structure with Externally Bonded Prestressed CFRP Strips, Conference Proceedings of 16th Congress IABSE, Luzern, Switzerland.

10 Berset T, Approval and testing of CFRP plate prestressing systems, ETHZ Zurich 2001

FRP STRENGTHENING OF BUILDING AND CIVIL STRUCTURES IN SWEDEN - A REVIEW AND FUTURE AIMS

Björn Täljsten[1,2] and Anders Carolin[1]

[1]*Divison of Structural Engineering*
Luleå University of Technology, Sweden
[2]*Skanska Teknik AB, Sweden*

ABSTRACT

Since buildings and civil structures usually have a very long life, it is not uncommon that the demands on the structure changes with time. The structures may have to carry larger loads at a later date or fulfil new standards. In extreme cases, a structure may need to be repaired due to an accident. Another reason can be that errors have been made during the design or construction phase so that the structure needs to be strengthened before it can be used. If any of these situations should arise it needs to be determined whether the structure should be strengthened or replaced. Over the past decade, the issue of deteriorating infrastructure has become a topic of critical importance in Europe, and to an equal extent in the United States and Japan.

The deterioration of decks, superstructure elements and columns can be traced to reasons ranging from ageing and environmentally induced degradation to poor initial construction and lack of maintenance. Added to the problems of deterioration, are the issues related to the needs for higher load ratings and the increased number of lanes to accommodate the ever-increasing traffic flow on the major arteries. As an overall result, a significant portion of our infrastructure is currently either structurally or functionally deficient. Beyond the costs and visible consequences associated with continuous retrofit and repair of such structural components, are the real consequences related to losses in production and overall economies related to time and resources caused by delays and detours. As we move into the twenty-first century, the renewal of our lifelines becomes a critical issue.

In this paper a short description is presented of the research and development regarding plate bonding as a repair and strengthening method carried out in Sweden. A background to the initiation of the research together with ongoing research and future aims and needs are discussed. In addition the importance of implementation processes and need of codes and standards are also debated.

INTRODUCTION

The motivation for research and development into repairing, strengthening and restoration of existing structures, particularly concrete systems, is increasing. If consideration is given to the capital that has been invested in the existing infrastructure, it is not always economically viable to demolish and rebuild the structure. The challenge must be to develop relatively simple measures such as restoration, reparation and strengthening that can be used to prolong the life of structures. This challenge places a great demand on both consultants and contractors. For example, there could be difficulties in assessing the most suitable method for an actual subject; for example, two identical columns within the same structure can have totally different lifespan depending on their individual microclimate.

Also strengthening structures to carry higher load or to change the use of a structures can be complicated, especially when the load at serviceability limit state is high. Therefore, it is important to analyse the problem thoroughly to be able to select the correct solution. The choice of an unsuitable reparation method can even deteriorate the performance of the structure. In the cases where upgrading is appropriate, the aim should be to improve the durability and the load-bearing capacity of the system.

At the end of the 1980s Luleå University of Technology commenced research into the repair and strengthening of existing concrete structures utilizing the plate bonding technique. Initially steel plates were used to strengthen members. Currently, however, all research is focussed on plate bonding using FRP composite materials in which, carbon fibre composite is the favoured material.

AN HISTORIC PERSPECTIVE

Strengthening existing structures with external reinforcement bonded on to the relevant face of the structure is not a new invention. The first known application in this field was reported from South Africa[1] at the end of the 1960s, where a concrete beam associated with an office building was strengthen by means of an epoxy bonded steel plate. Research in this field was then undertaken, and became an important technique during the 1970. At Luleå University of Technology, steel plate bonding, as a research field, was established in mid 1980. The reason commencing research in this field was that the Swedish National Road Administration, due to increased demand on the road network, in particular bridges, were keen to investigate different existing strengthening methods and in particular those that were new to the Road Administration. The main research in this field begun in 1988, when the first task was to produce a state of the art report. During the years after 1988 a considerable number of tests were performed, mainly on concrete beams strengthened in bending using steel plates, in addition, durability tests and different anchor lengths were also investigated. Furthermore, adhesives were also developed to enable a workable viscosity for field applications to be achieved as well as fulfilling upgrading demands. In addition, extensive theoretical studies were carried out, where in particular, the peeling stresses at the cut-off end of the plate were studied. Furthermore, concrete beam strengthening using steel plates, were tested and design formulae established. These formulae covered shear, bending and anchorage and advice was given on good working practice. In 1989 a full-scale test was performed on a concrete bridge, which was strengthened for bending upgrade with steel plates. With the successful completion of these tests the Swedish National Road Administration decided to accept steel plate bonding, as an additional strengthening method, as one of their standard maintenance techniques. Consequently the method was introduced into the Swedish bridge code.

At the end of the 1980s the steel plate bonding method was used on several bridges in Sweden, both for bending and shear. In 1995, one of the last applications to strengthen bridges with steel plates was carried out in Sweden, and this is shown in Figure 1. This project was considered successful, but the disadvantage of the technique viz.heavy plates, need of joints, bolting and pressure during curing of the adhesive, still remained. An inspection after 8 years shows no corrosion or degradation of the strengthening system. Since then, plate bonding applications have been with FRP (Fibre Reinforced Polymers) materials and in particular carbon fibre based products.

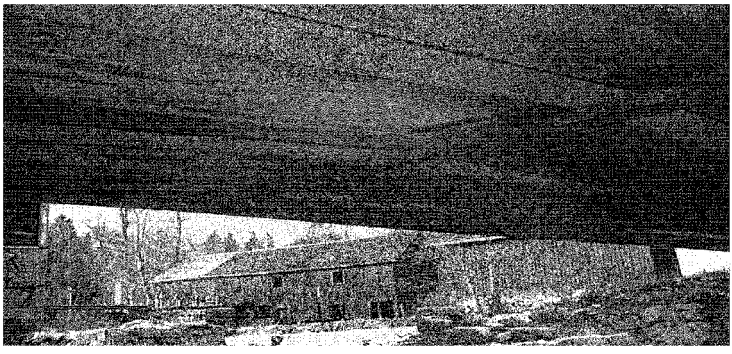


Figure 1 Underside of a concrete bridge in Sweden strengthen by steel plates in the mid 1990s.

Composite materials for strengthening were introduced in Sweden in early 1990s, when also the first tests were carried out at Luleå University of Technology on beams strengthen with CFRP laminates and GFRP laminates, these tests were considered as pilot tests.

The tests in which beams were strengthen with CFRP laminates were considered successful and a more systematic approach towards FRP strengthening was taken. In 1994 a PhD thesis[2] was presented. This thesis is considered to be the start of established repair and strengthening research in the field of plate bonding at the university.

ONGOING RESEARCH

Several areas of significant research from 1994 have been undertaken and a number of major projects are presented below with a brief description of each. Some of the areas have raised interesting problems and further research into these have been undertaken

Strengthening for shear

Strengthening for increased shear capacity has been one of the main research areas on CFRP in Civil Engineering at Luleå University of Technology and projects are still active in this area[3,4,5,6]. A large number of tests have been undertaken. To study parameters such as: fibre direction, fibre thickness, fibre quality, anchorage arrangements, matrix type (epoxy or cementitiuos), amount of steel stirrups, specimen size, strengthening of pre-damaged specimens, fatigue and the effect of cold climate. Tests have been undertaken on large scale beams specimens subjected to four-point bending; the beams were generally 4.5 m long. Comprehensive monitoring of these beams to measure the utilization of the material, strain profiles within the shear span, strain in the steel rebars and deflections of the beam. In some cases speckle pattern analysis has been used, this is shown in Figure 2. The laboratory testing on shear strengthening has provided the means for the derivation of equations to describe the behaviour in both in the Ultimate Limit State (ULS) and in the Service Limit State (SLS). The derived theory covers both linear-elastic material and anisotropic behaviour. Research in shear strengthening is further integrated with other activities such as, full-scale testing, monitoring, mineral-based matrix and non-destructive testing.

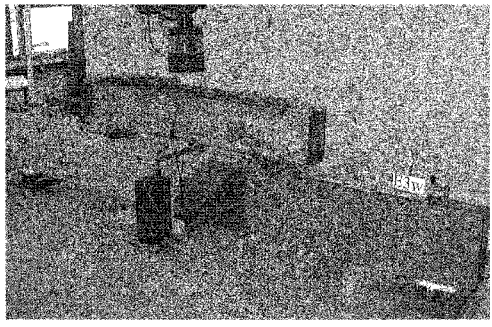


Figure 2 Typical test beam, here shown with non-touching measuring of strains in the right shear span

NSMR

Near Surface Mounted Reinforcement (NSMR) is a development for plate bonding with FRPs. The method implies that rods mainly of CFRP are bonded in sawn grooves in the concrete cover. The method was developed in Sweden during the 1940s[7], but at that time with steel bars instead of FRP. This method has now been developed into using quadratic rods of CFRP composites, which then are bonded either by epoxy polymer or a cementitious bonding agent.

The reason for using rods with quadratic cross-section is that the sawed groove will have parallel vertical sides and a uniform adhesive thickness around the rod is desirable, this may bee seen Figure 3. The research with NSMR covers traditional tests of flexural capacity but also tests with live loads acting during strengthening process and behaviour in cold climate[8,9].

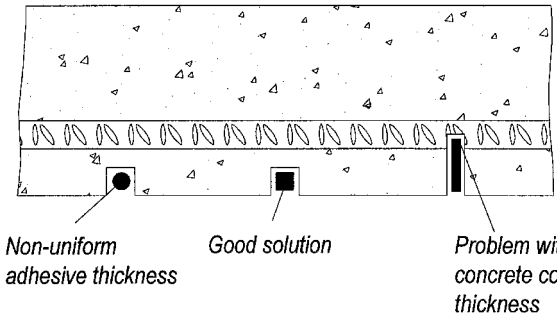


Figure 3 Plate bonding vs. different types of NSMR

Prestressed CFRP Composites

CFRP composites may be prestressed to achieve an effective utilization of materials. By prestressing the composite when a structure is strengthened the issue with dead loads during strengthening will decrease. In this area most research has been undertaken and is still performed on NSMR[10,11]. Tests have shown that very high stresses can be transferred into the concrete structure and in tests, so far, no mechanical anchor system has been used. Long-term applications utilizing this technique are currently being investigated and, in addition, a mechanical anchorage system for this purpose is under development.

Mineral based strengthening systems

If the epoxy adhesive could be replaced with a mineral based bonding agent a more environmental friendly strengthening system would be obtained. We have during the last two years investigated the possibility to replace the epoxy with mineral based bonding agents[8]. The results so far are very promising and the research is strengthened in this field.

Strengthening of openings

Strengthening of openings is a quite common application for CFRP strengthening, however, not much research has been presented in this field. We are now undertaking research on openings strengthen with composites[12]. Different types of composites are used, for example, laminates, fabrics and nets. The preliminary results show that CFRP composites can be used to maintain or even increase the original load-capacity of the tested two-way concrete slab specimens. The experiments showed that a simple design method used to calculate the cross-sectional area of CFRP laminates for strengthen a fabricated opening in an existing concrete slab gives a load-capacity higher than the as-built homogeneous slab. It was also found that the ductility of the strengthened or repaired slabs was considerably high if bond failure is to be avoided. This research has now moved into a second phase with the development of more advanced methods for design and a number of new parameters to be investigated.

Risk based design

The safety of structures is the most important issue for society. Several countries have their codes based on probabilistic models and are using partial coefficients both on loads and structural capacity. When new materials and methods are introduced it is not always clear whether the former partial coefficients can be used.

It is also believed that the partial coefficients should vary when evaluating an existing structure compared to those when designing a new one. Theoretical studies have shown that a structure strengthened by plate bonding offers good reliability but new failure modes and risk factors must be investigated and understood. A comprehensive study has begun where the new design methodology in Eurocode is one part of the base in the research.

Steel Structures

In the area of steel strengthening some research has also been carried out at Luleå University of Technology. This type of strengthening may be used to: repair damages, increase stiffness (both locally and globally) and to improve several other qualities. The method is of particular interest for the strengthening of wrought and cast iron; these materials are not suitable for the welding technique. In the area of strengthening of steel structures, research has been carried out in bending, flexure and buckling.

Tests and derived theory[3] also show that FRPs may be used as a reinforcement to improve buckling of steel pipes. When bonding fibres to a member critical in buckling the stiffness is changed. By placing fibres in the longitudinal direction of a pipe it is possible to increase the load before buckling occurs. Theories which establish how FRP may be used as strengthening to increase buckling loads have been derived. The theories have been compared to full-scale tests where steel pipes have been strengthened, with different fibre types (glass, carbon and aramid), fibre amount, fibre quality and strengthening lengths. The fibres are most efficient in the midsection of the member. This is illustrated by Figure 4 that shows how the buckling mode changes when pipes are strengthened.

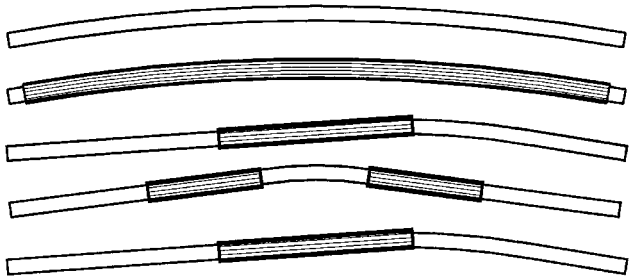


Figure 4 CFRP may be used as compressive reinforcement and increase buckling load for steel pipes

CODES AND STANDARDS

To be able to strengthen concrete structures in an optimum way and to use the FRP materials most effectively proper design guidelines are needed. Lack of guidelines will not only reduce the use of FRP for strengthening but may also risk the fact that the strengthening materials may be used incorrectly by the designer without understanding how the FRP material, and the structure work together. Accordingly, it is of utmost importance to develop and compile design guidelines and codes for FRP Plate Bonding.

Our philosophy about strengthening is that it shall only be carried out if absolutely necessary. If possible it is preferable to use administrative upgrading where refined calculation methods are used in connection with exact material properties and loading parameters to show that the existing structure has a higher load-carrying capacity than that which was earlier assumed. This may also be combined with advanced measurement methods. However, if it is found that a structure has to be strengthened a strict design methodology should be followed.

The first code covering plate bonding was implemented in the Swedish bridge code in 1989. This code covered steel plate bonding and was used for many years in connection with strengthening of concrete structures.

During, 1998 and 1999, an extensive piece of work involved writing a design guideline for FRP strengthening was carried out. The content of the guideline is mainly based on earlier research and development in FRP strengthening in Sweden, but also international experiences and knowledge has been included. The Swedish National Road Authorities accepted the design guideline for FRP strengthening of bridges in 1999. The first guideline was written in Swedish but due to large international interest the guideline was later extended and written in English[13]. The guideline concentrates on strengthening of existing concrete structures and covers strengthening for bending, shear, torsion and confinement. A short discussion is made about safety factors and also how the strengthening work should be carried out.

IMPLEMENTATION

The use of the results from research is essential and has been highly prioritised throughout all our work. Already in the planning phase this has been considered and a structured way to achieve this, is followed. This process can be described schematically, see Figure 5.

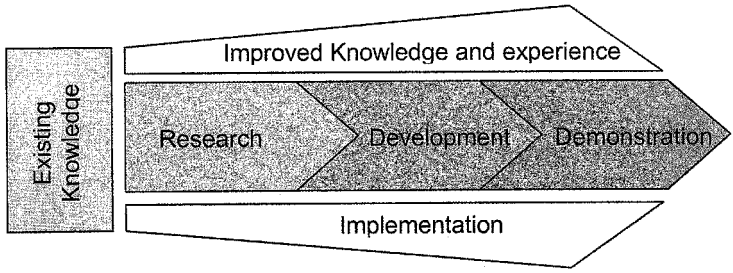


Figure 5 Structure of research

Research in civil engineering may be considered as applied science, this implies that demonstration and implementation are essential for success. In most of our projects we commence the investigation by studying the existing knowledge in the area and the research is then planned in more detail. Depending on the type of the project, the research, development and demonstration phases may contain other research groups, or specialists within or outside our own organization. Here we try to involve a large part international collaboration. Implementation is carried out throughout the whole project, with a larger extent of implementation at the end of the project. We also try to work closely with the client, for example the Swedish National Road Authorities, consultants or contractors, this has proven to be an successful way of working. In Figure 5 we have to divide between demonstration projects and implementation of the scheme. In the demonstration projects we have tried to "gear up" the research and development to existing large scale structures, such as for example, bridges. These projects contain a large amount of monitoring. In demonstration projects where CFRP strengthening has been applied, an objective is that full-scale loading and monitoring before and after strengthening should be carried out.

We have undertaken several demonstration projects, where one of the most interesting ones was strengthening and then loading of a railway bridge in Sweden. In this particular case theoretical studies and tests had been carried out at the university to investigate the most suitable FRP strengthening system for the bridge. A project group was formed and normal plans for the work were instigated. The installation of the monitoring equipment and a load test before strengthening was carried out. The next step was to strengthen the bridge. The bridge strengthening was in the cross-direction with two layers of carbon fibre fabric. More monitoring equipment was mounted onto the bridge and a test, after the bridge was strengthened, was performed. The bridge during loading is shown in Figure 6, which also shows the strain in a steel bar in the cross section before and after strengthening. A strengthening effect comparing to a stiffness increase of 17 % was obtained.

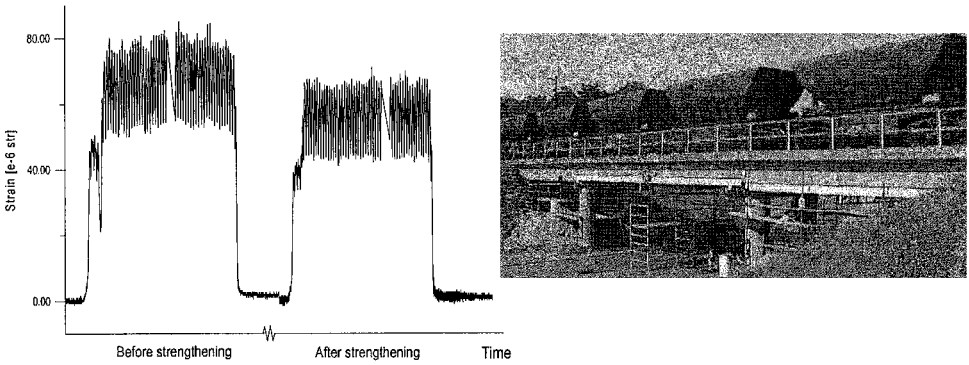


Figure 6 Railway bridge strengthened with carbon fibre fabrics.

FUTURE AIMS AND NEEDS

There are many areas that need to be further investigated regarding repair and strengthening of existing structures, we have planned during the next coming 10 years to work in the following areas; system thinking, standardisation, long-time behaviour, risk based design, environmental friendly strengthening systems, composites in construction in general, smart materials and structural health monitoring. In all fields we aim for a strong international collaboration where Luleå University of Technology is one of several important hubs in this research. We believe that more environmental friendly strengthening systems are essential for long time success in the area of repair and strengthening - here mineral based bonding agent could be an interesting path to follow. In addition, more research needs to be focused on systems, where for example one strengthened part would change the behaviour of the whole system. Furthermore, a more holistic view of the function of real structures must be built up, here SHM may be one research area to help to obtain this. Risk based and probabilistic design where real loads and material values are used could open up new ways of designing, in particular in regards to repair and strengthening of existing structures.

SUMMARY AND CONCLUSIONS

In this paper a short summary on past and ongoing research in the area of plate bonding has been presented together with our future plans for research and development. Our process for carry out research has also briefly been described. During the last decade, our focus has very much been towards advanced composites for strengthening of concrete structures. Fundamental theories as well as laboratory tests to verify this and full scale applications have been covered by our research. In addition design guidelines have been produced and an acceptance for FRP strengthening in Sweden has been obtained. Up to now, we consider our way of working and our research is successful. Now, we try to widen our views and are focusing harder on smart materials, structural health monitoring, risk-based design as well as more environmental friendly repair and strengthening methods.

ACKNOWLEDGEMENT

The research, development and implementation carried out in Sweden during the last decade have been funded by several organisations, here the Swedish National Road Administration, the Development fund of the Swedish Construction Industry and Skanska AB should be acknowledged. The work have not been possible without very committed people over on long period, not only PhD students and Master students have contributed to the work, but also laboratory personnel and persons from organisations outside the University - without mentions any specific person all should be acknowledged.

REFERENCES

1 Dussek I.J., 1974, Strengthening of bridge beams and similar structures by means of epoxy-resin bonded external reinforcement. Transport research record 785, Washington, USA, 1974, pp 21-24.
2 Täljsten B., 1994, Plate Bonding, Strengthening of Existing Concrete Structurers with Epoxy Bonded Plates of Steel or Fibre reinforced Plastics, Doctoral Thesis 1994:152D, Div. of Structural Engineering, Luleå University of Technology, ISSN 0348 – 8373, p 308.
3 Carolin, A (2003): "Carbon Fibre Reinforced Polymers for Strengthening of Structural Elements" Doctoral Thesis2003:18, ISBN 91-89580-04-4, Luleå University of Technology, Structural Engineering. 178 pp
4 Carolin, A and Täljsten, B. (2003): "Behaviour of Concrete Structures Strengthened in Shear with CFRP" FRPRCS-6, Singapore, July 2003
5 Täljsten, B. and Carolin, A (2003): "Strengthening Two Large Concrete Bridges in Sweden for Shear Using CFRP Laminates" Structural Faults and Repair, London, July 2003.
6 Täljsten B., 2002, Strengthening concrete beams for shear with CFRP sheets, Journal of Construction and Building Materials, Vol. 17, Issue 1, pp 15-26.
7 Asplund, S.O. (1949), "Strengthening Bridge Slabs with Grouted Reinforcement", Journal of the American Concrete Institute, Vol. 20, No. 6, January, pp. 397-406
8 Hejll, A, Carolin, A and Täljsten, B. (2003): "Strengthening with CFRP under Simulated Live Loads" FRPRCS-6, Singapore, July
9 Carolin, A., Nordin, H. and Täljsten B. (2001): "Concrete beams strengthened with near surface mounted reinforcement of CFRP" Proceedings of the International Conference on FRP Composites in Civil Engineering, Hong Kong, Volume II ISBN 0-08-043945-4, pp1059-1066
10 Nordin, H., Täljsten B. and Carolin, A. (2001): "Concrete beams strengthened with prestressed near surface mounted reinforcement, NSMR" Proceedings of the International Conference on FRP Composites in Civil Engineering, Hong Kong, Volume II ISBN 0-08-043945-4, pp1067-1076
11 Nordin Håkan. (2003), "Fibre Reinforced Polymers in Civil Engineering - Flexural Strengthening of Concrete Structures with Prestressed Near Surface Mounted CFRP Rods" Luleå, Luleå Univeristy of Technology, Division of Structural Engineering, Licentiate thesis 2003:25 ISBN 91-89580-08-7.
12 Enochsson O., Olofsson T. and Täljsten, B. (2003): Strengthening of holes in two-way concrete slabs using CFRP composites " Structural Faults and Repair, London, July 2003.
13 Täljsten, B. (2003): "FRP Strengthening of Existing Concrete Structures. Design Guidelines, Second edition" Division of Structural Engineering, Luleå University of Technology, Luleå 2003, 228 pp, ISBN 91-89580-03-6.

INDEX OF AUTHORS

Abbaker, A 437-444
Abbasi, A 445-456
Afifi, A 545-552
Aggelopoulos, E 284-291
Aiello, M A 213-221,457-464,501-508
Almajed, W B 187-194
Almenara, P C 319-326
Andreou, E 179-186
Ayers, S 101-113

Banerjee, J R 574-581
Bausano, J V 593-601
Bisby, L A 465-472
Bloodworth, J R 327-334
Broughton, J G 667-674
Brown, P 683-692

Cadei, J 235-244,693-700
Cao, S Y 117-125
Canning, L 667-674,683-692,747-754
Carolin, A 763-770
Case, S W 593-601
Ceroni, F 126-133
Chen, J-F 117-125,473-482
Chen, J 117-125
Chryssanthopoulos, M K 274-283,284-291
Ciupala, M A 195-202
Clark, J 258-265
Clarke, H 258-265
Clarke, J 651-658
Colombi, P 245-257
Conroy, A 335-342
Corvaglia, P 457-464
Cousins, T 738-746
Cuninghame, J R 483-492

Daly, A F 483-492
Darby, A 651-658
Davies, J M 3-17
De Lorenzis, L 308-315,493-500
Delpak, R 179-186,611-618
Denton, S R 134-143
Deng P J 266-273
Dharani, L D 501-508
Duke, J C 593-601
Dunscombe, G C 384-391

Erki, M A 428-433
Eslimy-Isfahany, H 574-581

Farmer, N 659-666,667-674
Frost, S 667-674

Galati, N 222-231,501-508
Garden, H N 343-352
Gheorghiu, C 585-592
Green, M F 465-472
Guan, H 18-29
Gűrtler, H 369-376

Hackman, I 353-360
Halliwell, S 335-342,719-726
Hann, L-H 203-212,633-640
Hao, Z 117-125
Heffernan, P J 428-433
Hogg, P J 445-456
Hollaway, L C 274-283,353-360,361-368,457-464,693-700
Hulatt, J 361-368
Hutchinson, A R 667-674

Ibell, T 144-151,651-658
Ikeda, K 412-419
Irannejad, H R 509-516

Jiang, J J 152-161
Jolly, C K 727-737

Karbhari, V M 18-29,30-42
Kasahara, H 602-610
Keller, T 369-376,641-648
Kessler, K 738-746
Khoei, A R 509-516
Kodur, V K R 465-472

Labossière, P 585-592
La Tegola, A 292-299,300-307,308-315,493-500
Lam, L 73-88,203-212
Lee, L 18-29
Lee, M M K 266-273
Lee, R J 667-674
Lees, J M 377-383,420-427
Lesko, J J 593-601,738-746

Liu, I 162-169
Loudon, N 675-682
Lu, X Z 152-161
Luke, S 667-674,683-692,701-708,747-754
Lutz, C 384-391

Maruyama, K 602-610
Matthys, S 126-133
McCartney, L N 517-524
Meier, U 43-44
Micelli, F 292-299,300-307
Mortazavi, A A 195-202
Mosallam, A 45-58
Mottram, J T 384-391,437-444
Moy, S S J 258-265,266-273,525-534
Mullin, B 170-178

Nanni, A 222-231,501-508
Nayak, A K 525-534
Nishimoto, T 412-419

Oehlers, D J 162-169
Ogin, S L 561-565,566-573
Owen, J S 701-708

Pan, W K 473-482
Panzeri, N 245-257
Pearson, S R 701-708
Pecce, M 126-133
Photoiu N 274-283
Pickett, A K 535-544
Pickering, S J 392-399
Pilakoutas, K 195-202
Poggi, C 245-257
Porter, A D 134-143
Post, N L 593-601
Proulx, J 585-592

Reed, G T 561-566,567-573
Reynolds, T 335-342
Richardson, M 755-762
Righiniotis, T D 284-291

Saadatmanesh, H 59-72,619-632
Scialpi, V 292-299,300-307
Sciolti, S M 213-221
Secondin, S 222-231
Sedlacek, G 400-411
Sekijima, K 412-419
Seracino, R 162-169
Shave, J D 134-143
Shimomura, T 602-610
Shenoi, R A 525-534
Shyu, C R 428-433
Sikorsky, C 18-29
Silva, P 144-151
Smith, I 667-674,711-718
Stratford, T 235-244,693-700
Szczerbicki, J R 327-334

Taerwe, L 126-133
Täljsten, B 683-692,763-770
Tan, C M 701-708
Tann, D B 179-186,611-618
Tanovic, R 428-433
Tao, Z 203-212
Taranu, N 195-202
Tavakkolizadeh, M 59-72,619-632
Taylor, S E 170-178
Teng, J G 73-88,152-161,203-212
Terrasi, G P 420-427
Thornburrow, P 319-326
Thorne, A M 361-368,561-566,567-573
Tirelli, T 641-648
Tjin, S C 561-566
Triantafillou, T 89-100
Trumpf, H 400-411
Tumialan, G J 222-231
Turvey, G J 545-552,553-560

Ussorio, M 561-566

Van Erp, G 101-113
Vollintine, B 501-508

Wang, H 561-566,567-574
Wang, Y C 3-17
Wong, P M H 3-17
Wight, R G 428-433

Xiao, R Y 187-194

Ye, L P 152-161
Yu, Q 633-640

Zhang, Y 553-560
Zhang, Z 633-640
Zhou, A 641-648